

NOV 24 1994

NAS 1.2: SP 2/3/v.2



Proceedings of the

International Symposium on

SPECTRAL SENSING RESEARCH

VOLUME II

10-15 July 1994

San Diego, California USA

COMPLETED

Q+

Proceedings of the
International Symposium on
SPECTRAL SENSING RESEARCH

VOLUME II

10-15 July 1994
San Diego, California USA

*Proceedings of the
International Symposium on Spectral Sensing Research '94
10-15 July 1994*

Sponsored by

U.S. Army Corps of Engineers (USACE)
Cold Regions Research and Engineering Laboratory (CRREL)
Topographic Engineering Center (TEC)
U.S. Army Night Vision and Electronic Sensor Directorate (NVESD)
U.S. Army Space and Strategic Defense Command (SSDC)
U.S. Army Research Laboratory (ARL)
U.S. Army Edgewood Research, Development and Engineering Center (ERDEC)
U.S. Army Research, Development and Standardization Group - United Kingdom (USARDSG-UK)
Air Force Office of Scientific Research (AFOSR)
U.S. Air Force Phillips Laboratory, Geophysics Directorate (PL/GD)
U.S. Air Force Systems Command (AFSC)
National Aeronautics and Space Administration (NASA)
Naval Research Laboratory (NRL)
National Oceanic and Atmospheric Administration (NOAA)
Wave Propagation Laboratory (WPL)
Nautical Charting Research and Development Laboratory (NCRDL)
Oak Ridge National Laboratory (ORNL)
Environmental Protection Agency (EPA)
Environmental Monitoring Systems Laboratory (EMSL)
U.S. Geological Survey (USGS)
NASA Stennis Space Center (SSC)

Under Contract No. DACA76-93-C-0028

PREFACE

These proceedings contain the papers presented at the International Symposium on Spectral Sensing Research '94 (ISSSR), held at the Doubletree Hotel at Horton Plaza, San Diego, California on 10–15 July 1994. Forty-eight papers are included in Volume I and forty-nine papers are included in Volume II of the proceedings. Thirteen papers are also included in the "proceedings only" portion of Volume II.

The ISSSR was sponsored by several U.S. government agencies and organized by the U.S. Army Corps of Engineers (USACE). Dr. Richard B. Gomez, Associate Director of Technology of the U.S. Army Topographic Engineering Center (TEC), was the ISSSR General Chair; Mr. John V.E. Hansen, Director of the Remote Sensing Laboratory at the U.S. Army Topographic Engineering Center, was the Steering Committee Chair; Dr. Jack N. Rinker, Senior Research Scientist at the U.S. Army Topographic Engineering Center, was the Technical Program Committee Chair; and Ms. Charlotte Lemen, U.S. Army Topographic Engineering Center, was the Organizing Committee Chair. The symposium theme was presented by Mr. Walter E. Boge, Director, U.S. Army Topographic Engineering Center. The keynote address was given by Professor John A. Richards, Head of the Department of Electrical Engineering and Deputy Rector at the University College, Australian Defence Force Academy, Australia. Science and Technology Corporation (STC) provided contractual support.

The theme of the ISSSR was "Dual-Use Technologies." The objective was to provide an international forum where people can meet to discuss scientific requirements, implementation issues, analysis problems, and scientific benefits of spectral sensing research, and to produce the symposium proceedings soon after the ISSSR meeting for the benefit of the scientific community. Members of the government, industry, and academia, as well as persons from allied nations, attended the symposium. Papers were presented in seven topical areas: (1) Data Collection; (2) Signal/Data Processing; (3) Spectral Analysis/Processing Systems and Tools; (4) Atmospheric Studies and Applications; (5) Oceanographic/Coastal Studies and Applications; (6) Terrestrial and Land Surface Studies and Applications; (7) Environmental Restoration and Disaster Evaluation.

On the day prior to the formal opening ceremonies of the symposium, attendees had the option of attending tutorials to enable them to update their technical knowledge and thus potentially increase their understanding of the technical presentations. Tutorials were given in the following topics: Introduction to Spectral Remote Sensing, *Lecturer*: Dr. Jack N. Rinker, U.S. Army Topographic Engineering Center; Spectral Measurements Demonstration, U.S. Army Topographic Engineering Center and University of Colorado; Imaging Spectrometer Data Analysis, *Lecturer*: Dr. Fred A. Kruse, University of Colorado; Spectral Sensors and Data Availability, *Lecturer*: Dr. Harlan L. McKim, U.S. Army Cold Regions Research and Engineering Laboratory.

Acknowledgment is made of the support and cooperation of the sponsoring organizations, steering committee members, technical program committee members, organizing committee members, session chairs, tutorial lecturers, and workshop chairs of the ISSSR; and of the technical contributions by both paper and poster presenters participating in the ISSSR. Special thanks are due to Professor John A. Richards, keynote speaker, Professor Emil Wolf, invited speaker, and Mr. Walter E. Boge, conference theme presenter.

Richard B. Gomez
Editor of the Proceedings

BLANK PAGE

CONTENTS

VOLUME I

Preface	iii
Message from Symposium General Chairman	v
Profile of Richard B. Gomez	xvii
Profile of Walter E. Boge	xviii
Profile of John V.E. Hansen	xix
Profile of Jack N. Rinker	xx
Profile of John Richards	xxi
General Information	xxii

TUTORIALS

Introduction to Spectral Remote Sensing	5
Jack N. Rinker, U.S. Army Topographic Engineering Center	
Imaging Spectrometer Data Analysis	44
Fred A. Kruse, University of Colorado	
Spectral Sensors and Data Availability	55
Harlan L. McKim, U.S. Army Corps of Engineers, Cold Regions Research and Engineering Laboratory	

OPENING SESSION

Conference Theme	59
Walter E. Boge, U.S. Army Topographic Engineering Center	
Keynote Address – Remote Sensing: An Australian Perspective on Opportunities and Challenges	62
John A. Richards, University College, The University of New South Wales, Australia	
Correlation-Induced Spectral Changes	71
Emil Wolf, University of Rochester	

SESSION I: DATA COLLECTION

Mapping and the Verification of Terrestrial Hyperspectral Information	77
John E. Estes, National Aeronautics and Space Administration/U.S. Geological Survey	
HYDICE: A Status Report	89
Lee J. Rickard, J. Fischer and M. Anderson, Naval Research Laboratory	
Operational Use of a Variable Interference Filter Pushbroom Scanning Multispectral Imager	93
James M. Anderson and X. Sun, University of Dundee, Scotland	
Development and Operation of a Real-Time Imaging Spectroradiometer	105
Mark Dombrowski, Surface Optics Corporation	
Spectral Significance of the MOMS-02 Sensor Flown Aboard STS-55/D2	116
Hermann Kaufmann and M. Berger, GeoResearch Center Potsdam, Germany; D. Meißner, German Aerospace AG, Germany	

Airborne Radioactivity Surveys for Routine and Emergency Applications	123
G.F. Schwarz, L. Rybach and E.E. Klingelé, Institut für Geophysik, ETH-Hoenggerberg, Switzerland	
Multispectral Background Measurements from an Airborne MWIR Sensor	133
Kevin D. Bishop, J.A. Granger and E.L. Jewett, Lockheed Palo Alto Research Labs	
A Hyperspectral Sensor and Investigation of Shallow Water Remote Sensing	149
Thomas B. McCord, Ronald G. Resmini, Michael Fené and Gregory C. Mooradian, SETS Technology, Inc.	
SMIFTS: A Flexible System for Collection of Hyperspectral Sensing Data in the 1–5 μm Region	160
Paul G. Lucey, Tim Williams, Keith A. Horton and John Hinrichs, University of Hawaii at Manoa	
High Resolution Multispectral Stereo Imager (HRMSI), A Step Toward the Future	168
George T. Elerding, Jerald R. Holt and Edgar E. Russell, Santa Barbara Research Center	
Wedge Imaging Spectrometer (WIS) Hyperspectral Data Collections Demonstrate Sensor Utility	180
Loren M. Woody and James C. Demro, Santa Barbara Research Center	
A State-of-the-Art Airborne Infrared/Ultraviolet Scanner for Oil Pollution Monitoring and Mapping	191
B.M. Sorensen, GER-Intradan, Denmark; S.-H. Chang, Geophysical and Environmental Research Corporation, USA; and T.E. Melhuish, Canadian Coast Guard, Canada	
Field Spectrometry: Techniques and Instrumentation	195
Brian Curtiss, Analytical Spectral Devices, Inc.; and Alexander F.H. Goetz, University of Colorado	
Comparative Study of Dielectric Constant Measurements of Soils Using Different Techniques	204
Ram M. Narayanan, Danny W. Rhoades, Paul D. Hoffmeyer, University of Nebraska; and John O. Curtis, U.S. Army Waterways Experiment Station	
A Field Portable Hyperspectral Imager: The Large Area Fast Spectrometer	216
Randall W. Zywicki, Keith A. More, Daedalus Enterprises, Inc.; J. Holloway and N. Witherspoon, Coastal Systems Station, Dahlgren Division	
TOPSAT: The Global Topography Mission	225
Thomas G. Farr, Howard A. Zebker, Jet Propulsion Laboratory; and David J. Harding, NASA Goddard Space Flight Center	

SESSION II: SIGNAL/DATA PROCESSING

Calibration and Atmospheric Compensation of Imaging Spectrometer Data for Vegetation, Geological and Water Applications and Research	229
Robert O. Green, Thomas G. Chrien, James E. Conel and Jeannette van den Bosch, Jet Propulsion Laboratory	
Mathematical Aspects in Modeling Material Reflectance Properties for Remote Sensing Applications	230
Michael D. Metzler, Environmental Research Institute of Michigan; James R. Baker, Virginia Polytechnic Institute and State University; and J.R. Maxwell, Environmental Research Institute of Michigan	

Scene/Object Classification Using Multispectral Data Fusion Algorithms	246
Thomas J. Kuzma, Laurence E. Lazofson, Howard C. Choe, E.B. Preston, and J.D. Chovan, Battelle	
An Assessment of the Effects of Data Compression on Multispectral Imagery	256
Ken Richl Jr. and Carey D. Erdman, Itck Optical Systems	
Automatic Identification of Spectral Endmembers in Hyperspectral Image Sequences	267
Joseph C. Harsanyi, Applied Signal and Image Technology Company; William H. Farrand, Science Applications International Corporation; Joseph M. Hejl, Applied Signal and Image Technology Company; and Chein-I Chang, University of Maryland	
Subpixel Detection Methods: Spectral Unmixing, Correlation Processing, and When They Are Appropriate	278
Alan Schaum, Naval Research Laboratory; and Alan Stocker, Space Computer Corporation	
Predicting Sub-Pixel Target Detectability	287
Michael J. Duggin, Research Associates of Syracuse, Inc. and State University of New York; R. Richter, DLR, German Aerospace Research Institute, Institute of Optoelectronics, Germany; W.N. Philpot, Cornell University; and J. Lamicela, Research Associates of Syracuse, Inc.	
Automating Linear Mixture Analysis of Imaging Spectrometry Data	302
Joseph W. Boardman, University of Colorado	
From a Natural to a Behavioral Classification	310
Jean Paul Rasson, F. Orban-Ferauge and V. Granville, Laboratory GEOSATEL, F.U.N.D.P. University, Belgium	
Application of the Natural and the Behavioral Approaches for Supervised Remote Sensing Classification	311
F. Orban-Ferauge, Jean Paul Rasson and V. Granville, Laboratory GEOSATEL, F.U.N.D.P. University, Belgium	
Assessment of the Linear Mixing Model for Subpixel Materials Detection in Thermal Infrared Multispectral Scanner (TIMS) Images	312
Ronald G. Resmini, Jessica M. Sunshine, SETS Technology, Inc.; Alan Schaum, Naval Research Laboratory; Thomas B. McCord, Jennifer L. Forsythe, SETS Technology, Inc.; and Alan R. Gillespie, University of Washington	
Linear Estimation of Hyperspectral Mixed Pixel Components	333
Edmundo Simental and Elisa C. Gonzalez, U.S. Army Topographic Engineering Center	
SESSION III: SPECTRAL ANALYSIS/PROCESSING SYSTEMS AND TOOLS	
Effects of Spectral and Spatial Resolutions on NDVI	365
P.M. Teillet, Karl Staenz, Canada Centre for Remote Sensing, Canada; and D.J. Williams, MacDonald Dettwiler and Associates Ltd., Canada	
Application of Dark Object Subtraction to Multispectral Data	375
James B. Campbell and Xiangdong Liu, Virginia Polytechnic Institute and State University	

Temporal Measurements of High Resolution Spectral Signatures of Plants and Relationships Indicating Water Status	387
Charles Bostater, Florida Institute of Technology; Carlton Hall, The Bionetics Corporation; D. Vieglais, John F. Kennedy Space Center; J. Rebbman, Florida Institute of Technology; and M. Provancha, The Bionetics Corporation	
Spectral Manipulation for the Detection of Man-Made and Small Objects in Multi-Spectral Images	403
Vittala K. Shettigara and Gordon M. Sumerling, Defence Science and Technology Organisation, Australia	
Optimal Routing Techniques for Feedforward Neural Networks and Parallel Distributed Processors	416
Perry J. LaPotin, U.S. Army Cold Regions Research and Engineering Laboratory/University of Vermont; and Harlan L. McKim, U.S. Army Cold Regions Research and Engineering Laboratory	
Application of AVIRIS Data to Estimate Dynamic Range Demands on HYDICE	430
William S. Aldrich, William H. Farrand, William W. Stoner, Science Applications International Corporation; and Robert W. Basedow, Hughes Danbury Optical Systems, Inc.	
Target Detection in Multispectral Images Using Relative Entropy Thresholding	456
Mark L.G. Althouse, U.S. Army Edgewood Research, Development and Engineering Center; Chen-I Chang, University of Maryland; and Joseph C. Harsanyi, Applied Signal and Image Technology	
Quantifying Multispectral Imagery Interpretability	468
Carey D. Erdman, Ken Riehl, Jr., Lawrence A. Maver, Itek Optical Systems; Jon Leachtenauer, Ellen Mohr, John M. Irvine, Julie Odenweller, Environmental Research Institute of Michigan; Rulon Simmons, Eastman Kodak Company; and D. Hothem, Booz-Allen and Hamilton	
Hyperspectral Image Processing	477
Samuel Barr, U.S. Army Topographic Engineering Center	
Real-Time Analysis of Spectral and Spatial Data From Hyperspectral Imaging Sensors	491
Wally T. Jansen, WTJ Software Services	
A Hyperspectral Image Processing System—Hips™	496
Nicholas J. Susner, Juliana T. Lo and Thomas B. McCord, SETS Technology, Inc.	
Spectral Characteristics (0.4 μm – 2.5 μm) and the Detection of Camouflage Materials	497
Timothy D. Evans and Ponder Henley, U.S. Army Topographic Engineering Center	
A Rationale for Pixel Colorations of Evaporite Mineral Deposits in Thermal Imagery of Death Valley, California	516
John W. Eastes, U.S. Army Topographic Engineering Center	
The Impact of System MTF on Sub-Pixel Target Detection, and on Spectral Demixing For Sub-Pixel Discrimination	518
Michael J. Duggin, State University of New York and Research Associates of Syracuse, Inc.	

VOLUME II

SESSION IV: ATMOSPHERIC STUDIES AND APPLICATIONS

Remote Sensing of Aerosols Using Passive Infrared Spectroscopy	539
David K. Lynch and Andrew B. Christensen, The Aerospace Corporation	
Optical Remote Sensing of the Dayside Ionosphere from Space Through Observations of the O ⁺ 834 Å Dayglow	549
Kenneth F. Dymond, J. Michael Picone, Robert R. Meier, Robert P. McCoy, Owen Kelley, Naval Research Laboratory; and Ronald J. Thomas, New Mexico Institute of Mining and Technology	
Hyperspectral Observations of the Earth's Atmosphere and Surface from the MSX Satellite in the Spectral Region 200–900 NM	562
Donald E. Anderson, G.J. Romick, D. Morrison, J.F. Carbary, L.J. Paxton, C.-I. Meng, J.-H. Yee and G. Crowley, The Johns Hopkins University Applied Physics Laboratory	
Coincident Surface and Aircraft Spectral Resolution Sensing of Atmospheric Parameters: A Joint American-Mexican-Russian Research Program	570
Oleg B. Vasilyev, St. Petersburg State University, Russia; now at: UNAM, Cd. Universitaria, Del. Coyoacan, Mexico; Ronald M. Welch, South Dakota School of Mines & Technology; Amando Leyva Contreras, Agustin Muhlia Velazquez, and Ricardo Peralta y Fabi, UNAM, Cd. Universitaria, Del. Coyoacan, Mexico	
Estimation of Cirrus Cloud and Aerosol Scattering in Hyperspectral Image Data	582
E. Ben-Dor, Alexander F.H. Goetz, and A.T. Shapiro, University of Colorado	
Estimation of Atmospheric Conditions and Surface Temperatures from Multispectral Data	594
James R. Johnson, E-System Garland Division	
Sensitivity Analyses to Identify Key Parameters for Use with a Radiative Transfer Model-Based Atmospheric Correction	595
Sally Westmoreland, San Diego State University; and Frederick C. Mertz, Photon Research Associates, Inc.	
The 1994 GEISA Program for Management and Study of Spectroscopic Information	604
Nicole Husson, B. Bonnet, A. Chedin, N.A. Scott, Laboratoire de Météorologie Dynamique, France; Alexey A. Chursin, Vl. G. Tyuterev and V.F. Golovko, Institute of Atmospheric Optics, Russia	
A New Doppler Imager for Thermospheric Dynamics	612
Randall W. Zywicki, D.S. Dilworth, Daedalus Enterprises, Inc.; B.C. Kennedy, University of Michigan; E.J. Weber, Phillips Laboratory, Geophysics Directorate; and Keith A. More, Daedalus Enterprises, Inc.	
SSM/T-2 Brightness Temperature Signatures	628
Vincent J. Falcone, Michael K. Griffin, Phillips Laboratory, Geophysics Directorate; John D. Pickle, Ronald G. Isaacs, Atmospheric and Environmental Research, Inc.; and James Wang, NASA Goddard Space Flight Center	
Precipitable Water Estimated from SSM/I	635
Charles Norris, John Roads, Shyh Chen, Scripps Institution of Oceanography; and Paul Weber, Los Alamos National Laboratory	

Sensitivity of SSM/T-2 Channels to Water Vapor	636
Michael K. Griffin, Vincent J. Falcone, Phillips Laboratory, Geophysics Directorate; John D. Pickle, Ronald G. Isaacs, Atmospheric and Environmental Research, Inc.; and James Wang, NASA Goddard Space Flight Center	
Satellite Observed Cloud Patterns Associated With Precipitation	641
Graciela Alicia Catuogno and Inés Velasco, Universidad de Buenos Aires, Argentina	
The Software Package for Managing Large-Scale Spectroscopic Data Bases and Spectral Sensing Applications: GEISA Based Version	649
Alexey A. Chursin, V.F. Golovko, V. G. Tyuterev, Institute of Atmospheric Optics, Russia; Nicole Husson, B. Bonnet, A. Chedin, and N.A. Scott, Laboratoire de Météorologie Dynamique, France	
Water Vapor Dependent Thermodynamics of the Lower Atmosphere	658
Fred Walter, Scientific Components Company	
SESSION V: OCEANOGRAPHIC/COASTAL STUDIES AND APPLICATIONS	
Processing and Analysis of AVIRIS Imagery of the Coastal Ocean	661
Curtiss O. Davis, Naval Research Laboratory	
Simulating Radiative Transfer in Aquatic Systems and Contrasting Results from Ambient Environmental Spectroscopy: Estuarine and Near Coastal Waters	673
Charles Bostater, Wei-Ming Ma and Andrew Lamb, Florida Institute of Technology	
Spectral Reflectance Properties of Wetlands Plants	683
John E. Anderson, U.S. Army Topographic Engineering Center	
Airborne Visible Imaging Spectrometry Applied to Limnology: Chlorophyll Variation in Mono Lake	691
John M. Melack and Mary Gastil, University of California	
Laser-Induced Signatures in Oceanographic Spectral Sensing: Dynamics, Pollution and Baseline Studies	696
Alexander E. Dudelzak, Canadian Space Agency, Canada; Sergei M. Babichenko and Larisa V. Poryvkina, Institute of Ecology, Estonian Academy of Sciences, Estonia	
An Analytical Model for Remote Sensing of Chlorophyll a in Inland Waters	697
H.J. Hoogenboom, A.G. Dekker, Vrije Universiteit, The Netherlands; and G.A. Farrington, Integrated Terrestrial Systems, Canada	
A Synergistic Approach to Monitoring Coastal Environments by Using a Suite of Remotely Sensed Imagery and Gound-Based Measurements	705
Elijah W. Ramsey III, Richard H. Day and Kevin McRae, National Wetlands Research Center, National Biological Survey	
The Littoral Remote Sensing Modeling and Simulation System (LRS-MASS)	706
Lee J. Rickard, G. Keramidas and J. Spencer, Naval Research Laboratory	
Use of Principal Components to Characterize Upwelling off the Coast of California	707
Eugene Molinelli and G. Muncill, Planning Systems, Inc.	

SESSION VI: TERRESTRIAL AND LAND SURFACE STUDIES AND APPLICATIONS

Monitoring Vegetation Health Status With Steady-State Chlorophyll Fluorescence	737
Arnold F. Theisen and Barrett N. Rock, University of New Hampshire	
Remote Sensing Hypermedia Terrain Database	749
Brian D. Leighty, Knowledge Sciences, Inc.; Robert D. Leighty, Leighty and Associates, Inc.; George E. Lukes, Jack N. Rinker and Phyllis A. Corl, U.S. Army Topographic Engineering Center	
The Application of Almaz Radar Imagery to Petroleum Exploration	761
Richard F. Pascucci, Autometric, Incorporated	
Multispectral Measurements of Active Lava Flows in the MWIR (2.0–5.0 μm)	775
Kevin D. Bishop, J.A. Granger and E.L. Jewett, Lockheed Palo Alto Research Labs	
Rock-Soil Background Effects on Narrow Band Vegetation Indices	785
Christopher D. Elvidge, Zhikang Chen, Desert Research Institute, University of Nevada System; and Walrave T. Jansen, WTJ Software Services	
Derivation of Inputs to a Biogenic Emission Model from Spectral and Ancillary Data	805
Siamak Khorram, John A. Brockhaus, Jayantha Ediriwickrema and Heather Cheshire, North Carolina State University	
RASTER-J: A Multisensor Testbed for Environmental Research	813
Lee J. Rickard, G. Hoskins, Naval Research Laboratory; and A. Skroch, Falcon Research, Inc.	
Diachronic Study of Crop Spectral Response in Central Greece	821
Leonidas G. Toullos, National Agricultural Research Foundation, Greece; and N. Silleos, Aristotle University of Thessaloniki, Greece	
Spectral Change Detection in Coniferous Forest Using Landsat TM and Elevation Models	836
Per Syrén, Stockholm University, Sweden	
Using Imaging Spectrometry for Modeling Soil Erosion	842
Steven M. de Jong, Utrecht University, The Netherlands	
Using Multitemporal, Multispectral Remote Sensing Data to Monitor Land Degradation	848
Terrill W. Ray, California Institute of Technology; Thomas G. Farr, Eric M. De Jong, Ronald G. Blom and Robert E. Crippen, Jet Propulsion Laboratory	
Applications of Remote Sensing for Tectonic Purposes in El-Rouge Depression, Northwest of the Syrian Arab Republic	859
Moutaz Dalati, General Organization for Remote Sensing, Syria	

SESSION VII: ENVIRONMENTAL RESTORATION AND DISASTER EVALUATION

Multispectral Remote Techniques of Studying the Consequences of Chernobyl Catastrophe and Technogenic Activity in Belarus	869
Alexander Kovalyov, Belarusian Republican Scientific and Technical Centre of Environment Remote Sensing, Republic of Belarus	
Environmental Applications of Remote Sensing in the Greek Islands	870
John N. Hatzopoulos, University of the Aegean, Greece	

Mapping a Biochemical Stress Gradient Across a Coniferous Forest with Airborne Visible/Infrared Imaging Spectrometer (AVIRIS) Data	878
C. Banninger, Institute for Image Processing and Computer Graphics, Joanneum Research, Austria; L. Johnson and D. Peterson, NASA Ames Research Center	
Texture Analysis of Remotely Sensed Data for Waste Site Characterization	880
John M. Irvine and Garth Barbour, Environmental Research Institute of Michigan	
An Infrared Hyper-Imaging Spectrometer for Atmospheric Studies and Environmental Remediation	893
Mark Massie and Michele Hinnrichs, Pacific Advanced Technology	
An Examination of Mine Waste Contamination in the Coeur D'Alene River Valley, Idaho, Using Imaging Spectrometer Data	908
William H. Farrand, Science Applications International Corporation; and Joseph C. Harsanyi, Applied Signal and Image Technology Company	
Dual Use in GosNIIAS Airborne Laboratories—Capabilities of Multizonal Remote Sensing	919
Edward Falkov, I.M. Formanuk, and V.A. Kosinov, State Research Institute of Aviation Systems (GosNIIAS), Russia	
Monitoring of Surficial Deposits in the Gulf War Zone Using Satellite Data	929
Kamel M. Sheikho, Saudi Centre for Remote Sensing, Saudi Arabia	
Rapid <i>In-Situ</i> Assessment of Organic Contaminants in Aquatic Sediments with the REMOTS® UV Imaging Spectrometer	936
Donald C. Rhoads, Jo Ann Muramoto, Chris Coyle, Roger H. Ward, and Richard Anderson, Science Applications International Corporation	
Using Spectral Data and Stressed Vegetation to Evaluate Hazardous Waste Sites	945
M.B. Satterwhite and John E. Anderson, U.S. Army Topographic Engineering Center	
Role of Saudi Civil Defence in Monitoring and Protecting Environmental Pollution	946
F. Al-Khodairy, King Faisal Specialist Hospital and Research Centre, Saudi Arabia; Majdi H. Al-Tukhi, Center for Studies and Research, Saudi Arabia; M.A. Hannan and A. Al-Dakan, King Faisal Specialist Hospital and Research Center, Saudi Arabia	
Analysis of the 1993 Flood Using Digital Remotely Sensed Data	954
Donn Rodekohr, ERDAS, Inc.	

APPENDIX A: PROCEEDINGS ONLY

CCD Sensors Applicable in Tracking and Imaging Spectrometers: Study and Correction of Their Spectral Characteristics	A-3
Valentin Atanassov, Alexandar Krumov and Valentina Boyceva, Bulgarian Academy of Sciences, Bulgaria	
Study on the Intertransputer Connections for an Image Processing	A-10
Doyno Petkov, T. Zdravev and H. Nikolov, Bulgarian Academy of Sciences, Bulgaria	
A New Technique for Solving Classification Problems in Remote Sensing	A-16
Doyno Petkov, T. Zdravev and H. Nikolov, Bulgarian Academy of Sciences, Bulgaria	

Satellite Images Data Compression Using Multiresolution Analysis Based on Optimal Edge Detection	A-20
A. Serir and B. Sansal, Institut d'Electronique, Algeria	
Spatial Resolution of Multispectral Survey Systems for Different Atmospheric Conditions	A-31
V.V. Gogohia, Russian Academy of Sciences, Russia	
Second Generation Database of the Ionosphere Disturbance Indices	A-38
Tamara L. Gulyaeva, Russian Academy of Sciences, Russia	
Precipitation Amount Long-Term Variability Over Romanian's Territory	A-50
Maria Colette Iliescu, National Institute of Meteorology and Hydrology, Romania	
A Method for Direct Retrieving the Planetary-Scale Wave Parameters from Satellite Measurements of Thermal Outgoing Radiation	A-59
Igor A. Podgorny and Gusiav M. Shved, St. Petersburg University, Russia	
Bathymetric Image Maps of Coastal Water Areas	A-70
Lee Estep, J. Lillycrop, U.S. Army Corps of Engineers, Waterways Experiment Station; R. Arnone, Naval Research Laboratory; and L. Parson, U.S. Army Corps of Engineers, Waterways Experiment Station	
Optimization of Water Quality Monitoring in Izmit Bay Using Landsat Spectral Radiance Differentials and SPOT Imageries	A-79
Hikmet Kurar and Krishnaier Natarajan, Turkish Council of Scientific and Industrial Research, Turkey	
Applications of Multispectral MM-Wave Technique for Diagnostics of the Deep Oceanic Processes and Critical Situations in the Atmosphere	A-89
Igor V. Cherny and G.M. Chernyavskiy, Russian Academy of Sciences, Russia	
A Review of Problems of Land Use and Cover Delineation Using SPOT and LANDSAT-TM Data of Sao Jose Dos Campos, Brazil	A-100
Sosthenes Kwadzo Kufogbe, University of Ghana, Ghana	
Detection of Rill Erosion with Digitized KFA-1000 Satellite Photographs	A-112
Fred Ernst, University of Çukurova, Turkey	
Temporal Environmental Changes in the Vicinity of Atatürk Dam Using Remote Sensing Techniques	A-118
Erhan Alparslan, M.T. Aygün and B. Bilge, TÜBİTAK, Marmara Research Centre, Turkey	

APPENDIX B

Author Index	B-3
--------------------	-----

APPENDIX C

List of Attendees	C-3
-------------------------	-----

BLANK PAGE

VOLUME II

SESSION IV - SESSION VII

PROCEEDINGS ONLY

APPENDICES A - C

000001

1

SESSION IV
ATMOSPHERIC STUDIES AND APPLICATIONS

000002

REMOTE SENSING OF AEROSOLS USING PASSIVE INFRARED SPECTROSCOPY¹

D. K. Lynch and A. B. Christensen
Space and Environment Technology Center
The Aerospace Corporation M2/254
P.O. Box 92957
Los Angeles, CA 90009 USA

ABSTRACT

Aerosols are common atmospheric constituents that occur both naturally (clouds, sea spray, dust, smoke, and volcanic emissions) and artificially (smog, smoke, certain hazes, detonation products, and industrial emissions). Some, like the great dust bowl storms in the U.S. in the 1930s, are a combination of natural and man-made agents. Most aerosols are difficult to model because they are composed of small, nonspherical particles whose optical constants and particle sizes are poorly known. Spectroscopic observations of aerosols in the thermal infrared atmospheric window between 8 and 13.5 μm offer the opportunity to detect aerosols both day and night down to very low column densities. Such observations can also identify the gross chemical composition of the particles and, in some cases, the actual sizes and shapes. In this paper, we discuss thermal IR observations of three types of aerosols: satellite measurements of volcanic dust, ground-based observations of airborne desert soil and both ground- and space-based measurements of cirrus clouds.

1. INTRODUCTION

An aerosol is any grossly homogeneous aggregate of finely divided liquid or solid particles suspended in a gas. By suspended, of course, we mean having very small settling velocities. An ordinary water drop cloud is a familiar aerosol. Other naturally occurring inorganic aerosols include cirrus clouds, dust clouds, sea spray, volcanic ash, and meteoritic dust in the atmosphere. Smog, rocket plumes, some smokes, and certain chemical and biological warfare clouds are manmade aerosols. Pollen clouds and some blue hazes like those of the Smoky and Blue Ridge Mountains in the eastern U.S. are biogenic in origin. We will refer to all aerosols generically as "clouds."

Aerosol particles are generally much less than 100 μm in diameter, and their separation is very large compared to their diameters. For example, a typical stratus cloud may consist of particles about 12 μm across and separated by roughly 1.5 mm (concentration $\approx 300 \text{ cm}^{-3} \mu\text{m}^{-1}$). The large separation/diameter ratios shown by most aerosols allow the particles to be treated as independent, incoherent, isotropic radiators for simulation and modeling purposes. Passive IR remote detection is not sensitive to concentration ($\text{cm}^{-3} \mu\text{m}^{-1}$), but rather to column density or optical depth τ ,

$$\tau = N \pi a^2 Q_{\text{EXT}} L,$$

where N is the number density of particles, a the mean particle radius, Q_{EXT} the extinction efficiency, and L the line-of-sight distance through the cloud. In general, optically thick clouds are easy to detect but offer the least amount of information about the cloud's microphysical properties.

¹This work supported by the Aerospace sponsored research program.

Four questions must be answered in order to specify the radiative properties of a cloud and to develop models:

- | | |
|-------------------------------------|--|
| 1. What is the cloud's composition? | chemical composition, crystallinity, optical constants |
| 2. How big is it? | cloud size, shape, height, temperature, optical depth |
| 3. How large are the particles? | particle size distributions |
| 4. What shape are the particles? | shape, orientation, filling factor |

In this paper, we will be concerned with using passive, moderate resolution ($0.05\text{--}1\text{ }\mu\text{m}$), thermal infrared spectroscopy to answer these four questions about clouds. High spectral resolution is not needed because of the dearth of narrow spectral features in solids and liquids. Techniques that depend on scattering, such as visible and near-infrared spectroscopy, or active illumination, such as lidars and radars, will not be discussed. We will review the important aspects of thermal IR spectroscopy by examining three types of aerosol particles that have recently yielded to advances in the field: chemical composition identification in dust clouds, particle size determination in volcanic clouds, and particle size and shape estimation in cirrus clouds. In each case, the influence of microphysical properties will be linked to measurable, systematic structure in the IR spectra, with particular emphasis on the $8\text{--}13.5\text{ }\mu\text{m}$ atmospheric window.

Passive spectroscopy in the $8\text{--}13.5\text{ }\mu\text{m}$ window can be used both day and night and requires relatively little power and optical equipment compared to lidars. Infrared-array detectors for this wavelength region are also becoming readily available, thereby allowing wider and simultaneous wavelength coverage as well as higher signal-to-noise ratios per detector.

2. DUST IN THE ATMOSPHERE

In this section, we show how composition and approximate particle shape can be determined from IR spectroscopy. A recent explosives test in the desert of New Mexico placed a large quantity of desert soil into the atmosphere and provided a good opportunity to carry out a controlled set of spectroscopic measurements (Lynch et al. 1994). The composition of this soil was typical of the world's dirt: 80% quartz and other complex silicates (Si_xO_y), 10% calcite (CaCO_3), and the rest iron oxide (Fe_xO_y) and other minor constituents (percentages by weight).

Figure 1 shows a spectrum of the dust cloud, along with a spectrum of a naturally occurring water ice cloud and one of the clear sky. All three were taken at the same elevation angle, and the water and dust cloud were at approximately the same altitude. Figure 2a shows the difference between the water and dust cloud spectra, i.e., $\text{FLUX}_{\text{difference}} = \text{FLUX}_{\text{dust}} - \text{FLUX}_{\text{water}}$. The subtraction gives a good first-order estimate of the dust cloud's excess emission over a water cloud's by removing the emission from atmospheric water vapor. Between about 8 and $11\text{ }\mu\text{m}$, there are two significant differences between the dust and water-drop cloud spectra: (1) the broad feature straddling the stratospheric ozone band and (2) a weaker feature at $11.4\text{ }\mu\text{m}$. This enhanced emission centered on the ozone band is caused by high opacity in the silicate molecule Si_xO_y due to the fundamental asymmetric vibrational mode of the O-Si-O structure. Although variable in shape, depending on the exact silicate compound and crystalline state, the feature extends between about 8 and $11\text{ }\mu\text{m}$ and is well known in laboratory spectra (Ferraro 1982; Salisbury et al. 1991) and in many astronomical sources (Hanner et al. 1994). The small but still prominent emission feature at $11.4\text{ }\mu\text{m}$ is due to the carbonate molecule's C-O bending mode in calcite, CaCO_3 . Figure 2b shows a laboratory spectrum of the dust. This spectrum verifies the chemical identifications made in the field because the same structures that appear in Figure 2a are present in Figure 2b, except in absorption.

The relatively simple operation shown above represents a powerful remote sensing tool because it allows so much information about the cloud to be deduced. First, the dust particles have been identified as being primarily silicates and carbonates. Second, the radius a of the silicate particles must be smaller than

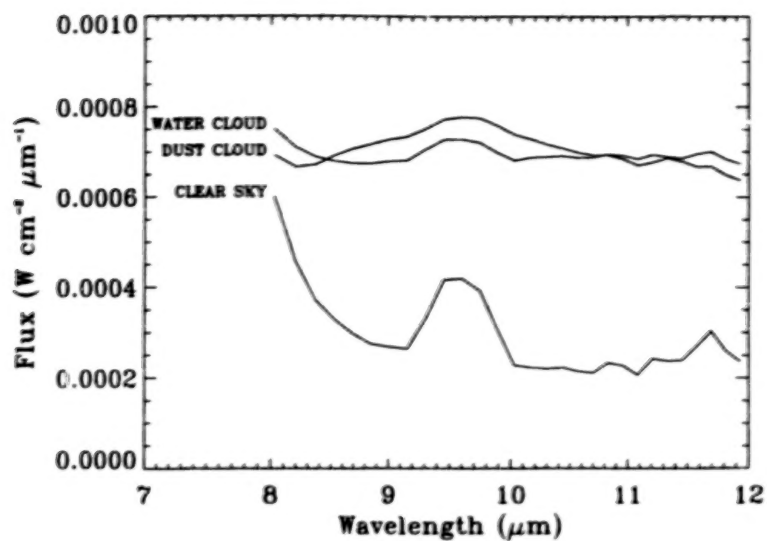


Figure 1. IR spectra of the clear sky (lower), water cloud (middle) and dust cloud (upper) from the explosives test in New Mexico.

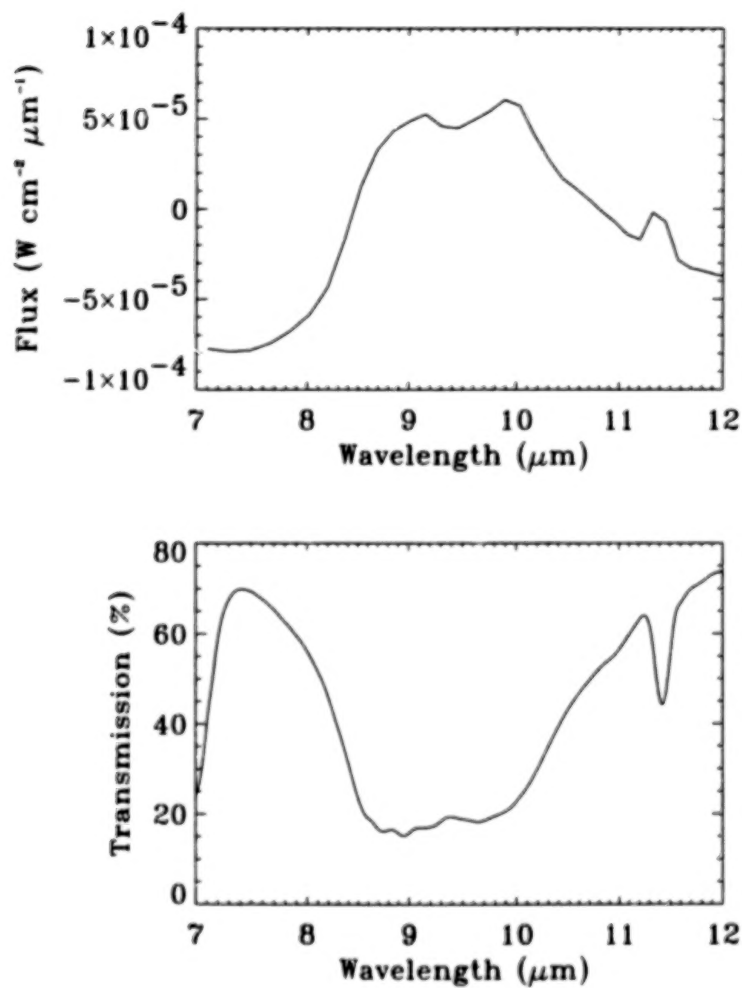


Figure 2. Spectral identification of dust. (Upper) Flux difference between dust cloud and water cloud in Figure 1; (lower) laboratory transmission spectrum of dust collected from the New Mexico Test.

about $a < 5 \mu\text{m}$. Larger particles would be optically thick and would radiate in a more Planckian manner. Third, the cloud has an optical depth of unity or less at wavelengths on either side of the resonance (8 and $12 \mu\text{m}$). Were it otherwise, no spectral features would be present, and the spectrum would simply appear as a smooth black-body function (Figure 3). The optical depth, τ , of the cloud was near 0.7. This was estimated by noting that the brightness was about half way between the clear sky value and the value of the Planck function at the ambient surface temperature ($\tau = -\ln(1/2) \approx 0.70$). From optical photographs, we estimate that the cloud thickness, L , was about 500 m. Since $\tau = N \pi a^2 Q_{\text{abs}} L$, where Q_{abs} is the absorption (= emission) efficiency around unity, we find the particle number density $N = 16 \text{ cm}^{-3}$. The column density, σ , can be determined because $\sigma = NLm$, where m is the mass of a single particle. With mass density $\rho = 2.5 \text{ gm cm}^{-3}$, we find $\sigma = 10^{-3} \text{ gm cm}^{-2}$. Thus, we have learned the cloud's approximate optical depth, principal chemical components, particle size, particle number density, and column density. In this instance, however, nothing as yet has been determined about particle shape.

With a knowledge of the optical constants of the levitated dust, an estimate can be made of the sensitivity of passive IR spectroscopy to the detection of aerosols. Providing that the atmospheric opacity between the observer and the aerosol cloud is small, Lynch (1994) has shown that the minimum detectable column density, σ_{min} , is between 6×10^{-7} and $6 \times 10^{-8} \text{ gm cm}^{-2}$. These estimates assume a signal-to-noise ratio between 100 and 1000, values that are characteristic of modern instruments like those described by Hackwell et al. (1990) and used in the present study.

The technique has a number of limitations. It will not be especially sensitive to dust that has no spectral features in the infrared. To estimate the particle number density, some estimate of the cloud's physical thickness must be made. For detecting very small amounts of dust, a spectrum of the "clear" sky must be available because the excess brightness due to the dust cloud is small compared to the background spectral structure. The technique may not, in its present incarnation, work on an optically thick dust cloud, although some information can be extracted from spectra of such clouds.

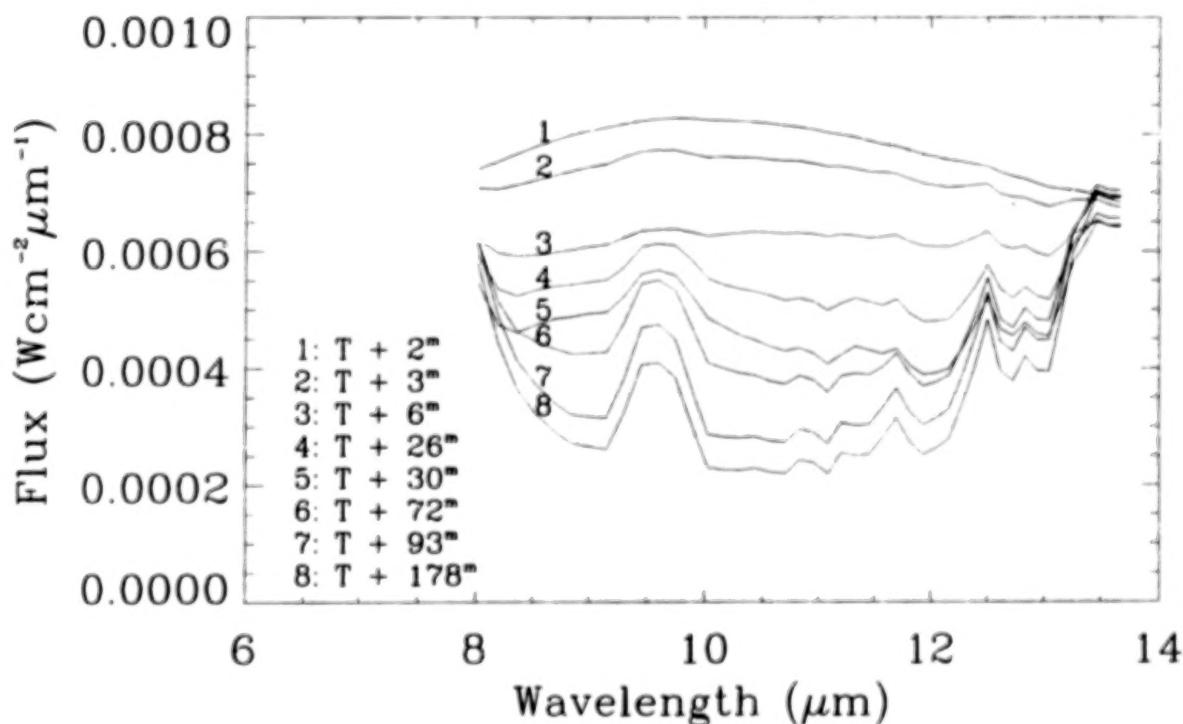


Figure 3. Time series of spectra of the dust cloud as it grew thinner with time. Note the transition from an optically-thick, Planck-like emission spectrum to an optically thin clear sky spectrum.

Infrared spectroscopy described above is ideal for demonstrating the physical processes and observational techniques by which clouds can be plumbed. In an operational setting where the vast amount of data taken automatically must be processed and interpreted, spectroscopy must give way to lower (spectral) resolution imaging spectrometers. We turn now to IR satellite remote sensing using, as an example, NOAA's Advanced Very High Resolution Radiometer (AVHRR).

3. VOLCANIC DUST

Volcanic dust clouds influence commercial aviation, climate, and global change and global transport processes. Being able to identify them, distinguish them from natural clouds, and follow their evolution is a major goal in remote sensing. Recent eruptions of Mt. Pinatubo in the Philippine Islands (1991) and Mt. Spurr/Redoubt in Alaska (1992) have provided timely events for IR study. Distinguishing volcanic clouds from natural water clouds by studying the colors in the thermal IR is possible because of the large difference in the optical constants between volcanic dust (primarily silicates) and water/ice. In this section, we will perform an analysis similar to the one above for desert soil, but rather than spectra, our tools will be the brightness temperatures of the cloud measured in various broadband thermal IR filters.

The Advanced Very High Resolution Radiometer (AVHRR) is an instrument aboard NOAA's TIROS satellites in low earth orbit. It measures absolute flux (radiance) from the earth in several channels in the 8–14 μm window. Two of these channels, bands 4 (10.3–11.3 μm) and 5 (11.5–12.5 μm), are particularly useful in cloud studies. The brightness temperatures in the two bands have been used by Prata (1989) and Holasek and Rose (1991) to distinguish volcanic clouds from natural water/ice clouds. The observational criterion is that when $T_4 - T_5 < 0$, the cloud is volcanic while the opposite is true for water and ice clouds.

By plotting temperature difference $T_4 - T_5$ vs T_4 on a theoretically derived template, the so-called temperature difference method TDM (Figure 4), Wen and Rose (1994) have shown that particle sizes can be determined, providing that the particles are not too large (optically thick), the cloud is not optically thick, and that the cloud exceeds some minimum optical depth. It is important to realize that Wen and Rose's TDM, like most others, relies on model calculations that assume solid spherical particles, and, thus, its results may contain systematic uncertainties.

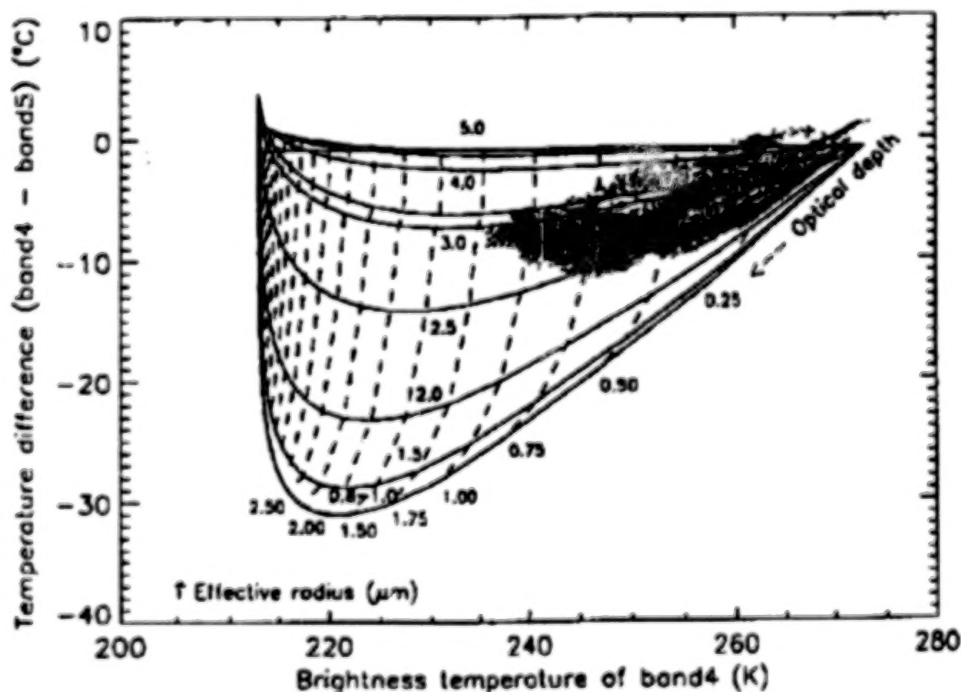


Figure 4. Temperature Difference Method (TDM) applied to AVHRR data of the Mt. Spurr volcanic ash cloud (from Wen and Rose 1994)

With the techniques by which particle composition and size may be determined, we will now look at deducing the most difficult microphysical property of all: particle shape. This will lead into the complex world of nonspherical particles.

4. CIRRUS CLOUDS

Cirrus clouds are high, cold clouds composed of nonspherical ice particles (See Dowling and Radke [1990] for a review). Cirrus is very wide spread (Henderson-Sellers et al., 1987; Prabhakar et al., 1988; Menzel and Wylie, 1989; Wylie and Menzel, 1993) and, in some cases, is present but almost undetectable (Lynch, 1993; Schmidt et al., 1993; Cornette and Shanks, 1993). In some parts of the tropics, cirrus may be nearly ubiquitous, occurring as a thin layer near the tropopause. Along with marine stratus, cirrus is thought to control the earth's radiation budget and, therefore, its mean surface temperature. A crucial issue in climate change is whether heating (or cooling) results in positive or negative feedback. Positive feedback of heating, for example, leads to run-away greenhouse effects. According to Stephens et al. (1990), whether the presence of cirrus results in a positive or negative feedback to the surface temperature depends on crystal size. Crystals larger than about $24\text{ }\mu\text{m}$ result in positive feedback, while those smaller than this lead to negative feedback. With the recent and somewhat unexpected result that cirrus contains a large number of particles smaller than $10\text{ }\mu\text{m}$ (Platt et al., 1989), the continued study of cirrus clouds will be crucial in understanding and modeling radiative feedback.

Because the chemical composition of cirrus clouds is known, the goal of IR spectroscopy is to assess the clouds' microphysical properties, i.e., particle sizes and shapes. To do this, quantities such as extinction, scattering, and absorption efficiencies (Q_{EXT} , Q_{ABS} , Q_{SCAT}), single scattering albedo ω , and asymmetry parameter, g , must be determined. Size and shape, however, are not uniquely determined by Q_{EXT} , Q_{ABS} , Q_{SCAT} , ω , and g . The system is degenerate in the sense that many crystal types can lead to nearly identical scattering properties. Thus, some additional information such as temperature and humidity inside the cloud may be used to narrow the range of possibilities.

For large particles (size parameter $2\pi a/\lambda > 30$), size and shape (and sometimes orientation) are vital for determining radiative properties. For smaller particles, size is more important than shape, providing that the particles are nearly spherical and not, for example, thin plates or long columns (Dungey and Bohren, 1992; Takano, Liou, and Minnis, 1992).

Determining cirrus particle sizes from passive IR spectroscopy alone requires comparing the observations against model calculations. Palmer et al. (1993) have shown that particle size (for assumed spherical ice particles) is correlated with slope of the continuum between 10 and $12\text{ }\mu\text{m}$ (Figure 5). This is possible because the extinction coefficients at these two wavelengths vary nonlinearly with the size of the particle. Such techniques are promising but rely on the ability of the observer to accurately take account of other sources of continuum slope, such as cloud temperature, optical depth, and water-vapor continuum.

Ackerman and Smith (1990) present a method of distinguishing ice spheres from ice cylinders by scatter plotting data from an IR spectrometer onto theoretically derived plots of $11\text{--}12\text{ }\mu\text{m}$ temperature difference vs $8\text{--}11\text{ }\mu\text{m}$ temperature differences. A similar technique has been used by Takano, Liou, and Minnis (1992) to distinguish between hexagonal/spheroidal and spherical crystals in the $10\text{ }\mu\text{m}$ window (Figure 6). The basis for their shape determination is the fact that at $8.35\text{ }\mu\text{m}$ equivalent-area spheres have smaller single-scattering albedos, and, as a result, absorb (emit) more radiation than they do at $11.16\text{ }\mu\text{m}$ (Liou and Takano, 1994).

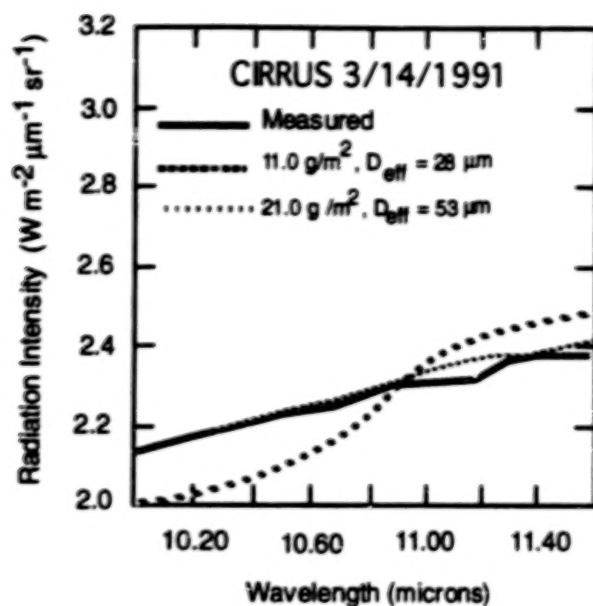


Figure 5. Measured cirrus cloud emission compared to theoretical predictions of mean particle diameter D_{eff} (after Palmer et al 1993)

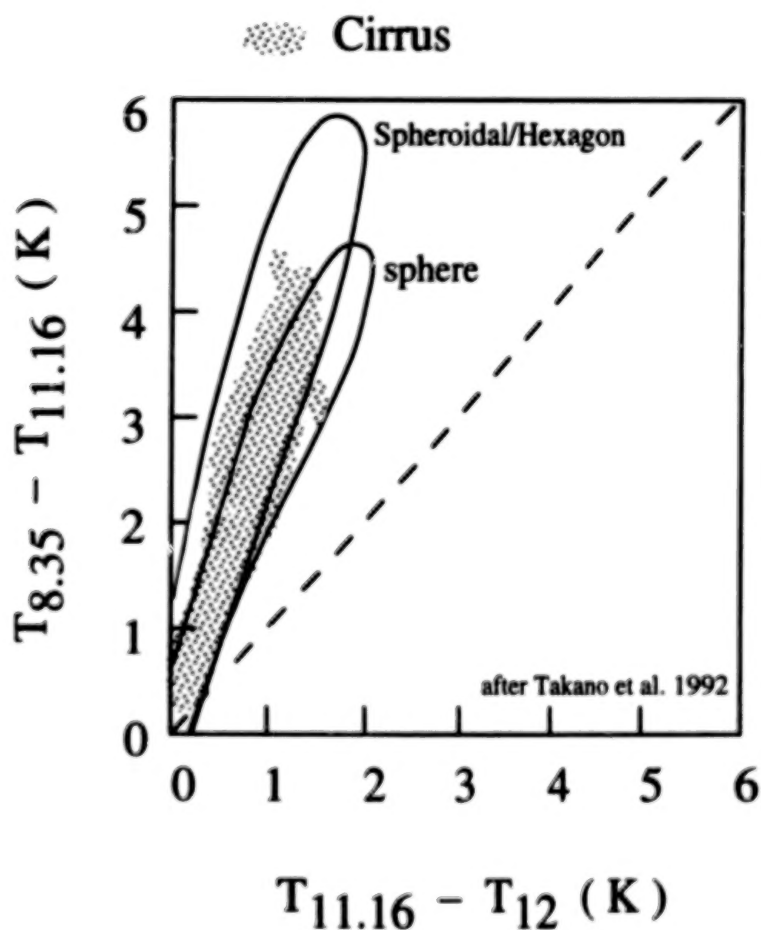


Figure 6. IR color plot of cirrus cloud and theoretical colors from two different clouds of cirrus with difference particle shapes. (after Takano, Liou and Minnis 1992)

5. DISCUSSION

Most passive IR observations can be enhanced by using radiance models to refine the analyses and more tightly limit the microphysical parameters derived. There are presently a number of atmospheric radiance codes available, such as FASCOD and MODTRAN that can be used for these purposes, providing that they are modified to include specific data and radiative properties of the types of particles under study (Mazuk and Lynch, 1994). In other cases (Wen and Rose, 1994) radiance codes can be by-passed in favor of more direct treatments where high spectral resolution is not necessary.

In most cases, the limiting assumption in either technique is that the particles are spherical and can, therefore, be modeled using spherical particle codes ("Mie theory"). Recent work has made significant advances towards modeling hexagonal ice crystals and other irregular particles (see Liou and Takano, 1994, for a review). This requires enormous amounts of computer time, and an acceptable solution for one irregular particle adds little to our knowledge about how another, differently shaped particle scatters radiation, or even how the same particle scatters radiation when oriented differently relative to the sun. Statistical approaches like those reviewed by Liou and Takano (1994) will probably be the best compromise for the foreseeable future. The other major unknown is the particle size distribution.

6. SUMMARY AND CONCLUSIONS

Passive IR spectroscopy and photometry can be used in many cases to detect aerosol clouds and determine a number of important quantities, including chemical composition, particle size and shape, and column density. Observations of airborne desert soil, cirrus clouds, and volcanic ash have demonstrated the capabilities and limitations of the technique. Future work must concentrate on making more laboratory measurements of aerosols with well-known properties in order to guide the interpretation of data obtained in the field or from satellite measurements. In most cases, theoretical models of the clouds enhance the quality of the results, although significant improvements in the models must be made. When the cloud particles are large and irregular, it is important to use nonspherical particle properties rather than rely solely on spherical particle results.

ACKNOWLEDGMENTS

IR spectroscopy and photometry of the atmosphere is an enormous field, and we have not tried to review all of it. Rather than touch on the vast works of many the scientists, we chose to bypass many important contributions in favor of focusing on a few specific techniques. To the extent that we might have omitted or offended in the process, we apologize.

Many people contributed to this review, and we would like to acknowledge Drs. Steve Ackerman and Sergei Matrosov. Stephen Mazuk and Ann Mazuk made many of the figures and performed a number of important calculations.

REFERENCES

- Ackerman, S. A., and W. L. Smith, 1990: Inferring cloud microphysical properties from high resolution spectral measurements in the 8–13 μm window region, Preprints of the Seventh Conference on Atmospheric Radiation (American Meteorological Society, Boston, Mass), 6–8.
- Cornette, W. M., and J. G. Shanks, 1993: Impact of cirrus clouds on remote sensing of surface temperature, *Passive Infrared Remote Sensing of Clouds and the Atmosphere*, D.K. Lynch (ed), SPIE Conference 1934, Bellingham, WA, 252–263.
- Dowling, D.R., and L.F. Radke, 1990: A Summary of the Physical Properties of Cirrus Clouds, *J. Appl. Met.*, **29**, 970–978, September.

- Dungey, C.E., and Bohren, C.F., 1992: Backscattering by nonspherical hydrometers as calculated by the coupled-dipole method: An application in radar meteorology, *J. Atmos. Oceanic Technol.* (in press).
- Ferraro, J.R. (ed.), 1982: *The Sadtler Infrared Spectra Handbook of Minerals and Clays*, Sadtler Research Laboratories, Philadelphia.
- Hackwell, J. A., D. W. Warren, M. Chatelain, Y. Dotan, P. Li, D. K. Lynch, D. Mabry, R. W. Russell, and R. Young, 1990: A Low Resolution Array Spectrograph for the 2.9–13.5 μm Spectral Region, *Proc. SPIE Conference 1235 on Instrumentation in Astronomy VII (1235)*, 171–180.
- Holasek, R.E., and Rose, W.I. 1991: Anatomy of 1986 Augustine Volcano Eruptions as revealed by digital AVHRR satellite Imagery, *Bull. Volcanol.*, 53, 420–435.
- Hanner, M.S., D.K. Lynch, and R.W. Russell, 1994: 10 μm Spectra of Comets and the Composition of Silicate Grains, *Astrophys. J.*, 425, 274–285.
- Henderson-Sellers, A.G., F. Seze, M. Drake, M. Desbois, 1987: Surface-Observed and Satellite Retrieved Cloudiness Compared for the 1983 ISCCP Special Study Area in Europe, *J. Geophys. Res.*, 92, No. D4, 4019–4033, April 20.
- Liou, K. N., and Y. Takano, 1994: Light scattering by nonspherical particles: Remote sensing and climate implications, *Atmospheric Research*, 31, 271–298.
- Lynch, D.K. 1993: Subvisual Cirrus: What It Is and Where You Find It, *Proc. Passive Infrared Remote Sensing of Clouds and the Atmosphere*, D.K. Lynch (ed), SPIE Conference 1934, Bellingham, WA, 264–274.
- Lynch, D.K., M. A. Chatelain, T.K. Tessensohn, and P.M. Adams, 1994: 3–14 μm Nonscanning Spectra of the Minor Uncle Dust Cloud, *Proc. Minor Uncle Symposium*, Defense Nuclear Agency, Alexandria VA, 1994 (in press).
- Mazuk, S., and Lynch, D.K., 1994: Application of the MODTRAN2 code to the modelling of silicate dust clouds, *Proc. 17th Annual Review Conference on Atmospheric Radiation Models*, 7–8 June 1994 Hanscomb AFB, Bedford (in press).
- Menzel, W. P., and D.P. Wylie, 1989: Cloud Cover Determinations with Multispectral VAS Observations: A Two Year Study, COSPAR, *Adv. Space Res.*, 9, No. 7, 167–173.
- Palmer, A.J., S.Y. Matrosov, T. Uttal, B.E. Martner, D.K. Lynch, M.A. Chatelain, J.A., Hackwell, and R.W. Russell, 1993: Combined Infrared Emission Spectra and Radar Reflectivity Studies of Cirrus Clouds, *IEEE Trans. Geosci. and Rem. Sens.*, 31, no.1, 64–69.
- Platt, C.M.R., J.D. Spinhirne, and W.D. Hart, 1989: Optical and microphysical properties of a cold cirrus cloud: Evidence for regions of small ice particles, *J. Geophys. Res.*, 94, 11151–11164.
- Prabhakara, C., R.S., Fraser, G. Dalu, Man-Li C. Wu, R.J. Curran, and T. Styles, 1988: Thin Cirrus Clouds: Seasonal Distribution over Oceans Deduced from NIMBUS-4 IRIS, *J. Appl. Met.*, 27, 379–399.
- Prata, A.J., 1989: Observations of volcanic ash clouds in 10–12 μm window using AVHRR/2 data, *Int. J. Rem. Sens.*, 10, 751–761.
- Salisbury, J.W., L.S. Walter, N. Vergo, and D. M. D'Aria, 1991: *Infrared (2.1–25 μm) spectra of Minerals*, Johns Hopkins Press, Baltimore, 267 pp.

- Schmidt, E. O., J. M. Alvarez, M. A. Vaughn, and D. P. Wiley, 1993: Review of subvisual cirrus morphology, *Passive Infrared Remote Sensing of Clouds and the Atmosphere*, D.K. Lynch (ed), SPIE Conference 1934, Bellingham, WA, 230-239.
- Stephens, G.L., S. Tsay, P. W. Stackhouse, and P. Flatau, 1990: The relevance of the microphysical and radiative properties of cirrus clouds to climate and climate feedback, *J. Atmos. Sci.*, **47**, 1742-1753.
- Takano, Y., K. N. Kiou, and P. Minnis, 1992: The effects of small ice crystals on cirrus infrared radiative properties. *J. Atmos. Sci.*, **49**, 1481-1493.
- Wen, S., and W.I. Rose, 1994: Determination of distributions of particle size, emissivity, and cloud cover for volcanic ash clouds by bi-spectral measurements, *J. Geophys. Res.*, **99**, no. D3, 5421-5431.
- Wylie, D.P., and W. P. Menzel, 1993: Trends in Global Cirrus Inferred from three years of HIRS Data, *Proc. Passive Infrared Remote Sensing of Clouds and the Atmosphere*, D.K. Lynch (ed), SPIE Conference 1934, Bellingham, WA, 197-205.

..

Optical Remote Sensing of the Dayside Ionosphere from Space Through Observations of the O⁺ 834-Å Dayglow

Kenneth F. Dymond, J. Michael Picone, Robert R. Meier, Robert P. McCoy, Owen Kelley

E. O. Hulburt Center for Space Research
Naval Research Laboratory
Washington, DC 20375-5320

and

Ronald J. Thomas
New Mexico Institute of Mining and Technology
Socorro, NM 87801

ABSTRACT

Vertical profiles of F-region ionospheric O⁺ ion (and electron) densities can be determined from observations of the ultraviolet O⁺ 834-Å dayglow from satellite and sounding rocket platforms. The 834-Å emission is produced primarily by solar photoionization of oxygen at low altitudes in the thermosphere. Part of this radiation undergoes multiple resonant scattering in the F-region of the ionosphere and thereby provides an illumination source for the ionosphere. Profiles of this emission obtained from either a limb scanning satellite or vertically traveling sounding rocket can be used to infer the O⁺ ion distribution.

We have developed new nonlinear algorithms using a radiation transport model and discrete inverse theory which allow the rapid inversion of airglow profiles to yield accurate ion densities over the entire F-region. Details of these algorithms and their potential for analyzing satellite and rocket data will be discussed.

Ionospheric remote sensing has wide-spread application to any system depending on transmission through, or reflection from the ionosphere. Examples include high frequency communication, frequency management, high frequency direction finding, and position location using the Global Positioning Satellites. These algorithms will be used for near real-time retrieval of ionospheric electron densities using the Special Sensor Ultraviolet Limb Imager sensors on the Defense Meteorological Satellite Program (DMSP) Block 5D3 satellites.

1. INTRODUCTION

The O⁺ ($2s^2 2p^3 \ ^4S^o \leftarrow 2s 2p^4 \ ^4P$) emission at wavelengths 832.67, 833.33, and 834.47-Å is the brightest O⁺ emission in the Earth's dayglow spectrum (Meier, 1991). This radiation is primarily produced by photoionization-excitation of atomic oxygen at the base of the thermosphere, in the 100-200 km altitude range. Additional sources are photoelectron impact excitation and resonance fluorescence with solar radiation; these two sources contribute roughly 10% and 5%, respectively (Meier, 1991). The volume excitation rate due to resonance fluorescence peaks in the ionosphere with the O⁺. Because the photoelectron flux peaks in the lower thermosphere, photoelectron excitation peaks below the ionosphere. Thus, the ionosphere is primarily illuminated from below. The 834-Å radiation is optically thick and undergoes multiple resonant scattering from the O⁺ in the F₂ region of the ionosphere (altitudes greater than 200 km). This multiple scattering imposes a signature characteristic of the altitude distribution of the O⁺ on the observed radiance as shown in Fig. 1. Without the multiple resonant scattering, the O⁺ 834-Å radiance would only be useful for inferring the O density and would provide no information about the ionosphere. Measurements of the O⁺ 834-Å emission can be used with a model of the illumination and scattering process to infer the O⁺ altitude distribution. Because O⁺ is the dominant ion in the F-region ionosphere, the electron density is then determined by charge neutrality.

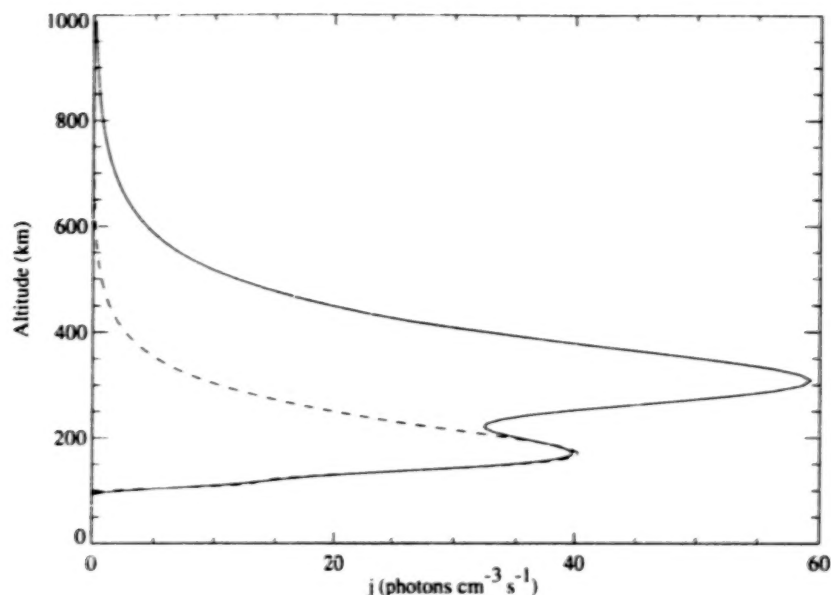


Figure 1. The volume emission rate for the O^+ 834.47 Å line is denoted by the solid line. The volume emission rate without multiple scattering is denoted by the dashed line. The enhancement of the volume emission rate in the F-region is caused by the multiple scattering of the photons by O^+ ions. Notice that the ionosphere is illuminated from below and that the volume emission rate peaks near 300 km. This peak corresponds to a change of the vertical scattering optical depth of approximately 1 from the value at the peak of the initial volume emission rate. Below the ionosphere, downward traveling photons are absorbed by the neutral atmosphere and are therefore lost. The ionospheric parameters were: $n_m = 2 \times 10^6 \text{ cm}^{-3}$, $z_m = 350 \text{ km}$, and $H_0 = 60 \text{ km}$.

The $O \text{ II } 834\text{-}\text{\AA}$ emission has been observed by sounding rocket experiments, shuttle experiments, and by satellites (Carlson and Judge, 1973; Christensen, 1976; Gentieu et al., 1979, 1981; Chakrabarti et al., 1983; Kumar et al., 1983). The satellite and sounding rocket observations have been analyzed using radiation transport models to determine the altitude distribution of the O^+ . McCoy et al. (1985) suggested that this emission could be used to infer the F-region ionospheric parameters such as the plasma scale height, F-region peak altitude, and the peak O^+ density (and electron density). McCoy et al. (ibid.) carried out a detailed parametric study using an ionospheric model with these three parameters. Based on that study, several experiments have been planned for future flights on Air Force DMSP satellites and on Air Force Space Test Program (STP) satellites. These experiments will exploit the O^+ 834-Å emission for ionospheric remote sensing.

The Naval Research Laboratory (NRL) is currently constructing several experiments for measuring the O^+ 834-Å radiance from satellites. The first experiment, called the *Remote Atmospheric and Ionospheric Detection System* (RAIDS), is a joint venture between the NRL and the Aerospace Corporation (McCoy et al., 1992; Christensen et al., 1992; McCoy et al., 1994; Christensen et al., 1993). The RAIDS is a suite of three photometers, three spectrometers, and two spectrographs. Seven of these instruments have their fields-of-view swept across the Earth's limb by a mechanical scan platform; the eighth instrument images the limb directly. The EUV spectrograph covers the extreme-ultraviolet passband, 550-1100 Å, with 12-Å spectral resolution. It will continuously observe the 834-Å emission throughout the nominal three year mission. NRL is also building a suite of five extreme- and far-ultraviolet spectrographs, called the *Special Sensor Ultraviolet Limb Imager* (SSULI), for flight on the U. S. Air Force's DMSP Block 5D3 satellites (McCoy et al., 1992; McCoy et al., 1994). These instruments will scan the Earth's limb covering altitudes 75-750 km at roughly 5 km altitude resolution; they observe the 800-1700 Å passband at 12-15 Å spectral resolution. The SSULIs will continuously observe the 834-Å emission, which will be used to determine the daytime electron density as a function of altitude in near real time. NRL is also building an experiment for flight on the Air Force STP P91-1 or *Advanced Research and Global Observing Satellite* (ARGOS). This experiment is called the *High Resolution Airglow and Auroral Spectroscopy* (HIRAAS) experiment. The HIRAAS experiment consists of three spectrographs, two of which operate in the extreme- and far-ultraviolet. One of these, called the *Low Resolution Airglow and Auroral Spectrograph* (LORAAS), is an exact copy of a SSULI instrument. The other spectrograph is the *High-resolution Ionospheric and Thermospheric Spectrograph* (HITS; Dymond and McCoy, 1993). The HITS operates in the 500-1500 Å passband at better than 0.5 Å spectral resolution everywhere. Its resolution is optimized at 834 Å and is 0.3 Å there. The HITS and LORAAS instruments will provide complimentary coverage of the O^+ 834-Å emission. The LORAAS will observe the emission at lower spectral resolution than the HITS but with higher sensitivity. However, the high spectral resolution of the HITS will

provide additional information on the O^+ by providing spectrally resolved altitude profiles of the triplet. The NRL has also constructed and flown a sounding rocket experiment for preliminary testing of the O^+ retrieval algorithms described in Section 2. This experiment called the *High Resolution Airglow/Aurora Spectrograph* (HIRAAS: McCoy and Carruthers, 1988) covers the 520-1750 Å passband at roughly 0.5-Å resolution.

The O^+ 834-Å emission is a triplet in which the scattering cross-section for each of the lines is approximately in the ratio of 1:2:3 for the 832.67, 833.33, and 834.47-Å lines. Because of the difference in cross-section, the lines undergo different amounts of multiple scattering and therefore the altitude distribution of their intensities differs. This difference in shape provides additional information which may be exploited to determine the O^+ density. Thus, an instrument like the HITS can obtain additional information about the ionosphere when compared to a lower resolution instrument even if both instruments had the same sensitivity. This idea was originally proposed by McCoy and Carruthers (1988) and has been explored experimentally by the HIRAAS sounding rocket experiment; although, the results of the rocket flights have not been fully analyzed. Meier (1991) explored the idea of using high resolution measurements to determine ionospheric densities by modeling the emission and comparing the altitude profiles. He concluded that high spectral resolution did produce additional information which might be exploited.

A new algorithm for inverting the high spectral resolution data returned by the HITS instrument and the HIRAAS sounding rocket experiment has been developed. This algorithm is based on a recently developed algorithm for routine reduction of the O^+ 834-Å data to produce the ionospheric O^+ and electron densities (Picone et al., 1994). The algorithm presented in Picone et al. will be used to invert lower spectral resolution data from the LORAAS, SSULIs, and RAIDS-EUV. Both algorithms use Discrete Inverse Theory (DIT: Menke, 1989; Tarantola and Vallette, 1982; Press et al., 1986) and a "forward model" which includes the effects of resonant scattering and pure absorption on the radiation field and a general parameterization of the ionospheric O^+ density. However, the "forward model" is general enough so that no parameterization of the O^+ density is required; instead, the O^+ densities at various altitudes can be determined directly. This paper will discuss the details, characterization, and preliminary results of the testing of this new High Spectral Resolution Algorithm (HSRA). The HSRA will be compared and contrasted with the Low Spectral Resolution Algorithm (LSRA) presented in Picone et al.

2. INVERSION ALGORITHMS

The inversion algorithms use an iterative approach based on Discrete Inverse Theory to seek the maximum likelihood estimate of the input parameters to the ionospheric model based on the "best" fit to the data. This estimate minimizes the chi-squared (χ^2) of the model fit to the data. The algorithm uses a non-linear model of the scattering process since the O^+ 834-Å radiance is a byproduct of multiple scattering. The model is very robust and general so it can provide an accurate description of the ionosphere and the radiation transport process. The modeling procedure is started by generating a neutral atmosphere using the Mass Spectrometer and Incoherent Scatter model (MSIS: Hedin, 1987). The initial excitation source or volume emission rate of O^+ 834-Å photons is calculated from the neutral atmosphere using the PEGFAC model of Strickland and Meier (1982). This is followed by the calculation of the O^+ density profile using an ionospheric model. The vertical opacities due to pure absorption by N_2 , O_2 , and O and scattering by O^+ are then calculated. The opacities and the initial volume emission rate are used to calculate the volume emission rate due to resonant scattering using the radiation transport model. After this, the volume emission rate is integrated along the line-of-sight through the instrument's field-of-regard; these integrations include extinction effects due to pure absorption and resonant scattering. Next, the χ^2 is calculated and a test for goodness of fit to the data is performed. If the fit is deemed to be "good", the calculation terminates; otherwise, new values for the model parameters are chosen and the whole process is repeated. During the testing for this paper, the neutral atmosphere was held fixed so that the model's ability to determine the ionosphere could be tested. Since the pure absorption opacities and the initial volume excitation rate are fixed, the calculations are continued for each improvement step starting with the calculation of a new vertical opacity due to resonant scattering. For accurate results, a physically accurate parameterization of the ionosphere is required along with an accurate model for the radiation transport process. The model is non-linear and one of the best methods for solving this type of problem is iteration starting from an initial guess at the model parameters. The Levenberg-Marquardt scheme (Press et al., 1986) is used to select subsequent sets of parameters. The partial derivatives of the model fit with respect to the model parameters at the current step are evaluated and used to determine how each of the model parameters need to be changed to improve the agreement between the model and the data. When far from the minimum, the Levenberg-Marquardt scheme approaches the minimum in χ^2 along the path of steepest descent, but slows down by selecting smaller steps when near the minimum χ^2 . This permits a quicker approach to the minimum because the step size is large where χ^2 is rapidly varying and is decreased where χ^2 is slowly varying. Once the model has converged, the inversion code returns the best fit values and a model covariance matrix. This covariance matrix has the squares of the variances of the model

parameters as its on-diagonal elements and the cross covariances as its off-diagonal elements. Using the standard technique for error propagation (Bevington, 1969), the variances in the density at each altitude can be calculated using the covariance matrix and the partial derivatives of the density with respect to the model parameters.

The Chapman layer is used as the ionospheric model for the O^+ density during the testing (Chamberlain and Hunten, 1987). This model uses three parameters to characterize the ionosphere: the altitude where the density peaks, Z_m ; the density at the peak, n_m ; and the O scale height, H_o , which is one-half the plasma scale height for the form of the Chapman layer given below. The Chapman function for describing the density, $n(z)$, is:

$$n(z) = n_m \exp \left\{ \frac{1}{2} \left[1 - \frac{z - z_m}{H_o} - \exp \left(- \frac{z - z_m}{H_o} \right) \right] \right\} \quad (1)$$

where z is the altitude. This function has a "roll-off" on the bottomside due to complete absorption of the Sun's ionizing soft x-ray and extreme-ultraviolet radiation. The topside follows the density variation of a species in diffusive equilibrium. The density peaks where the opacity along a line of sight to the Sun is unity, i. e., where photoionization is most effective. The Chapman layer is a reasonable approximation for describing the ionospheric density. However, a more robust parameterization should be used for modeling a "real" ionosphere. This work uses the Chapman function to describe the ionosphere since the primary concerns here are demonstrating that the technique works and evaluating how well the instruments are expected to perform.

The integral form of the radiation transport equation is solved using the complete frequency redistribution (CFR) approximation. CFR is a good approximation in this case because the maximum value for the vertical optical depth is ≤ 10 . The transport equation for the volume emission rate of the k^{th} line, is:

$$j_k(z) = j_k^0(z) + n(z) \sigma_k^0 \int_{z_{\min}}^{\infty} j_k(z') H(|\tau_k(z) - \tau_k(z')|, |t_k(z) - t_k(z')|) dz' \quad (2)$$

where $j_k^0(z)$ is the initial volume emission rate, in this case, the rate of production of excited O^+ ; σ_k^0 is the line center scattering cross-section; $n(z)$ is the O^+ density at z ; τ_k is the vertical optical depth for resonant scattering; t_k is the vertical optical depth for pure absorption; and H is the Holstein probability function. The essence of the CFR process is contained in the Holstein H function:

$$H(\tau, t) = \frac{1}{2\sqrt{\pi}} \int_0^{\infty} e^{-2x^2} E_1(\tau e^{-x^2} + t) dx \quad (3)$$

where x is the particle's speed in Doppler units, e^{-x^2} is the Gaussian line shape, and $E_1(x)$ is the exponential integral of the first kind. This function is proportional to the probability that a photon will propagate from region z' , $z' + dz'$ to the region z , $z + dz$.

The integration in equation 2 is evaluated from the bottom of the source region at approximately 100 km to the upper boundary at 1000 km, which for all practical purposes is infinity. The solution then progresses by rewriting the integral in equation (2) as a discrete sum using the trapezoid rule. The resulting set of linear equations are then solved by LU Decomposition (Press et al., 1986). LU Decomposition is faster than matrix inversion for this application and the problems associated with numerical errors are reduced because there are fewer calculations required. The CFR portion of the model requires the O^+ , O , O_2 , and N_2 densities; the cross-sections for scattering and pure absorption; and the initial volume emission rate. The pure absorption and scattering cross-sections in Table 1 were taken from Link and Evans (1994). The model atmosphere used in this calculation and throughout the testing is in Table 2. An example of the effects of multiple scattering on the volume emission rate for the 834.47 Å line is shown in Fig. 1.

Once the multiply scattered volume emission rate is known, the radiance can be calculated. The radiance in Rayleighs, $4\pi I$, is calculated using:

$$4\pi I = 10^{-6} \int j(z) T(\tau(z), t(z)) dz \quad (4)$$

where $T(\tau(z), t(z))$ is the Holstein transmission function, $\tau(z)$ is the vertical optical depth for scattering, $t(z)$ is the vertical

Table 1. Pure Absorption and Scattering Cross Sections for the O⁺ 834 Å Triplet

Wavelength (Å)	Upper State	Oscillator Strength	Scattering Cross Section (1000 K, cm ²)	Absorption Cross Section (10 ⁻¹⁸ cm ²)		
				N ₂	O ₂	O
834.4655	5/2	0.1371	1.68x10 ⁻¹³	10.1	10.44	3.90
833.3294	3/2	0.0916	1.12x10 ⁻¹³	0.29	14.40	3.89
832.7572	1/2	0.0459	5.61x10 ⁻¹⁴	0.049	31.80	3.89

All cross sections taken from Link et al. (1994).

Table 2. Model Atmosphere

Z (km)	[N ₂] (cm ⁻³)	[O ₂] (cm ⁻³)	[O] (cm ⁻³)	T (K)	j ₀ (cm ⁻³ s ⁻¹)
1000.0	2.9e+001	1.6e-001	1.2e+005	1199.7	0.0
926.1	1.3e+002	8.6e-001	2.8e+005	1199.7	0.0
857.7	5.4e+002	4.5e+000	6.4e+005	1199.7	0.0
794.3	2.1e+003	2.1e+001	1.4e+006	1199.7	0.0
735.6	7.7e+003	9.4e+001	2.9e+006	1199.7	0.0
681.3	2.6e+004	3.7e+002	5.8e+006	1199.6	0.1
631.0	8.0e+004	1.4e+003	1.1e+007	1199.6	0.1
584.3	2.3e+005	4.7e+003	2.1e+007	1199.5	0.2
541.2	6.4e+005	1.5e+004	3.7e+007	1199.4	0.4
501.2	1.6e+006	4.3e+004	6.3e+007	1199.1	0.7
464.2	4.0e+006	1.2e+005	1.0e+008	1198.6	1.1
429.9	9.0e+006	3.0e+005	1.7e+008	1197.7	1.7
398.1	2.0e+007	7.3e+005	2.6e+008	1196.0	2.7
368.7	4.0e+007	1.7e+006	3.9e+008	1193.4	4.0
341.5	8.0e+007	3.6e+006	5.8e+008	1189.1	5.8
316.2	1.5e+008	7.6e+006	8.3e+008	1182.6	8.3
292.9	2.8e+008	1.5e+007	1.2e+009	1173.0	11.3
271.2	4.9e+008	2.9e+007	1.6e+009	1159.2	15.1
251.2	8.5e+008	5.4e+007	2.2e+009	1139.9	19.5
232.6	1.4e+009	9.9e+007	3.0e+009	1113.8	24.5
215.4	2.4e+009	1.8e+008	4.1e+009	1079.3	29.7
199.5	4.0e+009	3.1e+008	5.6e+009	1034.8	34.6
184.8	6.7e+009	5.6e+008	7.6e+009	978.7	38.5
171.1	1.1e+010	1.0e+009	1.0e+010	909.6	40.3
158.5	2.0e+010	1.9e+009	1.5e+010	826.1	38.8
146.8	3.6e+010	3.7e+009	2.2e+010	727.1	33.3
135.9	7.1e+010	8.0e+009	3.4e+010	611.6	25.0
125.9	1.6e+011	2.1e+010	5.9e+010	479.1	17.1
116.6	5.0e+011	7.9e+010	1.2e+011	330.0	13.6
108.0	2.0e+012	4.0e+011	2.6e+011	230.1	9.6
100.0	8.5e+012	2.0e+012	4.3e+011	190.1	1.4

Square brackets represent density. Exponential notation d.de+nnn is to be read d.d×10⁺ⁿⁿⁿ.

pure absorption optical depth, and s is the distance from the observer along the line of sight. The Holstein transmission function is:

$$T(\tau, t) = \frac{1}{\sqrt{\pi}} \int e^{-x^2} \exp(-\tau e^{-x^2} - t) dx. \quad (5)$$

The ionospheric density enters into the calculation in two ways. First, it enters by affecting the volume emission rate through multiple resonant scattering. Second, it enters by affecting the transmission through the atmosphere. This second effect is very important because the transmission function can affect the observed intensity even if the ionospheric density is too small to affect the volume emission rate.

The HSRA generates look angle profiles for each line of the O⁺ triplet, because the satellite experiments described above measure the airglow radiance as a function of angle below the satellite's horizon. During the modeling, all three profiles are fit simultaneously. The satellite is assumed to be in a 850-km circular orbit, which is appropriate for all of the experiments mentioned above (except for the sounding rocket, of course). The experiments are assumed to be looking aft along the satellite track. The field-of-view of the instruments is swept downward. The motion of the tangent point is away from the observer during a downward scan, but the satellite is moving forward which partially compensates for the tangent point's apparent motion. Likewise, if the observer was looking forward the scan would be upward. In this way, the loci of the tangent points forms a more vertical trajectory with less latitudinal smearing. Most of the extreme and far ultraviolet airglow occurs above 100 km and the F-region O⁺ density typically peaks below 500 km. The angular scan range is set so that it starts below the region of interest and continues upward to a few scale heights above the F-region peak. For a satellite orbiting at 850 km, the look angles (angle below the space vehicle's local horizon) of interest are between 10° and 26.5°, corresponding to tangent altitudes of 750 and 90 km, respectively. During a typical 90 sec scan, the satellite moves approximately 6° of latitude. In all of the satellite experiments mentioned above, the scan rate is varied to concentrate observing time in the region below 300 km where more structure is expected in the altitude profiles. This is accomplished by scanning the instrument's field-of-view at 0.28 degrees sec⁻¹ during the first 30 seconds and at 0.14 degrees sec⁻¹ during the next 60 seconds. In the algorithms, a 31 point altitude grid is used in calculating the volume emission rates. This grid has exponentially varying spacing and covers the 100-1000 km altitude range. The radiances are calculated on this same altitude grid by calculating the look angle corresponding to each altitude in the grid and then evaluating equation 4 for each look angle. These radiances are interpolated onto the satellite look angle grid using a cubic spline function. Since the synthesized data are created in the same manner, the relatively low resolution of the altitude grid is not a problem. However, during the analysis of satellite data, this resolution should probably be increased.

The only differences between the HSRA and LSRA are in the generation of the data and the number of profiles that are fit. The LSRA model is generated from the three separate altitude profiles for the O⁺ lines by adding the three altitude profiles together. Then, instead of having three separate line profiles to fit, we have only a single profile. This is computationally faster than the HSRA. However, the advantage of the HSRA is in the ability to exploit the additional information from three profiles derived from the same physics.

3. DESCRIPTION OF TESTS

Two types of testing were performed. First, synthetic data were generated for a wide range of ionospheric parameters. These data were then inverted using the high and low resolution algorithms and the results were compared. Second, the global convergence properties of both algorithms were tested for initial guesses that ranged from very good (exactly the values used to synthesize the data) to very poor. During the global convergence testing, the synthetic data with noise were held fixed so that the effects of noise on the retrieved parameters could be minimized. This emphasizes the effects of different starting points for the ionospheric parameters. Because the low resolution algorithm has been the subject of intensive study at NRL, we will only summarize the results of the testing in this work; the details can be found in Picone et al. (1994). In all of the tests, the neutral atmosphere was held fixed. This emphasizes the sensitivity of the algorithms to the ionospheric parameters and de-emphasizes any sensitivity the algorithms have to the initial volume emission rate, which is determined by the neutral atmosphere. This is a reasonable approach because in practice the results of neutral density inversion algorithms will be used to determine the neutral atmosphere. The inversion algorithm for determining the neutral oxygen and molecular nitrogen densities from the O I 1356-Å and the N₂ 1385-Å Lyman-Birge-Hopfield band radiances is described by Meier and Picone (1993). The neutral atmosphere and the initial volume emission rate without multiple scattering are in Table 2. To save computing time, the ionospheric parameters used in the data synthesis were used as the initial guess for the inversions. This does not invalidate the results because additional testing of the global convergence properties of both the HSRA and LSRA has demonstrated excellent global convergence properties—even when starting with extremely poor initial guesses.

A calibration or sensitivity factor is used in the conversion of a model profile to synthetic data. The unit used for atmospheric radiances is the Rayleigh. The radiance of a source of strength 1 megaphoton cm⁻¹ sec⁻¹ emitted into 4π steradians is 1 Rayleigh (see Chamberlain and Hunten, 1987 for a discussion). Typical magnitudes of atmospheric radiances in the extreme and far ultraviolet are of the order of 1-10⁴ Rayleighs. The measured sensitivity for SSULI-1 is approximately 1.6 counts sec⁻¹ Rayleigh⁻¹ at 834 Å. The sensitivity of the HITS instrument and the RAIDS-EUV at 834 Å is roughly 0.5 counts sec⁻¹ Rayleigh⁻¹. To remove the effects of the sensitivity from the comparison of the HSRA and the LSRA, the same sensitivity factor, 1 count sec⁻¹ Rayleigh⁻¹, was used in both algorithms.

The results of an inversion for a particular set of synthetic data will show some sensitivity to the noise on the profile. The inversion algorithm will usually not converge to exactly the same "best fit" ionospheric parameters when

different noise is superimposed on the profile. However, the "best fit" values of the model parameters from fits to profiles generated with the same input ionospheric parameters and different noise will agree to within the uncertainties for the retrieved parameters. To remove the effects of the randomness of the noise on the synthetic data when the two algorithms were compared, the synthetic data from the HSRA were added together to generate the LSRA synthetic data. In this way, the same data were used to test both algorithms and the sensitivity to the noise was suppressed. The HSRA and LSRA synthetic profiles without noise were converted from units of Rayleighs to units of counts per bin per second by applying an intensity scaling factor. Error bars were calculated by assuming the data are shot noise limited (uncertainty equal to the square root of the number of counts). The shot noise limit assumption is valid because all of the instruments described above use microchannel plate based photon counting detectors which have a low dark count. These errors were then superimposed on the data by generating random numbers with a Gaussian distribution, zero mean, and standard deviation of 1 which were multiplied by the error bars and added to the profile. New error bars accurately representing the "noisy data" were derived by taking the square root of the profiles. The "noisy" profiles and their error bars were then converted back to intensities in Rayleighs. These synthetic data and error bars were then used in the inversion.

4. RESULTS AND DISCUSSION

The results presented here are of a preliminary nature as additional testing of both algorithms is continuing. The testing performed for this work is by no means exhaustive.

4.1 LSRA RESULTS

The LSRA was tested by synthesizing profiles for a variety of values for the ionospheric parameters. At three O scale heights (50, 60, and 70 km), the peak density was varied from $1 \times 10^5 \text{ cm}^{-3}$ to $1 \times 10^8 \text{ cm}^{-3}$ while the peak height was varied from 250 km to 750 km. These ranges are extreme since the upper limit to the tangent altitude for the experiments described above is approximately 750 km and the CFR approximation begins to break down at peak densities $\sim 10^7 \text{ cm}^{-3}$. The LSRA converges to the "true" values used to simulate the "data" to within a few sigmas in all cases and for initial guesses that range from exactly the input values to off by an order of magnitude for n_m , by a factor of 2 for H_O , and by a hundred kilometers for Z_m . This implies that there is a unique solution for the density based on the "data" used in the analysis. This also implies that the uncertainties in the derived solutions can be used as an indication of the accuracy of the determination of the ionospheric parameters as well as providing some estimate of the confidence in those parameters.

Figure 2d shows a typical LSRA fit to data simulated for ionospheric parameters $n_m = 2 \times 10^6 \text{ cm}^{-3}$, $Z_m = 350 \text{ km}$, and $H_O = 60 \text{ km}$. The reduced χ^2 for this fit is 0.99 and the probability of producing a model with a larger χ^2 is 0.51. The retrieved values are: $n_m = 2.07 \pm 0.08 \times 10^6 \text{ cm}^{-3}$, $Z_m = 358.2 \pm 3.7 \text{ km}$, and $H_O = 56.4 \pm 3.7 \text{ km}$ which differ from the "true" values by 3.5, 2.3, and 6.0 %, respectively. Figure 2e shows the agreement between the LSRA density (diamonds) and the "true" density (solid line). Above 300 km, the derived density matches the "true" density to within the error bars shown in Fig. 2f. The uncertainty is lowest near the F-region peak (350 km, in this case), but the uncertainty increases dramatically below the peak. The model is unable to determine the density below the F-region peak, because there is little or no information transmitted to the observer from regions where the scattering extinction is large. In fact, any information obtained from this region may be superfluous and is a result of the model extrapolating the density downward, which is an artifact of using the Chapman layer to describe the ionospheric density. This situation is analogous to the case of ground-based ionosonde measurements of the electron density, as an ionosonde cannot determine any topside information which must be extrapolated by fitting a model to the bottomside data.

Panels d, e, and f of Fig. 3 show contour plots of the fractional uncertainty in the retrieved parameters for various values of the peak density and peak altitude used in the "data" synthesis. The O scale height was fixed at 60 km for these simulations, but the contour plots for 50 and 70 km show similar structure and comparable magnitudes for the uncertainties. As shown in Fig. 3d, the peak density can be determined to within 10% for "true" peak densities less than 10^7 cm^{-3} and peak altitudes above 300 km. At the lowest altitudes, the loss of information due to extinction along the line-of-sight becomes apparent and increases the uncertainty in the retrieved peak density. At the highest altitudes, the uncertainty again increases because topside information, such as the O scale height, is overwhelmed by information from the tangent point. This is a geometric effect caused by limb viewing in a spherical geometry which strongly enhances the contribution from the tangent point. Figure 3e shows that the peak height can be determined to better than 10% for all peak densities and altitudes; in many cases, the peak altitude can be determined to within a few percent. The peak height determines the location of the "cut off" for the altitude information due to extinction along the line-of-sight and also determines where the volume emission rate peaks. Below the peak height, the models provide very little information, as

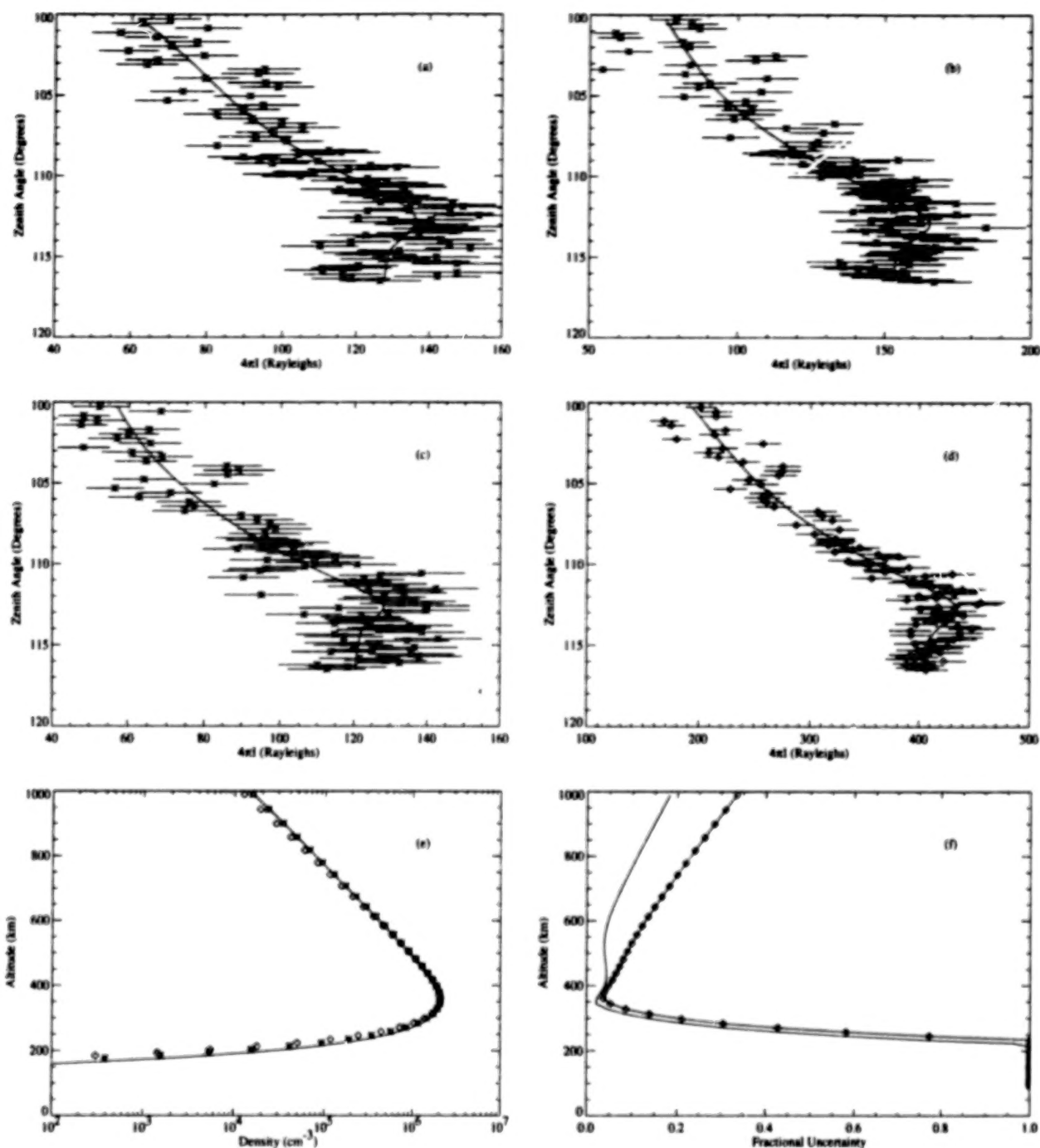


Figure 2. This figure shows the results for a typical simulation. Panels a, b, and c are the "data" and fits for the 832.67, 833.33, and 834.47-Å lines, respectively. Panel d shows the total triplet intensity data and fit from the LSRA. The "true" values used to synthesize the "data" are $n_m = 2.0 \times 10^6 \text{ cm}^{-3}$, $Z_m = 350 \text{ km}$, and $H_0 = 60 \text{ km}$. The HSRA returned $n_m = 2.05 \times 10^6 \text{ cm}^{-3}$, $Z_m = 356.0 \text{ km}$, and $H_0 = 58.8 \text{ km}$ with uncertainties of 1.95%, 0.76%, and 4.6%, respectively. The LSRA returned $n_m = 2.07 \times 10^6 \text{ cm}^{-3}$, $Z_m = 358.2 \text{ km}$, and $H_0 = 56.4 \text{ km}$ with uncertainties of 3.74%, 1.03%, and 6.52%, respectively. The error bars in panels a - d are one sigma. Panel e shows the overall fits to the "true" density. The solid line is the "true" density; the HSRA fit is marked by asterisks and the LSRA fit by diamonds. Both algorithms do a good job of fitting the data. The fractional uncertainties in the retrieved densities from the HSRA (solid line) and the LSRA (solid line with diamonds) are shown in panel f.

shown in Fig. 2f. Figure 3f shows that the O scale height is the most poorly determined of the three Chapman parameters. The information most critical for determining the O scale height comes from the top side of the data profile which is the faintest and consequently has the largest error bars. The effect of the relatively large uncertainty in H_0 is most obvious in Fig. 2f where it causes the error bars on the top side density to increase.

The uncertainties in all three ionospheric parameters increase toward higher peak density and the uncertainties for all three are largest near $4\text{--}5 \times 10^7 \text{ cm}^{-3}$. There are three potential causes for this "island" of high uncertainty. One potential cause of the "island" is the size of the error bars. The fractional uncertainty in the data increases with the peak density which causes the uncertainty in the retrieved parameters to increase. However, the decrease of all three uncertainties for peak densities larger $6\text{--}7 \times 10^7 \text{ cm}^{-3}$ suggests that size of the error bars on the data is not the only consideration. Another possible explanation of the high uncertainty "island" is that the CFR approximation no longer valid; this approximation begins to break down at peak densities $\sim 10^7 \text{ cm}^{-3}$. This is probably not the cause of the "island" because the "data" and the model both use the same approximation. However, the breakdown of the CFR approximation could potentially affect the calculation of the partial derivatives of the model with respect to the ionospheric parameters; these derivatives are used in the calculation of the uncertainties. The most likely cause of the "island" of high uncertainty is due to the competition between the extinction along the line-of-sight, which decreases the intensity, and the increase in volume emission rate due to multiple resonant scattering, which increases the intensity. At lower peak densities the extinction effects dominate. However, at high peak densities, the multiple resonant scattering effects become much more important. Figure 4 shows how the shape of the look angle profiles changes with peak density near the region where the uncertainties peak. For these plots, the O scale height was fixed at 60 km and the peak height was fixed at 300 km. As the peak density is increased from $1.5 \times 10^7 \text{ cm}^{-3}$ to $2 \times 10^7 \text{ cm}^{-3}$ there is only a small change in shape, although the magnitude of the intensity changes. However, as the peak density is further increased to $3 \times 10^7 \text{ cm}^{-3}$ the shape begins to change and the uncertainty in the retrieved parameters decreases. When the density is increased to 10^8 cm^{-3} the bulge due to the greatly enhanced volume emission rate becomes apparent.

4.2 HSRA RESULTS

The convergence properties of the HSRA were tested by simulating data with a fixed set of input values and then inverting the data using widely ranging initial guesses for the ionospheric parameters. The data were generated for $n_m = 1 \times 10^6 \text{ cm}^{-3}$, $Z_m = 350 \text{ km}$, and $H_0 = 60 \text{ km}$. Noise was then superimposed on the profile as described above. This profile was then used throughout the simulations. The initial guesses ranged from $10^5\text{--}10^7 \text{ cm}^{-3}$ for n_m , from 250–450 km for Z_m , and 30–120 km for H_0 . The HSRA converged to the values used to simulate the data in all cases tested.

The HSRA was tested over the same ranges of parameters as the LSRA. Panels a, b, and c of Fig. 2 show the fit to the synthetic high resolution data for the 832.67, 833.33, and 834.47 Å lines, respectively. The synthetic data were created using $n_m = 2 \times 10^6 \text{ cm}^{-3}$, $Z_m = 350 \text{ km}$, and $H_0 = 60 \text{ km}$. All three profiles were fit simultaneously and the retrieved ionospheric parameters were: $n_m = 2.05 \pm 0.04 \times 10^6 \text{ cm}^{-3}$, $Z_m = 356.0 \pm 2.7 \text{ km}$, and $H_0 = 58.8 \pm 2.7 \text{ km}$. These values differ from the true values by 2.5, 1.7, and 2.0 %, respectively. The reduced χ^2 for this fit is 0.95 with a probability of exceeding this χ^2 of 0.702. Figure 2e shows the derived density (asterisks) and its agreement with the "true" density (solid line). The propagated uncertainty of the derived densities are shown in Fig. 2f. The density uncertainty is a minimum near the peak height. The uncertainty increases above Z_m but not as much as the uncertainty returned by the LSRA. This is due to the difference in opacity for the three lines in the triplet. The 832.67 Å line has the lowest opacity and therefore more information is available on the topside to help determine the O scale height. The uncertainty increases on the bottomside because the opacity prevents any information about the bottomside from reaching the observer.

Panels a, b, and c of Fig. 3 show contour plots of the uncertainties in the peak density, peak height, and the O scale height, respectively. As in the LSRA algorithm, the peak density can be determined to within 6%, and in many cases to better than 4%, for all peak heights greater than 300 km and peak densities less than 10^7 cm^{-3} . The uncertainty in the retrieved peak height is less than 5% for all peak heights and peak densities tested. It can be determined to better than 1% over most of the parameter space considered. Again, as is the case with the LSRA, the O scale height is the poorest determined quantity. This is due to the large error bars on the topside data where the model is most sensitive to the O scale height. But, the algorithm can still determine the O scale height to better than 10% for all peak heights used in the test and for peak densities less than 10^7 cm^{-3} . The uncertainties in all three quantities show the largest uncertainties at peak densities of $2\text{--}4 \times 10^7 \text{ cm}^{-3}$ and at peak heights 350–500 km. Like the LSRA case, this is most likely caused by the competition between the extinction along the line-of-sight and the increase in the volume emission rate due to multiple resonant scattering; although, additional analysis is required to verify this claim.

4.3 ALGORITHM COMPARISON

Both algorithms are able to accurately determine the ionospheric parameters, but the HSRA is able to better determine the ionospheric parameters than the LSRA. Figure 2 f shows the uncertainty in the retrieved density for the two algorithms. The uncertainty in the retrieved density from HSRA (solid line) is lower than that returned by the LSRA at all altitudes where the algorithms obtain information. The HSRA uncertainties in the peak density, peak height, and O scale

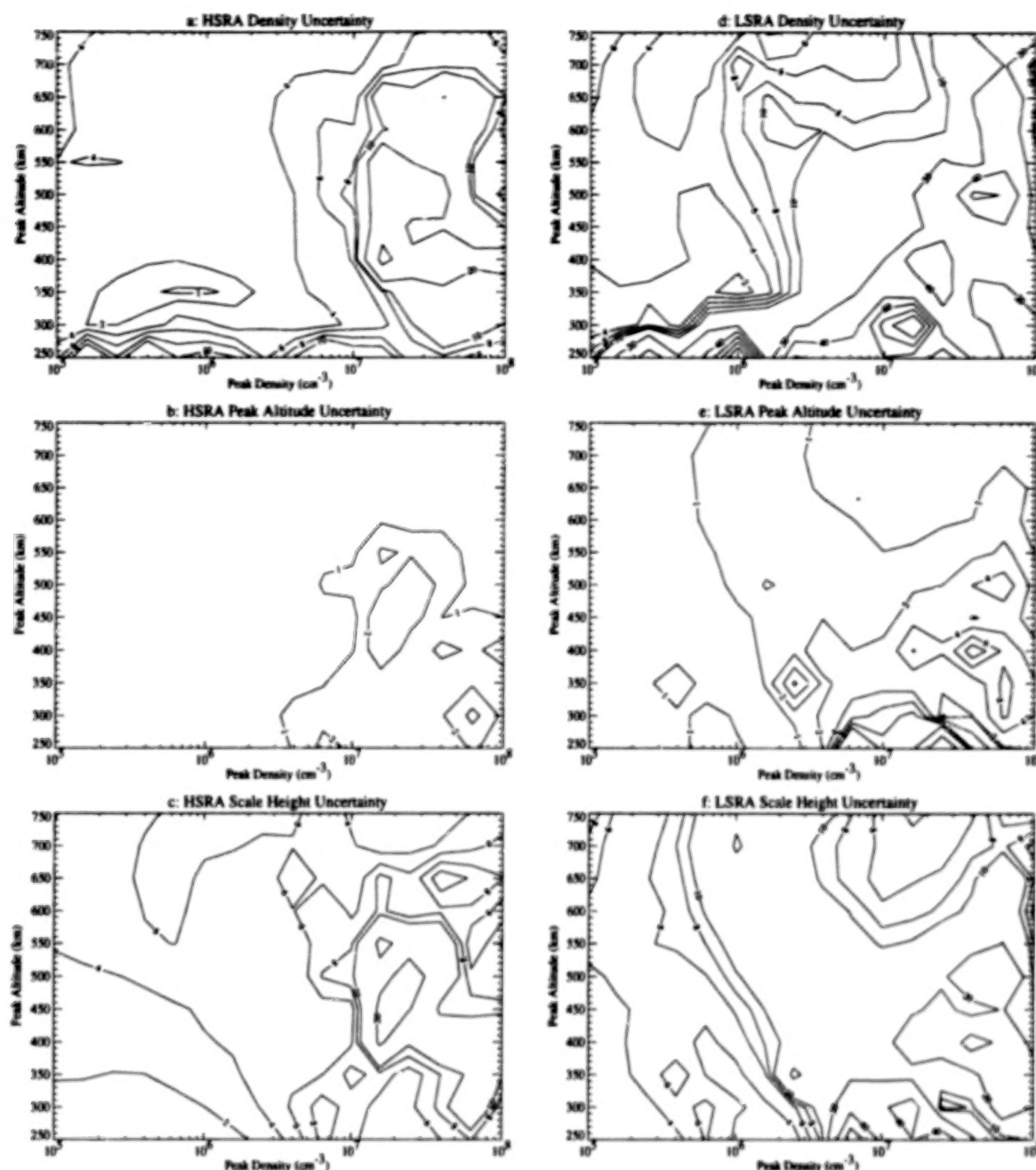


Figure 3. These are contour plots of the fractional uncertainties in percent for the retrieved parameters as functions of the peak density and peak altitude. Plots a, b, and c are for the HSRA and plots d, e, and f are for the LSRA. The O scale height was held fixed at 60 km for these simulations. However, simulations at 50 km and 70 km show the same general structure and relative sizes of the uncertainties. Note that the HSRA produces smaller uncertainties than the LSRA in all cases. The contour levels are at 1, 2, 4, 6, 8, 10, 20, 40, 60, 80, 100%. In plots b and e the uncertainty is sometimes less than 1%.

height, shown in Figs. 3 a, b, and c, are in all cases lower than the uncertainties returned by the LSRA, shown in Figs. 3 d, e, and f. In most of the simulations, the uncertainties retrieved by the HSRA were approximately half of those returned by the LSRA. The smaller uncertainties are a direct consequence of the increased information content available with high spectral resolution observations. There is information available in the lower resolution profile, as the LSRA simulations show; however, this information is more ambiguous due to the blending of the triplet. The LSRA is computationally faster

than the HSRA. Both algorithms use the same radiation transport and line-of-sight integration modules, but the discrete inverse theory section of the computer code takes considerably longer in the HSRA because there are 3 times as many points being used.

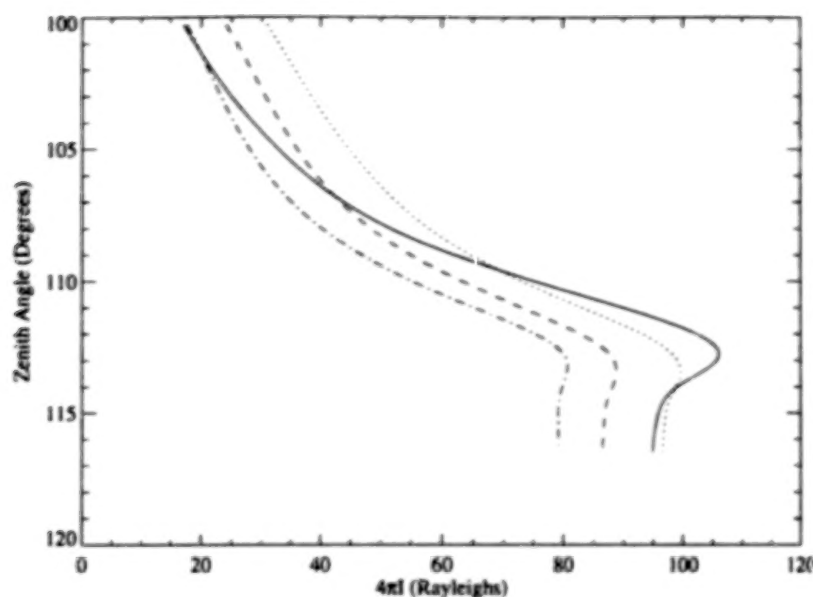


Figure 4. The intensity profiles for peak densities near where the uncertainties peak are shown. The solid line is for a peak density of $1 \times 10^8 \text{ cm}^{-3}$. The dotted line is for $1.5 \times 10^7 \text{ cm}^{-3}$. The dashed line is for $2 \times 10^7 \text{ cm}^{-3}$. The dot-dash line is for $3 \times 10^7 \text{ cm}^{-3}$.

5. CONCLUDING REMARKS

Two algorithms for inverting satellite and sounding rocket observations of the $\text{O}^+ 834\text{-}\text{\AA}$ emission have been presented. Both algorithms are based on Discrete Inverse Theory and use nonlinear models including radiation transport to seek an iterative, maximum-likelihood fit to the data. The Chapman layer was used as the ionospheric model for testing the algorithms. The High Spectral Resolution Algorithm (HSRA) has been shown to be superior to the Low Spectral Resolution Algorithm (LSRA), because high spectral resolution observations provide additional spatial information which can be exploited. The HSRA typically returns uncertainties in the retrieved ionospheric parameters that are approximately one half those returned by the LSRA. The global convergence properties of both algorithms were found to be excellent over a wide range of ionospheric parameters. Neither algorithm can accurately determine the bottomside of the O^+ density distribution because very little information is available from this region due to extinction by multiple scattering and pure absorption.

Link et al. (1994) suggest that densities based on analysis of the $\text{O}^+ 834 \text{ \AA}$ emission are not unique. We have demonstrated that our algorithms will uniquely retrieve the ionospheric parameters used to simulate the data. However, we have used a model which perfectly describes the data, which is rarely the case in a real-world situation. The approach used in this paper and in Picone et al. (1994) provides a robust approach for analyzing the data and generating uncertainties in the retrieved parameters. These algorithms can produce accurate ionospheric densities provided an accurate model for the physics is used. The parameters derived from inversions have uncertainties associated with them and therefore a range of solutions are admissible. However, the range of solutions admitted is strongly dependent on the uncertainty in the data and the uncertainty in the data is related to the instrument's sensitivity. As expected, the ability of an algorithm retrieve accurate ionospheric densities by inversion is strongly dependent on the data and on the uncertainties in the data. Part of the purpose of the simulations in this paper and in Picone et al. (ibid.) is to estimate how sensitive an instrument has to be to determine the ionospheric density to some level of confidence. Simulations of the type discussed in this paper indicate that the instruments described above are sensitive enough to accurately determine the F-region O^+ and electron densities on the Earth's dayside.

Additional study of these algorithms is required. We have used a simple ionospheric model which is not robust enough to describe the ionosphere in all cases. Further investigation is needed to determine the best parameterization to use to adequately model the ionosphere. The final step will be to compare the densities retrieved with our algorithms based on analysis satellite and sounding rocket data to "ground truth" densities measured by ionosondes and incoherent scatter radars.

REFERENCES

- Anderson, D. E., and R. R. Meier, 1985: The O II 834 Å Dayglow: a General Model for Excitation Rate and Intensity Calculations, *Planetary and Space Sci.*, **33**, 1179.
- Bevington, P. R., 1969: *Data Reduction and Error Analysis for the Physical Sciences*, McGraw-Hill, New York, N. Y.
- Carlson, R. W., and D. L. Judge, 1973: Rocket Observations of the Extreme Ultraviolet Dayglow, *Planet. and Space Sci.*, **33**, 1179.
- Chamberlain, J. W., and D. M. Hunten, 1987: *Theory of Planetary Atmospheres*, Academic Press, Orlando, Florida, 230.
- Chakrabarti, S., F. Paresce, S. Bowyer, R. Kimble, and S. Kumar, 1983: The Extreme Ultraviolet Day Airglow, *J. G. R.*, **88**, 4898.
- Christensen, A., 1976: A Rocket Measurement of the Extreme Ultraviolet Dayglow, *G. R. L.*, **3**, 221.
- Christensen, A. B., D. C. Kayser, J. B. Pranke, P. R. Straus, D. J. Gutierrez, S. Chakrabarti, R. P. McCoy, R. R. Meier, K. D. Wolfram, and J. M. Picone, 1992: Instrumentation on the RAIDS (Remote Atmospheric and Ionospheric Detection System) Experiment II: Extreme Ultraviolet Spectrometer, Photometer, and Near IR Spectrometer, *SPIE vol. 1745, Instrumentation for Planetary and Terrestrial Atmospheric Remote Sensing*, 89.
- Christensen, A. B., D. C. Kayser, J. B. Pranke, P. R. Straus, D. J. Gutierrez, S. Chakrabarti, R. P. McCoy, R. R. Meier, K. D. Wolfram, and J. M. Picone, 1993: Instrumentation on the Remote Atmospheric and Ionospheric Detection System Experiment: Extreme-ultraviolet Spectrometer, Photometer, and Near-infrared Spectrometer, *Optical Engineering*, **32**, 3054.
- Cleary, D. D., R. R. Meier, E. P. Gentieu, P. D. Feldman, and A. B. Christensen, 1989: An Analysis of the Effects of N₂ Absorption on the O⁺ 834-Å Emission from Rocket Observations, *J. G. R.*, **94**, 17,281.
- Dymond, K. F., and R. P. McCoy, 1993: Ultraviolet Spectrographs for Thermospheric and Ionospheric Remote Sensing, *SPIE vol. 1940, Small Satellite Technology and Applications III*, 117.
- Feldman, P. D., D. E. Anderson, R. R. Meier, and E. P. Gentieu, 1981: The Ultraviolet Dayglow 4. The Spectrum of Singly Ionized Oxygen, *J. G. R.*, **86**, 3583.
- Gentieu, E. P., P. D. Feldman, and R. R. Meier, 1979: Spectroscopy of the Extreme Ultraviolet Dayglow at 6.5 Å Resolution: Atomic and Ionic Emissions Between 530 and 1240 Å, *G. R. L.*, **6**, 325.
- Gentieu, E. P., P. D. Feldman, R. W. Eastes, and A. B. Christensen, 1984: Spectroscopy of the Extreme Ultraviolet Dayglow During Solar Active Conditions, *G. R. L.*, **8**, 1242.
- Hedin, A. E., 1987: MSIS-86 Thermospheric Model, *J. G. R.*, **92**, 4649.
- Kumar, S., S. Chakrabarti, F. Paresce, and S. Bowyer, 1983: The O⁺ 834-Å Dayglow: Satellite Observations and Interpretation With a Radiation Transfer Model, *J. G. R.*, **88**, 9271.
- Link, R., J. S. Evans, and G. R. Gladstone, 1994: The O⁺ 834-Å Dayglow: Revised Cross Sections, *J. G. R.*, **99**, 2121.
- McCoy, R. P., D. E. Anderson, and S. Chakrabarti, 1985: F₂ Region Ion Densities from Analysis of O⁺ 834-Å Airglow: A Parametric Study and Comparisons With Satellite Data, *J. G. R.*, **90**, 12,257.
- McCoy, R. P., and G. R. Carothers, 1988: Spartan-282: The High Resolution Airglow/Aurora Spectrograph (HIRAAS), *SPIE Vol. 932, Ultraviolet Technology II*, 297.
- McCoy, R. P., R. R. Meier, K. D. Wolfram, J. M. Picone, S. E. Thonnard, G. G. Fritz, J. S. Morrill, D. A. Hardin, A. B. Christensen, D. C. Kayser, J. B. Pranke, P. R. Straus, 1992: Instrumentation on the RAIDS Experiment I: Far-

ultraviolet Spectrograph and Scanning Grating Spectrometers for the Middle and Near Ultraviolet, *SPIE vol. 1745, Instrumentation for Planetary and Terrestrial Atmospheric Remote Sensing*, 75.

McCoy, R. P., R. R. Meier, K. D. Wolfram, J. M. Picone, S. E. Thonnard, G. G. Fritz, J. S. Morrill, D. A. Hardin, A. B. Christensen, D. C. Kayser, J. B. Franke, P. R. Straus, 1994: Far-ultraviolet Imaging Spectrograph and Scanning Grating Spectrometers for the Remote Atmospheric and Ionospheric Detection System, *Optical Engineering*, **33**, 430.

Meier, R. R., 1991: Ultraviolet Spectroscopy and remote Sensing of the Upper Atmosphere, *Space Sci. Rev.*, **58**.

Meier, R. R., and J. M. Picone, 1994: Retrieval of Absolute Thermospheric Concentrations for the Far UV Dayglow: An Application of Discrete Inverse Theory, *J. G. R.*, **99**, 6307.

Menke, W., 1989: *Geophysical Data Analysis: Discrete Inverse Theory*, *International Geophysics Series*, No. 45, Academic Press, San Diego.

Picone, J. M., K. F. Dymond, R. R. Meier, O. Kelley, R. P. McCoy, and R. J. Thomas, 1994: Retrieval of the Ionospheric O⁺ Concentration from O II 834-Å Airglow Using Discrete Inverse Theory I. The Chapman Layer Representation, *J. G. R.*, Submitted.

Press, W. H., B. P. Flannery, S. A. Teukolsky, and W. T. Vetterling, 1986: *Numerical Recipes: The Art of Scientific Computing*, Cambridge University Press, New York, NY.

Strickland, D. J., and R. R. Meier, 1982: A Photoelectron Model for Rapid Computation of Atmospheric Excitation Rates. NRL Memorandum Report, **5004**, Naval Research Laboratory, Washington, DC.

Tarantola, A., and B. Valette, 1982: Generalized Nonlinear Inverse Problems Solved Using the Least Squares Criterion, *Rev. Geophys. and Space Phys.*, **20**, 219.

HYPERSPECTRAL OBSERVATIONS OF THE EARTH'S ATMOSPHERE AND SURFACE FROM THE MSX SATELLITE IN THE SPECTRAL REGION 200 - 900 NM

**D.E. Anderson, G.J. Romick, D. Morrison, J.F. Carbary, L.J. Paxton,
C.-I. Meng, J.-H. Yee and G. Crowley**

**The Johns Hopkins University Applied Physics Laboratory
Johns Hopkins Road, Laurel, Maryland 20723**

ABSTRACT

The Midcourse Space Experiment Satellite (MSX) has a suite of Ultraviolet and Visible imaging spectrographs and imagers that cover the wavelength range from 110 to 900 nm. The versatile pointing capability of the satellite allows observations in the earth limb and below the horizon with observations during the day and night. The wavelength resolution (1-3 nm) for the spectrographs and high spatial resolution in the filtered imagers allows experiments covering a variety of remote sensing issues. Experiments are planned to retrieve ozone, aerosol and nitrogen dioxide from both dayside earthlimb observations and night time stellar occultation observations. Hyperspectral images of terrain and ocean features for specific locations are in the planning stages. Atmospheric emission sources during the day and night in different global locations from the poles to the equator will be observed.

INTRODUCTION

The primary purpose of the MSX satellite, is to collect and analyze phenomenology data related to military targets of interest to the Ballistic Missile Defense Organization (BMDO). This satellite, with an expected five year lifetime, is scheduled for launch in the Fall of 1994 (see Mill, et. al., 1994). The spacecraft, the 9 UVISI instruments, and the contamination investigation instruments were built by The Johns Hopkins University Applied Physics Laboratory (APL). In addition, APL contains the mission and flight operations center and is the primary site for data downlink from the spacecraft. Associated with this mission is a major program for the acquisition of specific global earthlimb and terrestrial backgrounds. Atmospheric and terrestrial backgrounds will be collected as a function of altitude, latitude, longitude and season, under conditions that vary from quiescent to geomagnetically disturbed and including both the presence and absence of auroral precipitation. Major emphasis will be placed on the analysis of the filtered imaging and spectrographic imaging of scenes in terms of the spatial structure seen in the intensity in different wavelength bands. The ultraviolet through the visible wavelength region provides a wealth of information on the atmosphere and the terrestrial surface with respect to both the identification of different stressing scenes and on the physics and chemistry responsible for the observed phenomena. Thus, although most of the emphasis of the early analysis will be directed to scene clutter issues, the successful modeling and prediction of the response of particular sensors requires a fundamental knowledge of the source functions. This leads to the need for well planned satellite observational experiments, detailed characterization of the scene conditions and an in-depth study of the data beyond that needed for just scene cataloging. We describe below a discussion of the ultraviolet and visible instrumentation, examples of proposed experiments and the approach to the organization and analysis of the data.

INSTRUMENTATION

The Ultraviolet and Visible Imagers and Spectrographic Imagers (UVISI) is a suite of nine instruments composed of five spectrographic imagers (SPIMs) and four filtered imagers covering the range from 110 nm to 900 nm. Figure 1 provides a schematic representation of the UVISI instruments on the MSX spacecraft. The nine instruments share a common boresight with each other and with the SPIRIT III IR radiometer, as well as the Space Based Visible (SBV) instrument. Figure 2 shows a sketch of the UVISI instruments, the scan mirror motion is described in Figure 3 and the focal plane

unit with the spectrograph and imager footprints on the focal plane are shown in Figure 4 (Carbary, et al., 1994). For the spectrographic imagers, the CCD detector plane collects an image of the slit length in one direction and spectral information in the other. One spatial dimension is resolved along the slit and the other spatial dimension information is obtained by moving the field of view either 0.05° or 0.1° before recording another observation. Thus, it takes about 10 seconds to complete a $1^\circ \times 1^\circ$ image in either 10 or 20 steps.

The wavelength range and spectral resolution of UVISI is given in Figure 5. With a dynamic range of near 10^{11} , UVISI will have the ability to obtain data ranging from noontime surface reflected visible radiation to observations of the diffuse ultraviolet celestial background. UVISI may be operated in manual or automatic gain selection modes, so that great flexibility is possible in selecting instrument settings for a particular observation.

The UVISI instrument derives from a succession of ultraviolet and visible instruments flown on orbital missions by the Johns Hopkins University Applied Physics Laboratory (APL). The Auroral Ionospheric Mapper flew on the HiLat spacecraft in 1983 (Meng and Huffman, 1984), and its cousin the Auroral Ionospheric Remote Sensor flew on the Polar BEAR spacecraft in 1986 (Schenkel and Orgorzalek, 1987). Both made measurements of the ultraviolet aurora of the Earth. The Hopkins Ultraviolet Telescope made astronomical measurements of 77 celestial objects from the Shuttle STS-35 mission in 1990 (Davidson, et al., 1992). APL instruments also flew on the Department of Defense/Strategic Defense Initiative series of Delta missions and made the first exoatmospheric observations of plume phenomena (Griffin and Fendine, 1988; Holland, et al., 1989).

OBSERVATIONS

MSX will be launched into a 900 km, 3am-3pm orbit in November 1994. Expected lifetime of the spacecraft is five years, with the cryogenically cooled SPIRIT III instrument lifetime estimated at 18-20 months. Except for solar exclusion zones, the MSX spacecraft is a fully steerable spacecraft and experiment plans may thus range from limb scans, to nadir or limb point and stare, to cross track scans. Thus it is possible to simulate a variety of flying, flown and/or planned missions. For example, the Air Force DMSP Block-4 spacecraft will have on board the Special Sensor Ultraviolet Spectrographic Imager (SSUSI) which will obtain nadir to limb scans of far ultraviolet emissions from which ionospheric characteristics will be determined. Experiment plans are under development to operate MSX and UVISI in a SSUSI mode to prototype and test observations and algorithms for the SSUSI Air Force mission. Many other examples have been planned, but we will focus here on two specific plans that are relevant to this community: stellar occultation and daytime limb observations for the retrieval of ozone, aerosol, pressure, temperature and NO_2 in the stratosphere; and land surface and ocean color retrievals.

Stellar occultation experiments require detailed planning sequences which move the spacecraft to lock on to candidate stars and view the stars as they pass through the earth limb. These occultations will utilize all five SPIMS. SPIMS 3,4 and 5 may observe radiation from the ground to space, whereas SPIMS 1 and 2 provide information above 50 km altitude to space. The major challenge in this experiment is to place the candidate star within a pixel and to hold it there as the star 'sets'. With an anticipated pointing accuracy of 0.1 degrees and a post-observation pointing knowledge and precision of 9 micro radians, this should be straightforward. The width of the wide slit of the UVISI SPIMs is 0.1 degree, which implies that, with the projected point accuracy, UVISI should be able to acquire the candidate star. During early stellar occultation experiments, the SPIM scan mirror will be dithered about its center by two steps to assure that the experiment be successful in viewing the star. The pointing knowledge accuracy leads to an observation altitude, or tangent altitude, accuracy of ~ 1 m at the limb. Offsets among the SPIMs will have been determined during the on orbit calibration phase. Figure 6 shows the variation in transmittance expected for a simulated stellar occultation sequence and a mid-latitude ozone profile. A test retrieval utilizing the POAM retrieval algorithms (Lumpe, private communication, 1993) indicates that ozone can be recovered from the tropopause to the mesopause (15-90 km) and NO_2 in the 20-40km altitude region. The Hartley-Huggins absorption bands are utilized for ozone retrieval in the mesosphere and stratosphere. Tropospheric ozone retrievals will utilize the Chappuis bands as well. Water vapor, aerosol, pressure and temperature will also be retrieved using simultaneous constrained least squares fitting techniques. Because of the presence of the narrow and wide field of view imagers, observations of the occultation scene will help provide supporting information regarding the emission sources observed by the spectrographs.

Daytime and nighttime retrievals from solar backscatter and chemiluminescence induced emissions are more straightforward. Retrieval algorithms for both the stellar occultation and solar backscatter will be based on the approach described by Anderson, et al. 1992. In addition to the species identified above, nightglow emissions will provide signatures of wave activity induced changes in the mesosphere and lower thermosphere density and temperature. Dayglow retrievals from observations will provide sodium profiles in the mesosphere, polar mesosphere cloud climatology, mesosphere density variations and solar and auroral energy deposition strengths.

Land Surface and ocean color retrievals are dependent upon wavelength resolution and atmospheric correction. As shown in Figure 6, UVISI has superior wavelength resolution when compared to any comparable satellite sensor, and in general has higher spectral resolution than necessary for ocean or land characteristics retrieval. In addition, because the wavelength range extends from the UV to the near IR, atmospheric correction is better estimated than for narrow band instruments. At UV wavelengths, ozone absorption and rayleigh scattering dominate the signal and by covering 300-900 nm, the aerosol contribution is better estimated because of the advantage that the $1/\lambda^n$ dependence can be determined. Also, at shorter wavelengths the rayleigh scattering signal is less affected by ground albedo, so it is easier to recover a good estimate of the rayleigh contribution. Figure 7 shows the anticipated effects of atmosphere and aerosol on observed radiance as a function of wavelength for a representative soil sample (TEC, 1990).

The spatial footprint when viewing the nadir is 900 m for the UVISI imaging spectrographs and 90 m for the narrow field-of-view imager. When this spatial resolution is combined with the unique spacecraft ability to point and stare with a post-observation pointing knowledge of better than a meter, the MSX UVISI investigation provides a unique opportunity to extract surface, ocean color, aerosol and cloud characteristics at previously unattainable spatial/spectral and time resolution.

DATA REDUCTION AND ANALYSIS

Data obtained from the UVISI instrument will be archived in the Naval Research Laboratory (NRL) Backgrounds Data Center (BDC) and the unclassified backgrounds data will become available to all interested users after the integrity of the data is established. Earlier access to the data is available through direct collaboration with the MSX investigator teams and their individual Data Analysis Centers (DACs). The UVISI-related data will be collected at APL and organized in INGRSS DBMS which allow meta data scanning at 5 second instrument time resolution. The downlink data rate for UVISI is expected to be ~6 Gbytes/day, thus providing a good test for the APL science data management paradigm. Analysis of the UVISI data as described is the primary responsibility of the The Johns Hopkins University APL DAC. The current system configuration includes six SGI and two HP workstations, an SGI XL Challenge with 0.5 Gbytes of memory and eight processors, an on line disc capacity of 80 Gbytes and a near line 350 Gbyte CD jukebox which will contain data subsets. Off line storage will be maintained within a 5 Gbyte exabyte tape storage archive. The archive, near line and on line data will be managed through the DBMS software.

SUMMARY

The UVISI instrument is a combination of narrow field $\sim 1^\circ$ (visible and mid-ultraviolet) and wide field $\sim 10^\circ$ (visible and far ultraviolet) filtered imagers co-aligned with five spectrographic imagers ($\sim 1^\circ \times \sim 1^\circ$) that span the wavelength interval from 110 nm to 900 nm. The spacecraft can make observations in the limb and below the horizon to the nadir in a variety of operational modes. These include constant tangent height scans, stare at a given geographical location either in the limb or below the horizon, fixed arbitrary angle from the spacecraft and combinations of these maneuvers during one experiment plan. Experiment plans now under consideration entail observations at different locations around the globe, at different seasons and at different levels of geomagnetic activity. Specific ground locations for terrain and ocean observations are being planned and other suggestions may be accommodated.

REFERENCES

- Anderson, D.E., J.-H. Yee, L.J. Paxton, G. Crowley, G.J. Romick, J.f. Carbary and C.-I. Meng, Global Modeling of UV/Visible Emissions Observed from Space: Retrieval of Mesosphere/Lower Thermosphere Pressure, Temperature and Ozone, *Proc. ISSSR*, Maui, HI, November, 1992.
- Carbary, J. F., E. H. Darlington, K. Heffernan, T. J. Harris, C. I. Meng, M. J. Mayr, P. J. McEvaddy and K. Peacock, Ultraviolet Imaging and Spectrographic Imaging (UVISI) Experiment, *SPIE, Surveillance Technologies III*, Orlando, Florida, April 6, 1994
- Davidson, A.F., K.S. Long, S.T. Durrance, W.P. Blair, C.W. Bowers, S.J. Conard, P.D. Feldman, H.C. Ferguson, G.H. Fountain, R.A. Kimble, G.A. Kriss, H.W. Moos, and K.A. Potocki, "The Hopkins Ultraviolet Telescope: Performance and calibration during the Astro-1 Mission," *Astrophys. J.* 392, 264-271, 1992.
- Griffin, M.D. and M.J. Rendine, "Delta 180/Vector Sum: the first powered space intercept," *AIAA 26th Aerospace Sciences Meeting*, Reno, NV, January 1988.
- Holland, B.B., J.C. Ray, and A.J. Green, "Delta 181, the Thrusted Vector Mission," *AIAA 27th Aerospace Sciences Meeting*, Reno, NV, January 1989.
- Meng, C.-I. and R.E. Huffman, Ultraviolet imaging from space of the auroral under full sunlight, *Geophys. Res. Lett.*, 11, 315-318, 1984.
- Mill, J.D. R.R. O' Neil, S. Price, G.J. Romick, O.M. Uy, E.M. Gaposchkin, G.C. Light, W.W. Moore, T.L. Murdock, The Midcourse Space Experiment--- MSX, submitted to *Journal of Spacecraft and Rockets*, 1994.
- Schenkel, F. W. and B.S. Orgorzalek, Auroral images from space: Imagery, spectroscopy, and photometry, *APL Tech. Dig.*, 8, 309-317, 1987.
- Satterwhite, M.B. and J.P. Henley, Hyperspectral Signatures (400 to 2500 nm) of Vegetation, Minerals, Soils, Rocks and Cultural Features: Laboratory and Field Measurements, U.S. Army Corps of Engineers, ETL-0573, 1990.

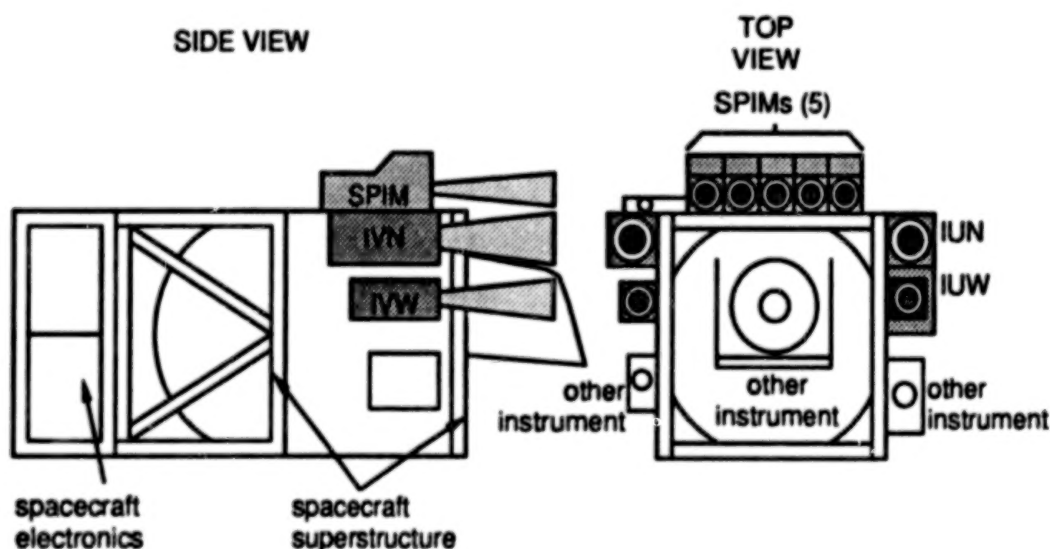


Figure 1. Mounting locations of the UVISI sensors on the MSX spacecraft. All sensors have a common forward-looking orientation.

000000

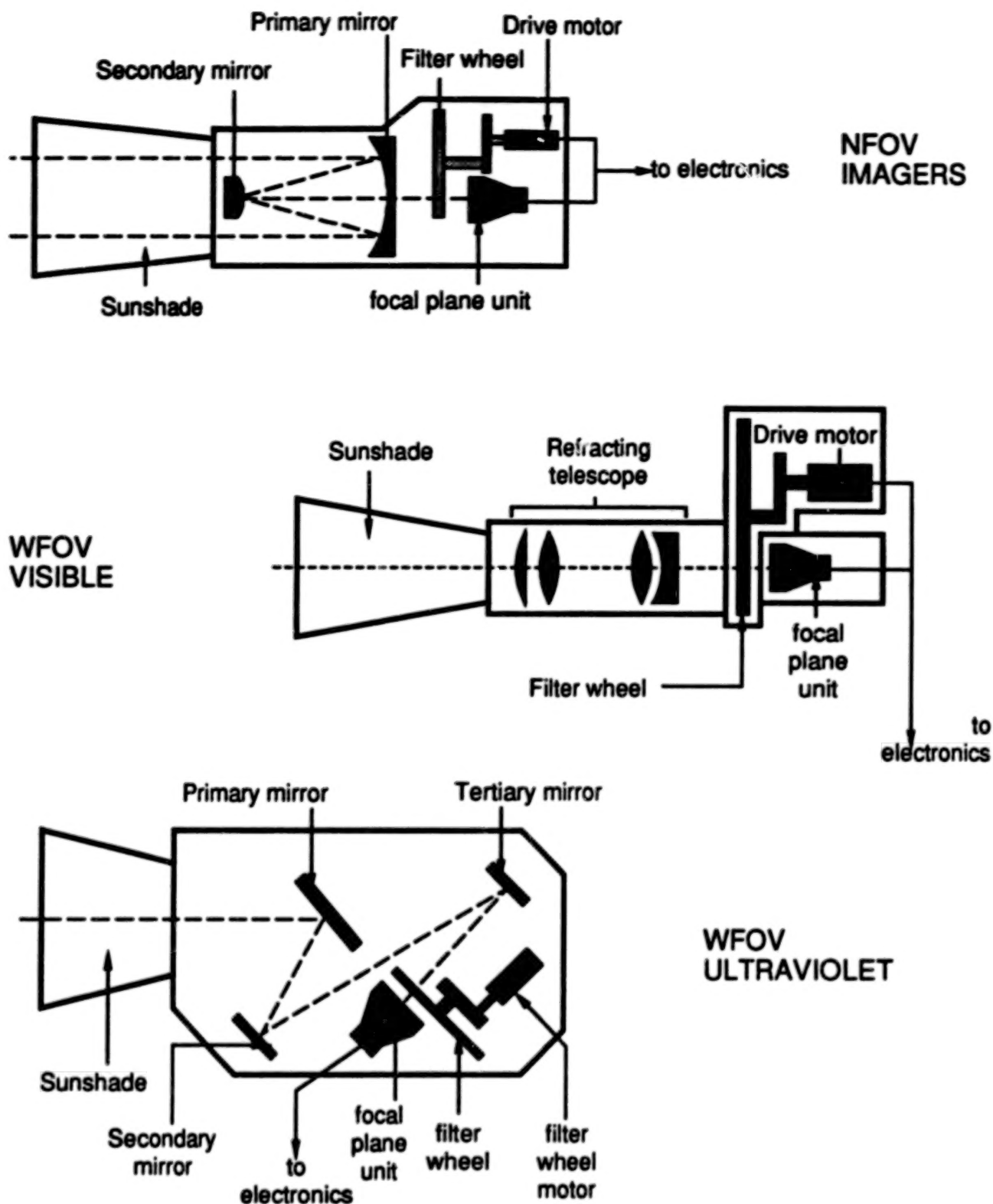


Figure 2a. Schematic diagrams of the three types of UVISI imagers.

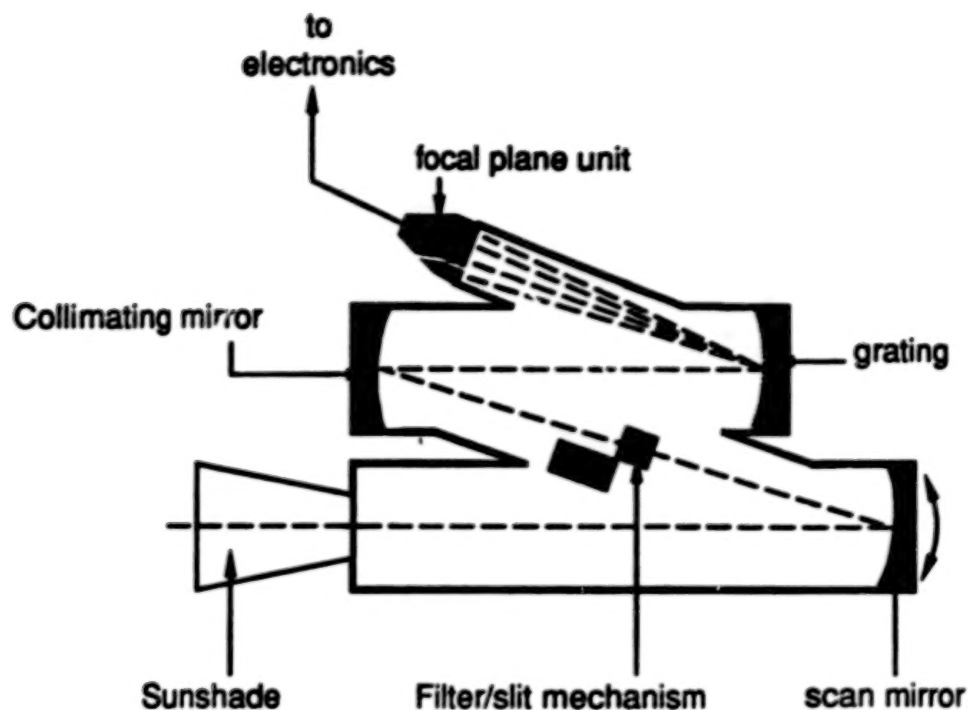


Figure 2b. Schematic diagram of a UVISI spectrographic imager (SPIM).

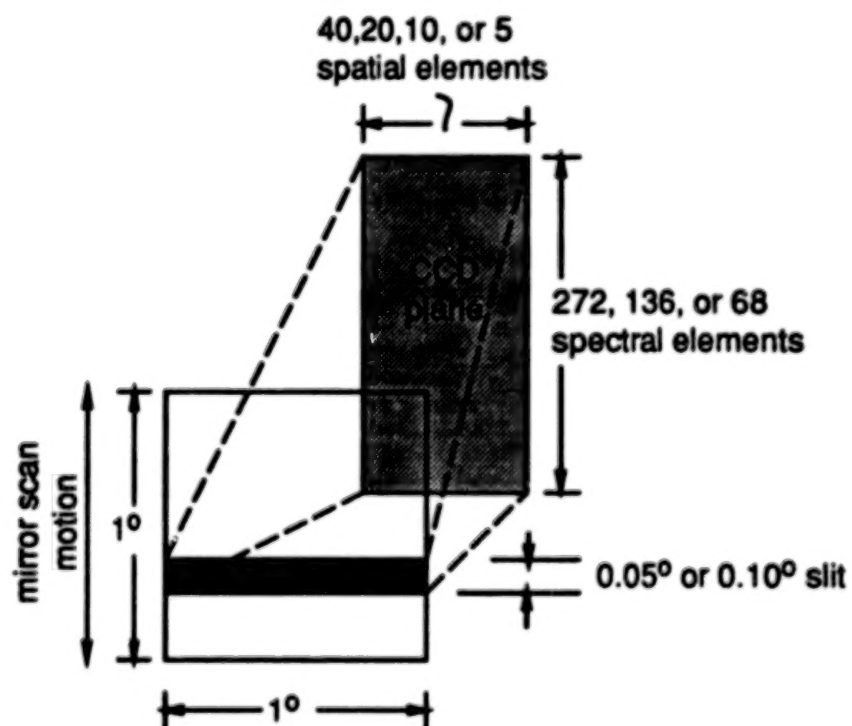


Figure 3. Schematic explanation of how spectrographic imaging works in UVISI SPIMs. On-chip summing of CCD pixels allows selection of various pixel sizes as shown.

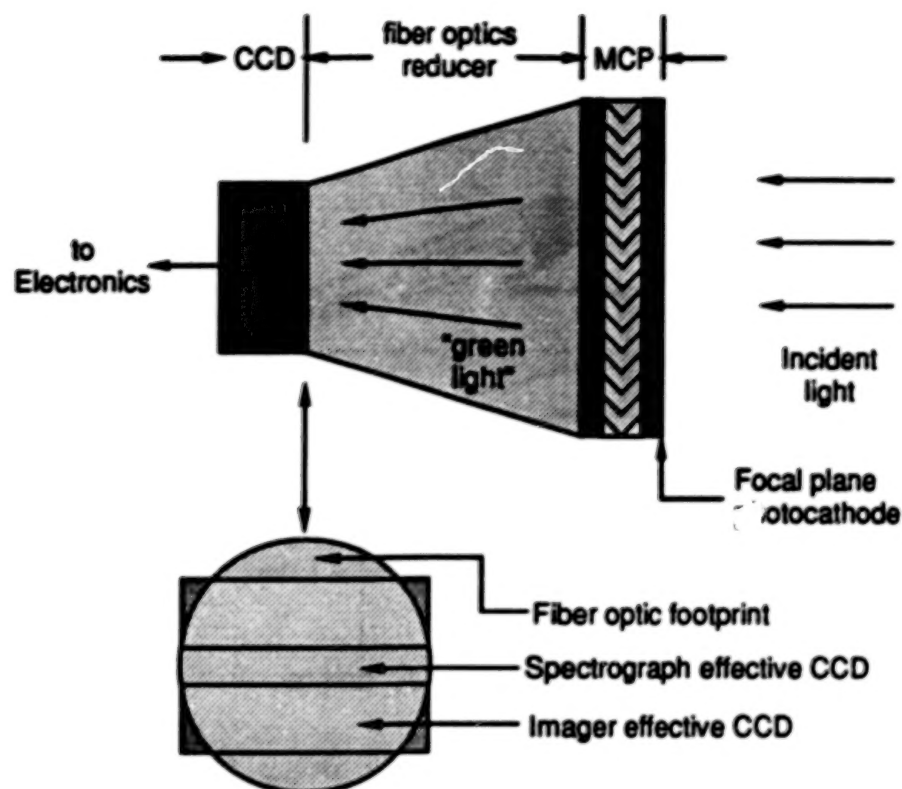


Figure 4. Schematic diagram of UVISI focal plane unit. All focal plane units share a common design that differs only in material of photocathode.

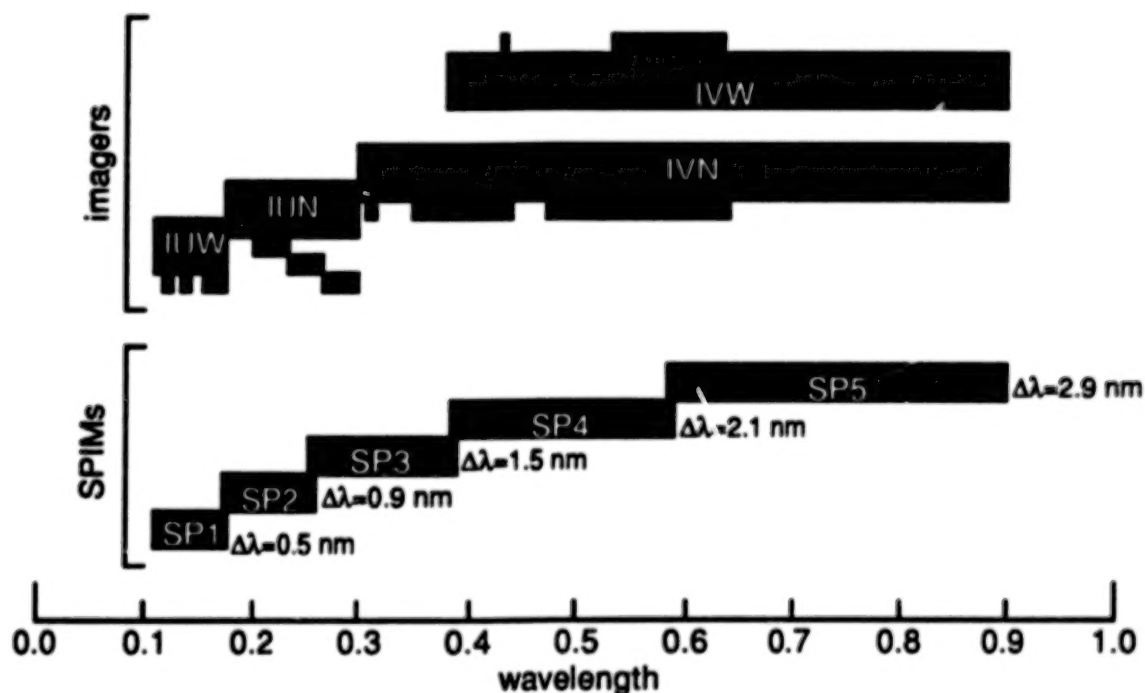


Figure 5. Wavelength coverage of each UVISI sensor. The several bandpass filters of the imagers are shown as smaller rectangles. For the imagers, U, V, N, W indicate ultraviolet, visible, narrow field of view and wide field of view, respectively. The spectral resolution of each SPIM is indicated by $\Delta\lambda$.

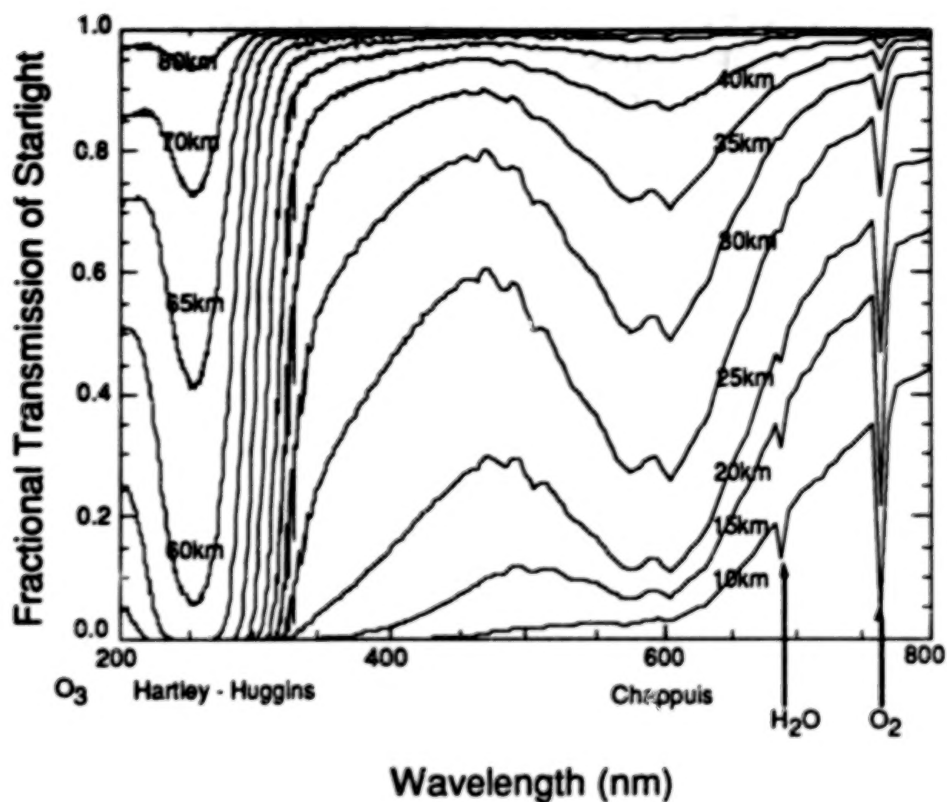


Figure 6. Atmospheric transmission through the atmosphere as a function of wavelength at the tangent altitudes indicated.

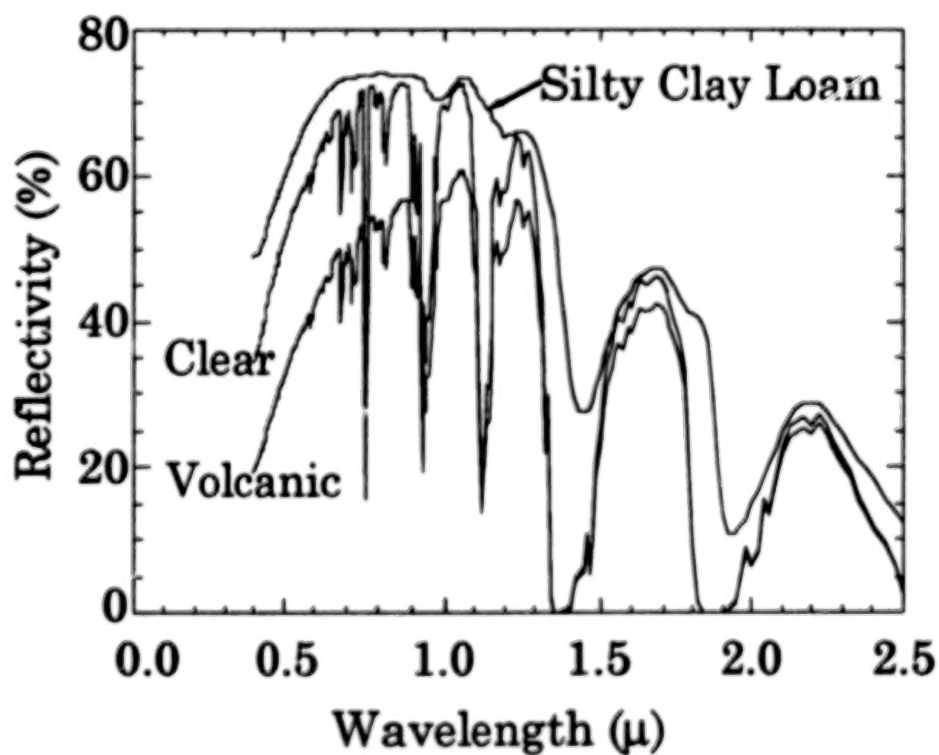


Figure 7. Effects on surface reflectivity of atmosphere and atmosphere plus volcanic aerosol as a function of wavelength.

**COINCIDENT SURFACE AND AIRCRAFT SPECTRAL RESOLUTION
SENSING OF ATMOSPHERIC PARAMETERS: A JOINT
AMERICAN-MEXICAN-RUSSIAN RESEARCH PROGRAM**

Oleg B. Vasilyev
St. Petersburg State University

Now at:
UNAM, Cd. Universitaria, Del. Coyoacan
04510 Mexico, D.F.

Ronald M. Welch
South Dakota School of Mines and Technology
Rapid City, S.D. 57701, U.S.A.

Amando Leyva Contreras, Agustin Muhlia Velazquez
and Ricardo Peralta y Fabi
UNAM, Cd. Universitaria, Del. Coyoacan
04510 Mexico, D.F.

ABSTRACT

On the basis of international collaboration, the development of improved techniques (instruments and methods) for remote sensing of aerosol content in the regional atmosphere is in progress. The SWIF spectroradiometer utilizing Wedge Interference Filters, designed and manufactured in Russia, was used in this research.

The atmosphere affects the retrieval of surface optical parameters in two ways. Radiation is scattered towards the sensor by atmospheric molecules and aerosols, and solar radiation is reflected from the Earth's surface and is attenuated by the atmosphere. In this experiment, large black and white plastic sheets are used as targets. With this approach, aerosol scattering and absorption optical thickness, along with aerosol concentration and size averaged distribution, can be retrieved over land. Spectral remote sensings of two plastic black and white surfaces were made in August 1993 in Rapid City, SD, and at the ARM program site in Oklahoma using the 224-channel AVIRIS instrument onboard the ER-2 aircraft. Simultaneous ground-based measurements at over 200 channels also were taken using the SWIF instrument. The paper presents the first results obtained under this program.

1. INTRODUCTION

It is recognized that aerosols are an important contributor to global climate change. However, accurate retrieval of their concentration, size distribution, optical properties and their spatial/temporal variability over land surfaces measured from surface based aircraft and space-based measurements remains a difficult problem. As a result of international collaboration (American-Mexican-Russian), improved instrumentation and retrieval methodologies were developed for remote and *in situ* sensing of aerosol content in the terrestrial atmosphere.

The atmosphere affects satellite images of the Earth's surface in the optical spectrum in two ways. Atmospheric molecules, aerosols, and clouds all scatter solar radiation. In addition, solar radiation reflected from the Earth's surface is attenuated by the atmosphere. This combined atmospheric effect is wavelength dependent, varies in time and space, and depends on the surface reflectance. Molecular scattering and absorption in the atmosphere are well understood and can be modeled satisfactorily. The effects of gaseous absorption may be minimized by choosing sensor bands in the atmospheric windows. Therefore, the problem reduces to aerosol scattering and absorption and the presence of sub-pixel clouds upon aircraft and satellite imagery. Note that by using high spatial resolution imagery, clouds are detectable. Therefore the retrieved signal can be assumed to be a function of aerosol optical properties alone.

A method for retrieving aerosol properties based on observations of two test surfaces with high contrast (light and dark) is presented. With the advent of new aircraft-based sensors, such as the Airborne Visible and Infrared Imaging Spectrometer (AVIRIS), new approaches are possible. However, natural high contrast surfaces in close proximity are not found everywhere. Therefore, in some cases, artificial surfaces must be constructed.

Using this high contrast surfaces approach, both aerosol scattering and absorption optical thicknesses can be retrieved, along with aerosol concentration and average size distribution. The retrievals then can be validated using surface-based measurements of the atmosphere's spectral transmission.

A research program of this type was initiated in 1993 in Rapid City, SD. Black and white plastic sheets about 140 ft by 140 ft in size were placed on the ground on the 8th of August 1993. Ground-based measurements of their spectral brightness (or reflectance) coefficients (SBC) were made on that date. Late in the morning, an ER-2 AVIRIS over-flight took place. Simultaneous measurements of atmospheric spectral optical depths (SOD) characterizing aerosol optical properties were made using the spectrometer based upon Wedge Interference Filters (SWIF).

This research program was continued at the Atmospheric Radiation Measurement (ARM) program site in Oklahoma during August 1993. A joint research expedition was organized between the American, Mexican, and Russian scientists. Late in the morning on 15 August, two over-flights of the ER-2 took place with the AVIRIS instrument. An overpass of LANDSAT TM (Thematic Mapper) also occurred on this date. Ground-based measurements of the SBC of the black and white sheets and several natural surfaces (soil, grass, concrete, and gravel), and atmospheric SOD using the SWIF were obtained.

This paper presents the first results obtained under this program.

2. INSTRUMENTATION

The Spectroradiometer utilizing Wedge Interference Filters (SWIF) uses a Charge-Coupled Device (CCD) matrix as a sensor. It was designed and constructed for obtaining ground-based and aircraft spectral atmospheric optical measurements. The SWIF's main parameters are given in Table 1.

The SWIF spectroradiometer was designed in the Laboratory of Atmospheric Optics of the Institute of Physics at Saint-Petersburg State University (SPbSU), in the Electronic Laboratory at Saint-Petersburg Electrotechnical University (SPbETU), and in Vavilov's State Optical Institute (VSOI), and

TABLE 1. MAIN PARAMETERS OF THE SWIF INSTRUMENT

Dispersing element	Wedge Interference Filters
Sensor	CCD - matrix
Spectral range	0.35 - 1.15 mm
Spectral resolution	Not less than 0.015-0.02 mm (UV), 0.025-0.03 mm (VIS), and 0.05-0.055 mm (IR)
Field of view	15' (or larger); 2p (flux measurements)
Measuring time	From 1.5 ms to 2 s
Operating voltage	24 - 32 V
Maximum output signal	10 V
Mean square value of output noise	Less than 20 mV
Consumed power	About 30 W
Temperature range	15 - 105°F (-10 - +40°C)
Relative humidity	Not more than 95%

constructed by the Experimental Plants at SPbETU and VSOI. The general view of the optical scheme of the SWIF are shown in Figs. 1 and 2.

To transfer the "image" signal of the CCD-matrix into a linear spectral one, a special computer unit is used which integrates the signal from an area of CCD-matrix, equivalent to some spectral band with a given spectral resolution. After pre-amplification and pre-processing, the output signal is interfaced with an IBM compatible computer. The "dark current" registered and test signals are displayed on the computer monitor. Further processing of the measurements depends on the type of the

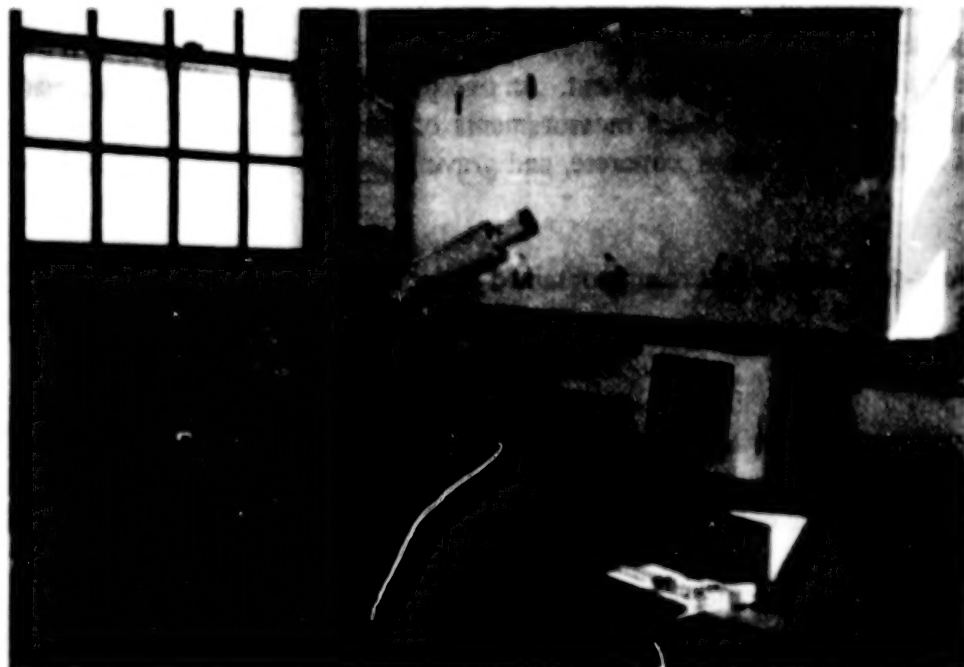
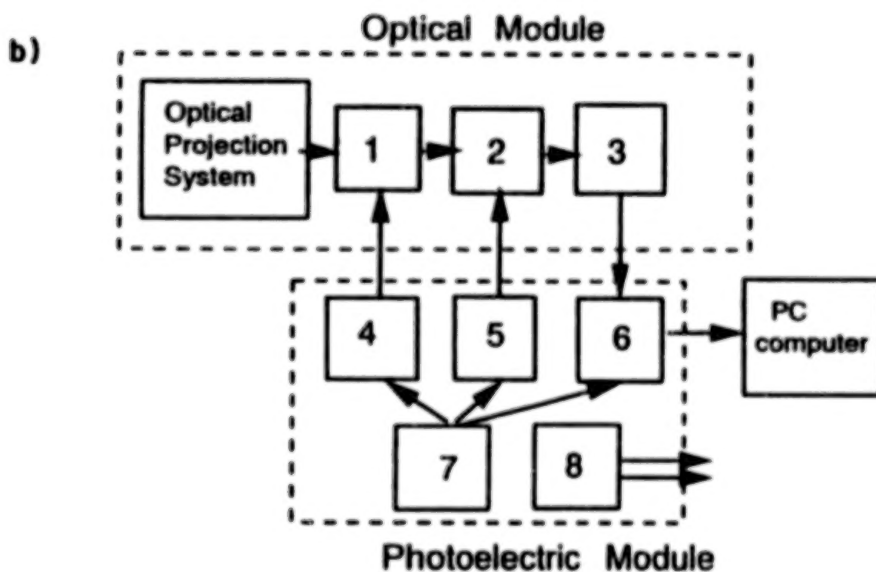
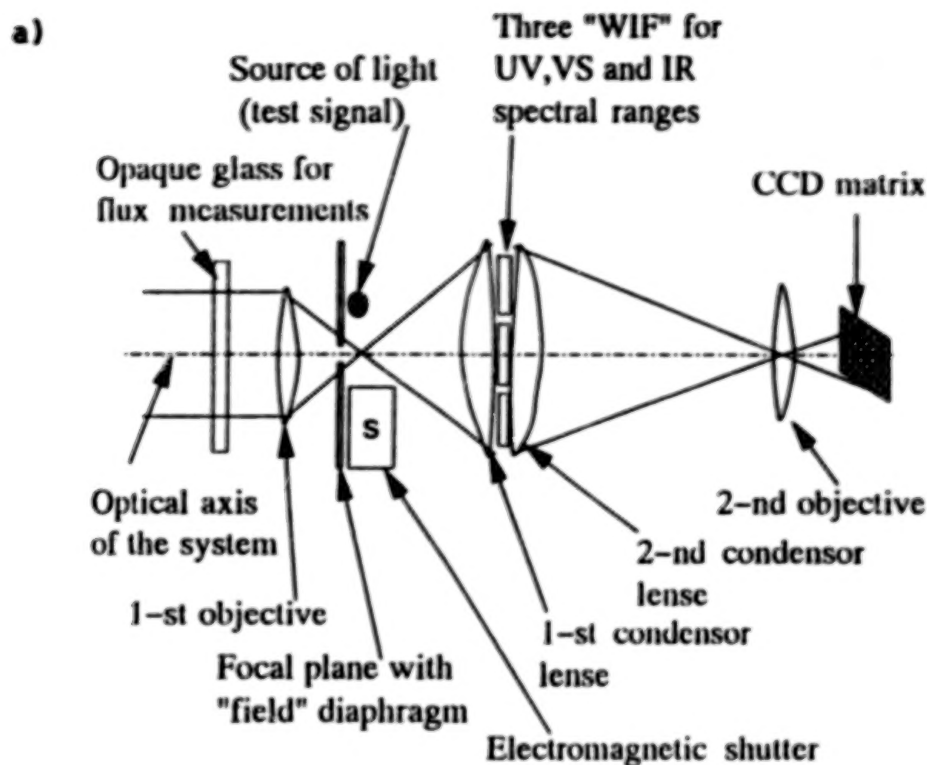


Figure 1. General view of SWIF.



1. Electromechanical shutter
2. 512 x 290 CCD matrix
3. Pre amplifier
4. Shutter control circuitry
5. CCD matrix operating controller
6. Amplifier with signal pre processing capability
7. Synchronizer
8. Power supply circuitry

Figure 2. (a) Optical and (b) block schemes of SWIF.

experiment being conducted. A more detailed description of the SWIF instrument, its wavelength and light calibration, accuracy estimates, etc., will be published soon.

3. SATELLITE/AIRBORNE RETRIEVALS OF AEROSOL PROPERTIES

Aerosol property retrievals from satellite measurements and atmospheric corrections are associated problems (Basu *et al.*, 1990). As mentioned previously, aerosol retrievals generally are made over dark surfaces. For example, aerosol optical thicknesses have been retrieved operationally over the oceans since 1987 (Rao *et al.*, 1989; Stowe, 1991). However, the problem of aerosol property retrievals and atmospheric corrections over variable land surfaces is more difficult. The intervening atmosphere affects satellite measurements in two ways (Fraser *et al.*, 1992). Radiation is scattered to the satellite sensors from atmospheric molecules, aerosols, and clouds. In addition, solar radiation reflected from the surface is attenuated by the atmosphere. This combined atmospheric effect: 1) is wavelength dependent; 2) varies in time and space; and 3) depends upon the spatial distribution of the reflecting surface. Molecular scattering and absorption are well understood and can be accounted for satisfactorily, and gaseous absorption may be minimized by the proper choice of atmospheric window regions. Therefore, aerosol scattering and absorption and the presence of clouds are the main variables. In most cases, clouds can be identified. Therefore, the problem is reduced to a retrieval of aerosol properties.

Aerosol optical thicknesses can be obtained from three sources. Climatology supplies the least accurate values, since the data are sparse and available only at a few wavelengths. Accurate values can be obtained from ground-based measurements of direct solar radiation and from aircraft platforms. Finally, aerosol optical properties can be retrieved from satellite measurements. The tradeoff is that the high accuracy of ground and aircraft measurements are limited both spatially and temporally, while the satellite measurements allow continuous and global coverage but require the use of indirect techniques which must be improved to properly account for aerosol absorption; and they must be validated.

Assume that the surface reflects radiation according to Lambert's law, and that the radiation scattered by the cloud-free atmosphere and the surface is unpolarized. Then the upward spectral radiance L is given by (Chandrasakhar, 1960)

$$L = L_0 + \frac{RF_s T}{\pi(1 - sR)} \quad ; \quad (1)$$

where L_0 is the upward radiance for a zero surface reflectance, R is the surface reflectance, F_0 is the downward flux at the surface, T is the direct plus diffuse transmission from the surface to the satellite sensor, and s is the backscattering ratio. The measured radiance L is a function of the solar zenith angle θ_0 , the observation angle θ , the azimuth angle ϕ , the Rayleigh optical thickness τ_R , the optical thickness of molecular absorption τ_{atm} , aerosol absorption and scattering optical thicknesses τ_a and τ_s , and the height of the surface H above sea level. In order to make reliable retrievals, first one must make radiative transfer calculations in terms of L_0 , F_0 , and s . Such models generally are based upon assumed wavelength dependent values of the aerosol scattering and absorption optical thicknesses (or the single scattering albedo) and the phase function. If L is measured, then R may be found; or if R is known, then L may be calculated using Eq. (1). On the other hand, if both L and R are measured, then it is possible to vastly improve the atmospheric model and to determine the aerosol optical parameters with acceptable accuracy. This is the basis for the proposed investigation.

As reviewed in King *et al.* (1992), methods for retrieving aerosol optical thickness can be classified into two categories: 1) methods using reflectance values in a single image; and 2) methods that rely upon consecutive images taken over the same geographic area. In methods of the first type, optical thicknesses are recovered over selected pixels of the image for which the surface reflectance is very low (i.e., 0.05 or less). This requires that the value of surface reflectance be known a priori with high precision (e.g., clear water or dense vegetation). In methods of the second type, the change in measured contrast between selected pixels in the image is used (Kondratyev *et al.*, 1975; Tanre *et al.*, 1988). The advantage is that they can be applied over terrain without dark pixels. Their disadvantage is that, in order to convert the image differences of optical thicknesses into absolute values, a clear day must be available in which the optical thickness is known from ground-based measurements or assumed a priori.

The use of standard deviations of the distribution of brightness (Tanre *et al.*, 1988), or the suggested use of textural measures, is an improvement over standard techniques. The limitation is that the aerosol absorption and scattering optical thicknesses cannot be separated (or, equivalently, the optical thickness and single scattering albedo). While such separations may not be important for some aerosols such as sea salt, the single scattering albedo for many aerosols over land can be about 0.80 or even smaller (e.g., urban aerosol, smoke, and dust). Note that if the single scattering albedo is on the order of 0.8, and if the surface reflectance is about 0.1, Fig. 3 (Fraser and Kaufman, 1985) shows that methods of the first type cannot retrieve the aerosol optical thicknesses at all. Furthermore, these approaches cannot retrieve optical thicknesses of more than about 0.2 even over the oceans (Durkee *et al.*, 1991; Singh, 1992).

The only method that retrieves both the scattering and absorption optical thicknesses requires the presence of two nearby surfaces of high contrast (Kondratyev *et al.*, 1973, 1974, 1975, 1977; Vasilyev, 1993). As noted by King *et al.* (1992), "For a dark surface ($R \ll 0.1$), the reflectance of the

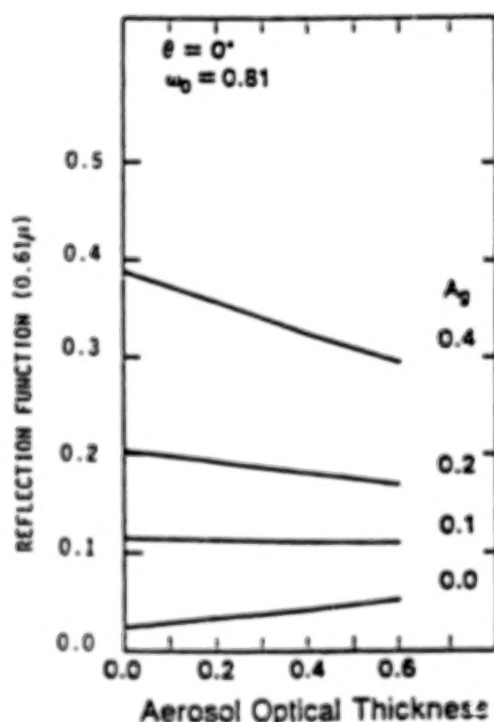


Figure 3. The reflection function for nadir observations ($\theta = 0^\circ$) as a function of aerosol optical thickness and surface reflectance for single scattering albedos $\omega_0 = 0.81$ and for a Junge size distribution given by $n(r) \propto r^{-4}$, where $\lambda = 0.61 \mu\text{m}$ and $\theta_0 = 40^\circ$.

atmosphere dominates such that the reflection function is enhanced over that of the surface alone for both high and low aerosol absorption models. For a bright surface ($R \gg 0.3$), on the other hand, aerosol absorption as well as backscattering of the surface-reflected radiation dominate such that the reflection function of the Earth-atmosphere system is reduced over that of the surface reflection alone." The proposed technique for determination of the spectral optical properties of the atmosphere is based upon experiments carried out on Soyuz-7, Soyuz-9, and on the Salyut space station (Beregovoy *et al.*, 1972; Vasilyev, 1993). It is assumed that the aerosol optical properties are invariant over a distance of several hundred meters.

The satellite measured radiance $L(\lambda)$ may be decomposed into components from the atmosphere $L_0(\lambda)$, radiation reflected once by the surface $L_1(\lambda) R(\lambda)$, radiation scattered twice by the surface $L_2(\lambda) R^2(\lambda)$, etc.:

$$L(\lambda) = L_0(\lambda) + L_1(\lambda) R(\lambda) + L_2(\lambda) R^2(\lambda) + \dots \quad (2)$$

From Monte Carlo experiments, it is found that only the first two components on the right-hand side of Eq. (2) need to be included. Now the spectral reflection function measured from space may be expressed as

$$R(\lambda) = R^h(\lambda) + R_0(\lambda) T(\lambda), \quad (3)$$

where $T(\lambda)$ is the spectral transmission function.

For two test surfaces, labeled "1" and "2",

$$R_1(\lambda) = R^h(\lambda) + R_{0,1}(\lambda) T(\lambda) \quad (4)$$

$$R_2(\lambda) = R^h(\lambda) + R_{0,2}(\lambda) T(\lambda) \quad (5)$$

The solution is:

$$T(\lambda) = [R_1(\lambda) - R_2(\lambda)]/[R_{0,1}(\lambda) - R_{0,2}(\lambda)] \quad (6)$$

$$R^h(\lambda) = R_2(\lambda) - R_{0,2}(\lambda)T = R_1(\lambda) - R_{0,1}(\lambda)T \quad (7)$$

While the contrasting surfaces method is excellent for local aerosol measurements and for in-flight instrument calibration, to be practical for global monitoring purposes, natural surfaces of reasonable contrast must be found. An example of such a contrasting surface is a sandy beach next to a body of water. However, the question remains as to the contrast necessary to retrieve aerosol properties. To make an error estimate, we assume that the error in measuring the surface properties is very low, or that $\delta R_{0,1} \approx 0$ and $\delta R_{0,2} \approx 0$. We find that

$$\delta R^h = R^h \frac{\delta R}{R} \quad (8)$$

$$\delta T \approx 1.4 \frac{\delta R}{R_2 - R_1} T \quad (9)$$

Therefore, the greater the contrast ($R_2 - R_1$), the smaller the error in T . Likewise, the smaller the value of T , the smaller the error in T . For example, taking a sandy beach with $R_2 = 0.35$, a water surface with $R_1 = 0.05$, a transmission of $T = 0.7$, and an error in the satellite measurements of $\delta R = 0.02$, then $\delta T = 0.065$. On the other hand, artificial clean white sheets of plastic have reflectances of about 0.95, while black sheets have values very close to zero. In such cases, the net accuracy is limited to that of the spacecraft sensor.

Note that King *et al.* (1992) propose to retrieve aerosol properties using vegetation as targets. Vegetation typically is dark at $0.66 \mu\text{m}$ and usually quite bright at $0.87 \mu\text{m}$. This characteristic, together with the assumption that single scattering albedo is independent of wavelength over this narrow spectral interval, permits the single scattering albedo to be retrieved. The principal drawback to this approach is that it does not provide the spectral response of the single scattering albedo.

4. SPECTRAL REFLECTANCE CHARACTERISTICS OF NATURAL AND ARTIFICIAL SURFACES USED IN THE EXPERIMENT

In field experiments carried out in Rapid City, SD, and at the ARM program site in Oklahoma during August 1993, measurements of reflectance characteristics of several test surfaces were obtained. These surfaces were both natural and artificial. In Oklahoma, natural surfaces such as soil, grass, concrete, and gravel were also measured. The results are shown in Fig. 4.

Measurements of Spectral Brightness (or reflectance) Coefficients (SBC) of these surfaces are made along with the brightness of a "reference" surface. A 40-cm square sheet of hard board coated with white plastic was used as a reference surface. To determine its absolute SBC, a small 30-square sheet of 18-gauge aluminum was first covered by white paint containing ZnO pigment. Then it was "smoked" by MgO. Such a screen is assumed to have the absolute SBC = 1.00; the reference surface then is compared with this screen. Measured absolute values of the reference screen SBC are shown in Fig. 5.

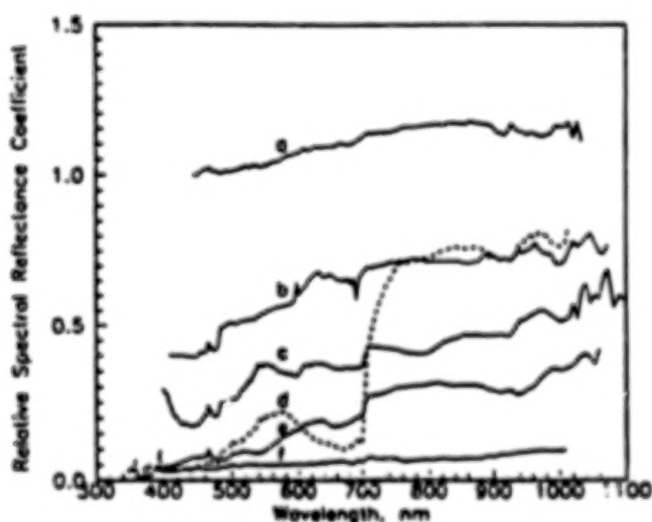


Figure 4. Spectral reflectance coefficients:
a) White pl. surf.; b) concrete;
c) gravel; d) grass (dashed);
e) soil; f) black pl. surf.
(Oklahoma, 16 Aug 1993)

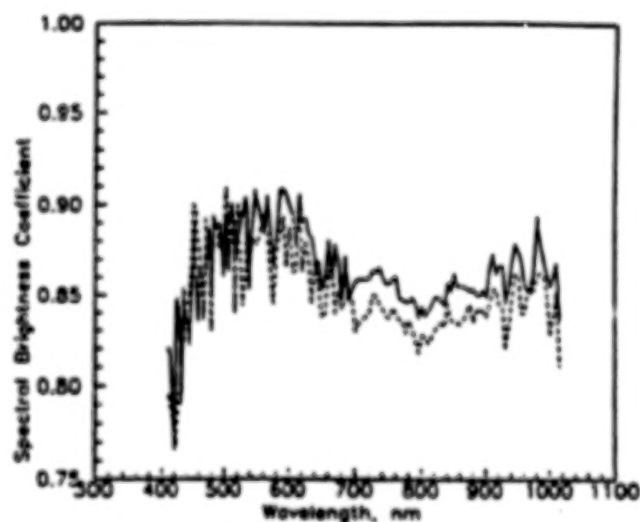


Figure 5. Absolute calibration of reference surfaces: Rapid City (solid); Mexico City (dashed).

In Rapid City, measurements of the reflectance characteristics of black and white plastic sheets were obtained at different angles to estimate their bi-directional dependencies. Further processing showed that the difference between measurements obtained at different angles is less than the observational errors caused by the specular reflectance characteristic of plastic sheets.

Figure 6a shows AVIRIS imagery obtained at the ARM program site in Oklahoma on August 15, 1993. The pixels with black and white sheets are shown at different scales. The spectral dependencies of the black and white sheets are shown at the bottom of Fig. 6.

AVIRIS measurements were compared to those obtained using the ground-based SWIF instrument in Rapid City, SD, and at the ARM program site in Oklahoma. The results show that the SBC of white surfaces from ground-based measurements differ considerably from those obtained from

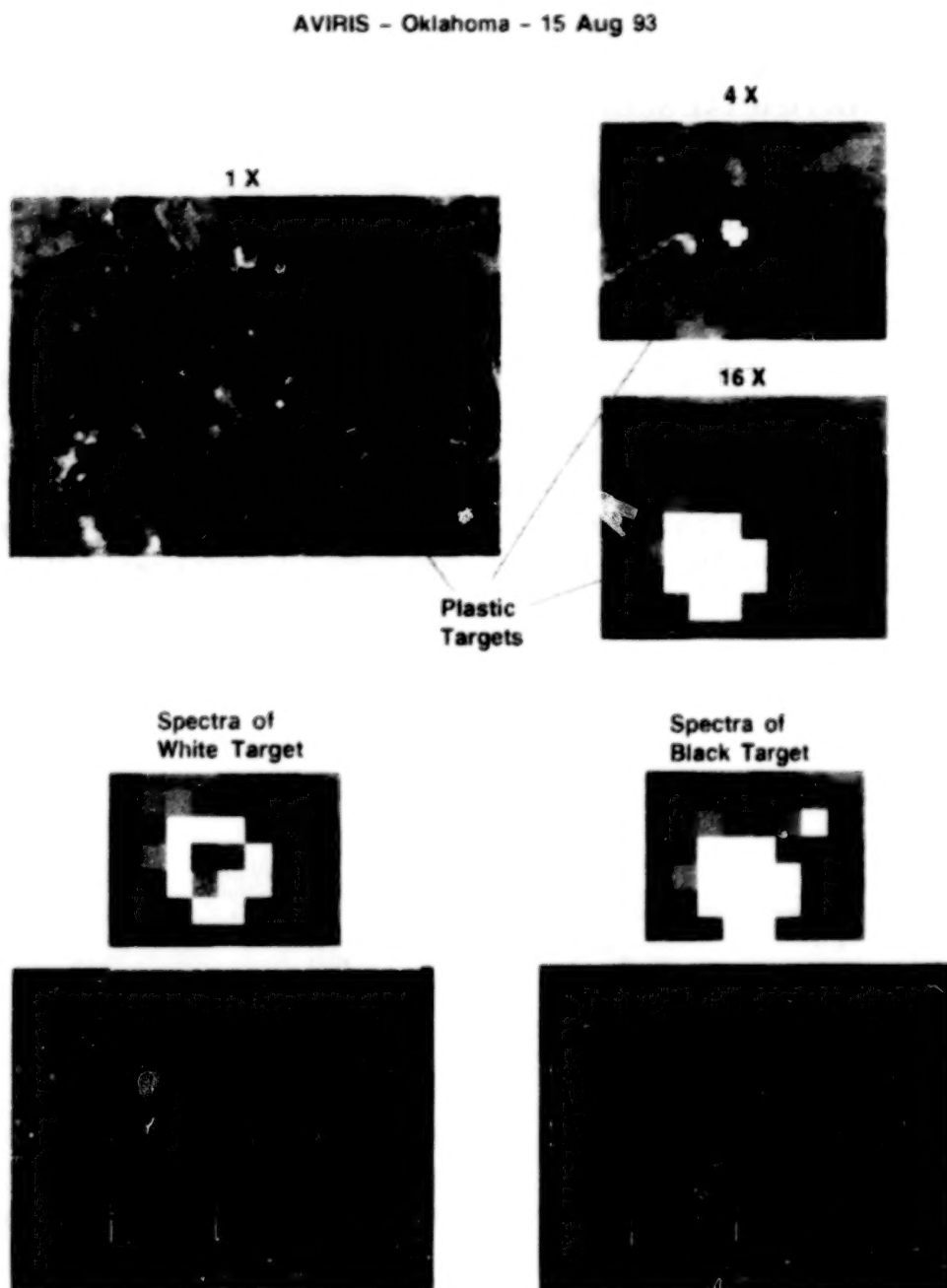


Figure 6. ER-2 imagery received using AVIRIS at ARM program site in Oklahoma on 15 Aug 1993.

the AVIRIS data. The reason is that the ground-based measurements of SBC were made with multiple layers of material. However, a more thorough examination of white plastic material proved that it is transparent. Laboratory measurements of SBC of the white plastic sheets over a dark background (like grass in Rapid City or soil in Oklahoma) provided a better agreement with the AVIRIS measurements (see corresponding curve on Fig. 7a).

Figures 7a and 8a show the SBC curves taken using both the ground-based instruments and the AVIRIS in Rapid City, SD, and at the ARM program site in Oklahoma, and Figs. 7b and 8b show the preliminary results of processing these data in the spectral range 450 through 700 μm using Eqs. (6) and (7). The effective spectral transparency coefficient of the atmosphere $t(\lambda)$ determined from AVIRIS is somewhat less than measured by SWIF, and the SBC of atmospheric haze $R^{(h)}(\lambda)$ is higher than determined by SWIF. Note that the angular field of view of the SWIF instrument is equal to 15'. Therefore, the size of the measured spot on the plastic material was approximately 1/2 - 1 cm, which is insufficient to average over inhomogeneities and undulations of the plastic surface. The angular field of view of the instrument must be enlarged (by about 10 times).

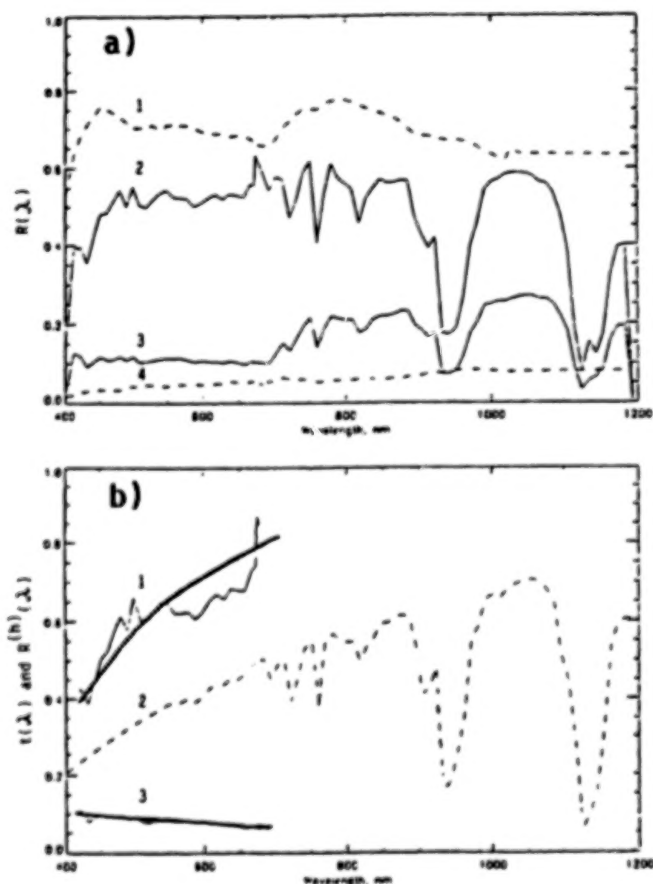


Figure 7. Results of the experiment in Rapid City, SD, on 9 Aug 1993.

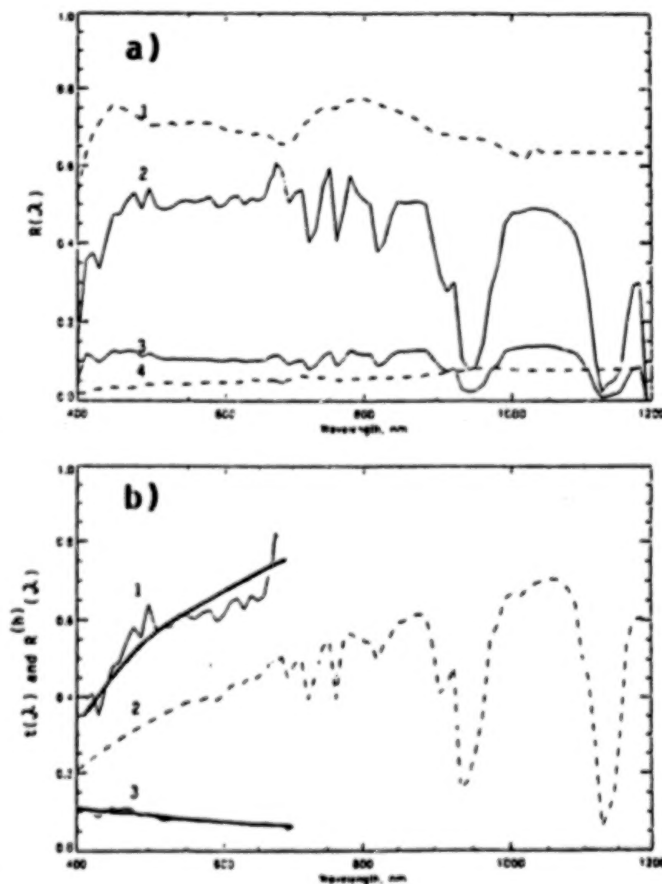


Figure 8. Results of the experiment at the ARM program site in Oklahoma on 15 Aug 1993.

[Note: For both figures: (a) Spectral brightness coefficients of white (1 and 2) and black (3 and 4) plastic sheets, measured by AVIRIS (2 and 3) and SWIF (1 and 4) instruments; (b) parameters of the transfer operator of the Earth's atmosphere $t(\lambda)$ -1 and $R^{(h)}(\lambda)$ -3 and $t(\lambda)$, according to LOWTRAN for the visibility equal to 15 km - 2.]

5. CONCLUSIONS

Experiments onboard the IL-18 airplane and the "Soyuz-7" and "Soyuz-9" spacecrafts conducted in the early 70's using natural high contrast test surfaces proved that optical properties of the terrestrial atmosphere and surface may be retrieved. However natural test surfaces, having high contrast and located in close proximity, are not found everywhere. Therefore, it is important to develop methods using artificial black and white surfaces. In August 1993, in Rapid City, SD, and at the ARM program site in Oklahoma, SBC of black and white plastic sheets (approximately 140 ft x 140 ft) were measured by the AVIRIS-instrument from the ER-2 airplane, which overflew them at the height of 20 km. Simultaneous ground-based (and later laboratory) measurements of SBC of these plastic sheets were made.

Processing of this data gave the parameters of the transfer operator of the terrestrial atmosphere. These turbidity values are higher than measured by the SWIF sunphotometer. The problem seems to be related to the angular field of view of the SWIF instrument which is too small to average the inhomogeneities and undulations of the plastic sheets.

ACKNOWLEDGMENTS

The authors express their gratitude for the excellent technical support of technical personnel of the ARM program site in Oklahoma, Remote Sensing Group of IAS at SDSM&T, the Observatory of Solar Radiation at IGf UNAM, and the Laboratory of Experimental Atmospheric Optics of IPh at SPbSU. Their special gratitude to Rand E. Feind, Todd Berendes, and Vladileu Isakov from IAS, SDSM&T, and to Vidal Valderrama from IGf UNAM.

The activities were financially supported from the funds of the Institute of Atmospheric Sciences at SDSM&T, the Institute of Physics at SPbSU, the Institute of Geophysics and the Institute of Engineering, both at UNAM, and also by the U.S. National Research Council and the National Council for Science and Technology (CONACyT) of Mexico. They were planned and fulfilled within the framework of the Agreements on Scientific Collaboration between IAS SDSM&T and IPh SPbSU for 1993-1995 and between UNAM and SPbSU for 1991-1995. One of us, Dr. Oleg B. Vasilyev, expresses appreciation to the U.S. National Research Council for a one-year research fellowship.

REFERENCES

- Basu, S., M. Tewari and V. K. Agarwal, 1990: A model for retrieval of surface spectral reflectance from satellite radiance measurements using realistic atmospheric aerosol profiles, *Intl. J. Remote Sensing*, 11, 395-407.
- Beregovoy, G. T., A. A. Buznikov and O. B. Vasilyev, 1972: *Investigations of Environment from Manned Space Stations*, Gidrometizdat, Leningrad, 400 pp. [In Russian]
- Chandrasakhar, S., 1960: *Radiative Transfer*, Dover, New York, 273 pp.
- Durkee, P. A., F. Pfeil, E. Frost and R. Shema, 1991: Global analysis of aerosol particle characteristics, *Atmos. Environ.*, 25A, 2457-2471.
- Fraser, R. S., and Y. J. Kaufman, 1985: The relative importance of aerosol scattering and absorption in remote sensing, *IEEE Trans. Geosci. Remote Sensing*, 23, 625-633.

- Fraser, R. S., R. A. Ferrare, Y. J. Kaufman, B. L. Markham and S. Mattoo, 1992: Algorithm for atmospheric corrections of aircraft and satellite imagery, *Intl. J. Remote Sensing*, **13**, 541-557.
- King, M. D., Y. J. Kaufman, W. P. Menzel and D. Tanré, 1992: Remote sensing of cloud, aerosol, and water vapor properties from the moderate resolution imaging spectrometer (MODIS), *IEEE Trans. Geosci. Rem. Sensing*, **30**, 2-27.
- Kondratyev, K. Ya., O. B. Vasilyev, A. A. Grigoryev and G. A. Ivanyan, 1973: An analysis of the Earth's Resources Satellite (ERTS-1) data. *Remote Sens. Environ.*, **2**, 273-285.
- Kondratyev, K. Ya., O. B. Vasilyev, *et al.*, 1974: Remote sensing of natural formations from measurements of radiance coefficients. *Acta Astronautica*, **1**, 1415-1426.
- Kondratyev, K. Ya., A. A. Buznikov, O. B. Vasilyev and O. I. Smoktiy, 1975: Influence of the atmosphere on the spectral brightness and contrasts of natural formations in spectrophotometry of the earth from space. *Izv. Atmos. Ocean Phys.*, **11**, 210-218.
- Kondratyev, K. Ya., A. A. Buznikov, O. B. Vasilyev and O. I. Smoktiy, 1977: Influence of the atmosphere on the albedo in aerospace photography of the earth in visible light. *Izv. Atmos. Ocean Phys.*, **13**, 330-340.
- Rao, C. R. N., L. L. Stowe and L. L. McClain, 1989: Remote sensing of aerosol over the oceans using AVHRR data: Theory, practice, and applications, *Intl. J. Remote Sensing*, **10**, 743-749.
- Singh, S. M., 1992: Accuracy of atmospheric correction algorithm using ATM data, *Intl. J. Remote Sensing*, **13**, 559-569.
- Stowe, L. L., 1991: Cloud and aerosol products at NOAA/NESDIS, *Palaeogeogr., Palaeoclimatol., Palaeoecol.* (Global Planet. Change Sect.), **90**, 25-32.
- Tanré, D., P. Y. Deschamps, C. Devaux and M. Herman, 1988: Estimation of Saharan aerosol optical thickness from blurring effects in Thematic Mapper data, *J. Geophys. Res.*, **93**, 15,955-15,964.
- Vasilyev, O. B., 1993: The methodology for determination of the optical properties of the atmosphere based on the observation of test surfaces from space. In *IRS '92: Current Problems in Atmospheric Radiation, Proceedings of the International Radiation Symposium*, Tallinn, Estonia, A. Keepak Publ., Hampton, VA, 345-348.

ESTIMATION OF CIRRUS CLOUD AND AEROSOL SCATTERING IN HYPERSPECTRAL IMAGE DATA

E. Ben-Dor¹, A. F. H. Goetz^{1,2}, A. T. Shapiro¹

¹Center for Study of Earth from Space (CSES), Cooperative Institute for Research
in Environmental Science (CIRES), University of Colorado, Boulder

²Department of Geological Sciences, University of Colorado, Boulder
Boulder, CO 80309-0216, USA

ABSTRACT

An algorithm based on the normalized depth of the oxygen band at $0.76\mu\text{m}$ was developed to correct raw AVIRIS data for aerosol scattering in this band. The basic assumptions for this development were that the oxygen is uniformly distributed in a given scene and there is no topographic relief. The natural logarithms of the radiance values obtained at the center of the oxygen absorption band (A), ratioed to the continuum radiance value at the same wavelength (R) was the basic parameter used to derive the scattering effect on a pixel-by-pixel basis. Three AVIRIS data sets containing different thickness and densities of cirrus clouds were selected for this study. Applying the algorithm produced scattering distributions that were highly correlated with the $1.38\mu\text{m}$ cirrus image maps. Compared to the 5S code in cirrus-free areas, the Oxygen Offset (OOS) method yields more scattering at $0.76\mu\text{m}$. The OOS scattering value can be used in conjunction with the 5S model enabling a more accurate modeling of scattering at all wavelengths.

1. INTRODUCTION

Scattering of aerosol particles and molecules in the atmosphere must be accounted for when calculating apparent reflectance of the Earth's surface (Gao et al., 1991; Goetz, 1993; Green and Conel, 1993). Many techniques have been developed to determine the scattering effects from a given scene (Conel et al., 1987; Kneizys et al., 1988; Bosch and Alley, 1991; Moran et al., 1992; Teillet, 1992; Carder et al., 1993). Aerosol models, visibility, and optical depth are the most important parameters used to estimate the scattering function (Kneizys et al., 1988; Gao et al., 1993b; Green and Conel, 1993; Green et al., 1993). Nevertheless, these parameters still assume that the scattering is uniform, and no correction for local scattering is available.

Hyperspectral imagers such as the Airborne Visible/Infrared Imaging Spectrometer (AVIRIS) (Vane, 1987) provide spectral information that allows direct identification of surface materials and atmospheric gases (Goetz, 1991, 1992). Using the narrow band characteristics of the unsaturated atmospheric water absorption features from AVIRIS data enables the quantification of the amount of water vapor and subsequent removal of its effect on a pixel-by-pixel basis (Gao and Goetz, 1990; Carrere and Conel, 1993; Gao et al., 1993b). This method is based on the values of the maximum absorption of water vapor at $0.94\mu\text{m}$ and $1.14\mu\text{m}$ to the continuum. Green and Conel (1993) showed that an empirical equation for predicting surface elevation can be developed by estimating the pressure altitude of oxygen using the ratio of the oxygen minimum at $0.76\mu\text{m}$ to the continuum. Whereas the scattering effect of aerosols is small in the water absorption band at $0.94\mu\text{m}$, around the oxygen absorption band at $0.76\mu\text{m}$ this component is more important (Teillet, 1990; Bosch et al., 1993). In addition to the information about the oxygen content from in the sun-surface-sensor path, both cirrus clouds and aerosols particles may affect the oxygen absorption depth at $0.76\mu\text{m}$. Since oxygen is considered to be a well-mixed gas, variations in uniformity may be attributed to scattering effects of aerosol and cirrus cloud particles as well as changes in elevation.

The scope of this paper is to study the above assumption and to develop an algorithm for detecting aerosol and cirrus scattering on a local basis from AVIRIS data using the oxygen band of $0.76\mu m$.

2. THE OXYGEN OFFSET (OOS) ALGORITHM APPROACH

The radiance at a downward-looking sensor for a given wavelength can be written, according to Esaias et al. (1986), in a simplified form as follows:

$$L_s(\lambda) = \frac{E(\lambda)R(\lambda)T(\lambda)}{\pi} + L_p(\lambda) \quad (1)$$

where λ is the wavelength, $L_s(\lambda)$ is the radiance at the sensor, $E(\lambda)$ is the solar irradiance on a horizontal surface above the atmosphere, $T(\lambda)$ is the total atmospheric transmittance in the sun-surface-sensor path, $R(\lambda)$ is the surface reflectance at the observational geometry, and $L_p(\lambda)$ is the scattered path radiance, including effects of single and multiple scattering.

Rearranging Equation 1 for a given wavelength (λ) reveals:

$$(L_s - L_p)\pi = ERT \quad (2)$$

Using a hyperspectral sensor such as AVIRIS provides sufficient spectral resolution to permit analysis of a specific absorption feature. By selecting the absorption feature for O_2 near $\lambda = 0.76\mu m$, we assume that the atmospheric transmittance T is mostly affected by the oxygen absorption along the sun-surface-sensor path as follows:

$$T = e^{(-kx_1l_1)}e^{(-kx_2l_2)} \quad (3)$$

Where x_1 and x_2 are the amount of oxygen (mole, gram, or mbar) per pixel volume along the sun-surface and surface-sensor pathways respectively, l_1 is the sun-surface pathway distance for the downward direction, l_2 is the surface-sensor pathway distance for the upward direction, and k is the integral coefficient of absorption for oxygen. Substituting Equation 3 in Equation 2 reveals:

$$(L_s - L_p)\pi = ER e^{(-kx_1l_1)}e^{(-kx_2l_2)} \quad (4)$$

Denoting $x_1 + x_2$ as the total oxygen amount along the sun-surface-sensor pathway (x), $l_1 + l_2$ as the optical pathway (l) and rearranging Equation 4 by applying natural logarithms to the results yields:

$$\ln\left(\frac{(L_s - L_p)\pi}{E}\right) = \ln(R) - (kxl) \quad (5)$$

If no oxygen absorption occurred at $\lambda = 0.76\mu m$ ($T = 1$ in Equation 1), the reflectance $R_{(\lambda=0.76\mu m)}$ could be obtained from Equation 1 as follows:

$$R = \frac{(L_s^* - L_p)\pi}{E} \quad (6)$$

where L_s^* is the radiance at the sensor assuming no oxygen absorption is present. In the presence of oxygen R is estimated by interpolating the continuum line around the minimum of the oxygen absorption feature and assuming that the reflectance there is a linear function of the wavelength. The scattering parameter is:

$$D = \frac{\pi L_p}{E} \quad (7)$$

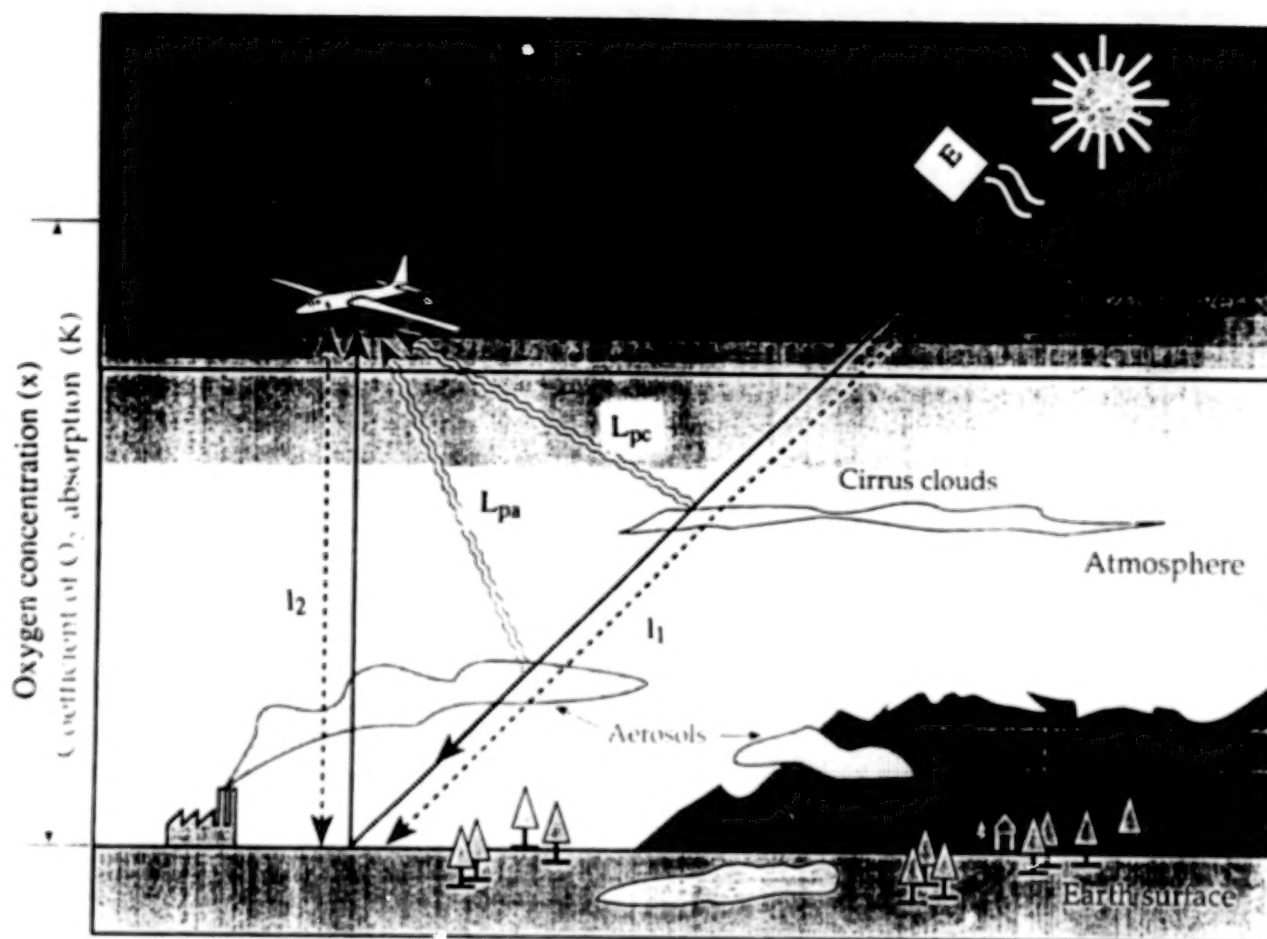


Figure 1. An illustration represents the radiation pathway from the sun via the surface to the sensor during typical AVIRIS flight. Also given are the oxygen distribution along the atmosphere, scattering parameters (aerosols and cirrus cloud) and typical landscape of a study scene.

Then, the optical depth

$$kxl = \ln \left(\frac{A - D}{R - D} \right) \quad (8)$$

Considering that k is a constant value for a given AVIRIS overpass, and assuming l has minimal variation within the scene i.e., ground elevation is relatively constant, Equation 8 shows that the ratio between the oxygen absorption band (A) and the surface apparent reflectance at this band (R), both corrected for the atmosphere scattering effects (D), is an exponential function of the oxygen amount from the sun-surface-sensor pathway (x). Assuming that the oxygen is a well-mixed gas and no topographic variation occurs, calculation of $\ln(A - D/R - D)$ on a pixel-by-pixel basis should yield a featureless image if the appropriate D value is used. Figure 1 gives a schematic illustration of the interaction of photons with oxygen and atmospheric particles through the sun-surface-sensor path.

We assume that two scattering mechanisms occur within a given scene. One is a scattering that occurs from aerosol particles uniformly distributed within the scene (L_{pa}), and the other is scattering that occurs from the existence of cirrus clouds (visual and sub-visual), which are nonuniformly distributed within the scene (L_{pc}).

Solving for D within Equation 8 within cirrus free areas represents aerosol scattering at the oxygen absorption wavelength. In order to determine this parameter, it is essential first to mask out

the cirrus covered areas by using the $1.38\mu\text{m}$ band image (Gao et al., 1993a). Then, in the cirrus free areas, it is assumed that two targets with non-similar reflectance characteristics will show similar optical depths. This is because the oxygen, as a well mixed gas, must be uniformly distributed above these targets. Thus, offsetting the original A and R parameters by D until a featureless oxygen image is obtained is the algorithm suggested for calculating the aerosol scattering parameter D .

3. DATA ANALYSIS

3.1 AVIRIS DATA

The Airborne Visible and Infrared Imaging Spectrometer (AVIRIS) acquires images in 224 channels (10nm intervals) between 400-2500nm from an altitude of 20km (Goetz, 1991). The swath subtends $\pm 15^\circ$ about nadir yielding an 11km width and a pixel size of 20m.

For this study, three AVIRIS data sets, having different amounts of cirrus cloud coverage, were selected. The data were: 1) Coffeyville, Kansas, acquired on December 5, 1991 (heavy cirrus), 2) Blackhawk Island, Wisconsin, acquired on June 21, 1992 (light cirrus), and Rogers Dry Lake, California, acquired on May 30, 1992 (no cirrus). All these locations were characterized by minor topographic variations and by targets that contain variations in the surface reflectance. The Coffeyville data were acquired in December and therefore were in an area mostly free of vegetation, consisting of urban areas, roads, and a river. Blackhawk Island is an area that was covered by dense vegetation, urban areas and roads crossed by the Wisconsin River. The Rogers Dry Lake image contains a playa and surrounding desert with a wide albedo variation.

AVIRIS is radiometrically and spectrally calibrated in the laboratory as well as with an onboard calibrator (Chrien et al., 1990; Green, 1990). Inflight radiometric calibration is achieved by using a reflectance-based method in which the spectral radiance from a uniform ground target is compared with the spectral radiance calculated at AVIRIS flight altitude using MODTRAN (Berk et al., 1989) or LOWTRAN (Kneizys et al., 1988) codes. The raw AVIRIS data used in this study were treated according to the above procedure. However, as Green (1990) has pointed out, errors in calibration may occur and they will directly affect the retrieved reflectance.

3.2 DATA PROCESSING

Processing was based on the above equations. The solar irradiance curve used was a combination of Neckel and Labs (1984) (for $0.4 - 1.2\mu\text{m}$) and ATMOS (for $1.2 - 2.5\mu\text{m}$) curves (Green and Gao, 1993). This spectrum was corrected for solar zenith angle based on the AVIRIS flight time and geographic location (latitude and longitude) of the scene. In order to generate the L_s^* , we calculated the continuum line around the oxygen absorption feature at $0.76\mu\text{m}$. This was done by generating a spline curve based on the six bands around the oxygen band. We then created a cirrus image map from the $1.38\mu\text{m}$ band according Gao et al. (1993a) and masked out the areas with cirrus cover.

In order to judge objectively the uniformity of the oxygen image, we applied a test that was based on two targets within the cirrus free areas. The test compares the $\ln(A/R)$ values of two contrasting albedo targets after offsetting the oxygen A and R values by D .

4. RESULTS AND DISCUSSION

Figure 2 presents a typical AVIRIS spectrum obtained for each of the data sets. In each of the three spectra the oxygen feature at around $0.76\mu\text{m}$ is very sharp. Due to different wavelength

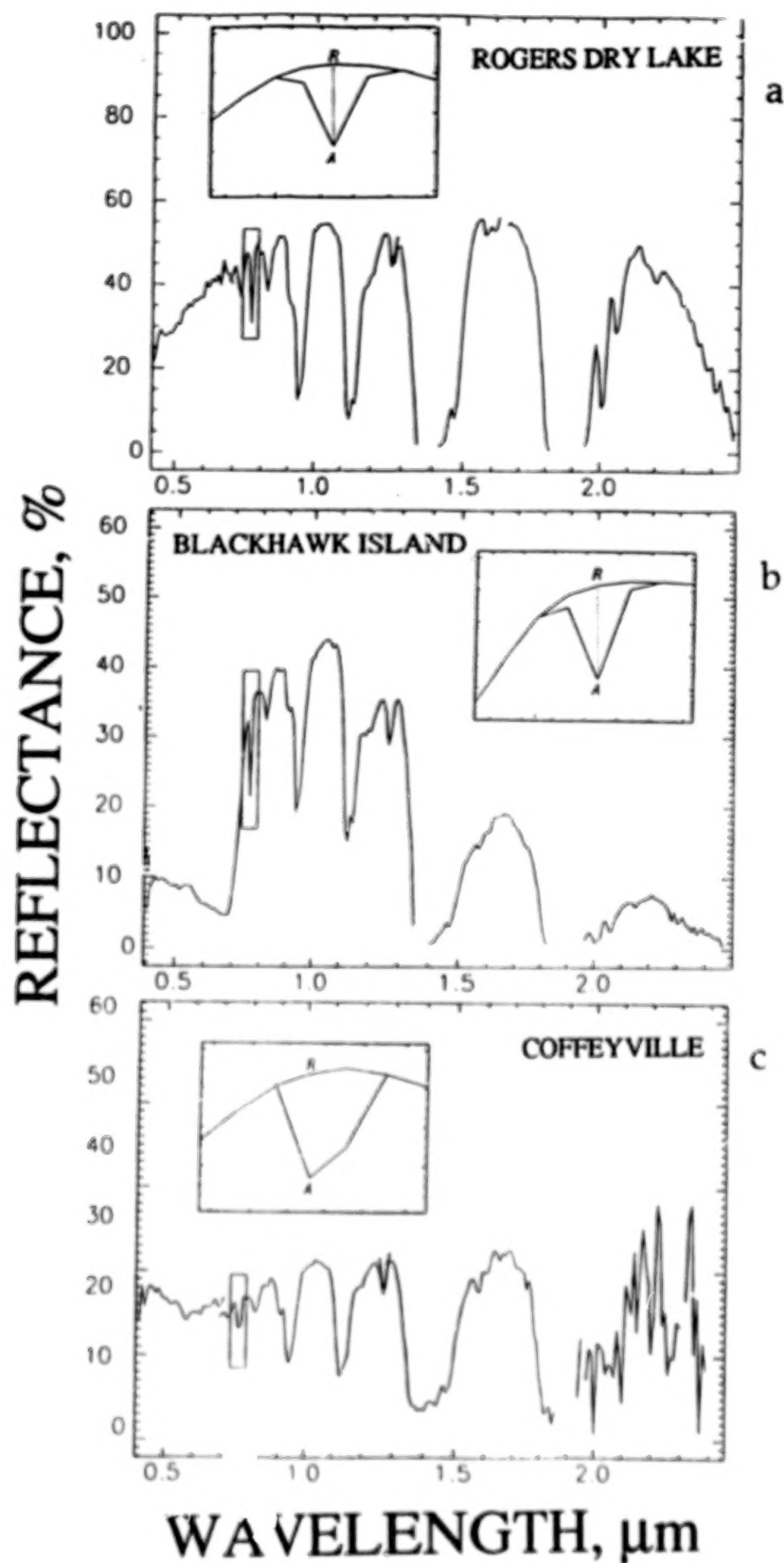


Figure 2. Typical AVIRIS spectra for (a) Rogers Dry lake, (b) Blackhawk Island and (c) Coffeyville data sets. Also shown is an expansion of the oxygen peak at around $0.76\mu\text{m}$, the derived continuum value (R), and the absorption depth (A).

calibrations for each of the flights, the oxygen peak appears at different wavelengths. For Rogers Dry Lake and Blackhawk Island the minimum was obtained at $0.764\mu\text{m}$ and for Coffeyville it was obtained at $0.756\mu\text{m}$. The signal-to-noise ratios at the oxygen peak were 105, 75, and 33 for Rogers Dry Lake, Blackhawk Island, and Coffeyville, respectively. An expansion of the oxygen band at $0.76\mu\text{m}$ is shown in each of the Figures together with the continuum line and with the A and R parameters.

4.1 APPLYING THE OOS ALGORITHM TO THE AVIRIS DATA

Figures 3, 4, and 5 give a series of images for each of the three data sets. image (a) shows the reflectance of each data set as obtained by taking a band that lies on the shoulder of the oxygen absorption feature. For Rogers Dry Lake and Blackhawk Island we used band 40 ($0.744\mu\text{m}$), and for Coffeyville we used band 41 ($0.746\mu\text{m}$). Image (b) presents the cirrus cloud map as extracted from the raw AVIRIS data at $1.38\mu\text{m}$. Images (c), (d), (e) and (f) present the $\ln(A/R)$ images as obtained by subtracting various offset values (D) from the original oxygen bands. Image (c): $D = 0$, image (d): $D = \text{optimum value}$ and images (e) and (f) D less and greater than the values used in (d), respectively.

In the Rogers Dry Lake case (Figure 3), it can be seen that no cirrus clouds are present in the scene (3b). The scene consists of high and low albedo targets (3a) that can still be seen in the original image (3c). In order to demonstrate the effect of extreme offset values on this data set, two extreme D values ($D = -3\%, +3\%$) were used to calculate new $\ln(A/R)$ images, 3d and 3f.

In order to obtain the scattering parameter D we changed the values of D and generated oxygen images based on Equation 8. Two contrasting albedo targets were used to run the calculation as discussed in section 2. For Rogers Dry Lake we found a D of -0.514% (equivalent to $-0.949 \mu\text{Wcm}^{-1}\text{nm}^{-1}\text{sr}^{-1}$ in radiance units) produced the low contrast image 3c. A field spectrum collected during the flight at one ground site on the dry lake agrees with the AVIRIS OOS data when a value of $D = -0.514\%$ is used.

For the Blackhawk Island case (Figure 4), it can be seen that cirrus clouds are dominant in several locations along the scene (Image 4b). Two extreme offset values $D = -2.5\%, +2.5\%$ were selected to demonstrate the effect of over- and underestimating the oxygen amount in this data set. The original $\ln(A/R)$ image ($D = 0$) is presented in Image 4c. A D value of -0.434% (equivalent to $-0.7673 \mu\text{Wcm}^{-1}\text{nm}^{-1}\text{sr}^{-1}$ in radiance units) produces the low contrast image 4c.

There is an inconsistency of about 4% between the AVIRIS OOS spectrum, that used a D of -0.434% , and a field spectrum collected during the overpass (see Figure 6b). The field area was covered by thin cirrus clouds, therefore the AVIRIS OOS spectrum contributed additional scattering not found in the field spectrometer data. Because the OOS method otherwise masks out the cirrus clouds, the extracted D for this particular location is a combination of the cirrus clouds and aerosol scattering. Using a similar correction for the cirrus cloud areas using different D values it is possible to distinguish between the two scattering mechanisms. This idea, however, requires further investigation, which is beyond the scope of this paper.

For the Coffeyville case (Figure 5), cirrus clouds (5b) cover almost the entire scene and appear to be very thick. Gao et al. (1993a) reported that the cirrus clouds could be observed easily from the ground, and hence confirmed the above observation. Setting $D = 0$, (5c) shows that ground features are still visible in the cirrus free areas. Two extreme offset values, $D = -10\%, +10\%$, in 5d and 5f respectively, demonstrate the effect of over- and underestimating the oxygen amount within cirrus free areas. A D of -3.516% (equivalent to $-1.37 \mu\text{Wcm}^{-1}\text{nm}^{-1}\text{sr}^{-1}$ in radiance units) shown in 5e yields the lowest contrast image. This relatively high D value retrieved for the Coffeyville data set indicates that these data contain more aerosol scattering than do Rogers Dry Lake and Blackhawk Island. The cirrus cloud distribution observed in figure 5e is highly correlated with the "cirrus map" in figure 5.

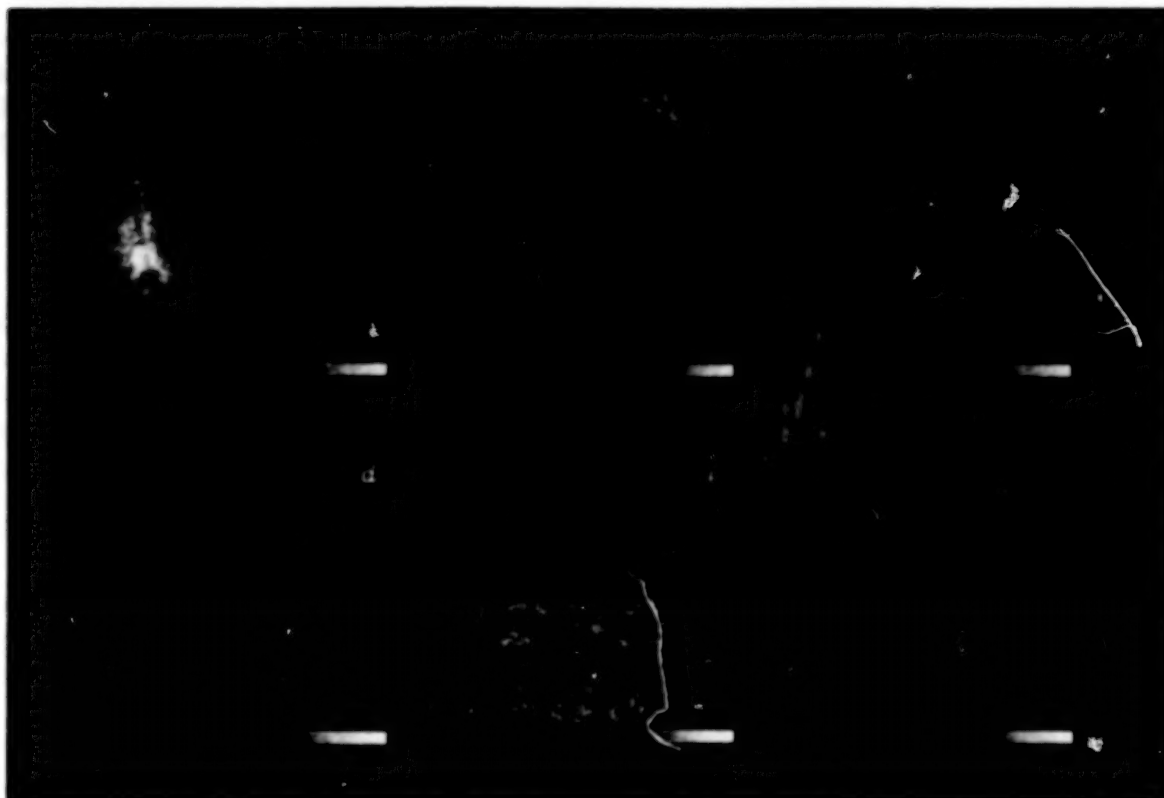


Figure 3. A set of images representing the Rogers Dry Lake data set results. (a) An "albedo" image as derived from a band that lies on the oxygen shoulder ($0.7161\mu\text{m}$); (b) A cirrus image map as derived from the raw data at $1.3825\mu\text{m}$; (c) An oxygen image as derived from the original oxygen band depth (see text for details); (d) An oxygen image as derived from a negative offset of 3% from the original oxygen band depth; (e) An oxygen image as derived from offsetting the original oxygen band depth by the correct offset (-0.514%); and (f) An oxygen image as derived from a positive offset of 3% from the original oxygen band depth.

4.2 COMPARING THE OOS TECHNIQUE TO THE 5S CODE RESULTS

In order to test the OOS method independently, we compared the OOS results with other radiative transfer codes. For that purpose, we ran the ATREM program (Gao et al., 1993a) which runs the 5S code (Tanre et al., 1986) to determine the scattering effects. For all three data sets we used a "continental aerosol" model and set the gas removal mode to off. The visibility parameters used in the code were: 40km for Rogers Dry Lake, 30km for Blackhawk Island and 20km for Coffeyville. After running the procedure, the oxygen absorption band depths at $0.76\mu\text{m}$ at several locations in the cirrus free areas were measured and plotted against the values obtained from the OOS algorithm. Figure 6 presents the results of the above procedure for the three data sets. In all examples, a 45° line is plotted in order to indicate a perfect match between the two methods. In all cases, the 5S code estimates less scattering than the OOS algorithm does. This is indicated by the higher reflectance values obtained by the 5S code compared to those obtained by the OOS algorithm. While in Blackhawk Island, the results of the two methods almost match each other, in Rogers Dry Lake and Coffeyville the OOS results differ widely from those obtained using the 5S code. Notice that in the Rogers Dry Lake case, a perfect match was obtained between the field spectrum and the AVIRIS OOS spectrum whereas in Blackhawk Island, as discussed previously, the field spectrum shows less scattering than does the AVIRIS OOS spectrum. Since the 5S code is based on parameters that are very general (aerosol model selection and estimation of visibility), this code may provide only an initial approximation of the aerosol scattering effect within



Figure 4. A set of images representing the Blackhawk Island data set results. (a) An "albedo" image as derived from a band that lies on the oxygen shoulder ($0.7447\mu\text{m}$); (b) A cirrus image map as derived from the raw data at $1.3825\mu\text{m}$; (c) An oxygen image as derived from the original oxygen band depth; (d) An oxygen image as derived from a negative offset of 2.5% from the original oxygen band depth; (e) An oxygen image as derived from offsetting the original oxygen band depth by the correct offset (-0.434%); (f) An oxygen image as derived from a positive offset of 2.5% from the original oxygen.

cirrus clear areas. In addition, this code assumes that a uniform scattering occurs throughout the scene. The OOS algorithm is based on the data itself. It uses the cirrus cloud image as a mask and requires no estimation of atmospheric model parameters. Thus, in cases where appropriate atmospheric information is absent the OOS method appears to be more accurate than the 5S code at $0.76\mu\text{m}$ for the assessing of aerosol scattering effects.

The OOS method is only capable of determining the scattering at one wavelength. However, it can provide an anchor at $0.76\mu\text{m}$ and the 5S code can be used to derive the wavelength dependence of the scattering on a local basis.

5. SUMMARY AND CONCLUSION

We showed in this paper that the oxygen absorption band at $0.76\mu\text{m}$ can be used for detecting scattering effects on a local basis. The method takes advantage of the well-mixed character of oxygen gas in the atmosphere as well as the relatively high spectral resolution of the AVIRIS spectrometer. Solving the radiance equation for oxygen reveals an expression $\ln(A/R)$ that describes the oxygen content in the sun-surface-sensor path. These parameters are generated on a pixel-by-pixel basis and

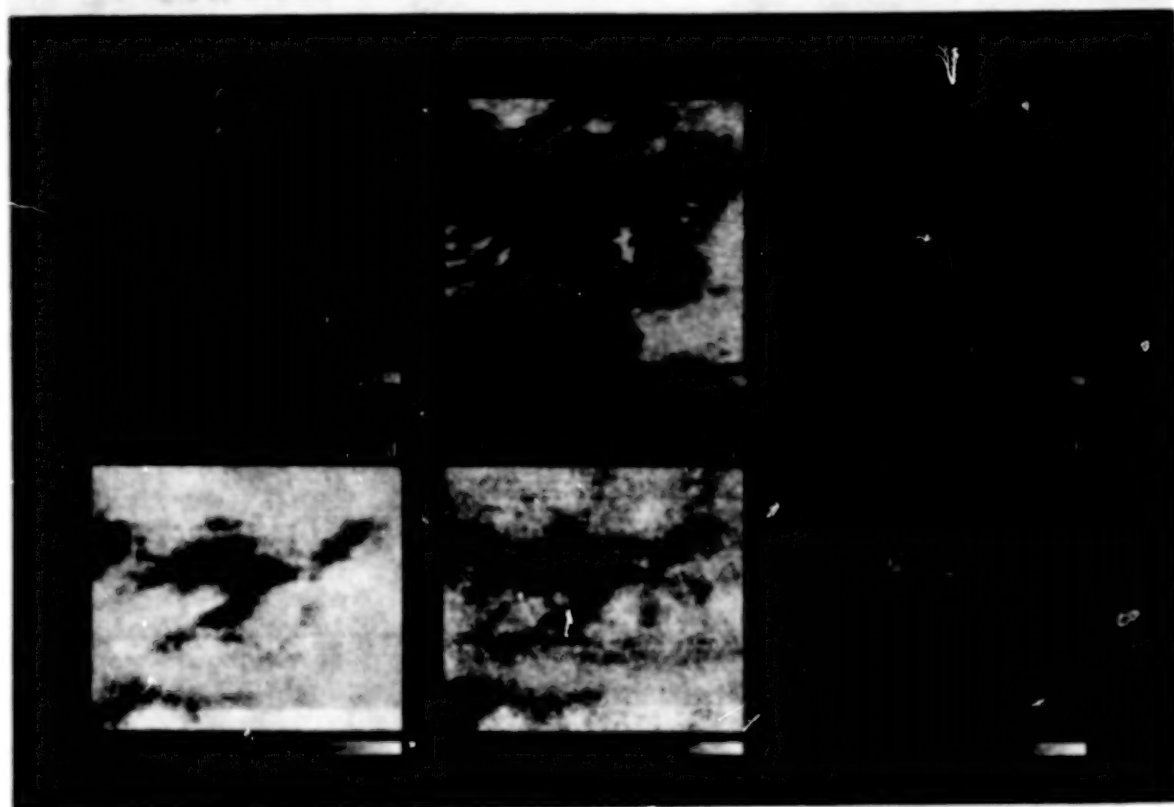


Figure 5. A set of images representing the Coffeyville data set results. (a) An "albedo" image as derived from a band that lies on the oxygen shoulder ($0.7464\mu m$); (b) A cirrus image map as derived from the raw data at $1.3820\mu m$; (c) An oxygen image as derived from the original oxygen band depth; (d) An oxygen image as derived from a negative offset of 10% from the original oxygen band depth; (e) An oxygen image as derived from offsetting the original oxygen band depth by the correct offset (-3.516%); (f) An oxygen image as derived from a positive offset of 10% from the original oxygen band depth.

are capable of describing local scattering variations. We applied a commonly used method (5S code) to assess the aerosol scattering effect in order to compare it with the OOS results. The OOS method estimates more scattering than the 5S code in the cirrus free areas. Positive agreement was obtained between the OOS and a field spectrum acquired in the cirrus-free areas. The OOS method can be used in conjunction with 5S to acquire scattering on a local basis in imaging spectrometer data.

ACKNOWLEDGMENTS

The authors wish to thank Ms. K. Heidebrecht and Mr. B. Kindel from CSES/CIREŞ, University of Colorado for their technical assistance in data processing. This work was supported by the Cooperative Institute for Research in the Environmental Sciences of the University of Colorado at Boulder through a Visiting Fellowship.

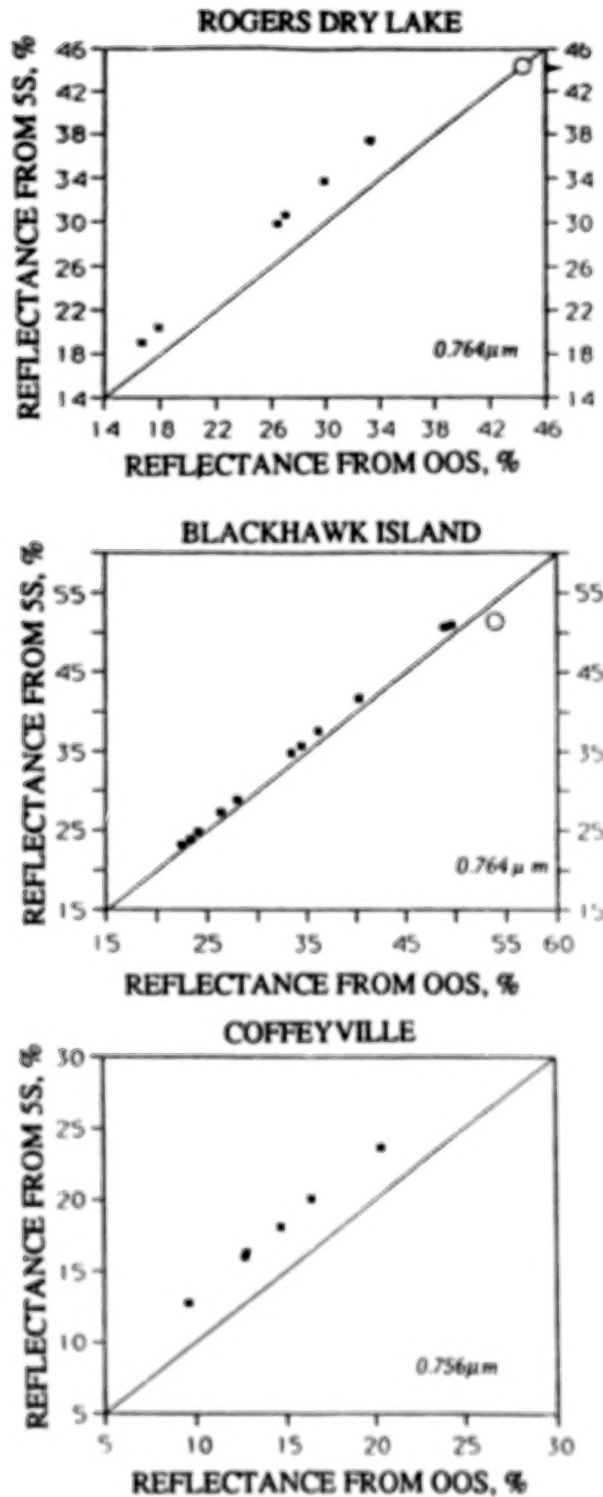


Figure 6. Absorption value expressed in reflectance units as derived from raw AVIRIS data by applying the 5S code and the OOS algorithm to the three data sets. Also shown is the line that denotes perfect correspondence between the two methods. The reflectances obtained by a field spectrometer are shown as a circle for Rogers Dry Lake and Blackhawk Island.

REFERENCES

- Berk, A., L. S. Bernstein, and D. C. Robertson, 1989: MODTRAN: A moderate resolution model for LOWTRAN 7. Final report, GL-TR-0122, Air Force Geophysical Laboratories, Hanscomb Air Force Base, Massachusetts.
- Bosch, J., and R. E. Alley, 1991: Quantitative analysis of three atmospheric correction models for Airborne Visible/Infrared Imaging Spectrometer (AVIRIS) data. *Proceedings of the Third Airborne Imaging Spectrometer Data Analysis Workshop*. JPL Publ. 87-30, Pasadena, CA, 87-95.
- Bosch, J., C. O. Davies, C. D. Mobley, and W. J. Rhea, 1993: Atmospheric correction of AVIRIS data of Monterey Bay contaminated by thin cirrus clouds. *Summaries of the Fourth Annual JPL Airborne Geoscience Workshop, AVIRIS Workshop*. JPL Publ. 93-26, Vol. 1, 85-188.
- Carder, K. L., P. Reinersman, and R. F. Chen, 1993: AVIRIS calibration using the cloud-shadow method. *Summaries of the Fourth Annual JPL Airborne Geoscience Workshop, AVIRIS Workshop*. JPL Publ. 93-26, Vol. 1, 15-18.
- Carrere, V., and J. E. Conel, 1993: Recovery of atmospheric water vapor total column abundances from imaging spectrometer data around 940nm- Sensitivity analysis and application to Airborne Visible/Infrared Imaging Spectrometer (AVIRIS) data. *Remote Sensing of Environment*. 44:179-204.
- Chrein, T. G., R. O. Green, and M. K. Eastwood, 1990: Accuracy of the spectral and radiometric laboratory calibration of the Airborne Visible/Infrared Imaging Spectrometer (AVIRIS). *Proceedings of the Second Airborne Visible/Infrared Imaging Spectrometer (AVIRIS) Workshop, Pasadena, CA.*, JPL Publ. 90-54, 1-14.
- Clark, R. G., S. Gregg, K. Heidebrecht, A. F. H. Goetz, and R. O., Green, 1993: Comparison of methods calibrating AVIRIS data to ground reflectance. *Summaries of the Fourth Annual JPL Airborne Geoscience Workshop, AVIRIS Workshop*. JPL Publ. 93-26, Vol. 1, 35-36.
- Conel, J. E., R. O. Green, G. Vane, C. J. Bruegge, and R. E. Alley, 1987: AIS-2 radiometry and a comparison of methods for the recovery of ground reflectance. *Proceedings of the Third Airborne Imaging Spectrometer Data Analysis Workshop*. JPL Publ. 87-30, Pasadena, CA, 18-47.
- Esaias, W., 1986: Moderate resolution imaging spectrometer. *Earth Observation System. vol. IIb, Instrument Panel Report, NASA, Washington, D.C.* 49-53, .
- Gao, B.-C. and A. F. H. Goetz, Column atmospheric water vapor retrievals from airborne imaging spectrometer data, *J. Geophys. Res.-Atmospheres*, 95, 3549-3564, 1990.
- Gao, B. C., A. F. H. Goetz and J. A. Zamudio, 1991: Removing atmospheric effects from AVIRIS data for surface reflectance retrieval. *Proceedings of the Third Airborne Visible/Infrared Imaging Spectrometer (AVIRIS) Workshop, August 1, 1991*. JPL Pub., 80-86.
- Gao, B.-C. , A. F. H. Goetz and W. J. Wiscombe, 1993a: Cirrus cloud detection from airborne imaging spectrometer data using the 1.38 μ m water vapor band. *Geophysical Research Letters*, 20(4), 301-304.

000056

- Gao, B.-C., K. B. Heidebrecht, and A. F. H. Goetz, 1993b: Derivation of scaled surface reflectance from AVIRIS data. *Remote Sensing of Environment*, 44:165-178.
- Goetz, A. F. H., 1991: Imaging spectrometry for studying earth, air, fire and water. *EARSeL Advances in Remote Sensing* 1:3-15.
- Goetz, A. F. H., 1992: Imagine spectrometry for earth remote sensing. In *Imaging Spectroscopy Fundamentals and Prospective Applications*, (Toselli, F. and Bodechtel, J. Eds.) 1-19.
- Goetz, A. F. H., 1993: Effect of water vapor and cirrus clouds on TM-derived apparent reflectance based on AVIRIS experience. *Proceedings of the Workshop on Atmospheric Correction of Landsat Imagery*, Torrance, Ca, June 29-2 July, 1993, 55-59.
- Green, R. O., 1990: Retrieval of reflectance from calibrated radiance imagery measured by the Airborne Visible/Infrared Imaging Spectrometer (AVIRIS) for lithological mapping of the Clark Mountains, California. *Proceedings of the Second Airborne Visible/Infrared Imaging Spectrometer (AVIRIS) Workshop*, Pasadena, CA. JPL Publ. 90-54.. 167-175.
- Green, R. O., and J. E. Conel, 1993: Application of Airborne Visible/Infrared Imaging Spectrometer (AVIRIS) to determine atmospheric aerosol optical depth and perceptible water content.
- Green, R. O., J. E. Conel and D. A. Roberts, 1993: Estimation of aerosol optical depth and addition atmospheric parameters for calculation of apparent reflectance from radiance measured by the Airborne Visible/Infrared Imaging Spectrometer. *Summaries of the Fourth Annual JPL Airborne Geoscience Workshop, AVIRIS Workshop. JPL Publ. 93-26*, Vol. 1, 73-76.
- Green, R. O. and B.-C. Gao, 1993: A proposed update to the solar irradiance spectrum used in LOWTRAN and MODTRAN. *Summaries of the Fourth Annual JPL Airborne Geoscience Workshop, AVIRIS Workshop. JPL Publication 93-26*, Vol. 1, 81-84.
- Kneizys, F. X., G. P. Anderson, E. P. Shettle, W. O. Gallery, L. W. Abreu, J. E. A. Selby, J. H. Chetwynd, and S. A. Clough, 1988: User Guide to LOWTRAN-7. Environmental Research Papers No.: 1010: AFGL-TR-88-0177: Air-Force Geophysical Laboratories.
- Moran, M. S., R. D. Jackson, P. N. Slater, and P. M. Teillet, 1992: Evaluation of A simplified procedure for retrieval of land surface reflectance factors from satellite sensor output. *Remote Sensing of Environment*, 41:169-184.
- Neckel, H., and D. Labs, 1984: The solar radiation between 3300 and 12500 angstrom. *Sol. Phys.*, 90:205-258.
- Tanre, D., C. Deroo and P. Duhaut, 1986: Simulation of the Satellite Signal in the Solar Spectrum (5S), User's Guide. Laboratory d'Optique Atmospherique, U.S.T. de Lille, 59655 Villeneuve d'asq, France.
- Teillet, P. M., 1990: Rayleigh optical depth comparisons from various sources. *Appl. Opt.*, 29:1897-1990
- Teillet, P. M., 1992: An algorithm for the radiometric and atmospheric correction of AVHRR data in the solar reflective channels. *Remote Sensing of Environment*, 185-193.
- Vane, G. (Ed.), 1987: Airborne Visible/Infrared Imaging Spectrometer (AVIRIS), *JPL Pub.* 87-38, Pasadena, CA.

ESTIMATION OF ATMOSPHERIC CONDITIONS AND SURFACE TEMPERATURES FROM MULTISPECTRAL DATA

James R. Johnson
E-System Garland Division
Dallas, TX 75266-0023
(214) 205-7613

The R&D activities at E-Systems have examined the applications of multispectral remote sensors for determining atmospheric temperature and water vapor profiles, and for applying these derived profiles to imagery from other sensors such as Landsat. The NOAA/AVHRR system has been demonstrated as a viable tool for atmospheric calibration and compensation of satellite imagery (Ingram and Johnson, 1992, and Johnson and Ingram, 1993). The E-Systems Multispectral Atmospheric Calibration Algorithm (MACA) utilizes all 5 AVHRR spectral channels. The temperature and water vapor density profiles are determined using the three IR channels, 3, 4 and 5. The shorter wavelength channels, 1 and 2, are then used to refine the water vapor profile and set the aerosol absorption model. A modified version of the MODTRAN radiative transfer modeling software is used to perform this analysis. This modified software integrates a Bidirectional Reflectance Distribution Function spectral database for a number of representative materials. It also performs the computations for atmospheric downwell radiance and adjacency effects. MACA utilizes standard atmospheric models for initial atmospheric states. The fitted atmospheric profiles are parameterized curves in temperature, water vapor density and visibility. Currently standard aerosol models are used for aerosol profile discrimination. A unique set of atmospheric profiles are extracted at selected locations within the imagery using bodies of water and uniform land regions. These profiles can be interpolated to specific points in the image. These interpolated atmospheric models can then be used to generate atmospheric compensation parameters specific to the acquisition system geometry and spectral response distribution. As a product, MACA determines the temperatures of all conjugate areas sampled for the atmospheric calibration process. A level of constraint on the material spectral properties can be used to define ground emissivities and reflectivities for possible surface identification and monitoring. This algorithm has been successfully tested on a number of NOAA/AVHRR images covering the North Texas area where ground truth temperatures and atmospheric radiosondes were collected. Typical errors in the conjugate target temperatures are less than 1.0 Kelvin.

The procedures for calibration and compensation of atmospheric effects in satellite imagery have been applied to the refinement of Normalized Difference Vegetation Indexes and in the generation of image fusion products. Such products incorporate E-Systems capabilities to automatically register Landsat to other sensor data, to generate mosaic reference images and to incorporate radiometrically derived parameters into color products. Such capabilities have applications in the areas of broad area search and monitoring of land areas.

Manuscript not available at time of printing. Please contact author for further information.

SENSITIVITY ANALYSES TO IDENTIFY KEY PARAMETERS FOR USE WITH A RADIATIVE TRANSFER MODEL-BASED ATMOSPHERIC CORRECTION

Sally Westmoreland
Department of Geography
San Diego State University
San Diego, CA 92182 USA

Frederick C. Mertz
Photon Research Associates, Inc.
10350 N. Torrey Pines Rd., Suite 300
La Jolla, CA 92037 USA

ABSTRACT

We present results from using a deterministic, physically-based model to correct Landsat Thematic Mapper image data for atmospheric effects and to calculate reflectances. Our analysis included evaluation of the accuracy of the correction for two different data sets and analysis of the sensitivity of the models to variations in characterization of the sensor and the atmosphere. The results showed accurate estimation of reflectances for the visible bands, but more variable results for the reflective infrared bands. The sensitivity analyses emphasized the need for well-defined calibration and sensor response. The model results appear to be more sensitive to estimates of visibility that affect boundary layer aerosol concentrations than specification of a model atmosphere.

1. INTRODUCTION

For a number of applications that use remotely sensed image data, correction of atmospheric effects is necessary to ensure temporal comparability among data sets or accurate measurement of some physical phenomena. In many circumstances, the atmospheric measurements needed for detailed correction of the image data may be unavailable or unfeasible to collect. In these situations, an alternative is to employ a radiative transfer model that incorporates standard models to characterize the atmospheric state.

In this paper, we present results from using a radiative transfer model-based approach for atmospheric correction. Our goal was to evaluate the accuracy of a physically-based model to calculate atmospherically corrected reflectances and to evaluate the sensitivity of the model to various model input parameters.

2. MODEL DESCRIPTION

As illustrated in Fig. 1, the atmospheric correction model is an integration of four separate models. MOSART (Moderate Spectral Atmospheric Radiance and Transmittance) was developed under funding from the Ballistic Missile Defense Office and direction of the Geophysics Directorate of the USAF Phillips Laboratory. MOSART performs the radiative transfer calculations for a given sensor band pass at spectral resolutions from 2 cm^{-1} to 20 cm^{-1} , using inputs of satellite and scene geometry and the atmospheric state. The code incorporates features from the earlier models of LOWTRAN (Kneizys et al. 1988), MODTRAN (Berk et al., 1989), and APART (Cornette, 1990) as well as additional features that allows a user to select standard model atmospheres, user-defined profiles, or interpolation over multiple model atmospheres. Radiative environment data sets may be generated for multiple targets, altitudes, and sensor geometries (Cornette et al., 1993; Cornette et al., 1994).

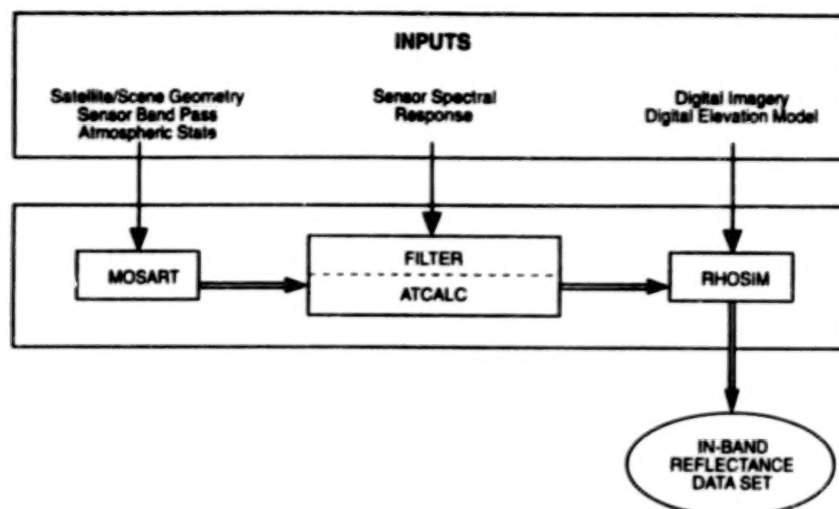


Figure 1. Atmospheric correction model.

In the ATCALC model, the radiative environment created by MOSART is convolved with the sensor spectral response function generated by the FILTER model to produce spectrally integrated "inband" radiative environment data. This spectral radiative environment with digital imagery, calibration coefficients, and a digital elevation model are inputs to the RHOSIM model. The user supplied calibration coefficients are used to convert the image digital values to radiances. The angle between the surface facet and the sun ($\cos(z')$) for each pixel is generated from the digital elevation model. Inband reflectance for each image pixel is determined by a physically-based computation (1) (Mertz et al., 1993):

$$\rho = \frac{\text{Radiance(sensor)} - \text{Radiance(path)}}{[(\text{Solar irradiance} * \cos(z')) + \text{Skyshine}]/\pi} \quad (1)$$

3. TEST DATA SETS

The data used in this analysis had been collected as part of two different multidisciplinary projects. The first data set was part of an experiment at the University of Arizona's Maricopa Agricultural Center (MAC) located south of Phoenix. Landsat 5 Thematic Mapper (TM) image data were collected for 7 dates between July 1985 through June 1986 with concurrent acquisition of Exotech radiometer measurements from a low-level aircraft platform. Data were obtained over two targets, bare soil and growing crops, for each date for the first four TM bands only (Moran et al., 1992).

The second data set was part of the First ISLSCP (International Satellite Land Surface Climatology Project) Field Experiment (FIFE) conducted over the Konza Prairie in Kansas. In this experiment image and atmospheric data were collected from ground, helicopter, aircraft and satellite based platforms throughout the 1987 growing seasons and again in 1989. For purposes of this analysis we used an August 15, 1987 Landsat 5 TM image and reflectance data calculated from radiances measured by a helicopter-mounted Barnes MMR radiometer. Sixteen observations collected from the radiometer within $\pm 1/2$ hour of the satellite overpass were compared with the corrected TM reflectances. The FIFE site, unlike the laser-leveled MAC site, has variable moderate terrain over the 15 km x 15 km area of the site with a predominant cover of tall grass prairie and crop/pasture (Sellers et al., 1992).

4. RESULTS

The accuracy from using the MOSART/RHOSIM models for atmospheric correction of the MAC and FIFE TM data sets is shown in Figs. 2 and 3. Based on using the US Standard 1976 model atmosphere and the desert aerosol model with a visibility greater than 61 km, the overall root mean square error (RMSE) of the TM corrected reflectances vs the Exotech-based reflectances was about .016 in reflectance. This result is comparable to the RMSE of about .015 obtained by Moran et al. (1992) with the same data using the LOWTRAN model for a US Standard 1976 model atmosphere and rural aerosol model.

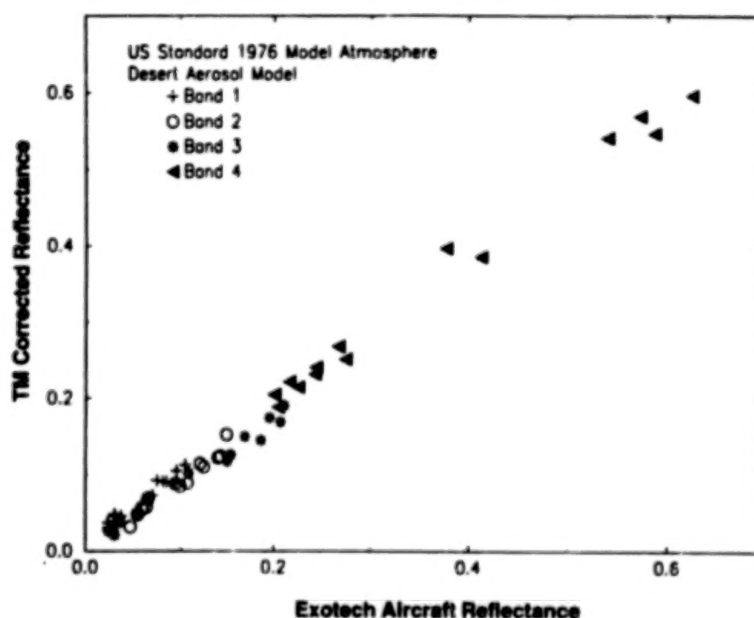


Figure 2. Reflectance estimates for two targets, MAC, 1985-86

The FIFE results were more mixed than the MAC as can be seen from Fig. 3. The agreement between the corrected TM reflectances and the uncorrected helicopter MMR reflectances for the lower reflectances of bands 1, 2, 3, and 7 is similar to that of MAC with individual band RMSEs of .016 or less. However, for the more variable and higher reflectances in bands 4 and 5, the RMSEs were on order of .062. These results are based on using a midlatitude summer model atmosphere with actual observations substituted for model temperature and humidity profiles. The rural aerosol model was used with visibility set to 50 km. In comparing the FIFE and MAC results, it should be noted that both the spatial and temporal registration of the MAC radiometer and satellite data were superior to that of FIFE. MAC was also superior for these purposes, in that it included high and low reflectance targets in each spectral band, while the FIFE data focused on vegetated surfaces providing low reflectance target in bands 1, 2, and 3 and higher reflectances targets in TM band 4, 5, and 7. However, the spectral coverage of the FIFE data included the six TM reflective bands while the MAC data included only TM bands 1, 2, 3, and 4.

As part of an analysis of the sensitivity of the model to input parameters, we investigated the effects of varying three different parameters: (1) calibration coefficients and bandwidth, (2) model atmospheres, and (3) horizontal visibility. The MAC and FIFE studies used different calibration coefficients to convert the TM digital values to radiances. The MAC calibrations were based on the 1984/85 in-flight calibration at White Sands, New Mexico by Slater et al., (1986). The FIFE image digital values were converted to radiances using the coefficients derived by Markham and Barker (1986). Similarly, the TM bandwidths may

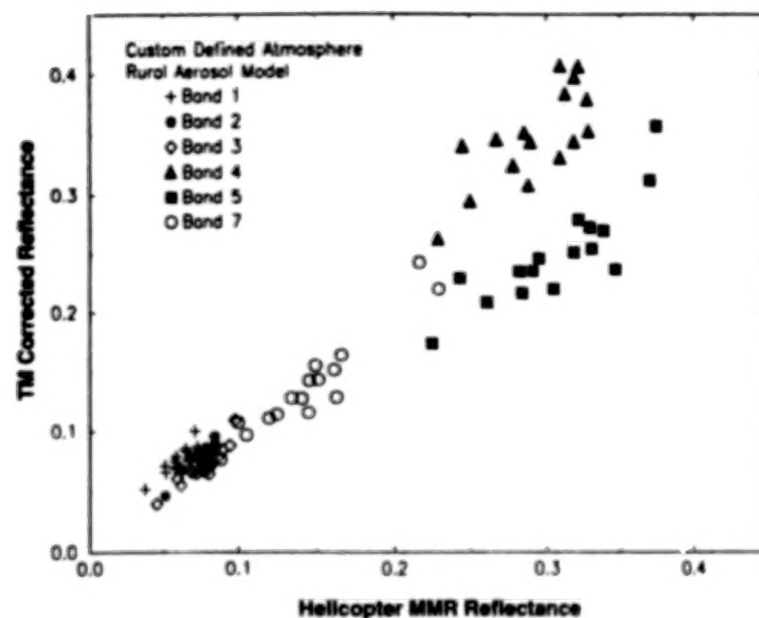


Figure 3. Reflectance estimates for 16 sites, FIFE, August 15, 1987

be defined in several ways. We compared results using bandwidths based on an integration of the shaped spectral response measured at .001 μm intervals (Markham and Barker, 1984), the EOSAT defined full-width at half maximum (Markham and Barker, 1986), and the Palmer (1984) moments analysis. Both the EOSAT full-width at half maximum and Palmer bandwidths are square responses unlike the integrated shaped filter. The variation in integrated width by TM band is shown in Table 1.

Table 1. Landsat Thematic Mapper bandwidths in μm

TM Band	Integrated Shaped Filter at .001 μm Intervals	EOSAT Full-Width at Half Maximum	Palmer Moments Analysis
1	.0602	.0654	.0701
2	.0757	.0813	.0889
3	.0649	.0668	.0767
4	.1199	.1281	.1343
5	.2146	.2167	.227
7	.2399	.2518	.268

The effect of varying both calibration coefficients and bandwidth is illustrated in Fig. 4 with the MAC data set. The original MAC study used the Slater et al. (1986) coefficients and the Palmer (1984) bandwidths as did the corrected TM data results shown in Fig. 2. However, for the conditions given in Fig. 4, midlatitude summer model atmosphere, rural aerosol model and 23 km visibility, the overall RMSE (.023) using EOSAT coefficients with the narrower shaped filter is lower than the RMSE based on Slater et al. (1984) coefficients for this atmospheric characterization. Fig. 5 shows the effect of varying only

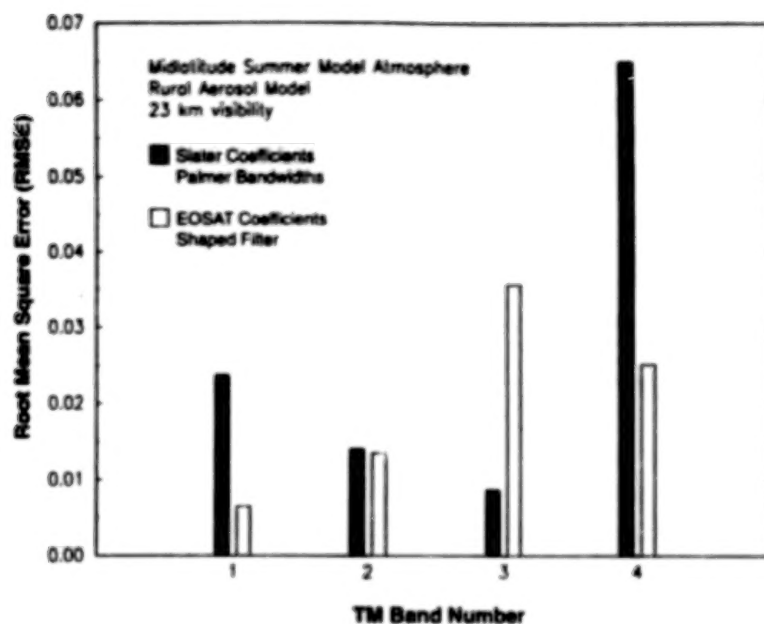


Figure 4. Effects of calibration and bandwidth on reflectance RMSE, MAC, 1985-86

bandwidth for the FIFE data set based on the same conditions used in Fig. 3. Overall, using the wider square EOSAT bandwidth produced a lower RMSE, but with considerable inter-band variability.

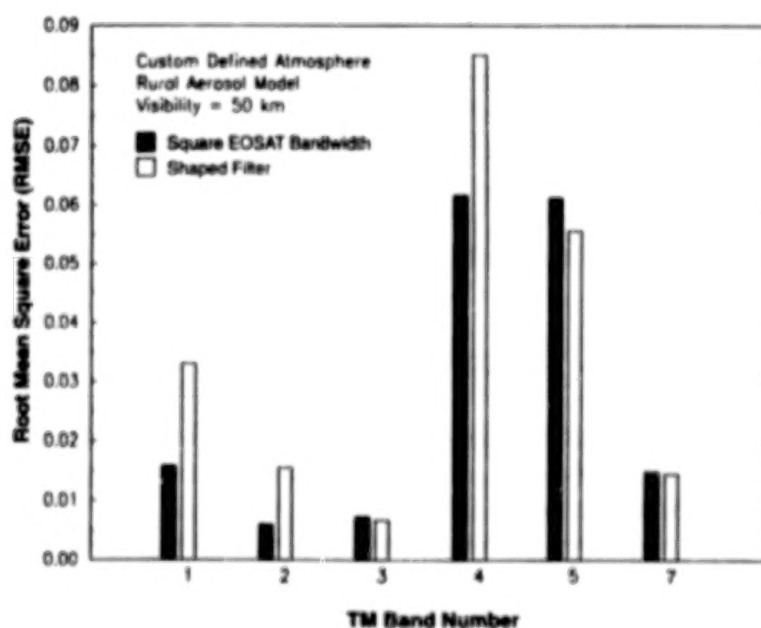
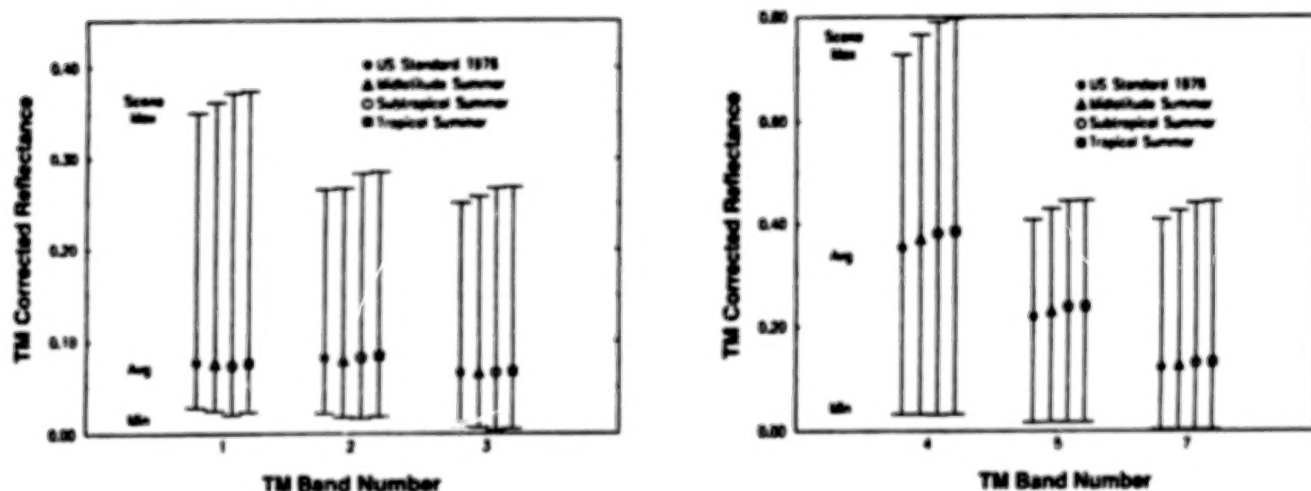


Figure 5. Effect of bandwidth on reflectance RMSE, FIFE, August 15, 1987

The variation in the FIFE scene reflectance as a result of using different model atmospheres is graphed in Figs. 6a and b. All six bands exhibited a similar response in terms of the overall variability, with the US Standard 1976 atmosphere resulting in the least variability, followed by the midlatitude summer, subtropical summer, to the most variable, tropical summer model atmosphere. At the lower reflectances of bands 1, 2, 3, and 7, the average reflectances for each model atmosphere were relatively constant. Bands 4 and 5 with higher reflectances showed more variability in their overall average reflectances among the four model atmospheres.



Figures 6a. and b. Variation in scene reflectance by model atmosphere, FIFE, August 15, 1987

Accurate estimation of horizontal visibility is important as this is used by MOSART to determine the aerosol concentrations in the boundary layer (Cornette, 1993). The effects on the FIFE scene reflectance of varying visibility from 23 km to 50 km is shown in Fig. 7. At the longer visibility range of 50 km, both overall variability and, generally, average scene reflectances were reduced. The magnitude of the decrease is again strongly band dependent. The effects on RMSE of varying both model inputs and visibility are illustrated in Fig. 8 with the MAC data. Here the effect on RMSE from using a midlatitude summer and rural aerosol model with 23 km visibility results in both greater variability among bands and higher overall RMSE than the correction using the US Standard 1976 atmospheric model and desert aerosol model with 61.8 km visibility.

6. CONCLUSIONS

The results presented here are part of an on-going evaluation of the MOSART/RHOSIM models for atmospheric correction of image data. While the accuracy of the initial results from using Landsat TM data are encouraging, the poor agreement from the FIFE data for TM bands 4 and 5 are of concern. With regard to the model sensitivity to input parameters, this initial analysis has demonstrated the importance of having a well-characterized calibration and sensor response to generate reliable reflectance data. In addition, accurate estimates of surface visibility were shown to be critical to the results. The effects of different model atmospheres appeared to be more subtle, affecting the overall scene variability. Future sensitivity analyses will include varying water vapor profiles and comparisons of non-nadir viewing geometries. In addition, further investigation is required not only with TM data, but also to test the model with other sensors, particularly hyperspectral instruments, and environments.

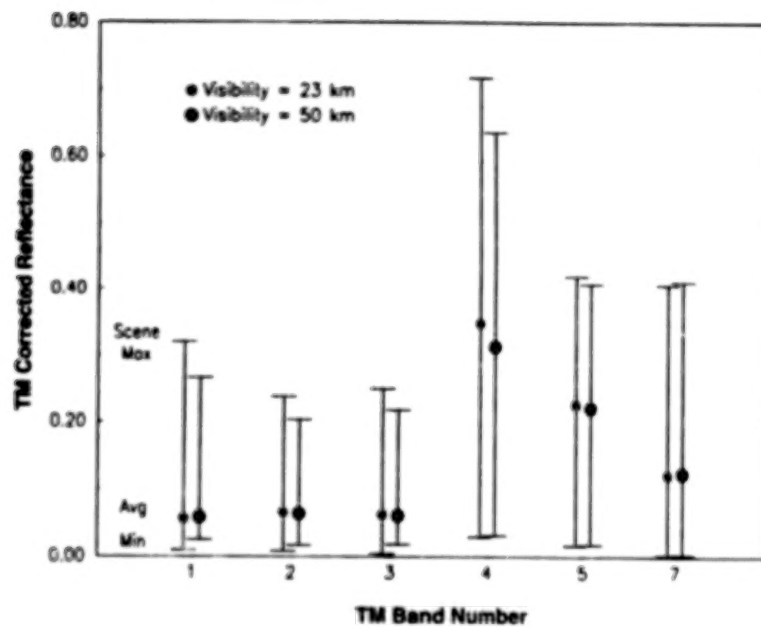


Figure 7. Variation in scene reflectance for changes in visibility, FIFE, August 15, 1987

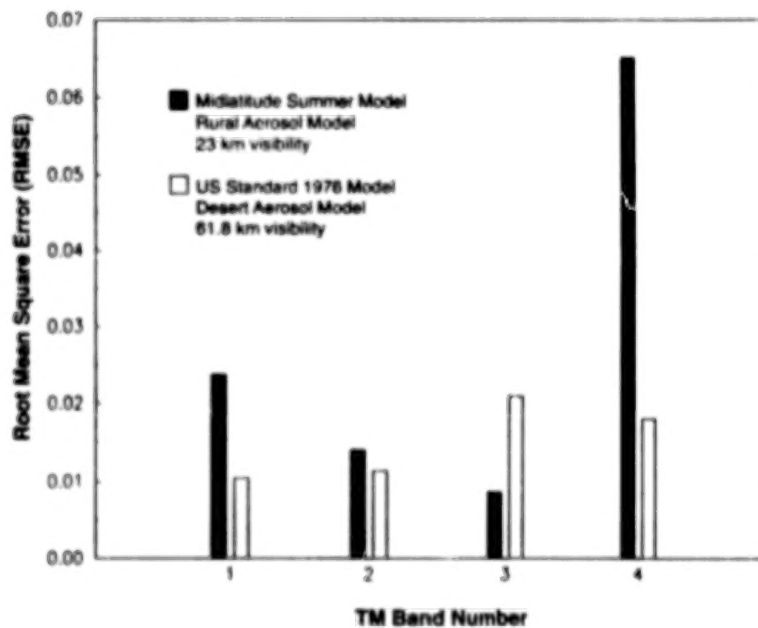


Figure 8. Effect of model parameters on reflectance RMSE, MAC, 1985-86

ACKNOWLEDGMENTS

We would like to thank Dr. Susan Moran and Dr. Bill Cornette for their assistance with data sets and MOSART, respectively.

REFERENCES

- Berk, A., L.S. Bernstein, and D.C. Robertson, 1989: *MODTRAN: A Moderate Resolution Model for LOWTRAN 7*. U.S. Air Force Geophysics Laboratory, GL-TR-89-0122.
- Cornette, W.M., P.K. Acharya, and G.P. Anderson, 1994: Using the MOSART code for atmospheric correction. *Proceedings of the International Geoscience and Remote Sensing Symposium '94*, IEEE Geoscience and Remote Sensing Society, Pasadena, California, August 1994 (in press).
- Cornette, W.M., D.C. Robertson, and G.P. Anderson, 1993: The moderate spectral atmospheric radiance and transmittance (MOSART) program. *Proceedings of the Workshop on Atmospheric Correction of Landsat Imagery*, Defense Landsat Program Office, Torrance, California, July 29 - July 1, 1993, 70-74.
- Cornette, W.M., 1993: *Moderate Spectral Atmospheric Radiance and Transmittance Program (MOSART), Version 1.1, Volume II: Users' Reference Manual*. Photon Research Associates, Inc., La Jolla, California.
- Cornette, W.M., 1990: *Atmospheric Propagation and Radiative Transfer (APART) Computer Code, Vol. I: Installation Reference Manual, Vol. II: Users Reference Manual, Vol. III: Technical Reference Manual, Vol. IV: Software Reference Manual*. Photon Research Associates, Inc., La, California.
- Kneizys, F.X., E.P. Shettle, L.W. Abreu, J.H. Chetwynd, G.P. Anderson, W.O. Gallery, J.E.A. Selby, and S.A. Clough, 1988: *Users Guide to LOWTRAN 7*. U.S. Air Force Geophysics Laboratory, AFGL-TR-88-0177.
- Markham, B.L. and J.L. Barker, 1986: Landsat MSS and TM post-calibration dynamic ranges, exoatmospheric reflectances and at-satellite temperatures. *EOSAT Technical Notes*, EOSAT, Lanham, Maryland, 3-8.
- Markham, B.L. and J.L. Barker, 1984: Spectral characterization of the Landsat Thematic Mapper sensors. *Proceedings of the Landsat-4 Scientific Characterization Early Results Symposium*, Greenbelt, Maryland, 22-24 February 1983, II-239.
- Mertz, F.C., S. Westmoreland, D.A. Stow, and A. Hope, 1993: A model for computing in-band reflectance data sets from digital satellite image data. *Proceedings of the Workshop on Atmospheric Correction of Landsat Imagery*, Defense Landsat Program Office, Torrance, California, July 29 - July 1, 1993, 80-84.
- Moran, M.S., R.D. Jackson, P.N. Slater, P.M. Teillet, 1992: Evaluation of simplified procedures for retrieval of land surface reflectance factors from satellite sensor output. *Remote Sensing of Environment*, **41**, 169-184.
- Palmer, J.M., 1984: Effective bandwidths for LANDSAT-4 and LANDSAT-D' Multispectral scanner and Thematic Mapper subsystems. *IEEE Transactions on Geoscience and Remote Sensing*, **22**, 336-338.

Sellers, P.J., F.G. Hall, G. Asrar, D.E. Strebel, and R.E. Murphy, 1992: An overview of the First International Satellite Land Surface Climatology Project (ISLSCP) Field Experience (FIFE). *Journal of Geophysical Research*, **97**, 18345-18371.

Slater, P.N., S.F. Biggar, R.G. Holm, R.D. Jackson, Y. Mao, M.S. Moran, J.M. Palmer, and B. Yuan. 1986. Absolute radiometric calibration of the Thematic Mapper. *SPIE*, vol. 660: 2-8.

THE 1994 GEISA PROGRAM FOR MANAGEMENT AND STUDY OF SPECTROSCOPIC INFORMATION

N. Husson, B. Bonnet, A. Chedin, N.A. Scott
Laboratoire de Météorologie Dynamique du CNRS
Ecole Polytechnique, 91128 Palaiseau, France

A.A. Chursin, V.I.G. Tyuterev, V.F. Golovko
The Laboratory of Theoretical Spectroscopy
Institute of Atmospheric Optics, 634055 Tomsk, Russia

ABSTRACT

The GEISA (Gestion et Etude des Informations Spectroscopiques Atmosphériques ; word translation: Management and Study of Atmospheric Spectroscopic Information) spectroscopic database oriented towards the Earth's and planetary atmospheres studies, has been developed, since 1976, and is maintained, at Laboratoire de Météorologie Dynamique (LMD) du CNRS, Ecole Polytechnique, France.

The last public edition of this database, GEISA-93, includes the data on 731206 spectral transitions of 40 molecules and 86 isotopic species from 0 to 22656 cm^{-1} , the infrared absorption cross sections data on chlorofluorocarbons (8 species), on N_2O_5 and ClONO_2 .

Since the origin, one of the major goals of this work has been to develop a software making possible various kinds of extractions covering applications in the field of Atmospheric Physics, as well as in the field of Molecular Spectroscopy. Formerly the above mentioned software was designed for use on large computer complexes, but recently an IBM PC/AT/XT compatible version of associated software, called GEISA-PC, has been created thanks to a collaboration between LMD and Laboratory of Theoretical Spectroscopy (LTS) of the Institute of Atmospheric Optics, in Russia.

Among the functional capabilities of the GEISA system, the development of an interface between the GEISA data base and other ones, such as data bases on different emission laser lines, on atmospheric constituents contents and on aerosols, is outlined.

1. INTRODUCTION

Increasingly more sophisticated satellite atmospheric remote sensing experiments are being proposed by NASA (USA), ESA (Europe), CNES (France), Japan ..., for possible implementation beyond the later part of this century. For example, high spectral resolution infrared sounders like AIRS (Atmospheric Infrared Sounder ; JPL publication, 1991) and IASI (Improved Atmospheric Sounding in the Infrared) are being developed to meet the needs of both the operational meteorology and atmospheric science communities. Achieving the anticipated improvements in retrieval accuracy from high spectral resolution (NATO Publication, 1993), infrared and microwave data will require adequate tools for the calculation of atmospheric radiative transfer. Among them, is a good knowledge of spectroscopic line parameters, which are particularly important given the increasing impact of physical retrieval techniques for space-based remote sensing of the planetary atmosphere structure.

TABLE 1. EVOLUTION OF THE GEISA DATABASE SINCE 1978

Year	1978	1979	1980	1981	1982	1984	1991	1994
# molecules	7	11	12	23	31	36	40	40
# isotopes	30	35	36	49	57	79	86	86
# lines	134 000	170 000	180 000	215 000	228 000	323 521	726 557	731 206

Consequently, computer accessible compilations of spectroscopic line parameters, extending from infrared to microwave, are required for molecules of interest for atmospheric remote sensing.

The first compilation, oriented towards the Earth's atmosphere, was initiated at Air Force Geophysics Laboratory (the so-called "AFGL tape") by McClatchey et al. (1973) and Garing et al. (1973). In 1976, a similar work was started at Laboratoire de Météorologie Dynamique with the development of the GEISA (Gestion et Etude des Informations Spectroscopiques Atmosphériques ; word translation: Management and Study of Atmospheric Spectroscopic Information) database which has been described by Chedin et al. (1980) and updated several times (see for example : Chedin et al., 1985 ; Husson et al., 1986, 1992, 1994). The evolution of the GEISA database since 1978 is presented in Table 1. From its origin, the major orientations of GEISA have been, first, to introduce molecules of interest not only for the Earth's atmosphere, but also for planetary atmospheres, in particular for the Giant Planets in connection with the NASA/VOYAGER mission (Chedin and Scott, 1984), and, second, to develop a software making possible various kinds of extractions covering applications in the field of atmospheric physics as well as in the field of molecular spectroscopy, thanks to a specific management.

Similar other compilations of spectroscopic line parameters, available for general use by the remote sensing community had different initial emphasis :

- the AFGL/HITRAN (Air Force Geophysics Laboratory ; Phillips Laboratory / High-Resolution Transmission) Database (McClatchey et al., 1973 ; Rothman et al., 1992) was intended for terrestrial atmospheric problems ;
- the ATMOS (Atmospheric Trace MOlecule Spectroscopy) Molecular Line-List, compiled by Brown et al. (1987) was tailored for the specific needs of the ATMOS experiment (Farmer et al., 1987) ;
- the JPL (Jet Propulsion Laboratory) catalog and atlas of microwave and submillimeter transmission by Poynter and Pickett (1985) was mainly devoted to astrophysical studies.

However, several alike spectroscopic parameters are currently incorporated into these various compilations (for more details, see Husson et al., 1993).

The purpose of this paper is to present a summarized review of GEISA in the frame of its contents and of its newly enhanced and extended management system. At present, the last public edition of GEISA contains 731206 entries (40 molecules, 86 isotopic species) between 0 and 22656 cm⁻¹.

2. DESCRIPTION OF THE GEISA DATA BANK IN ITS 1993 EDITION

Detailed information on GEISA contents regarding spectroscopic parameters and molecular species is given below.

2.1 GEISA DATA BASE SPECTROSCOPIC PARAMETERS

The spectroscopic parameters are provided for all significant transitions of molecular and atomic species of interest. Figure 1 presents the description of the direct image of a transition, with 120 characters per transition and the related FORTRAN format :

F10.6, E10.3, F5.3, F10.3, 4A9, F4.2, I4, I3, A3, I2, I1, E10.3, F5.4, F8.6, I3, I6

Figure 1. Description of the image of a transition in the GEISA data base

F10.6	E10.3	F5.3	F10.3	4A9	F4.2	I4	I3	A3	I2	I1	E10.3	F5.4	F8.6	I3	I6
A	B	C	D	E	F	G	H	I	J	K	L	M	N	O	P

In Figure 1, the A-J fields are those used in GEISA associated software as the following :

- (A) Wavenumber (cm^{-1}) of the line associated with the vibro-rotational transition.
- (B) Intensity of the line (cm molecule^{-1} at 296K).
- (C) Lorentzian collision halfwidth ($\text{cm}^{-1} \text{atm}^{-1}$ at 296K).
- (D) Energy of the lower level of the transition (cm^{-1}).
- (E) Transition quantum identifications for the lower and upper levels of the transition.
 - TRS1 (A9) lower state vibrational identification,
 - TRS2 (A9) upper state vibrational identification,
 - RN1 (A9) lower state rotational identification,
 - RN2 (A9) upper state rotational identification.
 Blank field corresponds to no identification information.
- (F) Temperature dependence coefficient n of the halfwidth ; when n is not available, its value is set to zero.
- (G) Identification code for isotope in GEISA
- (I) Identification code for molecule in GEISA.
- (J) Internal code for GEISA data identification.

The K-Q fields correspond to the information related to the actual transition, in a purpose of possible compatibility with the HITRAN data base. These fields, not involved in the GEISA software, correspond respectively to the following parameters, from HITRAN :

- (K) Molecule number.
- (L) Isotope number (1- most abundant ; 2- second, ...).
- (M) Transition probability (debyes).
- (N) Self-broadened halfwidth (HWHM) ($\text{cm}^{-1} \text{atm}^{-1}$ at 296K).
- (O) Shift of the transition due to pressure (cm^{-1}).
- (P) Accuracy indices for frequency, intensity and halfwidths.
- (Q) Indices for lookup of references for frequency, intensity and halfwidth.

2.2 CONTENTS OF THE GEISA DATA BASE IN ITS 1993 EDITION

Originally molecules of interest not only for the Earth's atmosphere have been included in GEISA. Consequently, at present time, certain molecules are specific to GEISA, such as C_2H_4 , GeH_4 , C_3H_8 , C_2N_2 , C_4H_2 , HC_3N , H_2S , $HCOOH$, C_3H_4 . However, because recent updates of GEISA (Husson et al., 1992) and HITRAN (Rothman et al., 1992) have been carried out at nearly the same time, both data bases include very similar data sources for many molecules. Independently of its line parameter file, GEISA includes files of cross-sectional data on heavy molecular species such as the chlorofluorocarbons (CFC's) which are not amenable to line-by-line representation, at the present time.

TABLE 2. SUMMARY OF THE MOLECULAR SPECIES CATALOGED IN THE LINE PARAMETER PORTIONS OF GEISA93

Molecules	# of isotopes	# of bands	# of lines	F_{MIN} (cm^{-1})	F_{MAX} (cm^{-1})
H ₂ O	5	136	49296	0.007	22587
CO ₂	9	598	62783	442	9649
O ₃	3	76	168881	0.026	3226
N ₂ O	5	140	24125	0.838	5131
CO	5	102	13205	3	8465
CH ₄	2	39	43346	0.010	6185
O ₂	3	18	2254	0.000	15928
NO	3	50	7385	0.000	3966
SO ₂	2	7	23659	0.017	2527
NO ₂	1	9	55468	0.498	2938
NH ₃	2	23	6784	0.231	2154
P H ₃	1	5	4635	18	2446
HNO ₃	1	13	143021	0.035	1388
OH	3	103	8676	0.003	9997
HF	1	6	107	41	11536
HCL	2	17	371	20	13458
HBR	2	16	398	16	9759
HI	1	9	237	12	8487
CLO	2	8	6020	0.015	890
OCS	4	23	4153	0.381	4118
H ₂ CO	3	10	2702	0.000	2999
C ₂ H ₆	1	2	8944	765	3000
CH ₃ D	1	9	6457	7	3146
C ₂ H ₂	2	13	1258	638	3397
C ₂ H ₄	1	1	203	903	1093
GEH ₄	1	1	824	1937	2225
HCN	3	41	2575	2	18408
C ₃ H ₈	1	1	9019	700	800
C ₂ N ₂	1	7	2577	204	2182
C ₄ H ₂	1	5	1405	190	654
HC ₃ N	1	20	2027	474	691
HOCL	2	6	15565	0.024	3800
N ₂	1	1	117	1992	2626
CH ₃ CL	2	6	6687	2907	3173
H ₂ O ₂	1	2	5444	0.155	1500
H ₂ S	3	6	4058	1	1574
HCOOH	1	1	3388	1061	1161
COF ₂	1	3	18242	725	1982
SF ₆	1	1	18242	940	952
C ₃ H ₄	1	1	3390	290	360
Total lines			731206		

2.2.1 Line parameters file

Table 2 (from Husson et al., 1994) summarizes the contents of the line parameters file of GEISA93. Column 1 gives molecular formulas and columns 2 and 3, respectively isotope and band number for each molecule. The total number of lines in GEISA93 is provided in column 4. The two last columns list the minimum and maximum range of the line positions for each molecule.

2.2.2 Cross section file

The additional cross section file includes the following data :

- New CFC's cross sections from NCAR (Massie et al., 1985, 1991 ; McDaniel et al., 1991) :
In 20 spectral regions , from 765.011 to 1334.995 cm^{-1} , the following CFC's species have been considered : CF_3Cl , CHF_2Cl , $\text{C}_2\text{Cl}_3\text{F}_3$, $\text{C}_2\text{Cl}_2\text{F}_4$, CFCl_3 , CF_2Cl_2 , C_2ClF_5 , CF_4 .
- ClONO_2 cross sections in the 700-1800 cm^{-1} spectral regions, from Ballard et al., 1988.

2.2.3 CFC-12 data from a line-by-line calculation in the 923 cm^{-1} region (Deroche et al., 1987)

Spectroscopic line parameters (line frequency, relative intensity, assignment and lower state energy) for 9 bands of the isotopic species : $\text{CF}_2^{35}\text{Cl}_2$, $\text{CF}_2^{35}\text{Cl}^{37}\text{Cl}$, $\text{CF}_2^{37}\text{Cl}_2$ are cataloged in GEISA specifically, as an independent file containing 375,962 entries. For more details, see Husson et al. (1992).

3. GEISA ASSOCIATED SOFTWARE PACKAGES

A software making possible various kinds of extractions covering applications in the field of atmospheric physics as well as in the field of molecular spectroscopy, has been developed and associated with the GEISA program from its origin (Chedin et al., 1980).

3.1 GEISA MAIN FRAME COMPUTERS ASSOCIATED SOFTWARE

The GEISA management programs have been currently running on an IBM 3090/600 J-VF under VM/XA-MSV/ESA software (Chedin et al., 1985 ; Husson et al., 1992). The GEISA main frame computers software makes possible, through direct access input, output processes on GEISA-compatible structure files, various kinds of extractions such as : copy or creation of sub-files compatible with the structure of the GEISA programs, analysis, list, extractions of transitions for one or several molecules.

There are seven possible options and each option is able to perform one or more functions. These options are the following : INFORMATION: 'INF' (4 functions) ; ANALYSIS: 'ANL' ; LIST: 'LST' ; TRANSITION: 'TRS' ; EXTRACTION: 'EXT' ; COPY: 'COP' ; CREATION: 'CRE'. Extensive information on how to use in practice the GEISA software is given in Chedin et al. (1980, 1985).

3.2 IBM PC/AT/XT VERSION OF THE GEISA SOFTWARE

An IBM PC compatible version of the GEISA database and a related associated software have been created because not all the potential users have rapid access to main frame computers, and because of the present generalized use of personal computing capabilities. This software is described extensively in Chursin et al. (1993, 1994) and in Husson et al. (1994).

The GEISA-PC software package is characterized by an on line access to the spectroscopic data allowing the use of highly developed service programs as well as of a graphics tool. Among the functional capabilities of this system, the following features should be pointed out :

- interactive display according to different selections of outputs of the spectroscopic characteristics of all the lines existing in any spectral region of the data base ;
- interactive display of various kinds of molecular spectra with a preselected resolution (adapted for simulation of low resolution spectra) ;
- development of the interface between the GEISA data base and other ones, such as databases on different emission laser lines (Beck et al., 1978 ; Freed et al., 1980), on atmosphere constituent profiles (Anderson et al., 1986), and on aerosol models (Zuev, 1972 ; Krekov and Rakhimov, 1986)

At present, the GEISA-PC software package includes four main programs using the spectroscopic information contained both in GEISA93 and in the emission laser line data bases :

The first program, called BASE.EXE, enables the simulation and the graphics display of various radiative characteristics of a gas mixture.

The second program, called GSUTIL.EXE, is designed for maintaining and managing the GEISA data base. It is, in fact, an adaptation for PC computers of the original main frame data base management system, with recently developed new capabilities.

The third program, called CROSSUTL.EXE, is designed to use and maintain the database on the absorption cross sections of chlorofluorocarbons.

The fourth program, called SPECTRUM.EXE, allows the visualization of either simulated (by BASE.EXE) or experimental spectra, or of both of them.

The GEISA-PC software is designed to facilitate a broad range of applications related with the information on high resolution molecular spectra incorporated in the database.

4. CONCLUSION

The GEISA program is worked out in the purpose to be able to meet the requirements for processing the increasing number of accurate observations from space. These observations will require better knowledge of spectroscopic parameters at conditions prevalent in the upper stratosphere, mesosphere and possibly at even higher altitudes. Considering an evaluation that has been made on the basis of all the entries included in the present public data bases (see Husson et al., 1993), many of the spectroscopic parameters needed for the future space-based programs require greater accuracy than presently available.

Copies of GEISA data and free demo-version of GEISA-PC are available upon request.

REFERENCES

- Anderson, C.P., S.A. Clough, F.X. Kneizys, J.H. Chetwynd, and E.P. Shettle, 1986 : AFGL atmospheric constituent profiles (0-120 km). Report ERP no. 954, AFGL-TR86-0110, Air Force Geophysics Laboratory, Hanscom AFB, Mass., USA.
- Ballard, J., W.B. Johnston, M.R. Gunson, and P.T. Wassell, 1988 : Absolute absorption coefficients of ClONO₂ infrared bands at stratospheric temperatures. *G. Geophys. Res.*, **93**, 1659-1665
- Beck, R., W. English, and K. Girs, 1978 : Table of laser lines in gases and vapors". Springer-Verlag.
- Brown, L.R., C.B. Farmer, C.P. Rinsland, and R.A. Toth, 1987. Molecular line parameters for the atmospheric trace molecule spectroscopy experiment. *Appl. Opt.* **23**, 5154-5182
- Chedin, A., N. Husson, N.A. Scott, I. Jobard, I. Cohen-Hallaleh, and A. Berroir, Oct. 1980 : La banque de données GEISA. Description et logiciel d'utilisation. Internal Note 108, Laboratoire de Météorologie Dynamique du CNRS, Ecole Polytechnique, F- 91128 Palaiseau Cedex (in French).
- Chedin, A., and N.A. Scott, 1984 : The impact of spectroscopic parameters on the comparison of the Jovian atmosphere discussed in connection with the recent laboratory, Earth and planetary observations programs. *JQSRT* **32**, 453-461.
- Chedin, A., N. Husson, N.A. Scott, I. Cohen-Hallaleh, and A. Berroir, Feb. 1985 : The GEISA data bank : 1984 version. Internal Note 127, Laboratoire de Météorologie Dynamique du CNRS, Ecole Polytechnique, F- 91128 Palaiseau Cedex (in French).
- Chursin, A.A., A.V. Nikitin, V.F. Golovko, Vl. G. Tyuterev, N. Husson, B. Bonnet, N.A. Scott, and A. Chédin, 1993 : GEISA-PC software : IBM-PC version of GEISA-92 optical spectroscopy data base. *Proc. of SPIEE*, **2205**, 413-418.
- Chursin, A.A., V.F. Golovko, Vl. G. Tyuterev, N. Husson, B. Bonnet, N.A. Scott, and A. Chédin, 1994 : GEISA-PC Manual. Internal Note LMD 192, Laboratoire de Météorologie Dynamique du CNRS, Ecole Polytechnique, F- 91128 Palaiseau Cedex, in press.
- Deroche, J.C., and A. Goldman, 1987 : Line-by-line calculation of CF₂Cl₂ (F-12) absorption profile in the 923 cm⁻¹ region. Tenth Colloquium on High Resolution Molecular Spectroscopy, Dijon, France, 14-18 sept. 1987
- Farmer, C.B., O.F. Raper, and F.G. O'Callaghan, Oct. 1987 : Final report on the first flight of the Atmos iInstrument during the Spacelab-3 mission, April 29 through May 6 1985. JPL Publication, 87-32, USA
- Freed, C., L.C. Bradley, and R.G. O'Donnel, 1980 : *IEEE J. of Quantum Electronics* **QE-16**, 1195.
- Garing, J.S., and R.A. McClatchey, 1973 : Atmospheric absorption line compilation. *Appl Opt*, **12**, 2545-2545
- Husson, N., A. Chedin, N.A. Scott, D. Bailly, G. Graner, N. Lacome, A. Levy, C. Rossetti, G. Tarrago, C. Camy-Perret, J.M. Flaud, A. Bauer, J.M. Colmont, N. Monnanteuil, J.C. Hilico, G. Pierre, M. Loete, J.P. Champion, L.S. Rothman, L.R. Brown, G. Orton, P. Varanasi, C.P. Rinsland, M.A.H. Smith, and A. Goldman, 1986 : The GEISA spectroscopic line parameters data bank in 1984. *Ann. Geophys.*, Fasc. 2, Series A, 185-190

- Husson, N., B. Bonnet, N.A. Scott, and A. Chédin, 1992 : Management and study of spectroscopic information. The GEISA program *JQRST*, 48, 509-518.
- Husson, N., B. Bonnet, and A. Chédin, 1993 : The GEISA program. Proc. of NATO advanced Research Workshop on "High Spectral Resolution Infrared Remote Sensing for Earth's Weather and Climate Studies", Paris, France, 23-26 March 1992, Springer-Verlag, 443-447. Edited by A. Chedin, L.T. Chahine & N.A. Scott.
- Husson, N., B. Bonnet, A. Chedin, N.A. Scott, A.A. Chursin, V.F. Golovko, and V.I.G. Tyuterev, 1994 : The GEISA data bank in 1993. A PC/AT compatible computer's new version. *JQSRT*, in press.
- JPL, 1991 AIRS (Atmospheric Infrared Sounder) science and measurement requirements. JPL Publication, D6665 REV.1 9/91. Jet Propulsion Laboratory, Pasadena, USA.
- Krekov, G.M., and R. Rakhimov, 1986 : The optical models of atmospheric aerosols (in Russian). Publication of the Institute of Atmospheric Optics of Siberian Branch of Soviet Academy of Sciences, Tomsk, Russia.
- Massie S.T., A. Goldman, D.G. Murcray, and J.C. Gille, 1985 : Approximate absorption cross sections of F12, F11, ClONO₂, N₂O₅, HNO₃, CC1₄, CF₄, F₂, F113, F114 and HNO₄. *Appl. Opt.*, 24, 3426-3427
- Massie S.T., A. Goldman, A.H. McDaniel, C.A. Cantrell, J.A. Davidson, R.E. Shetter, and J.G. Calvert, 1991 : Temperature dependent infrared cross sections for CFC11, CFC12, CFC13, CFC14, CFC22, CFC113, CFC114 and CFC115. NCAR Technical Note TN-358+STR, USA
- McClatchey R.A., W.S. Benedict, S.A. Clough, D.E. Burch, R.F. Calfee, K. Fox, L.S. Rothman, and J.S. Garing , 1973 : AFCRL atmospheric absorption line parameters compilation. Environmental Research Paper 434, AFCRL-TR-73-0096 : Air Force Cambridge Research Laboratories, USA
- McDaniel A.H., C.A. Cantrell, J.A. Davidson, R.E. Shetter, and J.G. Calvert, 1991 : The temperature dependent infrared absorption cross sections for the chlorofluorocarbons : CFC11, CFC12, CFC13, CFC14, CFC22, CFC113, CFC114 and CFC115. *J. Atmos. Chem.*, 12, 211-227
- NATO ASI Series, 1993. High Spectral Resolution Infrared Remote Sensing for Earth's Weather and Climate Studies. Series I : Global Environmental Change, vol. 9. Springer-Verlag. Edited by A. Chedin, L.T. Chahine & N.A. Scott.
- Poynter R.L., and H. Pickett, 1985 : Submillimeter, millimeter, and microwave spectral line catalog. *Appl. Opt.* 24 : 2235-2240
- Rothman L.S., R.R. Gamache, R.H. Tipping, C.P. Rinsland, M.A.H. Smith, D.C. Benner, V. Malathy Devi , J.M. Flaud, C.Camy-Peyret, A. Perrin, A. Goldman, S.T. Massie, L.R. Brown, and R.A. Toth, 1992 : The HITRAN Molecular Database : Editions of 1991 and 1992. *JQRST*, 48, 469-507.
- V.E. Zuev, 1972 : The propagation of visible and infrared emission into the atmosphere (in Russian), Sovetskoe Radio.

A NEW DOPPLER IMAGER FOR THERMOSPHERIC DYNAMICS

R.W. Zywicki¹, D.S. Dilworth¹, B.C. Kennedy², E.J. Weber³ and K.A. More¹

1. ABSTRACT

An innovative optical system design has been developed for the purpose of high spatial resolution measurements of thermospheric winds. The system will measure the Doppler shift imparted by the motion of the neutral atmosphere at altitudes of approximately 250 km at 630 nm over the full sky. Velocities of up to 4.7 km/s will be measured with resolution of 50 m/s, and with spatial resolution of 50 km.

The magnetosphere, ionosphere and thermosphere are highly coupled systems which interact at high latitudes through electromagnetic, energetic particle and mechanical processes. Previous measurements have established the large scale, average characteristics of the motion of these three regimes. More recent studies have focused on the detailed structure of thermal plasma flow and associated electrodynamics in the vicinity of auroral arcs. These types of studies require improved measurements of neutral flows on these same spatial and temporal scales in order to properly determine small scale coupling processes.

The designed system integrates wide field telecentric optics, a novel Fabry-Perot interferometer, a high precision cooled CCD camera and a controlling personal computer. The key innovation in this design is the use of a Fabry-Perot etalon as an imaging device. Previous techniques of imaging through a Fabry-Perot are limited to a spatial resolution of tens of spatial regions, whereas the instrument developed with this technique images 2200 regions. In addition, a set of software tools has been developed for image processing and data extraction.

Potential applications of the technology used in the prototype are any Fabry-Perot based system that would benefit from the addition of imaging capabilities. These include chemical detection, environmental monitoring and atmospheric research.

2. INTRODUCTION

During the past decade, significant progress in understanding thermospheric dynamics has been achieved through improved ground based and satellite diagnostics, and through the development and improvement of computer models. The average wind patterns and their dependence on geophysical forcing parameters are reasonably well understood at low-, mid- and high-latitudes. These are driven by relatively slowly varying solar U.V. and E.U.V. heating and by geomagnetic inputs at high latitudes. Good agreement is being obtained among actual measurements, empirical models and Thermospheric General Circulation Models. An excellent review by Crowley (1991) summarizes recent advances in experimental and modeling results. Conventional narrow beam Fabry-Perot Interferometers (FPI), which have to be mechanically scanned to various positions over the sky, were adequate to obtain large-scale, average wind patterns. These often required 10's of minutes to complete a limited number of line of sight measurements, which were then combined to derive a single velocity vector at that location. Variations in the wind field over the field of view from a ground station were not easily observed. In order to explore thermospheric wind variability at spatial scales of 10's of km and temporal scales of 10's of minutes, new instrumentation was required. These thermospheric "weather" type measurements would be required, for example, to investigate the detailed wind pattern associated with auroral arcs. Coordinated Incoherent Scatter Radar (ISR) and Imaging Photometer measurements (Weber, et al., 1991) have shown that large shears as well as flow jets in the thermal plasma velocity are associated with many auroral arcs. These velocity structures, which occur over spatial

¹Daedalus Enterprises Incorporated, Ann Arbor MI 48106-1869

²Space Physics Research Laboratory, University of Michigan, Ann Arbor MI 48109-2143

³Phillips Laboratory, Geophysics Directorate, Hanscom AFB MA 01731-5000

scales of 50 km, are the ionospheric signature of magnetospheric electric fields, mapped down along magnetic field lines, and responsible for horizontal (Pederson and Hall) as well as field aligned currents. Through ion drag, the plasma motion is expected to impart momentum to the neutrals, provided the arc is stable and persists for several 10's of minutes, and that the thermal plasma density is high enough to effectively collisionally couple to the neutrals. These conditions are often satisfied, however to date no similarly structured thermospheric flow patterns have been reported. The most relevant measurements, made by Batten and Rees (1990) using a Doppler Imaging system (DIS), provide spatial resolution of every 15° in azimuth by four measurements in elevation or 96 individual line of sight wind components over a field of view of 100°. Because of the smoothing techniques employed to convert the line of sight components to actual horizontal wind vectors and smearing due to air parcel motion during the relatively long (10 min) integration period, small scale flow structures tend to be suppressed in the DIS measurements. They do, however, reveal relatively rapid changes in thermospheric flow in the auroral region, presumably due to changes in the thermal plasma convection pattern.

Studies of the thermosphere/ionosphere have been conducted utilizing sounding rockets, satellites, and ground based remote sensing instrumentation. A wide variety of instrumentation has been employed including ion and mass spectrometry, particle detectors, radar, multichannel narrow and broad band photometers, imaging photometers, imaging spectrometers, grating spectrometers, and Fabry-Perot interferometers. Of great interest are the physical, chemical, dynamic and radiative processes in the upper atmosphere, ionosphere, and magnetosphere and the coupling between these regions. The ionosphere is of interest because it greatly influences most radio signal propagation and affects the operation of many commercial and military communication systems. Since the ionosphere is closely coupled to the thermosphere, studies of thermospheric dynamics yield important information on ionospheric and thermospheric structure, dynamics and the interactive processes, particularly when integrated with complementary measurements. Consequently, remote optical sensing of winds has provided considerable insight into these important processes.

Optical remote sensing of the thermosphere has been conducted by multichannel and imaging, narrow and broad band photometers. This class of instrumentation provides considerable information on intensities and geometrical structure in the upper atmosphere. Barium release experiments provide much useful wind information, but are localized and of relatively short duration. The use of remote sensing Doppler instruments adds the dynamics measurements needed to further the understanding of the complex interactions. Remote Doppler optical measurements provide an opportunity to obtain information over long periods of time and large geometrical regions.

The auroral region of the polar cap has received considerable attention because the earth's magnetic field concentrates solar energy input into this region providing an opportunity to examine the complex processes and interactions of interest. Observations of the high latitude neutral winds have been reported by several authors; see for example, Meriwether, et al., 1973 in which the results from 15 chemical release rocket experiments are reported. The chemical release results show that ion drag, (the effect of ions on neutrals) is a dominant force on neutral winds in the 200 to 300 km region at magnetic latitudes greater than 65° in the evening and midnight hours. A single etalon Fabry-Perot interferometer was flown on the Dynamics Explorer 1 satellite in 1981 obtaining global wind patterns as reported by Killeen and Roble, 1988. The Fabry-Perot measurements were combined with in situ mass spectrometer wind measurements to provide comprehensive global wind patterns over a period of 13 months. Frank, 1988, reported results from the Dynamics Explorer 2 high altitude satellite employing an imaging photometer which discovered the presence of the auroral centerline or "theta" arc. The use of a Photometric Imaging Etalon Spectrometer earth limb instrument used to measure temperatures in the earth's airglow has been reported by Mende, et al., 1988.

Of particular interest is the relative motion near auroral arcs and the observation of drifting 'patches' and their relationship to the ionosphere in the F region as reported by Weber, et al., 1986. The patches drift in the anti-sunward direction with speeds from 100 to 1000 m/s, are up to 1 km in size, and are accompanied by ionospheric irregularities of similar size. The patches are seen to convect over large distances (3,000 km). Higher temporal and geometric scale measurements have been reported by Batten and Rees (1990) using a modified ground based Fabry-Perot interferometer. Geometric scales as short as 50 km and time resolution down to 10 minutes are shown to be scientifically interesting with wind velocities of 100 to 200 m/s reported.

2.1 THE $O(^1D)$ MEASUREMENT

Since the primary focus for this instrument development is wind imaging, the $O(^1D)$ emission at 630 nm was chosen for the basic measurement. This ubiquitous oxygen emission occurs in a 'shell' approximately 100 km thick in the 200 to 300 km region of the upper atmosphere. Daytime intensities are on the order of 30 KRayleighs, while nighttime intensities are typically 50 to 100 Rayleighs. Auroral zone emissions can be much higher. Consequently, a useful emission is present essentially at all times and in all look directions. In addition, as noted above, this emission has been studied extensively which provides the input parameters needed for the instrument design. From Weber, et al. (1991) we have derived the following input parameter for the instrument:

Zenith angle	0 to 80°, maximum
Azimuth angle	0 to 360°
Spatial resolution	50 x 50 km
Brightness	50 to 2,000 Rayleighs
Temporal Resolution	1 to 15 minutes (Signal dependent)
Wind Velocity	0 to 2,000 m/s
Wind error	50 m/s
Emission Layer Temperature	1,000 to 3,000 K

2.2 OBSERVATION GEOMETRY

The observation geometry for a single pixel is shown in Fig. 1. Buildings, hills, etc. at site locations typically limit the zenith angle to about 80°. The 50 x 50 km nominal spatial resolution produces 2195 sky regions with this geometry and sets the pixel field of view at 3.6° full angle. Since the $O(^1D)$ occurs in a layer, the signal brightness is enhanced by about a factor of three as the zenith angle reaches 80° as shown in Fig. 2. This is shown as Delta 1 in the figure. During the daytime, the $O(^1D)$ signal is dominated by Rayleigh scattering from the lower atmosphere. Useful measurements of the bright daytime signal can be made past sunset since the lower atmosphere is no longer illuminated and the Rayleigh scattered component is significantly reduced. The twilight altitude at zenith is shown in Fig. 3 versus time past normal sunset.

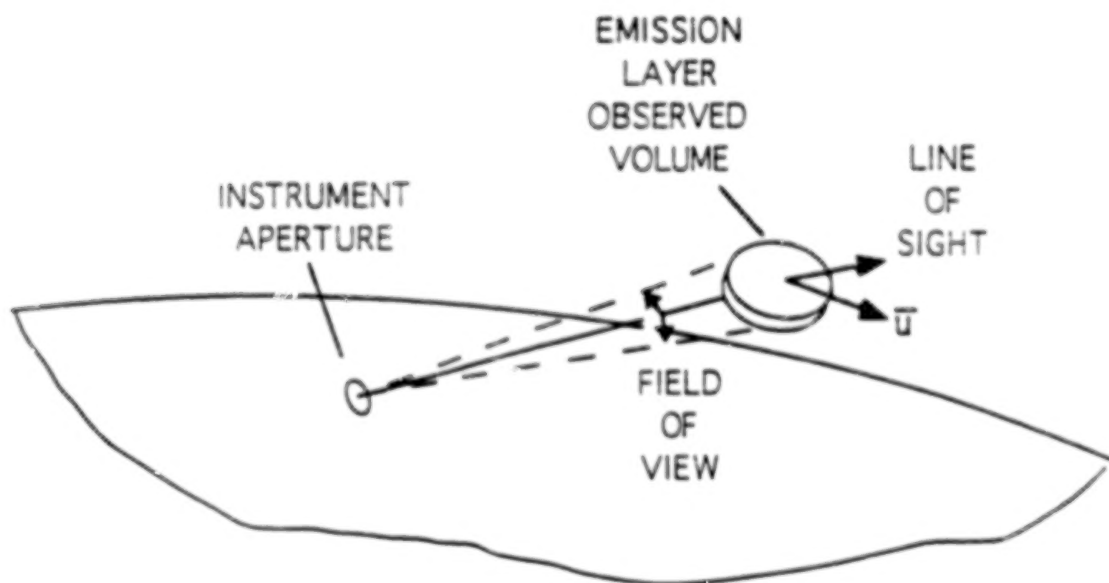


Figure 1. Upper Atmosphere Wind Velocity Observation Geometry.

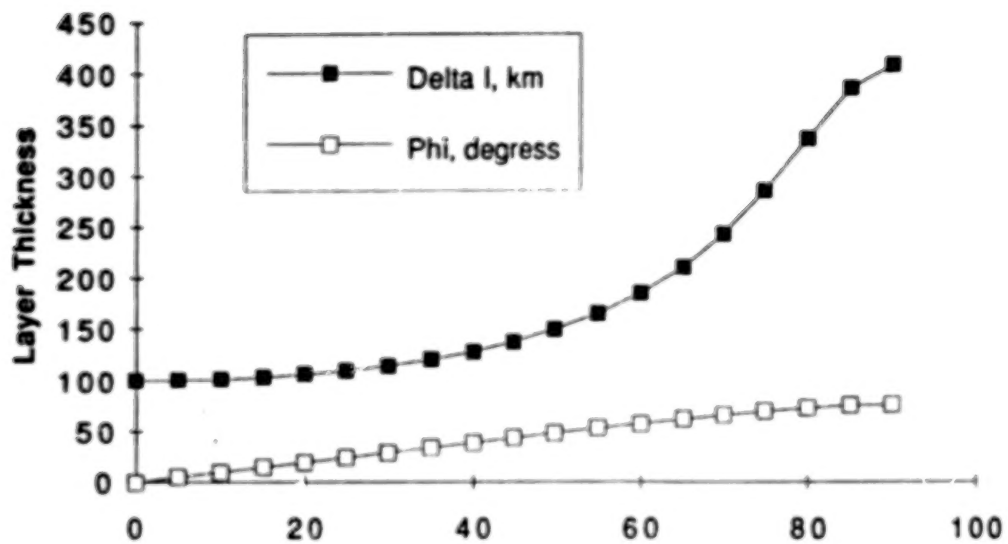


Figure 2. Von Rhijn Effect: Layer Thickness vs. Zenith Angle.

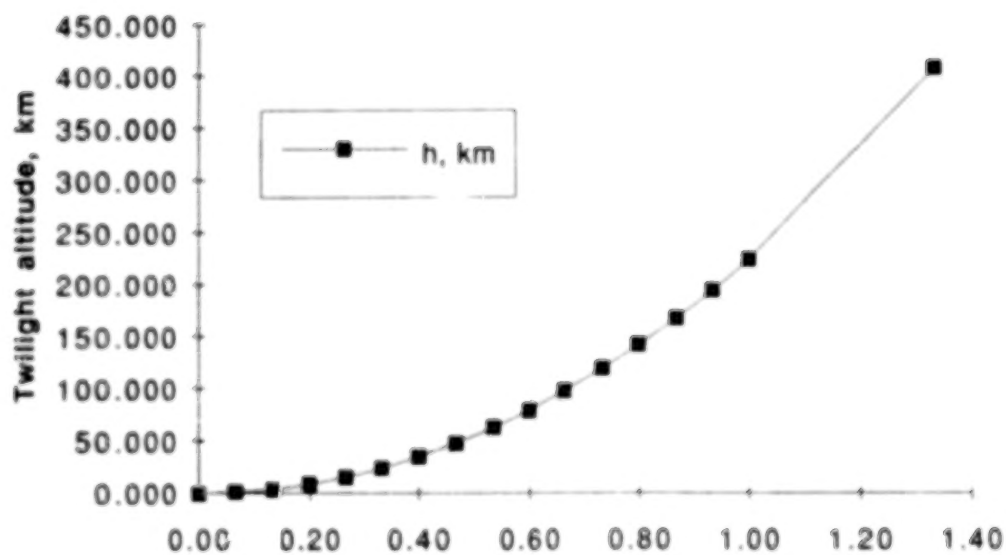


Figure 3. Twilight Altitude vs. Hours Past Twilight.

3. SYSTEM DESCRIPTION

Few of the previous Fabry-Perot instruments have been imagers, that is, they have not provided any spatial information about the portions of the sky that lay within their fields of view. In order to create an image, these single point interferometers needed to be mechanically scanned across the area of interest. This is not the optimal method for providing a high spectral and temporally resolved image, as only a fraction of the scan time is dedicated to any one portion of the sky. This method is inherently inefficient as compared to a staring system, which has a multiplex advantage.

The Batten and Rees instrument improves on the single point interferometer approach by resolving several dozen radial regions of the sky simultaneously. While this approach provides some degree of spatial resolution, it cannot be extended to allow high enough spatial resolution to adequately study the relative motion in the ionosphere.

The key to this problem of parallel image acquisition is in segmenting the image into discrete regions. Hernandez alludes to the use of fly's eye optics to segment an image presented to an etalon for filtering. This "Imaging Interferometer" concept, as applied in the Doppler Imager, is used to optically segment a large (150 mm) Fabry-Perot etalon into 2200 optically isolated regions. This effectively creates tiny, 3 mm individual etalons for each region.

In support of the Imaging Interferometer are optical and electrical subsystems that format the optical signal, gather the interferometer output, collect the raw imagery and process the quantified data. A block diagram showing the major subsystems is shown in Fig. 4.

The primary optics collect a 150 mm image of a 160° total field and project this into the imaging interferometer. These optics are throughput and angle matched to the Imaging Interferometer. This assembly segments the image, and selectively filters the signal with a Fabry-Perot etalon. (This codes the Doppler shift on the sky signal with an Airy ring pattern.) The resultant image is re-imaged onto a 1024×1024 pixel CCD camera system where the image is collected and quantified. Once transferred to the computer, the raw image is displayed for quality verification. The raw data may then be processed to decode the Doppler signal. The output of the signal processing algorithm is a set of files that contain the line of sight wind velocity in the image as well as amplitude and image quality information. In addition, the algorithm creates a set of velocity and amplitude images which may be displayed on the system monitor.

3.1 OPTICAL DESIGN

A layout for the optical system is shown in Fig. 5.

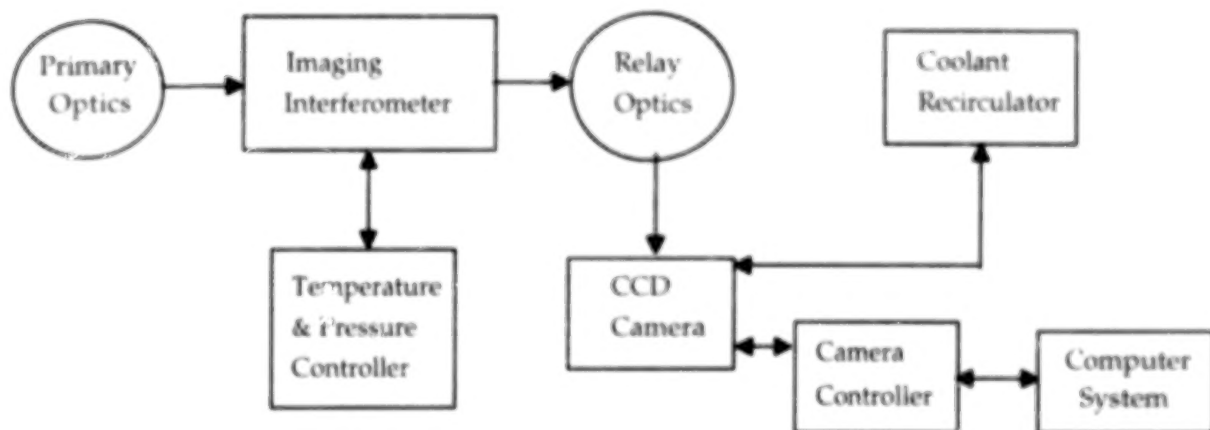


Figure 4. Doppler Imager Block Diagram.

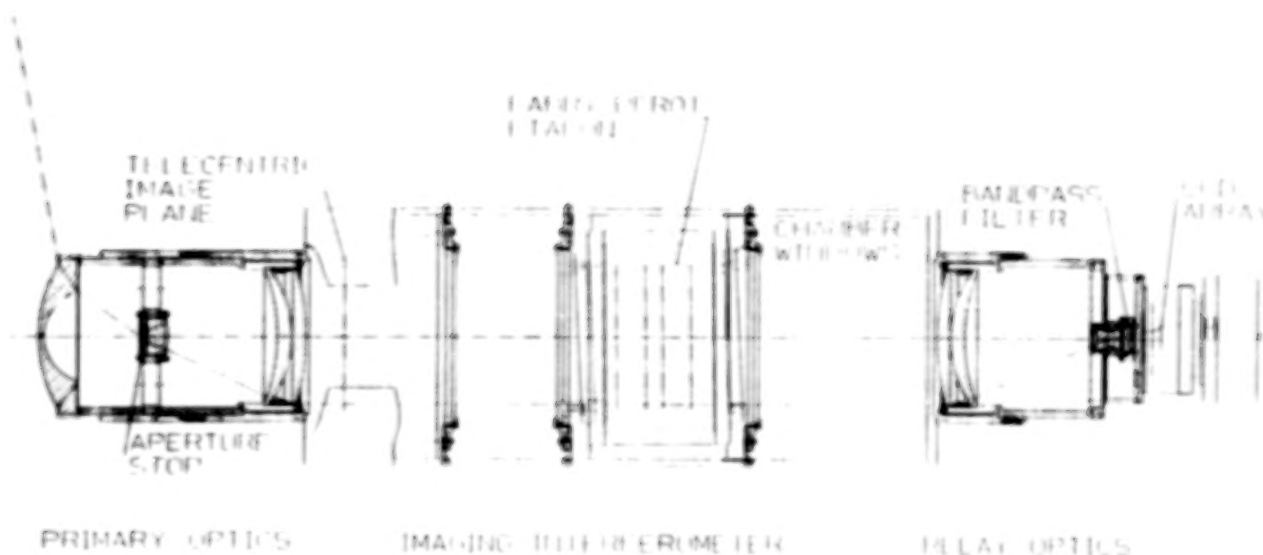


Figure 5. Doppler Imager Optical System Layout.

Table 1 outlines the optical performance of the system.

TABLE 1. DOPPLER IMAGER OPTICAL PERFORMANCE

Parameter:	Design Specification	Doppler Imager
TFOV:	160°	175° Maximum (Measured) 160° unvignetted
Region IFOV:	3.0°	3.6° (Measured)
Pixel IFOV:	None Specified	2.5 mrad/0.14° (Measured)
Relative Aperture:	f/89	f/91
Telecentricity (Maximum angle incident on the etalon):	<5.6 mrad	<6 mrad.
Spatial Resolution:	<48 μ m at CCD	Approx. 16 μ m at CCD (Diffraction limited)
Modulation Transfer Function (MTF):	>50% @ 20 lines/mm	>70% @ 20 lines/mm >50% @ 40 lines/mm
Obscurations:	None Specified	Three 6° x 30° obscurations (Sky coordinates) due to etalon mounting, at 0°, 120° and 240° azimuth.

BLANK PAGE

3.2 ELECTRICAL SYSTEMS

The electrical systems within the Doppler Imager include:

- CCD Camera Subsystem
- Temperature and Pressure Controller
- Computer Subsystem
- Power Distribution

The interconnection between these systems is shown in Fig. 6.

The camera head houses a Tektronics TK1024B back-thinned 1024^2 silicon CCD array. This is operated in MPP mode and is mounted on a four-stage thermoelectric cooler with a liquid heat exchanger. This combination cools the array to -60°C ensuring the least possible dark current signal without requiring liquid nitrogen. The output from the array is pre-amplified and sent to the camera controller, where a 50 kHz A/D converter digitizes the image. This slow scan minimizes read noise in the imagery. The controller also supplies the interface between the camera and the 80486 DX/2 66 host computer via a high speed serial interface using the PC's DMA channels.

The temperature and pressure controller regulates and controls the interferometer internal temperature to $\pm 0.1^\circ\text{C}$, and measures the sealed etalon pressure to $\pm .01\text{ PSIA}$. This stabilizes the phase of the Airy signals generated by the etalon.

3.3 MECHANICAL PACKAGE

The intended installation for this system is the Air Force laboratory at Sondrestrom, Greenland. Although the actual installation is in a laboratory environment, the remote location and severe weather precludes the transportation and operation of a "breadboard" instrument. As a result, the Doppler Imager was developed as a fully packaged, field portable system.

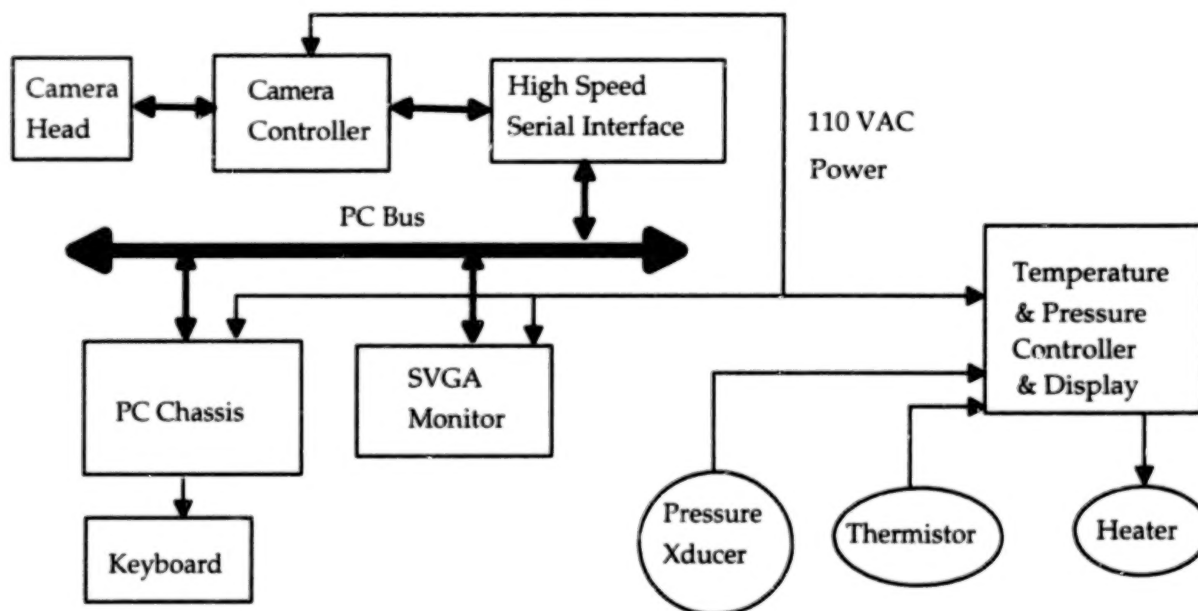


Figure 6. Electrical Systems Block Diagram.

The optical head as shown in Fig. 5 is a 59"x12"x12" assembly constructed primarily of aluminum and glass. The head weighs 175 lbs., and is designed to hang vertically from a supporting frame built into the installation ceiling.

The electronics consist of five 19" rack-mount chassis totaling 36.75" of rack space, plus a 8" high un-mounted coolant recirculator. The electronics are semi-permanently mounted in a shock resistant shipping case, and can operate without being removed from this package.

4. SIGNAL ANALYSIS

The geometric parameters of the Doppler Imager were stated in Section 2. Of particular interest is the relationship between wind error, and sample time. The basis for determining this relationship is the instrument throughput equation which relates input signal to output counts. This output provides input to the error analysis equation which permits a determination of the wind error versus sample time from which instrument parameters can be optimized. The instrument signal throughput can be shown to be:

$$S = \frac{10^6 BL_{VR} A \Omega \tau \eta t}{4\pi F} \quad (1)$$

Where:

<u>Term</u>	<u>Definition</u>	<u>System Value</u>
S	Detector counts per sample period	Signal Dependent
$10^6/4\pi$	Rayleigh conversion constants	N/A
B	Brightness in Rayleighs	Signal Dependent
L_{VR}	Von Rhijn path length effect of viewing layer obliquely	Varies from 1 to 3.5
A	Instrument (region) aperture	.08 cm ²
Ω	Instrument solid angle (region)	1×10^{-6} sr.
τ	Total optical transmission	61%
η	Detector quantum efficiency	80%
t	Sample period	1-15 minutes, signal dependent
F	Total instrument finesse	2.9

Wind error: In the absence of background noise, using a simple linear model of the instrument spectral response function, it can be shown that the wind error is related to signal by:

$$\Delta v = \frac{0.7\delta v}{\sqrt{C_{tot}}} \quad (2)$$

where Δv is the wind error, δv is the spectral width of the source, and C_{tot} is the total accumulated signal in the region.

For a Fabry-Perot, common terminology is Free Spectral Range, FSR, the spacing between recurring peaks, and Finesse, F, the ratio of FSR to spectral line width. Therefore, the Wind error equation can also be expressed as:

$$\Delta v = \frac{0.7FSR}{F\sqrt{C_{tot}}} \quad (3)$$

For this simplified case, wind error is inversely proportional to the square root of the signal counts, as would be expected for a Poisson statistically limited signal and is proportional to the spectral line width which is an inverse measure of the 'slope' of the spectral response function, which can be interpreted as the instrument 'sensitivity'. (In the actual calculation the finesse is multiplied by a factor of 1.3 to more closely represent the actual slope of the Fabry-Perot.)

For the charge coupled detector, CCD, used in this instrument, thermally generated current and readout noise must be added as background terms. When this is done the wind error equation becomes:

$$\Delta v = \frac{0.7FSR \sqrt{C_{tot} + 4C_{background}}}{FC_{tot}} \quad (4)$$

The theoretical wind error based on the Doppler Imager instrument parameters is shown in Fig. 7

5. SIGNAL PROCESSING

This section describes the computer algorithm developed to process raw Doppler Imager imagery into ionospheric wind velocity information. The raw image from the CCD camera is a 1024^2 pixel image that is sectioned into 2200 "regions", each of approximately 314 pixels. Each of these regions contains a spectral signature of a small (3.6°) area of the sky, encoded as an Airy ring. The prime goal of the wind velocity algorithm is therefore to decode these Airy rings and estimate the Doppler shift associated with that region.

Table 2 describes the more significant raw and processed data parameters.

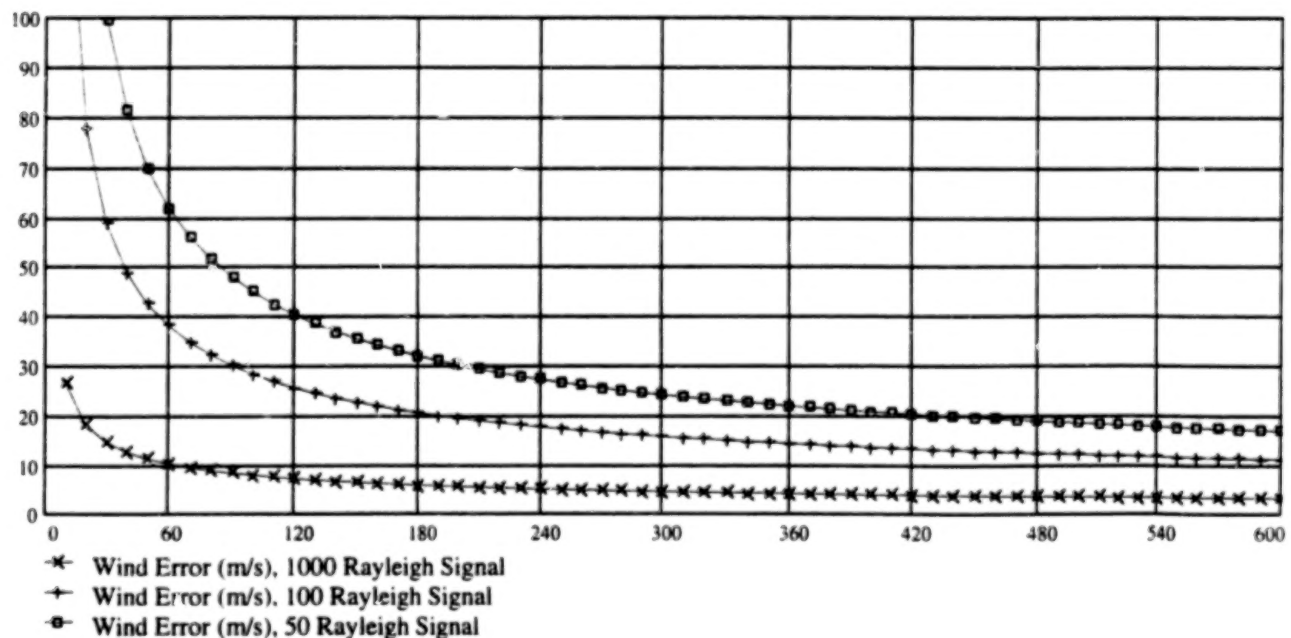


Figure 7. Theoretical Wind Error (m/s) vs. Integration Time(s).

TABLE 2. DATA PARAMETERS

Item	Value
Raw Image Size:	1024 x 1024 CCD Pixels
Image Amplitude Resolution:	16 bits
Raw Data File Size:	2.0 MByte
Usable Sky Regions:	2200 Regions
Area of Region:	314 CCD Pixels (20 pixel diameter)
Number of Calibration Files:	80
Total Amount of Library Data:	140 MByte (Derived from calibration files)
Standard Result File:	136 kByte Text File
Optional Result File:	2.1 MByte Text File
Velocity Image:	2.0 MByte
Amplitude Image:	2.0 MByte

5.1 DEVELOPMENT OF THE NORMALIZED CORRELATION ALGORITHM

The correlation method uses a library of Fabry-Perot ring images, one library per region, as references against which the raw data is compared. The acquired image is correlated against each library and the resulting correlations are used to determine the best match. An interpolation between library locations is then performed to produce the estimated wind velocity for that region.

Following are advantages of the normalized correlation method:

- The algorithm is well developed, documented, and easy to code and analyze.
- The libraries can be created from real instrument calibration data and hence includes non-modelable noise terms.
- Correlating one image with all the libraries produces a smooth and nearly symmetric function that has one peak.
- The algorithm can be adapted to use as many or few regions as desired.

Following are disadvantages of the normalized correlation method:

- The maximum correlation is affected by the presence of noise or clutter in the image. The critical parameter is the ratio of the standard deviations of the image to the image plus the noise.
- Normalized correlation is a computationally expensive algorithm. It requires calculation of:
 - Expected value of the product of the image with each library entry tested.
 - Expected value of the image and each library entry tested
 - The standard deviation of the image and each library entry tested.

The normalized correlation method correlates each region with the library of calibration images. The calibration images are collected with the same instrument and span the etalon free spectral range. The data processing then involves correlating each region with the same region in all library entries and then finding the library entry that produced the best match. This method allows for resolution beyond the number of library entries (similar to subpixelation). Matching pixels with real data from the same region of the CCD means that noise mechanisms that cannot be modeled will be considered in the process. This approach can be contrasted to using the ideal physical model of a Fabry-Perot image which doesn't include optical imperfections or other noise sources. Normalized correlation includes a normalization algorithm that adjusts to variations in the brightness between the sky data and the calibration data, and removes any dc biases. Since

the algorithm makes no assumptions about signal shape, it is tolerant to optical effects such as distortion, aberrations and vignetted as long as the imperfections are present both in the calibration and raw data.

The normalized correlation algorithm is well known and a common algorithm from computer vision. The typical computer vision application is to find a known object in a scene. An image of the object is correlated with regions of the scene and a high correlation results when the region of the scene matches the object. Correlation is limited to applications where the object image and the scene regions have the same lighting conditions. The normalized correlation method compensates for brightness variations by normalizing the mean and standard deviation of the object image and scene regions. Normalized correlation is typically used as a filter in conjunction with some other algorithm.

For this application, the normalized correlation operation results in one correlation reading for each library entry per region. The result is a 1-D array of correlations, one entry per calibration file, with the maximum correlation occurring (ideally) at the best match. The current algorithm finds the maximum correlation and then prepares a second array of 23 correlations with the maximum correlation in the middle. Hence, the second array has a peak correlation value in the middle and decreases on either side of the peak. The peak value is determined by fitting these 23 points to a cubic polynomial using the well known least squares method. The resulting polynomial is differentiated, and the differential set equal to zero, which represents the dependent variable at the peak of the cubic. Due to the tendency of this method to smooth out system noise, the resulting velocities can attain resolution beyond that of the number of library entries. From this calibration velocity the resultant Doppler wind velocity is then linearly scaled.

The noise model for this method (normalized correlation and polynomial curve fitting) is only partially understood. While the instrument noise mechanisms are well understood, we do not have a statistical model that describes how the instrument noise (in A/D counts) translates to wind velocity error. In general, it is known that the effect of instrument noise on the maximum normalized correlation is the ratio of the standard deviation of the noise-free image to the standard deviation of the image with noise. Hence, the effect of image noise on one correlation value is well understood. We do not have a model for how the polynomial curve fitting is affected by variations in normalized correlation.

5.2 ALGORITHM IMPLEMENTATION

Following is a series of flowcharts that illustrates the data acquisition process from camera calibration through signal processing and data storage.

In the first figure, the overall sequence of instrument calibration, data acquisition and signal processing is shown. A set of calibration images are acquired at pressure increments in the etalon and stored to disk. Then the experimental image is acquired, and stored in raw form. The raw image is then processed to calculate the wind velocity in the 2200 sky pixels. The resultant 2200 point wind image is then stored and displayed.

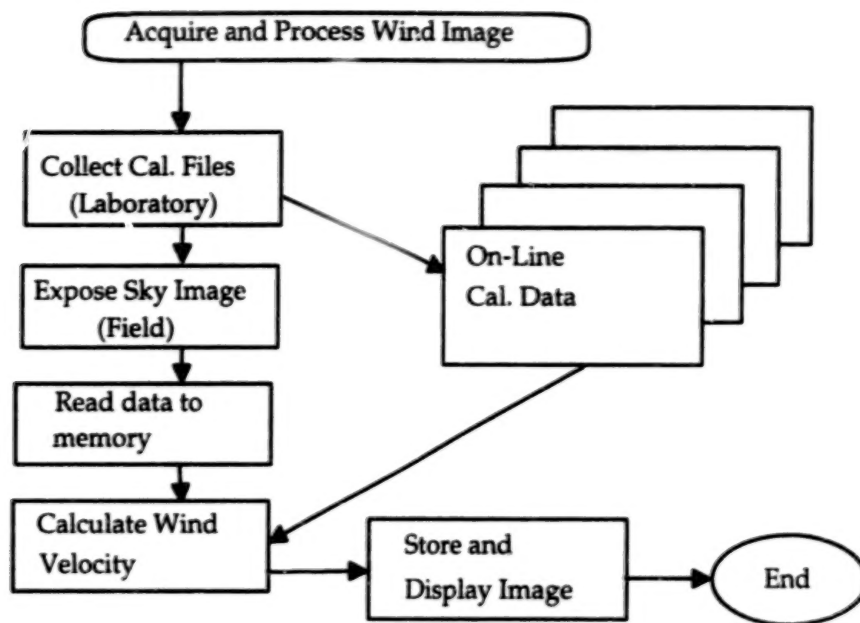


Figure 8. Image Acquisition and Processing.

Fig. 9 details the correlation and polynomial interpolation sequence. The raw imagery is compared to each calibration file image, and the score of that correlation is stored as a match. A polynomial fit is then run on the set of matches to interpolate between calibration files. The best fit between calibration files is recorded, and the wind velocity of that calibration image is recorded as data. This is done for all 2200 regions, and the result is written out as a 2200 point wind image in text or image format.

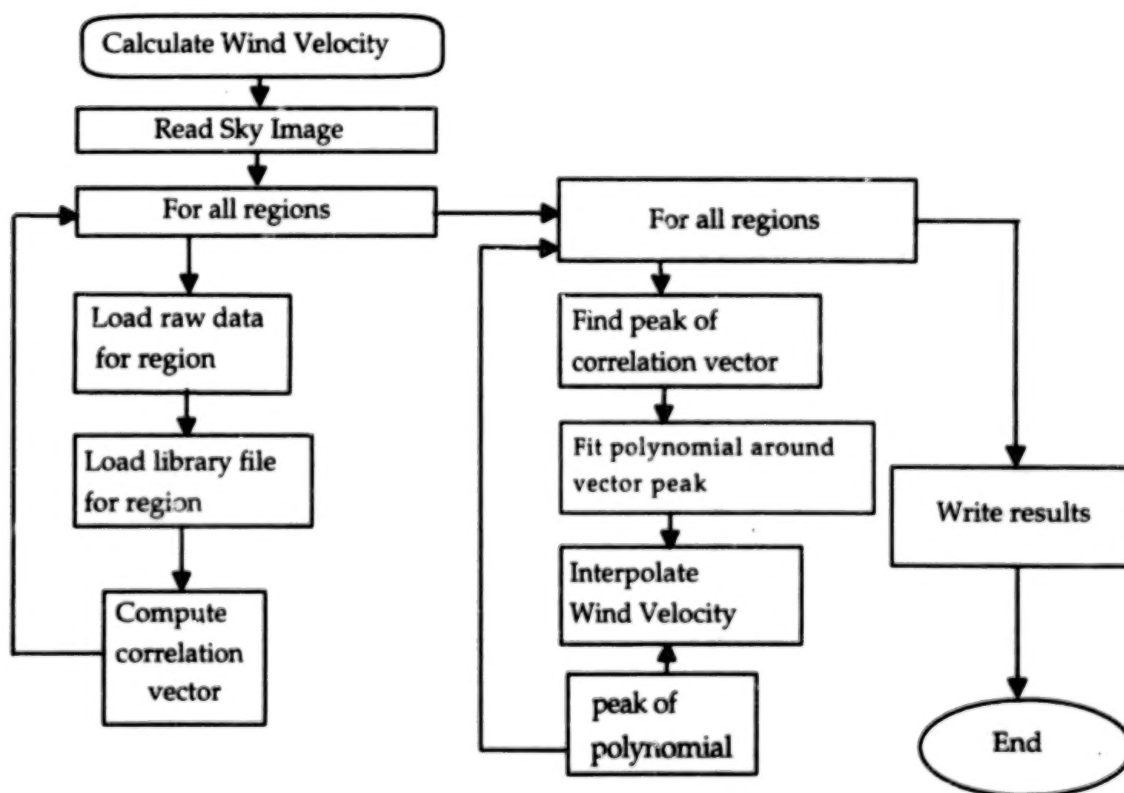


Figure 9. Signal Processing Detail.

6. RESULTS

We conducted a brief test program to quantify the performance of the system and to refine our signal processing algorithms. Two sets of tests were conducted: indoors, using Helium Neon lasers as a source with an integrating sphere; and out of doors, observing airglow near Ann Arbor. As the lasers provided a stable, bright signal and the airglow provided a dim cluttered signal, these tests represent the best and worst operating conditions for the Doppler Imager.

6.1 RADIOMETRIC PERFORMANCE

Before using the system to estimate Doppler velocities, we calibrated the radiometric response of the system. This was done by observing a stable, field filling source and computing the average signal response from all 2200 regions. Using the parameters from Section 4, we can solve Equation 1 for brightness. The average response per region is given below.

Parameter	Value
Measured Average Signal	384,911 counts
Average Electrical Signal	688,990 electrons
Integration Time	20 Seconds
Power incident on detector	.0136 picoWatts
Signal Brightness	562,736 Rayleighs

Note that although the optical flux is extremely low, the brightness measured here is four orders of magnitude higher than the expected airglow signal.

6.2 WIND VELOCITY ERROR

In order to quantify the system performance in terms of Doppler velocity resolution, we measured both high and low signal level performance in the laboratory. We then acquired and processed airglow data.

6.2.1 HeNe Laser Measurements

Full field measurements were made using four Helium Neon lasers and an integrating 16" sphere. These were acquired at several signal levels and for two integration times. These data were then processed, and the theoretical results for these signals were computed. These results are summarized in Table 3.

TABLE 3. COMPARISON OF MEASURED THEORETICAL AND MEASURED WIND ERRORS

Signal Brightness (Rayleighs)	Integration Time (Minutes)	Measured RMS Velocity Error (m/s)	Theoretical Velocity Error (m/s)
562,736	0.33	42.9	0.7
891	1	57.9	10.8
562	1	75.9	13.8
178	1	240.1	26.5
891	5	53.1	4.8
178	5	109.5	11.2
56	5	197.3	22.4

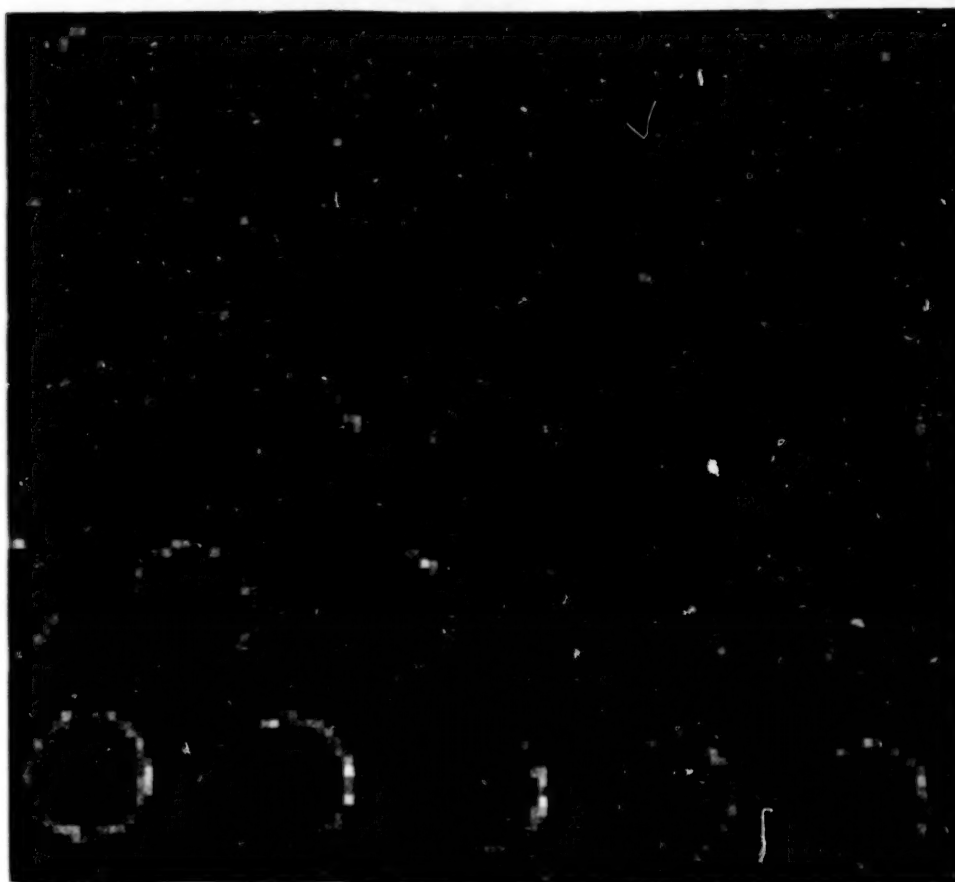


Figure 10. Calibration File: Expanded View.

An expanded view of a small portion of a typical calibration file is shown above in Fig. 10. Note the Airy structure, and the hexagonal region spacing. Each region covers 3.6° of sky.

6.2.2 Airglow Measurements

We made airglow measurements with the Doppler imager outside in Ann Arbor on three occasions between March and May 1994. On the last date, 29 May, we began making a 1-second measurement just prior to sundown, and acquired a sequence of 15 images over an hour and a half. The sky was partly cloudy with some haze; generally, the best available weather for spring in Michigan. Fig. 11 shows raw imagery from image 14, taken approximately an hour after sunset. To the left is the all-sky (175°) image with the top of the display relating to North-Northwest. The right-hand image is a magnified image of the center of the field. Note that due to the amount of broad-band stray light, airy rings are not obvious in this imagery. The gray scale on the top is in A/D counts.

In Fig. 12 we show a set of processed images. The left-hand image shows an amplitude image; each region displays the total signal in the region in A/D counts, scaled by 100. The bright area at the top-right is due to the sunset in the west. The right-hand image shows the calculated wind velocity of the full sky, referenced to 0 m/s at Zenith. The scale is in m/s. Note that over most of the image there is no apparent motion. Near the horizon, however, where the signal is brighter due to the Von Rhijn effect, there is a great deal of observed motion. These preliminary results show a great deal of variability in the wind velocity, and further processing is required.

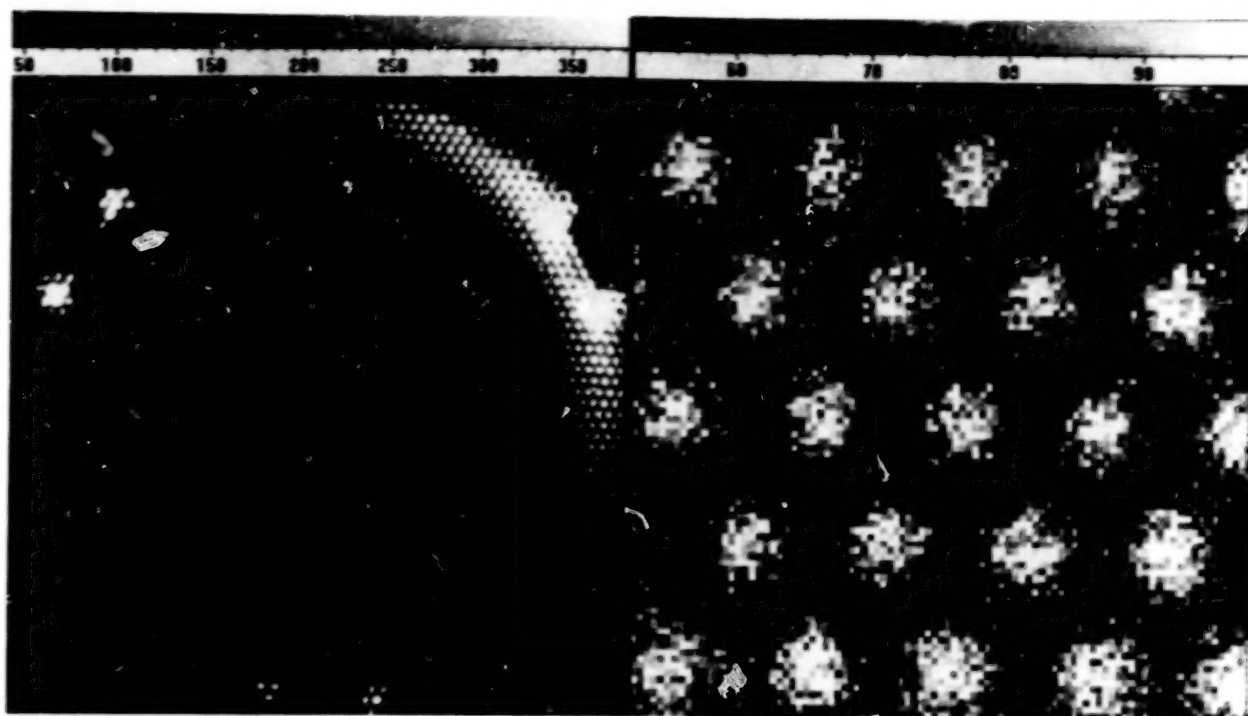


Figure 11. 29 May 1994: Raw Imagery.

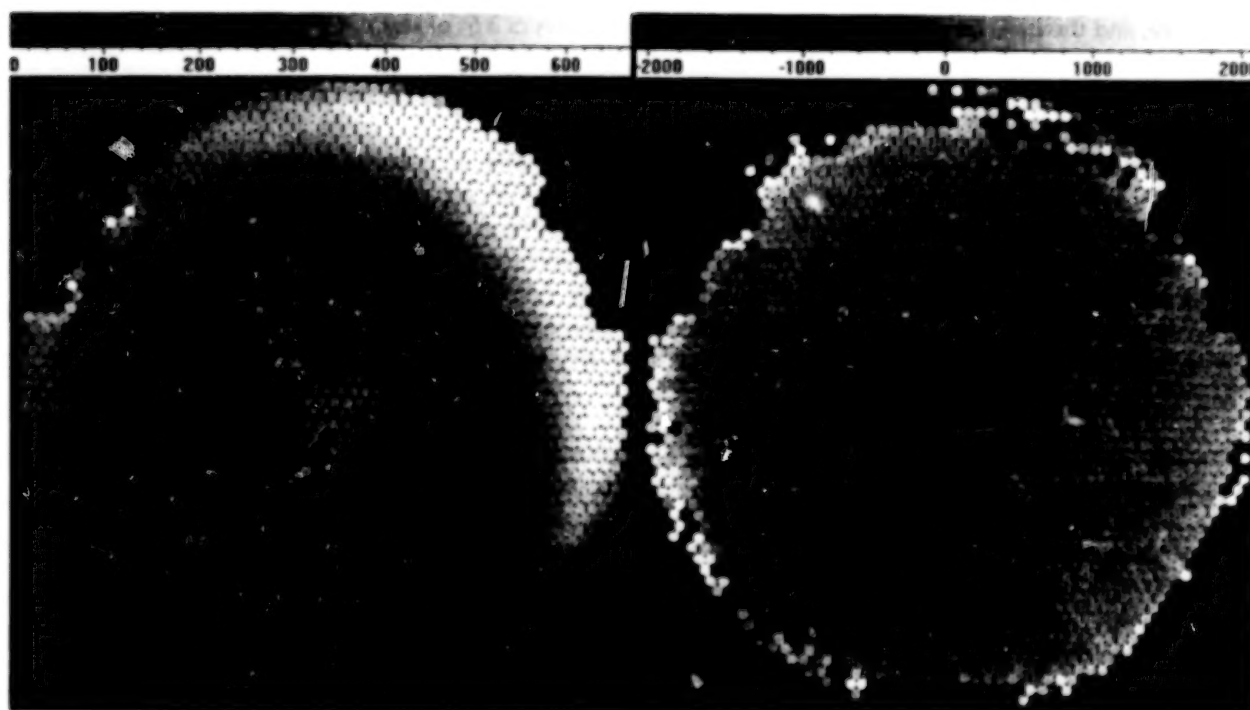


Figure 12. 29 May 1994: Processed Imagery.

7. CONCLUSIONS

The prototype resulting from the Doppler Imager development program represents a significant advancement in instrumentation for upper atmospheric wind velocity measurement. It provides spatial resolution of ionospheric emissions that have not previously been available, with excellent signal sensitivity and good velocity measurement accuracy. The instrument meets or exceeds all optical design specifications, and the signal performance matches that predicted by theory. To date, we have not been able to achieve wind velocity measurements that match the theoretical performance. We believe that this discrepancy is due to the practical limitations imposed by our signal processing algorithm, and that our initial performance figures do not represent the ultimate performance limits of this instrument. Other techniques involving a priori knowledge of the signal shape such as used by Skinner and Abrue, 1989, hold promise for extracting the theoretical wind velocity performance.

ACKNOWLEDGMENT

The work reported in this article was sponsored by the United States Air Force, Phillips Laboratory, Geophysics Directorate, Hanscom AFB MA 01731-5000, contract F19628-91-C-0097.

REFERENCES

- Abrue, V.J. and W.R. Skinner, 1989: Inversion of Fabry-Perot CCD Images: Use in Doppler Shift Measurements, *Applied Optics*, Vol. 28, No. 15, pp. 3382-3386.
- Batten, S. and D. Rees, 1990: Thermospheric Winds in the Auroral Oval: Observations of Small Scale Structures and Rapid Fluctuations by a Doppler Imaging System, *Planet. and Space Science*, Vol. 38, No. 5, pp. 675-694.
- Crowley, G., 1991: Dynamics of the Earth's Thermosphere: A Review, *Revs. of Geophys.*, **29**, 1143.
- Frank, L.A., 1988: Dynamics of the Near-earth Magnetotail Recent Observations, *Geophysical Monograph*, **44**, Washington, D.C.
- Hernandez, G., 1986: *Fabry-Perot Interferometers*, Cambridge University Press.
- Killeen, T.L., and R.G. Roble, 1988: Thermosphere Dynamics Contributions From the First 5 Years of the Dynamics Explorer Program, *Rev. of Geophys.*, Vol. 26, No.2, pp. 329-367.
- Mende, S.B., et al., 1988: Measurements of Rotational Temperature in the Airglow With a Photometric Imaging Etalon Spectrometer, *Journal of Geophysical Research*, Vol. 93, No. A11, pp. 12,861-12,870.
- Meriwether, J.W., et al., 1973: Neutral Winds above 200 km at High Latitudes, *Journal of Geophysical Research*, Vol. 78, No. 28, PP. 6643-6661.
- Weber, E.J., et al., 1991: Coordinated Radar and Optical Measurements of Stable Auroral Arcs at the Polar Cap Boundary, *Journal of Geophysical Research*, 1 October 1991.
- Weber, E. J., et al., 1986: Polar Cap F Patches Structure and Dynamics, *Journal of Geophysical Research*, Vol. 91, No. A11, pp. 12,121-122,129.

SSM/T-2 BRIGHTNESS TEMPERATURE SIGNATURES

Vincent J. Falcone, Michael K. Griffin
Phillips Laboratory, Geophysics Directorate
Hanscom AFB, MA, 01731 USA

John D. Pickle and Ronald G. Isaacs
Atmospheric and Environmental Research, Inc.
Cambridge, MA, 02139 USA

James Wang
NASA Goddard Space Flight Center
Greenbelt, MD, 20771 USA

ABSTRACT

During the calibration/validation study for the Special Sensor Microwave Water Vapor Sounder (SSM/T-2), brightness temperature (T_b) signatures were identified for various surface and atmospheric conditions. Additional sensor information were used (specifically SSM/I and GOES visible and infrared imagery) to determine the presence of clouds and precipitation in the SSM/T-2 field-of-view (FOV).

Using data collected along the east and west coast of the United States, clear FOVs over land displayed the warmest T_b s at 150 GHz; whereas, clear FOVs over water had the warmest T_b s at 183 ± 7 GHz. Non-precipitating clouds over water generally display T_b signatures similar to clear FOVs although some differences do occur, especially for the 91 GHz channel. Including data collected from the western equatorial Pacific, the presence of light rain over water caused the warmest T_b to shift to 150 GHz. As the rain rate and scattering in the FOV increased, the 183 ± 1 GHz T_b became the warmest of the three atmospheric channels. Globally, the warmest 183 ± 3 and 183 ± 1 GHz T_b s are associated with the upper-level subsidence within subtropical ridges. In the polar land regions the 183 ± 1 GHz channel was the warmest of all five channels.

1. INTRODUCTION

With the launch of the F-11 spacecraft in November of 1991, and its new microwave sensor, the SSM/T-2, a new era of atmospheric water vapor measurements was begun. While the retrieval of atmospheric temperature and to a lesser extent atmospheric water vapor profiles has been obtained for a number of years utilizing infrared (IR) sensors, they have always suffered from the inability to sense through clouds. Since clouds cover some 50% of the earth's surface, this has proven to be a severe limitation. While not totally transparent to clouds and their constituents, microwave measurements are much less sensitive to liquid and solid hydrometeors. This attribute has proven useful for studies of precipitating systems normally opaque to IR sensors. SSM/I measurements have allowed insight into the structure of tropical cyclones not possible with IR sensors.

While the main function of the SSM/T-2 is to provide water vapor profiles of the atmosphere, a look at the raw radiance or brightness temperature (T_b) has revealed a number of interesting and potentially useful channel signatures. This paper will explore some of these channel-parameter relationships in more detail, concentrating on those characteristics associated with clouds and precipitation.

2. INSTRUMENT DESCRIPTION

The SSM/T-2 is a five channel, cross-track scanning, sun-synchronous, passive, total power microwave radiometer system. At an altitude of approximately 870 km, the channel FOVs range from 48 to 88 km at nadir (Table 1). The sensor makes 28 measurements across a scan line at 3° increments ($\pm 40.5^\circ$) with a swath width of approximately 1480 km. The 3-4 FOVs at the edge of scan on the sunward side of the swath are generally not usable due to interference by the glare obstruction panel (GLOB). Calibration of the raw sensor counts is done onboard; antenna corrected radiance or brightness temperature is the standard sensor measurement used in this study.

A calibration and validation (CalVal) study was performed on the SSM/T-2 measurements (Falcone, et al., 1992 and Griffin, et al., 1993), the findings of which showed the instrument was performing well within specifications for both the measured T_b s and the retrieved water vapor profiles. In the CalVal study, a number of sensitivity experiments were performed on the measurements to estimate the effect of various surface, atmospheric and orbital phenomena. From these studies a number of relationships were discovered between the individual SSM/T-2 channels and specific surface or atmospheric parameters. The next section will explore these relationships in more detail beginning with some basic statistics about the channel measurements themselves.

Data for the CalVal study was collected over a multi-year period starting in late January, 1992 through October, 1993. Approximately 100 usable satellite overpasses were collected, of which only half could be considered full-orbits. The rest consisted of sporadic F-11 pass segments over target study areas (see Falcone, et al., 1992 for more information on the data collection periods).

3. SSM/T-2 CHANNEL SIGNATURES

In this section, an attempt to quantify the SSM/T-2 T_b s as a function of surface topography, clouds and precipitation occurrence will be made. At this time, surface topography is limited to basic parameters: water, ice, coastal and land surfaces as defined by the Air Force Global Weather Central (AFGWC) surface topography database for each SSM/T-2 FOV. Snow covered land surfaces which would have a significantly different microwave signature from that of dry soil or vegetation were not designated a separate topography type. This will influence the statistics for land surfaces especially at higher latitudes.

Cloud information for specific orbital segments was obtained using coincident GOES visible imagery. Unfortunately, only a small portion of the database has collocated cloud information. AFGWC Satellite Global Data Base (SGDB) cloud data is available for most of the orbits and may be incorporated into the database in the future.

Precipitation information for this study comes from the SSM/I precipitation algorithm (Hollinger, et al., 1991) for water surfaces. Cases containing precipitation occurrences that have been analyzed are limited; processing is continuing to expand this dataset to include more precipitation events.

3.1 CHANNEL STATISTICS

The data base described above was statistically processed to determine the range and distribution of SSM/T-2 channel T_b s. The results were categorized by latitude and surface topography and are shown in Table 2. Channels are displayed for increasing weighting function peak altitude from 91 GHz at the surface to 183 ± 1 GHz. As would be expected, in the latitude range from 0 - 60 degrees, the mean T_b s decrease in relation to their sampling altitude. Over land surfaces, both the 91 and 150 GHz channels have almost identical responses. Over coastal and water surfaces the decrease in surface emissivity (roughly from 0.9 to 0.6, see Felde, 1994) is most pronounced in the 91 GHz channel because of the larger surface contribution at this frequency. This is reinforced by the fact that the 91 GHz channel displays the lowest T_b s of any channel over water, even those peaking at high altitudes.

Since the contribution of the surface emittance to the 183 GHz channel signals is almost negligible in moist environments for latitudes below 60 degrees, it would be expected that the T_b s would remain relatively unchanged over changing topography. This appears to be the case for all three channels, except possibly over ice surfaces where the above condition does not hold true. Since all channels may have a surface contribution, the 91 GHz T_b s measured over ice surfaces are slightly larger than those over water surfaces. Combining this with the reverse relationship that exists at 183 ± 7 GHz may provide a technique to detect the location of ice in the polar regions.

3.2 CLOUD SIGNATURES

During the CalVal Experiment, the NASA ER-2 made seven flights over the West and East Coast of the U.S. in coordination with F-11 overpasses. For these overpass segments, contemporaneous GOES visible imagery was collected to be used for cloud fraction determination (DMSP OLS imagery was not obtained for these flights). By remapping the SSM/T-2 FOVs to the GOES image grid system, the fractional coverage of each SSM/T-2 FOV by non-precipitating clouds could be computed using a simple threshold technique (Table 3). The results in Table 3 are based on data over a limited region from 20 to 50 degrees north latitude.

For both of the window channels, clouds over land surfaces show a much weaker effect on the T_b s than over water surfaces. This is mainly due to the lack of contrast between the cloud emissions and those of the land surface. Water surfaces which have a much lower emissivity than typical land surfaces, contrast well with the cloud emissions and display a significant increase in the T_b at 91 GHz and to a lesser extent at 150 GHz. All channels show a slight decrease in the T_b with increasing cloud amount over land topography. This extends to all surfaces for the 183 GHz channels which have little or no surface contribution (see Pickle, et al., 1994). The overall effect of non-precipitating clouds on the SSM/T-2 T_b s is small except for the window channels where clouds significantly enhance the outgoing radiance over water surfaces due to the contrast between the warm clouds and the cool water surface.

3.3 PRECIPITATION SIGNATURES

Only two precipitation cases have been analyzed for this study: both in the Western Pacific during the Toga-Coare Experiment in February of 1993. One case included clouds and precipitation from a developing tropical cyclone (Typhoon Oliver) and provided the most dramatic effects on the SSM/T-2 channel T_b s. Utilizing the SSM/I CalVal algorithm (Hollinger, et al., 1991) for the detection of precipitation, areas of anomalous SSM/T-2 T_b s and precipitation events have been identified. Figure 1 displays the 150 GHz channel T_b s in image format along with the computed precipitation intensity from the SSM/I algorithm. The storm center is located over water south of Papua New Guinea and northeast of Townsville, Australia near 13° S and 150° E. All SSM/T-2 channels display some decrease in the measured T_b with some channels showing more sensitivity to the effects of the precipitation than others. For the 150 GHz channel, the general area of decreased T_b matches well the region of precipitation thereby providing the possibility of using the SSM/T-2 channels alone to define precipitation areas, which could then be treated uniquely in the operational water vapor retrieval model.

The effects of precipitation on the individual channels is clearly evident in Fig. 2, where measurements at a single beam position (13.5°) of the swath is plotted for the pass over the tropical cyclone. This region of the overpass is characterized by relatively clear skies over the ocean between the equator and 5 degrees south which provides a good background for comparison. In Fig. 3, plots of the T_b s shown in Fig. 2 are highlighted for three locations in the swath: clear ocean, light precipitation and intense precipitation. In the clear region the channels have the characteristic range of T_b s with the coldest occurring for the highest peaking channel (183 ± 1 GHz). During light precipitation this channel-to-channel relationship becomes less distinct until eventually the trend in the channel T_b s reverses: the 183 ± 7 GHz becomes the coldest of the three atmospheric channels, the 183 ± 1 GHz channel the warmest for more intense precipitation. The scattering of the microwave energy due to the precipitation and/or ice particles effects each channel differently in part due to its sensitivity to water vapor. The 183 ± 7 GHz channel peaks lower in the atmosphere and therefore would be most affected

Table 1. SSM/T-2 Channel Characteristics

Center Frequency (GHz)	Nadir FOV (km)	Beam Acceptance (degrees)	Peak Altitude (hPa)
91.655	88	6.0	Surface
150.00	54	3.7	1000
183.31 \pm 7	48	3.3	800
183.31 \pm 3	48	3.3	650
183.31 \pm 1	48	3.3	450
Altitude 870 km			
Swath 1480 km (40.5°)			
Ascending Node 1714 Local			

Table 2. Mean and Standard Deviation of the SSM/T-2 Channel T_{bs} (K) for three latitude bands and four surface topography types. Data is from seven F-11 orbital passes encompassing over 500,000 individual SSM/T-2 channel measurements.

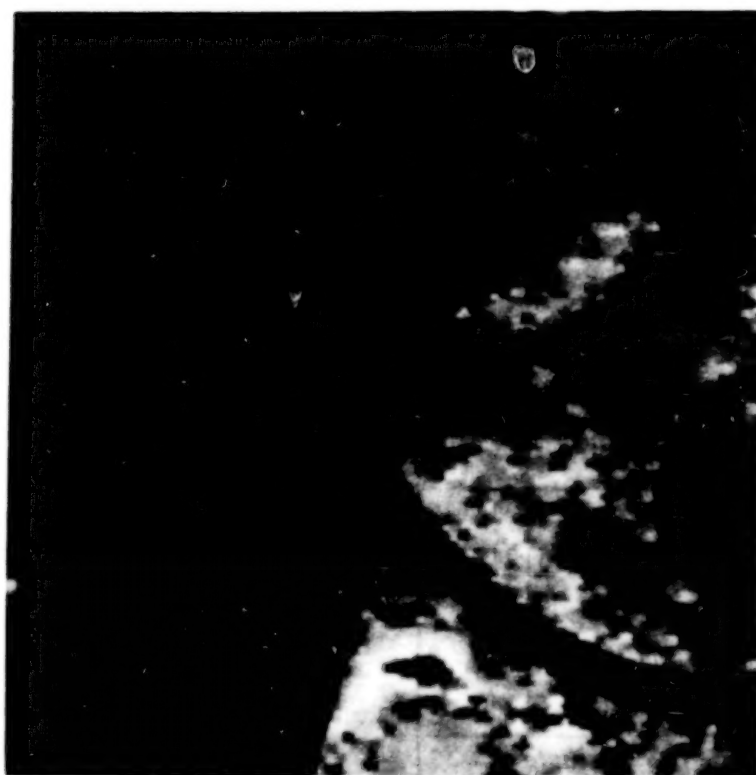
Channel	Land	Coast	Water	Ice
<i>0 - 30 Degrees N/S Latitude</i>				
91.655	284 8	261 16	243 15	
150.00	284 10	280 10	276 11	
183.31 \pm 7	272 9	273 10	275 9	
183.31 \pm 3	262 8	261 9	266 9	
183.31 \pm 1	249 8	248 8	253 9	
<i>30 - 60 Degrees N/S Latitude</i>				
91.655	275 10	247 23	218 15	224 10
150.00	277 10	264 17	248 15	240 6
183.31 \pm 7	271 7	271 8	266 8	256 5
183.31 \pm 3	261 6	262 7	259 6	249 3
183.31 \pm 1	249 6	249 7	248 6	240 2
<i>60 - 90 Degrees N/S Latitude</i>				
91.655	210 38	223 20	213 22	216 18
150.00	209 41	233 22	238 20	221 19
183.31 \pm 7	220 37	251 18	259 20	244 17
183.31 \pm 3	230 27	250 9	254 19	248 8
183.31 \pm 1	233 16	243 5	243 18	242 4

Table 3. Mean and Standard Deviation of the SSM/T-2 Channel T_{bs} (K) for three categories defining the percentage of the FOV covered by non-precipitating clouds and three surface topography types. Data is from seven F-11 orbital pass subsets over the West and East Coasts of the U.S. 2,681 individual SSM/T-2 channel measurements were used in the table.

Cloud	Land	Coast	Water
<i>91.655 GHz</i>			
< 25 %	275 8	245 22	218 13
25 - 75 %	270 9	249 20	227 14
> 75 %	272 8	254 19	232 16
<i>150.0 GHz</i>			
< 25 %	279 7	267 13	261 11
25 - 75 %	274 8	269 12	266 10
> 75 %	274 9	272 11	265 11
<i>183.31 \pm 7 GHz</i>			
< 25 %	277 5	276 6	278 5
25 - 75 %	272 6	275 6	277 6
> 75 %	270 8	271 10	272 10
<i>183.31 \pm 3 GHz</i>			
< 25 %	267 5	266 6	269 6
25 - 75 %	262 5	265 6	267 7
> 75 %	260 6	260 8	263 9
<i>183.31 \pm 1 GHz</i>			
< 25 %	253 5	253 6	255 7
25 - 75 %	250 4	251 6	252 8
> 75 %	247 5	246 6	249 8



a



b

Figure 1. SSM/T-2 150 GHz channel T_b (a) and precipitation intensity (b) over region in the Western Pacific. Image is bounded by the equator and 20 South and by 140 to 160 East; grid lines are every 5°. Bright grayshades indicate (a) warmer T_b s, (b) intense precipitation, darker grayshades indicate (a) cold T_b s, (b) light or no precipitation.

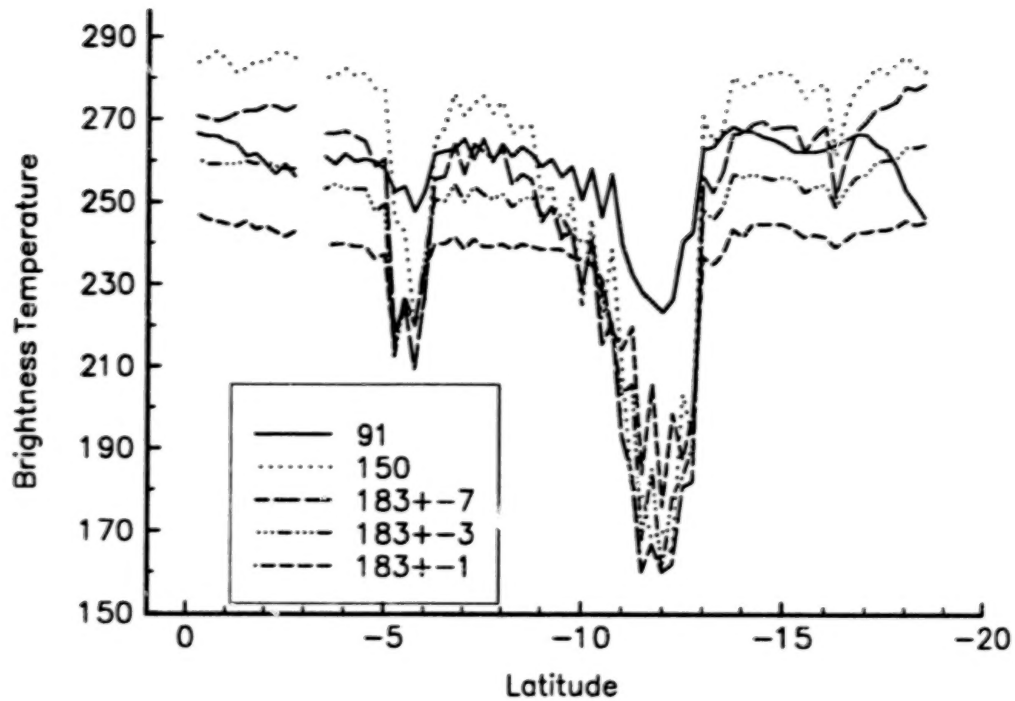


Figure 2. SSM/T-2 channel T_b s for the 13.5° beam position for a pass over the developing tropical cyclone Oliver in the Western Pacific. Gap in curves denotes missing data.

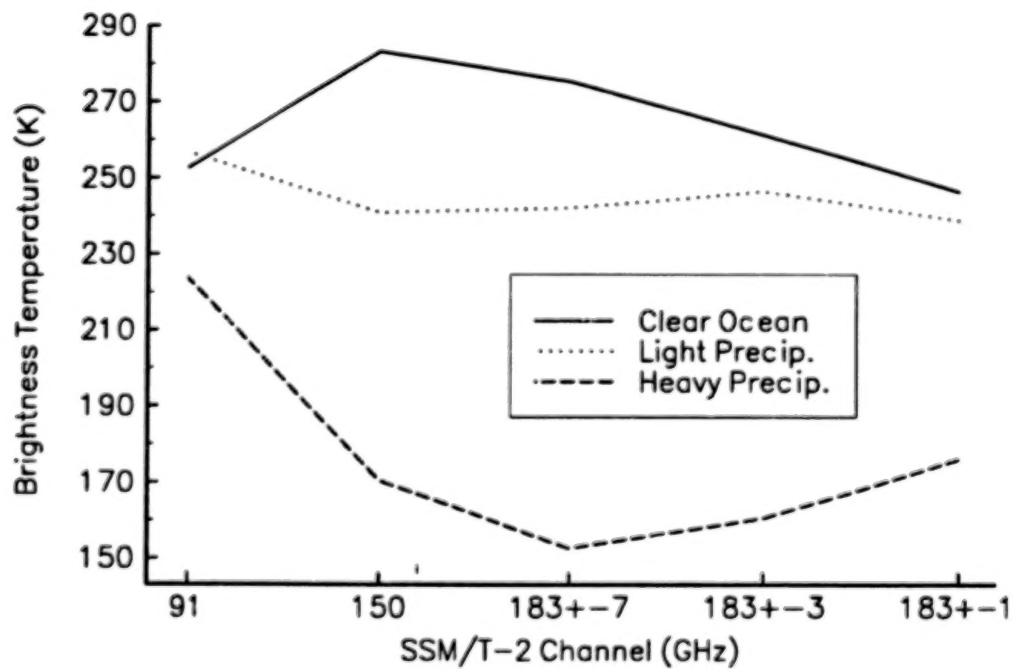


Figure 3. SSM/T-2 channel T_b s for three regions of the pass shown in Fig. 2.

by scattering which reduces the outgoing microwave energy resulting in a lower T_b . The 183 ± 1 channels peaks highest and therefore would be affected least by scattering. The balance between the normal emission from water vapor and the depletion of this energy by scattering is the key to using this information to depict areas of precipitation. A technique is being developed to use this information to define the precipitation regions utilizing SSM/T-2 data alone.

REFERENCES

- Falcone, V.F., M.K. Griffin, R.G. Isaacs, J.D. Pickle, J.F. Morrissey, A.J. Jackson, A. Bussey, R. Kakar, J. Wang, P. Racette, D.J. Boucher, B.H. Thomas, and A.M. Kishi, 1992: SSM/T-2 Calibration and Validation Data Analysis. *PL-TR-92-2293, Hanscom AFB, MA*, 432 pp.
- Felde, G.W., 1994: A Relationship Between SSM/I Brightness Temperatures and Earth Surface Emissivities at 91 and 150 GHz. *Preprints of the Seventh Conference on Satellite Meteorology and Oceanography*, AMS, Monterey, CA, June 1994.
- Griffin, M.K., V.F. Falcone, J.F. Morrissey, R.G. Isaacs, J.D. Pickle, R. Kakar, J. Wang and P. Racette, 1993: The Special Sensor Microwave Water Vapor Sounder (SSM/T-2): Calibration Study. *Preprints of the Eighth Symposium on Meteorological Observations and Instrumentation*, AMS, Anaheim, CA, Jan 1993.
- Hollinger J.P. and the DMSP SSM/I CalVal Team, 1991: DMSP Special Sensor Microwave/ Imager Calibration/Validation, Final Report. *Naval Research Laboratory*, 1, Washington, D.C.
- Pickle, J.P., R.G. Isaacs, V.J. Falcone and M.K. Griffin, 1994: Sensitivity of SSM/T-2 Channels to Water Vapor. *Preprints of the Seventh Conference on Satellite Meteorology and Oceanography*, AMS, Monterey, CA, June 1994.

PRECIPITABLE WATER ESTIMATES FROM SSM/I

Charles Norris, John Roads and Shyh Chen
Climate Research Division
Scripps Institution of Oceanography
LaJolla CA 92093-0224
(619) 534-7557

Paul Weber
Astrophysics and Radiation Measurements Group
Los Alamos National Laboratory
Los Alamos, NM 87545

The Special Sensor Microwave Imager (SSM/I), a scanning passive microwave remote sensing instrument flying on the Defense Meteorological Satellite Program (DMSP) series of spacecraft [Hollinger et al, 1987], has been used successfully to estimate the atmosphere's total precipitable water over the oceans [Schlüssel and Emery, 1990], but not over land. Variability of the background surface emission, caused by variation in surface emissivity and temperature, is larger over land regions than over the ocean. Moreover, surface emission over land regions is more difficult to determine than over the oceans. Therefore, microwave brightness values over land are generally eliminated from consideration by application of a land mask before determination of total atmospheric water vapor content. Essentially, it is assumed that the effect of water vapor on microwave brightness temperatures over land is indistinguishable from noise.

We examine this assumption of complete noise over land. In particular, we drive a statistical fit between SSM/I microwave radiances and precipitable water calculated from NMC analysis for several years over both land and ocean, treating each case separately. Although the errors are clearly larger over the land regions, the errors are still smaller than the signal and through appropriate corrections and statistical filters, we can derive precipitable water which is applicable to land regions. Such estimates are useful in regions lacking traditional meteorological measurements, or as an additional data source for global atmospheric analyses.

Manuscript not available at time of printing. Please contact authors for further information.

SENSITIVITY OF SSM/T-2 CHANNELS TO WATER VAPOR

Michael K. Griffin and Vincent J. Falcone
Phillips Laboratory, Geophysics Directorate
Hanscom AFB, Massachusetts 01731-3010 USA

John D. Pickle and Ronald G. Isaacs,
Atmospheric and Environmental Research, Inc (AER)
Cambridge, Massachusetts 02139 USA

James Wang
NASA Goddard Space Flight Center
Greenbelt, MD 20771 USA

ABSTRACT

One approach undertaken to calibrate the Special Sensor Microwave Water Vapor Sounder (SSM/T-2) was to compare satellite brightness temperatures (T_b s) with results from radiative transfer (RT) models using co-located global radiosondes. Since ground temperature, surface emissivity, and upper-level atmospheric moisture and temperature were not directly measured, climatological values were used as input into the models. From this the sensitivity of the model-generated T_b s and its components (atmospheric emission, surface emission and surface reflectance) to these parameters were examined. Two RT models were used in this study: a line model (Enhanced RADTRAN) and a bandwidth model based on Eyre's work.

Since each of the five SSM/T-2 channels sense different levels in the atmosphere, sensitivities to surface and atmospheric parameters differ for each channel. If the atmosphere is sufficiently dry, the three atmospheric channels can sense a significant contribution from the surface, and thus respond as a window channel. Conversely, when the atmosphere is sufficiently moist, the two window channels sense a significant atmospheric contribution and respond as an atmospheric channel. In light of these observations, sensitivities are examined with respect to total precipitable water in the radiosonde profile. A global set of 1600 radiosondes were used to provide realistic variation in temperature and moisture profiles for the sensitivity studies.

1. MODELING

The SSM/T-2 sensor, which was designed to provide vertical profiles of water vapor, consists of 5 channels: three dual-pass bands located on the 183 GHz water vapor absorption line, one on the wing of this line at 150 GHz and a 91 GHz window channel. Using a global set of radiosonde profiles as input, radiative transfer (RT) models were used to examine the sensitivity of the brightness temperatures (T_b) to atmospheric water vapor. Two approaches were undertaken: first, examine the response of the models with respect to total precipitable water (TPW), and second, vary each moisture profile in order to examine the change in the modeled T_b s. Other parameters such as surface emissivity, ground temperature, and viewing angle were set to constant values. Note that moisture was not modified beyond saturation or below 0.003 gm/kg. Cloud formation was not considered as saturation was approached. Note that $TPW = \int w/g dp$ where w = mixing ratio, g = acceleration of gravity and p = pressure.

The RT models used in this study included the RADTRAN transmission model which was developed by the Phillips Laboratory (GP) (Falcone et al., 1979, 1982), and the Eyre microwave simulation model (Eyre and Woolf, 1988). Since the models produced similar T_b s using a global set of radiosondes (an RMS difference of 1 K at 183 ± 3 GHz for 1169 radiosondes with TPW ranging from 10 to 70 kg/m²), the computationally faster Eyre model was used in the following calculations. In addition, the Eyre model was easily modified to calculate the contributions of atmospheric emission, surface emission and surface reflectance as well as the weighting functions.

A global set of 1601 radiosondes were used as input into the RT band model in order to provide a wide range of realistic temperature and moisture profiles (Table 1), although it has been shown that this data is biased toward land cases (Falcone et al, 1992). Radiosondes were collected during the last week of February to the first week of March, 1992; mid May, 1992; and late July to early August, 1992. Only moisture profiles extending up to at least 300 mb were used. Upper-air moisture climatology modeled after the work by Oltmans (1985) was supplied from the top of the radiosonde moisture profile to 0.1 mb. An isothermal temperature profile was assumed from the top of the temperature sounding to 0.1 mb. Colocated SSM/T-2 fields-of-view (FOV) were defined as those closest to the radiosonde release (maximum distance of 100 km) and within ± 1 hour from the balloon release time.

These soundings were measured by many different types of radiosonde instruments which have been shown to have both random and systematic differences when flown on the same balloon (Nash and Schmidlin, 1987; Schmidlin, 1988). Since data reduction techniques differ from country to country, the differences between radiosonde measurements were compounded (Garand, et al, 1992). However, the data provided a wide range of temperature and moisture profiles that were useful for studying SSM/T-2 T_b sensitivities.

Table 1. Statistics of atmospheric moisture profiles represented by the global set of radiosondes.

Latitude	Mean \pm 1 Standard Deviation of Mixing Ratio [gm/kg]					
	1000 mb	850 mb	700 mb	500 mb	400 mb	300 mb
70 - 90	2.3 \pm 1.6	1.7 \pm 1.3	1.1 \pm 0.8	0.4 \pm 0.3	0.17 \pm 0.15	0.05 \pm 0.05
60 - 70	3.3 \pm 2.5	2.5 \pm 1.8	1.4 \pm 1.1	0.5 \pm 0.5	0.25 \pm 0.25	0.08 \pm 0.14
50 - 60	4.7 \pm 2.7	3.8 \pm 2.4	2.2 \pm 1.6	0.7 \pm 0.6	0.33 \pm 0.26	0.10 \pm 0.09
40 - 50	5.7 \pm 3.1	4.6 \pm 2.5	2.9 \pm 1.7	1.0 \pm 0.7	0.41 \pm 0.32	0.11 \pm 0.10
30 - 40	10.4 \pm 4.9	7.0 \pm 3.5	4.2 \pm 2.3	1.6 \pm 1.1	0.69 \pm 0.60	0.22 \pm 0.20
20 - 30	15.9 \pm 4.0	10.2 \pm 3.5	6.2 \pm 2.5	2.5 \pm 1.4	1.20 \pm 0.79	0.42 \pm 0.28
10 - 20	17.5 \pm 2.9	11.1 \pm 3.0	6.6 \pm 2.2	2.7 \pm 1.3	1.34 \pm 0.74	0.44 \pm 0.23
0 - 10	17.4 \pm 2.0	11.5 \pm 2.4	7.1 \pm 2.0	3.1 \pm 1.2	1.47 \pm 0.91	0.41 \pm 0.24
TOTAL	9.4 \pm 6.8	6.0 \pm 4.2	3.6 \pm 2.7	1.3 \pm 1.2	0.60 \pm 0.64	0.19 \pm 0.22

2. SENSITIVITY TO WATER VAPOR

By integrating the weighting function with respect to pressure, statistical features of the weighting functions (e.g., the pressure levels of the 25th, 50th and 75th percentiles) were calculated. These statistics were valid provided that the functions approached zero above the surface. This condition was generally observed for the 183 GHz channels, unless the moisture profile was dry. The amount of moisture extending above these pressure levels were also calculated. The mean TPWs observed extending above the median and peaks of the atmospheric channel weighting functions is presented in Table 2. As expected, these TPWs were constant for the 183 \pm 3 and 1 GHz channels, regardless of the amount of moisture present. About 3 times the moisture was observed for the 183 \pm 3 GHz channel compared to that of 183 \pm 1 GHz. Variable amounts of moisture extended above the peaks and medians of the 183 \pm 7 GHz weighting function due to a significant surface contribution for all but the moistest conditions.

As seen from Table 1, moist environments (lower latitude regions of the globe) tend to have more moisture at all pressure levels. Therefore, since the regions of the atmosphere that are sensed by the 183 GHz channels are controlled by specific amounts of moisture, there is a steady decrease in the pressure levels (increase in altitude) of the median of the atmospheric channel weighting functions as TPW increased (Figure 1). This decreases the T_b s of the atmospheric channels as TPW increases because cooler, higher altitude regions of the atmosphere are being sensed (Griffin et al, these proceedings). All three weighting functions shifted downward in pressure by roughly the same amount, yet the vertical sampling regions of the atmosphere being sensed narrowed, resulting in a decreased overlap between the weighting functions.

As TPW increased, the surface emission contribution for all five of the SSM/T-2 channels decreased steadily as the atmospheric contribution increased (Table 3). For very moist environments, approximately half of the 91 GHz T_b comes from atmospheric moisture; for dry conditions, almost one quarter of the 183 ± 3 GHz T_b is from the surface.

Figure 2 illustrates the varied sensitivities of the five SSM/T-2 channels to moisture profile modification. Two profiles, one dry and the other moist, were used to generate the figure. The relative humidity was increased (decreased) by a constant percentage at all levels, resulting in a change in T_b with respect

Table 2. Mean TPW extending from the pressure levels of the peaks and medians of the weighting functions to the top of the atmosphere. TPW in the left column represents the atmospheric moisture used in the RT model. TPW values in kg/m^2 .

TPW	<u>183 ± 7 GHz</u>		<u>183 ± 3 GHz</u>		<u>183 ± 1 GHz</u>	
	Peak	50%	Peak	50%	Peak	50%
0-5	2.1	1.6	1.4	1.2	0.6	0.6
5-10	4.8	4.8	2.1	1.8	0.7	0.7
10-20	6.0	6.0	2.3	2.0	0.7	0.6
20-30	6.3	6.3	2.3	2.1	0.7	0.6
30-40	6.9	6.9	2.2	2.2	0.8	0.6
40-50	7.2	7.2	2.3	2.3	0.7	0.6
> 50	7.9	7.9	2.6	2.4	0.7	0.6

Figure 1. Statistical features of the weighting functions for the three 183 GHz channels with respect to TPW ranges (0-5, 5-10, 10-20, 20-30, 30-40, 40-50, and > 50 kg/m^2). Median values are connected across TPW categories. Vertical line extend between the 25th and 75th percentiles of the weighting function curves.

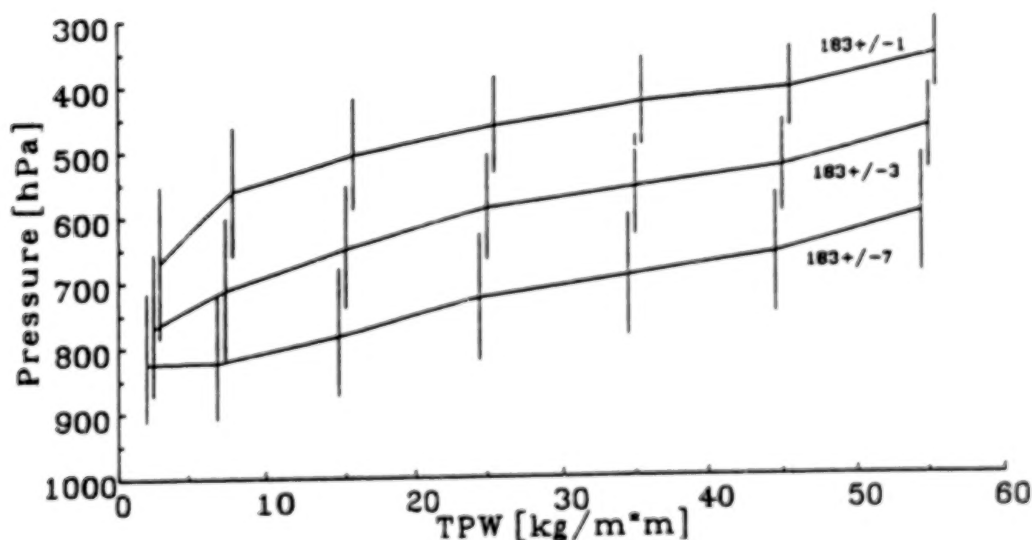


Table 3. Mean percent contributions of the three dominant components (atmospheric emission - surface emission - surface reflectance) of T_b with respect to TPW.

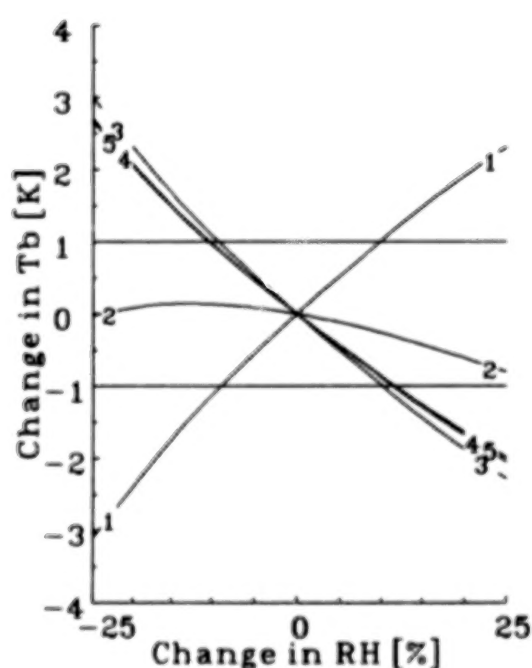
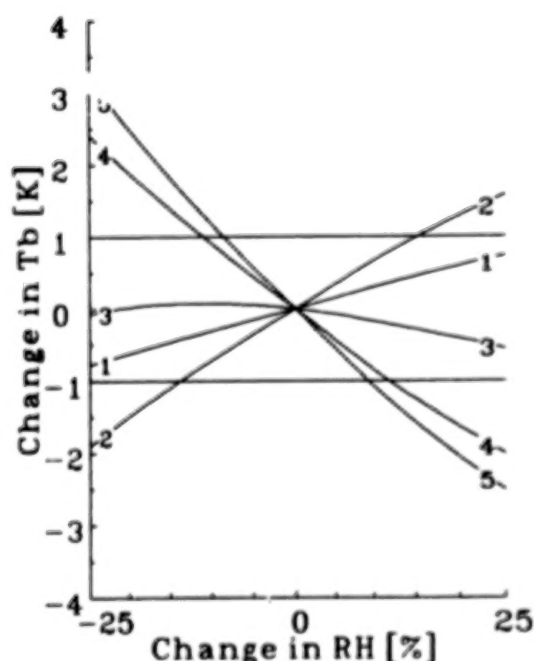
TPW [kg/m^2]	91 GHz	150 GHz	183 \pm 7 GHz	183 \pm 3 GHz	183 \pm 1 GHz
0 - 5	9 - 90 - 1	12 - 87 - 1	41 - 57 - 2	76 - 22 - 2	92 - 7 - 1
5 - 10	13 - 86 - 1	26 - 72 - 2	72 - 26 - 2	97 - 3 - 0	100 - 0 - 0
10 - 20	19 - 79 - 2	43 - 55 - 3	90 - 9 - 1	100 - 0 - 0	100 - 0 - 0
20 - 30	26 - 72 - 2	58 - 39 - 3	97 - 3 - 0	100 - 0 - 0	100 - 0 - 0
30 - 40	34 - 64 - 2	70 - 38 - 2	99 - 1 - 0	100 - 0 - 0	100 - 0 - 0
40 - 50	40 - 58 - 2	79 - 19 - 2	100 - 0 - 0	100 - 0 - 0	100 - 0 - 0
> 50	46 - 51 - 3	85 - 14 - 1	100 - 0 - 0	100 - 0 - 0	100 - 0 - 0

to the nominal (0% RH change) T_b . In general, when a channel senses predominantly surface radiation, as with the window channels (91 and 150 GHz), there is a positive relationship between moisture and T_b changes. When a channel senses predominantly atmospheric moisture contributions (the 183 GHz channels), there is a negative relationship. A non-monotonic relationship (see 183 \pm 7 GHz in Figure 2a and 150 GHz in Figure 2b) occurs when the channel senses significant contributions from both the surface and the atmosphere; as the moisture content is decreased, the channel behaves as a window channel, and when the moisture is increased, it becomes an atmospheric channel. Even the 183 \pm 1 GHz channel may sense the surface when the terrain is mountainous and/or the atmosphere extremely dry, and, conversely, window channels may have a significant atmospheric contribution when the profile is very moist, i.e. in the tropics, and/or for large viewing angles.

Figure 2. Change in T_b for the five SSM/T-2 channels as the moisture profile was modified in the RT model. The original sounding profiles had TPWs of (a) 7.8 and (b) 56.3 kg/m^2 . Channel 1 is 91 GHz, channel 2 is 150 GHz, and channels 3, 4 and 5 are 183 \pm 7, 3 and 1 GHz, respectively.

a) Dry Atmosphere

b) Moist Atmosphere



REFERENCES

- Eyre, J. and H. Woolf, 1988: Transmittance of Atmospheric Gases in the Microwave Region: a Fast Model, *Applied Optics*, 27, 3244-3249.
- Falcone, V.J., L.W. Abreu, and E.P. Shettle, 1979: Atmospheric attenuation of millimeter and submillimeter waves: Models and computer code, *AFGL-TR-79-0253*. [NTIS AD A084485]
- Falcone, V.J., L.W. Abreu, and E.P. Shettle, 1982: Atmospheric attenuation in the 30-300 GHz region using RADTRAN and MWTRAN. *Proc. Soc. Photo Opt. Instrum. Eng.*, 337, 62-66.
- Falcone, V.J., M.K. Griffin, R.G. Isaacs, J.D. Pickle, J.F. Morrissey, A.J. Jackson, A. Bussey, R. Kakar, J. Wang, P. Racette, D.J. Boucher, B.H. Thomas, and A.M. Kishi, 1992: SSM/T-2 Calibration and Validation Data Analysis. *PL-TR-92-2293*, Hanscom AFB, MA, 432 pp.
- Garand, L., C. Grassotti, J. Halle, and G.L. Klein, 1992: On differences in radiosonde humidity-reporting practices and their implications for numerical weather prediction and remote sensing. *BAMS*, 73, 9, 1417-1423.
- Griffin, M.K., J.D. Pickle, V.J. Falcone, R.G. Isaacs, and J. Wang, 1994: SSM/T-2 Brightness Temperature Signatures, AMS Seventh Conference on Satellite Meteorology and Oceanography Proceedings, Monterey CA.
- Nash, J., and F. J. Schmidlin, 1987: WMO International Radiosonde Comparison, Final Report. *World Meteorological Organization Instruments and Observing Methods Report No. 30*, WMO/TD-No. 195, 103 pp.
- Oltmans, S.J., 1985: Measurements of Water Vapor in the Stratosphere with a Frost-Point Hygrometer. *International Symposium on Moisture and Humidity Proceedings*, pp. 251-258, Instrument Society of America, Research Triangle Park, North Carolina.
- Schmidlin, F., 1988: WMO International Radiosonde Intercomparison Phase II, 1985. *World Meteorological Organization Instruments and Observing Methods Report No. 29*, WMO/TD-No. 312, 113 pp.

SATELLITE OBSERVED CLOUD PATTERNS ASSOCIATED WITH PRECIPITATION

Graciela Alicia Catuogno and Inés Velasco
Pabellón 2, Ciudad Universitaria
Departamento de Ciencias de la Atmósfera
Universidad de Buenos Aires
1428 - Buenos Aires - Argentina

ABSTRACT

The occurrence of significant Convective Weather Systems over most of continental Argentina along the year is established on the basis of AVHRR - IR imagery from NOAA 11 and 12. Examples of large and small cloud clusters, large and small convective lines, convective arcs and some hybrid systems that occurred between September 1992 - November 1993 are documented. Other attributes as size, life evolution and path are extracted from a large number of systems. This satellite data base of Mesoscale Convective Systems (MCSs) may be used as a research resource to help to improve our understanding of convective weather over most of Argentina.

1. INTRODUCTION

Convective weather systems in mid-latitudes occur over a broad spectrum of scales ranging from individual thunderstorms (1-10 km) to classic pre frontal squall lines (100-1000 km) and to large circular (500-1000 km across) long lived Mesoscale Convective Complexes (MCCs). Satellite imagery (NOAA) provides observations over this large range of spatial scale and from the basis of MCC definition (Maddox, 1980). Similarly, other Mesoscale Convective Systems (MCSs; Zipser, 1983) can be defined and documented using satellite imagery. MCCs and MCSs are probably responsible for much of the severe weather, including heavy rains and flash floods that occurs in South America mid-latitude during spring, summer and fall. Velasco and Fritch (1987) documented MCCs that occurred in this region during November - April.

The satellite data based sample presented here describes significant Mesoscale Convective Systems that occurred over the region of South America between 20° - 40° S during September 1992 - November 1993 (see Fig. 1). The term "mesoscale" is used because all the systems have an α -length scale (Orlanski, 1975).

2. SATELLITE DATA ANALYSIS PROCEDURES

The storm's classification method used in this paper has evolved from a method developed for Central North America using GOES imagery. The criteria for selecting MCS cases are based solely upon physical characteristics observable in enhanced infrared (IR) satellite imagery. The enhancement curve (Fig. 2) indicates specific ranges of IR black body temperature (T_{bb}). An example of a thunderstorm system displayed with such a curve is shown in Fig. 3. In Argentina the AVHRR satellite imagery are operational and routinely available at intervals of about 12 hours. Although this image set was not complete, enough images were available to document the existence of a large number of MCS. It is inevitable that the data gaps resulted in exclusion of some significant meso-systems.

The $\leq -52^\circ\text{C}$ (white) cold cloud top isotherm was the threshold value used for the selection of cases because it conveniently represents the cold IR cloud tops that is often associated with deep precipitating convective clouds (Schofield and Oliver, 1977). The requirement that large areas ($\geq 50,00\text{ km}^2$) have an IR T_{bb} $\leq -52^\circ\text{C}$ ensures that the system is active and precipitation is falling over a large area. It is recognized that precipitation occurs with warmer cloud top temperatures, especially as systems decay and weaken (Bartels and Rockwood, 1983) and when the tropopause is relatively low. Also an intense severe thunderstorm may be characterized by a large cold anvil and only small radar echo (personal communication, 1984, Maddox R. A. Boulder, Colorado). However, if the storm later develops into a meso-system, the entire cold ($T \leq -52^\circ\text{C}$) cloud shield is associated with precipitation. For this reason the $T \leq -52^\circ\text{C}$ cloud top criterion is adopted as representative of significant convective weather system, in an attempt to impart some sense of order to the documentation of a large number of MCCs.

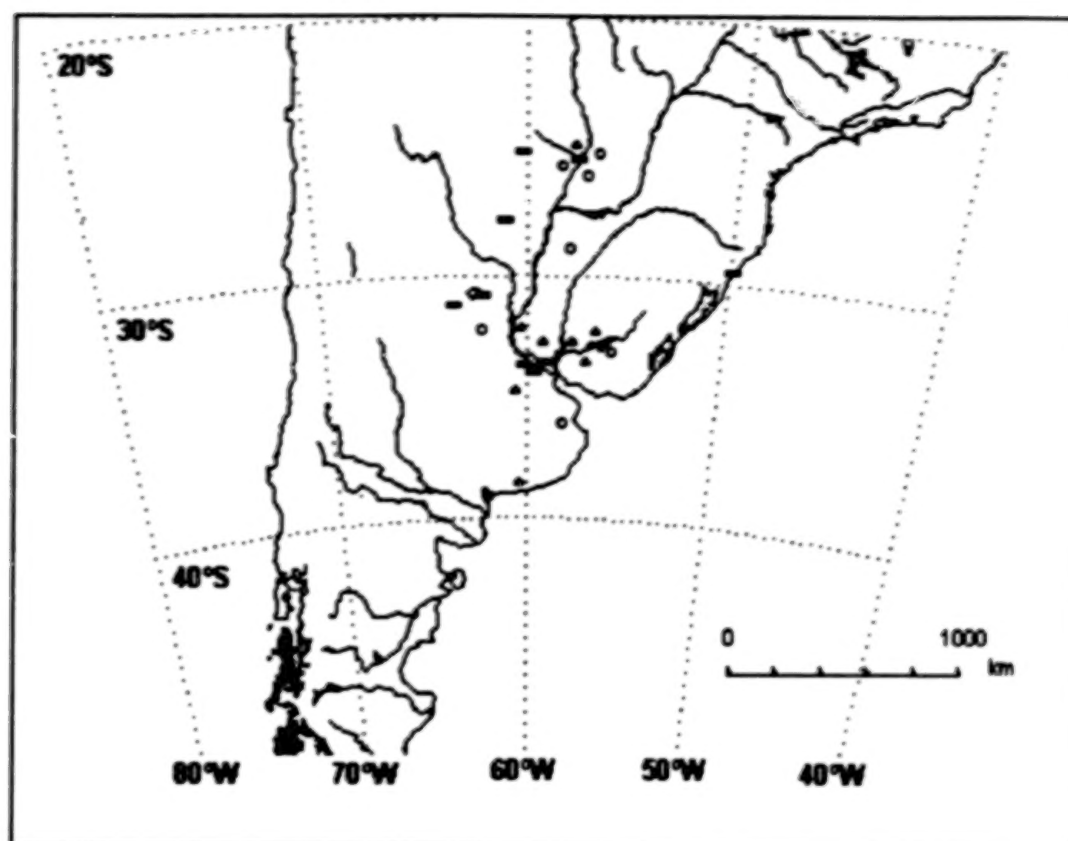
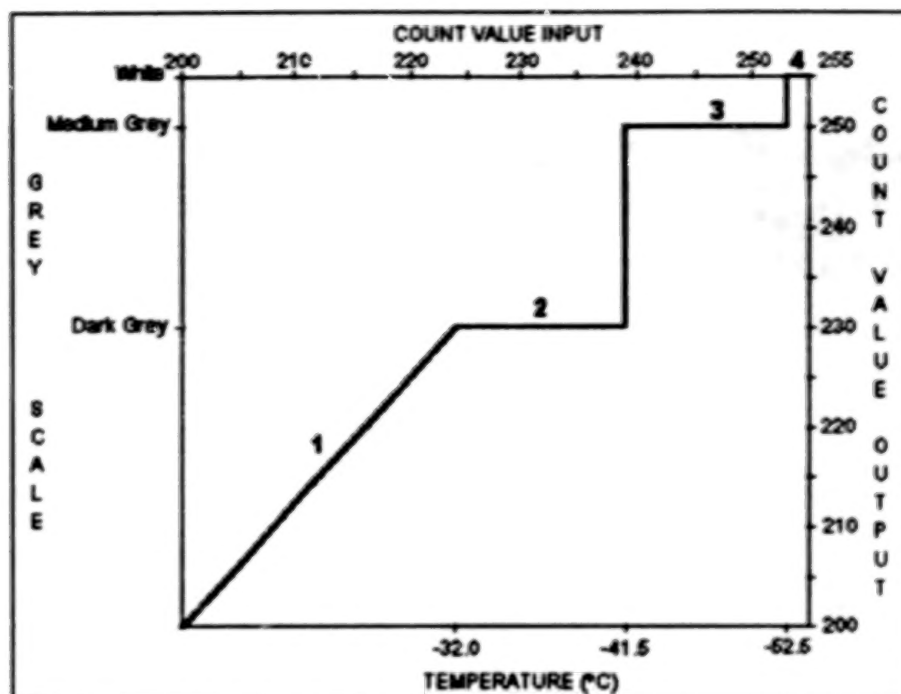


Figure 1: Geographic distribution of MCSs. Locations are for the MCSs cold cloud shields at the time of the maximum extent according to the available imagery.

- linear systems
- circular systems
- △ hybrid systems

3. DOCUMENTATION

Convective systems that are observable in satellite imagery reflect differing organizational characteristics (i.e., distinct line structures, circular cloud clusters, combinations of the two, etc.). Therefore, each mesoscale convective system was subjectively classified as having a linear, circular or hybrid organizational structure. Because some convective system exhibits both linear and circular structures during their lifetimes, the classification was based on the structure each system exhibited at the time of maximum extent in the imagery available. For some systems this was a difficult judgment to make. Fig. 4 shows an example of different shapes of the same storm. The definitional boundary between circular or linear system was based upon the characteristic criterion (minor axis/major axis ≥ 0.7 at the image time) according Maddox, 1980. Even so, included in this category are several systems that lie near the definitional boundary between circular and linear systems. The term MCC is avoided because it has a specific definition (Maddox, 1980) and because of the satellite imagery available. The date, time of occurrence, satellite, size, shape and significant weather for each mid-latitude South American MCS are listed in Table 1. The rain data was surveyed for 15 systems of a total of 24 to determine the rains of at least 25 mm (one inch) associated to each system. The geographical systems distribution is shown in Fig. 1. Fig. 5 shows some examples of the different types of convective systems considered here. Fig. 5a shows a large linear system in contrast to Fig. 5b that shows a small linear system (the labels "large" and "small" are relative only). The major axis of the large linear system is of 1200 km while in the small linear system the major axis reaches only 435 km. The minor axis in Fig. 5a is 380 km while in Fig. 5b it is 270 km. Fig. 5c shows a large circular system in contrast to Fig. 5d that shows a small one. Fig. 5e shows a linear system oriented in N-S direction. It certainly has circular proportions but is too elongated to meet the 0.7 minimal eccentricity criterion. Severe thunderstorm (included several tornados) were associated with the system of Fig. 5e



SEGMENT NUMBER	°C TEMPERATURE	COMMENTS
1	$T > -32$	No significant data
2	$-31 > T > -42$	First level contour for convection
3	$-41 > T > -53$	Thunderstorm enhancement
4	$T < -52$	Coldest cloud tops

Figure 2: Digital Enhancement Curve

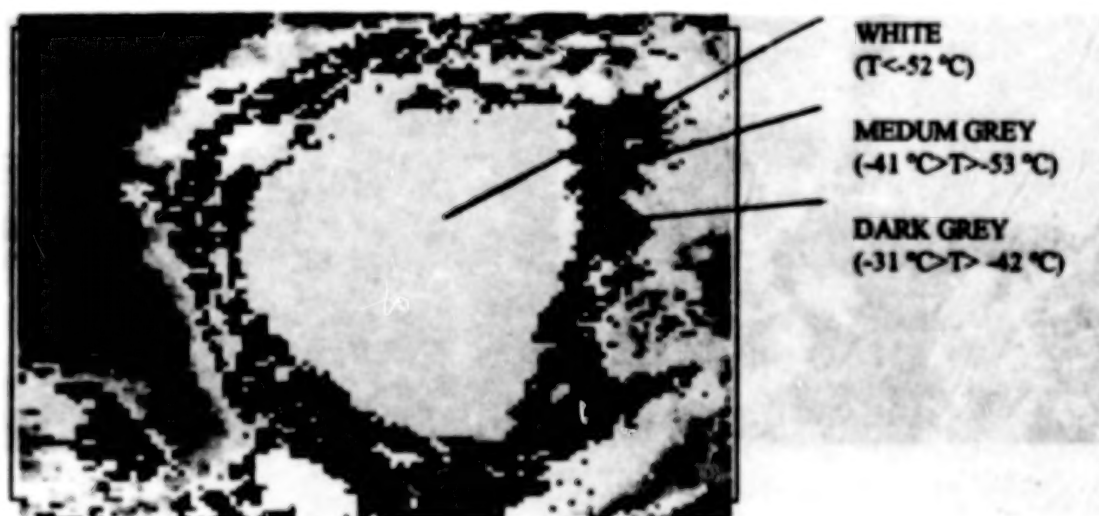
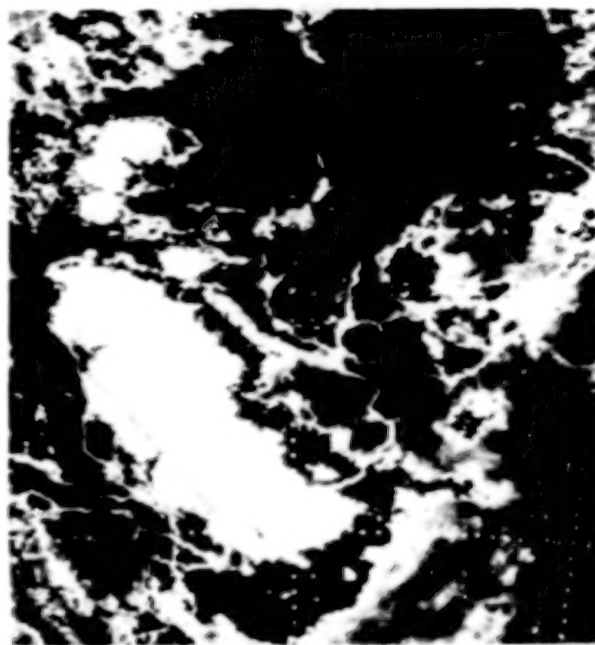


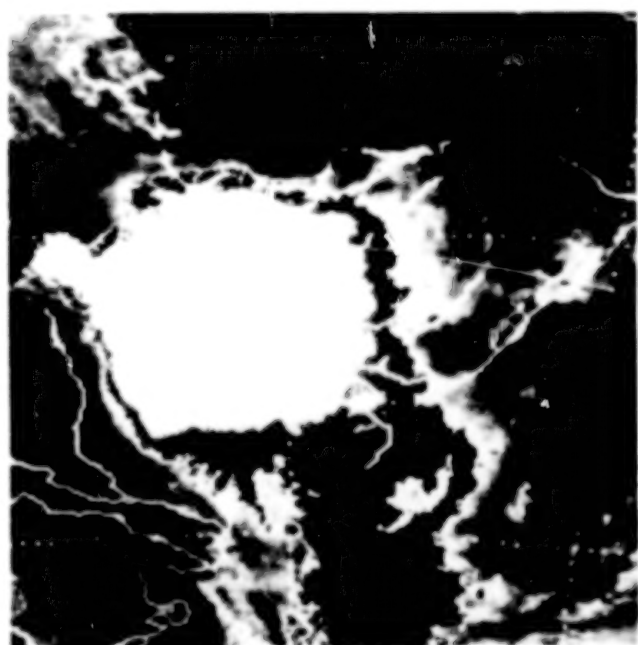
Figure 3: Enhanced Infrared Imagery



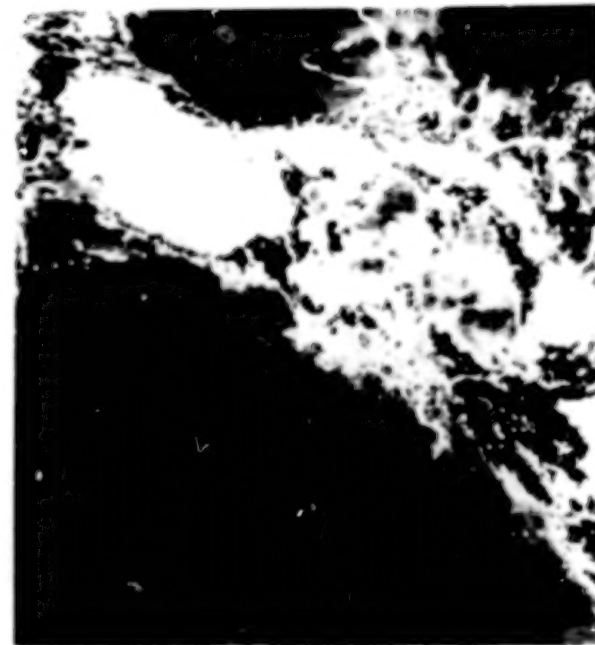
4a



4b



4c



4d

Figure 4: Evolution of a MCS occurred during December 22 and 23 of 1992

a - DEC/22/92 23:50 UTC

b - DEC/23/92 07:02 UTC

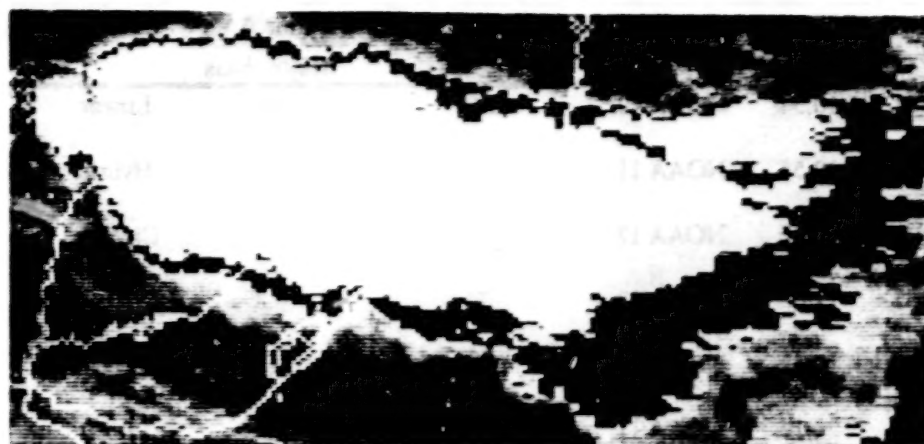
c - DEC/23/92 19:27 UTC

d - DEC/23/92 23:28 UTC

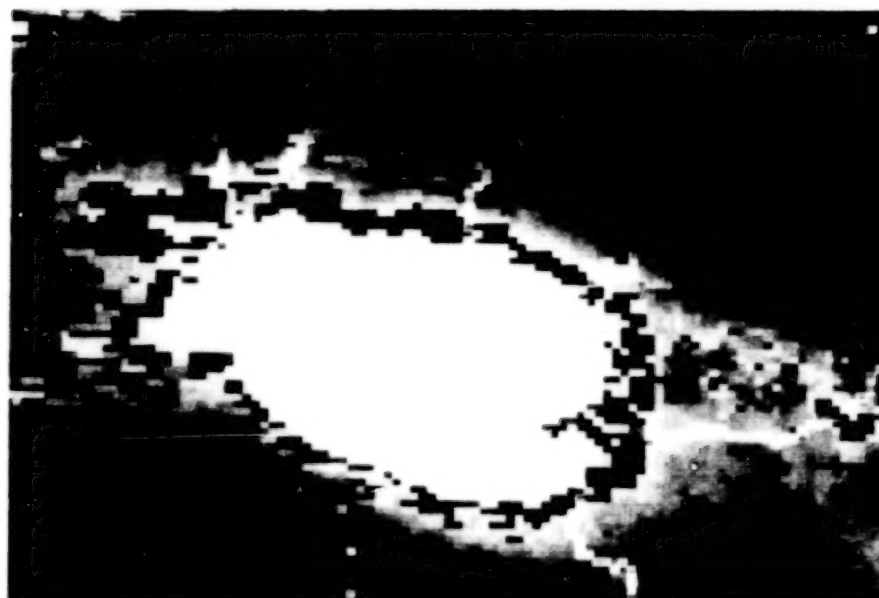
TABLE 1: MCSs over Mid-Latitude over South America for the October /November of 1992 - 1993

Nº	Date	Time (UTC)	Satellite	Area x 10 ³ Km ² T _{bb} ≤ -52°C	Minor Axis Major Axis	Shape	Significant Events
1	OCT/05/92	10:54	NOAA 12	230	0.6	Linear	N
2	OCT/15/92	19:55	NOAA 11	352	0.3	Hybrid	R
3	OCT/20/92	10:35	NOAA 12	360	0.7	Circular	N
4	NOV/11/92	11:05	NOAA 12	74	0.8	Circular	R
5	DEC/06/92	10:32	NOAA 12	303	0.8	Hybrid	R
6	DEC/19/92	20:16	NOAA 11	143	0.6	Linear	R
7	DEC/23/92	07:02	NOAA 11	470	0.9	Circular	R, H
8	DEC/29/92	10:40	NOAA 12	425	0.6	Linear	R, W
9	JAN/06/93	23:29	NOAA 12	366	0.3	Linear	R
10	MAR/12/93	23:39	NOAA 12	365	0.2	Hybrid	R
11	MAR/15/93	19:41	NOAA 11	149	0.3	Hybrid	R
12	MAR/16/93	07:03	NOAA 11	189	0.4	Linear	R
13	MAR/16/93	23:53	NOAA 12	134	0.9	Circular	R
14	MAR/19/93	06:27	NOAA 11	100	0.6	Linear	N
15	APR/13/93	23:54	NOAA 12	440	0.5	Hybrid	T
16	MAY/10/93	10:15	NOAA 12	196	0.8	Circular	R, H
17	JUN/07/93	19:25	NOAA 11	157	0.6	Hybrid	R, W
18	JUN/14/93	11:03	NOAA 12	246	0.9	Circular	R
19	SEP/20/93	07:28	NOAA 11	433	0.3	Linear	N
20	NOV/10/93	23:20	NOAA 12	437	0.5	Hybrid	RR
21	NOV/11/93	10:38	NOAA 12	399	0.6	Hybrid	N
22	NOV/24/93	10:58	NOAA 12	265	0.4	Linear	N
23	NOV/25/93	10:36	NOAA 12	159	0.5	Linear	R, W
24	NOV/30/93	10:29	NOAA 12	248	0.7	Circular	N

Mid-latitude South America is south of 20°S. Significant weather is coded as follows: R, heavy rain (25-100 mm); RR, very heavy rain (more than 100 mm); T, tornado; W, strong winds; H, hail; N, no report available at the moment



5a



5b

Figure 5: Examples of different types of convective systems

a - 20 SEP 1993

b - 19 MAR 1993

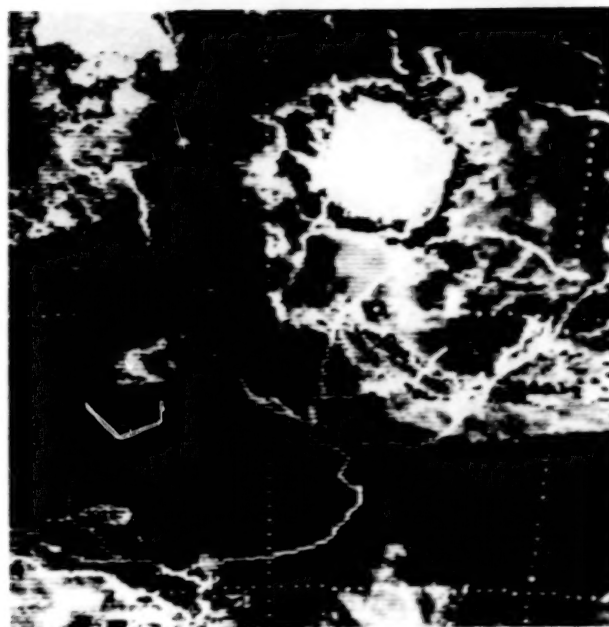
07:28 UTC

06:27 UTC

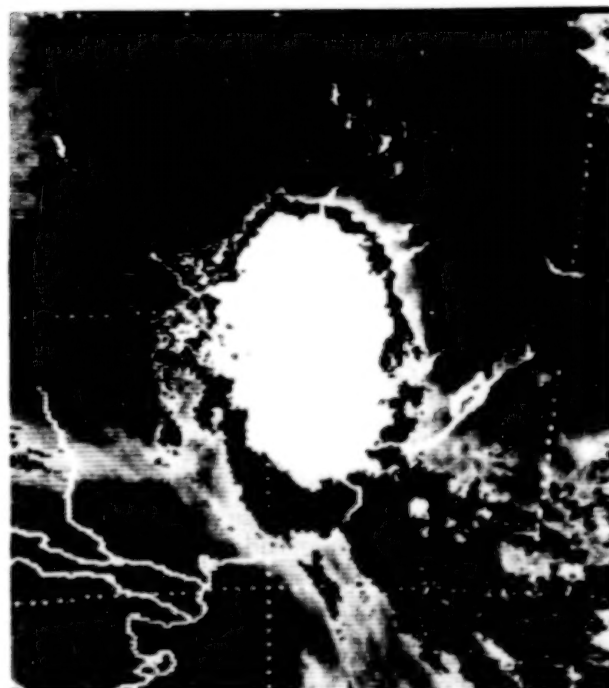
4. SUMMARY

The storm classification method used in this paper allow to classify a number of convective storms in linear, circular or hybrid systems. In some cases this classification was difficult to do because a number of systems show more than one shape during their lifetimes. In such cases they were classified according to the structure each system exhibit at the time of maximum extent in the available imagery. The lag between images was a restriction to study life evolution.

The distribution of convective storms (Fig. 1) shows a preferred regional occurrence. This result suggest the likelihood that certain configuration of surfaces features may be important to the development of these systems. The average area for hybrid systems (about 325,000 km²) is considerable larger than the average area of the rest of the MCSs (about 250,060 km²). It is also apparent from Table 1 that most of the systems occurred during the early morning. This results together with the restricted area condition imposed suggest a preference of big storms to reach considerable size (as suggested by satellite imagery) early in the morning, (around 4 to 8 local time). From the sample available it was not possible to distinguish any preference of occurrence in shape or time.

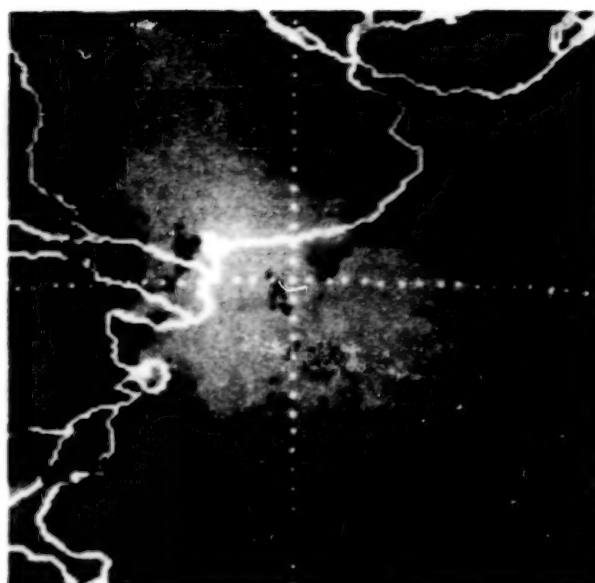


5c



5d

Figure 5: Examples of different types of convective systems
 c - 16 MAR 1993 23:53 UTC d - 05 OCT 1992 10:54 UTC



5e

Figure 5: Examples of different types of convective systems
e - 13 APR 1993
23:54 UTC

ACKNOWLEDGMENT

We acknowledge the support of the Universidad de Buenos Aires (UBA 92/94 - 19025/91), the Consejo Nacional de Investigaciones Científicas y Técnicas (PIA - 0379/92), and the Servicio Meteorológico Nacional (FAA) for the satellite imagery used in the investigation.

REFERENCES

- Bartels, D. L. and A. A. Rockwood, 1983: Internal structure and evolution of a dual mesoscale convective complex. *Preprints, 5th Conf. on Hydrometeorology*, Tulsa, Oklahoma. Amer. Meteor. Soc., 97-102.
- Maddox, R. A., 1980: Mesoscale convective complexes. *Bull. Am. Meteorol. Soc.*, **61**, 1374-1387.
- Orlanski, I., 1975: A rational subdivision of scales for atmospheric processes. *Bull. Am. Meteor. Soc.*, **36**, 390 - 396.
- Scofield, R. A. and V. J. Oliver, 1977: A scheme for estimating convective rainfall from satellite imagery. *NOAA Tech. Memo. NESS*, **86**, 47 pp.
- Velasco, I. and Fritsch, M., 1987: Mesoscale Convective Complexes in the Americas, *Journal of Geophysical Research*, **92**, 9561- 9613.
- Zipser, E. J., 1983: Preliminary program development plan for STORM - Central. (Draft document available through the National Center for Atmospheric Research, Boulder, Colorado.)

THE SOFTWARE PACKAGE FOR MANAGING LARGE-SCALED SPECTROSCOPIC DATA BASES AND SPECTRAL SENSING APPLICATIONS: GEISA BASED VERSION

A.A. Chursin, V.F. Golovko, and V.I.G. Tyuterev
Laboratory of Theoretical Spectroscopy, Institute of Atmospheric Optics,
Tomsk, 634055, Russia

N. Husson, B. Bonnet, A. Chedin, and N.A. Scott
Laboratoire de Météorologie Dynamique du CNRS, Ecole Polytechnique,
91128 Palaiseau, France

ABSTRACT

This paper presents a software package, designed for handling and use of the data bases on molecular spectra, which has been developed thanks to a cooperation between the Laboratoire de Météorologie Dynamique du CNRS, France and the Laboratory of Theoretical Spectroscopy, Russia. The IBM PC XT/AT version of the software is called GEISA-PC because the GEISA (Gestion et Etude des Informations Spectroscopiques Atmosphériques; word translation: Management and Study of Atmospheric Spectroscopic Information) (Chedin et al., 1980; Husson et al., 1992, 1994) data base is used as a work file, however any database written in suitable format can be processed. The Demo-Versions of GEISA-PC are available upon request from authors: E-mail address: HUSSON@ARA01.POLYTECHNIQUE.FR, FAX: +33-1-69-33-3005.

1. INTRODUCTION

The spectroscopic methods of gas analysis are the most promising ones for determining the concentrations of atmospheric constituents because of their selectivity, high sensitivity, and possibility of remote sensing (Chedin et al., 1993; Hinkley, 1976) which makes them most suitable for solving problems of pollution and global climate change monitoring. For successful application of spectroscopic methods reliable information on high-resolution spectra is needed as well as the perfect experimental equipment. Among the existing spectroscopic high-resolution infrared databases, the GEISA data base (Chedin et al., 1980; Husson et al., 1992, 1994), mostly involved in Earth and planetary atmospheric applications, has been selected for equipment with the software described in this paper. It should be noticed that this software, designed for using and managing spectroscopic information, is also adaptable with other large compilations of spectroscopic parameters information, such as the HITRAN database (Rothman et al., 1992) and the ATMOS molecular line list (Brown et al., 1987), or similar ones.

Since its origin (Chedin et al., 1980), the GEISA data base has been associated with a management software currently running on an IBM 3090/600 J-VF under VM/XA-MSV/ESA software (Chedin et al., 1985; Husson et al., 1992).

Recently, graphic software packages for personal computers (GRASSP, GEISA-PC, TDS, USF-HITRAN, AIRSENTRY) have been developed which are designed to manage large scale high-resolution spectroscopy databases, for the simulation of absorption/transmittance spectra and various optical spectroscopy applications. Basic features of the first three packages were described by

Golovko et al., 1992 (GRASSP); Chursin et al., 1993 and Husson et al., 1994 (GEISA-PC); Babikov et al., 1993; Tyuterev et al., 1994 (TDS). This paper reviews the recent developments of the GEISA-PC software and presents some examples of current applications.

2. GEISA-PC SOFTWARE.

2.1 GENERAL CLASSIFICATION

The GEISA-PC software can be divided into three groups of programs:

- 1) Programs simulating some radiative characteristics of a gas mixture, such as absorption coefficients, absorption/transmission functions, windows of transmittance suitable for sounding of the certain gases, etc... The calculations are based on the line parameters stored in GEISA-92.
- 2) Programs designed to obtain some information on the contents of the data base, in a preselected spectral range: the list of molecules and the corresponding list of transitions, the energy levels of the molecules etc. The user may choose the graphics form of the information representation, use it in a numerical form or write it into a disk file for use by further applications.
- 3) The third group of programs is designed to work simultaneously with experimental high-resolution molecular spectra and GEISA based transmittance simulations or with stick spectra. This group could probably be the most interesting and perspective utility for a large number of applications.

The whole package of software includes four executable codes, the data bases and the auxiliary files read by these programs.

2.2. THE PROGRAM BASE.EXE

It is the principal routine of the GEISA-PC software. It calculates the radiative characteristics of the gases and outputs the various information on the contents of the data base. Thus, **BASE** belongs to the groups 1) and 2) simultaneously and has the following main operational modes:

- *High resolution spectra* displays the theoretical absorption coefficient of a gas mixture.
- *Low resolution spectra* displays the result of a convolution of the theoretical absorption coefficient with a slit function of a spectral instrument.
- *Absorption/Transmittance* displays the absorption or the transmission function on a path into a gas with homogenous parameters (temperature, pressure, gas mixture). The path length and the above mentioned parameters have to be specified by the user;
- *Windows of transmittance* is designed to search for the spectral ranges, suitable for sounding of atmospheric constituents or gaseous impurities;
- *Survey spectra* - this option is designed to depict the spectral lines of any gas mixture in the form of "sticks" (in logarithmic or linear scale), without display of a line shape. By using this option the user can obtain express-information on lines and spectral bands of any molecule.
- *The Slant Path* calculates the transmittance of the terrestrial atmosphere on the slant paths (see Fig. 1). The six reference models of the atmosphere (Anderson et al., 1986) are used.
- *Save* allows to store the calculated spectra into a disk file to be used by the program **SPECTRUM.EXE**

For more details on **BASE.EXE** refer to Golovko et al., 1992 and Husson et al., 1994.

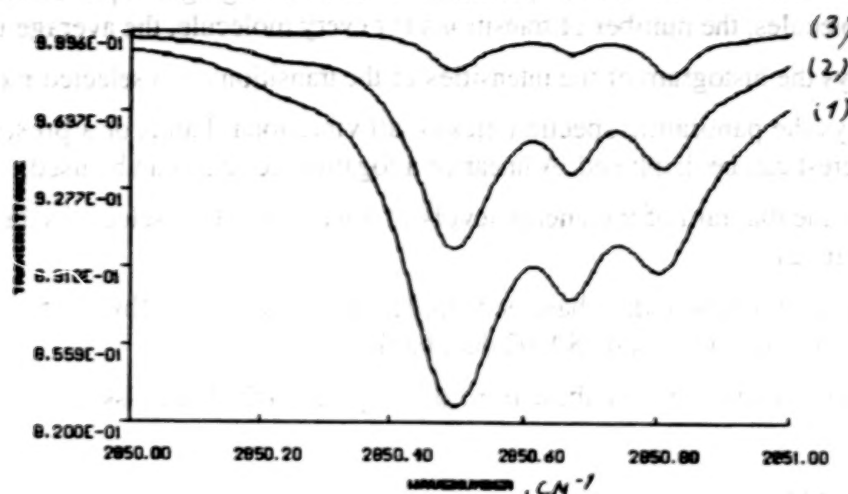


Figure 1. The GEISA-92 based simulation of the transmittance of the gas mixture corresponding to the composition of the US Standard Atmosphere (Anderson et al., 1986) on a horizontal 10 km path. (1) : near Earth's surface ; (2) : at 2 km of altitude ; (3) at 6 km of altitude.

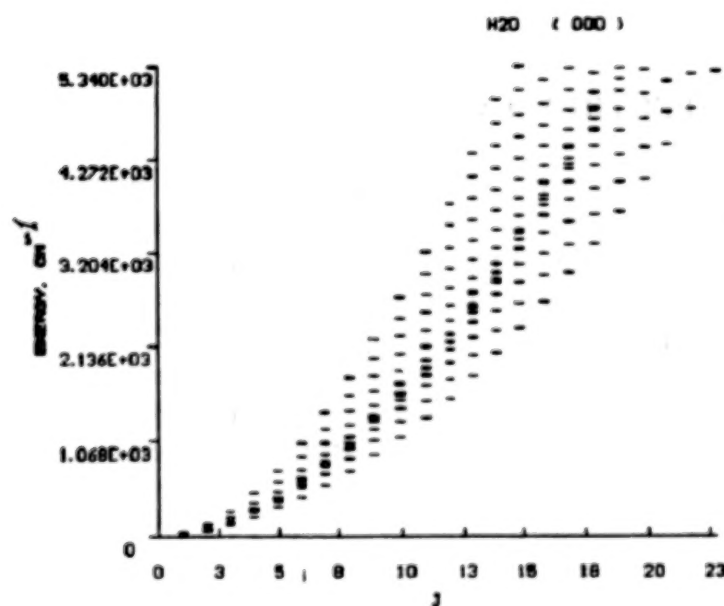


Figure 2. The rotational ground state energy levels of H_2^{16}O molecule versus rotational quantum number J , displayed by the program GSUTIL.EXE.

2.3 THE PROGRAM GSUTIL.EXE

This program is a special utility designed to manage the GEISA data base. It both reproduces the GEISA management capabilities already available for main frames and contains recently developed new ones. In particular, it has the following main options:

- **EXTRACT** designed to select a part of the whole data base and to write it in a separate file. Both ASCII and binary format may be used. The binary format files are the GEISA-PC type random access files which can be processed by **BASE.EXE**.

- *INFO* outputs the brief information on spectral transitions belonging to a preselected range (i.e. the list of active molecules, the number of transitions for every molecule, the average intensity etc.).
- *HISTOG* displays the histogram of the intensities of the transitions of a selected molecule;
- *STICKS* displays the panoramic spectra (sticks); all vibrational bands or a preselected band of a molecule of interest can be displayed. A linear or a logarithmic scale can be used.
- *DIAGR* displays the diagram of the energy levels of lower states of a selected vibrational state of a molecule (see Fig. 2).
- *BACK UP* backs up the whole data base on floppies. The fifteen 1,2 Mbytes (5 $\frac{1}{4}$ " , HD) diskettes are sufficient to store the whole GEISA-92 data bank.
- *RESTORE* allows to restore the database from the floppies to the hard disk.

2.4 THE PROGRAM CROSSUTL.EXE

This program is designed to use and to maintain the data base on the absorption cross sections of chlorofluorocarbons. It has the same options as GSUTIL.EXE, but in addition it allows the user to visualize the absorption cross sections of the molecules of interest as well as to plot the absorption coefficient for a gas mixture.

2.5 THE PROGRAM SPECTRUM.EXE

This program allows the user to visualize either the molecular spectra simulated and written in disk files by *BASE.EXE*, or experimental spectra, or both of them simultaneously. Special utilities have been developed to convert an ASCII-type file of experimental data into a binary file, readable by *SPECTRUM.EXE*. An option of this program allows to visualize simultaneously the pre-recorded simulated or experimental spectra, and the stick-spectra for molecules, selected by the user. We believe that this option will be especially useful for the treatment of experimental spectra, since it simplifies the identification of lines belonging to the impurities in a cell and provides swift estimate of their concentrations (see Section 3). The program *SPECTRUM* belongs to the third group of the software.

3. GEISA-PC APPLICATIONS

The GEISA-PC software is designed to facilitate a broad range of applications related to the information on high resolution molecular spectra incorporated in the data base.

Thanks to the possibilities of making easy "visualization" of a "digital line parameters compilation" (simulation of the absorption coefficient and of an absorption/transmittance for various gas mixtures with different temperatures and pressures; display of line-sticks - in different colors depending on bands and species - against experimentally recorded spectra), this software package can be used for the assignment of laboratory measurements.

A simultaneous display of high-resolution and low-resolution spectra and the simulation of the atmospheric transmittance on slant paths (up to the altitude of 120 km) by using different reference atmospheric models suggest applications for the modelling of atmospheric optical experiments.

Searching for spectral "micro-windows" suitable for sounding particular species in standard atmospheric conditions or in gaseous mixtures composed by the user, and for searching for their coincidence with laser emission lines can serve for the optimization of an experimental set up for a local gas analysis, in lidar remote sensing, optical communication, etc.

3.1 THE RETRIEVAL OF THE CONCENTRATIONS OF THE GAS IMPURITIES

The simultaneous use of data on high-resolution spectra from the GEISA data bank and of the experimental data visualized by the program SPECTRUM.EXE allows the user to make the express-analysis of gas impurities, contained in a sample, on the base of recorded high-resolution spectra. We will consider here a simple example based on the water vapour spectra recorded recently at the University of Giessen (Keppler et al., 1993).

3.1.1 The Method of Two Isolated Lines

Consider an experimental transmittance spectrum of a gaseous mixture recorded in a point-by-point format. By using a special command of SPECTRUM.EXE, we can visualize a range of this spectrum superposed with the sticks of transitions for molecules which could be hypothetically present into a cell (see Fig. 3). Suppose that we find two *isolated* lines belonging to a principal gas and to an impurity (Fig. 4). The transmission function τ is determined by well-known Beer-Lambert law:

$$\tau(x) = \exp(-k(x)L) \quad (1)$$

where x is a wavenumber (cm^{-1}); $k(x)$ is a profile of the absorption coefficient (cm^{-1}), and L is a path length (cm). The transmission $\tau_o(x)$ measured by a spectral device is expressed as:

$$\tau_o(x) = \zeta(x) \int_{-\infty}^{\infty} A(x-x') \tau(x') dx' + D \quad (2)$$

where $\tau_o(x)$ is the observed transmission; $A(x-x')$ is a normalized instrumental function of a spectral device; $\zeta(x)$ is the transmittance of the optical system of a spectrometer, and D is a non-selective contribution to the "transmittance base line" determined by conditions of the experiment.

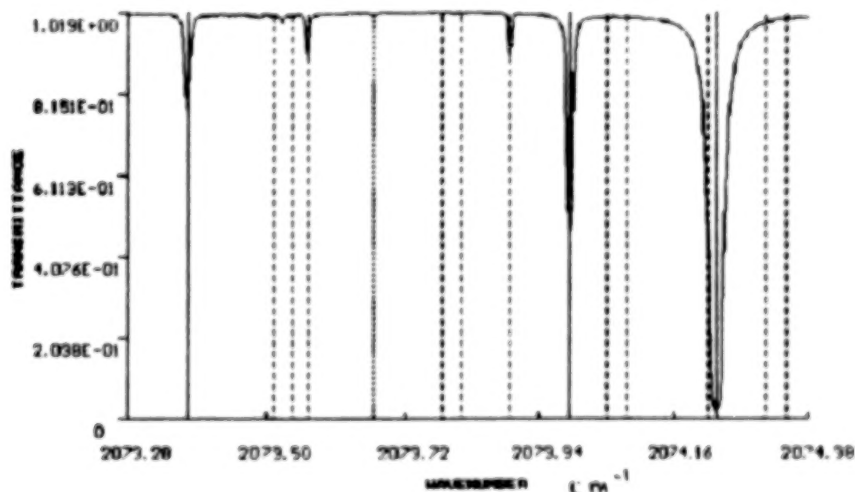


Figure 3. A part of the water transmittance spectrum (Keppler et al., 1993) superposed with the line sticks visualized by SPECTRUM.EXE. The sticks of H_2^{16}O are drawn by solid lines, of H_2^{17}O by a dotted line, and of $^{16}\text{O}^{12}\text{C}^{32}\text{S}$ by dashed lines.

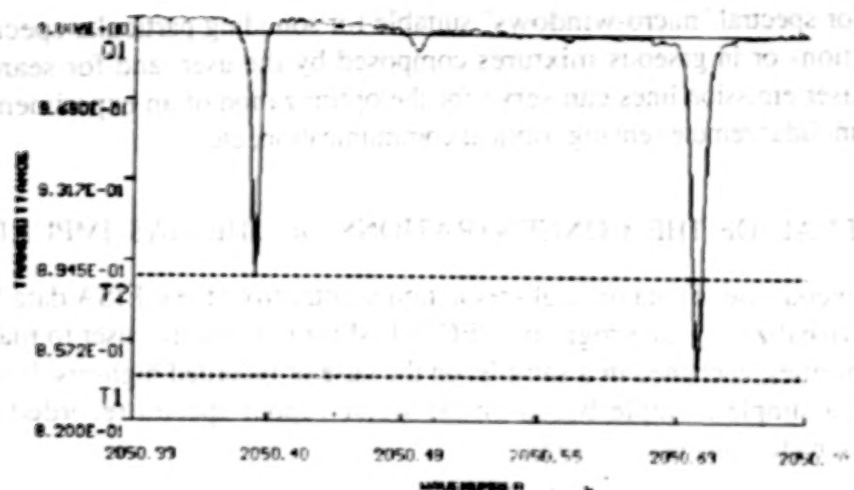


Figure 4. Two isolated lines in an observed spectrum : T1 and T2 are the transmittance values in centres of observed lines. Q1 is the shift of the base line for the transition T1.

In case of an isolated line, we can estimate the value of D by analysing of the experimental data as shown in Fig. 4:

$$D = Q - 1$$

where Q is a shift of a *base line*. Thus, the "corrected" transmission $\tau_c(x)$ is expressed as

$$\tau_c(x) = \tau_o(x) + (1 - Q) \quad (3)$$

It is $\tau_c(x)$ that will be used in all the following equations. To minimize the influence of the optical system $\zeta(x)$, we need to select two *isolated* lines $\tau_{1c}(x_1)$ and $\tau_{2c}(x_2)$, and to consider the ratio:

$$\frac{\tau_{1c}(x_1)}{\tau_{2c}(x_2)} = \frac{\int_{-\infty}^{+\infty} A(x_1-x') \tau_1(x') dx'}{\int_{-\infty}^{+\infty} A(x_2-x') \tau_2(x') dx'} \quad (4)$$

where x_1, x_2 are the centres of the absorption lines; $\tau_1(x')$ and $\tau_2(x')$ are the theoretical transmissions calculated by equation (1). We assumed that the transmittance of the optical system was a smooth function so that $\zeta(x_1) \approx \zeta(x_2)$, if the lines are not far from each other. The concentration of an impurity is involved in (4) via the absorption coefficient $k(x)$ used in (1), and thus can be derived from this equation.

The expressions for the concentrations of an impurity have been derived by using the approximation of (4) under several conditions and have been tested using the GEISA-PC software.

3.1.2 Approximation for the Voigt Profile

Assume, that the experimental spectrum was recorded under conditions when the Doppler and Lorentz broadenings are of the same order. In this case the absorption coefficient $k(x)$ is known to be described by the Voigt profile results from the convolution of a Lorentzian profile by a Gaussian one.

Consider the approximation which corresponds to the assumption of a cancellation of instrumental function effects in the right-hand side of Equation (4). In this case the latter takes the form:

$$\frac{\tau_{1c}}{\tau_{2c}} = \frac{\text{Exp}(-k_1 N_1 L)}{\text{Exp}(-k_2 N_2 L)} \quad (5)$$

where τ_{1c} and τ_{2c} are the "corrected" transmissions (3) in the peaks of the absorption; k_1 , k_2 are the peak values of the absorption cross section ($\text{mol}^{-1} \text{cm}^2$); N_1 and N_2 are the concentrations of the principal gas "1" and the impurity "2" ($\text{mol} \cdot \text{cm}^{-3}$), and L is the path length (cm).

To calculate the peak value of k , the absorption cross section described by the Voigt profile function, we used the approximation (Whiting, 1968):

$$k = \frac{S}{w_v [1.065 + 0.447 (w_l/w_v) + 0.058 (w_l/w_v)^2]} \quad (6)$$

where S is the line intensity (cm molecule^{-1}); w_l is the Lorentzian halfwidth, and w_v is the so-called Voigt halfwidth (cm^{-1}) expressed as (Van de Hulst and Reesinck, 1947):

$$w_v = 0.5 w_d + (0.25 w_d^2 + w_l^2)^{0.5} \quad (7)$$

where w_d is the Doppler halfwidth (cm^{-1}), depending on the temperature T , on the molecular mass M and on the wavenumber f :

$$w_d = 3.58 \times 10^{-7} (T/M)^{0.5} f \quad (8)$$

By solving the equation (5) we can derive the following expression for an unknown concentration of an impurity N_2 :

$$N_2 = \frac{k_1}{k_2} N_1 - (L k_2)^{-1} \text{Ln}(\tau_{2c}/\tau_{1c}) \quad (9)$$

It was expression (9) that was used for the estimation of the concentration of OCS in an experimental cell with the vapour of H_2O . The values of the absorption cross section k_1 and k_2 were derived by (6), the values of the line intensities were taken from the GEISA data base. An example of such estimates using the GEISA-PC package is listed in Table 1 where we used the volume *relative* concentrations C_i of the constituents instead of their *absolute* concentrations N_i (molecule cm^{-3}) used in (9). They are related by the expression:

$$C_i = 10^6 N_i K_B T / P \quad (10)$$

where $K_B = 1.38 \cdot 10^{-23} \text{ J/K}$ is the Boltzman constant; T is the temperature (K), and P is the total pressure of a gas mixture (Pa).

TABLE 1. THE CONCENTRATIONS OF THE MINOR IMPURITIES IN A SAMPLE.

Gas	Concentration	Remarks
H ₂ O	0.997317	The principal constituent, known concentration. Used as a reference gas.
HDO	3.1 10 ⁻⁴ (4 10 ⁻⁴)	Known concentration. The restored concentration is written in brackets. Used as a test of (9)
OCS	1.8 10 ⁻⁶	The concentration restored by the use of (9)

4. CONCLUSION

This paper gives only a brief description of the principal capabilities of the GEISA-PC software. More information is available in Chursin et al. (1994) and Husson et al. (1994).

The presented method can be used for the express-analysis of the constituents contained in a cell, and for the estimation of their concentrations. The perspective of the GEISA-PC development is to create new options and programs designed for the more reliable recovering of constituent concentrations, both in the laboratory experiments and in the atmospheric experiments related to climatology, environmental protection and to the global weather monitoring projects.

The Demo-Versions of GEISA-PC are available upon request from authors: E-mail: ROOT@LTS.ACAD.TOMSK.SU or HUSSON@ARA01.POLYTECHNIQUE.FR, FAX number : +33-1-69-33-3005.

REFERENCES

- Anderson G.P., S.A.Clough, F.X.Kneizys, J.H. Cherwynd, and E.P. Shettle, 1986: AFGL Atmospheric Constituent Profiles (0-120 km), Report, ERP, No. 954, AFGL-TR-86-0110, Air Force Geophysics Laboratory, Hanscom AFB, Massachusetts.
- Babikov Yu.L., S.A. Tashkun, V.I.G. Tyuterev, J.P. Champion, Cl. Pierre, G. Pierre, and Ch. Wegner, 1993: T.D.S. spectroscopic databank for spherical tops: present status. *Proceedings of SPIE*, 2205, 419-429
- Brown L.R., C.B. Farmer, C.P. Rinsland, and R.A. Toth, 1987: Molecular line parameters for the atmospheric trace molecule spectroscopy experiment. *Appl. Optics*, 26, 5154-5182.
- Chedin A., N.Husson, N.A.Scott, I.Cohen-Hallaleh, and A.Berroir, 1981: La banque de données GEISA. Description et logiciel d'utilisation. Laboratoire de Meteorologie Dynamique du CNRS, Internal note 108. Ecole Polytechnique, Palaiseau, France
- Chédin A., N. Husson, B. Bonnet, and N.A. Scott, 1985: The GEISA data bank, 1984 version. Laboratoire de Météorologie Dynamique du CNRS, Internal Note LMD 127, Ecole Polytechnique, Palaiseau, France

- Chedin A., M.T. Chanine, and N.A. Scott (Eds.), 1993: *High Spectral Resolution Infrared Remote Sensing for Earth's Weather and Climate Studies*, NATO ASI Series, Series I: Global Environmental Change, v.9, Springer-Verlag, 492 pp.
- Chursin A.A., Nikitin A.V., V.F. Golovko, V.I.G. Tyuterev, N. Husson, B. Bonnet, N.A. Scott, and A. Chedin, 1993: GEISA-PC software: IBM-PC version of GEISA-92 optical spectroscopy database. *Proceedings of SPIE*, **2205**, 413-418
- Chursin A.A., V.F. Golovko, V.I. G. Tyuterev, N. Husson, A. Chedin, N.A. Scott and B. Bonnet, 1994: GEISA-PC Manual, Internal Note LMD 192, Laboratoire de Météorologie Dynamique du CNRS, Ecole Polytechnique, Palaiseau, France (in press).
- Golovko V.F., A.A. Pozdnyakov, V.I.G. Tyuterev and A.A. Chursin 1992: Graphics Software of a Spectroscopic Information System. *Atmos. Oceanic Optics*, **5**, 706-710 .
- Hinkley E.D. (Ed.), 1976: *Laser Monitoring of the Atmosphere*, Springer Verlag, New York.
- Husson N., B. Bonnet, N.A. Scott, and A. Chedin, 1992: Management and study of spectroscopic information: the GEISA program. *JQSRT*, **48**, 509-518 .
- Husson N., B. Bonnet, A. Chedin, N.A. Scott, A.A. Chursin, V.F. Golovko, and V.I.G. Tyuterev, 1994: The GEISA Data Bank in 1993. A PC/AT Compatible Computers' New Version. *JQSRT* (in press).
- Keppler K.A., B.P. Winnewisser, M. Winnewisser, F.N. Rao, S.N. Mikhailenko, V.I. Starikov, V.I.G. Tyuterev, 1993: High Resolution Molecular Spectroscopy. *Proceedings of SPIE*, **2205**, 264-268
- Rothman L.S., R.R. Gamache, R.H. Tipping, C.P. Rinsland, M.A.H. Smith, D. Chris Benner, B. Malathy Devi, J.-M. Flaud, C. Camy-Peyret, A. Perrin, A. Goldman, S.T. Massie, L.R. Brown, and R.A. Toth, 1992: The HITRAN molecular Database: Editions of 1991 and 1992. *JQSRT*, **48**, 469-507
- Tyuterev V.I.G., Yu.L. Babikov, S.A. Tashkun, V.I. Perevalov, A.V. Nikitin, J.P. Champion, Ch. Wegner, Cl. Pierre, G. Pierre, J.C. Hilico, and M. Loette, 1994: T.D.S. spectroscopic databank for spherical tops. DOS version. *JQSRT*, (in press).
- Van de Hulst H.C. and J.J.M. Reesinck, 1947: *Astrophys. J.*, **106**, 121
- Whiting E.E., 1968: An Empirical Approximation to the Voigt Profile. *JQSRT*, **8**, 1379-1384

WATER VAPOR DEPENDENT THERMODYNAMICS OF THE LOWER ATMOSPHERE

Fred Walter
Scientific Components Company
Cottage Grove, OR 97424
(503) 942-3611

Solar radiation is the predominant source of heat received by the earth's atmosphere and, subsequently, by its land- and ocean areas. Water vapor, present in concentrations from highs of 4 to 5% in the equatorial tropics, to less than 0.1% in arctic and polar regions, is the principal gaseous absorber. Maps of temperature and dewpoint data from national weather services show temperatures to be closely related to insolation levels. Water vapor concentrations, as computed from dewpoint values, in turn exponentially increase with temperatures, according to the vapor pressure-vs-temperature function. A few areas show unusually small variations in daily, seasonally, and annual values; they may be good enough to serve as calibration and reference points for large-scale, remote sensing operations. Ocean- and air currents distribute solar heat collected in the tropics to higher latitude areas. Specific examples of primary distribution patterns are presented.

Manuscript not available at time of printing. Please contact author for further information.

SESSION V

OCEANOGRAPHIC/COASTAL STUDIES AND APPLICATIONS

121000

000123

BLANK PAGE

PROCESSING AND ANALYSIS OF AVIRIS IMAGERY OF THE COASTAL OCEAN¹

Curtiss O. Davis
Naval Research Laboratory, Code 7212
Washington, D.C. 20375

ABSTRACT

Global ocean color sensors, such as the Coastal Zone Color Scanner (CZCS) and Sea-viewing Wide Field-of view Sensor (SeaWiFS) provide excellent data on open ocean optical properties which are largely related to the abundance of phytoplankton and their degradation products. In the coastal ocean suspended sediments, bottom reflectance, river discharges, coral reefs, aquatic plants and other features result in a much more complex and spatially varying optical environment. To assess this complex environment we have been using data from AVIRIS, a well calibrated airborne imaging spectrometer system flying on an ER-2. This paper reviews the present validation, processing and analysis procedures for AVIRIS data from the coastal ocean with examples from a flight over San Pedro channel, CA. The present procedures are computationally intensive and possible alternative approaches that are more computationally efficient are discussed.

1. INTRODUCTION

The Coastal Zone Color Scanner (CZCS; Hovis, et al., 1980) was launched on NASA's Nimbus 7 satellite in 1978 and it continued to provide data through 1986. It was launched as a demonstration project and only operated about 10% of the time, but it provided the first picture of the global time varying distribution of phytoplankton in the world ocean. Many global and mesoscale features, such as the jets of phytoplankton that extent 300 km offshore from the coastal upwelling centers on the west coast of North America were discovered or documented with this data. As a follow-on the Sea-viewing Wide Field-of view Sensor (SeaWiFS; Hooker, et al., 1992) is scheduled to be launched in late 1994 or early 1995. SeaWiFS will provide ocean color data in 5 spectral bands (plus three for atmospheric correction), higher signal to noise and two day global coverage.

The CZCS worked well for the open ocean, but, in spite of its name, it did not work well for the nearshore coastal ocean. It was tuned for the dark ocean target, and the detectors would saturate over bright land or clouds and then ring providing false high data for the next 10 to 20 pixels (10 to 20 km). Also, the coastal ocean is a rich and varied place with high spatial and spectral variability (Table 1). An imager with a few discrete channels does not provide adequate information to separate the chlorophyll signal from the signal from dissolved organics, detritus, suspended sediments, bottom reflectance, kelp and other features that are often found in the coastal zone.

SeaWiFS will provide global ocean color data at 4.5 km resolution and regional data at 1.13 km resolution. This will be an excellent data set for many oceanic problems, and it is expected to be used by a large community of oceanographers for research and an even broader group for some commercial applications. However, SeaWiFS will not always provide useful data in the near coastal areas and in case II waters where dissolved organics, suspended sediments and bottom reflection can interfere with the chlorophyll signal, and where higher spatial resolution will be required for many studies. In addition, SeaWiFS is highly tuned for ocean applications and it saturates over bright land scenes, and over clouds. This means that if the scan is from the land to the ocean then the instrument is still 'ringing' from the saturation and the ocean data is not usable for the next 5 pixels, or 6 km from the shore. For many coastal ocean sites this is a huge loss. For example this will mean that the SeaWiFS data for San Francisco Bay is essentially all contaminated, as it is on average only 10 km wide and has a high concentration of suspended sediments. Even in our largest estuary, Chesapeake

¹ Support for this work was provided by the National Aeronautics and Space Administration and by the Office of Naval Research.

TABLE 1. SPATIAL AND SPECTRAL COMPLEXITY OF THE COASTAL OCEAN

Spatial complexity:

- Small scale patches, fronts
- Bottom reflectance
- Potential for "Ringing" from high land signals

Spectral complexity:

- High chlorophyll
- Suspended sediments
- High gelbstoff
- Pollution (sewage, oil, etc.)
- Kelp, sea grass and algal beds
- Coral reefs and reef bleaching
- Salt marshes
- Beach erosion

Bay up to half of the data will be contaminated from ringing. Also these estuaries have high levels of suspended sediment and dissolved organics and the SeaWiFS band set is inadequate to resolve the chlorophyll signal from these competing signals. Other areas that will provide difficulties are the Mississippi River Plume which has a high sediment load, and all of the other estuaries which either have ringing or case II water problems. Thus an alternate system is needed for the nearshore coastal environment.

To address the problems of the coastal ocean we have been working since 1989 using the Airborne Visible/InfraRed Imaging Spectrometer (AVIRIS; Porter and Enmark, 1987; Vane et al., 1993) which is operated by the Jet Propulsion Laboratory and flown on an ER-2 operated by NASA Ames. This has been a collaborative effort with Ken Carder and his group at the University of South Florida and in the work to date with AVIRIS we have demonstrated the ability to separate the chlorophyll signal from bottom reflectance in clear waters of Lake Tahoe (Hamilton et al., 1993) and the turbid waters offshore from Tampa Bay (Carder, et al. 1993a). In addition, spectral signals from re-suspended sediments and dissolved organics have been interpreted for the Tampa AVIRIS images (Carder, et al., 1993a,b), and for suspended sediments and kelp beds for AVIRIS images of San Pedro Channel (Davis, et al., 1993), and a general semi-analytical model for decomposition of the spectral signatures (Lee et al. in press).

Any system used for the measurement of ocean color requires high signal to noise, excellent calibration, and some method of accurately correcting for the atmosphere. Of the total signal measured by an ocean color instrument in space or on a high altitude aircraft over 90% of the signal is from the atmosphere (Fig. 1). Systems designed exclusively for ocean color measurements have very high signal to noise (CZCS, SeaWiFS) but they saturate over bright targets, reducing their effectiveness near the coast and in partly cloudy conditions. In 1991 AVIRIS has barely sufficient signal to noise for dark ocean targets. The 1992 AVIRIS data has significantly improved signal to noise and continued improvements to AVIRIS in 1993 and 1994 should give performance 1994 similar to that in line 3 which is the predicted performance of HYDICE (Rickard, this volume) which is an aircraft imaging spectrometer with approximately 10 nm spectral resolution and 3 to 6 meter spatial resolution depending on the altitude of the overflight. Both AVIRIS and HYDICE have sufficient dynamic range to image bright and dark targets in the same scene.

The following sections give an overview of our present procedures for the calibration, atmospheric correction and analysis of AVIRIS data for the coastal ocean. Data from an AVIRIS

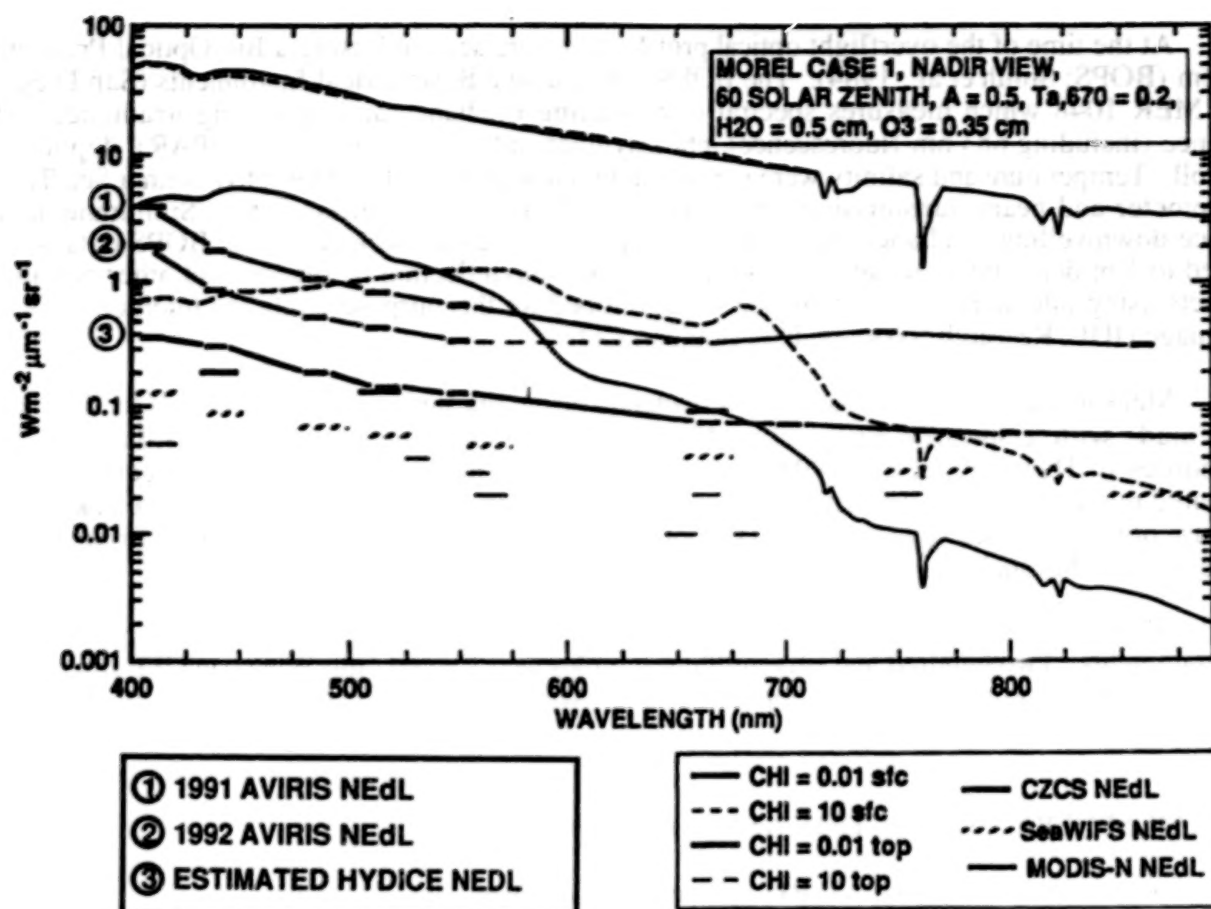


Figure 1. Ocean radiances and instrument noise equivalent delta radiances (NEdL). The signal from low chlorophyll ($0.01 \text{ mg Chl m}^{-3}$) and high chlorophyll (10 mg Chl m^{-3}) ocean waters at the water surface (sfc) and at the top of the atmosphere (top). Instruments whose NEdL is less than the ocean surface signal for each wavelength are suitable for ocean measurements. A lower NEdL is better. The signals and instrument performance were modeled using the conditions indicated in the upper right corner of the figure.

image of the coastal ocean off San Pedro, CA is used to illustrate the procedures. A discussion of the methods for extracting in-water components from the AVIRIS data follows. Consideration is also given to future directions for the design of imaging spectrometers for the coastal ocean, and the need for rapid, automated processing systems for that data.

2. METHODS

On March 21, 1991 AVIRIS imagery was acquired on two flight lines from the Palos Verdes Peninsula to Catalina Island. At the time of the overflight there were two research ships collecting ground truth data. On one ship measurements of surface reflectance, and profiles of pigments and optical properties were collected, and subsequently used in the calibration and analysis of the AVIRIS data. The other ship collected under-way measurements which are not discussed in this paper. Further details about the AVIRIS data and the study site are given in Davis, et al. (1993). The AVIRIS image was initially calibrated using the calibration factors supplied by the Jet Propulsion Laboratory's AVIRIS Processing Facility, and then recalibrated in the blue part of the spectrum as discussed in section 2.2.

2.1 IN-SITU MEASUREMENTS

891000

At the time of the overflight optical profile data were acquired using a Bio-Optical Profiling System (BOPS; Smith et al., 1984). The BOPS is based on a Biospherical Instruments (San Diego, CA) MER 1048 which measures spectral downwelling irradiance and upwelling irradiance and radiance (including 683 nm fluorescence), photosynthetically available radiation (PAR), depth, tilt and roll. Temperature and salinity were measured with a SeaBird CTD, chlorophyll with a Sea Tech fluorometer and beam transmission (660 nm) with a Sea Tech transmissometer. Simultaneously surface downwelling irradiance was collected with a four channel deck cell. The BOPS data were binned to 1 m depth intervals and processed to remove ship reflection or shadow and other possible artifacts using interactive software which we developed for this purpose using the Interactive Data Language (IDL, Research Systems, Inc., Boulder, CO).

Measurements of remote-sensing reflectance of the sea surface (R_{rs}), from 350 to 1250 nm were made with a Spectron Engineering Model 590 hand-held spectroradiometer following the procedures of Hamilton, et al. (1993) and references cited therein. Sea surface reflectance was measured relative to a gray 10% reflectance standard and corrections were made for reflected skylight. Because of the rough sea state and abundance of foam at station 1, only the R_{rs} spectrum from station 2 was used in this analysis.

Water samples were collected at four depths for determination of chlorophyll and phaeopigments. Two hundred and fifty milliliter samples were filtered onto Whatman GFF filters and processed for chlorophyll and phaeopigments following the method of Strickland and Parsons (1972).

2.2 ATMOSPHERIC CORRECTION AND RECALIBRATION

In each spectral channel AVIRIS measures the following sum of radiances:

$$L_{tot} = L_w t_d(\theta_1) + L_{path} + L_{sky} * (\rho t_d(\theta_1) + \rho t_d(\theta_2)), \quad (1)$$

where:

L_{tot} = Total radiance received at the aircraft (the AVIRIS data)

L_w = water-leaving radiance

$t_d(\theta_1)$ = diffuse transmission of the atmosphere at the instrument view angle

$t_d(\theta_2)$ = diffuse transmission at the solar zenith angle

L_{path} = path-scattered Rayleigh and aerosol radiance due to the atmosphere

L_{sky} = skylight as viewed looking up from the surface, at the instrument view angle

ρ = Fresnel reflectance of the water surface

Each of the terms on the right side of the equation, with the exception of water-leaving radiance, was modeled with the atmospheric radiative transfer code LOWTRAN-7 (Kneizys, et al., 1988).

Rearranging to solve for the water leaving radiance:

$$L_w(\text{image}) = [L_{tot} - L_{path} - L_{sky} * (\rho t_d(\theta_1) + \rho t_d(\theta_2))] / t_d(\theta_1). \quad (2)$$

LOWTRAN-7 was run in radiance mode with the proper geometry and environmental characteristics to get the path-scattered term. It was run again with the observer placed on the surface looking up into space to get a value for skylight, which is then reflected off the ocean using the Fresnel reflectance (ρ) and diffusely transmitted through the atmosphere to altitude.

Transmittance through the atmosphere was modeled as a function of optical thickness of the atmospheric components:

- τ_r the optical thickness for Rayleigh scattering
- τ_a the optical thickness for aerosol scattering
- τ_{O_2} the optical thickness for ozone absorption
- τ_{mg} the optical thickness for absorption by mixed gases, and
- τ_{wv} the optical thickness for water vapor

The optical thicknesses were modeled using the equations and databases from LOWTRAN-7 with two exceptions. First, the exact column ozone abundance was calculated for the date of the overflight using current ozone profiles provided by the UARS (Upper Atmosphere Research Satellite) project. As the gas profiles used by LOWTRAN-7 are based on 1976 measurements, $[O_3]$ was rescaled for the atmospheric correction. Second LOWTRAN-7 was modified to allow a variable input for atmospheric water vapor. This value (2.356 cm for the White Point scene) was derived from the depth of the water absorption feature at 1130 nm using the Continuum Interpolated Band Ratio (CIBR) method (Bruegge et al., 1990).

The water-leaving radiance thus derived from the image was then compared to in-situ measurements, collected by both in-water (MER 1048) and surface (Spectron hand-held spectroradiometer) instruments at station 2. The remote-sensing reflectance measurements taken with the Spectron were transformed to units of water-leaving radiance, using a surface irradiance spectrum (E_d^+) calculated for the scene conditions using LOWTRAN-7:

$$L_w(\text{Spectron}) = R_{rs} * E_d^+ \quad (3)$$

The uppermost 5m of the underwater light field measurements were propagated to just below the surface using a polynomial interpolation, and then transformed to just above the surface using a factor of 0.544¹²:

$$L_w(\text{MER}) = L_u * 0.544 \quad (4)$$

The independent estimates of L_w are shown in figure 2. Agreement between the various measurements is remarkably good, except in the short wavelengths. This is assumed to be an instrument calibration problem which is the result of a change in instrument performance between conditions in the laboratory where it is calibrated and conditions in the aircraft (Rob Green, personal communication). Carder et al. (1993a) developed a vicarious recalibration technique which we employ here. We used the Spectron data for the recalibration and for this purpose the higher spectral resolution measurements of the Spectron instrument were resampled to AVIRIS spectral channel positions and halfwidths. The ratio of the Spectron water-leaving radiance to the AVIRIS water-leaving radiance were then used to adjust the image calibration coefficients, and these new coefficients were applied to the entire image. This was performed only in the spectral region where the image calibration is unsatisfactory for a water target, i.e. for wavelengths less than 500 nm (the first 10 AVIRIS channels). This combination of modeling and vicarious recalibration (where necessary) was used to produce an atmospherically corrected and accurate image for analysis.

3. ANALYSIS OF WHITE POINT AVIRIS IMAGE

Given a calibrated, atmospherically corrected AVIRIS image the present procedures for the analysis of the spectral signatures from coastal waters fall into three general categories. The semi-analytical approach uses spectra from characteristic regions of the image and knowledge of the

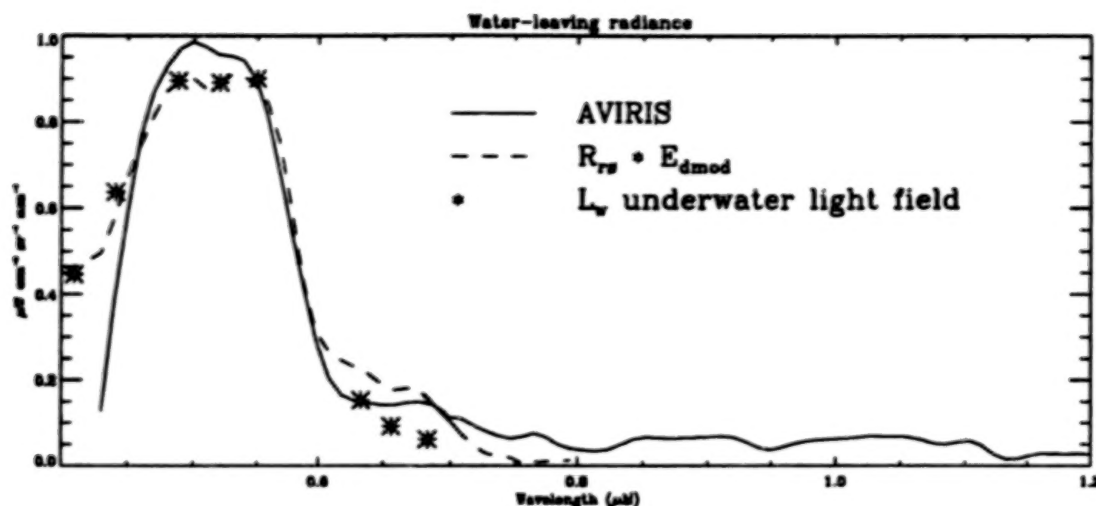


Figure 2. Comparison of shipboard and AVIRIS estimates of water leaving radiance (L_w) at the calibration station. There is close agreement for the three independent estimates of L_w except in the blue region of the spectrum where the AVIRIS values are low. Based on this comparison the first five bands of the AVIRIS data were recalibrated using the SPECTRON data.

components spectral properties to develop derivative or band ratio algorithms for those components. Statistical approaches use principal components or related methods to assess the spectral properties of the main components in the scene. The analytical approach involves the inverse solution of the radiative transfer equation, or a two stream approximation of it. Examples of each approach are given in the following subsections.

3.1 SEMIANALYTICAL PROCEDURES

Four distinct water types were identified in the image and representative spectra (Fig. 3) were extracted for further analysis. Spectra of kelp beds had a distinct red edge at $0.7 \mu\text{m}$ which is a function of pigment absorption at the shorter wavelengths and reflectance from the spectral components of the plant at longer wavelengths. An algorithm based on the slope at $0.7 \mu\text{m}$ was successfully used to delineate all of the kelp beds in the image regardless of the sediment load or other characteristics of the water where they were growing. Suspended sediments backscatter strongly in the visible and an increase in reflectance at $0.56 \mu\text{m}$ with increasing sediment load is evident for the three water spectra in Fig. 1. At wavelengths shorter than $0.56 \mu\text{m}$ the spectral shape is controlled by absorption by phytoplankton pigments and colored dissolved organic matter, however at wavelengths longer than $0.56 \mu\text{m}$ the spectral shape is controlled almost entirely by water absorption. Thus the slope of reflectance at $0.59 \mu\text{m}$ is a function of sediment backscattering and water absorption and is a good indicator of suspended sediment concentration (Chen, et al. 1992). An algorithm based on the slope at $0.59 \mu\text{m}$ produced an excellent map of sediment distribution in the image.

3.2 STATISTICAL PROCEDURES

Principle component or factor analysis (e.g. Fisher, et al., 1986) has been applied to coastal ocean spectral data with mixed success. It is excellent for finding how many independent factors are determining the radiance spectra, however, because the components are required to be orthogonal

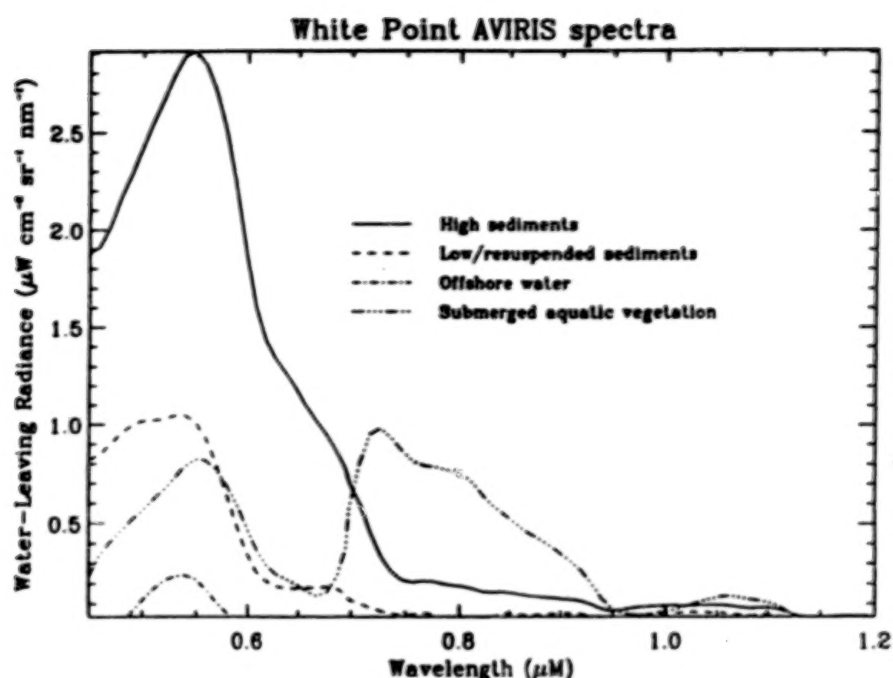


Figure 3. Characteristic spectra from the AVIRIS image. A kelp bed spectra is compared with water having low, medium and high levels of suspended sediments.

they are not always recognizable as actual components in the scene. Principle component analysis of a sub scene of the White Point image that contained kelp and suspended sediments (Fig 4., Hamilton, et al., In Press) resulted in three components explaining 97% of the variance. However, the first two components are some combination of the water and sediment spectrum, and neither can be related directly to the spectral signature of any known component. The third component is clearly related to the kelp spectra and explains 1.8% of the variance in the scene which is a good estimate of the percent of the sub scene that contained kelp.

A number of researchers are exploring alternate statistical approaches for the unmixing of hyperspectral image data. One of the most promising is the automated procedure developed by Joe Boardman which is based on the principles of convex geometry (Boardman, This volume). In this approach the data is represented as an n -dimensional scatterplot, where n is the number of spectral bands. A best fitting simplex is found which contains all of the points in the scatterplot. The vertices of this simplex represent the spectral endmembers. The sub scene was sent to Boardman for automated spectral analysis and the resulting spectra (Fig. 5) are recognizable as kelp, low sediment and high sediment waters. Boardman mapped these components to the image and they clearly show the kelp beds and sediment plumes coming off of the coast. The limitation of this approach is that it is computationally intensive and computation time increases rapidly with an increase in the number of components in the scene such that it is impractical for scenes with 10 or more components.

3.3 ANALYTICAL APPROACHES

From a theoretical basis the ideal approach for extracting the component spectra from the image is an inverse solution of the radiative transfer equation. In this formulation the light field is described as a function of the inherent optical properties (absorption, scattering and scattering phase function) of the optically active components in the water. Numerical models for the computation of the underwater light field are mostly Monte-Carlo solutions which require a great deal of computer time for each profile and wavelength (Mobley, et al., 1993). One of these models (Mobley, 1989) uses the method of invariant imbedding to numerically solve the radiative transfer equation, and is sufficiently rapid to use for remote sensing calculations. Hamilton et al. (In Press) made some preliminary calculations using this method, however they note that the primary limitation is the lack of optical parameters, particularly phase functions for the various components.

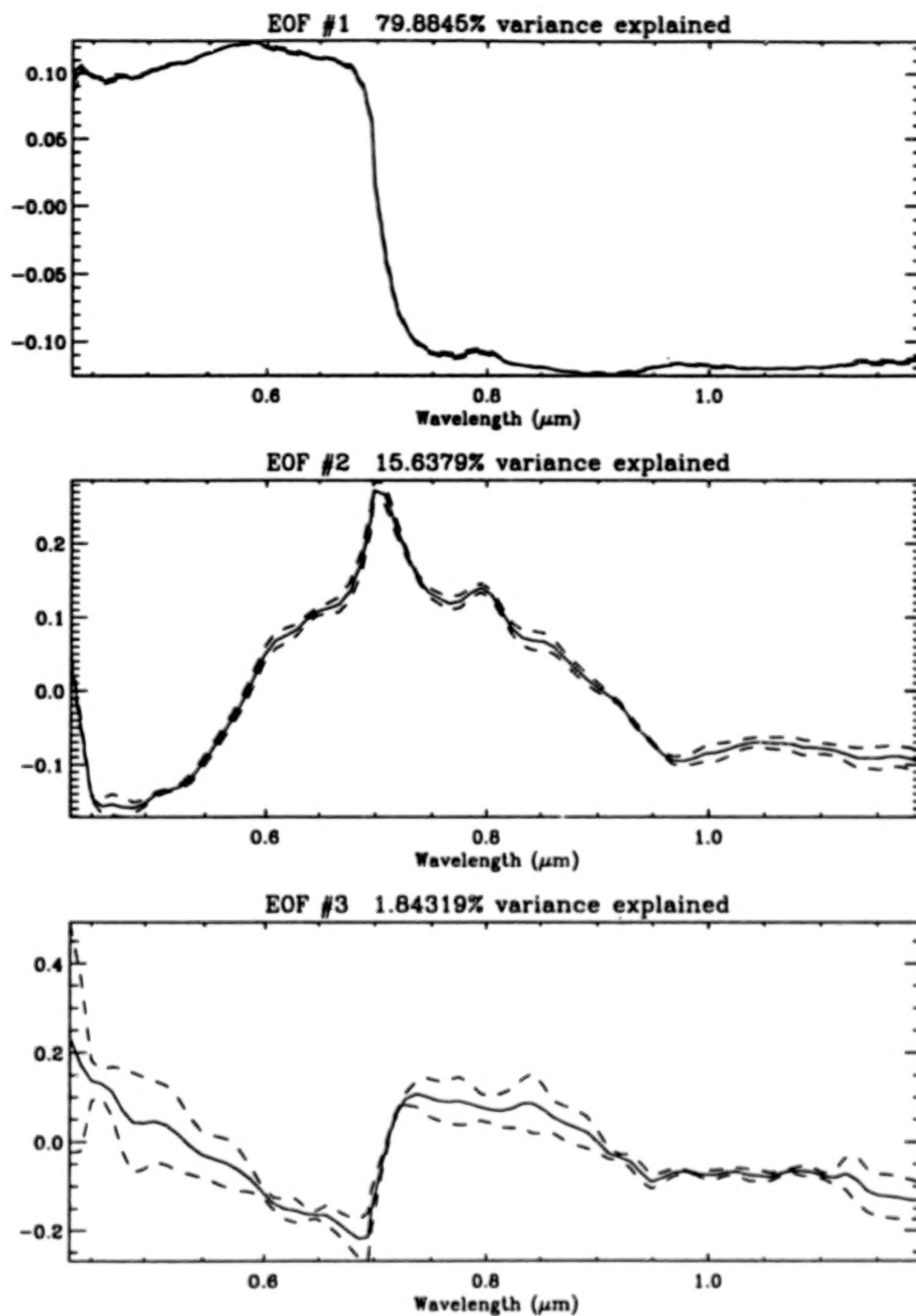


Figure 4. The first three principle components for the AVIRIS sub scene.

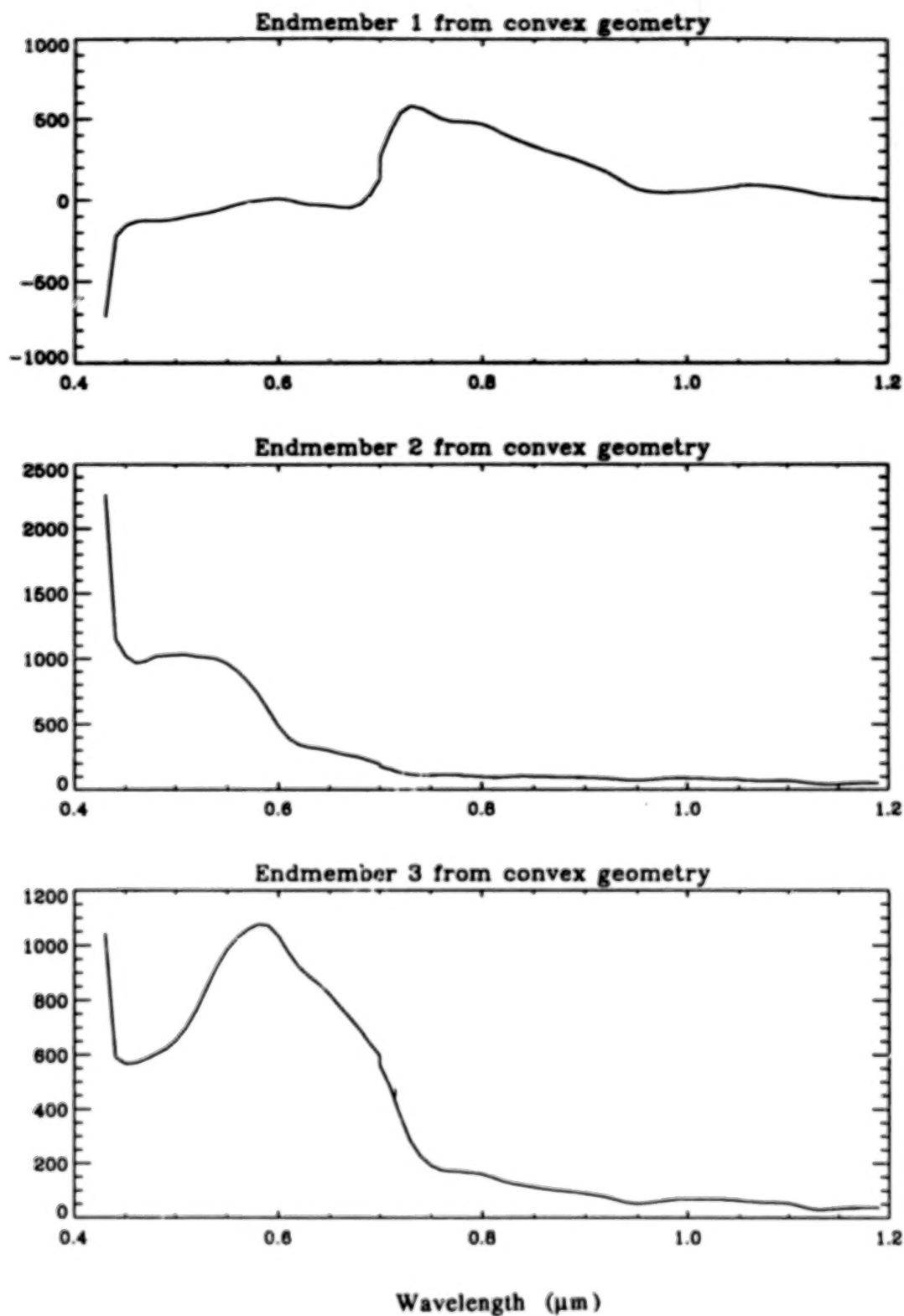


Figure 5. Components of the sub scene determined using the convex geometry method.

The present inverse approaches are iterative and use a two stream approximation of the radiative transfer equation (Doerffer, 1992; Lee et al., In Press). The approach is to simulate the radiance (or reflectance) from each component and compare that to the measured radiance. The concentrations of the unknown components are varied to achieve a best fit to the measured radiances. This approach requires a knowledge of the optical properties of all of the substances that contribute to the signal. It also requires a great deal of computing time, even with a two stream model.

4. DISCUSSION

Imaging spectrometry data is a powerful tool for the analysis of the complex properties of the coastal ocean. Systems such as AVIRIS and, next year HYDICE, provide calibrated data with adequate signal to noise for dark ocean targets. Procedures have been developed for the atmospheric correction and analysis of AVIRIS data, however, they are computationally intensive and may require many hours or days for the analysis of each scene. More efficient approaches are being sought. A simplified atmospheric correction scheme has been suggested by Doerffer (1992) that is much more efficient than the present LOWTRAN-7 or MODTRAN based methods. Doerffer assumes single scattering and makes other simplifications that are very appropriate for most nadir viewing aircraft systems, and that greatly speed computation time.

Statistical unmixing of scenes is particularly useful when there is limited knowledge about the spectral properties of the components in the scene. Standard principle components analysis has limited usefulness because of the requirement for orthogonality, however, approaches such as Boardman's convex geometry method give excellent results. Its limitation is that it takes a great deal of computer time, and is limited to less than ten components.

Inverse methods for the analysis of imagery are most promising, however, they require more efficient computational methods such as neural networks. Also, they require knowledge of the optical properties of the in-water components and, in shallow water, the bottom reflectance. The key to making use of the large amount of imaging spectrometry data that is becoming available is the development of the necessary spectral data bases and rapid computational methods.

ACKNOWLEDGMENTS

Special thanks to the Jet Propulsion Laboratory (JPL) AVIRIS team for their continuing efforts to improve the calibration and performance of AVIRIS for coastal ocean experiments. The AVIRIS team and the NASA Ames Research Center, High Altitude Branch collected the AVIRIS data. Mike Hamilton and Jeannette van den Bosch of JPL processed the White Point AVIRIS data, and Mike did most of the analysis of that data. Joe Rhea of JPL helped collect, and processed the in-water optical profile data. Bob Stewart of the University of South Florida collected and processed the Spectron data. Thanks to William Read for the UARS ozone data. Long and frequent discussions with Ken Carder of the University of South Florida helped develop many of the ideas expressed in this paper.

REFERENCES

- Boardman, J. W., 1994: Automatic mixture analysis of imaging spectrometry data, *ISSSR*, this volume.
- Bruegge, C. J., J. E. Conel, J. S. Margolis, R. O. Green, G. Toon, V. E. Carrere, R. G. Holm, G. Hoover, 1990: In-Situ Atmospheric Water-Vapor Retrieval in Support of AVIRIS Validation, *Proc. SPIE 1298 Imaging Spectroscopy of the Terrestrial Environment*, Int. Soc. Optical Eng., Bellingham, WA, 150-163.

- Carder, K. L., P. Reinersman, R. Chen, F. Muller-Karger and C. O. Davis, 1993a: AVIRIS calibration and application in coastal oceanic environments, *Rem. Sens. Environ.* **44**: 205-216.
- Carder, K. L., Z. P. Lee, R. F. Chen and C. O. Davis, 1993b: Unmixing of spectral components affecting AVIRIS imagery of Tampa Bay, *SPIE, 1937, Imaging Spectrometry of the Terrestrial Environment*, Int. Soc. Optical Eng., Bellingham, WA, 77-90.
- Chen, Z., P. Curran, and J. Hansom, 1992: Derivative reflectance spectroscopy to estimate suspended sediment concentration, *Rem. Sens. Environ.*, **40**, 67-77.
- Davis, C. O., M. K. Hamilton, W. J. Rhea and J. M. van den Bosch, K. L. Carder and R. Steward, 1993: Spectral analysis of an AVIRIS image of San Pedro Channel, *SPIE, 1937, Imaging Spectrometry of the Terrestrial Environment*, Int. Soc. Optical Eng., Bellingham, WA, 64-76.
- Doerffer, R., 1992: Imaging Spectroscopy for Detection of Chlorophyll and Suspended Matter. In *Imaging Spectroscopy: Fundamentals and Prospective Applications*, F. Toselli and J. Bodechtel (Eds.), ECSC, EEC, EAEC, Brussels and Luxembourg, 215-257.
- Fisher, J., R. Doerffer, and H. Grassel, 1986: Factor analysis of multispectral radiances over coastal and open ocean water based on radiative transfer calculations, *Applied Optics*, **25**, 448-456.
- Hamilton, M. K., C. O. Davis, W. J. Rhea, S. H. Pilorz and K. L. Carder, 1993: Estimating chlorophyll content and bathymetry of Lake Tahoe using AVIRIS data, *Remote Sens. Environ.*, **44**, 217-230.
- Hamilton, M. K., S. H. Pilorz, C. O. Davis, J. M. van den Bosch and W. J. Rhea, In Press: Analysis of high spectral resolution coastal ocean imagery: statistical, empirical and analytical investigations, *SPIE, Algorithms for Multispectral and Hyperspectral Imagery*, Int. Soc. Optical Eng., Bellingham, WA.
- Hooker, S. B., et al., 1992: SeaWiFS Technical Report Series, Volume 1, An Overview of SeaWiFS and Ocean Color, *NASA Tech. Memo.* 104566, **1**, 25 pp.
- Hovis, W. A., et al., 1980: Nimbus-7 coastal zone color scanner; System description and initial imagery, *Science*, **210**, 60-63.
- Kneizys, F. X., E. P. Shettle, L. W. Abreu, J. H. Chetwood, G. P. Anderson, W. O. Gallery, J. E. A. Selby, S. A. Clough, 1988: Users Guide to LOWTRAN 7, Air Force Geophysical Laboratory, AFGL-TR-88-0177, *Environmental Research Papers*, No. 1010.
- Lee, Z., K. L. Carder, S. K. Hawes, R. G. Steward, T. G. Peacock and C. O. Davis, In Press: A model for interpretation of hyperspectral remote-sensing reflectance. *Appl. Opt.*
- Mobley, C. D., 1989: A numerical model for the computation of radiance distributions in natural waters with wind-roughened surfaces, *Limnol. Oceanogr.*, **34**(8), 1473-1483.
- Mobley, et al., 1993: Comparison of numerical models for the computation of underwater light fields, *Applied Optics*, **32**(36), 7484-7504.
- Porter, W. M. and H. T. Enmark, 1987: System overview of the Airborne Visible/Infrared Imaging Spectrometer (AVIRIS), *Proc. SPIE 834, Imaging Spectroscopy II*, Int. Soc. Optical Eng., Bellingham, WA, 114-126.
- Rickard, L. J., 1994: HYDICE: A status report, *ISSSR*, this volume.

- R. C. Smith, C. R. Booth, and J. L. Star, 1984: Oceanographic Bio-optical Profiling System, *Applied Optics*, **23**, 2791-2797.
- Strickland, J. D. H. and T. R. Parsons, 1972: *A Practical Handbook of Seawater Analysis*, Fish. Res. Bd. Canada Bull. **167**, 311 pp.
- Vane, G., R. O. Green, T. G. Chrien, H. T. Enmark, E. G. Hansen and W. M. Porter, 1993; The Airborne Visible/Infrared Imaging Spectrometer (AVIRIS), *Remote Sens. Environ.*, **44**, 127-143.

SIMULATING RADIATIVE TRANSFER IN AQUATIC SYSTEMS AND CONTRASTING RESULTS FROM AMBIENT ENVIRONMENTAL SPECTROSCOPY: ESTUARINE AND NEAR COASTAL WATERS

by

Charles Bestater, Wei-Ming Ma and Andrew Lamb

**Marine & Environmental Optics Remote Sensing Center
Marine & Environmental Systems Division
Florida Institute of Technology, Melbourne FL., 32901**

ABSTRACT

A simplified solution to the radiative transfer problem for a water layer that is considered optically shallow is developed and described. The application of high resolution optical signatures are discussed with respect to coastal marine waters with examples from Atlantic and Pacific ocean coastal waters. The development and solutions to the two flow model equations are described and contrasted to the second derivative estimators of simulated and measured data derived from ambient environmental reflectance spectroscopy. The application of high spectral resolution optical signatures obtained from a solid state spectrograph suggest these instruments provide valuable data and platforms for studying coastal and marine water radiative transfer. Results show the need and role for further developments in modeling or optimization of solution techniques applicable to analytical solutions of radiative transfer for environmental quality applications. The quantitative relation between the 2nd derivative of reflectance signatures and analytical solutions to the radiative transfer problem is considered a preferred analysis technique for understanding high resolution reflectance signatures.

1. INTRODUCTION

The purpose of this paper is to present & discuss characteristic reflectance signatures of various water environments. The rationale for development of a radiative transfer model (two flow irradiance) is described and selected results show simulated sensitivity results of the analytical model. The concept of differentiating the analytical solution of reflectance is described in order to point out that $d^2R/d\lambda^2$ (the second derivative of reflectance as a function of wavelength) of either measured or modeled reflectance signatures, provide the signals of interest in materials detection in the aquatic environment. The goal of this research is to bring to the readers attention that relative absorption and backscatter spectral regions are made apparent in this signal (measured or modeled) in a *quantitative* manner. In general, these important spectral regions are our main interest in ambient environments using the reflectance signature.

2. BACKGROUND

A point source of electromagnetic radiation can be described in terms of it's steady state Lagrangian derivative or,

$$dL(\lambda)/dz = - [s(\lambda)+c(\lambda)]L(\lambda) + L'(\lambda) \quad (1)$$

where: $L(\lambda)$ = radiance ($\text{W cm}^{-1} \text{ str}^{-1} \text{ nm}^{-1}$),
 $L'(\lambda)$ = path radiance ($\text{W cm}^{-1} \text{ str}^{-1} \text{ nm}^{-1}$),
 $s(\lambda)$ = total volume scattering function (m^{-1}),
 $c(\lambda)$ = beam attenuation (m^{-1}),
 z = distance along the source path direction (m),
 λ = wavelength of electromagnetic.

The above formulation makes no specific distinction as to the wavelength or the portion of the electromagnetic spectrum being considered. It assumes a uniform medium through which the radiation travels. For this research one can think of visible light being transferred, transmitted, and scattered or thus attenuated. The last point to make is that the above formulation is also wavelength (λ) or frequency dependent. This point means that L , L' , c , and s can be measured in many different spectral regions or channels using hyperspectral marine and environmental optics instrumentation.

The scattering function in the above formulation can be considered to be made of two components, the backscattered, $b_s(\lambda)$ and the forward scattering, $b_f(\lambda)$ components of $L(\lambda)$. In the model developed below, we will utilize the concept of backscatter. This backscattering environmental process is conceptualized as being responsible for the measured signal of upwelling or upwards flowing light emitted from within the water (or medium) and even across the water surface. It is the backscattered fraction of $L(\lambda)$ originating from within the water that an instrument submerged or located just above water surface, or at altitude will measure. A sensor measuring the upwelled or backscattered light may measure the light reflected from the water surface or $R_s(\lambda)$. This quantity may be the specular and diffuse sky reflectance, as well as the light reflected off the bottom due to the bottom reflectance, $R_b(\lambda)$. In the model developed below, we will assume the influence of $R_s(\lambda)$ will or can be included within a surface boundary condition. The influence of $R_b(\lambda)$ will also be utilized directly in the model.

The measurements made from a sensor looking into the water (just above the water surface) or an *in-situ* optical instrument can also measure the integral of $L(\lambda)$ in a horizontal plane or the hemispherical irradiance. These irradiance signals (in the upwards and downwards directions) can be used to also calculate the fundamental remote sensing - reflectance or for the purposes of this paper, the reflectivity factor $R(\lambda)$. This is considered to be a measure of the volume reflectance of the water or medium (and may have $R_s(\lambda)$ or $R_b(\lambda)$ within it). Thus, measurement of this quantity is often influenced by the sea surface and as well as the bottom reflectance $R_b(\lambda)$. Of course, a sensor which views the sea surface (as from a satellite or aircraft or ship) has these other reflectance factors influencing the received signal unless $R_s(\lambda)$ is reduced by using a polarizing lens and or viewing is minimized by the radiance measurement at Brewsters angle. With the above in mind, we define the reflectivity factor as:

$$R(\lambda) = E_u(\lambda) / E_d(\lambda) \quad (2)$$

where:

$E_u(\lambda)$ = upwelled irradiance ($\text{W cm}^{-2} \text{ nm}^{-1}$),
 $E_d(\lambda)$ = downwelled irradiance ($\text{W cm}^{-2} \text{ nm}^{-1}$).

Thus this definition is the most general case for a sensor viewing the water from above the sea water surface. The values of $E_i(\lambda)$, $i=u,d$ above are assumed to be the hemispherical integrals of $L(\lambda)$ defined above, where we now note that $L(\lambda)$ or $E_i(\lambda)$ are defined as the energy traveling in a unit direction along a z axis as described in figure 1.

In general, equation 2 for the hemispherical irradiant energy fluxes in the water can be described in terms of an inherent backscatter $b_i(\lambda)$, and absorption $a(\lambda)$, processes and another type of apparent process, the diffuse attenuation with terms for each of the upwelling and downwelling directions or $k_d(\lambda)$ and $k_u(\lambda)$. In the model to be developed, we will avoid use of the apparent attenuation processes. A formulation for the irradiance quantities in terms of inherent adsorption and backscatter processes for a water layer of thickness z are then:

$$dE_d(\lambda)/dz = -a(\lambda) E_d(\lambda) - b_s(\lambda) E_d(\lambda) + b_s(\lambda) E_u(\lambda) , \quad (3)$$

$$dE_u(\lambda)/dz = -a(\lambda) E_u(\lambda) - b_s(\lambda) E_u(\lambda) + b_s(\lambda) E_d(\lambda) . \quad (4)$$

Figure 1 represents the conceptualization of the water layer for an idealized homogeneous medium or hydrosol. Note that for optically shallow waters, interface 1 represents the water surface and interface 2 would represent the bottom of the water column. These equations could be used on a layered basis for estimating the transfer of radiation through the water column where the value of the transferred light represents the light impinging the top of an adjacent layer.

A solution to these equations applicable to shallow waters can be obtained assuming appropriate boundary conditions with $E_d^0(\lambda)$ at the surface, a bottom reflectance factor $R_b(\lambda)$, the water depth, h and two unique parameters to be estimated, $\delta(\lambda)$ and $\beta(\lambda)$. A mathematically unique solution to these equations exist when (1) and (2) are decoupled in a second order differential equation. The general form of the decoupled O.D.E. can be written as:

$$\frac{d^2 E_i(\lambda, z)}{dz^2} - \psi(\lambda)^2 E_i(\lambda, z) = 0 , \quad (5)$$

where the coefficient ψ is given by:

$$\psi(\lambda) = \sqrt{a^2(\lambda) + 2a(\lambda)b(\lambda)} , \quad (6)$$

and represents a second order inherent attenuation coefficient as shown in (5).

The above 2nd order O.D.E. above can be solved for the upwelling light $E_u^0(\lambda)$ at the surface $z=0$, as seen by a satellite, or other airborne, shipboard or *in-situ* optical sensor system in shallow water environments such as inlets, in shallow coastal waters and in estuarine systems. It can be shown that a general solution (omitting λ for brevity) for $E_u(\lambda, z)$ and $E_d(\lambda, z)$ at any depth z are by:

$$E_d(z) = \frac{\psi E_d^0 + \delta}{2\psi} e^{\psi z} + \frac{\psi E_d^0 - \delta}{2\psi} e^{-\psi z} , \quad (7)$$

$$E_u(z) = \frac{\psi E_u^h + \beta}{2\psi} e^{\psi(z-h)} + \frac{\psi E_u^h - \beta}{2\psi} e^{-\psi(z-h)}, \quad (8)$$

where $k > 0$. These solutions satisfy the boundary conditions of:

$$E_d(\lambda, 0) = E_d^0 \quad \text{and} \quad \frac{dE_d(\lambda, 0)}{dz} = \delta, \quad (9)$$

$$E_u(\lambda, h) = E_u^h \quad \text{and} \quad \frac{dE_u(\lambda, 0)}{dz} = \beta. \quad (10)$$

The value of $E_u^h(\lambda)$ can be obtained from knowledge of the bottom reflectance and the value of $E_d^h(\lambda)$ obtained from (9) requires an estimate of $E_d^0(\lambda)$ just below or just above the water surface (depending on the application). With estimates or measurements of either $E_i(\lambda, z)$ and $a(\lambda)$, then $b_s(\lambda)$ can be estimated from the above (equations 5,6). The system can be inverted to obtain multiwavelength semi-analytical inversion estimates of the specific coefficients for estimation of water quality variables that may influence $R_s(\lambda)$, as well as the influence of $R_b(\lambda)$. Also note that the above formulation does not explicitly neglect forward scattering, but the model includes this process in an inherent fashion.

Note that the term $E_u^h(\lambda)$ or the light upwelling at the bottom can be specified using the solution for $E_d(\lambda)$ with a specified water depth and the bottom reflectance term given by:

$$R_b(\lambda) = E_u(\lambda)/E_d(\lambda) \quad (11)$$

and now we have a complete system of equations to describe the flow of energy that enters the water, reflects off of the bottom and then emerges at the water surface. The above solution methodology can in concept be further refined with the knowledge of the air-sea interface effects upon the values $\delta(\lambda)$ and $\beta(\lambda)$ if necessary, i.e., wave and foam effects using concepts from physical oceanography. Another utilization of the solution is to solve for h with the other values known or estimated from a multiwavelength inversion methodology.

3. Model Simulation Procedure

With the analytical radiative transfer solution as described above, the procedure to calculate the reflectance at the top of the layer is to define $E_d^0(\lambda)$, $a(\lambda)$, $b(\lambda)$, $R_b(\lambda)$, $\delta(\lambda)$, $\beta(\lambda)$, and h . Use the relation $E_u^h(\lambda) = R_b(\lambda) E_d(\lambda)$. Next, calculate $E_u^h(\lambda)$ with knowledge of $R_b(\lambda)$ and then calculate the upwelling light at $E_u^0(\lambda)$. Note that one can define $L_w(\lambda) = E_u^0(\lambda) / E\pi$ in order to obtain radiance. One then calculates the reflectance at an interface or $R_s(\lambda)$ using $E_u^0(\lambda) / E_d^0(\lambda)$.

Now the goal is to relate the above analytical form of the reflectance spectrum to observed measurements of reflectance and to show how the above work is related to differential reflectance spectroscopy.

4. RADIATIVE TRANSFER SOLUTIONS AND ENVIRONMENTAL SPECTROSCOPY

The analytical solution as described above can now be differentiated in order to demonstrate the very powerful relation between the radiative transfer solution and modern environmental spectroscopy techniques. We know that the first derivative and second derivative of observed reflectance signatures have been the basis of quantitative identification of relative material absorption and backscatter. The first derivative (or slope) is commonly used in remote sensing by using band ratios. The second derivative (inflection or curvature) is a more precise measure of the actual absorption region which is characterized by using 3 or more channels of data. For example Bostater (1992, 1991) developed an optimal band selection methodology using a second derivative estimator (Grew, 1988) based upon passive sensor data used to produce reflectance signatures of water. The analytical solution as described Note that $E_d(\lambda, z)$ is given by a similar equation and with $E_d^0(\lambda)$ specified as the light entering at interface 1. The above can be written (omitting the notation for λ) as:

$$R = \frac{2e^{h\nu} \beta - 2e^{3h\nu} \beta + E_d^0 \psi R_b + 2e^{2h\nu} E_d^0 \psi R_b + e^{4h\nu} E_d^0 \psi R_b - R_b \delta + e^{4h\nu} R_b \delta}{4e^{2h\nu} E_d^0 \psi} \quad (12)$$

Taking the 2nd derivative of the above, we then have a function that will describe the relative absorption and backscatter regions of the spectrum in terms of the curvature or inflection of the reflectance spectrum. This radiative transfer reflectance spectroscopy (RTRS) relation can enable one to analytically describe the spectral absorption regions given the specified coefficients and the two flow equations as developed and solved here. Also remember that for nadir viewing geometry, we have that radiance $L(\lambda) = E(\lambda)/\pi$ so the above becomes:

$$L_w(\lambda) = R(\lambda) E_d^0(\lambda) \pi \quad (13)$$

for nadir viewing geometry. Thus the first and second derivatives of $L(\lambda)$ could also be used for radiance spectroscopy applications. In general however, we will use the above equation for $R(\lambda)$ and differentiate twice with respect to λ and obtain a quantitative theoretical function that will provide an exact description of the adsorption and backscatter regions of a simulated reflectance spectrum derived from the analytical radiative transfer model.

Using the above analytical expression of reflectance, it can be shown that the results of the second derivative is a very complex mathematical formulation, even for this simplistic model. This fact is in itself important. First, it shows that the OPACS second derivative technique is actually representing a very complex function based upon simple theory. Second, this 2nd order derivative is easily calculated with observed reflectance signatures or model simulations between theory and observations. Third, once an analytical formulation is obtained as described above, it can be reduced objectively with specified assumptions to determine the most sensitive components. For example, assume that one finds that there are regions of the spectrum (at least 3 channels somewhere across the spectrum (not necessarily adjacent) where all of the model inputs can be constant and bottom reflectance changes. Under these 2 assumptions, the above approach yields:

$$\frac{d^2 R}{d \lambda^2} = \frac{(1 + e^{2h\nu})(E_d^0 \psi + e^{2h\nu} E_d^0 \psi - \delta + e^{2h\nu} \delta) d^2 R_b / d \lambda^2}{4e^{2h\nu} E_d^0 \psi} \quad (14)$$

Note that this relation can be solved for the second derivative of reflectance at interface 2 (or bottom reflectance). Thus this significant relation for coastal shallow water applications can be estimated using several different numerical operators. For example, a common nonlinear 2nd derivative, inflection or curvature operator is (Grew, 1990) is given by:

$$I(\lambda) = B(\lambda)_i^2 / [B(\lambda)_{i-m} * B(\lambda)_{i+n}] \quad (15)$$

where I is the inflection or second derivative estimator centered at channel i , and n channels forwards and m channels backwards along the spectrum. The channels or forward and backwards operators as well as channel i may vary from the first to last channel available in observed data or as specified in the simulated reflectance signatures. This is a nonlinear or power estimator of the 2nd derivative and yields good discrimination features for further analysis of reflectance spectrums. The double inflection ratio is just a ratio of the above with different channels in the numerator and the denominator.

The ratio of 2nd derivatives of the reflectance and/or the radiance has been shown to be invariant to atmospheric perturbations (Philpot, 1990), thus the double inflection ratio (D.I.R.) as described by Bostater, 1990, 1991, 1992 may prove to be a useful technique for reflectance spectroscopy.

5. MATERIALS IN THE MEDIUM

The information concerning concentrations of constituents in the medium are embedded in ψ or the relation containing only the inherent optical properties of the water layer or water column. The relation for ψ can be expressed as a function of $a(\lambda)$, the absorption coefficient and $b(\lambda)$ is the backscatter coefficient for the medium. Now the two terms, a and b are not only a function of wavelength but they are a function of constituent concentrations within the medium. The most common expression to describe a and b are in terms of a linear combination of specific absorption (α_j) and specific backscatter (ϕ_i) coefficients for the specific constituent C_k given by:

$$a(\lambda) = \alpha_w(\lambda) + \alpha_1(\lambda)C_1 + \alpha_2(\lambda)C_2 + \alpha_3(\lambda)C_3 + \alpha(\lambda)_j C_k, \quad (16)$$

$$b(\lambda) = \phi_w(\lambda) + \phi(\lambda)_1 C_1 + \phi_2(\lambda)C_2 + \phi(\lambda)_3 C_3 + \phi(\lambda)_i C_k. \quad (17)$$

The first two terms $\alpha_w(\lambda)$ and $\phi_w(\lambda)$ are special coefficients of absorption and backscatter terms specific to clear natural waters and the other terms are specific to the concentrations of constituents in the water. This formulation allows for an inversion of the constituent concentrations using the model solution developed above.

6. SUMMARY

The solutions of a 2 flow (irradiance) radiative transfer in a medium can be cast into analytical formulations of $d^iR/d\lambda^i$. Observed or measured high resolution spectral reflectance signatures can be used to directly calculate $d^iR/d\lambda^i$ signatures. The observed and modeled signatures can be used in multiwavelength inversions to estimate the necessary materials concentrations as well as the absorption and backscatter and/or other coefficients for target detection purposes. Utilizing the 2nd derivatives of the reflectance signatures for quantitative detection and empirical selection of optimum λ 's or spectral regions can thus be placed on a simple analytical formulation of irradiance.

7. ACKNOWLEDGMENTS

Andrew and Wie-Ming are thanked for mathematically checking the formulation of the model development scheme. Carlton Hall helped collect the data in San Diego Bay and nearby coastal Pacific ocean waters. Model simulations were performed in the Mathematica software on a SGI Indigo². Indirect support has been provided by Ken Marcks, Silicon Graphics Inc. for the Indigo². Dr.'s. William Naught & Ross Hinkle, NASA, Kennedy Space Center, Life Sciences Division are acknowledged for support of this research. Dr. R. Sullivan, Florida Tech, is thanked for his support in development of the Marine & Environmental Optics Lab and Remote Sensing Center at Florida Tech.

8. REFERENCES

Bostater, C., 1992, Mathematical Techniques for Spectral Discrimination Between Corals, Sea Grasses, Bottom and Water Types Using High Spectral Resolution Reflectance Signatures, US Army COE, In: Proceedings, International Symposium On Spectral Sensing Research, November, Vol. 1, pp 526-536.

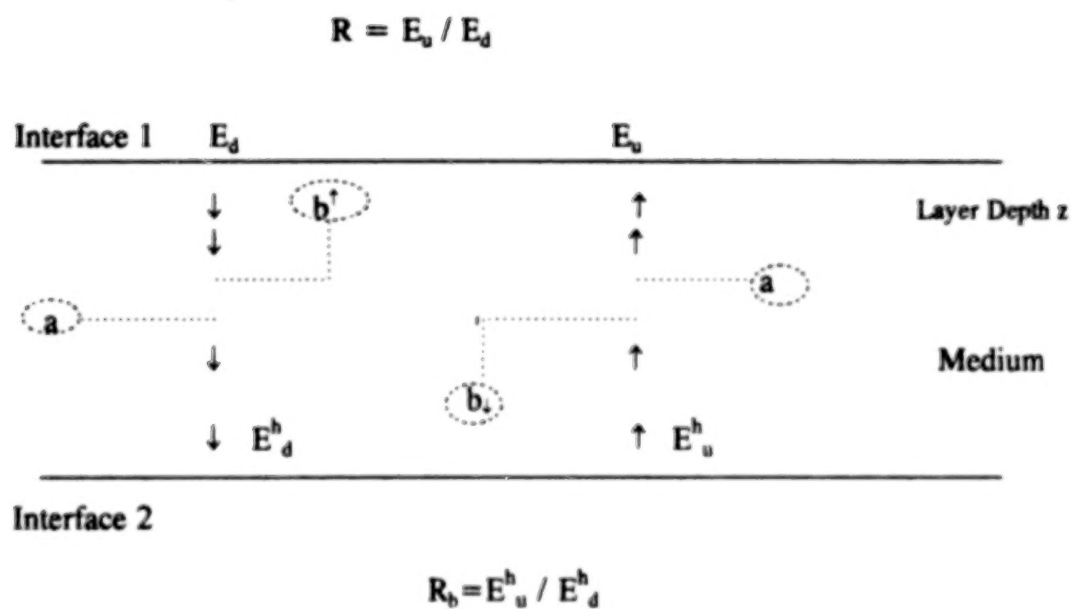


Figure 1. Idealized diagram depicting the 2 flow nature of light energy in a hydrosol or optical medium.

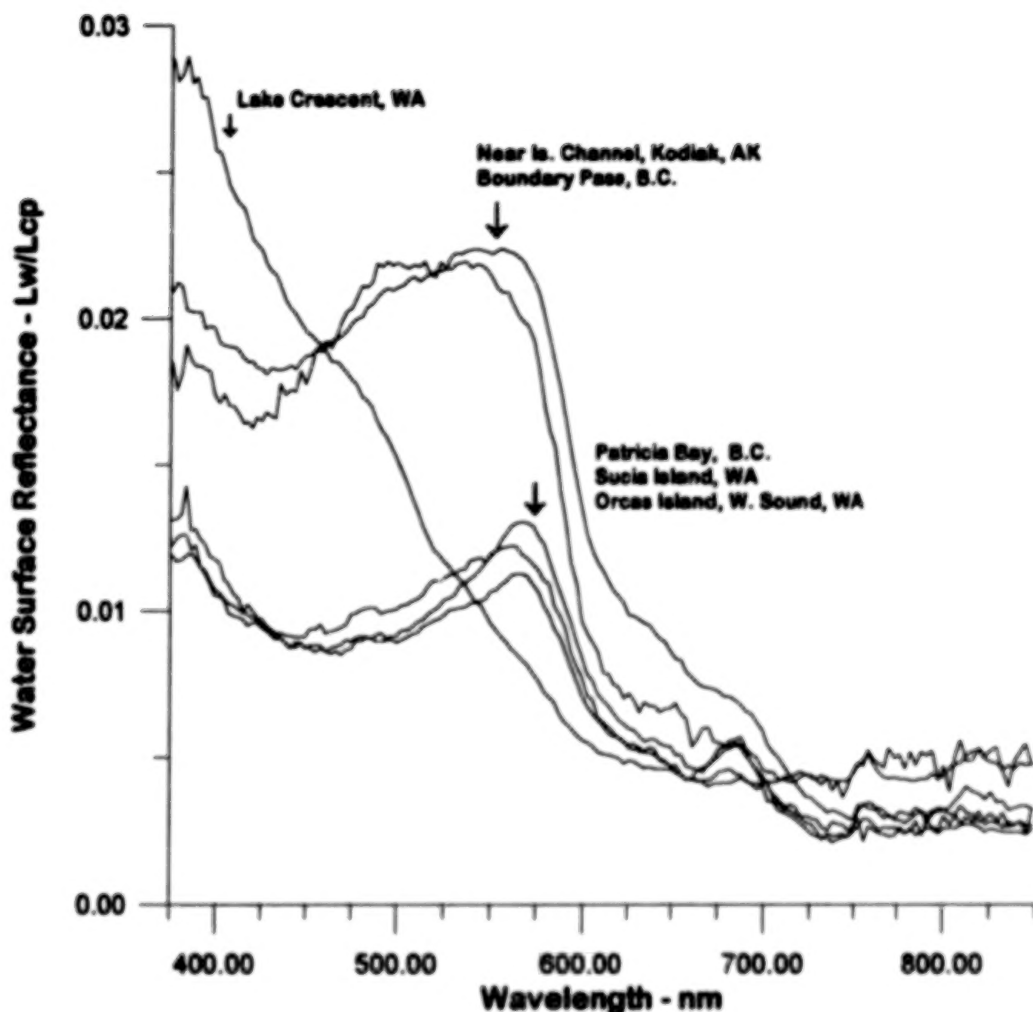


Figure 2. Example of reflectance signatures of the water surface taken from a 252 channel spectrograph. Data collected May-June, 1994. The suspended matter from Lake Crescent (depth=600 ft) was 0.45 mg/L. With this expanded vertical scale plot, note the hinge points above 450 nm and below 550 nm suggesting 2 distinct water types in addition to the very clear natural water from Lake Crescent located in Olympic National Park. The concentration data from Boundary Pass (US and Canadian Border) and Kodiak Island, Alaska ranged from approx 14 to 17 mg/L. Other measurements ranged from approximately 7 to 12 mg/L. These measurements were made from just above the water surface with an intensified SE590 solid state spectrograph and a Labsphere spectralon calibration panel (approximately 5 percent reflectivity).

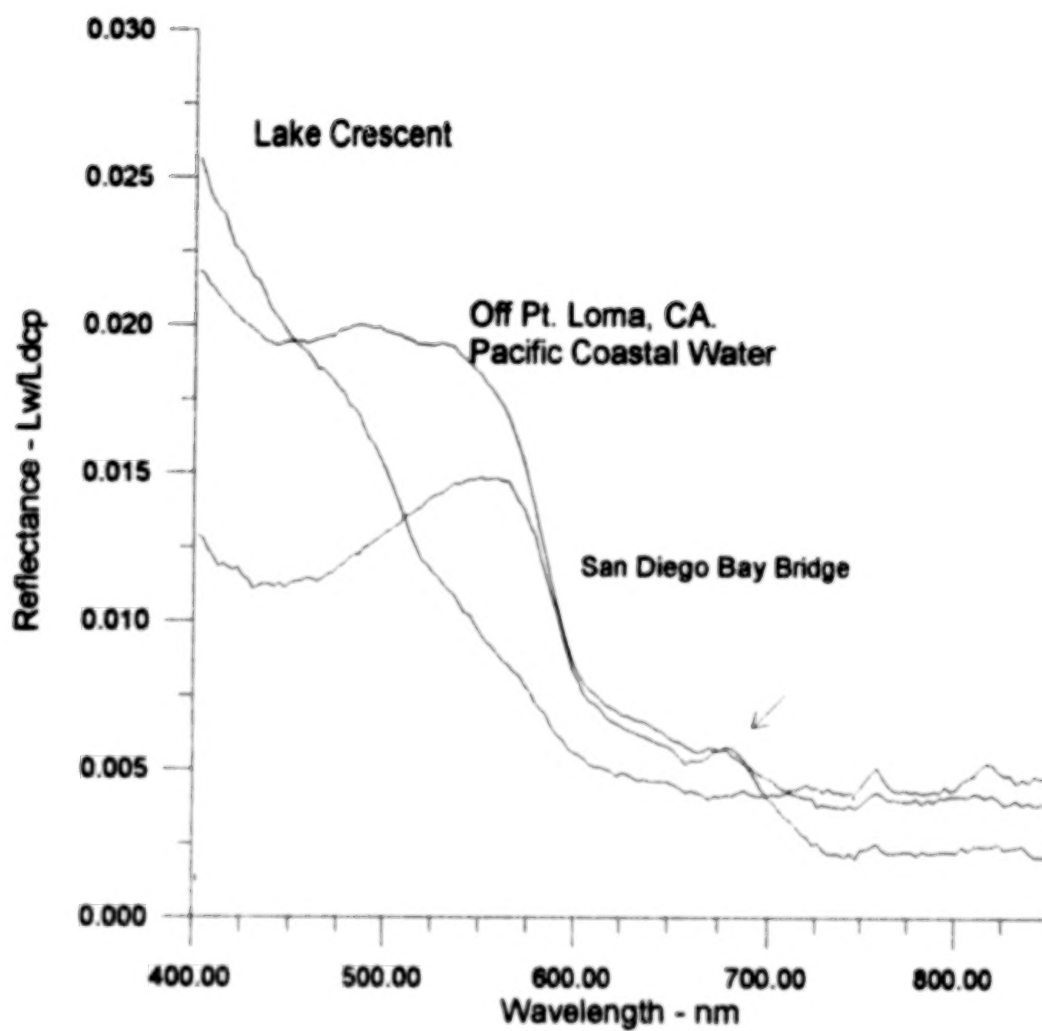


Figure 3. Comparison of clear natural waters from Lake Crescent, Olympic National Park, WA and reflectance near San Diego Bay Bridge and approx 2 miles off Pt. Loma, near the mouth of San Diego Bay, CA.

SPECTRAL REFLECTANCE PROPERTIES OF WETLANDS PLANTS

John E. Anderson, Biologist
U.S. Army Corps of Engineers
Topographic Engineering Center
Spectral Research Division
7701 Telegraph Road
Alexandria, Virginia, 22310-3864

Abstract

Wetlands occupy a unique position on the landscape. Being neither fully aquatic nor terrestrial, they are poorly understood from a standpoint of seasonal characterization and detection using spectral sensors. Wetlands ecotones and their associated plant communities offer a seasonally dynamic ecology which is governed primarily by fluctuations in local hydrologic regimes. Biogeochemical dynamics, caused by fluctuations in hydrology, work to manifest changes in plant physiology and provide a challenge for the spectral characterization and detection of wetlands. This paper presents information on the spectral reflectance characteristics of wetland plants and attempts to relate changes in spectral reflectance to the seasonal stresses experienced by wetlands plant communities.

1. INTRODUCTION

Numerous studies have documented the relationship between spectral and morphological changes in plants growing in a wide array of medium types and substrates (*Milton et al., 1991*). This research supports geobotany and agriculture with respect to vegetation growth stages and condition. Attempts to correlate changes in plant spectra and physiology due to uptake of pollutants have also been carried out (*Clark, 1982*). Most of these studies, however, have involved terrestrial plants grown in controlled environments to limit the effects of cation exchange, which could influence desired experimental results.

Wetlands plants differ greatly from terrestrial plants in response to stress. Depending on hydrologic regime, wetlands plants undergo biophysical changes during the growing season to cope with flooding and the resulting anaerobiosis. Anaerobic respiration requires a completely different energy requirement from plants than does aerobic respiration. The efficient production of biological energy is lost in the anaerobic pathway and, provided anaerobic conditions are extended throughout the growing season, this pathway can be lethal to plants not adapted to flooded conditions. For example, flood tolerance has been linked to the production and accumulation of non-toxic malate as a by-product of metabolism (Figure 1). Flood-intolerant plants also produce malate; however, malate is converted to pyruvate, which is further reduced to ethanol. Although ethanol is toxic to root tissues, *Mitsch and Gosselink, (1986)* suggest that ethanol diffuses out of the roots of flood-tolerant plants. Additionally, metals speciation and nutrient availability modified by the anaerobic environment place an extra burden on plants.

The goal of this study was to test the hypothesis that the stress experienced by wetlands plants (due to seasonal flooding) can be characterized using ground-level spectral reflectance data in the .4 to .9 μ bandpass. This in turn would form the basis for developing a seasonal "wetland signature," therefore allowing data acquisition strategies to be developed for imaging spectrometers. In this experiment, stress is a function of the reduction-oxidation (Redox) potential. Redox potential describes the reducing condition of soils whereby the availability

of oxygen and cation exchange capacity is altered due to a positive or negative electric potential (recorded in millivolts) (Wetzel, 1983). In strongly reduced conditions such as flooded environments, the Redox potential can fall to low levels (-200 mv) causing the transformation of metals and nutrients and rendering them unavailable for uptake by plants (Table 1). This serves to cause stress in plants (Mitsch & Gosselink, 1986).

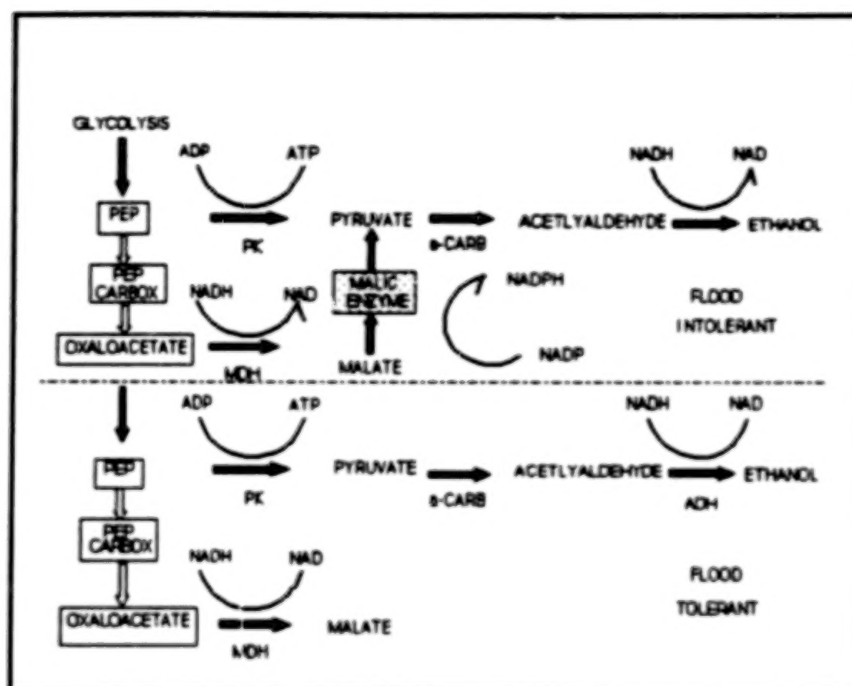


Figure 1. Metabolic pathways for flood intolerant and flood tolerant plants. (Adapted from Mitsch and Gosselink, 1986)

Table 1. Transformed Elements and Redox Potentials

ELEMENT	Oxidized Form	Reduced Form	Redox Potential
Nitrogen	Nitrate	Nitrous Oxide	220 mv
Manganese	Manganic	Manganous	200 mv
Iron	Ferric	Ferrous	200 mv
Sulfur	Sulfate	Sulfide	-75 to -150 mv
Carbon	Carbon Dioxide	Methane	-250 to -350 mv

Adapted from Mitsch & Gosselink, 1986.

2. METHODS

2.1 SITE SELECTION

Two wetland areas bordering the Rappahannock River in Virginia were selected for this study. These areas were colonized by the facultative (FAC) wetland species *Acer rubrum* (red maple). Red maple was selected owing to its tolerance to flooded environments and its status as a FAC wetland species. This categorization means that the species occurs in wetlands 33% to 66% of the time. For this investigation, it was important to select two of the same species of wetland plants to ensure similar physiological responses to stress. The sites have their own distinct hydrological regime and are close to one another on gradients characterized by zones III and V along the stream terrace. Site 1, lying along a stream tributary (zone III), is "semi-permanently flooded" (Cowardin *et al.*, 1979) and subjected to standing water periodically throughout the growing season. Site 2 (zone V) is drier, "temporarily flooded" (Cowardin *et al.*, 1979), and not subject to total seasonal inundation. The soils of each site are mapped as Congaree loam and Wehadkee local hydric soil units.

2.2 Redox AND SPECTRAL REFLECTANCE MEASUREMENTS

Redox and spectral measurements were collected during the early part of the growing season for both sites on a weekly basis for three weeks. Other measurements such as water level, pH, specific conductivity, and dissolved oxygen were also collected. Redox measurements were made using a Cole-Parmer pH meter with a platinum ORP probe. *In-situ* Redox measurements were made on moist and inundated soils adjacent to the plant specimens. All measurements were averaged and recorded in millivolts (mv).

Spectral measurements were taken in the field from leaves excised from 25 trees sampled at random along a 30-meter transect. The tree stands averaged 13.4cm diameter breast height (DBH). As accessibility permitted, three leaf samples were obtained from different portions of the tree canopy to limit spectral anomalies between leaf samples occurring high or low in the canopy. Leaf spectra were obtained using an Analytical Spectral Devices (ASD) PS II field spectroradiometer (350 nm–1100 nm) with a 5 degree field-of-view (.0872 rad). This is approximately equal to a 8 cm diameter field-of-view at a 1 m sampling distance. Three spectra of each leaf sample were taken and then averaged to help improve signal-to-noise levels in the resulting spectral file. All measurements were taken as close to local (solar) noon time as possible. Procedures for obtaining spectra were followed according to those established by Satterwhite and Henley, 1991. All measurements were referenced to a Labsphere Spectralon reflectance standard. All targets and reflectance standards were leveled with a bubble level, and data were collected at a nadir viewing angle.

Raw spectral data files were processed using an existing software routine to convert all binary files into ASCII. The resulting spectral data sets were smoothed and reduced to 5 nm data using an interpolation program which applied a cubic spline algorithm.

3. RESULTS

3.1 SPECTRAL CHARACTERISTICS AND Redox

Figure 2 is an example of the averaged spectral data and corresponding Redox measurement taken from wet and dry site red maple specimens. In comparison to the dry site where Redox

Averaged Spectral Data and REDOX

Acer rubrum

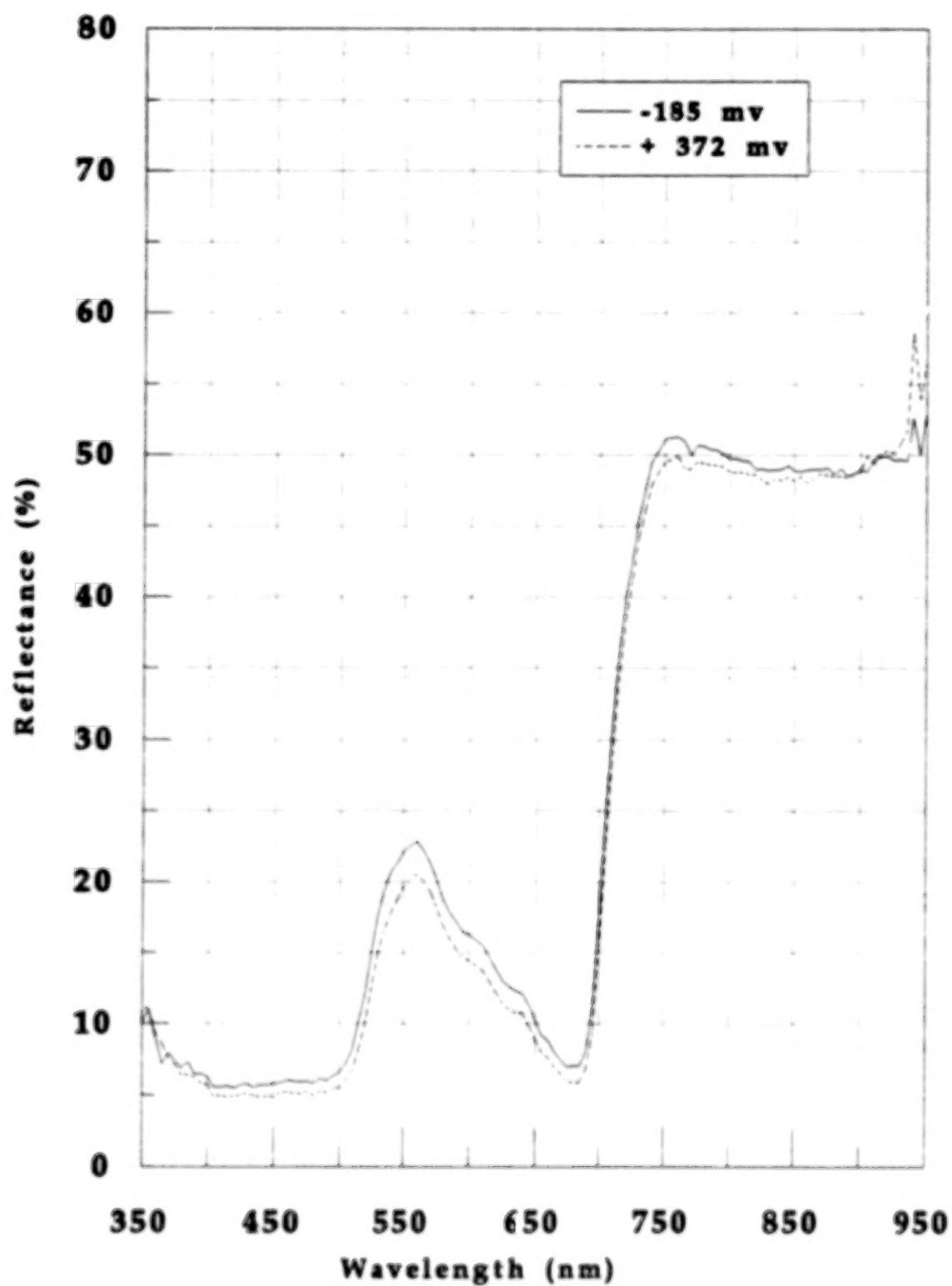


Figure 2. Averaged spectra for red maples from wet and dry sites.

potentials averaged +372 mv, wet site Redox potentials averaged -185 mv during the two-week period of saturation. Spectrally, chlorophyll reflectance in stressed red maples was slightly elevated at 560 nm. There was also an insignificant elevation in the chlorophyll absorption bands at 435 and 675 nm. Most notably, a displacement between the averaged spectral curves exists along the "red edge" boundary between 740 and 780 nm. This suggests that a red edge shift may exist for (FAC) wetlands plants stressed by prolonged flooding. The red edge shift is a theoretical spectral characteristic diagnostic of maturing, healthy green vegetation. It is described as the position of the chlorophyll absorption edge shifting toward longer wavelengths as plants mature (Collins, 1978, Campbell, 1987).

3.2 STATISTICAL EVALUATION OF RED EDGE INFLECTION POINTS

First derivative curves for the spectral samples were generated for the wet site and dry site red maples. Established methods (Salisbury et al. 1987; Milton et al. 1991; and Horler et al. 1980) were used to analyze the maxima of the first derivative spectra to characterize the inflection points associated with the red edge. The resulting first derivative curves illustrate a detectable red edge shift between the wet and dry specimens (Figure 3). A t-test (two-sample analysis) was employed to test the variability of the sample first derivatives between wet and dry site red maple specimens. Table 2 shows the descriptive statistics and Table 3 provides statistical results of the t-test for the first derivatives.

Table 2. Descriptive Statistics for Sample First Derivatives

Variable	DRY SITE (+372 mv)	WET SITE (-185 mv)
Sample Size	25	25
Average	715.4nm	706.5nm
Median	715nm	707nm
Mode	719nm	708nm
Mean	715.3nm	706.4nm
Variance	9.75	2.75
Standard Deviation	3.12	1.66
Standard Error	0.62	0.33

4. DISCUSSION

The results computed for the red edge first derivative maxima indicate that a statistically significant difference exists between the spectral characteristics of red maples on wet and dry sites having different Redox potentials. Since plant chemical assays were not performed, it can only be speculated that the transformation of available plant nutrients under severely reduced conditions contributed to the stress of the wet site specimens. However, the rejection of the null hypothesis confirms the statistical significance of the variability between wet and dry site specimens and warrants

Spectra First Derivatives and REDOX

Acer rubrum

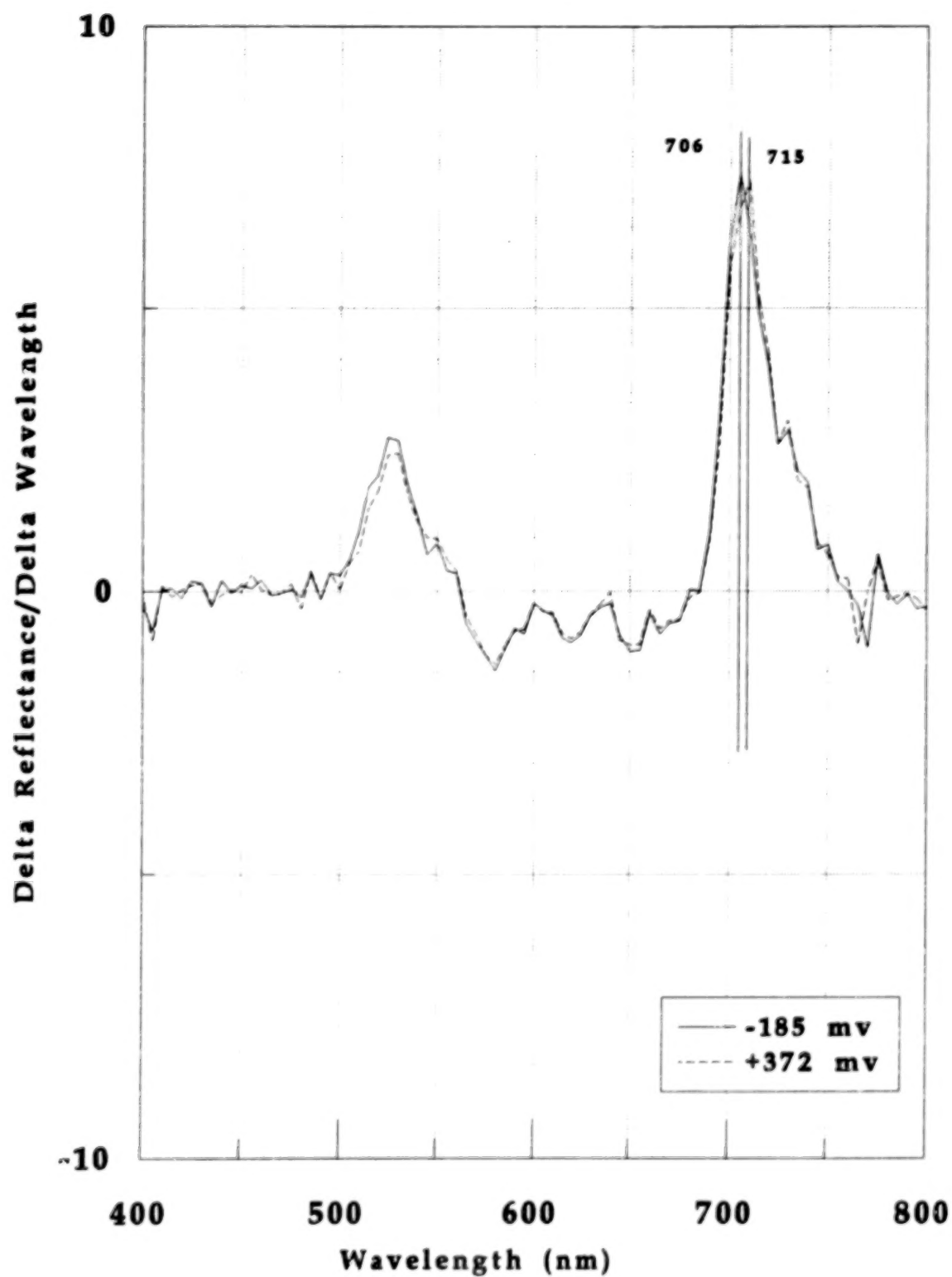


Figure 3. Spectra first derivatives illustrating displaced inflection points.

further investigation. The differences in maxima characterizing the red edge is consistent with other investigations involving nutrient and metals stress in plants (Milton *et al.*, 1987 & 1991). The difference here is that the stress is not anthropogenic, but due to natural phenomena.

Table 3. t-Test Results for First Derivative Inflection Points

SAMPLE STATISTICS	DRY SITE (+372 mv)	WET SITE (-185 mv)
Number of Observations	25	25
Average	715.4nm	706.59nm
Variance	9.75	2.75
Std. Deviation	3.12	1.66
Median	715nm	707nm
Difference between Means = 8.84 Conf. Interval for Diff. in Means: 95% (Equal Vars.) Sample 1-Sample 2 -10.2624 -7.41756 48 D.F. (Unequal Vars.) Sample 1-Sample 2 -10.274 -7.40598 36.6 D.F.		
Hypothesis Test (HO) at Alpha= 0.05	Computed t Statistic = -12.49	Reject HO

The results of this study suggest that wetlands occupied by monotypic stands of (FAC) vegetation, subjected to prolonged flooding, can be stressed to the degree that subtle changes can be detected with spectroradiometers. If this is the case, a strategy may exist for mapping wetlands that are cloaked within stands of characteristically upland and FAC plant species. Ecotypic and adaptive variations within plant species are well documented and are ecologically significant (Brewer, 1979). Golet and Lowry (1987) documented the biophysical differences in the obligate species *Chamaecyparis thyoides* (Atlantic White Cedar) on six different sites in Rhode Island having six different hydrological regimes. Most of the variations between the sites occurred as a function of flooding, pH, tree crown cover, and stand density. Although spectral measurements and Redox potentials were not considered, wide variations existed between the biophysical characteristics of the trees. Lowry (1984) also discovered growth variations among red maples on seven hydrologically distinct sites.

Although recordable with field and laboratory instruments, the detection of this phenomenon with imaging spectrometers may only be possible if the spatial and temporal variability of wetlands plants is observed long enough to characterize the specific stress signatures. In the case of facultative plants subjected to prolonged periods of flooding, the gap between the inflection maxima may widen to afford use of broader band sensors.

Clearly, a better understanding of the spectral behavior of wetlands plants is needed. These dynamic ecosystems are adapted to extreme and severe stresses which disrupt and prove fatal to flood-intolerant, upland plants. Furthermore, the spectral characterization of plants translates into observing a facet of the energy budget of an ecosystem. Changes in the way energy is transferred by wetland plants on a seasonal basis could provide a powerful diagnostic tool in managing wetland (and terrestrial) ecosystems.

REFERENCES

- Brewer, R., 1979: *Principles of Ecology*, Holt, Rhinehart, and Winston, Orland, Florida.
- Campbell, J.B., 1987: *Introduction to Remote Sensing*, The Guilford Press, New York, New York.
- Clark, R.B., 1982: Plant response to mineral element toxicity and deficiency, In *Breeding Plants for Less Favorable Environments*, M.N. Christiansen and C.F. Lewis, (Eds.), Wiley, New York, pp.71-142.
- Collins, W., 1978: Remote Sensing of Crop Type and Maturity, *Photogrammetric Engineering and Remote Sensing*, Vol. 44, pp. 43-55.
- Cowardin, L.M., V. Carter, F.C. Golet, and E.T. LaRoe, 1979: Classification of wetlands and deepwater habitats of the United States. U.S. Fish and Wildlife Service Pub. FWS/OBS-79/31, Washington, D.C., 103pp.
- Golet, F.G. and D.J. Lowry, 1987: Water regimes and tree growth in Rhode Island Atlantic White Cedar Swamps, In *Atlantic White Cedar Wetlands*, Aimlee D. Laderman, Editor, Westview Press, Boulder, Colorado, 91-110.
- Horler, D.N., J. Barber, and A.R. Barringer, 1980: Effects of Heavy Metals on the Absorbance and Reflectance Spectra of Plants, *International Journal of Remote Sensing*, 1(2):121-136.
- Lowry, D.J., 1984: Water regimes and vegetation of Rhode Island forested wetlands, Master's thesis, Univ. of Rhode Island, Kingston, R.I.
- Milton, N.M. C.M. Ager, B.A. Eiswerth, and M.S. Power, 1989: Arsenic- and Selenium-Induced Changes in Spectral Reflectance and Morphology of Soybean Plants, *Remote Sensing Environment*, 30:263-269.
- Milton, N.M., B.A. Eiswerth, and C.M. Ager, 1991: Effect of Phosphorus Deficiency on Spectral Reflectance and Morphology of Soybean Plants, *Remote Sensing Environment*, 36:121-127.
- Mitsch, W.J. and J.G. Gosselink, 1986: *Wetlands*, Van Nostrand Reinhold, New York, New York.
- Salisbury, J.W., N.M. Milton, and P.A. Walsh, 1987: Significance of Non-isotropic Scattering from Vegetation for Geobotanical Remote Sensing, *International Journal of Remote Sensing*, 8(7):997-1009.
- Satterwhite, M.B. and J.P. Henley, Hyperspectral signatures (400 to 2500 nm) of vegetation, minerals, soils, rocks, and cultural features: laboratory and field measurements. U.S. Army Engineer Topographic Laboratories Report. ETL-0573, Fort Belvoir, Virginia, 484pp.
- Wetzel, R.G., 1983: *Limnology*, Saunders College Publishing, Fort Worth, Texas.

AIRBORNE VISIBLE IMAGING SPECTROMETRY APPLIED TO LIMNOLOGY: CHLOROPHYLL VARIATION IN MONO LAKE

John M. Melack and Mary Gastil
Marine Science Institute,
University of California, Santa Barbara, CA 93106 USA

ABSTRACT

Remote sensing reflectance (R_{rs}) spectra and water samples obtained from Mono Lake were used to test several algorithms to calculate chlorophyll concentrations. To simulate the ability of the 10 nm full width at half maximum (fwhm) bands of Airborne Visible/Infra-Red Imaging Spectrometer (AVIRIS) to resolve features in the R_{rs} spectrum well enough to permit calculation of chlorophyll concentrations, the field radiometer spectra were resampled to correspond to the AVIRIS band centers and band widths. The ratio of $R_{rs}(656 \text{ nm})$ to $R_{rs}(443 \text{ nm})$ correlated well with the log of chlorophyll concentration over the range from 0.9 to 47 $\mu\text{g L}^{-1}$ ($r^2, 0.84$). Fluorescence peak height, defined as $R_{rs}(688 \text{ nm} - 675 \text{ nm})$, fit the measured chlorophyll data from Mono Lake linearly ($r^2, 0.89$). These results from field spectra, resampled to simulate AVIRIS spectra, indicate that when accurate atmospheric corrections can be applied, chlorophyll concentration can be calculated from AVIRIS data with a single predictive equation over a wide range.

1. INTRODUCTION

Many lakes are eutrophic and contain moderate to high concentrations of phytoplankton and other particulates which vary in their optical properties. Hence, we are applying high resolution imaging spectrometry to optically complex lakes with an objective of estimating concentrations of suspended material with remotely sensed data. One of our first goals is development and testing of algorithms to calculate chlorophyll concentrations in eutrophic lakes (Melack and Gastil 1994).

AVIRIS is an airborne imaging spectrometer with high spatial and spectral resolution: nominal pixel width 20 m and 224 bands between 400 to 2400 nm with spacing and fwhm of about 10 nm (Vane 1987). We use a span of about 40 bands between 400 nm and 750 nm for testing algorithms to calculate chlorophyll concentrations.

We aim to develop robust relations which can be applied to spectral images obtained with AVIRIS to produce images of chlorophyll distribution. Here we assess whether the 10 nm fwhm bands of AVIRIS are of sufficient spectral resolution to calculate chlorophyll concentrations. Instead of using AVIRIS images for this purpose, we have resampled spectra obtained with a high resolution field spectrometer to avoid the problem of atmospheric correction of AVIRIS imagery.

2. METHODS

2.1 Study site and chlorophyll measurements

Mono Lake, California, is a large (160 km²), deep (mean depth 17 m at an elevation of 1943 m), saline lake located on the western edge of the North American Great Basin. The phytoplankton community has few species and varies widely in abundance seasonally (Jellison and Melack 1993).

Samples for the measurement of the chlorophyll *a* (chl *a*) content of the phytoplankton were collected from the surface waters at the same time that the reflectance spectra (described below) were

obtained. The lake water was filtered through Gelman A/E glass fiber filters to separate the phytoplankton, and the filters were kept frozen at -14 °C until pigments were analyzed. Except during periods of low biomass, chl *a* was determined by spectrophotometric analysis with correction for pheopigments (Golterman 1969) after a 40-minute extraction of the macerated filters in 90% acetone at room temperature in the dark. Low chl *a* concentrations (<5 µg L⁻¹) were measured on a fluorometer calibrated against spectrophotometric measurements with large-volume lake samples.

2.2 Field measurements of reflectance spectra

To obtain reflectance spectra we used a Personal Spectrometer II (PS-II) from Analytical Spectral Devices Inc. (Boulder, CO). The PS-II records digital counts in 512 spectral bands from a linear array of silicon detectors. The full width at half maximum of the detector response functions are 1.4 nm, and the 512 detectors cover approximately 350 nm to 1040 nm. The spectral calibration of the bands was adjusted so that the sharp absorption bands in the skylight spectrum coincided with a Lowtran 7 skylight spectrum of the same spectral resolution. Integration times used were under a second (usually 350 msec). Up to ten integration times were averaged, and the average was recorded as a binary file. The real-time display of the instrument proved useful in checking for saturation, jaggedness and variability in the spectra. A 1.5 m fiber optic cable extended the reach of the detector and made boat-side measurements feasible. We used a 22 degree total field of view.

Our procedure for measuring remote sensing reflectance (*R_{rs}*) was adapted from the method described by Hamilton et al. (1993). Spectra were collected from three targets: a 10% reflectance gray card, lake surface, and blue sky. The gray card was a 25 cm x 25 cm slab of Spectralon SRS-Gray, a calibrated lambertian reflecting material (LabSphere, Inc., New Hampshire). The spectrum from the lake surface included the skylight reflected off the water (Fresnel reflectance) and the light upwelling through the surface from below. We avoided effects from the side of our small boat by holding the fiber optic cable one meter off the side of the sunny side of the boat with the fiber optic tip pointed vertically down. The tip was pointed vertically up to measure the spectrum of the blue sky at zenith. Three series of card, water, and sky spectra were recorded at each survey station.

2.3 Analysis of spectra

The spectra were used in the following equation to calculate *R_{rs}* (Hamilton 1993):

$$R_{rs} = \frac{(S_{water} - S_{sky} \cdot \rho_{water})}{(\pi \cdot S_{card} \cdot \rho_{card})}$$

where *R_{rs}* is remote sensing reflectance; *S_{water}*, *S_{sky}*, and *S_{card}* are the spectra in digital numbers from the three targets as described above; ρ_{water} is the Fresnel reflectance coefficient of hypersaline water, and ρ_{card} is the calibrated reflectance coefficient of the gray card. The card, water, and sky spectra were not radiometrically calibrated because the radiometric calibration factor would cancel in the numerator and denominator of the above equation.

The Fresnel reflectance coefficient for sea water was extrapolated to the salinity of 90 g L⁻¹ found in Mono Lake for three temperatures (0, 10, 15 °C) for the spectrum from 400 to 750 nm using data on the index of refraction of sea water reported by Mobley (1992). The *R_{rs}* calculated with precise spectral reflectance coefficients ρ_{water} and ρ_{card} differed by only two percent from *R_{rs}* calculated using constant (non-spectral) values.

The 39 AVIRIS bands spanning the visible region (400 - 750 nm) correspond to 245 field spectrometer bands. We resampled the high resolution spectra to the AVIRIS bands by Gaussian convolution. This assumes a Gaussian response function for each AVIRIS band using the exact fwhm and band center wavelengths for each band distributed with the AVIRIS data tapes.

3. RESULTS AND DISCUSSION

A total of 45 reflectance spectra were obtained at Mono Lake at four times; chlorophyll *a* concentrations ranged from $0.9 \mu\text{g L}^{-1}$ in early September to $47 \mu\text{g L}^{-1}$ in December. Average spectra, calculated by combining three to twenty separate spectra from each survey, are shown in Figure 1. Spectral features apparent in these resampled spectra are similar to those reported by Melack and Gastil (1994) for high resolution spectra.

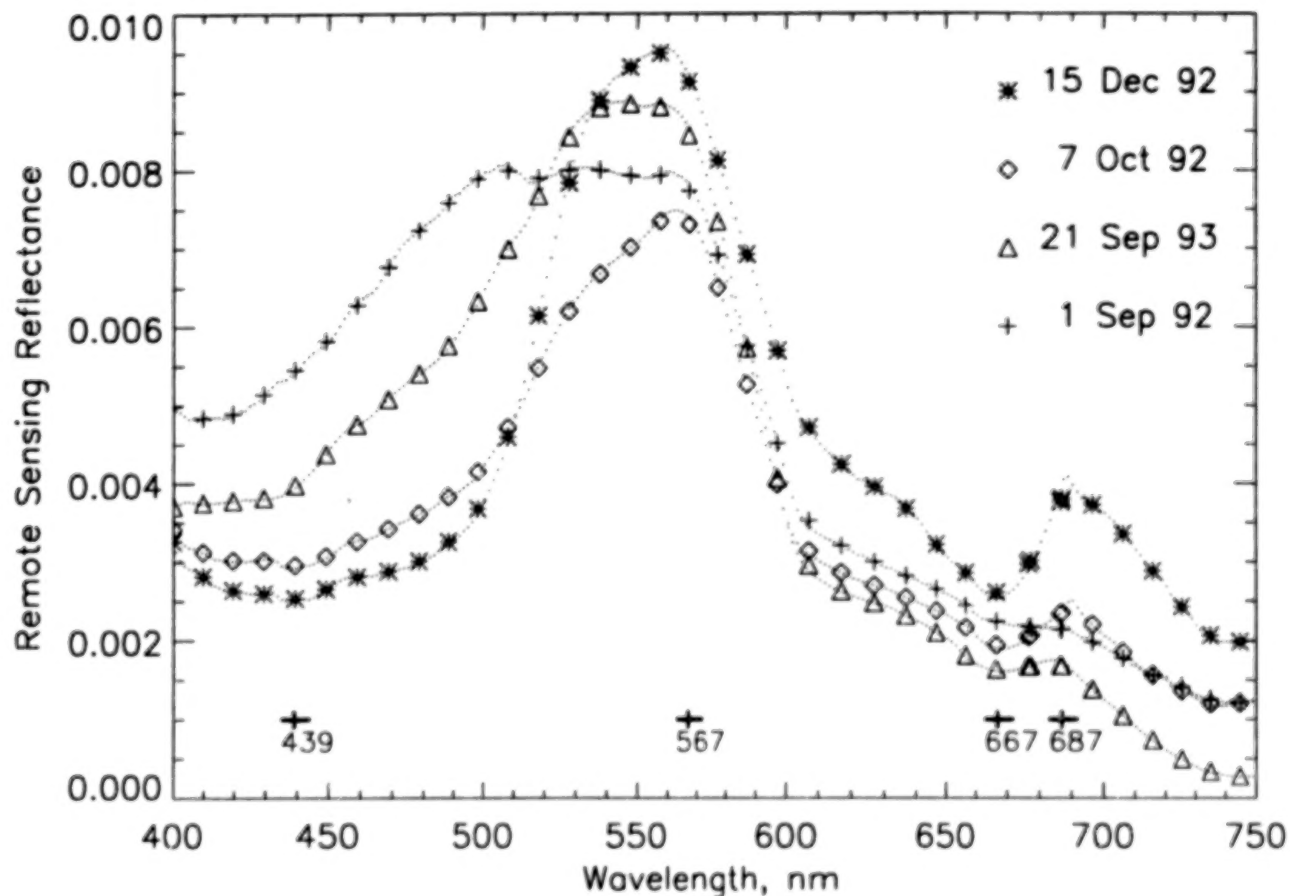


Figure 1. Remote sensing reflectance spectra at Mono Lake for four surveys, showing band centers of AVIRIS 1992 bands resampled from the field spectra. The dotted curves are the spectra before resampling. AVIRIS bands used in this analysis are marked, centered at 439, 567, 667, and 687 nm. The average of three to twenty stations in each survey is shown for 1 Sep 92 (+), 7 Oct 92 (\diamond), 15 Dec 92 (*), and 21 Sep 93 (Δ), when average chl *a* for those surveys were 0.9, 15.4, 46.3, and $4.6 \mu\text{g L}^{-1}$, respectively.

Smith and Baker (1978) describe the combined effects of absorbance and scattering on the reflectance spectra of water as chlorophyll content increases. At low chl *a* concentrations, the shape of the absorption spectrum of phytoplankton, with its broad maximum around 440 nm and narrow peak at 675 nm, dominates the shape of the reflectance spectrum. In waters turbid with phytoplankton, the backscatter in the 500 nm to 600 nm region dominates. Whereas in the clear waters the increased pigment lowers the reflectance (with stronger absorption), in more turbid waters the reflectance rises with increasing chl *a* concentration because the particulate concentration covaries with pigment concentration.

In the spectra from Mono Lake, the absorption around 440 nm increases (i.e. R_{rs} decreases) with increasing chl *a*. The slope from 440 nm to 565 nm becomes steeper with increasing chl *a* (i.e. the ratio $R_{rs}(565\text{nm})/R_{rs}(440\text{nm})$ increases as chl *a* increases). The chl *a* absorption around 670 nm is apparent. The sharpest peak, around 687 nm, increases in height and narrows with increasing chl *a*.

With increasing chl *a* concentration, the curvature of the spectra increases: the absorption centered around 440 nm deepens and broadens toward 500 nm; the 565 nm peak sharpens; and the fluorescence peak at 687 nm rises. This trend extends from the spectra of ultra-oligotrophic, clear waters (such as Lake Tahoe, Hamilton, et al. 1993) to the eutrophic conditions at Mono Lake.

We examined how several combinations of spectral features were related to chlorophyll concentrations, and summarize here those most promising for the calculation of chlorophyll. We determined the correlation of several band ratios to chlorophyll (Table 1). We chose the AVIRIS bands centered closest to 410, 440, 565, 667, and 687 because they describe the change in Rrs spectral shape with changing chl *a*. The best correlation with a band ratio was Rrs(410nm)/Rrs(440nm). However, AVIRIS signal to noise is low at 410 nm, and predictive equations using this band may be problematic. The best correlation was with the fluorescence peak height ($r^2=0.89$). This is remarkable because that peak width itself is comparable to the AVIRIS band fwhm.

TABLE 1. R^2 VALUES FOR RELATIONS AMONG BAND RATIOS OR PEAK HEIGHT TO CHLOROPHYLL ($n=45$) Each of three band ratios and one peak height was separately regressed to the measured chlorophyll, to produce a table of regression coefficients (r^2).

	410/440	440/565	687/667	687-667
ratio=A + B*chl _a	0.65	0.52	0.78	0.89
ratio ⁻¹ =A + B*chl _a	0.62	0.74	0.69	---
ratio=A + B*log(chl _a)	0.87	0.84	0.82	0.76
ratio ⁻¹ =A + B*log _e (chl _a)	0.88	0.78	0.84	---

The change in spectral shape which distinguishes clear water from water rich in phytoplankton is expressed by the ratio of Rrs at 565 nm (AVIRIS band centered at 567 nm) to Rrs at 440 nm (AVIRIS band centered at 439 nm). A line fit to the 45 samples from four surveys of Mono Lake show a strong correlation between the measured chlorophyll concentration and this band ratio (Figure 2).

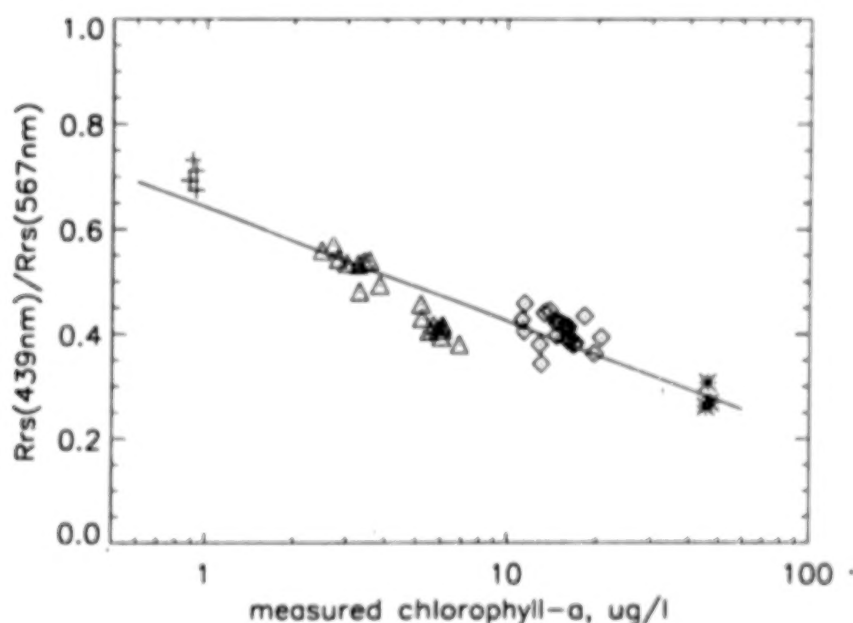


Figure 2. Band ratio Rrs(439nm)/Rrs(567nm) versus measured chlorophyll. Symbols same as in Figure 1. $Rrs(439nm)/Rrs(567nm) = 0.642 + -0.217 \cdot \log(chl_a)$; $r^2=0.84$, $p<0.00001$

The reflectance peak around 687 nm (ranging from 685 to 690 nm), which we attribute partially to solar induced fluorescence, can be related to chlorophyll concentration (Figure 3.). We found the peak height, expressed as the difference between the AVIRIS-resampled Rrs bands centered at 687 nm

and 667 nm, to be an excellent predictor of chlorophyll ($r^2=0.89$, $p<0.0001$). These are the band centers of the AVIRIS bands which are closest to the maximum and minimum of the peak. When using the full resolution of the field spectra, bands were selected precisely at the maximum and minimum, and the regression coefficient for the linear fit to measured chl *a* was $r^2=0.94$.

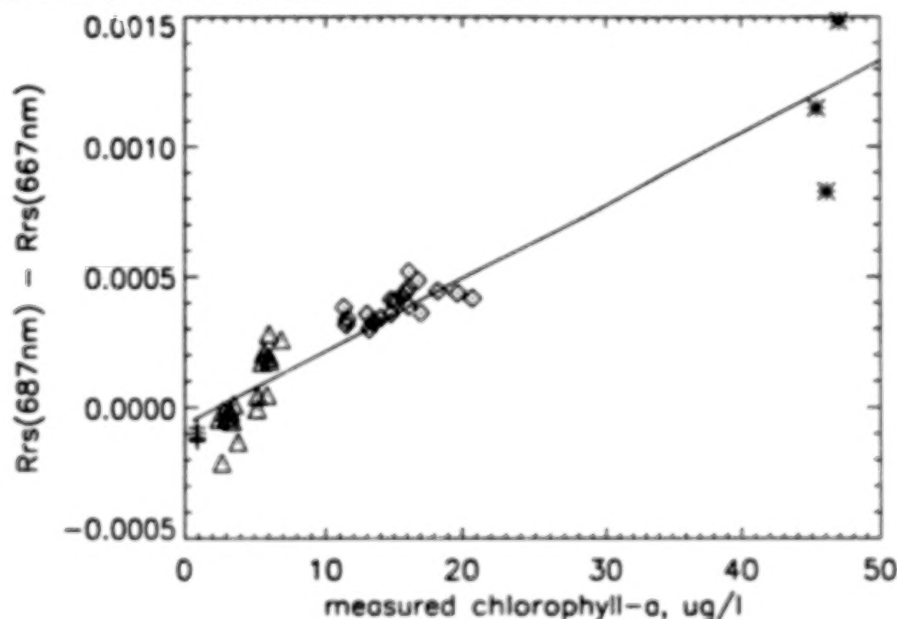


Figure 3. Fluorescence peak height versus chlorophyll in Mono Lake. Symbols same as in Figure 1. The solid line is the fit of 45 Mono Lake samples to the equation:

$$Rrs(687nm) - Rrs(667nm) = (-0.0000665) + (0.0000280) \cdot chl a, r^2=0.89$$

4. CONCLUSION

The result that the resampled spectra retained correlation to chl *a* demonstrates that instruments such as AVIRIS are appropriate for estimation of plant pigments in eutrophic lakes.

REFERENCES

- Golterman, H.L., 1969: *Methods for Chemical Analysis of Fresh Waters*. IBP Handbook 8. Blackwell.
- Hamilton, M.K., C.O. Davis, W.J. Rhea, S.H. Pilon and K.L. Carder, 1993: Estimating chlorophyll content and bathymetry of Lake Tahoe using AVIRIS data, *Remote Sens. Environ.*, **44**, 217-230.
- Jellison, R. and J.M. Melack, 1993: Algal photosynthetic activity and its response to meromixis in hypersaline Mono Lake, California, *Limnol. Oceanogr.*, **38**, 818-837.
- Melack, J.M. and M. Gastil, 1994: Comparison of spectral feature algorithms for remote sensing of chlorophyll in eutrophic lakes. *Proc. International Geoscience and Remote Sensing Symposium* (in press)
- Mobley, C.D., 1994: *Light and Water: Radiative Transfer in Natural Waters*, Academic Press, San Diego, California.
- Smith, R.C., and K. Baker, 1978: Optical classification of natural waters, *Limnol. Oceanogr.*, **26**, 260-267.
- Vane, G. (Ed.), 1987: *Airborne Visible/Infrared Imaging Spectrometer (AVIRIS)*, JPL Publication 87-38, Pasadena, California.

LASER-INDUCED SIGNATURES IN OCEANOGRAPHIC SPECTRAL SENSING: DYNAMICS, POLLUTION AND BASELINE STUDIES

Alexandre E. Dudelzak
Canadian Space Agency
Saint-Hubert, Québec
J3Y 8Y9 CANADA
(514) 926-4619

Sergei M. Babichenko and Larisa V. Poryvkina
Institute of Ecology, Estonian Academy of Sciences
2 Kevade Street, Tallinn
EE0031 ESTONIA
(372-2) 524-385

The original results of applying analytical laser spectroscopy to remote diagnostics of sea water conditions and their spatial variability are overviewed. The concept of laser-induced, multi-dimensional fluorescent signatures is described. Such signatures can serve as representative indicators of both statistically "normal" baseline situation and the stress generated deviations from it. Analysis of natural aquatic targets containing phytoplankton, humic substances and organic pollutants is based on the previously prepared laboratory catalogs of the signatures of various substances, and real-time data correlation or neural-network processing. Quantitative conclusions are made with normalization of fluorescent signal on the intensity of water Raman-scattering. Using this approach, it is possible to detect and identify pollutants in water surface layers (e.g., oil products from about 1 ppm to spill-level concentrations), and to determine different water types by the signatures of naturally dissolved organic matter.

Lidar sensing using the "inner spectroscopic bench-mark calibration" allows for the highest spatial resolution in analytical oceanographic measurements. Regularities in the spatial distribution of sea surface phytoplankton have been found. Possibilities of the application of this technique to studying surface manifestations of the deep-water processes (such as internal waves or dynamic fronts) are discussed.

The description of a spectroscopic lidar used in the measurements is given. The system operates either automatically (programmable) or manually controlled, resulting in a multi-wavelength pattern of a target or in plotting concentrations versus spatial coordinates.

Future development directions and possible spin-off applications of the technique, based on recent technological achievements, are considered.

Manuscript not available at time of printing. Please contact authors for further information.

An analytical model for remote sensing of chlorophyll *a* in inland waters

H.J. Hoogenboom, A.G. Dekker
Institute for Environmental Studies
de Boelelaan 1115
1081 HV Amsterdam, The Netherlands
Tel: (31) 20 444 9506 Fax: (31) 20 444 9553

G.A. Farrington
Integrated Terrestrial Systems
Box 61221, 217K, 3630,
Brentwood Road, N. W.
Calgary, Alberta, Canada. T2L 1V8
Tel/Fax: 403-283-7814

Abstract

An analytical method was developed based on a physical model in which the subsurface irradiance reflectance is related to the absorption and (back)scattering properties (i.e. the inherent optical properties) of the water constituents. The analytical method was demonstrated for the estimation of the sum of chlorophyll *a* and phaeopigments (CHL) in inland waters. The analytical algorithm coefficients give insight into the sensitivity of the algorithm due to the absorption and scattering of other components than CHL. The coefficients of the algorithm were calculated using the average inherent optical properties of 14 lake samples with large variations in water quality. The CHL estimated with the analytical algorithm showed good agreement with *in vivo* measured CHL. A linearised version of the algorithm was successfully applied on remote sensing images in 1990 and 1993. It was concluded that the analytic method provides a good basis for remote sensing algorithms for water quality. However, for the further development of an analytical method, spectral volume scattering functions are required for the various components of suspended matter (detritus, inorganic matter and phytoplankton) in turbid inland waters.

1. Introduction

Research was carried out into the development of multi-temporal valid remote sensing algorithms for retrieval of water quality parameters of inland waters. The water quality parameters that can be estimated from remotely sensed data are phytoplankton pigments such as the sum of chlorophyll *a* and phaeophytin (CHL), cyanophycocyanin, seston dry weight (suspended matter), the vertical irradiance attenuation coefficient and Secchi depth. The inland waters in this study, in the central western part of The Netherlands, are turbid and eutrophic in comparison to ocean or coastal waters. They may contain various (high) concentrations of phytoplankton, tripton (dead organic and inorganic particles) and aquatic humus (also denoted as gelvin, gelbstoff, yellow matter).

In the development of remote sensing algorithms of turbid waters research has shifted from a (semi)-empirical approach towards algorithms based on an analytical approach. In an empirical model statistical relationships are sought between measured spectral values and measured water quality parameters. In a semi-empirical model knowledge of the spectral characteristics of the water quality parameters is included in the statistical analysis by using appropriate bands or combinations of bands. In an analytical approach a physical model is developed in which the influence of the water constituents on the subsurface light field is analysed by their inherent optical properties (IOP), i.e. the absorption coefficient and (back)scatter coefficient. From this model analytical algorithms can be derived which allow sensitivity analysis and assessment and improvement of accuracy.

The physical relation between the (specific) inherent optical properties (IOP) of the water constituents and the subsurface irradiance reflectance $R(0^-)$ has been investigated by several authors (Dekker *et al.* (1994), Krijgsman (1994), Dekker (1993), Kirk (1991) and Whitlock (1981)) based on the work of Gordon *et al.* (1975). They found that for turbid waters the following linear relationship was valid:

$$R(0^-) = r_1 \frac{b_b}{a + b_b} \quad (1)$$

where a is the total absorption coefficient, b_b the total backscatter coefficient and r_1 a coefficient. Algorithms based on $R(0^-)$ are minimally effected by atmospheric conditions, the air-water interface, solar angle etc.

In August 1990 water samples of 18 waterbodies were taken simultaneously with *in situ* measurements of $R(0^-)$. The IOP spectra of phytoplankton, tripton, and aquatic humus were determined from laboratory spectrophotometric measurements (see Dekker (1993)). Based on the IOP measurements an analytic algorithm was developed. The algorithm was successfully applied to remote sensing data from a multispectral scanner (CEASAR) and an imaging spectrometer (CASI) flown at three days in August and September 1990 and in August 1993. During the remote sensing campaign in 1993 $R(0^-)$ was measured *in situ* in 6 of the 18 waterbodies and in the IJ-lake, a large lake in the central part of The Netherlands.

2. The analytical method

The development of a RS algorithm using an analytical method is demonstrated for the sum of chlorophyll *a* and phaeopigments (CHL). The objective is to find a model which yields an estimate of CHL from a (remote sensed) *R* (0-) spectrum. In addition, the model should be applicable to different waterbodies with large variations in water quality. Within the study area four watertypes are recognised based on eutrophic status and chemical composition: shallow eutrophic lakes, shallow mesotrophic lakes, deep lakes and rivers and canals. In this paper all lake samples are put together in one data set (thus excluding river and canal data).

The analytical method involves 5 steps. First, the IOP of the water samples are separated into the four main components that influence the underwater light field. The total absorption coefficient is equal to the sum of the coefficients of phytoplankton (*a*(ph)), tripton (*a*(tr)), aquatic humus (*a*(ah)) and the absorption coefficient of water (*a*(wa)) which was obtained from literature

$$a = a(\text{ph}) + a(\text{tr}) + a(\text{ah}) + a(\text{wa}) = a(\text{ph}) + a(\text{re}), \quad (2a)$$

where *a*(re) is the absorption coefficient of *a*(tr) + *a*(ah) + *a*(wa). For the backscatter coefficient the backscattering of aquatic humus may be ignored yielding

$$b_b = b_b(\text{ph}) + b_b(\text{tr}) + b_b(\text{wa}). \quad (2b)$$

Figures 1 and 2 show the absorption and backscatter coefficient spectra respectively. Separate absorption spectra of the individual components are given in Dekker (1993). Figure 1 shows that *a* first decreases with increasing wavelength due to the decreasing absorption of tripton, phytoplankton and aquatic humus. In several samples there is a local maximum around 624 nm caused by cyanophycocyanin. The maximum around 676 nm is due to CHL; the absorption at this wavelength can be as large as 3.5 - 4 m⁻¹ in eutrophic lakes.

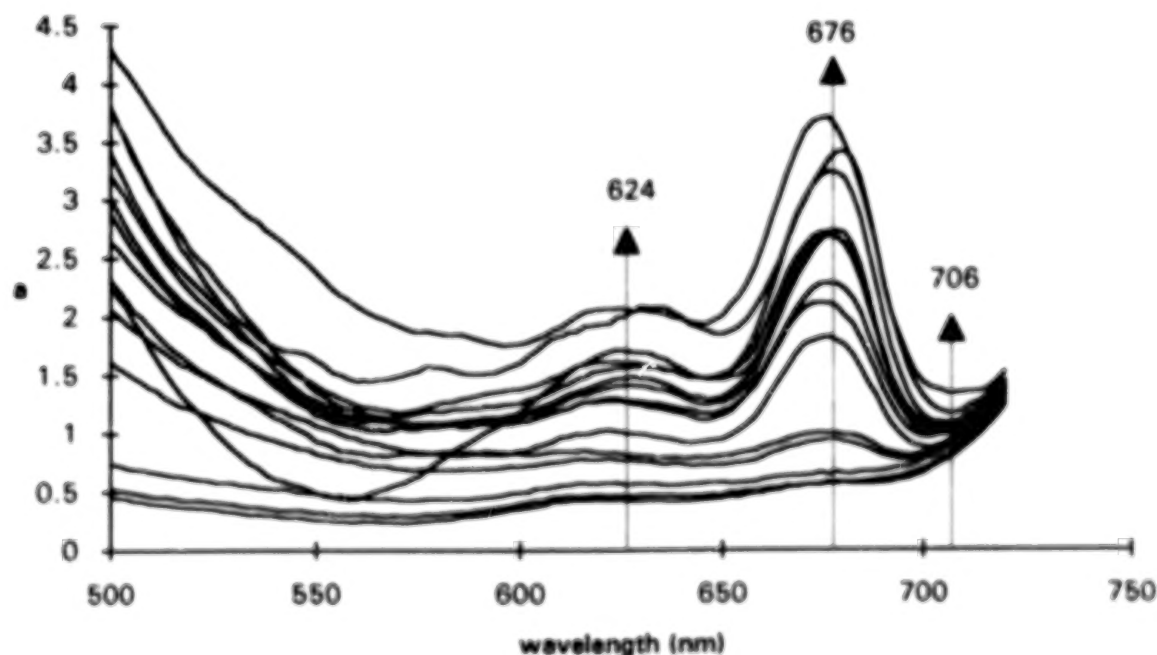


Figure 1. The total absorption coefficient of 14 inland water samples in 1990.

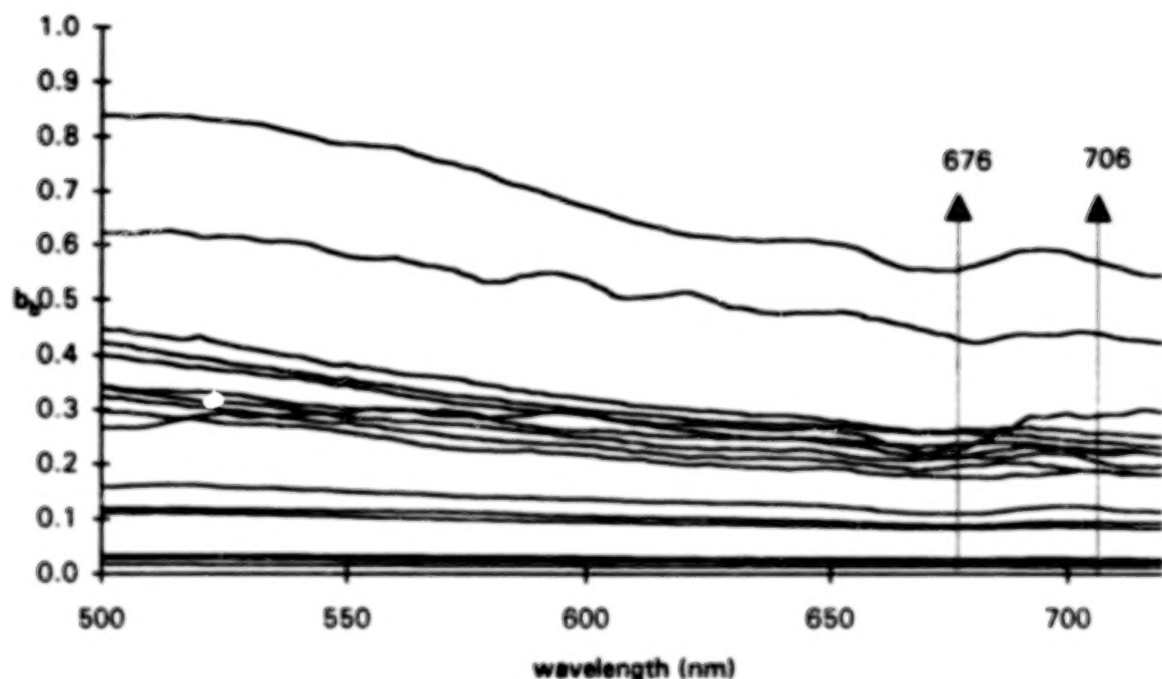


Figure 2. The total backscatter coefficient of 14 inland water samples in 1990

A minimum occurs at 706 nm and for longer wavelengths the absorption of water dominates the absorption coefficient. The backscatter coefficient spectra in Fig. 2 show that the backscattering in turbid waters with values of up to 0.8 m^{-1} is not negligible compared to the absorption, which means that the b_b in the denominator of Eq. 1 should be taken into account; for ocean waters this term often can be neglected (see e.g. Morel & Prieur (1977)). Since the b_b shows no distinct spectral features it is not yet feasible to split the total b_b into its components. Therefore, an assumption must be made about the amount of scattering due to phytoplankton. In this study two extreme assumptions are analysed: in model I it is assumed that the b_b is not correlated to CHL, hence all backscattering is caused by tripton and water; in model II the b_b is linear correlated to the CHL.

In the second step the $R(0-)$ is measured and substituted in Eq. 1 and subsequently analysed. The $R(0-)$ of the lake samples in 1990 are shown in Fig. 3. Together with the substitution of the IOP the r_1 of every sample was estimated (see Dekker *et al.* (1994)). It was found that the constant r_1 varies largely between different waterbodies, especially in shallow eutrophic lakes. Therefore, it was concluded that an algorithm for CHL preferably contains a spectral band ratio. This has the additional advantage that multiplicative errors in the determination of (remote sensed) $R(0-)$ are diminished.

Thirdly, the $a(\text{ph})$ is correlated to the CHL. Since physical relations were not available a statistical correlation was used yielding the specific absorption coefficient a^* defined by

$$a(\text{ph}) = a^* \text{CHL} \quad (3)$$

From the correlation spectrum two appropriate wavelengths were found for the reflectance ratio. It appeared that the ratio of $R(0-)$ at 706 nm to the $R(0-)$ at 676 nm was most suitable. The average value of a^*_{676} was $0.0164 \text{ m}^2 \text{ mg}^{-1}$ and of a^*_{706} $0.0012 \text{ m}^2 \text{ mg}^{-1}$. In model II, a specific (i.e. CHL-correlated) back-

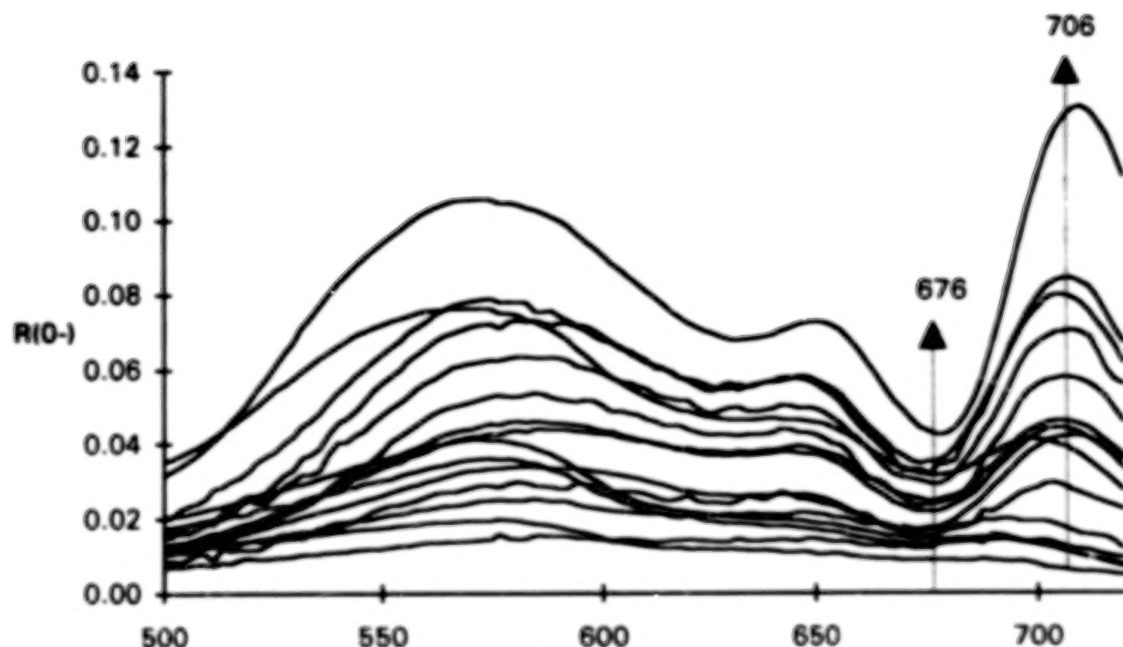


Figure 3. The in situ measured $R(0-)$ in 14 inland waters in 1990 in The Netherlands

scatter coefficient b_b^* was determined. The average values were equal for both wavelengths within the statistical error $b_b^*_{676} = b_b^*_{706} = 0.0040 \text{ m}^2 \text{ mg}^{-1}$ (see Dekker (1993)).

In the final step the analytic algorithm is constructed by substituting Eqs. 2a and 3 in Eq. 1. The reflectance ratio was calculated and rewritten in an explicit form for CHL:

$$\text{CHL} = \frac{k_0 + k_1 \frac{R(0-)_{706}}{R(0-)_{676}}}{1 - k_2 \frac{R(0-)_{706}}{R(0-)_{676}}} \quad (4)$$

where k_0 , k_1 and k_2 are constants which in model I (no correlation between CHL and backscattering) are given by

$$k_0 = -\frac{[a(\text{re}) + b_b]_{676}}{a^*_{676}}, \quad k_1 = \frac{[a(\text{re}) + b_b]_{706} b_{b676}}{a^*_{676} b_{b706}}, \quad k_2 = \frac{a^*_{706} b_{b676}}{a^*_{676} b_{b706}} \quad (5)$$

and in model II (linear correlation between CHL and backscattering) are given by

$$k_0 = -\frac{a(\text{re})_{676}}{[a^* + b_b^*]_{676}}, \quad k_1 = \frac{a(\text{re})_{706} b^*_{b676}}{[a^* + b_b^*]_{676} b^*_{b706}}, \quad k_2 = \frac{[a^* + b_b^*]_{706} b^*_{b676}}{[a^* + b_b^*]_{676} b^*_{b706}} \quad (6)$$

In general an analytic algorithm such as Eq. 4 has several advantages. It allows a sensitivity analysis for varying water compositions which makes it possible to predict the accuracy when applying the algorithm to a certain waterbody. Moreover, only a limited or maybe no set of *in situ* measurements is required for the calculation of the algorithm coefficients, since no statistical analysis has to be carried out. Another advantage is the possibility of specifying the required accuracy of the (remote sensed) $R(0-)$ in order to meet a predefined accuracy of CHL.

3. Results

The algorithm coefficients of model I were calculated using the average IOP of all lake samples. The model was linearised by the approximation $k_2 \approx 0$ assuming that $a^*_{706} \ll a^*_{676}$ (see Eq. 5). A linear model is preferable since the non-linear model is less robust, especially for higher CHL. Furthermore, linear algorithms generally require less computational time in processing remote sensing images. The results are given in Table 1 and Fig 4. Model II could not be linearised directly since the calculated k_2 is larger than in model I. Linearisation can only be achieved by fitting a line through the calculated curve. The results in Fig. 4 and Table 1 show that for average IOP both models agree within the measurement errors with the measured data of 1990 and 1993.

For both 1990 and 1993 also the semi-empirical method is applied using the measured $R(0^-)$ and CHL. The algorithm coefficients k_0 and k_1 in Eq. 4 were estimated by linear regression (thus assuming $k_2 = 0$). In 1990 the *in situ* spectroradiometric measurements were carried out with a Spectron SE590 field spectrometer whereas in 1993 a Personal Spectrometer II was used. In the analysis of the 1993 data one sample with a CHL of $291 \mu\text{g l}^{-1}$ was omitted since it falls outside the range in which the semi-empirical method is valid. The results given in Table 1 indicate a difference between the semi-empirical methods of 1990 and 1993. However, the number of data samples is too limited to test this difference statistically. Furthermore, with the present results it is not possible to draw definite conclusions about the multitemporal validity of both the analytical and semi-empirical method.

The linearised version of the analytic model II was successfully applied to remote sensing images yielding quantitative maps of chlorophyll *a*. In 1990 two airborne instruments were used: the Compact Airborne Spectrographic Imager (CASI) and the CCD Airborne Experimental Scanner for Application in Remote Sensing (CAESAR). In order to achieve a better signal to noise ratio broader bandwidths were used: 13-14 nm. In 1993 good results were obtained from CASI images with bandwidths of 9-10 nm. Table 1 shows that broader bandwidths have a small effect on the coefficients found by the semi-empirical method.

TABLE 1. The coefficients k_0 and k_1 of the algorithm for CHL (see Eq. 4) with their statistics. s is the estimated error k_0 , k_1 and CHL respectively. r^2 is coefficient of determination.

method	year	bandw	n	k_0	k_1	est. error			r^2	range CHL
		nm				s_{k_0}	s_{k_1}	s_{CHL}		$\mu\text{g l}^{-1}$
an. model I	1990	2	14	-55.6	75.8	-	-	-	-	1-200
semi-emp	1990	2	14	-54.6	76.5	5.1	2.9	7.1	0.98	5-140
semi-emp	1990	13	19	-59.9	78.9	6.1	3.6	9.5	0.97	5-140
semi-emp	1993	1	10	-44.3	59.1	7.1	5.7	4.9	0.93	6-56
semi-emp	1993	10	10	-44.6	59.8	7.8	6.2	5.4	0.92	6-56

4. Discussion and Conclusions

An analytical method is proposed based on a physical model which relates the subsurface irradiance reflectance to the inherent optical properties of the water constituents. This method enables the development of a general, non-linear remote sensing algorithm for the estimation of the sum of chlorophyll *a* and phaeopigments (CHL) in inland waters. From the results in Fig. 4 it is concluded that a linearised version of model I still provides accurate estimates for CHL. Model II, in which the backscattering is correlated to CHL cannot be linearised directly.

The analytical algorithm coefficients give insight into the sensitivity of the algorithm for the absorption and scattering of other components. The coefficients of the algorithm were calculated from the average IOP of 14 lake samples with a large variation in water quality. The analytical algorithm showed good agreement with *in vivo* measured CHL. A linearised version of the algorithm was successfully applied on remote sensing images in 1990 and 1993.

It is concluded that the analytic method provides a good basis for the development of remote sensing algorithms for water quality. However, there is a lack of knowledge on the inherent scattering properties of turbid inland waters. Therefore, for the further development of the analytical method spectral volume scattering functions are required for the various components of suspended matter (detritus, inorganic matter and phytoplankton).

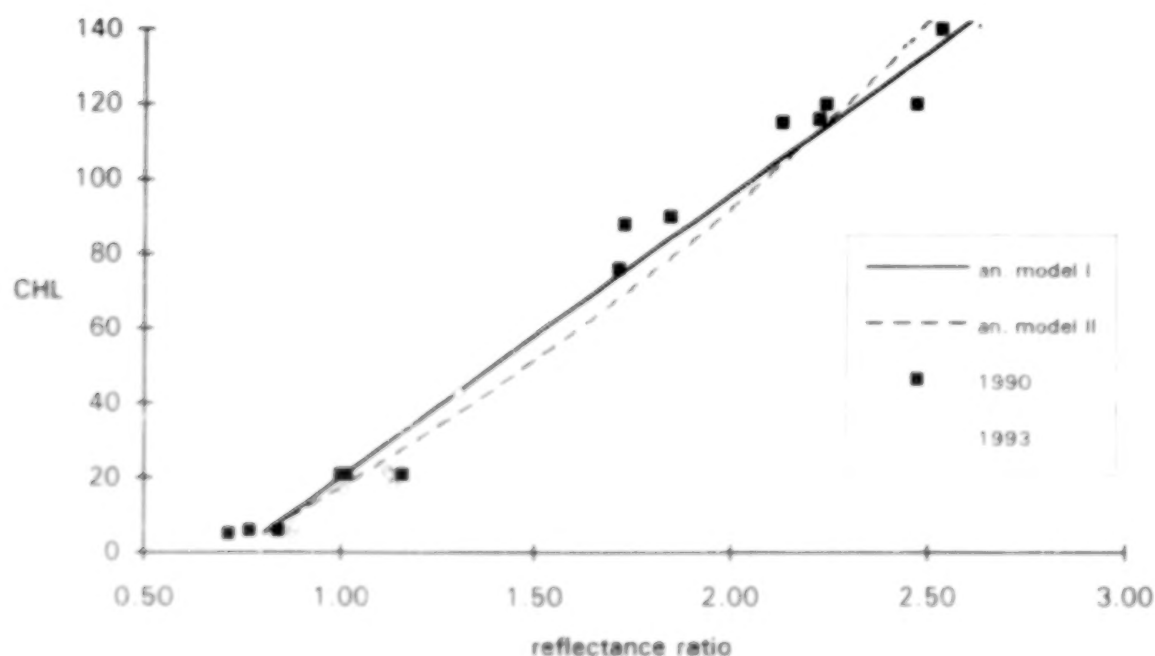


Figure 4. The analytic algorithm for CHL assuming no correlation between CHL and the total backscatter coefficient (model I, solid line) and assuming a linear correlation of CHL with the backscattering (model II, dashed line). Measured reflectance ratio versus measured CHL for 1990 and 1993.

Acknowledgements

The Spectron SE-590 was provided by the University of Nottingham and calibrated by the equipment pool of the National Environmental Research Council, UK. The PSII was provided by the Survey Department Rijkswaterstaat. A grant from NERC made it possible for Dr T.J. Malthus to perform and analyse the measurements. In 1990 the spectrophotometric measurements were performed by J. Krijgsman and H. Hakvoort at the Faculty of Civil Engineering of the Technical University of Delft (NL) in 1990 and in 1993 by A. Veen of the National Institute of Public Health and Environmental Protection. This work was funded by the National Remote Sensing Programme of The Netherlands via the Dutch Remote Sensing Board (BCRS) and by the Institute for Inland Water Management and Wastewater Treatment (NL).

References

- Dekker, A.G., Hoogenboom, H.J., Goddijn, L.M. & Malthus, T.J.M. (1994), The relationship between spectral reflectance, absorption and backscattering for four inland water types; Proc. sixth Symposium on Physical Measurements and Signatures in Remote Sensing, France, 17-21 Jan. 1994 (in press).
- Dekker, A.G., (1993). Detection of optical water quality parameters for eutrophic waters by high resolution remote sensing, PhD-thesis, Amsterdam, The Netherlands (ISBN 90-9006-234-3).
- Gordon, H.R., Brown, O.B., Jacobs, M.M. (1975); Computed relationships between the inherent and apparent optical properties of a flat homogeneous ocean; *Applied Optics*, 14(2): p 417-427
- Kirk, J.T.O., (1991); Volume scattering function, average cosines, and the underwater light field; *Limnol. Oceanogr.*, 36(3): p 455-467.
- Krijgsman, J., (1994); Optical remote sensing of water quality parameters; interpretation of reflectance data with spectra, PhD-Thesis, Delft, The Netherlands (ISBN 90-6275-952-1).
- Morel, A. & Prieur, L., (1977); Analysis of variations in ocean colour; *Limnol. Oceanogr.*, 22(4): p 709-722
- Whitlock, C.H., Poole, L.R., Usry, J.W., Houghton, W.M., Witte, W.G., et al., (1981); Comparison of reflectance with backscatter and absorption parameters for turbid waters; *Applied Optics*, 20 (3) p 517-522.

A SYNERGISTIC APPROACH TO MONITORING COASTAL ENVIRONMENTS BY USING A SUITE OF REMOTELY SENSED IMAGERY AND GROUND-BASED MEASUREMENTS

Elijah W. Ramsey III, Richard H. Day and Kevin McRae
National Wetlands Research Center
National Biological Survey
Lafayette, LA 70506
(318) 266-8575

Wetland resources are under increasing detrimental pressure from human and natural causes. To protect these environments, resource managers require tools to assess the status and to monitor changes of each resource. Remote sensing offers a valuable tool for describing the physical and biological characteristics of regional resources, however, methods must be generated that can consistently discriminate wetland types and identify changes within each wetland type. Described within this paper are the results of using different imagery sources and ground based measurements to discriminate marsh types and to detect and monitor marsh alterations, especially from acute stresses, e.g., burning and storm surges.

As part of a global climate change study, helicopter reflectance spectra and ground-based light attenuation curves and continuous water depths and salinities have been acquired for a number of forested and marsh sites--including sites where fires had occurred in the past two years within the St. Marks National Wildlife Refuge, Florida. Marsh and forested sites include: pine and pine/cabbage palm forests, sawgrass (fresh), and black needlerush (saline) marshes. Imagery collected of the study area include: satellite [Thematic Mapper and ERS-1 radar], aircraft [Multispectral Scanner (CAMS and TMS), AVIRIS, Radar (Navy P3 and USGS Star-1), and natural and CIR photography]. Unique and common information available from the suite of helicopter, ground-based, and imagery data sources are discussed, especially the advantages of radar as a marsh monitoring tool, singularly and in conjunction with other imagery sources. Finally, how decision makers may use the resulting information to assist in protecting wildlife and wetland resources is discussed.

Manuscript not available at time of printing. Please contact authors for further information.

**THE LITTORAL REMOTE SENSING MODELING
AND SIMULATION SYSTEM (LRS-MASS)**

Lee J. Rickard, G. Keramidas and J. Spencer
Naval Research Laboratory
Washington, DC 20375-5351
(202) 404-7877

As a part of a program to conduct integrated basic research/exploratory development programs in remote sensing, the Office of the Chief of Naval Research is supporting a joint program among NRL, ONR, NCCOSC/NRaD, and NSWC/CSS to construct an end-to-end, physics-based simulation system for remote sensing of coastal regions. This system will link together a number of physical models to simulate the performance of three categories of remote sensing device; passive optical imaging spectrometers, active optical imagers, and synthetic aperture radars. The results should support both environmental measurements as well as military target evaluations. We will report on the models being incorporated into the system, and the status of the end-to-end structure.

Manuscript not available at time of printing. Please contact authors for further information.

USE OF PRINCIPAL COMPONENTS TO CHARACTERIZE UPWELLING OFF THE COAST OF CALIFORNIA

E. Molinelli and G. Muncill
Planning Systems Incorporated
McLean, Virginia 22102, United States

ABSTRACT

One component of monitoring U.S. fishing resources is monitoring fishery habitats as indicated by regions of upwelling. Upwelling regions are areas characterized by cold, nutrient-rich surface waters. Such upwelling is indicative of high biological productivity and marks favorable habitats for several species of commercially valuable fish, including rockfish. Daily analyses of upwelling regions are needed even in the presence of some cloud cover to allow reliable daily monitoring. We here present work that can support daily analyses of coastal upwelling.

First we define meaningful principal components for satellite imagery of coastal sea surface temperature (SST) and upwelling. These principal components retain the high resolution of the original image. We show that an image constructed from only the mean and the 8 most significant components (modes) does an adequate job of describing SST and upwelling for 35 cloud free images spanning two years of SST observations in the coastal waters of northern California. We demonstrate this quantitatively by defining two different measures of effectiveness -- 1) the root mean square (rms) temperature difference between the reconstructed image and the original image, and 2) the upwelling misclassification rate, i.e. the percentage of pixels classified in the reconstructed image differently than they were classified in the original image. Our 8 mode reconstructions had half the rms temperature difference, and about half the misclassification rate, of a "mean image" made up of mean values at each pixel.

We further show that a neural network is capable of recognizing, in imagery partly obscured by clouds, enough of each mode to estimate the amplitudes for the 8 modes needed for reconstructions. The cloud free image generated from these estimated 8 amplitudes (and the fixed mean and modes) performed better than the mean image, and performed almost as well as 8 mode reconstructions using amplitudes computed directly from cloud free images. We quantify how the images constructed from neural network amplitudes improved on the mean image. Even in the case of cloud coverage from 40% to 50%, the neural network still performed better than the mean field -- the neural network amplitudes provided a 40% reduction in rms temperature error and a 13% reduction in misclassification rate.

1. INTRODUCTION

Satellite imagery provides a compelling view of the Earth, rife with detail on surface features. The technologies are advanced sufficiently that surface properties with electromagnetic signatures can be reliably sensed and located with reasonable estimates of parameter and positional accuracies. Among the properties of the ocean surface that can be sensed are sea surface temperature (SST) from infrared imagery and chlorophyll concentration from the visible band. In infrared images involving an ice free ocean surface, clouds often can be automatically detected and cloud detail can be removed from the images. These characteristics of spectral remote sensing are taken as given and will not be treated further.

The concern here is to perform meaningful interpretations of ocean spectral imagery by extracting ocean features. Extracting ocean features from imagery is a task still performed operationally by humans; yet, humans can not be expected to keep pace with the new sources and increasing volume of data. It is clear that automated extraction of features from imagery reduces a daunting task, involving gigabytes of information which is impossible for a human being to properly assimilate, to a task involving kilobytes which can be managed more reasonably by humans. With the onslaught of new volumes of data, organizations, like the National Oceanic and Atmospheric Administration (NOAA) which are responsible for providing analysis, will either employ automated feature extraction, or they will perform analyses that do not utilize all the data that will be available.

Automated extraction is impeded by "noise" in the imagery caused by sensor error (such as scan dropout), algorithm error (such as imprecise atmospheric corrections) and natural variability due to processes other than the feature of interest (such as shingles at the Gulf Stream front). Automated extraction from visible and infrared sensors is also impeded by the progression of clouds across the satellite sensor's field of view. There is a need to develop automated feature extraction procedures that are robust in the presence of noise and clouds.

There are promising techniques for describing ocean features numerically and quantitatively. Principal components (PC, also called empirical orthogonal functions) characterize variability in any series of observations (including a series of images) as the eigenvectors of a covariance matrix (Preisendorfer et al., 1981). The details will not be presented here, but the image is converted to a vector before applying PC analysis. The results of a PC analysis are a mean vector and a set of orthogonal vectors called modes that characterize the dataset. Any member of the original dataset is a vector that can be reconstructed by adding a linear combination of the modes to the mean. The linear combination consists of a scalar coefficient (which we call an amplitude) multiplied by a mode and the result added to the next amplitude multiplied by the next mode until all modes have been utilized. There is one scalar amplitude needed for each vector mode, so a set of amplitudes are needed to reconstruct each original vector. The set of amplitudes are different for different original vectors. However, the modes are the same for all of the original vectors. It is this property that leads us to think of the modes as "features" in the dataset.

One other property of PCs make them useful for extracting features in imagery data. If all modes that can be defined for a dataset are used then there has been no savings in information. However, it is not necessary to use all modes. Different amounts of the total variability in the dataset are attributable to different modes. Often very few modes describe 90% of the variability. Thus one can keep just the important modes that explain the most variance. These are the principal components and they constitute the main features in the dataset. In the ocean PCs have been used to describe many forms of variability in datasets of coastal sea level and Gulf Stream position. PCs are used for imagery of SST in recent work (Lagerloef and Bernstein, 1988).

There are promising techniques of artificial intelligence that can be employed to extract ocean features automatically from imagery. One of these is neural network technology which emulates the processing believed active in the human retina and brain, and has shown the ability to detect features in imagery (Cybenko, 1988). Moreover, they are capable of deducing principal components of ocean features within ocean imagery contaminated by noise (Molinelli and Flanigan, 1989, and Molinelli et al., 1991). Neural networks tend to converge on solutions in a least squares sense that make them robust against noise and missing data. These properties are extremely important for detecting ocean features even when obscured by clouds.

The opportunity exists to develop a system that will meld these potent technologies to process information pertinent to ocean activities such as those undertaken by coastal fisheries. The feasibility of such a system for detecting coastal upwelling in the presence of clouds was the goal of research sponsored by NOAA through the Small Business Innovative Research (SBIR) Program. In this research we use PCs as the interpolating functions and neural network as the procedure to fit those functions to the gappy observations.

2. TECHNICAL OBJECTIVE

The objective is to test whether a system composed of a neural network operating in concert with a principal component analysis can classify coastal zone areas in the presence of clouds better than a climatic average can classify them. As an example, we test the system's ability to classify nutrient rich, cold water upwelling areas in the California coastal ocean in the presence of clouds. Such upwelling is important because it leads to phytoplankton blooms which initiate a prolific food chain. This classification is to rely on sea surface temperature from infrared imagery (channel 4) of the Advanced Very High Resolution Radiometer (AVHRR) on the current NOAA polar orbiting satellite. The effects of noise and cloud coverage on the classification are to be quantified.

3. RESEARCH WORK COMPLETED

The work presented here was performed with a three person month effort undertaken between August and December 1992. With limited resources of Phase I funding through the SBIR program, the goal is simply to show feasibility, not to predict or achieve peak performance.

3.1 IMAGE PREPARATION.

A set of 41 Advanced Very High Resolution (AVHRR) images depicting the Exclusive Economic Zone (EEZ) off southern California during 1991 and 1992 were received from M. Laurs, National Marine Fisheries Service (NMFS) Southwest Fisheries, LaJolla, California. These images are 512x512 bytes (8 binary digits) of channel 4 uncorrected temperatures geolocated with 1.1-km resolution and have few to no clouds. Cold water regions adjacent to the coast are indicative of high productivity upwelling and are to be characterized by our work. Table 1 lists the images by date and time and indicates their disposition during our research. The notations in Table 1 will be explained in the following.

A 200 pixel by 200 pixel region for analysis was defined that is cloud free on most images. Twenty one images were selected for defining the principal components (PCs). Fourteen of the remaining images can be used to test the PCs. Five are redundant or have clouds in the area of interest so that they are useful for testing the neural network but not the PCs. One image from 1992 Julian day 252 at 2200Z, has warm clouds not easily masked and will not be used in our work. Our intention was to select the 200 pixels immediately west of the westernmost land pixel on each line. We found that land registration varied slightly among the images and some land pixels were not masked to zero values. The land signal thus peeking into our area of interest is highly variable and dominates the variance we are trying to characterize. We were able to reduce this contribution to the total image variance by moving our area of interest 3 pixels further westward.

An arbitrary criterion for classifying a pixel as upwelling or not was established. The purpose of this classification is to have a performance measure more akin to a parameter of operational interest than simple temperature. The criterion is that upwelling pixels must be colder than 9° C, or more than a threshold temperature TT colder than waters found in the southwestern 11x11-km of the area of interest. TT was set to 2.5°C by default; but, it was found that TT must be diminished when the coldest waters in the image approach the southwest corner, this occurs for about one third of the images. Figure 1 shows the original image (a) in terms of pixel values ($10 \times (25.5 - \text{temperature})$), and the upwelling pixels in the 200x200 area of interest (b) on an arbitrary scale (200 for upwelling, 100 for non-upwelling). The complete set of 21 images selected to define the principal components are in a separate report (Molinelli et al., 1993)

3.2 PRINCIPAL COMPONENT COMPUTATION.

Both temporally removed and spatially removed means were considered for the computation of principal components. Spatially removed means (for the computation of "gradient" EOFs, Lagerloef and Bernstein, 1988) are inappropriate for the application we have in mind, to interpolate under cloudy regions. To apply principal components one must add them to the mean; yet, because it is impossible to compute the spatial mean in the presence of clouds, no mean would be available. By using a temporal mean, every pixel visible between clouds has a well defined mean value.

The mean of the 21 images used to define the principal components is depicted in Figure 2a in terms of pixel values. The upwelling associated with the mean temperature field (using the default criterion) is depicted in Figure 2b. To be useful, the principal component analysis must provide better estimates of upwelling than the mean in Figure 2b. It must be noted that the images used for defining the coastal conditions are predominantly taken in the summer and fall seasons when upwelling is active. Consequently our mean conditions show upwelling; and, the mean is likely to do a very good job for some of the upwelling images, which it does, as we will show.

The computation of principal components provides not only the spatial pattern associated with each component but also the percent of the total variance about the mean associated with that component. The components are ranked in order from highest to lowest percentage of total variance explained. The first component is called mode 1, the second mode 2, and so on. For data consisting of 200x200 pixels

there are 40,000 pixels in each mode. Theoretically, it takes then 40,000 modes to completely describe the variability of every such image. However for 21 images there are only 20 significant modes. The remainder are essentially degenerate modes consisting of zeros in every one of the 40,000 pixel locations. The details of the computation follow the discussion of Kelly (1991).

TABLE 1. DISPOSITION OF 41 IMAGES RECEIVED FROM NOAA NMFS, SOUTHWEST FISHERIES

Number	Year	Julian day	hour (GMT)	TT* #	PCA image #	Test image	Remarks
1	91	066	21		1	-	
2	91	119	21		-	1	bad scan line
3	91	134	21		2	-	
4	91	151	21		3	-	
5	91	167	22	1.5	-	2	
6	91	245	22		-	3	
7	91	281	22		4	-	
8	91	293	23		-	4	
9	91	303	22	0.5	5	-	
10	91	322	22	0.0	6	-	
11	91	342	22	0.5	7	-	
12	92	056	11		8	-	
13	92	144	22		9	-	
14	92	156	12		-	5	
15	92	187	22		10	-	
16	92	204	22		11	-	
17	92	205	12		-	6	
18	92	205	22		-	7	
19	92	217	23		12	-	
20	92	222	22	0.5	13	-	
21	92	234	11		-	8	
22	92	234	23		14	-	
23	92	236	11		-	9	
24	92	236	22		-	-	redundant
25	92	250	11		-	-	redundant
26	92	251	11		-	-	redundant
27	92	251	22		15	-	
28	92	252	11		-	10	
29	92	252	22		-	-	warm clouds can't be masked
30	92	257	22		16	-	
31	92	268	22		17	-	
32	92	269	11	1.5	-	11	
33	92	269	22	1.5	-	12	
34	92	270	11	1.0	-	13	
35	92	278	11	0.0	-	14	
36	92	280	12	1.5	19	-	
37	92	281	23	1.5	18	-	
38	92	282	23		20	-	
39	92	296	22	0.5	21	-	
40	92	308	11		-	-	too many clouds
41	92	308	23		-	-	too many clouds

*TT, threshold temperature = 2.5 unless noted

BLANK PAGE

000120

711

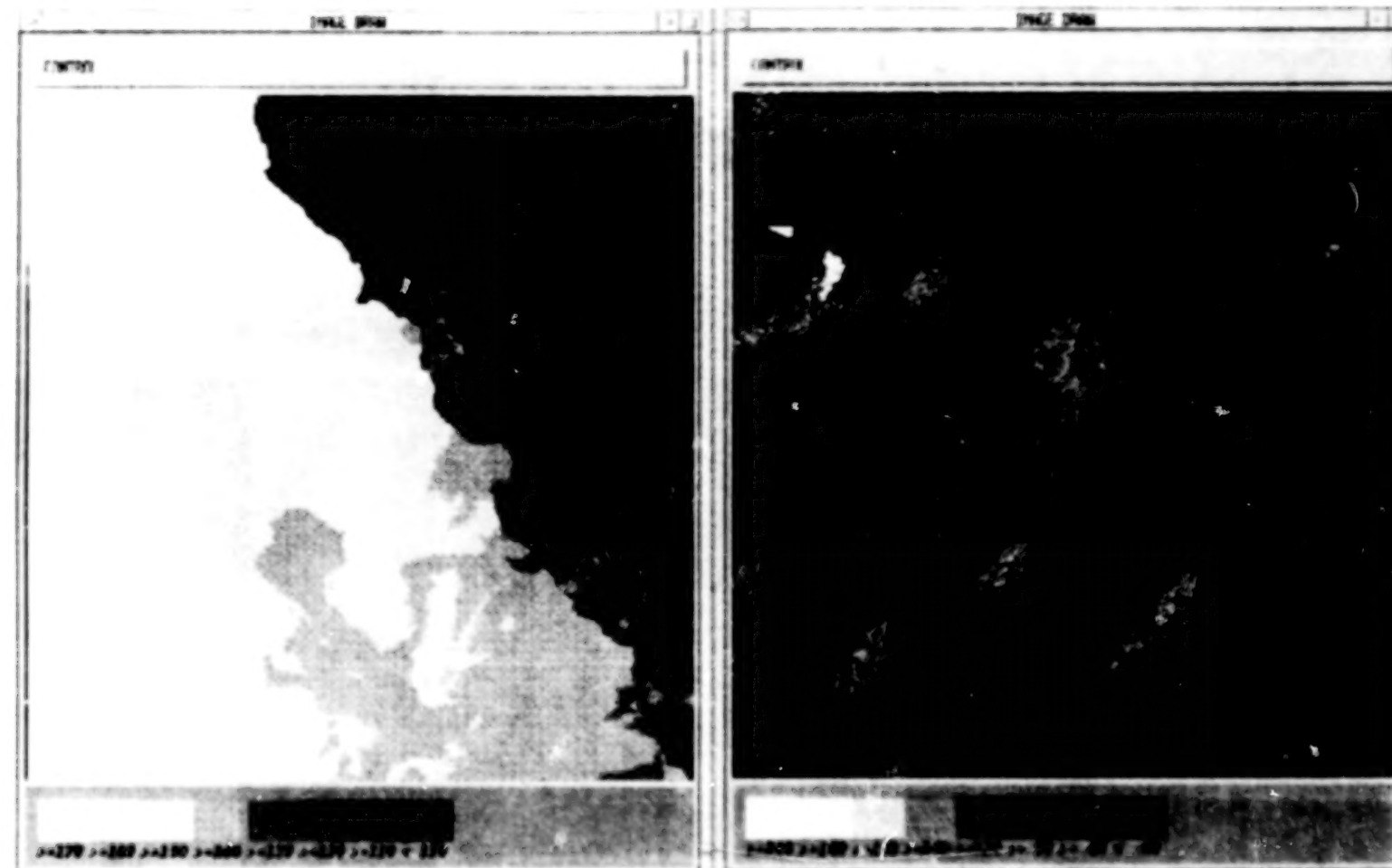
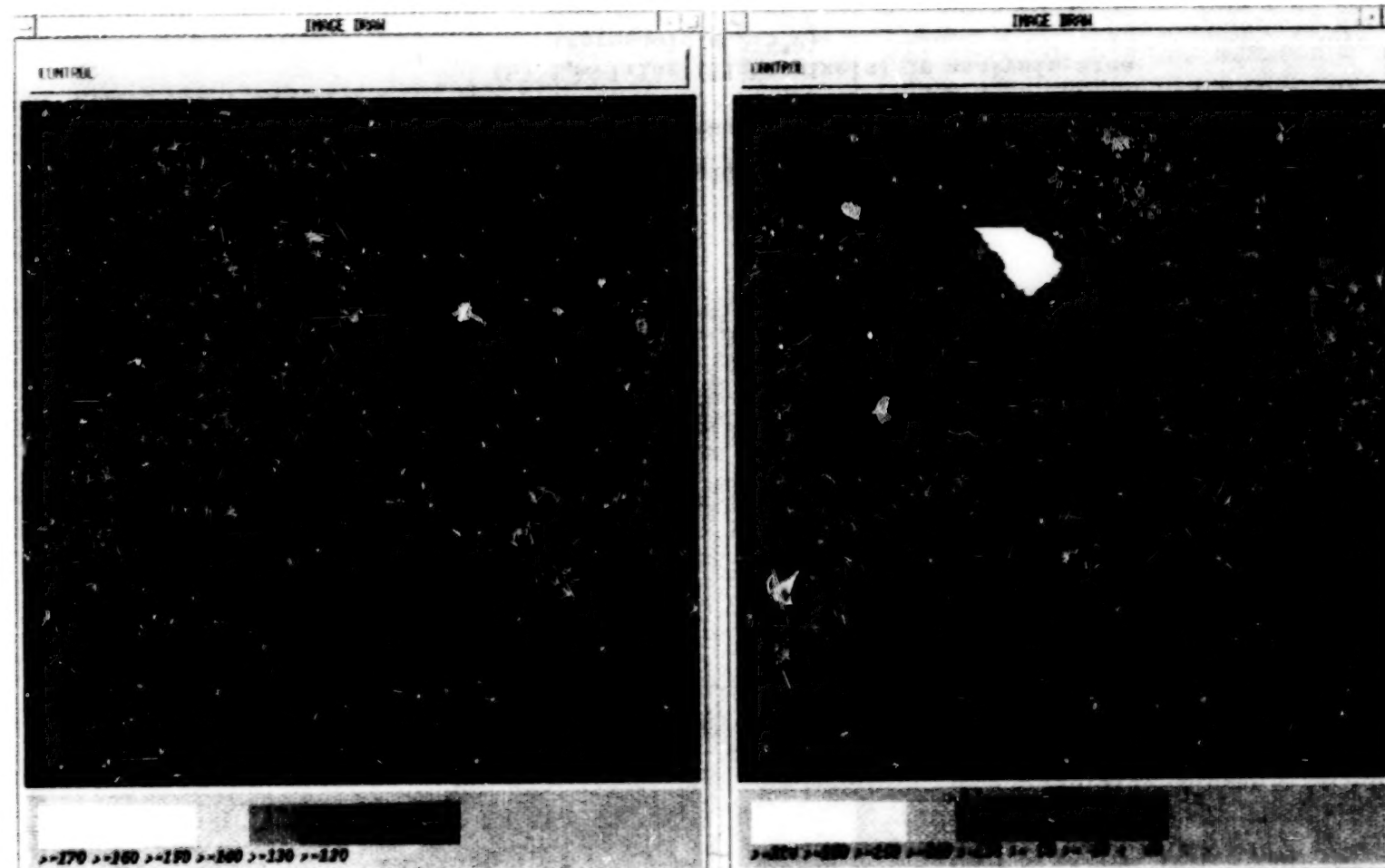


Figure 1. Year 91 Julian Day 066 Time 2100Z
 (a) Original image [(temperature = $\frac{255 - \text{value}}{10}$)]
 (b) Upwelling (light pixels) in analysis area
 (threshold = 2.5°C)

000175

BLANK PAGE

000152



712

Figure 2. (a) Mean field (pixel values) in analysis area
(b) Upwelling deduced from mean field

000176

BLANK PAGE

Table 2 lists the percentage of the total variance associated with each mode. Figures 3a through 7b show the spatial patterns associated with the first ten modes rescaled to lie between 100 and 200 so that they can be displayed with the imagery software. The actual values of each pixel in a mode are small floating point numbers so that the sum of the squares of the values are about 1.0.

The modes show some patterns that are satisfactorily oceanographic. Mode 1 (Figure 3a) shows cold water offshore that roughly negates the pattern evident in the mean (Figure 2a). This allows mode 1 to generate more uniform temperatures as are needed in the non-upwelling seasons; mode 1 essentially contains the seasonal signal. Mode 2 reflects the strong circular cold region found in the image from 1992 Julian Day 144 at 22:00Z.

Some modes are not so satisfactorily oceanographic. In particular, mode 5 (Figure 5a) shows hot spots along the coastal edge that hints it may be dominated by land registration problems not fully eliminated by our 3 pixel standoff. Modes 6 and 8 may also be similarly affected to some degree. Such a problem will have the effect of giving importance to oceanic features that just happen to occur in images with slight errors in land registration. In spite of this problem, however, the modes so defined perform sufficiently well for our work to demonstrate the feasibility of a combined neural network/PCA for interpolating under clouds. In future work, we can reduce this problem by better land registration or by defining our area of interest farther offshore (e.g., one pixel farther south, F. Schwing, personal communication).

Any image in the defining set of 21 images can now be reconstructed by a linear combination of the modes. The modes contain the spatial pattern of variability but not the magnitude of the variability. Each mode must be multiplied by a scalar amplitude specific for a particular image and added to the next mode multiplied by the next amplitude for that image. Using all 20 modes completely reconstructs the original image (within the roundoff error of the computations). Using fewer modes gives a good approximation. The correct amplitude for a given mode of a given image is provided by the computation of the principal components, but also can be computed by multiplying each pixel of the mode by the corresponding pixel of the image and summing over all pixels. This procedure for computing amplitudes is only possible if the entire area is in view. It cannot be used with clouds present; that is the problem we will invoke neural networks to solve.

TABLE 2. PERCENTAGE OF TOTAL VARIANCE ASSOCIATED WITH EACH MODE

Mode	% of Total Variance	Cumulative % of Total
1	88.76	88.76
2	3.44	92.20
3	1.97	94.17
4	1.27	95.44
5	0.69	96.13
6	0.65	96.78
7	0.49	97.27
8	0.40	97.67
9	0.33	98.00
10	0.31	98.31
11	0.30	98.61
12	0.28	98.89
13	0.24	99.13
14	0.19	99.32
15	0.16	99.48
16	0.15	99.63
17	0.11	99.74
18	0.10	99.84
19	0.10	99.94
20	0.04	99.98

771000

714

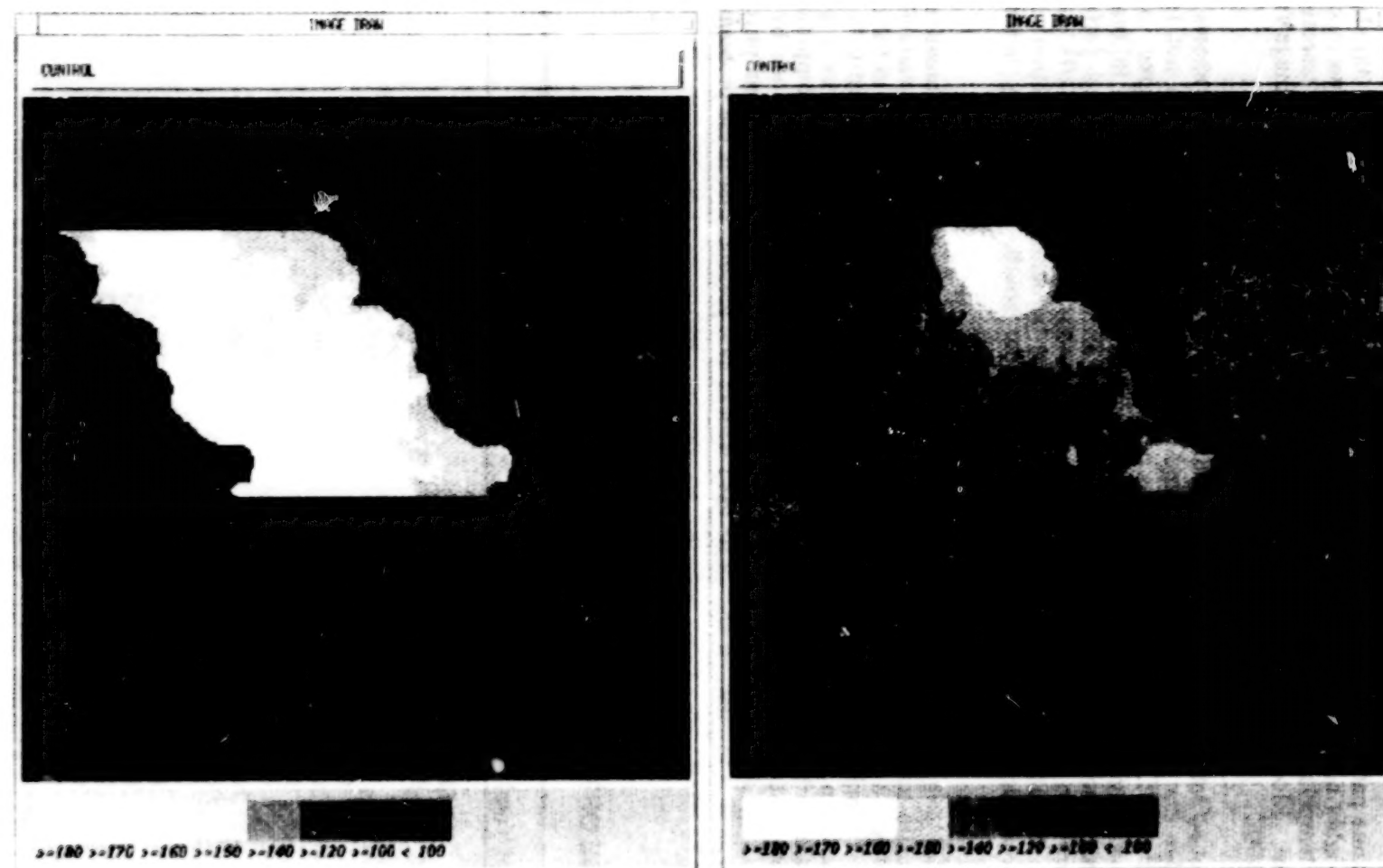


Figure 3. (a) Spatial pattern of mode 1 (arbitrary units) in analysis area
(b) Spatial pattern of mode 2

000178

000120

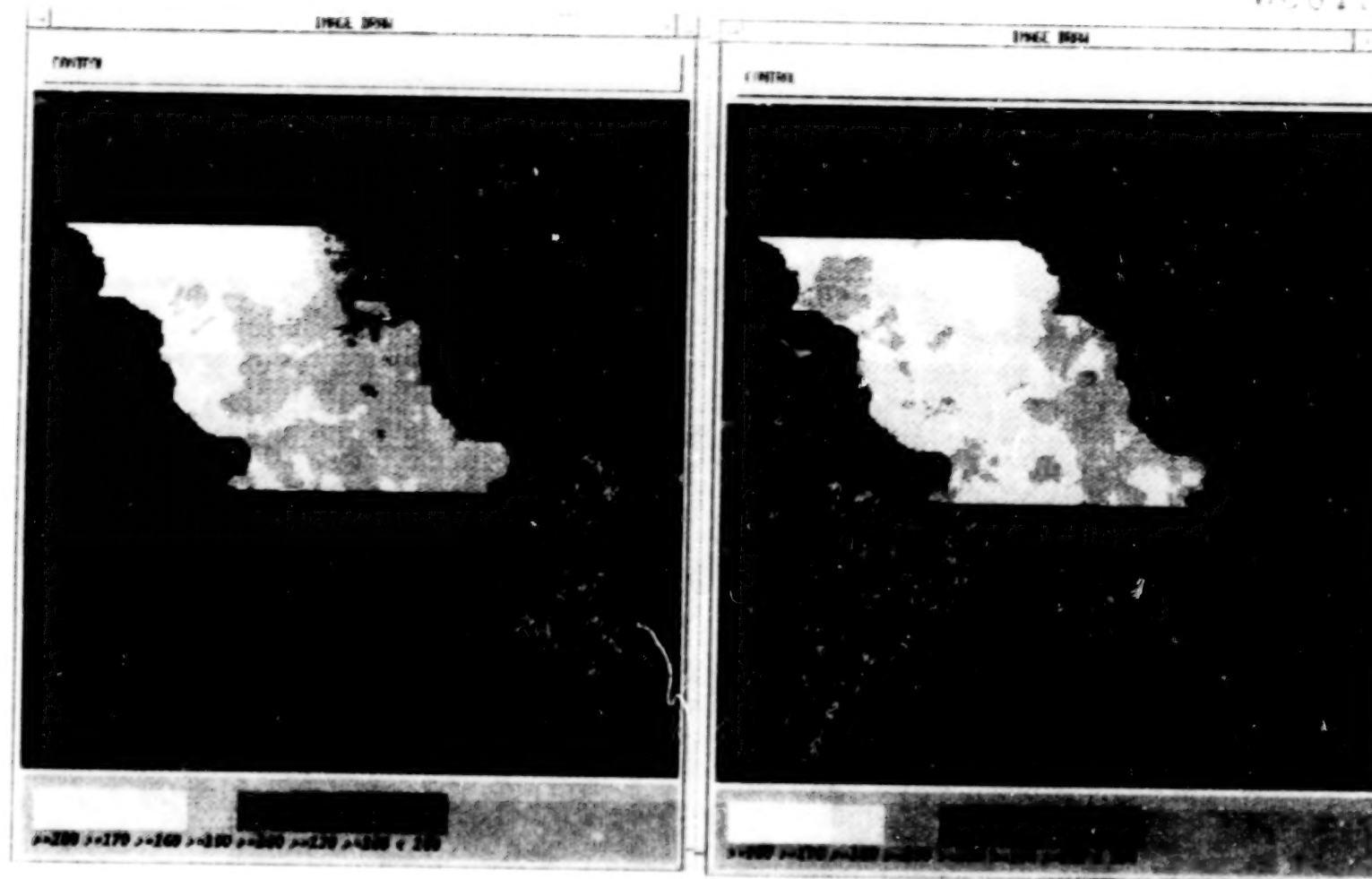


Figure 4. (a) Spatial pattern of mode 3
(b) Spatial pattern of mode 4

000179

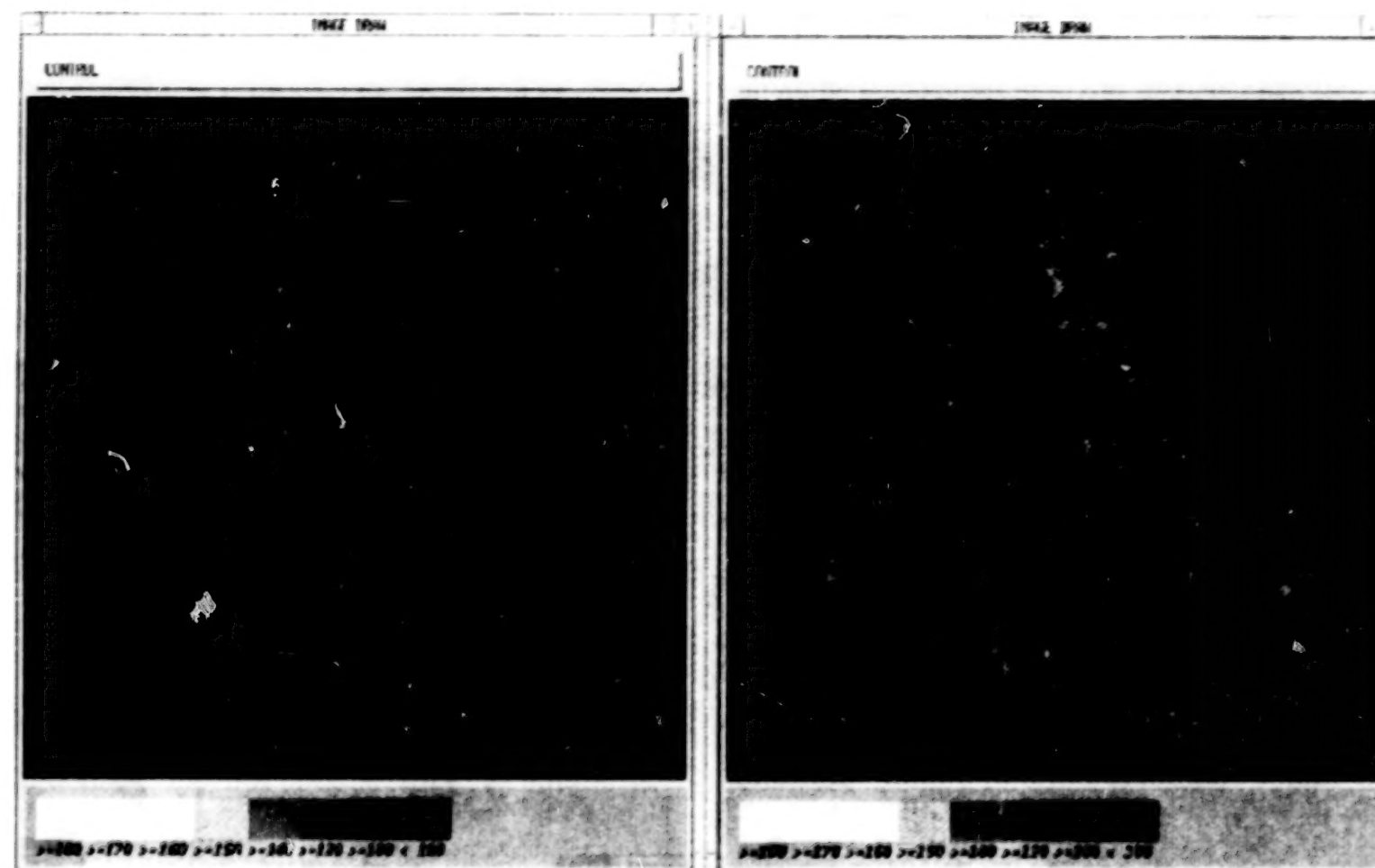


Figure 5. (a) Spatial pattern of mode 5
(b) Spatial pattern of mode 6

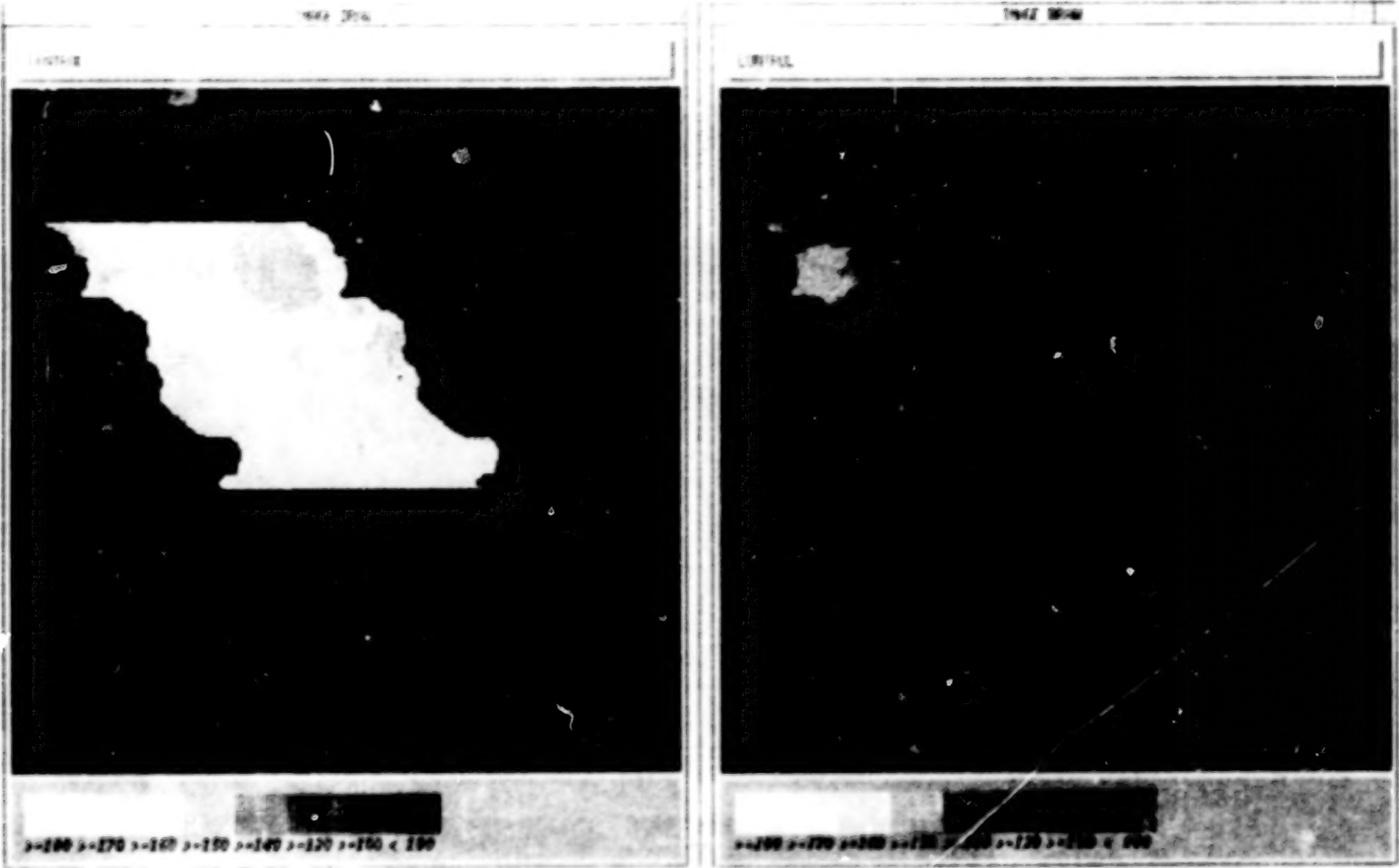


Figure 6. (a) Spatial pattern of mode 7
(b) Spatial pattern of mode 8

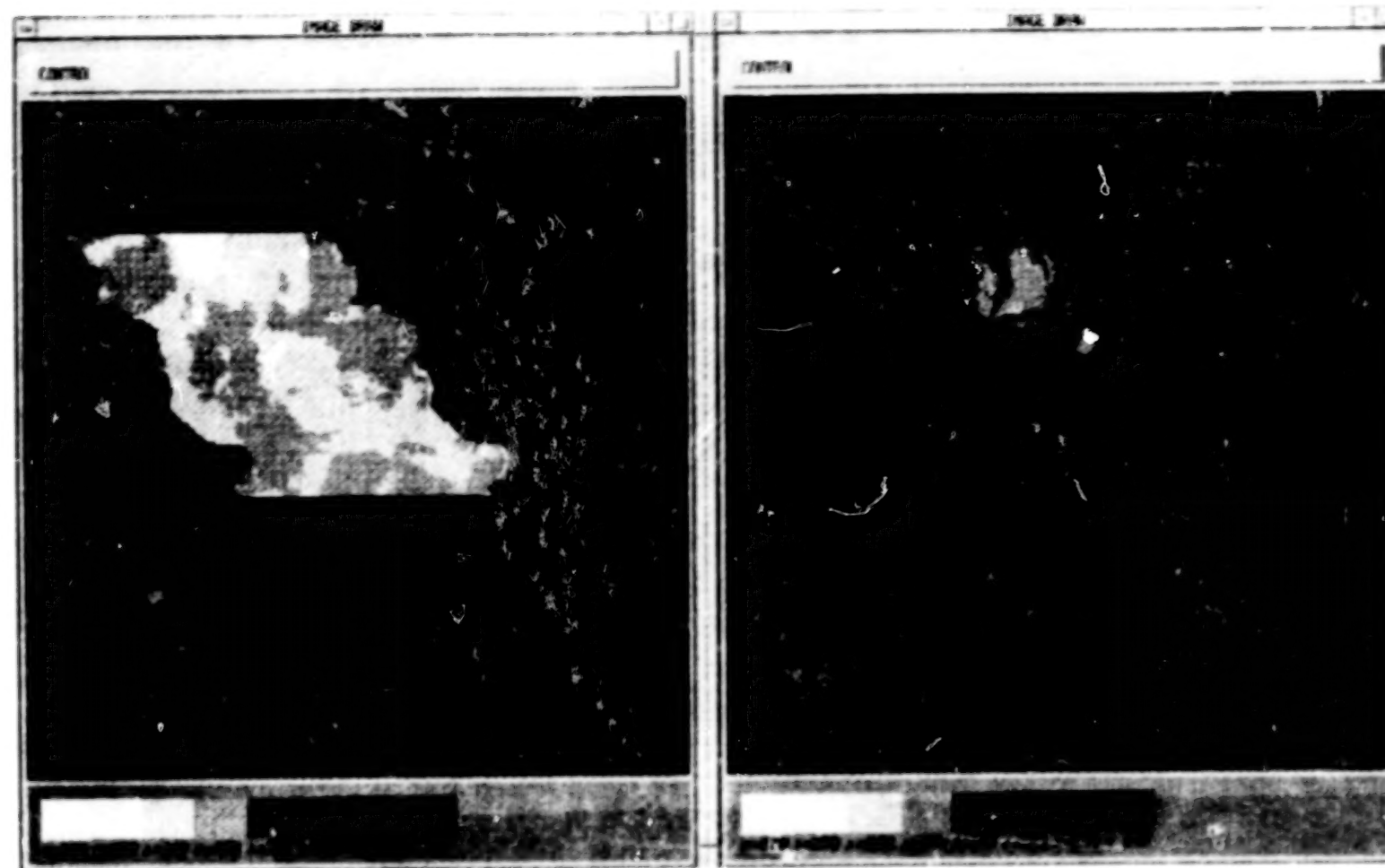


Figure 7.

- (a) Spatial pattern of mode 9
- (b) Spatial pattern of mode 10

BLANK PAGE

We determined how many modes to keep for our characterization of the upwelling off southern California by looking at the root mean square (rms) temperature difference between the original and reconstructed image and by looking at the misclassification rates of the reconstructed image. Misclassification rate was defined as the percent of pixels classified as upwelling or non-upwelling contrary to their classification in the original image. Using the data in Table 3 for two of the 21 images, we decided to use 8 modes for reconstructions. Table 4 shows that 8 modes did an adequate job of reconstructing all the original images with misclassification rates superior to misclassification rates of the mean temperature field except for images 15 and 16. For these two images the mean is a very good representation of conditions. On average, 8 mode reconstructions halved the rms temperature error and reduced misclassifications by 8 percentage points.

Figures 8a shows the 8 mode reconstruction of the image from 1991 Julian Day 066 21:00Z, and Figure 8b shows the resulting upwelling classifications. These figures should be compared to the original image in Figures 1a and 1b. The reconstructed image is somewhat warmer (darker) than the original but shows the same gradual south to north gradient. The upwelling criterion based on the reconstructed temperatures shows no upwelling in the area of interest, which is a good result; in fact, the few upwelling pixels in the original (Figure 1b) are highly suspect classifications given their distance offshore, and the reconstructed result of no upwelling is probably a better, though accidental, diagnosis. Figures 9a and 9b show the reconstructed temperatures and upwelling classifications for 1991 Julian Day 134 21:00Z. These are to be compared with the originals in Figures 10a and 10b, respectively. Again the reconstructed image is slightly warmer than the original with gradients similar in magnitude and direction to the original, and an annulus shaped feature is correctly located. The upwelling criterion gives a reduced area of upwelling for the reconstructed temperatures (Figure 9b) than for the original (Figure 10b), but the locations are correct.

Before using the modes to interpolate under clouds, we need to see how well they reconstruct images not used to define the modes. Mathematically, the modes defined for the 21 originally selected images should have little resemblance to the variability observed in the next 14 images. However, we make a critical assumption here. We assume that the modes of variability observed in a reasonable sample of the ocean are characteristic of the modes of variability for that part of the world. Since our samples are from all seasons off the California coast, we hope that they provide good statistics for variability at other times. The 14 test images are interspersed in time with the 21 defining images. Some test images (e.g. #9, #12 on Table 1) were excluded from the defining set because they are nearly redundant observations; so, we expect good performance for them. Other test images (e.g. #1, #4, #6 in Table 1) are not redundant but were kept out of our defining set because of some contamination by clouds or bad scan lines that we did not want to affect our modes. They provide a more severe test.

We test how good our assumption is by reconstructing the 14 test images using our 8 modes. Table 5 shows that results are again superior to the mean image. The average rms errors again have decreased to about half (from 0.96 degrees to 0.38 degrees); and, misclassification rates have been reduced by more than 6 percentage points. Eight mode reconstructions are compared to the original images for one of the test cases in Figure 11 (test image #1). Note in Figure 11 how the bad scan line does not appear in the 8 mode reconstruction; it may add amplitude to several modes, but there is no mode that reconstructs it. This is good. The dropout of bad scans and other spurious features in the mode reconstructions is highly advantageous for producing inputs to numerical models and human analysis.

The results of Table 5 and the example in Figures 11 show that the modes we have defined based on 21 cloud free images do a good job in describing 35 essentially cloud free images. Though this property of our modes is useful for such functions as image compression, image transmission, and smoothing out small artifacts, it is otherwise of little operational use to reconstruct an image that is already as cloud free as the 35 we have selected so far. For operational settings, we want to use these modes for interpolating sea surface temperature to areas under clouds.

For interpolating under extensive clouds we need to be able to estimate the 8 amplitudes that go with an image. We can not compute these amplitudes directly by the summation of values obtained by pixel by pixel multiplications, as we did for the 21 defining and 14 test images; too many of the pixels would have cloud values and not appropriate sea surface temperature values. Instead, we hope we can estimate the 8 amplitudes from the cloud-free portion of the image we are able to view. Estimating these 8 amplitudes from partly obscured imagery is the role we have turned over to a neural network.

221000

720

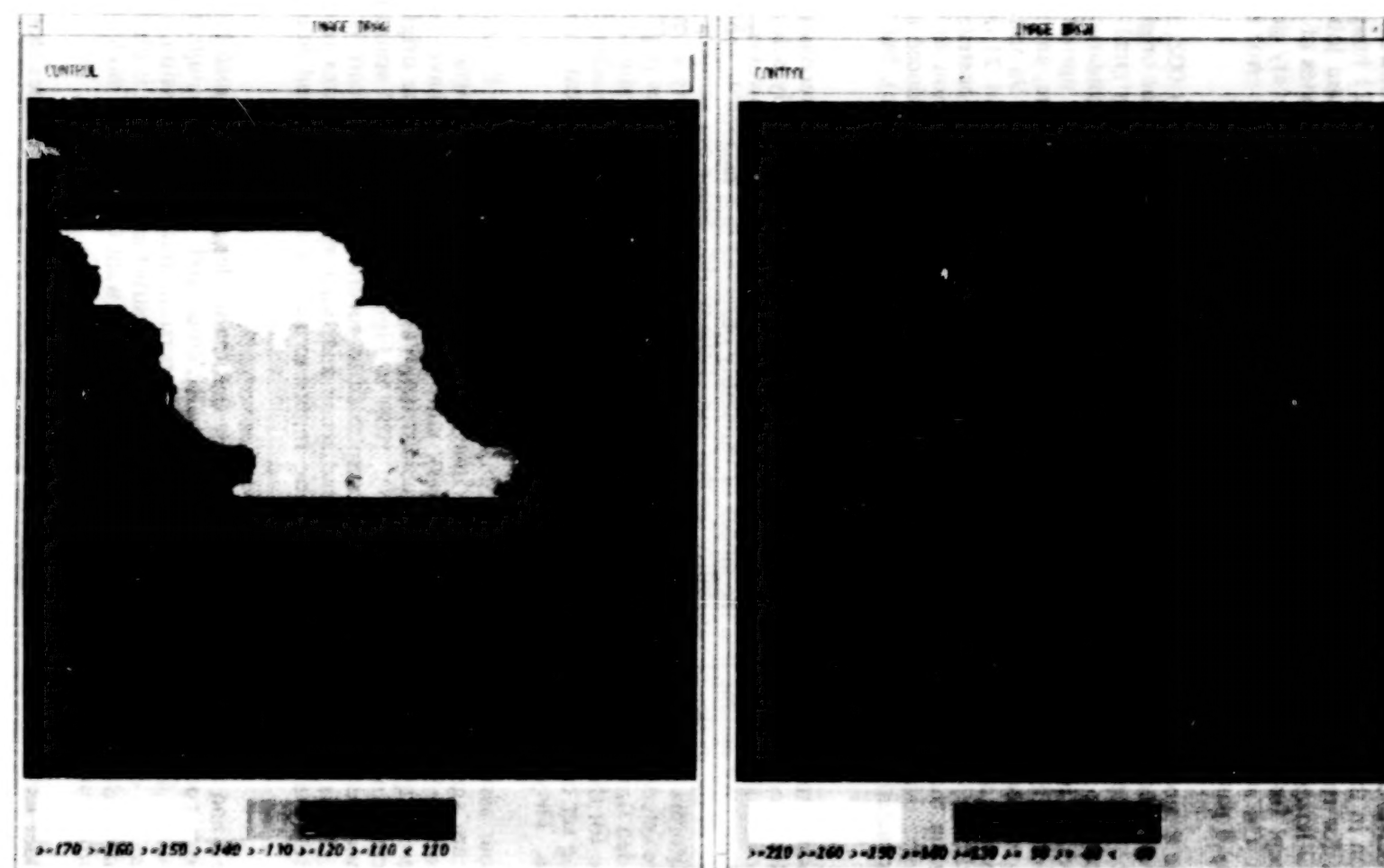


Figure 8.

Year 91 Julian Day 066 Time 2100Z

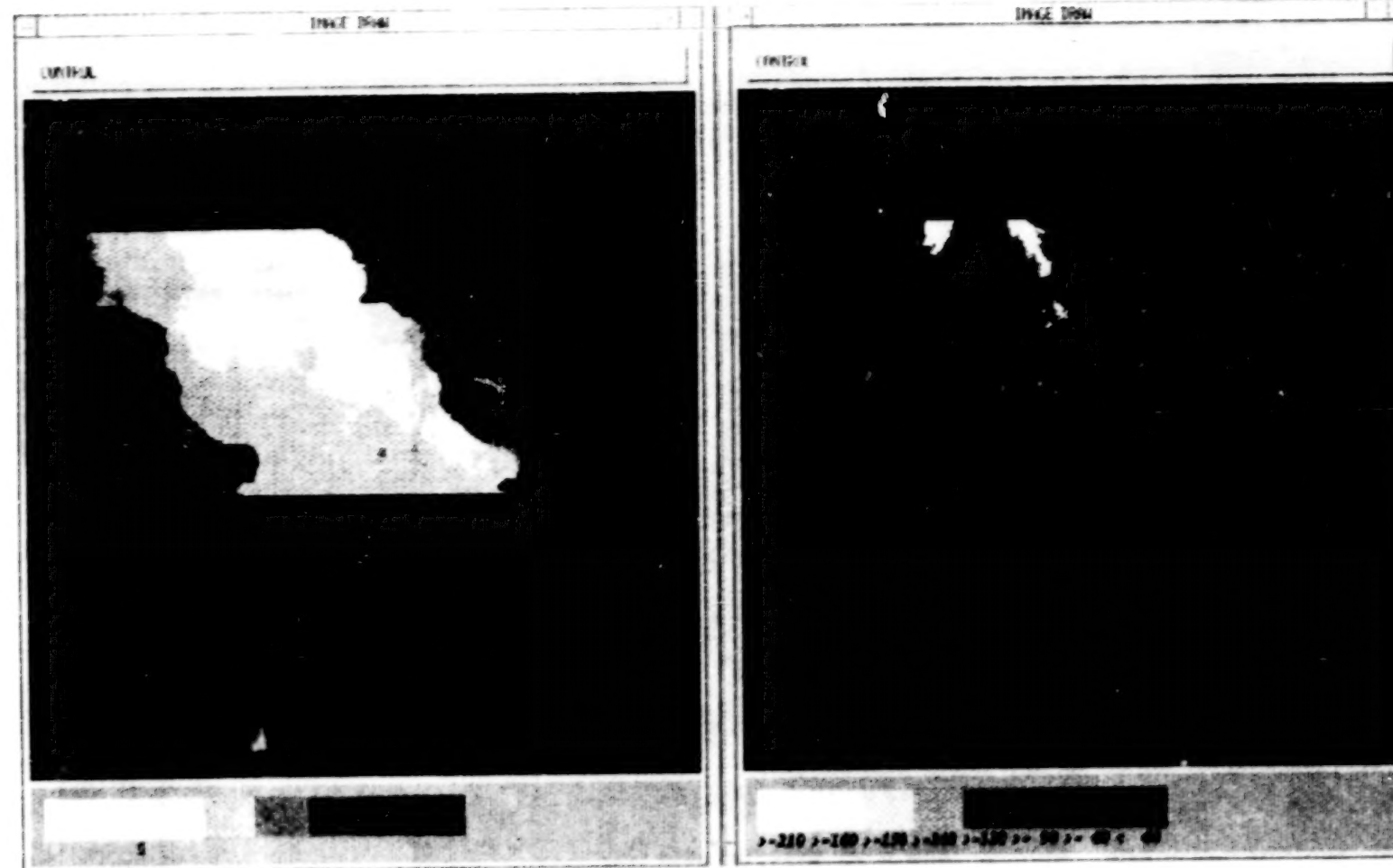
Reconstruction of original image

(a) 8 mode reconstruction in analysis area for image of
Figure 1 [(temperature = $\frac{255 - \text{value}}{10}$)]

(b) Upwelling deduced from a

000184

000182



721

Figure 9. Year 91 Julian Day 134 Time 2100Z
 Reconstruction of original image
 (a) 8 mode reconstruction in analysis area of image
 of Figure 2
 (b) upwelling deduced from a

000185

000182

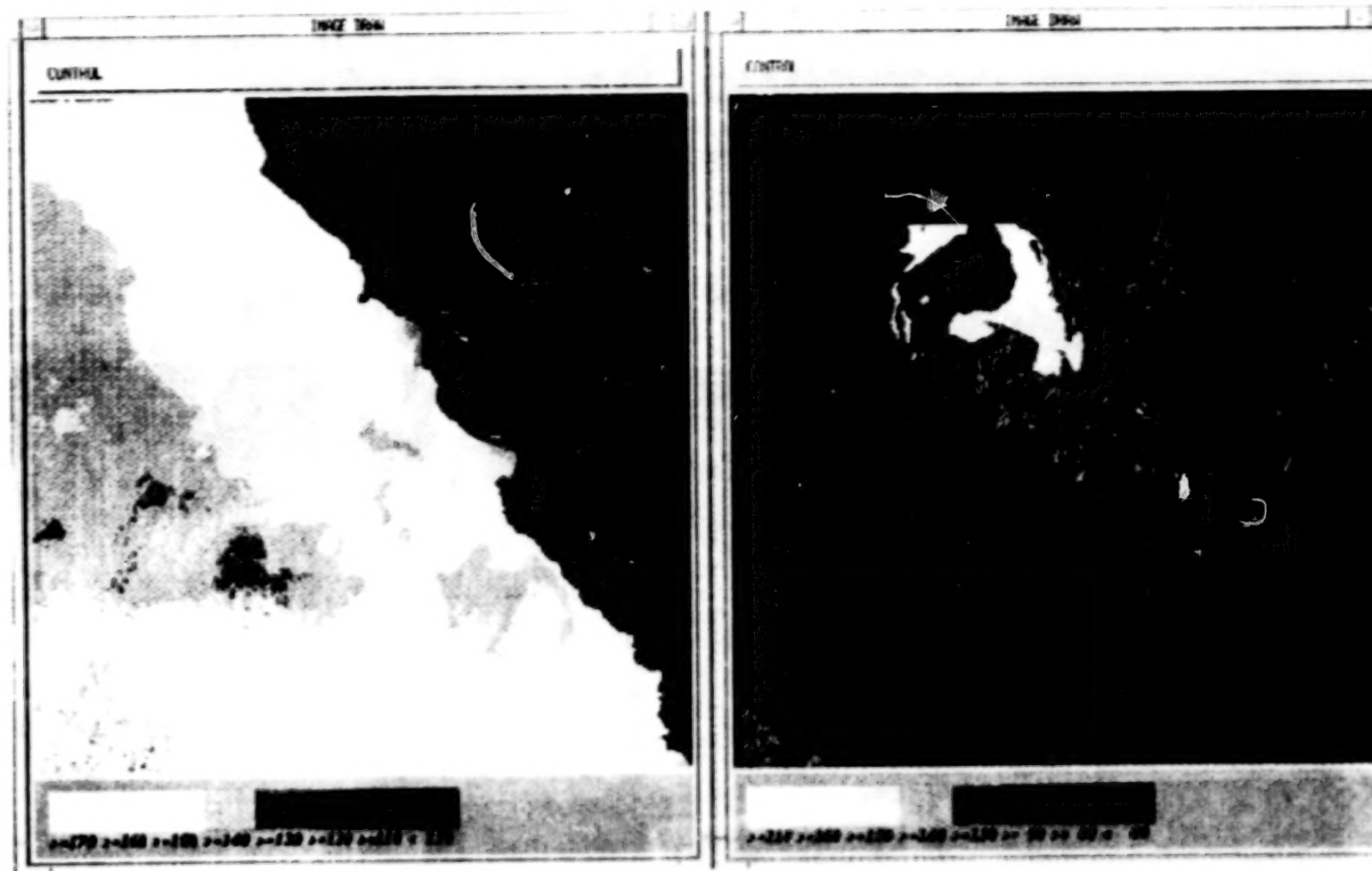


Figure 10. Year 91 Julian Day 134 Time 2100Z
(a) Original image
(b) Upwelling in analysis area (threshold = 2.5°C)

000186

000183

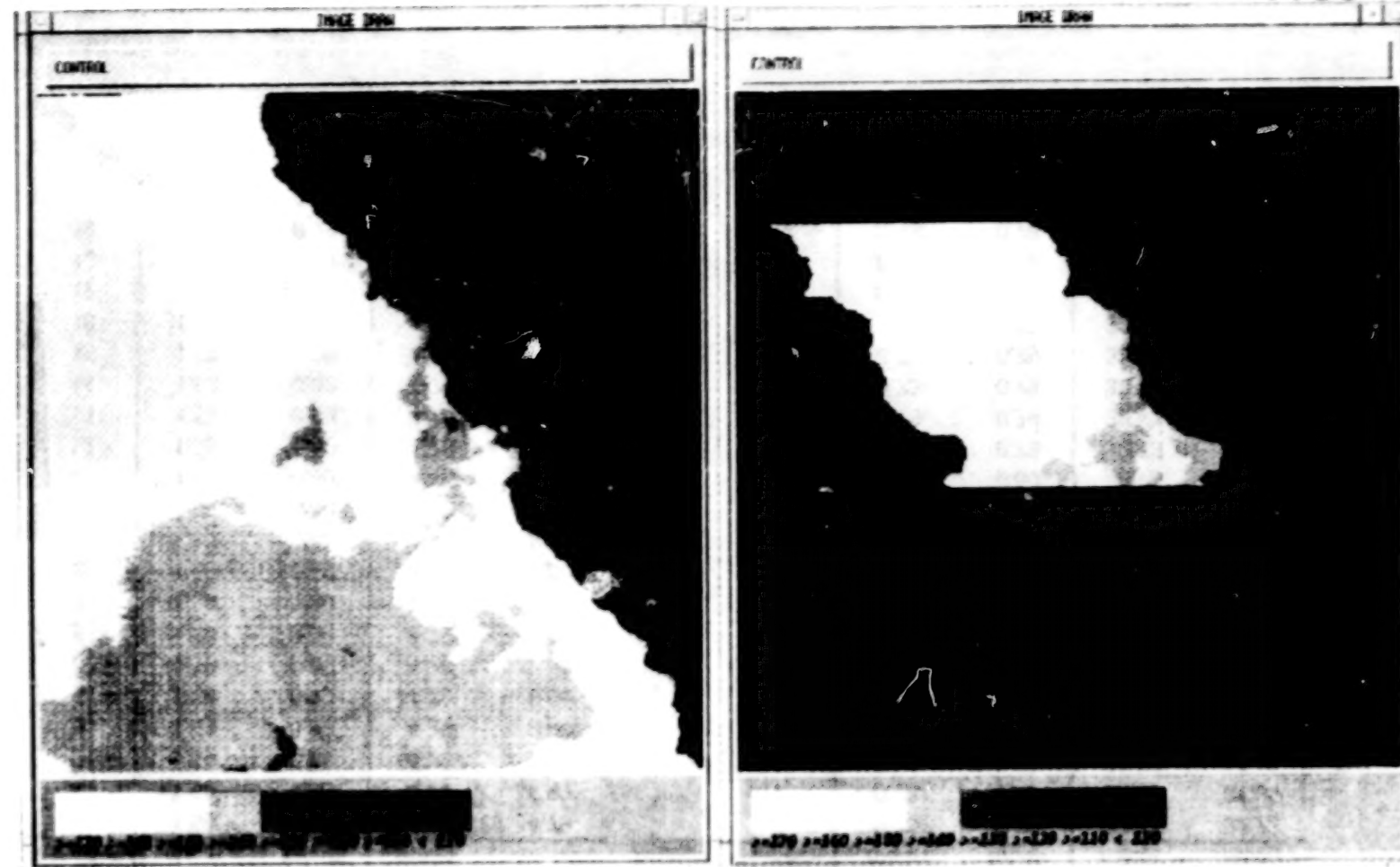


Figure 11. Year 91 Julian Day 119 Time 2100Z
 Reconstruction of test image
 (a) test image from Year 91, Julian Day 119, Time 2100Z
 (b) 8 mode reconstruction of a

000187

TABLE 3. ERRORS IN RECONSTRUCTING TWO IMAGES AS A FUNCTION OF NUMBER OF MODES USED

image 8	rms temperature error (deg C)		misclassification rate (%)	
# modes	mean	recon	mean	recon
0	1.59	1.59	4.79	4.79
1	1.59	1.03	4.79	4.23
2	1.59	0.82	4.79	0.00
3	1.59	0.82	4.79	0.00
4	1.59	0.80	4.79	0.00
5	1.59	0.80	4.79	0.00
6	1.59	0.80	4.79	0.00
7	1.59	0.80	4.79	0.00
8	1.59	0.80	4.79	0.00
9	1.59	0.80	4.79	0.00
10	1.59	0.80	4.79	0.00
11	1.59	0.80	4.79	0.00
12	1.59	0.80	4.79	0.00
13	1.59	0.80	4.79	0.00
14	1.59	0.80	4.79	0.00
15	1.59	0.80	4.79	0.00
16	1.59	0.80	4.79	0.00
17	1.59	0.79	4.79	0.00
18	1.59	0.79	4.79	0.00
19	1.59	0.79	4.79	0.00
20	1.59	0.78	4.79	0.01

image 14	rms temperature error (deg C)		misclassification rate (%)	
# modes	mean	recon	mean	recon
0	0.73	0.73	32.73	32.73
1	0.73	1.05	32.73	31.95
2	0.73	0.98	32.73	16.16
3	0.73	0.94	32.73	15.98
4	0.73	0.91	32.73	12.63
5	0.73	0.91	32.73	12.51
6	0.73	0.85	32.73	10.12
7	0.73	0.85	32.73	9.95
8	0.73	0.82	32.73	7.07
9	0.73	0.80	32.73	5.26
10	0.73	0.80	32.73	4.90
11	0.73	0.80	32.73	4.13
12	0.73	0.79	32.73	3.97
13	0.73	0.79	32.73	3.92
14	0.73	0.79	32.73	3.82
15	0.73	0.79	32.73	3.80
16	0.73	0.78	32.73	3.67
17	0.73	0.78	32.73	3.62
18	0.73	0.78	32.73	5.87
19	0.73	0.78	32.73	5.88
20	0.73	0.78	32.73	5.89

BLANK PAGE

TABLE 4. COMPARISON OF ERRORS IN MEAN AND 8 MODE RECONSTRUCTED IMAGES FOR 21 IMAGES USED TO DEFINE MODES

Defining Image	mns temperature error (deg C) mean	misclassification rate (%)			
		8 modes	mean	8 modes	improve
1	4.01	0.81	6.07	1.28	4.79
2	4.17	0.83	13.07	11.23	1.84
3	3.89	0.85	6.12	5.31	0.81
4	0.63	0.86	9.31	5.66	3.65
5	1.82	0.89	36.76	27.31	9.45
6	2.19	0.85	43.19	42.60	0.59
7	3.50	0.84	42.65	32.44	10.21
8	1.59	0.80	4.79	0.00	4.79
9	0.90	0.83	11.39	3.94	7.45
10	0.49	0.83	3.91	2.45	1.46
11	0.59	0.83	6.18	2.92	3.26
12	0.83	0.81	9.93	7.95	1.98
13	0.69	0.82	40.89	15.4	25.49
14	0.73	0.82	32.74	7.07	25.67
15	0.65	0.85	11.26	13.86	-2.6
16	0.87	0.83	8.04	20.76	-12.72
17	1.19	0.84	5.44	5.05	0.39
18	1.91	0.85	21.93	1.40	20.53
19	1.22	0.84	21.87	2.61	19.26
20	1.54	0.79	13.75	1.23	12.52
21	0.63	0.84	62.24	33.25	28.99
average:	1.62	0.83	19.60	11.61	7.99

TABLE 5. COMPARISON OF ERRORS IN MEAN AND 8 MODE RECONSTRUCTED IMAGES FOR 14 TEST IMAGES

Defining Image	mns temperature error (deg C) mean	misclassification rate			
		8 modes	mean	8 modes	improve
1	4.18	0.68	13.94	13.81	0.13
2	3.28	0.44	11.76	9.54	2.22
3	1.99	1.10	4.86	0.90	3.96
4	0.91	0.67	8.74	4.18	4.56
5	1.90	0.74	24.20	20.28	3.92
6	0.93	0.54	13.79	5.98	7.81
7	0.97	0.44	4.59	3.95	0.64
8	0.80	0.53	29.06	13.25	15.81
9	1.12	0.51	34.98	21.47	13.51
10	0.79	0.42	13.46	6.00	7.46
11	0.60	0.42	16.94	7.80	9.14
12	0.90	0.46	18.57	8.19	10.38
13	0.74	0.43	27.53	18.67	8.86
14	0.99	0.58	66.12	20.94	45.18
average:	0.96	0.38	13.74	7.38	6.36

3.3 NEURAL NETWORK TRAINING.

A neural network is a set of connected nodes that emulate the circuitry of neurons in a biological system. As Figure 12a shows, a layer of input nodes is multiply connected to a set of nodes in another, "interior", layer (many input nodes to one interior node and each input node to many interior nodes). These nodes may, in turn, be multiply connected to nodes in a still different layer, and so on until the final layer of nodes which we call the output layer. Information is processed in the network by passing it from the input layer through the intervening layers to the output layer. At each step the information is operated on by weighted connections and a non-linear transform. That is, information is presented at each node in the input layer. The information presented to the input node can be as simple as a binary digit (0 or 1), or as complex as needed (such as a signed, complex, double precision number). The information is passed to every node in the next layer for which a connection has been defined, but is multiplied by a number, i.e. "weight", that is unique for a given connection. At each node in the next layer all the weighted inputs connected to it are combined, often summed. The combined value is then transformed to a new number through a non-linear transform like the sigmoid in Figure 12b. The purpose of the non-linear transform is to prevent very large positive or very large negative values from overwhelming the values in a layer. For the sigmoidal transform, all sums are constrained to lie between zero and one. The transform is sensitive to changes near the middle of the range, but insensitive to changes at large positive or negative values. This emulates the saturation of neurons and provides a neural network with its characteristics of graceful degradation in the absence of data and insensitivity to noise. A network is defined by the number of nodes in its input, interior, and output layers, the weights of each connection, and its non-linear transform function.

The weights for each connection are not established *a priori*, but, again in analogy with the nervous system in animals, are learned by forcing a given input to produce a known output. The process of adjusting weights to give desired answers is called training, and the set of given inputs with known outputs is called the training set. Several methodologies are in use for training networks. Once trained, a network can be built that very rapidly produces output values when presented with an input set. Currently, networks are built in software, functioning on a single central processing unit (cpu) rather than as truly multiply connected circuits. The potential exists for hardware neural networks that will operate many thousands of times faster than the software versions.

Our purpose here is to design and train a neural network that will estimate upwelling below clouds. Our design calls for the input layer to consist of 40,000 nodes, each of one byte representing the pixel values of an image with clouds and noise. Our output layer consists of eight nodes, one each for the eight mode amplitudes necessary to approximately reconstruct an entire image in the area of interest. We want to use such a network as part of a system to estimate upwelling below clouds.

Since the size of the Phase I effort precluded much experimenting with network characteristics, we employ a network configuration that builds on our previous experience. Our network is in no sense optimal. Based on previous experience, we introduce one interior layer of nodes to allow the network to retain other clues about the input imagery that may help the network assign values to the 8 output modes. Our prior experience had shown better performance with an interior layer with more nodes than the output layer. Our experience also showed *no improvement* in network performance as the number of nodes in the interior layer increased beyond about twice the number of output layer nodes. Network performance did not degrade with more nodes, so the only penalty for selecting a value too large is the increase in the number of connection weights that must be determined. The number of nodes in the interior layer was selected to be 20 with no experimentation to verify the merits of this selection. If this network performs well enough, feasibility is demonstrated, and experimentation to optimize performance can be deferred to later research.

This network has 40,000 times 30, plus 30 times 8, connections (i.e. 1,200,240) connections, and thus needs a great deal of training information. In the 21 to 41 images at our disposal, there are 8 times 41 (i.e., 328) outputs, a number of outputs well short of sufficient to determine 1.2 million connections. We need something on the order of 100,000 images for training. Also, our 41 images have essentially no clouds, so a network trained with them will not have learned how to ignore clouds. Clearly we must generate a large training set and introduce clouds. Our earlier experience with training networks showed the importance of an expansive training set -- without it, we consistently obtained excellent agreement with the few dozen cases in our training set, but very poor agreement with test cases. Our earlier work also showed the necessity of scaling the outputs so that the values at each node vary between 0.0 and 1.0.

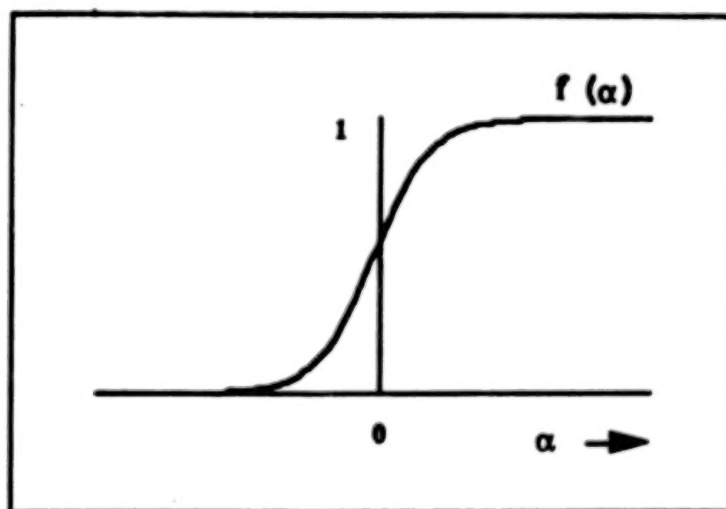
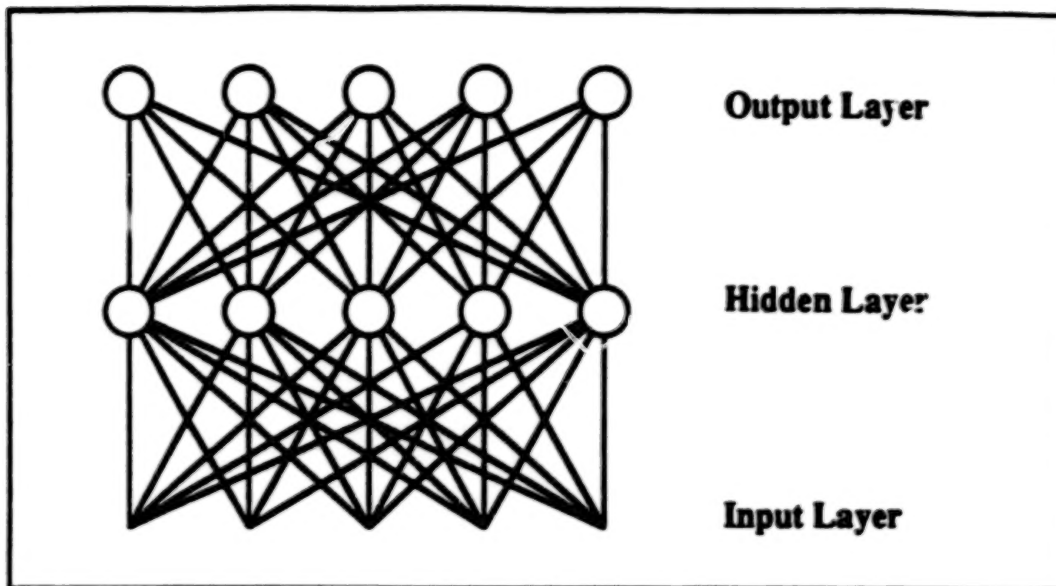


Figure 12. Neural Network Connections and a Non-Linear Transform.

- a) This diagram shows the scheme of connections between an input layer and a hidden layer, and those between the hidden layer and the output layer that constitute the framework of a neural network. Different feed forward weights are assigned to each connection through some learning algorithm.
- b) This plot shows the Sigmoid Transfer function used to combine the contributions at a node via various connections from a previous layer. This nonlinear transfer function gives this type of network many of its distinctive features.

To expand the training set we develop thousands of synthetic images. These synthetic images are constructed by random combinations of our 20 modes. To be sure that the resulting images are realistic we choose amplitudes in the range between the maximum and minimum amplitudes observed in the original set of 21 images for each of the 20 modes. Table 6 lists for each of the 20 modes the range of amplitudes needed to reconstruct the 21 images that defined our principal components. For each synthetic image thus produced, we know the values of the eight mode amplitudes that belong on the output nodes of our neural network. The other 12 modes add realistic noise to our synthetic images because the amplitudes of the last 12 modes are not provided to the network. By this method we generate 7500 synthetic images.

To simulate the effects of clouds, we generate randomly centered and oriented ellipses with a major axis of 100 pixels (110-km) and minor axis of 50 pixels (55-km). This cloud would never obscure more than 50% of the area of interest. By randomly positioning it, most pixels would be obscured at one time or another, preventing the network from keying on a particular pixel or small group of pixels and giving such a small set unwarranted significance. By this method we generated 100 clouds. The range of cloud covers produced by our 100 clouds are presented in Table 7 as a frequency histogram in bins of 10% cloud cover.

We randomly select one of our synthetic images and randomly select one of our 100 clouds and combine them, assigning a pixel the value zero where a cloud occurs. This combined image constitutes the input provided to the network. There are 750,000 different possible synthetic, cloud infested inputs, with small chance of any being equal to one of our real images. The known amplitudes for the first 8 modes are each scaled by its range to lie between 0 and 1 and then provided to the output. The network weights are then adjusted to reduce discrepancies between the network outputs and the correct ones. The process is repeated tens of thousands of times until the network weights begin to converge on a set that minimize the errors in the outputs in a least squares sense. We expect to be satisfied with tens of thousands of iterations, rather than hundreds of thousands, because we don't expect significantly different weights on connections from nodes representing neighboring pixels. Rather, we expect that connections from nodes representing neighboring pixels are similar in weight because the modes we are trying to detect have spatial patterns which usually are correlated over dozens of pixels. The test of our expectations will be how rapidly the network converges on a successful set of connection weights.

TABLE 6. MAXIMUM AND MINIMUM VALUES OBSERVED FOR AMPLITUDES OF 20 MODES AMONG THE 21 DEFINING IMAGES

Mode	maximum Amplitude	Minimum Amplitude
1	6770.31	-5012.91
2	1324.49	-920.74
3	1295.94	-1247.60
4	806.26	-889.14
5	908.60	-570.79
6	698.10	-878.83
7	573.35	-715.42
8	400.44	-413.45
9	397.21	-522.57
10	402.66	-397.42
11	333.69	-436.03
12	717.71	-345.57
13	248.10	-500.93
14	272.36	571.30
15	301.16	-428.85
16	210.13	-471.53
17	261.07	-320.42
18	336.26	-185.14
19	270.16	-230.95
20	271.06	-174.39

TABLE 7. HOW THE 100 RANDOMLY GENERATED CLOUDS PROVIDE A RANGE OF CLOUD COVER PERCENTAGES

CLOUD COVER PERCENT BIN	NUMBER OF OCCURRENCES
0%	27
0 to 10%	34
10 to 20%	20
20 to 30%	9
30 to 40%	6
40 to 50%	4
0 inclusive to 50%	100

As stated earlier, there are several methods available to adjust weights in the network but limited resources for Phase I compel us to rely on prior experience and existing capability. Based on previous work, we favor the back propagation algorithm and employ in the present study software we had already developed to implement it. Our C language software was modified to handle different input and output array sizes and to operate on the SUN 4/330 SPARCStation to take advantage of its 40 Megabyte random access memory (RAM), and large virtual memory, and fast speed cpu.

Even on the capable SUN machine made available for this work, the back propagation algorithm takes almost 30 seconds to adjust weights for one training image -- 50,000 iterations takes over 17 days. The network was trained for most of the time from 2 through 18 December 1992. Figure 13 plots the root mean square (rms) error between the network values and the correct values for 100 sequential occurrences of each of the 8 modes in the training set. The rms error declines throughout the 50,000 iterations, from about 20% errors in modes two through 8 over the first 100 iterations to about 15% errors in those same modes over the last 100 iterations; there is a slight tendency for the lower, more significant modes, to have smaller errors than the higher modes. Separate from the pack made up of the other modes, mode one starts off at only a 10% error over the first hundred iterations and decreases to about 6% error in the last 100 iterations. Thus Figure 13 shows that throughout this interval the neural network outputs continued to converge on the correct values. Training stopped at this point to allow testing of the network's performance in terms of rms temperature error and misclassification rates of the image reconstructed from the output amplitudes.

The network performance is next tested on 2079 input images constructed from the 21 original images each masked by 99 clouds in turn (the 100th cloud cover, another case of 0% coverage, was skipped). These 2079 images are expected to be different than any of the synthetic images upon which the network was trained, so they provide a true test of the network's performance. Running the network in a forward direction after the weights have been set takes much less time than adjusting weights with the back propagation scheme -- about 1 versus 30 seconds, including all disk access and input/output time. The mode amplitudes output by the network are then rescaled, multiplied by the appropriate modes, and added together with the mean to produce a neural network image. The difference between the neural network image and the original cloud free image are measured using both rms temperature difference and misclassification rate. These differences are then compared to the differences already observed between the mean temperature field and the original images.

For the method to be considered feasible, the network images must agree with the original cloud free images better than the mean image agrees with the original. The best we can hope for is that the neural network images perform almost as well as the 8 mode reconstructions operating on cloud free images.

001000

730

RMS for Neural Network Training on 7500 Synthetic Images
30 Hidden nodes - 40000 input nodes - 8 mode output

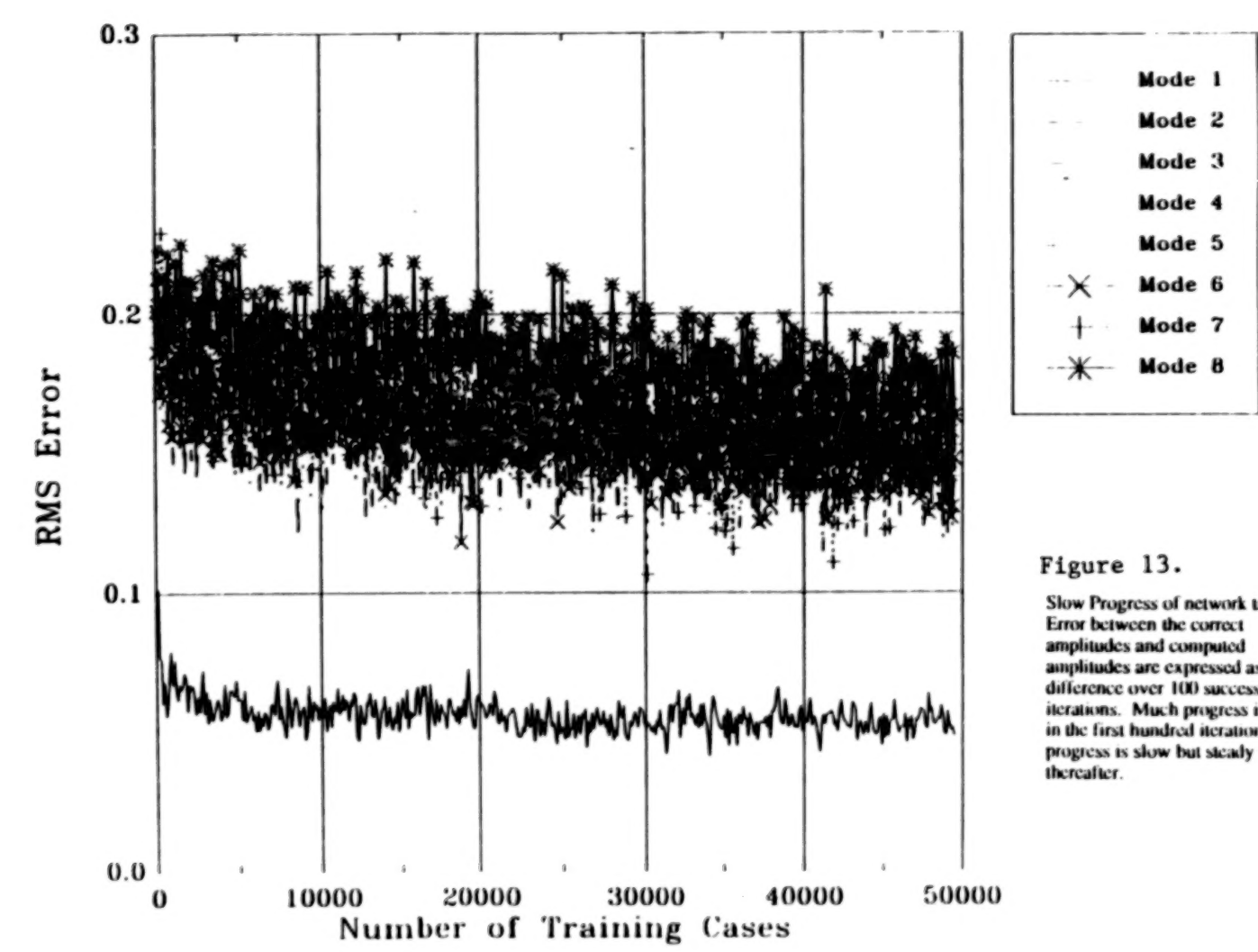


Figure 13.
Slow Progress of network training.
Error between the correct
amplitudes and computed
amplitudes are expressed as rms
difference over 100 successive
iterations. Much progress is made
in the first hundred iterations and
progress is slow but steady
thereafter.

000194

BLANK PAGE

4. RESULTS OBTAINED.

Table 8 (based on rms temperature differences) and Table 9 (based on misclassification rates) compare the performance of three approximations to the 21 original cloud free images in the area of interest. The first approximation is the mean of all 21 images, and the second approximation is the 8 mode reconstructions -- both these results already appear in Table 4 and are based on cloud free imagery. Recall the result of that comparison: 8 mode reconstructions are superior to the mean field and represent an improvement of about a factor of two.

The third approximation, offering a new set of comparisons, is the neural network image generated from cloud infested inputs. The differences from the original are presented for all cloud covers combined and are also broken out by cloud cover in 10% bins. The result of these comparisons is remarkable. Overall, the neural network images are superior to the mean field and represent an improvement almost as great as that of the 8 mode reconstructions. Though the improvement decreases somewhat as the cloud cover increases, even up to 50% cloud cover, the neural network provides a better estimate of the temperature field and upwelling region than does the mean field.

5. CONCLUSIONS AND RECOMMENDATIONS

We have shown that a neural network, without benefit of numerical experiments to optimize performance, can produce estimates of sea surface temperature that out perform the mean temperature field in terms of both rms temperature difference and misclassification rate. We expect that it is possible to achieve even better performance with further work.

First, an operational requirement should be established, such as rms errors less than 0.5°C for the reconstructed image. This must be done in the context of the application. Next, the principal component analysis should be revised. The set of images used to define the principal components should be expanded and cleaned up to remove land registration problems. We would like to improve the fit of principal component reconstructions to exceed the operational requirement, since this is a limiting factor on the neural network performance. Next, the neural network will be retrained, experimenting with number of nodes in the internal layer and other parameters of training, to speed convergence. Finally the network will be run until the operational requirement is met or convergence of weights ceases, whichever comes first.

Next, other methods of fitting the amplitudes to a partially obscured image of SST should be tried. Neural networks have the potential to provide great speed of operation once they are implemented as hardware nets, but their results may not be the most accurate fitting that is possible. Two other interpolation fitting procedures we have used for PC are gradient search techniques and simulated annealing. Both should be implemented and compared to the neural network in terms of both rms temperature error and misclassification rate.

The resulting system can provide an estimate of the sea surface temperature beneath clouds. That estimated temperature field can be used in several ways. It can be used directly, it can be merged with the cloud free portions to produce a composite image, it can be used to initiate another mode fitting process, or it can be used as input to numerical models.

In addition, the process of defining modes and fitting amplitudes can be modified for other applications. The resolution can be reduced and the area of interest can be expanded for a system of the same complexity, or using more capable computer equipment in the training process, a larger neural network can be developed with the same resolution but expanded area of interest. The system can be defined to operate on other imagery, from LANDSAT/SPOT or SeaWiFS. Also possible is a system with two input images from different sensors, one from a cloud infested sea surface temperature sensor, the other from a radar imager such as a synthetic aperture radar (SAR). The system would use information in the SAR imagery to cue the amplitudes for the modes in the temperature field.

Once the useful system has been defined it can be periodically updated, say annually, with the most recent year's clear imagery. New principal components would be defined and a new training session executed if needed.

001000

732

TABLE 8. COMPARISON OF ERRORS IN MEAN AND 8 MODE RECONSTRUCTED IMAGES AND NEURAL NETWORK OUTPUT FOR 21 IMAGES USED TO DEFINE MODES

Defining Image #	rms temperature error (deg C)								
	mean	PCA 8 modes	Neural Network (by cloud cover)						
			0 to 50%	0%	0 to 10%	10 to 20%	20 to 30%	30 to 40%	40 to 50%
1	4.01	0.81	0.54	0.50	0.51	0.59	0.57	0.57	0.66
2	4.17	0.83	0.74				0.81		
3	3.89	0.85	0.54				0.61		
4	0.63	0.86	0.62				0.60		
5	1.82	0.89	1.15				1.10		
6	2.19	0.85	1.58				1.52		
7	3.50	0.84	0.53				0.52		
8	1.59	0.80	1.60				1.66		
9	0.90	0.83	0.60				0.57		
10	0.49	0.83	0.94				0.95		
11	0.59	0.83	0.74				0.68		
12	0.83	0.81	1.51				1.42		
13	0.69	0.82	0.64				0.75		
14	0.73	0.82	0.96				0.98		
*15	0.65	0.85	0.62				0.59		
*16	0.87	0.83	0.71				0.69		
17	1.19	0.84	0.61				0.65		
18	1.91	0.85	1.00				1.16		
19	1.22	0.84	0.57				0.63		
20	1.54	0.79	0.86				0.89		
21	0.63	0.84	1.26	1.30	1.30	1.22	1.19	1.14	1.07
average:	1.62	.83	.87	.84	.86	.89	.88	.91	.95

000196

201000

733

TABLE 9. COMPARISON OF ERRORS IN MEAN, 8 MODE RECONSTRUCTED IMAGES WITH NEURAL NETWORK OUTPUT FOR 21 IMAGES USED TO DEFINE MODES

Defining Image #	misclassification rate (%)								
	mean	PCA 8 modes	Neural Network (by cloud cover)						
			0 to 50%	0%	0 to 10%	10 to 20%	20 to 30%	30 to 40%	40 to 50%
1	6.07	1.28	1.29	1.29	1.29	1.29	1.30	1.28	1.34
2	13.07	11.23	13.85				13.80		
3	6.12	5.31	9.59				9.59		
4	9.31	5.66	8.90				8.73		
5	36.76	27.31	22.73				24.49		
6	43.19	42.60	36.43				40.98		
7	42.65	32.44	25.82				27.32		
8	4.79	0.00	0.01				0.00		
9	11.39	3.94	4.86				4.69		
10	3.91	2.45	5.69				3.23		
11	6.18	2.92	4.18				4.72		
12	9.93	7.95	5.38				5.26		
13	40.89	15.40	26.62				35.25		
14	32.74	7.07	20.02				19.32		
*15	11.26	13.86	6.49				6.20		
*16	8.04	20.76	8.06				8.56		
17	5.44	5.05	2.16				3.42		
18	21.93	1.40	13.82				16.79		
19	21.87	2.61	13.35				16.37		
20	13.75	1.23	7.25				8.22		
21	62.24	33.25	38.63	36.35	36.41	37.14	39.08	50.05	61.65
average:	19.60	11.61	13.20	12.25	12.39	13.93	14.16	15.30	17.11

000197

We here reprise our main result. Even without optimizing experiments, a neural network has been defined that can provide sea surface temperature fields with 1.1-km resolution that performs better than the mean temperature field in all cases of cloud cover tested (up to 48%). This proves the technique is worthwhile and makes it feasible to attempt to produce a network that, acting alone or in concert with other techniques, can meet operational requirements for real time cloud free sea surface temperature, color, or upwelling. Neural networks can potentially provide several functions in an overall system to classify ocean areas of high productivity important to National Marine Fisheries Service missions of monitoring commercially significant habitats in the Exclusive Economic Zone of the United States.

ACKNOWLEDGEMENTS

This report is based upon work supported by the Department of Commerce under contract number 50-DKNA-2-00125. Any opinions, findings, and conclusions or recommendations expressed in this publication are those of the authors and do not necessarily reflect the views of the Department of Commerce.

REFERENCES

- Cybenko, G., 1988: Continuous Valued Neural Networks with Two Hidden Layers are Sufficient., Technical Report, Department of Computer Science, Tufts University, March.
- Kelly, K., 1988: Comment on 'Empirical Orthogonal Function Analysis of Advanced Very High Resolution Radiometer Surface Temperature Patterns in Santa Barbara Channel' by G.S.E Lagerloef and R.L. Bernstein, *J. Geophysical Research*, 93, C12, 15753-15754, December.
- Lagerloef, G., and R. Bernstein, 1988: Empirical Orthogonal Function Analysis of Advanced Very High Resolution Radiometer Surface Temperature Patterns in Santa Barbara Channel. *J. Geophysical Research*, 93, C6, 6863-6873.
- Molinelli, E., and M. Flanigan, 1989: Preliminary Neural Network Detection of a Gulf Stream in Images of Sea Surface Temperature Gradients. PSI TR 477421.
- Molinelli, E., G. Muncill, and K. Pepe, 1991: Progress with Neural Network Gulf Streams. TR 545445, in *Proceedings: Automated Interpretation of Oceanographic Satellite Images Workshop*, M. Lybanon, Ed., NOARL SPOOL:321:91, Naval Research Laboratory, Stennis Space Center, MS, February.
- Molinelli, Harpel and Muncill, 1993: SBIR Phase I Final Report: Feasibility of Using Neural Networks in a System to Estimate Upwelling Features. PSI TR 634468.
- Preisendorfer, R., F. Zwiers, and T. Barnett, 1981: Foundations of Principal Component Selection Rules. SIO Ref. Ser. 81-4, Scripps Institution of Oceanography, LaJolla, CA, May.

SESSION VI

TERRESTRIAL AND LAND SURFACE STUDIES AND APPLICATIONS

002.000

000199

BLANK PAGE

MONITORING VEGETATION HEALTH STATUS WITH STEADY-STATE CHLOROPHYLL FLUORESCENCE¹

Arnold F. Theisen and Barrett N. Rock
University of New Hampshire
Durham, NH 03824 USA

ABSTRACT

Steady-state chlorophyll fluorescence provides non-destructive information for the analysis of vegetation health status. White pine (*Pinus strobus* L.), grown in open-top chambers at Acadia National Park, Maine, was subjected to ozone at predetermined levels for short durations. Red/far-red (R/FR) fluorescence ratios increased significantly from pre- to 24 hrs post-fumigation. In July and August 1992, laboratory fluorescence spectrophotometer measurements were made of clonal grafts of white pine, prior to, one hour after, and 24 hrs after exposure to ozone (3 hrs duration at $180 \text{ mm}^3 \text{ m}^{-3}$). The R/FR fluorescence ratio mean ($n = 16$) derived from spectra collected 24 hrs after exposure in July, 1992 was significantly different from the pre-fumigation R/FR ratio mean ($P = 0.10$). In August, 1992, the R/FR ratio mean ($n = 16$) at 24 hrs post-fumigation was significant at $P = 0.05$. August, 1993 measurements, with a different set of white pine exposed to 120 and $220 \text{ mm}^3 \text{ m}^{-3}$ ozone for 3 hrs, produced R/FR ratio means ($n = 6$) at 24 hrs post-fumigation that were significant at $P = 0.05$ and $P = 0.20$, respectively. For white pine exposed to ozone at $120 \text{ mm}^3 \text{ m}^{-3}$, the 1 hr post-fumigation R/FR fluorescence ratio mean exceeded the pre-fumigation R/FR ratio mean with a significance from 90 to 95 percent ($0.10 > P > 0.05$). Differences in the R/FR ratio means of pre- and 24 hrs post-fumigation measurements for 120, 180, and $220 \text{ mm}^3 \text{ m}^{-3}$ ozone indicate dose dependent responses.

At the University of New Hampshire, five replicates of common beans (*Phaseolus vulgaris* L.) were grown in low pH soil (4.9) in July, 1993 and exposed to 6 treatments of cadmium (0 to 50 mg Kg^{-1}). A significant ($r = 0.95$) above ground plant dry weight gradient was produced. Fluorescence intensities in the far-red (735 nm) were strongly correlated with cadmium dose ($r = 0.96$) and with plant dry weight ($r = 1.0$). However, no significant difference ($P = 0.05$) in R/FR fluorescence ratios among the cadmium treatments was noted. Chlorophyll levels, a controlling factor for R/FR fluorescence ratios, were also not significantly different ($P = 0.05$). In April, 1994 the experiment was repeated. Again, a strong correlation between plant dry weight and cadmium dose was noted ($r = 0.95$). In contrast, the April planting did produce a strong correlation between R/FR fluorescence ratios and cadmium dose ($r = 0.91$) and a high correlation between R/FR ratios and dry weights ($r = 0.86$). Preliminary measurements of chlorophyll levels were significantly different ($P = 0.05$) among the treatments, strongly correlated with cadmium dosage ($r = 0.92$) and plant dry weights ($r = 0.96$), and well correlated with the R/FR fluorescence ratio means ($r = 0.85$).

1. INTRODUCTION

The results in this report represent a portion of the ongoing study of the use of steady-state chlorophyll fluorescence as a tool for the early detection of stress in vegetation due to abiotic factors. The two examples provided show the potential of the fluorescence technique whether the source of the stressing factor is airborne (ozone) or taken up by the vegetation root system (cadmium). Although the manner in which the two agents affect the vegetation is different, and the visible symptoms of damage done by sufficient levels of the two agents is also different (chlorotic tip burn, and severe stunting and deformation), pre-visual detection of stress due to either is possible with the same method. The following paragraphs give a brief description of fluorescence and the basis for the use of steady-state chlorophyll fluorescence as a remote sensing tool.

¹Research supported by a NASA grant for the Spectral Characterization of Ozone Damage in Boreal Forest Species, NAGW2741, the National Park Service cooperative agreement CA-1600-9-8005 with the University of New Hampshire, by NRSP-3, scientific contribution #1815 from the New Hampshire Agriculture Experiment Station, and by the US Army Topographic Engineering Center.

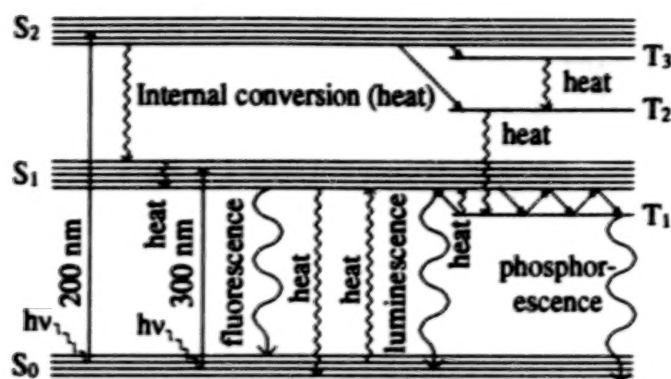


Figure 1. Jablonski Diagram of electron energy action and emission upon photon excitation. S_0 is the ground state, S_1 is the first singlet excited state, S_2 is the second excited state, and T_{1-3} are the excited triplet states. The figure combines elements from similar diagrams in Hercules (1966) and Lumb (1978).

1.1 FLUORESCENCE AND CHLOROPHYLL FLUORESCENCE

Fluorescence arises from the excitation of an electron in an atom, ion, or molecule, from the ground state (S_0) to some level of an excited singlet state (usually S_1 or S_2) by the energy it receives from a photon, and the subsequent path back to the ground state, first by internal conversion to heat, until the excited electron reaches the lowest level of S_1 . From that energy level it makes the photon-releasing radiative transfer back to S_0 (Fig. 1). The released photon has a longer wavelength than the exciting photon resulting from the loss of energy as heat. The difference in wavelength is known as a Stokes' shift (Hercules, 1966; Lumb, 1978). The loss of energy by heat takes place within 10^{-12} seconds and the radiative decay, or fluorescence, occurs within 10^{-9} seconds. An alternative way of expressing this phenomenon is that a singlet-singlet transition produces "prompt" fluorescence.

When an excited electron is passed from a singlet excited state (i.e. S_2) to a triplet excited state (T_3 or T_2), decays through heat loss to the lowest triplet level (T_1), and returns from that triplet state, radiatively, to the ground state (S_0), the emission is termed phosphorescence. The decay time is much longer than for fluorescence and can take from milliseconds to tens of seconds. While a singlet-triplet transition is formally forbidden by quantum mechanics, Lumb (1978) explains that there is still a finite rate constant of approximately 10^6 s^{-1} , and the long-lived phosphorescence emission is the result of this large rate constant. The phosphorescence transitions also produce an emission spectrum different from fluorescence.

Luminescence has had multiple meanings applied to it. D.M. Hercules (1966) states that luminescence is the radiation emitted by a molecule or atom after it has absorbed energy to go to an excited state, and further that, as far as the analytical chemist is concerned, luminescence is the inclusive term for fluorescence and phosphorescence. M.D. Lumb (1978) subdivides luminescence into photo-, cathodo-, radio-, bio-, thermo-, sono-, and electroluminescence according to the exciting process. When the intention is to relate the spectral emission studies of plants to the natural environment, it is assumed that the excitation energy will be from UV or visible light, which would therefore refer to photoluminescence. Photoluminescence is further subdivided by Lumb dependent on whether the material being excited is organic or inorganic. That inorganic materials are held together by ionic and covalent bonds, and organic materials are held together by van der Waals forces between molecules is the basis for Lumb creating these separate categories. Whereas the emissions of inorganic materials are associated with defects or impurities in a crystal lattice, or the excited states of isolated atoms or ions, organic materials owe their emissions to the excited states of delocalized π -electrons of whole molecules. In the study of vegetation, luminescence refers to the delayed fluorescence phenomenon (Fig. 1).

Energy from a wide range of the UV and visible spectrum can be absorbed for use by leaves, needles, or even bark by chlorophyll and other molecules. This is called light harvesting, and the molecules responsible are known collectively as light harvesting complexes (LHCs) and antenna pigments. The absorbed energy is then transferred from one molecule to another, sometimes in a so-called "random walk" (see Fig. 2), until it reaches a special chlorophyll molecule known as a reaction center (RC). This "bucket brigade" passage of

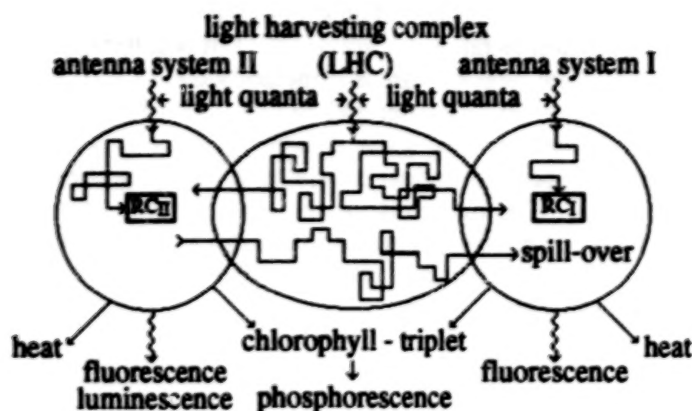


Figure 2. Tripartite model for the antenna system. Absorbed quanta are funneled by multiple resonant energy transfer steps into reaction centers (RC_{II} and RC_I). Energy is lost by the processes of heat, fluorescence, luminescence, and phosphorescence (Junge, 1977, figure 2).

energy is called the Förster mechanism after its discoverer (Junge, 1977). When the RC receives energy to excite one of its π -electrons the excitation energy is not passed on. Rather, an electron is lost to a pheophytin molecule oxidizing the RC. The oxidized RC cannot accept additional excitation energy from the LHC and antenna pigments and, if the RC is not returned to the reduced state rapidly enough, the excited π -electron of this chlorophyll molecule can drop to the ground state releasing a new photon known as chlorophyll fluorescence.

In a healthy, mature, green leaf in direct sunlight the apparatus of photosynthesis should be functioning to maximum capacity, assuming that there is no lack of water or required nutrients, that the leaf is adapted to function in direct sunlight and will therefore not be suffering from photoinhibition, and further that temperature and vapor-pressure-deficits are within optimal ranges. This leaf will absorb between 44 and 88 percent of the photosynthetically active radiation (PAR, 400-700 nm) available at its surface. Far-infrared radiation also reaches the leaf from the surrounding environment and is a contributing factor in raising electrons to excited states, higher levels within excited states, or even to different states (i.e. the triplet-singlet transition producing delayed fluorescence or luminescence; see Fig. 1). The leaf also emits far-infrared radiation at levels that, normally, exceed 50 percent of the total solar and far-infrared energy it receives, and can exceed 80 percent of the total received energy.

At moderately high light levels ($800 \text{ mol quanta m}^{-2} \text{ s}^{-1}$) only 10-50 percent of incident light energy is used for photosynthesis, and in full sunlight ($2000 \text{ mol quanta m}^{-2} \text{ s}^{-1}$) the percentage is even lower. The excess energy is mainly lost as heat, with some fluorescence (Walker, 1992). Under these conditions the system is overexcited, all the RCs are oxidized most of the time, and excess excitation energy not lost as heat cannot be passed on as an electron to pheophytin, or is passed back to the LHCs or antenna pigments. The chlorophyll molecules will dissipate the excess energy as fluorescence rather than as phosphorescence or luminescence.

1.2 THE RED/FAR-RED FLUORESCENCE RATIO

The ratio of red (ca 680 nm) to far-red (ca 740 nm) emission was recognized by Lichtenthaler et al. (1986) to be an indicator of physiological activity, in addition to being a measure of relative chlorophyll content. Incubating a leaf with the herbicide diuron (DCMU) greatly increases red and far-red emission intensity, although red emission is increased to a greater degree than is far-red emission (Lichtenthaler et al., 1986). Diuron acts to block the Q_B binding site, a major link in the electron transport pathway between photosystem II (PSII) and photosystem I (PSI), interfering with the electron transport process.

Fluorescence at 690 nm was compared to that at 735 nm by Lichtenthaler and Rinderle (1988) for several plants and different chlorophyll contents of those plants. For Norway spruce (*Picea abies* (L.) Karst.), the ratio F_{690}/F_{735} varied directly with chlorophyll content which increases up to a point as a plant matures, and decreases under conditions of stress, such as mineral or water shortage or excess, as well as high light or

heat. The increase in the F690/F735 ratio with loss of chlorophyll is explained by a decrease in self absorption by chlorophyll in the red spectral region (Krause and Weis, 1991). It is generally accepted that the fluorescence peak in the red portion of the spectrum near 685 nm is principally due to PSII emission, and the fluorescence peak near 735 nm is principally due to PSI (Strasser and Butler, 1977; Mullet et al., 1980; Stahl et al., 1988; Gruszecki et al., 1991), although there is still some disagreement as to whether PSI makes a significant contribution to the 735 nm emission peak at normal physiological temperatures (Krause and Weis, 1991). At normal physiological temperatures, 735 nm emission is less variable than 690 nm emission and the effectiveness of the F690/F735 fluorescence ratio, in relation to electron flow, may be due to low sensitivity of PSI fluorescence in response to PSI photochemistry changes, whereas PSII fluorescence is more responsive to photochemical change (Bradbury and Baker, 1981).

1.3 LISTING OF CONTENTS

1. INTRODUCTION
 - 1.1 FLUORESCENCE AND CHLOROPHYLL FLUORESCENCE
 - 1.2 THE RED/FAR-RED FLUORESCENCE RATIO
 - 1.3 LISTING OF CONTENTS
2. MATERIALS AND METHODS
 - 2.1 THE OZONE EXPERIMENT
 - 2.2 THE CADMIUM EXPERIMENT
 - 2.3 GENERAL METHODS
3. RESULTS
 - 3.1 OZONE
 - 3.2 CADMIUM
4. DISCUSSION AND CONCLUSIONS
 - 4.1 OZONE
 - 4.2 CADMIUM
5. REFERENCES

2. MATERIALS AND METHODS

2.1 THE OZONE EXPERIMENT

In 1992, current-year needles of two-year old grafted seedlings (ramets) of eastern white pine (*Pinus strobus* L.), from trees in Acadia National Park were used in short-term ozone exposure experiments. Reflectance properties were measured with a Visible/Infrared Intelligent Spectrometer (VIRIS) from Geophysical Environmental Research Corporation; data on the net rates of photosynthesis were collected with a Li-Cor 6200 portable gas exchange analyzer; and fluorescence response was measured with a Perkin-Elmer MPF-44B Fluorescence Spectrophotometer using techniques described below. Ozone was supplied from liquid oxygen using a Griffin Model 1A generator, and ozone levels in open-top chambers were measured with Thermo Environmental Instruments Inc. (TECO) Model 49 monitors².

Pre-fumigation fluorescence measurements were made from 0830 hours to 1200 hours, after the plants had time to reach normal photosynthetic activity, on each of 16 randomly selected ramets to be fumigated and 8 control ramets left unfumigated. Plants were then fumigated from 1200 to 1500 hours with ozone levels of 180 $\mu\text{mol m}^{-3}$ maintained for 3 hours to simulate the average high concentration ozone episodes on record for Acadia National Park (personal communication, Robert Breen). The 1 hr post-fumigation measurements were made from 1600 to 1700 hours on fumigated ramets only due to the low sun angle and presence of a small mountain, the Beehive, east of the investigation site. It was decided that the measurement of the control plants would be invalid because conditions were not consistent with the treated ramets. The 24 hour post-fumigation measurements were begun two hours early (1400 hours) to include all control as well as all treated ramets.

²Reference to brand names is made as a matter of convenience and does not imply endorsement by the authors, the University of New Hampshire, or any of the sponsors of this research.

In August, 1993, the short-term experiment was repeated with ramets from a different set of white pines from the park area. The trees were divided randomly into three groups of 6 ramets each, one group for control, and one group each for fumigation at 120 and 220 $\text{mm}^3 \text{m}^{-3}$ ozone for 3 hours. Control plants were not measured at the 1 hr post-fumigation time.

2.2 THE CADMIUM EXPERIMENT

Experiments conducted at the University of New Hampshire in 1993 and 1994 involved the growing of bean plants (*Phaseolus vulgaris* L.) in a greenhouse in soil contaminated with predetermined levels of cadmium. Low pH forest soil, to ensure the mobility of cadmium cations, was screened, thoroughly blended with additions, and distributed to 6 in. pots. A cadmium chloride (CdCl_2) solution was prepared to provide 5 replicates of 5 treatments at 10, 20, 30, 40, and 50 mg Kg^{-1} Cd compared to the weight of soil found in a single pot, plus a control of 0 mg Kg^{-1} Cd. Because the soil was deficient in magnesium and raising the pH was not desirable, Epsom salt, at 600 mg Kg^{-1} , was added to the soil in each pot. An initial fertilization of the soil was provided with the inclusion of 250 mg Kg^{-1} NPK 20-20-20 per pot, and a twice weekly application of NPK 20-20-20 at 24 mg Kg^{-1} was continued until the third trifoliate leaf was fully expanded to ensure that the root mass had enough time to gain access to as much of the Cd contaminated soil as possible. Fluorescence spectral measurements from 650 to 800 nm, at a 470 nm excitation, were taken with the fluorescence spectrophotometer. The two lateral lobes of the third trifoliate leaf were measured and a 1 cm^2 portion was removed for chlorophyll analysis. The above-ground portion of each plant was harvested and the fresh weight was measured. Plants were then oven dried at 70° C for a minimum of 24 hrs and dry weights were taken.

2.3 GENERAL METHODS

The fluorescence spectrophotometer has excitation and emission scanning monochromators with a measuring range from 200 to 900 nm. Adjustable slit widths accommodate bandwidth limiting, and a ratio mode is used to minimize the effects of any potential drift in the excitation source (a 150 watt Xenon lamp powered by a current-stabilized supply). The signal detectors are Hamamatsu R928 photomultipliers. For these experiments, emission intensity levels were collected at 5 nm increments, from 650 to 800 nm with an excitation wavelength of 470 nm. Intensity levels were corrected for the response characteristics of the instrument excitation source, photodetector, and excitation and emission optics that vary with wavelength. The emission spectra thus produced provided the data from which R/FR ratios were derived for analysis. Data were stored in digital format on floppy disk. A light excluding extension was added to the sample compartment to accommodate whole potted plants. This feature allows live plants to be measured repeatedly throughout the growing season, if necessary, without removing portions of leaf or needle material. Any potential adverse effects on the plants due to material removal are therefore avoided. Although this modification was more useful for chronic experiments than for the short-term experiment reported here, the small numbers of available pine ramets in 1992 did require the use of the same samples for both the July and August measurements.

Chlorophyll extractions were made with dimethyl sulfoxide (DMSO) after Hiscox and Israelstam (1979), and the calculations of pigment concentration were based on formulas presented by Lichtenthaler (1987) for 80% acetone following Hiscox and Israelstam's use of Arnon's formulas for 80% acetone. The process is straight forward: a leaf sample (1 cm^2), collected from a leaf lobe so as to include the area of fluorescence measurement, is placed in a vial with 7 ml of DMSO and incubated at 65° C until the leaf material no longer retains any color. The leaf sample is then removed from the solution which is, in turn, brought to 10 ml by adding more DMSO. The solution can be measured immediately with an absorption spectrometer or stored at around 4° C for later analysis.

Because of the small number of observations in each statistical sample of the ozone experiments, Student's t test was used. The R/FR fluorescence ratio data used for the analyses presented here meets the qualifying criteria for this test described in Sokal and Rohlf (1981). The t value significance varies with the number of degrees of freedom of the statistical sample, and this was an important consideration for the short-term ozone exposure experiments because sample sizes differed for 1992 and 1993. Standard least squares analysis was used for correlations between variables in the cadmium contamination experiments, and Student's t test was used to evaluate standard analysis of variance (ANOVA) tests of differences among treatments for single variables such as R/FR fluorescence ratios, above ground plant dry weights, and total chlorophyll contents.

3. RESULTS

3.1 OZONE

Normalized mean fluorescence emission spectra for red/far-red emission comparison are presented in Fig. 3. The spectra shown include the pre- (I), 1 hr post- (P), and 24 hrs post-fumigation (D) measurements, respectively, of 16 ramets each for the August, 1992, 180 mm³ m⁻³ ozone exposure (Fig. 3A). August, 1993 measurements of 6 ramets exposed to 120 mm³ m⁻³ ozone collected at the same time steps are plotted in Fig. 3C, and spectra from measurements, also made in August, 1993, of 6 ramets each exposed to 220 mm³ m⁻³ ozone are displayed in Fig. 3E. The mean R/FR ratios, with standard errors, of the fluorescence emission data for the fumigated ramets measured in August, 1992 and 1993 are shown in bar graph format in Figs. 3B, 3D and 3F. Before exposure, the R/FR ratio mean for the 1992 control ramets (0.20, not included in Fig. 3) was not statistically different ($P = 0.50$) from the R/FR ratio mean of the ramets that were fumigated. Although the R/FR ratio mean of the 1992 control ramets at the 24 hour measurement increased to 0.26, this was not significant ($0.25 > P > 0.20$), and the 24 hrs post-fumigation R/FR ratio mean of the 1992 control ramets fell significantly below ($P = 0.05$) the R/FR ratio mean of the 1992 fumigated ramets.

In August, 1993 results in white pine were comparable to the 1992 R/FR ratio means at the 24 hrs post-fumigation measurement. However, in contrast to the responses seen in the 1992 measurement results, the R/FR ratio means for both the 120 and 220 mm³ m⁻³ ozone exposures showed a more immediate response to exposure, as the 1 hr post-fumigation R/FR ratio means were considerably greater than the pre-fumigation R/FR ratio means in both cases, producing t values of 2.14 ($0.10 > P > 0.05$, $df = 5$) and 1.40 ($0.25 > P > 0.20$, $df = 5$) respectively, versus 0.50 ($P = 0.50$, $df = 15$) for the August, 1992 180 mm³ m⁻³ ozone exposures. Comparison between the pre- and 24hrs post-fumigation R/FR ratio means for ramets fumigated at 120 mm³ m⁻³ ozone produced a result more significant ($t = 2.88$, $P = 0.05$, $df = 5$) than the August, 1993 220 mm³ m⁻³ ozone fumigation ($t = 1.67$, $P = 0.20$, $df = 5$), but less significant than the August, 1992 180 mm³ m⁻³ ozone fumigation ($t = 5.50$, $P = 0.05$, $df = 15$). The R/FR ratio mean for control ramets, measured in August, 1993, rose significantly ($0.10 > P > 0.05$) from the pre-fumigation level (0.08) to the 24 hrs post-fumigation level (0.13), but when the spectra and the R/FR ratio means for the 120 and 220 mm³ m⁻³ ozone treated ramets and data from the control ramets were compared, the control R/FR ratio mean was seen to lie significantly below ($P = 0.05$) the R/FR ratio means of the fumigated ramets (data not shown).

Gas exchange measurements for 1992 indicate that the rates of photosynthesis for all ramets were unaffected by ozone treatments (Eckert et al, 1993). White pine was not measured for gas exchange with the August, 1993 experiment. Preliminary assessment of concurrent spectral reflectance measurements indicate that no obvious changes occurred in the visible portion of the spectrum in either 1992 or 1993 between the pre- and post-fumigation measurements (Rock, unpublished data).

3.2 CADMIUM

Thirty five days after planting in July, 1993, data was gathered for 30 bean plants subjected to cadmium doses of 0 to 50 mg kg⁻¹. Mean fluorescence emission spectra ($n = 10$) are shown in Fig. 4. Mean dry weights of above ground growth produced a gradient that was strongly correlated ($r = 0.95$) with cadmium dosage (Fig. 5A). During the analysis of the spectral information, the data for the 40 mg kg⁻¹ treatment was judged to be anomalous due to unknown causes, but is included here for completeness. The mean R/FR fluorescence ratios showed no significant increase ($P = 0.05$) with increased cadmium dosage (data not shown). The chlorophyll content of samples removed from the leaves at the time of the fluorescence measurements also showed no significant differences among the treatments and no correlation with either the cadmium dosages or plant dry weights (data not shown). However, the general increase in the mean fluorescence intensities in the far-red (ca 735 nm, Fig. 4) produced a high correlation with cadmium dosage ($r = 0.96$) when the anomalous 40 mg kg⁻¹ treatment was ignored (Fig. 5B). An even stronger correlation was seen between the mean far-red fluorescence maxima and the mean dry weights ($r = 1.0$, Fig. 5C). All of the measured leaves were a "healthy" dark green.

A second set of beans were planted in April, 1994 using the same soil type, pot sizes, nutrient additives, and cadmium treatments as before, with data collected for fluorescence, dry weights, and chlorophyll content after 39 days of growth. The mean fluorescence emission spectra ($n = 10$) displayed in Fig. 6 show a general increase in fluorescence intensity with cadmium treatment similar to that noted for the beans measured in 1993.

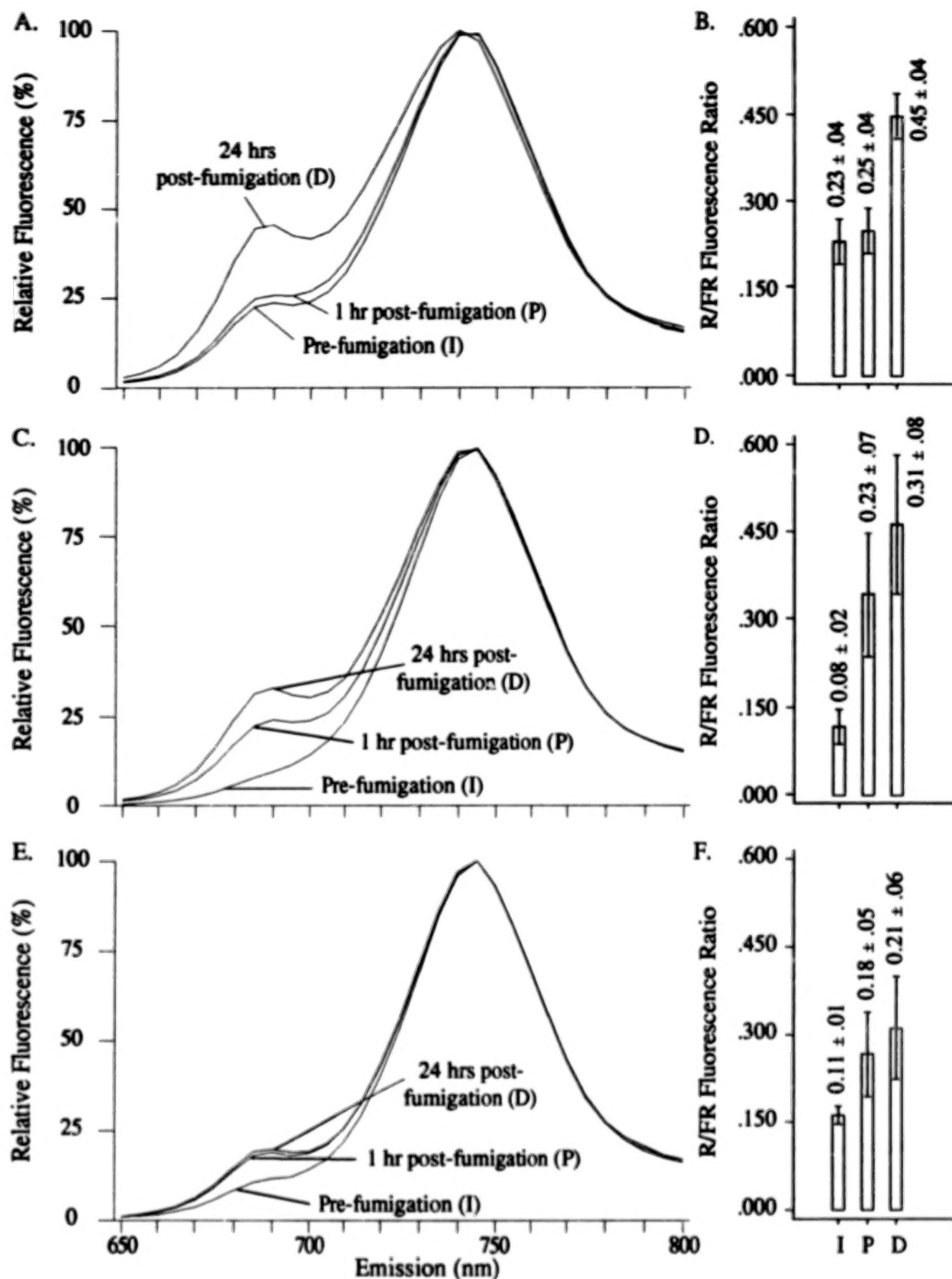


Figure 3. Normalized mean fluorescence emission spectra and the mean R/FR fluorescence ratios, with standard errors, from data collected prior to (I), 1 hr (P), and 24 hrs (D) after ozone fumigation in August, 1992 ($n = 16$, $180 \text{ mm}^3 \text{ m}^{-3}$, A and B) and August, 1993 ($n = 6$, $120 \text{ mm}^3 \text{ m}^{-3}$, C and D; $n = 6$, $220 \text{ mm}^3 \text{ m}^{-3}$, E and F). The excitation wavelength for all measurements was 470 nm.

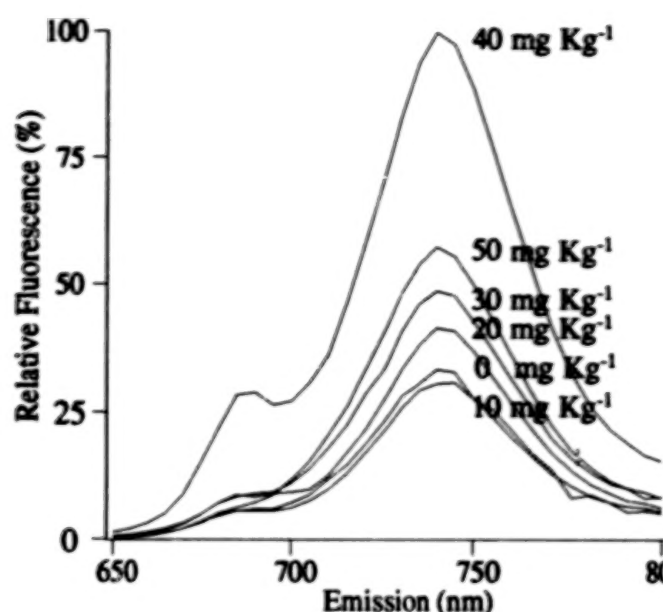


Figure 4. Beans planted in July, 1993 and measured after 35 days, produced mean fluorescence emission spectra shown normalized ($n = 10$). The beans were grown in soil contaminated with predetermined levels of cadmium.

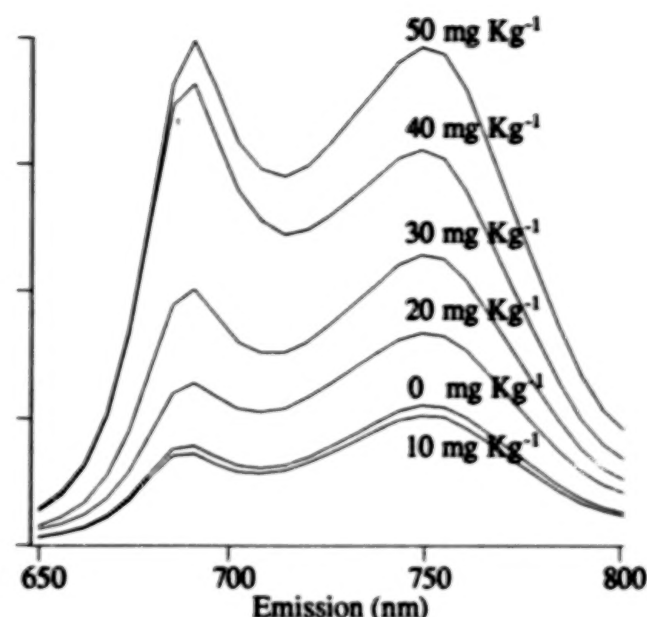


Figure 6. Beans planted in April, 1994 and measured after 39 days, produced mean fluorescence emission spectra shown normalized ($n = 10$). The beans were grown in soil contaminated with predetermined levels of cadmium.

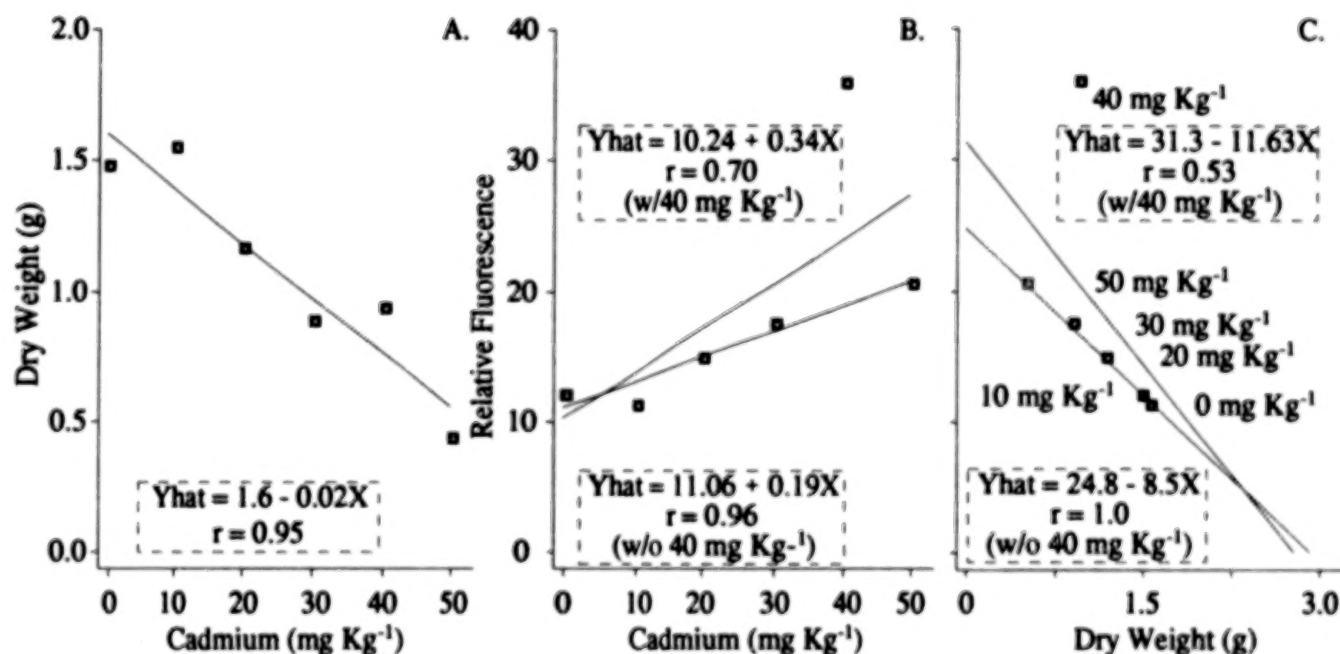


Figure 5. Beans planted July, 1993 were grown in soil contaminated with predetermined levels of cadmium. Correlations between (A) the mean dry weights of above ground growth ($n = 5$) and cadmium dosage, (B) the mean far-red fluorescence maxima ($n = 10$) and cadmium dosage, and (C) the mean far-red fluorescence maxima and the mean dry weights of above ground growth are shown with the least squares fit line for each set of data.

Dry weights for plant above ground growth again produced a strong correlation ($r = 0.95$) with cadmium dosage (see Fig. 7A). The mean far-red fluorescence maxima were also strongly correlated with both cadmium dosage and mean plant dry weights ($r = 0.97$ and $r = 0.91$, respectively in Figs. 7B and 7C). Unlike the plants grown in 1993, mean R/FR fluorescence ratios for the 1994 beans showed strong differences among treatments (i.e. 0 vs 30 mg Kg⁻¹ Cd, $t = 6.2$), a high correlation with cadmium dosage ($r = 0.91$) and a good correlation ($r = 0.86$) with mean plant dry weights (Figs. 8A and 8B). Preliminary measurements of chlorophyll contents of samples from each individual leaf lobe showed significant differences among all the treatments ($P = 0.05$), a strong correlation with cadmium dosage ($r = 0.92$) and mean plant dry weights ($r = 0.96$), and a good correlation with mean R/FR fluorescence ratios ($r = 0.85$). The data for these analyses are shown in Figs. 9A, 9B and 9C). From a qualitative analysis of the measured leaves, it was noted that though they were green, they were not as dark as the leaves from the July planting.

4. DISCUSSION AND CONCLUSIONS

4.1 OZONE

It has been determined that pre-visual evidence of physiological changes in white pine, related to short-term ozone exposure, can be detected with steady-state fluorescence techniques as opposed to the use of visible symptoms, such as chlorotic fleck, chlorotic mottle, and emergence tip burn, that are generally accepted as diagnostic (mites and fungi can cause similar symptoms). Our data show significant increases in R/FR fluorescence ratio means at the 24 hour measurement for the 180 mm³m⁻³ ozone exposure in August of 1992 ($P = .05$) and for the 120 mm³m⁻³ ozone exposure in August, 1993 ($P = .05$). The 220 mm³m⁻³ ozone exposure produced an increase that was not as great ($P = .20$). The reduced response at 220 mm³m⁻³ ozone exposure compared to the 180 and 120 mm³m⁻³ ozone exposures, is consistent with the conclusions of Schreiber et al. (1978) that chronic exposure to lower ozone concentrations can be more injurious than brief exposures to higher, acute exposures.

Significant increases from pre- to 1 hr post-fumigation R/FR ratio mean levels also occurred for both the 120 and 220 mm³m⁻³ ozone exposures ($.10 > P > .05$ and $.25 > P > .20$, respectively). The August, 1992 ramets were the same ramets that were fumigated in July, 1992 and may have suffered some damage or been under some stress, due to handling and measurement, producing a pre-existing condition could that have masked most of the response to the August fumigation, while the 1993 ramets had not been previously exposed to other than ambient ozone. The R/FR ratio mean for the pre-fumigation measurements in August, 1992 is significantly higher than the other two pre-fumigation R/FR ratio means ($P = .05$).

The dramatic increases in R/FR ratio means at the 24 hour measurement seen in the August, 1992 and 1993 white pine data, resulting from an increase in intensity in the red region of the spectrum may be caused by a reduction in chlorophyll levels (Lichtenthaler et al., 1986). However, reflectance parameters such as the red edge inflection point, a good indicator of chlorophyll content (Rock et al., 1988; Vogelmann et al., 1993), showed no change that corresponded to the R/FR ratio mean increases at the 24 post-fumigation measurements in 1992 (Rock, unpublished data). Preliminary analysis of the 1993 reflectance data indicates similar results.

The results of this research are in agreement with the conclusions of previous investigators that white pine does respond, physiologically, to the presence of ozone. The fact that significant fluorescence changes were measured while no significant changes were seen in the reflectance or gas exchange data, indicates that fluorescence monitoring of vegetation in areas geographically and climatologically susceptible to the formation of ozone should be pursued. This monitoring could be accomplished with passive instrumentation that uses the sun as an excitation source (Theisen et al., in press).

4.2 CADMIUM

It has also been determined that R/FR fluorescence ratios can be used to detect different levels of stress in bean plants due to cadmium contamination when that stressing factor affects chlorophyll content. While the cadmium treatments did produce obvious size differences in the bean plants in agreement with most previous studies (Jastow and Koeppe, 1980), the reduction in chlorophyll content did not produce visible differences in the intensity or shades of green among the leaves of the different treatments in the separate studies. The strong

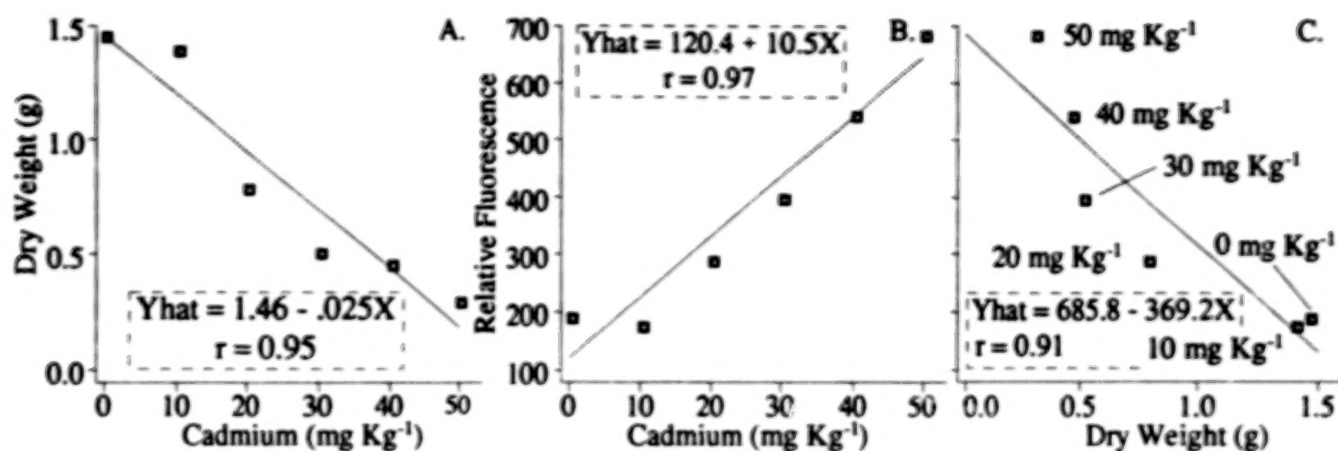


Figure 7. Beans planted in April, 1994. Correlations between (A) the mean dry weights of above ground growth ($n = 5$) and cadmium dosage, (B) the mean far-red fluorescence maxima ($n = 10$) and cadmium dosage, and (C) the mean far-red fluorescence maxima and the mean dry weights of above ground growth are shown with the least squares fit line for each set of data.

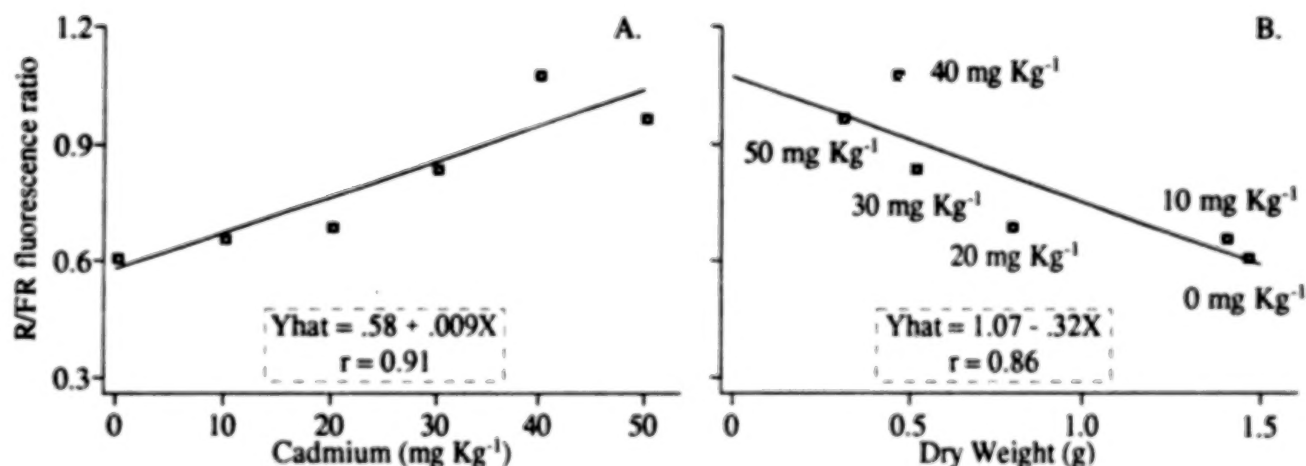


Figure 8. Beans planted in April, 1994. Correlations between (A) the mean R/FR fluorescence ratios ($n = 10$) and cadmium dosage, (B) the mean R/FR fluorescence ratios and the mean dry weights of above ground growth ($n = 5$) are shown with the least squares fit line for each set of data.

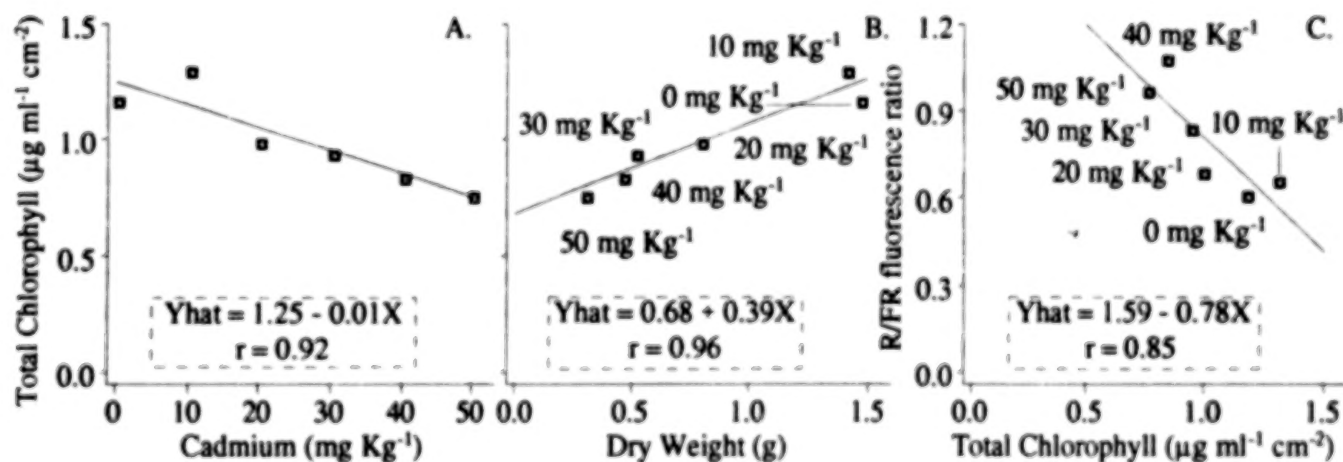


Figure 9. Beans planted in April, 1994. Correlations between (A) the mean total chlorophyll values ($n = 10$) and cadmium dosage, (B) the mean total chlorophyll values and mean dry weights of above ground growth ($n = 10$), and (C) the mean R/FR fluorescence ratios ($n = 10$) and the mean total chlorophyll values are shown with the least squares fit line for each set of data.

correlations between chlorophyll contents and R/FR fluorescence ratios for the April, 1994 plants, and the lack of any differences in either chlorophyll contents or R/FR fluorescence ratios among treatments for the July, 1993 plants is in direct agreement with the conclusions of Lichtenthaler et al. (1986).

In previous studies of vegetation subjected to differing levels of cadmium in the nutrient solutions, the effects were found to be dose dependent. Murata et al. (1970) noted no significant effects on fluorescence yields from isolated spinach chloroplasts doped with concentrations of cadmium below 5 mM. Cadmium at a concentration of 15 mM was found to inhibit electron transport on the electron donor side and action site of PSII (Van Duijvendijk-Matteoli and Desmet, 1975). Uptake of cadmium is also dependent on the concentration in soil (Turner, 1973) and soil pH (Reber, 1989). Although chlorophyll levels have been shown to be reduced in bean seedlings grown only in solutions of cadmium acetate (Padmaja et al., 1990), the greatest amount of cadmium taken up by plants is retained in the roots (Narwal et al., 1990).

The results of the 1993 cadmium study seem to be in agreement with findings of Krupa et al. (1992) who found significantly reduced growth with increased cadmium dosage in beans grown in Hoagland solution, and Turner (1973) who found no change in fluorescence yields. On the other hand, the 1994 results agree with the information provided by Van Duijvendijk-Matteoli and Desmet (1975) that cadmium affects PSII electron transport and therefore R/FR fluorescence ratios (Lichtenthaler, 1986), and Padmaja et al. (1990) who noted reduced chlorophyll levels that would also produce increased R/FR fluorescence ratios (Lichtenthaler and Rinderle, 1988).

The answer to this apparent problem between the two experiments is that, while the variables under direct control of the investigators (e.g. soil type, soil quantity, nutrient additives, and cadmium concentration) were constant for both, growing conditions, even in the greenhouse, differed with the times of the year (i.e. temperature ranges and hours of natural light). That these parameters would have a major effect on the cadmium concentration in the leaves that would determine chlorophyll levels and therefore R/FR fluorescence ratios is a matter for further investigation.

5. REFERENCES

- Bradbury, M. and N.R. Baker, 1981, Analysis of the slow phases of the *in vivo* chlorophyll fluorescence induction curve / Changes in the redox state of photosystem II electron acceptors and fluorescence emission from photosystems I and II, *Biochim. Biophys. Acta*, 635, 542-551.
- Eckert, R., T. Lee, K. Stapelfeldt, A. Theisen, R. Kohut, J. Laurence, and P. King, 1992, Studies to assess the effects of ozone on native vegetation of Acadia National Park. 1992, Annual Report to the Natl. Park Serv., 144 pp.
- Gruszecki, W.I., K. Veeranjaneyulu, B. Zelent, and R.M. Leblanc, 1991, Energy transfer process during senescence: fluorescence and photoacoustic studies of intact pea leaves, *Biochim. Biophys. Acta* 1056, 173-180 (1991).
- Hercules, D.M., 1966, Fluorescence and Phosphorescence Analysis Principles and Applications, Interscience Publishers, 258 pp.
- Hiscox, J.D. and G.F. Israelstam, 1979, A method for the extraction of chlorophyll from leaf tissue without maseration, *Can. J. Bot.*, 57, 1332-1334.
- Jastrow, J.D. and D.E. Koeppe, 1980, Uptake and effects of cadmium in higher plants, in *Cadmium in the Environment Part I: Ecological Cycling*, J.O. Nriagu (ed.), 607-638.
- Junge, W., 1977, Physical aspects of light harvesting, electron transport, and electrochemical potential generation in photosynthesis of green plants, *Encyclopedia of Plant Physiology*, vol 5, Photosynthesis I, 179-186
- Krause, G.H. and E. Weis, 1991, Chlorophyll fluorescence and photosynthesis: the basics, *Ann. Rev. Plant Physiol. Plant Mol. Biol.*, 42, 313-349.

- Krupa, Z., G. Öquist, and N.P.A. Huner, 1992, The influence of cadmium on primary photosystem II photochemistry in bean as revealed by chlorophyll a fluorescence - a preliminary study, *Acta Physiol. Plant.*, 14, 71-76.
- Lichtenthaler, H.K., C. Buschmann, U. Rinderle, and G. Schmuck, 1986, Application of chlorophyll fluorescence in ecophysiology, *Radiat. Environ. Biophys.* 25, 297-308.
- Lichtenthaler, H.K., 1987, Chlorophylls and carotenoids: Pigments of photosynthetic biomembranes, *Methods in Enzymology*, 148, 349-382.
- Lichtenthaler, H.K. and U. Rinderle, 1988, The role of chlorophyll fluorescence in the detection of stress conditions in plants, *Critical Reviews in Analytical Chemistry*, Vol. 19, Supplement 1, CRC Press, Inc, S29-S85.
- Lumb, M.D., 1978, *Luminescence Spectroscopy*, Academic Press, 375 pp.
- Mullet J.E., J.J. Burke, and C.J. Arntzen, 1980, Chlorophyll proteins of photosystem I, *Plant Physiol.*, 65, 814-822.
- Murata, N., H. Tashiro, and A. Takamiya, 1970, Effects of divalent metal ions on chlorophyll a fluorescence in isolated spinach chloroplasts, *Biochim. Biophys. Acta*, 197, 250-256.
- Narwal, R.P., M. Singh, and D.J. Dahiya, 1990, Effects of cadmium on plant growth and heavy metals content of corn (*Zea mays* L.), *Crop Research*, 3, 13-20.
- Padmaja, K., D.D.K. Prasad, and A.R.K. Prasad, 1990, Inhibition of chlorophyll Synthesis in *Phaseolus vulgaris* L. seedling by cadmium acetate, *Photosynthetica*, 24, 399-405.
- Reber, H.H., 1989, Threshold levels of cadmium for soil respiration and growth of spring wheat (*Triticum aestivum* L.), difficulties with their determination, *Biology and Fertility of Soils*, 7, 152-157.
- Rock, B.N., T. Hoshizaki, and J.R. Miller, 1988, Comparison of *in situ* and airborne spectral measurements of the blue shift associated with forest decline, *Remote Sensing of Environment*, 24, 109-127.
- Schreiber, U., W. Vidaver, V.C. Runeckles, and P. Rosen, 1978, Chlorophyll assay for ozone injury in intact plants, *Plant Physiol.*, 61, 80-84.
- Sokal, R.R. and F.J. Rohlf, 1981, *Biometry*. W.H. Freeman and Company, San Francisco, 859 pp.
- Stahl, U., V.B. Tusov, V.Z. Paschenko, and J. Voigt, 1988, Spectroscopic investigations of fluorescence behaviour, role and function of the long-wavelength pigments of photosystem I, *Biochim. Biophys. Acta*, 973, 198-204.
- Strasser, R.J. and W.L. Butler, 1977, Fluorescence emission of photosystem I, photosystem II, and the light-harvesting a/b complex of higher plants, *Biochim. Biophys. Acta*, 462, 307-318.
- Theisen, A.F., B.N. Rock, R.T. Eckert, 1994, in press, Detection of changes in steady-state chlorophyll fluorescence in *Pinus strobus* following short-term ozone exposure, *J. Plant Physiol.*, 1-10.
- Turner, M.A., 1973, Effect of cadmium treatment on cadmium and zinc uptake by selected vegetable species, *J. Environ. Quality*, 2, 118-119.
- Van Duijvendijk-Matteoli, M.A. and G.M. Desmet, 1975, On the inhibitory action of cadmium on the donor side of photosystem II in isolated chloroplasts, *Biochim. Biophys. Acta*, 408, 164-169.
- Vogelmann, J.E., B.N. Rock, and D.M. Moss, 1993, Red edge spectral measurements from sugar maple leaves, *Internat. J. Remote Sensing*, 14, 1563-1575.
- Walker, D., 1992, Tansley Review No. 36, Excited leaves, *New Phytol.*, 121, 325-345.

REMOTE SENSING HYPERMEDIA TERRAIN DATABASE

FOR IMAGE INTERPRETATION

B. D. Leighty
Knowledge Sciences, Inc.
Atlanta, GA 30350, U.S.A.

R. D. Leighty
Leighty and Associates, Inc.
Vienna, VA 22180, U.S.A.

G. E. Lukes, J. N. Rinker, P. A. Corl
U.S. Army Topographic Engineering Center
Fort Belvoir, VA. 22060, U.S.A.

ABSTRACT

Military mission planning requires detailed terrain information at a level usually not found in existing maps or databases. Examples of required terrain information include the identification of geologic landforms, surface materials, surface conditions, and vegetation. This information can be extracted from aerial imagery that exists for most of the world. Presently, very little of this imagery has actually been interpreted. Image interpretation is a slow, knowledge intensive, manual process performed by terrain analysts using a significant amount of collateral material. Image interpretation collateral material consists of satellite imagery, aerial photos, radar imagery, ground photos, synthetic imagery from elevation data, spectrographic data, climatic data, existing maps, area physiography descriptions, etc.. The integral use of this material in the image interpretation process provides important clues when inferring terrain features. A tool is needed to efficiently integrate these diverse forms of collateral data into the image interpretation process. Additionally, as the defense budget is reduced image interpretation expertise will be in less supply. Thus, this tool should also incorporate image interpretation knowledge to aid less experienced analysts in performing at higher levels. A proof-of-principle software system has been developed utilizing hypermedia technology to integrate all these forms of information into an interactive database for use in inferring terrain characteristics from imagery. The Hypermedia Terrain Database (HTD) currently contains imagery consisting of: air photos; LANDSAT MSS and TM; SPOT; SAR; synthetic shaded relief DTED, and 35 mm photos. Textual data consists of information on: landform patterns; physiography; geology; climate; vegetation; surface conditions; landform engineering and military usage; and terminology definition. Graphics include data such as maps and spectrographic line plots. Knowledge conveying how an expert utilizes this information for different applications is implemented using guided tours of the database with expert commentary. The HTD effectively demonstrated the capability to efficiently integrate these diverse forms of collateral material in the image interpretation process. This tool will also have civil applications.

1.0 INTRODUCTION

Military operations require detailed terrain information at a level usually not found in existing maps or databases. For mission planning, detailed terrain maps must be rapidly developed. In the case of virtual world training simulations, high fidelity terrain databases must be rapidly constructed. The objective of this work was to assess the potential of hypermedia technology to efficiently integrate the various forms of collateral image interpretation data, into a computer based, softcopy form. In this form the collateral material can be efficiently exploited during the process of inferring terrain characteristics from imagery. A proof-of-principle Hypermedia Terrain Database (HTD) was developed implementing portions of the U.S. Army Topographic Engineering Center (TEC) "Remote Sensing Field Guide - Desert" [Rinker, et al, 1991] as well as collateral materials from the Fort Irwin, California area as gathered by a team led by J.N. Rinker.

A hypermedia database is essentially an implementation of a semantic network of concepts and relations. Concepts consist of nodes containing text, imagery, or graphics. Relations consist of associative links that provide the capability to rapidly move from one concept to a related concept. Using a pointing device the user selects highlighted information resulting in the traversal of the link and the display of the related information. Besides related information being linked together, networks of links exist that organize information relative to specific applications. This essentially presents windows into the database according to the users desired viewpoint. For example, the database appears differently if being accessed for landform feature classification versus cross country mobility analysis.

It is expected that a full scale implementation of the proof-of-principle system can be useful in military mission planning and virtual world database development. In addition, the HTD will be useful in civil applications such as environmental impact monitoring, natural resource planning, and natural disaster evaluation. This paper first presents background information in hypermedia technology. This is followed by a descriptions of the database design, the user interface, and the system hardware and software implementation. Conclusions and discussion of future work are also provided.

2.0 BACKGROUND

The following paragraphs provide background information on hypermedia technology and some advantages of its use.

2.1 HYPERMEDIA TECHNOLOGY

Hypermedia provides a fundamental new way of storing and retrieving information. A hypermedia database is essentially an implementation of a semantic network of concepts and relations. Concepts can consist of text, images, and graphics or combinations thereof. Relations consist of associative links that provide the capability to rapidly move from one concept to a related concept. For instance, within a body of text a group of words representing a concept would be highlighted by color indicating that there exists a link from it to related information. Using a pointing device the user may select the highlighted words resulting in traversal of the link and the display of the related information. The typically sequential process of reading as is done with conventional textual material is replaced by a multidimensional, interactive process involving text and images. Semantic nets are a model of memory. They lend themselves to graphic display, and their meaning tends to be intuitively clear. Hypermedia has only recently become practical with the advancement of computer hardware technology. Hypermedia requires a certain degree of computing power, storage, graphics, and user interface capability that is now widely available at the microcomputer level.

2.2 ADVANTAGES OF THE HYPERMEDIA APPROACH

A Hypermedia approach has many potential advantages over other forms of database management systems. Most typical database systems access carefully structured data records using numbers, keywords, names, or other identifiers. Sophisticated, conventional databases require the user to know complex query languages and to understand the concept of a relational data model. Relational databases are most useful for data structures that can be organized into structured fields of information, however if the data consists largely of text, graphics, and images, then this data model is less effective. In addition, relational or other conventional forms of database organization are generally less effective if the data is more complex in organization. Hypermedia databases have been shown to be object oriented in nature [Campbell and Goodman, 1988]. They can handle more complex structured or interconnected data items consisting of text, graphics and images. A hypermedia database supports structured as well as arbitrary links among pieces of information and as such can be very large. In addition, the computer can exploit the pattern of links in a hypermedia database and give the user different perspectives on the database. For instance, the user may express an interest in "causes", and the system could organize information so as to emphasize the causal links.

3.0 DATABASE DESIGN

The design of the HTD is first discussed in terms of the structure of some of its components. The concept of database viewing perspectives is then discussed. This involves the organization of the components based on a particular application. There is also discussion presented of how the semantic network organization lends itself to an object oriented representation.

3.1 STRUCTURE

As discussed earlier, a hypermedia database is an organization of nodes and links where pieces of information (concepts) are nodes and the links are cross references (relations). The most important concept in hypermedia is the link. Links are the labels that link one node (text, graphics, etc.) with another. When a link is activated by the user (via selection by a mouse) the link becomes activated and a jump is made to the node that it points to. The link may be embedded in a body of text or embedded as part of a graphic or imagery display. Links are usually denoted by words or phrases that are highlighted by color or special symbology. The highlighting used typically indicates the type of link, for instance whether it is to text versus a graphic.

Hypermedia database links can be established in hierarchical or non hierarchical structures (i.e., networks). In a hierarchical organization, nodes are arranged in a tree structure. Hierarchical structures allow data to be organized and searched in a well prescribed way. Each level of the tree provides more detail or certain types of information. However, network organizations can provide very useful cross referencing links that are not necessarily hierarchical. In practice, most database applications result in a hybrid of the two approaches. The user first is presented a hierarchy to initially launch into the database. Once in the database the user may continue to follow a hierarchy but may also pursue references across the hierarchy at any level. The initial hierarchies for the HTD consist of the following: access by desert landform feature class; access by imagery; access by operations; access by surface conditions; access by location; access by regional environment; how-to guided tours; and the image index. These initial hierarchies consist of links that organize pertinent portions of the database relative to the particular application of interest. This essentially provides a set of application dependent windows showing varying perspectives on the data contained within the database. The concept of database viewing perspective is further addressed after the discussion of each of these individual perspectives. The following paragraphs discuss each access perspective in greater detail.

3.1.1 Access By Desert Landform Feature Class

Access by desert landform is organized according to a hierarchy of major desert landform feature classes. The top level of this hierarchy consists of the following top level features: depositional patterns and transported material; erosional patterns and residual material; special and minor features; and cultural features. The selection of "depositional patterns and transported material" from the hierarchy results in the display of a textual outline that consists of all landforms formed as the result of material deposited from wind or water. Each landform within this hierarchy (e.g. Dunes, Linear Dunes, Crescentic Dunes, etc.) is then linked to a landform description and discussion of its military uses and wind regime. For example, selection of Linear Dunes in the hierarchy results in transversing the link to a text node that contains a description of the Linear Dune landform. From this node there are separate links to other textual nodes that describe the wind regime, military uses, and display example imagery. This organization is shown in figure 1.

3.1.2 Access By Imagery

The emphasis of this method of access is to give the user the ability to browse through images in an organized way. Images are organized according to the desert landform hierarchy as discussed above. The initial display presents a gallery of postage stamp size images or chips. These chips are of the major desert landforms resulting from wind depositional processes (e.g. Dunes, Ripples, Sand Plains/Sheets, etc.). Above each chip is displayed a button that links to the textual description of that landform. Selection of a chip such as the one for dunes results in traversing a link to another image gallery node of chips showing the different types of dunes (e.g. Linear, Crescentic, Dome, etc.). Above each of these chips is also a button that links to the textual description of that landform.

Selection of a chip such as the one for Linear Dunes results in the traversal to an image node containing an example photo of a linear dune. From this image one may sequentially pursue links through other example images, the last image links back to the original image. From any of these images one may jump forward or backward through the hierarchy at the dune level. For instance one may jump from images of Linear Dunes to the first image of the Crescentic dunes. In this way the user can easily flip through images of the same type of landform or move along the hierarchy to images of other types of landforms.

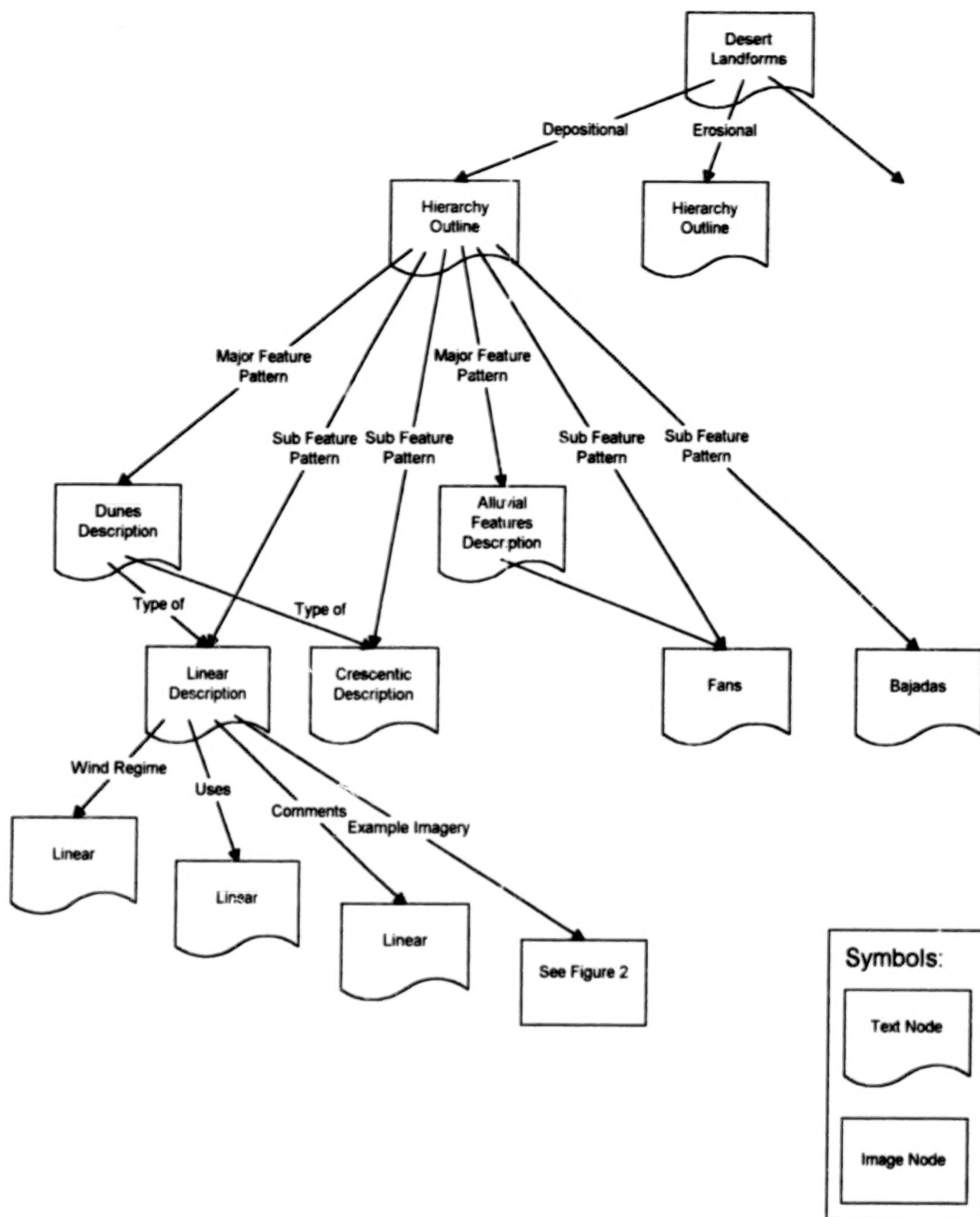


Figure 1. Access by Feature Class

The image node described above has more detailed structure as shown in figure 2. A button exists that links to the a node as described in the paragraph on access by landform feature class. Separate button links exist to different text nodes for image data (i.e., location, source, data, time, etc.), comments, and uses. Within the node containing image data text there can be a link to a map indicating the precise location of the image or, links to other data such as spectral reflectance and radiance plots. Utilizing interactive regions, links can also be made directly from areas of the image itself. For instance, the internal area of a green rectangular outline overlaid on top of the image can be linked to another image that represents an enlargement of the area contained within the rectangle. This in effect results in a zoom. On the zoom image one may place markers on sample sites that link to nodes such as ground photos or spectral plots. This is a very effective way of linking spectral data to the precise sample site as indicated by imagery.

3.1.3 Access By Operations

Access by operations presents a list of operational considerations such as: foot traffic; use of dune buggy and light 4 wheel drive vehicles; use of fixed wing aircraft; obstacles to cross country movement; obstacles to traffic; observation points; navigation aids; terrain to avoid; cover and concealment. For each operational consideration there is a list of landforms that are relevant to that particular operation. Links take the user directly into the pertinent database text describing the landform in relation to these operations. This text may also include links to illustrative images. For example if the user selects "Playas" under "obstacles to traffic" he would traverse a link into the text node containing "Playas, Engineering and Military Uses" where it is described that dry Playas with a high clay content can have large desiccation cracks that present formidable obstacles to ground mobility. A link to a ground photo of a large desiccation crack can be selected from the text for viewing.

3.1.4 Access By Surface Conditions

Access by surface conditions presents a list of surface conditions including: Soft - Dry; Soft - When Wet; Quick Conditions - When Wet; Hard; etc.. For each surface condition a list of pertinent landforms is provided. Just as in the case of operations, this is essentially a cross reference between surface conditions and landforms. The design of the HTD in this case is the same as for access by operations. Links from the landforms listed as a function of surface condition are implemented directly into the pertinent database material.

3.1.5 Access By Location

The access by location method is not structured in terms of landform but rather specific geographic location. To best illustrate this method of access data was used from the Fort Irwin area as gathered by J.N. Rinker (TEC) and his team. This data, along with other imagery provided by TEC personnel, provided a comprehensive data package including maps, satellite imagery (LANDSAT MSS, SPOT), SAR, aerial photos, synthetic imagery (e.g. synthetic shaded relief generated by TEC), ground photos, low altitude aerial oblique photos, ground sample spectra, and textual descriptions. In the future imagery from the Desert Guide will also be linked geographically.

Access by location first presents the user with a display of a world map as well as a list of major continents. The user may select the region of interest from either the map or list. Selection of the continental United States results in the display of a U.S. map with a portion of southern California highlighted with a transparent, rectangular button. This button indicates that data is available for the area under the button. Selection of the button results in the display of a map of southern California and southwestern Nevada from Los Angeles to Las Vegas. On this map, centered around the Fort Irwin area, is another transparent rectangular button that includes the Silurian Valley. Selection of this button results in the display of a larger scale map that includes Fort Irwin and the Silurian Valley. All of these maps were generated from the Defense Mapping Agency's Digital Chart of the World map database and were included in the HTD as image files.

On the large scale map of the Silurian Valley are two transparent rectangular buttons, one covering a major portion of the Silurian Valley (running north-south) and one covering the Dumont Dunes that are located in the northern section of the valley. At this level, there are several other types of links available for selection that are not located on the map but are relevant to the area at this scale. These additional links include: maps; small scale imagery; area physiography; and other data. The following describes these links:

- a. **Maps** - Selection of the maps link provides a list including a topographic map, and a geologic map. These are linked to the corresponding map image and include both the Silurian Valley and the Dumont Dunes.

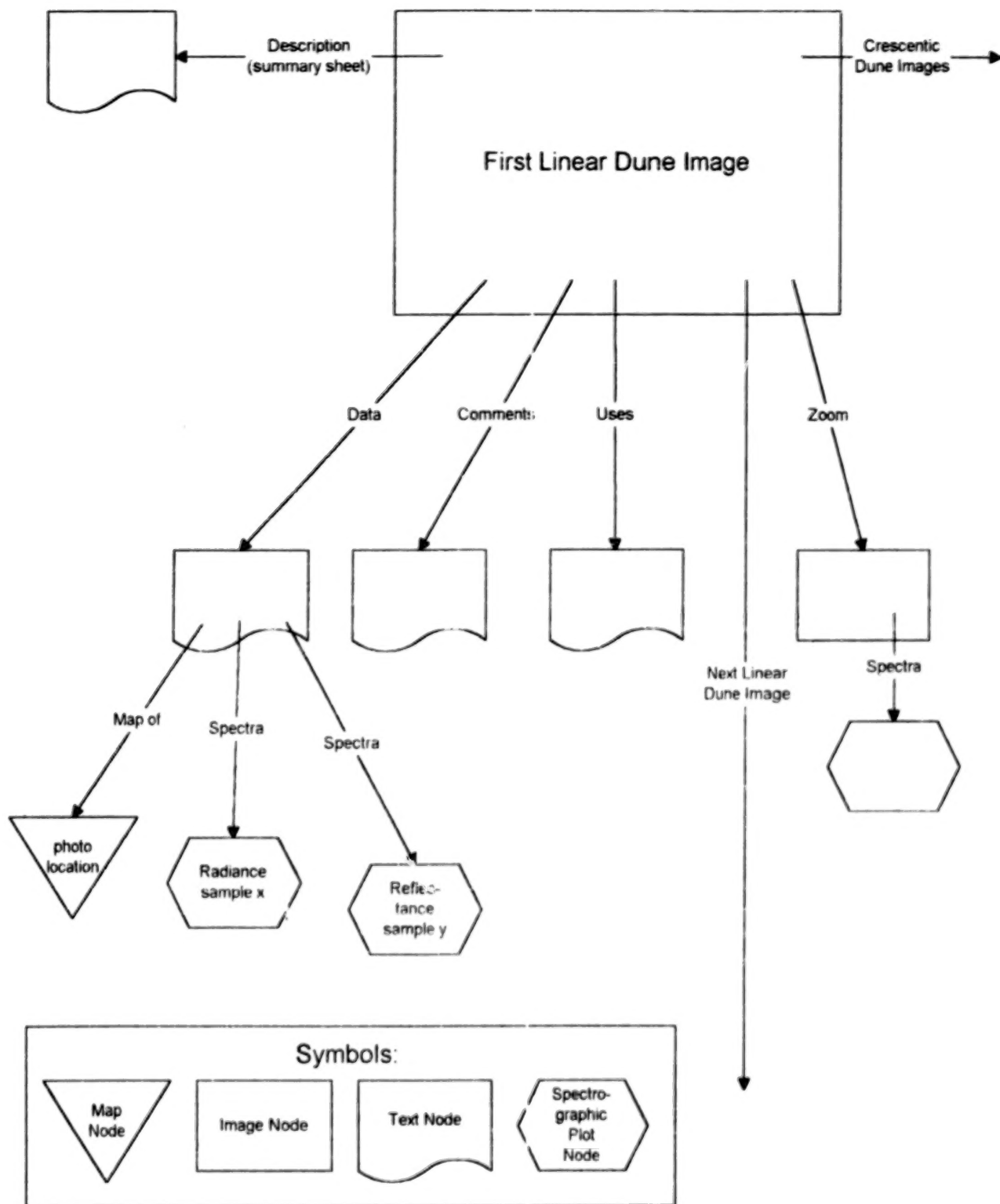


Figure 2. Example of Detailed Structure - Landform Image Nodes

- b. **Small Scale Imagery** - Selection of the small scale imagery link provides a list of small scale imagery including: an aerial photo; LANDSAT MSS image; small scale SPOT (synthetic color); large scale SPOT (synthetic color); high resolution gray scale SPOT; SAR; and a synthetic shaded relief using high resolution DTED (generated by TEC). Selection of any of these entries results in the display of the corresponding image. All of these images are approximately of the same scale as the map selections described above.
- c. **Area Physiography** - Selection of the area physiography link results in transversal to the specific point within the physiographic descriptions that is most pertinent to the Fort Irwin geographic region. Specifically, this link goes to the Great Basin physiographic section textual node.
- d. **Other Data** - Selection of other data link provides a list of miscellaneous data pertinent to this area. In this case it includes a USGS Geologic Reconnaissance and Test-Well Drilling report written on the Fort Irwin area. Selection of this item results in linking to the complete report in hypertext form.

Selection of the transparent, rectangular button covering the Silurian valley results in the display of a topographic map that includes Silver Lake Road that runs east-west across the valley that runs north-south. On this display there are the following links: site markers; area markers; maps; imagery; high altitude aerial photo; and spectral data. This database structure is shown in figure 3. These links are described as follows:

- a. **Site Markers** - These consist of small green squares that mark site locations where ground photos were taken. Selection of one of the green site markers on the topographic map results in the display of a photo gallery that contains chips of ground photos taken at this site. On the gallery display there is a link to a text node that describes the site in general and a link that results in the display of a list of any spectrographic plots that from samples taken at the site. Selection from the list of spectrographic plots results in the display of the particular plot. The photo chips are generally recognizable but little if any detail can be seen. Cursor selection of a chip results in the full scale display of the photograph. On the full scale photo is a link to pertinent data such as a description of the scene, time of day, etc. The photo may also include a link to a spectrographic plot if a such a sample was taken within that particular scene.
- b. **Area Markers** - These consist of large green rectangular outlines that overlay certain areas. Selection of one of the area markers on the topographic map results in the display of a high altitude aerial photo (HAP). The HAP encompasses the area enclosed by the area marker on the map. On the HAP (a gray scale image), are green markers that indicate the approximate ground position and direction for which a low altitude oblique image exists. Selection of one of these markers results in the display of the corresponding oblique photo. The oblique photo contains a link to text that describes associated photo data such as direction, time, location, etc.. On the display of the HAP is also a link to text that provides any data associated with the HAP such as date, time, location, altitude, etc..
- c. **Maps** - Same as provided on the preceding level (Fort Irwin area map). This should give the user more direct access to small scale maps that could be useful even at the larger scale levels.
- d. **Imagery** - Same as provided on the preceding level (Fort Irwin area map). This should give the user more direct access to small scale imagery that could be useful even at the larger scale levels.
- e. **High Altitude Aerial Photo (HAP)** - Selection of HAP results in the display of a HAP image that is approximately of the same scale as the topographic map that has the site and area markers. The HAP also has the same site and area markers indicated on it. The user may select sites from this HAP as is done from the topographic map.
- f. **Spectral Data** - Selection of spectral data results in the display of a list of spectral samples collected in the area. Selection of a sample from the list results in the display of the spectral plot. Even though these plots can be accessed at the site level, this allows easy access to all plots within a given area.

Selection of the transparent rectangular button covering the Dumont Dunes results in the display of a topographic map that includes the Dumont Dunes. This display could have been designed in the same way as the Silurian Valley but because of time limitations no ground sites were used, only the aerial oblique photos were used with the HAP. An area marker appears over the topographic map, and when selected, results in the display of a HAP image that corresponds to that area. In a fashion analogous to the Silurian Valley HAPs, the Dumont Dunes HAP image contains markers indicating links to aerial oblique images.

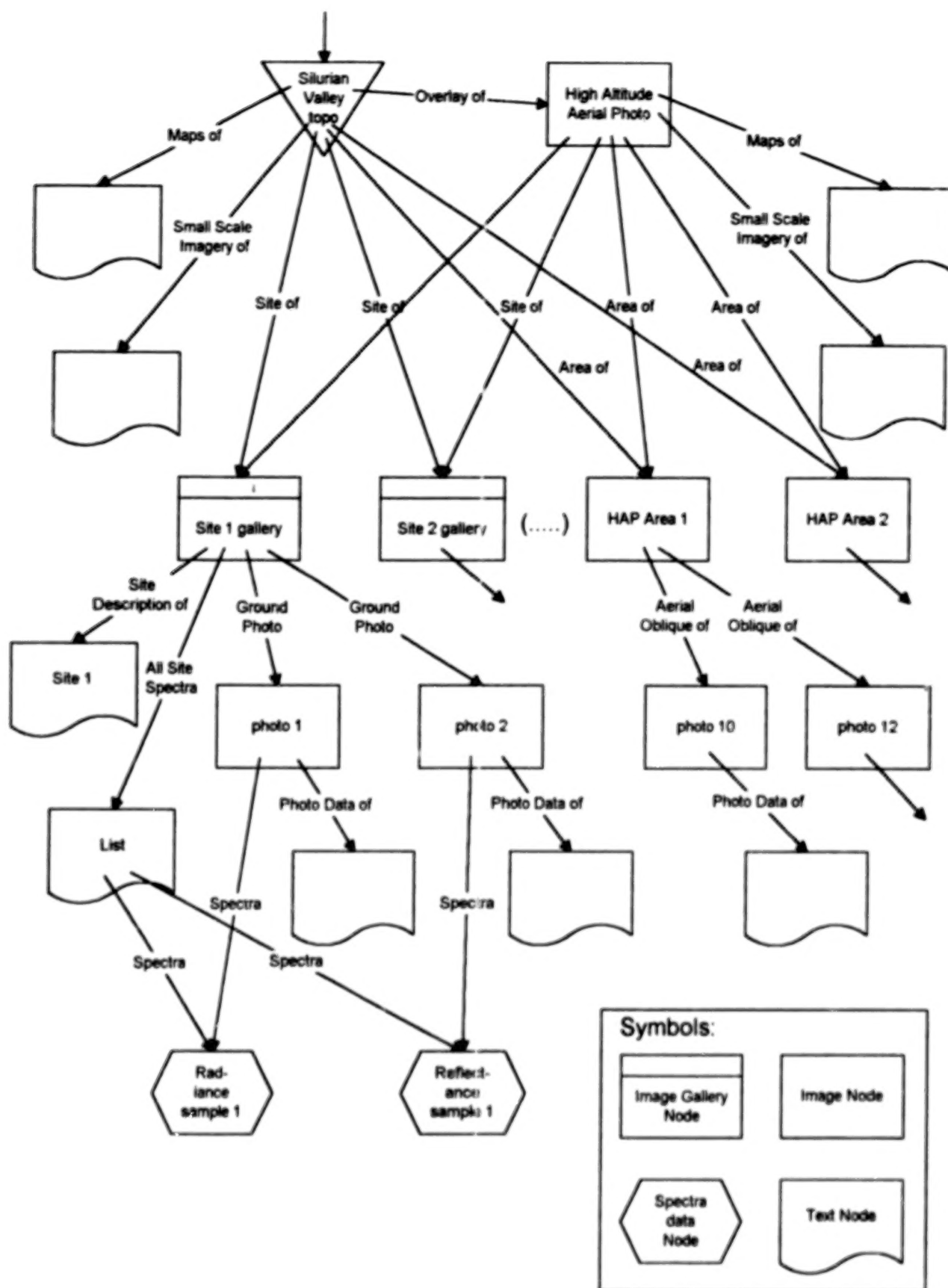


Figure 3. Access by Location - Silurian Valley Link

3.1.6 Access By Regional Environment

Access by regional environment provides the user with access to physiography, climate and vegetation data for various geographic regions. In this study only selected portions of the United States physiography was implemented. In this mode the user may select to access physiographic information for a U.S. region from: an outline of major physiographic divisions (based on Fenneman, 1928); from a U.S. map of major physiographic provinces (Rocky Mountain System, Intermontane Plateaus, etc.); or from a list of U.S. regions (i.e., SWUS, NEUS, etc.). Selection of a physiographic division by any of these methods results in the display of an outline or detailed map indicating the major physiographic provinces (e.g. Intermontane Plateaus division includes the Columbia Plateaus, Colorado Plateaus and the Basin and Range provinces). Selection of a province results in the display of a textual description of the province that includes links to textual descriptions of the various sections within the province. Other areas of the hypermedia database link directly into the physiographic data at the section level. For instance, from the Silurian Valley map node, selection of the Physiographic Area link results in linking directly into the Great Basin section which is applicable to the Silurian Valley geographic area.

The links described above are bi-directional allowing access upwards in a physiographic hierarchy. This is particularly important if access to the physiographic section data is from some other point in the database and by coming down the physiographic hierarchy. In this case it will allow the user to explore links upwards through the hierarchy. In the future, climatic data or models and vegetation data would be accessed from this function.

3.1.7 "How-To" Guided Tours

Although hypermedia systems typically let you choose your own path in accessing information, they can also be setup to guide the user through a predefined path. In a guided tour all link selections are activated automatically by the system. A tour may be interrupted to pause, review a previous screen, or to stop. The tour may be of information most pertinent to a given topic, or perhaps an overview of a single topic, or a quick look at related topics. Experiments have shown that guided tours provide more accurate overviews of the available material and result in a higher rate of exposure to new, rather than repeated information [Allison and Hammond, 1989].

As such, this guided tour facility is used to capture and convey expert information. For a particular subject, an expert tutorial is presented using data from the database to provide examples. Text developed just for this tour is presented along with examples that consist of images and maps already contained in the database. The user selects a "continue" button that automatically sequences him through the various database nodes that are part of the tour. Along this tour the user may also select to jump off and pursue links that are contained in the material. A guided tour was implemented that explained the kind of terrain information that could be inferred from the various forms of imagery and maps in the database. It used imagery from the database to specifically show how various terrain features could be inferred from image patterns. Another possible tour would be to show in detail, how to infer terrain information using spectral data. It would also be interesting to incorporate knowledge in the form of expert system knowledge bases that could be embedded and used to provide expert advice in the inferential procedure.

3.1.8 Image Index

It is believed that with the large quantity of imagery contained in a terrain related database, an index would be useful to directly access any image. The index developed in the HTD organizes images by landform.

3.1.9 Glossary

A partial glossary of terminology applicable to terrain analysis was developed. Terms used throughout the database that may not be readily familiar to the user were linked into the glossary. A full glossary could become quite substantial.

3.2 VIEWING PERSPECTIVES

Each application dependent viewing perspective (i.e. method of database access) was addressed in detail in the above paragraphs. It can now be seen in general, how the application hierarchies link into the primary data of the database depending on a particular perspective. For instance, Access by Operations ultimately links directly into the landforms in the Uses nodes where the particular military operations are typically addressed. It can be seen how

Access by Feature Class primarily links into textual descriptions of the landforms while the Access by Imagery follows the same feature class hierarchy but links primarily into imagery.

This type of organization provides a very efficient, flexible and powerful means of access. New viewing perspectives can easily be added. For instance, it could be very useful to have a window that organizes and accesses all of the spectrographic data in the database just as Access by Imagery does. Perhaps galleries of reduced spectrographic plots could be used to organize this data into some sort of hierarchy such as was done in Access by Imagery. By using bi-directional links once a spectrographic plot of interest is found, one could traverse a link from it to a photo of the sample site and then perhaps ultimately to a geological map of the sample area.

3.3 OBJECT ORIENTATION

As can be seen from the figures that depict the semantic networks of the database there are recurring structures throughout its design. For instance the landform descriptions in figure 1., the landform image node shown in figure 2, and the site galleries shown in figure 3. The landform object class in figure 1. could be defined as the landform description that includes, a wind regime node, a uses node, a comments node and an example imagery node. The landform object would actually inherit the structure of the image node object class in figure 2. The image node object includes the image data node object, comments node, etc.. The image data node object includes a map node, and spectral plot nodes. One can see that the various landforms and available data instantiate this object structure.

An object oriented representation is important because it can make the development and maintenance of large databases much more manageable. This could be true to the extent that newly instantiated objects could be integrated into the database networks using an automated procedure. Some of the object class definitions (i.e., object attributes and inheritances) could also come from standards established by other object oriented terrain databases. This will further enhance the ability of the HTD to exploit external sources of data.

4.0 USER INTERFACE

User friendliness is an important aspect of any man/machine system. Software that is difficult to learn, frustrating or confusing to use, or results in an unduly large number of errors, is not acceptable. Hypermedia systems, like all other systems must meet certain usability criteria. Learning time must be minimal. Through the use of menus rather than command languages, it is possible for a novice to begin using the system immediately. The design of the user interface should make errors unlikely. The use of pointing devices eliminates the possibility of errors from incorrectly entered commands. This form of direct manipulation simplifies learning and enables rapid traversal with low error rates [Shneiderman, 1983, 1986]. Clear directions, help messages, and consistent system responses all reduce the likelihood of errors.

The HTD user interface consists of a color graphics display, mouse and keyboard. Text, images and graphics are presented on either full screen displays or in windows. In either case text and images are scrollable when larger than the display window. With the display of large images contained in scrollable windows it can be difficult to maintain an orientation relative to the full context of the image. To aid in orientation, the full image is reduced in size and placed directly adjacent to the scrollable window containing the full scale image. This reference image should be very useful in maintaining position context within the windowed image.

4.1 DATABASE NAVIGATION FUNCTIONS

Database links can be interactively selected via the pointing device from text, graphics, and images. In hypermedia systems various navigation functions are also provided to the user to help in selecting information links, finding information and determining current location within the database linkage network. The following user interface functions were included in the HTD. These functions are activated via soft buttons displayed at the bottom of the full screen display and are described as follows:

- 1) **EXIT** - Exits the database back to the computer operating system.
- 2) **MENU** - Returns to the main database menu.
- 3) **HELP** - Provides access to the HTD help capability. This function was not designed but would be analogous to the Windows style of "help".

- 4) **MARK** - Allows the operator to set a marker at the current location within the database. The user specifies a label for this marker. This is analogous to setting a bookmark.
- 5) **GOTO** - A list of previously defined marker labels is displayed that the user may select from. This results in "going to" the location within the database where the marker was defined.
- 6) **LINKS** - Displays a graphical representation of the database link structure. Links may be selected from this graphical display for activation.
- 7) **HISTORY** - Displays a list of all database nodes visited and the amount of time spent at each node. A node can be selected from the history resulting in its display.
- 8) **SEARCH** - A complex Boolean search can be specified on textual patterns within the database.
- 9) **NOTES** - At any point within the database the user may select to leave a note. This note may be for his own benefit or for that of others accessing the database.
- 10) **PRINT** - Provides a hardcopy printout of the text contained in the currently viewed database node.
- 11) **BACK** - Returns to the previously visited database node.

5.0 SYSTEM IMPLEMENTATION

The following paragraphs discuss the hardware and software implementation of the proof-of-principle HTD.

5.1 HARDWARE

The HTD was developed on a 66 MHz DX2 80486 personal computer utilizing standard 640 by 480 pixels VGA graphics (256 colors). This relatively powerful platform worked well for the development effort due to the extensive amount of image processing that was required. Images were scanned by an HP ScanJet IIc. The HTD contained 124 image files requiring approximately 22 MB of storage and 46 hypermedia files requiring approximately 900 kB of storage. Once developed, the demonstration database was hosted on a 25 MHz 80486 laptop personal computer. The lap-top had the capability for displaying 640 by 480 pixels but could only do so using 16 colors. An external video port was capable of the same resolution but with 256 colors. This video port could be connected to a monitor or projection system. Although the lap-top had adequate speed, the display of 16 colors presented a limitation for some images but in general was still very usable. The lap-top provided a highly portable platform for the HTD.

5.2 SOFTWARE

The hypermedia database was implemented using the authoring tools of the Microsoft Windows based commercial hypermedia package HyperWriter 3.0 (Ntergaid, Inc.). A substantial portion of the text and image data was entered utilizing a full page scanner with optical character recognition (OCR) software. Some of this material was provided by TEC already in digital form. The material was linked as defined in the database design. System display buttons, graphics, and window definitions were developed. The application unique user interface was implemented using the facilities of the commercial hypermedia package.

6.0 CONCLUSIONS

The proof-of-principle HTD demonstrated that it could very effectively integrate the diverse types of collateral material used in the image interpretation process. The following are a few of the more important observations made relative to the HTD's use in image interpretation:

- a. Areas were selectable from topographic maps for display of imagery relating to the area including LANDSAT, SPOT, SAR, synthetic shaded relief and aerial photos. In this way features could be correlated across different forms of imagery.
- b. Areas or points on small scale imagery were linked to larger scale imagery such as aerial photos, ground photos or low altitude oblique images. For example, points on a high altitude aerial photo were selected resulting in the display of low altitude aerial oblique or ground photos corresponding to those points. More

specifically, it was very effective to interactively select using the mouse pointer, a marker on an alluvial fan in a high altitude aerial photo resulting in a view of the fan from a low altitude oblique or ground photo. Features seen in high altitude imagery could easily be correlated with features seen in ground level imagery.

- c. As described above, ground photos could be directly linked onto aerial imagery. Some of these ground photos were of areas where samples were taken for spectrographic analysis. The results of this analysis were linked directly to these photos in the form of graphical plots. This provided the ability to correlate colors from high altitude small scale imagery directly to surface consistency (ground photo) and composition (spectral plot). These same spectral plots could also be grouped in related lists for selection.
- d. The ability to link new site imagery into the landform hierarchy was very useful. For instance, one of the low altitude oblique images from the Dumont Dunes area (Fort Irwin data) indicated a Star dune. The fact that it was a Star dune was described in the image data text linked to the image. When this photo was added a link was implemented between "Star" in this text and the Star dune landform description already in the database. The user could then directly access text describing Star dunes, which then leads to links with separate text nodes that provide information on Star dune military uses, and wind regime. Conversely, the new Star image was linked in with the other Star image examples already in the database. This provided another example of a Star dune for access from other areas of the database. This demonstrated how new imagery could be added into the system and cross linked in a very synergistic way.

7.0 FUTURE WORK

Future work will implement stereoscopic imagery as well as hyperspectral datasets. Various analytical facilities will also be added to aid in the comparative analysis of the various forms of remote sensing imagery within the database. In addition, because the HTD cannot contain all of the data that may be useful in terrain image interpretation the HTD will be integrated with other databases and models. While the brute addition of more data does not necessarily lend itself to increased efficiency, the use of the HTD to access these data in a context sensitive fashion will allow the efficient application of collateral data that may otherwise be difficult to utilize. Future work will also include adding the ability to provide the user with advice during the inferential process. This will involve the integration of an inferential expert system knowledge base with the HTD. In addition, a conferencing capability will be added that will allow analysts in the field to interactively solve difficult terrain problems with other, remotely located terrain analysis experts.

REFERENCES

- Allison, Lesley and Nick Hammond, "A learning support environment: the hitchhikers guide", in *Hypertext: Theory Into Practice*, R. McAleese (ed.), Intellect Books, Oxford, pp. 45-61, 1989.
- Cambell, B., J. Goodman, "HAM: A general purpose hypermedia abstract machine," *Communications of the ACM*, vol. 31, no. 7, pp. 856-861, 1988.
- Rinker, J.N., C. Breed, J.F. McCauley, and P.A. Corl, "Remote Sensing Field Guide - Desert," U.S. Army Engineer Topographic Laboratories Report ETL-4588, Fort Belvoir, Virginia 22060-5546, 1991.
- Schneiderman, B., "Direct Manipulation: A Step Beyond Programming Languages," *IEEE Computer*, vol. 16, no. 8, pp 57-71, 1983.
- Schneiderman, B., *Designing the User Interface*, Addison-Wesley, Reading, Mass., 1986.

THE APPLICATION OF ALMAZ RADAR IMAGERY TO PETROLEUM EXPLORATION

R.F. Pascucci
Autometric, Incorporated
5301 Shawnee Road
Alexandria, VA 22312-2333 USA

ABSTRACT

Imagery acquired by the Russian satellite-borne radar system, Almaz, has recently been declassified and made available for civil use. A frame of this imagery, covering an area measuring 28 by 50 km in central Peru, was analyzed to determine the applicability of the Almaz to petroleum exploration.

The investigation was conducted in three phases. The first phase involved the collection of geologic evidence of structure and stratigraphy. This consisted of inferring geologic information from the Almaz image data and plotting this information on an overlay to the ground-plane image to produce a detailed geologic map. In the second phase, a hypothesis was developed that accounted for all the observational data and that explained these data in the form of a geologic model. The third phase of the analysis involved testing the model by using it to predict geologic features that should be present if the model was valid but that had not yet been observed on the imagery. One of the predictions — that if oil had been formed in the area, it would have migrated to, and accumulated along, the structural traps formed by the crests of the anticlines — was confirmed by the *ex post facto* discovery of an existing oil well located just eight km outside the area of interest on the prolongation of one of the postulated anticlines.

In summary, the Almaz imagery proved to be highly effective in providing the evidence needed for the development of a geologic model that could serve as an excellent basis for geophysical exploration for petroleum.

1. INTRODUCTION

For more than 30 years, airborne radar systems have proven their value in geoscience programs that have included engineering geologic evaluations, a broad variety of environmental projects, and exploration programs for petroleum, minerals, and ground water. In 1978, data from NASA's Seasat demonstrated the potential of satellite-borne radar for the analysis of complex geology, especially in regions characterized by dense vegetation and persistent cloud cover. These results were subsequently confirmed by data from the Shuttle Imaging Radar (SIR) series, A, B, and C launched in 1981, 1984, and 1987, respectively. The single most important contribution of these airborne and satellite-borne synthetic aperture radar (SAR) systems to geologic investigations has been their superior depiction of surface morphology and their sensitivity to micro-topography, two of the most important indicators of geologic structure and lithology.

It is this background of proven radar capabilities that led to the investigation of the application of data from the Russian satellite-borne SAR system, Almaz, to petroleum exploration. Imagery from the Almaz is offered for sale by the Russian space program through U.S. representatives.

2. TECHNICAL APPROACH

The epistemological process of deriving geologic knowledge from radar imagery (that is, from a two-dimensional, gray-toned approximation of a three-dimensional, multi-hued terrain) is

carried out in three phases. In the first phase, image data are observed and converted by inference to geologic information (first-phase inference). This process leads the investigator out of the image world into the object world.

In the second phase, the geologic phenomena are used as a basis for the inferential development of a hypothesis — a geologic model that accounts for, and explains, the data (second-phase inference). The conceptual framework provided by the model organizes the disparate geologic phenomena into a unified whole that reconstructs the series of events that occurred throughout geologic time, ending with a three-dimensional picture of the lithology and structure of the area of interest as they exist at the present time.

In the third phase, the hypothesis is tested by using it to make predictions. (The second phase explains all the data that have been observed; the third phase leads the investigator to data that have not yet been observed.) The hypothesis is validated to the extent that the predictions are borne out.

2.1 AREA OF INTEREST

The study area is located in central Peru (8°41'S, 75°19'W) just east of, and bordering on, the Cordillera Oriental. (See Fig. 1.) The area is rectangular in shape and measures 50 km by 27.8 km, having its long axis oriented N 20°E. Topographically, the area is mountainous in the southwest corner of the image (approximately 10 percent of the area) and moderately hilly to flat over the remainder. Geologic information is sparse, but the "Mapa Geologico del Peru," at a scale of 1:1,000,000, shows a folded series of Mesozoic marine sedimentary strata in the mountains of the southwest corner and a blank area referred to as simply "Tertiary Continental" sediments over the northwestern 90 percent of the area. In other words, as of 1977, 90 percent of the area had not been mapped geologically even at a reconnaissance scale. The area is traversed from south to north by the Rio Aguaytia, which follows the gentle regional slope into the Amazon basin.

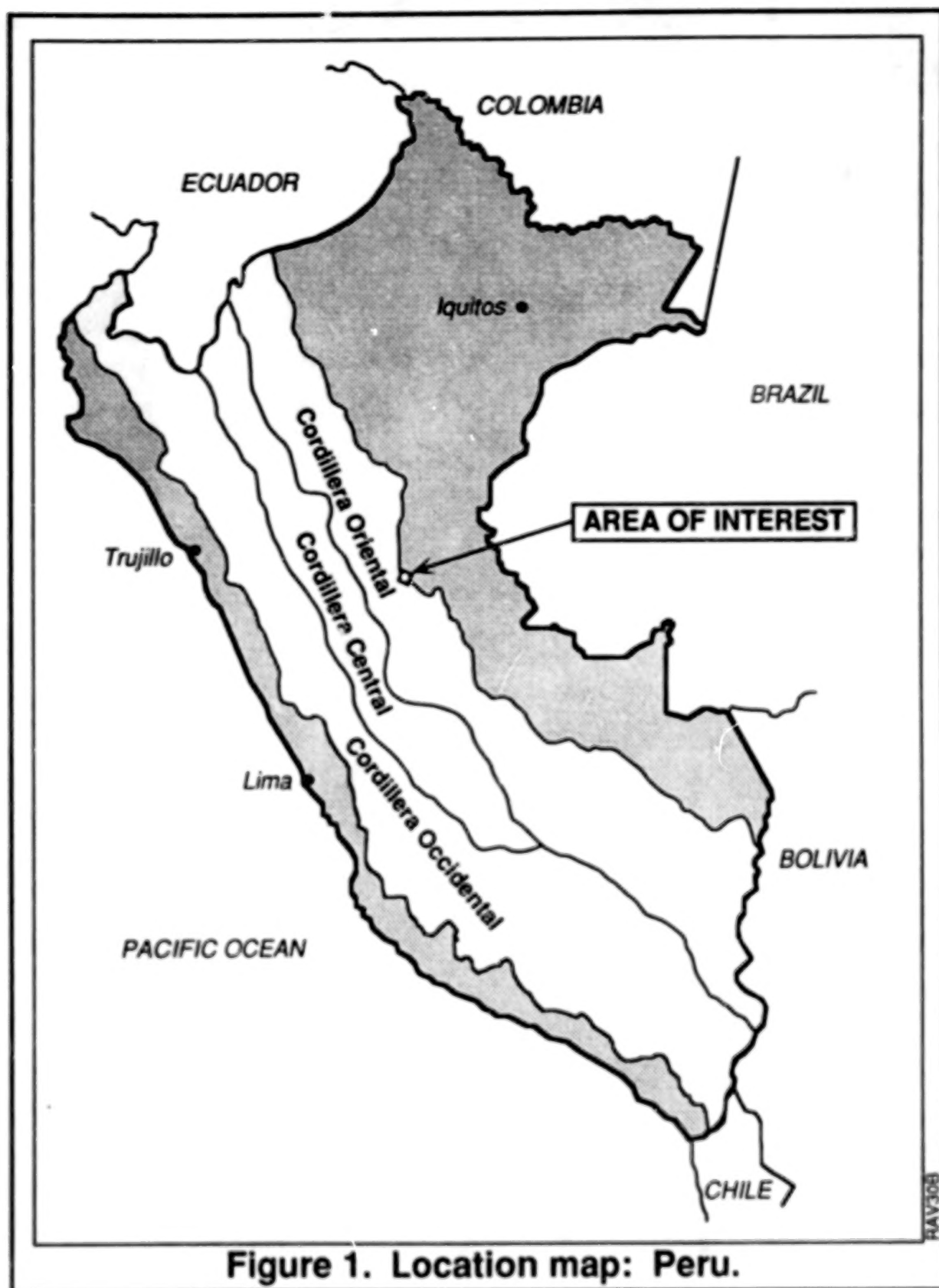
2.2 IMAGERY USED

A single frame of Almaz imagery covers and defines the area of interest. Figure 2 shows the image, and Table 1 lists the acquisition parameters of the system at the time the image was acquired. The quality of the original image was excellent but the process of digitization has somewhat degraded the reproduction. Although a grazing angle 20 degrees lower would have been preferable, the azimuth angle was excellent, bisecting the trends of the lithologic contacts and faults and making an angle of 70 degrees with each.

2.3 PHASE 1 — EXTRACTION OF THE DATA

The Almaz image is analyzed by inferring geologic phenomena from the image data, as shown in Table 2 (first-phase inference). Organized spatially, the data are in the form of a geologic

TABLE 1. ACQUISITION PARAMETERS	
Acquisition Parameters	Values
Frequency	S-band
Resolution	15m
Polarization	HH
Grazing Angle	43°
Azimuth Angle	292°
Format	Ground range (i.e., orthogonal projection)
Field of View	27.8 by 50 km



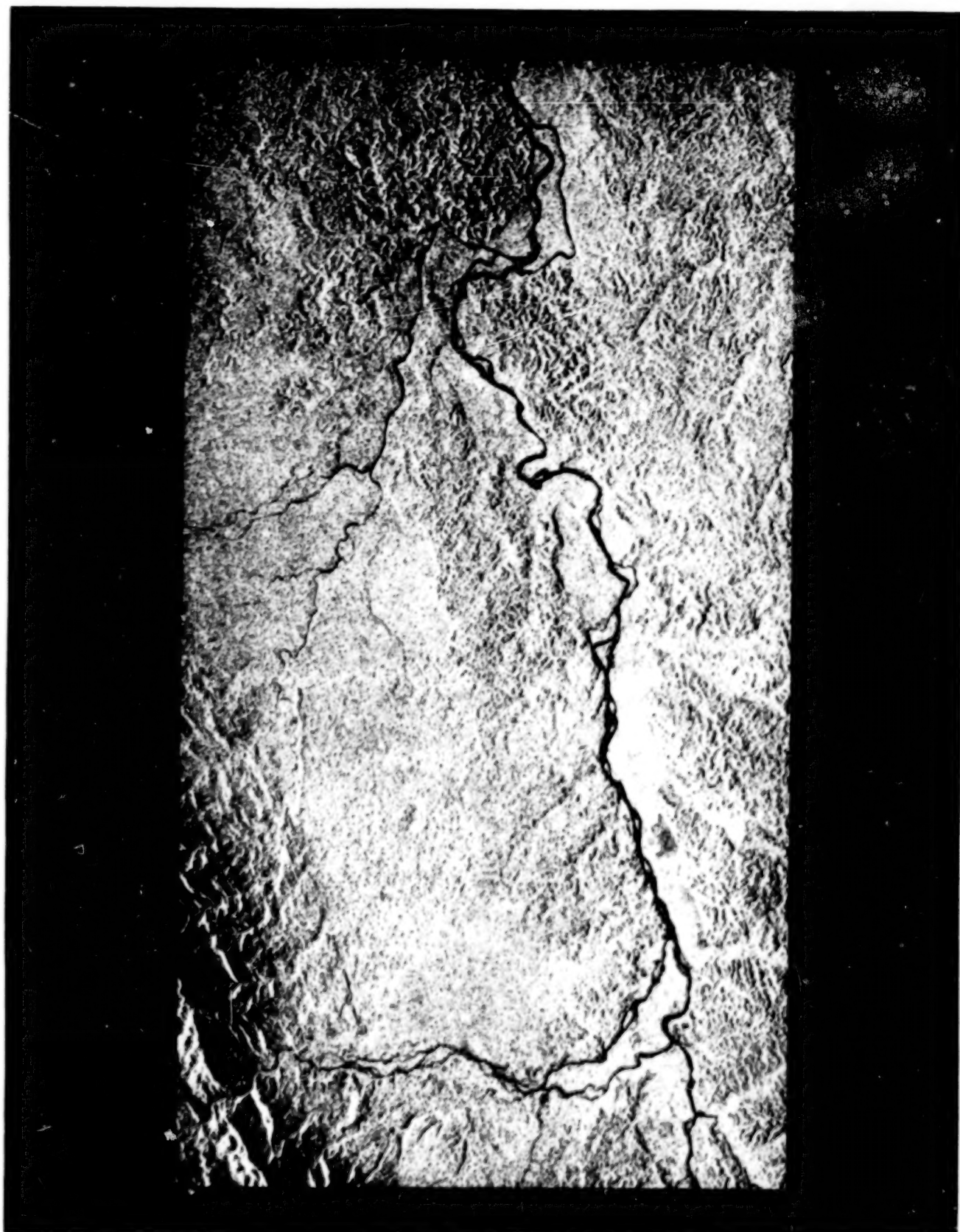


Figure 2. Almaz image.

map (Fig. 3) having a high density of both lithologic and structural information. A sedimentary sequence of 13 lithologic units was found trending nearly north-south. These beds, labeled from 1 to 13 (oldest to youngest) dip toward the east with an angle of inclination that decreases progressively from west to east. As there was no way to measure the dips, symbols representing steep, moderate, and gentle have been used.

Evidence identifying 37 faults and fractures was observed, all but four having a northeast trend. These faults have a total length of 287 km, an average length of 7.7 km, and a median length of 5.8 km. The longest fault is 22.7 km in length and the shortest is 1.8. The sense of movement was seen on only eight of these, five of which were right-lateral and three left-lateral. No evidence of vertical movement was observed, but that does not mean that none was present. Where offset was observed, the feature was called a "fault" and was delineated with a solid gray line. Where only alignment was observed, the feature was called an "inferred fault/fracture" and was delineated with a dashed gray line. (Strictly speaking, all of the mapped features are inferred; a standard terminology and line type have been used to differentiate between higher and lower probability of inference.)

When organized chronologically, the data produce the stratigraphic column shown in Fig. 4. Collateral information (Mapa Geologico del Peru) tells us that strata were deposited more or less continuously from the Triassic through the Cretaceous Periods and again throughout the Tertiary. The orogeny following stratum 4 and the uplift following stratum 12 were inferred from geologic phenomena (second-phase inference) and are, of course, universally recognized.

TABLE 2. RELATION OF IMAGE DATA TO GEOLOGIC INFORMATION

Image Data (image world)	Geologic Phenomena (object world)
<u>Surface Drainage</u>	
density	lithologic type
pattern	fold structure (anticline, syncline, dome)
alignment	fault or fracture
offset	fault
<u>Topography</u>	
elevation (relative)	lithologic type
frequency of slope reversal	lithologic type
angularity (subjective)	lithologic type
alignment	fault, fracture, intrusive
offset	fault
slope (degree & azimuth)	lithologic type, fold structure
landform	lithologic type, fold structure, geologic process
<u>Vegetation</u>	
density	lithologic type
tone	lithologic type
texture	lithologic type
alignment	fault or fracture
offset	fault
<u>Rock</u>	
alignment	fault, fracture, intrusive
offset	fault
strike	fold structure
dip	fold structure
tone	lithologic type
texture	lithologic type

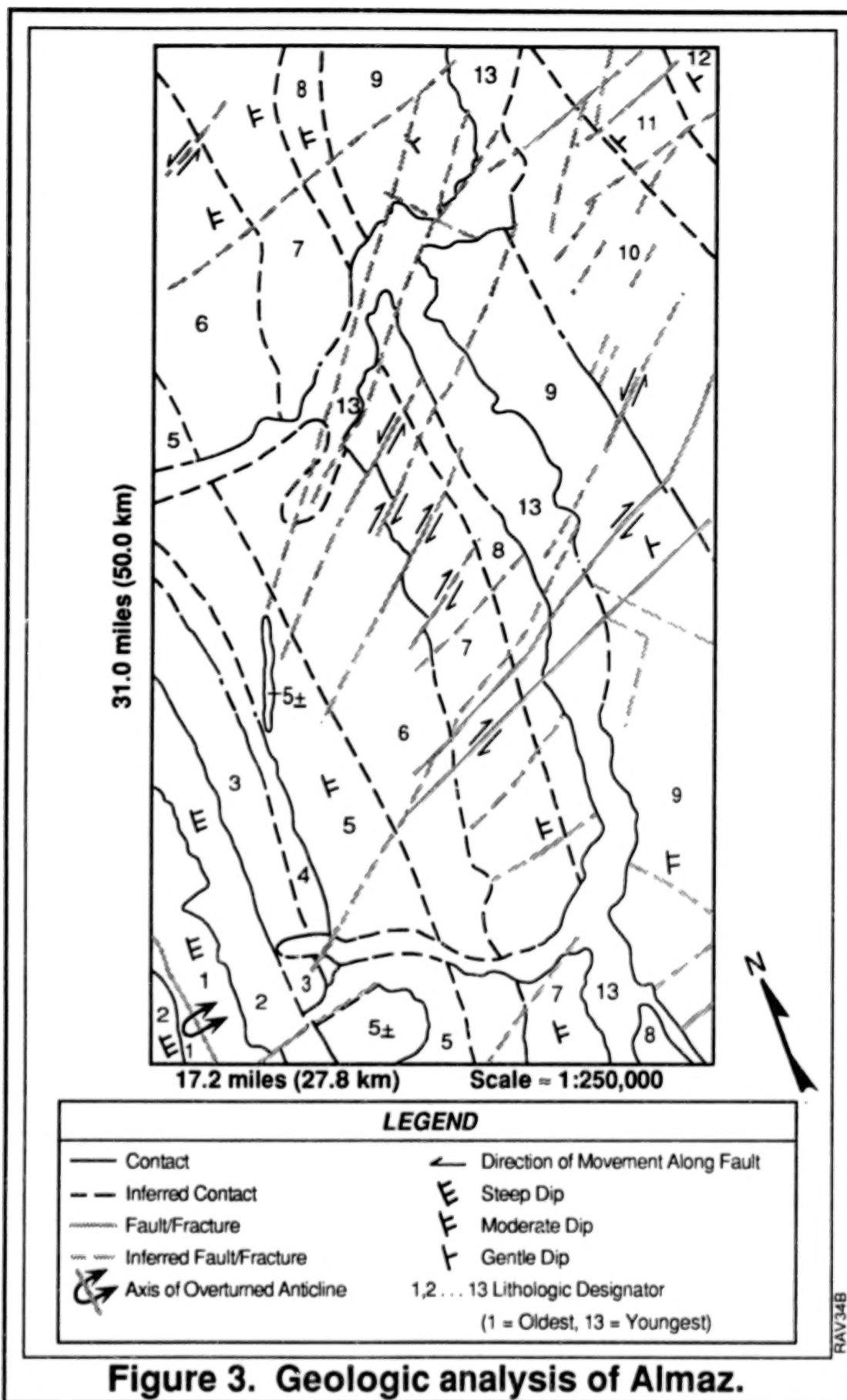
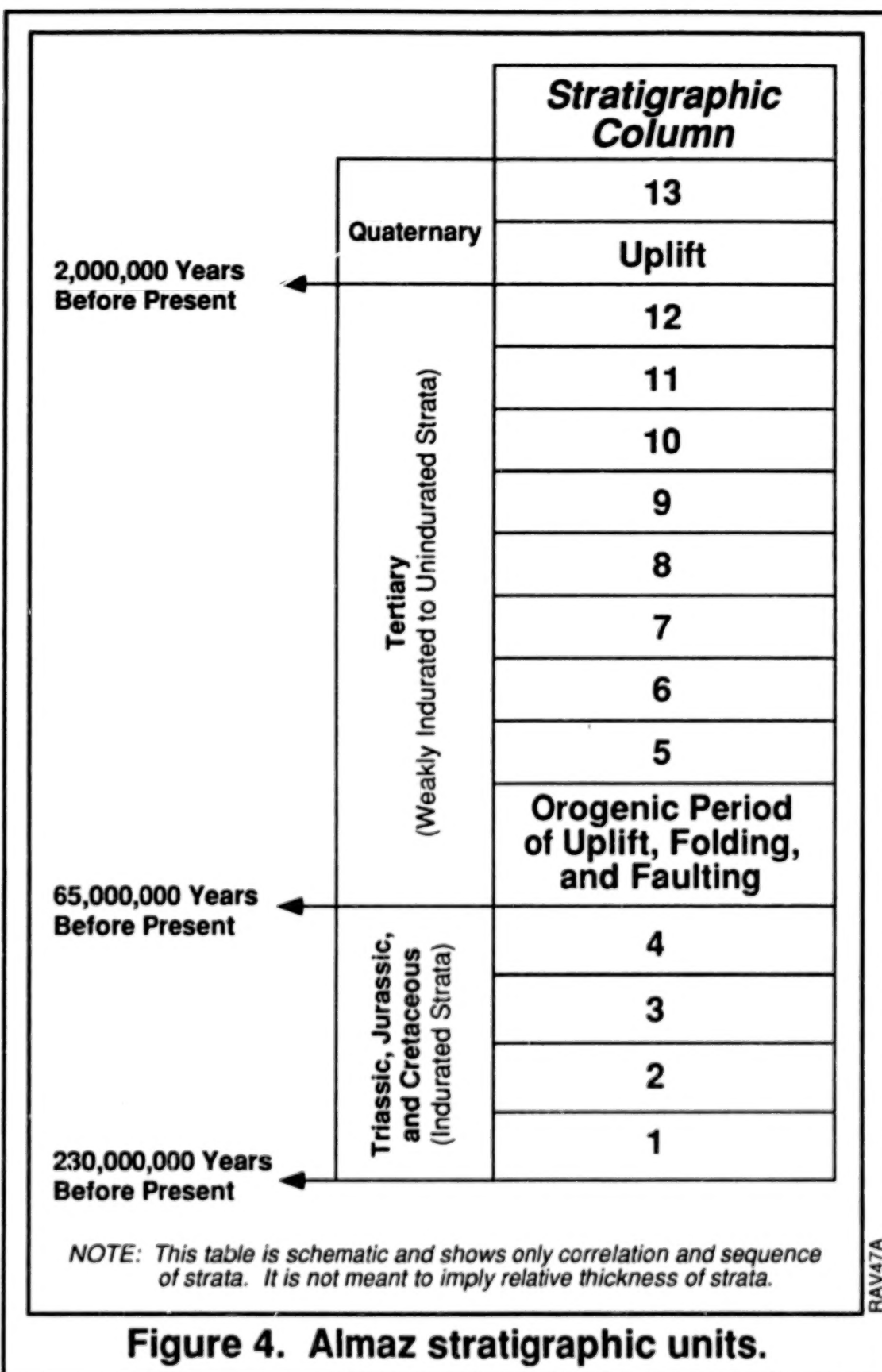


Figure 3. Geologic analysis of Almaz.



2.4 PHASE 2 — FORMULATION OF THE GEOLOGIC HYPOTHESIS

The first-phase analysis converted the image data to a large quantity of geologic information, displayed spatially in Fig. 3 and chronologically in Fig. 4. The second phase of the geologic analysis was to develop a hypothesis that would explain the disparate information elements by subsuming them under a comprehensive paradigm of general geologic principles. The hypothesis (or model) takes the form of a series of cross sections that display the geologic history of forces acting on material over time. (See Fig. 5.) The final stage in the model brings us up to the present time and shows, in section, the three-dimensional disposition of lithology and structure that conforms to (because induced from) the two-dimensional disposition of the individual lithologic units and structural features displayed on the map (Fig. 3) and the stratigraphic column (Fig. 4).

The hypothesis illustrated in Fig. 5 postulates a four-stage sedimentary/tectonic scenario. Stage 1 consists of the deposition of sedimentary materials in a marine environment with the possible formation of petroleum.

In stage 2, an overturned anticline has formed in the western part of the cross section. Such an anticline is the result of severe compression, and it was inferred that compressive stress of such magnitude, when countered by the gravitational force exerted by the uplifted anticline, was probably dissipated in the production of subsidiary folds, such as those shown in the center and eastern third of the section. The presence of such subsidiary folds was predicted solely from the overturned anticline because, at that point in the analysis, no surface evidence of subsidiary folds had been seen. These folds, if they do indeed exist, would serve as structural traps into which petroleum could migrate. The cross section depicting stage 2 shows the hypothetical petroleum as solid black lenses located at the crests of the two subsidiary anticlines.

Stage 3 is characterized by erosion of the Mesozoic rocks and the deposition of Tertiary strata. Stage 4 shows uplift, continued erosion, and the truncation of the Tertiary deposits. Stage 4 conforms to the geologic map of Fig. 3, with steeply dipping beds in the west, moderately dipping beds in the center, and gently dipping strata in the east. (It should be noted that all of these cross sections are essentially sketches that are meant only to convey the concepts of the hypothesis. They are not drawn to scale either vertically or horizontally.)

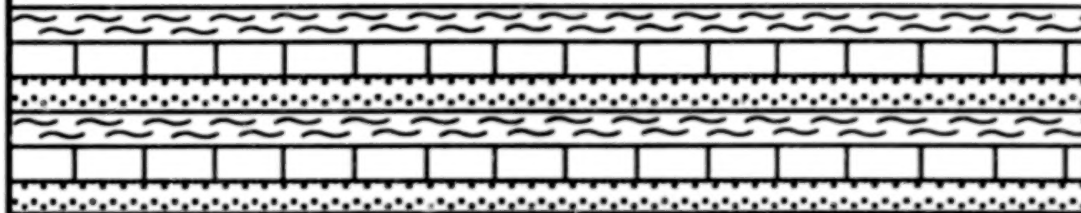
2.5 PHASE 3 — TESTING THE GEOLOGIC HYPOTHESIS

At this point, the investigation has entered its third phase in which the hypothesis is tested by using it to make predictions. The first prediction was made back in stage 2 of the hypothetical model in which it was predicted that subsidiary folds (of unknown number or amplitude) had been produced. In order to determine if such folds do, in fact, exist, it became necessary to make another prediction — a prediction that a not-uncommon geological phenomenon known as differential compaction had taken place. Differential compaction is the relative change in thickness of unindurated strata due to the reduction in pore space caused by the weight of the overlying beds. All else being equal, the percentage of compaction varies directly as the thickness of the deposit, being least over the crest of the anticlines and greatest over the troughs of the synclines. The result of differential compaction is that the surface of the terrain assumes a generalized topographic expression that is a subdued replication of the generalized topography of the underlying terrain, much like a damped waveform. Figure 6 is a schematic representation of differential compaction. If it can be demonstrated that differential compaction has occurred, the hypothesis would be validated and the buried anticlinal axes could be located.

In order to determine the generalized topographic configuration of the present day, which is obscured by small-scale topographic features, a detailed delineation of all visible drainage channels was performed. The result of the drainage delineation is shown in Fig. 7, in which two north-trending rivers and the drainage divides between and adjacent to them can be plainly seen. Analysis of this drainage map confirms the prediction of differential compaction and, thereby, the prediction of the existence of subsidiary anticlines. (See Fig. 8.) Indeed, this analysis not only confirms the presence of these anticlines, it gives us their number and location as well. The location of the anticlinal and

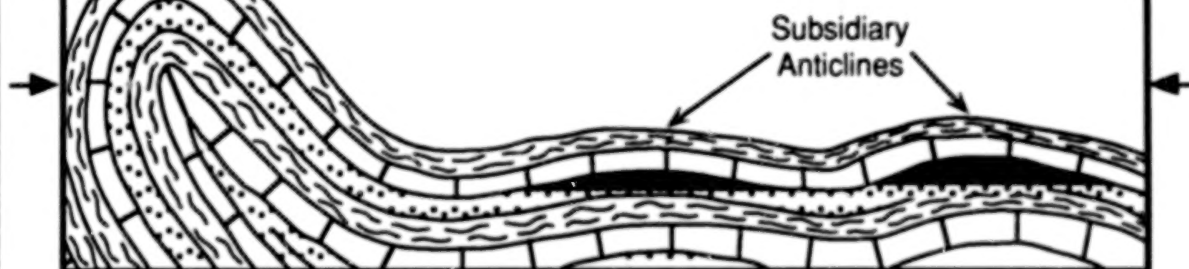
Stage 1, Mesozoic Era

Deposition of Marine Sedimentary Deposits; Formation of Petroleum?



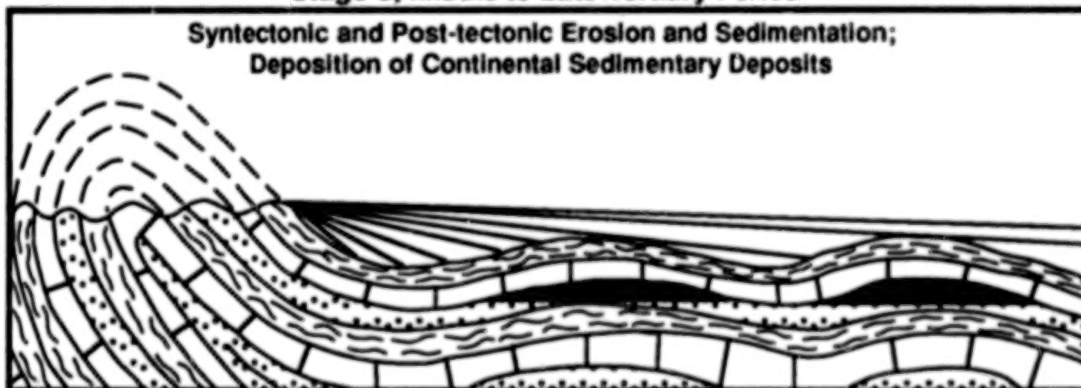
Stage 2, Early Tertiary Period

Compression with Development of Faults and Folds; Migration and Accumulation of Petroleum in Structural Reservoirs (Traps)?



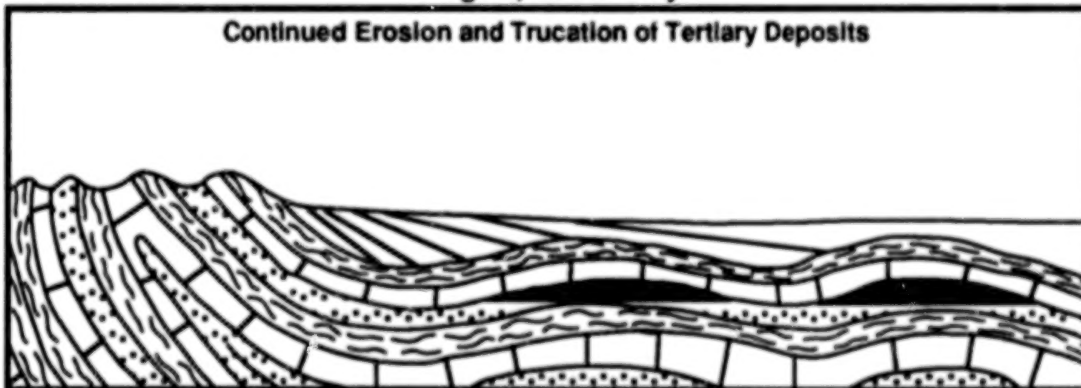
Stage 3, Middle to Late Tertiary Period

Syntectonic and Post-tectonic Erosion and Sedimentation; Deposition of Continental Sedimentary Deposits



Stage 4, Quaternary

Continued Erosion and Truncation of Tertiary Deposits

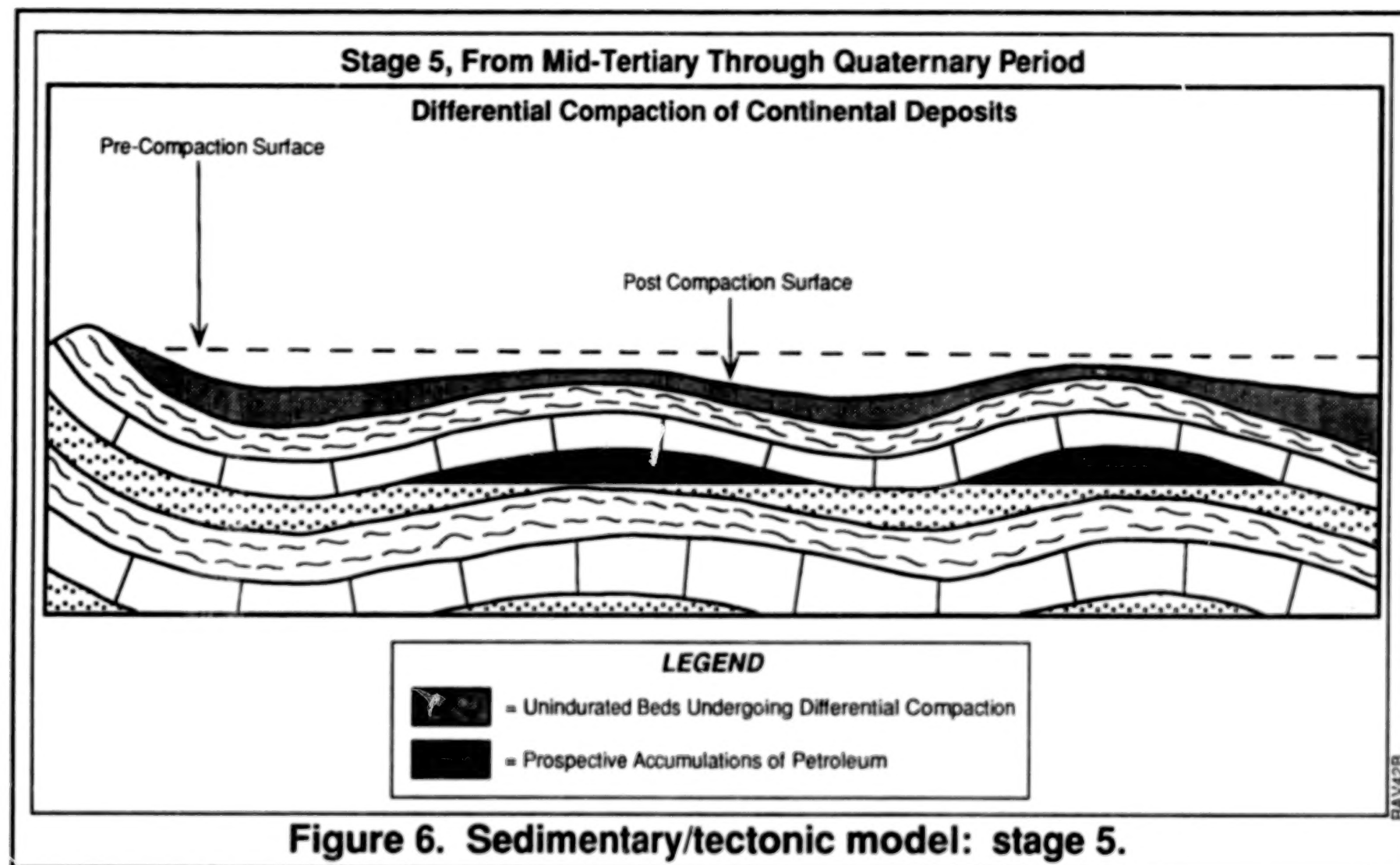


RAV41B

Figure 5. Sedimentary/tectonic model: stages 1-4.

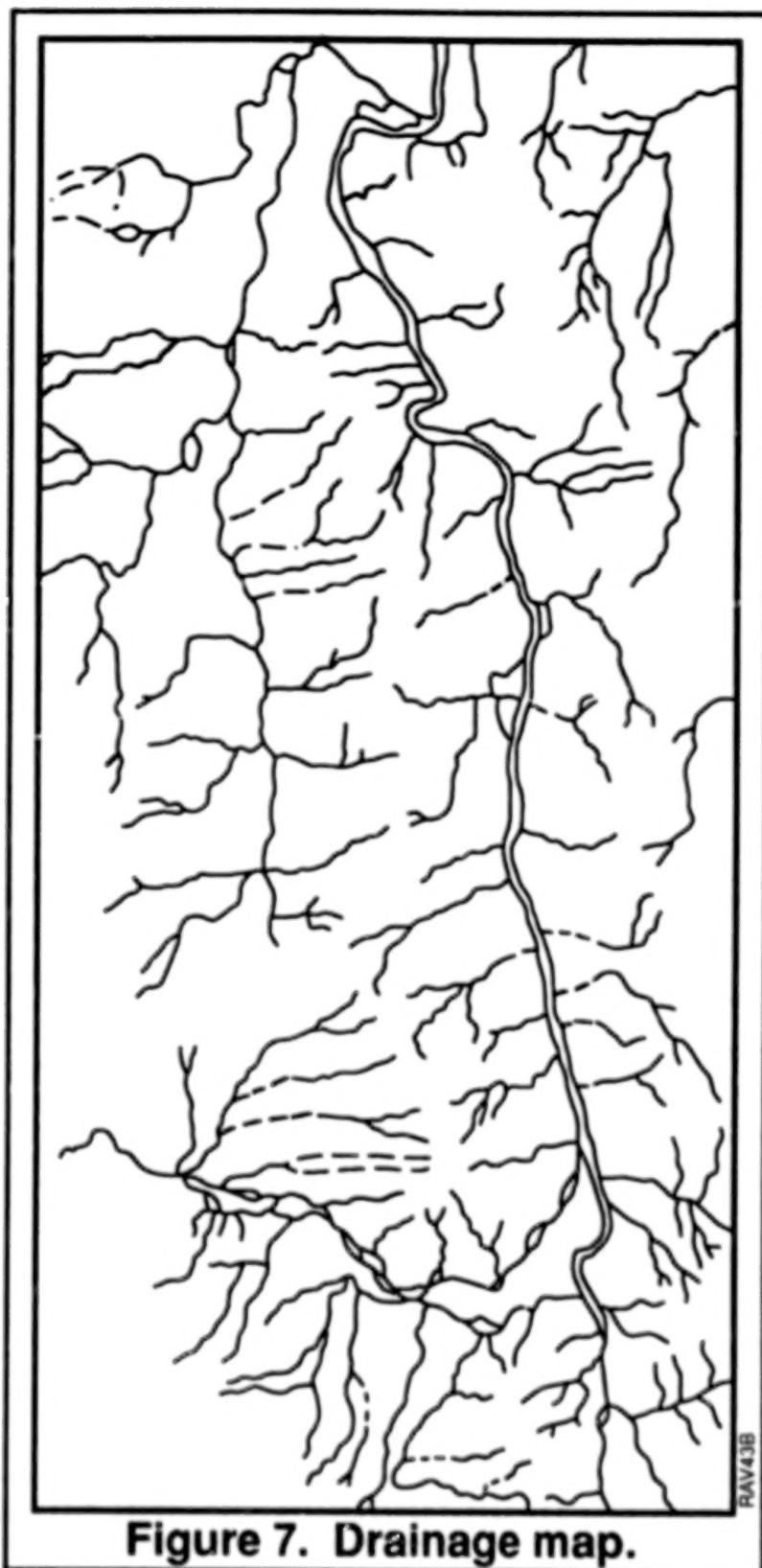
000233

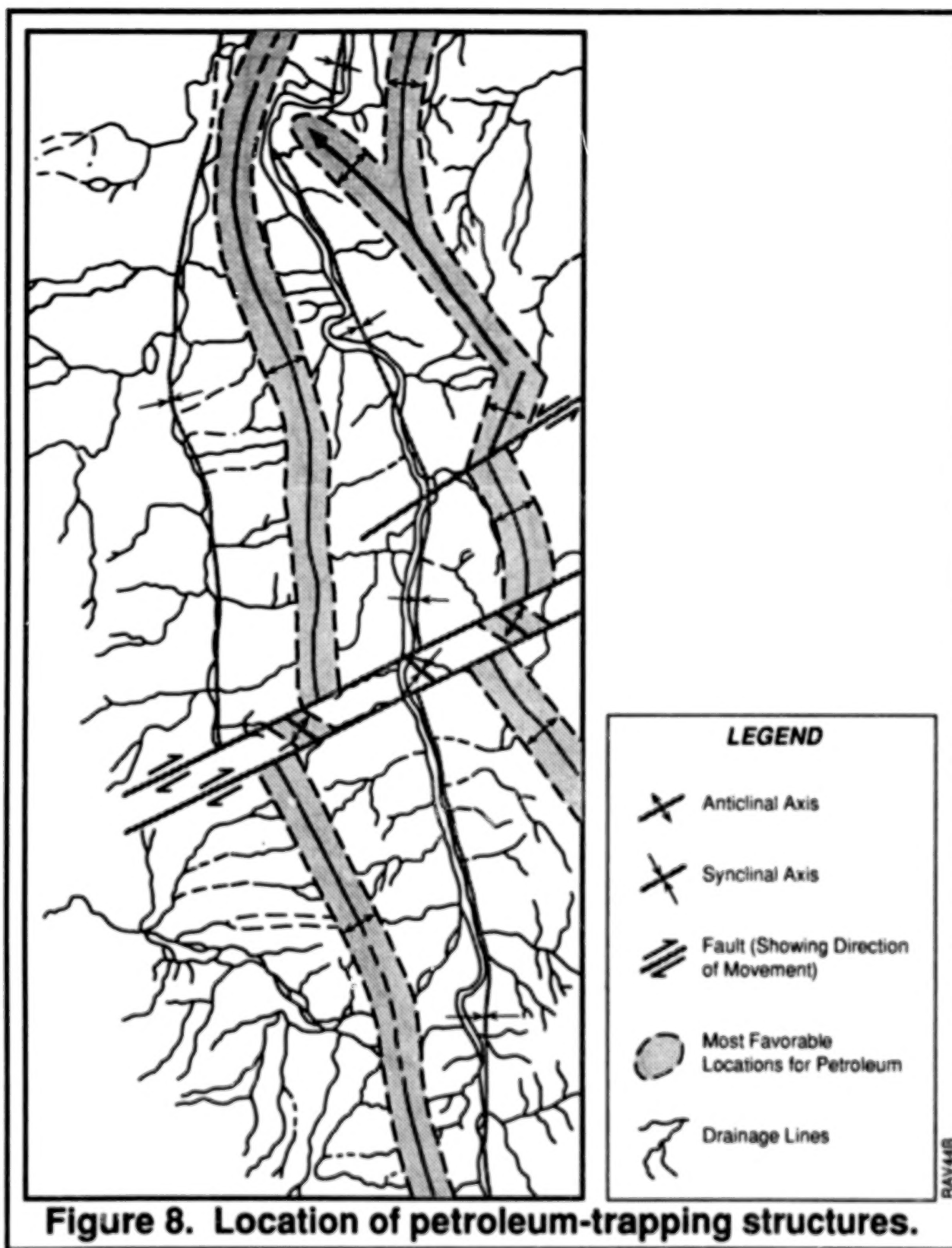
770



000234

BLANK PAGE





synclinal axes that are shown in Fig. 8 were derived solely from the evidence of the drainage map on the basis that differential compaction produces a surface configuration that is a muted manifestation of the underlying topography.

2.6 APPLICATION OF THE HYPOTHETICAL MODEL TO THE LOCATION OF PETROLEUM

Once the Almaz-based hypothesis had gained a large measure of confirmation based on the two successful predictions, it became a relatively easy matter to apply the implication of the hypothesis, with some confidence, to predicting areas in which petroleum, if present, would be trapped and accumulated.

Since it is known that petroleum migrates updip to the crests of anticlines, the locations of prospective accumulations are shown in Fig. 8 as shaded zones (of necessarily arbitrary width) that lie along the drainage-derived locations of anticlinal axes. Pending confirmation from seismic surveys (which are costly, laborious, and, in this area of interest, highly dangerous because of drug producers and Shining Path guerrillas), the shaded zones in the figure are where petroleum is predicted to be found if it is present in the area.

"If petroleum is present," is a cautionary phrase that has been used several times in this paper, since geologic exploration, whether conducted through the use of remote sensors or on the ground, can identify only the conditions of petroleum accumulation but not petroleum itself. It is a geological truism that "Oil is discovered only by a drill bit."

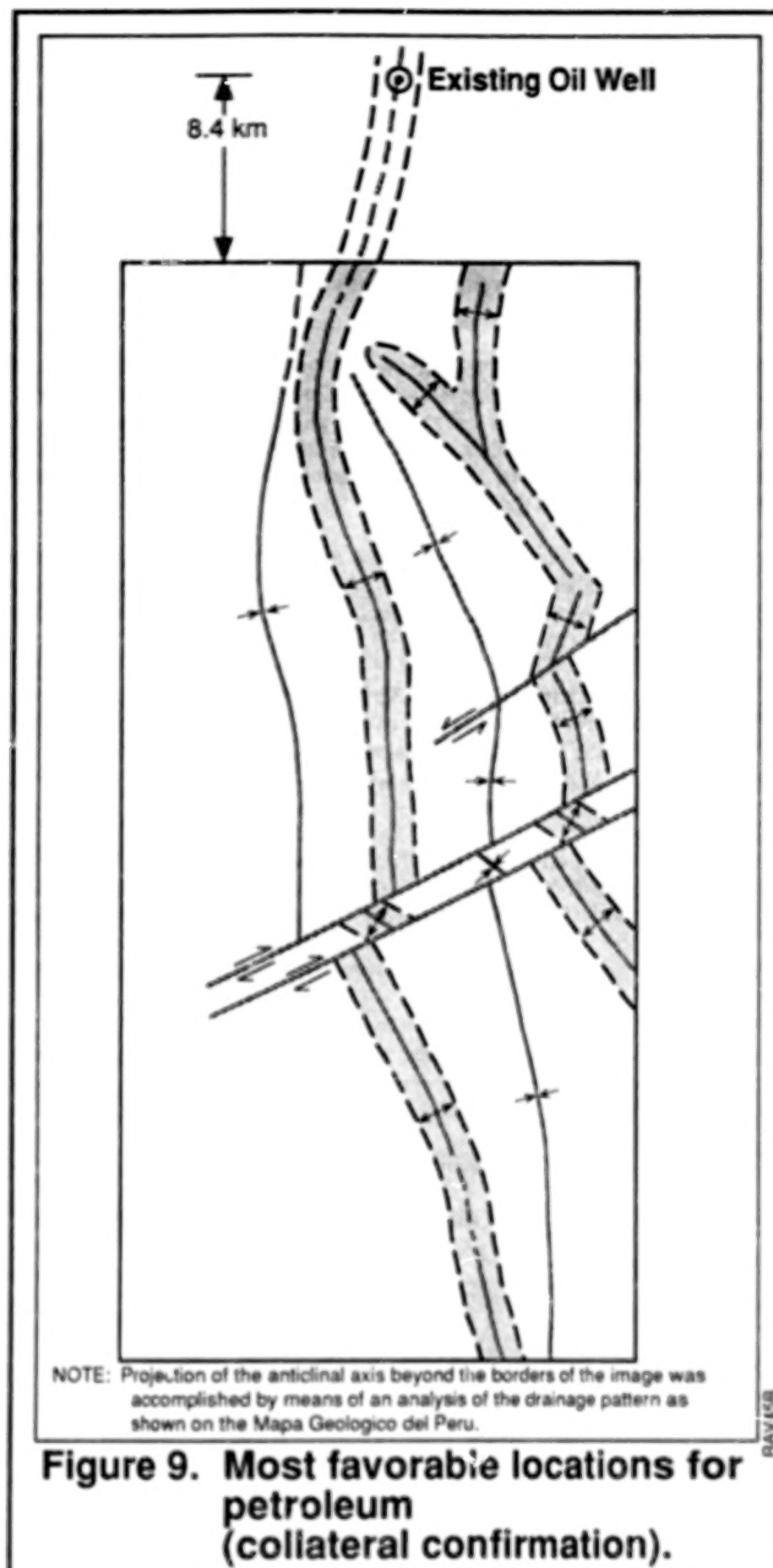
However, following the completion of the Almaz investigation, one additional, collateral (i.e., non-inferential) bit of information was unearthed in the form of an untitled map that showed an oil well in the general vicinity of the study area. This well, when transferred to the Almaz image map, appears as is shown in Fig. 9. As can be seen, the well lies on the projection of one of the anticlinal axes only 8.4 km north of the area of interest.

Thus, three predictions based on the hypothetical model have been fulfilled: 1) that there are subsidiary anticlines; 2) that differential compaction has occurred and can reveal the number and location of these anticlines; and 3) that if oil exists in the area, it will be found along the crest of an anticline. On the basis of these fulfilled predictions, it appears highly likely that a new oil field has been discovered within the confines of the area of interest defined by the Almaz image.

The next step in the exploration process would be, eventually, to conduct a seismic survey that would: 1) confirm the geologic model (either positively or negatively); 2) refine the model (by adjusting the location of the fold axes and the number and thickness of the lithologic units); and 3) produce a three-dimensional model having a much more realistic vertical scale.

REFERENCES

Instituto Geologico del Peru, 1977: Mapa Geologico del Peru, scale = 1:1,000,000.



MULTISPECTRAL MEASUREMENTS OF ACTIVE LAVA FLOWS IN THE MWIR (2.0-5.0 μm)

K.D. Bishop, J.A. Granger, E.L. Jewett
Lockheed Palo Alto Research Labs
Palo Alto, California 94304

ABSTRACT

The currently active flows from Kilauea and subsidiary vents on the island of Hawaii offer an extraordinary opportunity for geologic study through the use of multispectral remote sensing techniques. Utilizing an airborne 45 channel imaging spectrometer, the active flow areas between the Pu'u O'o vent and the sea were mapped over the 2-5 μm range on 23 May 1993. The resulting spectra and spatially reconstructed imagery described both the structure of the subterranean flow tubes as well as recent changes in flow patterns including a new (as compared to USGS mapping data of Jan '93) subsurface opening to the sea. Various aspects of sensor/platform characteristics, calibration, image processing and spatial reconstruction, spectral and thermal analysis, and a comparison of published flow/topological mapping data to the measured MWIR structure will be presented.

1. INTRODUCTION AND SYSTEM DESCRIPTION

The Airborne Instrument Program (AIP) is a Multispectral Mid-Wave Infrared (MWIR) data collection activity conducted by the Lockheed Palo Alto Research Labs in conjunction with the NASA Johnson Space Center's WB-57F high altitude research aircraft program. The data presented here summarize the Kilauea thermal mapping flight experiment of 24 May 1993.

1.1 AIRCRAFT PLATFORM

Based at Ellington Field, an offsite extension of the NASA Johnson Space Center in Houston Texas, the WB-57F is a high altitude, two-place, twin-engine aircraft with a maximum ceiling of 19 km (62,000 ft). The F-model is a descendant of the earlier B-57, originally modified for high altitude reconnaissance (larger wingspan, more powerful engines), with the bomb bay areas converted over to house scientific instrument packages such as the AIP sensor. Due to fuel efficiency and operational safety constraints, the aircraft is typically operated at altitudes of either 14 km or 18 km with the latter requiring the use of full body pressure suits by the aircrew. Cruising speed, at 14 km, is typically 390 knots with a maximum flight duration, limited primarily by fuel capacity, of approximately 6 hours. The aircraft cockpit is two-seat with a pilot and instrument operator/navigator making up the flight crew.

1.2 AIP SENSOR PAYLOAD

The instrument itself is both a scanning spectrometer and staring radiometer utilizing common pointing optics, imaging lens and Indium doped Silicon photoconductive 45x90 element detector array. An internal motor driven mirror is commanded into or out of the optical path to bypass the spectrometer and reflect the incoming light directly into the imaging lens and onto the focal plane to provide a two dimensional staring capability as well as a multichannel (currently approximately 60 useful channels) MWIR spectrometer. The spectrometer utilizes a narrow reflective slit as a field stop and a two-element prism to provide spectral dispersion. Additionally, two motorized 5-position filter wheels, one containing 4 bandpass filters and an open, and the other with 4 neutral density filters and an open, are housed within the vacuum-cryocooled dewar enclosing the telescope optics. Spectral resolution, determined by the projection of the prism dispersion onto the multi-element detector array,

ranges from 25 nm at 2.2 μm to 70 nm near 5 μm . The total spectral coverage of the spectrometer extends from 2.0 to 6.3 μm , however for most down-looking applications, typically 50-60 of the 90 focal plane columns receive useable signal levels due to atmospheric absorption. As the focal plane array (FPA) is oriented with the dispersion direction along the 45 element (row) axis, a frame of spectrometer data consists of 50-60 narrow band line images of the projected footprint of the reflective entrance slit.

A diagram of the AIP optical system is presented as Fig. 1 below. The task of pointing and acquiring an object of interest are performed by a Stabilized Mirror Pointing System (SMPS) in conjunction with visible-band TV cameras feeding into a monitor in the instrument operator's console. Operator joystick commands, a pre-programmed position/angle timeline, or a closed loop video tracker system can all be used to control instrument pointing over a range of 30 deg forward to 20 deg aft in pitch (along the axis of the aircraft) and 90 deg either side of straight down (NADIR) in roll. Additionally, a commercial Short Wave Infrared (SWIR) camera utilizing a Pt:Si detector array and Charge Couple Device (CCD) readout structure is installed in the system as an alternate tracking source to the wide and narrow field TV cameras.

To sweep the projection of the spectrometer entrance slit across the target area, a motorized, commandable, fine scan mirror system may be used as an alternative to the simple fixed angle/aircraft motion pushbroom commonly used on down looking systems. The angular resolution or detector instantaneous field-of-view (IFOV) is 1.17×10^{-3} rad/detector element for the radiometer or the spatial axis of the spectrometer. The projected angular width of the entrance slit is currently 360 μrad , having been recently increased from 150 μrad at the time of these data collections. The practical angular resolution of the scan-axis of the spectrometer however is generally a function of scan mirror angular rate and/or aircraft velocity. External optical elements are sized for 45x45 detector array with some oversizing in the scan direction to allow for scan mirror motion, bringing the total Field of View (FOV) to 53 mrad or 3 deg.

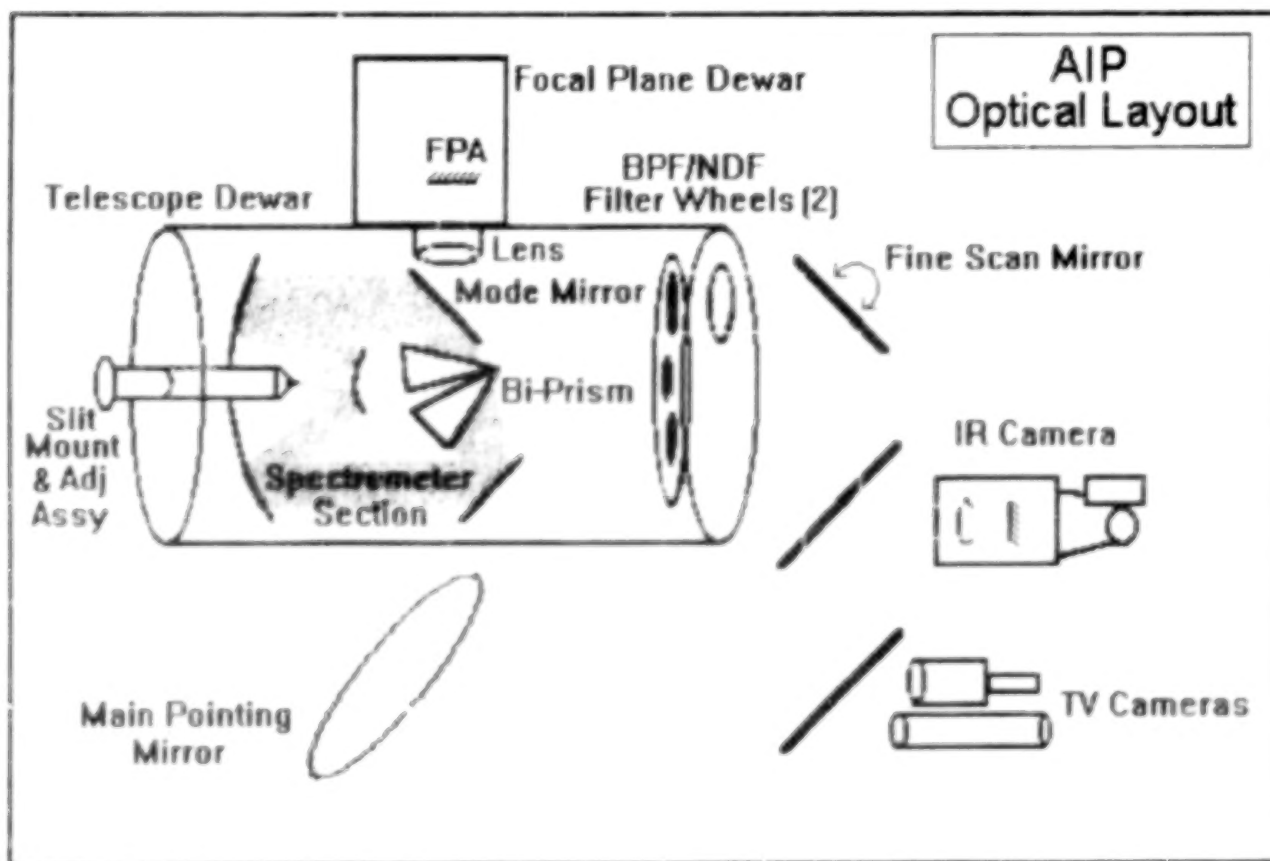


Figure 1 AIP Optical System Diagram Radiometer and Spectrometer Paths Shown in Two-Tone Gray Scale

2. BACKGROUND : THE KILAUEA ERUPTION

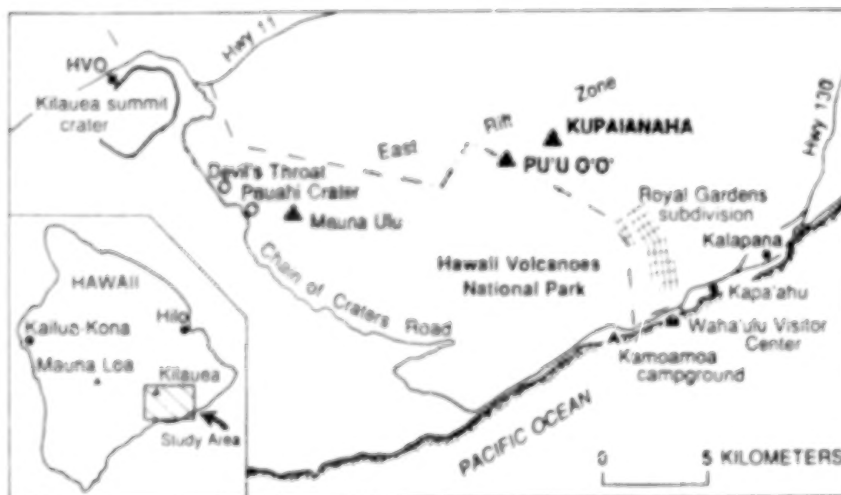
The eruption of Kilauea is a unique phenomenon where geologic change is measured in years, sometimes even days, as opposed to centuries. To appreciate the significance of the Kilauea eruption, which is now entering its 11th year, a brief discussion of its background and history is in order. Much of the material to following has been synopsized, or in some cases directly re-printed, from an excellent summary paper by Clague and Heliker (1992). This paper is highly recommended for anyone interested in a general overview of the Kilauea eruptions as it is concise and understandable with just the right amount of technical detail to appeal to a wide range of professional and educational backgrounds.

The Kilauea volcano on the island of Hawaii has been in nearly continuous eruption since January 1983. Some 52 geologic episodes of flow activity have been recorded centering primarily on the string of vents and fissures called the East Rift Zone which extends on a south-eastward arc some 30 km down from the main Kilauea summit crater.

By mid-1983, the site of a new vent, called Pu'u O'o, became the center of activity for some three years or 44 eruption episodes. In July 1986, another vent, named Kupaianaha, formed 3 km to the east of Pu'u O'o. In a quiet, continuous outpouring of lava, first a lava pond and then later a channel formed which eventually roofed over and became the beginning of a 12 km long lava tube carrying the flow down to the Pacific by December 1986. The smooth, billowy flow, called pahoehoe, covered almost 200 homes, the Hawaii Volcanoes National Park Visitor's center at Waha'ula and the entire towns of Kapa'ahu and Kalapana by the end of 1990.

The most recent series of episodes (50-52) began in February 1992 with the opening of a 150 m long fissure on the west side of the Pu'u O'o cone. Later, in March 1992, the fissure extended higher onto Pu'u O'o and formed several new vents which have been intermittently active to the present day (Episode 51). In October 1992, a new eruptive fissure opened co-incident with a magnitude 4.3 earthquake beneath the southern slope of Kilauea. The flow from this event (Episode 52) was fairly short-lived but permanently altered the flow pattern of the episode 51 vents. Since that earthquake, there has only been a single 24-hour long pause in the eruption. By December of 1992, through a network of newly formed lava tubes, a continuous flow of virtually all of the lava erupted at the episode 51 vents, reached the Pacific covering the Kamoamoa campgrounds and forming a triangular delta extending 300 m into the sea.

Figure 2, a reprint of a map from Clague and Heliker (1992), illustrates the relative locations of the Kilauea crater, the East Rift Zone (as indicated by the wide gray arc), and the Pu'u O'o and Kupaianaha vents. Also shown in Fig. 2 are the ill-fated Royal Gardens subdivision, Waha'ulu Visitor Center, Kamoamoa campgrounds, and the towns of Kapa'ahu and Kalapana. The small corner map in Fig. 2 indicates the location of the Kilauea/East Rift Zone area relative to Mauna Loa, the other currently active volcano on the island having last erupted in 1984, and the cities of Hilo and Kona.



The area covered by this flight experiment extends on a line between the Pu'u O'o vent and the Kamoamoa campgrounds.

The area covered by this flight experiment extends on a line between the Pu'u O'o vent and the Kamoamoa campgrounds.

Figure 2 - Kilauea, the P'u O'o and Kupaianaha Vents, and the East Rift Zone

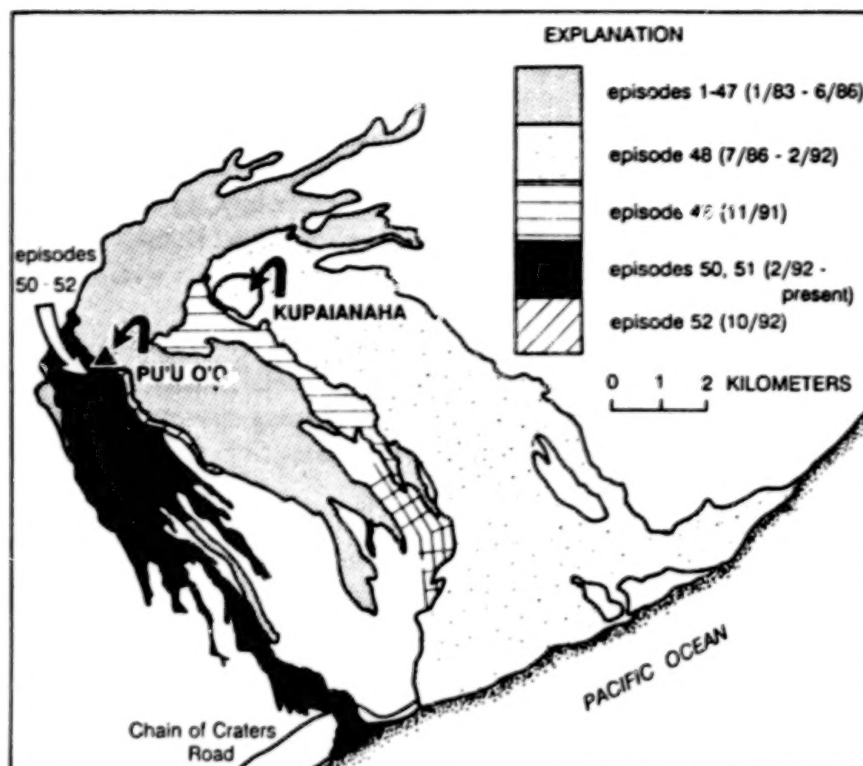


Figure 3 - Kilauea Flow Episodes : Areas Affected by Recent Flows in Black

Kilauea summit. There is however no evidence that the eruptions along the East Rift Zone will stop entirely. The current series of eruptions, begun in 1955, marked the end of 115 years of quiet for this part of the rift.

In summary, the Kilauea eruptions, which have lasted over 11 years so far, have extruded more than a billion (10^9) m^3 of lava, destroyed homes, towns and parks and formed a 12 km long chain of underground tubes to carry the river of molten rock to the sea. The scale of geologic change and destruction left by Kilauea is immense. The eruptions of Kilauea are truly an interesting and unique feature for scientific study.

3. MISSION PLANNING - THE FLIGHT EXPERIMENT

As the current flow is almost entirely subsurface, the thermal infrared capability of the AIP spectrometer was used to map the upwelling heat flow, by its subsequent infrared emission, and thereby construct a map of the underground lava tube network. The overall approach was to overfly the area with a series of parallel nadir staring pushbroom (using the aircraft motion to sweep the projection of the spectrometer's entrance slit across the scene as opposed to active scanning) swaths which could be registered and superimposed to form a composite map of the entire flow. Initially five tracks were planned with a 680 m track to track spacing. At an altitude of 18.3 km (60,000 ft) the cross-track swath width of the AIP spectrometer would be approximately 960 m providing for a track to track overlap of approximately 30%. The original flight plan called for the use of a hand-held Global Positioning System (GPS) receiver unit to provide periodic accuracy updates to the aircraft's Inertial Navigation System (INS) and minimize the effect of track-track positioning errors and thus ensure complete, overlapping ground coverage of the flow areas. A graphical view of the flight plan is shown in Fig. 4.

In terms of sensor and radiometric measurement parameters, the desire to maximize thermal contrast was deemed more important to the thermal mapping mission than avoiding transient detector saturation effects while crossing exposed flow areas. The spectrometer was therefore configured for maximum sensitivity : open spectral and neutral density filters at a 40 hz data rate. In order to minimize the impact of diurnal heating and cooling of the solidified flow surface and surrounding rock, the flight experiment was planned for local midnight.

Figure 3 is a map detailing the areas affected by the respective flow episodes (1-52) and their approximate dates. The most recent flows, episodes 50-52, are denoted in black. Currently, only the episode 51 vents are flowing. As long as this trend continues, no further damage to residential areas appears likely.

There is evidence that the lava flow process from Kilauea may be winding down as the lava extrusion rates are significantly lower than those measured only a few years ago. The Kupaianaha vent shut down completely in February 1992.

Additionally, the locations of the active vents appear to be slowly migrating toward the

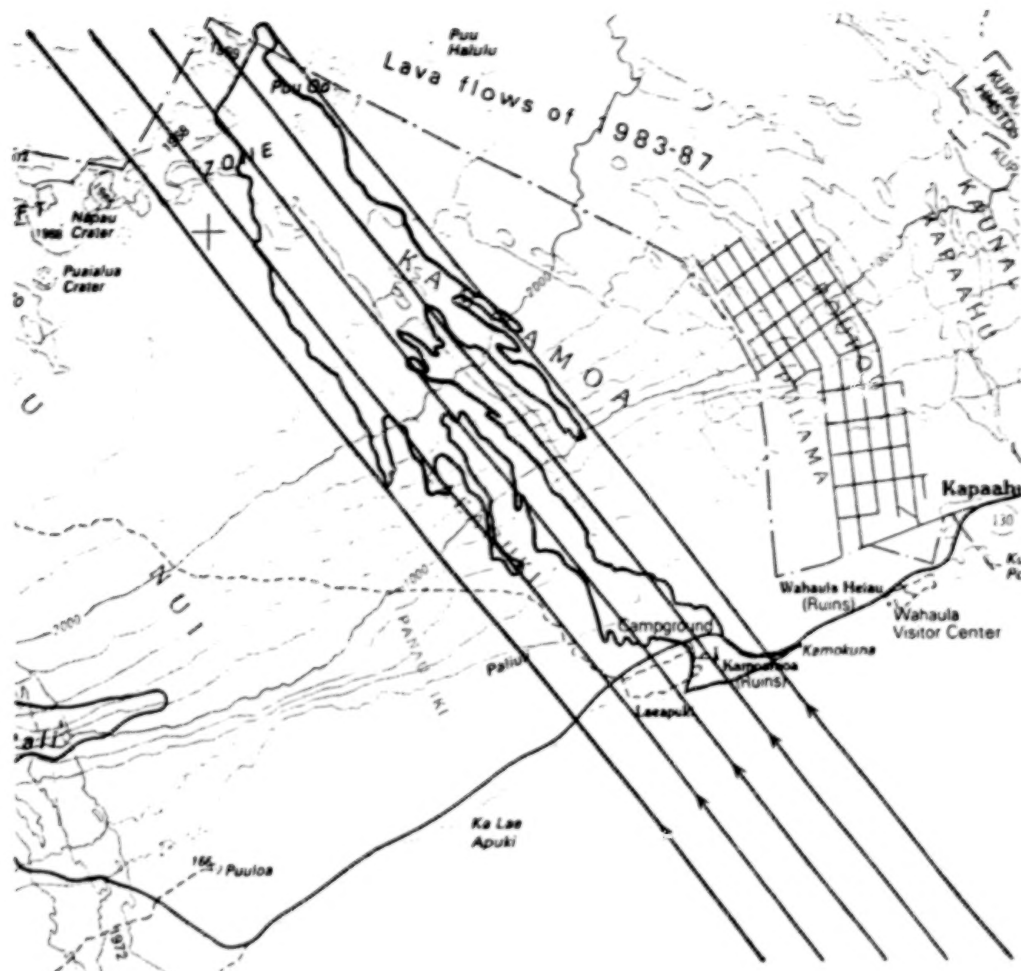


Figure 4 - Kilauea Lava Flows Flight Collection Plan : Layout of 5 Parallel Flight Tracks Over Active Flow Area. Topological Map With Tracks and Episode 50-52 Flow Outlined

In actuality, the execution of the flight experiment, in the early morning hours of 24 May 1993, was somewhat different than the original plan. An in-flight failure of the on-board GPS receiver forced the tracks to be flown by relying entirely on the aircraft INS for navigation. Typical drift errors in the WB-57F's INS system are on the order of 0.1 to 0.3 nautical miles (185-560 m). A random track-track positioning error of this size could prove fatal to a complete mapping reconstruction later on; and so an in-flight decision was made to collect two complete sets of the five track flight plan. Utilizing the data from seven of the ten flight tracks, a complete mosaic of the flow area was finally constructed; a single band sample of which is shown in Fig. 5.

4. IMAGING SPECTROMETER DATA ON THE ACTIVE FLOW

A total of 10 tracks were flown accounting for 40,000 frames of 45 channel MWIR spectrometer data. Spectral coverage extends from 2.3 to 5.2 μm , with spectral channel widths of 0.03 μm (at 2.3 μm) to 0.07 μm (around 4.5 μm). The spectral dispersion curve is somewhat non-linear with a rapid rise in spectral bandwidth, with wavelength, to about 4.5 μm , and a gradual fall-off in bandwidth beyond ($\Delta\lambda \sim 0.068 \mu\text{m}$ at 5.2 μm). Instrument sensitivity, in terms of a Noise-Equivalent-Spectral-Radiance (NESR) was approximately 1.0 $\mu\text{W}/\text{cm}^2\text{-SR-}\mu\text{m}$, corresponding to a surface Noise-Equivalent-Temperature-Difference (NEAT) of 0.23 K at 4.7 μm (A LOWTRAN 5B calculation was used to estimate atmospheric transmittance).

Figure 5 at right is a single band false color thermal IR (4.7 μm) mosaic reconstruction of the active flow areas between the Episode 51 vents, near Pu'u O'o, and the Pacific. The composite image was produced by the registration and superposition of data from 7 of the 10 flight tracks. Track-track seams are still faintly visible in the final image. To properly reconstruct the spatial along-track axis, a graphical display of the data at a 4:1 aspect ratio was used to represent the distance traveled by the sensor line-of-sight in a single frame time in proportion to the apparent width of a pixel footprint in the cross-track direction. In this fashion, the data at right represents the radiometry collected over a 2500 frame by 225 pixel (12.3 x 4.8 km) area.

Detector saturation effects are evident in the image as white horizontal lines or 'spill-over' of charge within the focal plane's Charge-Coupled-Device (CCD) readout; the heaviest region of which occurs directly over the main vent and lava pool at Pu'u O'o as seen in the upper right of the mosaic. The chain of small sources extending through the main vent and diagonally across the upper portion of the image are the fissures and vents marking the East Rift Zone. The Kilauea summit could be reached by following the chain back up the slope, approximately 17 km to the left. The Kupaianaha vent, scene of the 1986-90 eruptions which buried Kalapana and the Royal Gardens subdivision, would be found about 3 km further to the right.

Immediately below the main vent, the apparent flow is diffuse, covering an area 1.5 x 3 km with several localized hot spots or 'skylights' (small areas of exposed flow usually caused by collapse of a piece of the solidified 'roof' over the flow) as evidenced by detector saturation. The flow begins to converge on a single, clearly defined channel mid-way down the slope (around the 2,000 ft elevation level). The flow then divides first into two channels and ultimately a complex network of flow tubes before separating again into two major flow channels.

The left of these two arms of the flow exits directly to the shoreline forming a triangular delta at the mouth. The right channel, initially narrower and more distinct, divides into a maze of tunnels and empties into the ocean in at least two, but probably more, locations. A massive delta of lava 0.5 km wide by 300 m deep forms at the rightmost entrance to the sea. Thermal plumes in the ocean surface spread more than 1 km in any direction outward from the discharge point, and can be clearly be seen at the bottom of the image.

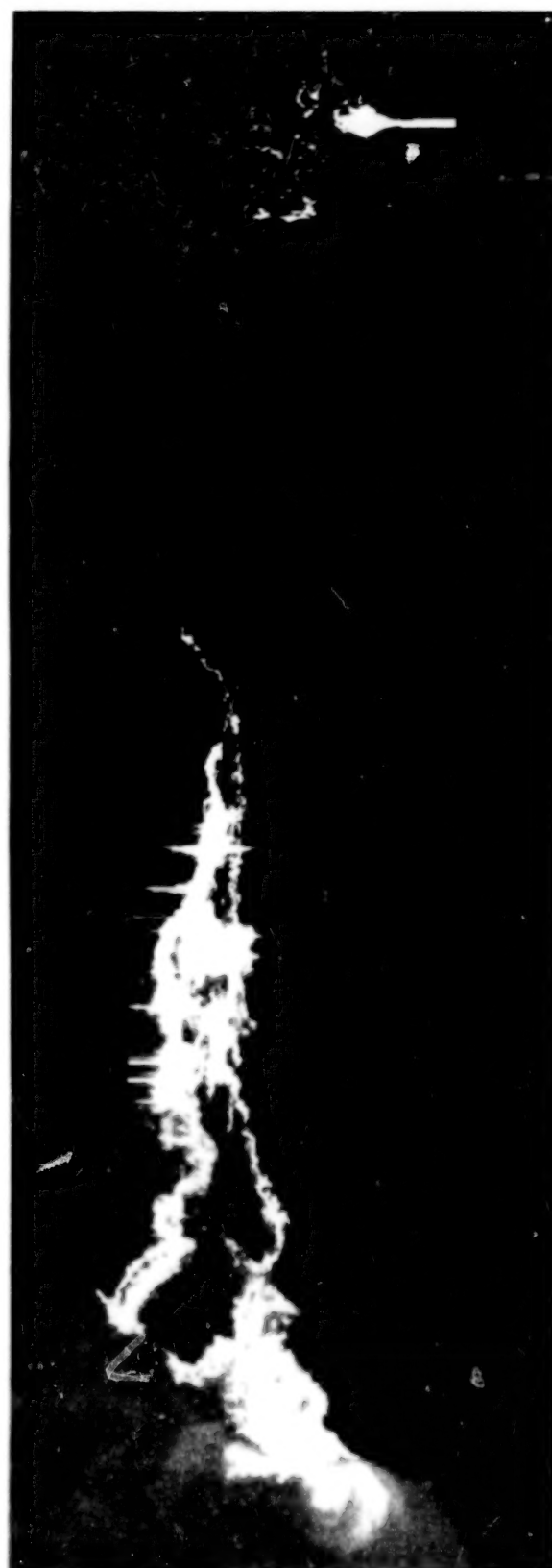


Figure 5 - False Color IR Map of the Active Flow Areas between Pu'u O'o and the Sea



Figure 6 - False Color Thermal Map of Lava Flow Delta : Computed Temperature
Based on 4.7 μm Measured Radiance. Color Scale Range : 295-330 K

In terms of a more quantitative look at the data, Fig. 6 is a 45 x 45 pixel reconstruction of one of the lava flow deltas as seen in the lower left of the area map in Fig 5. In order to compute surface temperature, a Lowtran 5B transmission model was used to back out the effects of atmospheric absorption before applying an iterative Planck-Function based equivalent blackbody temperature convergence algorithm. As with the mosaic, the band selected for processing was 4.7 μm due to its excellent thermal contrast and relatively high atmospheric transmission.

The ground surface temperature, near 295 K, appears dark, surrounding the brighter flow. The ocean, at nearly 300 K, appears slightly warmer but essentially featureless. The absence of a thermal plume indicates little actual discharge into the ocean as cooled layers of rock form a barrier forcing the flow to extend laterally outward along the coastline, forming the 'fingers' to the upper left and lower right hand corner of Fig. 6. The single pixel hot-spot, just above center in Fig. 6, is probably a sub-pixel 'skylight' or collapse of the overlying solidified material above the main flow. Although the temperature of the flow itself is undoubtedly much greater than 330 K, the relative area occupied by the skylight is probably quite a small fraction of a pixel footprint (21.4 m at 18.3 km or 60,000 ft altitude). In all a surprisingly modest range of temperatures are detected at the surface of the lava flow delta indicating that the body of the flow is deeply subsurface.

A low level periodic pattern can be seen in the data, particularly against the featureless ocean surface, as a slight diagonal banding pattern in the image. However, an inferred surface Noise-Equivalent-Temperature Difference

Lava Flow and Background Spectra

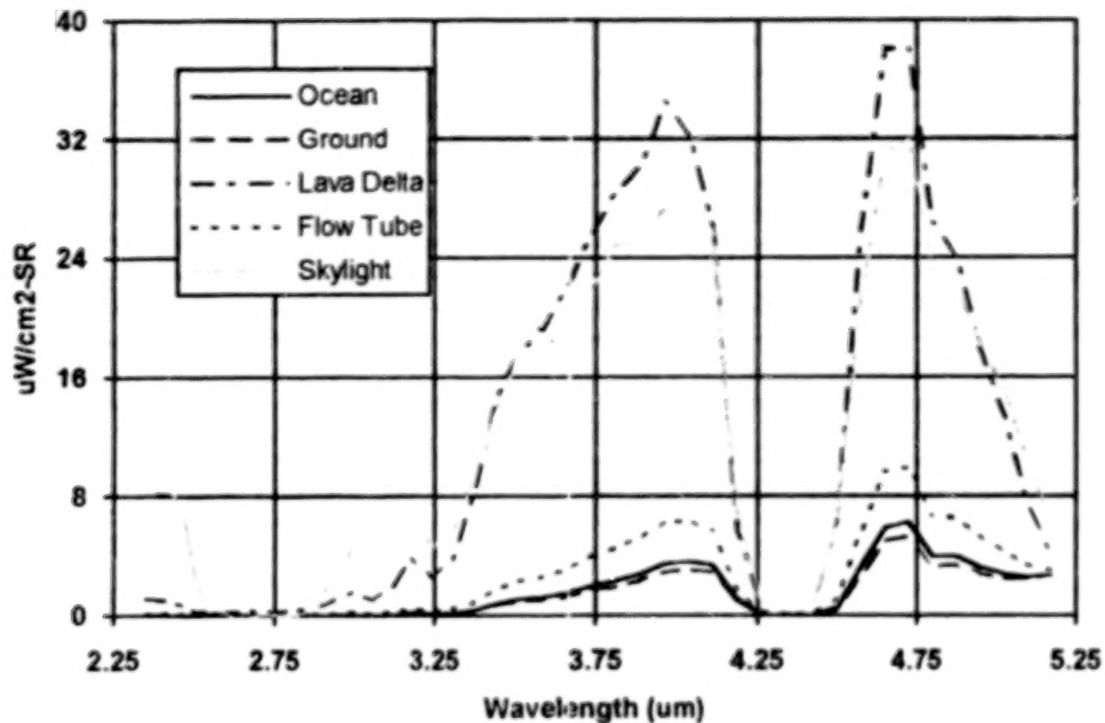


Figure 7 - Lava Flow and Background Spectra : Ocean (300 K Blackbody), Cold Mid-Slope Surface Background (Ground), Lava Flow Delta, Lava Flow Tube (mid-slope), Small Area Skylight (near Pu'u O'o)

(NEAT) calculation of 0.2 K, limited primarily by an atmospheric transmission, estimated by Lowtran 5B at 0.4, indicates little was lost in the way of useful sensitivity, as this performance is excellent for the AIP sensor.

In terms of spectral data, Fig. 7 above illustrates some of the background and lava flow spectra collected during the Kilauea thermal mapping flight experiment. The lava delta curve refers to the spectra collected over the large, triangular delta where the primary flow discharges into the Pacific (seen at lower right in the mosaic of Fig. 5). The skylight curve was chosen from the one of the many small area broken and exposed flow regions just below the main vent. Both of these spectra are composites in the sense that they cannot be described by a single blackbody source term, but rather have short wavelength components characteristic of high temperature sources on top of a strong long wavelength (low temperature) background. The strong short wavelength component of the skylight curve indicates the at least some small portion of the detector footprint imaged the exposed lava flow. In fact, the composite spectra could be modeled by a series of blackbody temperature terms where the relative constants or weighting factors express the product of emissivity and detector footprint fill factor. A simple example of this technique is illustrated in the technical report accompanying the Kilauea thermal mapping data package. Without supporting ground truth data however, the validity and 'unique-ness' of information inferred from a multi-term blackbody model solution is in question.

The lava flow tube spectra in Fig. 7 was chosen from a point 3/4ths of the way down the slope between Pu'u O'o and the Pacific where the flow again separates into two distinct channels to the sea. The spectra here is characteristic of an area blackbody at a single, relatively modest temperature (approximately 320 K).

The ocean spectra, due to an inadequate cold-sky background collect, is essentially that of a 300 K blackbody as seen through a Lowtran 5B modeled atmosphere. In the calibration process, the featureless ocean background was used as a pattern and sensor internal background reference and subtracted off with the analytic approximation of the ocean spectra, (i.e. - the transmitted 300 K blackbody radiance) added back in as spectral offset constants. Spatial imagery is unaffected. A complete tabulation of these computed radiance offsets are provided with the data package. As these constants are small numerically in comparison with the flow radiance, and published average ocean surface temperatures in the Hawaiian islands range from 26-28° C, the residual error (i.e. the difference between the real ocean spectra and the model), and hence the effect on flow spectra, in most cases is quite small, particularly in the shorter wavelength bands.

The ground spectra, somewhat colder than the ocean, is also a near-blackbody as the surface of the slope is entirely covered by episode after episode of lava flow. The absolute intensity values of low level background spectra are impacted somewhat by the 'ocean background' calibration procedure, however radiometric and temperature differences are preserved.

4. SUMMARY

The Kilauea thermal mapping experiment of 24 May 1993, produced an interesting set of multi-spectral MWIR data on one of the most unique geologic phenomenon on Earth. The use of an airborne MWIR thermal mapping instrument provided a detailed, feature-filled mosaic of the intricate network of surface skylights and underground flow tubes carrying the erupted flow from Kilauea's Pu'u O'o vent to the sea. The flow from Kilauea is by no means a static event, with some 52 recorded episodes of new flow or flow movement over the

last 11 years. As further evidence of the dynamic nature of these active flows, Fig. 8 depicts the topological view of the flow areas south of Pu'u O'o with the episode 50-52 flow regions outlined in black. The newly measured flow pattern, from the mosaic of Fig 5, is shown superimposed onto the areas already described in Fig. 8.

The triangular delta-shaped flow mouth detailed in Fig. 6, appears as a new feature of the flow when compared to the previously mapped regions outlined in Fig. 8. (i.e. - relative to USGS mapping data from Dec 1992).

A complete data package on the Kilauea MWIR thermal mapping experiment, including calibrated spectrometer data, 45 single-channel reconstructed mosaics, video tapes, a technical summary report and aircraft and sensor telemetry data, is available to support further investigation into this amazing geologic event.

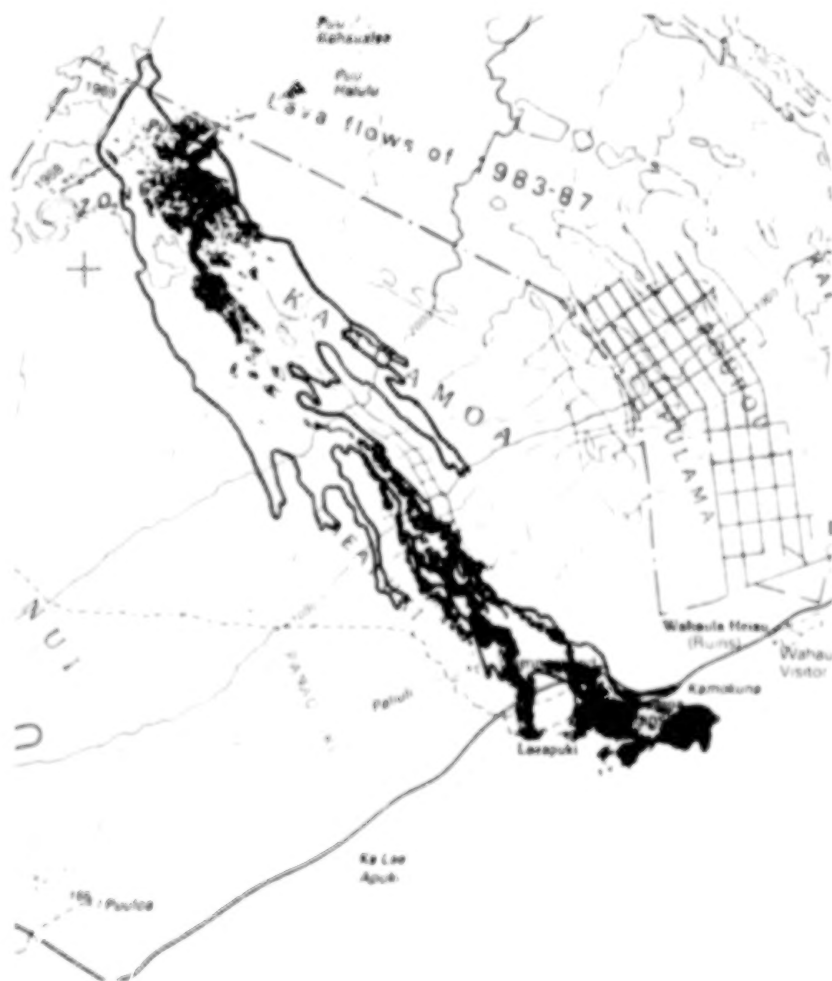


Figure 8 - Newly Measured Flow Pattern vs. Episode 50-52 Regions

REFERENCES

- Clague, D.A and C. Heliker, 1992 : The Ten-Year Eruption of Kilauea Volcano,
Earthquakes & Volcanoes, Vol 23, No 6, U.S. Geological Survey 1992, 244-254
- U.S. Geological Survey, 1986 : Hawaii Volcanoes National Park and Vicinity,
Map 19155-D3-PF-100

BIBLIOGRAPHY

The following references, while not explicitly cited in the text, provide useful background, additional technical detail and striking color photography :

- deGruy, M., Hollis, R., and J. TenBruggencate, 1990 : *Hawaii's Kilauea Volcano The Flow to the Sea*
C.F. Boone Publishing Co., Sun City West, Arizona, 81 pp
- Heliker, C., 1989 : Volcanic and Seismic Hazards of the Island of Hawaii,
U.S. Geological Survey, U.S. Government Printing Office : 1991-287-376
- Heliker, C., and D. Weisel, 1990 : *Kilauea The Newest Land on Earth*,
Bishop Museum Press, Honolulu Hawaii, 76 pp
- Jewett, E.L. and K.D. Bishop, 1993 : AIP Data User's Manual
Internal Lockheed Palo Alto Research Labs Publication
- Jewett, E.L., Granger, J.A. and K.D. Bishop, 1993 : AIP Technical Report : Kilauea Thermal Mapping,
Internal Lockheed Palo Alto Research Labs Publication
- Tilling, R.I., 1991 : Volcanoes,
U.S. Geological Survey, U.S. Government Printing Office : 1992-316-653

Rock-Soil Background Effects on Narrow Band Vegetation Indices

Christopher D. Elvidge and Zhikang Chen
Desert Research Institute
and Nevada Agricultural Experiment Station
University of Nevada System
Reno, Nevada 89506-0220

Walrave T. Jansen
WTJ Software Services
San Mateo, California 94401

ABSTRACT

An experiment has been conducted to contrast vegetation indices calculated with continuous spectra across the chlorophyll red edge versus traditional discrete band (red versus NIR) vegetation indices, using both broad and narrow bands. The results indicate that background spectral variations seriously degrade the accuracy with which discrete band indices estimate percent green cover and Leaf Area Index (LAI) for discontinuous plant canopies. The performance of the discrete band indices improved as bandwidth decreased, but were substantially out-performed by the continuous narrow band vegetation indices which measure the amplitude of the chlorophyll red edge feature.

1. INTRODUCTION

Red versus NIR vegetation indices are mathematical transforms designed to assess the spectral contribution of green vegetation to remote sensing observations. The most widely used green vegetation indices are formed with data from discrete red and near infrared (NIR) bands. This includes the Ratio Vegetation Index (RVI: Jordan, 1969), Normalized Difference Vegetation Index (NDVI: Rouse et al., 1973), Perpendicular Vegetation Index (PVI: Richardson and Wiegand, 1977), and the Soil Adjusted Vegetation Index (SAVI: Huete, 1988). These vegetation indices operate by contrasting intense chlorophyll pigment absorptions in the red against the high reflectivity of plant materials in the NIR (Tucker, 1979).

Ideally, there should be a linear relationship between vegetation index values and the quantity of green vegetation being observed. However, variations in the spectral properties of background rock, soil and litter materials can have adverse effects on vegetation indices, especially at low levels of vegetation cover. There are three main types of rock-soil effects on vegetation indices, listed here in their general order of prominence: The brightness of the background materials can have a pronounced impact on the vegetation index values derived using ratio based formulas (Huete et al., 1985; Elvidge and Lyon, 1985), with bright backgrounds producing lower vegetation index values and dark backgrounds producing higher vegetation index values. Variations in the slope from red to NIR reflectance in background materials produce variations in vegetation index values (Elvidge and Lyon, 1985). Non-linear spectral mixing

results when NIR light transmitted through plant canopies is reflected by bright background materials (Huete et al., 1984 and Roberts et al. 1993).

Preliminary research reported by Elvidge et al. (1993) indicated that the chlorophyll red edge, located between 700 and 800 nm, can be observed even in sparsely vegetated pixels. In analyzing the three adverse effects of background variations on vegetation indices, we have hypothesized that a green vegetation index derived from a continuous set of narrow bands across the chlorophyll red edge feature, would be capable of reducing the first two listed adverse background effects (albedo and red to NIR slope) on vegetation index performance. In order to test this hypothesis we designed and conducted an experiment to acquire narrow band reflectance spectra for a set of plant canopies with varying backgrounds. For our experiment we designed a matrix of observations, with plant canopy variations in LAI and percent green cover on one axis and a set of five different gravel backgrounds on the other. Vegetation indices for calculated from the resulting spectra using the original narrow bands and simulated broad band red and NIR reflectance for the Landsat Thematic Mapper (TM), the Landsat Multispectral Scanner (MSS), and the Advanced Very High Resolution Radiometer (AVHRR). The data has been analyzed to determine the predictive power of the vegetation indices for estimating LAI and percent green cover.

2. MEASUREMENTS

Five sets of wooden trays were used to place gravel materials under a plant canopy. Each set of trays contained a left and right pair, 60 by 35 cm in size, with 1 cm rims on all four sides, and circular notches at the mid-point of the adjoining 60 cm sides. The trays were painted a flat black color, to minimize the contribution of the trays to the spectra. The trays were loaded with five varieties of fine sized gravel: black, red, gray, brown, and white.

Spectral measurements of the plant canopy and gravel background combinations were made of a pinyon pine (*Pinus edulis*) canopy with an Analytical Spectral Devices Personal Spectrometer (PS-2). This instrument acquires spectra in the 0.4 to 1.0 μm region with 4 nm bandpasses (full width half maxima) with 1.4 nm sampling interval. Using a 25 degree field of view and a height above tray level of 86 cm, the observed ground area was a circle with a 38 cm diameter. This was sufficient to encompass the entire plant canopy, which had a diameter of 15 cm.

Spectra of the pinyon canopy were measured with each of the five gravel backgrounds. Each set of spectra made with the five gravel backgrounds was preceded by the acquisition of three dark current spectra and ten spectra of a Spectralon panel, which was used as a reflectance standard. For each gravel background ten individual spectra were acquired. After completing the spectra for one gravel background, trays were manually switched to place the next set in position. When spectra had been acquired for all five gravel backgrounds, a portion of the pinyon needles were manually removed and spectra with the five gravel backgrounds were repeated. The pinyon needles were sealed in plastic bag and placed on ice until the area was measured using a leaf area meter. At the beginning of each round of five gravel backgrounds, a 35 mm color slide was taken of the pinyon canopy from a near-nadir view. A one foot ruler

was placed in the gravel in each photograph to provide scale. This procedure was repeated seven times, with the seventh set of spectra made with the pinyon entirely defoliated.

A complete set of spectra for the Spectralon and the five gravel backgrounds averaged five minutes to acquire. The measurements were started at 12:10 pm Pacific Standard Time on September 21, 1993. The entire data collect was completed in 35 minutes.

3. DATA ANALYSIS

The needle areas were used to derive an LAI value for each of the cover levels. Percent green cover was estimated using gridded point counts made of the 35 mm slides. The PS-2 spectra were processed to units of percent reflectance. The reflectance factors for the red and near infrared bands for the Landsat Thematic Mapper, the Landsat Multispectral Scanner (MSS), and the Advanced Very High Resolution Radiometer (AVHRR) were derived from the narrow band reflectance spectra by passing them through the relative response curves for the red and NIR bands of the broad band sensors.

Standard red versus NIR vegetation indices (RVI, NDVI, SAVI, PVI) were calculated with the simulated TM band reflectance factors. The same indices were also calculated using narrow red and NIR bands at 674 nm and 755 nm. In addition, a narrow band Difference Vegetation Index (DVI) was calculated by subtracting the red reflectance from the NIR reflectance in the two narrow bands.

Three types of derivative based vegetation indices were calculated using the continuous narrow band data across the chlorophyll red edge, from 650 to 800 nm. Two of the indices were calculated from the first derivative of the reflectance spectra by integrating the area under the derivative curve, with and without the subtraction of a local baseline. The third index was calculated by integrating the absolute values of the second derivatives of the reflectance spectra.

Linear regressions were performed to develop equations for estimating percent green cover and LAI using the vegetation indices. The predictive power of the vegetation indices can then be evaluated based on the standard errors of the green cover and LAI estimates.

4. RESULTS

The maximum green cover level was 17.75 %, with a corresponding LAI of 0.2858. The minimum value for both LAI and percent green cover was zero. At the upper level of green vegetation cover the chlorophyll red edge can be readily observed in the reflectance spectra (Figure 1). The amplitude of the chlorophyll red edge, located between 700 and 750 nm, decreased as green needles were incrementally removed from the canopy. The chlorophyll red edge feature persists visually in the reflectance spectra to green cover level of 5.69% (Figure 2) and even 2.76%. This feature was not observable in the reflectance spectra of the canopy and gravel materials with all the green needles removed (Figure 3). A visual examination of Figures 1 and 2 indicates that non-linear mixing is occurring, with higher red edge amplitudes for the plant canopy over a bright substrates and a lower red edge amplitudes for canopies underlain by

BLANK PAGE

the dark substrates.

Figures 4 to 7 show the TM band vegetation indices (NDVI, RVI, SAVI, and PVI) versus percent green pinyon cover. The corresponding narrow band vegetation indices showed little improvement over the results obtained with the broader TM bands (Figure 8 to 11). Results were somewhat worse for the vegetation indices calculated with the MSS and AVHRR bands.

The 1st order derivative green vegetation index calculated with a local baseline provided the most linear relationships to percent green cover (Figure 12). This was closely followed by the 2nd derivative green vegetation index (Figure 13). Without the local baseline correction, the 1st DGVI produces substantially poorer results (Figure 14). The local baseline correction is not required for the 2nd order DGVI.

Our results indicate that there is an interactions between bandwidth, vegetation index formula, and the predictive power of the vegetation indices for estimating LAI and percent green cover. This is shown graphically by plotting the width of the red band against the standard error of the percent green cover estimates (Figures 15). From this figure it can be observed that the RVI and NDVI produced the highest errors in estimating percent green cover. The level of error is constant between AVHRR and MSS but gradually declines as bandwidth is reduced. The errors in green cover estimation are substantially reduced for the PVI and SAVI, with a gradual decline in the level of error as bandwidth decreases. The value of the narrow bands are not apparent for the RVI, NDVI, SAVI, PVI, 1st order DGVI using the zero baseline or the difference vegetation index (DVI). The 2nd order DGVI and the 1st order DGVI calculated with the local baseline produced a two-fold decrease in error relative to the TM band PVI and SAVI, and three-fold decrease in the error relative to the TM RVI and NDVI.

5. CONCLUSION

Using high spectral resolution field spectra of plant canopies of known green cover levels we have examined the adverse effects of background variations on the performance of broad-band and narrow-band vegetation indices. Our results indicate that the estimation of LAI and percent green cover based on broad band vegetation indices can be highly inaccurate in broad-band (e.g. AVHRR and TM) datasets of regions having discontinuous plant canopies and spectral variations in background rock, soil, and litter materials. We found that the PVI and SAVI performed substantially better than the RVI and NDVI. The background effects persist in the discrete band vegetation indices calculated with the narrow band data, yielding little improvement over the performance of their broad band counterparts. In contrast, background effects can be largely eliminated using continuous narrow-band derivative based vegetation indices, which measure the amplitude of the chlorophyll red edge.

REFERENCES

- Elvidge, C.D. and R.J.P. Lyon, 1985, Influence of rock-soil spectral variation on the assessment of green biomass. *Remote Sensing of Environment*, v. 17, p. 265-269.
- Elvidge, C.D., Z. Chen and D.P. Groeneveld, 1993, Detection of trace quantities of green vegetation in 1990 AVIRIS data. *Remote Sensing of Environment*, v. 44, p. 271-279.
- Huete, A.R., 1988, A soil-adjusted vegetation index (SAVI). *Remote Sensing of Environment*, v. 25, p. 295-309.
- Huete, A.R., R.D. Jackson and D.F. Post, 1985, Spectral response of a plant canopy with different soil backgrounds. *Remote Sensing of Environment*, v. 17, p. 37-53.
- Jordan, C.F., 1969, Derivation of leaf area index from quality of light on the forest floor. *Ecology*, v. 50, p. 663-666.
- Richardson, A.J. and C.L. Wiegand, 1977, Distinguishing vegetation from soil background information. *Photogrammetric Engineering and Remote Sensing*, v. 43, p. 1541-1552.
- Roberts, D.S., M.O. Smith and J.B. Adams, 1993, Green vegetation, nonphotosynthetic vegetation and soils in AVIRIS data. *Remote Sensing of Environment*, v. 44, p. 255-269.
- Rouse, J.W., R.H. Haas, J.A. Schell, and D.W. Deering, 1973, Monitoring vegetation systems in the great plains with ERTS. *Third ERTS Symposium, NASA SP-351*, v. 1, p. 309-317.
- Tucker, C.J., 1979, Red and photographic infrared linear combinations for monitoring vegetation. *Remote Sensing of Environment*, v. 8, p. 127-150.

Raw and Smoothed PS2 Spectra (Pinyon - Green Cover Level 2)

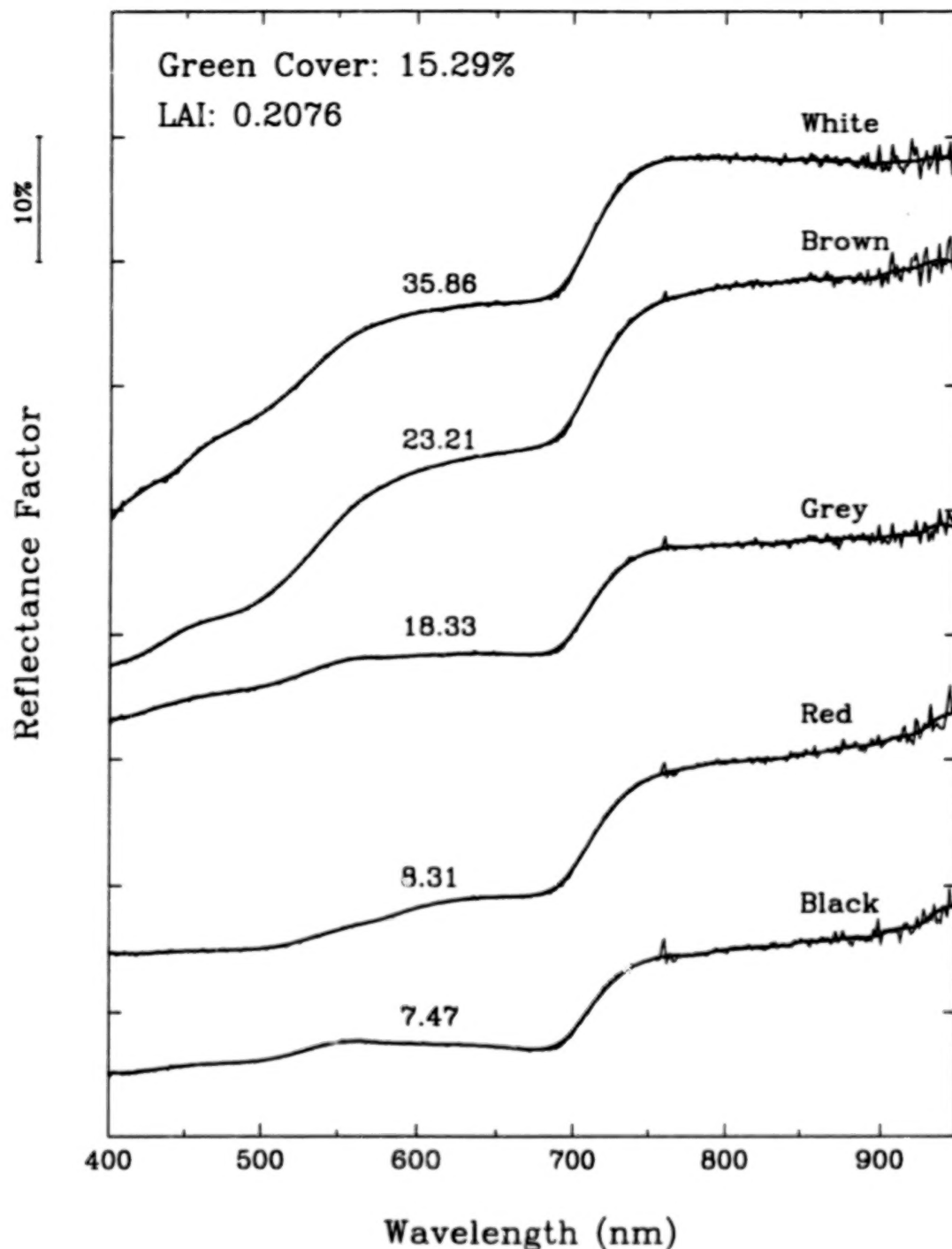


Figure 1. Raw and smoothed reflectance spectra of the pinyon canopy at green cover level 1 with five different gravel backgrounds. The pinyon canopy had a green cover value of 15.29% and an LAI of 0.2076. The spectra have been offset vertically to avoid overlap. The reflectance at 600 nm is provide for each curve. Note that the amplitude of the chlorophyll red edge feature is larger in spectra acquired with bright gravel backgrounds (white and brown) than the spectrum acquired with the black gravel background.

Raw and Smoothed PS2 Spectra (Pinyon - Green Cover Level 4)

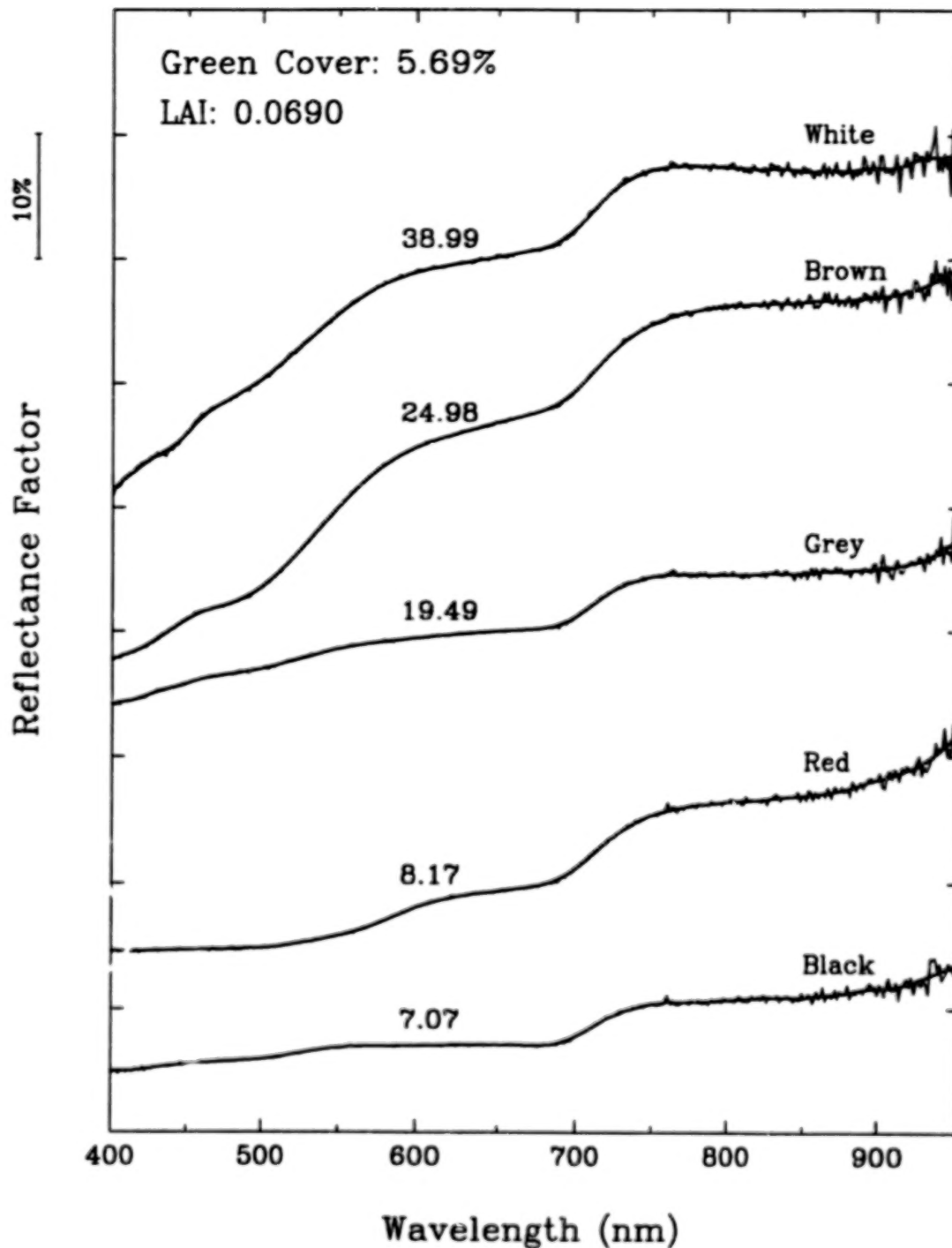


Figure 2. Raw and smoothed reflectance spectra of the pinyon canopy at green cover level 4 with five different gravel backgrounds. The pinyon canopy had a green cover value of 5.69% and an LAI of 0.0690. The spectra have been offset vertically to avoid overlap. The reflectance at 600 nm is provided for each curve. Note that the amplitude of the chlorophyll red edge features in the spectra are reduced relative to the spectra in Figure 1.

Raw and Smoothed PS2 Spectra (Pinyon - Green Cover Level 7)

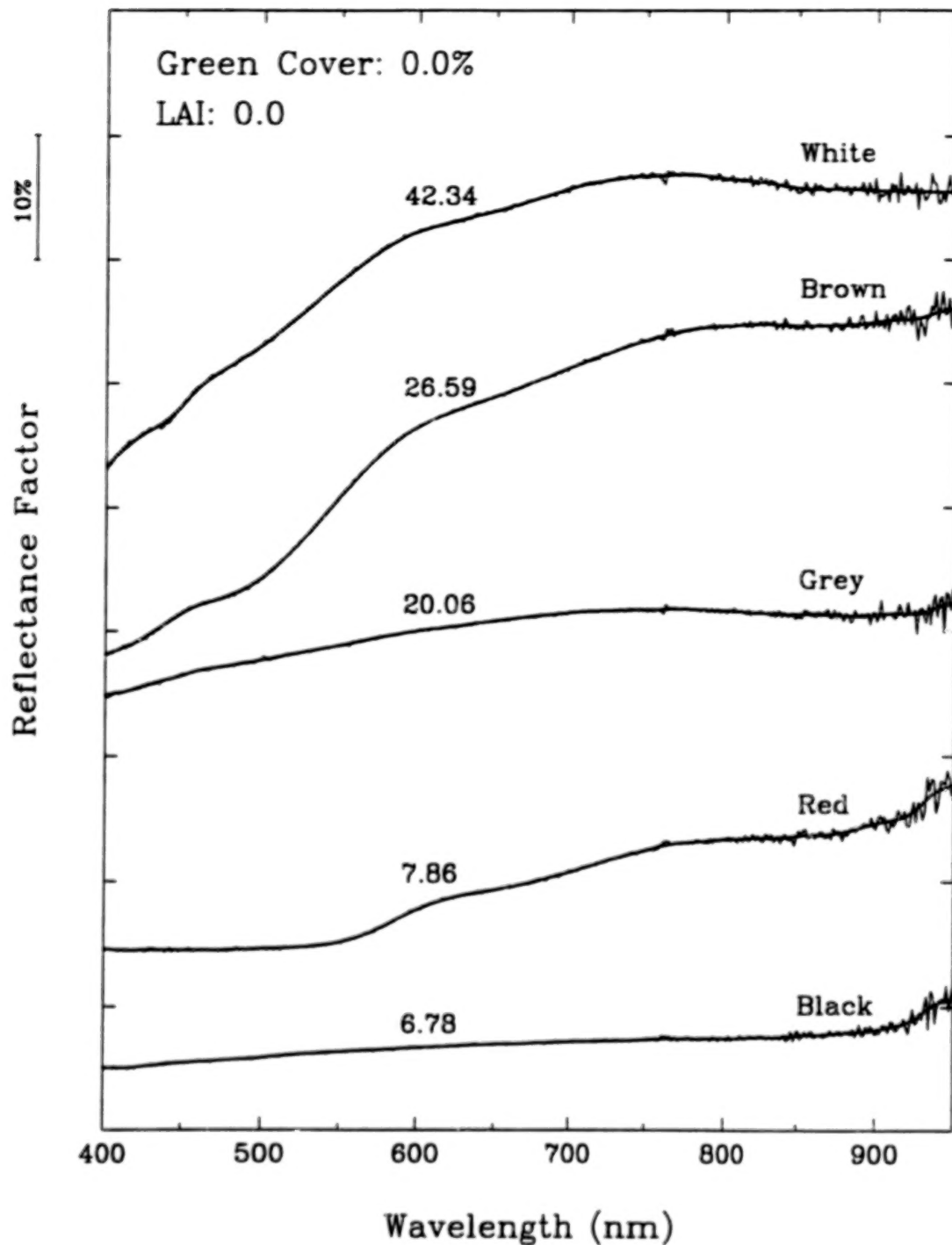


Figure 3. Raw and smoothed reflectance spectra of a pinyon canopy at green cover level 7 with five different gravel backgrounds. The pinyon canopy had 0.0% green cover and an LAI of 0.0. The spectra have been offset vertically to avoid overlap. The reflectance at 600 nm is provided for each curve. Note the lack of the chlorophyll red edge features in the spectra.

Percent Green Cover vs TM NDVI

(TM NDVI simulated using PS2 data)

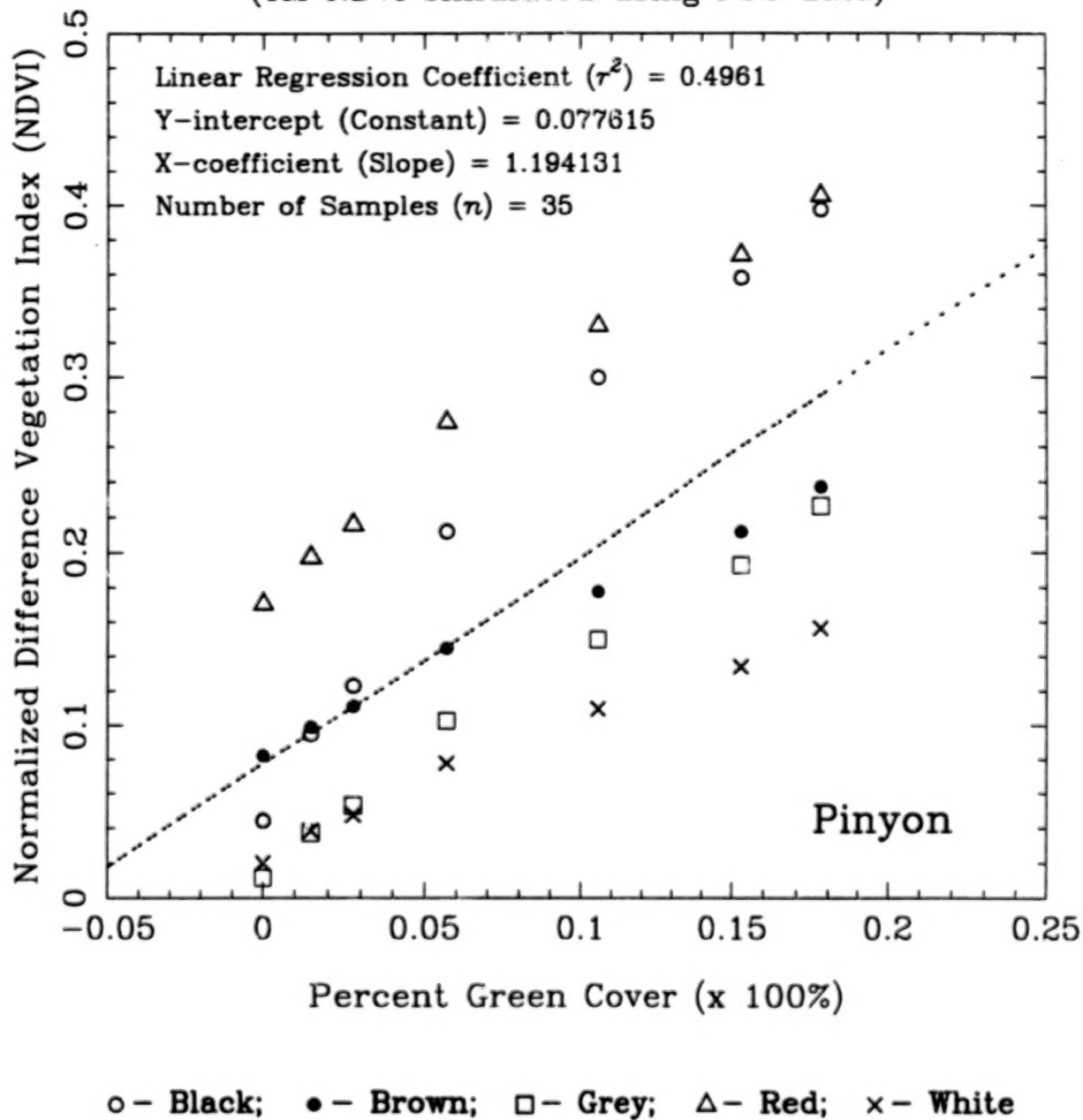


Figure 4. TM NDVI versus percent green cover for the seven pinyon pine canopy levels.

Percent Green Cover vs TM RVI

(TM RVI simulated using PS2 data)

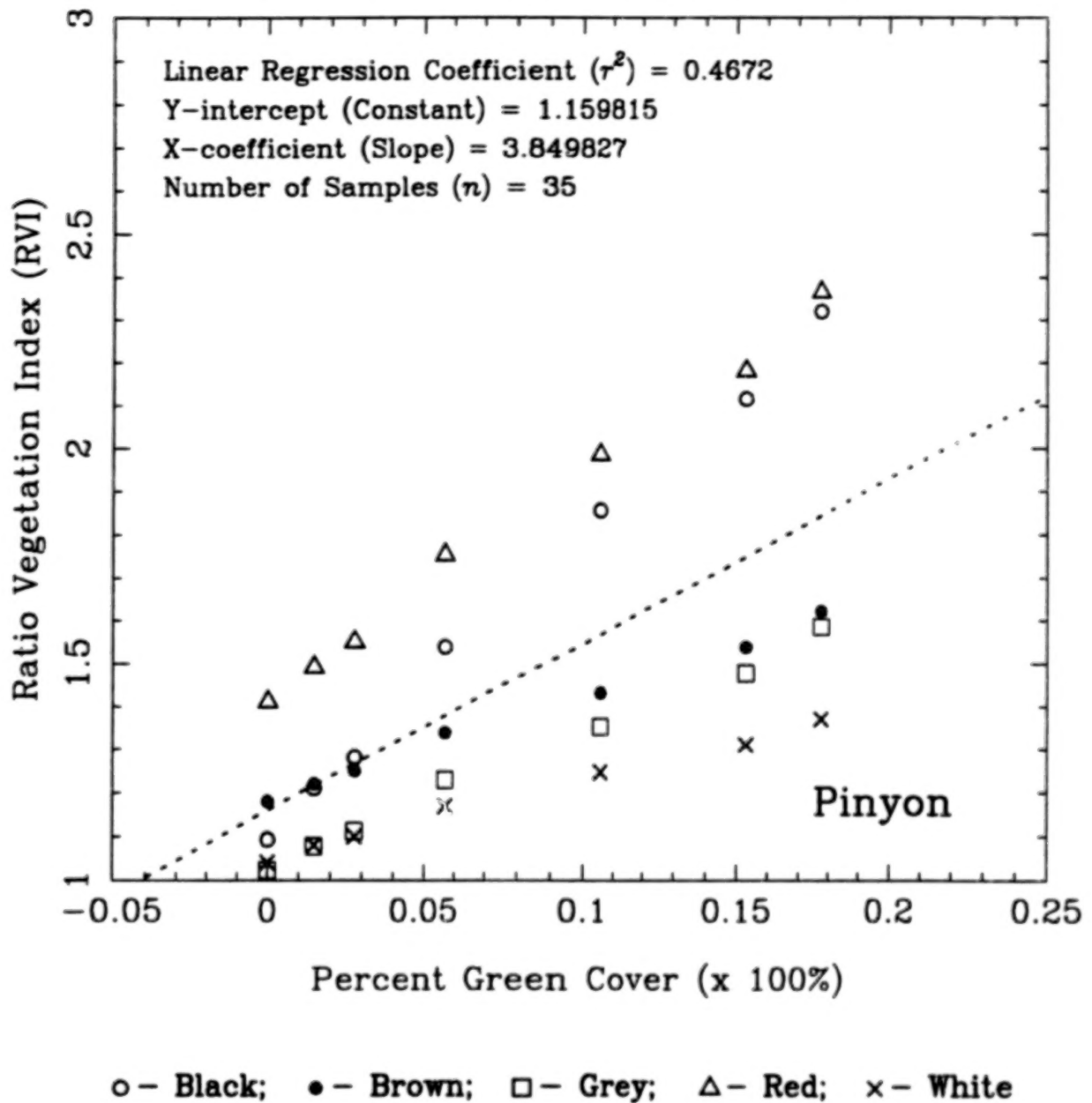


Figure 5. TM RVI versus percent green cover for the seven pinyon pine canopy levels.

(TM SAVI simulated using PS2 data)



Percent Green Cover vs TM PVI

(TM PVI simulated using PS2 data)

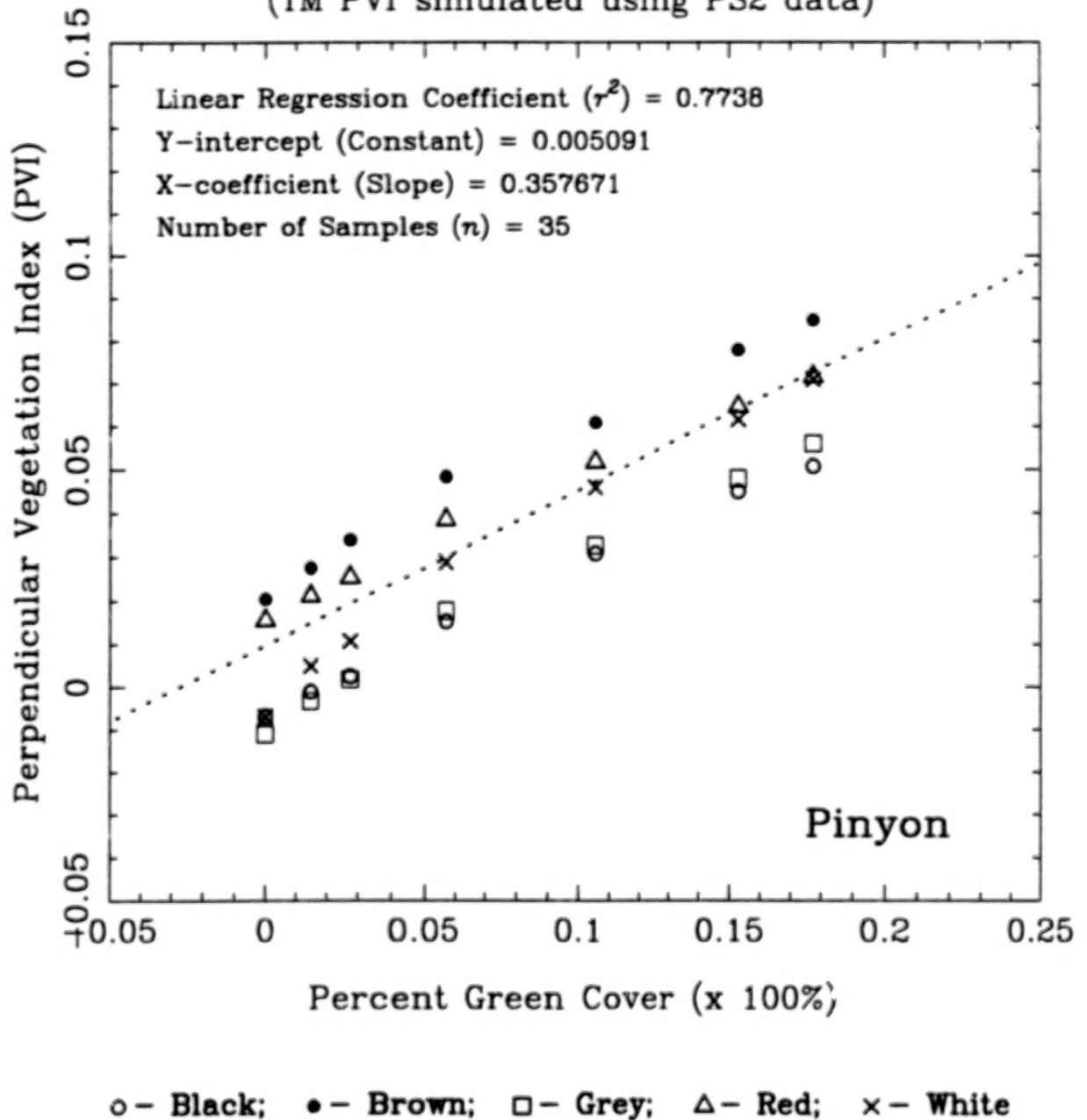
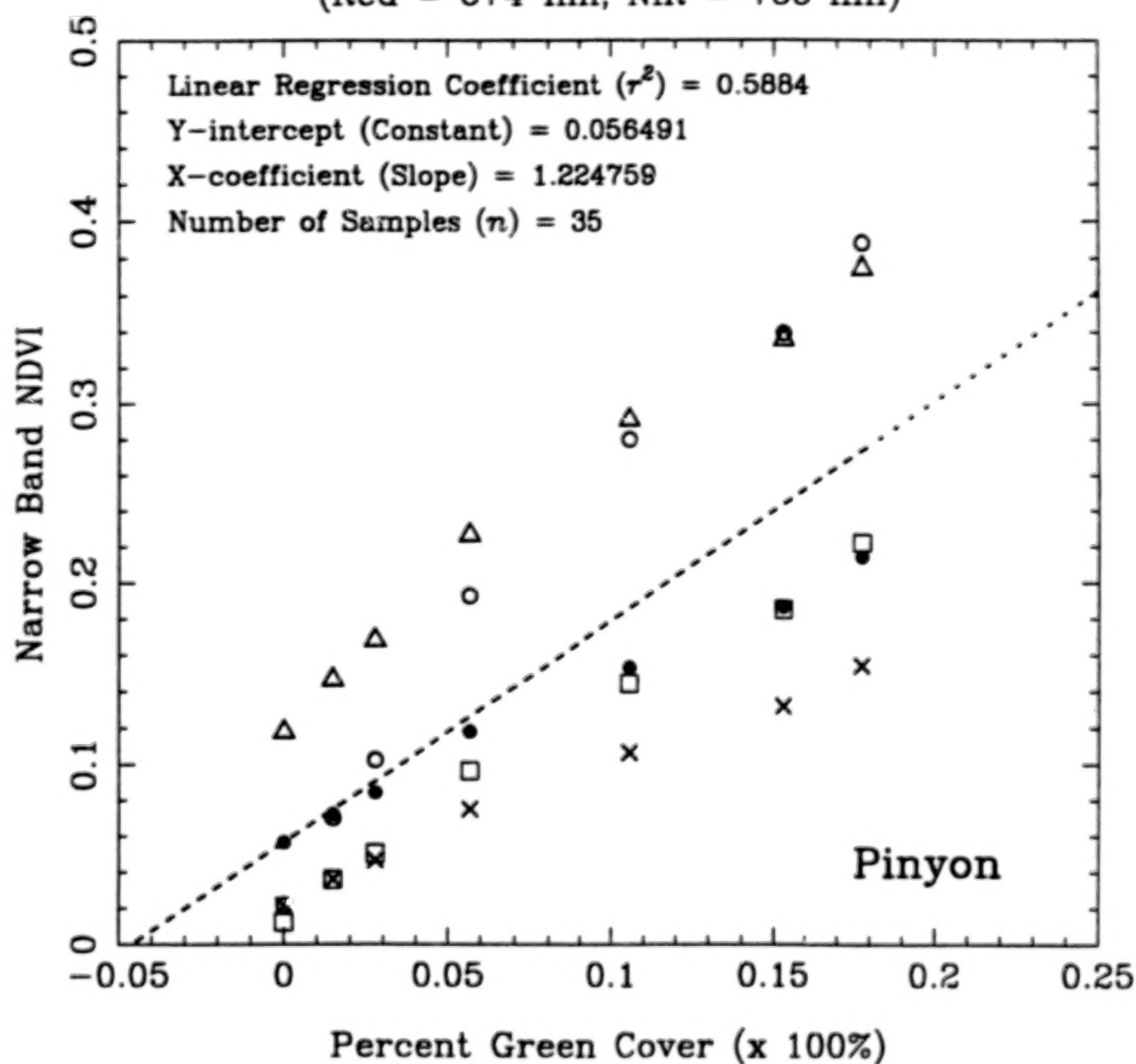


Figure 7. TM PVI versus percent green cover for the seven pinyon pine canopy levels.

Percent Green Cover vs Narrow Band NDVI

(Red = 674 nm; NIR = 755 nm)



○ - Black; ● - Brown; □ - Grey; △ - Red; × - White

Figure 8. Narrow band NDVI versus percent green cover for the seven pinyon pine canopy levels.

Percent Green Cover vs Narrow Band RVI

(Red = 674 nm; NIR = 755 nm)

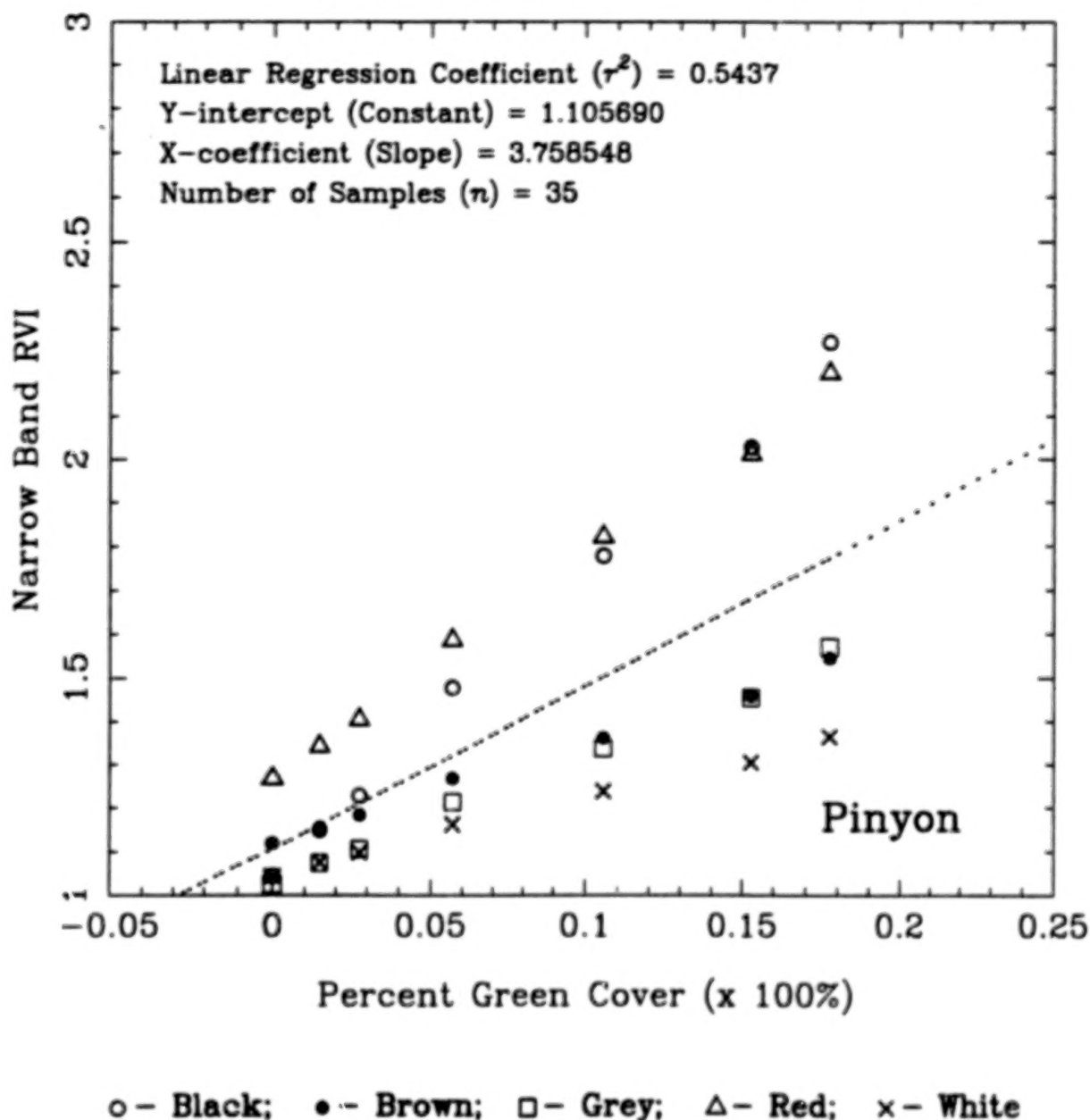


Figure 9. Narrow band RVI versus percent green cover for the seven pinyon pine canopy levels.

Percent Green Cover vs Narrow Band SAVI

(Red = 674 nm; NIR = 755 nm)

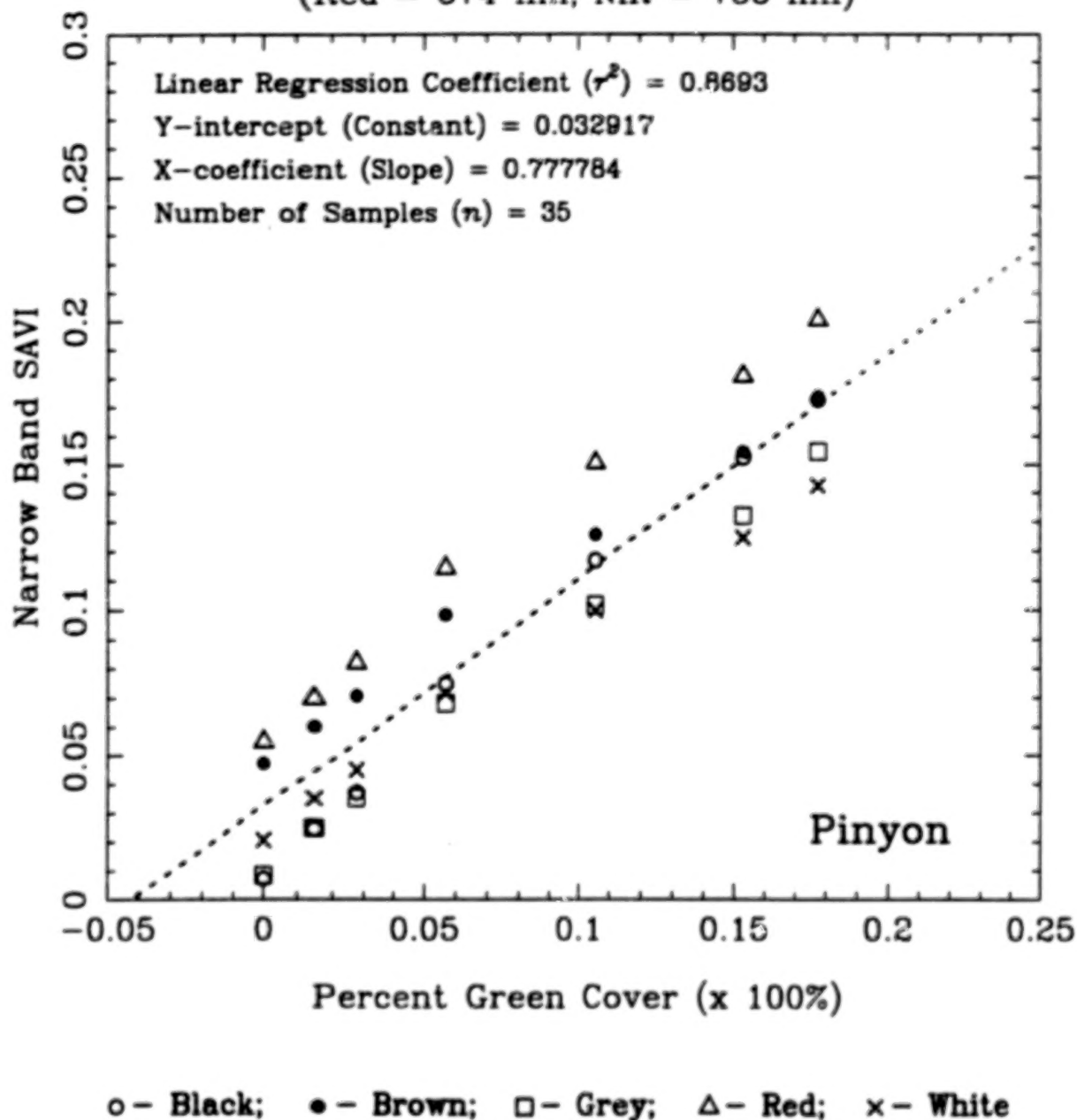
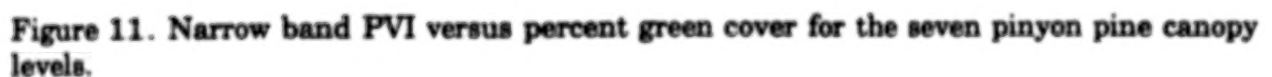


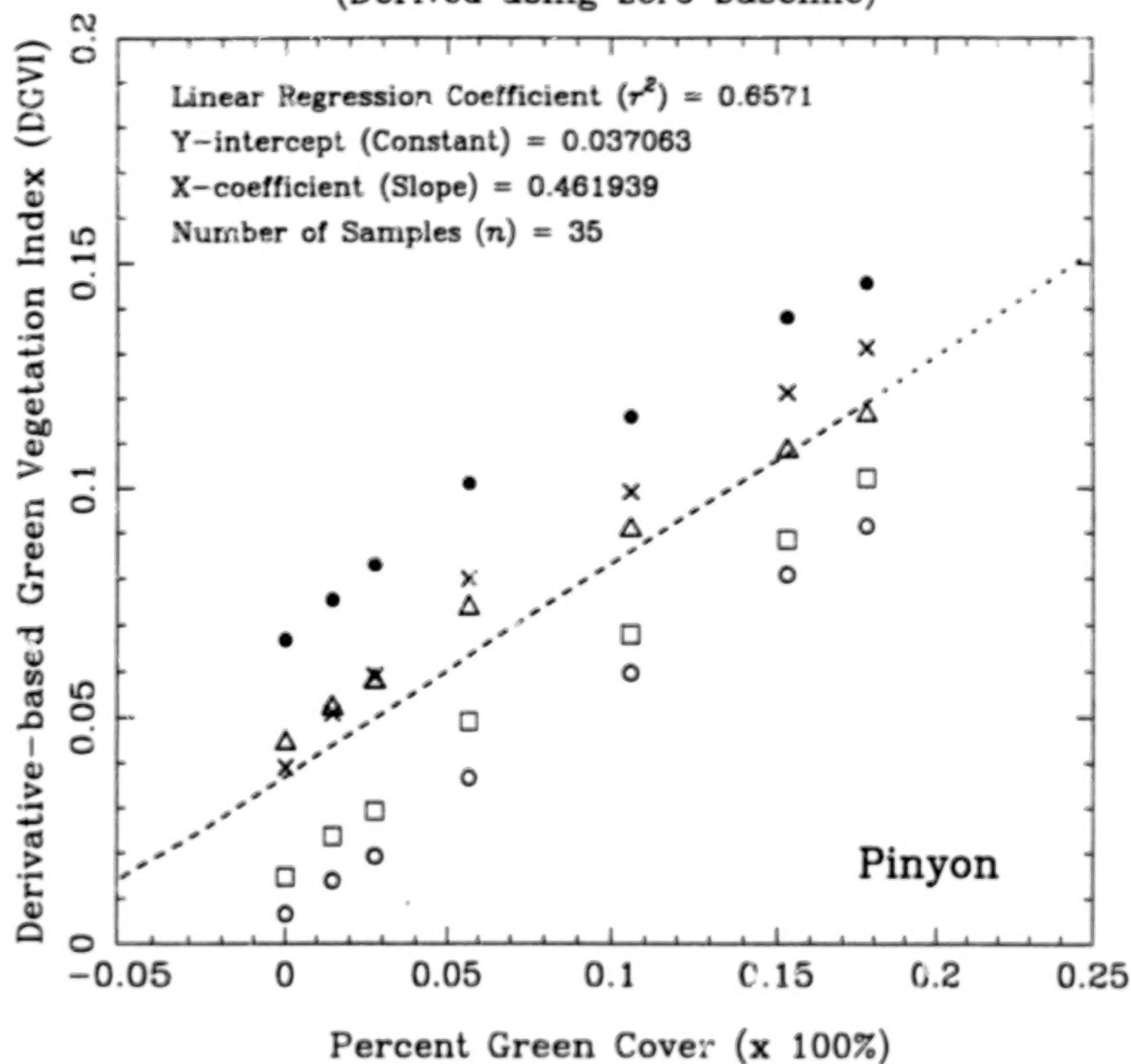
Figure 10. Narrow band SAVI versus percent green cover for the seven pinyon pine canopy levels.

(Red = 674 nm; NIR = 755 nm)



Percent Green Cover vs 1st Order DGVI

(Derived using zero baseline)



○ - Black; ● - Brown; □ - Grey; △ - Red; × - White

Figure 12. First order DGVI calculated with a zero baseline versus percent green cover for the seven pinyon pine canopy levels.

Percent Green Cover vs 1st Order DGVI

(Derived using local baseline)

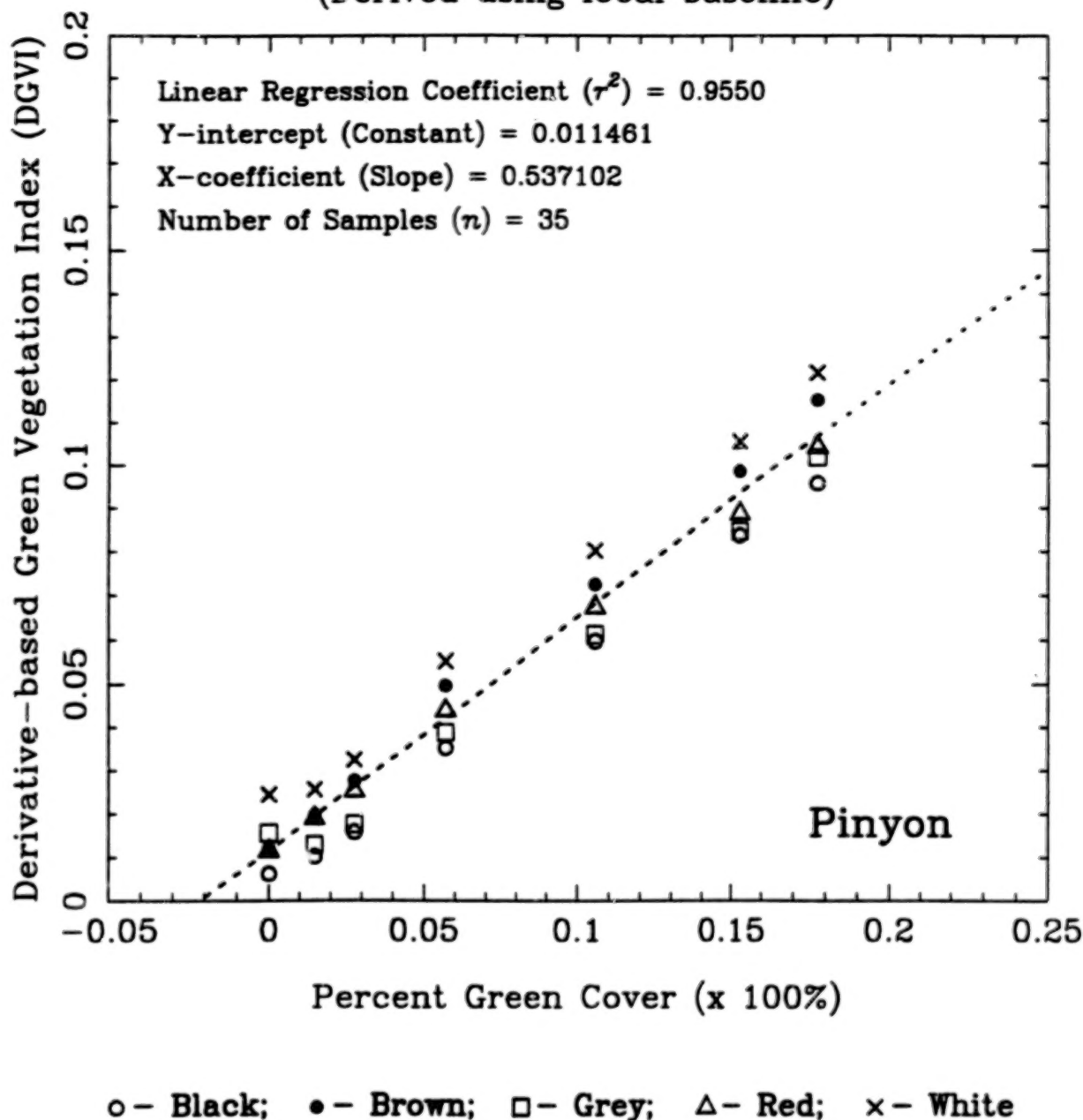


Figure 13. First order DGVI calculated in reference to a local baseline (set at 625 nm) versus percent green cover for the seven pinyon pine canopy levels.

Percent Green Cover vs 2nd Order DGVI

(Derived using zero baseline)

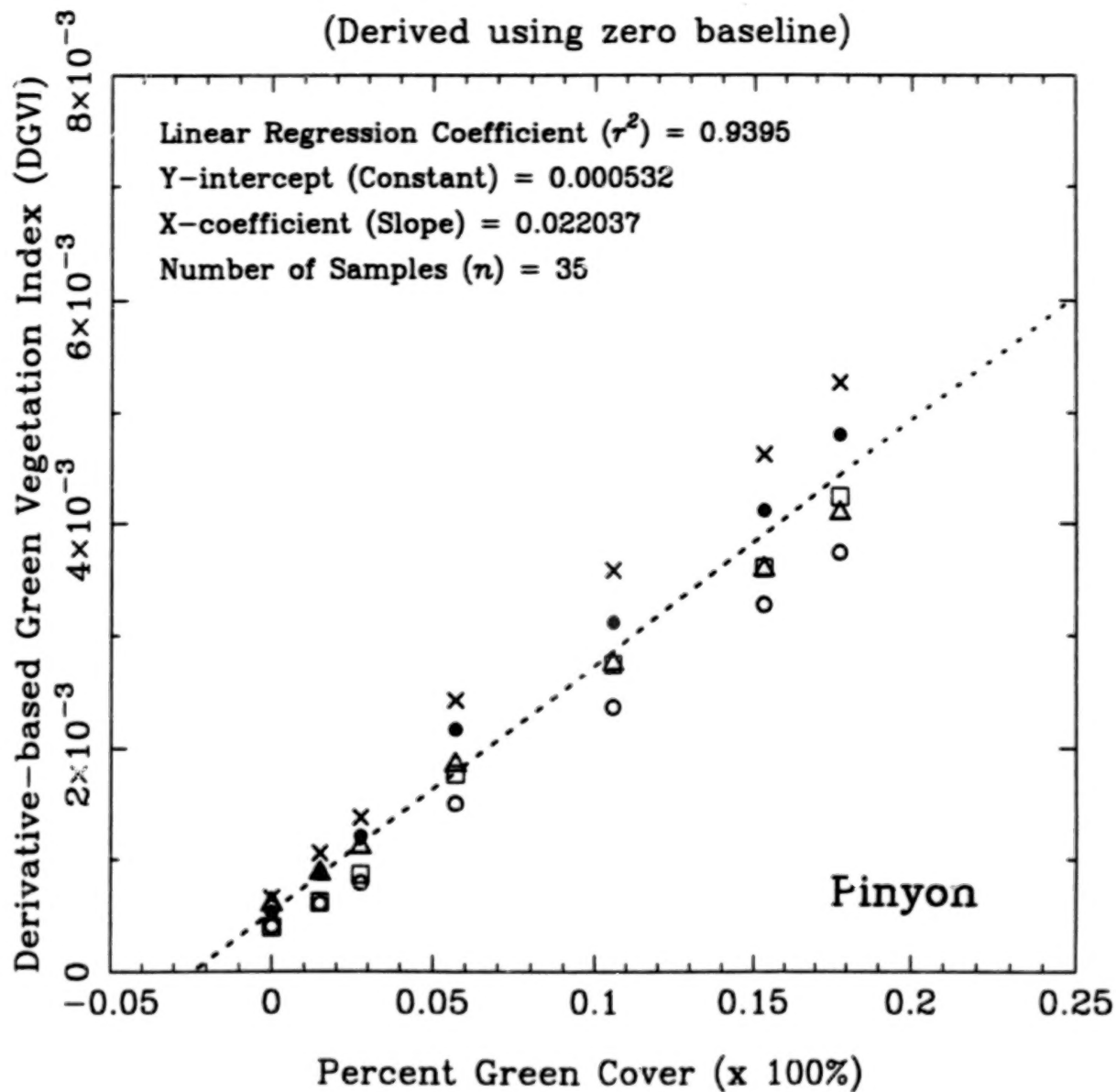


Figure 14. Second order DGVI versus percent green cover for the seven pinyon pine canopy levels.

Vegetation Index Predictive Power For Pinyon Pine Percent Green Cover

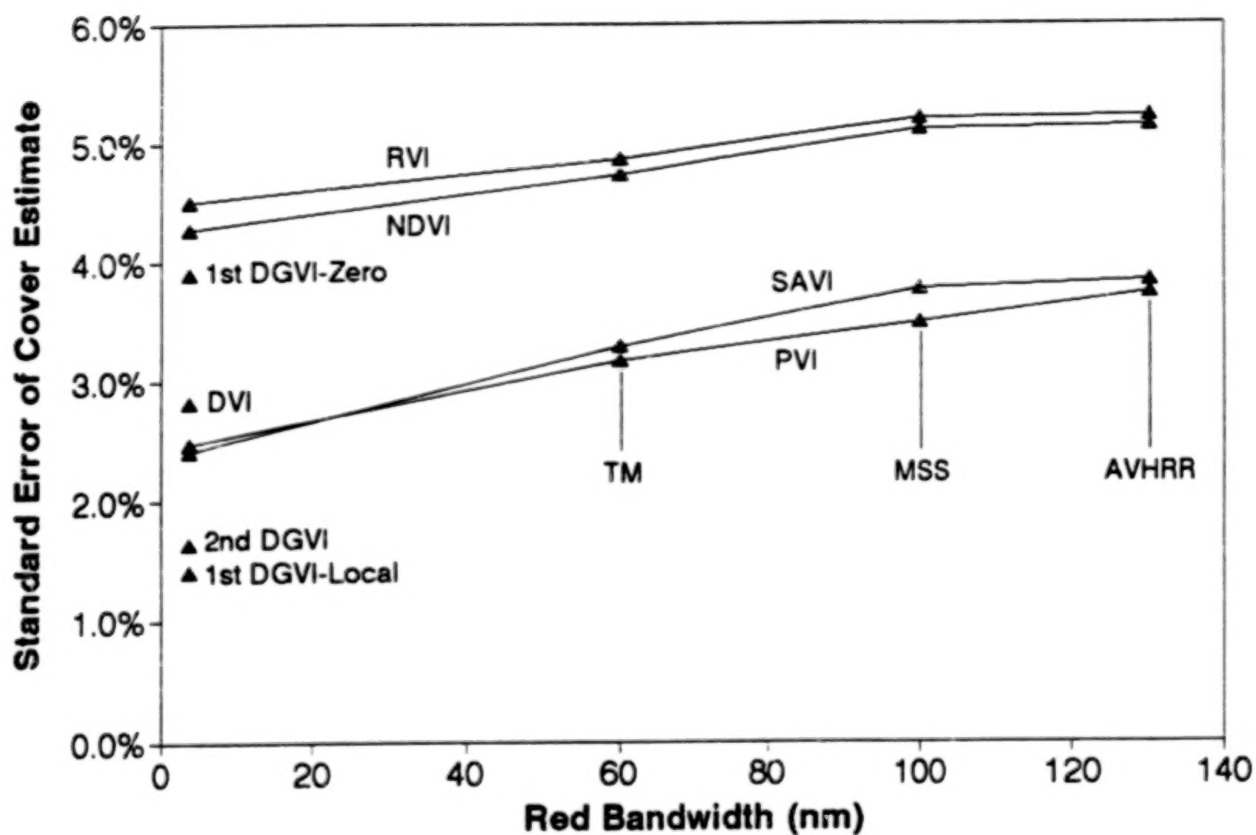


Figure 15. The standard error of the percent green cover estimates versus red bandwidth for the tested vegetation indices. Reducing the bandwidth only marginally improved the performance of NDVI, RVI, SAVI, and PVI. The best results were obtained for the first order DGVI using a local baseline.

DERIVATION OF INPUTS TO A BIOGENIC EMISSION MODEL FROM SPECTRAL AND ANCILLARY DATA

S. Khorram, J. Brockhaus, J. Ediriwickrema, and H. Cheshire
Computer Graphics Center/Forestry Department, North Carolina State University
Raleigh, NC 27695-7106, USA

ABSTRACT

An integrated inventory system designed to provide detailed spatial estimates of inputs to a forest biogenic emission model is described. Data layers currently being used as input to the Environmental Protection Agency's Biogenic Emissions Inventory System include natural vegetation data layers dating back to 1967 documenting the distribution of three forest cover types and two average leaf area index values. Several sources of forest inventory information of varying spatial resolutions including field acquired forest species and leaf area index data, color infrared aerial photography, Landsat Thematic Mapper imagery, and Advanced Very High Resolution Radiometer data were utilized to generate more detailed information describing the spatial distribution of eight forest cover types and associated average leaf area index conditions within a three state study site encompassing North Carolina, South Carolina, and Georgia. Geographic Information Systems (ERDAS and ARC-INFO) and a least squares linear mixture model were utilized to integrate and spatially analyze these data producing a new set of forest cover type data layers which may be utilized to generate estimates of volatile organic compound emission rates from forested areas.

1. INTRODUCTION

Emissions of volatile organic compounds from biogenic sources have been shown to be an important factor controlling several atmospheric processes such as: tropospheric chemistry, photochemical oxidant formation, global carbon budgets, and atmospheric organic acid production (Fehsenfeld et al., 1992). Regulatory policies concerning ozone levels in the United States (U.S.) have focused on the control of anthropogenic emissions of volatile organic compounds (VOC) while effectively ignoring biogenic inputs. It is important that these emissions be investigated so as to determine whether anthropogenic nitrogen oxides or VOC should be regulated in order to reduce ozone levels (Geron et al., in press).

It has been estimated that forests are responsible for approximately 90% of biogenic volatile organic compound (BVOC's) emissions with the remainder coming from agricultural areas and brushlands (Lamb et al., 1987). The regulatory model, Biogenic Emission Inventory System (BEIS), currently being used by the U.S. Environmental Protection Agency (EPA) produces estimates of the spatial distribution of BVOC emissions from three general forest cover types (oak forest, other deciduous forests, and coniferous forests). Inputs to this model include forest cover type land area and average leaf area index (LAI) conditions for each type (Pierce et al., 1990). Forest cover type land area is being extracted from the GEOECOLOGY land use database (Olson et al., 1980). Natural vegetation data layers within this database date back to 1967, although updated to account for urbanization and agricultural encroachment in 1978. Though dated, the GEOECOLOGY database is the most readily available, comprehensive database documenting the spatial distribution of forest cover types on regional and national scales. Average leaf area index factors used for each of the three forest cover types were generated from data published in 1987 (Lamb et al., 1987).

Recent research has resulted in estimates of genus specific BVOC emission rates (Guenther et al., 1994). These data cannot, however, be utilized to obtain more precise estimates of emission rates from the BEIS due to the lack of corresponding genus level LAI and forest cover type information. This paper describes a set of methodologies designed to produce data layers which may be used as input to the BEIS to exploit the availability of genus level emission rates. Specific objectives were to: (1) generate a forest cover type data layer describing the spatial distribution of eight forest types instead of the three currently available from the GEOECOLOGY database; (2) determine average LAI conditions for each of the eight forest cover types; (3) integrate the spatial forest cover data and the tabular LAI information within a geographic information system (GIS) to facilitate input to the BEIS; and, (4) to assess the accuracy of the resulting database.

2. METHODS

A "bottom up" approach integrating data from field surveys such as the U.S. Department of Agriculture (USDA) Forest Inventory and Analysis (FIA) database, field measurements of LAI, and nested scales of remotely sensed data was used. Integration of these data took place within the framework of a GIS (ARC-INFO) to produce estimates of the percentage of forest cover types and average LAI conditions corresponding to individual cells within a grid system specified by the EPA.

2.1 STUDY SITE

A study site encompassing the states of North Carolina, South Carolina, and Georgia was selected for the development and evaluation of the methodology described in this paper. A great diversity of cover types and land use activities occur within this three state area. The region is heavily forested containing several forest cover types ranging from riverine swamps in coastal areas to high elevation boreal montane spruce-fir forests in the Blue Ridge Mountains. Soils may be derived from marine, lagoonal, deltaic or fluvial processes and can be sandy, peaty or clayey. Agriculture represents an important cover type within the region and several major metropolitan areas (Atlanta, Georgia; Columbia, South Carolina; Charlotte, North Carolina; Raleigh, North Carolina) are located within the study site.

The study area encompasses three major physiographic provinces: Coastal Plain, Piedmont and Blue Ridge. In addition, a small portion of the Appalachian Ridge and Valley Province extends through the extreme northwest corner of Georgia. The Coastal Plain is bounded on the west by the Fall Zone which marks the eastern boundary of the Piedmont. The gently rolling topography of this province is underlain by igneous and metamorphic rocks, though basins of sedimentary materials can also be found. The Piedmont reaches its greatest width in North Carolina (approximately 201 kilometers) and its greatest elevation (550 meters) in Georgia. The Blue Ridge province is a mountainous upland which extends into northeastern Georgia. Elevations reach a maximum at Mt. Mitchell in the Black Mountains of North Carolina (2037 meters). Drainage is mainly to the west and many outliers of the Blue Ridge lie east of it in the Piedmont. The Blue Ridge does not extend as far south as the Ridge and Valley province which abuts the Piedmont in northeastern Alabama (northwestern Georgia) without a marked contrast in topography in the study area. Within each of these provinces there are also several variations in underlying geology and in topographic expression which can affect the abundance and distribution of vegetation types.

2.2 DESCRIPTION OF THE BEIS

The BEIS computes gridded, hourly emissions of speciated biogenic hydrocarbons for the eastern U.S. Data required as inputs to the system include: (1) land use; (2) forest leaf area; (3) emission factors; and, (4) environmental effects (Pierce et al., 1990). The system can be characterized by the following equation:

$$ER_i = [A_j \times BF_j \times EF_{ij} \times F_{ij}(S,T)] \quad (1)$$

where ER_i is the emission rate of chemical species i , A_j is the area of vegetation class j , BF_j is the LAI for vegetation class j , EF_{ij} is the emission factor of chemical species i for vegetation class j , and $F_{ij}(S,T)$ accounts for the environmental effect of solar radiation S and leaf temperature T .

GEOECOLOGY natural vegetation data layers currently used as input to the BEIS contain information describing the occurrence of 105 plant communities within a county and are used to generate data documenting the spatial extent (A_j) of six general land cover types: (1) oak forest; (2) other deciduous forests; (3) coniferous forests; (4) scrub; (5) grassland; and, (6) barren land. Summaries of the occurrence (# of hectares) of each land cover type within each cell of a 20 kilometer (km) x 20 km grid system are determined utilizing a GIS (ARC-INFO). These grid cells represent the minimum mapping unit for BVOC emission estimation within the BEIS. Average LAI factors (BF_j) for the forest types are taken from research conducted by Lamb (1987) and are divided into four emission categories. Speciated emission factors (EF_{ij}) are derived from work completed in 1977 (Zimmerman, 1979). Solar radiation and leaf temperature (F_{ij}) are computed from equations adapted for use in studying isoprene and monoterpane emissions from slash pine and live oak (Tingey et al, 1980 and 1981). Output products generated from the application of the BEIS to these data include hourly estimates of speciated chemical emissions from forests for each 20 km² cell within the grid system.

2.3 GENERATION OF A SPECIES LEVEL FOREST COVER TYPE DATA LAYER

A hierarchical classification scheme in which the level of information provided increases as the classification process advances was implemented. Initially, the spatial distribution of six general land cover types were mapped within eight sample sites utilizing Landsat Thematic Mapper (TM) data: (1) coniferous forests; (2) deciduous forests; (3) mixed coniferous/deciduous forests; (4) agriculture; (5) water; and, (6) developed areas. Data output from this process were then used to calibrate a least squares linear mixture model which predicted the occurrence of the six cover types within Advanced Very High Resolution Radiometer (AVHRR) data. Existing field survey data collected by the USDA-Forest Service FIA group were used to increase the level of information describing the distribution of individual species and species complexes within the forest cover types. Integration of these data with the classified AVHRR data produced from the application of the linear mixture model provided information regarding the following forest cover types: (1) southern yellow pine; (2) spruce-fir; (3) oak-hickory; (4) sweet gum-yellow poplar; (5) cypress-water tupelo; (6) sweet bay-black gum-red maple; and, (7) sugar maple-beech-birch.

2.3.1 Classification of Landsat TM Data

Spectral and spatial resolution characteristics of the AVHRR restrict the level of information which may be extracted from these data (Twonshend et al., 1987; Iverson et al., 1987; Belward and Lambin, 1990). AVHRR spatial resolution for LAC data (1.1 km) is such that it is likely that several cover types will occur within a single pixel, referred to as the mixed pixel effect. Thus, in areas containing a heterogeneous mixture of cover types, such as the southeastern U.S., it would be unusual to be able to classify individual AVHRR pixels as belonging to a single cover type. Therefore, a method was needed which was capable of determining the complex of cover types occurring within AVHRR mixed pixels.

Eight sets of multitemporal Landsat TM moveable mini-scenes were selected for use in characterizing land cover patterns within the AVHRR data. Each mini-scene covered an area of approximately 5,000 km² (50 km x 100 km). Two mini-scenes, one acquired during mid summer the other during late fall/early winter, were selected for each of the eight locations within the study area. It was felt that the use of multitemporal Landsat TM data would reduce the confusion often encountered between cover types with similar spectral signatures when a single acquisition date is used. For example, confusion between highly reflective exposed agricultural soils and developed areas in urban environments is common in the classification of Landsat TM data. Utilization of multitemporal data may alleviate much of this confusion by including reflectance information acquired when agricultural fields are occupied by crops. Reflectance patterns associated with paved areas in urban settings will not exhibit the temporal flux observed in agricultural environments resulting in multitemporally unique spectral signatures for the two cover types. Late fall/early winter acquired Landsat TM will also help in the discrimination of deciduous and coniferous forests due to the leaf-off condition of deciduous species during this time period (Khorram et al., 1993).

Each of the multitemporal Landsat TM data sets were registered to a Lambert Azimuthal Equal Area map projection corresponding to that of the AVHRR data. Color infrared (CIR) aerial photography acquired as part of the National High Altitude Photography (NHAP) program and the National Aerial Photography Program (NAPP) were systematically selected so as to provide representative coverage of each of the Landsat TM mini-scenes. A minimum of five training sites for each of the six land cover types to be mapped were delineated on the CIR aerial photography, each site encompassed a minimum of thirty pixels. The location of each training site was transferred to United States Geological Survey (USGS) 7.5' orthophotoquads and the map coordinates corresponding to the approximate center of each site was taken from the map. These map coordinates were input to coordinate transformation algorithms within the ERDAS GIS/image processing software system to determine the location of each training site within the appropriate set of Landsat TM data. Training site locations were also verified through a visual comparison with the aerial photography and orthophotoquads. Boundaries of each site were delineated through the use of the on-screen digitizing capabilities of the ERDAS software and spectral data were extracted for each site based on these boundaries. Spectral signatures were developed from the training site data and used as input to a maximum-likelihood classification algorithm assigning each pixel within a Landsat TM mini-scene to one of the cover types being studied.

An assessment of the accuracy of the classified Landsat TM data is currently being conducted by an independent subcontractor (Research Triangle Institute, Research Triangle Park, NC). Aerial photography is being used as the source of the "ground truth" information which the classified database will be compared against. Photo interpreted land cover polygons will be digitized and registered to the

classified Landsat TM data. A vector to raster conversion will then be performed to facilitate a pixel by pixel comparison of land cover types between the photo interpreted data and the classified Landsat TM data.

2.3.2 Classification of the AVHRR Data

The 1990 counterminous U.S. AVHRR data set produced by the EROS Data Center, Sioux Falls, South Dakota was the remotely sensed database selected to provide wall to wall coverage of the three state study site. This data set consists of 19 bi-weekly normalized difference vegetation index (NDVI) composites generated from 1-km AVHRR data and contains the following data files: (1) calibrated AVHRR channels 1 to 5; (2) the NDVI; (3) satellite zenith viewing angle; (4) solar zenith angle; (5) relative solar/satellite azimuth angle; and, (6) the acquisition date of each pixel within the data set (Eidenshink, 1992). Only the visible and near infrared channels (channels 1 and 2) of the AVHRR were utilized in this work.

An AVHRR pixels reflectance value is a composite of the reflectance from several cover types occurring within a single pixel. Mathematically this can be expressed in the following form:

$$A_{ii} = F_{ij} \times RP_j + F_{ij} \times RP_j + \dots + F_{ij} \times RP_j \quad (2)$$

where A_{ii} is the reflectance value of AVHRR pixel ii , F_{ij} is the frequency of occurrence of cover type j in pixel i , and RP_j is the reflectance value of an AVHRR pixel which contains only cover type j . The basic assumption of this equation is that the average reflectance value of a pixel which is homogenous for a cover type is known. However, the patchwork distribution of cover types throughout the study site and the 1-km resolution of the AVHRR data preclude the existence of pixels which include a single cover type. Therefore, these values (RP_j) were estimated using regression techniques.

Equation two may be expressed in the following regression matrix form:

$$A = F \times RP \quad (3)$$

where A is a matrix of the AVHRR pixel reflectance values, F is a matrix of the frequency of occurrence of the six cover types for each AVHRR pixel, and RP is a matrix of the AVHRR reflectance values for pixels which contain a single cover type. Matrix A consists of AVHRR pixel values corresponding to the areas encompassed by the Landsat TM mini-scenes, data values for matrix RP are unknown, while cover type proportions in matrix F were calculated from the classified Landsat TM data utilizing GIS functions within ARC-INFO. Cover type data derived from the Landsat TM data were converted into a vector polygon file with each pixel/polygon being assigned a cover type attribute. A 1-km grid system corresponding to the AVHRR data set for the study site was generated and then overlaid onto the Landsat TM cover type polygon data layer. The occurrence of cover types within each AVHRR pixel were then used to calculate the cover type proportions for matrix F . Only half of the available classified Landsat TM data were utilized to generate the information in matrix F . Half of the data were withheld for use in determining the accuracy of the linear mixture model developed from the data contained in the F matrix. Using matrix algebra to solve for RP , homogenous AVHRR cover type reflectance values, equation three becomes:

$$RP = (F^T F)^{-1} \times F^T A \quad (4)$$

This estimated value of RP may now be substituted into equation two. Solving for F , cover type proportions, and including a variance/covariance term to account for between band correlation in the AVHRR data equation two becomes:

$$F = (RP \times COV^{-1} \times RP)^{-1} \times (RP \times COV^{-1} \times A) \quad (5)$$

where:

$$COV = ((A - RP) \times (A - RP)^T) / N \quad (6)$$

and is the variance/covariance matrix for the AVHRR wavebands. Equation five is a least squares linear mixture model capable of predicting cover type proportions within an AVHRR pixel. Least squares linear mixture models (LSLMM) have been used to model land cover patterns on regional scales in Africa, Europe, and South America using AVHRR data (Townshend et al., 1987; Cross et al., 1991; Detchmندی

et al., 1993). However, past efforts have focused on the modeling of two to four land cover categories with LSLMM. Results from previous studies have shown that the reliability of the model generally decreases as the number of cover types increases.

Application of equation five to the appropriate data sets produced a database consisting of cover type proportions for six land cover classes within a 1-km grid system corresponding to the AVHRR data. The output data file consisted of an ARC grid coverage corresponding to the AVHRR data for the study site and attribute files for each pixel/polygon containing the cover type proportion information. The basic resolution element used as input to the BEIS to compute emission estimates is a 20-km² grid cell. Thus, the 1-km² cover type proportion data were aggregated over each 20-km² cell within the grid system used as input to the BEIS. This was accomplished by generating a 20-km grid system within the GIS and then intersecting this with the 1-km cover type proportion data layer. Cover type percentages for all 1-km² pixel/polygons occurring within a 20-km² cell were then aggregated to produce an estimate of the cover type proportions for that cell. This was done for each 20-km² cell within the grid system.

2.3.3 Integration of FIA Field Survey Data

The level of information extracted from the Landsat TM data describing the distribution of forest cover types is limited to a discrimination of coniferous, deciduous, and mixed coniferous/deciduous forests. In certain areas, for example the coastal plain, it may have been possible to distinguish hardwood types associated with unique species or species complexes such as cypress-tupelo marshes. In general, however, it is not possible to discriminate between other types such as oak-hickory and maple-beech-birch without the inclusion of additional ancillary data. Thus, it was necessary to integrate field survey data collected by the USDA-Forest Service FIA group with the classified AVHRR data, aggregated over 20-km² grid cells, to generate more detailed information describing the seven species complex forest cover types.

Over 20,000 FIA inventory plots occur within the study area. Sixty percent of these are located within forested areas. Data collected at each plot includes: (1) forest cover type; (2) size class; (3) age class; and, (4) plot location in latitude/longitude. The seven species complex forest cover types being studied in this effort were selected from the set of types mapped by the FIA. The FIA inventory data were provided to the investigators in the form of an ARC coverage with associated attribute files documenting conditions at each plot. This data layer was spatially reprojected to the aggregated AVHRR cover type proportion coverage and the two data sets intersected so as to identify the FIA plots occurring within each 20-km² grid cell. Forest cover type information from the FIA plots found within a 20-km² grid cell were used to determine the percentage of specific species complex types existing within that cell. For example, it may be determined that 35% of a grid cell is deciduous forest and 65% of that cell is coniferous forest. Analysis of the 33 FIA plots located in that cell shows that 15 of these have been identified as oak-hickory types, 10 have been typed as sweet gum-yellow-poplar, and the remaining 8 are southern yellow pine. Therefore, 100% of the coniferous forests found within this grid cell are southern yellow pine, while 60% of the deciduous forests are oak-hickory and 40% are sweet gum-yellow poplar. These forest cover type percentage values would then be converted to acreage estimates for input to the BEIS. The format of the output file generated from this process is an ARC grid coverage of the 20-km² grid system along with attribute files documenting the extent, in acres, of each of the seven species complex forest cover types within each cell.

2.4 GENERATION OF FOREST COVER TYPE LAI DATA

In the past, intensive data collection efforts have been required to obtain estimates of LAI (Vose and Allen, 1988; Running et al., 1986; Herwitz et al., 1990). Such techniques typically involved destructive sampling of trees at several locations throughout a study area. New techniques for estimating LAI have recently been developed which are non-destructive. These techniques utilize instruments which measure light penetration through a vegetation canopy and convert this information into an estimate of LAI.

Data describing the variations in LAI for southern yellow pine were taken from previously published research (Vose and Allen, 1991). Similar data for the deciduous forest cover types and the spruce-fir type were not available. Field data collection efforts were necessary in order to develop estimates of LAI for these cover types. A LI-COR LAI-2000 Plant Canopy Analyzer was used to perform non-destructive measurements of LAI within these types. This instrument computes an estimate of LAI for a vegetative canopy from measurements of light interception made at various angles simultaneously. The LAI-2000 was developed and tested for broadleaf deciduous vegetation and has been shown to provide reliable estimates of LAI (Daughtry and Hollinger, 1984; Lang et al., 1986; Perry et al., 1988).

A representative sample of thirty field sites were selected for each of the five deciduous types and the spruce-fir type. Within each site several measurements were taken with the LI-COR LAI-2000 to obtain an estimate of LAI for that plot. Plot estimates within a forest cover type were aggregated to derive an average LAI for that type (Table 1). Mean projected LAI for the sample plots ranged from 2.30 for southern yellow pine to 5.05 for the maple-beech-birch cover type. Although mean LAI appeared to vary substantially, closer inspection suggests that four of the seven types had somewhat similar mean projected LAI. Mean LAI for cypress-water tupelo, blackgum-red maple, sweetgum-yellow poplar, and oak-hickory was 4.04, with no significant differences among these types observed. Additionally, the range in LAI for these four types was essentially the same; LAI ranged from approximately 2.5 to 5.5 across these cover types. The data in Table 1 were attached to the attribute tables for the ARC coverage containing the acreage estimates for each of the seven forest cover types.

3. RESULTS AND DISCUSSION

At this time the following output products have been generated: (1) classified Landsat TM data for selected areas throughout the study site; (2) a least squares linear mixture model predicting cover type proportions found within 1-km² AVHRR pixels; (3) classified AVHRR data containing cover type proportion information for every AVHRR pixel within the study area; (4) aggregated cover type proportions for grid cells within a 20-km² grid system; (5) estimates of cover type proportions for seven species complex forest cover types within each 20-km² cell; and, (6) estimates of average LAI conditions for each of the seven species complex forest cover types. All output data files were generated as ARC coverages with associated attribute tables to facilitate input to the BEIS.

Table 1. Average LAI conditions for the seven forest cover types

Cover-Type	Mean LAI (projected)	Std of LAI	Sample Size	Range in LAI
Cypress-Water Tupelo	4.02	0.89	30	2.68 - 5.44
Blackgum-Red Maple	3.89	0.71	30	2.73 - 5.20
Southern pine	2.30	0.25	30	1.49 - 3.56
Sweetgum-Yellow Poplar	4.18	0.81	30	2.34 - 5.90
Oak-Hickory	3.87	0.82	30	2.78 - 5.95
Maple-Beech-Birch	5.05	0.98	30	2.74 - 6.30
Spruce-Fir	3.46	0.68	30	2.20 - 4.89

Efforts to verify the classification of the Landsat TM and AVHRR data are currently being conducted. The outcome of these efforts will determine the operational utility of the methodologies developed in this research. The investigators recognize the difficulty in developing a reliable LSLMM which predicts the occurrence of six land cover types when the literature demonstrates that the best results are obtained when two or three types are modeled. Alternative approaches to the classification of the AVHRR data have been formulated so as to reduce the number of types to identified. Ancillary data describing the spatial distribution of urban areas and water bodies could be obtained from the U.S. Bureau of the Census and the U.S.G.S. and used to account for those two cover types. This would reduce the number of types to be included in the LSLMM to four which may have the effect of improving the performance of the model.

Sensitivity analyses will be conducted following the completion of the verification of the accuracy of the classified Landsat TM and AVHRR data. These analyses will include a comparison of emission estimates obtained utilizing the data layers produced from this research to those generated using the existing GEOECOLOGY database. Additional work will be conducted to investigate the use of classified Landsat TM data alone to obtain aggregated cover type proportion estimates for the 20-km² grid cells, and to compare these results to those obtained when AVHRR data are utilized.

ACKNOWLEDGEMENTS

The authors would like to gratefully acknowledge the following individuals for their input and guidance in the completion of this research: (1) Mr. Chris Geron, AREAL Lab, EPA, Research Triangle Park, NC; (2) Mr. Tom Pierce, NOAA, Research Triangle Park, NC; and, (3) Dr. Lee Allen and Dr. Arthur Sampson, Forest Nutrition Cooperative, College of Forest Resources, North Carolina State University, Raleigh, NC. This research was funded by the U.S.-EPA, Atmospheric Research and Exposure Assessment Laboratory, Research Triangle Park, NC, contract #68D20009.

REFERENCES

- Belward, A., and E. Lambin, 1990: Limitations to the Identification of Spatial Structures From AVHRR Data, *International Journal of Remote Sensing*, 11(5), 921-927.
- Cross, A., J. Settle, N. Drake, and R. Paivinen, 1991: Subpixel Measurement of Tropical Forest Cover Using AVHRR Data, *International Journal of Remote Sensing*, 12(5), 1119-1129.
- Daughtry, C., and S. Hollinger, 1984: Costs of Measuring Leaf Area Index of Corn, *Agronomy Journal*, 76, 836-841.
- Detchmendy, D., and W. Pace, 1993: Linear Mixing and the Estimation of Ground Cover Proportions, *International Journal of Remote Sensing*, 14(6), 1159-1177.
- Eidenshink, J., 1992: The 1990 Conterminous U.S. AVHRR Data Set, *Photogrammetric Engineering and Remote Sensing*, 58(6), 809-814.
- Fehsenfeld, F., J. Calvert, R. Fall, P. Goldan, A. Guenther, C. Hewitt, B. Lamb, S. Liu, M. Trainer, H. Westberg, and P. Zimmerman, 1992: Emissions of Volatile Organic Compounds From Vegetation and Their Implications for Atmospheric Chemistry, *Global Biogeochemical Cycles*, 10, 63-102.
- Geron, C., A. Guenther, and T. Pierce, In press: An Improved Model for Estimating Emissions of Volatile Organic Compounds From Forests in the Eastern United States, *Journal of Geophysical Research*.
- Guenther, A., P. Zimmerman, and M. Wildermuth, In press: Biogenic Volatile Organic Compound Emission Rate Estimates for U.S. Forest and Woodland Landscapes, *Atmospheric Environment*.
- Herwitz, S., D. Peterson, and J. Eastman, 1990: Thematic Mapper Detection of Changes in the Leaf Area of Closed Canopy Pine Plantations in Central Massachusetts, *Remote Sensing of Environment*, 29, 129-140.
- Iverson, L., E. Cook, and R. Graham, 1989: A Technique for Extrapolating and Validating Forest Cover Across Large Regions: Calibrating AVHRR Data with TM Data, *International Journal of Remote Sensing*, 10(11), 1805-1812.
- Khorram, S., K. Siderelis, H. Cheshire, and Z. Nagy, 1991: Mapping and GIS Implementation of Land Use and Land Cover Categories for the Albemarle-Pamlico Drainage Basin. Albemarle-Pamlico Estuarine Study Report, North Carolina Department of Environment, Health and Natural Resources, Raleigh, North Carolina.
- Lamb, B., A. Guenther, D. Gay, and H. Westburg, 1987: A National Inventory of Biogenic Hydrocarbon Emissions, *Atmospheric Environment*, 21, 1695-1705.
- Lang, A., and Y. Xiang, 1986: Estimation of Leaf Area Index From Transmission of Direct Sunlight in Discontinuous Canopies, *Agricultural and Forest Meteorology*, 37, 229-243.
- Olson, R., C. Emmons, and M. Nunsgesser, 1980: GEOECOLOGY: A County-Level Environmental Data Base for the Conterminous United States. Oak Ridge National Laboratory Report, ORNL/TM-7351, Oak Ridge National Laboratory, Oak Ridge, Tennessee.
- Perry, S., A. Fraser, D. Thomson, and J. Norman, 1988: Indirect Sensing of Plant Canopy Structure with Simple Radiation Measurements, *Agricultural and Forest Meteorology*, 42, 255-278.

872000

Pierce, T., B. Lamb, and A. Van Meter, 1990: Development of a Biogenic Emissions Inventory System for Regional Scale Air Pollution Models. Proceedings of the 83rd Air and Waste Management Association Annual Meeting, Pittsburgh, Pennsylvania, 49-66.

Running, S., D. Peterson, M. Spanner, and K. Teuber, 1986: Remote Sensing of Coniferous Forest Leaf Area, *Ecology*, 67, 273-276.

Tingey, D., R. Evans, and M. Gumpertz, 1981: Effects of Environmental Conditions on Isoprene Emissions From Live Oak, *Planta*, 152, 565-572.

Townshend, J., C. Justice, and V. Kalb, 1987: Characterization and Classification of South American Land Cover Types Using Satellite Data, *International Journal of Remote Sensing*, 8(8), 1189-1207.

Vose, J., and L. Allen, 1988: Leaf-Area, Stemwood Growth and Nutrition Relationships for Loblolly Pine, *Forest Science*, 34, 547-563.

Vose, J., and L. Allen, 1991: Quantity and Timing of Needlefall in N and P Fertilized Loblolly Pine Stands, *Forest Ecology and Management*, 37, 133-146.

Zimmerman, P., 1979: Determination of Emission Rates of Hydrocarbons From Indigenous Species of Vegetation in the Tampa Bay/Petersburg, Florida Area. U.S. Environmental Protection Agency Report, EPA-904/9-77-028, Atlanta, Georgia.

Tingey, D., M. Manning, L. Grothaus, and W. Burns, 1980: Influence of Light and Temperature on Monoterpene Emission Rates From Slash Pine, *Plant Physiology*, 65, 797-801.

RASTER-J: A MULTISENSOR TESTBED FOR ENVIRONMENTAL RESEARCH

L. J. Rickard
G. W. Hoskins
Remote Sensing Division
Naval Research Laboratory
Washington, DC 20375-5351, USA

A. Skroch
Falcon Research, Inc.
9727 Cinnamon Creek Dr.
Vienna, VA 22182-1482, USA

ABSTRACT

The U.S. Naval Research Laboratory is developing an airborne testbed to develop techniques for efficiently collecting and analyzing simultaneous and near-simultaneous multisensor observations, and to demonstrate their utility for environmental research and applications. Sponsored by the Strategic Environmental Research Development Program, this program exemplifies the dual-use approach, in that it leverages on-going advanced sensor development programs, and targets environmental processes common to climate research, civil environmental applications, and military environmental applications.

1. INTRODUCTION

Many basic environmental variables cannot be adequately characterized by remote sensing with a single system. Yet even when multiple sensor data sets are available, the analysis is often limited by the fact that one is usually combining "one-dimensional" views provided by independent sensors, seldom contemporary and often only roughly coregistered. The importance of addressing this aspect of the multisensor approach to remote sensing in environmental research is fundamental to NASA's Earth Observing System concept, and has been tested in a number of multiplatform experiments. However, combining data from different sensors on different platforms at different altitudes and viewing geometries is quite difficult, especially when trying to maintain comparable spatial and spectral resolution.

The U. S. Naval Research Laboratory is developing a multisensor testbed to determine whether the use of a common platform, a common control and data handling system, and novel methods of visualization and analysis for data aggregation would make it possible to achieve the anticipated advantages of simultaneous (or near-simultaneous) multisensor imaging. The initial effort has been supported by the Strategic Environmental Research and Development Program (SERDP) in order to make advanced DoD and DOE remote sensing technologies available to the research community for studies of process variables relevant to global environmental change. The program is called the Responsive Airborne Sensor Testbed for Environmental Research - Joint Program, or RASTER-J.

We have recommended a three-phase approach to the development of an operational multisensor platform. We are currently completing Phase 0, a system study of sensors and aircraft trades, highlighted by three "Quick Look" flights using off-the-shelf hardware to support the analysis and to better define the system issues. The purpose of Phase 0 was to provide guidelines for putting together a research testbed that could conduct more

detailed utility studies. This Phase I testbed would integrate into a research aircraft a Core Sensor Suite (currently envisaged as a hyperspectral imager, a passive microwave imaging radiometer, a SAR, and a lidar) drawn from current DoD and DOE advanced sensor development programs. After eighteen months of flight tests, the utility of such a multisensor platform for environmental research would be reviewed. The third phase would be development and deployment of an operational system, should it be considered desirable.

2. ANALYSIS

2.1 SENSOR TRADES

The RASTER-J sensor study addresses the sizing of a sensor suite capable of supporting an optimized collection of environment and terrain features. The initial analysis focused on the use of this suite to provide unique synergistic information on process variables relevant to global environmental change, with an emphasis on those variables poorly addressed by existing or planned systems. Of course, the requirements analysis for this problem has already been done (thoroughly!) by NASA in preparation for Mission to Planet Earth (MTPE), and the planning of the satellite-based Earth Observing System (EOS). Furthermore, as budgetary constraints have required rescoping EOS, the resulting gaps provide us with our direction. In particular, as EOS has moved to emphasize global coverage, long time-series observations (with relatively low spatial resolution), the task of performing targeted, opportunistic observations at high spatial resolution naturally falls to airborne platforms. The RASTER-J Core Sensor Suite (CSS) includes a hyperspectral imager reminiscent of HIRIS, and a synthetic aperture radar reminiscent of EOS-SAR.

To develop an initial sensor list, we turned to the 1988 report of the Earth System Sciences Committee of the NASA Advisory Council, identifying which environmental variables were least addressed by existing data sets. We attempted to account for the anticipated capabilities of currently planned components of MTPE. Note that, because of the DoD applications that RASTER-J must also address, we must distinguish US and international capabilities. The resulting list of key process variables identified for the RASTER-J study is shown in Table 1, together with the relevant desirable sensors. The Core Sensor Suite for Phase I would likely have four primary systems. In addition to the hyperspectral imager and SAR, the CSS would include a microwave imager (probably operating at millimeter wavelengths to optimize imaging performance) and lidar.

As will be discussed later, it is obvious that RASTER-J has numerous applications outside that of research into global change. Much of the generality of RASTER-J arises from the fact that many of these applications require analysis of similar variables; for example, hydrological analyses for waste stream assessment require measurements of soil moisture. One application that has been de-emphasized in this study, however, is oil pollution, for which the desirable multiple sensor combination (UV/VIS imagery, SAR, two-frequency millimeter-wave imagery, and laser fluorescence) is well known and has been implemented (at least in part) on a number of platforms.

The sensor configuration will be defined to meet both technical and data exploitation objectives. Beyond the primary criterion of relevance to global change research and environmental applications, we will consider status of hardware and software development, intrinsic instrumental parameters, instrumental parameters relevant to integration, matching operating characteristics to enhance mutual operation, and cost and schedule constraints. Issues critical to the utility of the testbed results, such as the degree of data coregistration achievable with the available sensors and platform, or the sensitivity mismatches imposed by driving sensors at a common V/H ratio, will be analyzed in detail. The sensor configuration scheme utilized will stress modular components to allow for inclusion and testing of new sensors and applications as they are developed.

TABLE 1. GLOBAL ENVIRONMENTAL CHANGE PROCESS VARIABLES

Problem	Desired Sensors
Soil Moisture	IR, PMW, SAR, HSI, MSI, LIDAR
Ocean Surface Moisture/Energy Flux	HSI, IR, PMW, LIDAR
Volcanic Emissions	IR, LIDAR, US
Tectonic/ Alteration & History Modeling	HSI, MSIR, SAR
Net Primary Production in Coastal Oceans	HSI, SAR, MSI, LIDAR
Arctic Chimneys	MSI, IR, SAR
Snowpack	HSI, PMW, SAR, IR
Wetlands	HSI, SAR
Forest Fires	IR, PMW, US

KEY: IR = Infrared Imager; PMW = Passive Millimeter-Wave Imager; SAR = Synthetic Aperture Radar; HSI = Hyperspectral Imager; MSI = Multispectral Imager; US = Ultraspectral Sensor; MSIR = Multispectral IR; RASTER-J Core Sensors are highlighted in **bold** type.

An example of the sort of trades that must be analysed is shown in Figure 1. This is a combination of data from our first Quick Look flight in 1994 January (discussed in more detail later). We have here combined data from a passive 90 GHz imager and a 9.3 GHz imaging RAR, hoping that the opposing responses of the two devices to variations in soil moisture would provide an enhanced signal. At the same time, we were using a 1 μ m lidar to detect variations in canopy cover and the presence of standing water. The sensitivity limits of the lidar required taking data at low altitudes (700 ft); this led to the obvious heavy shadowing in the radar data (because of the low grazing angle) as well as less obvious (but no less troublesome) problems in matching the scanning speed of the millimeter imager with the ground speed of the platform.

2.2 DATA HANDLING

Fundamental to successful multisensor data is the use of a common control system to direct, initiate, and monitor all sensors. This anticipation was strongly reinforced by our experience in the Quick Look flights. Common time stamping on the data stream is particularly important. In addition, the need to handle a large total data rate, and to optimize post-collection recovery and analysis demands a central data recording site.



Figure 1. Combined RAR and millimeter-wavelength data for a region near Aberdeen, MD. North is left.

Data collection from each sensor will be handled by a central computer/common data bus network and recorded on high speed digital tape at 400 mbit/s. Figure 2 outlines the data handling architecture. The concept is modular with standard sensor interfaces (16bit and RS 232) on a fiber optic Asynchronous Transfer Mode (ATM). To maintain electrical isolation all sensors are on Uninterruptable Power Supplies.

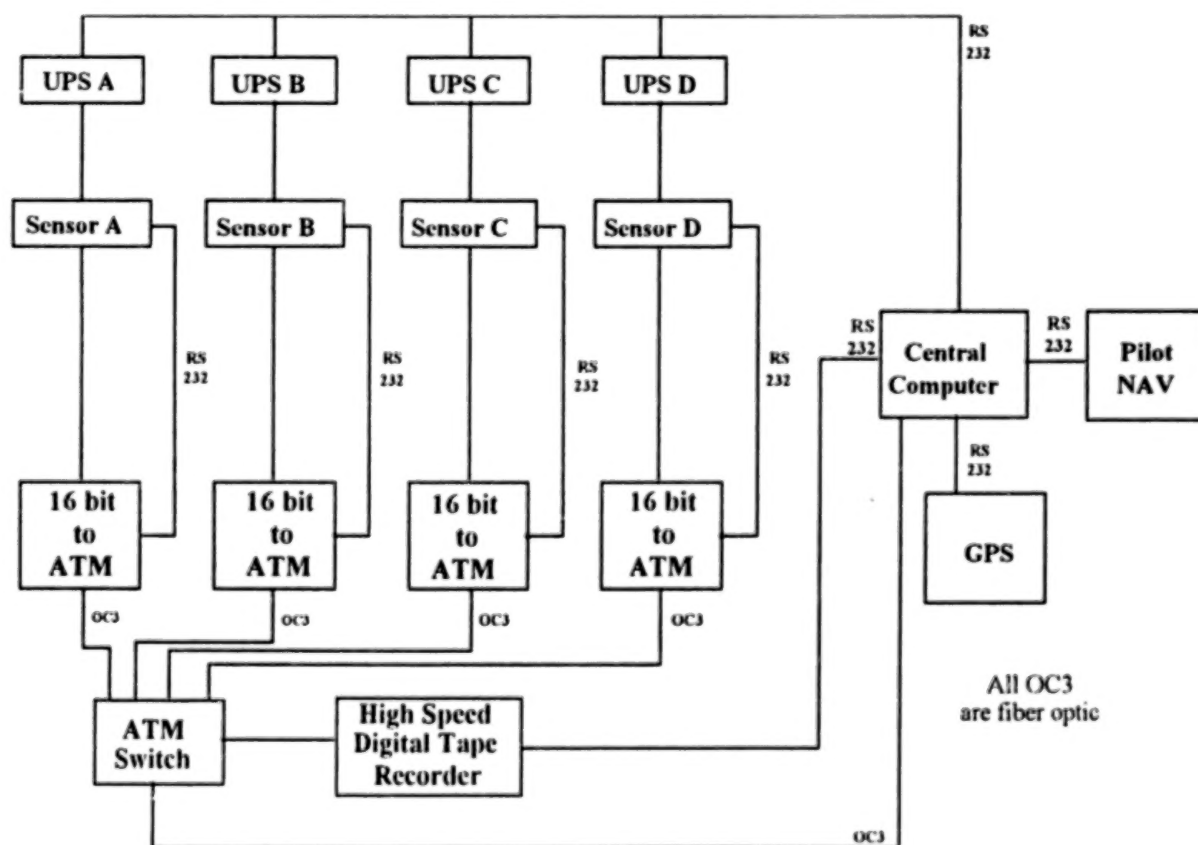


Figure 2. Airborne data handling architecture.

2.3 DATA AGGREGATION

The temptation in discussing combination of multisensor data is to call it "data fusion". This term, however, has acquired a very particular meaning in defense research. The standard military approach is focused on targeting against clutter, and relies on interpreting the output from each of several sensors separately and then combining the results in some heuristic scheme to make an identification. By contrast, the RASTER-J approach emphasizes early combination of sensor outputs, aggregating the calibrated sensor data as part of the interpretation process. This can be as simple as piping each output to the different RGB inputs of a color display. More sophisticated methods, involving algorithmic combinations of the data before display are well known in remote sensing (e.g., the tasseled cap transform).

The best method of aggregating data would be to feed the sensor outputs into a model for the formation of the desired signature, including simulation of the sensor responses, atmospheric transmission, etc. Elsewhere in this meeting, we describe an ONR-sponsored program to develop a general simulator for remote sensing signatures in the littoral regime. Part of the RASTER-J Phase I activity would be to use this simulator as the modeling nucleus for such an aggregation process.

To a large extent, the use of data aggregation enables us to get around the deficiencies of individual sensors. For example, the ideal sensor for measuring soil moisture would be a microwave radiometer operating at centimeter wavelengths, which would be sensitive to the changes in dielectric constant produced by moisture differences and yet insensitive to covering vegetation. But such a system is inadequate to the spatial resolution requirements of most real problems. We seek sufficient resolution by use of the higher frequency millimeter-wavelength imager, but at the cost of needing to correct for vegetation cover. By coupling the millimeter-wavelength data with a vegetation cover correction inferred from multispectral or hyperspectral imagery, we can hope to come to a better solution.

2.4 AIRCRAFT SELECTION AND EVALUATION CRITERIA

The RASTER-J concept is to mount multiple sensors with all attendant control and recording systems on an aircraft, and to operate those sensors in a cooperative manner over a broad range of environmental phenomena and insults. Most pre-existing sensors have been developed to fly as a stand alone system and are neither compact nor light. Most sensors require a minimum of one operator. These conditions drive the testbed aircraft towards a larger platform with a large payload and range. Large aircraft burn larger amounts of fuel, require larger crews, and, therefore, cost more money to modify and operate.

TABLE 2. AIRCRAFT EVALUATION

	Operator	Max. Payload (X 1000 lbs)	Range (X 1000 NM)	Flight Cost (X \$1000/Hr.)	Modifications Required
CV-580	ERIM	3-4	1.2 - 1.8	1.5	Minor
RP-3A	NRL	7	3	1.4 - 3.0	Minor
C-141A	412 TW	28	7.3	5.2	Moderate
RP-3B	NRL	11	3	1.4 - 3.0	Moderate
C-23	412 TW	3	0.75	0.76	Major
757	Boeing	68	1.5	3.0	Major
DC-9-30	Lockheed	15	3	2.6	Major
C-130	NASA Ames	20	1.9	4.0	Moderate
C-18	412 TW	25	8.7	4.8	Major

000281

As part of the aircraft trade studies, we consulted with government and industry personnel who are actively involved in the selection, integration and/or operation of aircraft for environmental remote sensing. Table 2 summarizes the aircraft evaluation.

3. APPLICATIONS

It should be recognized that, while instigated as a research program into processes relevant to Global Environmental Change, RASTER-J has potential application to most environmental applications. These are summarized in Table 3.

TABLE 3. POTENTIAL APPLICATIONS OF RASTER-J

Application Area	Utilization
Pollution Prevention	Detect hazards and measure process variables affecting waste stream pollution.
Compliance	Develop monitoring techniques for hazards and waste water. Develop rapid response capability to assess accidents.
Conservation	Develop monitoring techniques for land management and rehabilitation assessment.
Installation Restoration/Cleanup	Develop methods for site characterization, site certification, and assessment of pollution transport

One particular application of interest to the Navy is the base remediation problem. The requirement to return old bases to civil use demands detailed understanding of the consequences of decades of use and storage of often hazardous materials to the coastal environment. The methods needed to assess the hydrological behavior of a coastal region for environmental change research are quite similar to those required for determining the waste stream and pollution transport in those regions. Consequently, we have tended to direct our data collection activities (despite their primary focus on system engineering) toward coastal regions and remediation targets.

000282

4. DATA COLLECTION FLIGHTS

To support the sensor trade studies and data handling/aggregation efforts, data collection flights were flown with an NRL P-3. It must be emphasized that these collections were not intended to be proper scientific experiments, with the required calibration and ground truthing; rather, they were done to explore the system engineering issues involved with multiple sensor installation, operation, and data analysis. Nonetheless, the data collected during these flights provided an excellent benchmark in supporting the trade-off studies. The sensors used were mostly existing devices immediately at hand, with one loaned from another laboratory (the NOAA multispectral camera), and (in the case of the hyperspectral imager) one newly developed instrument in its first field deployment.

TABLE 4. "QUICK LOOK" SENSOR CONFIGURATION

Sensor	Spectral Range	Parameters Sensed
Passive Microwave Imager	90 GHz	Soil moisture content, temperature
NOAA Multispectral Imager	Visible	Ocean color & vegetation color
Hyperspectral Imager	Visible/NIR	Soil & plant spectral variations
LIDAR	1 μ m	Ground roughness & plant vigor
Real Aperture Imaging Radar	9.3 GHz	Ground roughness, soil moisture & ice cover
PRT-5	Infrared	Ground temperature

The flights were conducted in January and March 1994. The aircraft, based at the Naval Air Station Patuxent River, MD was flown over Aberdeen Proving Grounds, MD and Calvert Cliffs, MD in January, and, in addition, over the Naval Surface Warfare Center at Dahlgren, VA in March. Both flights also covered parts of the Chesapeake Bay. Given the focus on system issues, we have thus far only reduced the data for the Aberdeen overflights, concentrating on a single part of the peninsula.

The Department of Energy has been exploring the use of a multisensor platform to develop synergistic products, with a particular emphasis on the remote measurement of variables related to non-proliferation treaty activities. This program, the Airborne Multisensor Pod System (AMPS), employs a modified P-3 platform with wing-mounted multisensor pods. NRL and DOE have planned a joint data collection activity to investigate our rather different multisensor architectures. This test flight will have the AMPS pods mounted on an NRL P-3 that will simultaneously carry a pallet with many of the Quick Look sensors. We will overfly Duck, NC, where an extensive oceanographic experiment is being conducted by the Office of Naval Research, from which we hope to obtain calibration and ground truthing data.

5. SUMMARY

The emphasis of the RASTER-J Program is in exploring the potential synergistic value of merged multiple sensor data for civil and military applications. Information gathered from this suite of sensors, either individually or synergistically, will spawn understanding and requirements and specifications for future airborne and space borne sensor designs. The long term goal is to build an operational multiple sensor platform which could respond nationwide or even worldwide to collect environmental data in response to a natural or man-made catastrophe, in addition to supporting continued environmental monitoring and research and base remediation efforts.

We will continue to evaluate current data products, collection techniques and data distribution techniques. Exploitation algorithms and methods, concept of operations, tasking procedures, etc., will be developed. Active and passive EO and RF sensors - SAR, RAR, LIDAR, MSI, HSI, MWIR and LWIR imagers, ultraspectral sensors, and standard stereo mapping cameras - will be evaluated. The sensors, however, will be existing equipment, rather than specially designed for RASTER-J. Parallel analyses and trade studies will be conducted to define the most effective sensor and platform combinations for future data collections and for meeting our long term goal of an operational, responsive multisensor platform. In addition to the sensor evaluation criteria discussed above, we will evaluate potential operational platforms on the basis of availability, payload capabilities, integration requirements, modification requirements, flight envelopes, range and endurance, flight cost per hour, and recurring costs.

RASTER-J will be capable of addressing many of the environmental questions important to improving our understanding of global environmental change. It will also be capable of addressing many of the current environmental problems confronting both civil and military agencies, such as contaminant assessment, effectiveness of restoration efforts, compliance monitoring, and hazards and risk assessment.

ACKNOWLEDGEMENTS

We thank the NRL RASTER-J team for their many contributions underlying the work presented here, with special thanks to J. Antoniadis, A. Clegg, N. Hubbard, and C. Freise. Financial support for this work was provided by the Strategic Environmental Research and Development Program.

DIACHRONIC STUDY OF CROP SPECTRAL RESPONSE IN CENTRAL GREECE

L. Toullos

National Agricultural Research Foundation (N.A.G.R.E.F.)
Institute of Soil Classification and Mapping
Larissa, 413 35, Greece

N. Silleos

Aristotle University of Thessaloniki
Laboratory of Remote Sensing Applications in Agriculture
Thessaloniki, 540 06, Greece

ABSTRACT

The purposes of this work are the identification and the discrimination of the main agricultural crops in Central Greece, using spectral data. The main crops in this area are cereals (wheat) for the non irrigated land and cotton, maize and sugarbeets for the irrigated land. For the performance of this target, including the designation of the period most suitable for receiving satellite data, a series of frequent measurements of the spectral behavior of the above named crops during the cultivation period, has been carried out. All measurements were taken using a Cimel type field radiometer with three channels (the same as SPOT satellite). The whole studied area was divided into several subareas (according to the geomorphological, the pedological and the hydrological characteristics), representative of the main soil types of the Central Plain. Based on the diachronic spectral data themselves, as well as the calculated Ratio Vegetation Index and Normalized Difference Vegetation Index, it was concluded that differences among the spectral data are existing not only between crops and between their phenological stages, but also between the subareas and between the parcels of the same subarea. Compared with cereals, the industrial crops cotton and sugarbeets, appear the most uniform spectral behavior. On the other hand maize and alfalfa appear the most extreme reflectance values due to their unstable cultivating range during the year. However, it was found that there are some Julian days in which both the identification and the discrimination of these crops are potentially feasible.

1. INTRODUCTION

Remote sensing is rapidly becoming a practical tool for obtaining information about the earth's resources and especially the vegetation resources. Satellite measurements of spectral radiance have been successfully used for identification of crops species and area estimation in many countries (MacDonald and Hall, 1980; Badhwar, 1984; Williams *et al.*, 1987; Baret *et al.*, 1988; Silleos, 1988, Silleos *et al.*, 1992), but usually problems concerning the accuracy (using one date data) and the cost (using multirate data) are mentioned. A significant amount of research has been conducted to develop remote sensing techniques for evaluating spatial and temporal variations in crop biomass and conditions as well as the influence of external factors. One difficult and challenging problem in remote sensing is the development of techniques that minimize the influence of the soil background on the spectral signatures of vegetation. The successful application of techniques for accurate estimation of canopy development depends on the degree to which such influence can be minimized.

Wheat, cotton, maize and sugarbeet are very important crops in Thessaly (Central Greece) and if satellite imagery is to play a role in providing timely, accurate landcover information, it will be necessary to discriminate between different species of cereals and the principal irrigated crops such as cotton, maize and sugarbeet. The objective of this study is to determine the extent to which SPOT simulated data discriminate between the predominate arable land cover types within the study area. This objective is of practical significance for the Ministry of Agriculture and local authorities to supplement their existing data collection methods, and to apply these data to improve the accuracy and cost-efficiency of the crops inventory and monitoring.

This study is based on the analysis of multi-date spectral reflectance data and relies on the fact that crops can be discriminated and identified according to changes which occur at various stages in their growth. The need for a multi-date approach is that single-date data rarely possess sufficient spectral differentiation between crop types for accurate classification (Jewell, 1989). This paper presents the results of an application of multitemporal data, collected by a field radiometer, for crops discrimination, based on spectral differences of each crop occurring between the main districts of the study area.

2. METHODS AND MATERIALS

For the performance of this work, first the proper study sites in the whole area were chosen carefully. The study area, the phenological stages of the studied crops as well as the used radiometer and the reflectance measurements are described directly below.

2.1. STUDY AREA

The study area (Fig. 1) is a part of the most important area in Greece for agriculture and it



Figure 1. Location map of the study area.

is irrigated mainly by pumping the underground water. For the needs of the research the whole area is divided into four subareas (Fig. 2) based on the geological, the geomorphological, the pedological and the hydrological characteristics. These four main subareas, chosen for study the main annual crops and alfa-alfa in central Greece, differ mainly in topography and soils but not in climate, due to relatively small distance between them.

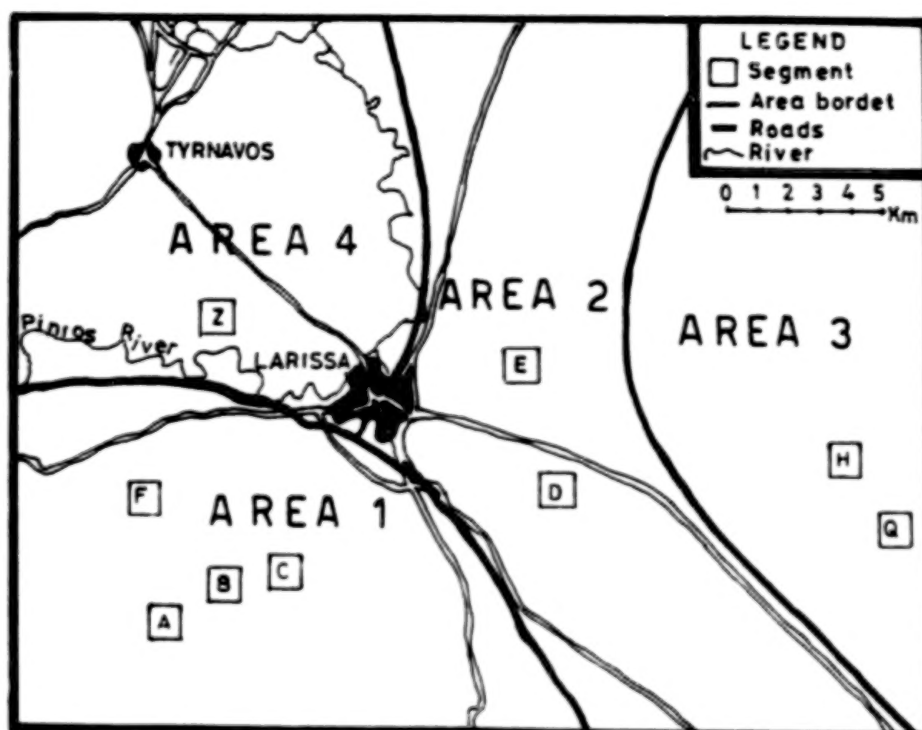


Figure 2. The four study subareas and their segments.

The first subarea (AREA 1) covers the hilly tertiary deposits at the southwest of the city of Larissa and mainly is consisted by eroded soils developed on fluvial and lake deposits (central raising of Thessaly). On the top of the convex slope are Entisols with A,C horizons (Soil Survey Staff, 1975) and on the lower part of the concave slope are deep dark clay soils (Inceptisol and Vertisol). The second (AREA 2) is in between the city and the former lake Karla, consisting from recent alluvial deposits of Pinios river and older clay to clay-loam soils, very fertile (Entisol and Inceptisol). The third subarea (AREA 3), is extended to the northeast, in the former lake Karla (with Entisols -recent alluvial soils with vertic characteristics- and Vertisols). The fourth subarea (AREA 4) covers the northwest alluvial fan with mostly flat old leached red soils without calcium carbonates (Alfisol). The soil moisture regime is xeric for the whole area.

Geologically, the first subarea is placed in the Pontian-Plio-Pleistocene with fluvio-terrestrial formations overlying lacustrine and fluviolacustrine deposits, consisting of sandy-clay material and loam with dispersed angular and rounded pebbles of different origin. The lacustrine deposits consist of marls and marly sandstones. The other three subareas are placed in the Holocene with alluvial deposits, light-grey to brown-grey unconsolidated material consisting of clays, sand, angular and rounded pebbles and fluvio-torrential-lacustrine material, deposited in the main Larissa basin, as well as in small internal basins. In the basins borders the material is coarse-grained, gradually passing to fine-grained towards the center (IGME, 1985).

The spectral reflection of crops, cultivated on these different parent materials, was measured using a field three-channel spectrometer, in smaller test sites (segments) representative for the vegetation and the soil as follows: Segments A, B, C and F in area 1, segments D and E in area 2, segments H and Q in area 3 and segment Z in area 4 (Fig. 2). The data for this study contain information of about 10 separate fields in each one 1 by 1 kilometer of the 9 segments in the 4 main districts in Larissa area. Thus, the target of the investigation was an approach to determine the spectral characteristics of wheat, cotton, maize and sugarbeet, using features derived from diachronic profiles of SPOT simulated radiometer measurements, in early, middle and full season. So carrying out crop identification separately in each segment could be result in easier selection of satellite imagery for agricultural inventory, the most suitable in each area. Hard wheat was examined in all segments, cotton in all segments except A, maize in segments C, D and E, sugarbeet in segments C, F and H, and alfalfa in segment Q.

2.2. SPECTRAL REFLECTANCE MEASUREMENTS

Radiometer data were examined in order to assess their discriminating power with regard to the crops of interest. Multispectral observations for the intensive farming area around Larissa, were made for these annual crops and alfalfa during the 1990 cultivating period. Table 1 describes the phenological stages of the main crops in Central Greece (Silleos *et al.*, 1992).

TABLE 1. PHENOLOGICAL STAGES OF THE MAIN CROPS

Wheat :	SEEDING: 10-30 November
	GERMINATION: About 30 days after
	STEM ELONGATION: In the end of March
	HEADING: From the 15th of April
	FLOWERING: In the end of April
	MILK STAGE: May 1-15th
Cotton :	MATURITY-HARVESTING: June 5-15th
	SEEDING: April 15-30th
	GERMINATION: After 15 days
	FLOWERING: Continuously from June 20th to the beginning of September
	MATURITY: In the end of September
Sugarbeet :	HARVESTING: October - December
	SEEDING: About the 15th of March
	GERMINATION: 20 days after
Maize :	HARVESTING: August - October
	SEEDING: About the 15th of April
	GERMINATION: 15 days after
	VEGETATIVE STAGE: About 40 days after seeding
	REPRODUCTIVE STAGE: A month later (depending on the variety)
	SEED FILLING: 130 days after seeding
	HARVESTING: Two months later

Spectral reflectance measurements of the canopies over the wavelength range 400-1100 nm were made using a SPOT portable radiometer developed by Cimel électronique in collaboration with CNES and INRA in France (Guyot *et al.*, 1984). The instrument is composed of a radiance head for ground sighting, an irradiance head for sky sighting and an electronic box for direct reading of the 3 reflectance

factors. A telescopic support was used in the field and the two head fixed on the support remain on vertical position, mounted on the boom of a mobile aerial tower. The wave lengths for the three radiometer bands are 0.50-0.59 μm for channel 1, 0.61-0.69 μm for channel 2 and 0.79-0.89 μm for channel 3 (Guyot *et al.*, 1984).

Radiation measurements were taken for more than ten locations, over each field-plot vertically (nadir view) from 2.0 m above the soil surface. With a 12° field of view, the sensor viewed an area 1.5 m in diameter. The use of small sample sizes for characterizing a spatially complex site, is a major source of error in remote sensing investigations (Curran and Williamson, 1985). But 2 meters are enough high to surpass the variability problem of the spectral response of the plant canopy, which depends on the size of the viewed area (Guyot, 1989). All spectral measurements were made during cloudless or near cloudless days prior to solar noon and the solar elevation was at least 45° . No reflectance measurements were made when clouds blocked any direct beam solar radiation, nor when cloud cover exceeded 30 %. Most observations were made when cloud cover was less than 10 % (by visual estimate) and between 10:00 and 14:00 solar time, although other times are presented. Reflectance data were collected on 42 days in 1990, and all major stages of development from seeding (tillering) to maturity were included. The spectral measurements of the ratio radiance/irradiance were expressed as % reflectance with a 0-100 scale.

3. RESULTS AND DISCUSSION

3.1. DATA ANALYSIS

A radiometer measures the sum of the electromagnetic energy which emerges from the plant-soil complex and the reflected and emitted sky radiation, so, the study of green vegetation using a field radiometer is hampered by the influence of the variability of soil background and its properties (Baumgardner *et al.*, 1985). The emergence of green vegetation over a soil causes composite red radiance to decrease, because of chlorophyll absorption and increase of overall infrared response, as a result of leaf mesophyll structure. Thus, deviations of spectral data from the bare soil line, in an appropriate direction, may be attributed to the presense of green biomass.

Spectral response was represented in several forms for further analysis. In addition to the reflectance factors of individual wavelength bands, two vegetation indices were considered in an attempt to maximize the spectral contribution from green vegetation, while minimizing soil background influences. The ratio indices use ratios of linear combinations of near infrared and red wavelengths, to enhance contributions from green vegetation. Jackson *et al.* (1983) found ratios to be effective in reducing of soil moisture-induced soil reflectance variations on a uniform soil type. The ratio of IR/red was calculated as channel 3 divided by channel 2, and Normalized difference vegetation index was computed as $(\text{channel 3} - \text{channel 2})/(\text{channel 3} + \text{channel 2})$. These indices are sensitive to soil type and soil moisture condition.

Reflectance spectra were measured at several stages of development (tillering, seeding, heading, flowering, harvest maturity) between February and August, in 1990. The phenologies of the crops were considered identical and the differences in the agronomic characteristics among the crops and the segments were generally small, in the 4 different areas. Visually, it was not possible to produce distinct groups of canopies, except for segment H due to severe drought in Area 3. Maximum green leaf area of wheat crop was reached prior to heading and then declined as the lower leaves senesced. Cotton plants reach this stage during flowering and stay at this situation for a long period. Sugarbeet covers the soil background in a short time and its phenology looks steady till harvesting. The vegetative and

reproductive stages of maize depend on the variety but can be distinguished from the prior and next stages. The analysis of the field measurements on the different crops indicates that these seasonal changes of the crop features could discriminate between crops and stages. As it was expected the great differences were in the near infrared band for all crops and all dates of measurements. There was a very high correlation between bands 1 and 2 with $r > 0.9$. Because of this correlation, data from band 1 was largely discarded from the analysis in favour of using vegetation indices derived from a ratio of band3/band2.

A first comparison of different reflectance data for the 9 test sites (segments) is presented in Fig. 3. This figure compares the mean radiometric values in channel 3 (CBAND3) of hard wheat, in groups of a few days intervals, corresponding to four separate stages. The time interval February 15 - March 5 represents the stage of germination, the interval March 19-26 represents stem elongation, the interval May 7-11 represents milk stage and the fourth interval May 22 - June 6 represents maturity. It is clearly seen that there are differences between stages and between segments and the highest values of reflectance appear during stem elongation. Only in segment Q the highest values appear later (May) possibly because of tardy seeding and the lack of measurements during April. The lowest values appear in segment H, as it was expected due to the lack of rain water. However these differences in the mean values of reflectance, in near infrared, are not able to support distinct criteria for site by site crop discrimination. Similar results were obtained also for the irrigated crops. Cotton and sugarbeet appear the most uniform spectral behavior and maize and alfa-alfa appear the most extreme one.

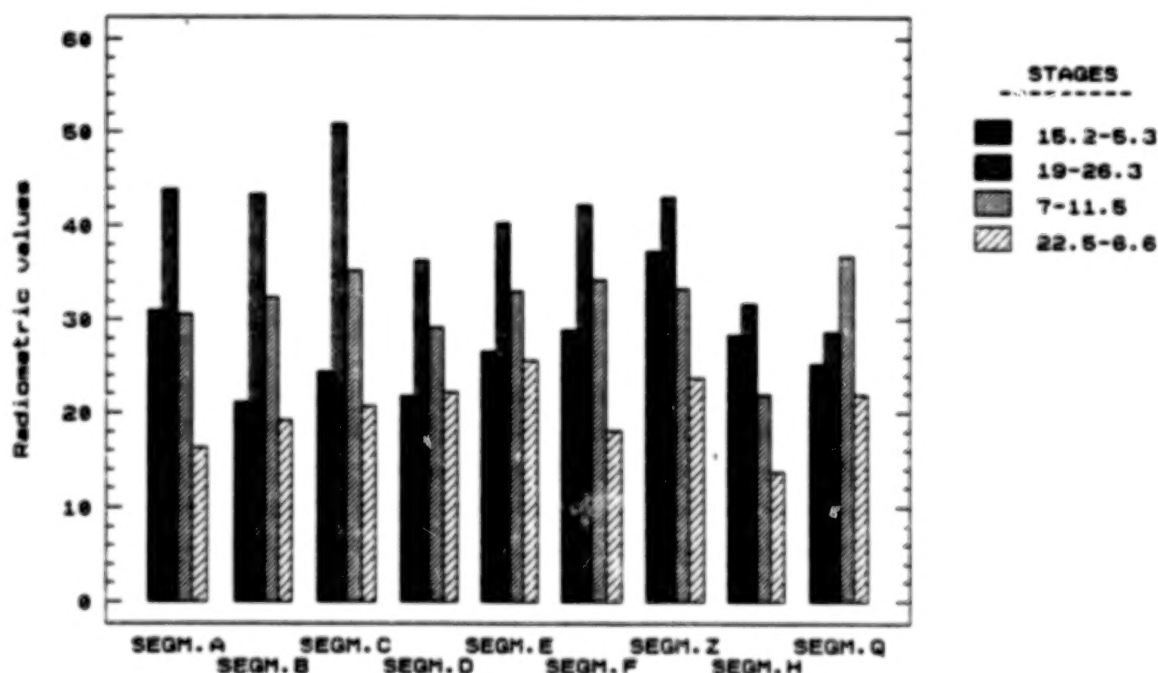


Figure 3. Mean reflectance values in near infrared, in 4 stages of Hard Wheat, in the 9 segments.

3.2. CROP DISCRIMINATION BASED ON MULTITEMPORAL SPECTRAL SIGNATURES

Figure 4 presents the differentiation of the spectral signatures of hard wheat for each of the 9 studied test sites (segments) during crop evolution. Radiometric values represent the reflectance as it was recorded by the radiometer, for each of the three channels, in several dates (Julian days) : 3 for segments D, E, and Z, 4 for segments A, B, C, H and Q, and 7 dates for segment F. These data are the mean values of measurements in 10 different parcels in each segment and each parcel value is the

mean of more than 10 repetitions in the same parcel, recorded within a time interval of a few minutes. With Fig. 4 it is concluded that almost in all segments the shape of the multitemporal spectral signature of hard wheat is altered in the same way during the time. A small differentiation occurs in segment Q (Karla area) where the maximum values of infrared channel appear late in the spring (May) instead of March, as mentioned above. The highest values in infrared channel appear in segment C and the lowest in segment H (the area with severe drought during 1990). In all segments is clear the effect of soil type on crop reflectance. The other two channels, due to the chlorophyll absorbance of the radiation, give less reflectance. The relation between these values is at the first stages $CBAND1 > CBAND2$, after the critical point of the highest value of $CBAND3$ and during flowering, it is $CBAND1 = CBAND2$, and by the end of milk stage and during maturity, the relation becomes opposite ($CBAND1 < CBAND2$).

Figure 5 presents the spectral signatures of cotton in 8 segments, for 5 or 6 dates. The shape of these signatures is almost similar in all segments with small differences mainly in segments H and Q (Karla area) and in bands 1 and 2, due to surface salts which reflect strongly in the visible spectrum. The highest values in infrared channel are observed in C and F segments, which represent the typical cotton fields with the highest yield. A comparison between wheat and cotton spectral signatures, shows that the greatest differences in infrared reflectance occur between the 50th and the 130th day, when wheat is in the stage of stem elongation, heading or flowering and cotton is at the stage of seeding or germination. In segment C cotton data of the 47th day refer to bare soil. Compared with the next measurement (129th day) we can see that there is no significant change in mean reflectance values during about 80 days.

The other irrigated crops (sugarbeet and maize), because of long vegetative period, show spectral signatures with small differences between measurements (Fig. 6). Sugarbeet in segments C, F and H keep the radiometric values as well as the relation $CBAND3 > CBAND1 > CBAND2$ steady for all the vegetative stage, with the highest greenness in segment C. Maize has also steady signature shape but the remoteness between channel 3 and the others is smaller. Alfalfa will be always a problematic crop for image crop discrimination. Its multitemporal spectral signature (Fig. 6) easy can be confused with the other crops as it is a semipermanent crop (about 4 years cycle) and the cuttings are repeated randomly in the time between parcels.

Spectral signatures of 3 different crops (cotton, sugarbeet, maize) in the same segment (C) at the same day, can be compared in the diagrams for days 129 (9 May 1990), 156 (5 June 1990) and 172 (21 June 1990) (Figs. 4,5,6). Sugarbeet has the highest reflectance in infrared channel in both 129th and 156th day and the highest difference between $CBAND3$ and the other two and seems to discriminate this crop very well. That means the time interval between the second half of May and the first days of June are the best for the identification of this crop. During the 172th day (21 June) maize and cotton appear similar as sugarbeet and discrimination is impossible. This problem continues during July (diagram for day 191) between sugarbeet and cotton.

Diagrams for days 64, 85, 131, 157, 176, 193 and 232 in segment Q (Figs. 4,5,6) compare hard wheat, cotton and alfalfa. Based on these data we can discriminate hard wheat during the first 15 days of May (with the relation of high values in band 3 and the lower in the others as well as the positive difference $CBAND1 - CBAND2$). Cotton can be distinguished only in the 131th day or near that date, based on the high values of bands 1,2. Alfalfa produces confusion in the most part of the cultivating period and only very early in the spring (end of February) can be identified well.

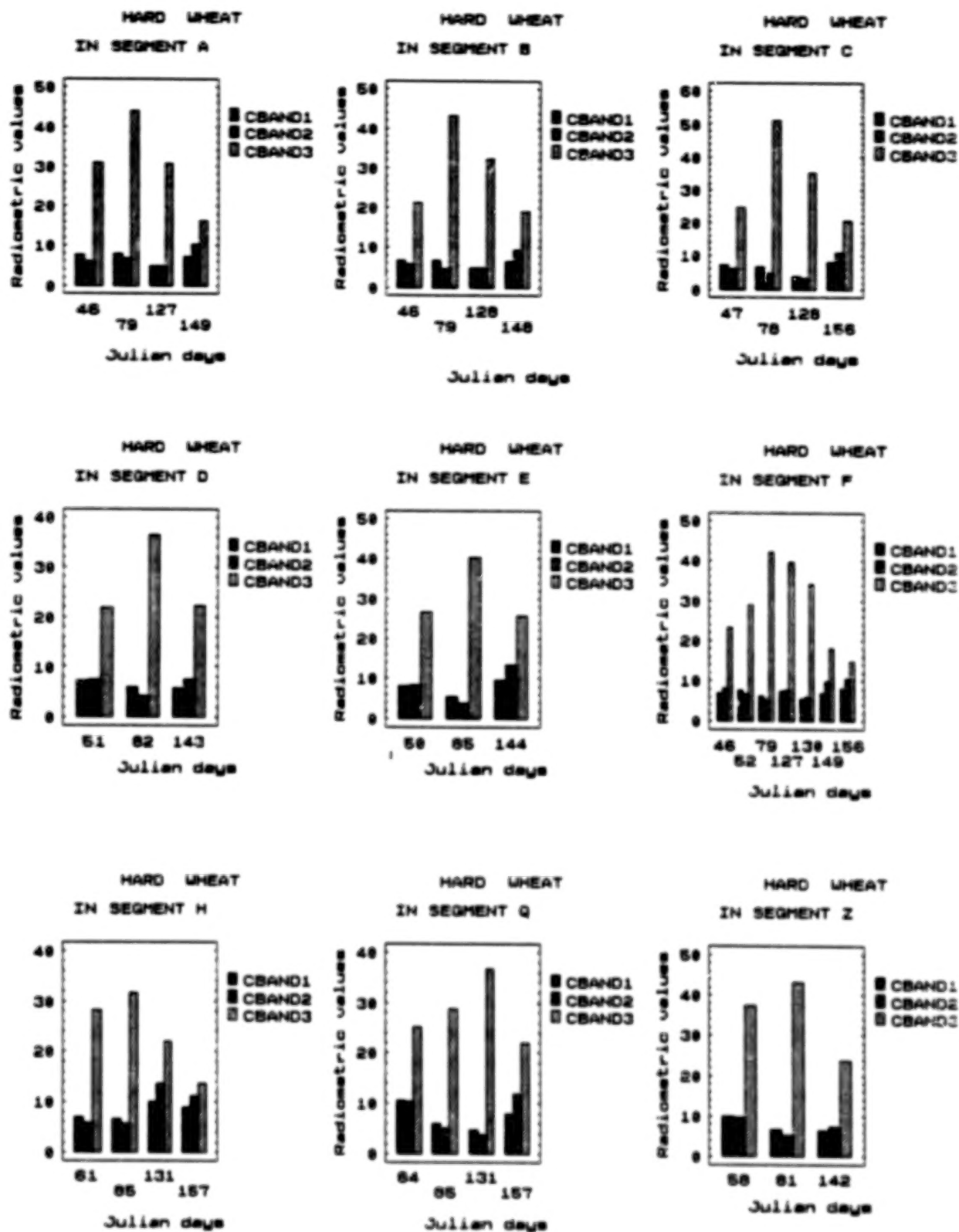


Figure 4. Multitemporal spectral signatures of Hard Wheat for several Julian days, in the 9 studied segments.

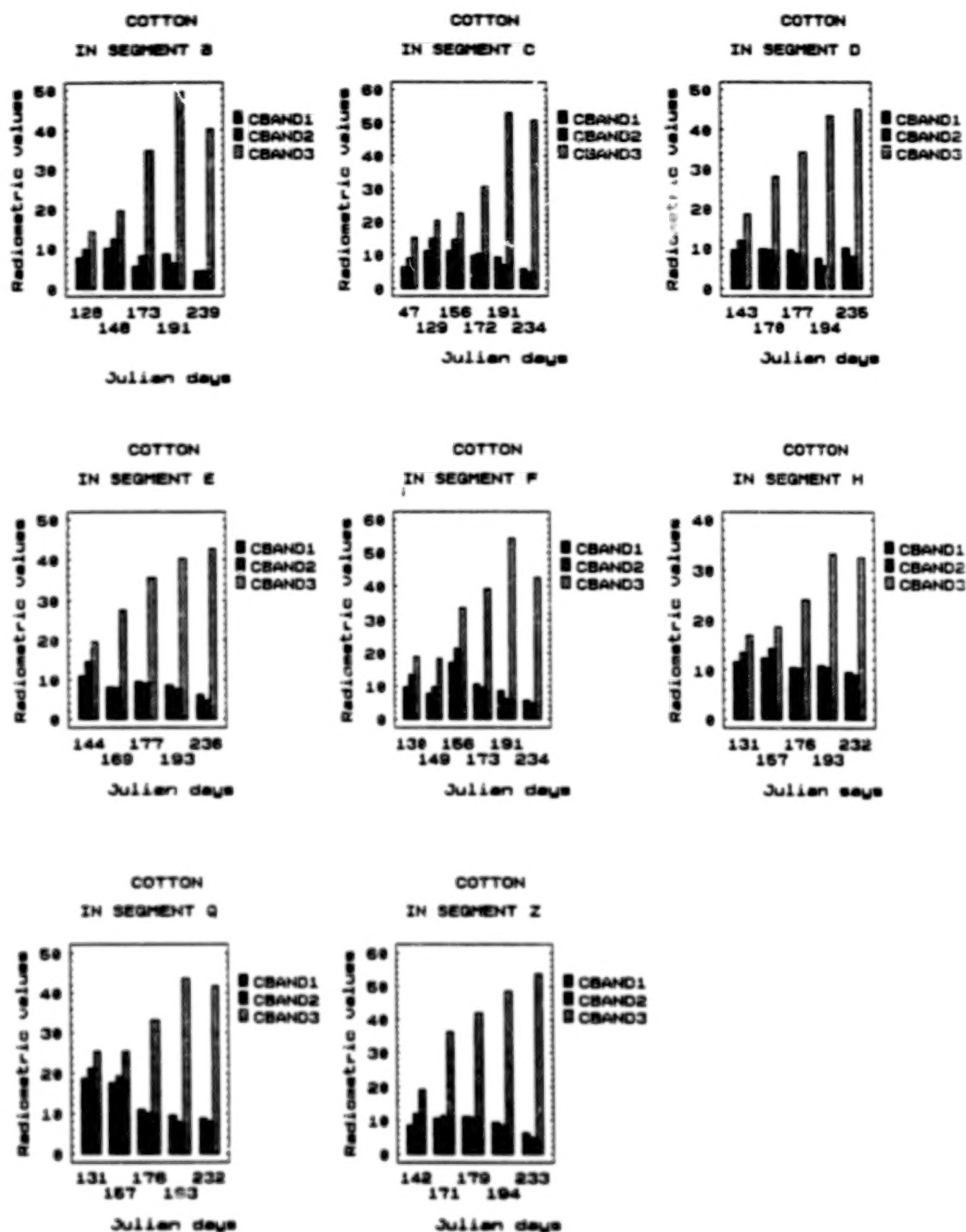


Figure 5. Multitemporal spectral signatures of Cotton for several Julian days, in the 8 studied segments.

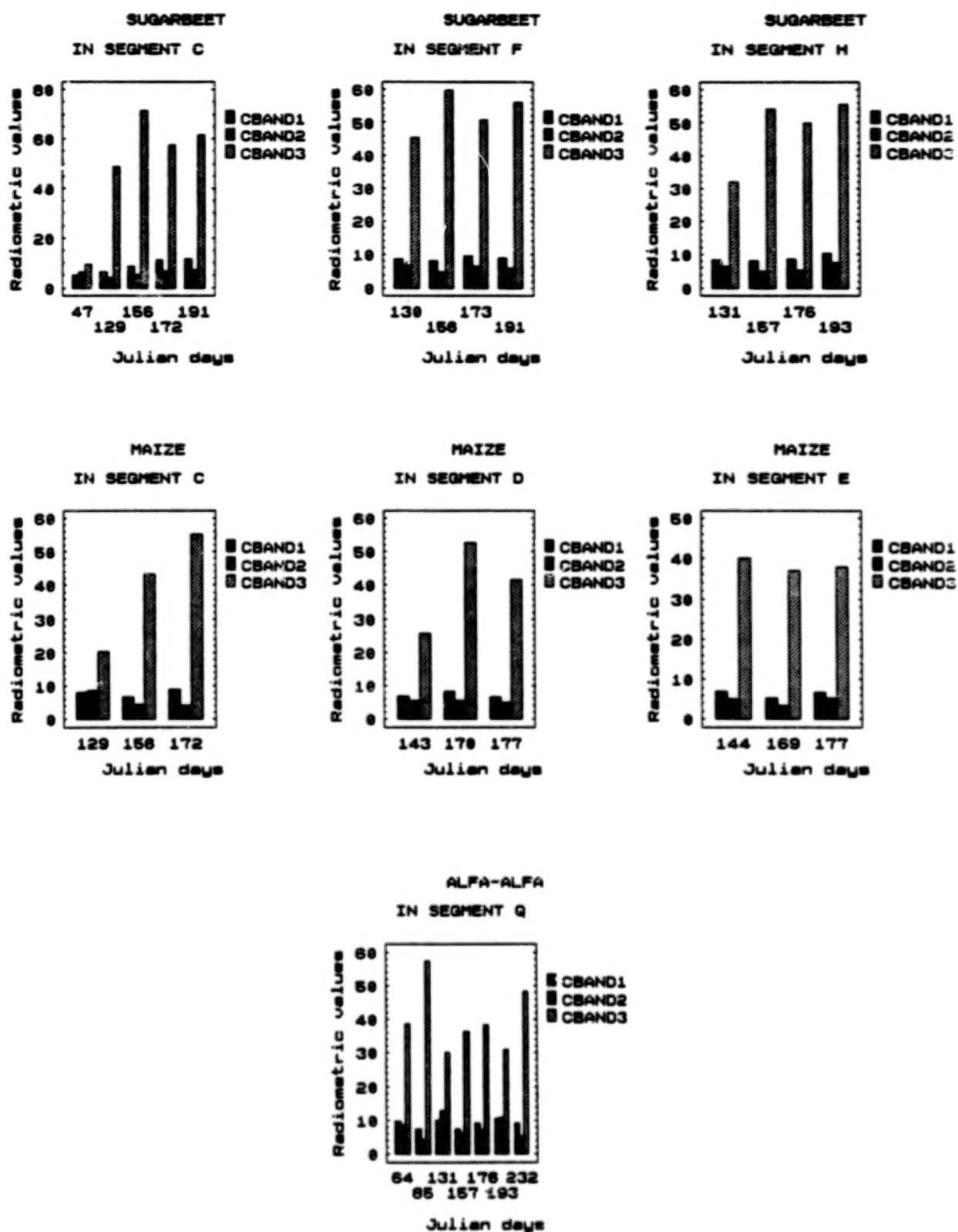


Figure 6. Multitemporal spectral signatures of Sugarbeet, Maize and Alfa-alfa for several Julian days.

3.3. CROP DISCRIMINATION BASED ON VEGETATION INDICES

Given the high correlation of bands 1 and 2, nearly all the information on crop discrimination can be obtained by producing a ratio of band 3 against band 2, the Ratio vegetation index (RVI). In addition to this ratio, the normalized difference vegetation index (NDVI) enables removal of reflectance differences due to soil type. Figure 7 shows the mean RVI values of all parcels in each segment, in the four study subareas and for all dates during the growing season of hard wheat. In segments D, E and Z there are only 3 dates of reflectance data and in the others 4 dates. Comparing these diagrams it can be concluded that there are no significant differences between areas. The only differences occur in area 3 where in segment H drought affected the vegetation and reduced the growing period (Boissard *et al.*, 1987). In segment Q the effect of delayed seeding is obvious. The mean NDVI values against Julian days of gathering data, in all parcels of each segment and for all the segments of the hard wheat, have parallel evolution in all segments, as the RVI data. Figure 8 represents in four plots all diagrams for RVI, one for each area, for cotton. The data are based on 5 dates during crop growing for all segments except for A. We can see the similar RVI values during germination, but from the flowering stage these values appear with differences between segments. These differences are smaller for the NDVI data. Figure 9 represents the NDVI mean values for sugarbeet, maize and alfa-alfa in their segments.

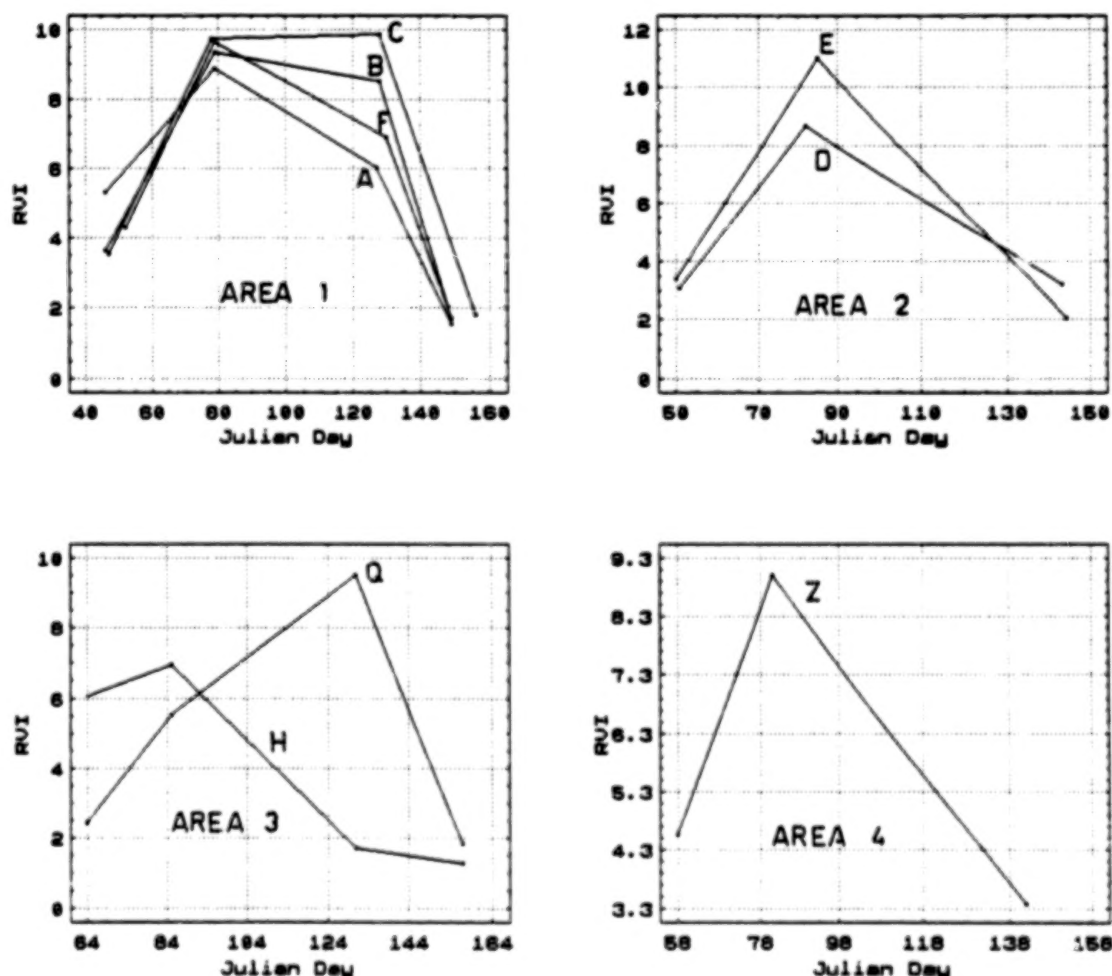


Figure 7. Mean Ratio Vegetation Index (RVI) values for Hard Wheat in the segments of each one of the 4 study areas.

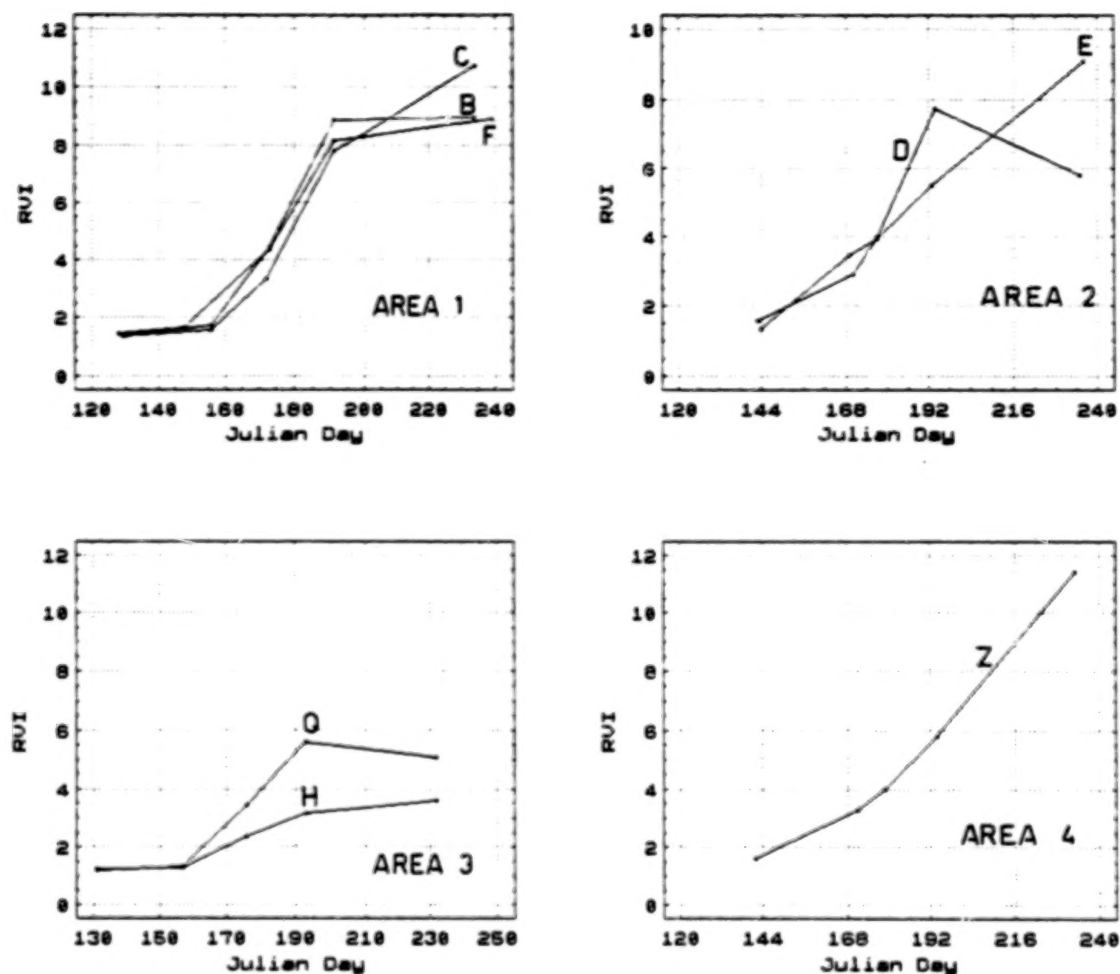


Figure 8. Mean Ratio Vegetation Index (RVI) values for Cotton in the segments of each one of the 4 study areas.

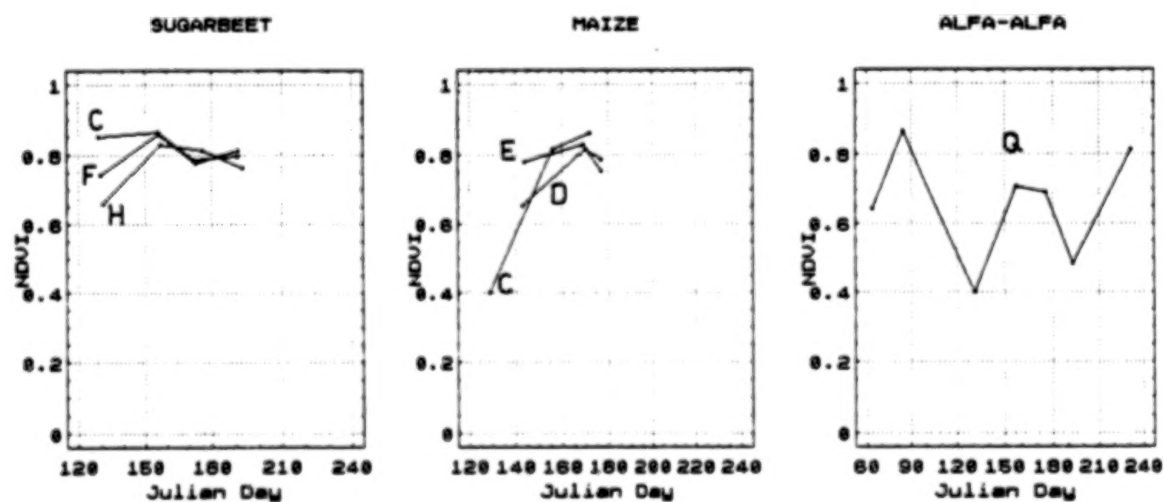


Figure 9. Mean NDVI values for Sugarbeet, Maize and Alfa-alfa in the corresponding segments.

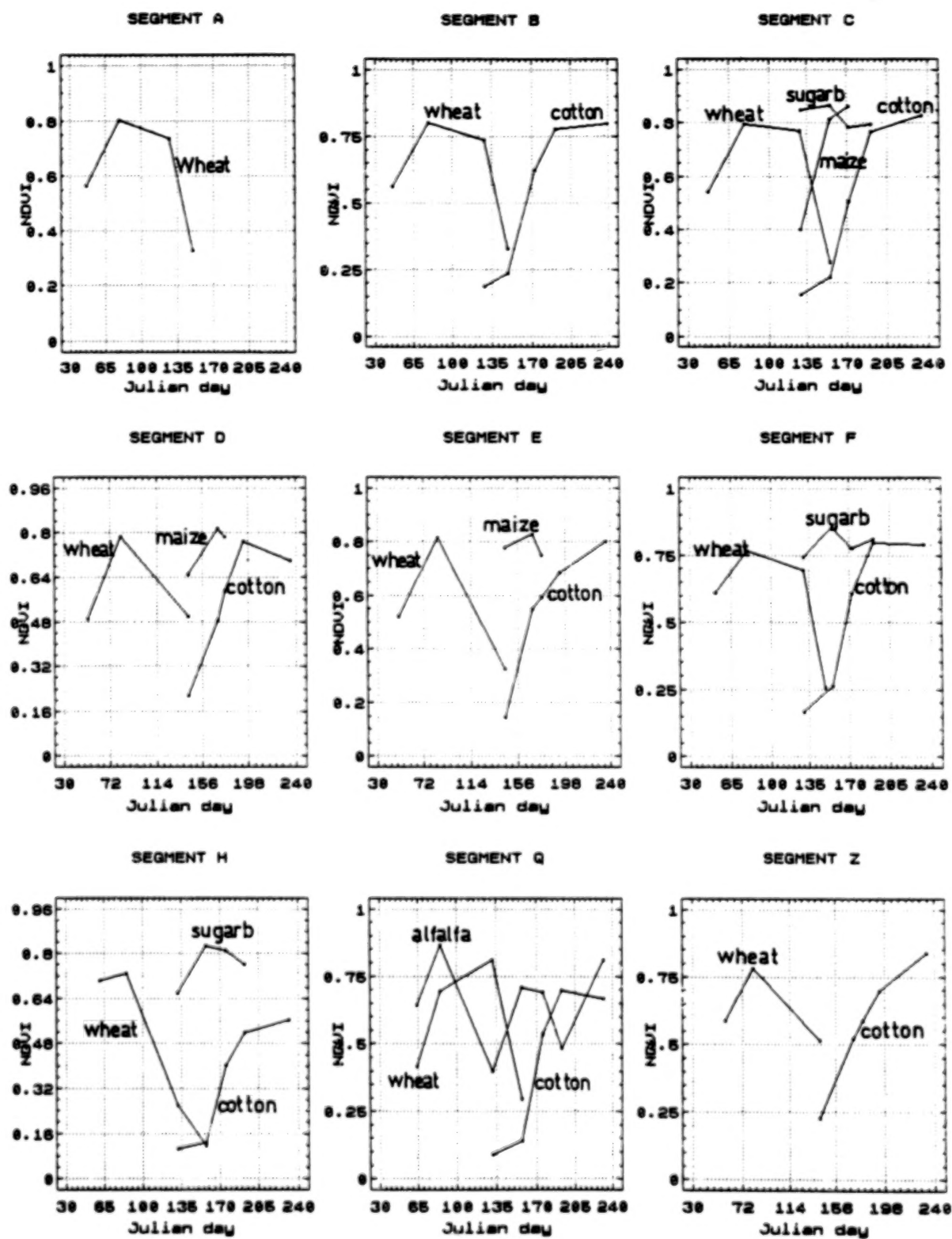


Figure 10. NDVI profiles for all studied crops in each segment.

Finally Fig. 10 shows the NDVI profiles of all the crops in each segment, during the measurements period. Here it is clear that with these values is possible to identify and discriminate the main crops in each segment. In the area 1 (segments A, B, C and F) we can select satellite data for one noncloudy day in the time interval between the 60th and the 100th julian day (March and April), during stem elongation, for wheat perfect inventory. For the irrigated crops a scene close to the 170th day of the year (end of June) will allow the inventory of sugarbeet, cotton and maize, with combining of RVI data. In the area 2 (segments D and E) the three major crops (wheat, maize and cotton) can be discriminated sufficiently with a scene of the period 20th-30th of May, based on crop differences in NDVI values. In the area 3 (segments H and Q) we need at least images of two days. One in the spring for wheat and the other in the end of June (as for area 1) for the successful discrimination of cotton and sugarbeet. Finally, in the area 4 (segment Z) we need the same scene as for area 1 and the inventory will be very accurate. Alfa-alfa will be always a confusion challenging crop for all areas.

4. CONCLUSION

Based on the above analysis of mean reflectance values as well as the vegetation indices data, it is concluded that an early spring SPOT satellite image could provide information on the distribution of wheat and other cereals. A combination of May/June images and a July image can help in the discrimination within and between irrigated crops, while an autumn image could provide special information for the discrimination of cotton.

Greece has the gift to be a sunny part on the earth surface. This allows remote sensing to receive uncloudy images many times a year. On the other hand the high spatial resolution of SPOT and Landsat-TM overcomes the relatively small parcel size of Greek farms. With only 2-3 scenes of the proper days per year, it is possible to have a sufficient accurate inventory of the arable land in central Greece. Ground truth is always needed and a close cooperation with the farmers is necessary too.

ACKNOWLEDGMENT

Professor G.P. Gilg from the University of Paris is acknowledged for providing the Cimel Spot radiometer.

REFERENCES

- Badhwar, G.D., 1984: Classification of corn and soybeans using multitemporal Thematic Mapper data, *Remote sensing of environment*, 16, 175-181.
- Baret, F., G. Guyot, A. Begue, P. Maurel, and A. Podaire, 1988: Complementarity of Middle-Infrared with Visible and Near-Infrared reflectance for Monitoring Wheat Canopies, *Remote sensing of Environment*, 26, 213-225.
- Baumgardner, M.F., L.F. Silva, L.B. Biehl, and E.R. Stoner, 1985: Reflectance properties of soils, *Advances in Agronomy*, 38, 1-44.
- Boissard, P., J.P. Pointel, and D. Lanquetuit, 1987: Etude de deux images multitemporelles rapprochees de SPOT 1 acquises a la maturation du b'e d' hiver (Ile-de-France, France), *Photo-Interpretation*, 4 (4), 25-28.
- Curran, P.J., and H.D. Williamson, 1985: The accuracy of ground data used in remote sensing investigations, *Int. J. Remote sensing*, 6, 1637-1651.

- Guyot, G., 1989: Les signatures des surface naturelles, *Teledetection Satellitaire*, 50, Paradigme Caen (France).
- Guyot, G., J.F. Hanocq, J.P. Buis, and G. Saint, 1984: Mise au point d' un radiometre de simulation de SPOT (Study of a SPOT simulation radiometer). *1^{er} Coll. Int. Signatures spectrales d' objets en teledetection*. Les Colloques de l' INRA, 23, P.I. 17, 233-242.
- Jackson, R.D., P.N. Slater, and P.J.Jr. Pinter, 1983: Discrimination of growth and water stress in wheat by various vegetation indices through a clear and turbid atmosphere, *Remote Sensing of Environment*, 113, 187-208.
- Jewell, N., 1989: An evaluation of multi-date Spot data for agriculture and land use mapping in the United Kingdom, *Int. J. Remote Sensing*, 10 (6), 939-951.
- IGME, 1985: Geological map of Greece, Larissa sheet. Athens.
- MacDonald, R.B., and F.G. Hall, 1980: Global crop forecasting, *Science* 208, 670-679.
- Silleos, N., 1988: Visual and digital classification of Landsat TM data for soil, physiography and Land Use mapping in Axios alluvial plain, Thessaloniki, Greece, *Geocarto International*, 4, 55-65.
- Silleos, N., N. Misopolinos, and K. Perakis, 1992: Relationships between remote sensing spectral indices and crops discrimination, *Geocarto International*, 7, (2), 41-51.
- Soil Survey Staff, 1975: *Soil Taxonomy*, USDA Handbook No 436, U.S. Government printing office, Washington DC.
- Williams, V.L., W.R. Philipson, and W.D. Philpot, 1987: Identifying vegetable crops with Landsat Thematic Mapper data, *Photogrammetric Engineering and Remote Sensing*, 53, (2), 187-191.

SPECTRAL CHANGE DETECTION IN CONIFEROUS FOREST USING LANDSAT TM AND ELEVATION MODELS

P. Syrén

Department of Physical Geography, Laboratory of Remote Sensing
Stockholm University, Sweden

ABSTRACT

Reliable estimates of spectral change between two or more satellite registrations require a strategy to systematically handle sources of error. The proposed correction scheme consists of 4 major steps. Reflectance calibration of satellite imagery through simultaneous low altitude reflectance measurements. Correction for topographic effects, using a digital elevation model and Minnaert constants. A standwise approach for estimate of reflectance statistics, i.e., each forest stand is segmented according to slope-aspect intervals. And finally, an object dependent reflectance correction, using empirically derived relationships between stand characteristics and solar angle for standardization of reflectance to a standard solar angle. The spectral changes obtained in visible, near-, and middle-infrared wavelengths were statistically evaluated on the level of stands and forest class.

1 INTRODUCTION

Change detection in coniferous forest, with the use of satellite imagery, can be divided into two broad categories. That which deals with spatial difference of specific object classes from one time to another, and that where the spectral development over time is investigated. The first case is easily studied with image enhancement techniques, preferably integrated with a geographical information system. The latter category is much more complex to investigate, since the spectral response to a change in health status or biomass may be obscured by a number of factors; natural spectral variation and development of the object, differences in atmospheric conditions and illumination and viewing geometry between registrations, non-Lambertian behaviour of the object and instability in the sensor system. In order to make reliable estimates of spectral change between two or more satellite registrations it is necessary to systematically handle these sources of error in a correction scheme, figure 1.

2 METHOD

In this study¹, such a scheme, was applied to coniferous forests of Norway spruce (*Picea abies*) and Scots pine (*Pinus Sylvestris*) in the Stockholm area, Sweden. Two Landsat TM-scenes, acquisitions dates 1986-09-17 and 1992-07-24 (09.21 and 09.17 GMT), were analysed in combination with a digital terrain model. Both images and the terrain model were resampled at 25 m resolution and georeferenced.

The 1992 image was classified with a maximum likelihood classifier. The areas classified as mature stands of spruce or pine were used as feature images to extract digital numbers from the 1986 and 1992 image, as well as slope and aspect values from the terrain model.

¹Founding was provided from the Swedish National Space Board

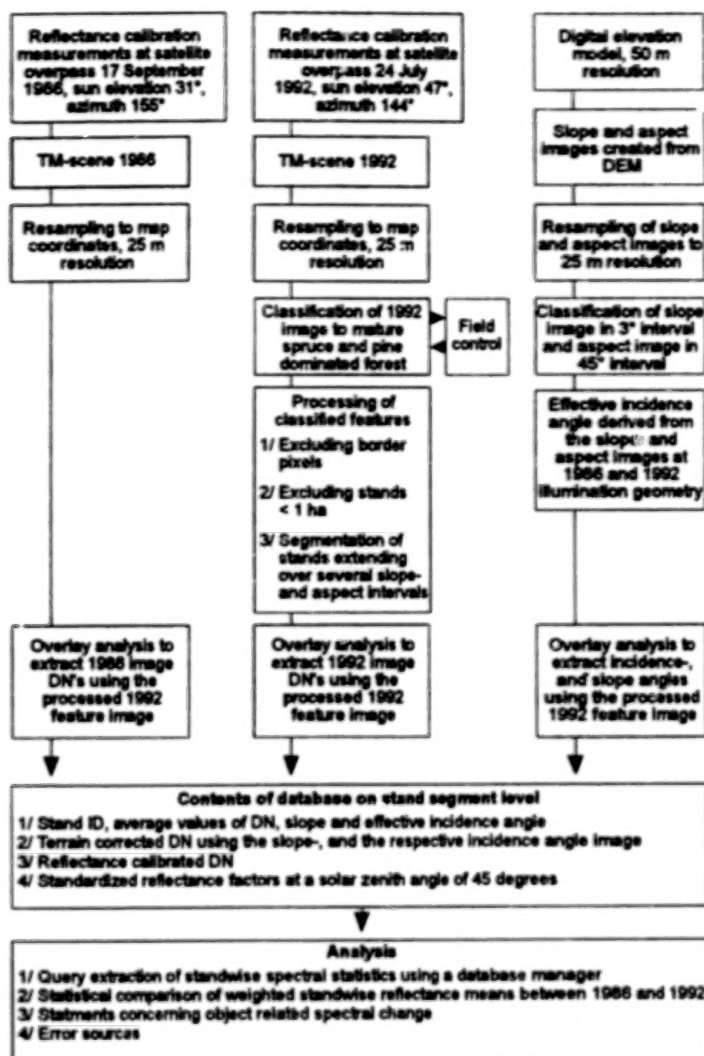


Figure 1. The correction scheme applied to coniferous forest of mature spruce and pine dominated forest in the test area, Stockholm, Sweden.

2.1 PROCESSING OF THE FEATURE IMAGE

Spectral comparisons of mean object reflectance over time, should be carried out with a standwise approach. Depending on available information of the object in question, e.g. inventory data or forest maps, the rules for defining homogenous stands will differ somewhat. When using a traditional computer based classifier, the classified image must be processed to achieve standwise homogenous objects. This post-processing includes steps to:

- Shrink the classified areas with a "mixed-pixel" border zone. Depending on resampling errors this step was found relevant in order to exclude a border zone around each classified area to assure comparison of reflectance means from corresponding objects. Also, this procedure will reduce adjacency effects from neighbouring objects with high spectral difference.
- Clear up the image of objects of a specified minimum size, and to assign an index to each remaining stand.
- Create a standwise segmentation depending on slope- and aspect intervals. For stands that extend over several slope-aspect classes it was necessary to compute standwise reflectance means weighted according to the segment area in each slope and aspect class.

2.2 REFLECTANCE CALIBRATION OF LANDSAT TM DATA

Image normalisation is achieved through simultaneous low-altitude reflectance measurements from helicopter and satellite overpass (Vogelman and Rock, 1988; Kleman and Alm, 1989). This empirical method depends on accurate reflectance measurements from objects of a wide spectral range that can be localised in the satellite image. Within the test area, spectral observations with the sensor in nadir position were collected from low-, high- and medium reflectance objects, in wavelength bands corresponding to the Landsat TM-bands 1, 3, 4 and 5, visible blue and red (485 and 654 nm), near-infrared and middle-infrared (NIR, 841 and MIR, 1676 nm).

Spectral irradiance estimates from a fully illuminated and horizontal barium sulfate panel, corrected for deviation from the Lambertian assumption Kimes and Kirshner (1982), made before and after the flight were used to interpolate the expected value at the time of object measurement. The reflectance factor per band was calculated as the ratio of the object radiance and corrected irradiance estimate. In order to identify the location in the satellite images, colour prints were taken of each object using a fisheye-lens.

For each object at least 5 pixels were chosen to give an average digital number of the corresponding measured reflectance. The regressions were used to recalculate the image data to reflectance factors. At this point irradiance-, atmospheric- and sensor system differences between the images were removed. The remaining discrepancies are composed of topographic effects, true spectral change of the object and differences in sun-target-sensor geometry between registrations.

2.3 CORRECTION FOR TOPOGRAPHY

The influence of topography on forest canopy reflectance has been described in several papers e.g. Leprieux *et al.* (1988), Teillet *et al.* (1982) and Ekstrand (1993). Terrain location indices, defined as the effective incidence angle (Smith *et al.*, 1980; Holben *et al.*, 1980), were used to calculate Minnaert constants for radiometric correction of forest reflectance in each spectral band Teillet *et al.* (1982).

2.4 REFLECTANCE STANDARDISATION

The relationship between solar zenith angle (SZA), forest characteristics and canopy reflectance can be described by linear functions in different wavelength bands (Syrén, in press). The functions for mature spruce and pine canopies were used to calculate the object dependent reflectance correction factor, as the ratio of the regression estimate at the acquisition solar zenith angle (SZA_a) and the regression estimate at the standard solar zenith angle (SZA_s). The factor obtained corrects the reflectance factor at SZA_a to that expected at the standard solar zenith angle. The difference in SZA between the 1986 and 1992 image was 16° (59.3° and 43.3°), and the SZA_s was set to 45° . In figure 2, the linear functions between SZA and canopy reflectance (near-infrared) for mature spruce and pine are shown.

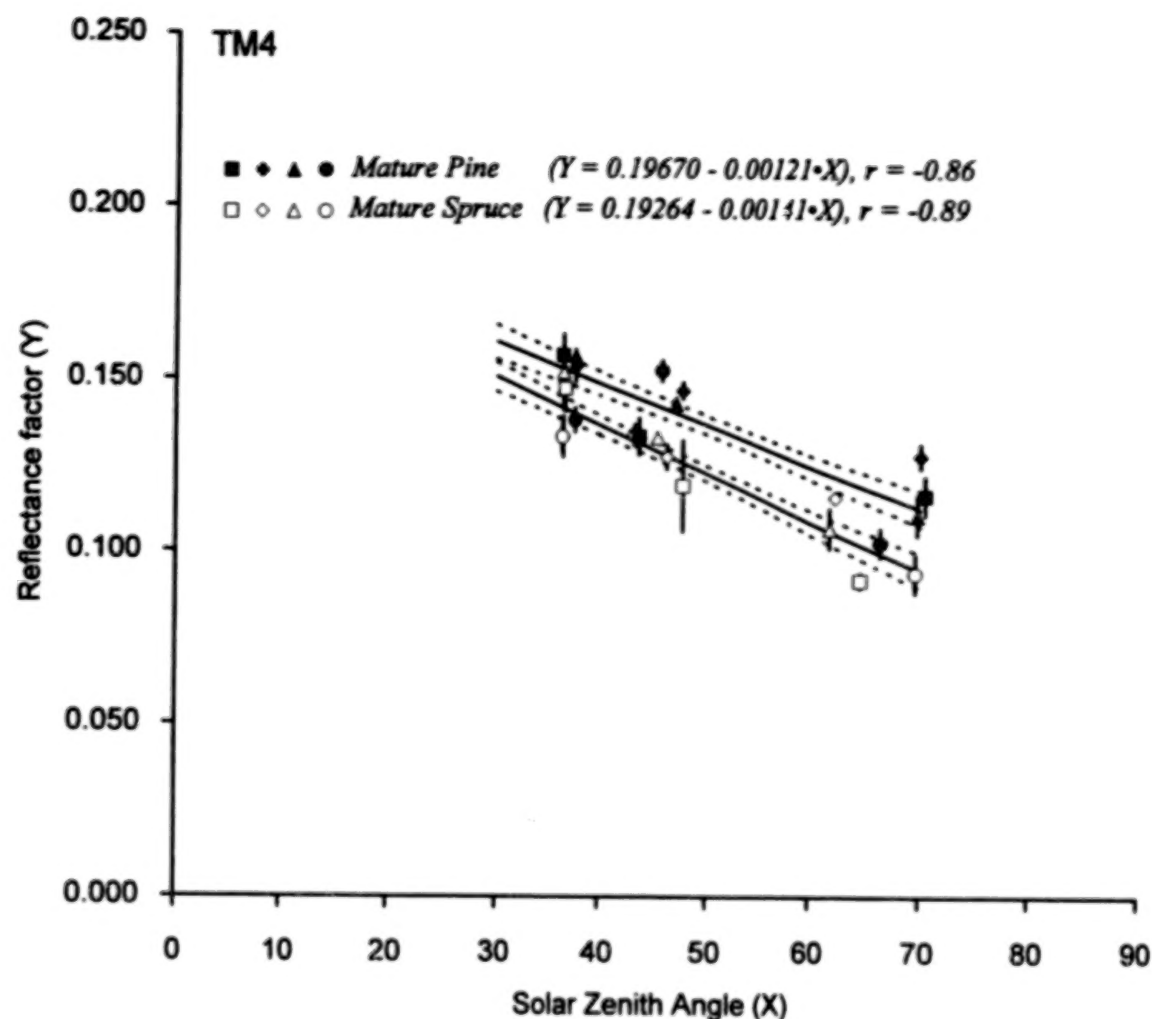


Figure 2. Linear functions for reflectance standardisation of mature spruce and pine in TM-band 4 (NIR). Dotted lines show the confidence limits of prediction means at the 0.05 level.

2.5 DATABASE CONTENTS

The processed feature images of mature spruce and pine stands were used to extract mean values of DN, incidence angle, slope and aspect for each feature segment in the 1986 and 1992 images and entered to a database. From the database, standwise mean values of terrain corrected DN, reflectance, and standardised reflectance with the corresponding standard errors were calculated.

3 RESULTS

In figure 3 the spectral difference between 1992 and 1986 (1992 minus 1986) are plotted for each stand, using the slope-aspect weighted mean values with confidence limits at the 0.05 level, together with the respective difference in class mean with confidence limits.

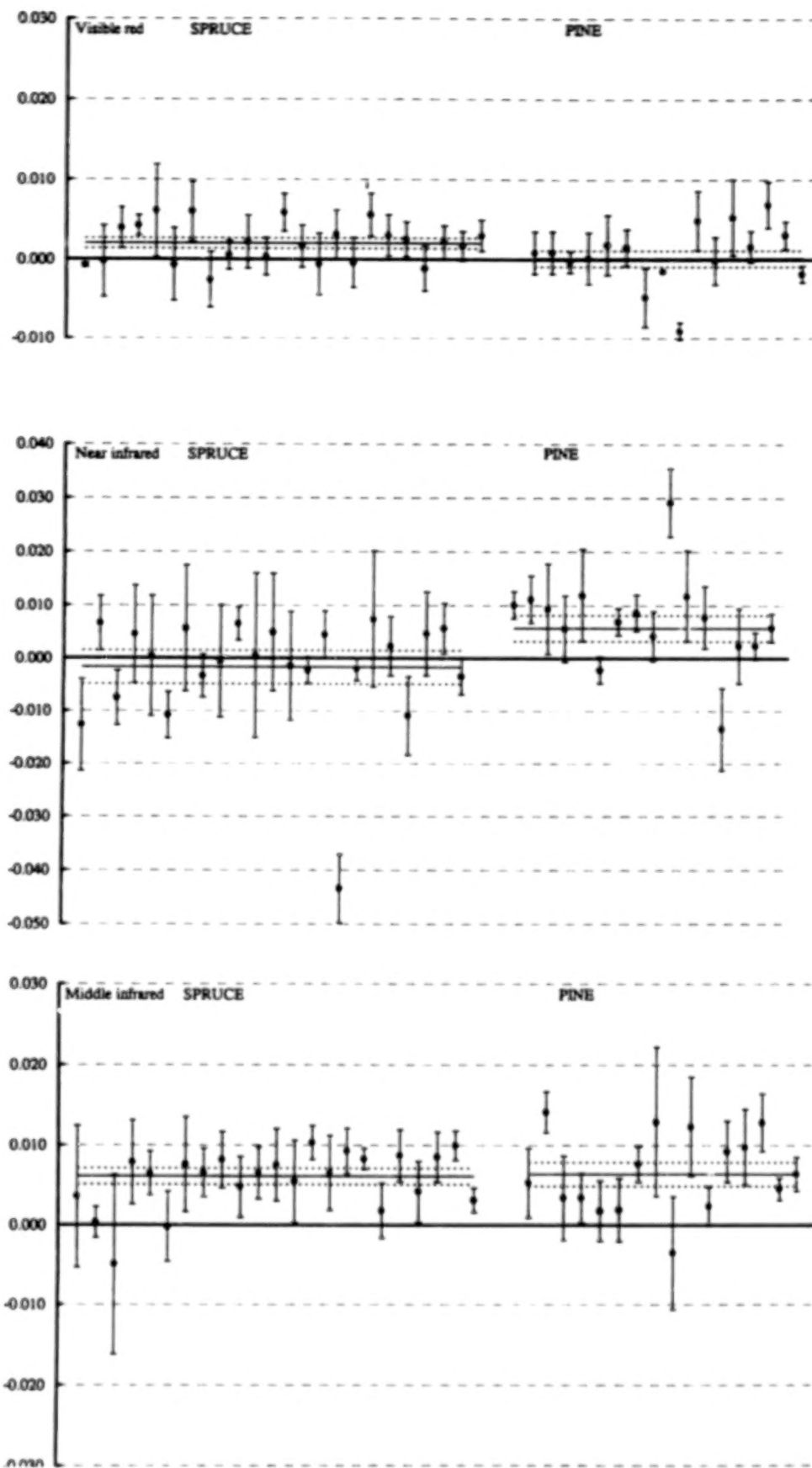


Figure 3. Reflectance difference (1992 minus 1986) of mature spruce and pine stands, with confidence limits at the 0.05 level

REFERENCES

- Ekstrand, S., (1993): Assessment of forest damage using Landsat TM, elevation models and digital forest maps. Doctoral dissertation. Royal Institute of Technology, Stockholm, Sweden.
- Holben, B. N. and Justice, C. O., (1980): The topographic effect on Spectral Response from Nadir-pointing sensors.. *Photogramm. Eng. Remote Sens.* 46:1191-1200.
- Kimes, D. S., Kirchner, J. A., (1982): Irradiance measurement errors due to the assumption of a Lambertian reference panel, *Remote Sens. Environ.* 12:141-149.
- Kleman, J. and Alm, G., (1989): Estimation of the atmospheric influence in a Landsat TM-scene using simultaneous low-altitude radiometer data. Research report 75, Department of Physical Geography, Stockholm University, pp. 28.
- Leprieux, C. E., Durand, J. M., and Peyron, J. L., (1988): Influence of topography on forest reflectance using Landsat Thematic Mapper and digital terrain data, *Photogramm. Eng. Remote Sens.* 54:491-496.
- Smith, J. A, Lin, T. L. and Ranson, K. J., (1980): The Lambertian assumption and Landsat Data, *Photogramm. Eng. Remote Sens.* 46:1183-1189.
- Syrén, P., (in press): Reflectance Anisotropy for Nadir Observations of Coniferous Forest Canopies, *Remote Sens. Environ.*
- Teillet, P. M., Guindon, B. and Goodenough, D. G., (1982): On the slope-aspect correction of multispectral scanner data, *Can. J. Remote Sens.* 8:84-106.

USING IMAGING SPECTROMETRY FOR MODELLING SOIL EROSION

Steven M. de Jong
Utrecht University
3508 TC Utrecht, The Netherlands

ABSTRACT

Soil erosion is a severe threat for Mediterranean areas. Modelling soil erosion processes at a regional scale helps to understand the processes and to indicate which areas are most prone to erosion. Data requirements of soil erosion models comprise topography (slope steepness and slope length), vegetation cover, climatic characteristics and soil physical variables. For this study a digital elevation model provides information on topography and meteorological stations provide data on rainfall volumes and rainfall intensities. Remotely sensed information in visible and infrared wavelengths is useful to assess the spatial distribution and the temporal changes of vegetation cover. The required model input of soil physical variables is often deduced from a digitized soil map. A serious drawback of this approach is that the spatial variability of soil physical components is often very large as is demonstrated by the (semi-)variograms. This study investigated the use of imaging spectroscopy to survey the spatial variability of soil physical variables and to use the image derived information as input for models. It is concluded that imaging spectroscopy is useful to assess the spatial variability of a limited number of soil variables only for bare or nearly bare areas. Wherever vegetation cover exceeds approximately 30%, the spectra are deteriorated by the vegetation and information on soil properties fades.

1. INTRODUCTION

In 1989 and 1991, experimental airborne campaigns (EISAC'89: European Imaging Spectroscopy Airborne Campaign and MAC-Europe'91: Multi-Sensor Airborne Campaign) were carried out in Europe (Bodechtel and Sommer, 1992; Hill, 1991). During these campaigns spectroscopical images were acquired by GERIS and AVIRIS of several test sites over Europe. One of the selected test sites was the southern part of the Ardèche province (southern France), which is located in a Mediterranean area and suffers from land degradation. Past and present human activities have caused the development of landscapes with vegetation ranging from maquis, garrigue and rangelands to badlands and unfavourable natural conditions hampers the ecosystem to regenerate (De Jong, 1994a; Grenon and Batisse, 1989). The usefulness of imaging spectroscopy was investigated for providing distributed maps for erosion models of variables such as soil and vegetation properties.

2. SOIL EROSION

Soil erosion is the result of a complex interaction of many variables changing over time and space. Although plot studies have yielded detailed information on the process-controlling variables and their interaction, the process is not yet fully understood (De Roo, 1993; Morgan, 1986). Due to the aggressive climate Mediterranean landscapes are vulnerable to land degradation processes such as soil erosion and the natural conditions in many Mediterranean areas are such that disturbed ecosystems do not regenerate easily. Consequently, Mediterranean areas need to be treated with care and methods for sustainable land use need to be developed. In order to develop methods for sustainable land use, information is needed on the present state of these areas and knowledge is required on the functioning of Mediterranean ecosystems.

The erosion processes that play a key role in the study area are soil surface crusting and rill and gully formation which result in badlands. Computer models were used to simulate the erosion processes and to

produce regional maps of erosion hazard. Input of these kinds of models comprise data on rain-fall volume and intensities, data on soil physical properties such as particle size distribution, organic matter content and saturated hydraulic conductivity, data on vegetation properties such as structure and cover percentage throughout the growing season and data on topography such as slope steepness and slope length. The erosion model used in this study is SEMMED (De Jong, 1994a) and was built on the physical basis of the Morgan, Morgan and Finney method (Morgan, 1986; Morgan et al., 1984). The model predicts annual soil losses. The model considers soil erosion to result from the detachment of soil particles by raindrop impact and the transport of these particles by overland flow. Energy of the rainfall for splash soil particle detachment is computed from the rainfall volume and intensity using the relation developed by Wischmeier and Smith (1978). The splash detachment rate is computed from this energy factor, the vegetation cover and a soil detachability index. The volume of overland flow is computed using the mean rain per rain day (Kirkby, 1976) and a critical value of the soil moisture storage capacity which is a function of the soil's bulk density, rooting depth, initial soil moisture content and a correction factor for evapotranspiration.

As the Mediterranean regions are extended and complex, remote sensing techniques may contribute significantly to data acquisition of complex spatial patterns of vegetation and soils to feed these kind of erosion models. Remote sensing can aid the mapping of the spatial and temporal distribution of vegetation variables (cover, patterns, land use) and some soil properties. Vegetation cover in the study area was mapped using the relations between spectral indices and field variables determined in the Ardèche region and is described in detail in De Jong (1994b). The use of remote sensing information in most erosion studies is limited to the survey of vegetation attributes. Information on soil properties is mostly derived from a conventional choropleth soil map with large soil units having a probably large, but mostly unknown 'within-unit' variance. Geostatistics can aid by quantifying the spatial variability and next, by sampling at a appropriate scale but such an approach is time-consuming and laborious. Imaging spectrometers might be a quick and useful alternative to provide information on the spatial distribution of soil properties. This study aims at comparing field mapping results with results derived from spectroscopical images.

3. FIELD SURVEY

The scale and structure of the spatial variation of the soil physical input variables were determined within the flight paths of the airborne campaigns following a geostatistical approach (Isaaks and Srivastava, 1989; McBratney and Webster, 1983). Such an approach generally requires two steps:

- 1) An approximation of the scale of spatial variation can be determined economically by a nested analysis of variance where stages incorporate spatial scale (Oliver and Webster, 1986). A nested analysis of variance, carried out in the study area (1.1 by 2.5 km) yielded an average optimal sampling distances shown in table 1. Next, a regular grid was put over the study area and the input variables for the model were determined at 208 locations. From these data points the spatial pattern of each soil variable can be described quantitatively in terms of the semi-variance function. This technique is based on the idea that the statistical variation of data is a function of distance (Journel and Huijbregts, 1978). The variogram (the graph of semivariance versus sample spacing, or lag) relates distances between sample points to the variance of the differences in the data.

TABLE 1. DISTANCE OF SPATIAL DEPENDENCE (RANGE OF THE VARIOGRAM) FOR A NUMBER OF SOIL PHYSICAL VARIABLES IN THE ARDÈCHE TEST SITE (VAN BEURDEN AND RIEZEBOS, 1988; RIEZEBOS, 1989).

Organic matter content	55.9 m
Clay content	77.8 m
Bulk density	105.0 m
Drainage	40.0 m
Stoniness	60.0 m

- 2) The structures of the spatial distribution of the input variables is commonly characterized by fitting an approved mathematical function (a variogram model) which is then used for interpolation (Isaaks and Srivastava, 1989). Following this technique, the experimentally-derived variograms were modelled and applied in ordinary point kriging. The spatial interpolations resulted in continuous raster maps of predicted values and corresponding kriging errors of the soil physical variables.

4. SOIL SPECTRAL ANALYSIS

Knowledge of the spectral behaviour of the local soils is a prerequisite for proper image interpretation. Therefore, soil samples of the five most important soil types with and without surface crusts were taken in the field and brought to the laboratory. Their spectral reflectance between 400 and 2500 nm was measured using the SIRIS-spectrometer and analyzed (De Jong, 1994a; De Jong, 1992). For reference purposes spectral measurements were also performed on a two pure (weathered) limestone, on a limestone with an iron crust and on a sample of marls. The SIRIS-spectrometer measures reflectance in 864 bands in the region from 477 to 2443 nm, it has a band-width of approximately 3 nm and its single field of view covers an area of 8 by 2 cm. The distance between target and spectrometer was 30 cm and targets were illuminated by quartz-halogen lamps.

Physical properties of the soils such as texture, lime content, iron content and organic matter content of the soils (Van Reeuwijk, 1992) were determined to relate the absorption features in the soil spectra to physical properties. Furthermore, mineralogical analysis by X-ray diffraction was carried out on the soil samples used for the spectroscopical measurements. The clay mineral composition of the five soils is very similar, they consist of mixed-layers of illite/smectite and some kaolinite and illite. A library of local soil spectra was created and used for spectroscopical image interpretation and classification as described in the paragraph.

5. IMAGE ANALYSIS

The airborne spectroscopical images were analyzed on their usefulness for erosion modelling. Spectroscopical images contribute to soil erosion modelling studies in two ways: 1) they can be used to assess the vegetative cover in the study area, 2) they can provide information on certain soil properties, which is useful to classify the soils, which is useful to assess the spatial distribution of erosion controlling soil physical variables. A library of local soil spectra was created by matching the spectral coverage of the GER and AVIRIS image with the SIRIS laboratory measurements. The images were classified into soil maps by using a algorithm developed by Jansen (1993) referred to as the 'Similarity Index'. The Similarity Index computes a normalized Euclidian distance between two spectra in a user-defined spectral window on a pixel-by-pixel basis.

The SI-value is a measure for the goodness of fit between the pixel's spectrum and the reference spectrum. Consequently, the SI-value presents a kind of probability that a certain soil type is present in that pixel: large SI-values indicate a poor match and the likelihood that this soil type is present in the pixel is small, small SI-values indicate a good match and it is more likely that this soil type is present in the pixel. Using the SI-values, a soil map of the flight path was produced (De Jong, 1994a). The 14 images with SI-values were exported from the image processing software into a GIS. The decision to assign a certain pixel to a specific soil type, was based on the smallest SI value in each of the 14 images. Pixels having a SI-values exceeding 150 for all soil types were rejected from the classification and a missing value was assigned to that pixel. All pixels with a vegetative cover exceeding approximately 35% had a SI value larger than 150 and were consequently rejected from the classification. A field survey and infrared aerial photographs were used to check the produced soil map.

The use of convex-hull transformation and derivative transformation (Green and Graig, 1985; Sedgewick, 1983) could not successfully be used to discriminate between the different soil types because they use only a very limited part of the spectra.

6. EROSION MODELLING RESULTS

The erosion model SEMMED (De Jong, 1994a) was used to produce erosion hazard maps of the study area. SEMMED comprises several modules each of which describes a part of the erosion process such as soil particle detachment, moisture storage in the top soil and transport of soil particles by overland flow. The empirical Morgan, Morgan and Finney Method to predict annual soil losses (Morgan 1986; Morgan et al., 1984; Morgan and Finney, 1982) yielded the physical basis for SEMMED. Despite the desirability of physically-based models, the present state of model development is such that a simple empirical model such as SEMMED is often more successful in predicting soil erosion than a complex physically-based one which is difficult to operate and has been only partially evaluated.

Input for the model were gathered from remotely sensed data, from a digital terrain model stored in a GIS and from a limited amount of field data. The soil map produced by spectral matching was reclassified into the by the model required soil physical variables. This is only possible if sufficient knowledge of the occurring soil types in the study area is available. The digital terrain model was used to compute slope steepness and to produce a distributed map of the transport capacity. The hydrological process that is modelled is the following (Chow et al., 1988): when the (top-)soil moisture capacity is exceeded, the excess rainfall (defined as the rainfall which is neither retained on the land surface nor infiltrated into the soil) becomes overland flow until it is drained in one of the catchment channels. Consequently, the transport capacity increases in a downslope direction if overland flow is generated.

Vegetation cover was assessed by using an empirical relation between spectral indices and vegetation cover (De Jong, 1994b).

As SEMMED is composed of individual modules, the model output consists of a number of intermediate products such as a overlandflow map, the transport capacity map and the soil particle detachment map. The advantage of these intermediate products is that they can be judged on their accuracy before the final erosion map is considered. The modules are also useful to work out scenarios to assess the effect of changing one variable on the predicted soil loss.

The predicted rate of splash detachment ranges from 0 to 10.16 kg/m². Areas with low interception values show the largest values e.g. the marl areas surrounding the village of Lussas and at the edges of the limestone plateaux. The estimated transport capacity ranges from zero to some peak values of 274.4 kg/m². More than 70% of the values are below 50 kg/m². The largest values are located at the foot of extended slopes e.g. at the edges of the Coiron plateau and the limestone plateaux (Plateau de Gras).

SEMMED demonstrated that it is possible to produce regional maps of erosion hazard, which are much better than simple extrapolations of plot experiments. Although the pattern of predicted erosion seems reliable, the model results should be interpreted with caution because a number of assumptions and simplifications had to be made to run the model. The use of input from remote sensing facilitates the gathering of information compared to a geostatistical approach, which requires large amount of field work. However, the spectroscopical images provide only information on soil properties from bare or nearly bare soils.

7. CONCLUSIONS

A field survey following a geostatistical approach (nested analysis of variance and kriging) yielded maps of soil properties such as iron and lime content. These maps were compared with the information content of the spectroscopical images. A laboratory study using a SIRIS spectrometer yielded a library of local soil spectra, which was used to interpret and classify the spectroscopical images into soil types.

The advantage of the geostatistical approach is that it yields continuous raster maps of each soil physical variables with a known (estimated) error (i.e. kriging error). The main drawback of the geostatistical approach is that the required amount of field work is considerable due to the small to very small distances of spatial dependence of the soil variables. Consequently, the grid used for field sampling must be very dense.

The advantage of the approach using the spectroscopical images is that it is quick and does not demand much computer power. However, this method does not yield directly information on the soil physical input variables required by the model. Soil properties that can be monitored in the study area are lime content, iron content and some clay minerals. As a result, a translation must be made from soil properties that can be detected using imaging spectroscopy into soil types into soil physical variables required by the model. Furthermore, the spectroscopical images yield only information for bare or nearly bare areas.

ACKNOWLEDGMENT

The author would like to thank the DEMON-project supported by the Environment Programme of the European Community DGXII (contract EV5V-CT92-0035) for providing data and financial support for this study.

REFERENCES

- Bodechtel, J., and S. Sommer, 1992: The European Imaging Spectroscopy Airborne Campaign (EISAC). In: *Imaging Spectroscopy: Fundamentals and Prospective Applications*, F. Toselli & J. Bodechtel (Eds.), Kluwer Academic, Dordrecht, 73-102.
- Chow, V.T., D.R. Maidment & L.W. Mays 1988: *Applied Hydrology*. McGraw-Hill, New York.
- De Jong, S.M., 1992: The Analysis of Spectroscopical Data to Map Soil Types and Soil Crusts of Mediterranean Eroded Soils. *Soil Technology*, **5**, pp. 199-211.
- De Jong, S.M., 1994a: Applications of reflective Remote Sensing for Land Degradation Studies in a Mediterranean Environment. *Netherlands Geographical Studies*, **177**, KNAG Utrecht.
- De Jong, S.M., 1994b: Vegetation Parameters Derived from Satellite Images for Erosion Modelling. *Earth Surface Processes and Landforms*, **19**, No. 2.
- De Roo, A.P.J., 1993: Modelling Surface Runoff and Soil Erosion in Catchments using Geographical Information Systems. Validity and Applicability of the 'ANSWERS' Model in Two Catchments in the Loess Area of South Limburg (The Netherlands) and One in Devon (UK). *Netherlands Geographical Studies*, **157**, KNAG Utrecht.
- Green A.A. & Graig M.D., 1985: Analysis of Aircraft Spectrometer Data with Logarithmic Residuals. *Proc. Airborne Imaging Spectroscopy Workshop*, 8-10 April, JPL-Publication 85-41, Jet Propulsion Laboratory, Pasadena, CA, pp. 111-119.
- Grenon, M., and M. Batisse, 1989: *Futures for the Mediterranean Basin: The Blue Plan*. Oxford University Press.
- Hill, J., 1991: Analysis of GER Imaging Spectrometer Data Acquired During the European Imaging Spectrometry Aircraft Campaign (EISAC'89). Quality assessments and first results. *EARSeL Advances in Remote Sensing*, **1**, 64-77.
- Isaaks E.H. & R.M. Srivastava, 1989: *An Introduction to Applied Geostatistics*. Oxford University Press, New York. 561 pp.
- Jansen W.T., 1993: *General Imaging Spectrometry Interpretation Systems: GenIsis*. WTJ-Software, San Mateo CA.
- Journel A.J. & C.J. Huijbregts, 1978: *Mining Geostatistics*. Academic Press.
- Kirkby, M.J., 1976: Hydrological Slope Models: The Influence of Climate. In: E. Derbyshire (Ed.), *Geomorphology and Climate*. Wiley, London. pp. 247-267.
- McBratney A.B. & R. Webster, 1983: Optimal Interpolation and Isarithmic Mapping of Soil Properties: V. Co-regionalisation and Multiple Sampling Strategy. *Journal of Soil Science*, **34**, pp. 137-162.
- Morgan, R.P.C., 1986: *Soil Erosion and Conservation*. Longman Group, Essex, 298 pp.
- Morgan, R.P.C., D.D.V. Morgan & H.J. Finney 1984: A Predictive Model for the Assessment of Soil Erosion Risk. *J. Agric. Engng. Res.* **30**, pp. 245-253.
- Morgan R.P.C. & H.J. Finney, 1982: *Stability of Agricultural Ecosystems: Validation of a Simple Model for Soil Erosion Assessment*. Int. Inst. Applied Systems Analysis. Collab. Paper No. CP 82-76.
- Oliver, M.A. & Webster, R., 1986: Combining Nested and Linear Sampling for Determining the Scale and Form of Spatial Variation of Regionalized variables. *Geographical Analysis*, **18**, pp. 227-242.

- Riezebos H.Th., 1989, Application of Nested Analysis of Variance in Mapping Procedures for land Evaluation. *Soil Use and Management*, 5, pp.25-30.
- Sedgewick R., 1983: *Algorithms*. Addison-Wesley, Reading Massachusetts.
- Van Beurden S.A.H.A. & H.Th. Riezebos, 1988, The Application of Geostatistics in Erosion Hazard Mapping. *Soil Technology*, 1, pp.349-364.
- Van Reeuwijk L.P. Ed., 1992: Procedures for Soil Analysis. *Technical Paper*, 9, International Soil Reference and Information Centre (ISRIC), Wageningen. 90 pp.
- Wischmeier, W.H. and D.D. Smith, 1978: Predicting Rainfall Erosion Losses, a Guide to Conservation Planning. *Agriculture Handbook*, 282, United States Department of Agriculture, Washington.

USING MULTITEMPORAL, MULTISPECTRAL REMOTE SENSING DATA TO MONITOR LAND DEGRADATION

Terrill W. Ray
Division of Geological and Planetary Sciences,
California Institute of Technology
Pasadena, CA 91125, USA

Thomas G. Farr, Eric M. De Jong, Ronald G. Blom, and Robert E. Crippen
Jet Propulsion Laboratory
Pasadena, CA 91109, USA

ABSTRACT

In this study, data from the Jet Propulsion Laboratory Airborne Visible/Near-Infrared Imaging Spectrometer (AVIRIS), the Landsat MultiSpectral Scanner (MSS), and the ex-Soviet RESOURCE satellite have been combined into a co-registered temporal dataset covering the period from 1972 to 1991. The data cover the Manix Basin Area of the Mojave Desert, which is located NE of Barstow, California. This area has been cultivated with center-pivot irrigation systems since the mid-1960's. Since 1973, several fields have been abandoned at various times producing a sequence of abandoned fields at different stages of evolution. Analysis of this time series indicates that the vegetation cover on recently abandoned fields typically exceeds that in the surrounding desert for a few years. There is then a rapid decline in vegetation cover leading to the abandoned fields becoming more barren than the adjoining desert. Three significant sand mobilization events can be observed in the temporal dataset and quantitative measurements of the area covered by active sand can be made for each.

The time series of remote sensing data has served to corroborate the reports of abandonment dates of the fields that have been gathered from local interviews and water well records. Other on-site investigations have confirmed the relationships between the undisturbed desert and fields abandoned for varying lengths of time deduced from the remote sensing data. Regions that have been identified in the remote sensing data as areas undergoing sand mobilization show evidence of wind erosion when observed on the ground.

1. INTRODUCTION

The World Resources Institute (1992) reports that "over the past 45 years, about 11 percent of the Earth's vegetated soils became degraded to the point that their original biotic functions are damaged, and reclamation may be costly or in some cases impossible." The United Nations Conference on Desertification (UNCOD) estimated that due to the degradation of drylands there was a global loss of \$42.3 billion of agricultural productivity that represented a substantial increase from the \$26 billion UNCOD estimate for 1977 (United Nations Environment Programme, 1992). The United States is not immune from this problem. Dregne (1983) reported that nearly 1.3 million square kilometers of North American drylands have been "severely" or "very severely" degraded. This problem is likely to get worse, not better: "The introduction of sprinkler irrigation systems, especially the center pivot systems, has enabled previously unsuitable rolling sandy lands to be cropped successfully. If and when those soils are abandoned, for reasons of economy or shortage of

water, the United States will face an even greater wind erosion threat than it has had to cope with in the past" (Dregne 1983).

Desertification is not, as sometimes envisioned, an invasion of non-desert areas from a desert core. Sheridan (1981) compares desertification to guerilla warfare with no real "front line." Dregne (1983) describes desertification as a patch of land degraded through human abuse that then spreads outward if the abuse continues. A United Nations report (United Nations, 1978) describes the spread of desertification as follows: "These degraded patches, like a skin disease, link up to carry the process over extended areas."

The extent of this "subtle and insidious process" (United Nations, 1978) of land degradation can be difficult to assess from observations on the ground. Ground observations can readily see that there is a patch of degradation at a certain locality, but this is an inefficient way to survey an area to determine the status of land degradation. UNEP (1992) reports that there are virtually no reliable global data on the present status or rate of desertification, and UNEP also stressed the need for methodologies for making global assessments of land degradation on an ongoing basis. Remote sensing techniques provide the most obvious way of addressing this problem, since remote sensing provides a way of rapidly observing substantial areas of the Earth's surface. Remote sensing can observe the distribution, number and size of degraded patches on the synoptic scale. This paper describes the application of remote sensing techniques to the problem of land degradation in an area of the southwestern United States.

2. STUDY AREA

The Manix Basin area of California's Mojave Desert was chosen as a test site for developing remote sensing techniques to detect and estimate land degradation due to land use changes in an arid region. This area was the site of a series of lakes during the late Pleistocene and early Holocene (Jefferson, 1982). Much of the area is now covered by soils which are classified as very to extremely wind erodible by the Soil Conservation Service (Tugel and Woodruff, 1986).

This area has been extensively used for growing irrigated crops since the mid-1960's. The principal crop grown in this area has been alfalfa with some small production of other field crops and pistachios. Most of this agriculture has been performed using sprinkler irrigation systems, with center-pivot systems being used on most fields since 1978. Little water exists on the surface in this area, so these irrigation systems are groundwater fed.

The part of the Manix Basin being focused on in the study is that part bounded by the Calico mountains on the west, the Alvord Mountains and Coyote Dry Lake to the north, a major alluvial fan originating in the Alvord Mountains on the east, and the course of the Mojave River on the south. This area is centered at 35°00"N latitude 116°36"W longitude. The native vegetation in this area is primarily creosote bush and white bursage along with small desert grass. The soil is generally well drained and sandy with poorly developed horizons present in some areas (Ray *et al.* 1992; Tugel and Woodruff, 1986). A series of 16 center-pivot fields located in this area have been abandoned during the past 22 years as shown in table 1.

According to the residents of the area, these fields were abandoned for economic reasons. Many of the farmers have found that the cost of electricity needed to pump the groundwater for irrigation made growing the alfalfa unprofitable. The general trend was for the fields located at the greatest distance north from the Mojave River to be abandoned first and those nearest the river abandoned last. This sequence of abandoned fields provides an opportunity to see different stages of the evolution of abandoned fields each time the area is observed by remote sensing platforms or on-site expeditions.

Table 1.

Year	Number of Center-Pivot Fields Abandoned
before 1974	1
1974-1978	2
1981	2
1982	2
1984	5
1986	1
1989	1
1992	2

3. DATA

A series of 14 Landsat MSS (MultiSpectral Scanner) images covering the summers of 1973-74, 1975, and 1978-88 have been acquired. No Landsat MSS or TM (Thematic Mapper) data are available for the time from 1988 through 1992, so other data must be found to fill this gap. In the summer of 1990, the JPL AVIRIS (Airborne Visible/Infra-Red Imaging Spectrometer) instrument was flown over the study area and data collected by the Russian RESOURCE instrument in 1991 were made available by the Institute for Space Devices Engineering in Russia. These two datasets were used to fill the gap in Landsat coverage. These data were co-registered as described by Ray *et al.*, (1993a).

Field reflectance data of soils and plants have been collected in four separate expeditions. Data were collected using an Analytic Spectral Devices Personal Spectrometer II™ (ASD PS2), which covers 0.355-1.064 μm in 512 spectral bands, on July 23 and 24, 1993; October 9 and 10, 1993; (Ray *et al.*, 1993b); and February 9 and 10, 1994. The JPL GER spectrometer, which covers 0.4-2.5 μm in 826 bands, was used to collect data on February 24, 1994. Along with the collection of field spectra, measurements of plant cover were performed, and soil samples were collected for measurements of soil pH, salinity, particle size, and laboratory spectra. On March 29, 1994, 108 low-level aerial photos of the study area were acquired using standard 35mm color film.

4. CALIBRATION

The characteristics of the atmosphere and the calibration of the Landsat MSS instruments were variable among the images used in this study. Also the Russian RESOURCE instrument is not an exact copy of any of the MSS instruments. In order to eliminate these differences, the images must be co-calibrated. This was done by picking certain alluvial fans as spectrally invariant targets. Low-level aerial observation of these alluvial fans showed them to be nearly devoid of vegetation, they are of low relief and, unlike playas, they do not suffer large-scale periodic resurfacing with evaporites. A modification of the Crippen (1987) regression-intersection method was used to determine the relative gains and offsets to apply to each MSS image and the RESOURCE image to eliminate variations in atmosphere and instrument characteristics between each of the images and the 1988 MSS image. This process was not performed on the AVIRIS synthetic MSS data.

The AVIRIS data were calibrated to apparent reflectance using the empirical line technique of Conel *et al.*, (1987) with field spectra collected the day after the AVIRIS flight. A modified empirical line technique (Roberts, 1991; Gamon *et al.*, 1993) was used to calibrate the 1988 MSS data. The

standard empirical line technique uses spectra collected from specific targets that can be identified in the image and a least squares fit is performed to find the set of gains and offsets to convert from radiance to apparent reflectance. The modified empirical line technique requires that the user select areas of known surface type such as green vegetation, bare soil, and basalt. The spectra of these targets collected from the image are then compared with a library of spectra of that type of target. The gains and offsets are computed from the sets of spectra that best meet the criteria specified by the users.

Since all the MSS data and the RESOURCE data were co-calibrated to the 1988 MSS image, these values can be used to determine the apparent reflectances for all the images. These results were compared to the AVIRIS data calibrated with the standard empirical line calibration using an alluvial fan as an unchanging target, and the results of this comparison showed there to be a relative error between the MSS calibration and the AVIRIS calibration of 15–20% of the expected (AVIRIS) apparent reflectance and an absolute error of 5–7% apparent reflectance..

5. VISUALIZATION

One way of observing temporal changes using this data set is to display it as a movie. This can be done using any of a number of software packages that provide the ability to display a sequence of images on the computer monitor. It is also possible to transfer the image to video tape, although this leads to an appreciable loss of image resolution and color fidelity. Both of these techniques provide a compact and intuitively clear way of observing qualitative temporal changes in either the original image data or a derived data set such as vegetation index images. A multitemporal data set of this kind can be easily manipulated using software designed for looking at multiband image data. Since most of the inter-image biases have been removed through the co-calibration described above, it is possible to do quantitative comparisons of this series of images.

6. VEGETATION CHANGES

Crippen (1990) noted the subtraction of the red band radiance or reflectance that is done in the calculation of NDVI (Normalized Difference Vegetation Index) was irrelevant, and introduced the IPVI (Infrared Percentage Vegetation Index), which is linearly related to NDVI.

$$NDVI = \frac{NIR - R}{NIR + R};$$

$$IPVI = \frac{NIR}{NIR + R};$$

$$IPVI = \frac{1}{2}(NDVI + 1)$$

where NIR = Near-infrared (MSS Band 7) and R = Red (MSS Band 5).

Figure 1 shows the IPVI for two abandoned center-pivot fields. The IPVI values have been normalized so that the background desert, defined as the average IPVI value of several large areas located away from the fields, is equal to 1.0. Figure 1 shows a strong drop in IPVI levels when a field is abandoned. It is also seen that the fields remain at slightly higher IPVI values than the background desert for the first 5 years of abandonment. After that time, the IPVI values are seen to dip below those of the surrounding desert. It is important to note that field 6b, which is downwind of field 6a,

has lower IPVI values from 1985 through 1991 than field 6a. We might expect this if field 6a was acting as a source of blowing sand.

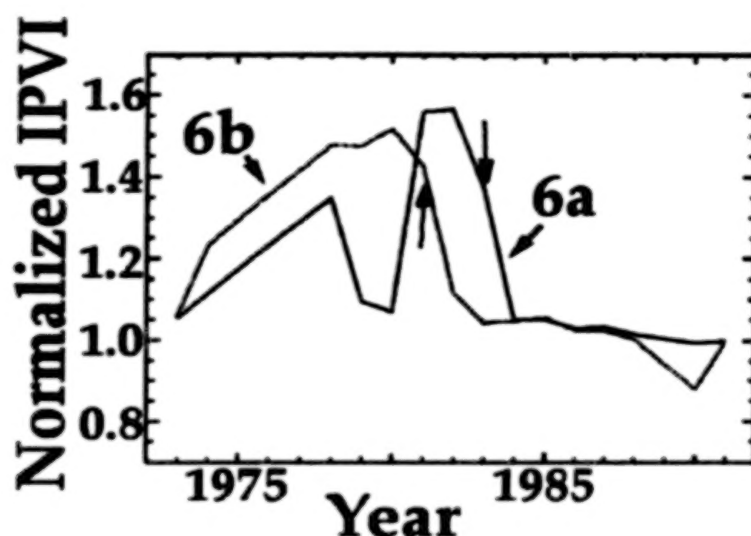


Figure 1: Normalized IPVI values for two fields in the Manix Basin. Field 6a, abandoned in 1983 (arrow), is upwind of field 6b, abandoned in 1981. The values are normalized so that the background desert has a value of 1.

Ray *et al.*, (1993b) and Ray and Murray (1994) have shown that arid region vegetation cannot be easily quantified by currently existing remote sensing vegetation indices. However, they do indicate that qualitative differences in plant cover can be assessed using such indices. Ray and Murray (1994) note that the two dominant shrub species in this area, creosote bush and white bursage, have inherently different IPVI values. The plots of the two shrub spectra in figure 2 show that this will occur because the red edge (the region from 0.7–0.8 μ m) is a smaller step in the bursage spectrum than it is in the creosote bush spectrum. Creosote bush tends to dominate the climax community in this area, while bursage is more dominant in areas that have been disturbed. The consequence of this is that lower values of vegetation indices in this area indicate either less plant cover or a change from climax vegetation to non-climax vegetation.

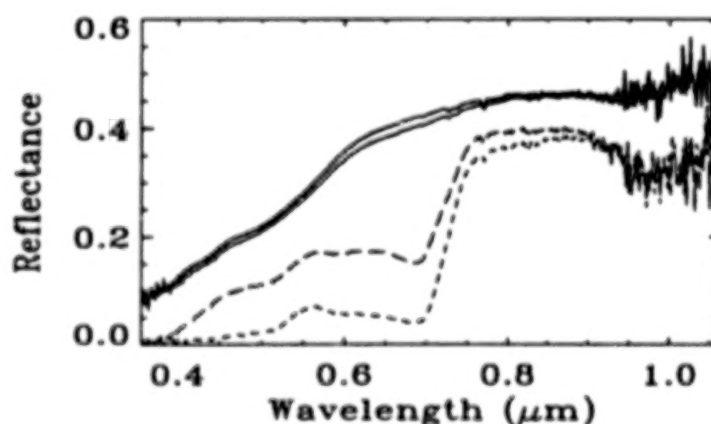


Figure 2: Plot of two soil spectra and the spectra of two common Mojave desert shrubs: bursage (long dashes) and creosote bush (short dashes). (From Ray and Murray, 1994)

Figure 2 shows that desert vegetation is generally darker than the desert soil in this area across the entire spectral range of 0.5–1.1 μ m covered by Landsat MSS (Ray and Murray 1994). Consequently, areas in this dataset that appear brighter tend to have lower vegetation cover. Abandoned fields tend to remain darker than their desert surroundings for the first few years after abandonment. This may occur because of residual fertilizer coupled with the fact that the deep roots of the alfalfa plants may still be providing some resistance to wind erosion. After the residual fertilizer is consumed and the alfalfa root systems decay, much of the invading desert grasses die off and wind erosion begins. On-site observations and low-level aerial observations confirm that recently abandoned fields tend to support higher levels of vegetation cover than the surrounding desert, and that old abandoned fields tend towards less vegetation cover than the surrounding desert.

7. BLOWING SAND

Another type of feature that is apparent in these data is high albedo areas of windblown sand (Ray and Murray, 1994). Many of these areas appear to extend from abandoned (and sometimes active) fields. These areas appear during some years and are not apparent in others. Many times a formerly high albedo area that returned to the same appearance as the undisturbed desert for a few years will become bright again. When these areas become bright again, they often cover a larger area than they were seen to cover during their previous period of high albedo. Table 2 shows how the size of various areas near abandoned fields identified as blowing sand because of their high albedo has changed over time. The identification of several of these areas as blowing sand has been confirmed by on-site investigations which have revealed Sand drifting onto roads, heavily wind-rippled surfaces and small dunes.

Table 2. Area (in hectares) of Blowing Sand Associated with Abandoned Fields Measured from Remote Sensing Data

Year	Field #2	Fields #6ab	Field #7	Field #8	Field #11	Field #AA
1979	0.0	0.0	0.0	2.6	0.0	16.6
1980	0.0	0.0	0.0	0.0	0.0	16.9
1981	0.0	8.8	17.5	13.0	6.5	18.2
1982	0.0	0.0	0.0	9.4	13.3	23.1
1983	0.0	12.3	0.0	0.0	0.0	0.0
1984	0.0	0.0	0.0	28.3	0.0	15.9
1988	18.5	61.1	0.0	0.0	48.7	0.0
1990	0.0	122.2	0.0	90.6	-----	41.6
1991	0.0	137.1	0.0	98.1	79.9	44.8

Although an abandoned field may be the initial source of blowing sand, the very nature of blowing sand can lead to a strong positive feedback. Wind erosion leads to a loss of the fine particles in the soil that provide much of the soil's ability to support plant life. Additionally, wind-driven sand can be highly destructive to plant life because of its ability to abrade and shred the leaves of plants (Dregne 1983). Plants may also be buried by mobilized sand.

The ability of windblown sand to adversely affect plant life leads to a further problem. It is well recognized that vegetative cover is an important factor in controlling wind erosion (Bagnold, 1942; Woodruff and Siddoway, 1965). Less vegetation cover leads to a greater potential for wind

erosion, and wind erosion in one area can lead to less vegetation cover in the area immediately downwind. This process may then cause the downwind area to become a new source of wind-driven sand. The positive feedback suggests that successful remote monitoring of arid regions requires techniques to identify and measure both of these properties of arid lands. Figure 1 shows how this synergism works in the case of fields #6a and #6b. The downwind field of the pair has lower vegetation values than its upwind counterpart, and, as shown in table 2, this pair of fields produces a much larger area of blowing sand than the single fields.

Blowing sand can spread the damage in yet another related way. The sand can damage the irrigation system that is being used for the downwind field. This is not just a hypothetical problem as illustrated by the following statement from a local resident reported by Gorman (1993): "I used to grow alfalfa on 40 acres, but my fields have been sandblasted. All my equipment is destroyed. The sand has ruined the magnetic switches in my irrigation equipment." The abandonment of the downwind field will provide an additional source of blowing sand that may spread the land degradation even further.

Figure 3 shows the changes in several areas of blowing sand over the period from 1984 through early 1991. Figure 3A shows a few small areas of blowing sand that disappear by the time of the 1985 image (figure 3B). The areas of blowing sand seen in 1984 seem to be inactive in 1985, 1986, and 1987. Between the MSS image taken in 1987 and the MSS image taken during the summer of 1988 (figure 3C), significant areas of blowing sand appear. These areas persist and spread over the period from 1988 through 1990 and shrink very slightly by the early part of 1991 as shown in figure 3D. Figure 3 shows why it is important to observe areas multiple times. From comparing figures 3A and 3B, we would conclude that the area has recovered, but the addition of figures 3C and 3D suggest that the area is being further degraded.

The NOAA National Solar Radiation Data Base (NSRDB) hourly meteorological data for Daggett, California indicates that over the period 1980–1984 there was an increase in average hourly windspeed in the southern part of the study area and that another even greater increase in average hourly windspeed over the period 1988–1990, with the average hourly windspeed in 1990 exceeding the 5.56 km/hr windspeed considered to be the threshold for mobilizing sand (Tugel and Woodruff, 1986). An analysis by Tugel and Woodruff (1986) indicated that 82.7% of the time winds exceeded the sand mobilization threshold they were blowing from between WNW and WSW, which is consistent with the direction that the areas of blown sand extend from the source fields. The lack of precipitation data for Daggett in the NSRDB precludes an analysis of the relationship of rainfall to the periods of blowing sand until another source of rainfall data can be found.

8. CONCLUSIONS

Land degradation is a serious problem for both the world as a whole and the United States itself. The spotty way in which desertification proceeds makes it difficult to quantify from on ground observations, even though on-site investigations can effectively document the fact of desertification in a given area. In order to monitor this problem on a regional or global scale, techniques are required which can rapidly survey substantial areas. Remote sensing techniques are the logical candidates for doing this. Additionally, as shown in this study, desertification occurs in a patchy manner in time as well as in space. Satellite-borne remote sensing allows for repeat coverage which can be used to observe the temporal progress of land degradation. As shown in this study, temporal coverage gaps may be filled using data from other orbital or airborne platforms given either similar bandpasses or higher spectral resolution. Airborne data that, at present, can be more accurately calibrated than satellite data can be wedded to satellite data and used to aid in calibration.



A)



B)

Figure 3: A series of remote sensing images of the Manix Basin area of the Mojave Desert taken by multispectral satellite systems. A, B and C were taken by the Landsat Multispectral Scanner (MSS) instrument, and D was taken by the ex-Soviet RESOURCE instrument. All images cover the spectral range of $0.6\text{--}0.7\mu\text{m}$ (MSS Band 5, RESOURCE Band 2). North is to the top. The double dark lines crossing diagonally from lower left to upper right is Interstate-15, and Interstate 40 can be seen as a pair of dark lines near the bottom of the images. Daggett Airport can be seen as a small 'V', which opens towards the upper right, located just above Interstate-40 in the lower left part of each image. The bright area in the upper left of each image is a playa called Coyote Dry Lake. The dark circles and squares are irrigated fields, and between the playa and the interstate are other circular patches (some slightly darker than the surrounding area and some brighter) which are abandoned fields. A) MSS band 5 obtained on June 23, 1984. A bright region of sand blowing off a field is indicated by arrow at upper right. A very bright abandoned field is indicated by an arrow at center. (JPL P43868A) B) MSS band 5 obtained on July 28, 1985. The bright areas pointed out in figure A have disappeared, suggesting that some vegetation has grown on them. (JPL P43868B)



C)



D)

C) MSS band 5 obtained on June 20, 1988. Two new bright patches of blowing sand are marked by arrows at upper center and center. The field that was bright in 1984 is bright again, which means that it has lost its vegetation. (JPL P 43689B) D) RESOURCE band 2 obtained January 23, 1991. The three bright patches of blowing sand have grown substantially. At this point they cover as much area as the fields that produced them. Notice that the patch of blowing sand indicated in A has reappeared (arrow at upper right).

Using the data set covering the Manix Basin we see that IPVI values for abandoned fields remain higher for the first few years following abandonment and then that the IPVI values drop rapidly to levels at or just below those of the surrounding desert. The sparse cover of vegetation common in arid regions coupled with the spectral characteristics of arid region vegetation presents problems for standard vegetation indices, but some of the spectral characteristics may, paradoxically, make the identification of degraded areas easier. This series of remote sensing data makes it possible to track the area affected by blowing sand. The results show that each time sand mobilization occurs from the abandoned fields it covers a large area, even though there appears to be some recovery from the condition of blowing sand between mobilization episodes. Measurements of IPVI for fields downwind of other abandoned fields indicate a greater suppression of vegetation on downwind fields, which is consistent with the expected effect on vegetation of an upwind source of blowing sand. There appears to be a relationship between the sand mobilization and changes in the wind regime of this area, but it has not yet been possible to determine the relationship between sand mobilization and local precipitation. These results clearly demonstrate that remote sensing techniques in alliance with on-site observations can be used to monitor and quantify land degradation.

ACKNOWLEDGMENTS

Parts of this work presented in this paper were performed using the Spectral Image Processing System (SIPS) created at the University of Colorado at Boulder's Center for the Study of Earth from Space. Parts of the work presented in this paper were performed at the Jet Propulsion Laboratory, California Institute of Technology, under contract with the National Aeronautics and Space Administration. Substantial funding for this work was provided by NASA Graduate Student Fellowship NGT-50891.

REFERENCES

- Bagnold, R.A., 1942: *The Physics of Blown Sand and Desert Dunes*, William Morrow & Co., New York, 265pp.
- Conel, J.E., Green, R.O., Vane, G., Bruegge, C.J., Alley, R.E., and Curtiss, B.J., 1987: Airborne Imaging Spectrometer-2: Radiometric Spectral Characteristics and Comparison of Ways to Compensate for the Atmosphere, *Imaging Spectroscopy II, Proc. SPIE*, **834**, 140-157.
- Crippen, R.E., 1987: The Regression Intersection Method of Adjusting Image Data for Band Ratioing, *Int. J. Remote Sens.*, **8**, 137-155.
- Crippen, R.E., 1990: Calculating the Vegetation Index Faster, *Remote Sens. Environ.*, **34**, 71-73.
- Dregne, H.E., 1983: *Desertification of Arid Lands*, Harwood Academic Publishers, Chur, London, Paris, New York, 242pp.
- Gamon, J.A., Field, C.B., Roberts, D.A., Ustin, S.L., and Valentini, R., 1993: Functional Patterns in an Annual Grassland During an AVIRIS Overflight, *Remote Sens. Environ.*, **44**, 239-253.
- Gorman, T., 1993: Sand Trapped: Residents Along Part of Mojave River Dig In for Battle Over Drifting Dunes, *Los Angeles Times*, May 24, 1993, pages A3&A22.

- Jefferson, G.T., 1982: Brief History of Pleistocene Lake Manix, *Quarterly San Bernardino Co. Museum Assoc.*, **29**, 7-14.
- Ray, T.W., Farr, T.G. and van Zyl, J.J., 1992: Detection of Land Degradation with Polarimetric SAR, *Geophys. Res. Lett.*, **19**, 1587-1590.
- Ray, T.W., Farr, T.G., Blom, R.G., and Crippen, R.E., 1993: Monitoring Land Use and Degradation Using Satellite and Airborne Data, *Summ. of the 4th Ann. JPL Airborne Geoscience Workshop: AVIRIS Workshop*, 145-148.
- Ray, T.W., Farr, T.G., Blom, R.G., Crippen, R.E., and DeJong, E.M., 1994: Using Airborne And Satellite Data for Multitemporal Studies of Land Degradation, *IGARSS '94*, (in press).
- Ray, T.W. and Murray, B.C., 1994: Remote Monitoring of Shifting Sands and Vegetation Cover, *Proceedings of IGARSS '94*, (in press).
- Ray, T.W., Murray, B.C., Chehbouni, A., and Njoku, E., 1993: The Red Edge in Arid Region Vegetation: 340-1060 nm Spectra, *Summ. of the 4th Ann. JPL Airborne Geoscience Workshop: AVIRIS Workshop*, 149-152.
- Roberts, D.A., 1991: *Separating Spectral Mixtures of Vegetation and Soils*, Ph. D. dissertation, Univ. of Washington, 180p.
- Sheridan, D., 1981: *Desertification of the United States*, United States Government Printing Office, Washington, D.C., 142pp.
- Tugel, A.J. and Woodruff, G.A., 1986: *Soil Survey of San Bernardino County, California Mojave River Area*, USDA-Soil Conservation Service, 211pp.
- United Nations, 1978: *United Nations Conference on Desertification: Roundup, Plan of Action and Resolutions*, United Nations, New York.
- United Nations Environment Programme, 1992: *Status of Desertification and Implementation of the United Nations Plan of Action to Combat Desertification*, United Nation Environment Programme, Nairobi, 88pp.
- Woodruff, N.P. and Siddoway, F.H., "A Wind Erosion Equation." *Proc. Soil Soc. Am.*, **29**, (1965).
- World Resources Institute, 1992: *World Resources 1992-1993*, Oxford University Press, Oxford. 385pp.

APPLICATIONS OF REMOTE SENSING FOR TECTONIC PURPOSES IN
EL-ROUGE DEPRESSION, NORTH-WEST OF THE SYRIAN ARAB REPUBLIC

MOUTAZ DALATI

Director of Int'l and Scientific Affairs
General Organization for Remote Sensing (GORS)
Damascus, Syrian Arab Republic

ABSTRACT

Since Spaceborne Remote Sensing data were first made available, investigations have demonstrated their high potential, but also their restrictions for tectonic applications. On the basis of the early results of Landsat-MSS and airborne validation campaigns, the advanced Landsat Thematic Mapper(TM) with improved spectral, spatial and radiometric characteristics, was realized in 1983. The aim of the present study is to investigate the improved capabilities of Landsat TM data and their applicability for tectonic purposes and to evaluate the capabilities and limitations of spaceborne data to prove that the El-Rouge depression is the extension of Al-Ghab depression and in line with the African-Lebanon rift system.

The area under study El-Rouge depression is situated in the marginal part of the Arabian platform in the zone of the rift system which stretches from the Red Sea across the Gulf of Aqaba, the Dead Sea and the Jordan valley. Within Syria it is represented by the Al-Ghab depression which stretches in a meridional direction. El-Rouge depression is located Northeast of Al-Ghab depression. It is limited from the West by Jabal El-Wastani horst-anticline and from the East by Jabal AzZawiye range and from the North by Jabal Barisha horst-anticline and from the South by the Al-Ghab depression. Landsat-TM, MSS and RBV scenes were studied in detail for a better discrimination of the different types of tectonical structures. The interpretation of photographic data shows that the El-Rouge depression is a graben and evidently possesses complicated internal tectonics. The graben is separated by a linear fault which is accompanied by a series of step-like faults parallel to the master fault. In the Southern part, the graben is separated by a system of faults trending North-West and Southeast. The final results of this study are represented as tectonical components and different levels of spatial resolution in El-Rouge graben.

1. INTRODUCTION

The urge to know is as old as the human race itself. Galileo put his new telescope to work to look at the Moon in 1610. In 1858 a French photographer made excellent aerial photos from balloons in the vicinity of Paris. In the 20th Century the balloon gave way to the airplane, and film technology came of age. Air-craft provided a better platform for mounting photographic cameras, and the field of aerial survey was born. Advanced in cameras, lenses, and films moved aerial survey from curiosity to a science. Color film in 1935 and infrared film in 1943 further enhanced the value of aerial photography. The first photo of the Earth taken from a satellite, was made in 1959 by a camera aboard the MARK II Re-entry Vehicle. By the early 60's the TIROS and Nimbus meteorological satellites were sending images of the Earth's cloud cover. A hand-held Hasselblad camera, used by the Gemini astronauts, showed the potential for global survey via satellite. These photos were the first ventures into the technology of Remote Sensing from Space. Remote Sensing from Space is a widely used and potentially powerful tool in the mapping of large-scale geological structures. Landsat MSS is familiar to many geologists but the poor resolution of the MSS has minimised its use.

NSC 100

000323

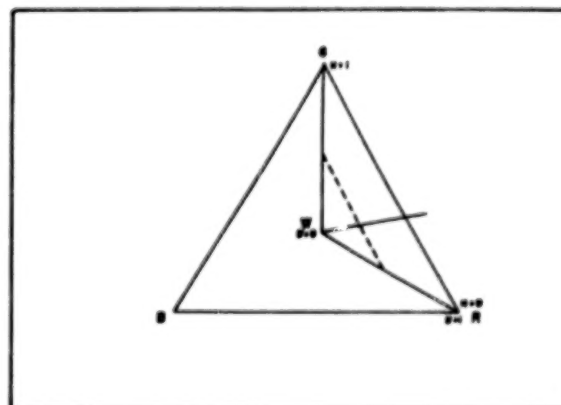
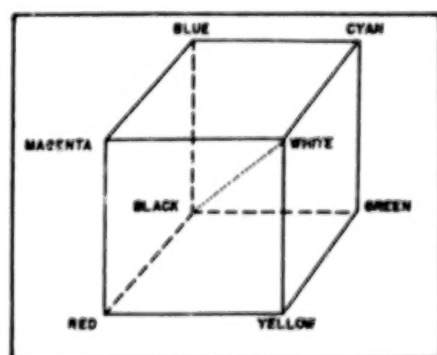
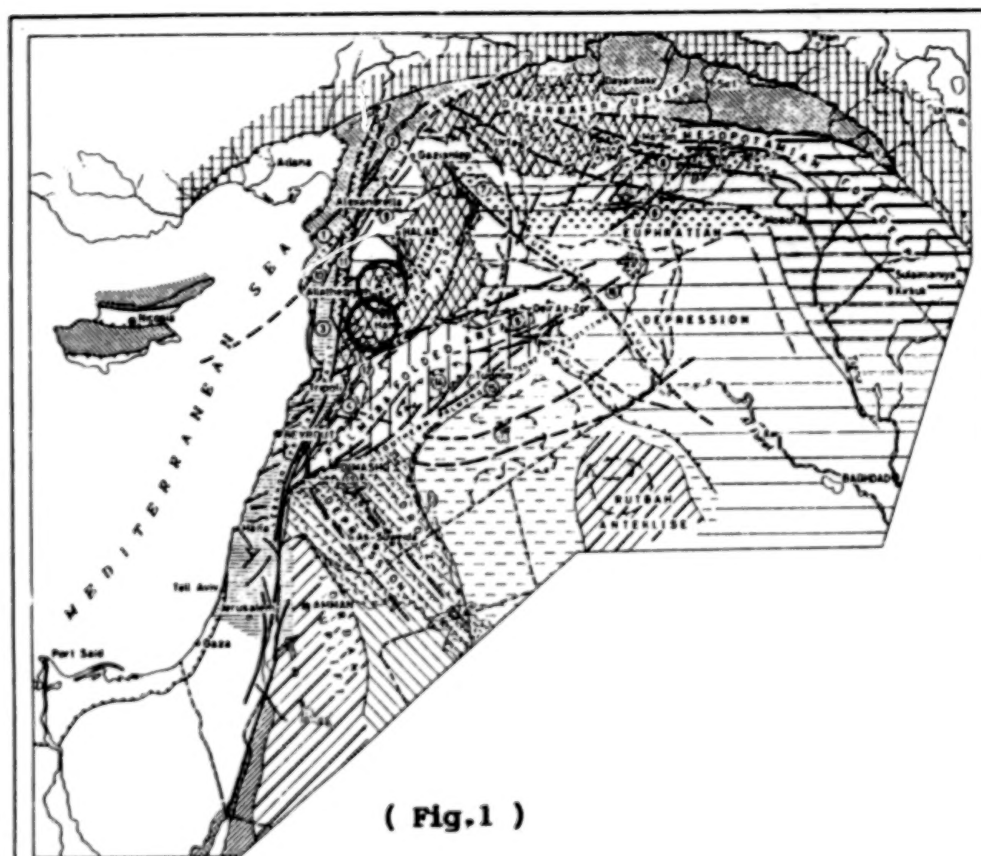
The amount of data has increased from MSS to TM Thematic Mapper because of an increase in the number of spectral bands(4-7), in radiometric resolution(64-256 digital levels) and in geometric resolution(80-30 m.). Using of Remote Sensing techniques shows the pronounced margin of the tectonical traces which can be traced clearly. The aim of this study was to evaluate the benefit of Landsat imagery in the mapping of tectonical phenomena in El-Rouge depression North-West of Syria. In particular, the work aimed to compare TM data with older Landsat MSS data from the same area , and to exemplify the utility of space photographs in establishing the origin and evaluation of arid landscapes.

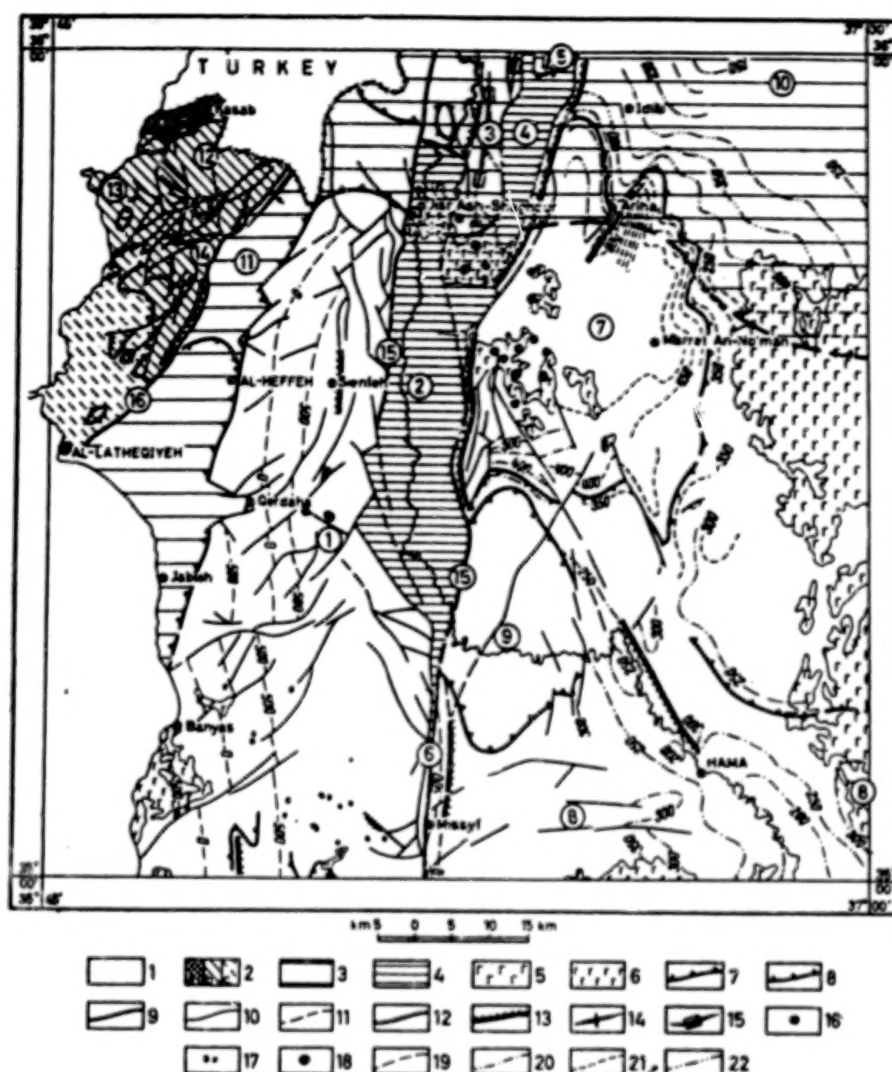
2. AREA OF INVESTIGATION

The area of investigation is located North-West of Syria (fig.1) and includes an area of about 5000 Km². Sedimentary and volcanic rocks occupy most of the area. The age of the basalts was determined to be Quaternary. The age of sedimentary rocks is Jurassic, Cretaceous, Paleogene, Neogene, and Quaternary (fig.2). The area under study El-Rouge depression is situated in the marginal part of the Arabian platform in the zone of the rift system which stretches from the Red Sea across the Gulf of Aqaba, the Dead Sea and the Jordan valley. It is limited from the West by Jabal El-Wastani horst-anticline and from the East by Jabal Az-Zaviyeh range and from the North by Jabal Barisha horst-anticline and from the South by the Al-Ghab depression. The geological study of North-Western Syria was started by M. Blanckenhorn. According to this investigator, the stratigraphic schemes became obsolete in many respects but his paleontological tables retain their significance up to now. E. Vaumas studied early volcanism in the region of Al-Ghab, El-Rouge, and Jabal Az-Zaviyeh. He marked all the volcanic bodies known in this region. E. Vaumas performed a geomorphological subdivision of the North-West of Syria. He has forwarded interesting ideas about neotectonic movements and the idea about the young age of the Al-Ghab depression, in particular. The age of the lacustrine sediments filling the Al-Ghab depression, according to E. Vaumas, is in Upper Pliocene and Quaternary. The growth and development of the uplift in connection with the movements along the Lebanon-Syrian fault were of irregular character and this is illustrated by the arrangement of the facies and thicknesses of the Upper Cretaceous and Tertiary sediments on both limbs of the structure. It is known that the movements along the eastern fault of the Dead Sea graben were reflected in the distribution and mode of occurrence even of the Lower Cambrian deposits.

3. RESULTS OF THE INVESTIGATIONS , USING SPACE IMAGERY

The investigations were carried out on the basis of multispectral data of the Landsat MSS, TM, in addition to the data of Landsat RBV mosaic (Landsat-3, Return Beam Vidicon,) which cover the investigated area. The interpretation of space data shows that El-Rouge represents a flat depression with a closed drainage covered on the surface with Quaternary sediments. In the north the depression is divided into two branches with the Jabal Barisha horst-anticline situated between them, the latter is similar to the Jabal El-Wastani structure and composed of limestones. The Jabal Barisha horst-anticline enters the region of the explorations only by its southern periclinal closure. The Jabal El-Wastani horst-anticline is a fold with an echelon-like squeeze of the bend to the South-East of the village of Darkoush. The fold has a gently sloping, almost horizontal arch and steeply dipping limbs. The dip of the beds on the limbs reaches in the southern up to 45°. The anticline is dissected by a system of longitudinal (submeridional) and diagonal faults, along which individual blocks composed of limestones were uplifted at various heights. The conjugation with the neighbouring troughs is performed through a steep bend of beds and accompanied by faults. This indicates a horst nature of the structure. Its apex as a whole gently dips to the North. In the South it terminates with a steep periclinal closure at the branching of the Al-Ghab depression.





1 - region of relatively stable uplift (the uplift of An-Nusseiriyeh and the North-Western Syrian block); 2 - region of the marginal part of the platform disturbed by Alpine movements with possible allochthonous occurrence of rocks belonging to the ophiolitic formation (the Bassit block: a Jurassic-Cretaceous sedimentary complex, b - the ophiolitic formation, c - rock complex of Upper Cretaceous-Paleogene age); 3 - Neogene depressions filled with marine deposits; 4 - Pliocene troughs filled with continental deposits; 5 - Upper Miocene basalts; 6 - Pliocene basalts and tuff-breccias; 7 - boundaries of depressions and troughs; 8 - contours of anticlines and synclines; 9 - faults of deep-seated occurrence; 10 - faults; 11 - faults supposedly seated under Pliocene deposits; 12 - overthrusts; 13 - flexures; 14 - anticline folds (linear, asymmetric); 15 - coffer-shaped anticline folds, horst-anticlines; 16 - volcanoes of Pliocene age; 17 - stocks of Pliocene basic rocks; 18 - volcanic vents of Upper Jurassic-Lower Cretaceous age; 19 - structure contours along the floor of Cretaceous age; 20 - structure contours along the floor of the Campanian; 21 - structure contours along the floor of Middle Eocene deposits; 22 - structure contours along the floor of Helvetian layer deposits.

Key to figures on the map (in circles):

1 - the western limb of the An-Nusseiriyeh uplift; 2 - the Al-Ghab graben; 3 - the Jabal El-Wastani horst-anticline; 4 - the Al-Balou's trough; 5 - the Jabal Barish horst-anticline; 6 - the Missyif graben; 7 - the M'arret An-No'man anticlinal projection; 8 - the Hama anticlinal projection; 9 - the Asharneh trough; 10 - the Idlib depression; 11 - the Nahr El-Kabir depression; 12 - the Qesal Dagh peridotite massif; 13 - the Bassit massif of peridotites; 14 - the south-eastern massif of peridotites; 15 - the Lebanon-Syrian fault; 16 - the Al-Latheqiyeh fault

(Fig.2)

000326

The visual interpretation of space images MSS and TM Landsat-5 presents good results, because the human eye is able to discriminate much more colors than grey tones. Figure 3 shows a geometrical representation of the RGB space, where one color can be specified by its three-dimensional coordinates. However, the color display coordinate system can also be defined by three independent and orthogonal parameters, named intensity (I), Hue (H) and Saturation (S). In this case, Intensity considers the total energy of the image (brightness); hue is the color sensation (average wavelength) and saturation is the relative index of the color purity (percentage of white light). The attributes of IHS express another type of color perception since they can be manipulated in a controlled way providing a quantitative image interpretation. Being so, it is necessary to decompose the IHS attributes of the image, considering them individually, in opposition to the RGB space, which allows only simultaneous changes at the IHS parameters. In this paper, the triangular coordinates were used (Hayden et al., 1982) to test the usefulness of the IHS transformation (fig.4).

4. METHODOLOGY

Figure 5 shows a diagram of the methodology used in this study.

5. CONCLUSION

Data from the TM-instrument onboard the Landsat-5 satellite has proved very useful for detailed interpretation of geological structures. Compared with MSS-data, the TM-data (fig.6) gives more information about structures less than 5 km in length. This means that TM can provide considerably more information about tectonics than an MSS (fig.7). The fact that TM has more spectral bands than MSS means that certain structural features are more easily detected than by conventional MSS-analysis. The MSS image resolution is so low that it is impossible in many cases, to distinguish between valleys eroded along foliation zones and valleys developed along fractures or faults. The lineament features derived from TM scenes took roughly same higher content of information of the RBV data. On the other hand, the resolution offered by TM imagery, plus the fact that it is recorded directly in digital form, appears to offer a more satisfactory approach to this type of study. In addition, the TM multispectral mode offers additional data of considerable use to geologists. The analysis of the MSS and TM imagery indicated that El-Rouge depression is the extension of Al-Ghab depression and in line with the African-Lebanon rift system and the El-Rouge depression is a graben and separated by a linear fault which is accompanied by a series of step-like faults parallel to the master fault. The graben is separated by a system of faults trending North-West and Southeast. The final results of this study are represented as tectonical components and different levels of spatial resolution in El-Rouge graben (fig.8).

6. REFERENCES

- 1) CHAVEZ, P.S.; BERLIN, G.L. ; SOWERS, L.B., 1982. Statistical method for selecting LANDSAT MSS ratios. *Journal Applied Photographic Engineering*, 8:23-30.
- 2) Doyle, F.J., 1984: Surveying and mapping with space data, *ITC Journal* 1984.
- 3) Explanatory Notes of the Geological Maps, Syria, Damascus.
- 4) Lillesand, T.M., and Kiefer, R.W., 1979, *Remote Sensing and Image Interpretation*, John Wiley & Sons.

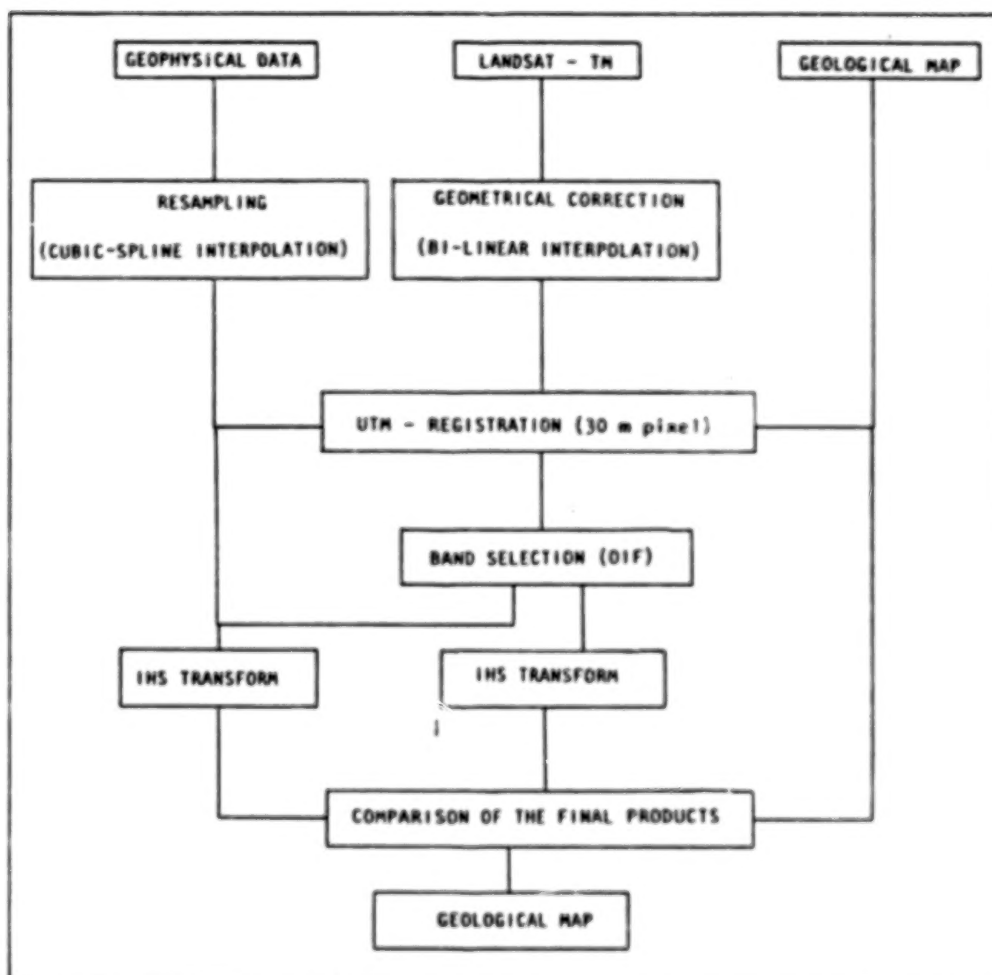


(Fig.5)



(Fig.6) TM-5 image covers the studied area .



(Fig.7) MSS- 5 image covers the area under study.

- 5) HAYDN , R. ; DALKE, G.W. ; HIROSE, T. ,1982. Application of the IHS color transform to the processing of multisensor data and image enhancement. In: Int'l. Symp, on Rem.sens., of Arid and Semi Arid Lands, Them.Conf. 2., Cairo, Egypt, pp. 559-616.
- 6) Heipke C.,1990: Joint Workshop on Hardware and software for fast image data processing, ISPRS JPhRS .
- 7) Renz H., Aman F., Baltsavias E., Forstner W.,1991: Tutorial, ISPRS Conference on : digital photogrammetric systems, Chair for photogrammetry and Remote Sensing , Technical University Munich.



(Fig.8) Technical components resulting from the interpretation of TM and MSS images covering the area under study .

SESSION VII

ENVIRONMENTAL RESTORATION AND DISASTER EVALUATION

000331

000331

BLANK PAGE

**MULTISPECTRAL REMOTE TECHNIQUES OF STUDYING
THE CONSEQUENCES OF CHERNOBYL CATASTROPHE
AND TECHNOGENIC ACTIVITY IN BELARUS**

Alexander Kovalyov
Belarusian Republican Scientific
and Technical Centre of Environment Remote Sensing
Minsk
REPUBLIC OF BELARUS 220072
0172 39 55 81

More than 35 million curies of different radionuclides were ejected into the atmosphere as a result of Chernobyl accident and about 70% of them fell out on the territory of our Republic. 5 from 6 districts of Belarus have large territories with different degrees of radionuclide contamination. The technogenic activity enhance the negative impact on living organisms and the environment. The Republic of Belarus is declared a zone of ecological disaster. Belarussian Scientific and Technical Centre of Environmental Remote Sensing "COMIR" realize the international program of complex radiation and ecological monitoring of Belarus territory using aerospace spectrometric multispectral photo- and scanner methods, mobile laboratories, ground technical facilities and geoinformation systems. A special helicopter-laboratory is constructed allowing of board spectrometers of ultraviolet, visible, approach and mean infrared ranges of spectrum, topographic and multispectral aerophotocameras, six-channel scanner of visible and infrared ranges of spectrum, three-channel microwave radiometer and lidar station. The remote sensing is accompanied with measurements from a mobile radiation and ecological laboratories, mobile lidar station and special laboratory for film development and digital data processing from helicopter-laboratory. Using measurement data of aerogamma-spectrometry, ground sampling and taking into consideration radionuclides absorption the maps of exposure dose rate, caesium-137 and potassium-40 distribution were made and published. The influence of natural and technogenic potassium-40 on the radiation situation has been analyzed, as well as 30-years prognosis of radionuclides migration was made. Using the results of complex aerospace and ground measurements, 12 types of radiation maps of the scale 1:50 000 were made for some districts with complicated technogenic situation. Remote spectrometric methods of inner basin state evaluation as well as determination of biomass of cereals crops were worked out.

Manuscript not available at time of printing. Please contact author for further information.

ENVIRONMENTAL APPLICATIONS OF REMOTE SENSING IN THE GREEK ISLANDS

John N. Hatzopoulos
University of the Aegean, Department of Environmental Studies
17 Karadonli Street, Mytilene T.K. 81100, GREECE

ABSTRACT

Applications of Remote Sensing to help with Environmental problems in the Greek Islands are described and analysed. Results from monitoring of olive grows in the Greek islands using Landsat-TM imagery, help to map the farms abandoned in recent years and thus monitor the desertification process. Methodologies and results related to land cover classification in order to determine the ecological sensitivity of certain areas using satellite images, are presented. Preliminary results from ongoing research on satellite oceanography are also presented. The process to monitor using satellite images, the extend of damage from natural hazards such as forest fires is given in detail and results are analysed.

1. INTRODUCTION

Spectral reflectances of the earth environment which are sensed and recorded by satellite sensors are carrying valuable information for environmental management planning and monitoring. Remote sensing and other space technologies are particularly useful for less favoured areas such as isolated islands where the cost prohibits the conventional methods to be used. Many Greek islands are located close to border areas and the effort of the Greek Government is to help developing those areas in terms of infrastructure developments and in providing motives for people to stay there or even having more people moving in from other places. This can be considered as a measure to tackle the desertification process which consequently has environmental, socio/economic and defence impact on those islands. It must be noted that a part of the defence strategy is to maintain high standards of living in the Greek islands in order to attract more people. To proceed with the development of those areas it is important to have reliable information especially for the environment since a great asset of those places is the tourism which is based on the excellent weather conditions, natural beauty, sunny beaches and the hospitality of the inhabitants. To provide such information, the University of the Aegean, decided to work on several remote sensing projects covering the land and marine environment.

The Department of Environmental Studies of the University of the Aegean, is located on the island of Lesbos in the North Eastern part of Greece. There is a Laboratory of Remote Sensing and GIS which is very well equipped with Unix workstations and PC-based systems for image processing and data manipulation and management, and those systems are also connected to local, National and International networks. There are several projects, as mentioned above, using remote sensing to collect information for the environment of those islands and there will be presented results from four of those projects. The projects to be presented are: Monitoring of olive grows in the Greek islands using Land-

sat-TM imagery, land cover classification in order to determine the ecological sensitivity of certain areas using satellite images, preliminary results from ongoing research on satellite oceanography and the extend of damage from natural hazards such as forest fires.

2. OLIVE GROVS MONITORING

Olive grows have been for thousands of years the main source of income to many of the people in the Greek islands. The production of seed oil resulted to lower olive oil prices kicking many farmers in the islands out of business. Those people abandoned their farms and they moved to the big cities in the continental Greece. This caused the gradual transformation of the olive grows to pasture land which due to heavy grazing resulted to soil erosion which is the final step in the desertification process. This study was conducted at the University of the Aegean (Hatzopoulos et al, 1992) to use Landsat-TM imagery to monitor the olive grows and make estimates about the desertification process. The results of this report come from the island of Lesbos while the study was later extended to cover more islands.

2.1 CLASSIFICATION

The precise estimate of spectral signatures to determine the land cover encounters many difficulties due to the nature of the agroecosystems which are developed in the island. The class categories were selected after running several experiment and they are shown in Table 1. Five classes represent the various types of olive grows while the remaining classes were composed of uniform groups such as: (6) sea water, (7) bamboo or calm, (8) pine trees, (9) Phrygana or garig, (10) urban areas, rock & bare soil, (11) maki-like olive trees, (12) a group of wooded type of vegetation composed of a large number of different species called maki, (13) the remaining grass type of vegetation. In Table 1 is also shown the ground samples which was taken from different areas of the island involving all class categories.

TABLE 1. Representative samples of all categories from different parts of the island.

No.	CLASS CATEGORY [symbols on the map Fig. 2]	x1000 m ² Area	Pixels
1	Olive trees of high crop production [e1]	235	261
2	Olive trees of moderate crop production [e2]	120	134
3	Olive trees suffering from frost, disease or drought [e5]	9	10
4	Olive trees abandoned in recent years [e11_g7]	12	13
5	Olive trees abandoned for many years [e11_t3]	22	24
6..13	Different types of landcover		

The magnitude of those samples was chosen to be sufficient according to the size of the corresponding areas of land cover (Lillesand & Kiefer

1987, Mather 1987, Swain & Davis 1978). Some of the ground samples were also used for quality control. The location of the ground samples was estimated from 1:50000 scale maps.

The image classification was performed using the Maximum Likelihood method on the original Landsat-TM image which was obtained on June 20 1992. The first four bands of the TM were used plus one composite band No. 5 based on the NDVI and defined as follows:

$$\left[\frac{\text{TM4} - \text{TM3}}{\text{TM4} + \text{TM3}} + 1 \right] * 127$$

The signatures of first five categories of land cover are shown in table 2:

TABLE 2. Signatures of olive tree categories

No.	Band 1		Band 2		Band 3		Band 4		Comp-b-5	
	min μ	max σ	min μ	max σ	min μ	max σ	min μ	max σ	min μ	max σ
1	18	23	16	18	23	27	63	75	179	192
	20	1.5	17	0.6	25	1.4	67	3.6	184	5.2
2	24	41	21	31	32	48	67	87	160	178
	32	4.2	26	2.9	40	4.6	79	5.0	168	4.3
3	21	29	18	21	26	28	57	65	172	177
	24	2.5	19	1.2	27	0.5	60	3.0	175	1.8
4	21	28	19	21	28	31	53	57	164	170
	25	2.6	20	0.8	29	1.2	56	1.6	167	2.0
5	30	34	23	29	38	48	64	70	150	161
	32	1.7	26	1.5	42	2.8	67	2.4	156	3.5

2.2 RESULTS

The final results, shown in Table 3, were compared with data obtained from the Hellenic National Statistical Service which keeps records for the total area covered by olive trees which was 449326 x1000 m². The difference of this value and the total area shown in Table 3 is about 17% which is considered acceptable for this project.

TABLE 3. Results of olive tree classification (Lesvos)

CLASS CATEGORY	x1000 m ²	%
Olive grows of high crop production	66860	18
Olive grows of moderate crop "	141560	38
Olive grows suffering of frost etc.	70850	19
Olive trees abandoned in recent yrs	63426	17
Olive trees abandoned for many "	29790	8
TOTAL	372489	100

3. ECOLOGICAL SENSITIVITY

This project involved Landsat-TM imagery for land cover classification to produce thematic maps with classes to be used for the calibration of the model of ecological sensitivity. In order to calibrate the model of ecological sensitivity, (Hatzopoulos, Troumbis, et al, 1993) it is need to relate the diversity and productivity to the term of ecological sensitivity. The criteria which were used, are:

1. Forestry ecosystems tend to have higher values of diversity and productivity than other ecosystems.
2. Every natural ecosystem (not disturbed by human activity) receives higher values of diversity and productivity than simplified plant communities of agricultural and urban settings.
3. The productivity of an area is highly increased if water is easily available.
4. Ecotones and transition zones are considered to be the most productive and diverse ecosystems in an area.
5. Proximity to roads and settlements, reduces the ecological value because of the likelihood of man-caused disturbance.

3.1 RESULTS

Fig. 1 shows the classification results over the area of Kolpos Geras in the island of Lesvos. There are several classes such as: (1) Olive trees, (2) Pine trees, (3) Maki type of vegetation, (4) Pasture land, (5) Wetlands, (6) other types of vegetation. The emphasis in the classes is given to isolate the wetlands and the pine trees from the cultivated land (olive trees), which is important to the ecological sensitivity model.

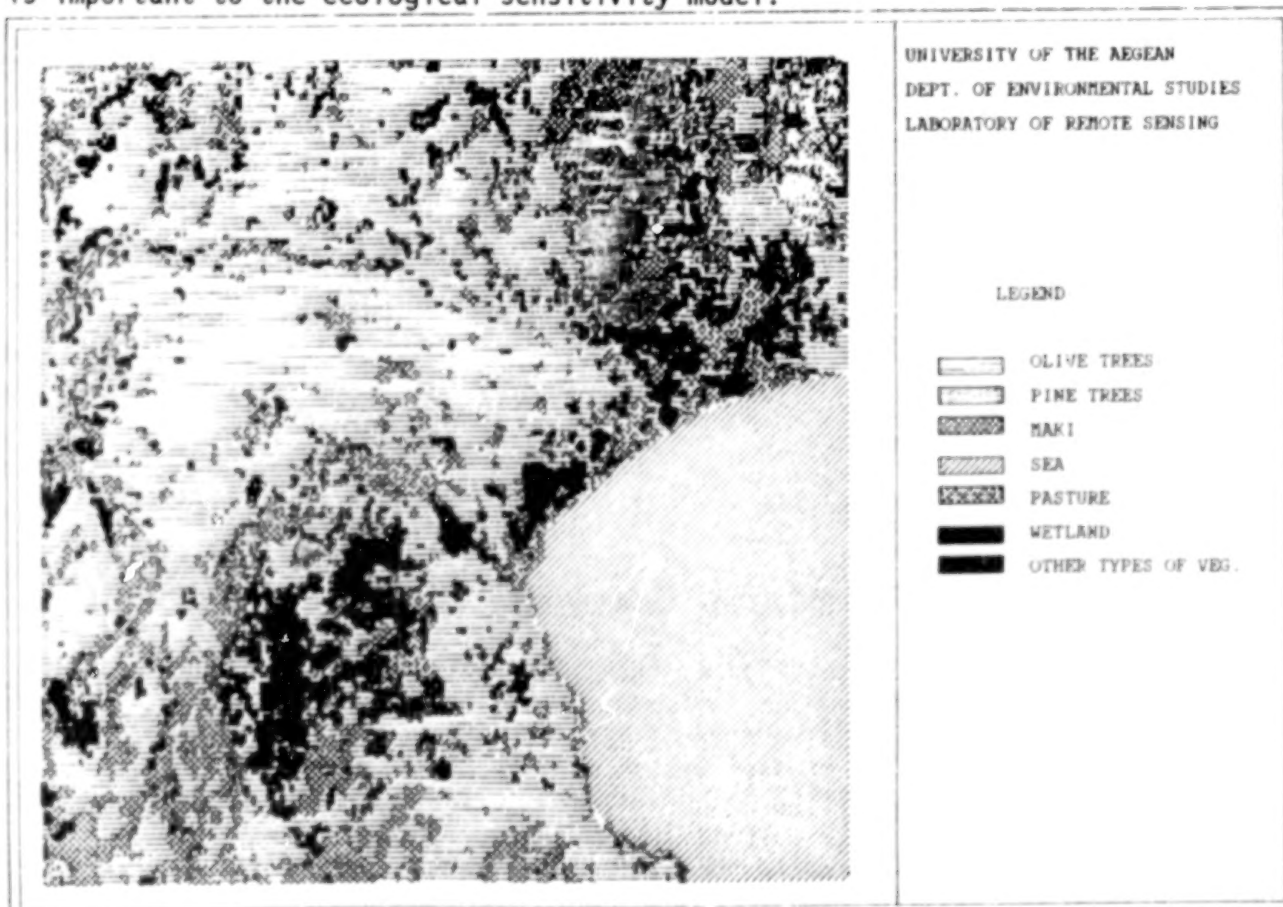


Figure 1. Landsat TM classification for ecological sensitivity.

Some of the factors used by the sensitivity model together with their weights are given in Table 4.

TABLE 4. ECOLOGICAL SENSITIVITY - CONCEPTUAL MODEL OUTLINE

CONSIDERATION	SPECIFIC DATA CLASS	VALUE
Vegetation Diversity	Vegetation type and Productivity	
	Forest (chestnut trees)	10
	Agriculture	1
	Pasture	-3
	Vineyards	2
	Barren	0
	Other vegetation	-2
	wetlands	10
Proximity to human disturbance	Existing Road Class	
	Primary roads	
	-500m	-6
	500-1000m	-5
	1000-1500m	-3
	Settlement Areas any kind	
	-1000m	-3
	1000-1500m	-2
Other ecological	Corine Biotopes properties	
	within a range of 500m	10

The final results of this process are obtained by running the ecological sensitivity model through a GIS system where by using buffering, polygon overlays and logical and arithmetic expressions the area is classified in the following categories:

- Low Sensitivity
- Medium Sensitivity
- High Sensitivity
- Extremely high Sensitivity

4. SATELLITE OCEANOGRAPHY

This project was supported by the Greek Secretariat for research and technology and the British Council in Athens Greece. The project was executed in cooperation between the University of the Aegean and the University of Dundee. The objectives of this project was to monitor the quality of the sea water environment using satellite images of Landsat TM, and AVHRR. A continuous such monitoring from satellites, helps in the early detection of sea water quality problems and activation of the environmental protection mechanism.

4.1 METHODOLOGY

In-situ sampling of sea water was performed and measurements of certain parameters of water quality were recorded using a light boat, at the same date and close to the same time that landsat-TM was passing over the area. The parameters measured were sea water temperature and depth of visibility in the water by a sechi disk. The sea water samples were analysed at the University of the Aegean laboratory and concentrations of chlorophyll, suspended matter and turbidity were determined. There were four sets of data obtained in the following 1992 dates: March 5, June 9, July 11 and August 27. The location of the sea sampling stations are around the Mytilene harbour and they are shown in Fig. 2.

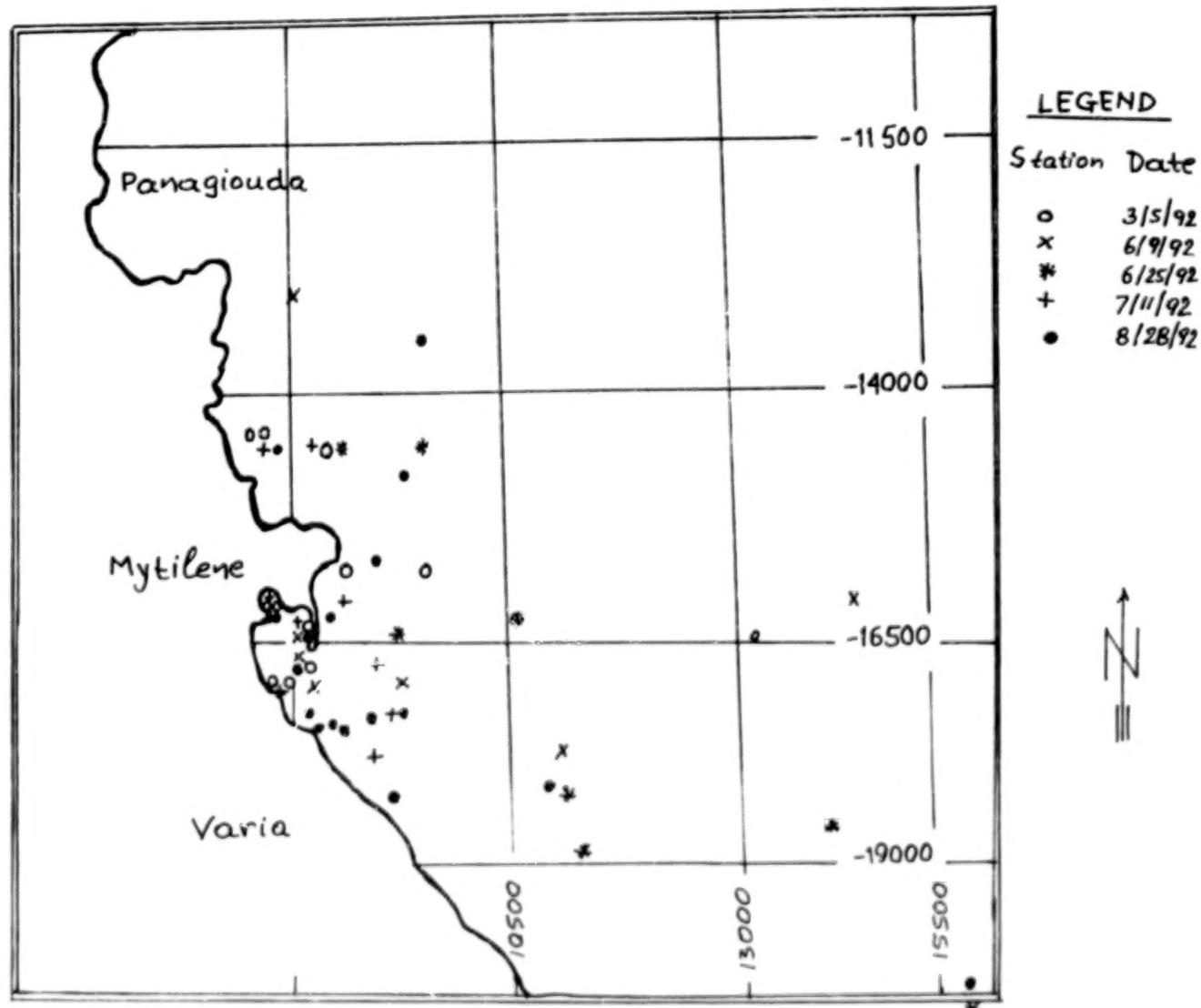


Figure 2. Location of sea water sampling stations.

Four Landsat-TM cloudless mini scenes (50x50Km coverage) were purchased corresponding to the in-situ sampling dates.

The position of the sampling boat was determined by photogrammetry

and later by GPS.

The image processing was performed at the University of Dundee (Cracknell et al, 1994) and water quality maps were generated by using correlation equations which were established by regression. Separate process was followed to produce sea surface temperature (SST) maps.

AVHRR data were also captured by the University of Dundee receiving station and they were analysed to indicate the circulation patterns of the wider area.

The image processing still continues at the University of the Aegean with different approaches and the results are expected to be finalized by the end of the year.

5. ASSESSMENT OF FOREST FIRE DAMAGES

In May 1992, a large fire in the island of Lesbos burn about 2000 acres of pine forest. During that period the university of the Aegean was involved in the satellite oceanography project and two mini scenes of the burn site March 5 (Fig. 3) and June 9 (Fig. 4) were obtained.

5.1 RESULTS

The image processing was performed using channel 4 of the Landsat-TM image. This included rectification to fit to a UTM projection and radiometric enhancement. The burned area was extracted by density slicing. The burned area was computed and it was found 9500 m²

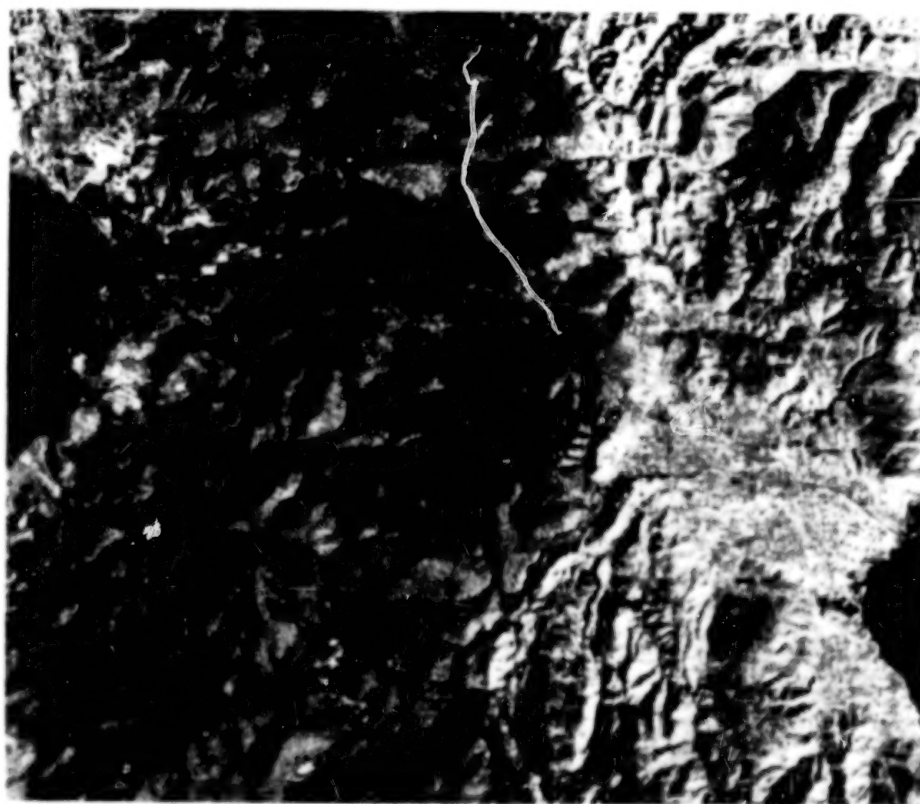


Figure 3. Landsat-TM image of band 4, on March 5, 1992.



Figure 4. Landsat image of band 4, on June 9, 1992.

REFERENCES

- Cracknell A. P., K. Abdullah, J. N. Hatzopoulos, M. Karydis, and D. Gazis, 1994, "Monitoring for Protection of the Marine Environment Using Landsat-TM and AVHRR Data", Preliminary report to the British Council of Athens, Greece.
- Hatzopoulos J.N., C.Giourga, S.Koukoulas & N.Margaris, 1992 "Land Cover Classification of Olive Trees in the Greek Islands Using Landsat-TM Images", proceedings of the ASPRS at the International Conference in Washington D.C., August 2-7 1992.
- J. N. Hatzopoulos, A. Troumbis, D. Andronikides, A. Antoniou, K. Dimitriou, Z. Karavanis, Ch. Kontos, and G. Skribas, 1993 "Ecological Sensitivity Using GIS Based Models", Proceedings of the 8th European ARC/INFO Conference, Athens Greece.
- Lillesand T.M. & R.W. Kiefer 1987, "Remote sensing and Image Interpretation", Second Edition, University of Wisconsin, Madison.
- Matther J.A. 1986, "Computer Processing of Remotely Sensed Images, an Introduction", University of New Nottingham, England.
- Swain P.H. & S.M. Davis, 1978 "Remote Sensing: The Quantitative Approach", McGraw-Hill, Inc., New York, N.Y., 396p.

MAPPING A BIOCHEMICAL STRESS GRADIENT ACROSS A CONIFEROUS FOREST WITH AIRBORNE VISIBLE/INFRARED IMAGING SPECTROMETER (AVIRIS) DATA

C. Banninger
Institute for Image Processing and Computer Graphics
Joanneum Research
Wastiangasse 6, A-8010 Graz
AUSTRIA
(316) 8020-735

L. Johnson and D. Peterson
NASA Ames Research Center
Moffett Field, CA 94035-1000

The forests of Austria are a major source of revenue to the national economy, not only for the wood products derived from the harvested timber, but also for the recreational and aesthetic setting they provide for tourism, as well as the local inhabitants. The health of the forests is, therefore, of prime importance to the continuing high prosperity and quality of life of the nation. These standards are however, under threat by the steady decline in the health and vitality of the nation's forests, particularly in the alpine regions of the country. The principal cause of this decline is the damaging effects that air pollutants (primarily SO_x , NO_x , and O_3) emitted from industrial and motor vehicle sources have on the forests. Conventional approaches to detecting and monitoring forest damage (e.g., ground surveys and aerial photography) have proven inadequate to the task, especially in light of the marked increase in areal extent and severity of forest degradation since the late 1970's. This has spurred government agencies responsible for the welfare of the forests to seek new means to monitor their status in an efficient and cost effective manner.

In the summer of 1986, Austria participated in a NASA-sponsored airborne imaging spectrometer (AIS-2) campaign involving several forested test sites in the alpine regions of the country and, in the summer of 1991, took part in the follow up NASA MAC-Europe campaign that acquired Airborne Visible/Infrared Imaging Spectrometer (AVIRIS) data from a large tract of air pollution damaged coniferous forest situated in the southeastern Alps of the country. The forest lies adjacent to a major industrial and power-generating centre, which is serviced by a heavily trafficked arterial road network, and has been the focus of an intensive ground study since the mid-1980's by several university research institutes on the precise causes and effects that the air pollutants have on the forests.

Complementary to these studies, the AVIRIS data acquired from a 15 km long and 6 km wide area of the forest are being examined in conjunction with ground data collected along a clearly recognizable stress gradient defined by canopy needle loss and chlorosis. Needle/twig samples collected from 56 individual tree stands representing all tree damage classes (healthy to severely damaged) present across the stress gradient provided a total of 312 samples that were analyzed for total nitrogen, lignin, cellulose, and pigment (chlorophyll and carotenoid) content. From these data sets, relationships between needle chemistry and tree damage have been derived and are currently being used with atmospherically corrected and geocoded AVIRIS data

from the 56 stands used in the ground sampling, to develop appropriate models for the prediction of canopy biochemical constituents from high spectral resolution remote sensing data. The results of this work will form the basis of the presentation at the symposium.

Manuscript not available at time of printing. Please contact author for further information.

TEXTURE ANALYSIS OF REMOTELY SENSED DATA FOR WASTE SITE CHARACTERIZATION¹

John M. Irvine and Garth Barbour
ERIM, Arlington, VA, 22209

ABSTRACT

A major environmental concern today is the characterization, remediation, and monitoring of Federal waste sites, such as those operated by the Department of Energy. Remotely sensed imagery data offers a rich source of information for characterizing and monitoring these sites. This paper explores the use of texture analysis of the imagery data as a technique for identifying and classifying features within the sites. Texture measures are derived from the spatial covariances, higher order moments, and estimates of the fractal dimensions of the imagery data. Application of classification procedures to these texture measures offers a way to identify features of interest, such as vegetative stress, surface contaminants, subsidence, and soil moisture.

1. INTRODUCTION

A major environmental concern today is the characterization, remediation, and monitoring of Federal waste sites, such as those operated by the Department of Energy. Remotely sensed imagery data offers a rich source of information for characterizing and monitoring these sites. This paper explores the use of texture analysis of the imagery data as a technique for identifying and classifying features within the sites. Texture measures are derived from the spatial covariances, higher order moments, and estimates of the fractal dimensions of the imagery data. Application of classification procedures to these texture measures offers a way to identify features of interest, such as vegetative stress, surface contaminants, subsidence, and soil moisture.

The analysis of imagery data often relies on the human observer to recognize features of interest in the image. Various image processing techniques, such as filtering, sharpening, etc., can be used to enhance the visual appearance, thereby making the features of interest more evident to the human observer. The use of texture analysis can supplement the visual analysis in several important ways. Texture analysis of the digital image data can:

¹ This project was supported under the Strategic Environmental Research and Development Program (SERDP). The Dystal artificial neural network was developed by ERIM under NIH grants NOINS02389 and NOINS32304 and ONR grants N00014-88-K-0659 and N00014-92-C-0018.

- Help identify subtle features that may not be apparent to the human observer,
- Assist in understanding the phenomenology that gives rise to certain signatures,
- Provide a basis for automated image exploitation.

The objective of this study is to develop and assess methods for detection, identification, and classification of environmental insults based on the application of mathematical procedures to digital imagery data. The initial step in characterization is to detect the environmental insult, i.e., distinguish between the insult and an unaffected area. Using classification methods, the characterization can be carried further by distinguishing among types of features (classes) in the image, where these classes could be defined by the severity or extent of the damage, the age of the insult, and the type of contamination.

Classification procedures can be applied once categories have been properly defined. This method of analysis requires relatively large samples of imagery. The performance of the classification procedures is indicated by a "confusion" matrix. The general approach to the texture analysis requires six steps:

- (1) Digitize the imagery, if necessary
- (2) Chip the imagery, to obtain samples depicting environmental insults and samples which are free from environmental stress
- (3) Preprocess the data, as appropriate
- (4) Compute measures of texture, spatial variation, and other relevant image features
- (5) Develop classification procedures, using a "training set" of the imagery-derived data
- (6) Evaluate performance of the classification procedures, using a separate "testing set" of imagery-derived data

2. IMAGE SELECTION

The chips for the initial experiments were selected from images containing two different types of environmental concerns. The two sites studied in this effort are the Oil Test Site at Savannah River and the Coal Ash Pond at Oak Ridge. Multiple collections at Savannah River imaged the surface oil and control plots that were set out in 1975. A separate image collection at Oak Ridge covered the coal ash pond and surrounding area. From each image, relatively small non-overlapping 64x64 chips were used for the feature calculations. The resulting features were the inputs for training and testing the classification procedure.

The Savannah River Oil Test Site offers a unique opportunity to assess the long-term effects of surface oils and lubricants. A controlled experiment was set up in 1975 to examine the degradation of oil over time. (See Pendergast and Nalezny (1994), Watts, Corey and McLeod (1976).) Careful plots were set up, some

410090

contained various types of oil and others were control plots. (See figure 1.) The image chips contain three types of features: the oil plot, oil free and the oil-contaminated soil storage area at the test site.

The coal ash pond at Oak Ridge, Tennessee, was a holding area for coal ash produced by a power generating plant. A slurry of coal ash and water was pumped into the pond formed by an earthen dam. (See figure 2.) The coal ash is known to contain high acidity and more radionuclides than are typical for the region. The major environmental concern is the effect of the coal ash on the surrounding vegetation. Recently, the dumping of coal ash was halted and the vegetation over the pond area is recovering. Four types of chips were extracted from the coal ash imagery: the ash pond, bare soil from and adjacent site, the drainage area for the ash pond, and the surrounding forest. The drainage area is a creek that runs through the woods from the ash pond to Rogers Quarry. Vegetation in this area closely resembles the surrounding forest, but the moisture content should be higher due to the presence of the creek.

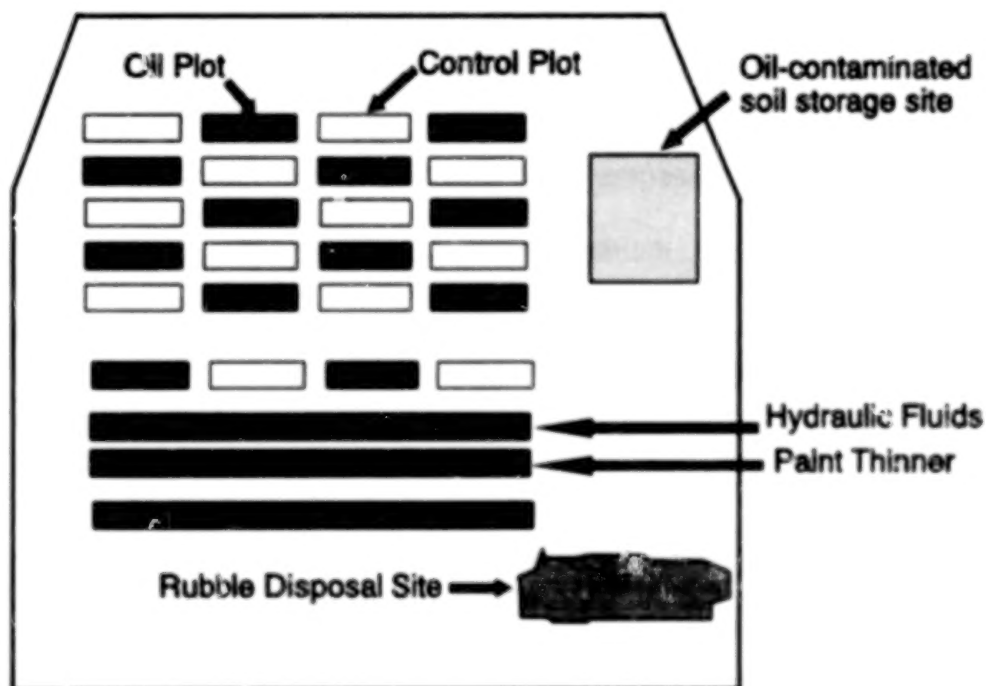


Figure 1. The Savannah River Oil Test Site. Oil plots and control plots were set up in an alternating pattern.

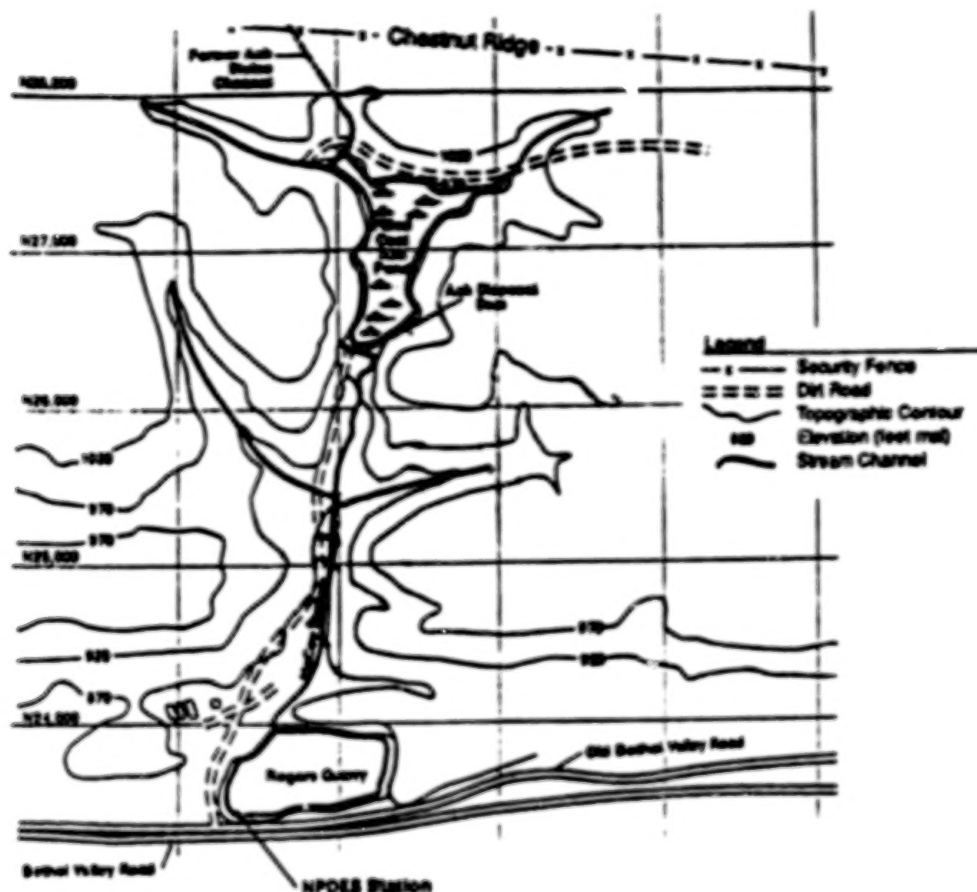


Figure 2. The Coal Ash Pond at Oak Ridge, Tennessee. Coal ash from a power plant was mixed with water and the slurry was pumped into the pond formed by the earthen dam. Excess water drained into Roger's Quarry.

3. TEXTURE ANALYSIS

Fractal analysis offers one method for characterizing remotely sensed imagery data. Although the mathematical treatment of fractals is complex, an intuitive understanding can be gained by considering examples. A conventional geometric object has a regular relationship between its area and perimeter. A fractal object, by comparison, may have a fixed area but a virtually infinite perimeter, due to the behavior of its boundary. If the fractal is studied under greater magnification, the complex boundary pattern remains present. One indication of this complex phenomenon is the fractal dimension². For the image features considered here, the

². Mathematically, the fractal dimension is the Hausdorff dimension of an object. For fractals, it differs from the topological (intuitive) dimension. For objects defined on a grid (such as images composed of pixels) the perimeter P and area A are related by:

$$P = c A^{D/2}$$

BLANK PAGE

fractal dimensions range between 1 and 2, where 1 corresponds to a conventional geometric figure and 2 corresponds to a boundary that actually fills up the real plane.

Terrain features that appear on imagery exhibit behavior similar to fractal processes. Because of their erratic appearance, fractal objects resemble shapes arising in nature. Furthermore, patterns observed on a large scale look similar to small scale patterns, a property which is called self-similarity. Consequently, various researchers have explored the use of fractals for analysis of imagery-derived data. (See Harrington (1988), De Cola (1989).) In particular, the terrain features observed on overhead imagery can be modelled by a fractional brownian motion, which is a generalization of brownian motion in two dimensions. If $B(s,t)$ is standard brownian motion then the fractional brownian motion $B_H(t,s)$ is defined by:

$$B_H(t,w) - B_H(0,w) = \int_0^t [(H + \frac{1}{2})^{-1/2} \{ -((t-s)^{(H-1/2)} - (-s)^{(H-1/2)}) dB(s,w) + \int_0^s ((t-s)^{(H-1/2)}) dB(s,w) \}]$$

The parameter H indicates the "ruggedness" of the process. (See figure 3.) If $H = 1/2$, then $B_H(t,s)$ is standard brownian motion. Values of H near 1 give relatively smooth surfaces, while H close to 0 corresponds to turbulent processes. Contours of the fractional brownian motion are fractals with dimension $D = 2 - H$.

When the fractional brownian motion is sampled on a grid, the behavior of the points resembles the pixel values for images of terrain. The increments to this discrete process have a Gaussian distribution, but exhibit strong dependencies. If N adjacent points are aggregated, the variance of these increments is proportional to N^{2H} . Thus, the fractal dimension indicates the persistency of the spatial correlations and can be estimated from the variances of subsets of the data. (See Harrington (1988).) To illustrate the calculations, let Q_1 and Q_2 be the means estimated from different size squares from the image chip, with $Q_1 > Q_2$. (For example, Q_1 could be the mean of the pixels for 8 by 8 squares and Q_2 could be from 4 by 4 squares.) Then H is estimated by:

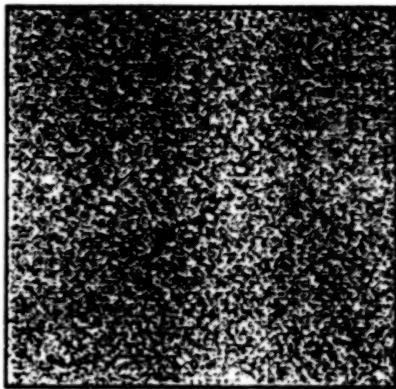
where D is the fractal dimension of boundary, with $1 \leq D \leq 2$. For conventional geometric objects, such as squares, circles, etc., $D = 1$. If the grid is made finer (i.e., the resolution of the image is improved) the area remains unchanged, but the perimeter increases by a factor that depends on D .

000348

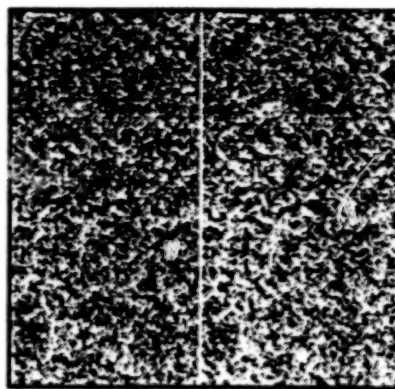
364

$$H = \frac{1}{2} \left[\frac{\ln(\text{var}(Q_1)) - \ln(\text{var}(Q_2))}{\ln(Q_1) - \ln(Q_2)} \right]$$

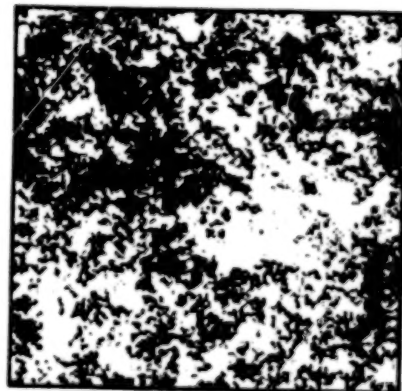
Different values of the estimated H parameter correspond to various terrain and target features on specific segments of an image. Classification of the image chips relies on estimates of the fractal dimensions and other summary statistics computed for each chip. An artificial neural network was used to develop classification rules for image chips, based on the H parameters and other statistics derived from the raw pixel data.



H = 1/2



H = 3/4



H = 1

Figure 3. Examples of Fractional Brownian Noise. The examples depicted here demonstrate the effect of changing the H parameter of the two-dimensional fractional Brownian noise. Large values of H correspond to high spatial correlations.

4. THE CLASSIFICATION ANALYSIS

Classification analysis was performed using an artificial neural network. The measures described above were used to train and test the Dystal (DYNAMICALLY STABLE Associative Learning) network for the classification tasks. These measures were calculated for each chip and the chips divided roughly evenly between training and testing.

Dystal is an artificial neural network based on properties of associative learning found in biological neural networks. (See Vogl, et al (1989, 1991, 1992), Alkon, et al (1990), Blackwell, et al (1992), Irvine, et al (1994)) The basic properties are derived from studies of the marine snail *Hermissenda crassicornis* (Alkon (1987) and supplemented by results from rabbit hippocampus (See Olds, et al (1989)). These studies suggest that learning takes place at a "patch", or local dendritic area of the post-synaptic neuron when temporal pairing of two (or more) input signals occurs. These signals are the Conditioned Stimulus (CS) and UnConditioned Stimulus (UCS). After training, presentation of the CS alone elicits the same response as presentation of the UCS. In these experiments, the CS pattern is the vector of measures described above and the UCS is a classification vector indicating to which group the chip belongs.

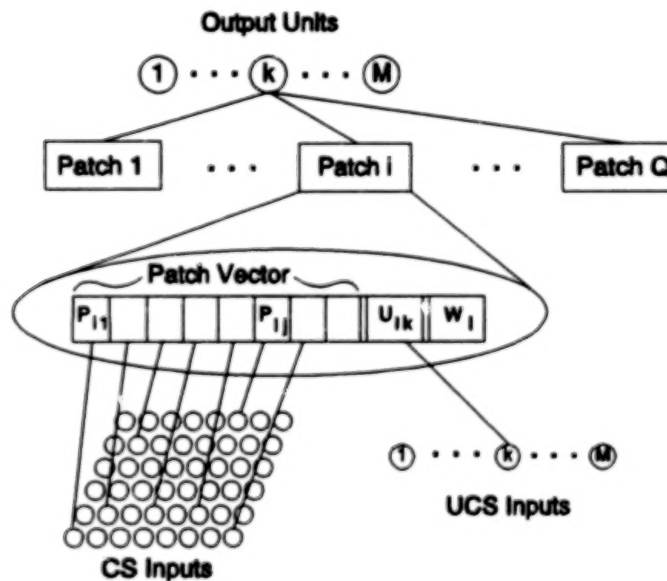


Figure 4. A diagram of the patch structure of output units. There is one output unit for each component of the UCS vector. Patch structure is shown for one patch of a single output unit. A subset of the CS inputs (receptive field) connects to each patch (the same subset for all patches of a given output unit).

In Dystal, the CS and UCS are modeled as separate input patterns (see figure 5). Each output unit is considered "tied" to one of the UCS elements. Each output unit has a dynamically allocated number of memory storage locations known as patches. Each patch stores an association between a portion of the CS and that element of the UCS vector that is tied to the patch's output unit. Each patch consists of a patch vector, a UCS value, and a weight. The patch vector is the memory of the CS patterns associated with this patch. The UCS value is the expected value of the input UCS associated with the CS patterns that match the patch. The weight is an indication of the frequency of match for the patch.

Dystal is self-organizing: each output unit starts without any patches and creates them as necessary. Dystal's training algorithm is illustrated in figure 5. During testing, the algorithm is the same as during training, except that no UCS pattern is presented, so patches are neither created nor modified. As in the biological systems, Dystal learns to output the associated UCS pattern upon presentation of the CS alone.

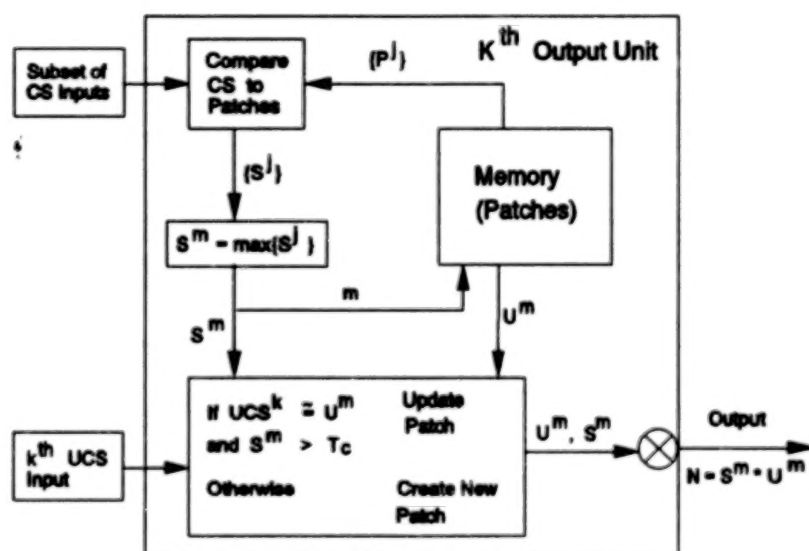


Figure 5. Dystal's training algorithm. This process occurs for each output unit independently. The input CS pattern is compared to the patch vector of each patch. (P^j is the patch vector of the j^{th} patch and S^j is the similarity between the CS inputs and P^j .) The patch with a patch vector most similar to the input CS is selected (S^m is the maximum taken over S^j and m is the index of the most similar patch). If the measure of similarity is sufficiently high ($S^m > T_c$) and the stored UCS value (U^m) is the same as the input UCS value, the patch is considered matched; its patch vector, UCS value, and weight are updated. Otherwise, Dystal creates a new patch, initializing the patch vector and UCS value to the input values. The unit then outputs the UCS value from the matched patch multiplied by the calculated similarity.

5. ASSESSING PERFORMANCE

Classification procedures use the imagery data to predict the category of the image chip. Two forms of error are possible -- errors of omission and errors of commission. One measure of performance is the frequency with which a procedure correctly predicts the class of an image chip. Performance depends on the nature of the procedure, the level of noise in the data, and the degree of separation between the classes. There is a trade-off between the two types of prediction errors. (See table 1.)

Although classification procedures are possible for multiple classes, the limitation is that performance is evaluated at only a single point. Running the analysis with two categories, e.g., insult and non-insult, associates a single score with each observation. Values of this score above a certain threshold are assigned to one category and values below are assigned to the other. Varying this threshold produces different estimates for the probability of detection (P_D) and the probability of a false alarm (P_{FA}). Thus, by using only two categories in the classification analysis, a complete performance curve, called the ROC curve, can be constructed.

		PREDICTION	
		INSULT	NON-INSULT
TRUE CLASS	INSULT	CORRECT	ERROR
	NON-INSULT	ERROR	CORRECT

TABLE 1. CLASSIFICATION ERROR TRADE-OFF.

Standard Receiver Operating Characteristic (ROC) analysis considers experiments in which each stimulus (in this case, a single chip) contains at most one realization of the signal of interest. For this problem, a single image chip contains either the image feature of interest, embedded in the background, or background only. The classic ROC framework represents each stimulus by a random variable X which arises either from a "noise" distribution or a "signal" distribution. The detection procedure, unaware of which distribution generated a given observation of X , will assign each to either the "target" category (feature) or the "background" category based on the observed values of X . Denote the underlying distributions by:

$$X \sim F(X, \theta_s) \text{ for signal-plus-noise}$$

and

$$X \sim F(X, \theta_n) \text{ for noise only.}$$

For a particular threshold, C , the detection procedure assigns values less than C to the background category and values greater than C to targets. The specific value of C

determines the theoretical probabilities of detection and false alarm:

$$P_D = 1 - F(C, \theta_n)$$

and

$$P_{FA} = 1 - F(C, \theta_s)$$

Varying the value of C generates different values for P_D and P_{FA} , which will trace the ROC curve. Each image chip, either target or background, corresponds to a single value of the random variable X .

In practice, the underlying distributions are not known. From a sample of data, we obtain only the observed P_D and observed P_{FA} at various thresholds. These observed points form the empirical ROC curve. For particular distributions $F(X, \theta_n)$ and $F(X, \theta_s)$, a model-based ROC curve can be fit to the data. The parameters θ_n and θ_s are estimated from the data. Different choices for the distribution function $F(\dots)$ produce different shaped ROC curves. We considered the exponential model for this study. The exponential model used $F(X) = 1 - e^{-\theta X}$, where the value of θ indicates the separation between targets and background. (See Egan (1975), Irvine (1990) and Irvine (1991).)

6. RESULTS

Dystal was trained and tested on separate image sets corresponding to the different sensors. For each of the Oil Test Site images, Dystal was trained to discriminate between the three classes: oil plots, control plots, and the contaminated soil storage area. The classification results can be substantially improved by pooling multiple sources of imagery. Looking only at the two primary categories, the oil plots and the control plots, ROC curves can be constructed based on the two imagery collections. By pooling the information from the two collections, superior classification accuracy is achieved. (See figure 6.) As one should expect, combining independent information from multiple sources enhances the capability to distinguish between the oil plots and the oil-free area.

Dystal was similarly trained to classify the four types of chips in the coal ash imagery: the coal ash pond, bare soil, the drainage area, and forest. Dystal's performance is summarized in table 2. These are preliminary results, using a small number of examples for training Dystal. Note that the drainage chips are like forest, with a small stream running through the chip. Thus, it is not surprising that the major confusion in classification is between plain forest and forest with a small creek. The encouraging result is that even in these initial experiments, the ash pond is seldom confused with the other classes. There are only two ash pond chips that are misclassified and two chips that are misclassified as ash pond.

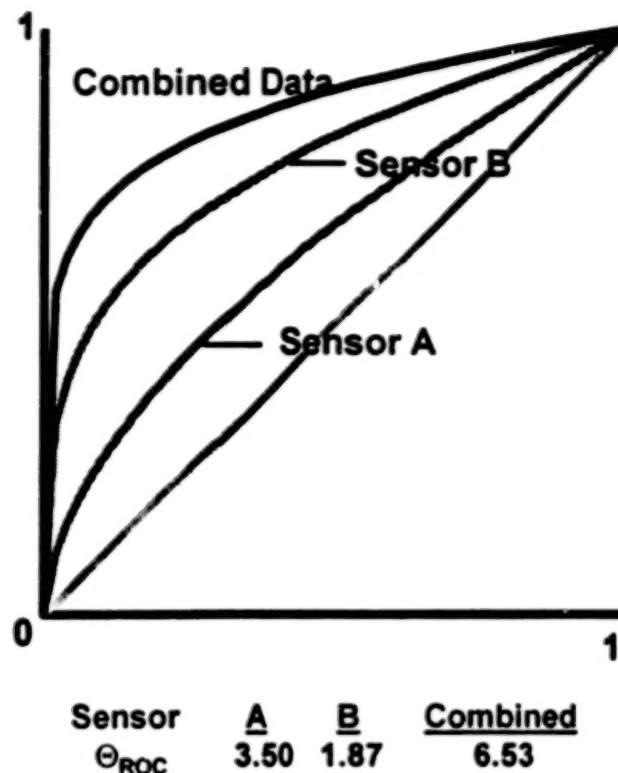


Figure 6. ROC Curve for Detection of Oil Plots Using Dystal. Curves A and B correspond to single sensors. By combining information from the two sensors, substantial improvements can be realized, as indicated by the "pooled" curve.

CLASSIFICATION RESULT

	Coal Ash	Bare Soil	Drainage Area	Forest	Rejected	TOTAL
Coal Ash	11	1	1	0	0	13
Bare Soil	1	6	0	0	3	10
Drainage Area	1	0	4	4	0	9
Forest	0	0	6	9	3	18
TOTAL	13	7	11	13	6	50

Table 2. Confusion matrix for the Coal Ash Pond. Dystal correctly classified 60.0% and rejected 12.0%. Note that the major area of misclassification is between the forest and the drainage area that consists of forest with a small creek.

7. APPENDIX: DEFINITIONS OF THE VARIABLES

Each chip is 64 pixels on a side, for a total of 4,096 pixels. Many of the variables are standard summary statistics calculated on the 4,096 individual observations. In addition, one could partition the chip into a set of K by K disjoint sets of pixels. If K=2, for example, each chip contains 1,024 separate 2 by 2 squares of pixels. Averaging the values within each 2 by 2 square reduces each chip to 1,024 observations. Statistics were computed for these observations. This entire process was repeated for K=4 and K=8. In all, 67 variables were calculated from the raw pixel data.

The summary statistics used in this study included the standard deviation, skewness, and kurtosis. These statistics were computed for various aggregations of the pixels (i.e., K = 1, 2, 4, 8). Spatial correlations were calculated from the raw data in four directions--across the rows of pixels, down the columns, diagonal to the right, and diagonal to the left.

The final set of variables are indicators of the persistency of the spatial correlations in different directions. These are based on estimates of the H parameter for fractional Brownian motion. (See Harrington (1988).) To illustrate the calculations, let Q_1 and Q_2 be the values estimated from different size squares from the chip, with $Q_1 \geq Q_2$. (For example, Q_1 could be the sum of the pixels for 8 by 8 squares and Q_2 could be from 4 by 4 squares.) Then H is estimated by:

$$H = \frac{1}{2} \left[\frac{\ln(\text{var}(Q_1)) - \ln(\text{var}(Q_2))}{\ln(Q_1) - \ln(Q_2)} \right]$$

Similar estimates of H were obtained by examining sequences of pixels in one direction. This was done in the horizontal, vertical, right diagonal, and left diagonal directions.

REFERENCES

D.L. Alkon, Memory Traces in the Brain, Cambridge University Press, Cambridge, 1987.

D.L. Alkon, K.T. Blackwell, G.S. Barbour, A.K. Rigler, T.P. Vogl, (1990) "Pattern-Recognition by an Artificial Network Derived from Biological Neuronal Systems," *Biological Cybernetics* 62, 363-376, 1990.

K.T. Blackwell, T.P. Vogl, S.D. Hyman, G.S. Barbour, D.L. Alkon, (1992) "A New Approach to Hand-Written Character Recognition," *Pattern Recognition*, In Press, 1992.

De Cola, Lee (1989) "Fractal Analysis of a Classified Landsat Scene",

Photogrammetric Engineering and Remote Sensing, vol.55, no. 5, pp.601-610.

Egan, J.P., (1975) Signal Detection Theory and ROC Analysis, New York: Academic Press.

Harrington, Leigh, (1988) "Computer Generation of Fractional Brownian Noise", ERIM Working Paper.

Irvine, J. (1990) "Estimation of Free Response Operating Characteristic Curves", Meetings of the American Statistical Association, 1990.

Irvine, J. (1991) "Model Selection for ROC Curves Using AIC", Meetings of the American Statistical Association, 1991.

Irvine, J., Blackwell, K.M., Alkon, D.L., Vogl, T.P. (1994) "Angular Separation in Neural Networks", *Journal of Artificial Neural Networks*, Vol.1, 1994.

Mandelbrot, Benoit (1982), The Fractal Geometry of Nature, San Francisco: Freeman.

J.L. Olds, M.L. Anderson, D.L. McPhie, L.D. Staten, D.L. Alkon, (1989) "Imaging Memory-Specific Changes in the Distribution of Protein Kinase C within the Hippocampus," *Science* 245, 866, 1989.

Peitgen, Heinz-Otto, and Dietmar Saupe (eds.) (1988) The Science of Fractal Images, New York: Springer-Verlag.

M.M. Pendergast, C.L. Nalezny (1994) "Application of Optical and Thermal Imagery to Detect Oil Contaminated Soil," Tenth Thematic Conference on Geologic Remote Sensing, May 1994.

T.P. Vogl, D.L. Alkon, K.T. Blackwell, (1989) "Dynamically Stable Associative Learning (Dystal): a Biologically Motivated Artificial Neural Network," *Proceedings of the IJCNN 1989*, II:101-103, 1989.

T.P. Vogl, K.T. Blackwell, S.D. Hyman, G.S. Barbour, D.L. Alkon, (1991) "Classification of Hand-Written Digits and Japanese Kanji," *Proceedings of the IJCNN 1991*, I:97-102, 1991.

T.P. Vogl, Blackwell, K.T., Irvine, J.M., Barbour, G.S., Hyman, S.D., Alkon, D.L. (1992) "Dystal: A Neural Network Architecture Based on Biological Associative Memory," Progress in Neural Networks, III, C.L. Wilson and O.M. Omidvar, Eds., Ablex Publishing Co., Norwood, N.J. 1992.

J.R. Watts, J.C. Corey, and K.W. McLeod (1976) "Land Application Studies of Industrial Waste Oils and Solvents"

AN INFRARED HYPER-IMAGING SPECTROMETER FOR ATMOSPHERIC STUDIES AND ENVIRONMENTAL REMEDIATION

July, 1994

International Symposium on Spectral Sensing Research '94 (ISSSR)

Mark Massie and Michele Hinnrichs
Pacific Advanced Technology
1623 Mission Dr., Suite 3
Solvang, CA 93464-0679
(805) 688-2088
FAX (805) 686-2723
email 73424.1666@compuserve.com

ABSTRACT

Under SBIR programs to the Air Force, Navy and BMDO, Pacific Advanced Technology has successfully developed a new and innovative imaging spectro-radiometer, the Image Multi-Spectral Sensing (IMSS) system. This instrument has the capacity to satisfy operational requirements in the following areas:

- Atmospheric absorption measurements
- Remote sensing of Earth resources
- Early warning and surveillance
- Tactical missile warning
- Missile seeker applications
- Biological and chemical warfare agent detection
- Laser warning applications
- Remote sensing of smoke stack and automobile exhaust emissions
- Drug interdiction

The current configuration of the IMSS instrument has a spectral bandwidth from 2.5 to 5.0 μm with a spectral resolution of $\Delta\lambda/\lambda$ of 0.15%. It is tuned for a peak performance at 3.9 μm , a region where the missile and aircraft spectral signature is strongest. The field of view of the instrument is 2.5 degrees with an IFOV of 0.3 mrad. At maximum spectral resolution and frame rate, this instrument can collect full image frames of data with a spectral resolution of 640 spectral bins/ μm at a rate of 0.191 $\mu\text{m}/\text{sec}$. Alternatively stated, this represents the capability to measure data at a spectral resolution of approximately 0.006 μm at a data collection speed of 5.24 sec/ μm . Higher data collection speeds are available with a corresponding linear reduction in spectral resolution.

To date we have measured greybody targets, the emission spectrum of propane, butane and kerosene flames and the absorption spectra of acetone in the laboratory. We have also remotely measured a Titan II booster and automobile exhaust emissions in the field. Preliminary measurements have been made which characterize an object's signature in a cluttered infrared background, and permit object identification using multispectral features. The spectral and spatial resolution of the IMSS instrument permits imaging of the above referenced sources and the measurement of spectra in any desired spatial location on the source.

1.0 INTRODUCTION

What originally began as a phase I SBIR to the Air Force Space Division, LAAFB, for ballistic missile defense was successfully carried to a phase II program with the Air Force Phillips Lab, Kirtland AFB. Pacific Advanced Technology has developed a prototype laboratory system, IMSS, a Hyper-spectral Imaging Radiometer. The instrument is shown in figure 1.0-1. The present configuration of the IMSS prototype instrument has an $f/3.5$, 160 mm focal length lens with an IFOV of 0.3 mrad and a full field of view of 2.3 degrees. The instrument is approximately 12 inches in length, and uses a conventional LN_2 pour-fill dewar.

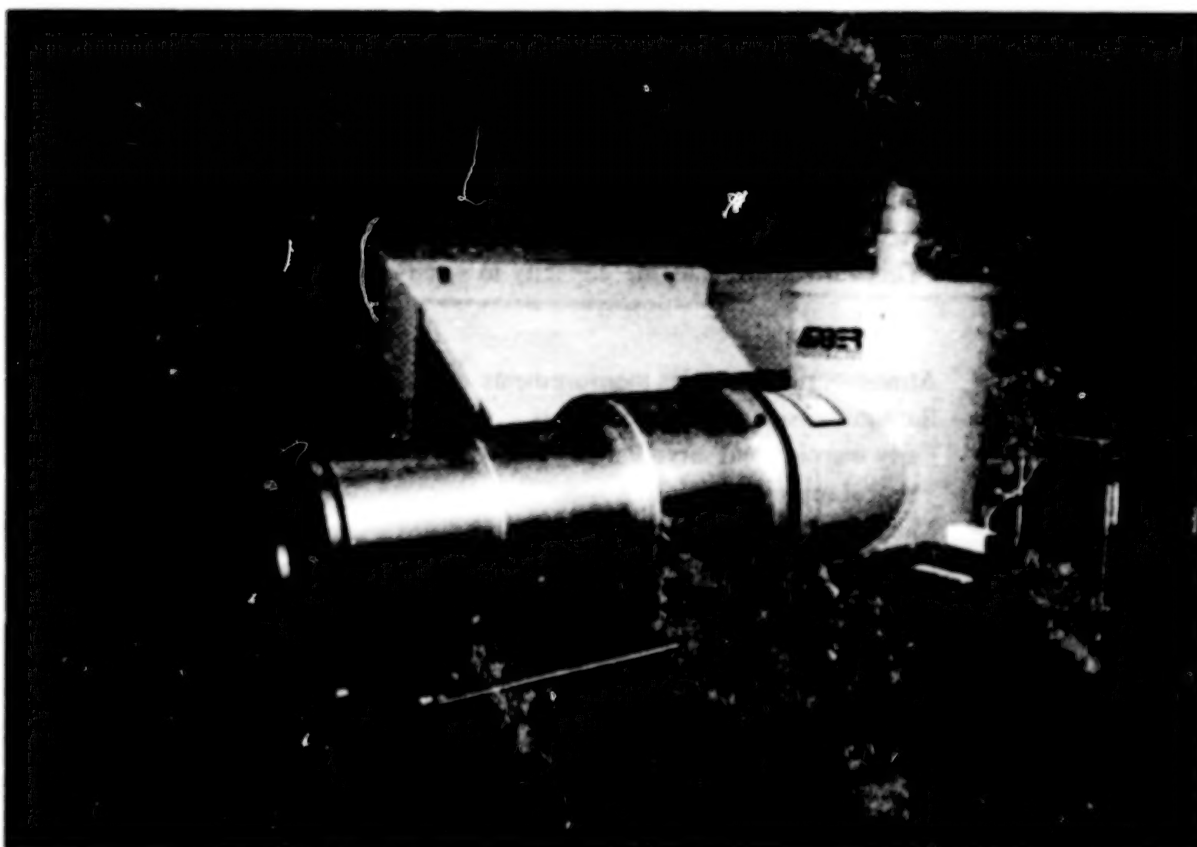


Figure 1.0-1. The Image MultiSpectral System (IMSS) prototype instrument.

This approach to image hyper-spectroscopy utilizes a very simple diffractive optical system as contrasted with the more traditional approach. It is also lightweight, low cost and relatively insensitive to normal vibration effects inherent in an airborne platform.

The IMSS instrument has undergone spectral and radiometric calibration at Pacific Advanced Technology. The spectral point spread function, the spatial point spread function and the spectral purity of the instrument have been measured, and will be reported in future disclosures of device performance.

2.0 MEASUREMENTS AND PERFORMANCE

The predicted spectral resolution for the IMSS instrument is $\Delta\lambda/\lambda = 0.3\%$, (at $4.0\ \mu\text{m}$ that is 7.6 wave numbers) as shown in figure 2.0-1. At shorter wavelengths the spectral resolution is better. A calibration polystyrene film was supplied to PAT by the Jet Propulsion Laboratory (JPL) along with the absorption spectrum as measured by their spectro-photometer. The JPL measured data points, (indicated by square boxes in figure 2.0-2), is superimposed on the spectrum measured using the IMSS system. The measured spectral resolution is better than the predicted performance by a factor of 2, ($\Delta\lambda/\lambda = 0.15\%$) as shown in figure 2.0-2. The IMSS system can resolve 5 wave numbers at $3.23\ \mu\text{m}$.

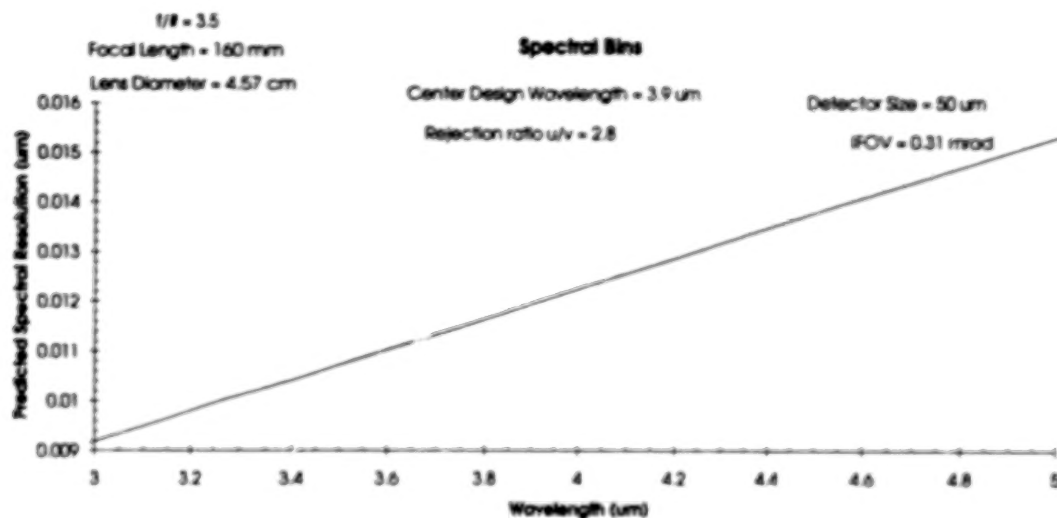


Figure 2.0-1 Predicted spectral resolution of the IMSS instrument.

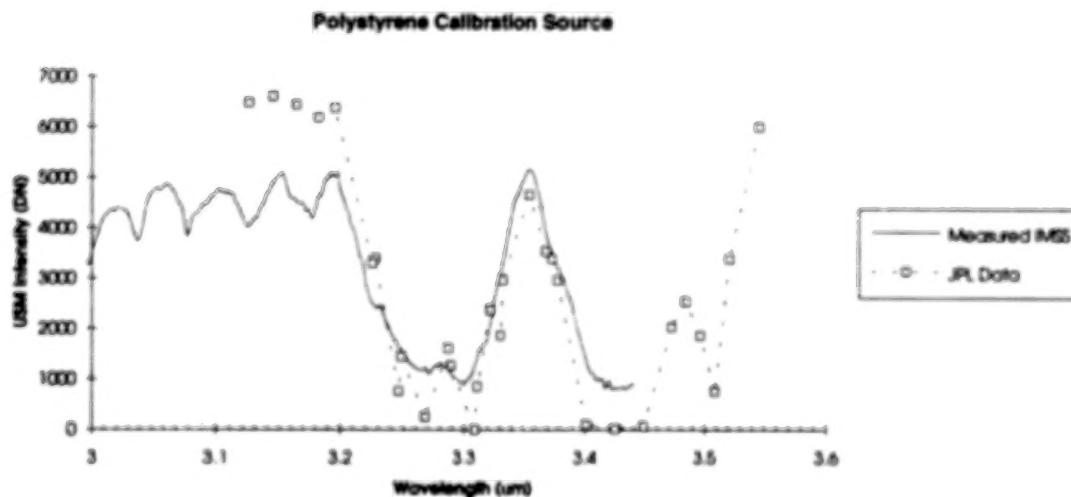


Figure 2.0-2 Comparison of IMSS-measured spectrum and reference spectrum of a polystyrene film.

Figure 2.0-3 shows a series of measurements of sources with known spectral characteristics. Two narrowband spectral filters were used to assess the spectral accuracy of the system over its overall passband from approximately 3.0 to 5.0 μm . Filter N03035-6 has 50% transmission points at 2.976 and 3.101 μm , as indicated with vertical lines in the figure. The characteristic polystyrene absorption profile near 3.35 μm using a JPL-supplied polystyrene film combined with the 3.391 μm spectral line present in a helium-neon laser provided spectral markers near the center of the system passband. On the far end of the overall bandpass region, filter number N04324-4 was used which has 50% points at 4.223 and 4.426 μm .

The cutoff 50% point for the midwave bandpass filter #N04324-4 is accurately measured, but the CO_2 absorption in the 30-foot air path between the instrument and the target contributes to a quenching of the signal at the 50% cuton condition. The CO_2 absorption was measured with IMSS using a soldering iron behind a pinhole. The left-most bump in this filter's bandpass response is produced by the multiplication of the filter's bandpass response with the absorption effect of the CO_2 in the air path. As the air path begins to transmit on the longwave side of the CO_2 absorption, the measured filter transmission recovers to a peak value, and then falls as the longwave side of the filter transmission is mapped out by the IMSS system. Notice that the measurements for the short and midwave bandpass filters favorably correspond to their expected bandpasses.

First Order Spectral Calibration for IMSS

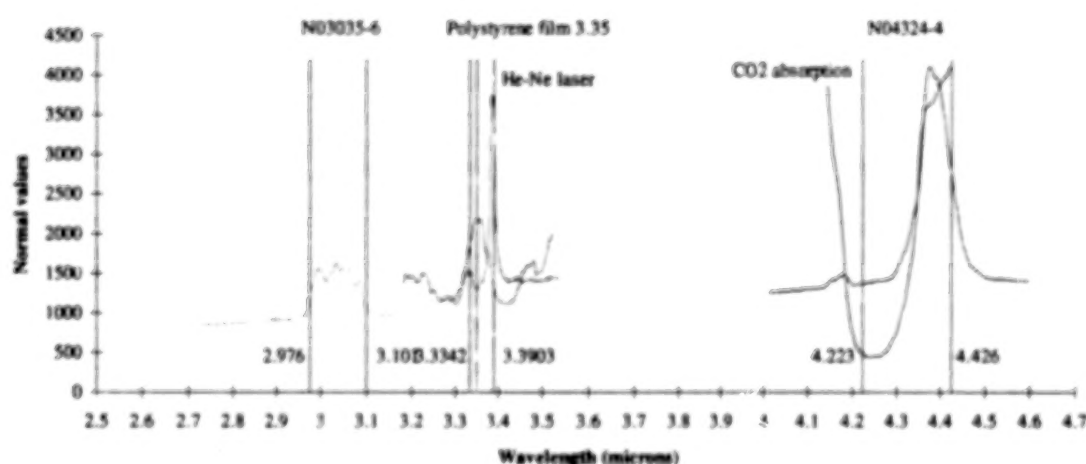


Figure 2.0-3. IMSS data with spectral calibration corrections applied.

Figure 2.0-4 presents the IMSS-measured spectrum of a 0.5 mw helium-neon laser cavity. To make this measurement, we imaged the laser cavity through the front window of the laser from a distance of approximately 30 feet.

Neon Laser Lines and Plasma Discharges over IMSS Data

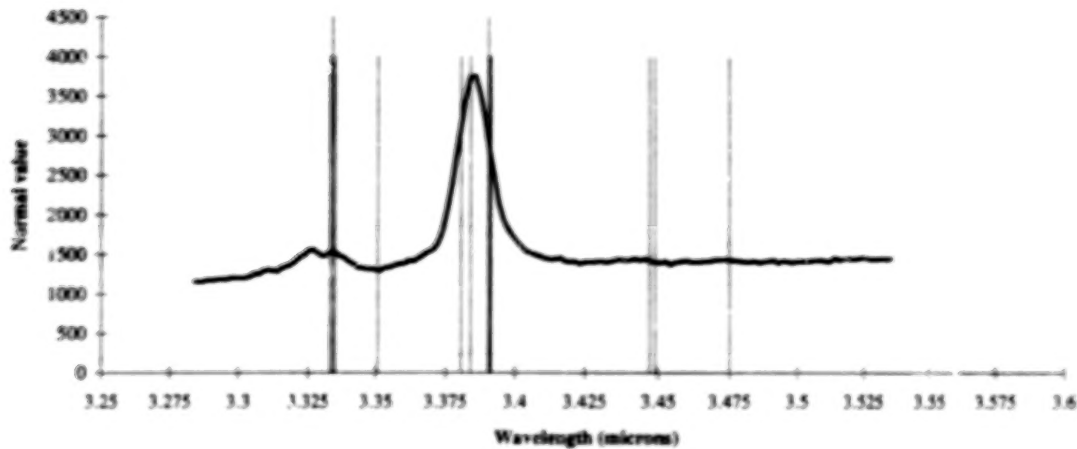


Figure 2.0-4. A helium-neon laser cavity spectrum shows plasma radiation.

The peak around 3.39 μm was expected, but the shorter small peak near 3.325 μm was an unexpected result. Discussions of this with colleagues at the IRIS Targets, Backgrounds and Discrimination meeting did not point to a potential mechanism, but further investigation with Melles Griot (a manufacturer of HeNe lasers) has revealed that the plasma contained in the tube has two strong $3s^2$ electronic transitions which occur at 3.3903 and 3.3303 μm . Superimposed on the spectral measurement of figure 2.0-4 are the two $3s^2$ transitions (shown as taller indicator lines) as well as numerous laser lines. A probable explanation for why the 3.39 μm line is so broad and not centered at precisely 3.391 μm is due to the fact that the laser mirrors are coated to quench this signal in order to enhance the red HeNe laser emission. Our measurement may be indicating the slight inefficiency of the spectral notch filter provided by the mirror coatings. It is also interesting that we have been told that conventional non-imaging spectrometers cannot measure these two emissions because this measurement requires the imaging of the laser cavity itself so as to monitor transitions occurring in the plasma. Non-imaging spectrometers can only measure the spectral content in the energy transmitted out of the cavity.

Signal Processing Applied to HeNe Cavity Spectra

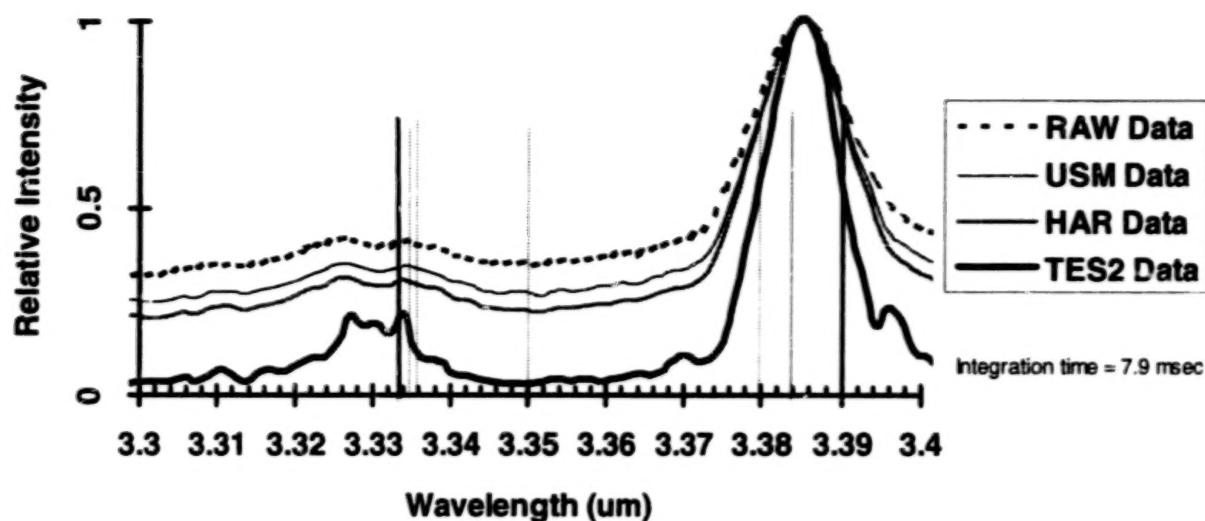


Figure 2.0-5. Signal processing techniques applied to measured spectra enhance the spectral resolution of the data.

Efforts are now underway to increase the spectral resolution of the IMSS system by performing detailed image processing operations on the recovered spectra. These techniques will be the topic of a following paper. Figure 2.0-5 shows the improvement in spectral contrast which is achievable with the use proprietary algorithms which extract spectral information from the infrared images.

Figure 2.0-6 shows how the cuton bandpass of the coldfilter (which is internal to the IMSS dewar) compares to the spectral measurement of the short bandpass filter, #N03035-6. This filter's 50% point is approximately 0.2 microns longer than the coldfilter's (AE-C0048) 50% point. The reduced amplitude of the narrowband filter's transmission is modulated by the turn-on slope of the internal cold filter.

AE Cold Filter C0048 v Short Band Filter N03035-6

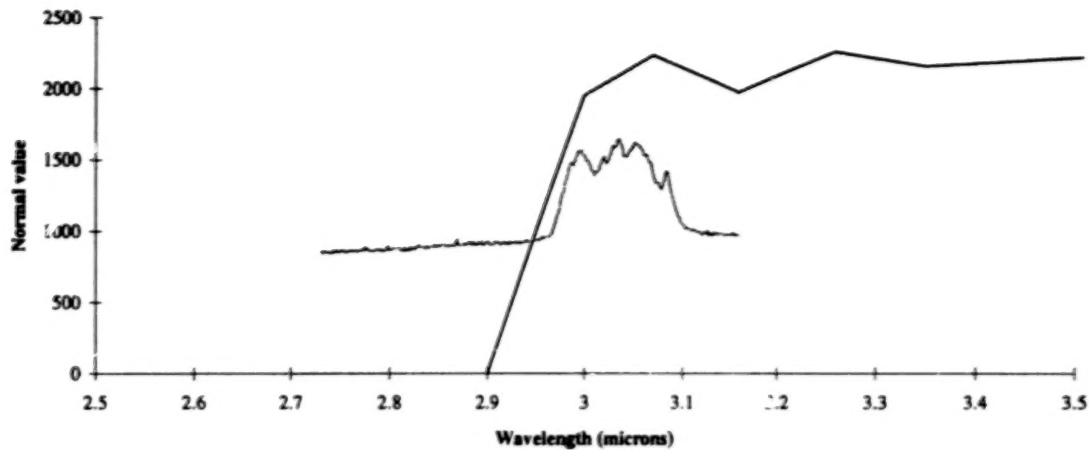


Figure 2.0-6. IMSS internal coldfilter cuton response with respect to a narrow passband filter transmission measured with the device.

Two overlaid spectra are presented in figure 2.0-7, representing the spectrum of a butane flame for each of two fuel-air mixture ratio conditions. Each of the plots in the figure represent the average of three spectral runs at the indicated condition. The strongest spectral features are the CO₂ emission lines, the blue and red spike showing at 4.2 and 4.5 μm region and the unique butane spectrum at 3.4 μm . This data was taken using 320 spectral bins per μm , 1/2 of the full spectral resolution of the IMSS system..

Dirty & Clean Burning Butane Flame

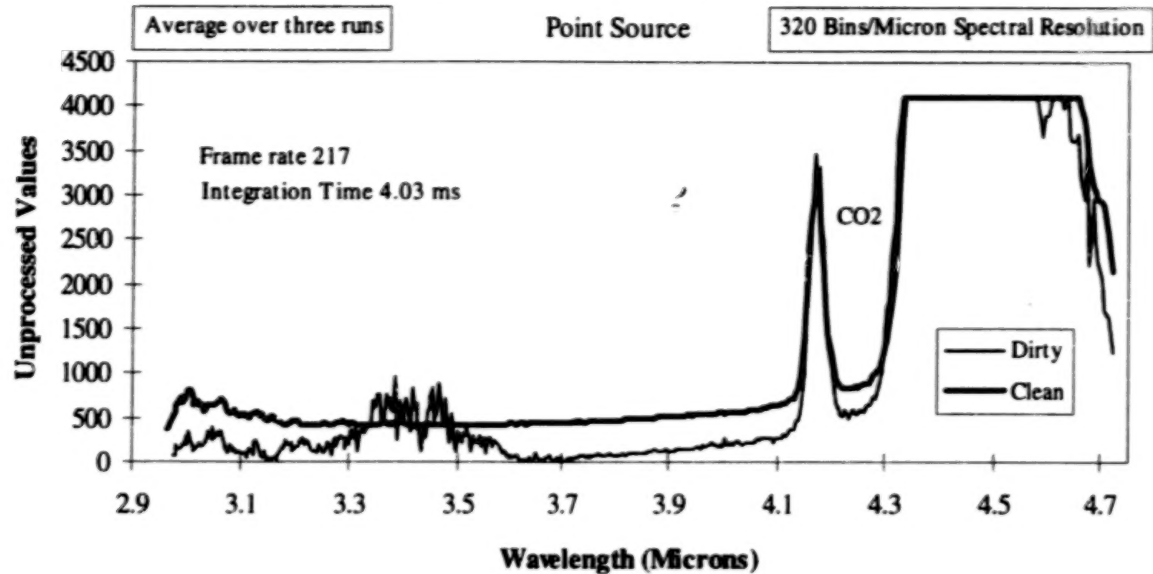


Figure 2.0-7. Butane flame spectra for two fuel-air mixture ratio conditions as measured using the IMSS instrument.

The difference between a clean and a dirty burning butane flame is clearly seen in the spectral region 3.0 to 3.7 μm as shown in figure 2.0-8. This data was taken at a spectral resolution of, 260 spectral bins per μm .

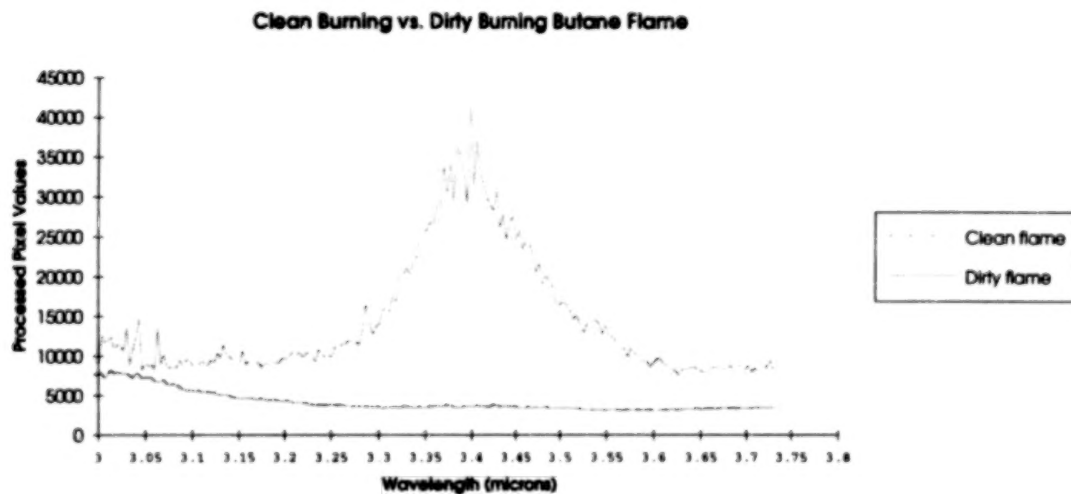


Figure 2.0-8. Clean and dirty burning Butane flame emission spectrum.

Two spectral images of a dirty burning butane flame are shown in figure 2.0-9. The first image is for a spectral bin centered at 3.40 μm and the second is 4.57 μm . Notice the difference in shape for the

two spectral regions. The two distinct spectral lobes in figure 2.0-9 a) are characteristic of all dirty burning butane flames in this spectral region. The spectra for both the lower and upper regions of the flame are shown in figure 2.0-10. The distinct difference in the two regions is clearly discernable. Notice the butane spectral signature in the lower portion and a spectrally flat but temporally varying signal for the upper portion characteristic of shot noise. The significance of this demonstration is that the IMSS instrument provides the capability to measure spectra for different spatial locations in an extended source.

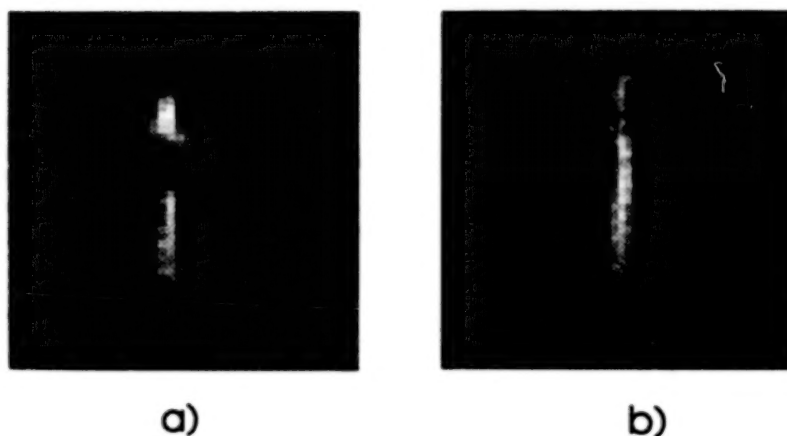


Figure 2.0-9. Spectral images of a Butane flame, a) for a spectral bin centered at 3.40 μm , b) a spectral bin centered at 4.57 μm .

Dirty Burning Butane Flame

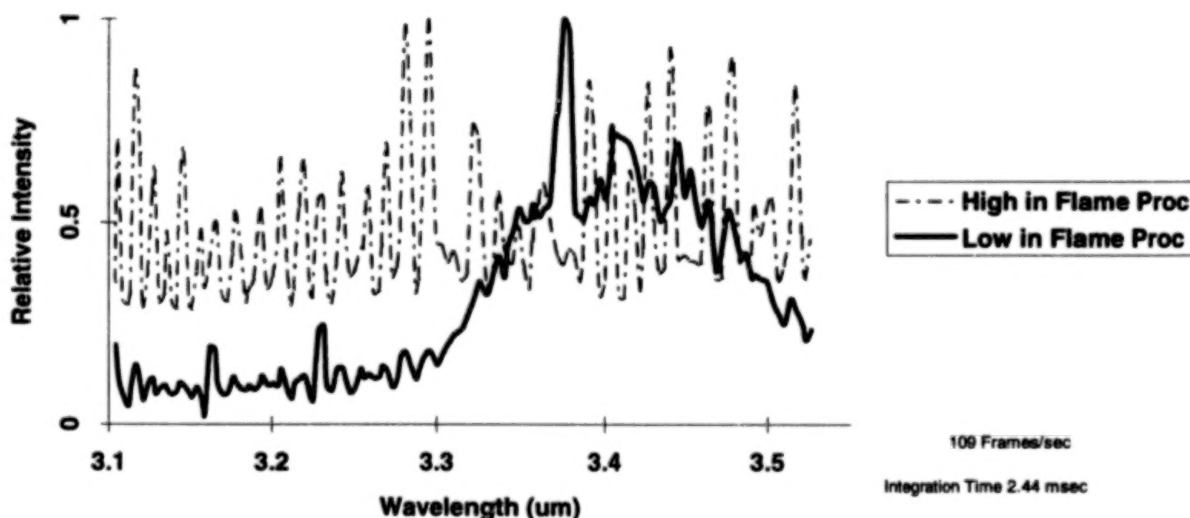


Figure 2.0-10. Spectrum of flame in figure 2.0-9.

To determine the measured spectral structure caused by temporal noise, a ten frame average over each spectral bin was generated. Due to limited frame-grabber memory we were only able to collect the ten frames of high resolution data, (640 bins/ μm) for each spectral bin over a narrow spectral region, (4.35 to 4.47 μm). The data was collected several times in order to determine repeatability and is shown in figure 2.0-11. The data for both a clean and dirty burning butane flame in the transition to the red spike spectral region is shown. As a comparison a 1 frame average per spectral bin is shown. The two spectral measurements for the dirty burning flame are almost identical and slightly lower value than the single frame average. This is the opposite for the clean burning flame.

The most significant point in these measurements is the difference between the fine spectral signature of the clean and dirty flame in the red spike region. For the clean flame there is an emission line at 4.43 μm where this line does not exist for the dirty burning flame.

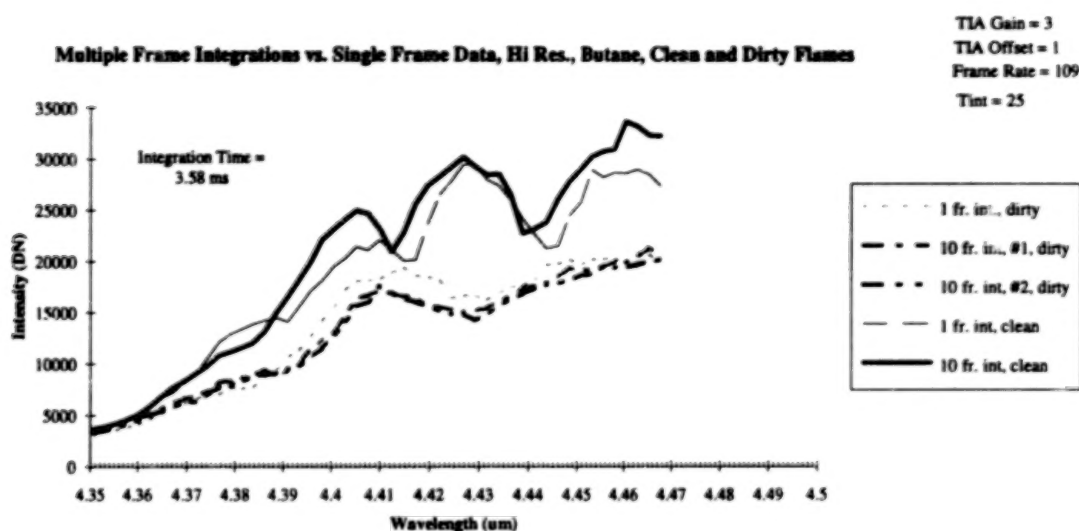


Figure 2.0-11. High resolution spectral data for a clean and dirty burning butane flame in the CO_2 spectral region.

An acetone absorption spectrum was measured using a soldering iron as a blackbody source. The acetone was contained in a plastic bag. Unfortunately the plastic bag has an absorption line right near the acetone absorption line. The spectra for the blackbody transmitted through air, the plastic bag and finally the bag containing the acetone were measured and are shown in figure 2.0-12.

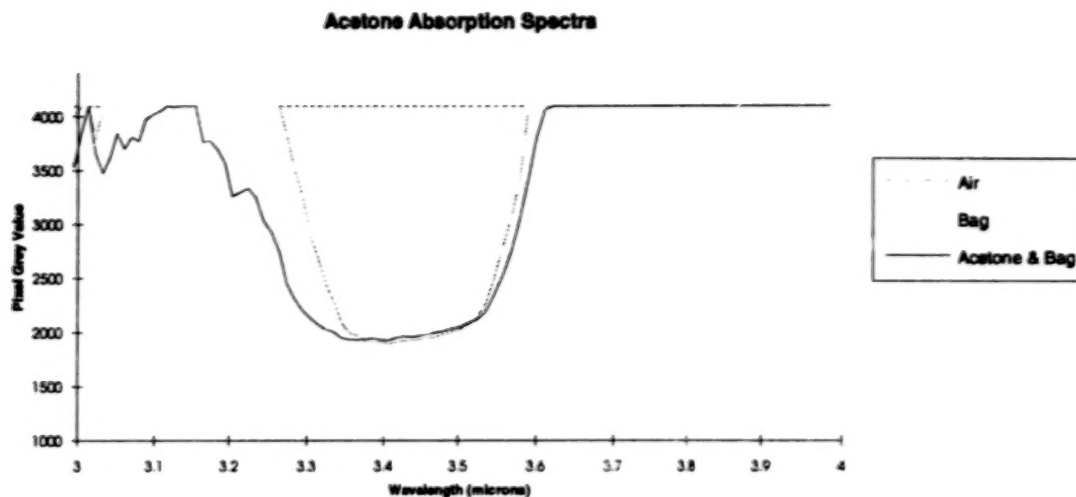


Figure 2.0-12. Acetone, plastic bag and air absorption spectrum.

The spectrum of the acetone alone is shown in figure 2.0-13. The acetone spectrum can be recovered by dividing the combined absorption profile by the absorption profile of the bag alone because absorption is a multiplicative transfer function. This is only truly accurate where none of the components are in a saturated condition.

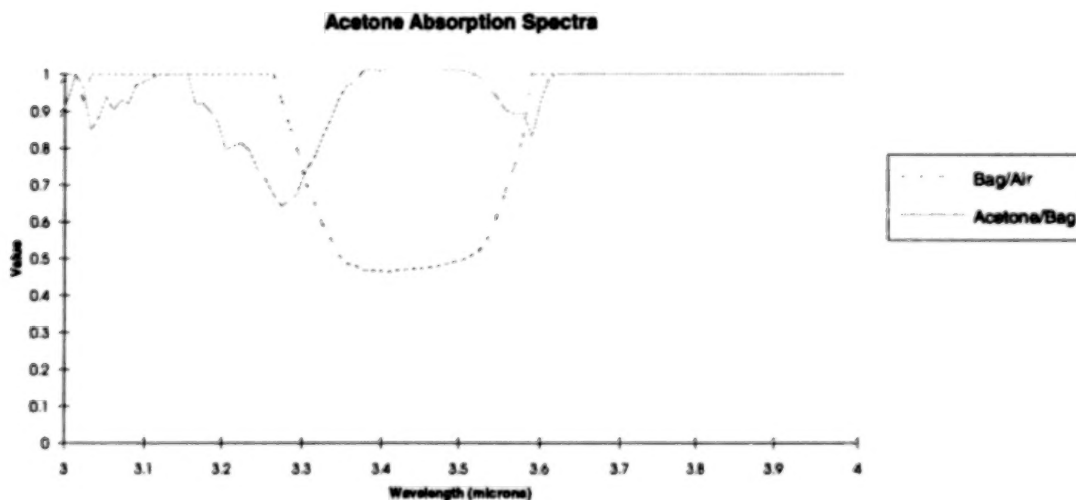


Figure 2.0-13. Acetone absorption spectra as measured using the IMSS instrument.

A series of tests were performed to determine the transmission spectrum from a narrowband infrared filter with its passband centered at 3.90 microns. The purpose of these tests were to determine if the recovered spectra were repeatable; i.e., are the measured variations truly of a spectral nature, or are they the result of temporal variations in the respective data sets? Figure 2.0-14 presents data from two independent runs in which the 3.90 micron filter was placed in front of a pinhole, behind which was located an extended-area blackbody with a surface temperature of 150C. The pinhole subtended a 1x1 pixel angular width at the focal plane. The figure shows the "raw" spectral data as well

as the result of a post-measurement signal processing process which has been implemented to improve the spatial and spectral resolution of the data.

Notice the high degree of correlation which exists for the two spectral measurement datasets. This test indicates that the recovered spectral data for this experiment is due mainly to the combined spectral characteristics of the blackbody source and the narrowband filter, not due to temporal effects which could have influenced the data. The applicability of using the IMSS approach for measuring and analyzing the spectral characteristics of unresolved point objects has also been demonstrated with this test.

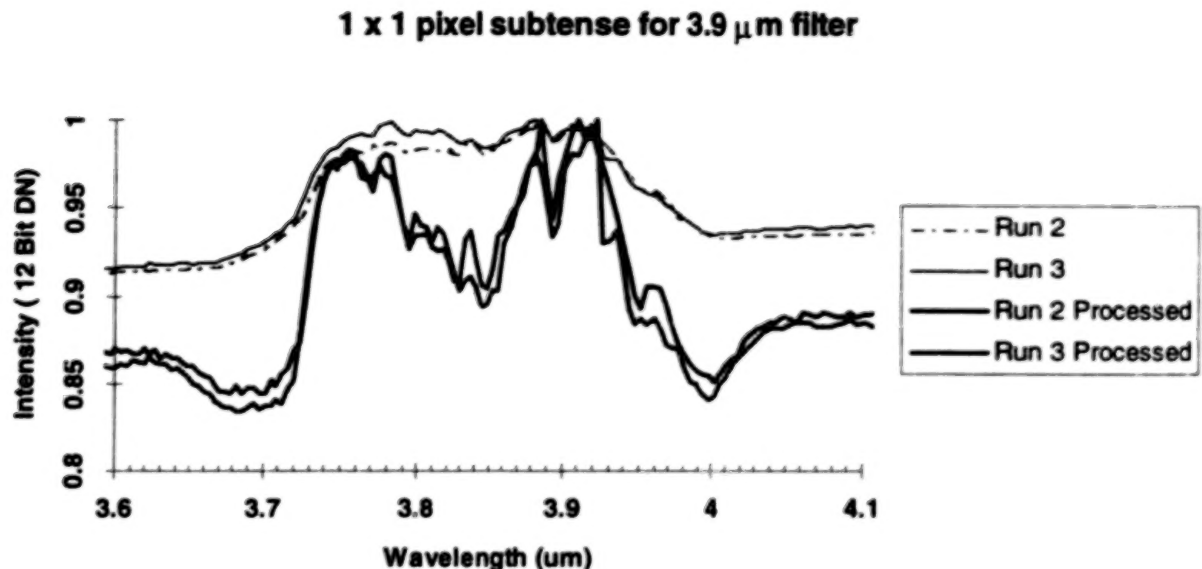


Figure 2.0-14. A high degree of correlation is achieved when measuring the transmission spectrum of a narrowband infrared filter at 3.90 microns.

The task of discriminating objects from a cluttered infrared background is a particularly difficult processing task for wideband infrared sensor systems, but the spectral sensing capability of the IMSS permits such assessments to be made in a straightforward manner. Figure 2.0-15 shows a 4.4990 μ m image of a houseplant with a house key embedded within the foliage. Also included in this image are other background types such as mylar wrapping around the base of the plant. A similar image was recorded at 3.9001 μ m, and a plot of pixel-specific sensor signal values plotted at these two specific wavebands is shown in Figure 2.0-16.



Figure 2.0-15. A houseplant with an embedded key is imaged at 4.4990 microns.

Cederquist has shown that there exists a high degree of spectral correlation for infrared detections produced by a given material¹. Notice, for example, that the mylar foil produces detections which are correlated into a clearly discernible line in this two-wavelength space. The house key which was embedded in the plant produces higher signals because it has characteristic specular reflections. Measurements of terrestrial targets embedded in clutter using IMSS is performed with high temporal, spatial and spectral resolution.

This data suggests the possibility of using the IMSS system (or a derivative of the technology) to remotely monitor environmental conditions and to discriminate between different geological or vegetative regions based upon their differences in spectral emissivities. It should be possible to discriminate groundwater from soil, and perhaps healthy from stressed vegetation.

Discrimination Between Objects and Clutter Using Unprocessed IMSS Data

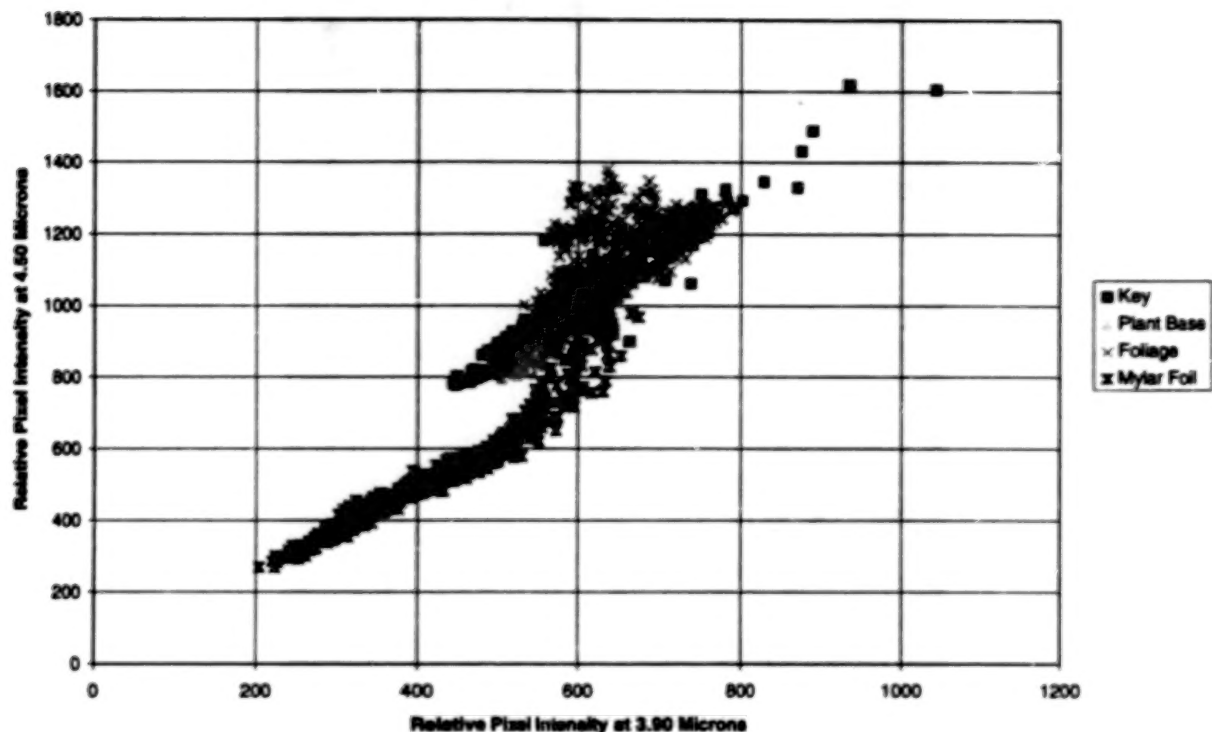


Figure 2.0-16. Preliminary clutter discrimination studies indicate the suitability of using the IMSS technique for discriminating targets with known spectral signatures from clutter.

4.0 PLANNED FUTURE ACTIVITIES

Atmospheric absorption properties may be measured with this instrument because the random access nature to the spectral tuning characteristics of the device permit the analysis of path-length absorption using known thermal emission profiles. For example, the absorption properties of the Earth's atmosphere were recently measured by observing a full moon with the IMSS instrument in the spectral region from 4.0 to 4.6 μm . The known spectral profile of reflected solar energy was used to evaluate the path-length absorption property of the atmosphere.

Measurement tasks have been proposed to remotely discriminate groundwater from soil or other groundcovers from an airborne platform. Similar techniques could be used to remotely monitor the condition of oil fields or ground-contamination of soil by detecting hydrocarbon-containing compounds on the surface of the soil.

IMSS technology has applications in the areas of target detection in the presence of infrared clutter, chemical vapor detection, remote monitoring of automobile and airborne pollutants, and other applications where high spectral resolution is required with the added capability of simultaneous imaging. Spectral calibration of the system is a continuing process. Preparations are being made to bring the prototype system to a test facility that will permit the direct comparison of the IMSS spectral data

000370

000000

with that of more conventional spectrometers. An automobile emissions test facility will also be used to determine the suitability of IMSS to the remote measurement of pollutants in moving automobiles.

A longwave infrared (LWIR) version of the IMSS is planned, which will use a 128 x 128 array of LWIR detectors. The characteristic absorption profiles of certain chemical and biological agents reside in the 9.0 to 11.0 μm spectral region, so a detector applicable to this spectral region must be used in place of the currently-installed InSb detector array.

5.0 SUMMARY

Based upon the work as presented in this paper we have shown how the IMSS instrument can measure the fine structure in the emission of a butane flame. We have also shown how IMSS can measure the absorption spectra of acetone as well as the ease with which IMSS can measure the spectral correlation function of cluttered backgrounds and targets. Using this instrument, differences in the fuel-to-air mixture ratio of hydrocarbon burning fuels can be measured, and aircraft types can be identified.

The IMSS is a versatile instrument that can be used in many different applications. The IMSS instrument can be used to collect signature data on different aircraft and missiles. In addition, the IMSS technique can be used in fieldable systems for non-cooperative target identification and identification of friend or foe (IFF). The IMSS instrument can also be used to image and measure the absorption spectrum of gases and therefore detect the presence of biological and chemical warfare agents. Clutter rejection applications for this system abound, and further measurement studies must be made to optimize system performance for a wide range of object and background types.

We have made important advances in the spectral calibration of the IMSS system. More narrow bandpass spectral filters have been ordered to continue the refinement of the spectral calibration of the system. Radiometric calibration is proceeding with the use of an extended area controlled-temperature blackbody source, as well as a variable aperture controlled blackbody source. At the same time, we are developing image processing kernels to improve the spectral resolution of the system for point and extended objects.

We would like to recognize and thank both Phillips Lab and the Air Force Space Division for their support in this program. We would especially like to thank Dr. Paul Le Van, Capt. Alan Hahn both of Phillips Laboratory PL/VTRS Kirtland AFB, and Capt Gordon Pardo of Air Force Space Division SSD/XRF Los Angeles Air Force Base, and Dr. Robert Chambers of the Aerospace Corp. for their continued support and guidance in our efforts. We would like to recognize the support from Cliff Alexander with Wright Laboratory Armament Directorate WL/MNGS for support under a Phase I SBIR to apply IMSS to missile seeker applications. We gratefully acknowledge the assistance of numerous individuals including Harry Gilmore of Toyon Research, Merlin Miller at Physical Sciences, Inc., Ralph Hill at Southwest Research, Inc., Clayton LeBaw at the Jet Propulsion Laboratory, John Selby at Grumman and Richard Sanderson at the Wright Labs. Their technical inputs have helped us to further understand the spectral and radiometric performance of the IMSS system. And finally we would like to thank Jim Buss at ONR for his support on a recently funded Phase I SBIR to use IMSS for shipboardIRST applications.

¹ Cederquist, Jack, "Infrared Multi-Spectral Target/Background Field Measurements", 1994 IRIS Targets, Backgrounds and Discrimination Meeting, 1-3 February, 1994, Monterey, CA.

AN EXAMINATION OF MINE WASTE CONTAMINATION IN THE COEUR D'ALENE RIVER VALLEY, IDAHO USING IMAGING SPECTROMETER DATA

W.H. Farrand^{1,2} and Joseph C. Harsanyi^{1,3}

1) HYDICE Project Office
Naval Research Laboratory
Code 9120
Washington, DC 20375

2) Science Applications International Corporation
1710 Goodridge Drive
P.O. Box 1303, M.S. E-7-3
McLean, VA 22102

3) Applied Signal and Image Technology Co.
9193 Rolling Meadow Run
Pasadena, MD 21122

ABSTRACT

AVIRIS data collected over the Coeur d'Alene river valley in northern Idaho in May 1993 were examined in order to map the distribution of sediments believed to contain heavy metals and to examine variations in the mineralogy of those sediments. Trace metals associated with mine wastes have been observed to aggregate in amorphous iron oxide and/or oxyhydroxide phases. The distribution of such iron-rich sediments in the Coeur d'Alene river valley were mapped using a Low Probability Detection (LPD) algorithm derived from the theory of orthogonal subspace projection. A principal components analysis was applied to the shortwave infrared channels of a set of pixels identified by the LPD technique. This analysis and subsequent observation of the data using a data visualization tool identified four endmembers: an illite-rich sediment, one dominated by kaolinite, one dominated by dickite and a fourth endmember which has some spectral features indicative of the presence of gypsum.

1. INTRODUCTION

The new technology of imaging spectrometry has been used successfully in several important application areas. Among these are mineral and lithologic mapping, mapping and monitoring of vegetation communities, mapping of atmospheric constituents, and the study of alpine snow packs. An area in which this technology has been largely underutilized has been that of remediation of environmentally stressed areas. The work presented herein describes the early stages of an investigation into the use of data from NASA's Airborne Visible/Infrared Imaging Spectrometer (AVIRIS) for mapping the spread of, and assessing changes in the mineralogic character of, tailings from a major silver and base metal mining district.

The area under investigation is the Coeur d'Alene river valley in northern Idaho. Mining has been going on in and around the towns of Kellogg and Wallace, Idaho since the 1880's. In the Kellogg-Smelterville Flats area, west of Kellogg, mine tailings were piled up alongside the South Fork of the Coeur d'Alene River. Until the construction of tailings ponds in 1968 much of these waste materials were washed directly into the South Fork. The Kellogg-Smelterville area was declared an EPA Superfund site in 1983 and remediation efforts are currently underway. Recent studies (e.g., Horowitz et al., 1992) have demonstrated that sediments in the Coeur d'Alene River and in the northern part of Lake Coeur d'Alene, into which the river flows, are highly enriched in Ag, Cu, Pb, Zn, Cd, Hg, As, and Sb. These trace metals have become aggregated in iron oxide and oxyhydroxide minerals and/or mineraloids. Reflectance spectra of iron-rich tailing materials is shown in Figure 1. Also shown in Figure 1 are spectra of hematite and goethite. The broad bandwidth and long band

center (near 1 μm) of the Fe^{3+} crystal-field band of the iron-rich sediment samples combined with the lack of features on the Fe^{3+} - O^{2-} charge transfer absorption edge indicates that the ferric oxide and/or oxyhydroxides in these sediments is poorly crystalline to amorphous in character. Similar features are seen in poorly crystalline basaltic weathering products (e.g., palagonites) (Farrand and Singer, 1992).

The problem of mapping and analyzing the downriver occurrences of iron rich tailings in the Coeur d'Alene (CDA) River Valley using remotely sensed data is complicated by the full vegetation cover present in the area. Because exposures of rock and soil were sparse, the data processing techniques used in this study were sensitive to detecting materials at subpixel scales. The methods used included spectral mixture analysis (Adams et al., 1993) and a low probability detection technique (Harsanyi et al., 1994).

2. DATA

The CDA River Valley is currently under investigation by the Spokane field office of the USGS (C. Smith, pers. comm.). In a cooperative endeavor between the USGS, the EPA and the Naval Research Laboratory's HYDICE (Hyperspectral Digital Imagery Collection Experiment) Project Office an AVIRIS flight was scheduled over the CDA River Valley. Data was collected on May 24, 1993 at 21:40 UTC. Incomplete coverage of the target area led to a reflight on September 17 at 19:40 UTC. The data examined for this paper consists of two scenes from the May 24 data collection that cover an area extending down river from approximately the Cataldo Mission to Killarney Lake (see Figure 2).

The reflectance of samples collected in the field were measured in the laboratory. A subset of the samples were measured at Brown University's RELAB. The majority of the samples were measured on the USGS Reston Beckman¹ (UV5240).

The AVIRIS data was analyzed in a radiometrically calibrated format and also in a format with DN equal to apparent surface reflectance. The conversion from radiance to reflectance was done using both surface reflectance data and the ATREM (Gao et al., 1993) radiative transfer based approach. First the data were converted to apparent surface reflectance through the use of ATREM. As noted by Farrand et al. (1994), radiative transfer based approaches produce reflectance spectra that are inherently noisier than those derived from empirical approaches that make use of the image data. A flat field or empirical line method (Farrand, 1992) correction effectively damps down noise in the hyperspectral data by dividing the image cube through by gain values derived from the data itself. Gain factors derived from a radiative transfer based approach divide the noisy radiance data by a noise-free model radiance spectrum and thus accentuate the noise in the data. The advantage that radiative transfer approaches offer over empirical or surface based approaches is that they can calculate a different gain and offset value for each pixel and thus can better account for atmospheric variability within a scene. Thus for the CDA data, atmospheric variability was removed using ATREM and this was followed by the application of a modified flat field (MFF) method (Farrand, 1992) applied to the ATREM corrected data.

3. ANALYSIS

The AVIRIS radiance data were initially examined with a spectral mixture analysis. An iterative approach utilizing several runs and successive examination of the resulting RMS error images (Adams et al., 1993) suggested four endmembers: shade, vegetation, an agricultural soil, and an iron oxide or oxyhydroxide rich soil. ATREM+MFF corrected AVIRIS spectra of the three material endmembers are shown in Figure 3. As was discussed above, the iron-rich soil is the most likely candidate for bearing heavy metals leached from the mine tailings. Inspection of the fraction image for this endmember produced a poor correspondence between the occurrence of such soils and the areas

¹ The use of brand names is for descriptive purposes only and does not imply endorsement by the authors or their respective institutions.

appearing bright on the fraction image. Many other materials (for instance, the pavement on I-90) were being modeled as iron-rich soil.

In order to cut down on the false alarm rate, a recently developed detection algorithm that has already shown good success in detecting poorly exposed lithologies (Farrand and Harsanyi, submitted) was brought to bear on the problem. Although it was used as an endmember in the spectral mixture analysis, the iron-rich soil was not thought to be very prevalent within the scene, thus it is a good candidate for use with the Low Probability Detection (LPD) routine (Harsanyi et al., 1994). For greater detail on the LPD method, the reader is referred to the above references; however a brief description of the method is given below. The technique accounts for the effects of linear mixtures by treating the mixed pixel as being composed of desired and undesired spectral signatures. Viewed in this manner, the equation describing a mixed pixel becomes:

$$L = da + Ug + n \quad (1)$$

where L is the reflected radiance reaching the sensor from the mixed pixel, d is the desired spectral signature of the material of interest, a is the desired signature abundance, U is a matrix whose columns are the undesired spectral signatures, and g is a vector containing the abundances of the undesired signatures. The vector n is assumed to be Gaussian noise which is independent and identically distributed.

In the case where the columns of U are known, an orthogonal subspace projection operator, P can be constructed:

$$P = (I - UU^{\#}) \quad (2)$$

where $U^{\#} = (U^T U)^{-1} U^T$ is the pseudoinverse of U . Multiplying this operator against every term in equation (1) has the effect of eliminating the Ug term thereby leaving only a transform of the desired target signature.

When the columns of U are not known, an estimate of their contribution can still be gleaned from the data. In this case, an estimate of the projection operator in equation (2) can be obtained from the first and second order statistics of the scene or scene subsection being processed. It is shown in Harsanyi (1993) and Harsanyi et al. (1994), that an operator:

$$w^T = d^T \tilde{P} \quad (3)$$

can be formed which will not only act to null the unknown, undesired background signatures, but also will maximize the SNR of the desired low probability target spectrum.

LPD was applied to the subsections of the two AVIRIS scenes shown in Figure 4 (a) and (c). The target spectrum for input to the LPD routine was derived from the data itself. The RELAB measured laboratory reflectance of a sample (designated BH-3 and shown in Figure 1) from the Cataldo Flats area was used as input to the Spectral Angle Mapper (SAM) program contained in the SIPS software package (Kruse et al., 1993) and applied to a portion of the AVIRIS scene containing Cataldo Flats. Since the SAM program provides a measure of spectral similarity, three pixels most like the BH-3 sample were thus identified. The radiance spectra of these pixels were then extracted from a radiance data set that was subsectioned to 190 bands to exclude several of the shortest and longest wavelength bands, spectrometer overlap regions and atmospheric water absorptions at 1.4 and 1.9 μm . These radiance spectra were averaged and the average was used as input to the LPD routine. The resulting LPD component images are shown in Figure 4 (b) and (d). As might be expected, the iron-rich sediments are concentrated primarily along the CDA River. Weaker responses are returned from some fields in the CDA River Valley.

The LPD routine identified 86 pixels in the two scenes that were most like the iron-rich sediments at Cataldo Flats. These were then extracted from the ATREM+MFF corrected data cube and transformed via a principal components analysis. Because of the small number of iron-rich sediment pixels, not all 190 bands could be analyzed at once. Instead, two PC analyses were conducted one utilizing 41 SWIR bands and another utilizing 82 VNIR bands. The results of the VNIR analysis were rather inconclusive due primarily to the contaminating effect of vegetation reflectance features. In the SWIR, the reflectance of green vegetation closely resembles that of liquid water, thus the variation in spectral properties in the SWIR is due more to mineralogical variations than to vegetation.

The first three principal components of the SWIR analysis were examined interactively using the "XGobi" data visualization program (Swayne et al., 1992). By rotating the data cloud, spectrally extreme "endmember"² pixels could be identified. A two dimensional projection of the 2nd versus the 3rd PC is presented as Figure 5. This figure shows the outline of a rough tetrahedron. The vertices of the tetrahedron in Figure 5 equate to approximate endmembers within the set of iron-rich sediment pixels. Figure 6 shows spectra of these iron-rich sediment endmembers. For discriminating differences in iron mineralogy, one would need to do the analysis in the VNIR. Since this analysis focused on the SWIR, variations in clay and evaporite mineral mineralogy is highlighted. Thus the four endmembers consisted of an illite-rich sediment, one dominated by kaolinite, one dominated by dickite and fourth endmember which has some spectral features indicative of the presence of gypsum.

A number of iron-rich sediment samples whose reflectance spectra were measured in the laboratory had features more reminiscent of the illite-rich "endmember". Closer analysis of the "illite-rich" pixel spectra in the 2.2 to 2.3 μm region (see inset in Figure 6a) indicates that the phyllosilicate mineralogy might more aptly be described as muscovite altering to illite. The "illite-rich" pixels have reflectance minima in the 2.203 and 2.342 μm AVIRIS bands. The PS-11a illite sample in the JPL spectral library (Groves et al., 1992) have band minima at 2.216 and 2.336 μm . The PS-16a muscovite sample in the JPL spectral library has reflectance minima at 2.192 and 2.344 μm . Thus the AVIRIS pixel spectra probably contain a mixture of muscovite and its decomposition product, illite.

Two of the other endmembers appear to represent variations in the internal structure of the clay mineral kaolinite. One of these endmember spectra (shown in Figure 6b) appears more representative of kaolinite and the other more representative of the compositionally identical but structurally dissimilar mineral dickite.

The interpretation that the final endmember contains gypsum is based primarily on reflectance minima at 1.44 and 1.48 μm . Overall the single pixel spectrum shown in Figure 6a shows evidence of the presence of several materials including the iron oxide or oxyhydroxide phase that is present in all 86 of the LPD-identified spectra, vegetation (evidenced by a weak red edge slope feature at 0.7 μm) and abundant liquid water as is indicated by the strong absorptions at 1.4, 1.9 and the wing dipping beyond the measured wavelength range towards 2.7 μm . Some of the water is probably contained in the vegetation, but the doublet longwards of 1.4 μm is indicative of molecular water bound in a mineral phase. The specific locations of the minima are more indicative of gypsum than of clays or zeolites. In dry weather, an efflorescent crust has been observed to form along the banks of the CDA River (C. Smith, pers. comm.), a primary component of which is gypsum. The weather at the time of the May overflight had not been particularly dry so perhaps what is being seen is due to fine-grained solid particles of gypsum and gypsum in solution in wet bankside sediments.

4. CONCLUSIONS

The problem of tracking and analyzing mine waste contamination remotely through the use of imaging spectrometer data is a challenging one. This paper has presented early results from a study examining the distribution of, and compositional variations in, ferric oxide bearing fluvial sediments

² The term "endmember" is used with some caution here. Because of the limited number of pixels included in the analysis and the wide GIFOV of AVIRIS (effectively 20 by 40 m over all spectral bands, see Farrand and Harsanyi (1994)) few if any of the identified "endmember" pixels are "pure" (pure in the sense that they contain only one material).

carried by the Couer d'Alene (CDA) river in northern Idaho. Other studies (e.g., Horowitz et al., 1992) have identified such sediments as the carriers of trace metals released by silver and base metal mining activities in the area. Laboratory spectroscopy of samples collected from the CDA river valley suggests that the ferric oxides and/or oxyhydroxides carrying the trace metals are poorly crystalline to amorphous in character.

In order to map the distribution of these sediments, a Low Probability Detection (LPD) algorithm was employed. The LPD algorithm treats spectral mixtures as a linear problem and provides a means of detecting and mapping materials which are not widely distributed within a scene. LPD was applied to two scenes of AVIRIS data collected in May 1993. The target spectrum was the average radiance of three pixels within the exposed iron-rich sediments at Cataldo Flats. 86 pixels within the two scenes were identified as being most like Cataldo Flats sediments. Mineralogic variations within this set of pixels were examined through the use of principal components analysis and an interactive data visualization tool. Four "endmembers" within the ferric oxide rich sediments were identified. Since the PCA analysis utilized SWIR channels, the endmembers express differences in clay and sulphate mineralogy. The four endmembers display spectral features judged characteristic of illite, kaolinite, dickite and gypsum.

Much work remains to be done on the CDA AVIRIS data set. More scenes from both the May and the September flights need to be examined. By studying more scenes, more ferric oxide rich pixels can be identified and the PCA analysis can be repeated with a larger number of samples. Repeating the analysis with a greater number of pixels will help to show if the mineralogic variations identified in this study are present over a broader region. Field work is also necessary. First, such work can be used to verify the results indicated by the remotely sensed data. Secondly, geochemical analysis of sample areas identified in the imaging spectrometer data will indicate if the changes in mineralogy of the iron-bearing sediments has any correlation with trace metal content.

ACKNOWLEDGEMENTS

Several sediment samples were provided by Cole Smith and Steve Box of the USGS Spokane. Thanks to Mel Podwysocki of the USGS Reston for allowing the first author access to the USGS Reston Beckman spectrometer and for helpful discussions. Thanks to Steve Pratt of Brown University's RELAB for measuring the reflectance of several samples. Special thanks to Mark Landers and Pete Mitchell of the HYDICE Project Office for their interest and support.

REFERENCES

- Adams, J.B., M.O. Smith, and A.R. Gillespie (1993) Imaging spectroscopy: Interpretation based on spectral mixture analysis. in *Remote Geochemical Analysis: Elemental and Mineralogical Composition*, (C.M. Pieters and P.A.J. Englert, ed.s), Cambridge University Press, New York, pp. 145-166.
- Farrand, W.H. (1992) A comparison of methods for retrieving apparent surface reflectance from hyperspectral data. *Proceedings of the International Symposium on Spectral Sensing Research*, pp.1154-1164.
- Farrand, W.H. and R.B. Singer (1992) Alteration of hydrovolcanic basaltic ash: Observations with visible and near-infrared spectrometry. *Journal of Geophysical Research* 97, pp. 17,393-17,408
- Farrand, W.H., R.B. Singer, and E. Merenyi (1994) Retrieval of apparent surface reflectance from AVIRIS data: A comparison of empirical line, radiative transfer, and spectral mixture methods. *Rem. Sens. Env.*, 47, 311-321.

- Gao, B.-C., K.B. Heidebrecht, and A.F.H. Goetz (1993) Derivation of scaled surface reflectances from AVIRIS data. *Rem. Sens. Env.* 44, 165-178.
- Groves, C.I., S.J. Hook, and E.D. Paylor (1992) Laboratory reflectance spectra of 160 minerals, 0.4 to 2.5 μm , JPL Publication 92-2, Pasadena, CA.
- Harsanyi, J.C. (1993) Detection and classification of subpixel spectral signatures in hyperspectral image sequences, Ph.D. thesis, The University of Maryland Baltimore County, 116 pp.
- Harsanyi, J.C., W.H. Farrand, and C.-I. Chang (1994) Detection of low probability, subpixel targets in hyperspectral image sequences with unknown backgrounds (submitted to) *Trans. Image Proc.*
- Horowitz, A., K.A. Elrick, and R.B. Cook (1992) Effect of mining related activities on the sediment trace element geochemistry of Lake Coeur d'Alene, Idaho, USA: Part 1. Surface sediments, U.S. Geological Survey Open-file Report 92-109, 30 pp.
- Kruse, F.A., A.B. Lefkoff, J.W. Boardman, K.B. Heidebrecht, A.T. Shapiro, P.J. Barloon, and A.F.H. Goetz (1993) The Spectral Image Processing System (SIPS)- Interactive visualization and analysis of imaging spectrometer data. *Rem. Sens. Env.* 44, 145-164.
- Swayne, D.F., D. Cook and A. Buja (1992) User's manual for XGobi, *Bellcore Technical Memorandum*

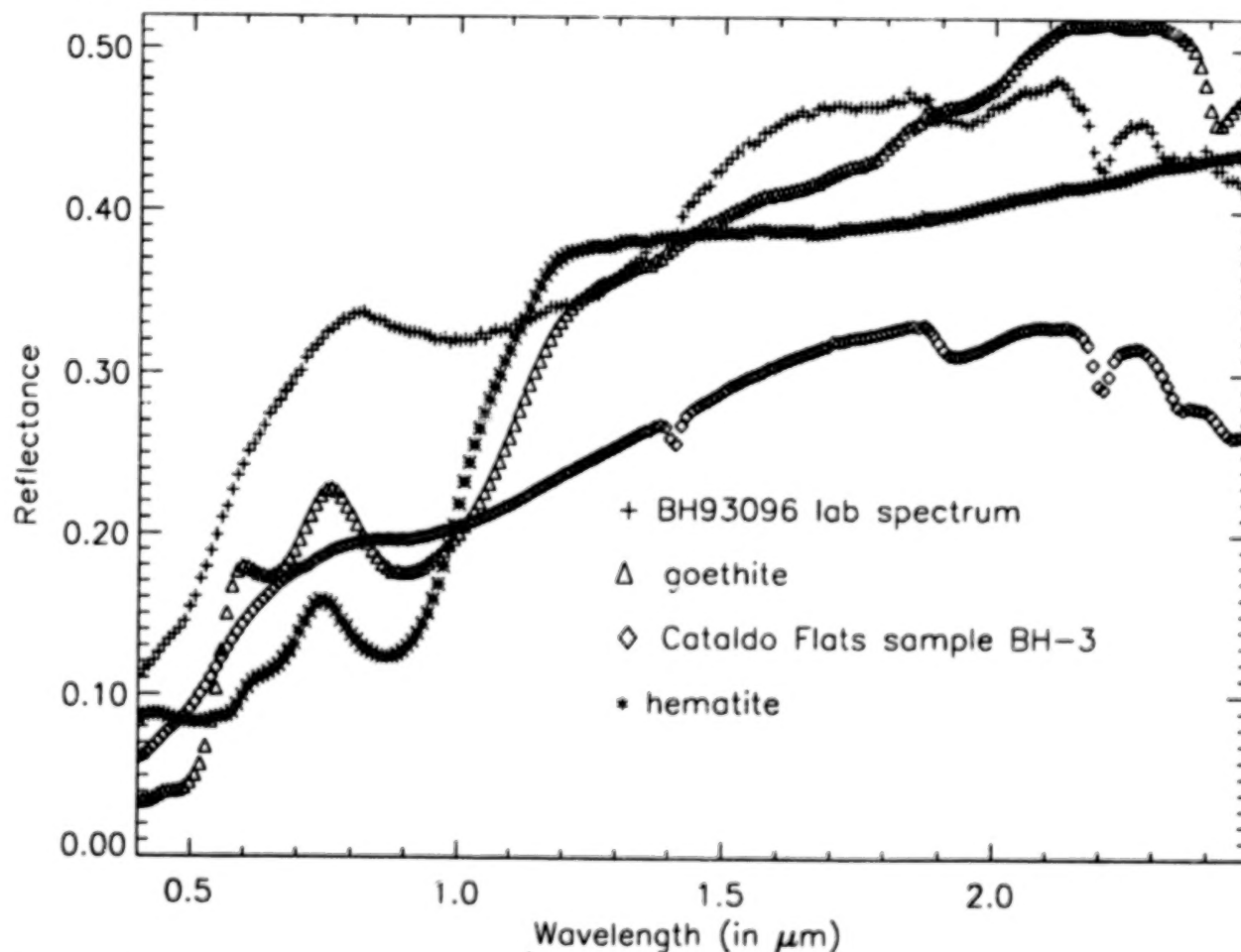


Figure 1. Laboratory reflectance spectra of iron-rich sediments collected near the Coeur d'Alene River compared against library spectra of goethite and hematite. The longer wavelength of the band center of the primary Fe^{3+} crystal field absorption in the CDA sediment samples combined with its broader character along with the lack of any distinct features on the UV absorption edge indicates that the ferric ion bearing minerals in the CDA sediments is amorphous in character.

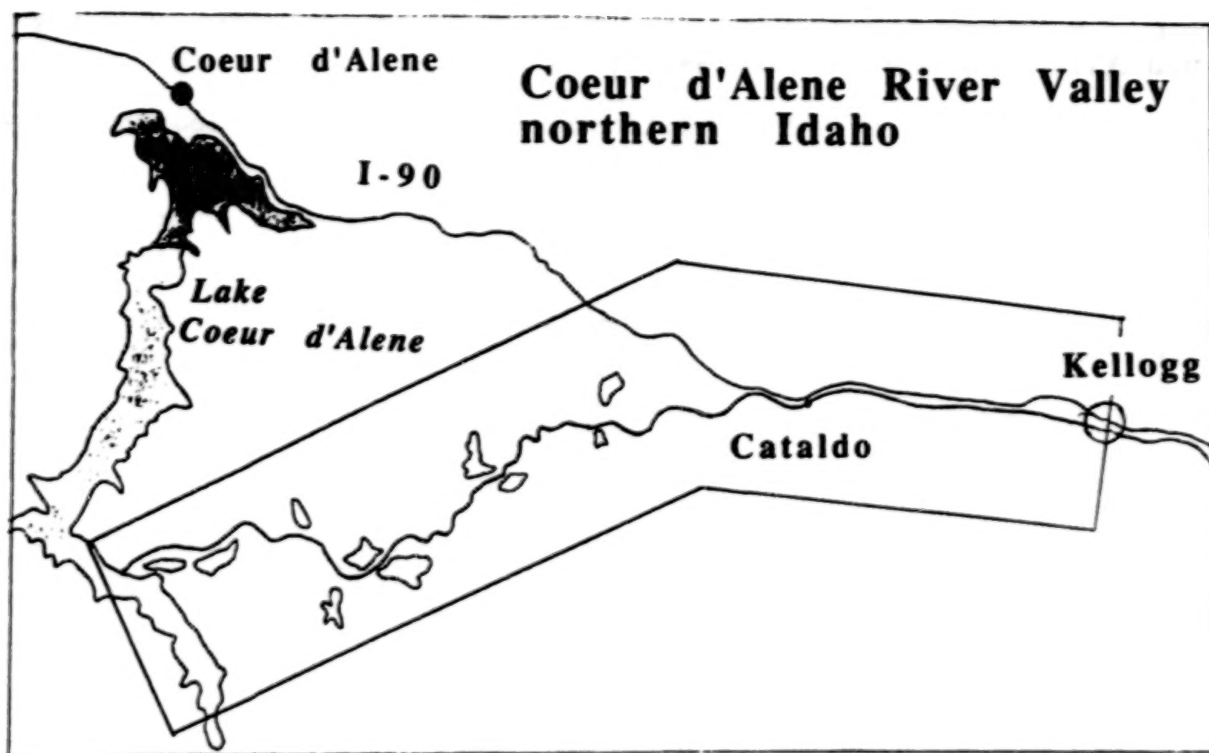


Figure 2. Sketch map of Coeur d'Alene River Valley in northern Idaho. The AVIRIS flightlines are outlined by the box.

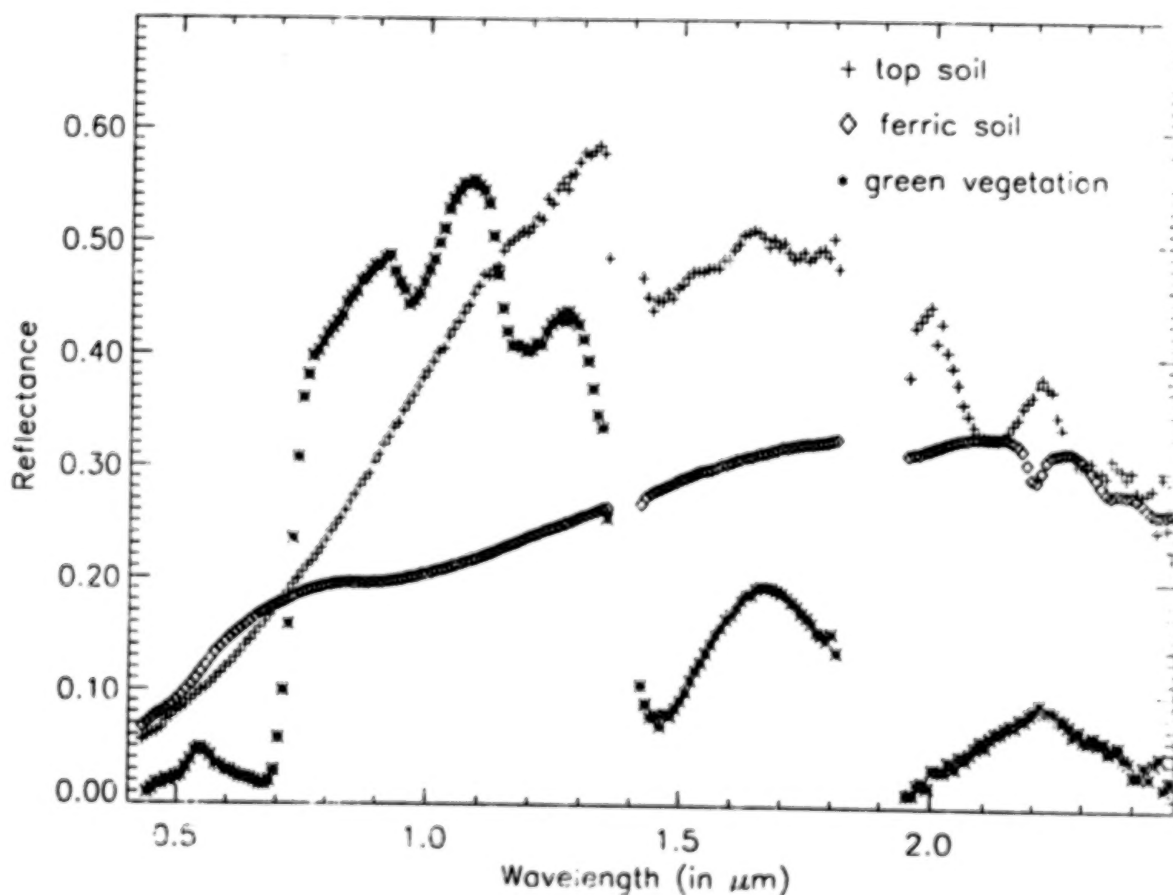


Figure 3. Three material image endmembers resulting from spectral mixture analysis: an agricultural, or top, soil, a ferric oxide or oxyhydroxide rich sediment, and green vegetation.

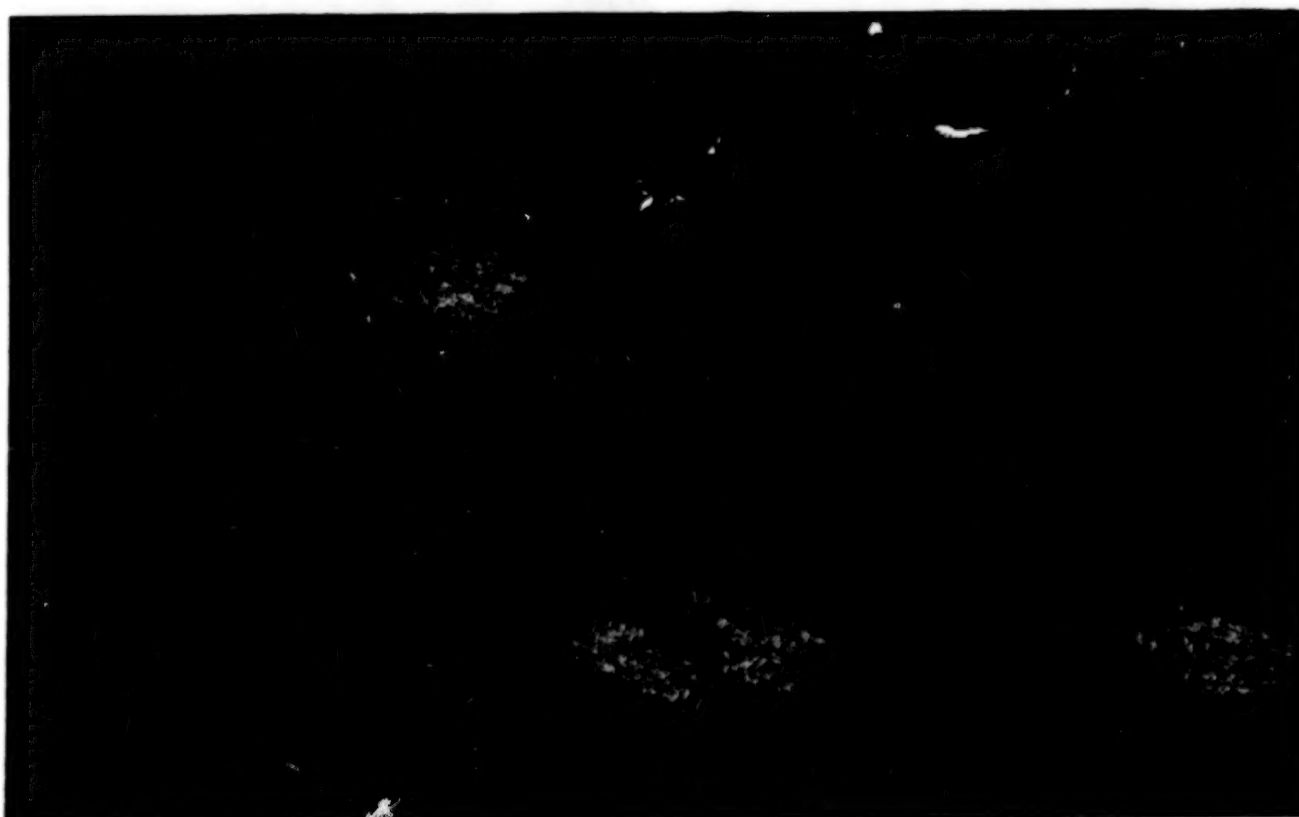


Figure 4. (a) Subsection of band 50 ($0.82\ \mu\text{m}$) of scene 1 of AVIRIS data that were analyzed by LPD. North is at the top of the page. Killarney Lake is the body of water on the left. (b) LPD detection image for iron-rich sediments in scene 1. Best exposures are along the Coeur d'Alene River, but some agricultural fields display the signature as well.

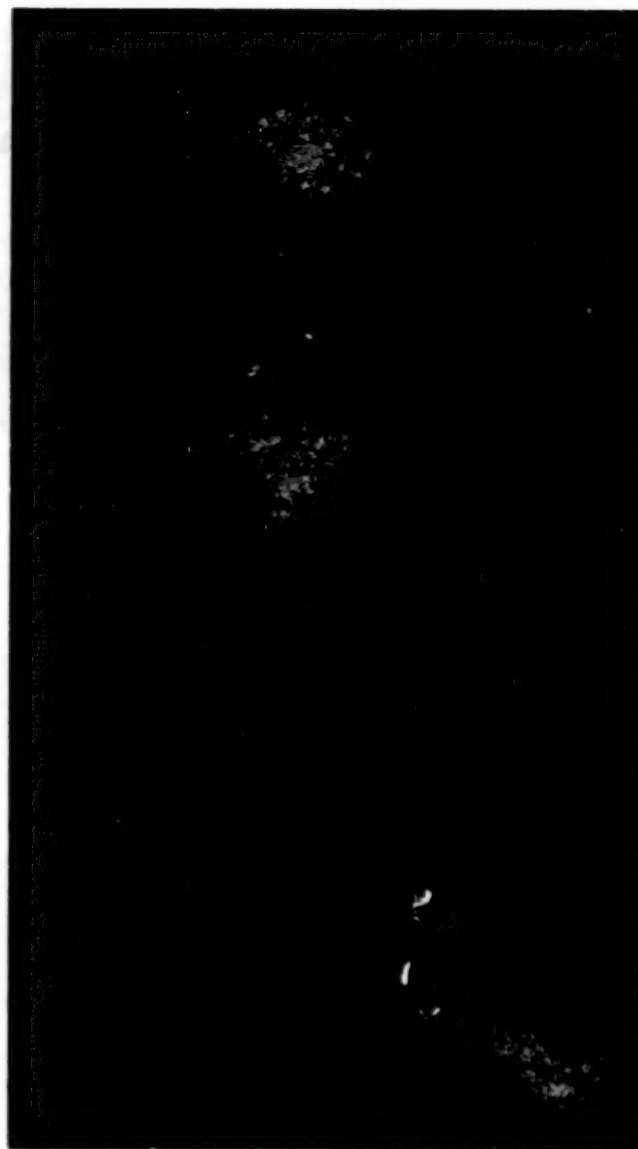


Figure 4. (c) Subsection of band 50 ($0.82 \mu\text{m}$) of scene 2 of AVIRIS data that were analyzed by LPD. West is at the top of the page. Cataldo Flats is near the bottom of the image near the large bend in the Coeur d'Alene River.
(d) LPD detection image for iron-rich sediments in scene 2. Note the exposures at Cataldo Flats.

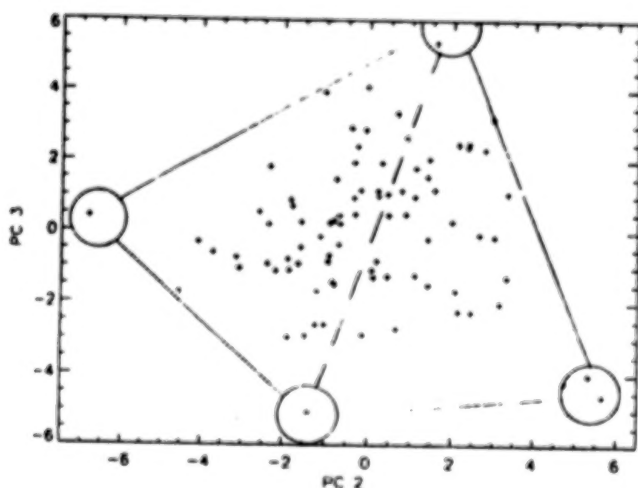


Figure 5. Plot of second vs. third principal component resulting from PCA of SWIR channels for pixels determined through LPD to be rich in iron-bearing sediments. A tetrahedron is outlined whose vertices correspond to the endmember spectra shown in Figure 6.

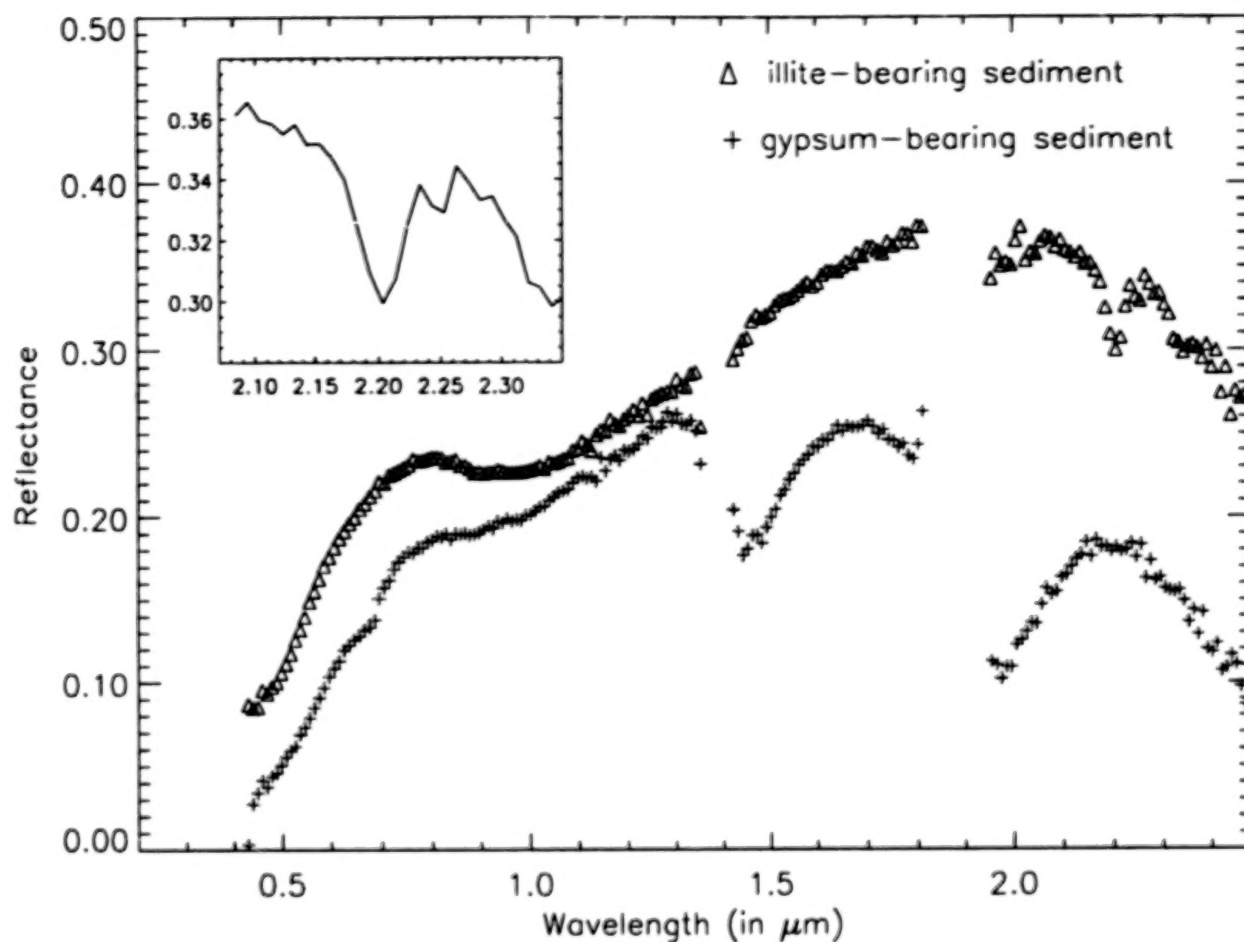


Figure 6. Iron-rich sediment endmembers. (a) Illite bearing sediment and a vegetation contaminated endmember which has some spectral feature reminiscent of gypsum. The inset shows the 2.20 μm absorption attributed to illite, perhaps with some contribution from muscovite.

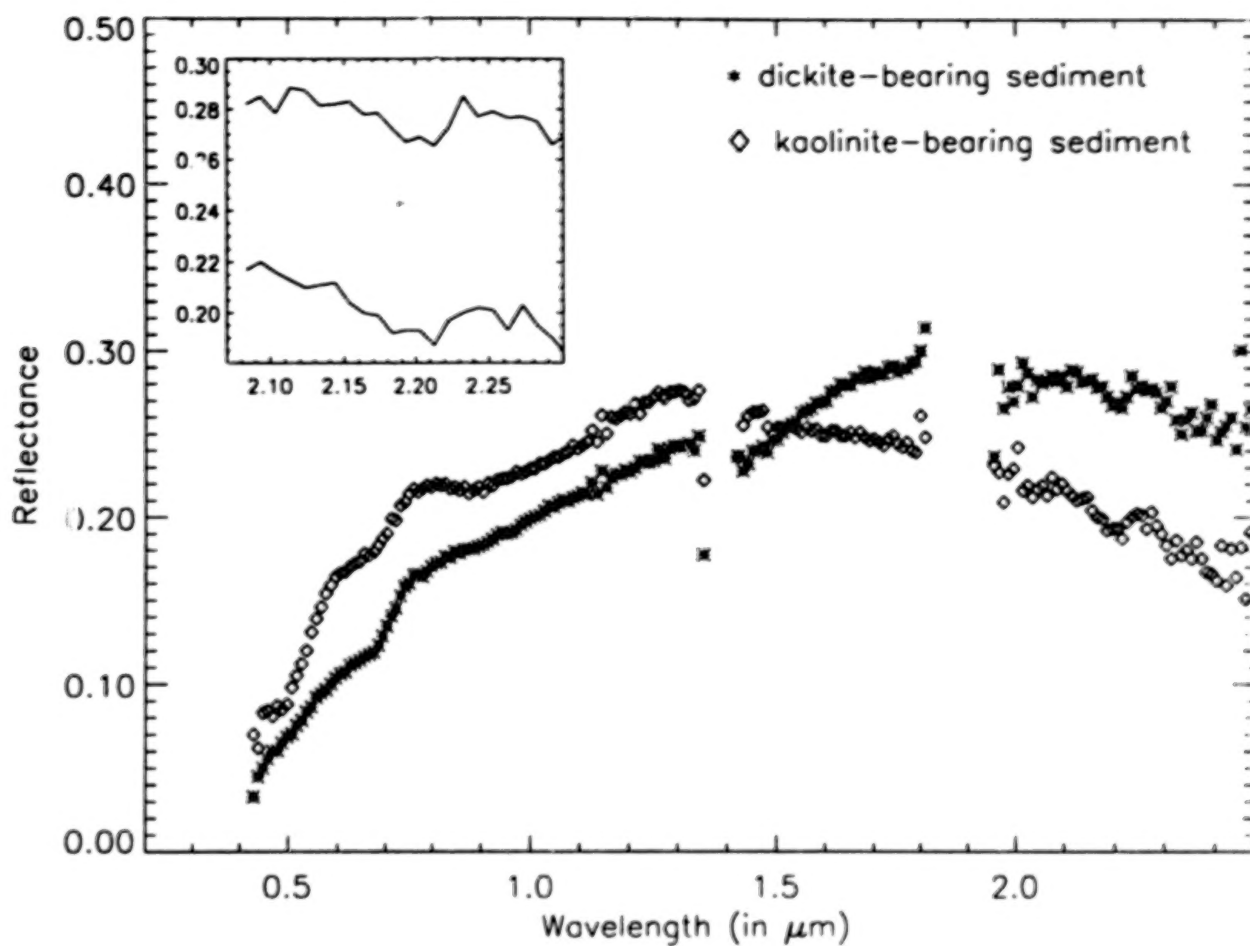


Figure 6. Iron-rich sediment endmembers. (b) Dickite and kaolinite bearing endmembers. The inset shows the doublet absorption features attributed to dickite (top) and kaolinite (bottom).

DUAL USE IN GOSNIAS AIRBORNE LABORATORIES – CAPABILITIES OF MULTIZONAL REMOTE SENSING

E.J.Falkov, I.M.Formanjuk, V.A.Kosinov
State Research Institute of Aviation Systems (GosNIAS)
Moscow, 125319, Russia

ABSTRACT

The capabilities of Tu-134 and An-2 airplanes and Mi-6 helicopter testbeds for carrying out tasks of remote sensing in the range of 0.4-14 μm are described. Through estimation of videosystem resolution and spectral investigations in the range of 8-14 μm to determine the surface temperature and emissivity are given as examples of dual use technologies.

1. AIRBORNE TESTBEDS EQUIPMENT

GosNIAS airborne testbeds were created in 1990-1991 boarded Tu-134 and An-2 airplanes and Mi-6 helicopter for the purpose of determining informational features of ground objects in the range of 0.4-14 μm . Forming images is performed with aerotopographical and aviation reconnaissance apparatuses. Digital recording of information from all the optical-electronic units and navigational equipment is done into a common frame of Schlumberger tape recorder. Plane Tu-134 as a carrier of remote sensing apparatuses allows to provide survey of objects in the range of altitudes from 100 m to 10 000 m along the routes of up to 3000 km long. The bottom part of the plane fuselage is additionally equipped with the specially designed gondola for installation up to 9 image receivers simultaneously, the maximum dimension of each receiver being 1170x800x600 mm. Three sections of the gondola are equipped with gyroplatforms. In the front section the rotating two-degree drive platform with remote control is mounted. It allows to orientate the optical axis of the apparatuses installed on the platform in the range of $\pm 30^\circ$ in horizontal plane and from horizon to 90° down in vertical plane. The list of on-board equipment and its main features in brief are given in the Table 1. Mi-6 helicopter is equipped with similar apparatuses but in the less quantity. An-2 plane allows to carry on plan either photosurvey or thermal survey.

2. CHARACTERISTIC FEATURES OF GOSNIAS TESTBEDS

Distinctive features of remote sensing (RS) complexes of GosNIAS are:

1. Obtaining of synchronous multizonal images with use of photographic, TV, infrared and laser scanning equipment which is partly installed on gyro-stabilized platforms, with registration of data from all optical-electronic devices and navigation equipment into a common frame on high efficient digital tape recorder Schlumberger.
2. Realization of ground objects observations by means of photo- and TV-systems in all the upper hemisphere with a possibility of manual or automated (using the correlation algorithm) watching of selected objects; realization of convergent survey for construction of a highly precise stereomodel of the locality.
3. Perfect navigational supply, including modern inertial systems and Doppler speed-and-drift meters, satellite navigation systems GPS and GLONASS and on-board computers.

Synchronous spectrally spread images in combination with topographical survey (item 1) serve as a basis for deciphering and construction of thematic maps as geological, forestry, soil, geobotanical etc. Multizonal topographically referenced images can be widely used for construction of different ecological maps and study of nature control problems.

188000

TABLE 1. THE EQUIPMENT OF GosNILAS Tu-134 TESTBED

Equipment	Fulfilled tasks	Notes
Interchangeable (3 from 5) topographic aerocameras TK-10, TAFA-10, LMK, TEA-35, 4-zonal aerocamera AS-707	Down-looking topographic and multizonal photogra- phing; plan reference of airplane location in the course of perspective survey	Visual range f=100 mm f=150 mm f=350 mm
TV-system T-2	Operative surveillance, tracking and video tape recording of forward-looking space images, direction of sight can vary from 0° (horizon) to ±90° (nadir), field of view (FOV) 20° or 3.5°	Visual range
Aerocamera BAF-40R , laser rangefinder LDI-3	Perspective photographing with slanting distance measurement for the shot centre; the optical axis is monitored automatically by TV-system T-2	Visual range f=400 mm
Optical sight OD-4M	Search and tracking with magnification up to ×80, photographing of images	Visual range f=1 m
TV-scanner	Plan panoramic survey, FOV=156°×40°, angular resolution 5 min.	Visual range
IR-scanner M	Plan survey in the range of 3-5 μm, FOV=120°, instantaneous field of view (IFOV) 10 min.	Middle IR range
IR-scanner L	Plan survey in the range of 8-14 μm, FOV=120° or 60°, IFOV=9 or 3.5 min. respectively	Thermal range
4-band IR-radiometer IKR4-2	Measurement of Earth surface radiation temperature in the ranges of 3-5, 8-10, 10-12 and 8-12 μm, FOV=3°, threshold sensitivity 0.1 K	Thermal range
Laser scanner	Down-looking survey with the laser 0.55 μm, FOV=120°, IFOV=3.5 min.	Active (at night) Passive (day time)
Supplementary to the regular navigation devices: radioaltimeter RV-21 , inertial navigation system I-21 , equipment of satellite navigation systems GPS and GLONASS , digital tape recorder Gamma	Registration of navigation parameters (altitude, coordinates, course, ground speed, angular velocities, angles of drift, pitch, heading, roll)	
Onboard information system with recording on a 27-channel digital tape recorder Schlumberger and 14- channel analog tape recorder SE-7000A	Normalization and analog-to-digital transformation of scanner- and video-images for a band up to 6 MHz, registration of scanner- and video-images and navigation information into a common digital frame, recording of analog signals with a band up to 150 kHz	Total output of a Schlumberger recorder is up to 96 Mbit/s, probability of recording failure is 10 ⁻⁶
Portable computer Compaq 486/66 MHz/ 525 Mb	Real time navigational data processing, control of airborne experiment	

During investigations of local ecologically unfavorable situations and disasters there can become useful the possibility of automated observing the object that is interesting almost in all the upper hemisphere (item 2). Similar situation can occur, for instance, in the process of a shipwreck observation, can arrive as a result of earthquakes, throw down of contaminations in river mouths and so on. Automated watching for the object is done by a narrow-field TV system, which then operates the two-degree drive of the platform with the long-focused aerocamera (Fig.1).

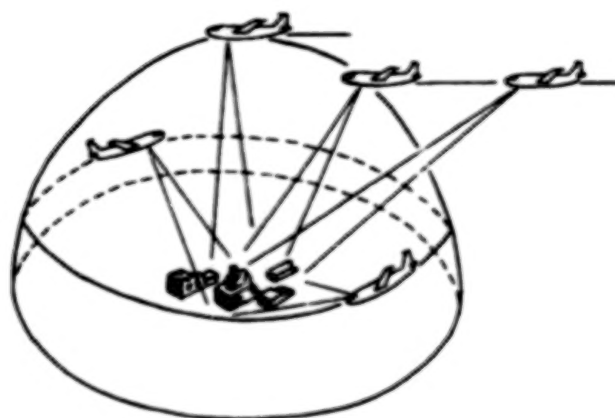


Figure 1. The scheme of possible observing of ground scene by GosNIIAS airborne testbeds.
The object can be observed nearly in all the upper hemisphere.

Precise spatial reference of the RS results by means of modern navigation aids (item 3) permits to carry out remote sensing in landmarkless surroundings and from large altitudes with automated account of drift angle, altitude and speed of aircraft movement, that is essential for sound operation of scanning system.

The peculiarity of aviation optical-electronic systems of reconnaissance type is the mode of their work with automated regulation of amplification, when the image that is being formed is optimized according to current relative contrast. For a number of validation tasks of the after-effects of ecological breaches such a mode turns to be optimal. In case if the purpose of remote sensing is to obtain absolute meanings of brightness, it is necessary to make alterations to optical and electronic channels of devices, to use additionally on-board calibrated radiometers and ground largesized test objects. It is expedient to realize a ground tracking of flight investigations in the part of measurement of optical and physical atmospheric parameters and definition of initial elements brightness of ground scene. GosNIIAS organizes systematic ground and space investigations of different regions, in this case space photographs have the highest local resolution less than 1 m.

The processing of the results and attendant information is being done in the specialized Center of processing at the institute. Data banks for efficient and personal computers contain images archives, attendant information, a catalogue, a data bank management system which includes a subsystem of automated search of necessary images on request with an arbitrary logical structure, and an application package of image processing for general and special purposes.

3. JUST CREATED SYSTEMS

3.1. AIRBORNE MULTISPECTRAL SCANNER

A great amount of various scanners for the acquisition of images from aircraft was worked out and constructed recently. Nevertheless, the use of a multipurpose device, which covers a large spectral range of survey (from visual to far IR area) and has high space resolution attracts great interest.

Below it is shortly described this very multispectral scanner (MS), developed in Russia during the last years.

MS is constructed due to the standard optomechanical scheme, where the line-by-line scanning of images is done by means of a rotating flat mirror, placed before the input pupils of the lenses. The rotation axis is parallel to the reflective surface, its both sides are covered with a mirror coating. Thus, during one turn of the mirror two image lines are formed. The frame scanning is done due to the aircraft movement.

In the MS construction a modular principle was used, that means that each information channel was built on the basis of an optical module, consisting of a lens objective, removable filters with a switching mechanism and a radiation receiver with a preamplifier.

In optical modules of the visible and near IR ranges the radiation flow is divided into two subranges by means of a dichroic mirror placed behind the lens. Each of optical channels formed in this way has its own set of replaceable light filters and a radiation sensor with a preamplifier. From the output of the preamplifier the signal passes to the videochannel module, where it is amplified and digitized. In the videochannels modules the mode of automatic alignment of amplification is realized by the help of controls, allowing to change the output slope (the amplification factor) of the videopass and the minimal and maximal meanings of the energy flow at the entrance of the information channel, which correspond to the bottom and top levels of the videosignal.

Main features of MS are given in Table 2.

TABLE 2. MAIN MULTISPECTRAL SCANNER FEATURES

Features	Meanings		
Scanning angle, degrees	70		
Instantaneous field of view, min.	5		
Scanning rates, lines/sec	18, 36, 72		
Spectral ranges, μm	0.43-0.46	0.50-0.59	0.61-0.69
(the nominals of the spectral ranges may change depending on the stated problems and demands of the consumer)	0.43-0.51	0.52-0.60	0.63-0.69
	0.57-0.60	0.53-0.58	0.66-0.69
	0.63-0.67	0.54-0.57	0.70-0.72
	0.70-0.69	1.50-2.50	3.50-4.10
	0.76-0.90	1.55-1.75	3.00-5.00
	0.79-0.89	2.00-2.50	8.00-12.5
	0.83-0.89		10.52-12.5
The signal/noise ratio in the spectral range of 0.43-2.5 μm	100-200		
Radiometric accuracy in the spectral range of 0.43-2.5 μm , %	0.5		
Temperature difference (at 300 K level) equal to noise, K	0.1		
Range of measured temperatures, K	240-330		
Absolute accuracy of infrared channels calibration, K	2		
The resource of non-stop work of infrared channels with one filling of the cryostat with liquid nitrogen, hours	5		
Dimensions of the device, mm	550×600×500		
Mass of the device, kg	100		

3.2. THE INTELLECTUAL SYSTEM FOR DATA COLLECTION AND PACKING

Airborne Data-Processing and Measurement System (ADPMS) is the on-board complex of equipment designed for sensors interrogatory according to the preset program as well as for normalization, analog-to-digital converting, packing into the frames of the appropriate format and matching with high-capacity digital tape recorder. Not-synchronous both analog and digital units for images acquisition, navigation instruments and other facilities operate as sensors. ADPMS controls the data collection process, forms the data flows with their timing, appropriately logs the data into the on-board tape recorder, generates the operator required signals for the system's main units operational direction. The ADPMS modular structure allows the configuration to be enlarged and developed according to the feature of the problems being solved. Data normalization and transformation are performed in a thermostable module which makes it possible to install it near sensors located sometimes beyond the aircraft interior. High protection from noise and accuracy are achieved through thermostabilization. Selection of the sensitivity range based on the measurements accuracy requirements is executed in automatic mode. Both compensation and coding for further taking into account of the constant component of the measured analog signal are performed. The ability of coding the sequence of cyclic selection of data coming from the sensors is available. A number of measures providing further reliable on-ground digital data unpacking is realized. For this purpose the data coming from each sensor are disintegrated to blocks whose sizes are defined by the sensor's both line and frame format. Each block is supplemented with 32-bit marker which has programmable contents, 8-bit code of channel marking as well as service and attendant information. Intelligence on the sensors mode, navigation data and other slowly alternating information and service parameters are shaped into the common frame of the low-speed magnetic logger and through the ADPMS are dubbed into the common frame of the efficient tape recorder together with the images.

Main technical data of the ADPMS when supplied with minimum suit are given below:

- number of input channels 16;
- the frequencies band width of input signal up to 6 MHz;
- the analog-to-digital converter digits number 8 (mantissa)
3 (characteristic);
- number of communication channels with digital logger from 1 to 24;
- velocity of transfer of data to the logger up to 90 Mbit/s;
- power supply 115 V, 400 Hz, 5 A.

Several ADPMS modules are mounted in the GosNIIAS airborne testbeds Tu-134 and Mi-6.

4. ESTIMATION OF VIDEOSYSTEMS RESOLUTION

Restoration of the geometrical parameters of objects based on their images depends on videosystems resolution. Accuracy of restoration for small details of the objects observed from testbeds is affected by own optical-electronic system features through modular transfer function, as well as by various noises due to atmospheric channel, testbed vibration etc. Through estimation of resolution while observing the scene from the testbed is of a special interest. For this purpose using TV and IR systems on GosNIIAS testbeds observation of multibar targets in visual and IR ranges was carried out. At the same time on-ground measurements of bar targets brightness parameters took place.

While estimating resolution on ground the bar target should provide receiving both resolved and non-resolved bars in the image. The most preferable is the bar target which has the set of bar groups, each of the groups consists of three dark and light pairs of bars. The width of both dark and light bars in the groups is the same. The ratio of the bar widths in the neighbouring groups was $\sqrt[6]{2}$, the width of the bar changing from 0.06 to 0.4 m.

By resolution on ground we understand the average value of the bar width in the group, visible on the image as a number of intermittent dark and light bars.

While surveying optical-electronic system is the spatial frequencies filter [Матиясевич (1989)], the passband limit of which is resulted by this system resolution. To detect in the image high frequencies corresponding to on-ground resolution it is necessary to use suitable high-frequency filter. A man can be such a filter who would sort out the group with the thinnest bars in the image and measure their width.

The procedure of visual resolution analysis used by us and adopted in the "Open Skies Treaty" project is as follows:

- 1) images of bar targets obtained by a videosystem are transformed to a digital form with tact frequency not less than the Nyquist frequency and a number of bits not less than 8 and stored in the computer;

- 2) the image of bar target is displayed on the terminal;

- 3) the brightness, contrast and magnification may be adjusted by an operator;

- 4) the image of the target is studied by several experienced observers;

- 5) the group of bars is resolved when the operator can distinguish at least one pair of bars from the group;

- 6) for each image the narrowest group is resolved when at least 80% of all the observers consider so. Being rather simple nevertheless the visual technique of resolution determination has some drawbacks:

- the method is rather labour-consuming;

- using of the computer and the terminal with limited number of brightness levels could result in non-adequate bar brightness values in the computer to their visual images on the terminal;

- the results of resolution estimation depend on observers experience.

In such conditions it is more preferable to apply rational automated evaluation procedure of resolution. The most precise, fully automated methods of resolution determination are based upon the use of image spatial frequency spectrum. In this case the image spectrum is convenient to calculate using Fast Fourier Transform (FFT) [Rabiner and Gold (1975)]. The description of automated resolution evaluation algorithm based on FFT analysis along target groups is given further.

The algorithm represents tracking zone filter which selects the frequency corresponding spatial frequency of the bars in the group $F_i = 1/L_i$, $L_i = 2 \Delta l_i$, being the bar period in the group. Making a decision about resolving is performed on the basis of analysis of the amplitudes for selected and background frequencies.

Automated algorithm consists of the following:

- 1) i -th group of bars in the target image is selected. The line of analysis for this group is chosen then (Fig.2);

- 2) by means of FFT spectra modulus of signal along the chosen line of analysis is calculated (Fig.3);

- 3) the component with spatial frequency F_i is selected;

- 4) the intensity of this component $|F(f_i)|$ is compared with the one of the background, noise and others, $N(f)$;

- 5) the weaker is the target image signal, the less is the intensity of the F_i component. Resolution is determined by the width Δl_R of the bars for the group, where the intensity of Fourier spectral component for F_i frequency in the given ratio, for instance, not less than the intensity of surrounding background components, noise, etc.;

- 6) the number of analysis lines in the group is determined by the necessity of getting their reliable statistic processing (not less than 5).

The algorithm considered is adjusted to the spectral characteristics of the target image including the noise components and doesn't need any agreement on the threshold. Using the data obtained from airborne testbeds, through estimation of resolution in both visible and thermal ranges was performed. Comparison of the both visual and automated methods was fulfilled. The automated one appeared to be simpler and was agreed to the results of visual estimation. The main advantage of the suggested technique is the threshold to be adjusted automatically in accordance

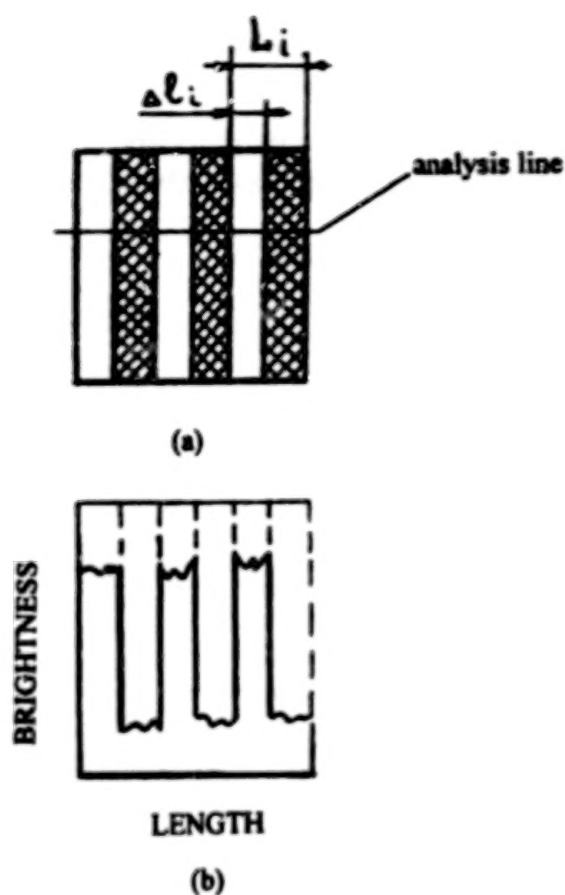


Figure 2. Half-tone image of i -th group of bars (a) and brightness function across the group (b).

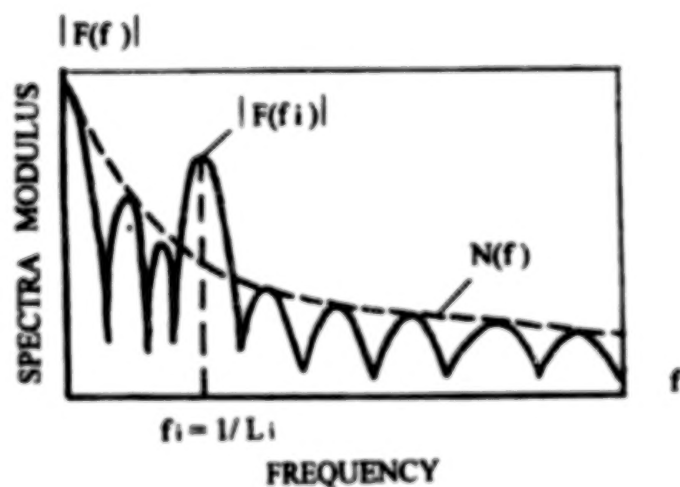


Figure 3. Modulus of image signal spectrum along the analysis line. $|F(f_i)|$ is the value of the spectrum component for frequency f_i ; $N(f)$ is the skirting line for noise and others.

with signal/noise ratio for each concrete image. That's why the conclusion about resolution doesn't depend on human factors.

5. THE DETERMINATION OF THE TEMPERATURE AND THE EMISSIVITY OF OBJECTS ON THE BASIS OF SPECTRAL INVESTIGATIONS IN THE THERMAL RANGE

The signal formed by an IR-system is proportional to:

$$u = \sigma \epsilon T^4 + (1 - \epsilon) E$$

where T is the temperature of the object, ϵ is its long-wave emissivity, σ is the Stefan-Boltzmann constant, E is the incident irradiance.

Three unknown quantities T , ϵ and E correspond to one measured datum called radiative temperature. For the number of tasks, for instance, to evaluate heat losses from buildings and central heating lines, it is necessary to know real temperature T . Knowing value of ϵ , one can use it in the problem of distinguishing and identification of the objects observed. How to separate quantities ϵ and T ?

Concerning remote sensing tasks, simultaneously with recording of IR-signal it is necessary to measure incident irradiance E . For this purpose a bolometer is installed on board the Mi-6 helicopter. The bolometer is directed to the upper hemisphere and measures spherical irradiance E' on the level of the flight altitude. Spectral characteristics of the bolometer are adjusted to spectral ones of the IR-system. Extinction of radiance in the atmosphere and the own radiance of the atmosphere are taken into account by LOWTRAN program.

For separation of quantities T and ϵ spectrally distinguished filters in the range of 8-14 μm are used. The high signal/noise ratio requirement demands the use of the filters with half-width not less than 2 μm . It results in spectral curves overlapping and brings to sufficient non-correctness of the task. It requires the regularization method for task solution [Тихонов и Арсенин (1979)].

Mathematically the task is formulated as follows. Radiance of the object in several spectral ranges is measured:

$$u_i(T) = \int_a^b \varphi_i(\lambda) \xi(\lambda) r(\lambda) [\epsilon(\lambda) m(\lambda, T) + (1 - \epsilon(\lambda)) e(\lambda)] d\lambda \quad (1)$$

$$i = 1, 2, \dots, n$$

where n is the number of channels (filters), (a, b) is the range of detector sensibility, $\varphi_i(\lambda)$ is the spectral function of i -filter, $\xi(\lambda)$ is the apparatus function of IR-system, $r(\lambda)$ is the atmospheric effects function, $\epsilon(\lambda)$ is the emissivity, $m(\lambda, T)$ is the spectral intensity of a blackbody radiation after Plank, $e(\lambda)$ is the incident radiation.

Emissivity is supposed to be described by some analytical model as a function of wave-length and several numbers of unknown parameters $a_1, a_2, \dots, a_k, k < n$

$$\epsilon(\lambda) = f(\lambda; a_1, a_2, \dots, a_k)$$

For the chosen model of the emissivity the problem of temperature determination consists of the solving equation system (1) for the quantity T and the parameters a_1, a_2, \dots, a_k . The results of solution depend on accuracy of radiative temperature measurement. The process of mathematical modeling of solution discending to true values of ϵ, T depending on accuracy of initial data (mainly accuracy of radiative temperature measurement) is shown in Fig. 4.

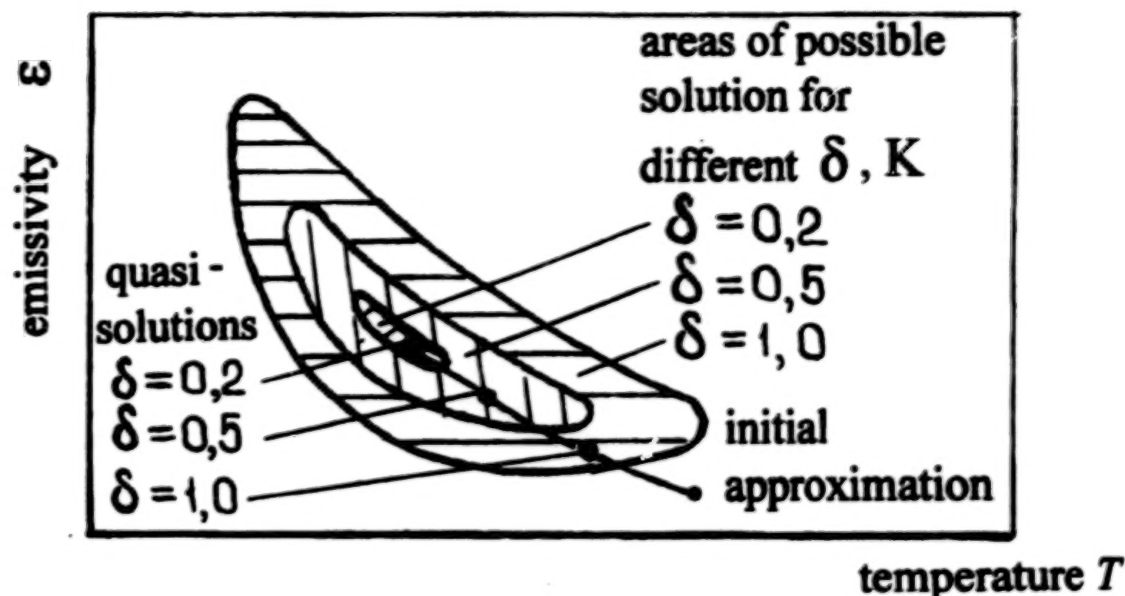


Figure 4. Influence of accuracy of radiative temperature measurement upon accuracy of temperature and emissivity separation.

6. POSSIBLE DIRECTIONS OF USE

General mind is that the GosNIIAS testbed Tu-134 for remote sensing in the range of 0.4-14 μm is the very best equipped among those in Russia and one of the best equipped in the world. Up to this year the airplane will be equipped with one of Ashtech sets of GPS Receiver Z-12. Together with on-ground Z-12 set the accuracy of location of the photograph centres in the differential mode will be expected about several centimeters. Up to this year the airplane will be equipped with a 6-channel scanner in 0.4-14 μm range with improved metrological features. Different scanners are interfaced with the recording system by means of on-board data measuring systems.

The analysis shows that the possibilities of GosNIIAS concerning remote sensing to a considerable extent satisfy the demands, made to the means of realization of remote sensing in traditional and new domains. At present in the bounds of conversational activities the institute carries out precision aerosurvey of Moscow region districts in order to work out a land cadastre with the use of satellite navigation system GPS in the differential mode, when the error of definition of an aircraft location is the least. Test flights were carried out, the results were processed, the expediency is shown, a long-term contract with Moscow government for aerothermovision monitoring of urban network of heat control is concluded.

The described above technical means of RS are supposed to be used for ecological monitoring of nature in the following directions:

1. Disclosure and identification of oil spread. It is known that on traditional black-and-white photographs the images of oil and water spread are in most cases shown by one and the same phototone, that hampers the distinguishing. The use of multizonal survey by means of aerocamera AS-707 with further-on synthesizing creates the necessary prerequisites for differentiation. The use of 8-14 μm heat channel and of an active laser scanning system must essentially increase the authenticity of identification. It seems that the combination of multizonal images would permit to carry out a confident identification of petroleum and oil spread on the water, including sea water areas. The possibility of night work allows to reveal unsanctioned sewages to urban river networks.

2. Disclosure of damages in gas- and oil-products pipelines. The gas under high pressure comes out of damaged pipe and due to adiabatic expansion causes cooling of near-by surroundings. The use of

multizonal survey will allow to carry out efficient disclosure of faults and possible subsequent accidents.

3. Forestry monitoring (stress situations, forest fires), ecological monitoring of geotechnical systems (mining industry, control of engineering protection of main transport routes from mudslides and screes), hydrological monitoring of territories with use of convergent survey for precise relief construction and consideration of polluted sewage migration etc.

REFERENCES

Матиясевич Л.М. *Введение в космическую фотографию* (Matijasevich L.M. *Introduction to Space Photographing*) . М., Недра, 1989.

Rabiner L.R., Gold B. *Theory and Applications of Digital Signal Processing*, Englewood Cliffs, N.J., Prentice-Hall, Inc., 1975

Тихонов А.Н. , Арсенин В.Я. *Методы решения некорректных задач* (Tichonov A.N., Arsenin V.Ja. *Methods of Solution of Non-correct Tasks*) .М., Наука, 1979.

MONITORING OF SURFICIAL DEPOSITS IN THE GULF WAR ZONE USING SATELLITE DATA

Dr. K. M. SHEIKHO
Saudi Centre for Remote Sensing
King Abdulaziz City for Science and Technology
P.O. Box 6086
Riyadh, 11442, Saudi Arabia

ABSTRACT

The Gulf war has changed the environment in many different ways, one of these being surficial deposits. In the course of last decade, remote sensing has proven its high potential for earth observation and became a powerful tool in quite different fields of application. A registered multi-temporal data (1990 and 1993) of LANDSAT -5 satellite (Thematic Mapper TM) images and SPOT (MLA) satellite images has been examined over the war zone area in Saudi Arabia. Different image processing techniques were applied to TM data. The final results showed a desertification process in the study area. The soil cover also has been disturbed providing a new source for sand dunes. The size, type and the patterns of the new sand dunes were different. Long term program for monitoring the changes in surface features in the area are needed.

1. INTRODUCTION

The Gulf war is regarded as a major environmental disaster in the Gulf region. The terrestrial environment was under continuous assault during the Gulf war. The objective of this study was to show the surface changes within part of the war zone using LANDSAT -5 and SPOT data. The natural vegetation in the war zone was sparse and the surface stabilized by biological, chemical and even mechanical factors (Sadiq and McCain, 1993).

The term surficial materials was defined by Townshend and Hancock, 1981 as " the materials above bedrock whether they have arrived there by transport or have developed in situ". Sand dune was defined by Mainguet, 1984, "as an accumulation of loose particles, deposited or reworked by the wind, with diameters varying from two or three millimetres to tens of micrometers". Sand dunes movement and reactivation of stabilized dunes and sand encroachment are one of major

manifestations of desertification. The composition, height and the shape of dunes are different from region to regions. In general, sand dunes were subdivided into three categories according to decreasing amounts of activity: vegetated dunes, inactive (fixed) dunes and active dunes.

In arid regions, monitoring environmental changes with remote sensing has become a valuable tool for assessing desertification (eg. Paisley et. al. 1991; Nichol, 1991). The region of Saudi Arabia lies in the "Arid bioclimatic zone" which is characterized by a precipitation/potential evapotranspiration ratio (p/E_{tp}) of between 0.03 and 0.2 (UNESCO, 1977). The study area is located in northeastern part of Saudi Arabia (Figure 1).

2. IMAGE PROCESSING

To achieve the objective of this study LANDSAT -5 (path 166 row 40) and SPOT (column 145 row 293) data of 1990 and 1993 (before and after the war) were processed and interpreted. The TM bands 4 and 3 were found to be the best in terms of contrast, definition of topographic features (compared with SPOT MLA bands). Therefore, only TM data was enhanced and interpreted. Repeated coverage of LANDSAT satellite data can be used as a tool for monitoring the surficial deposits (e.g. sand movements).

Image-to-image registration is necessary to form image mosaics or to map temporal changes accurately, from different images for the same area. The accuracy of the registration depends on many factors. Among these factors, which are relevant to Saudi Arabian desert areas was the availability or rather, the lack of ground control points (GCPs). Very few 'cultural' features were available to be used and many 'natural' boundaries were not defined. A regression method was used to define the relationship between the co-ordinates of two images (different date). Once the best regression equation had been found, the images were resampled. A very low accuracy was achieved using multi-temporal registration images. The result showed multi-temporal image registration error 3 to 4 pixels. For this reason the registered TM images were ignored.

3. IMAGE INTERPRETATION

Figure 1 shows the Gulf war zone area. Fig. (2) and (3) are false colour composites of bands 4, 3 and 2 in red, green and blue respectively. Figure (2) shows the full scene covering all the war zone areas including Kuwait city before the war (July 1990). Figure (3) shows the full scene covering all the war zone areas including Kuwait city after the war (June 1993). Both images were compared and interpreted separately in order to find the differences. The most important differences between these images were:

(a) There are new born sand dunes around the Saudi and Kuwait border (b) The sand dunes are moving towards northwest (c) The sand dunes have different shapes, size, and patterns . Figure (4) Shows a linearly stretched TM band 4 which show some of the new born dunes which cant be seen clearly in Fig 3.

There were no field visits because of inaccessibility in the study area, but according to Sadiq and McCain,1993), the ground surfaces in Gulf war zone were badly damaged over large area (Fig 1).

The sand deposition and movements can be controlled by many natural or physical factors such as vegetation covers, general wind direction, grain size, surface roughness, amount of rainfall, and underlying topography (Al-Hinai, 1989). Therefore, in the study area the author propose a three reasons for creating and activating the sand dunes ; (1) Exposure and disaggregation of near surface soil (sediments) may have resulted from troop deployment and military installations, or from the entrenchment of trenches. Therefore the desert soil was badly damaged, (2) bombardment of the training sites, and (3) the flood in rain season.

ACKNOWLEDGMENTS

The author would like to thank the saudi center for remote sensing for providing the satellites data .

REFERENCES

- AL-Hinai, K.G., 1989:Evaluation of Remote Sensing data for Sand Studies in Saudi Arabia proce. workshop on desert studies in Saudi Arabia : Scope and Concerns. Riyadh, Saudi Arabia, 67-90.
- Mainguet, M., 1984: A classification of Dunes Based on Aeolian dynamics and sand budget, In Deserts and Arid Lands, F. EL-Baz (ED.), Mrtinsus Nijhoff Publishers,Boston, U.S.A .
- Nichol, J.,1191:The Extent of Desert in Northern Nigeria as Shown by Image Enhancement, The Geo. Journal, 157:1, 13-24.
- Paisley, E. C.I., N. L. R. G.,Lisa, and R. Greeley, 1991: Discrimination of Active and Inactive Sand from Remote Sensing: Kelso Dunes, Mojave Desert, California Rem. Sens. Environment, 37,153- 166.
- Sadiq,M., and McCain,1993: The Gulf War Aftermath; An Environment Tragedy, Kluwer Academic Publishers, London, 298 pp.
- Townshend, J.R, and Hancock,P.J;1981,The Role of Remte Sensing in Mapping Surficial Deposits . In Terrain Analysis and Remote Sensing, J.R. Townshend (Ed.),George Allen & Unwin, London, 204-218.
- UNESCO, 1977, Map of the world distribution of arid Regions and explanatory note, united nations, paris, 54 p.
- General Soil Map for Saudi Arabia,1986: Ministry of Agriculture and Water,226 pp., Saudi Arabia.

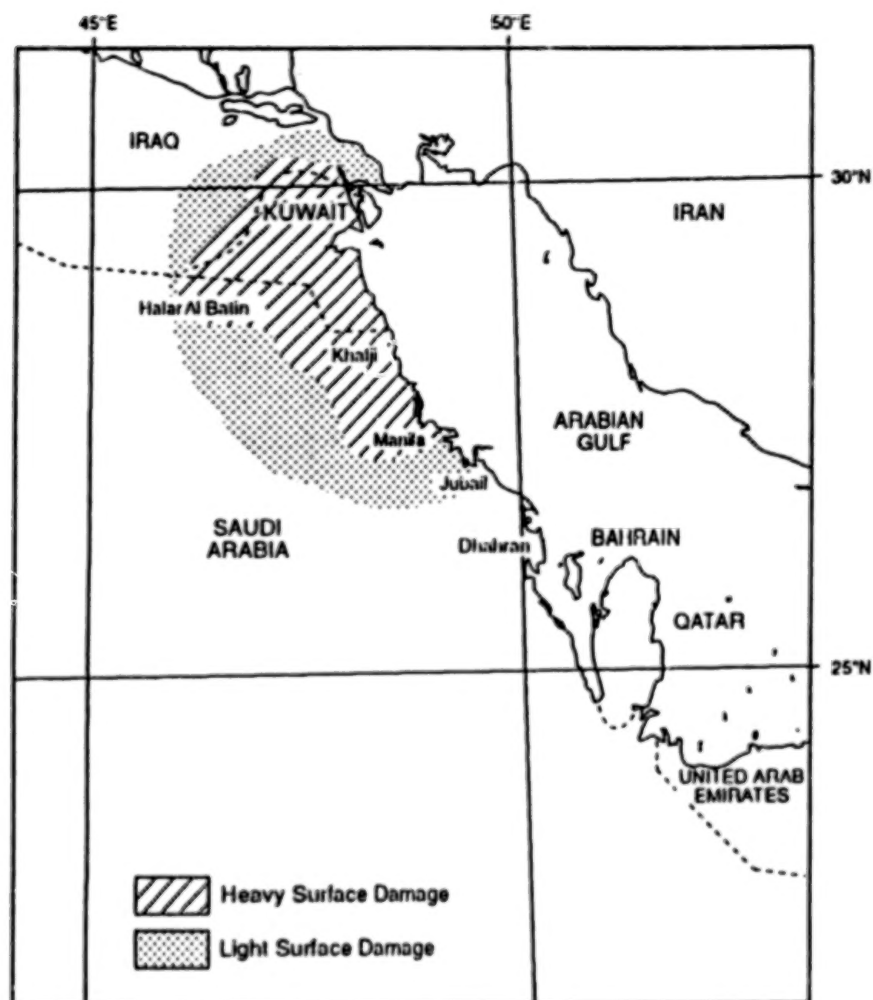


Figure 1. Map showing the location of the Gulf war zone and the surface disturbances during the war (After Sadiq and McCain, 1993).

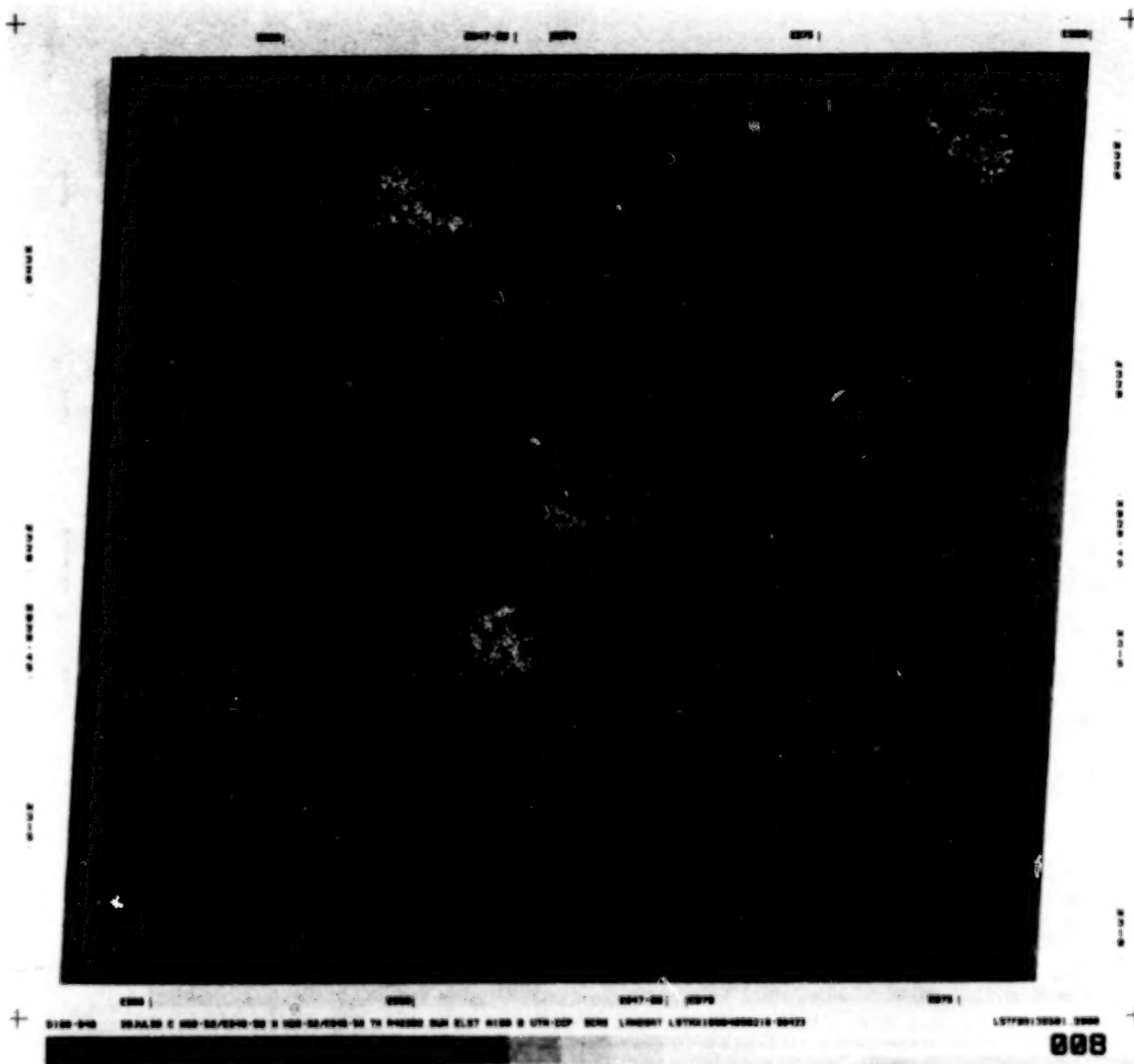


Figure 2. Bulk imagery for LANDSAT (TM) bands 4,3 and 2 in red, green and blue, cover the war zone including Kuwait city before the war (July,1990).

000000

000397

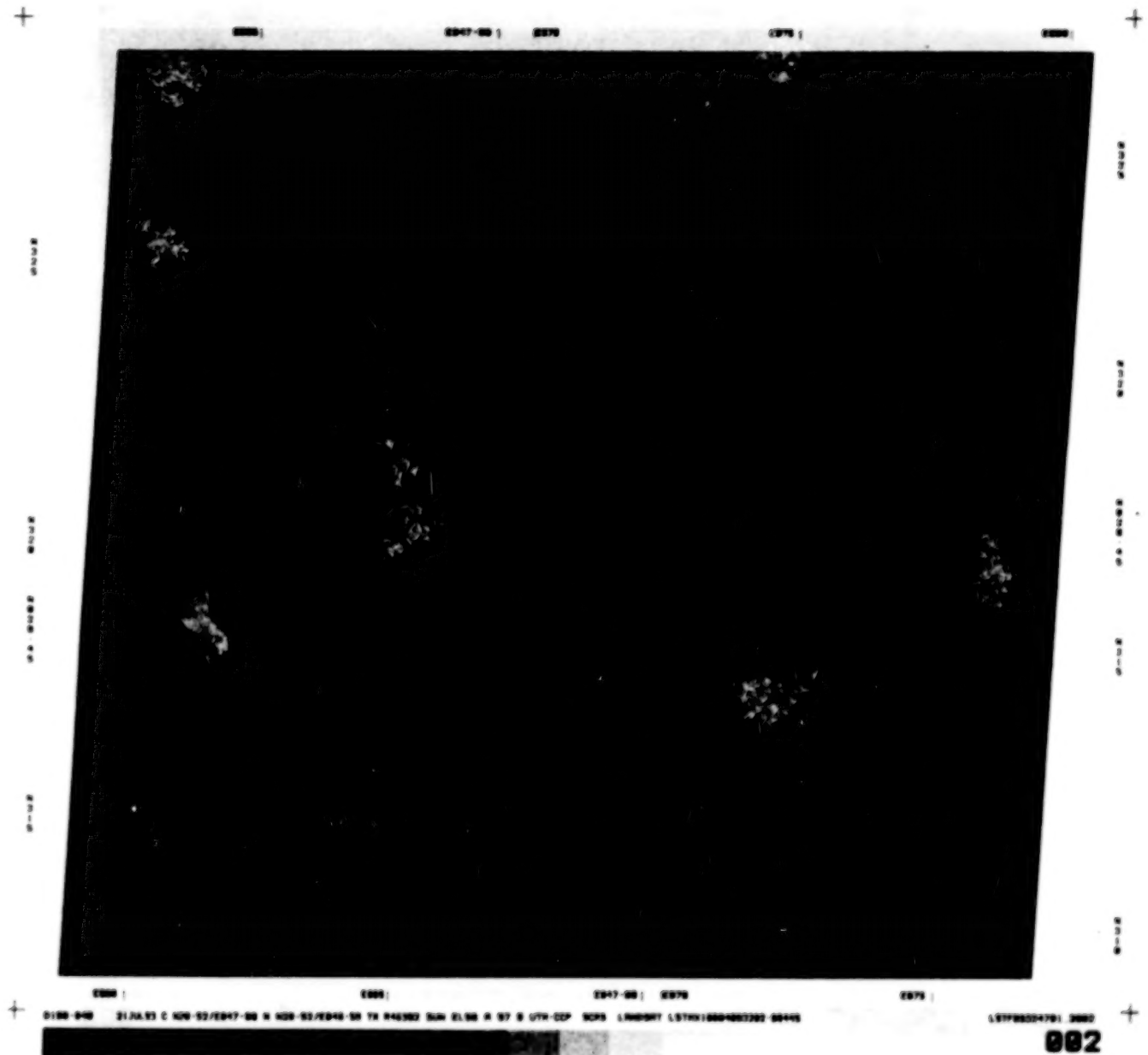
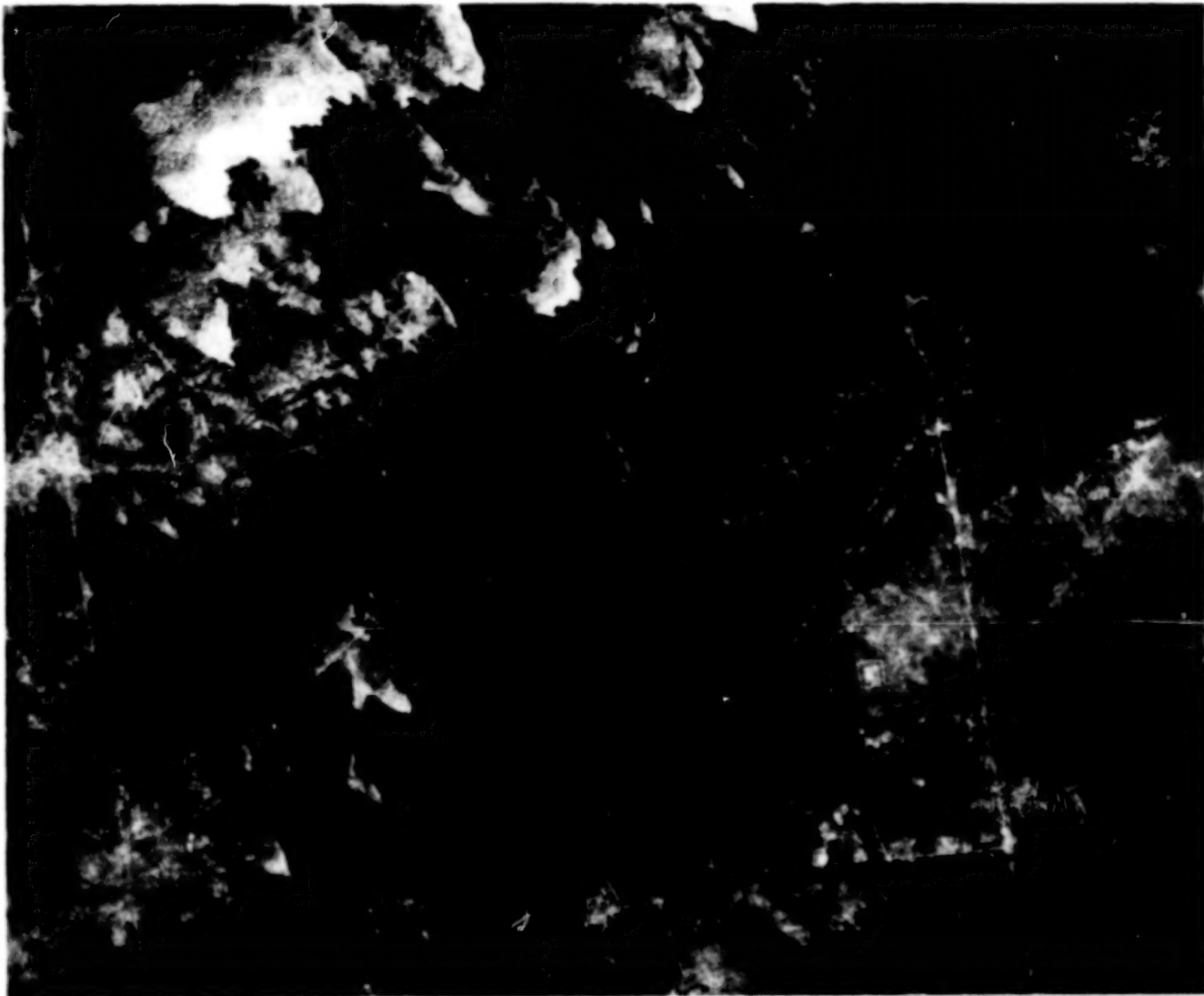


Figure 3. Bulk imagery for LANDSAT (TM) bands 4,3 and 2 in red, green and blue. This image cover the Gulf war zone and Kuwait city after the war (June 1993). The subcene shown in Fig. (4) is shown by ssuperimposed rectangle.

000000



0 2 4 6 8 10 12 km
 WISDIN-40/ HAPRO LANDSAT TM SC 10830/047-12 SUNEL: 56 AZ117 UNDOWN prog/UNIVERSAL NO 04G04 SCRS/VACST Scale: 1:25000

Figure 4. A subscene of TM band 4 (Linearly stretched) to show the new sand dunes in the Gulf war zone.

000000

000399

RAPID *IN-SITU* ASSESSMENT OF ORGANIC CONTAMINANTS IN AQUATIC SEDIMENTS WITH THE REMOTS® UV IMAGING SPECTROMETER¹

Donald C. Rhoads, Jo Ann Muramoto, Chris Coyle², Roger H. Ward³, and Richard Anderson²
Science Applications International Corporation (SAIC)
Woods Hole, MA 02540, USA

ABSTRACT

There is a need for high search-rate sensors to screen sediment quality at military bases, prospective dredging sites, and disposal areas. Traditional laboratory chemical methods used to identify contaminant "hot spots" typically have slow data turn-around and per sample costs are high (\$700 to \$1000).

SAIC is developing a hyperspectral UV imaging field sensor for rapid sediment quality screening of contaminant "hot spots" related to concentrations of polyaromatic hydrocarbons (PAHs), fuels, and crudes. The system is to be deployed from a small vessel. The optical sensor automatically penetrates the bottom in the vertical plane and images a vertical slice of the bottom 15 cm wide by 20 cm deep. A conventional color (RGB) CCD image is taken first followed by a series of images taken at 1 or more excitation bands and 17, 10 nm wide UV emission bands. Blanks and spiked standards are located at the top of the imaging window. Spatial/spectral data files are rapidly displayed on board the vessel for real-time analysis.

Software is employed to collect, store, and analyze the data in near real-time. Organic compounds have been spectrally imaged, identified, and measured at concentrations of 10's of ppm from a unique spectral library. Sources of contamination may be inferred from the mapped spatial relationship of fluorescing contaminants to imaged dredged material layers, sewage sludge layers, oil globules, deposits proximal to industrial/municipal effluents, or combustion sources. The resulting reconnaissance maps are to be used to select a subset of "hot" stations for traditional chemical analysis.

1. INTRODUCTION

Science Applications International Corporation (SAIC) is developing an *in-situ* imaging sensor for visually locating and measuring UV excited emission spectra from fuel oils, polycyclic aromatic hydrocarbons (PAHs), and other fluorescing materials in the upper 20 cm of bottom sediments. The camera/sensor is a hyperspectral (20 channel) sediment profile imaging spectrometer (Patent applied for) based on SAIC's existing REMOTS® sediment profile camera platform (Rhoads, Germano, and Hightower, 1992).

There is a need for high search rate sensors to rapidly screen sediment quality over large areas of the seafloor, lake or river bottom, in a short period of time. Applications include screening of prospective dredging sites, monitoring of disposal and fill areas, and oil spill evaluation. Another application of this instrument is time-series mapping of introduced fluorescent particles for bottom sediment dispersion studies.

Traditional wet chemical methods for measurement of hydrocarbon contaminants in sediments, such as gas chromatography (GC) or high performance liquid chromatography (HPLC), require sediment sampling,

¹ An SAIC IR&D Project (0704-0111)

² SAIC, San Diego, CA 92121

³ SAIC, Newport, RI 02840

solvent extraction, and laboratory measurement resulting in slow data turn-around and high per sample costs. The REMOTS® spectrometer will allow near real-time field measurement and identification of contaminant "hot spots" while a field survey is in progress. The source of the contaminants may be inferred by relating imaged fluorescence emission patterns to conventional color red, green, blue (RGB) images of sedimentary bottom structures, as viewed in vertical profile, such as dredged material layers, sewage layers, oil globules, and biogenic features.

2. TECHNICAL DESCRIPTION

The method of deployment and mechanical operation of the camera/sensor will be similar to that employed for the existing REMOTS® sediment profile camera (Fig. 1). The imaging window size is 15 cm wide by 20 cm high. Beyond this, the REMOTS® imaging spectrometer bears little resemblance to the existing optical system which consists of a 12 W tungsten strobe and 35 mm film camera.

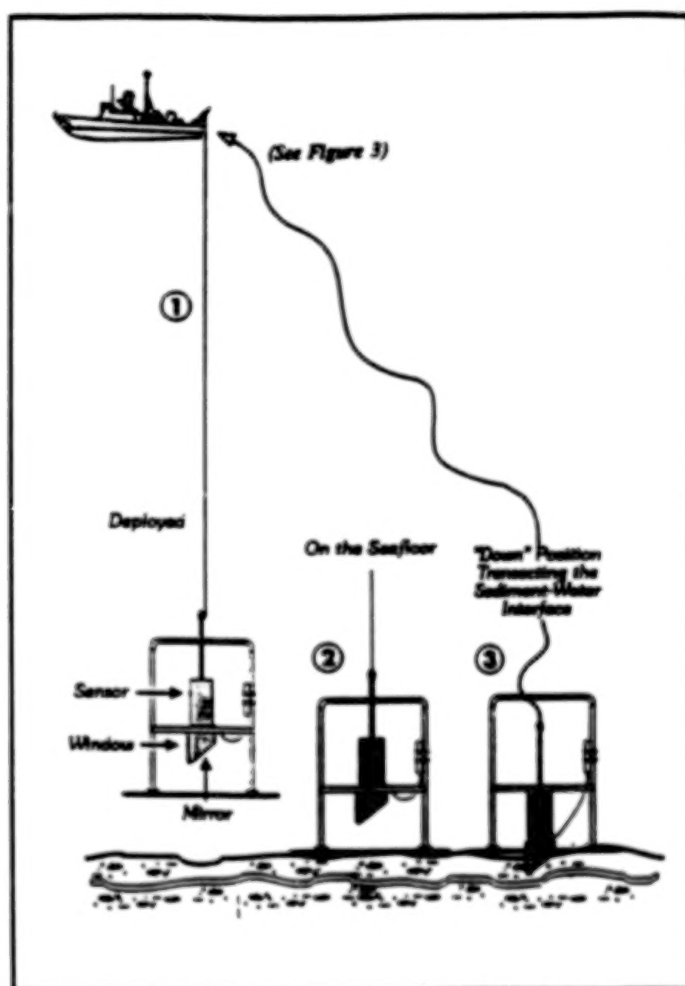


Figure 1. Deployment of the REMOTS® UV Imaging Spectrometer. 1) Lowering from vessel with the sensor held in an "up" position above the base frame. 2) On the bottom with the sensor still in an "up" position above the base frame to avoid disturbing the surface by a pressure wave. 3) When the winch wire goes slack, the sensor slowly penetrates the bottom to acquire a sediment profile color image and spectroscopic measurements of contaminants in the imaged field (up to 17 emission bands per excitation band).

The new REMOTS® UV imaging spectrometer presently exists as an unruggedized laboratory prototype. A high intensity UV-rich lamp illuminates the sediment profile. Blocking filters define discrete UV excitation bands and exclude all visible light. An electrically cooled UV-sensitive CCD camera is used for conventional RGB color imaging and for collecting discrete emission spectra from up to 17 x 10 nm wide emission bands. Appropriate blocking and collection filters are contained in mechanized filter wheels for sequential excitation/emission imaging. Because of the blocking filters, no image is produced unless there are fluorescent compounds in the field of view (sediment column) that have converted excitation UV bands into visible light (Fig. 2).

The camera/sensor communicates with an on-board computer via a power and communication cable, and receives operational commands from this deck computer. Collected images and spectral data are transmitted up to the deck computer for storage, display, and analysis (Fig. 3).

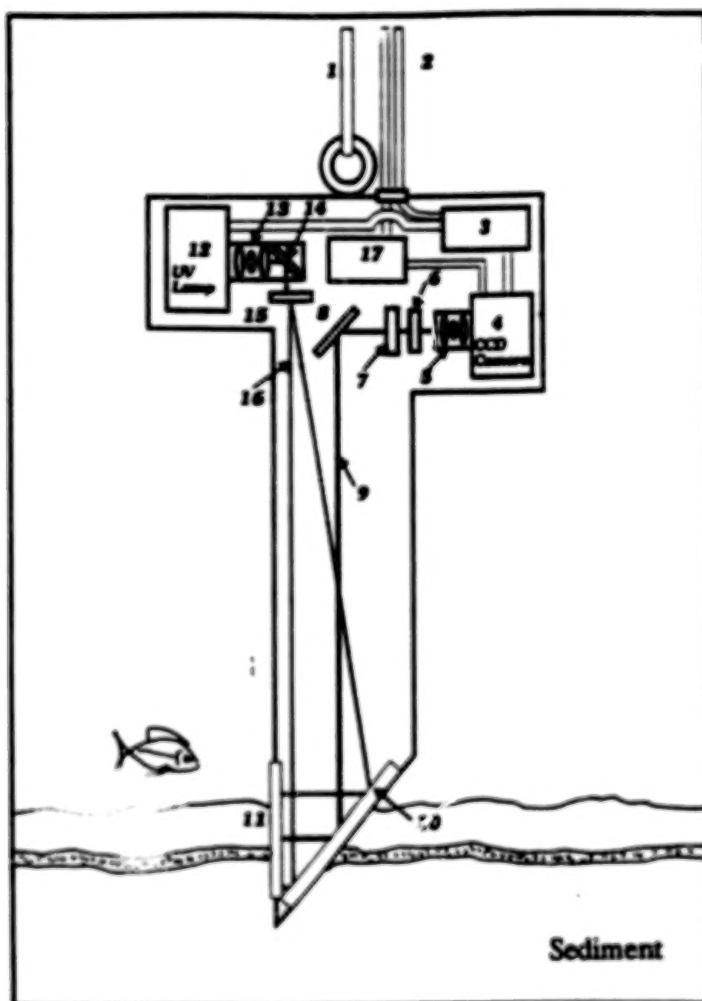


Figure 2. Schematic cross-section of the optical sensor showing major components: (1) lowering cable, (2) power and signal cables, (3) controller for camera and mercury lamp, (4) thermal electrically cooled CCD camera, (5) lenses, (6) spectral filter mounted in a filter wheel, (7) excitation blocking filter in a filter wheel, (8) 45° UV coated mirror, (9) sediment profile image path, (10) 45° first surface UV coated mirror, (11) quartz pressure window, (12) Hg lamp, (13) collimating lenses, (14) UV coated mirror, (15) excitation filter in a filter wheel, (16) excitation light path, (17) power control/conditioner for light and camera.

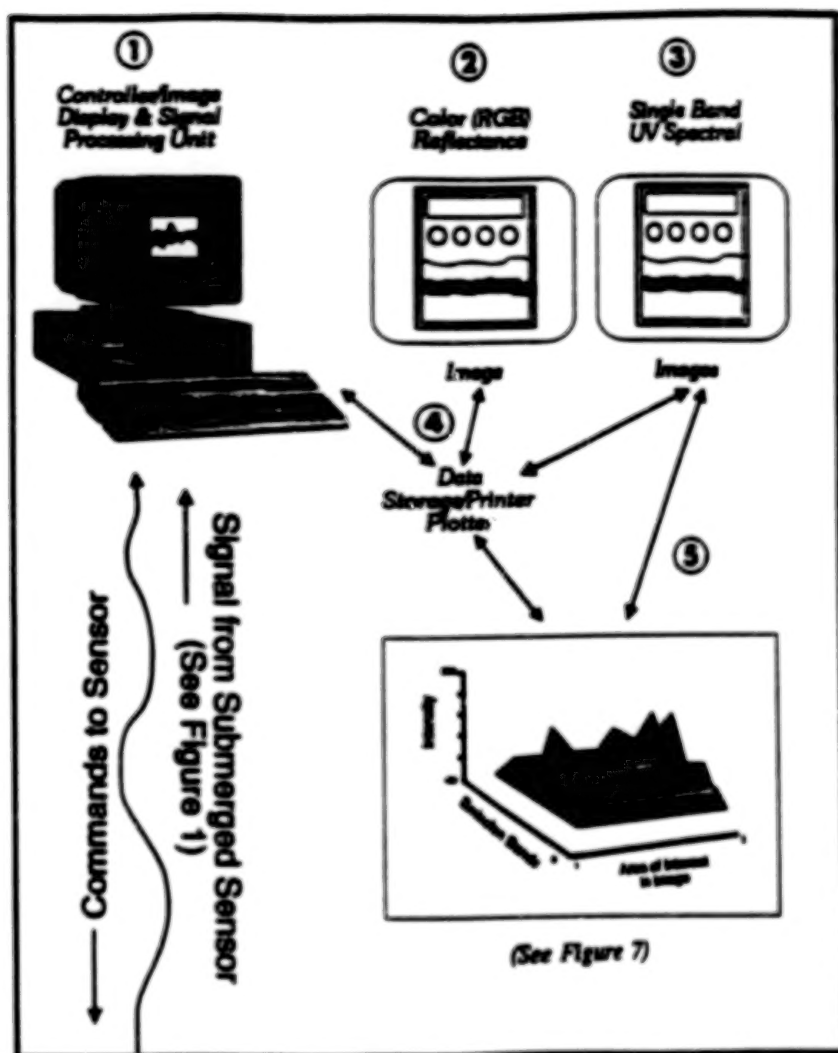


Figure 3. Shipboard controller and image acquisition/storage/processing unit (1). Commands are down-linked to control sensor functions and coordinate measurement sequencing. RGB color image (2) and UV emission spectra (3) are up-linked to the deck computer where they are stored, displayed, printed (4), and spectrally analyzed (5).

The sediment imaging window, as seen by the CCD camera, is shown in Fig. 4. Reference cells are placed at the top of the quartz window above the sediment-water interface. These cells are a unique feature of this spectrometer because they contain blanks (unspiked sediment + water occupying pore spaces between sediment particles) and sediment spiked with known concentrations of compounds of interest + pore water. The blanks allow one to correct sample spectral returns for sediment matrix effects, background fluorescence, and pore-water effects. Spiked references provide quantitative calibration curves for calculating concentrations from fluorescence emission intensities. In addition, the imaged references are part of the QA/QC protocol, allowing evaluation of sensor performance (accuracy and precision) for each excitation wavelength.

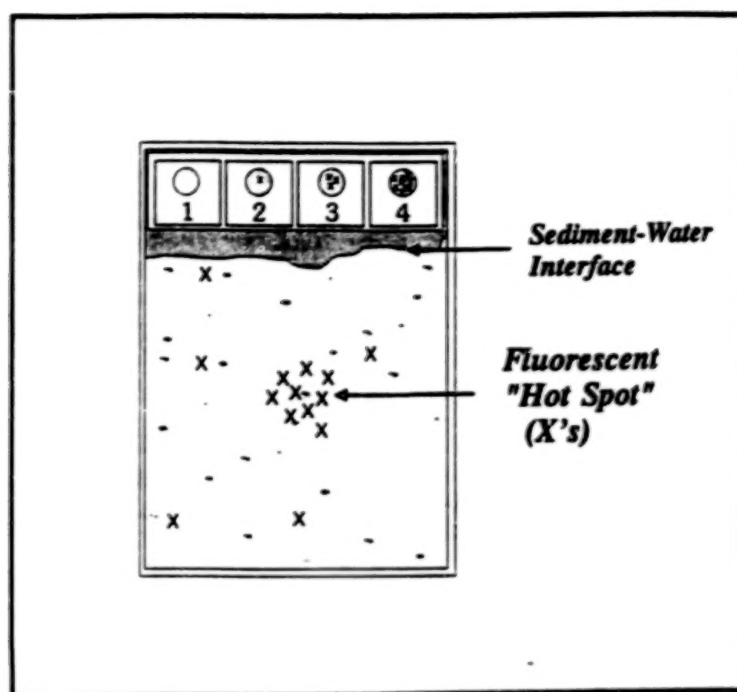


Figure 4. The imaged sediment profile as seen by the CCD camera. The field is divided into the sediment profile (below arrow) and water column (above arrow). Areas of intense fluorescence are shown as x's. Areas within the sediment that are uncontaminated occupy the rest of the sediment profile. The four cells at the top of the imaged field represent: (1) a blank containing uncontaminated sediment + clean ambient pore water, (2-4) spiked references containing contaminants of interest or a single contaminant at three different spiked concentrations. The number of reference cells is not limited to four. Smaller diameter cells can be used to increase the number of cells placed at the top of the imaging window.

3. PRE-SURVEY PREPARATION

Because survey goals differ from project to project, the instrument may require some pre-survey preparation. First, the client needs to list compounds of interest and threshold concentrations of concern. Small representative samples of reference (low contaminant or background) sediment from the survey area may also be needed to prepare blanks and spiked standards (see Measurement Sequence).

Information on target compounds and threshold concentrations will be entered into a computer program that specifies optimal instrument settings for specific compound identification and quantification including: excitation/emission frequencies, spacing of emission filters, pixel binning requirements, and emission read times. Once the appropriate excitation and emission filters have been installed in the filter wheels (Fig. 2), signal acquisition times for each emission wave length programmed, and appropriate blanks and spiked sediment standards have been prepared, the system is ready for deployment.

Optimal instrument settings will be based on a unique spectral library of fuel oils, crudes, and individual PAHs that is being developed for this instrument by SAIC. The spectral library is based on spectrometer measurement of spiked sediments having a defined grain-size, mineralogy, organic carbon content and pore water salinity.

4. MEASUREMENT SEQUENCE

After the camera/sensor is deployed on the seafloor and the optical prism has cut a vertical profile of the bottom (see Fig. 1), the CCD camera obtains a conventional color image of the sediment column by rotating red, green, and blue (RGB) filters in front of the CCD camera lens. Once the RGB image is obtained, deck commands begin sequential collection of UV emission spectra ($n=1$ to 17 bands) at a programmed excitation wave length ($n=1$ to 3 bands). The ideal rate of measurement is one emission band within 1 to 5 seconds. The pre-survey preparation will have determined the minimum number of excitation/emission bands and read times required to identify the compound(s) of interest within 45 seconds. The limit on bottom deployment time is based on many years of experience with the existing REMOTS® system.

The system can be deployed from small (40-60') vessels of opportunity which do not have special station-keeping equipment such as thrusters. If bottom times are greater than 45 seconds, cable angles become large due to vessel drift-off and the additional time required to reposition the vessel for acquiring replicate measurements compromises survey efficiency. Actual bottom times will be dictated by fluorescence yield of target compounds, specified concentration thresholds for detection, and the number of excitation/emission channels required to identify target compounds as determined by the spectral library and pre-survey preparation protocol.

5. ONBOARD ANALYSIS

Proprietary software called SARC (Spectral Analysis of Remots® Chemistry) has been developed to collect, store, and analyze imaged spectra while a survey is underway. Data acquisition and analysis consists of three steps: 1) Display of the conventional RGB image to identify stratigraphic features of interest such as dredged material or sludge layers, or oil globules, 2) Visual display of total UV fluorescence intensity summed over all emission bands in order to rank a replicate as falling above or below the threshold concentration of concern, and 3) Analysis of component compounds and their concentrations for the station subset falling above the pre-selected threshold concentration ("hot spots"). An example of such a quick-look analysis is shown in Figs. 5, 6, and 7 for an experimental mixture of anthracene, pyrene, and benzo(a)pyrene. At a minimum, by the end of a survey day, a map of hot spots will be prepared. The degree of quantification and compound identification will depend on the number of stations/replicates and spectral complexity of the data files.

6. POST-CRUISE ANALYSIS

Spectral unfolding of complex mixtures, and relating these mixtures to imaged sedimentary structures, may require post-cruise analysis using algorithms for extracting spectra from each pixel in the imaged field of interest. For example, the triple mix spectrum shown in Fig. 5 (h) shows three distinct peaks. By comparing the positions of these peaks with the spectral library of the three component PAHs, we can identify the peak at (b) as being anthracene, the peak at (d) being anthracene + pyrene, and the broad peak at (f) being anthracene + benzo(a)pyrene + pyrene. Again, the degree of quantification and spectral analysis is determined by a client's requirements. For example, mapping of negatively buoyant globules of crude oil may require less sophisticated analysis than a broad mixture of PAHs bound to sediment grains.

The field screening sensor described here is not intended to replace traditional methods such as gas chromatography-mass spectroscopy (GC-MS) or High Performance Liquid Chromatography (HPLC). Rather, the REMOTS® UV Imaging Spectrometer is a rapid field screening system for efficiently defining hot spots and monitoring the effectiveness of remediation. If required, REMOTS® hot spot maps can be used to identify a parsimonious subset of stations for more detailed chemical analysis using traditional methods.

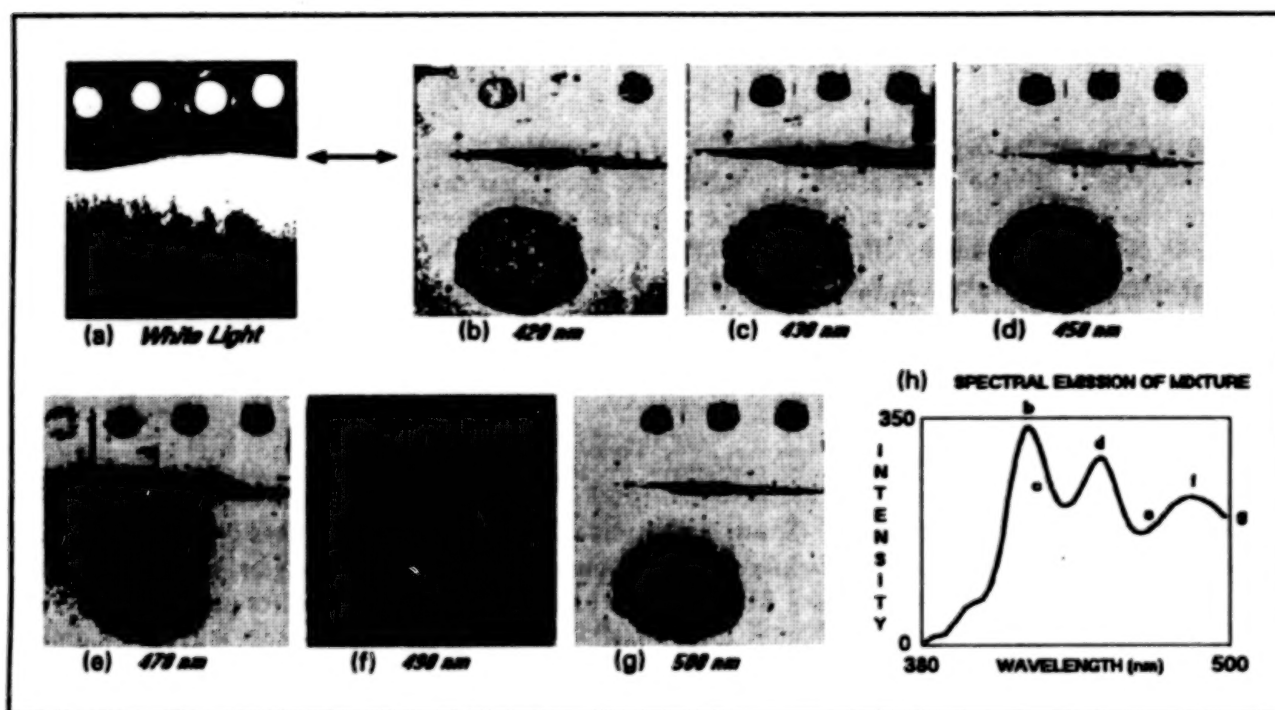


Figure 5. Example of spectral imaging and analysis from the laboratory prototype spectrometer. a) "White light" reflectance image of the test sediment column to be spectrally analyzed, and 4 reference cells at the top of the imaging window. An arrow marks the sediment-water interface. Note that the large circular area (spiked hydrocarbon patch) in the sediment column seen in the following 6 images (b-g) cannot be seen in the white light reflectance image. Images (b-g) are obtained from the same image field as a) using a 314 nm excitation band. Grey scaled emission intensities are imaged for discrete emission bands at 420, 430, 450, 470, 490, and 500 nm. The large circular area of high emission intensities contains a mixture of anthracene (500 ppm), pyrene (500 ppm), and benzo(a)pyrene (500 ppm). Reference cells 2 through 4 contain sediments spiked with 1000 ppm of anthracene (cell #2), benzo(a)pyrene (cell #3) and pyrene (cell #4), respectively. Spectral intensities are corrected for the blank (cell #1 at top of fig. 4). The emission spectrum of the mixture, including the 6 emission bands, is shown at the lower right (h) using a cubic spline curve fit. See Fig. 6 for calibration curve.

7. FUTURE WORK

Construction, testing, and calibration of a field prototype rated to 100 m depth is planned for 1995, including continued development of the spectral library of EPA priority hydrocarbon pollutants adsorbed onto sediment grains in the presence of pore water.

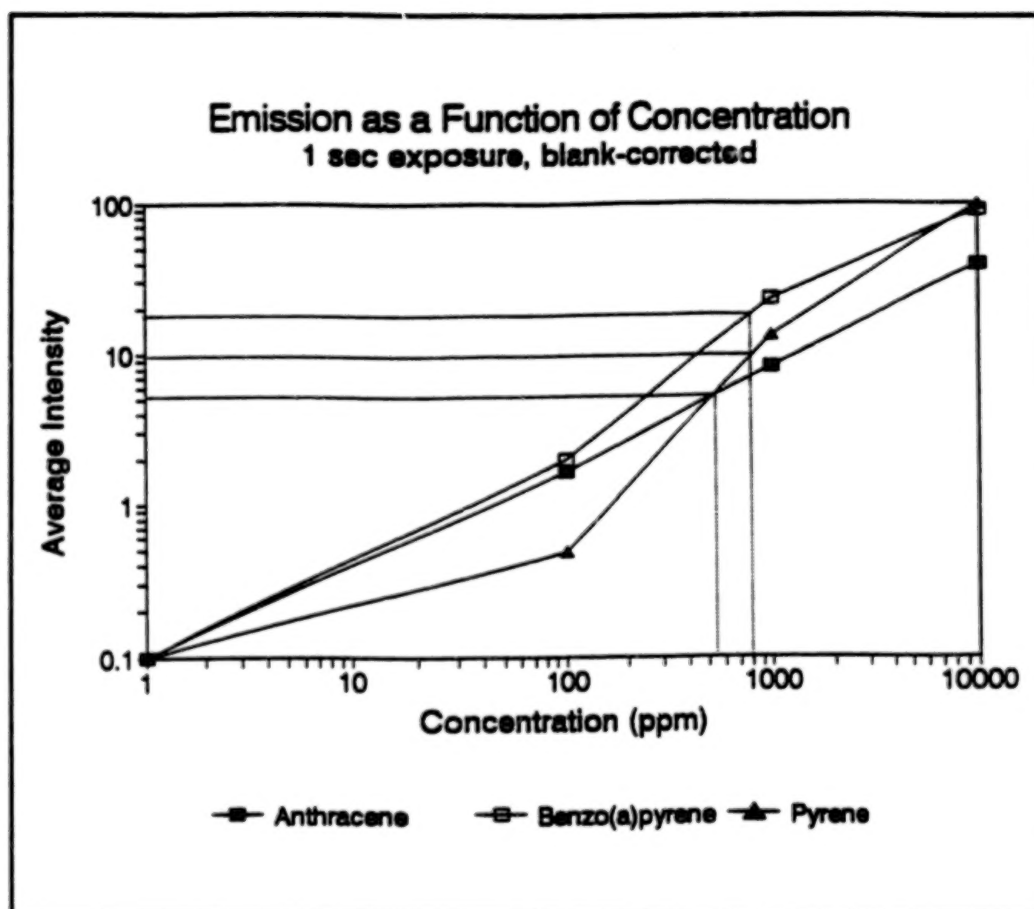


Figure 6. Method of estimating imaged hydrocarbon concentrations in the sediment column. Estimates are made by preparing a calibration curve. This is done by preparing a plot of average emission intensities (at specific emission bands) against concentrations of the spiked reference cells (2 through 4 as shown in Fig. 4). Reference emission intensities are corrected for the sediment blank (reference cell #1 as shown in Fig. 4) and normalized to a 1-sec. exposure time.

This calibration curve is used to estimate concentrations of unknowns in the imaged field by projecting the measured emission intensity (y-axis) onto the concentration axis (x-axis) (shown as dotted lines). The imaged test sediment is estimated to have individual PAH concentrations falling within the range 550 to 800 ppm. The actual spiked concentrations were prepared at 500 ppm.

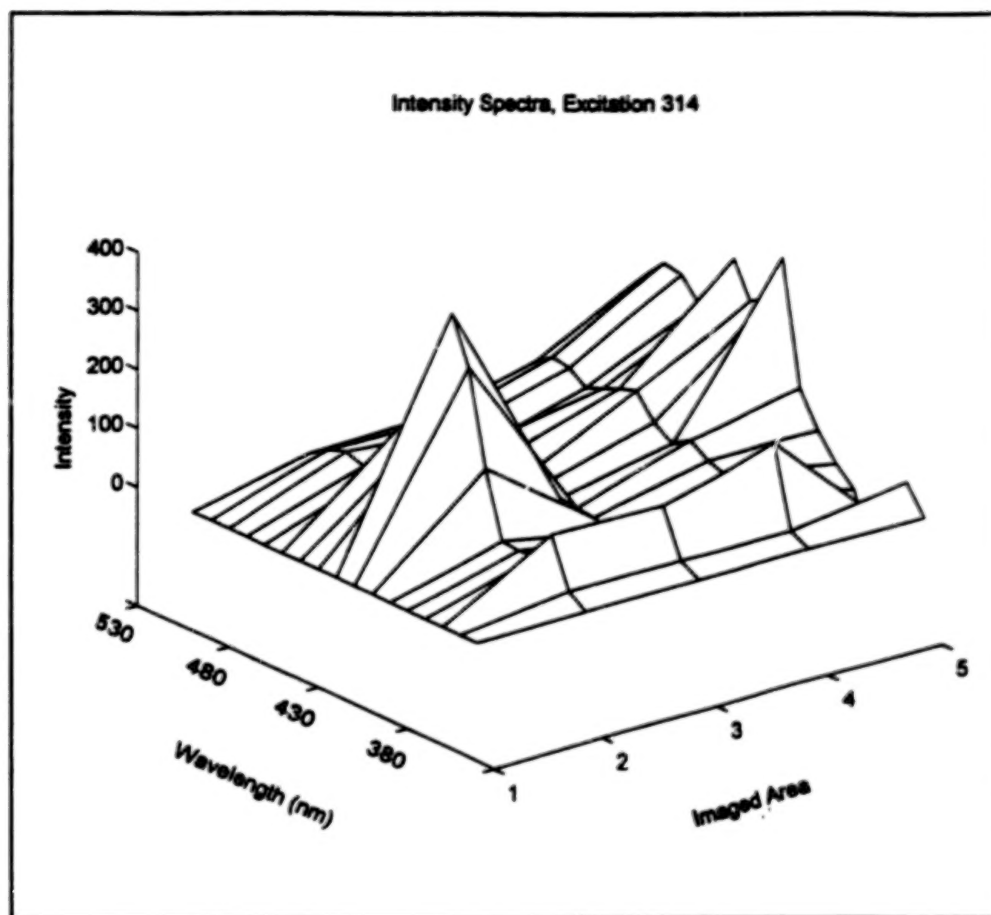


Figure 7. A 3-D plot of spectral intensity versus emission wavelength for imaged areas as shown in Fig. 5. A 3-D plot can be generated for each excitation band (314 nm shown here). Imaged areas (x-axis) refer to reference cells 1-4 (see Figs. 4 and 5) and the spiked triple mixture of PAHs (imaged area 5). These 3-D plots are used to compare spectral intensity signatures of imaged unknowns to the spectral library of known compounds.

ACKNOWLEDGEMENTS

We wish to thank Dr. Neil Blough, Dept. of Marine Chemistry and Geochemistry, Woods Hole Oceanographic Institution, for assistance in preparing spiked test samples and for evaluating the performance of the REMOTS® imaging spectrometer relative to a research quality spectrofluorometer (SLM-AMINCO 500C). Dr. Donald Cobb (SAIC) also assisted in the preparation of spiked standards. Richard Anderson (SAIC) set-up, calibrated, and operated the laboratory prototype. Alan Massey (SAIC) developed the analytical software used in this study.

REFERENCE

- Rhoads, D. C., J. D. Germano, and J. D. Hightower, 1992: The technology of remote ecological monitoring of the seafloor - REMOTS®: 18th meeting of the Marine Facilities Panel of the United States-Japan Cooperative Program in Natural Resources (UJNR). Conference Record, Oct. 1993, U.S. Dept. of Commerce, NOAA, 8 pp.

USING SPECTRAL DATA AND STRESSED VEGETATION TO EVALUATE HAZARDOUS WASTE SITES

M.B. Satterwhite and John E. Anderson
Army Corps of Engineers
Army Topographic Engineering Center
Alexandria, VA 22315-3864
(703) 355-3203

ABSTRACT

The Remote Sensing Division (RSD) at the Corps of Engineers Topographic Engineering Center is currently examining the feasibility of using imaging spectrometry to detect and evaluate hazardous waste sites. Recently, RSD used ground-level reflectance measurements and hyperspectral imagery to evaluate the extent of toxic-induced stress on vegetation at the Savannah River Nuclear Site in Aiken, Georgia. This presentation describes the findings of a study involving hazardous materials leaching out of failed containment facilities at the Savannah River Site.

DESCRIPTION OF WORK

During the summer of 1993, the Remote Sensing Division (RSD) collected field spectral measurements on a variety of contaminated and uncontaminated, vegetated sites at the Savannah River Nuclear Facility (SRS). These spectral collection efforts were made during July and August. Spectral samples of vegetation were obtained along a transect representing a vegetation transition gradient from wetland to upland. The resulting spectra indicate that vegetation contained within two emergent marshes fed by seep zones along the Four Mile Creek drainage area have been stressed by some abiotic mechanism. The spectra provides evidence of chlorosis and possible cellular damage to sampled marsh vegetation. The presence of obligate and facultative wet hydrophytes and hydric soils represented by the Pickney (Pk) sand series and associated Fluvaguents suggests periodic flooding can not fully explain the extent of the stress in the marsh. Additionally, published literature on chemical assays obtained for the watershed reveal moderate to high inputs of tritium, volatile organics, and heavy metals. Hydrologically, the recharge zone for each marsh is located in the vicinity of the F and H reactor site burial grounds and their associated containment facilities.

Analysis of historical Daedalus 1268 (hyperspectral) image data sets obtained over the site from 1988 to 1992 indicated detectable changes in the areal extent of each marsh. The changes in areal extent are evidenced by vegetation stress and death occurring predominantly in trees. Image analysis was performed using an algorithm applied to the band set most indicative of stress. Band selection was made based upon spectral measurements and analysis. Resulting algorithm images provided a multi-temporal description of changes in each marsh based on the signature of stressed vegetation. The success of using ground-level measurements in concert with imaging spectrometers can not be over emphasized.

The results of this study will be used by RSD to pursue research issues involving true spectral characterization of vegetation stressed by hazardous waste. Further research issues involve establishing baseline data using spectral analysis and analytical chemistry to understand the physiological changes in vegetation under stress. New instruments are also being designed to evaluate florescence as well as reflectance.

ROLE OF SAUDI CIVIL DEFENSE IN MONITORING AND PREVENTING ENVIRONMENTAL POLLUTION

F. Al-Khodairy¹, M.H. Al-Tukhi², M.A. Hannan¹, and A. Al-Dakan¹
King Faisal Specialist Hospital and Research Centre¹
Center for Studies and Research, Directorate of Civil Defense²
Riyadh, Saudi Arabia

ABSTRACT

Saudi Civil Defense by definition is a governmental agency which is responsible for protecting lives and belongings of all Saudi citizens during the time of peace and war. This responsibility has been carried out since the establishment of the agency in 1965. The development in the field of environmental protection in the past ten years, forced our Civil Defense to formulate its rules and regulations consistent with the current concepts in the field. One of the major goals is to target the public for increasing their general awareness about the role of the Civil Defense in protecting them against environmental hazards. In this regard, a project was designed to identify and evaluate the possible environmentally catastrophic areas. This project involves three phases. The first phase is concerned with the collection of information about the nature, extent, sources and classification of environmental hazards. The second phase involves analysis of the information from different regions of the country and making efforts to specify and define the needed tools, expertise and methods of operation to solve the environmental problems. These information are also shared with other governmental and private agencies to coordinate their efforts to prevent environmental pollution resulting from industrial growth, life-style changes and uncontrolled use of hazardous materials. Environmental terrorism such as the case of burning Kuwaiti oil wells is given a special attention. As part of the national efforts, the General Directorate of Civil Defense collaborates with other institutes to obtain experimental data on specific and vital environmental problems. For example, preliminary data have been generated by the King Faisal Specialist Hospital and Research Centre on the extent of air particulate mutagenicity in different regions of Saudi Arabia to assess the impact of rapid development in the industrial, agricultural and communication sectors. These data were useful in assessing the extent of mutagenic air pollution due to the burning of oil wells in Kuwait during the Gulf war. Collaborative efforts between the department of Civil Defense and the King Faisal Specialist Hospital and Research Centre proved to be helpful in identifying the source of air pollution and planning strategies for protecting public health. The final phase involves the enforcement of the Civil Defense policies for environmental protection.

INTRODUCTION

Saudi Civil Defense is one of six departments of the Ministry of Interior. Civil Defense by definition is responsible for the protection of lives and belongings of all citizens during the time of peace and war. This responsibility has been carried on since the establishment of this department in 1965. Increase in population, local challenges and Gulf war forced the department of Civil Defense to update its duties and responsibilities. Environmental pollution, transporting and using toxic chemicals and radioactive materials are some of these challenges. Citizens are at risk due to increasing exposure to many pollutants. Some of these exposures maybe accidental or due to the by-products of industrial growth and urbanization, while others are due to man made efforts deliberately designed to harm people. In order to prevent human exposure to these factors it was necessary to develop a proper environmental policy and implement it effectively, (Al-Tukhi & Taj Al-Din, 1994). Therefore, the Civil Defense department has an important role in enforcing some of these policies and penalizing the outlaws. Cooperative programs between the Civil Defense department and other governmental and private agencies concerned with the field of environmental pollution are often developed to study and/or resolve specific problems. In this context, a project was designed in collaboration with the King Faisal Specialist Hospital and Research Centre to examine air samples from different parts of the Kingdom for the presence of mutagenic (potential carcinogenic) agents, as such materials in the air could increase due to industrialization and urban growth as well as the release of toxic chemicals and fumes causing serious health problems (Poli et al, 1992), (Lewtas and Gallagher, 1990); (Chou & Lee, 1990). Our aim is to assess the degree of such problems in Saudi Arabia during the time of peace and such occasions as the Gulf war which was believed to have contributed toward air pollution through burning of oil wells.

Air particulates were collected from the City of Riyadh before the Gulf war (1988), a few months after the torching of oil wells in Kuwait during the war (1991) and several months after the burning oil wells were fully capped (1992), extracted with acetone and the solid residues obtained after evaporation of the solvent were tested for mutagenic activity by using the Ames Salmonella strains for histidine reversion (Ames, 1979); (Maron & Ames, 1983). Results indicated that mutagenicity of air samples from Riyadh during the war was 4-5 times higher than that of both pre-war and post-war levels. This strongly suggested that there would be a significant impact of burning oil wells on the public health and, hence, the appropriate agencies including the Civil Defense department should find ways and means to minimize the exposure of general public to hazardous substances generated by the environmental disaster like the Gulf war.

MATERIALS AND METHODS

A plan of three phases was designed to determine the role of the Civil Defense department and other Governmental and private agencies to address the problems of environmental pollutions. The preparatory phase is to collect and pool all available information needed. Environmental hazard analysis is one important activity of this phase. The planning phase involves the development of strategies in cooperation with the relevant agencies for solving environmental problems. The final phase involves the Civil Defense department in applying the rules and regulations for the safety of all citizens. Air pollution studies fall in the first phase of this overall plan. Air samples were collected on glass filters (whatman GF-A) with a pore size of 1.6µm. the sampling was carried out for 24 hrs. Samples were extracted from filters by acetone and a solid residue was obtained by evaporating the acetone. This residue was redissolved in acetone and tested for mutagenicity by Ames assay (Maron and Ames, 1983) which is designed to screen mutagenic activity of environmental agents using various histidine requiring strains of *Salmonella typhimurium* with or without the addition of a metabolic activation system. Any agent increasing the number of mutations leading to histidine independence in specific strains of *S. typhimurium* is considered as a mutagen and a potential carcinogen. Briefly, 0.1 ml of an overnight bacterial culture was added to 2ml of soft agar, containing 10% of 0.5mM histidine/ biotin, and then different concentrations of the test materials were added and vortexed together with or without a metabolic activation system (S9 mix + co factors) and plated onto minimal glucose agar plates. The plates were incubated at 37°C for 72 hours and the number of histidine revertants per plate were counted and the dose response curves were drawn.

RESULTS

Organic residues of air samples collected from several cities of Saudi Arabia were tested for mutagenicity using the tester strain TA98. Both direct and indirect mutagens (with or without metabolic activation) were found in some cities/sites included in our study. Mutagenicity of air samples varied depending on the environmental conditions of the sites investigated. There was a general indication that air samples from areas near industries or oil refineries, automobile traffic and construction sites were the most mutagenic. Air samples from Ras Tanurah, a site of oil refineries, showed the highest number of histidine revertants/m³ of air as shown in Fig. 1. In this area a 7-8 fold increase air particulate mutagenicity was observed while air samples from Dharan, Al Salam avenue in Riyadh, Buraidah, Al Mulaida farms, and Al Kharj were the least mutagenic with about 1-2 fold increase (Fig. 2). The areas showing the lowest air particulate mutagenicity included those with the least industrial development, little construction activities and low automobile traffic on the roads (Fig 3). Samples collected from the Riyadh city during oil well burning in Kuwait at the time of Gulf war (Fig. 4) showed a notable increase in mutagenicity which reflected a sudden deterioration of the environmental quality. A study conducted six (6) months after the oil wells were capped showed a decrease in mutagenicity which assumed the pre-war level (Fig. 4). The increase in air particulate mutagenicity in Riyadh during the period of oil well burning in Kuwait could only be attributed to the airborne particles and smoke arising from the torching of oil wells.

DISCUSSION

A difference in the levels of mutagenicity of air samples collected from different locations suggested a variation in the air quality of these areas. Samples from polluted places like industrial areas and oil refinery sites such as Ras Tanurah showed the highest number of revertants/m³ of air analyzed. Mutagenicity of air samples collected from the city of Riyadh was in general low indicating a better air quality compared to Ras Tanurah. However, a sudden increase in air pollution caused by the burning of oil fields in Kuwait resulted in increased mutagenic air particulates in Riyadh and possibly a greater increase in areas bordering Kuwait. Data showed that mutagenic materials were released in the environment by industrial emissions as well as wartime activities. People living around petrochemical refineries are at greater risks, for health hazards. The threat to human health can considerably increase by sudden acts of war.

Therefore, there is a need for continuous monitoring of air quality by both physical tools and bioassays to identify the nature of environmental pollutants and ascertain the potential risks to human health. Our Civil Defense department is currently pursuing such studies with an aim to identify the pollutants, their sources and to take appropriate measures to prevent or minimize exposure of our population to harmful agents.

REFERENCES

- Al-Tukhi, M.H. and M. Taj Aldin, 1994: Role of Saudi Civil Defense in Monitoring and Preventing Environment from Pollution in Peace and War time. Report, 1-5 Saudi Civil Defense Publications, Riyadh, Saudi Arabia.
- Ames, B. 1979: Identifying Environmental Chemicals Causing Mutation and Cancer, *Science*, **204**,587-593
- Maron, D.M., and B.N. Ames, 1983: Revised methods for the salmonella mutagenicity test. *Mutation Research*, **113**,173-215.
- Chou, M.C., and H. Lee, 1990: Mutagenicity of airborne particles from four cities in Taiwan.
- Lewtas, J., J. Gallagher, 1990: Complex mixtures of urban air pollutants: Identification and comparative assessment of mutagenic and tumorigenic chemicals and emission sources [Review] *IARC Scientific Publications-Lyon*, **104**,252-160.
- Poli, P., A. Buschini, N. Companini, M.V. Veltori, F., Fassoni, S. Cattani and C. Rossi, 1992: Urban air pollution: Use of different mutagenicity assays to evaluate environment genetic hazard. *Mutation Research*, **298**(2),113-123.

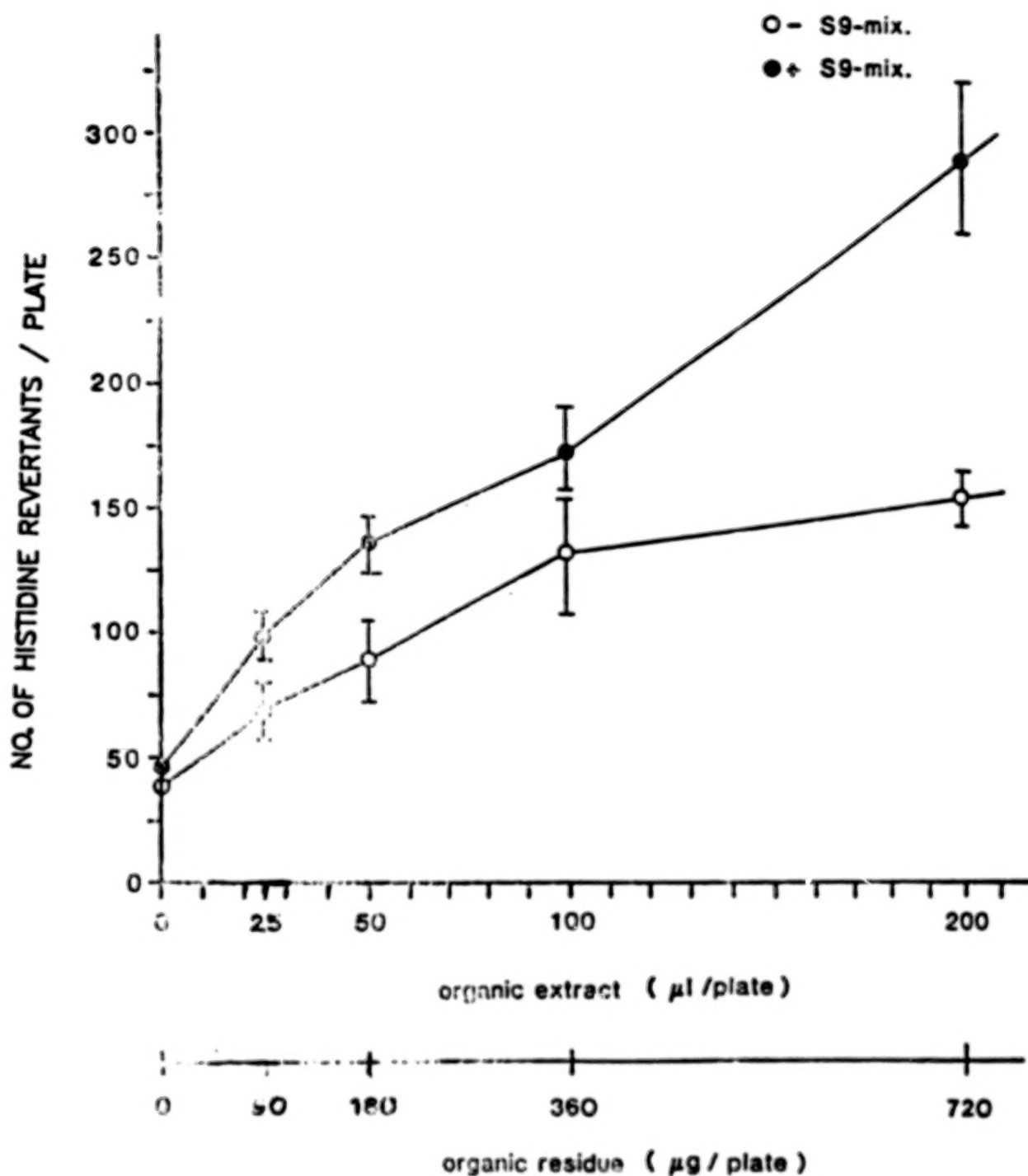


Fig. 1 Dose-response curves for histidine revertants/plate resulting from different concentrations of an organic extract of the air sample obtained from Ras Tanurah (residential area).

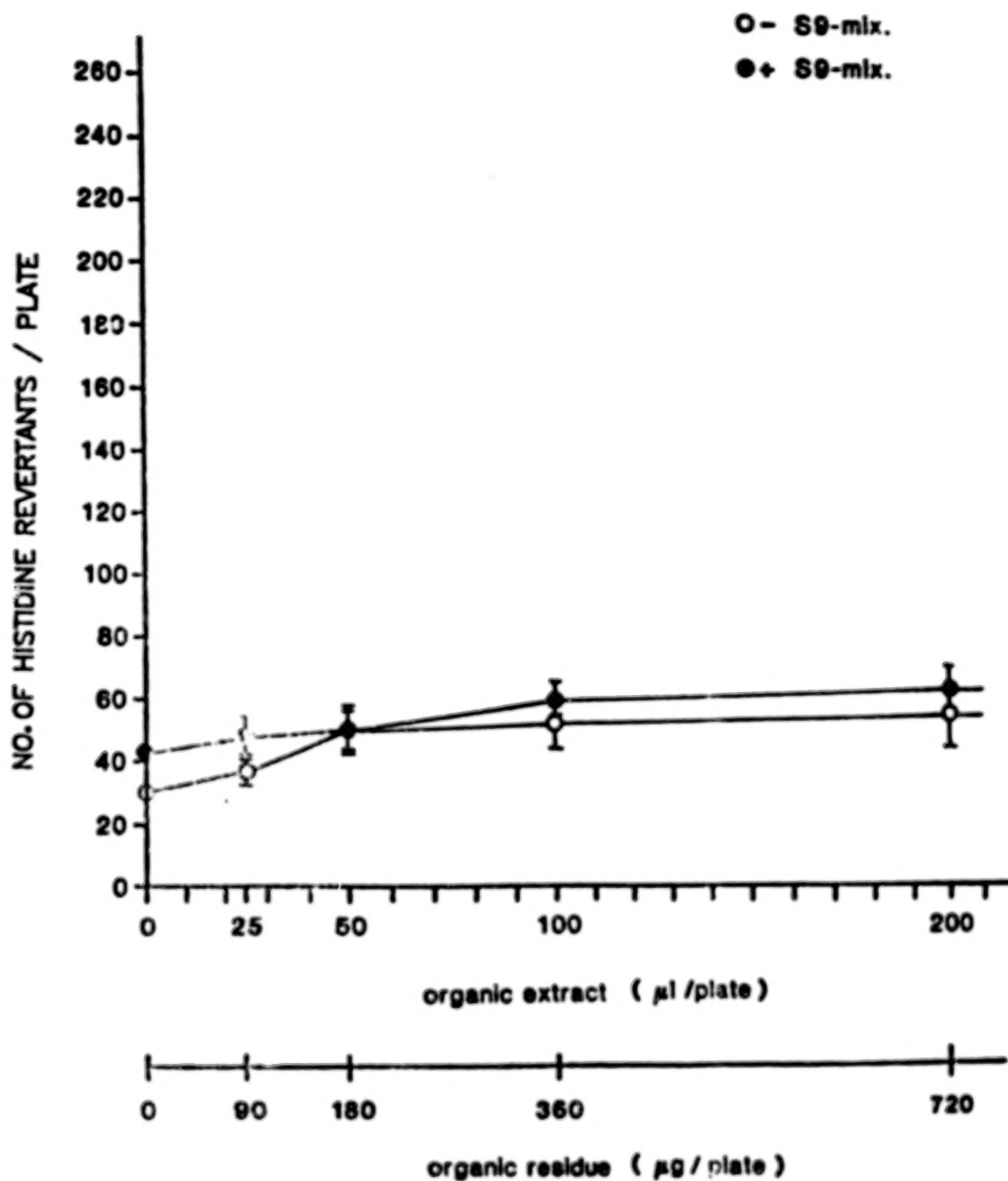


Fig. 2 Dose-response curves for histidine revertants/plate resulting from different concentrations of an organic extract of the air sample obtained from Al-Salam Avenue (in Riyadh).

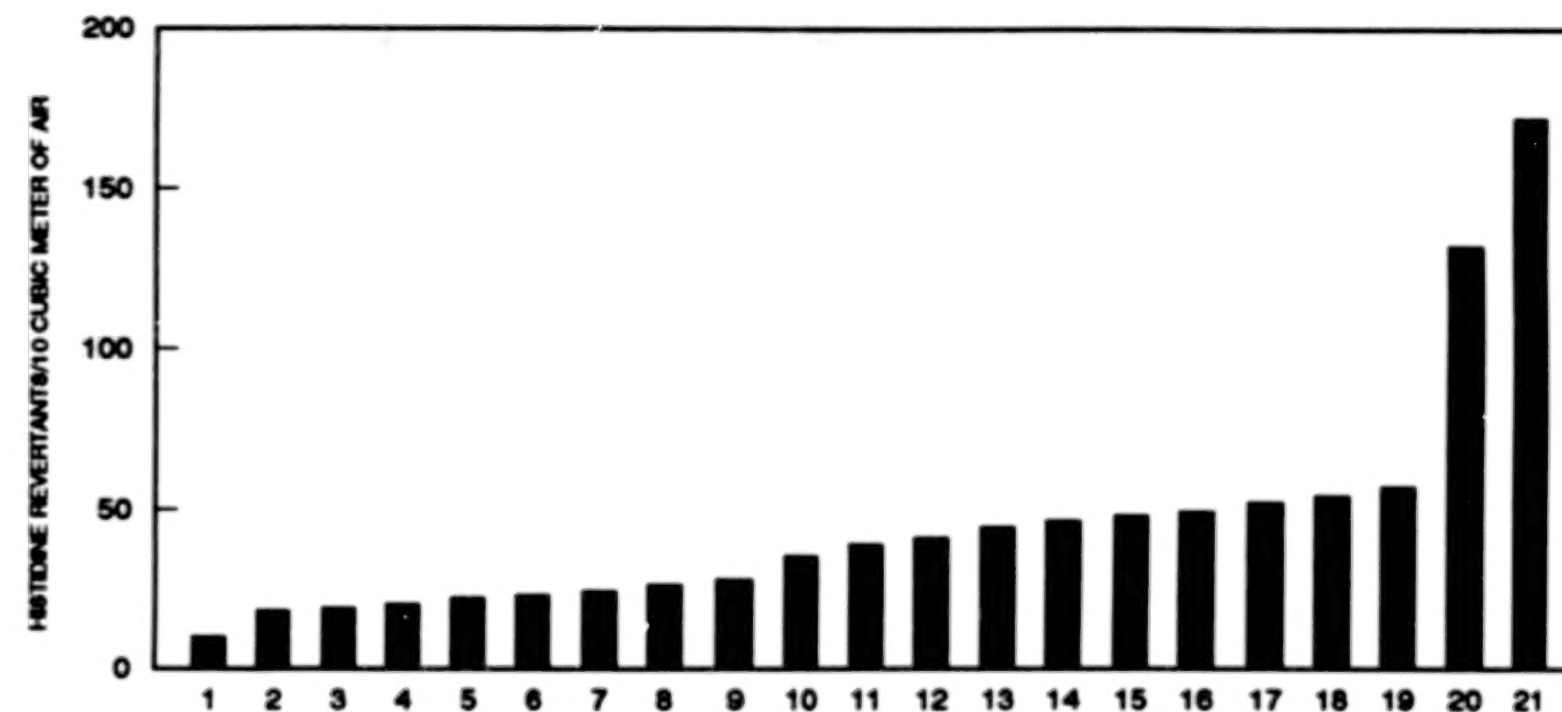


Fig. 3: Rank ordering the investigated areas according to the mutagenicity of their air samples (revertants/m³ of air) with S9-mix (nos. 1-21 represent the areas are as follows):

- | | | |
|-----------------------------------|---------------------------|------------------------------------|
| 1) Dharan (Dharan/Dammam Highway) | 8) Buraidah City | 15) Medinah Center |
| 2) Dharan (Aramco compound) | 9) Al-Kharj farm | 16) Medinah North |
| 3) Al-Salm Avenue (Riyadh) | 10) Batha street (Riyadh) | 17) Riyadh zone site 2 |
| 4) KFSH & RC roof (Riyadh) | 11) KAC roof (Riyadh) | 18) KAC basement (Riyadh) |
| 5) Al-Kharj City | 12) Riyadh zone site 1 | 19) Medinah South |
| 6) Al-Mulaida farmland (Qassem) | 13) Jubail zone 1 | 20) Ras Tanurah (residential area) |
| 7) Jubail residential area | 14) Jubail zone 2 | 21) Ras Tanurah (oil refinery) |

000416

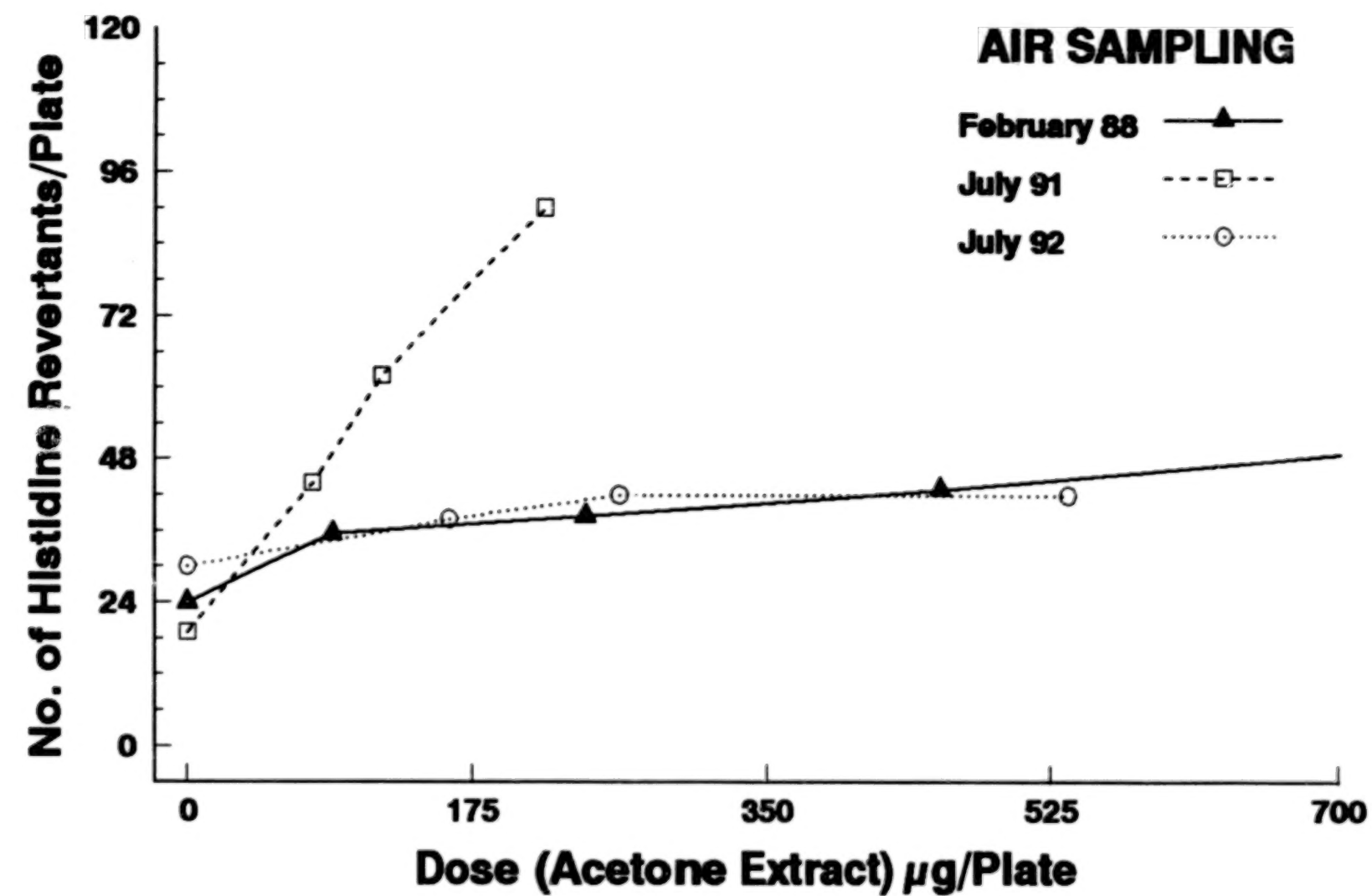


Fig. 4: Air samples from Riyadh City after Gulf war and during oil wells burning

000417

ANALYSIS OF THE 1993 FLOOD USING DIGITAL
REMOTELY SENSED DATA

Donn Rodekohr
ERDAS, Inc.
Atlanta, GA 30329
(408) 778-1100

The 1993 flood caused extensive damage in the Midwestern United States including property and agricultural losses. Although the flood was a terrible natural disaster, it provided an opportunity to demonstrate the advantages of using remote sensing technology for disaster analysis. Remotely sensed imagery was used to provide information to emergency response agencies that would not otherwise have been available. The ability to acquire remotely sensed data over very large areas, in a timely manner, is a distinct advantage for this type of analysis.

EOSAT, Inc., Geodynamics Corporation, and ERDAS, Inc. coordinated efforts to assemble an emergency response team to provide information that was derived from remotely sensed data. These three companies analyzed and processed Thematic Mapper imagery (TM) to generate hard copy maps and digital data that were delivered to the U.S. Army Corps of Engineers Emergency Operations Center in Washington, D.C. and the Federal Emergency Management Agency (FEMA). The Army Corps of Engineers received maps of TM imagery that could be used for an overview of the situation and briefings. The Corps of Engineers also received digital files derived from TM data showing the water-land boundary. These files were used in conjunction with existing Corps of Engineers data bases for further analysis of flood damage.

ERDAS, Inc. has continued to use satellite imagery to assess the flood now that the initial emergency phase is over. Additional information was incorporated into the analysis of a study area along the Mississippi River near Quincy, Illinois. Digital Elevation Models (DEM) were used to determine a more accurate water-land boundary, and analyzed to predict areas that were at a high risk of flooding if dikes or levees failed. More work was done to determine the number of flooded or high risk acres for each land cover type in the study area.

Manuscript not available at time of printing. Please contact author for further information.

APPENDIX A
PROCEEDINGS ONLY

**The following papers were not presented at ISSSR '94
and should be recognized as proceedings only status.**

BLANK PAGE

**CCD SENSORS APPLICABLE IN TRACKING AND IMAGING SPECTROMETERS:
STUDY AND CORRECTION OF THEIR SPECTRAL CHARACTERISTICS**

Valentin Atanasov, Alexander Krumov, Valentina Boycheva
Solar-Terrestrial Influences Laboratory
Bulgarian Academy of Sciences
1113 Sofia, Bulgaria

ABSTRACT

The spectral characteristics of charge-coupled devices (CCD), used in tracking and imaging spectrometers influence essentially the metric characteristics of such systems. Studying the parameters of the existing systems corroborates the opinion that their basic characteristics are determined mainly by the specific CCD. The paper presents some important characteristics of CCD when operating in tracking and imaging spectrometers. Relationships between CCD functional modes and photo-electric characteristics are established and their effects on the metric characteristics of such systems are highlighted. Experimental data is shown related to the spectral response as a function of temperature, integration time, etc. A particular attention is being paid to remove or compensate the changes of CCD sensors spectral characteristics depending on the specific operating conditions. The suggested methods cover both hardware solution to remove possible deviations and subsequent correction of already obtained characteristics. Conclusions are drawn and recommendations are suggested concerning tracking and imaging spectrometers designers and users.

1. INTRODUCTION

Charge-coupled devices (CCD) are widely applicable nowadays in designing modern spectrometers and imaging spectrometers (Mishev et al., 1991; Kovachev et al., 1992; Krumov et al., 1992). This fact is based on a series of advantages compared to the foregoing vacuum devices, namely, wide spectral range, high noise stability and aptitude for big optical overloads, high linearity of the optical-electronic transformation, exact geometric size of the image, easy control, low energy consuming, small size and weight.

2. THEORETICAL BACKGROUND

From designer's point of view CCD represent a series of MOS capacitors that are periodically charge coupled. The size of the charge packet collected on a definite element (Nosov and Shimin, 1986) is proportional to the integration time t (when the photo-generated charges fill only partly the potential well within the period of integrating the luminous flux Φ):

$$Q_p = q \Phi T_{tr} \eta [1 - \exp(-\alpha x)] / (1 + \alpha L_n) \quad (1)$$

where α is the absorption coefficient of the material, T_{tr} - transmission coefficient of the multi-layer structure; η - quantum yield of the photoemissive effect; x - the depletion layer width, L_n - the diffusion length.

Authors turn their attention to some photo-electrical characteristics of CCD image sensors, namely, light-signal and spectral response which exert a significant influence upon the metric characteristics of spectrometers.

The spectral response, defined as a dependency of the collected and transferred toward the output photogenerated charge packet upon the wavelength, is viewed as one of the most important characteristics of CCD sensors embodied in imaging spectrometers. The spectral characteristic is determined by three factors: the absorption coefficient $\alpha(\lambda)$, the spectral transmission coefficient of the multi-layer structure $T_{tr}(\lambda)$, and the quantum yield $\eta(\lambda)$.

3. CASE STUDY

A light source with known spectral density of the luminous flux $\Phi(\lambda)$ has been used to measure the spectral characteristics - the monochromator VSU2 (Karl Zeiss). The voltage amplitude of the output signal U_{out} is being measured vs. the dark current signal U_d . The output voltage U_{out} variation when the charge packet Q_p comes in, is determined by the expression (Norsov and Shimin, 1986)

$$U_{out} = \gamma Q_p / C \quad (2)$$

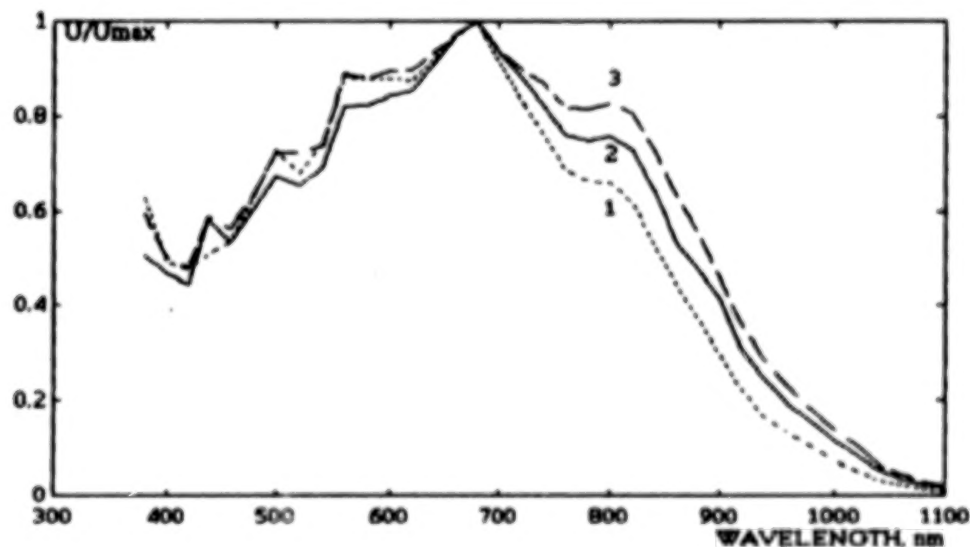


Figure 1. Spectral sensitivity of CCD array K1200CL7 at different temperature values: curve 1 - $T_1 = 24$ deg C, curve 2 - $T_2 = 35$ deg C, curve 3 - $T_3 = 46$ deg C.

where: γ is a proportionality coefficient, C - CCD's output capacitance. Usually, the spectral characteristics are displayed in relative units.

Experimentally obtained spectral characteristics of the CCD K1200CL7 (Press, 1991) depending on the temperature are shown in Fig. 1. Apart from the featuring drops in the device response within the short-wavelength region (caused by absorption in the material) and within the long-wavelength region (conditioned by the fundamental absorption's edge of silicon), a variation in the spectral response of device depending on the temperature is being observed. The analysis of obtained results proves that change in spectral sensitivity occurs in two ways. First, the spectral characteristics move towards the long-wave region, and second, they expand as the temperature rises.

This variation accounts for a spectral characteristic widening as the temperature rises which is due to the quantum yield increase when the transition temperature goes up. It is conditioned by the alteration of the forbidden energy gap, the absorption coefficient and the bulk charge thickness. This effects can be removed by ensuring a constant working temperature of CCD in thermostat which is a comparatively easy way. The results are discussed in greater details in (Atanasov et al, 1992). At the same time we know that for each 7deg C drop in temperature the dark leakage current is cut in half. Therefore, the signal/noise ratio of CCD can be improved by reducing its temperature. Basically, the application of CCD embodied in various spectrometric systems is related to the necessity of meeting requirements for wide dynamical range and/or long integration time. All of these can be efficiently achieved by cooling the devices using one of multiple known methods: built-in thermoelectrical coolers using the Peltier-effect; multiple stage coolers; Joule-Thomson cooler; by mounting the image sensor on a "cold finger" which is attached to a dewar of liquid coolant.

Usually, the specifications of CCD offered by manufacturers are not totally adequate for application in spectrometric and video-spectrometric systems. Such special requirements as low dark leakage current or improved non-uniformity of sensitivity can be achieved through a special selection of devices. A universal method of removing the non-uniformity of sensitivity which can as well be efficiently used for a correction of warped spectral characteristics depending on operational modes (temperature, integration time), is a subsequent software correction of the obtained spectral characteristics.

In most practical cases the application of CCD arrays in imaging spectrometers is connected to the device performance under poor illumination conditions. Many manufacturers supply photodiode CCD and several wide aperture devices for increased sensitivity. The coupling of the image intensifiers available from several magnifications can improve the sensitivity of the arrays. A widespread method of generating large enough charge packets under low luminance conditions is having the integration time (t) increased. That is why dependency of CCD spectral response on integration time proves to be very interesting. It is known that

$$\text{Exposure (E)} = \text{Light Intensity (I)} * \text{Integration Time (t)} \quad (3)$$

In Fig. 2 is shown a family of experimental dependencies of CCD spectral response at fixed light intensity I and different integration times $t_1 > t_2 > t_3$. From this figure we can deduce that noticeable variance in the spectral response (over 10%) exists within given wavelength range e.g. 500-600 nm, 750-850 nm. Obviously, despite the linear increase of the integral response as the integration time (t) increases, the CCD spectral response does not stick immediately to a linear law.

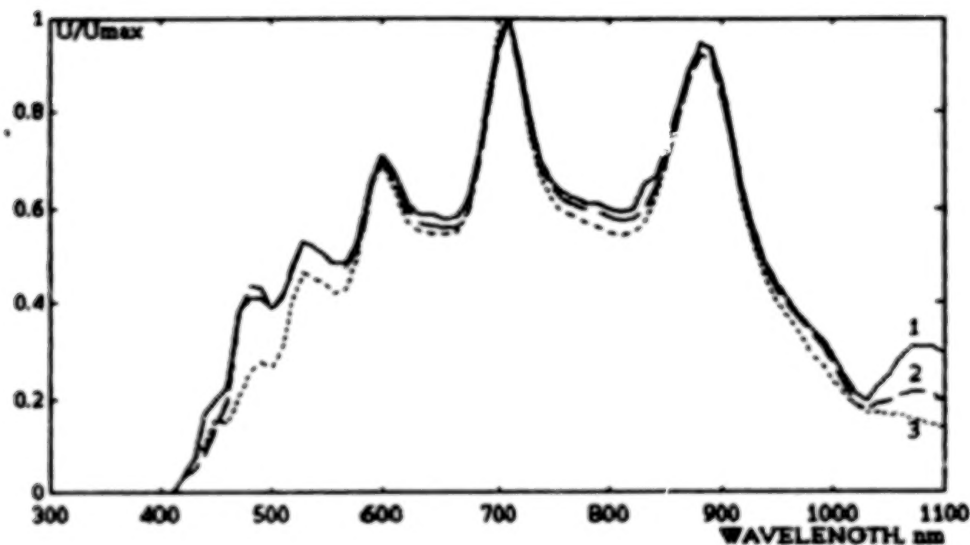


Figure 2. Spectral sensitivity of CCD array at different integration times: curve 1 - $t_1 = 10$ ms, curve 2 - $t_2 = 5$ ms, curve 3 - $t_3 = 1$ ms. Light intensity = const.

In Fig. 3 are shown spectral characteristics of a line array for different light intensity values ($I_1 > I_2 > I_3$) with a constant integration time t . The curves demonstrate a change in the spectral sensitivity for the same wavelengths and of the same order (10-20%). Therefore, in order to control the device response by varying the integration time, a preliminary additional calibration is needed which consists in applying a set of correction factors on images obtained at different integration times. A comparison of changes in spectral sensitivity from Figs. 2 and 3 highlights their reverse trends.

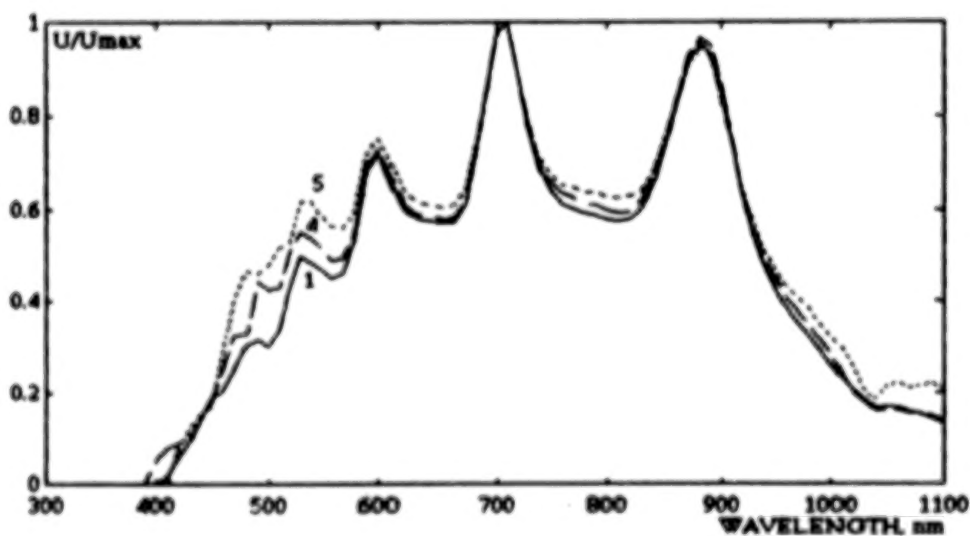


Figure 3. Spectral sensitivity of CCD array at different light intensity values: curve 1 - I_1 , curve 4 - I_4 , curve 5 - I_5 . ($I_1 > I_4 > I_5$).

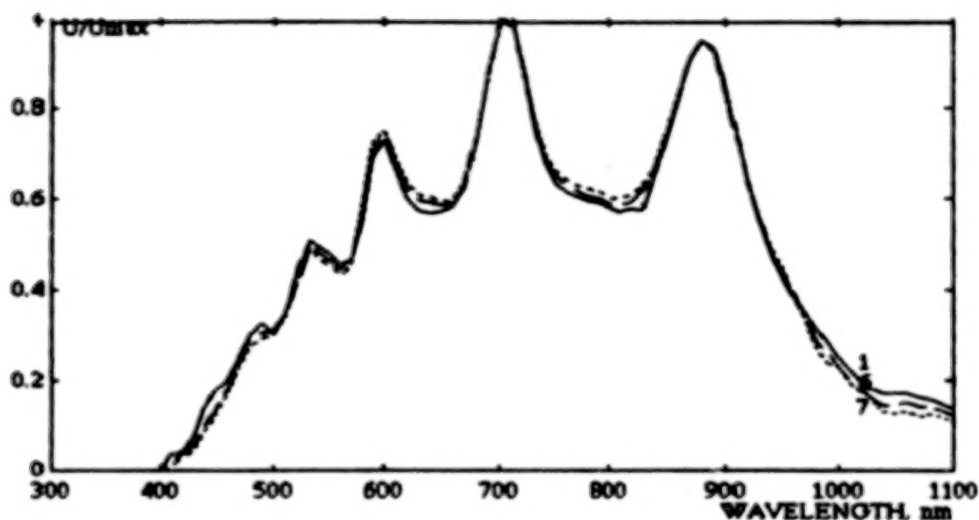


Figure 4. Spectral sensitivity of CCD array when simultaneous unidirectional changes in integration time and light intensity occur: curve 1 - I_1, t_1 ; curve 6 - I_6, t_6 ; curve 7 - I_7, t_7 . ($I_1 > I_6 > I_7, t_1 > t_6 > t_7$).

Figure 4 presents the spectral sensitivity of CCD array at a simultaneous unidirectional change in integration time $t_1 > t_6 > t_7$ and light intensity $I_1 > I_6 > I_7$, i.e. reduction of both intensity and integration time. Applying this stabilization method brings about a relative constancy compared to the preceding cases (Figs. 3 and 4). The differences

$$\Delta = U_j - U_1 \quad \text{at } j = 4, 5 \text{ (Fig. 5) and } j = 6, 7 \text{ (Fig. 6).} \quad (4)$$

between spectral characteristics obtained under conventional and stabilized conditions and the root mean square

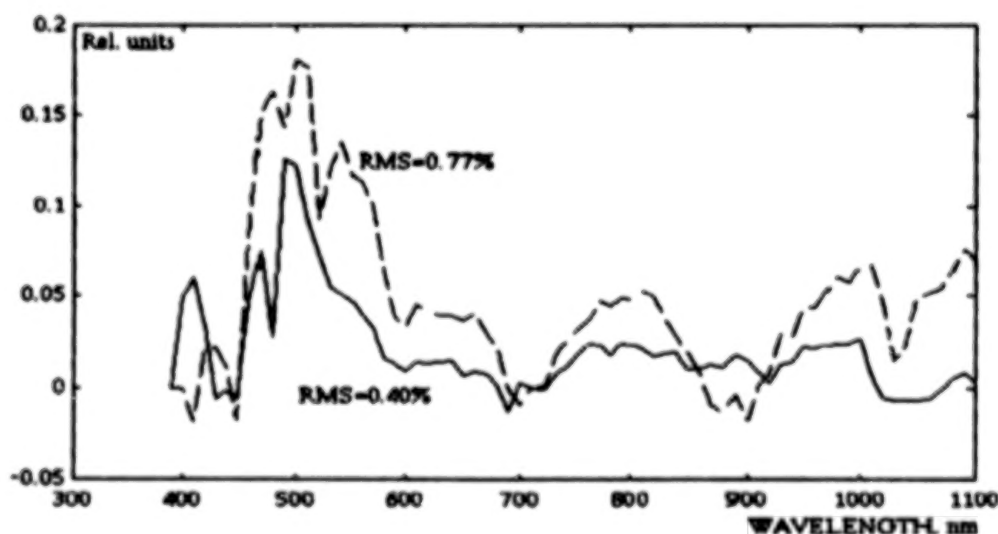


Figure 5. Difference between conventionally obtained spectral characteristics (curves 4 and 5) and the reference characteristic (curve 1).

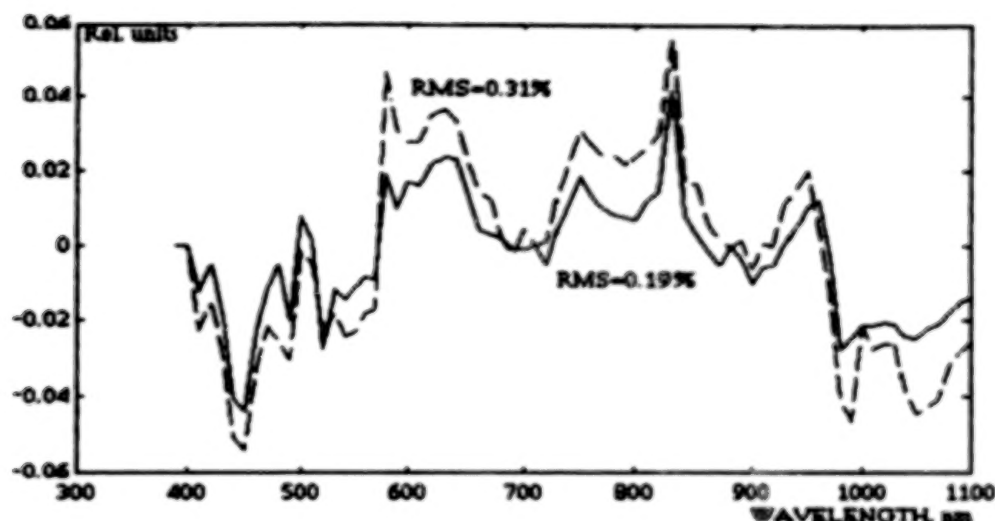


Figure 6. Difference between stabilized spectral characteristics (curves 6 and 7) and the reference characteristic (curve 1).

(RMS) error exemplify the obtained results. Here j is curve number. From the analysis of errors in both cases we can deduce that stabilizing the spectral characteristics by a thorough selection of operating modes will result in a performance improvement several times better than the traditional modes would provide.

4. CONCLUSIONS

1. The study of spectral response of CCD arrays as a function of temperature shows that besides the obligatory in most cases cooling of devices to ensure a wide dynamic range and high signal/noise ratio the use of thermostat is needed, as well, to provide stability of the spectral characteristics.

2. Changing the integration time in order to secure the required dynamic range brings about some changes in the spectral response. Therefore, when using CCD in imaging spectrometers we must account for the integration time effect on the spectral sensitivity. One method to remove this influence is software correction of spectral characteristics changes and thus saving the system metric characteristics. Another one, considered in the paper, promotes the spectral characteristics stabilization through a careful selection of the operational modes. The suggested method allows characteristics stability improvement several times.

REFERENCES

- Atanasov, V. I. et al., 1992: CCD Sensors Applicable in Tracking and Imaging Spectrometers: Dependences between Physical Processes, Operating Modes and Metric Characteristics, *Analytical Lab.*, 2, 47-49.
- Krumov, A.H. et al., 1992: Optoelectronic Converters - CCD Arrays, Operating in Slow Frame Mode, *Compt. Rend. Acad. Bulg. Sci.*, 45, 8, 43-45.
- Kovachev, S. T. et al., 1992: Optoelectronic Block of a Multi-Channel Spectrometric System for Remote Sensing, *Compt. Rend. Acad. Bulg. Sci.*, 45, 7, 29-31.

- Mishev, D.N. et al., 1991: Results of TV Imaging of Phobos (Experiment VSK-Pragat), *Planetary and Space Science*, 1/2, 281-295.
- Nosov, V. R. and V. A. Shimin, 1986: *Physical Basics of Charge-Coupled Devices* (in Russian), Nauka, Moskva, pp. 203, 233.
- Prens, F.P., 1991: *Photosensitive Charge-Coupled Devices* (in Russian), Radio i svyaz, Moskva, p.161.

STUDY ON THE INTERTRANSPUTER CONNECTIONS FOR AN IMAGE PROCESSING

Petkov D., T. Zdravev, H. Nikolov
Solar-Terrestrial Influences Lab.,
Bulgarian Academy of Sciences
"Acad. G. Bonchev" str. bl. 3, 1113 Sofia, Bulgaria

ABSTRACT

Image processing has a long years history now. The tasks in this field are characteristic for their high complexity. Solving such a problem in real time needs a huge computational power. To obtain real looking images 256 colors and a great number of pixels 512×512 for each image are required. To satisfy this need it is essential to use high resolution visualization system and high computational power. The transputers, which represent a contemporary "state of art" of computers for parallel environments, offer high computational possibilities at relatively low price i.e. high price/performance ratio, for building such systems. Other goal to achieve transputers are used is flexibility.

Recently a study has been conducted, which aimed to examine a pattern structure of parallel environment for image processing with pattern algorithm for process an image. In this paper are presented results from experiments carried out with different number of transputers and different kind of connections between them - tree and ring.

Equipment used for experiments was as follows - system video camera, frame grabber, host computer (PC 386/486) with transputer board or directly connected to transputer complex APS 48.

Each pixel from the frame (image) obtained was described by row, column and 3 bytes of data (1 byte for each color component) i.e. $512 \times 512 \times 3$ bytes of data are acquired. The structure of the implemented parallel environment is shown on fig. 1.

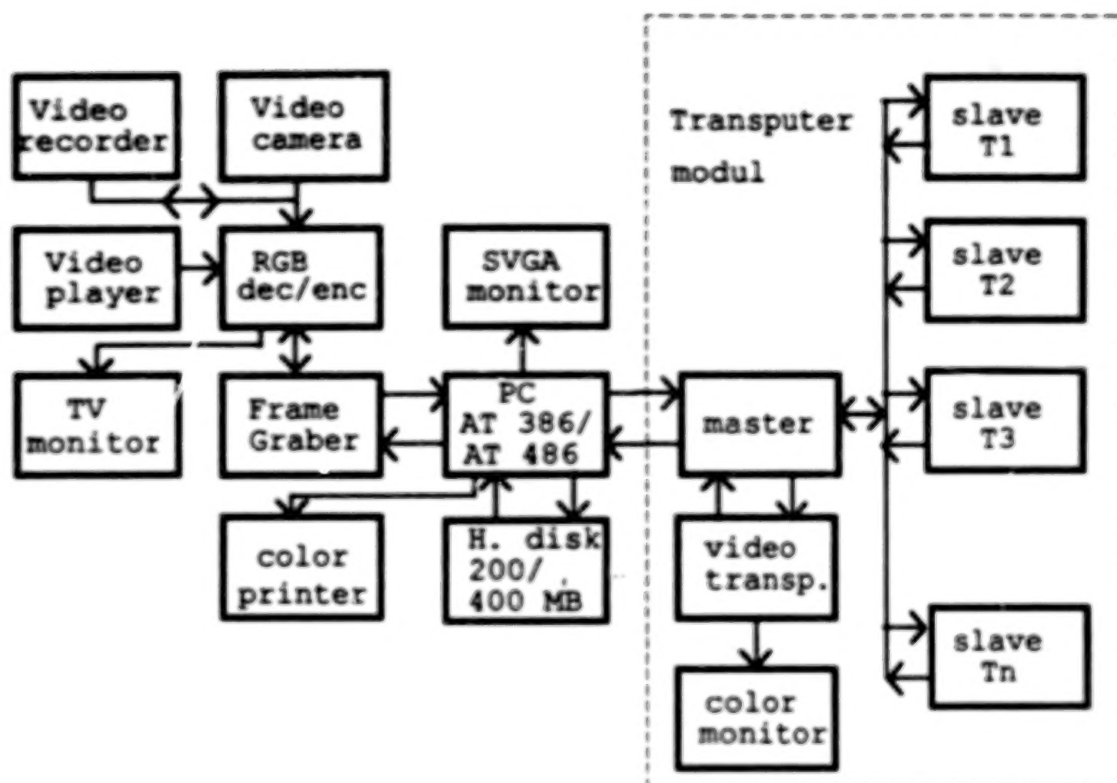


fig. 1 The structure of the implemented parallel environment

In the presented work the handling of the image was done under "Helios" operation system with "C" programming language. The number of transputers used is $N+1$ - on one transputer the main program was disposed and on the rest N transputers there were copies of the processing program. Consequently two programs have to be written. The main, conventionally called "master", containing an algorithm for separation of input data stream receiving and transmission of the data. The other was processing program conventionally called "slave", which containing an algorithm for processing the whole image or a certain part of it.

The chosen algorithm was the convolution algorithm, which allows separation of the input data stream (an image) in pieces so that they could be processed independently. These pieces, then, can be treated in parallel. The optimal number of input data streams for the "slaves" was determined during the execution of the "master". When using "Helios" it is possible to load both programs - "master" and "slave" - on one and the same transputer.

Obviously it isn't suitable to use the mentioned possibility, because of the increase of computational time in comparison with the pure parallel execution. This increase in time is caused by the additional time needed from the Helios server to load the components and to emulate parallelism. That is why we used 9 transputers the task being separated into 8 pieces - on 8 of them the program "slave" was loaded and on the last the program "master". When a matrix $M \times K$ and N programs "slave" are used, each of the transputers receives M/N rows and K columns.

The experiment were carried out with transputers T800. The chosen algorithm required bi-directional logical connection of each "slave" with the program "master". This suggested hardware links between the transputers which were similar to logical. Two kinds of hardware connection were applied - tree and ring. Some of the links between the transputers, when 65 transputers were used, are shown on fig. 2 and fig. 3

The research was carried out on transputer complex including 256 transputers, linked in tree and ring. Both configurations are exhibited on Fig.2 and Fig.3

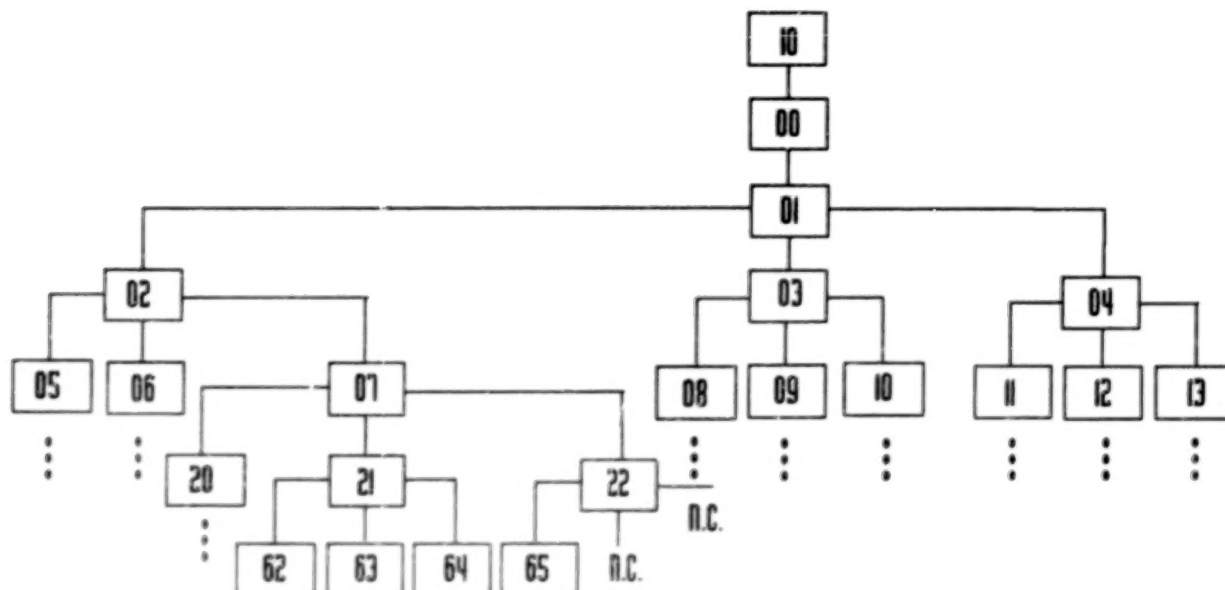


fig 2 "TREE"

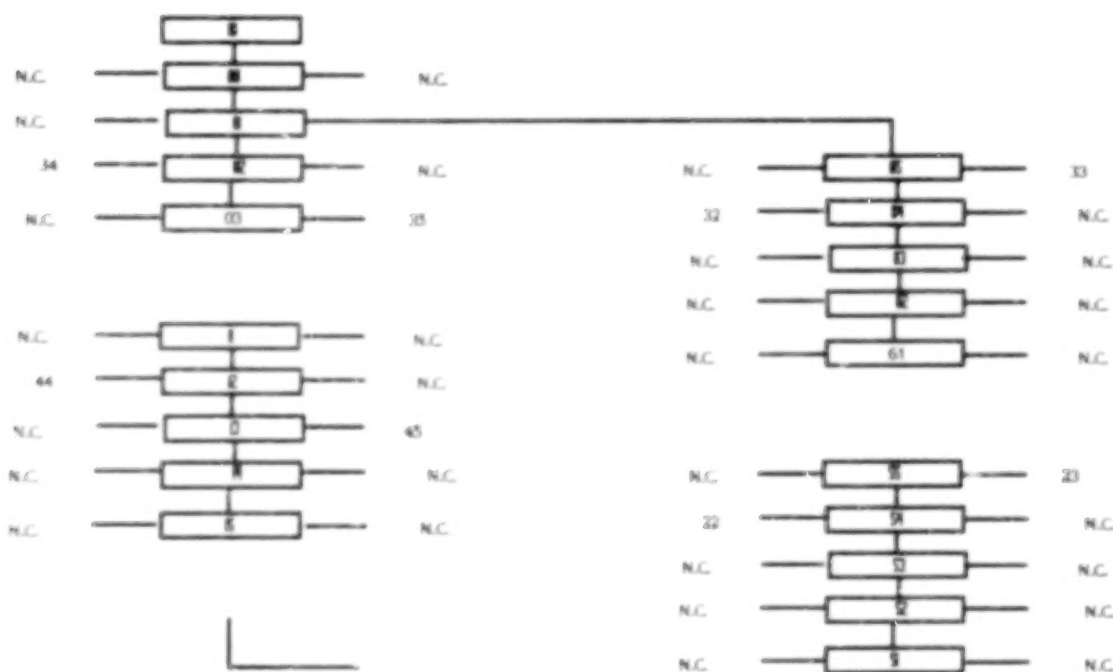


fig.. 3 "RING"

Since the transputer complex involves limitations for configuration ring, some additional hardware links were introduced. Herewith we present only part of obtained results. We measured : the time for execution, the time for communications and the complete time for execution. In tables 1 and 2 are shown the results for the both kinds of logical separation into 64 "slave" programs using different number of transputers - 128, 65, 64, 32, with hardware links tree and ring.

Table 1 64 slaves

Maps	Tcomp	Tcom	Tcomp+Tcom
tree128.map	3.17	1.15	4.32
tree65.map	3.17	1.13	4.30
tree64.map	3.17	2.18	5.35
tree32.map	3.17	2.97	6.14

Table 2 64 slaves

Maps	Tcomp	Tcom	Tcomp+Tcom
ring128.map	3.17	1.33	4.50
ring65.map	3.17	1.28	4.45
ring64.map	3.17	2.32	5.49
ring32.map	3.17	2.96	6.13

In tables 3 and 4 are shown the results for the both kind of logical separation into 32 "slave" programs using different number of transputers - 65, 64 and 32. The time is measured in seconds and is for one layer of processed image.

Table 3. 32 slaves

Maps	Tcomp	Tcom	Tcomp+Tcom
tree64.map	4.73	0.74	5.47
tree33.map	4.73	0.70	5.43
tree32.map	4.73	0.84	5.57

Table 4. 32 slaves

Maps	Tcomp	Tcom	Tcomp+Tcom
ring64.map	4.73	0.80	5.53
ring33.map	4.73	0.74	5.47
ring32.map	4.73	0.85	5.58

As it can be seen from the tables, less time for execution is obtained with N+1 transputers, when N "slaves" should be implemented. In tables 5 and 6 are given the time intervals needed for

complete execution with varying number of transputers from 4 to 64. As it was pointed above these data reflect the most convenient number of transputers to be used and are tested for both kinds of hardware links: tree and ring. In tables 5 and 6 the acceleration is given, compared to that, obtained by using only four programs "slave".

Table 5 TREE

Slaves	Tcomp	Tcom	Tcomp + Tcom	(Tcomp4+Tcom4) / (Tcompx+Tcomx)
64 slaves	3.17	1.13	4.30	8.15
32 slaves	4.73	0.70	5.43	6.45
16 slaves	8.95	0.74	9.69	3.62
8 slaves	17.40	0.49	17.89	1.96
4 slaves	34.59	0.48	35.07	1

Table 6 RING

Slaves	Tcomp	Tcom	Tcomp + Tcom	(Tcomp4+Tcom4) / (Tcompx+Tcomx)
64 slaves	3.17	1.28	4.45	7.88
32 slaves	4.73	0.74	5.47	6.41
16 slaves	8.95	0.76	9.71	3.61
8 slaves	17.40	0.54	17.94	1.95
4 slaves	34.59	0.50	35.09	1

CONCLUSIONS

In the presented article we give a pattern structure of image processing parallel environment and a pattern algorithm for processing an image. Image processing tasks are easily solved in parallel environment, because of the possibility to separate the input data stream into independent items and their successive processing with one and same algorithm.

In the future we plan to work on implementation of different algorithms for parallel processing of images, as well as on creation and exploration of different structures of logical links between transputers. Such systems are going to be studied on their price-performance ratio.

ACKNOWLEDGEMENT

This research was fully financed by National Fund for Scientific Research, the Ministry of Science and Education of Republic of Bulgaria.

References:

1. "Digital Image Processing", Pratt W., 1978
2. "Digital Picture Processing", Rosenfeld, Florida, 1992
3. "The Helios Parallel Programming Tutorial", Noble W., Ganz R., Veer B.
4. Perihelion Software Limited, "The Helios Operating System", Printed by Prentice Hall.
5. Perihelion Software Limited, "The Helios Network Guide", Printed by DSL.
6. Garnett, N.H., Perihelion Technical Report No 8, "Writing a Helios Server".
7. Perihelion Software Limited, "The CDL Guide", Printed by DSL.

A NEW TECHNIQUE FOR SOLVING CLASSIFICATION PROBLEMS IN REMOTE SENSING

Petkov D., T. Zdravev, H. Nikolov
Solar-Terrestrial Influences Lab.,
Bulgarian Academy of Sciences
"Acad. G. Bonchev" str. bl. 3, 1113 Sofia, Bulgaria

Abstract

An object classification problem, where the pixels belongs to an image obtained from a multichannel videospectrometer, in the matter of fact is an object recognition task. In this case, having the spectral irradiance characteristics of the studied by remote sensing techniques objects, is possible to join them to one of the previously formed set with well known properties. The way we do such a reference, always done with preliminary estimated and admitted error, resembles the processes of human thinking and perception. The aim of proposed study is to formalize the mentioned process using methods similar to these a man applies about appurtenance of an object to a defined set. As we consider, such a "human-like" system should be able to perceive and identify more than one object at once, and should be realized in parallel environment.

The classification of multichannel videodata, received from airborne based videospectrometers, is a final step in their thematic processing for remote sensing needs. As a result from this classification a digital image and a map of classified pixels [Swann et al. 1980] are produced. This image allows us to correlate each pixel to a previously formed group of objects (cluster) with well known and studied spectral characteristics. This action makes coordinate transformation from the coordinate system of the wavelengths, used in the classification, to other, where the newly attached attributes to each pixel give a clear differentiation between the classes.

For the remote sensing needs it is highly appropriate to use neural net based classifier, because of two main reasons :

- the first one is the low dependence of the output result from noisy input data. (as it is well known it is impossible to acquire noiseless data from air-based videospectrometers);
- the second one is the possibility of user-needs oriented data processing on the preprocessing level, which allows to decrease the needed storage capacity for each of the real images. The degree of the acquired compression K is given by the equation:

$$K=(N*n)/B$$

where :

N - is the number of the used channels;

n - is the number of bits per channel;

B- is the number of bits needed for all class's representation + 1 for all the pixels that are not included in the formed classes.

The structure of the proposed neural network based classifier is a three-layer perceptron trained by "Back propagation" method, which guarantees a better cluster separation (Lippmann, 1987). To satisfy the requirements of the teaching algorithm we have created a set of patterns, consisting of representative images. They were obtained automatically in accordance with their variance, as it was mentioned above.

The chosen structure is more convenient, since the neural network would be able to form correctly the decision surface even if the input values are close. Having optimized the configuration of the neural network, we acquired the best results with number of neurons in a hidden layer equal to number of clusters + 1 [Bischof et al. 1991].

The training of the neural network is in fact a fine tuning of the weight coefficients connecting the layers, until the output layer forms the desired output values. Using matrix presentation, this process has the following form :

$$OUT = W \times OUT^* = W \times (W^* \times IN)$$

where:

$OUT = \{OUT_1 \dots OUT_n\}$ is the set of output values (clusters);

$OUT^* = \{OUT^*_1 \dots OUT^*_n\}$ is the set of output values from the hidden layer;

$$W = \begin{pmatrix} w_{11} & w_{12} & w_{13} & \dots & w_{1n} \\ w_{21} & w_{22} & w_{23} & \dots & w_{2n} \\ \dots & \dots & \dots & \dots & \dots \\ w_{n1} & w_{n2} & w_{n3} & \dots & w_{nn} \end{pmatrix}$$

is the matrix with coefficients connecting hidden and output layers;

$$W^* = \begin{pmatrix} w^*_{11} & w^*_{12} & w^*_{13} & \dots & w^*_{1n} \\ w^*_{21} & w^*_{22} & w^*_{23} & \dots & w^*_{2n} \\ \dots & \dots & \dots & \dots & \dots \\ w^*_{n1} & w^*_{n2} & w^*_{n3} & \dots & w^*_{nn} \end{pmatrix}$$

is the matrix with coefficients connecting the input and hidden layers;

$IN = \{IN_1, \dots, IN_n\}$ is the set of input values.

The chosen kind of neural network, forming the classifier kernel, has an open, tree-like structure, which allows, after special training, to alter its utilization by including more classes of objects (increasing the number of the clusters in the classification). To do this it is essential to apply adaptive algorithms with different criteria for estimation the appurtenance to specified cluster.

With the aid of neural network based classifier it is possible, step by step, to extend the range of problems solved. In the present work are used spectral characteristics from three spectral ranges to form the classes. As it was shown in [8], this number of spectral channels is sufficient to achieve 90% accuracy of classification and at the same time increasing of the number of the channels do not cause a proportional increase of the accuracy, but only computational time arises.

To use the above mentioned fact, the classification is carried out in two steps: first, "rough" classification is done, determining to which one of the principle clusters from the set $OUT^* = \{OUT^*_1, \dots, OUT^*_n\}$ the pixel belongs to, and after this the same pixel is attached to some of the "subclusters" $OUT = \{out_1, \dots, out_n\}$. This process is shown on fig. 1.

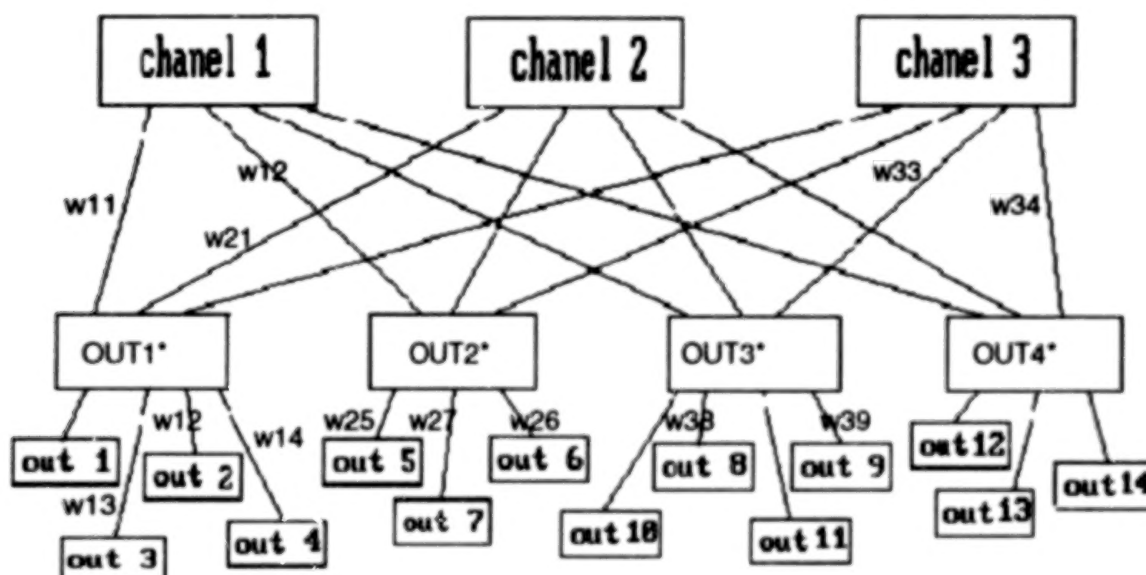


fig. 1.

Conclusions

The application of the described neural network based classifier is suitable in solving one of the important remote sensing problems. Its parameters can easily be tuned so as to identify different sets of clusters, including environmental pollutants.

Acknowledgement

This study is due to the support of the Bulgarian Ministry of Science and Education.

REFERENCES

1. Spectral Characteristics of Natural Formations, Mishev D., Publ. House of Bulg. Acad. of Sci., Sofia, 1986.
2. Remote Sensing: Quantitive Approach, Swain F., Davis Sh., N. Y., 1980.
3. Neural Computing, Wasserman F., 1990.
4. "An Introduction to Computing with Neural Network," Lippmann R. L., IEEE Trans. Acoustics, Speech and Signal Processing Magazine 4, 4-22, 1987.
5. AI-methods for Remote Sensing: Neural Networks and Knowledge-Based Vision, Bischof H., Bartl R., and others, proceedings of the 11th EARSel Symposium, Graz, Austria, 3-5 July 1991.
6. A massively parallel architecture for a self-organizing neural recognition machine., Carpenter G., Grossberg S., Computing vision, Graphics and Image Processing 37:54 - 115.
7. SPOT IMAGE, The Catalogue of SPOT Products and Services, Toulouse Cedex - France.

SATELLITE IMAGES DATA COMPRESSION USING MULTIREOLUTION ANALYSIS BASED ON OPTIMAL EDGE DETECTION

A. SERIR & R. SANSAL

USTHB - Institut d'Electronique
Bp 32, Bab Ezzouar, 16111. Alger. Algeria

ABSTRACT

This paper proposes a new scheme for image compression taking into account the edges and textures informations and describes a compact coding algorithm based on the wavelet transform modulus maxima. A close approximation of the original image can be reconstructed from multiscale edges, which are detected and characterized with a dyadic wavelet transform. For a particular class of wavelets, here we focus on an optimal edge detector, the local maxima of the wavelet transform modulus provide the locations of edges in images. This type of coding don't produce distortions such as Gibbs phenomena, but it removes the image texture. Therefore, we have extended this method by developing an algorithm that takes a specific coding of textures, and uses the low frequency wavelet transform component. It is shown that this coding scheme is particularly well adapted to very low bit rate (0.1485 b per pixel).

1. INTRODUCTION

The most serious disadvantage associated with the conversion of information from analog to digital form is the substantial increase in storage and/or transmission bandwidth requirements. The information contained in the image must, therefore, be compressed by extracting only the visible elements, which are then encoded.

Images are typically composed of structures or features that are scale-invariant in some sense over different spatial scales. Multiresolution signal decomposition is a new approach to image analysis in which information contents can be interpreted and studied in scale invariant fashion. This transformation is achieved by projecting the data on a basis of functions. The compression is performed by encoding this transform.

Because of the nature of the image signal and the mechanism of human vision, the transform used must accept nonstationarity and be localized in both the space and frequency domains. To avoid redundancy, the transform must be at least biorthogonal and lastly, in order to save CPU time, the corresponding algorithm must be fast. The two dimensional wavelet transform defined by Meyer and Lemarié [13][8] with Mallat's implementation satisfies each of these conditions. Biorthogonal wavelet is a simple and powerful tool to compress images by quantizing the wavelet coefficients, without any a priori knowledge on the geometric structures. It is, then well adapted to compress the micro textures.

In order to reach very low bit rate, one has to use the structural properties of the images and the way they are perceived by human observer [12]. The image information can be roughly divided between edges and textures. Multiscale edges can be detected and characterized with a dyadic wavelet transform [11]. For a particular class of wavelets, the local maxima of the wavelet transform modulus provide the locations of edges in images. A close approximation of the original image can be reconstructed from these multiscale edges, and this local maxima representation can be used for compression. The important advantages of this method, introduced recently by S. Mallat and Zhong are the low algorithmic complexity, flexibility in choosing the basic filter and accurate numerical reconstruction results from maxima representation. However it presents a poor reliability in selecting most significant edges.

We have resolved this problem by deducing a basic filter from an optimal multiscale edge detector adapted to wavelet transform [16].

The compression method we have developed associates, wavelet transform, maxima wavelet representation and vector quantization coding scheme. The textures and edges informations are coded separately by using respectively biorthogonal wavelet transform and maxima wavelet representation based on an optimal edge detector.

Sections II and III describe respectively the wavelet transforms and maxima wavelet representation. After a quick review of wavelets in general, we explain in more detail the construction of a particular maxima wavelet based on optimal edge detector. The new coding scheme is next presented in section IV. In section V, experimental results for satellite images are provided.

2. REVIEW OF WAVELET TRANSFORM

Wavelets are functions generated from one single function Ψ by dilation and translation :

$$\Psi^{a,b}(x) = |a|^{-1/2} \Psi\left(\frac{x-b}{a}\right)$$

The mother wavelet Ψ has to satisfy $\int \Psi(x) dx = 0$;

which implies at least some oscillations.

The basic idea of the wavelet transform is to represent any arbitrary function f as a superposition of wavelets. In practice, one prefers to write f as a discrete superposition (Sum rather than integral). Therefore, one introduces a discretization $a = a_0^m, b = n \cdot b_0 a_0^m$ with $m, n \in \mathbb{Z}$ and a_0, b_0 fixed. The wavelet decomposition is then :

$$f = \sum C_{m,n}(f) \Psi_{m,n} \quad \text{with} \quad \Psi_{m,n}(x) = a_0^{-1/2} \Psi(a_0^{-m} x - b_0 n).$$

For $a_0 = 2; b_0 = 1$ there exist very special choices of Ψ such that the $\Psi_{m,n}$ constitute an orthonormal basis, so that :

$$C(f) = \langle \Psi_{m,n}, f \rangle = \int \Psi_{m,n}(x) \cdot f(x) dx$$

and the synthesis formula

$$f(x) = \sum_{m,n} C_{m,n} \Psi_{m,n}(x)$$

can be used to recover $f(x)$ from its wavelet coefficients

Different bases of this nature were constructed by Stromberg [17], Meyer [13], Lemarié [8] and Daubechies [3]. All these examples correspond to a multiresolution analysis, a mathematical tool proposed by Mallat [10], which is particularly well adapted to the use of wavelet bases in image analysis, and which gives rise to a fast computation algorithm.

To construct the mother wavelet $\Psi(x)$ we may first determine a scaling function $\Phi(x)$ which, satisfies the two scale difference equation [3]:

$$\Phi(x) = \sqrt{2} \cdot \sum_k h(k) \Phi(2x - k)$$

Then the mother wavelet $\Psi(x)$ is related to the scaling function via

$$\Psi(x) = \sqrt{2} \cdot \sum_k g(k) \Phi(2x - k) \quad \text{where} \quad g(k) = (-1)^k h(1-k)$$

The coefficients $h(k)$ and $g(k)$ play a very crucial role in a given discrete wavelet transform. To perform the wavelet transform does not require the explicit forms of $\Phi(x)$ and $\Psi(x)$ but only depends on $h(k)$ and $g(k)$. The pair of filters H and G correspond to the halfband lowpass and highpass filters, respectively.

* Extension to the two-dimensional case : There exist various extensions of the one-dimensional wavelet transform to higher dimensions. We follow Mallat [10] and use a two dimensional wavelet transform in which horizontal and vertical orientations are considered preferential.

In two-dimensional wavelet analysis, one introduces, like in the one-dimensional case, a scaling function $\Phi(x, y)$ such that :

$$\Phi(x, y) = \Phi(x)\Phi(y)$$

where $\Phi(x)$ is a one-dimensional scaling function.

Let $\Psi(x)$ be the one-dimensional wavelet associated with the scaling function $\Phi(x)$. Then, the three two-dimensional wavelets are defined as :

$$\Psi^H(x, y) = \Phi(x)\Psi(y)$$

$$\Psi^V(x, y) = \Psi(x)\Phi(y)$$

$$\Psi^D(x, y) = \Psi(x)\Psi(y)$$

A multiscale pyramidal decomposition of an image : wavelet coefficients of the image are computed as follows:

An image $A_1 f$ is completely represented by $3J + 1$ discrete images

$$(A_{2^{-j}} f), (D_{2^{-j}}^H f), (D_{2^{-j}}^V f), (D_{2^{-j}}^D f)_{-j \leq j \leq -1}$$

where :

$$A_{2^{-j}} f = ((f(x, y), \Phi_{2^{-j}}(-x), \Phi_{2^{-j}}(-y))(2^{-j}n, 2^{-j}m)_{(n, m) \in \mathbb{Z}^2}$$

$$D_{2^{-j}}^H f = ((f(x, y), \Phi_{2^{-j}}(-x), \Psi_{2^{-j}}(-y))(2^{-j}n, 2^{-j}m)_{(n, m) \in \mathbb{Z}^2}$$

$$D_{2^{-j}}^V f = ((f(x, y), \Psi_{2^{-j}}(-x), \Phi_{2^{-j}}(-y))(2^{-j}n, 2^{-j}m)_{(n, m) \in \mathbb{Z}^2}$$

$$D_{2^{-j}}^D f = ((f(x, y), \Psi_{2^{-j}}(-x), \Psi_{2^{-j}}(-y))(2^{-j}n, 2^{-j}m)_{(n, m) \in \mathbb{Z}^2}$$

$A_{2^{-j}}$ is the approximation at the coarse resolution. D are detail images which give the difference in information between the approximation at resolution 2^{j+1} and at 2^j for different orientations. Figure 1 illustrates classical wavelet representation of satellite image.

The pyramidal-type wavelet transform decomposes subsignals recursively in the low frequency channels. Therefore, bi-orthogonal wavelet is a simple and powerful tool to compress images by quantizing the wavelet coefficients, without any a priori knowledge on the geometric structures. It is then well adapted to compress the micro textures.

3. MAXIMA WAVELET TRANSFORM

An important problem in image processing is to code images with a minimum number of bits for transmission or storage. To obtain high compression rates in images coding, we cannot afford to code all the information available in the image. It is necessary to remove the parts of the image components that are not important for visualization. Since edges provide meaningful features for images interpretation, it is natural to represent the image information with an edge based representation in order to select the information to be coded. Multiscale edges can be detected and characterized with a dyadic wavelet transform [11]. For a

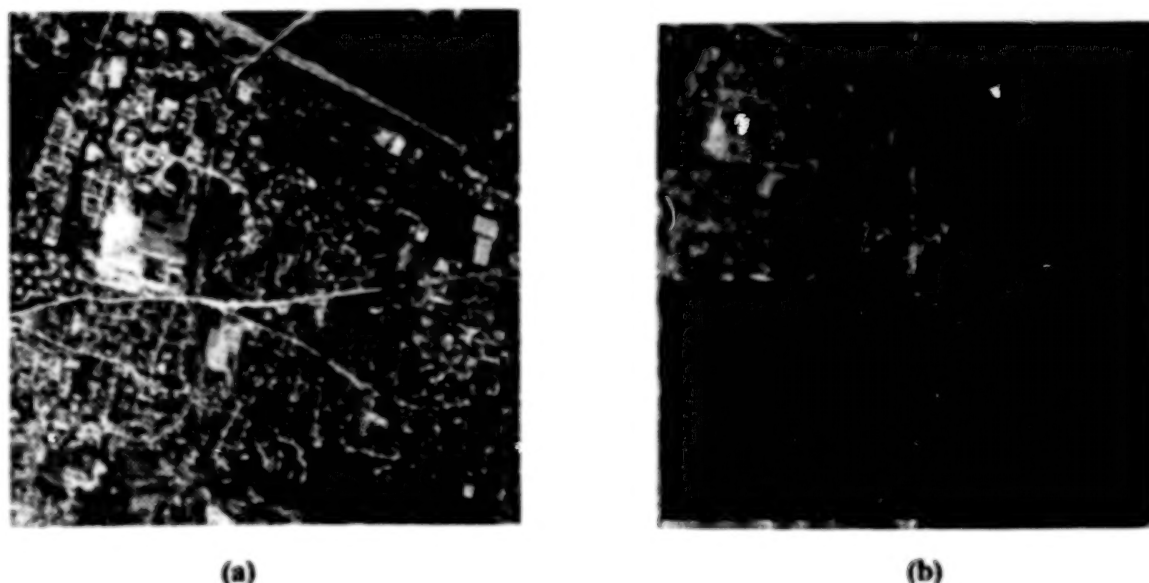


Figure 1 : Bi-orthogonal wavelet representation. (a) original image 256 x 256. (b) wavelet representation at resolution 2. The size of approximation image is 64 x 64.

particular class of wavelets, the local maxima of the wavelet transform modulus provide the locations of edges in images. A close approximation of the original image can be reconstructed from these multiscale edges. The above idea leads naturally to a new type wavelet transform called maxima wavelet representation.

3.1 Maxima wavelet representation

In two dimension, a multiscale edge detection can be reformalized through a wavelet transform defined with respect to two wavelets $\Psi^1(x, y)$ and $\Psi^2(x, y)$. We denote that :

$$\Psi_{2^j}^1(x, y) = \frac{1}{2^j} \Psi^1(x/2^j, y/2^j)$$

$$\Psi_{2^j}^2(x, y) = \frac{1}{2^j} \Psi^2(x/2^j, y/2^j)$$

The wavelet of a function $f(x, y) \in L^2(\mathbb{R}^2)$ at the scale 2^j has two components defined by

$$W_{2^j}^1 f(x, y) = f \bullet \Psi_{2^j}^1(x, y)$$

$$W_{2^j}^2 f(x, y) = f \bullet \Psi_{2^j}^2(x, y)$$

Let $\hat{\Psi}^1(\zeta, \eta)$ and $\hat{\Psi}^2(\zeta, \eta)$ be the Fourier transforms of $\Psi^1(x, y)$ and $\Psi^2(x, y)$

To ensure that a dyadic wavelet transform is a complete and stable representation of $f(x, y)$, we impose that the 2-D Fourier plane is covered by the dyadic dilatations of $\hat{\Psi}^1(\zeta, \eta)$ and $\hat{\Psi}^2(\zeta, \eta)$.

This means that there exist two strictly positive constants A and B such that :

BLANK PAGE

$$A \leq \sum_{j=-\infty}^{+\infty} |\hat{\Psi}^1(2^j \zeta, 2^j \eta)|^2 + |\hat{\Psi}^2(2^j \zeta, 2^j \eta)|^2 \leq B$$

Most multiscale edge detectors smooth the signal at various scale and detect sharp variation points from their first or second -order derivative [12] [2] [4]. The extrema of the first derivative correspond to the zero crossings of the second derivative and the inflection points of the smoothed signal. A smoothing function is any function $\phi(x, y)$ whose integral is equal to 1 and that converges to 0 at infinity.

Therefore, a multiscale sharp variation points can be obtained from a dyadic wavelet transform if

$$\Psi^1(x, y) = \frac{\partial}{\partial x} \phi(x, y) \quad \text{and} \quad \Psi^2(x, y) = \frac{\partial}{\partial y} \phi(x, y)$$

Then, the wavelet transform can be rewritten

$$\begin{bmatrix} W_{2^j}^1 f(x, y) \\ W_{2^j}^2 f(x, y) \end{bmatrix} = 2^j \begin{bmatrix} \frac{\partial}{\partial x} (f * \phi_{2^j})(x, y) \\ \frac{\partial}{\partial y} (f * \phi_{2^j})(x, y) \end{bmatrix}$$

The two components of the wavelet transform are proportional to the two components of the gradient vector $\bar{\nabla}(f * \phi_{2^j})(x, y)$.

At each scale 2^j , the modulus of the gradient vector is proportional to

$$M_{2^j} f(x, y) = \sqrt{|W_{2^j}^1 f(x, y)|^2 + |W_{2^j}^2 f(x, y)|^2}$$

The angle of the gradient vector with the horizontal direction is given by

$$A_{2^j} f(x, y) = \text{argument}(W_{2^j}^1 f(x, y) + i W_{2^j}^2 f(x, y))$$

Like in the Canny algorithm [2], the sharp variation points of $f * \phi_{2^j}(x, y)$ are the points (x, y) , where the modulus $M_{2^j} f(x, y)$ has a local maxima in the direction of the gradient given by $A_{2^j} f(x, y)$. We record the position of each of these modulus maxima as well as the modulus and the angle at the corresponding locations.

The important advantages of this method are the low algorithmic complexity, flexibility in choosing the basic filter and accurate numerical reconstruction results from maxima representation. However, it presents a poor reliability in selecting most significant edges. We suppose resolve this problem by deducing a basic filter from an optimal multiscale edge detector adapted to wavelet transform.

3.2 Maxima wavelet representation using optimal edge detector

This section reformalizes an optimal multiscale edge transform through pyramidal multiresolution representation. We first define the smoothing filter $g(x)$, which is the primitif of the optimal edge detector $h(x)$ [4].

$$g(x) = (c_1 \sin(w|x|) + c_2 \cos(w|x|))e^{-\alpha|x|} \quad h(x) = -k \sin(wx) e^{-\alpha|x|}$$

$$c_1 = \frac{k\alpha}{\alpha^2 + w^2} \quad c_2 = \frac{k w}{\alpha^2 + w^2} \quad k = \frac{(1 - 2e^{-\alpha} \cos w + e^{-2\alpha})(\alpha^2 + w^2)}{2\alpha \cdot e^{-\alpha} \sin w + w(1 - e^{-2\alpha})}$$

Taking $\alpha/w \gg 1$ assures the detection-localization optimality [2]. In a pyramidal transformation, the smoothing filter is used in the restriction operator scheme. The original image synthesis from restriction coefficients is possible under the following conditions

let,

$$\Phi(x, y) = \overline{g(-x, -y)} \quad \Phi_h(x, y) = \frac{1}{h^2} \Phi\left(\frac{x}{h}\right) \Phi\left(\frac{y}{h}\right)$$

with the sampling period h .

1. $\Phi(x)$ is a continuous function with a fast decrease at infinity. This condition is verified by $g(x)$ and then by $\Phi(x)$
2. The Fourier transform $\Phi(0, 0) = 1$; the smoothing filter $g(x)$ normalization and the parameters fitting ($\alpha = 1.4179$ and $w = 0.0001$) ensure this condition.
3. Fourier transform $\Phi(2k\pi, 2l\pi) = 0$ if $(k, l) \in \mathbb{Z}^2$ and $(k, l) \neq (0, 0)$. This condition requires $\Phi(\xi)$ periodicity, whereas, it isn't periodic.

Therefore, we have defined a new frequential response $\Phi^*(\xi)$ as the repetition of $\Phi(\xi)$ truncated by a 2π width rectangular window.

The pyramidal transformation implementation is made easier by introducing fine to coarse causality relations [14]. In frequential domain, it is written as :

$$\Phi^*(2\xi) = m_0(\xi) \Phi^*(\xi)$$

One can prove [16] that it is possible to associate a multiresolution analysis to the pyramidal transformation defined above. In two dimensions, a multiscale edge detection can be reformalized through wavelet transform defined [11] with respect to two wavelets $\Psi_1(x, y)$ and $\Psi_2(x, y)$:

$$\begin{aligned} \Psi_{2^j}^1 &= \frac{\partial}{\partial x} \Phi_{2^j}^*(x, y) & \Psi_{2^j}^2 &= \frac{\partial}{\partial y} \Phi_{2^j}^*(x, y) \\ \Phi_{2^j}^*(x, y) &= \frac{1}{2^j} \Phi(2^j x, 2^j y) \end{aligned}$$

The wavelet transform can be written :

$$\begin{bmatrix} W_{2^j}^1 I(x, y) \\ W_{2^j}^2 I(x, y) \end{bmatrix} = 2^j \begin{bmatrix} \frac{\partial}{\partial x} (I * \Phi_{2^j}^*)(x, y) \\ \frac{\partial}{\partial y} (I * \Phi_{2^j}^*)(x, y) \end{bmatrix}$$

This two components are proportional to the gradient vector. Like in edge transform, the sharp variation points on the smoothed image are the points (x, y) , where the modulus has a local maxima in the direction of the gradient.

In order to compute the wavelet transform with a minimum amount of operations, we choose two wavelets $\Psi_1(x, y)$ and $\Psi_2(x, y)$ that can be written as separable products of functions of x and y variables. Let $\Psi(x)$ be a wavelet defined as the first derivative of $\phi^*(x)$ and $\hat{\phi}^*(x)$ its Fourier transform :

$$\Psi^1(x, y) = \Psi(x) * \Phi^*(y) \quad \Psi^2(x, y) = \Phi^*(x) * \Psi(y)$$

$\Phi^*(x)$ is completely defined by $m_0(\xi)$ filter. We consider a 2π -periodic filter $m_1(\xi)$ such that :

$$\hat{\Psi}(2\xi) = m_1(\xi) \cdot \hat{\Psi}(\xi) = 2i\xi m_0(\xi) \hat{\Phi}^*(\xi)$$

$$m_1(\xi) = 2i\xi m_0(\xi)$$

Let us impose that the reconstructing wavelets $\chi^1(2^j \zeta, 2^j \eta)$ and $\chi^2(2^j \zeta, 2^j \eta)$ can be written

$$\chi^1(2^j \zeta, 2^j \eta) = m_1^*(\zeta) m_0^*(\eta) \hat{\phi}(\zeta) \hat{\phi}(\eta)$$

$$\chi^2(2^j \zeta, 2^j \eta) = m_0^*(\zeta) m_1^*(\eta) \hat{\phi}(\zeta) \hat{\phi}(\eta)$$

where $m_1^*(\zeta)$ and $m_0^*(\zeta)$ are 2π -periodic functions related to m_0 and m_1 by

$$m_1^*(\zeta) = \frac{1 - |m_0(\zeta)|^2}{m_1(\zeta)} \quad m_0^*(\zeta) = \frac{1 + |m_0(\zeta)|^2}{2}$$

Finite impulse response of m_0 , m_1 , m_0^* and m_1^* filters that correspond to the generated wavelets are shown by fig. 2.

4. NEW CODING SCHEME

This section describes an algorithm for computing a discrete wavelet transform and the inverse algorithm that reconstructs the original image from its wavelet transform. We suppose that the wavelet is characterized by the four discrete filters m_0 , m_1 , m_0^* and m_1^* described in section 2.2.

We denote by m_{0p} , m_{1p} , the discrete filters obtained by putting 2^p-1 zeros between each of the coefficients of the filters m_0 , m_1 . The following algorithm illustrated by fig 3, computes the 2-D mixed discrete wavelet transform of an image S_1 . At each scale 2^j , the algorithm decomposes by classical wavelet transform S_{2^j} into $S_{2^{j+1}}$. Edges modulus and orientation are given by maxima wavelet representation.

To code efficiently the edge information, we need to take advantage of the similarities between edges obtained at different scales. It was observed [11] that the edges of the main image structures have similar positions at the three finer scales : 2^1 , 2^2 and 2^3 . These three finer scales also carry more 90% of the image frequencies

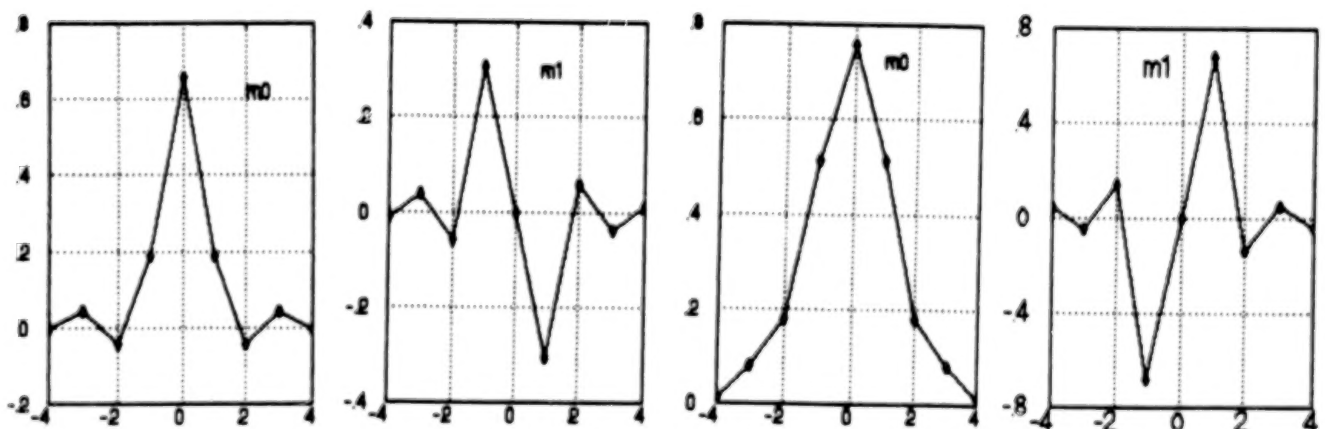


Figure 2 : Finite impulse response illustrations of m_0 , m_1 , m_0^* and m_1^* filters

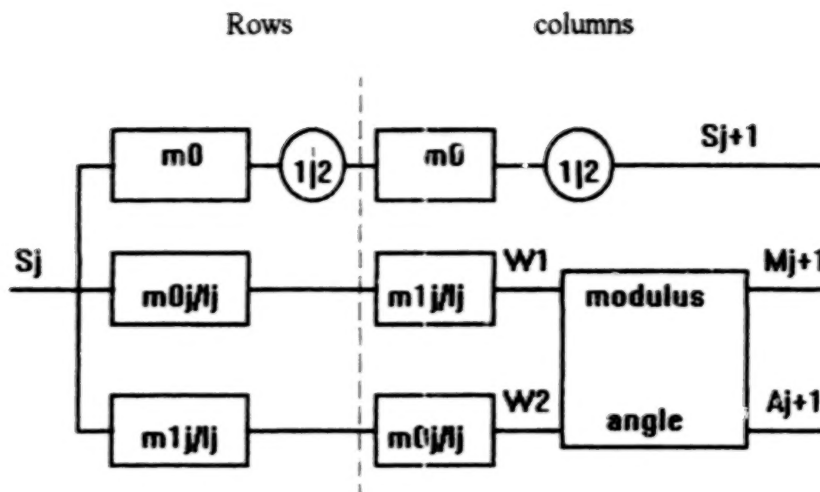


Figure 3 : algorithm scheme of wavelet representation. l_j is a normalization coefficient. $1/2$ means suppress every two columns or two rows.

bandwidth and, thus, cover most of the image information. The coarse scale information, corresponding to the wavelet transform at scales $2^j > 2^3$, is kept as low-frequency image S_{2^j} , defined in section 2.1. The edge selection is performed by thresholding. This is done by removing the edge curves along which the average value of the wavelet transform modulus is smaller than a given amplitude threshold.

Once the selection is done, we must efficiently code the remaining information (see fig 4). This requires coding the position, modulus value, and angle value of each modulus maximum along maxima curves at the scales 2^1 , 2^2 and 2^3 , plus the low frequency image S_{2^j} . The geometry of the edge curves is coded only at the scale 2^2 because we neglect the differences between the maxima positions at the scales 2^1 and 2^3 . The angle is coded by four possible directions $0^\circ, 45^\circ, -45^\circ$ and 90° . The modulus of maxima edges and image approximation are coded using vector quantization.

4.1 PRINCIPLE OF VECTOR QUANTIZATION

Developped by Gersho and Gray (1980) [5,6], vector quantization has proven to be a powerful tool for digital image compression [1,15] and classification. The principle involves encoding a sequence of samples (vector) rather than encoding each sample individually. Encoding is performed by approximating the sequence to be coded by a vector belonging to a catalogue of shapes, usually known as a codebook.

The codebook is created and optimized using the well known Linde-Buzo-Gray (LBG) [9] classification algorithm with a mean square error (MSE) criterion. This algorithm is designed to perform a classification based on a training set comprised of vectors belonging to image; it converges iteratively toward a locally optimal codebook.

Each codeword is indexed. At the encoding stage, the vector index in the codebook most closely describing (in terms of MSE criterion) the sample set to be encoded, is selected to represent this set.

4.2 GENERATION OF INITIAL REPRODUCTION ALPHABET.

The preceding paragraph explained why VQ outperforms other methods. Nonetheless, major problems are encountered in the VQ of images.

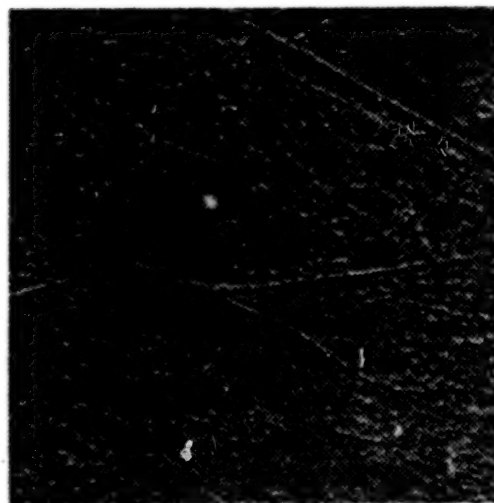
* The optimal codebook depends on the initial reproduction alphabet. In this case, it is deduced from image min and max values, the desired number of classes and different configurations of edges in neighborhood, which reduce the number of edge localization points. The different configurations are illustrated by fig 5.

* The training sequence or the modulus image is partitioned into (usually square) blocks of pixels centred on edge point, which are encoded as separate entities. In these scheme, the bloc size is a fundamental design parameter.

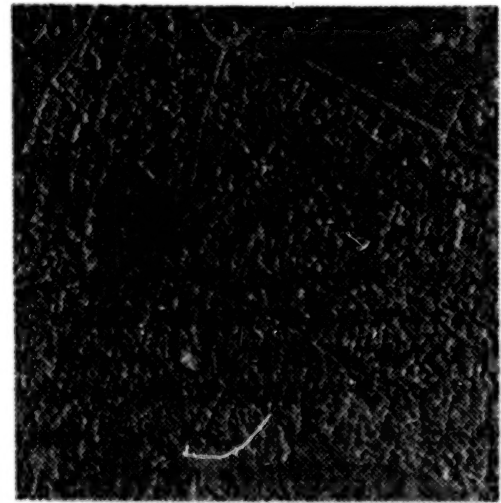
The image approximation, containing the textural information is encoded by using scalar quantization.

The storage information after quantization consists on :

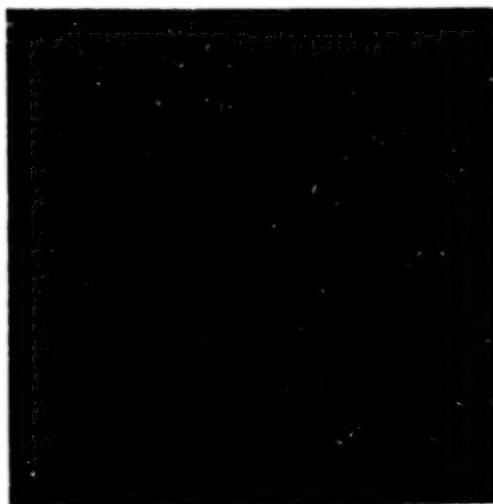
- optimal codebook of low frequency component and the index image at the last resolution ($j = 3$).
- positions of central edge points of a considering neighborhood.
- The coded edge points direction.
- The codebook of edges modulus at each scale and the index images.



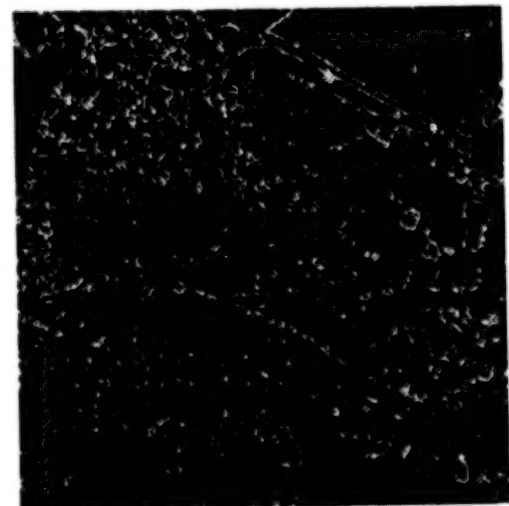
(a)



(b)



(c)



(d)

Figure 4 : Maxima wavelet representation. (a) horizontal edges (b) vertical edges (c) and (d) are respectively modulus and orientation representation

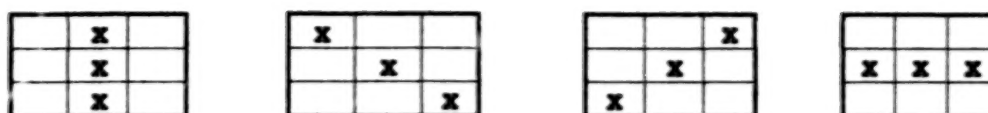


Figure 5 : Different configurations of maxima modulus in neighborhood 3x3. X may be take min or max values.

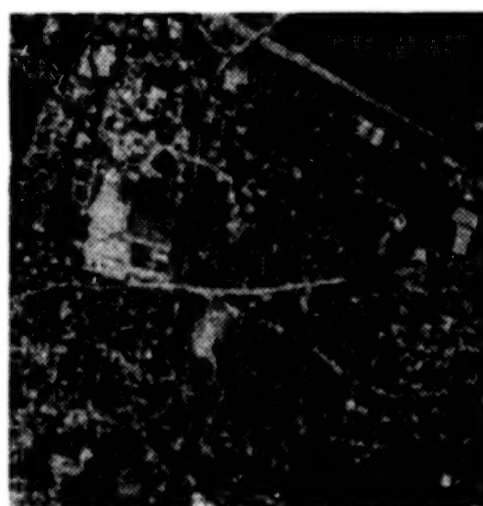
In order to reconstruct the original image from the storage informations a decodage operation followed by inverse transformation are performed. The horizontal and vertical edges are provided from modulus projection.

5. RESULTS AND CONCLUSIONS

We give, in figure 6, an example of images coded with this algorithm. The total amount of data to code reconstructed images is 0.4 b per pixel (block size 3x3) for figure 6-a and 0.145 b per pixel (block size 5x5) for figure 6-b. . The compression rate varies with the number of edge points that remain after the selection operation and the block size used in vector quantization. The maxima wavelet representation coding removes the image textures. It was improved by using the image approximation coding, which contains texture information. The performance of maxima wavelet representation as make easier the principal edges selection was improved by using an optimal edge detector.



(a)



(b)

Figure 6 : Reconstructed images. (a) image compressed at 0.4 b per pixel (b) image compressed at 0.1485 b

6. REFERENCES

- [1] M. Antonini, B. Barlaud P. Matieu and I. Daubechies. April 1990 : 'Image coding using vector quantization in the wavelet transform domain' in Proc ICASSP pp 2297-2300
- [2] J. Canny. 1986 : 'A computational approach to edge detection' IEEE trans PAMI -8 pp 679-698.
- [3] I. Daubechies 1988 : 'Orthonormal bases of compactly supported wavelets comm. pure Appl. Math Vol 41 pp 909-996.
- [4] R. Deriche. 1987 : 'Optimal edge detection using recursive filtering' International Journal of computer vision.
- [5] R. M. Gray. Apr 1984 : 'Vector quantization' IEEE ASSP Mag pp 4-29.
- [6] A. Gersho. March 1982 : 'On the structure of vector quantizers' IEEE Trans Inform. Theory vol. IT-28.
- [7] R. M. Haralick and L. Shapiro. 1992 : 'Computer and robot vision' Addison Wesley publishing company
- [8] P. G. Lemarié. 1988 : 'Une nouvelle base d'ondelettes de $L^2(\mathbb{R})$ ' J. Maths Pures et Appl. Vol 67 pp 227-238.
- [9] Y. Linde, A. Buzo and R. M. Gray Jan 1980 : ' An algorithm for vector quantizer design' IEEE Trans. Comm. Vol COM-28 pp 84-95.
- [10] S. Mallat. July 1989 : 'A theory for multiresolution signal decomposition the wavelet representation' IEEE Trans. PAMI.
- [11] S. Mallat and S. Zhong. July 1992 : 'Characterizations of signals from multiscale edges' IEEE PAMI Vol 14 pp 710-732.
- [12] D. Marr. 1982 : 'Vision' New York Freeman.
- [13] Y. Meyer. 1986 : 'Principe d'incertitude, bases hilbertiennes et algèbres d'opérateurs' Seminaire Bourbaki n° 662
- [14] Y. Meyer. 1992 : 'Les ondelettes Algorithmes et Applications' Armand Colin Edition Paris.
- [15] N.M. Nasrabadi and R.A.King Aug 1988 : 'Image coding using vector quantization : A review' IEEE Trans. Comm, Vol 36.
- [16] A. Serir and B. Sansal. March 1994 : "Maxima wavelet representation using an optimal edge detector' International workshop TOM Lyon France.
- [17] J.O. Stromberg ' A modified Haar system and higher order spline systems' in conf in Harmonic Analysis in Honor of Antoni Zygmund, Vol II pp 475-493.

000448

SPATIAL RESOLUTION OF MULTISPECTRAL SURVEY SYSTEMS FOR DIFFERENT ATMOSPHERIC CONDITION

Gogohia V. V.

Scientific Geoinformation Centre.
Russian Academy of Sciences, Moscow

ABSTRACT

A method to estimate spatial resolution of surveying optical systems using images of test sites is presented. The test sites are analysed applying the Fourier transform method. An analytical model is proposed for the variations of the spatial resolution of the TV and FOTO surveying systems with taking into account intensity of illumination, atmospheric conditions, reflection characteristics of the sites. The estimates are given for spatial resolution of same scanner systems for remote sensing of Environment. Developed methods and program complex may be used for atmospheric correction of TV and FOTO images, for control and calibration of survey systems in fly and for same other applications.

INTRODUCTION

The minimal angular sizes of object, which can be resolved by optical devices with aperture D are limited by diffraction and as it is known from optics have angular value $\theta = 1.2\lambda/D$, where λ is the wavelength of radiation. In practice diffractive limit of survey systems may be not achieved because of same reasons. Spatial resolution can be decreased because of discrete character of matrix of photoelements or when transmitting the images by radioline. Below we consider the influence of atmospheric condition and illumination of objects of survey on spatial resolution of images.

Real spatial resolution of devices may be defined from independent control analysis of test images with taking into account all parameters (digitizing of images, its transmitting, recording and e. t. c.).

For the determination of real spatial resolution of devices usually are used the results of analysis of sites like TV quality gratings. The spatial resolution can be determined as the minimal period of harmonic grating, which can be recognised yet on the reproduction of quality grating. To define the quality gratings for

calibration of optical survey devices we must define constant part of brightness of grating, alternative part (amplitude of modulation) and periods of quality gratings. It is very difficult to prepare quality gratings for calibrating of space devices in natural conditions because of wide range of necessary periods 10 m - 2 km. We developed the method of estimation of spatial resolution of devices by analysis of special test sites.

THEORY

The real image chosen for analysis may be performed as superposition of plane two dimensional waves:

$$F(x, y) = \sum_K F(K_1, K_2) \cdot \exp[i(K_1 x + K_2 y)] \quad (1)$$

$F(x, y)$ - two dimensional discrete function, describing the test image. $F(K_1, K_2)$ amplitude of two dimensional harmonic. As follows from relation (1) test site may be interpreted as superposition of harmonic gratings with different amplitudes $F(K_1, K_2)$ and different directions of two dimensional wave vectors (K_1, K_2) . Contrast of test grating on Earth surface may be defined as:

$$FK/F_0$$

FK - amplitude of K spatial harmonic with wave number K . F_0 - constant part of brightness of test image. The test grating will be considered as resolved if

$$FK > g \text{ NEP} \quad (2)$$

where NEP is the noise equivalent power. g - the threshold relation signal/noise when quality grating may be recognised yet. The threshold condition for detecting of grating may be written in form

$$FK > \text{NEP} + 2b \quad (3)$$

NEP is determined as mean value of noise found from image. b - dispersion of noise. So expression for threshold relation is:

$$g = 1 + 2b/\text{NEP} \quad (4)$$

From the analytical solution of equation of radiation transfer for alternative part of upward radiation we can obtain

$$FK = AKF_0R \quad (5)$$

Where F_0 is the illumination of Earth surface. AK - alternative part of Earth reflection (Albedo). Parameter R is defined as the ratio of alternative parts of upward radiation for space to Earth level.

For aerosol atmosphere from the analytical solution of equation

of radiation transfer for periods of quality gratings in range 20 m-15 km we obtain:

$$R = \exp(-\tau) \left[1 + \frac{\sigma M}{2} \int_0^h dh' \int_0^\infty \frac{dt}{t^2} \exp(-\alpha h' t - 2\beta \frac{t-1}{t}) I_0(kh' \sqrt{t^2-1}) \right] \quad (6)$$

Where M, β - parameters of phase function $P(\gamma) = \frac{M}{2\pi} \exp(-\beta\gamma^2)$, γ - angle of scattering, σ - coefficient of scattering, α - coefficient of attenuation, τ - optical thickness, $h = \tau/\alpha$, $I_0(x)$ - Bessel function.

Value of R as function of spatial wave number K slightly increases when $K \rightarrow 0$. For periods of gratings less than 20 m effects of atmospheric turbulence must be taken into account and dependence for $R(K)$ becomes more expressed. Let consider that function $f(x)$, corresponding any line of image describes stochastic stationary process. So mean value $\langle f(x) \rangle$, and correlation function $W(a) = \langle f(x) \cdot f(x+a) \rangle$ are independent from a . Fourier transformations $W(\omega)$ and $f(\omega)$, are related as:

$$W(\omega) \sim |f(\omega)|^2 \quad (7)$$

Integral Fourier presentation of $W(\omega)$ may be written as:

$$W(\omega) = \frac{1}{2\pi} \int_{-\infty}^{\infty} dt W(t) \exp(i\omega t) = \frac{1}{\pi} \int_0^{\infty} dt W(t) \cos(\omega t) \quad (8)$$

Integrating by part right side of (8) and using boundary conditions $W(\infty) = 0$, $W'(\infty) = 0$ we receive:

$$W(\omega) = -\frac{1}{\pi\omega^2} \left(A + \int_0^{\infty} \cos(\omega t) W''(t) dt \right) \quad (9)$$

where $A = \lim_{t \rightarrow 0} W'(t)$ when $t \rightarrow 0$.

If l is the radius of correlation then $W'(t) \approx -\frac{1}{l} W(t)$, $W''(t) \approx \frac{1}{l^2} W(t)$. If $(\omega l)^2 \gg 1$

$$W(\omega) \approx -\frac{A}{\pi\omega^2}, \quad |f(\omega)| \sim |W(\omega)|^{1/2} \sim 1/\omega \quad (10)$$

We may consider that $FK \sim BK/K$ and $BK \approx \text{const}$. So order of harmonic, which may be detected yet can be defined from relations:

$$BK R F_0 / K_B = g \text{ NEP} \quad K_B = BK R F_0 / g \text{ NEP} \quad (11)$$

Let derive the relation for spatial resolution. Line of scanner

images obtained from Russian space system "Okean-O" is formed by 1434 byte. For fast Fourier transformations we must take 2^M bytes. So for processing we used 1024 pixels ($M=10$). As example on fig.1 is shown mean dependence of amplitudes of spatial harmonics as function of order of harmonic for test image. Dependence is averaged over 124 lines of image. F_0 - constant part, F_1 - amplitude of first harmonic on spatial frequency $\omega = 2\pi/S$, F_2 - amplitude of second harmonic on spatial frequency 2ω , S - distance on Earth surface corresponding 2^M pixels. As it is seen from figure 1 for $K \approx 280$ dependence practically is constant with superposition of irregular fluctuations. This irregular fluctuations when $K \rightarrow \infty$ are interpreted as noise. Order of maximal detectible harmonic defined from figure 1 is $K_B = 280$. Period of detectible grating is calculated as $L = S/K_B$. Spatial resolution for arbitrary atmospheric conditions R , amplitudes of modulation A_K , intensities of illumination F may be found from the relations (11) in form:

$$L = L_0 \left(\frac{R_0}{R} \right) \left(\frac{F_0}{F} \right) \left(\frac{A_K^0}{A_K} \right) \quad (12)$$

Where L_0 - spatial resolution corresponding to: atmospheric condition R_0 , amplitude of modulation A_K^0 , illumination F_0 .

RESULTS

The developed theory was applied for estimation of spatial resolution of some Russian space systems. Results corresponding to clear atmosphere, zenith angle of sun $\theta < 35^\circ$ are shown in table 1.

For the exact calculations of the spectral density of the radiance and of integral intensities in the canals of survey systems we used program complex TEST [1]. The key peculiarity of our program complex, which makes it different from other analogues, is the possibility of exact calculation of the thermal radiation of the aerosol particles and atmospheric gases and also of the Earth surface in the thermal region and the exact calculation of the multiscattered radiation in the visible and nearest infra-red spectrum region. The accuracy of calculations makes it possible to use the program complex in the solution of the following problems:

- forecasting of the intensity of radiation in the canals of survey devices for the proper choice of the survey regimes (exposures, gain, magnitudes of intensifications).

- calculation of the light flows on the receiving elements when working out the new types of the apparatus for plane and space surveys.

Our program complex permits to calculate spectral radiance for every pixel in $W/m^2 mkm$ sr for upper border of atmosphere, arbitrary (plane) level and on the surface of Earth. As the example in the table 2 are performed the values of spectral radiances corresponding to wavelength: 0.65mkm, 1.0mkm, 3.75mkm, 9.65mkm, 12mkm obtained over water surface on the upper border of atmosphere, arbitrary (plane) level and on the Earth surface. From this data can be evaluated contribution of the atmospheric radiation to the integral value of thermal radiation and part of the multiple scattered radiation in the visible. More detailed description of our program is given in [1]. There are some other applications of our program. We can also calculate signal component and scattered radiation for every pixel of images. Applying atmospheric correction and filtering of spatial long wave components we have got good increase quality of space images. One of examples of the corrected images is shown on right side of figure 2. For comparison on the left side of fig.2 is shown uncorrected image.

Partially this work was supported by scientific program of Russian academy of science "Global changes of climate and environment".

TABLE 1

Comparison of passport and experimental values of spatial resolution of same Russian space systems (height of fly 600 km).

Type, wave length	spatial resolution, km	
	pasport	experimental
MCY-3 (0.5-0.9 nkm)	1.0	1.5 ± 0.3
RLS B0 (3 cm)	1.3	1.8 ± 0.4
Klimat IK (10-12 mkm)	4.0	4.0 ± 0.5
Klimat IK* (10-12 mkm)	15	18 ± 3.5

TABLE 2
Spectral radiances $W/m^2 mkm$ sr. (zenith angle of sun 60° ,
water content 1.4 cm, ozone content 0.3 cm, temperature
of surface 283 K).

	0.03	0.03	0.01	0.0	0.0
			Optical thickness		
	0.907	0.90	0.107	0.124	0.161
			wavelength, mkm		
	0.65	1.0	3.75	9.65	12.0
dIBT	99.07	39.95	0.77	7.16	6.87
dICT	96.31	39.07	0.76	7.22	6.89
dSTB	1.34	0.55	0.32	6.51	5.94
dSTC	1.40	0.56	0.33	6.53	5.99
dIPD	62.37	26.88	0.28	0.67	0.92
dITT	3.33	1.36	0.36	7.37	7.02
drBA	97.73	39.40	0.44	0.65	0.90
drCA	94.91	38.51	0.43	0.63	0.89

dIBT upward radiation on the upper border of atmosphere (UBA);
dICT upward radiation on plane level (PL);
dSTB signal component on UBA;
dSTC signal component on PL;
dIPD downward radiation at the Earth surface;
dITT reflected radiation at the Earth surface;
drBA upward scattered and thermal atmospheric component on UBA;
drCA upward scattered and thermal atmospheric component on PL;

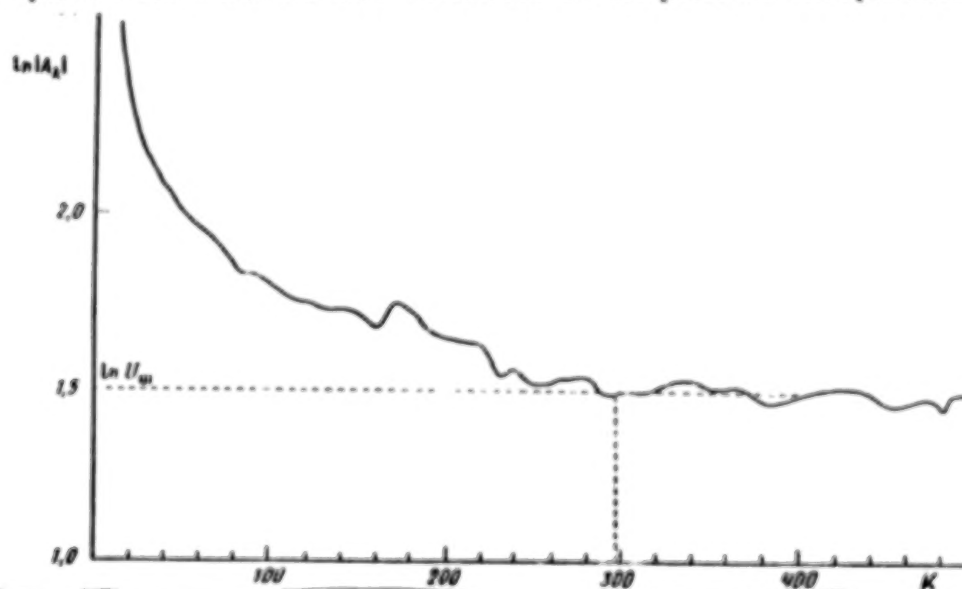


Fig 1.

Dependence of spatial harmonics amplitudes as function
of order of harmonic for test image. A_k amplitudes of
harmonic, K - order, U_n - noise level.

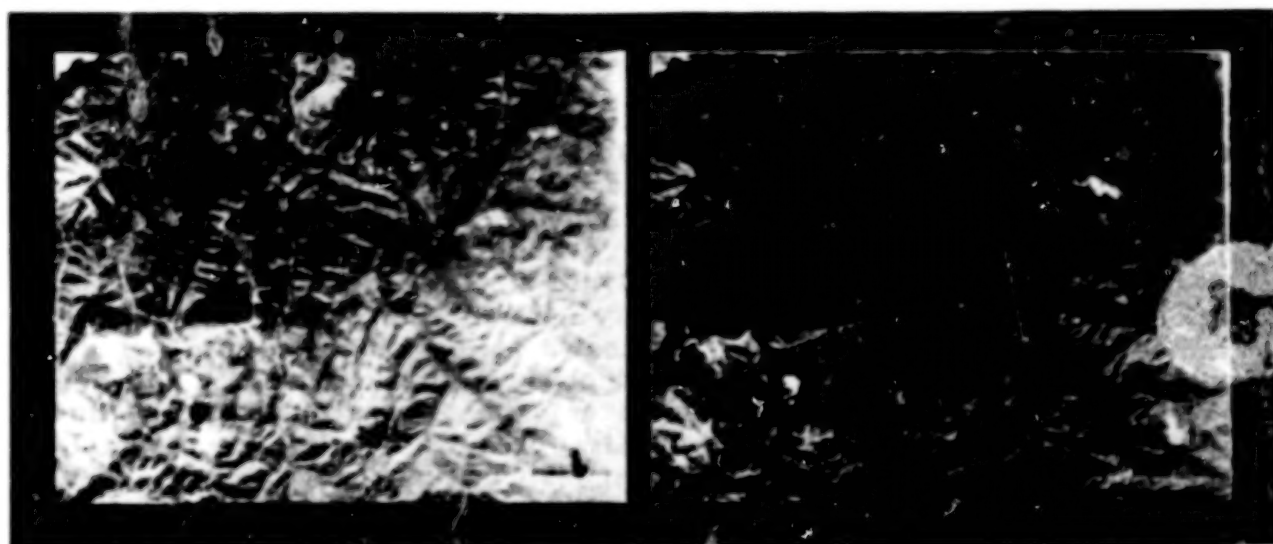


Figure 2.

Input and corrected images of the test syte.

1. Gogolia V. V. Atmospheric correction of the Multispectral Scanner Images in the Region 0.3-27 mkm for Change Analysis. Presented on 25th International Symposium - Remote sensing and Global Environmental Change. C-44, Graz. Austria, april 1993.

SECOND GENERATION DATABASE OF THE IONOSPHERE DISTURBANCE INDICES

T. L. Gulyaeva

Institute of Terrestrial Magnetism, Ionosphere and
Radio Wave Propagation, Russian Academy of Sciences,
142092 Troitsk, Moscow Region, Russia

ABSTRACT

Subject of study presents ionized envelope of the outer Earth's atmosphere at altitudes of 100 to 1000 km. Information technology is developed for evaluating the ionosphere disturbance indices from the long-term first generation database of ground-based vertical-incidence sounding observations. Spectrum of frequencies of occurrence of successive levels of disturbance is analysed with different temporal filters (hourly, 3-hours, half-diurnal, diurnal, monthly, annual and 11-years solar cycle variations). Statistics takes into account positive ionosphere disturbances (enhanced electron peak density) and negative disturbances (depression of ionization). Missed or aberrant hourly data are taken as signatures of disturbance. The latter reveals a few percents of occurrence at mid-latitudes but can reach 30 to 70% of times at equatorial, arctic and antarctic zones. Limiting acceptable level of disturbances is discussed. Specification of the ionospheric quiet and disturbed times is applied to incoherent scatter radar observations. Long-term trend of growing the ionosphere and geomagnetic disturbance is discussed. Extension of our second generation database of the ionosphere disturbance indices to world-wide scale could be helpful to study planetary perspective of the ionosphere variability.

1. INTRODUCTION

There is a need for distinction of quiet and disturbed conditions for the geophysical data analysis however results of separation depend on activity thresholds. Planetary three-hour-range index Kp presents one example of separation of the geomagnetic disturbances with 28 fixed levels 0, 0+, 1, ..., 9 (Solar Geophys. Data, 1951-1994). Kp is the mean standardized K-index from 13 geomagnetic mid-latitude observatories. Local K-index presents range between maximum and minimum deviations of geomagnetic field for 3 hours UT (Menvielle and Berthelier, 1991).

To present monthly pattern of disturbance one can build up a histogram of Kp frequencies. An example of such histogram for December 1990 (lines) and December 1991 (circles) near the solar maximum is given in Figure 1. The first period presents a weak disturbed pattern and second - more disturbed geomagnetic field. Maximum Kp frequency is shifted right along the Kp axis to the greater values (2nd period).

The well established system of indices of geomagnetic disturbance has no equivalents in ionosphere research. To fill the gap, information technology is proposed for producing the ionosphere disturbance indices from the routine observations by vertical-incidence sounding technique at global network of the ionospheric stations. First generation data base produced by standard URSI ionogram interpretation rules (Piggot and Rawer, 1976) is accumulated by the World Data Centers. Description of technology of the statistical analysis producing second generation database and its possible applications are presented below.

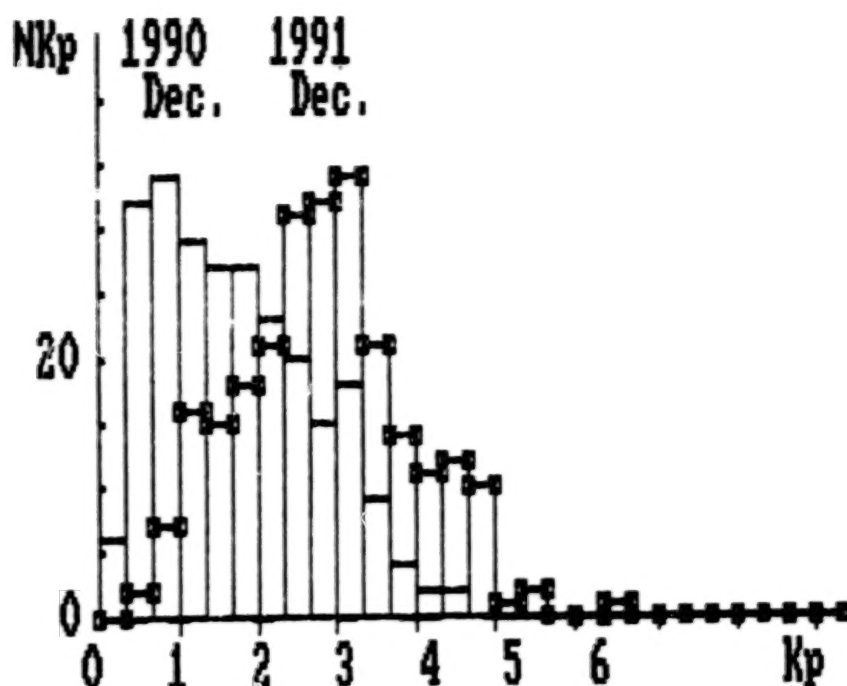


Figure 1. Histogram of frequency of occurrence of Kp indices during month: December 1990 (lines) and December 1991 (circles).

2. STATISTICAL ANALYSIS OF THE PRIMARY INFORMATION

Building up a histogram of frequency of occurrence of a disturbance index for the different time ranges, we can evaluate the skewness of the histogram and use it as the disturbance measure. This quantity could be calculated as a sum of number of occurrences of the index within successive fixed ranges weighted from $W_1=1$ to greater values and normalized by counts of all the data included in the histogram (Gulyaeva, 1994a):

$$D_m = \frac{\sum_{i=1}^m W_m C_m}{\sum_{i=1}^m C_m} \quad (1)$$

TABLE 1. RANGES AND WEIGHTS OF THE GEOMAGNETIC INDICES KP, AE AND DEVIATIONS OF THE F2 LAYER CRITICAL FREQUENCY FROM THE MEDIAN

Kp	0	0+	1-	1	1+	2-	2	2+	3-	3	3+	4-	4	4+
Wm/Kp	1.	1.3	1.7	2.	2.3	2.7	3.	3.3	3.7	4.	4.3	4.7	5.	5.3
Kp	5-	5	5+	6-	6	6+	7-	7	7+	8-	8	8+	9-	9
Wm/Kp	5.7	6	6.3	6.7	7.	7.3	7.7	9.	11.	13.	15.	18.	24.	30.
AE[nT]	0	100	200	300	400	500	600	700	...	2600	2700	2800		
Wm/AE	1	2	3	4	5	6	7	...			27	28		
DfoF2%	-200	-50	-40	-30	-20	-10	0	10	20	30	40	50	200	
Wm	6	5	4	3	2	1	1	2	3	4	5	6		
Wm(missed observations)=1,2,3,4: Wm=Wm(hr-1)+1														

Disturbance measure Dm is equal to 1 under absolutely quiet conditions when all given values of index fit the first range of histogram ($m=1$), and value of Dm increases at greater disturbances. Such unique integral quantity is convenient because the whole spectrum of values of data available can be taken into account. They also allow a comparison of different indices to be made if the ranges and weights for each parameter are specified properly. Examples of different ranges and relevant weights for a few indices are given in Table 1. The quasi-logarithmic scale is selected for the planetary Kp index. Local K -index has the same weights as planetary Kp index.

The auroral electrojet index AE is presented by linear scale of weights. AE index is computed by superposing the time series of magnetic perturbation field from 8 contributing observatories in Northern auroral zone uniformly distributed by longitude. AE presents a range between the maximum positive and negative values at superposition of magnetograms. Increase of AE index testifies on start of the magnetic-ionospheric storm with intervention of charge particles into the polar ionosphere accompanied by increased electric currents at 100-150 km.

The ionosphere disturbance level for each observatory could be quantified by deviations of critical frequency f_oF2 of the ionospheric $F2$ layer (peak electron density at the altitudes of 250-350 km) from the monthly median with appropriate weighting of qualifying and descriptive letters. Two linear scales are taken for the ionospheric disturbance of critical frequency - one for negative disturbance $Dm-$ if the observed f_oF2 is less than median and another for positive disturbance $Dm+$ (Table 1). Weights for the both types of deviations are enhanced by 1 if the numerical value f_oF2 is followed by a descriptive or qualifying letter. More involved procedure is adopted in cases of no readable records (missed or predicted observations) with weight varying from 1 to 4 periodically depending on weight for the preceeding hour. Counts are separated for negative and positive deviations; cases of zero deviation representing quiet conditions are excluded from counts of $Dm-$, $Dm+$.

Missed hourly observations in the primary database implicitly inform on the ionosphere disturbance. They reveal dependence on local time (occur more frequently by night), season (enhanced by winter) and latitude of observation (Gulyaeva, 1991). Figure 2 presents monthly percentage of missed values of f_oF2 at arctic zone (Sodankyla), middle latitudes (Slough, Washington and Wallops Is), equatorial zone (Huan-cayo) and Southern sub-auroral zone (Kerguelen).

Limiting acceptable level of missed (not readable) records is readily calculated according to minimum set of values necessary for determining the monthly median (Piggot and Rawer, 1978) or 27-day running median (Bremer, 1992). When there is less than 5 hourly measurements for each hour during a month the median cannot be found reliably. Besides, to obtain running median those available numerical data should be distributed uniformly during a month. Since parameters are scaled for 3 consecutive Regular World Days each month, this increases the number of required observations to 7 days per month. Thus, limiting acceptable level of missed hourly observations should not exceed 75% of times. Such constraint is not taken into account in planning incoherent scatter radar observations (EISCAT, 1991) nor it is relevant to satellite borne space observations. However to determine negative and positive ionosphere disturbances from the ISR and topside

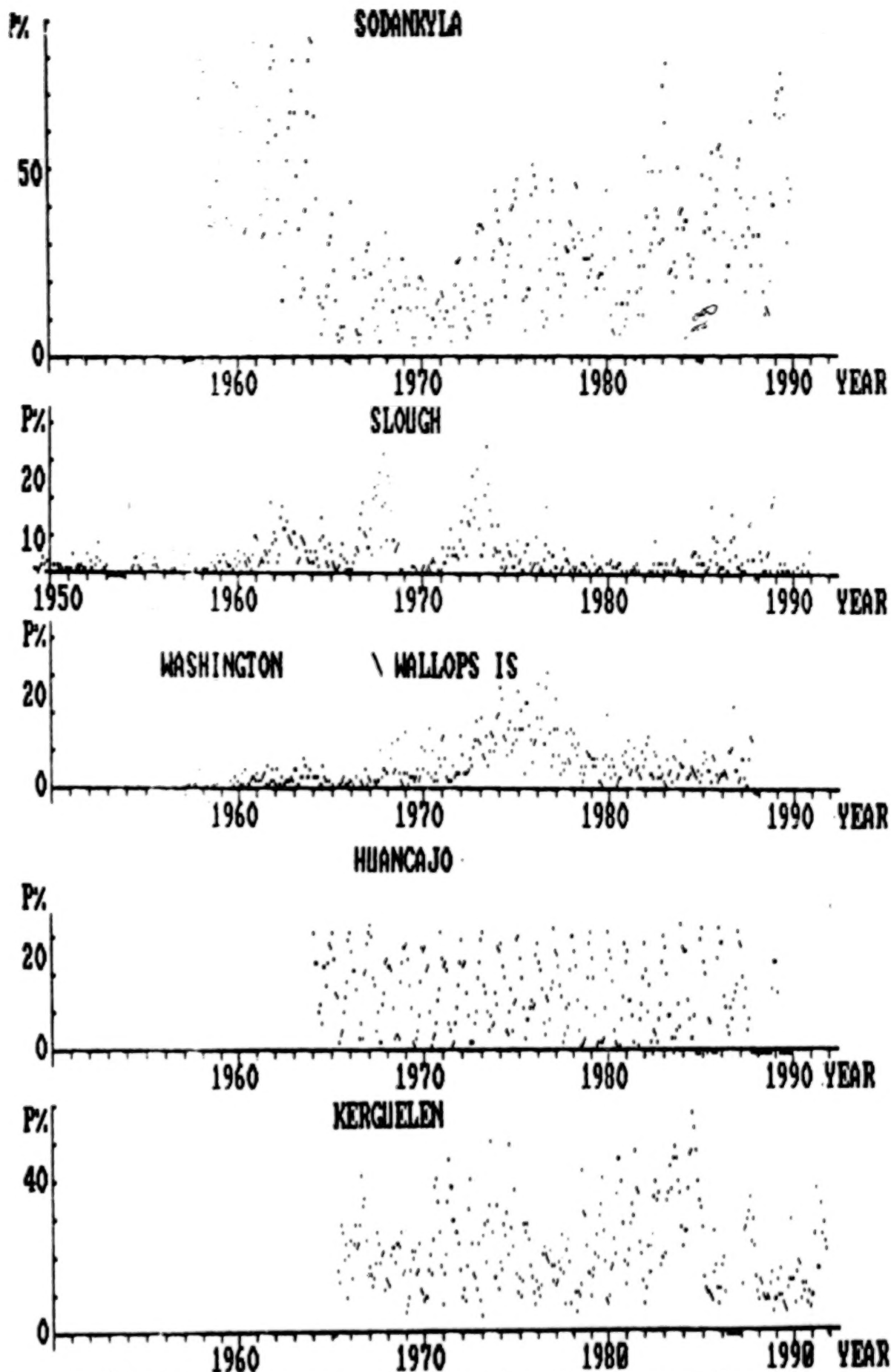


Figure 2. Monthly percentage of missed hourly observations.

sounding measurements, median could be found from the regional subset of ground-based vertical-incidence sounding data (Gulyaeva, 1994b).

The statistical estimates of the ionosphere disturbance indices (1) are greatly affected by a number of noisy observations. Incomplete sets of the data (for example, due to no measurements) could show unacceptable high level of missed values which could reach 90% at mid-latitudes (see Table 2). Also absence of numerical values could be due to inability for programmable identification of data with automatic system of digital ionosondes (Wright and Paul, 1981). The ionosphere disturbance indices obtained from such incomplete data sets should be clearly identified and excluded from further consideration of local, regional and global disturbances of the ionosphere.

TABLE 2. PEAK PERCENTAGE NUMBER OF MISSED DATA PER MONTH FOR INDICATED PERIOD OF OBSERVATIONS AT THE GLOBAL NETWORK OF IONOSPHERIC STATIONS

Station	Lat1	Long1	Period	Time/Peak%
Heiss Is	60.60N	58.00E	1944-1988	01.1967/89%
Kiruna	67.84N	20.42E	1957-1993	12.1984/70%
Sodankyla	67.40N	26.60E	1957-1989	12.1963/85%
Lycksele	64.62N	18.76E	1957-1989	01.1988/60%
Salekhard	60.00N	66.50E	1958-1990	03.1986/71%
Uppsala	59.80N	17.60E	1957-1993	12.1967/59%
Moscow	55.50N	37.30E	1946-1992	01.1986/14%
Kaliningrad	54.70N	20.62E	1964-1989	04.1966/72%
Irkutsk	52.50N	104.00E	1957-1988	06.1957/40%
Slough	51.50N	359.43E	1949-1990	05.1973/34%
Kiev	50.70N	30.30E	1964-1989	02.1986/37%
Pruhonice	50.00N	14.56E	1983-1992	05.1989/97%
Lannion	48.75N	356.55E	1971-1993	06.1985/32%
Poitiers	46.57N	0.35E	1964-1992	07.1976/22%
Alma-Ata	43.20N	77.00E	1957-1989	06.1978/58%
Rome	41.90N	12.52E	1968-1991	08.1968/61%
Boulder	40.00N	254.70E	1958-1989	09.1967/28%
Lisbon	38.72N	350.73E	1987-1992	07.1987/18%
Washington	38.70N	282.90E	1957-1967	07.1967/10%
Wallops Is	37.90N	284.50E	1968-1987	07.1976/31%
Kokobunji/Tokyo	35.70N	139.50E	1968-1992	07.1976/51%
Point Arguello	35.60N	239.40E	1969-1989	12.1976/25%
MauI	20.80N	203.50E	1957-1989	12.1965/11%
Dakar	14.76N	342.58E	1971-1993	02.1973/70%
Ouagadougou	12.37N	358.47E	1966-1993	11.1966/48%
Huancayo	12.00S	284.70E	1964-1989	11.1983/33%
Tahiti	17.73S	210.66E	1971-1993	01.1987/29%
La Reunion	21.10S	55.90E	1981-1993	07.1982/19%
Canberra	35.32S	149.00E	1950-1988	01.1952/34%
Kerguelen	49.35S	70.24E	1965-1991	06.1984/57%
Port Stanley	51.70S	302.20E	1967-1992	04.1968/23%
South Georgia	54.27S	323.50E	1971-1978	12.1974/16%
Argentine Is	65.25S	295.73E	1971-1992	07.1984/21%
Terre-Adelie	66.66S	140.02E	1964-1990	04.1967/74%
Halley Bay	75.50S	333.40E	1971-1980	06.1976/57%

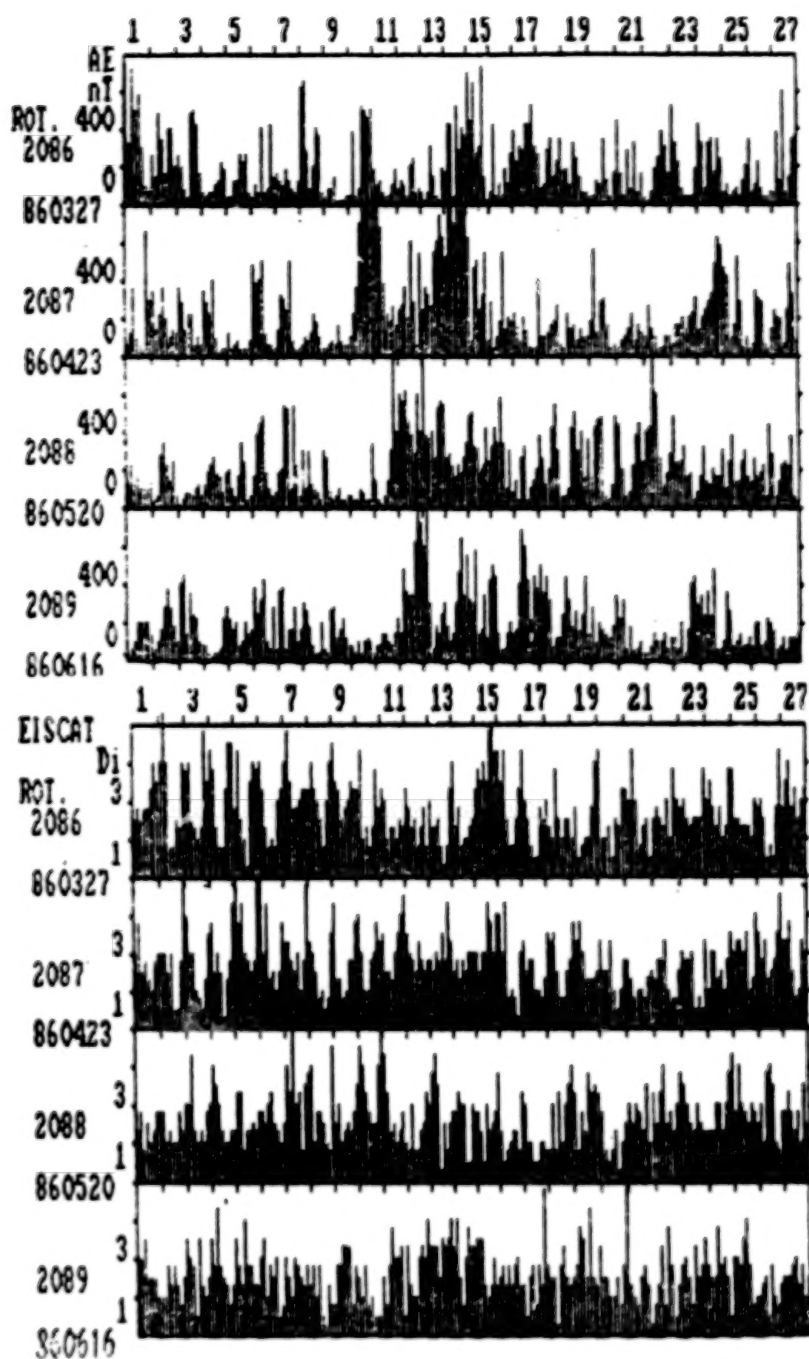


Figure 3. 3-hour range ionospheric indices at Scandinavian area and the auroral electrojet AE indices for four Bartels rotations. Starting date of each rotation is indicated at the left side.

3. SHORT-TERM INDICES AND CATALOGUES OF IONOSPHERIC DISTURBANCES

The most intense natural ionospheric disturbances are induced by solar proton flares accompanied by large disturbances in the solar wind and ejection of very high energy particles. The subsequent geomagnetic and ionospheric storms are a world-wide disturbance of the geosphere, of maximum intensity in the auroral zones and decreasing toward the poles and equator, manifested by abnormalities in critical frequency and peak heights, increased radio waves absorption and, in general, re-distribution of ionization density with height. Duration of such after-flares effects is of 10 min to 2-3 hours (Boska and Blahak, 1993). Similar effects could be observed at Earthquakes, nuclear explosions in the atmosphere (Kotadia et al., 1966) and other natural and manmade phenomena (Dea et al., 1991).

To recognise the ionosphere disturbance or quietness under such conditions we have hourly and 3-hours produced indices. The hourly indices are specified by weights introduced for the calculation of the histogram distortion when the deviations from quiet level are obtained (see Table 1). 3-hours ionospheric indices $Dm-$, $Dm+$ and Di are similar to geomagnetic Kp -indices, they are taken as the range between the greatest $Dm-$ and $Dm+$ for every 3 hours of Universal Time, UT. While observations at an ionospheric station allow to obtain local $Dm-$, $Dm+$ and Di values, their mean for a specified geographical region characterizes the regional quietness or disturbance.

An example of 3-hours Di indices near EISCAT averaged from indices of four ionospheric stations Kiruna, Sodankyla, Lycksele and Uppsala during four Bartels rotations from 27 March to 12 July 1986 is presented in Figure 3 (bottom section). Also 3-hours auroral electrojet AE values are shown (top section) where periods of enhanced AE activities are correlated with relevant Kp values (Rostoker, 1991). However there is no correlation between the two auroral indices - the ionospheric index Di (characteristic of disturbance of the critical frequency at heights of about 300 km over Scandinavian area) and the auroral electrojet AE index (measure of electric currents at the lower ionosphere heights of 100-150 km).

To simplify further analysis, the results could be denoted by two symbols: quiet state (0) and disturbed state (1). Similar approach is applied to produce Bartels diagrams which can be compared by simple voting procedure with relevant geomagnetic diagrams (Gulyaeva, 1992). Example of such results for Washington during 1946 is presented in Figure 4. Here comparison of our half-diurnal indices has been made with criteria applied earlier by NBS (Lincoln, 1970). The quiet periods comprise 34% of total half-diurnal pixels during 1946. The NBS stormtime figures $I=0,1,\dots,9$ are given under half-diurnal pixels. The values $I>3$ were taken as the storm conditions, they occurred about 14% of time. Our results confirm the ionospheric storm at all those periods with $I=4,5,\dots,9$ but also show small scale disturbances.

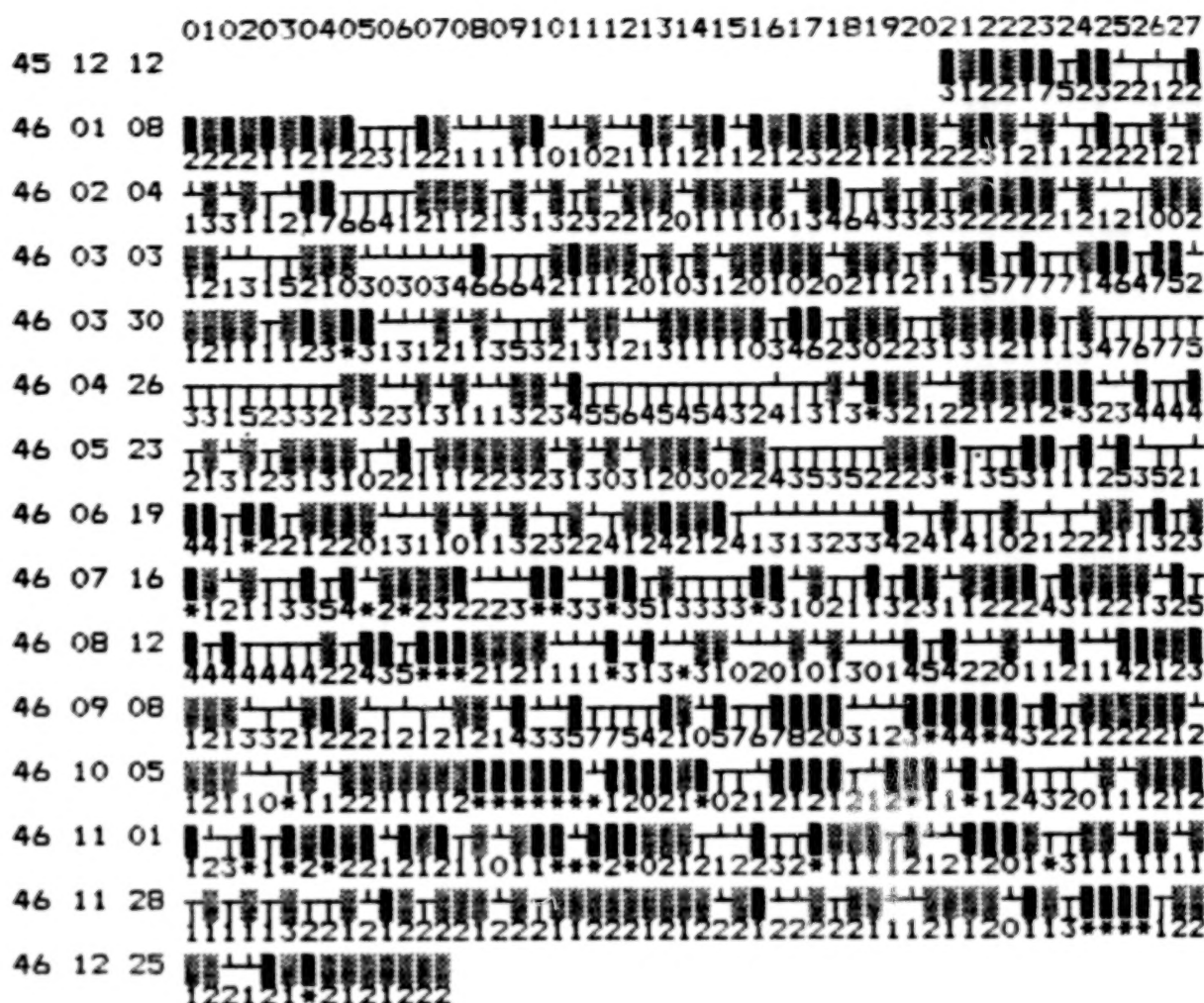


Figure 4. Comparison of half-diurnal diagram of foF2 positive (▲), negative (▼), the both types mixed (■) disturbances and quiet (□) values at Washington with HBS index of the ionosphere storminess 0,1,...,9, 9 representing the greatest disturbance (* no readable record of foF2).

Specific criteria for obtaining catalogue of 5 the most disturbed days and 10 quiet days for each month are proposed (Gulyaeva, 1993). Three signatures of disturbance are taken into account (diurnal indices Dm- for negative deviations from the median, diurnal indices Dm+ for positive deviations and their range Di for each day of the month). Similar to the planetary geomagnetic Kp index, the diurnal values of Dm-, Dm+ and Di are ranked in decreasing order and sum of current ranks is calculated for each day of the month. The most disturbed day is identified by the greatest sum of current ranks (as used to judge sport competitions), and the quietest day has the least sum of current ranks. An example of these results is presented in Table 3 for the ionospheric data at Wallops Is and planetary geomagnetic Kp index. In some months there is coincidence of some quiet and disturbed days in the ionosphere and geomagnetic field, sometimes - there is not. What happens at the larger time scale we will show in the following section.

4. LONG-TERM TRENDS OF GEOMAGNETIC AND IONOSPHERIC DISTURBANCES

With similar scale of weights we can make estimates of disturbance measure of any parameter of different time scales. Such calculations are carried out with some indices of solar-terrestrial physics for producing diurnal, monthly and annual results. Calculated monthly and annual values of disturbance measure D_m of the geomagnetic K_p indices (1932-1991) and AE indices (1957-1986) are presented elsewhere (Gulyaeva, 1992). Figure 5 illustrates correlation of the long-term monthly disturbance measure D_m during 1964-1989 for geomagnetic planetary K_p indices and auroral electrojet AE indices (top section), regional mid-European ionospheric negative disturbance indices D_m^- (middle section) and positive disturbance indices D_m^+ (bottom section).

Anti-correlation of annual number of geomagnetic quiet days of an amplitude value $A_p < 10$ nT and above disturbance measure D_m of planetary K_p index during 1932 to 1991 has been shown elsewhere (Gulyaeva, 1992). At the same time trend of gradual decreasing of number of geomagnetic quiet days since the beginning of 20th century can be deduced after Legrand and Simon (1991). Mean rate of decay of annual number of quiet days (defined by threshold $a_a < 20$ nT by Legrand and Simon) is about 1.5% per year. A 1.5% decrease in annual number of quiet days which reach nowadays about 100-150 days per year can cause ceasing of the quiet days in a foreseen future (about 2080). All possible consequences of such state should be thoroughly studied.

TABLE 3. 5 DISTURBED DAYS AND 10 QUIET DAYS AT IONOSPHERE OVER WALLOPS IS (WI) AND IN THE PLANETARY GEOMAGNETIC FIELD (K_p) DURING 1979. D1 - THE MOST DISTURBED DAY, Q1 - THE MOST QUIET DAY.

STYRMN:	D1	D2	D3	D4	D5	Q10	Q9	Q8	Q7	Q6	Q5	Q4	Q3	Q2	Q1
WI7901:	04	26	27	28	05	30	12	24	06	20	18	08	31	10	11
WI7902:	03	21	22	23	24	01	09	07	12	17	14	13	19	08	18
WI7903:	29	28	01	02	03	23	30	22	27	19	16	13	14	18	31
WI7904:	25	28	29	30	05	15	07	14	21	10	24	19	17	16	18
WI7905:	09	22	19	06	07	04	18	13	20	12	16	05	08	31	27
WI7906:	14	20	07	28	08	01	12	03	27	19	18	16	25	29	02
WI7907:	27	07	14	12	30	13	20	18	16	02	24	23	21	05	31
WI7908:	06	13	24	29	18	10	08	01	16	17	28	31	11	02	09
WI7909:	18	11	19	05	24	06	03	04	13	09	12	30	08	07	16
WI7910:	01	02	12	04	21	05	16	19	18	10	13	22	15	14	28
WI7911:	26	28	27	13	11	01	23	24	17	06	22	02	12	15	21
WI7912:	05	04	29	30	18	15	27	13	03	17	09	31	10	02	14
KP7901:	04	25	26	07	23	18	21	12	01	08	14	17	13	11	10
KP7902:	21	22	23	27	26	03	08	16	01	07	10	20	17	14	13
KP7903:	29	10	28	22	08	16	15	13	18	08	07	12	20	21	14
KP7904:	25	05	29	22	04	07	13	10	26	09	17	18	11	19	20
KP7905:	22	25	24	26	19	13	08	05	04	10	03	31	06	16	17
KP7906:	07	06	22	23	16	29	12	19	04	02	18	01	28	03	05
KP7907:	07	29	06	27	20	01	09	23	10	22	24	11	02	25	31
KP7908:	29	13	20	19	21	11	08	05	14	17	10	09	16	23	15
KP7909:	18	21	20	26	25	15	12	13	23	22	19	08	07	02	09
KP7910:	08	06	07	09	10	20	23	14	05	31	27	30	19	17	18
KP7911:	13	24	09	08	01	27	18	29	26	23	15	06	22	05	28
KP7912:	29	30	04	28	22	10	11	20	21	14	12	07	23	13	25

884000

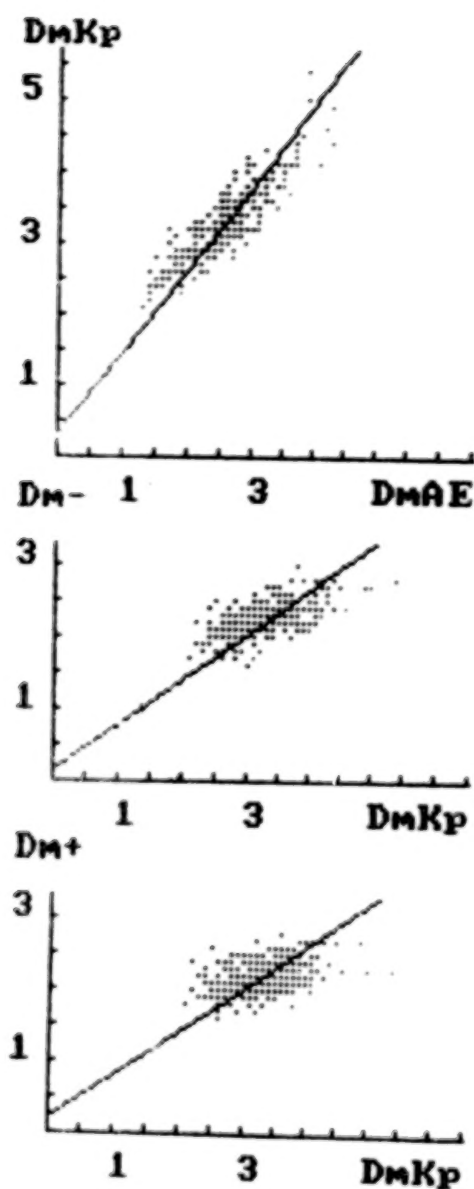


Figure 5. Correlation of monthly measure of disturbance by proposed weighted statistical criterium: for planetary geomagnetic Kp index, auroral electrojet AE index, negative ionosphere disturbance $Dm-$ and positive ionosphere disturbance $Dm+$ averaged over European area during 1964-1989.

001000

5. CONCLUSION

Development of second generation database of the ionosphere disturbance indices allowed to compare the ionosphere degree of disturbance of different time scale with relevant geomagnetic field parameters.

On a short-term scale the ionosphere instability is not correlated with the geomagnetic variation. Hence, it is recommended to arrange service producing hourly and 3-hours ionospheric indices to recognize quiet or disturbed state of the ionosphere from the global ground-based vertical-incidence sounding data in support of ionospheric and atmospheric space borne observations (Gulyaeva, 1994c).

On a long-term scale the above results confirm gradual growth of both the geomagnetic and ionospheric disturbances (Gulyaeva and Gulyaev, 1993). This may be caused by technogenous impacts on geosphere related with increasing usage of space environment for exploration, broadcasting, radio-telecommunications, etc. With knowledge of adverse effects of electric and magnetic fields of natural and artificial origin on living organisms (Plekhanov, 1990), the above trends should evoke concerns for their environmental effects.

ACKNOWLEDGMENTS

Author is grateful for geomagnetic and ionospheric data provided by WDC A for STP, Boulder, CO, USA; CHET, Lannion, France; WDC B2, Moscow, Russia; WDC C1 for STP, Oxford, UK; WDC C2 for Ionosphere, Tokyo, Japan; Dr. K. Schlegel, MPI, Germany (EISCAT Scientific Association). This work was supported by travel grants of European COST-238 Project (1992, 1993, 1994), the International Science Foundation, USA (1993), COSPAR (1994) and COSTED (1994).

REFERENCES

- Boska J. and F. Blahak, 1993: Changes of spectra of foF2, h'F2 and H3000F2 during SPE events. *Proc. of COST238 Workshop, Part 1*, Universitat Graz, Austria, 199-204.
- Bremer J., 1992: Ionospheric trends in mid-latitudes as a possible indicator of the atmospheric greenhouse effect. *J. Atm. Terr. Phys.*, 54, 1505-1512.
- Dea J.Y., W.L. Van Bise, E.A. Rauscher, and W.H. Boerner, 1991: Observations of ELF signatures arising from space vehicle disturbances of the ionosphere. *Can. J. Phys.*, 69, 690-698.
- EISCAT Scientific Association, 1991: Catalogue of operations 1981-1990. S-981 28 Kiruna, Sweden.
- Gulyaeva T.L., 1991: Incomplete information problem at ionospheric modelling with vertical-incidence sounding data. *Adv. Space Res.* 11, No. 10, 67-75.

- Gulyaeva T.L., 1992: Voting procedure for distinction of geomagnetic quiet and disturbed conditions for the ionospheric data analysis and modelling. *Publicaciones del Observatorio del Ebro, Memoria No. 16*, Roquetes (Tarragona), Spain, 305-324.
- Gulyaeva T.L., 1993: Criteria for the definition of the quiet ionosphere. *Proc. of COST238 Workshop, Part 1*, Universitat Graz, Austria, 129.
- Gulyaeva T.L., 1994a: Development of data base of the ionosphere disturbance indices. *Adv. Space Res.*, 14, No.12, 149-152, 163-166.
- Gulyaeva T.L., 1994b: Developing countries service with ground-based vertical-incidence sounding observations for enhanced utilization of space data. *Adv. Space Res.*, in press.
- Gulyaeva T.L., 1994c: Ionospheric variability and indices of solar-terrestrial environment. *Adv. Space Res.*, in press.
- Gulyaeva T.L. and R.A.Gulyaev, 1993: Climate change in the ionosphere parameters dependent on solar and geomagnetic activity. *Adv. Space Res.* 13, No.3, 63-66.
- Kotadia K.M., K.G.Jani, and K.Rawer, 1988: Ionospheric effects on nuclear explosions-II. *Ann. Geophys.*, 24(1), 91-100.
- Legrand J.P. and P.A.Simon, 1991: A Two-Component Solar Cycle. *Solar Phys.* 131, 187-209.
- Lincoln J.V., 1970: Ionospheric Forecasting in the United States 1942-1966. *AGARD Conf.Proc. No.49 on Ionospheric Forecasting*, Ed. by Vaughn Agy, ITS, ESSA, Boulder, CO, 80302, USA, 2-39.
- Menvielle M. and A.Berthelier, 1991: The K-derived Planetary indices: Description and availability. *Reviews of Geophys.*, 29(3), 415-432
- Plekhanov G.F., 1990: *Main regularities of the low frequency electric-magnetic biology*. Tomsk State University, Tomsk, Russia, 186 p.
- Piggot W.R. and K.Rawer, 1978: URSI Handbook of ionogram interpretation and reduction. UAG Rept.23A, WDC-A for STP, Boulder, Colorado, USA.
- Rostoker G., 1991: A quantitative relationship between AE and Kp. *J. Geophys. Res.* 96, A4, 5853-5857.
- Solar Geophysical Data, 1951-1994: Prompt Reports. WDC A for STP, Boulder, Colorado 80303, USA

PRECIPITATION AMOUNT LONG-TERM VARIABILITY OVER
ROMANIAN'S TERRITORY

Maria Colette Iliescu

National Institute of Meteorology and Hydrology
Bucharest 71552 Romania

ABSTRACT

The precipitation amount long-term variability is studied on the basis of the slid means computed from the secular series of monthly, annual and seasonal values from several meteorological stations. The obtained results offer the possibility to climatologically forecast precipitation long-term trends.

The issue of the climate's secular variability has become an object of study in Romania as early as the end of the last century (Hepites, 1898) - presently being in the focus of numerous researches not few of the climatologists (Topor, 1967; Stoenescu, 1968; Iliescu, 1993).

The present work gives estimations of water quantities variability resulted from precipitations on the basis of instrumental measurements made at Romanian meteorological stations which have been functioning ever since the second half of the 19-th century (Sibiu - from 1851, Piatra - from 1853, Bucharest - from 1865).

To stress long range systematic variabilities of precipitations quantities which may follow the trend of non-periodical variabilities induced by atmospheric circulation, the former variabilities were dumped using running means (WMO, 1990).

Thus, relatively short-term variabilities are diminished giving way to stressing long-term changes.

Secular strings of precipitations values were processed as running means over ten years periods - the latest such considered interval being 1984 - 1993.

The chronological succession of precipitation secular variability in Romania is complexly rendered by drawing the isopleths (Fig. 1).

These ones point at average quantities deviations compared to the "normal" (i.e. the multi-annual average of the 1891-1990 period) considered the "relatively zero" value.

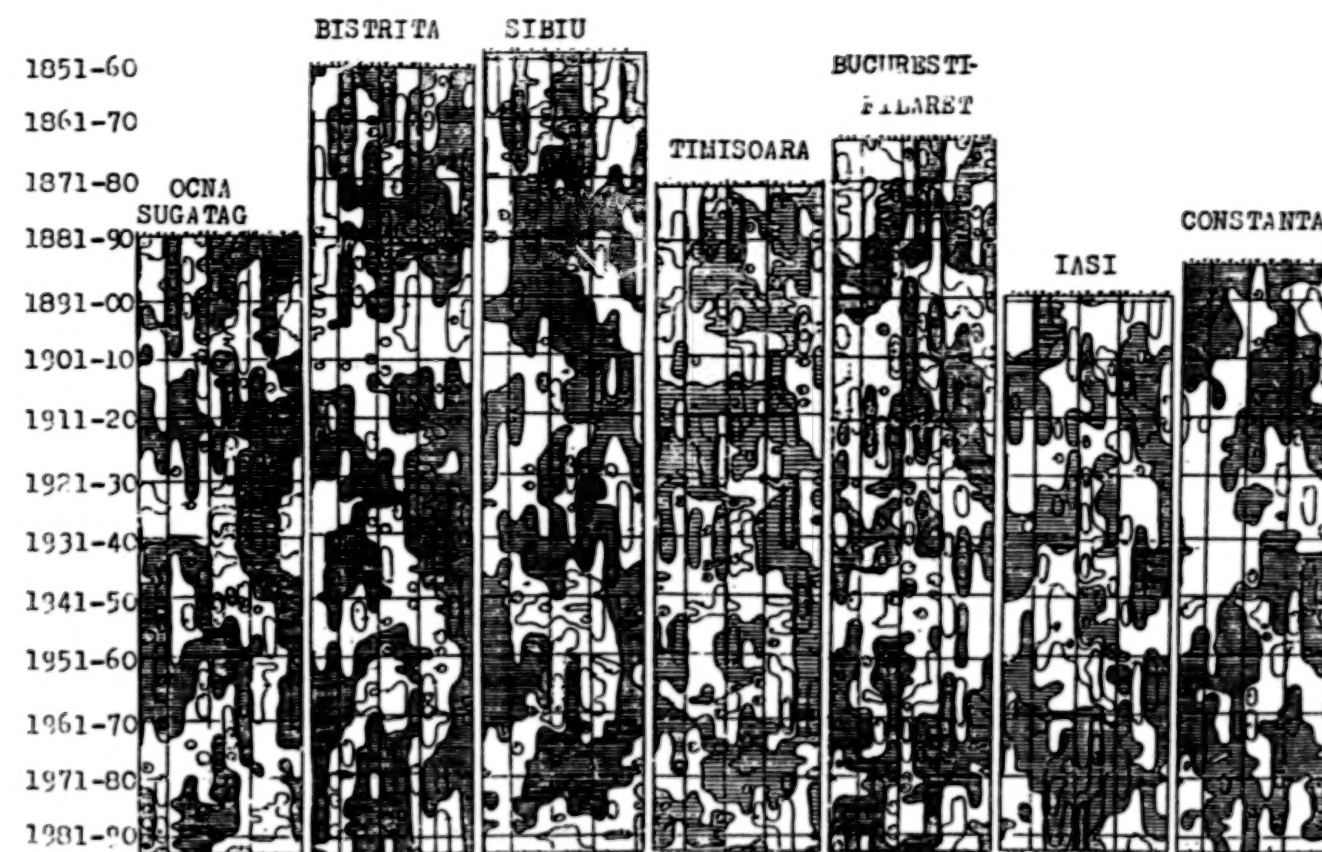
The isopleths shape the repartition in time of intervals with exceedent or deficit precipitation at different meteorological stations over the Romanian territory.

Isolines are drawn every 10 mm. The shaded areas mark deviations in the positive field (i.e. decades wetter than normal) while the blank areas correspond to negative deviations (i. e. to the droughty decades).

BLANK PAGE

000000

A-51



000470
Precipitation variability intervals are characterized by the sign of deviations, by their duration and territorial repartition.

Following the general aspect of the isopleths there are noticed increments or abatements of the precipitations. The aggregate long-term variabilities are characterized by rhythmicity, but not by cyclicity.

The succession of the precipitations quantities showed not always synchronical fluctuations over the whole territory of Romania.

The similitude in variability is rather a regional characteristic.

In fact, this regional synchronism is a projection of the specific way in which precipitations quantities occur and distribute within the baric systems, the same being valid for local thermo-convective precipitations.

Most part of the fluctuations have the same sense and chronology on the whole territory of the country which reveals the connection with the variability of the general atmospheric circulation.

As an example, the droughty intervals in the decades closing the 19-th century and those from the beginning of the 20-th century (including droughty years like: 1894, 1896, 1904, 1907), as well as the decades which comprise droughty years like: 1917, 1920, 1924, 1926, 1934, 1942, 1945-1948, 1950, 1951, 1953, 1961, 1983, 1986, 1989, 1990 and 1992 are noticeable on the whole territory of Romania. Isophlets drawn for different meteorological stations reveal a regional component in point of intensity and duration of the droughts (Figure 1).

Rainy intervals are generally detected in decades with rainy years like: 1884, 1887, 1912, 1915, 1939, 1941, 1969, 1972 and - in Moldavia - 1991.

The succession along the years of rainy and droughty intervals has a non-single rhythm and it generally comprises periods longer than one month.

Opinions roughly converge in the conclusion that the rhythms of variability have phases of several tenths of years each.

As for the latest decades (1984-1993 included), the isopleths contour a rainy interval in the months from the end of the summer and autumn respectively and from the beginning of spring.

The Southern part of the Transylvanian Plateau is to be remarked for its drought expanded over almost the entire year (December excepted where an excedent occurs).

In these latest decades, the months from the end of spring and summer are generally wetter than normal which correspond to the thermal tendency - i.e. summers are colder than normal in Romania in the mentioned decades.

Taking into account secular evolution of ten years running means for annual precipitations, large rhythmical deviations are

noticed every 30, 35 or 40 years (Figure 2).

The intervals with particularly rainy years as well as those severely droughty are easily noticeable.

The rainiest decades in Romania were: 1876-1885, 1910 - 1919, 1932-1941, 1966-1975, while 1902-1911, 1942-1951 and 1983-1992 were the droughtiest (personal communication, 16 March 1992, Maria Colette Iliescu, Romanian Academy, First Symposium I.G.B.P. - Romanian Research with implications on the topics of the Geosphere-Biosphere International Program, Bucharest).

In the last part of the analysed time-interval annual precipitations decreased over the whole territory of Romania.

The deviations of the precipitations reached 20-160 mm below "normal" excepting the East-North-East part of Romania where although the general tendency of the precipitations decrease also existed, the last deviation of the decades maintained in the "positive" domain with quantities from 35 to 50 mm above "normal".

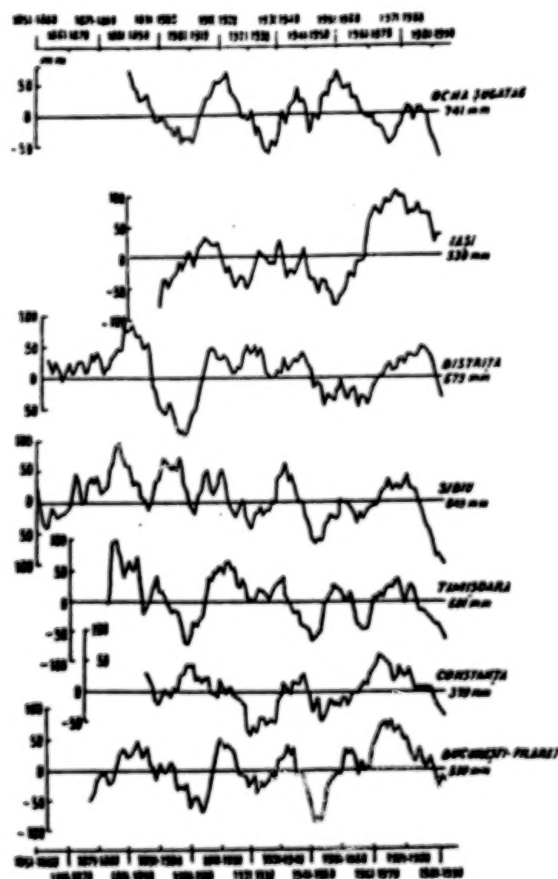


Figure 2. Annual precipitation 10 years running means deviation towards the "normal" (mm).

In the 1983-1992 decade, the least negative deviations occurred in Bucharest and in the Northern area of the Transylvanian Plateau (less than -20 mm) while the largest deviations were traced in the central and Southern part of the Transylvanian Plateau (-100 to -165 mm).

The decrease tendency below the "normal" of mean running precipitations has become obvious in Romania after the 1971-1980 decade and mainly after the 1976-1985 period. If the precipitations decrease is maintained, it is possible that until around the end of the century annual precipitation should decrease at the whole scale of the country by 30 to 50 mm. This would equal the lowest level previously reached in Romania as an example in the 1902-1911 and 1942-1951 decades.

It is a fact that in the North-Western part of our country, in the North of Transylvania and in the East-North-East of Romania a precipitation increase of a 5 to 10 mm in the 1983-1992 decade average was detected which could be the start of a certain precipitation normalization.

W.M.O. regional estimates made in 1990 for the winter season forecast precipitation augmentation; but in Romania a decrease tendency was observed: -5 to -25 mm below "normal" in most part of the country (Fig. 3).

In the Northern area of the Transylvania Plateau and in the West and centre of the Romanian Plain also, decade running means show positive deviations from 5 to 10 mm.

The general tendency of precipitation quantities is to maintain at approximatively the same level.

The largest negative deviations of the running means are localized in the Southern part of the Bărăgan (-25 mm) and in the middle part of the Siret river basin (-20 mm) where the probability of a higher deficit compared to the rest of the territory of the country maintains.

In spring (fig. 3) precipitations quantities have a general tendency over the whole Romanian territory - a fact which has become obvious after 1979-1988.

Decadic running means though decreasing showed positive deviations in the Northern part of the country as well as in the East - North-East area (15 to 25 mm).

Average decade precipitation show a deficit in the greatest part of the Transylvanian Plateau (-15 to -45 mm), in the Eastern border of the Danube Delta (-25 mm) and in the Southern part of the country also, where negative deviations towards the "normal" are eloquent.

The Northern part of the Transylvanian Plateau, the Western part of the country and the Bucharest area show averages of the 1983-1992 decade close to the "normal".

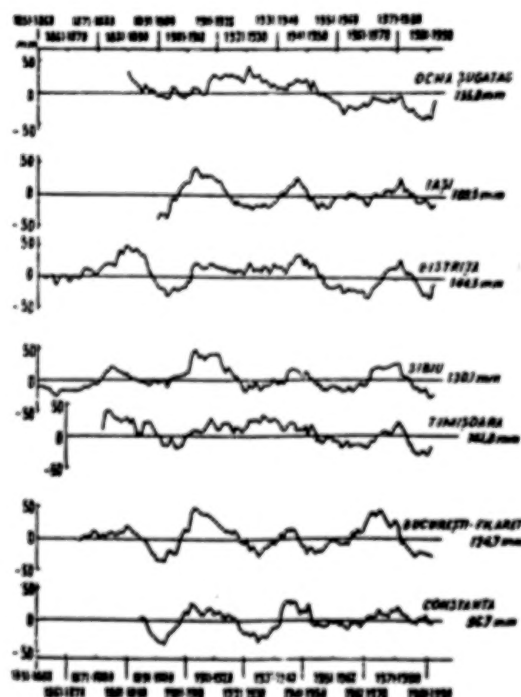
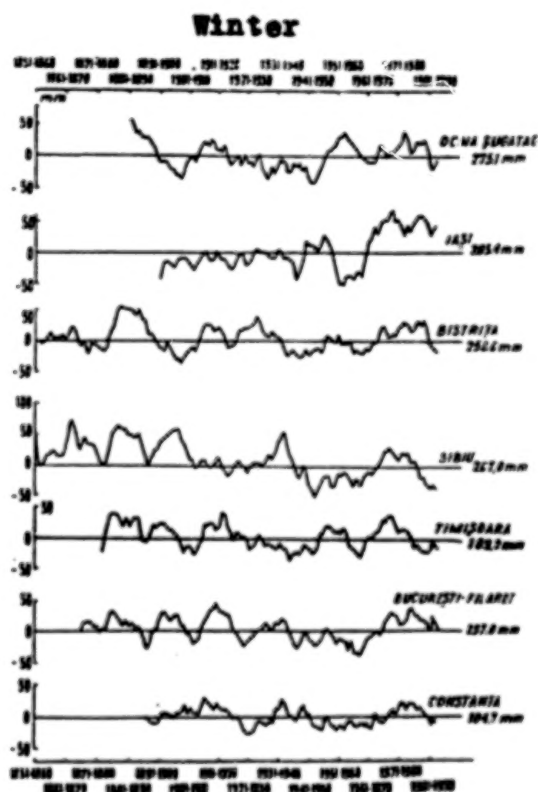
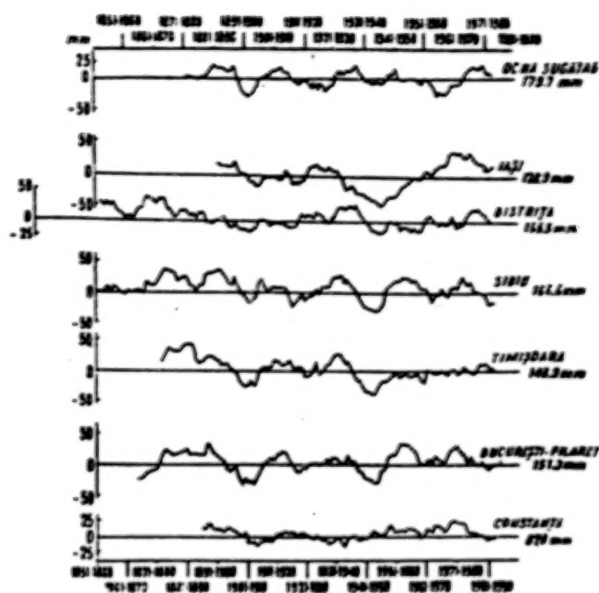
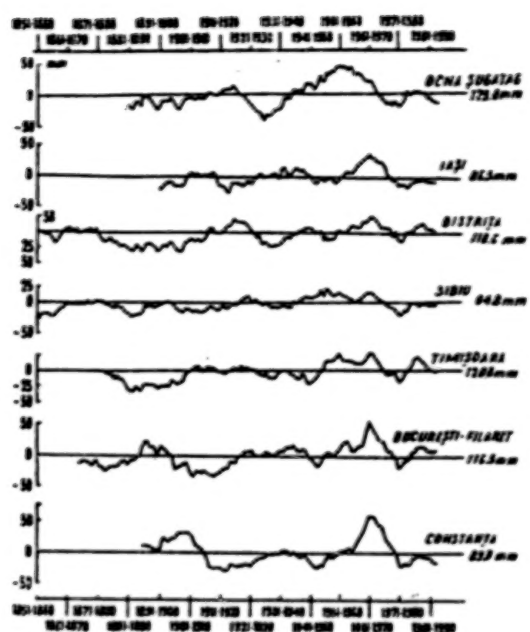


Figure 3. Seasonal precipitation 10 years running means deviation towards the "normal" (mm).

W.M.O. regional estimates made in 1990 forecast a precipitations decrease of 5 to 15% in the summer season.

To Romania, it means that, compared to multiannual averages of about 100-290 mm, summers will benefit by less than 85-250 mm in zones below 500 m height.

Indeed, in summer precipitations quantities have a decrease tendency all over the country approximatively beginning in the 1977-1986 decade (fig. 3).

In the North and centre of Romania, as well as in the littoral area, the precipitation decrease tendency maintained in the latest decade (1984-1993), while in the East, the South-South-West and in the South of the Bărăgan an increment of running means values has started.

Running means deviations towards the "normal" - i.e. small precipitations quantities - maintain in the North (-5 to -35 mm), centre (-20 to -60 mm) and in the South (-10 to -25 mm).

Precipitation quantities are higher than "normal" - i.e. positive deviations - in the Eastern part of the country (40 to 60 mm), while in the Bucharest area they equal the "normal".

The highest positive deviation of precipitations quantities occurs in the central area of the Siret river basin (60 mm) while the highest negative deviation - in the central (-50 mm) and Southern (-60 mm) part of the Transylvanian Plateau.

Such deviations are - regionally - extremes of the long-term precipitation variabilities. Regional occurrence in the 1984 - 1993 decade are unprecedented in the secular variability.

In autumn, in the decades of the 80s and 90s precipitation quantities were by 10 to 60 mm smaller than "normal", having the tendency to maintain at the present level or even to augment (fig. 3).

The negative deviations in the 1981-1990 ... 1984-1993 decades equalled and even surpassed the lowest recorded limit throughout 142 years of observations in the North, centre and South-West of Romania, in the sub-Carpathians of the Oltenia region and in the Eastern border of the Danube Delta.

In Romania, the general tendency of autumn precipitation decrease has started in the 1983 - 1992 decades.

As for the rest of the Romanian territory, as shown previously precipitation quantities seem to preserve the level reached in the latest decades. This level shows deficits mostly in the West of the Romania Plain (-60 mm) and in the Getic sub-Carpathians (-55 mm).

CONCLUSIONS

To stress some systematic precipitations long-term variations which might overlap non-periodical variations induced by the atmospheric circulation, a method was used to smooth the mentioned variations using the running means.

It was thus attempted to diminish the variations within the relatively short observational periods and give way to revealing the possible long-range climate changes.

The increases or decreases as compared to the "normal" are characteristic to precipitations regime which, as a whole, shows long-range rhythmic variations and whose oscillations are non-cyclic and reveal no long-range tendency.

The utmost part of both increases and decreases are approximately synchronic but differ in point of repartition and amplitude. Despite all these the succession of precipitations qualities did not always prove synchronic variations.

This is characteristic to precipitation occurrence and repartition manner for within the baric systems physico-geographic peculiarities mark their print.

The impact of atmospheric warming due to "greenhouse effect", supposed to have acted until now is impossible to separate from the natural variation known limits; although the mentioned warming also influences the precipitations regime.

It is possible that natural variability limits be exceeded in the following years, but not necessarily due to the "greenhouse effect". The real reason is that ancient values might have occurred within the Romanian latitudes but were not measured since no observations were performed in ancient times.

The decrease below the "normal" of average running precipitations quantities over 10 years, which became obvious after the 1971-1980 decade and mostly after 1976-1985 is not outside natural variability limits.

The present droughty interval is comparable in point of amplitude to that in the second half of the 19-th century and that around the middle of the 20-th.

In the first decades of the 21-st century, Romania is likely to experience decadic average precipitations values close to the "normal" and even higher.

REFERENCES

- Hepites, St., (1898): Did the Climate Change? Basileescu Printing House and Foundry, București, 77 pp.
- Iliescu, M.M., (1993): Considerations Concerning the Precipitation Amount Variability over Romania's Territory. Proc. International Symposium on Precipitation and Evaporation (September 20-24, 1993), vol.2, Slovak Hydromet.Inst. Bratislava, Swiss Federal Inst. of Technol., Zurich, 211-216.
- Stoenescu, St.M., (1968): Chronological Oscillations of the Amounts of Atmospheric Precipitations in the Southern Part of Romania. N.I.M.H. Works for 1966, București, 235-252.
- Topor, N., (1967): Does the Climate Change? Scientific Publishing House, București, 80 pp.
- World Meteorological Organization, (1990): Guide des pratiques climatologiques No.100, Deuxième édition, OMM, Genève.

A METHOD FOR DIRECT RETRIEVING THE PLANETARY-SCALE WAVE PARAMETERS FROM SATELLITE MEASUREMENTS OF THERMAL OUTGOING RADIATION

I. A. Podgorny, and G. M. Shved
Institute of Physics, St. Petersburg University
Petrodvorets, St. Petersburg, 198904, Russia

ABSTRACT

A method to retrieve the planetary-scale waves for the stratosphere and mesosphere from measurements of thermal outgoing radiation is presented for the nadir sounding of Rossby normal modes of the Lamb wave type in the $15\ \mu\text{m}$ CO_2 band. A dimensionless form for the main formulae is used which is believed to increase applicability of the results. The method proposed consists of EOF-filtering to extract a wave-induced signal and of Hermite polynomials expansions to describe vertical structure of the wave. Accuracy of retrievals is estimated as dependent on the record period as well as the number of channels. The method allows retrieving the planetary-scale wave parameters under condition of significant noise.

1. INTRODUCTION

The planetary-scale waves cause many peculiarities of both circulation and gas constituent distributions in the middle atmosphere. Also, they may be considered as some indicators of the atmospheric state and processes (stratospheric sudden warmings, quasi-biennial and semi-annual oscillations and so on). In the latter sense, the weak modes are interesting as well as the gravest ones.

At present, there are numerous investigations of the planetary-scale waves based on satellite measurements of thermal outgoing radiation. The frequency, zonal wavenumber, latitudinal and vertical structure have been found for a number of the gravest Rossby modes in the stratosphere and mesosphere (e.g., Rodgers and Prata, 1981; Hirota and Hirooka, 1984; Prata, 1984 and 1989; Hirooka and Hirota, 1985 and 1989; Venne, 1985 and 1989). All the wave parameters are derived from the temperature or geopotential fields constructed with the use of satellite radiation measurements in a set of radiometer channels. Only frequency and zonal wavenumber are obtained by the Fourier analysis of measured radiation in some channel directly.

The importance and peculiarities of the planetary-scale wave investigations require development of special methods to retrieve the wave parameters from measurements of thermal outgoing radiation. What is important, the determination of wave disturbances of the temperature or geopotential as an intermediate stage to obtain the wave parameters seems to be unnecessary. That must yield an improved accuracy of retrievals due to using an a priori information about space-time coherency of the planetary-scale waves. On the other hand, background temperatures may be omitted while retrieving the wave. That allows the preliminary processing of measured radiation with regard to remove experimental errors as well as slow background components. A special attention should be paid to measurements performed over short record periods (down to several days), when the planetary-scale wave parameters may be considered as invariable.

This paper presents a method to retrieve the planetary-scale wave for the stratosphere and mesosphere. The case of the Lamb wave not travelling in vertical is examined. That is believed to be appropriate, however, since Rossby normal modes in an isothermal motionless atmosphere are just the

Lamb waves according to the classical theory (Diky, 1969). Moreover, observations of the Rossby waves in the middle atmosphere are favourable to describing its vertical structure by that of the Lamb wave (Rodgers and Prata, 1981; Hirota and Hirooka, 1984; Hirooka and Hirota, 1985; Prata, 1989; Venne, 1989). First, the phase has little change with height for those modes ever been observed. Second, for the gravest modes, the amplitude change with height was found to be close to that given by the classical theory for the Lamb wave.

The method is elaborated for nadir measurements of thermal outgoing radiation. A dimensionless form for the main formulae is used that is believed to increase applicability of the results obtained. It should be emphasized, however, that we do not claim to give a technique for any up-to-date satellite instruments, since several simplifying assumptions are used to make the problem more tractable. So, this paper should be implied as an introduction to the problem.

2. APPLIED MODELS

2.1 THE RADIATIVE TRANSFER EQUATION

In this Subsection we consider a non-scattering atmosphere in the local thermodynamic equilibrium. The optical thickness of the atmosphere is assumed to be great to not take into account the radiation contribution from the ground and clouds. The transmission of the atmosphere from a dimensionless height $x = \ln(p_0/p)$ (p is pressure, $p_0 = 1000$ mb) to the upper boundary $P_v(x, \infty)$ (v is frequency) is suggested to be independent of temperature T . As a result, the variations of vertical thermal outgoing radiance $\Delta I(v)$ are caused by those of the Plank function $B(v, T)$ only. The departure of temperature $\Delta T(x)$ from the mean profile $T_0(x)$ is assumed to be small. Therefore, the disturbance of the Plank function linearly depends on $\Delta T = T - T_0$.

Let radiation is measured in N narrow spectral intervals (channels) so that $B(v, T)$ within the n -th interval (from $v_{n,1}$ to $v_{n,2}$) may be set to $B(v_n, T)$, where $v_n = (v_{n,2} + v_{n,1})/2$. As a result, a radiance fluctuation, registered in the n -th channel, is as follows

$$\Delta I_n = \int_0^\infty dx K_n(x) \frac{\partial B(v_n, T)}{\partial T} \Big|_{T=T_0(x)} \Delta T(x) + \varepsilon_n, \quad (1)$$

where

$$K_n(x) = \int_{v_{n,1}}^{v_{n,2}} dv \frac{\partial P_v(x, \infty)}{\partial x} \quad (2)$$

is the n -th weighting function. The values of $(\Delta v)_n = v_{n,2} - v_{n,1}$ are taken as equal to Δv irrespective of n . Experimental error of radiance ε_n is assumed to be the white Gaussian noise with variance σ^2 independent of n . The relevant covariance is $S_\varepsilon = \sigma^2 I_N$, where I_N is the identity matrix of rank N .

2.2 DIMENSIONLESS FORMULATION

Dividing (1) by σ and marking dimensionless values by tilde, the main formulae are introduced in a dimensionless form

$$\Delta \tilde{I}_n = \int_0^{\infty} \tilde{W}_n(x) \Delta \tilde{T}(x) dx + \tilde{\epsilon}_n, \quad (3)$$

$$\tilde{W}_n(x) = \tilde{K}_n(x) \frac{\partial \tilde{B}(\alpha)}{\partial \alpha} \bigg|_{\alpha = \frac{k_B T_p(x)}{h \nu_0}}, \quad (4)$$

$$\tilde{K}_n(x) = \frac{K_n(x)}{\Delta \nu}, \quad (5)$$

$$\tilde{B}(\alpha) = \frac{1}{\exp(\alpha^{-1}) - 1}, \quad (6)$$

$$\Delta \tilde{T}(x) = \frac{2 \nu_0^2 k_B \Delta \nu \Delta T(x)}{c^2 \sigma}. \quad (7)$$

where ν_0 refers to some representative frequency of the interval, whereas c , k_B , and h denote the light speed, and the Boltzmann and Planck constants, respectively. The dimensionless noise in (3) has the unit variance, a fact profitable for further consideration.

The dependence of $\Delta T(x)$ on time t is introduced with the use of dimensionless time

$$\tilde{t} = \frac{t}{\delta t}, \quad (8)$$

where δt is an interval between two subsequent measurements. To simplify things, satellite measurements are treated as performed on a fixed latitude. So, δt is assigned to be the satellite orbital period.

2.3 WEIGHTING FUNCTIONS

Two sets of hypothetical weighting functions $\tilde{K}_n(x)$ are employed for numerical simulations, which should provide retrieving waves in the stratosphere and lower mesosphere. That corresponds to the altitude range approximately from 15 to 70 km (or from $x_L=2$ to $x_U=10$). Although the 15 μm CO_2 band is of interest, the radiation transmission within a single isolated line is used, for simplicity, to calculate $\tilde{K}_n(x)$. The typical Voigt shape parameters are taken, namely, 0.1 cm^{-1} for the Lorentz half-width at the standard pressure and $\alpha_D = 0.65 \times 10^{-3} \text{ cm}^{-1}$ ($\sqrt{\ln 2} \alpha_D$ is just the Doppler half-width).

For numerical simulations, two ways to determine the sets of $\tilde{K}_n(x)$ are employed.

Way 1. The N intervals of the width $\Delta \nu = \alpha_D$ are put on the line having $s = 10^{23} \text{ cm}^{-1} / \text{mol m}^{-2}$. The lower boundary of the n -th interval is $\nu_{n,1} = \nu_0 + \delta \nu_n$ with $\delta \nu_n$ to control the position of the weighting function over the altitude range of interest. The weighting functions obtained (Fig. 1) are close to those providing the best vertical resolution for nadir sounding.

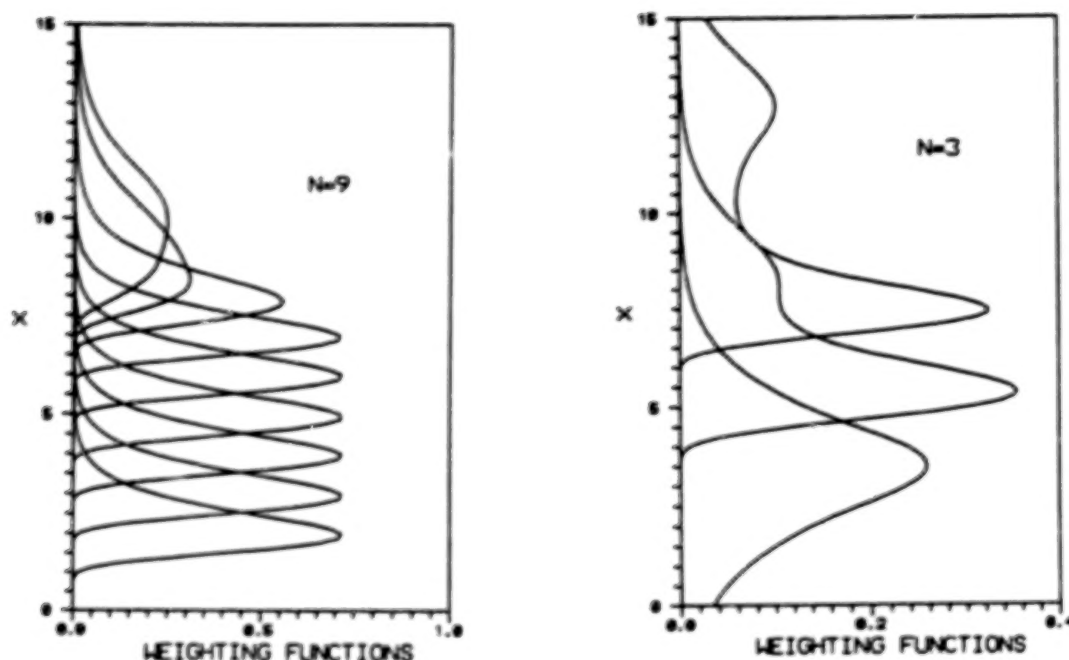


Figure 1. Two sets of weighting functions $\tilde{K}_n(x)$ obtained according to Way 1 ($N=9$) and Way 2 ($N=3$).

Way 2. The N intervals of the width $\Delta\nu=10\alpha_D$ are centred by the line center. The equidistant distribution of weighting functions is achieved varying s ($s \leq 10^{-23} \text{ cm}^{-1} / \text{mol m}^{-2}$). The relevant weighting functions are plotted in Fig. 1.

2.4 WAVE PARAMETERS

We focus on the case of a single wave defined as a temperature disturbance which, first, is correlated in vertical and, second, may be separated from the wave spectrum (as well as from relatively slow components of temperature variability and from noise) by band-pass filters without distortions. In this case, generalization for parallel retrieving several single waves is easy to make. Now $\Delta\tilde{T}(x, \tilde{t})$ (hereafter a wave-induced temperature fluctuation) may be written in the form

$$\Delta\tilde{T}(x, \tilde{t}) = X(\tilde{t})\tilde{\theta}(x). \quad (9)$$

Although variability of real Rossby waves is multiform, two extreme cases are only examined, allowing relatively easy mathematical treatment. The first case is that of the stationary wave, whereas the second one corresponds to a wave with frequent and occasional phase shift. In the latter case, a phase shift is assumed to take place between any two subsequent measurements. In spite of an observer does not detect the wave in this case, it is taken to estimate the maximum error in retrieving real waves.

In the frequent phase shift case, the wave amplitude is hard to be introduced. Therefore, the general principle to define $\tilde{\theta}(x)$ for both above mentioned cases is formulated considering the integral

$$\mathbf{w} = \int_0^{\infty} \tilde{\mathbf{W}}(x) \tilde{\theta}(x) dx, \quad (10)$$

where components of $\tilde{\mathbf{W}}$ are given by (4), and \mathbf{w} is prescribed to be a unit vector. Equation 10 does provide correct determination of $\tilde{\theta}(x)$ from $\Delta \tilde{\mathbf{T}}(x, \bar{i})$.

According to the classical theory, the amplitude the Lamb wave varies with height as

$$\tilde{\theta}(x) = \tilde{\theta}(0) \exp(\kappa x), \quad (11)$$

where $\kappa = (\gamma - 1)/\gamma$, and γ is the ratio of the specific heat of air at constant pressure to that at constant volume.

The mean profile $T_0(x)$ is derived from reference model CIRA 1972.

2.5 FORMULATION OF THE PROBLEM

Signal-to-noise ratio R is introduced as follows

$$R = \sqrt{\frac{E(\Delta \tilde{\mathbf{I}}, \Delta \tilde{\mathbf{I}})}{N}}, \quad (12)$$

where the components of $\Delta \tilde{\mathbf{I}}$ are given by (3) under condition of zero noise, E represents expected value operator, and $(\mathbf{a}_1, \mathbf{a}_2)$ defines scalar product for any given vectors \mathbf{a}_1 and \mathbf{a}_2 . As seen from (12), $R \sim 1$ is just the case when outgoing radiance disturbance, wave-induced and averaged over all the channels, is equal to noise radiance by the order of magnitude. When real measurements are dealt with, the time average should be, naturally, employed to find an estimate for R .

The problem is now formulated as follows. Sets of weighting functions $\tilde{\mathbf{K}}_n(x)$ and parameters R , L (number of measurements), and N are given. It is known a priori that wave amplitude departs from that given by (11). It needs to estimate the relative error in retrieving a wave for both cases described in Subsection 2e, - (1) frequent phase shift (FPS) and (2) stationary wave (SW).

3. METHOD TO PROCESS MEASUREMENTS AND RETRIEVE $X(\bar{i})$

3.1 EOF-ANALYSIS

Empirical orthogonal function (EOF) analysis is applied to extract the wave-induced component from satellite measurements of thermal outgoing radiation.

Making use of (9) and (10), we get

$$\Delta \tilde{\mathbf{I}}(l) = X(l) \mathbf{w} + \tilde{\mathbf{e}}(l), \quad (13)$$

where the components of $\Delta \tilde{\mathbf{I}}(l)$ correspond to a measurement performed at the l -th sampled time, whereas $\tilde{\mathbf{e}}(l)$ is the vector with components $\tilde{e}_n(l)$. Now we, first, determine the eigenvectors $\mathbf{e}(1), \dots, \mathbf{e}(N)$ of the covariance matrix

$$V = E(\Delta \tilde{I} \Delta \tilde{I}^T), \quad (14)$$

where the superscript T denotes transposition, and, second, label them so that the relevant eigennumbers $\lambda_1 \geq \dots \geq \lambda_N$ be in descending order. The vectors determined are EOFs for the measurements given by (13) and form a basis in the "measurement space" (Rodgers, 1976). According to the theory of EOF-analysis, the variance of X_k (a coefficient at $e(k)$ in expansion $\Delta \tilde{I}(1)$) is just λ_k (e.g. North et al., 1982). Furthermore, noise is uniformly distributed over coefficients at $e(k)$, whereas the wave-induced signal with variance $R^2 N$ accumulates in X_1 . In other words, retrieving X comes to the determination of X_1 .

3.2 FPS CASE

In this case, the matrix (14) is derived just from measurements. Inserting (13) into (14), we get

$$\lambda_1 = R^2 N + 1, \quad \lambda_2 = \dots = \lambda_N = 1, \quad (15)$$

$$e(1) = w. \quad (16)$$

The eigenvectors $e(2), \dots, e(N)$ form a degenerate multiplet. Using (15), we determine relative error of estimating X by X_1

$$\Delta_X = \frac{1}{R\sqrt{N}}. \quad (17)$$

In practice, to obtain the covariance matrix (14), time averaging is employed instead of applying expected value operator. Accordingly, sampling errors in estimating $e(1)$ take place. The relevant error covariance matrix, required to estimate accuracy in retrieving $\tilde{\theta}(x)$

$$S_e = \frac{R^2 N + 1}{R^4 N^2 L} (I_N - e(1)e^T(1)). \quad (18)$$

It should be pointed out that the determination of the true $e(1)$ (a vector relevant to the wave-induced signal) is unrealizable when sampling error of estimating λ_1 becomes comparable to $(\lambda_1 - \lambda_2)$. After North et al. (1982), a criterion for the correct selection of $e(1)$ is written in the form

$$R^2 N \gg \sqrt{\frac{2}{L}}. \quad (19)$$

3.3 SW CASE

The term "stationary wave" indicates here waves which, first, keep their amplitude and phase invariable through the record, and, second, have dimensionless period much less than L ,

$$\tilde{\omega}'L \gg 2\pi, \quad (20)$$

where

$$\tilde{\omega}' = \delta t(\omega - m\Omega) \quad (21)$$

is the Rossby wave dimensionless frequency observed from a satellite, Ω is the angular frequency of Earth's rotation, ω is the intrinsic frequency of a wave, m is its zonal number, and Ψ is the phase shift.

A priori information of time coherency of the wave favours to preliminary filtering of radiation measured in a channel to obtain the covariance matrix V with less errors than in the FPS case. Briefly, the preliminary filtering reduces error variance by factor $L/2$ (to the accuracy of the first-order terms on L^{-1}). As a result, the relative error of estimating X by X_1 , the error covariance matrix for the components of $e(1)$ and the criterion for the correct selection of $e(1)$ may be determined for the SW case from (17)-(19) through formal replacing R by $R\sqrt{L/2}$:

$$\Delta_X = \frac{1}{R\sqrt{N}} \sqrt{\frac{2}{L}}, \quad (22)$$

$$S_e = \frac{2R^2NL + 4}{R^4N^2L^3} (I_N - e(1)e^T(1)), \quad (23)$$

$$R^2N \gg \left(\sqrt{\frac{2}{L}}\right)^3. \quad (24)$$

4. METHOD TO RETRIEVE $\tilde{\theta}(x)$

Equation 11 for the ideal non-dissipating Lamb wave is derived for a isothermal motionless atmosphere, whereas the real atmosphere has more complex spatial temperature and wind distributions, and the wave is dissipating. As a result, the dependence of the wave amplitude on height for the real atmosphere is not that given by (11). However, observational evidences exist for a number of the gravest Rossby modes that functions like $\tilde{\theta}(x)$ are rather smooth and do not depart very much (at least over the altitude range of interest) from those given by (11) (Hirota and Hirooka, 1984; Hirooka and Hirota, 1985; Prata, 1989; Venne, 1989).

Hermite polynomials $H_k(x)$ are, probably, mostly suitable basis function set to parameterize $\tilde{\theta}(x)$, since they provide a convenient expansion just for the exponential profiles

$$\exp(\kappa x) = \exp(1/4) \sum_{k=0}^{\infty} \frac{H_k(\kappa x)}{k! 2^k}. \quad (25)$$

Let us consider the first-kind Fredholm integral equation

$$\hat{e}(1) = \int_0^{\infty} \tilde{W}(x) \tilde{\theta}(x) dx, \quad (26)$$

where $\tilde{\theta}(x)$ is an unknown function. The left part of (26) contains sampling errors as labelled by a cover over $e(1)$. Expanding $\tilde{\theta}(x)$,

$$\tilde{\theta}(x) = (q, H(\kappa x)), \quad (27)$$

where $H(\kappa x) = (H_0(\kappa x), \dots, H_{K-1}(\kappa x))$, $q = (q_0, \dots, q_{K-1})$, and inserting the expansion into the right part of (26), a linear system is obtained

$$Aq = \hat{e}(1). \quad (28)$$

The ij -th component of the matrix A is given by

$$A_{ij} = \int_0^\infty \tilde{W}_i(x) H_j(\kappa x) dx. \quad (29)$$

Here $i=1, \dots, N$; $j=0, \dots, K-1$, and K is the number of Hermite polynomials retained in (28).

The solutions for (28) are found in the form

$$\hat{q} = B\hat{e}, \quad (30)$$

$$B = S_q A^T (A S_q A^T + S_e)^{-1}, \quad (31)$$

where S_q is a diagonal matrix

$$(S_q)_{ii} = \frac{\exp(1/2)}{((i-1)!)^2 2^{2(i-1)}}. \quad (32)$$

The algorithm to retrieve $\tilde{\theta}(x)$ used below for numerical simulations is as follows. At the beginning, an approximation $e^{(0)}(1)$ is found from (11) which is just equal to w for the ideal Lamb wave. Then X_1 is computed to evaluate the value of R . After that, an approximation $S_e^{(0)}$ is determined from (18) (the FPS case) or (23) (the SW case), basing on $e^{(0)}(1)$ and R . Finally, $B^{(0)}$ is obtained, following (31) and (32), which is used to retrieve $\tilde{\theta}(x)$ from $\hat{e}(1)$.

Random $\Delta_R(x)$ and systematic $\Delta_D(x)$ relative errors in retrieving $\tilde{\theta}(x)$ are expressed by

$$\Delta_R(x) = \frac{\sqrt{(H(\kappa x), B S_e B^T H(\kappa x))}}{\tilde{\theta}(x)}, \quad (33)$$

$$\Delta_D(x) = \frac{(B e(1), H(\kappa x))}{\tilde{\theta}(x)} - 1. \quad (34)$$

Equations 33 and 34 include $e(1)$ and S_e found for $\tilde{\theta}(x)$ to be retrieved.

5. NUMERICAL SIMULATIONS

Numerical simulations are performed for the typical variation of the wave amplitude with height. That is believed to be like that for the ideal Lamb wave in the stratosphere but decreasing in the mesosphere (Prata, 1989; Rodgers and Prata, 1981). It is convenient to describe the amplitude for x less than some x_0 by the function

$$\tilde{\theta}(x) = \tilde{\theta}(0)(\exp(\kappa x) + \varphi(x)), \quad (35)$$

where $\varphi(x) < 0$ is close to zero for small x . When $x > x_0$ we put $\tilde{\theta}(x) = 0$. We take below $\varphi(x) = -0.00001x^6$, and $x_0 = 12$.

Two mostly interesting cases are concerned: that of approximate equality of the wave-induced signal and noise, $R=1$, and that of significant noise comparing to the signal, $R=0.1$. The value of L is prescribed to be enough large to satisfy, first, the conditions given by (19) or (24) and, second, (20) (for the SW case only). At the same time, one should not take L more than the dimensionless life time of a Rossby mode [this time is equivalent to approximately one month for the modes detected confidently in the stratosphere (Hirooka and Hirota, 1989)]. For the majority of the modes, wave period is no less than two days (e.g. Ahlquist, 1982). As the minimum zonal number $m=1$, the maximum period of the wave as observed from a satellite is about 2 days due to (21). Accordingly, $L=100$ is taken as corresponding to the record period of about 7 days for the typical value of $\delta t \approx 100$ min. The calculations for $R=0.1$ are made for the SW case only, since inequality (19) is broken at $L=100$ ($N \leq 9$ in our study) for the FPS case.

For the accepted values of R and L , both the sets of weighting functions, plotted in Fig. 1, the optimum value of K has been found to be 8.

Fig. 2 gives $\Delta_R(x)$ and $\Delta_D(x)$ found from (33) and (34) for $K=8$. Here the error covariance S_e is obtained either from (18) (the FPS case) or (23) (the SW case). As seen from Fig. 2a, the record period $L=100$ provides acceptable accuracy in retrieving vertical structure of the wave even for the FPS case. Fig. 2b evidences some chance to retrieve stationary wave under condition of significant noise ($R=0.1$). As expected, errors decrease with increasing N , but it is Δ_D that only depends on N strongly.

6. CONCLUSION

The goal of this paper was to present a method to retrieve the planetary-scale waves for the middle atmosphere from nadir measurements of thermal outgoing radiation. As the first step, the retrieving of the Lamb wave has been examined. The principal elements of the method proposed are (a) EOF-filtering to extract the wave-induced component just from measurements, (b) using Hermite polynomials expansions to describe the vertical structure of a wave and to find the solution of corresponding integral equation as a correction to that obtained for the ideal Lamb wave. The method allows retrieving the planetary-scale wave parameters under condition of significant noise.

The consideration has been presented for thermal outgoing radiation measurements performed at a fixed latitude. So, a priori information of space coherency of a wave in the meridional direction has been not utilized yet. Consequently, (1) the error estimations obtained may be overestimated and (2) further increasing in accuracy of the method is likely.

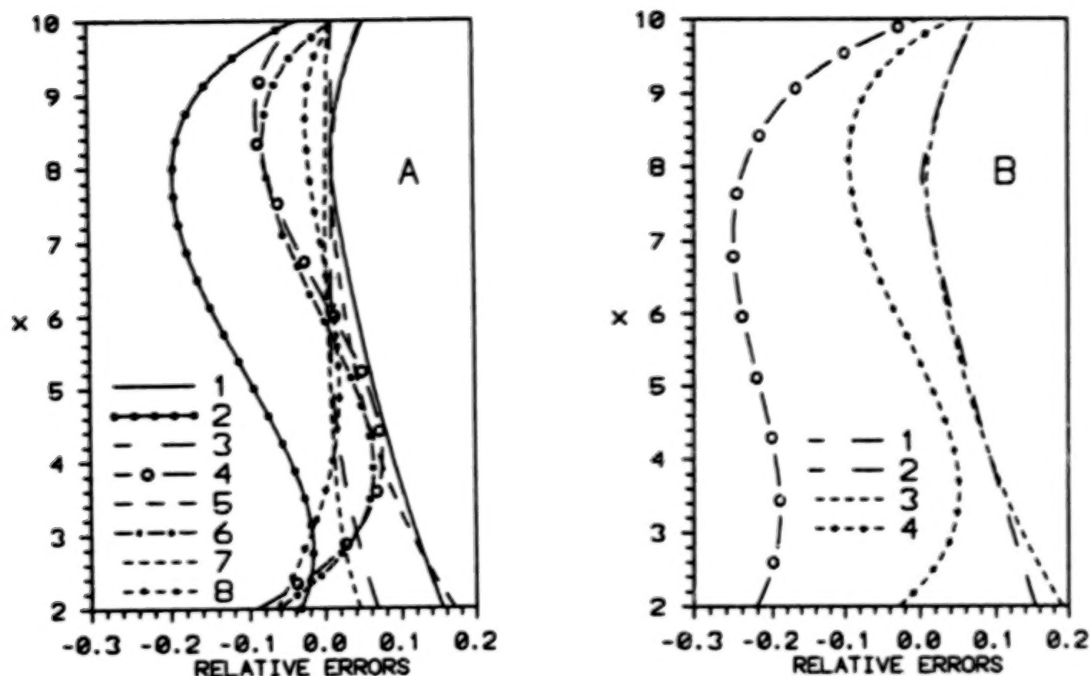


Figure 2A. Random $\Delta_R(x)$ (odd lines) and systematic $\Delta_D(x)$ (even lines) relative errors of retrieving vertical profile of Rossby normal modes of the Lamb wave type ($R=1$, $L=100$) for the cases of frequent phase shift [$N=3$ (lines 1 and 2) and $N=9$ (lines 5 and 6)] and stationary wave [$N=3$ (lines 3 and 4) and $N=9$ (lines 7 and 8)].

Figure 2B. As in Fig. 2A but only for the case of stationary wave and $R=0.1$. $N=3$ (lines 1 and 2), $N=9$ (lines 3 and 4).

ACKNOWLEDGEMENTS

The authors are grateful to Drs. V. Rozanov, G. Ryzhikov and Yu. Timofeev for many fruitful suggestions and discussions.

REFERENCES

- Ahlquist, J.E., 1982: Normal-mode global Rossby waves: Theory and observations, *J. Atmos. Sci.*, **39**, 193-202.
- Diky, L.A., 1969: *Theory of oscillations of Earth's atmosphere*, Gidrometeoizdat, Leningrad, 195 pp.
- Hirooka, T., and I. Hirota, 1985: Normal mode Rossby waves observed in the upper atmosphere. Part II: Second antisymmetric and symmetric modes of zonal wavenumber 1 and 2, *J. Atmos. Sci.*, **42**, 536-548.

- Hirooka, T., and I. Hirota, 1989: Further evidence of normal mode Rossby waves, *Pure Appl. Geophys.*, **130**, 277-289.
- Hirota, I., and T. Hirooka, 1984: Normal mode Rossby waves observed in the upper atmosphere. Part I: First symmetric modes of zonal wavenumber 1 and 2, *J. Atmos. Sci.*, **41**, 1253-1267.
- North, G.R., Bell, T.L., Cahalan, R.F., and F.J. Moeng, 1982: Sampling errors in the estimation of empirical orthogonal functions, *Mon. Wea. Rev.*, **110**, 699-706.
- Prata, A.J., 1984: The 4-day wave, *J. Atmos. Sci.*, **41**, 150-155.
- Prata, A.J. 1989: Observation of the 5-day wave in the stratosphere and mesosphere, *J. Atmos. Sci.*, **46**, 2473-2477.
- Rodgers, C.D., 1976: Retrieval of atmospheric temperature and composition from remote measurements of thermal radiation, *Rev. Geophys. Space Phys.*, **14**, 609-624.
- Rodgers, C.D., and A.J. Prata, 1981: Evidence for travelling two-day wave in the middle atmosphere, *J. Geophys. Res.*, **86**, 9661-9664.
- Venne, D.E., 1985: The horizontal structure of travelling planetary scale waves in the upper stratosphere, *J. Geophys. Res.*, **90**, 3869-3879.
- Venne, D.E., 1989: Normal-mode Rossby waves observed in the wavenumber 1-5 geopotential fields of the stratosphere and troposphere, *J. Atmos. Sci.*, **46**, 1042-1056.

BATHYMETRIC IMAGE MAPS OF COASTAL WATER AREAS

L. Estep¹, J. Lillycrop¹, R. Arnone², and L. Parson¹

¹ US Army Corps of Engineers
Waterways Experiment Station
Coastal Engineering Research Center
Vicksburg, MS. 39180

² Naval Research Laboratory
Code 7240
Stennis Space Center, MS. 39529

ABSTRACT

Bathymetric data represents valuable information to various US and International government agencies - for both national defence and internal domestic use. Furthermore, private businesses often require accurate water depth information for planning projects of various sorts. Examples of such businesses would include, but not be limited to, petroleum firms, shorefront planning and construction businesses, and dredging companies.

The US Army Corps of Engineers (USACE) has recently successfully field tested the Scanning Hydrographic Operational Airborne LIDAR Survey (SHOALS) system in Sarasota, FL. The SHOALS is a state of the art Airborne LIDAR Hydrographic (ALH) system to be used by the USACE (leasable to other US government agencies) for performing bathymetric surveying in support of maintaining the nations public waterways, flood control, and beach erosion and renourishment projects.

A funded exploratory spin-off project that merges the SHOALS system and an imaging spectrometer as a proposed permanent dual sensor system, provides, over a survey area, both SHOALS depth information and hyperspectral imagery of the survey area. This paper discusses the use of this dual sensor system in bathymetric charting of coastal water areas.

1. INTRODUCTION

The SHOALS uses a pulsed, 200 Hz, Nd:YAG laser, which provides two different transmitted wavelengths, to sense the air-sea interface and the sea bottom. The time difference between the reception of the surface and bottom signals, corrected for angle of entry, provides an estimate of the water depth. The SHOALS is presently flown on a NOAA Bell 212 helicopter and operates, nominally, at 200 m altitude and 25 m/sec velocity. The pulse pattern on the water surface results in a uniform sounding grid with about 5 m grid spacing. Table 1 provides other information concerning the SHOALS system. For more in depth information on the SHOALS system see Lillycrop and Banic (1992).

The SHOALS provides water depth information accurate to International Hydrographic Organization (IHO) standards. However, in the near future, the SHOALS will also be capable of providing an estimate of the rate at which a light field (at the LIDAR wavelength) will decay as it transits the water column. Such information is embedded in the fall-off of the backscattered LIDAR light seen at the SHOALS receiver. This water optical information, treated as environmental information, is as valuable as depth information. In fact, the computation of the depth in the post-processing of the SHOALS survey data, is enhanced if water optical information is available on a shot-to-shot basis. The water optical information provided by SHOALS is in the form of a system attenuation coefficient, or k_{sys} . This system attenuation coefficient can be related to the water optics of the coastal waters overflown (Gordon, 1982). In particular, k_{sys} approaches the absorption coefficient, a (Jerlov, 1976), of the water for a large receiver field of view. At the other extreme, for a very small receiver field of view, k_{sys} approaches the beam attenuation coefficient, c (Jerlov, 1976). Billard (1986) has shown how to use the results of Gordon (1982) to extract relevant water optical parameters. Using this water optical information together with the depth data, the effective optical depth of the water mass can be reckoned for each

781000

LIDAR pulse. Since little coastal water optical data is available, such information is valuable - especially on a seasonal basis.

SYSTEM PARAMETER	PARAMETER VALUES
Maximum Depth	kd > 3, day; kd > 4, night
Minimum Depth	1.0 m
Vertical Accuracy	+/- 0.3 m
Horizontal Accuracy	+/- 6 m
Sounding Density	3 to 15 m
Nominal Altitude	200 m
Nominal Platform Speed	50 m/sec
Operating Temperature Range	5 to 40 degrees Celsius
Data Processing Ratio	1:5
Platform	Bell 212
System Mod/DeMob Time	8 hrs/6 hrs

Table 1. SHOALS system parameters values summary

CASI SYSTEM PARAMETER	PARAMETER VALUE
Operational Modes	Spectral/Spatial
Spectral Coverage	420 - 900 nm
Spectral Resolution	1.8 nm spectral/3 nm spatial
Number of pixels	288 spectral/578 spatial
RFOV	35.5 degrees
Pixel Spatial Resolution	0.12% of altitude or about 1.2 mrad
Number of look angles in spectral mode	39
Integration Times	Typically 50 msec(spatial), 100 msec spectral
Digitization	12 bits on chip
Detector Type	CCD Array
Optics	Reflective diffraction grating with f2 lenses
Data Recording	Exabyte™, 8mm video cassettes
Data Recording Rate	280 Kbits/sec
Weight/Power	655 kg/20VDC 20A

Table2. CASI system parameter summary

An imaging spectrometer can be defined as providing access to several tens of spectral channels (not necessarily simultaneously) with very narrow spectral channel widths - emulating laboratory spectrometers. A relatively inexpensive and readily available version of an imaging spectrometer is the Compact Airborne Spectrographic Imager (CASI). The CASI is rentable from several groups, both commercial and academic, and has provided researchers with reliable datasets which have been published in the remote sensing literature.

The CASI is a line scanner that uses a diffraction grating to produce 288 spectral channels. The CASI can be operated in either a spectrometer mode or a spatial mode. The spectrometer mode provides for 39 'look' angles over a scene with high resolution spectral information at 1.8 nm width. The 39 spectral look angles are overlaid on a reference image collected in a single band. The spatial mode provides for scene imagery in up to 15 channels - however the channels accessible by the CASI run from 420 nm to 900 nm at 3 nm spectral resolution. The channel selection is set in hardware and is quickly and easily changeable at the computer console. Recently, an updated version has become available that provides increased signal to noise in the blue by 2:1. This is due to a new coating that has been placed on the grating. This means that spectral resolution attainable in the blue will be enhanced. Table 2 provides more information on the CASI scanner. For more in-depth information on the CASI sensor see Borstad (1989).

2. RELATED EARLIER WORK

Lyzena (1985) using the M8 active/passive scanner at two sites in the Bahama Islands, showed the feasibility of combining LIDAR depths with image data. The LIDAR data had to be manually interpreted for each used point. The LIDAR depths were then used to calibrate the passive image data. Then, using a band ratio technique, each band ratio was plotted against the lidar depths to see which ratio correlated best. This formed the basis of a regression derivation between the selected band ratio and depth. This regression relation was then applied to the entire image to extract depth from the information represented by the image.

The Airborne Bathymetric Survey (ABS) of the US Navy endeavored to use the Hydrographic Airborne LASER Sounder (HALS) together with the NORDA scanner (which, in effect, emulated a TM bandset) to provide depth and image data fusion (Haimbach et al., 1988). However, continual problems with the HALS and scanner caused the project to produce little useable data.

Borstad and Vosburg (1993) used LIDAR data from the Larsen 500 - an operational ALH system since the mid-1980's - and CASI imagery to produce a fusion of imagery with a Digital Depth Model (DDM) based on Larsen bathymetric data near the Bruce Peninsula in Lake Huron. Although several lines of overlapping Larsen and CASI data were taken, only a relatively small subset of the data was ever processed. However, the results of this work were readily recognized by the authors as a potentially valuable environmental product.

3. BACKGROUND: SHOALS + CASI SARASOTA OVERFLIGHT

During the SHOALS field trials the CASI was flown over the SHOALS test flightlines. The imagery was recorded in a bandset which had 12 different wavelengths. These are provided in Table 3.

This bandset emulated (with considerations for water vapor and oxygen atmospheric absorption lines and CASI SNR constraints in the blue region) NASA's proposed SeaWiFS ocean color sensor bandset. The CASI data was radiometrically corrected, roll and pitch corrected, and georeferenced using a GPS system. Thus, each pixel of a CASI image could be referenced to a particular latitude and longitude. Data were acquired at three different altitudes so that an atmospheric correction could be computed. Also, 'deep' water scenes were imaged for potential subtraction from shallow water imagery (Philpot, 1989).

The SHOALS datasets over the flightlines and benchmark areas were provided in X,Y,Z format with the X and Y representing latitude and longitude and Z as depth. The depth and position data were read onto a PC harddisk along with the CASI imagery in preparation for deriving the bathymetric image maps.

4. FUSING THE CASI AND SHOALS DATA

Figure 1 shows a schema that outlines the steps taken to produce bathymetric image maps.

BANDSET (nm)
426-470
473-501
504-527
540-569
598-621
625-656
656-667
671-684
686-690
701-714
744-760
839-869

Table3. CASI bandset used in Sarasota

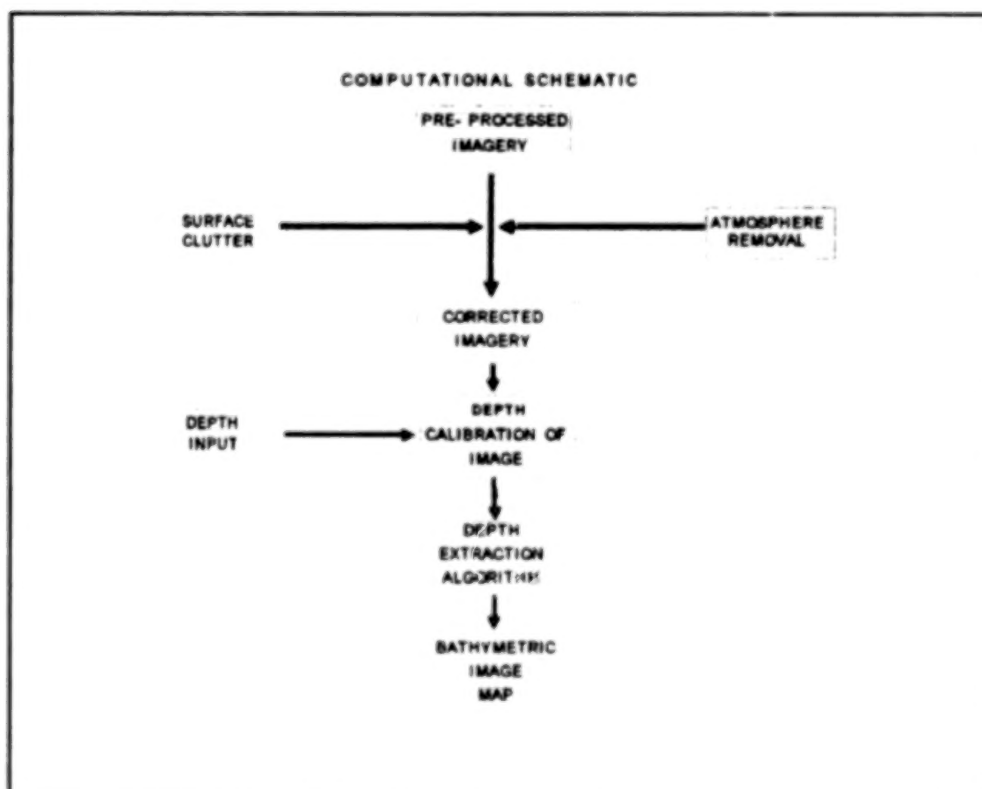


Figure 1. Computational schema for the derivation of the bathymetric image maps shown

The preprocessed data block shown in Figure 1 indicates CASI image data that has already been roll, pitch, and radiometrically corrected as well as georeferenced. The atmosphere correction uses the three altitudes at which data was collected to compute an atmospheric correction for each band under consideration. The atmospheric correction also takes into account the fact that towards the edges of the swath seen by the CASI the atmospheric slant range increases. This increase is corrected for in the atmospheric correction process and results in a 'flattened', atmospherically corrected image. The surface clutter removal uses the standard approach of weighting a band in the red and subtracting it from the water penetrating bands in the blue-green region. Since light of different colors penetrate to different depths, with blue penetrating more and red much less, the red band sees only the topmost portion of the water column. The red band, when weighted appropriately, removes the surface (clutter) which is the layer of water it sees.

The merging of the depth data with the CASI imagery involves searching the SHOALS database for LIDAR shots that are within the boundaries of a CASI image pixel. That is, a routine queries the SHOALS database for depths within a CASI image on a pixel-by-pixel basis to determine whether the bounds represented by the coordinates of the bounds of a pixel area has matching depths in the database.

There are several depth extraction techniques that are readily available. We will discuss four generic approaches: 1) gridding the depth database, 2) correlation of spectral data to depth, 3) adaptive filter (moving window) approach, and 4) using water optical information to obtain depth from the spectral data.

Technique 1 does not use image spectral intensity information at all. That is, in the stead of the imagery helping to 'grid' the LIDAR calibration depth data through relative intensity values, a computer routine simply grids up the LIDAR depth data so that the image array and depth array are the same size. In this case, the image serves to 'present' or 'integrate' the depth data for the user of the coastal water image map. Of course, observable bottom information and other scene information is embedded in the image presentation.

Technique 2 (Borstad and Vosburg, 1993) uses single spectral bands to correlate against depth data to see which band correlates best. One would use the band with the best correlation to derive an intensity to depth regression relation. The regression relation would then be used to compute depth over the entire image. A variant of this technique was used by Lyzenga (1985) which uses ratios of bands for the correlation computation and subsequent regression derivation. The use of ratios, it is felt, helps to offset some of the atmospheric and surface noise effects.

Technique 3 uses an adaptive filter, or 'moving window', approach. The need for the moving window is to take into account changing water optics and bottom reflectances over a scene. Pixel intensity values are a function not only of water depth but of light attenuation and bottom reflectance (assuming atmosphere and surface effects have been dealt with). With calibration depth data available, then shifting water optics and bottom reflectance can be effectively managed by moving sequentially through the image while tying a calibrated depth to small subsetting regions. Using this kind of moving window within the image tends to minimize the non-signal (non-signal = changing bottom reflectance, changing water optics; signal = changing depth) sources of variation in light field intensity.

Technique 4 uses the fact that the light reaching the sensor is composed of light due to water column reflectance and bottom reflectance (assuming atmosphere and surface light are removed). At this point, two different approaches can be followed: 1) compute depth based on changes in water column light (assuming the benthic interface still influences the upwelling light stream) neglecting any bottom contribution to the upwelling light stream, and 2) compute depth by modeling out the influence of the water column leaving only the bottom reflectance contribution to the upwelling light stream.

Ji et al. (1992) suggests that when the bottom reflected signal is relatively small, one ought to use water reflectance rather than bottom reflectance to estimate water depth. Use is made of a simple radiative transfer model (Philpot, 1987) to compute the water reflectance values when the presence of a bottom, at z , is felt in the upwelling light stream. The expression used (Ji et al., 1993) is

$$R(0-) = R_{\infty} [1 - \exp(-kz)] \quad (1)$$

where k is the irradiance attenuation coefficient of the water mass, $R(0-)$ is the reflectance of the water mass just below the air-sea interface at the coastal water site of interest, and R_{∞} is the water reflectance for a nearby deep water site. Notice that $R(0-)$ and R_{∞} are obtainable from the scanner information. However, k must be

provided to enable the water depth computation.

Estep (1993) used the converse approach. The water reflectance is modeled and subtracted from the atmospherically and surface corrected signal seen at the sensor to leave only the signal due to the bottom light field. The water optical models were based upon Case 1 and near Case 1 waters. The water reflectance just under the surface was computed using the Morel and Prieur (1977) formula

$$R(\lambda, 0-) = \frac{1}{3} \frac{b_b(\lambda)}{a(\lambda)} \quad (2)$$

where spectral a is the absorption coefficient and spectral b_b is the backscattering coefficient of the water. This form is for infinitely deep water masses and must be corrected for waters of finite depth (Estep, 1994). The absorption and backscattering values must be determined to compute the water reflectance. Once computed and subtracted from the sensor signal, the bottom component remains. This can be modeled as (Philpot, 1987)

$$R(\lambda, z) = R_b(\lambda) \exp(-2 k_e z) \quad (3)$$

where k_e is an effective attenuation coefficient, and spectral R_b is the reflectance of the bottom sediment facies. In this approach, then, as in the approach of Ji et al. (1992), we still need concomitant, measured water optical parameters to compute the water depth.

5. RESULTS AND DISCUSSION

Figure 1 shows a stacked image of a section of Sarasota Bay, Florida. The image provides information on how the bottom type varies across the scene while the top layer of the figure shows a contour plot of depth to the nearest foot. To read the stacked plots, first locate the point of interest on the image and, then, look at the contour overlay to read the associated depth contour. The coordinate values shown are in array pixel coordinates. However, these are relatable to geographic coordinates. The depths for the contouring were computed using Technique 3 - obviating the need for water optical data while allowing for a varying bottom reflectance. The calibrated depths used with the imagery were from SHOALS depth data as well as from depth data provided locally.

Once water optical information becomes available from the SHOALS data stream, Technique 4 approaches will become feasible. At that time, a combined approach of the Ji et al. (1992) and Estep (1993) methods could be used in depth calculations. That is, when a clearly evident bottom is shown in the imagery, the Estep (1993) approach could be used. However, when the bottom is dark or not plainly visible, the Ji et al. (1992) approach would be selected.

An interesting variant of this technique would be to use the water optical information and depth information from the SHOALS to compute the diffuse optical depth at each calibrated point in the image. This would allow, upon the modeling of the water reflectance, a direct computation of the in situ spectral bottom reflectance values using Equation (3).

Figure 2 shows the same bottom area draped over a Digital Depth Model (DDM) of the sea bottom. This image display format is effective for giving an observer a feeling for the relative 'lay of the land', the bottom types present, and how they vary across the scene.

6. SUMMARY AND CONCLUSIONS

Steps for the preliminary production of bathymetric image maps using combined SHOALS LIDAR depth data and CASI hyperspectral imagery has been discussed. A listing of possible applicable algorithmic approaches for calculation of the water depth is outlined. Actual bathymetric image map information in two different image formats is provided.

The combined sensor system is seen to provide crucial information in the form of environmental spectral information, greater depth resolution, and water optics. It is this set of information which is necessary to begin to produce reliable remotely sensed bathymetric data. Moreover, as suggested above, such a data

set allows for the unraveling of other environmental information such as bottom reflectance values - which leads to bottom type classification image maps.

ACKNOWLEDGMENTS

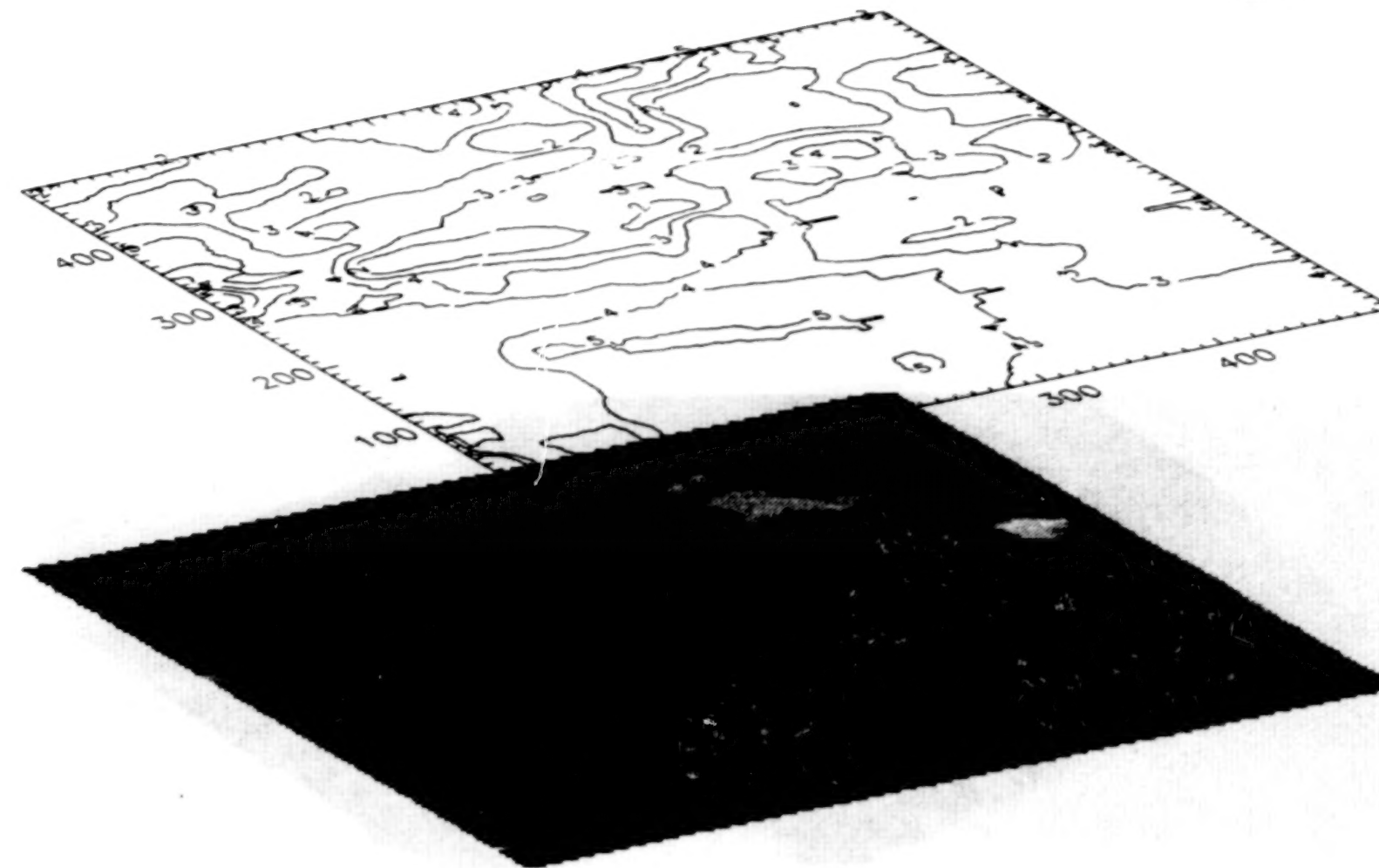
Results and information presented, unless otherwise noted, are based on the work funded by Headquarters, U.S. Army Corps of Engineers, Operations, Construction, and Readiness Division and the Department of Industry, Science, and Technology, Canada. Permission to publish this paper was granted by the Chief of Engineers.

REFERENCES

- Billard, B. 1986. Remote sensing of the scattering coefficient for airborne laser hydrography. *App. Opt.*, **25**, July.
- Borstad, G. and D. Hill. 1989. Using visible range imaging spectrometers to map ocean phenomena. *Proceedings of the Conference on Advanced Optical Instrumentation for Remote Sensing of the Earth's surface from Space, International Congress on Optical Science and Engineering, Paris, France, April 24-29, 1989.*
- Borstad, G. and J. Vosburg. 1993. Combined active and passive optical bathymetric mapping: using the Larsen LIDAR and the CASI imaging spectrometer. *Proceedings of the Canadian Symposium on Remote Sensing May 1993.*
- Estep, L. 1993. A suggested approach to the passive optical bathymetry problem by a component analysis of the upwelling remote sensing signal. *The Hydrographic Journal*, No. 69, July 1993.
- Estep, L. 1994. Bottom influence on the estimation of chlorophyll concentration in water from remotely sensed data. *Int. J. Rem. Sens.*, **15**, March.
- Haimbach, S., H. Mesick, J. Byrnes, and D. Hickman. 1988. Optical Bathymetry for the US Navy. *Proceedings of SPIE Ocean Optics IX, Orlando, FL, April 1988.*
- Gordon, H. 1982. Interpretation of airborne oceanic lidar: effects of multiple scattering. *App. Opt.*, **21**, 16.
- Jerlov, N. 1976. *Marine Optics*, Elsevier, Amsterdam.
- Ji, W., D. Chiriac, and W. Kennard. 1992. Satellite Remote Bathymetry: A New Mechanism for Modeling. *PE&RS*, 58.
- Lillicrop, J. and J. Banic. 1992. Advancements in the US Army Corps of Engineers Hydrographic Survey Capabilities: The SHOALS System. *Marine Geodesy*, 15.
- Lyzenga, D. 1985. Shallow-water bathymetry using combined lidar and passive multispectral scanner data. *Int. Journ. Rem. Sens.*, 6.
- Philpot, W. 1987. Radiative Transfer in Stratified Waters: A Single-Scattering Approximation for Irradiance. *App. Opt.*, 26.
- Philpot, W. 1989. Bathymetric Image Mapping with Passive Multispectral Imagery. *App. Opt.* 28.

BLANK PAGE

000180

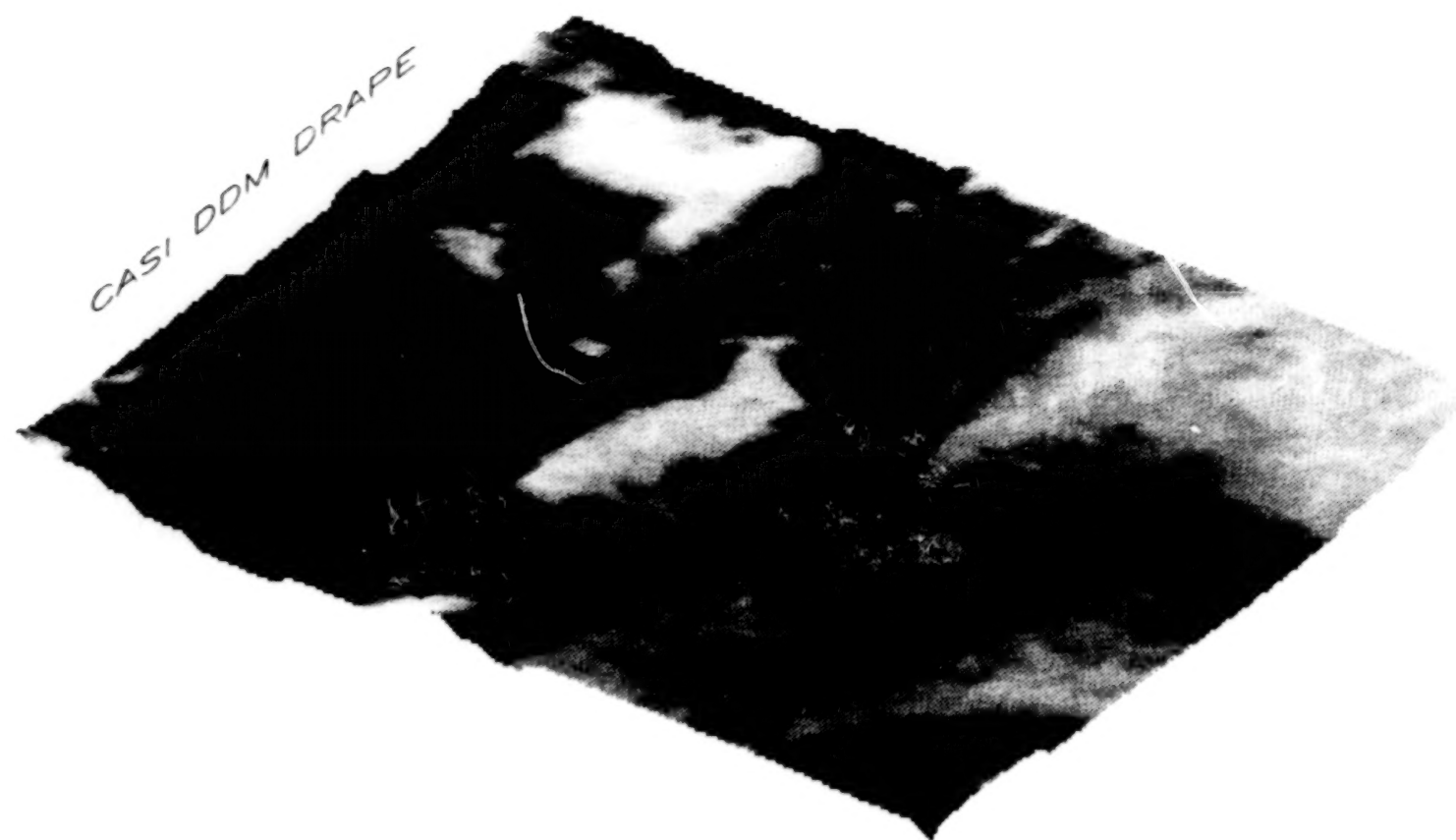


A-77

Figure 1.

000495

000482



A-78

Figure 2.

000496

BLANK PAGE

**Optimization of Water Quality Monitoring in Izmit Bay Using
Landsat Spectral Radiance Differentials and SPOT Imageries**

Hikmet Kurar and Krishnaier Natarajan
Space Technologies Department, Marmara Research Center
Turkish Council of Scientific and Industrial Research,
P.K. 21, 41470, Gebze-Kocaeli, Turkey.

Ph.: (90) 262 6412300 Ext.: 3307 FAX: (90) 262-619412309
e-mail: "nat@trmbeam.net"

ABSTRACT

This paper describes the first results of monitoring water quality parameters, especially, total suspended sediments (TSS) in Izmit Bay using Landsat and SPOT spectral radiance differentials. The Landsat MSS spectral bands 1 to 4 and all SPOT bands have been used and the digital data compared with the sea truth. It is observed that there is good correspondence between the Landsat digital values especially, for bands 3 and 4 and sea-truth data. The SPOT bands 2 and 3 data exhibit good correspondence amongst themselves; nevertheless, they do not portray the TSS information as accurately as the Landsat spectral bands.

1. INTRODUCTION

During the past decade, Marmara Research Center (MRC) has been actively involved in the estimation of pollutional loads of domestic and industrial wastewaters and surface runoff waters in the drainage area of the Bay. Recent oceanographic studies conducted at MRC within the framework of NATO-TU Waters Project during 1984-88 show that the Bay has a strong permanent salinity and temperature stratification during certain months. The MRC has also used Landsat digital data for mapping suspended sediments (SS) in the Bay. The Landsat radiance values of TSS for different bands are compared with the ground truth data. It is shown that such spectral data can be effectively used to quantify water quality parameters in the Bay, which is subject to environmental degradation. The object of this study is to investigate the appropriate combination of Landsat spectrum from the point of view of optimum investigation of sea pollution in the Izmit Bay. Spot spectral data are also used for a comparative study.

* Presented at the "International Symposium on Spectral Sensing Research, '94" (ISSSR '94), at San Diego, California, during July 10-15, 1994.

Satellite remote sensing provides an alternative means for obtaining relatively low-cost, simultaneous information on surface water conditions from the Bay. *In situ* measurements of water quality characteristics tend to be limited, especially in the temporal and spatial domains, because of the costs associated with data collection and laboratory analyses. Natarajan and Kurar (1994a) have given a detailed analysis of various water quality parameters in the Ömerli Lake using Landsat spectral data. Kurar and Natarajan (1994a) have studied the SS using Landsat spectral data. Natarajan and Kurar (1994b) have also examined the SS, dissolved oxygen and turbidity in the Golden Horn using Landsat MSS and TM bands. Further, for the Izmit Bay, Natarajan and Kurar (1994c) have studied the water quality parameters using Landsat as well as SPOT spectral data. This paper presents initial results of TSS analysis of the Izmit Bay using Landsat MSS and SPOT bands.

2. STUDY AREA

Figure 1 shows the study area. The Izmit Bay is an offshoot of Marmara Sea and is situated in the north-western part of Turkey. It stretches approximately 49 km long and 2-10 km wide and has an area of 310 km², mean depth of 20 m and 180 m in the inner and outer parts of the Bay respectively. This is one of the most polluted areas of this region. The Bay consists of three parts which are connected to each other with narrow openings. The eastern portion is about 15 km long and approximately 35 km deep. The middle section extends up to 20 km. The bottom topography of this part shows considerable variation from the north to south. It is also connected to the outer section by a narrow opening called "Dil Burnu", which is 3 km wide and 40-50 m deep. The northern part of the Bay is approximately 60 m deep. It joins to the southern portion by a sharp topographical slope. The southern section is about 180 m deep. The

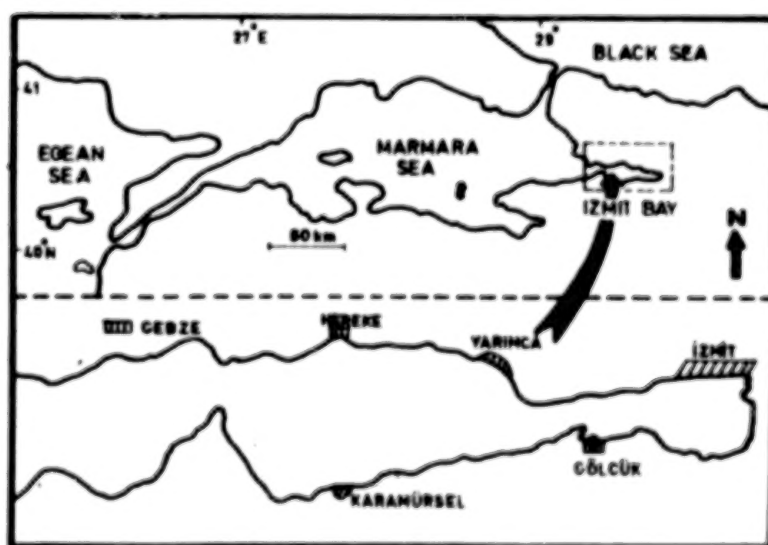


Figure 1. Study area.

outer Bay is connected to the open sea. It shows oceanographic characteristics of the eastern Marmara Sea. Around this Bay, several big cities and industrial towns such as Istanbul, Kocaeli, Gebze, Gölcük etc. constantly discharge domestic wastes and industrial effluents from pulp, paper chemical and petrochemical industries into the Bay. The highest density of population in this region of Turkey, coupled with large-scale industrial activities, put considerable pressure on this Bay.

3. RESEARCH METHODOLOGY

The research methodology for SS evaluation consists of:

- * Acquisition of water quality samples using Landsat MSS and SPOT imageries.
- * Extraction of digital numbers from the relevant spectral bands.
- * Examination of color-coded images, each depicting the generic water quality distribution for different spectral bands.
- * Comparison of the digital values of TSS as obtained from Landsat and SPOT spectral data with the extrapolated ground truth values.

Image analysis has been performed using the I²S image processing system on Sun Sparc II workstation. The image processing techniques such as image enhancement, and scaling have been used. This paper has compared the extrapolated ground truth values of TSS at different locations of the Bay with the pixel values obtained from Landsat imageries for the year 1984. The SPOT imageries for the year 1990 have also been compared.

Landsat MSS bands 1, 2, 3, and 4 are used for spectral investigation of TSS. The water quality data have been taken from TÜBİTAK Technical Report (DEE, 1992). These have formed the basis for the ground truth data based on linear extrapolation. The actual ground truth data at different sample sites are being collected and compiled, and further research is in progress. The study is limited by the lack of availability of a large number of ground truth data across wide-spread locations of the Bay at different times in the past. The spectral bands used are shown in Table 1. (Here, b.w. = width of the wavelength channel; c.w. = center of wavelength channel; nm = nanometer).

TABLE 1. DETAILS OF LANDSAT MSS SPECTRUM USED FOR THE STUDY

MSS Band no.	Band region	Band range (μm)	b.w. (nm)	c.w. (nm)
MSS 1	green	0.50-0.60	100	550
MSS 2	red	0.60-0.70	100	650
MSS 3	near-infrared	0.70-0.80	100	750
MSS 4	near-infrared	0.80-1.10	300	950

4. RESULTS AND DISCUSSIONS

The Landsat MSS spectral data for bands 1 through 4 have been collected for the year 1984 in different stations in all the four directions of the Izmit Bay. The raw as well as scaled data have been obtained for different stations in order to improve precision of investigation. In actual computation however, the scaled data have been used. The locations of the stations have been chosen to represent fairly uniform spatial distribution. Tables 2 to 5 show the Landsat MSS spectral data (raw/scaled) for different spectral bands in East, West, North and South directions of the Izmit Bay, respectively. Table 6 shows the ground truth data for the Izmit Bay.

TABLE 2. LANDSAT MSS SPECTRAL DATA (RAW/SCALED): IZMIT BAY EAST

BAND NO.	1	2	3	4	5	6	7	8	9	10
1.	32/ 221	24/ 165	21/ 145	20/ 138	20/ 138	20/ 138	21/ 145	25/ 172	21/ 145	26/ 179
2.	33/ 227	19/ 131	16/ 110	16/ 110	15/ 103	15/ 103	15/ 103	24/ 165	16/ 110	28/ 193
3.	18/ 74	11/ 46	10/ 42	8/ 33	9/ 37	8/ 33	9/ 37	13/ 54	13/ 54	19/ 79
4.	7/ 39	6/ 34	4/ 22	4/ 22	4/ 22	4/ 22	5/ 28	5/ 28	9/ 50	8/ 45

TABLE 3. LANDSAT MSS SPECTRAL DATA (RAW/SCALED): IZMIT BAY WEST

BAND NO.	1	2	3	4	5	6
1.	21/ 117	23/ 128	21/ 117	19/ 106	19/ 106	20/ 111
2.	14/ 58	15/ 62	14/ 58	13/ 54	13/ 54	13/ 54
3.	8/ 55	9/ 62	8/ 55	7/ 48	6/ 41	8/ 55
4.	3/ 21	3/ 21	4/ 28	3/ 21	3/ 21	4/ 28

**TABLE 4. LANDSAT MSS SPECTRAL DATA (RAW/SCALED):
IZMIT BAY NORTH**

BAND NO.	1	2	3	4	5	6	7	8	9	10	11	12	13	14	15	16	17	18
1.	23/ 159	22/ 152	21/ 145	20/ 138	21/ 145	20/ 138	20/ 138	20/ 138	21/ 145	21/ 145	23/ 159	22/ 152	22/ 152	21/ 145	22/ 152	23/ 159	21/ 145	20/ 138
2.	19/ 106	18/ 100	17/ 95	15/ 83	14/ 78	15/ 83	15/ 83	14/ 78	16/ 89	17/ 95	20/ 111	18/ 100	16/ 89	17/ 95	17/ 95	16/ 89	15/ 83	14/ 78
3.	10/ 42	10/ 42	10/ 42	8/ 33	10/ 42	9/ 37	8/ 33	8/ 33	10/ 42	11/ 46	10/ 42	12/ 50	10/ 42	10/ 42	12/ 50	9/ 37	8/ 33	8/ 33
4.	6/ 34	5/ 28	4/ 22	4/ 22	4/ 22	5/ 28	4/ 22	4/ 22	3/ 17	5/ 28	7/ 39	6/ 34	4/ 22	6/ 34	7/ 39	7/ 39	3/ 17	4/ 22

**TABLE 5. LANDSAT MSS SPECTRAL DATA (RAW/SCALED):
IZMIT BAY SOUTH**

BAND NO.	1	2	3	4	5	6	7	8	9	10	11
1.	20/ 138	19/ 131	19/ 131	17/ 117	17/ 117	18/ 124	18/ 124	18/ 124	20/ 138	19/ 131	18/ 124
2.	14/ 78	15/ 83	13/ 72	13/ 72	13/ 72	13/ 72	13/ 72	13/ 72	13/ 72	11/ 61	12/ 67
3.	9/ 37	8/ 33	7/ 29	8/ 33	7/ 29	6/ 25	6/ 25	6/ 75	6/ 25	5/ 21	5/ 21
4.	4/ 22	6/ 34	4/ 22	4/ 22	3/ 17	4/ 22	3/ 17	4/ 22	4/ 22	3/ 17	4/ 22

TABLE 6. TSS GROUND TRUTH DATA IN THE IZMIT BAY: ESTIMATED TSS LOADS OF DOMESTIC AND INDUSTRIAL WASTEWATERS (IN TONS/DAY)
(SOURCE: DEE, 1992)

Source of sediments	Eastern Bay	Northern Bay	Southern Bay	Total sediments
Industrial	5.6	70	1.26	76.86
Domestic	2.1	36	9.2	47.3
Runoff	43.6	42	85.9	171.5
TOTAL	51.3	148	96.36	295.7

Figure 2 shows the Landsat MSS data for different locations of the Bay along with the estimated TSS loads in different directions of the Bay. It can be seen that all the bands viz. 1, 2, 3 and 4 show almost identical trends along different locations of the Bay. Amongst these, the Bands 1 and 2 show mutually compatible trends, as also the bands 3 and 4. When compared with the ground truth data, the bands 3 and 4 show reasonably good correspondence.

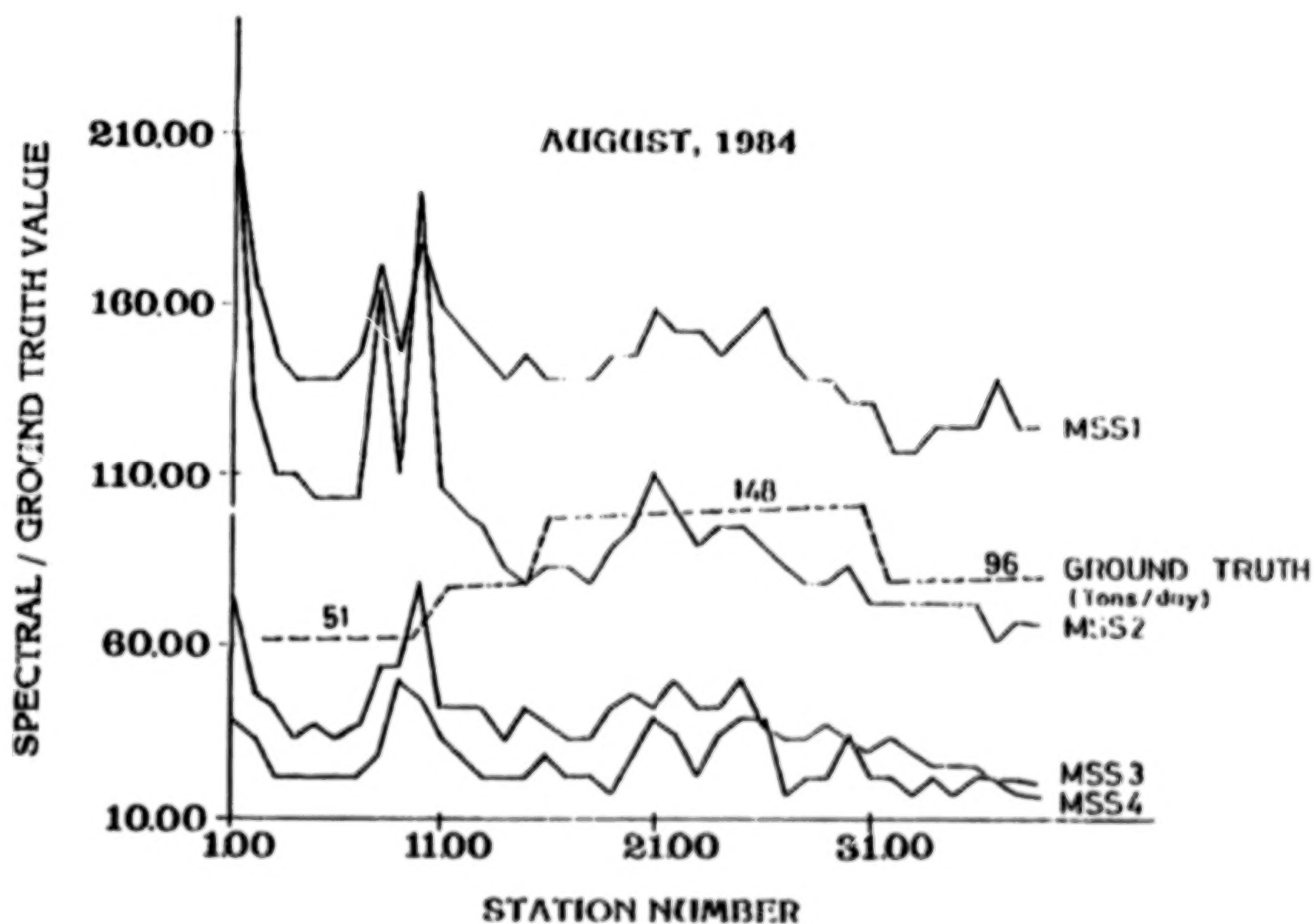


Figure 2. Landsat TSS data for MSS bands 1-4 along with estimated ground truth.

However, it can be seen that in the Eastern Bay, there are striking TSS variations at different locations, which are not evident in the ground truth. This is because, the TSS estimates in different directions were made based on the samples obtained in selected places. This is obviously misleading considering the fact that the pollutional loads at different locations can vary drastically depending on the number and nature of industries around a given station. For instance, the TSS pollutional load of pulp and paper mill can be as high as 42.1 ton/day, while that of textile mill can be as low as 0.19 ton/day (Table 7). Along the entire coast of the Izmit Bay, there are several factories manufacturing products such as food, textile, leather, pulp & paper, chemicals, refineries, cement, glass, ceramics, metal finishing, machine tools etc. These factories release pollutional loads of varying quantities at different sites. In such a scenario, ground truth measurements taken at a given site will not be truly representative of the actual value applicable to a vast area. Clearly, considerable work needs to be done to facilitate more reliable evaluation of TSS.

TABLE 7. ESTIMATED TSS LOADS OF INDUSTRIAL WASTEWATERS IN IZMIT BAY (TONS/DAY)
(SOURCE: DEE, 1992)

Type of Industry	TSS
Food	1.4
Textile	0.19
Leather	0.23
Pulp and paper	42.4
Chemicals	10.9
Refineries	1.1
Cement, glass and ceramics	18.8
Metal finishing and machinery	1.2
TOTAL	76.9

The SPOT pixel values as obtained for 1990 for the same stations along the Izmit Bay have also been plotted (Fig. 3). It is seen that the bands 2 and 3 are in overall agreement along different locations of the Bay, while the Band 1 shows considerable variation. The SPOT bands however, do not follow the ground truth values to a reasonable degree of confidence.

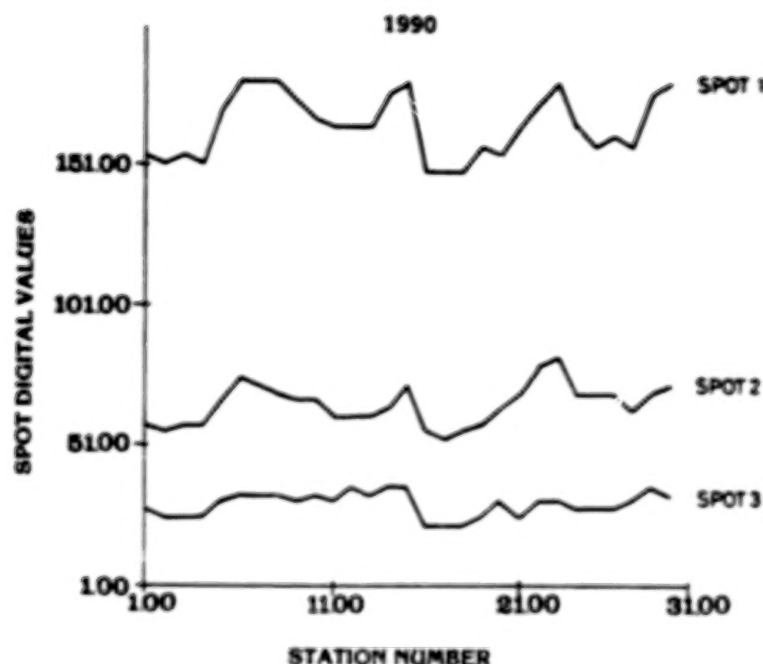


Figure 3. SPOT pixel values for different stations of Izmit Bay

5. SCOPE FOR FURTHER RESEARCH

The spectral data need to be properly correlated with the ground truth values, and the results will be reported separately. To facilitate this, radiance values may have to be used, rather than the pixel values. Reddy (1993) has given an account of investigating SS in Krishna Bay estuary of India, for which he resorted to radiance values, using the equation given by Robinove (1982). Previous research has also demonstrated that exoatmospheric reflectance, calculated by correcting the satellite data for differences in sensor characteristics and sun elevation angle, can provide better explanation of the SS concentration; i.e., higher coefficients of determination when compared with either radiance or raw digital numbers. Thus, in principle, Landsat data transformed to exoatmospheric reflectance should preferably be used in the analysis of this study. Simple linear regression techniques can be used to analyze the relationship between the water quality parameters and exoatmospheric reflectance, as suggested in previous studies, for instance, by Lyon *et al.* (1988); Ritchie *et al.* (1987); and Shih and Gervin (1980). In addition, simple linear regression has to be performed following a natural logarithmic transform of both variables. Finally, an optimized curve-fitting technique (DeCoursey and Snyder, 1969) based on the use of an exponential relationship between water quality parameters and exoatmospheric reflectance will be relevant. Theoretical considerations involving Beer's law should also be used in accordance with the procedures explained in detail by Harrington, Jr. *et al.* (1992). Here,

the accent is on atmospheric path radiance attributable to Rayleigh and Mie scattering with the reflectance from clear water, considering the atmospheric path reflectance and saturation reflectance values. Though the present investigation has considered only the digital values as obtained from different Landsat spectral data, further research is in progress at Marmara Research Center on the above lines considering the exoatmospheric reflectance and radiance values as well. The study itself needs to be updated based on more extensive and reliable ground truth data.

6. LIMITATIONS OF THE STUDY

(A). A proper evaluation of water quality parameters requires reliable ground truth data. Systematic records of water quality in the temporal and spatial domains are not available in this regard, imposing serious constraints on water quality research. However, some are indeed available in isolated cases, and one has no option but to use these limited data, and extrapolate them temporally and spatially. Obviously, this constitutes the major limitation of this study. Indeed, this is a limitation for water quality researchers across the world because of the fact that satellite techniques are relatively new and large-scale ground truth data have not been collected in the past at different locations of major oceans, rivers and lakes of the world, necessitating the need for linear extrapolation based on the available data. In Turkey also, systematic records have not been kept in this respect. Consequently, only very limited data are available, imposing serious limitation of this, as well as any related study.

(B). While satellite tapes are cost-effective in relation to *in situ* measurements, Landsat tapes, by themselves are expensive from the point of view of the developing nations. Whereas, some tapes are available in Turkey, maintaining an up-to-date archive of Landsat tapes is prohibitively expensive for most of the developing nations. In such a scenario, investigation is possible only by using the available tapes, rather than the actual one appropriate for a particular situation. This procedure gives rise to inevitable inaccuracies in data collection and interpretation.

(C). Digital numbers for all the stations have been extracted for the single pixel. It will be more appropriate to extract these values from an n-pixel-block, say nine-pixel-block encompassing the center pixel corresponding to each sample site. It is necessary to carry out investigation using single-pixel values and kernel (block) averages to verify that kernels represent spectrally uniform areas. For instance, if a site is close to a rock jetty, there may be substantial deviation between single-pixel and kernel average values.

(D). The Landsat and SPOT digital values do not correspond to the same time slot, as is highly desirable. However, the pollutional loads in the Bay area do not vary considerably in terms of tons/day. In such a scenario, it has been observed that the Bay does not exhibit drastic time-variation of TSS.

ACKNOWLEDGMENTS

The authors thank the authorities of Marmara Research Center, Turkish Council of Scientific Research (TÜBİTAK), for their support in this study.

REFERENCES

- DeCoursey, D.G., and Snyder, W.M., 1969: Computer-Oriented Method of Optimizing Hydrologic Model Parameters, *J.Hydrol.*, **9**, 34-56.
- DEE, 1992: Towards the clean Izmit Bay, Department of Environmental Engineering, TÜBİTAK-Marmara Research Center, Project Pre-proposal, 1992.
- Harrington, Jr., J.A., and Schiebe, F.R., 1992: Remote Sensing of Lake Chicot, Arkansas: Monitoring Suspended Sediments, Turbidity and Secchi Depth With Landsat MSS Data, *Remote Sens. Environ.*, **39**, 15-27.
- Kurar, H., and Natarajan, K., 1994a: Evaluation of suspended sediment concentration in Ömerli Lake using Landsat spectral data, *Journal of Faculty of Engineering and Architecture, Çukurova Üniversitesi, Special Issue*, ISSN 1019-1011, April, 1994, pp. 75-82.
- Lyon, J.C., Bedford, K.W., Yen, J.C., Lee, D.H., and Mark, D.J., 1988: Determinations of Suspended Sediment From Multiple Day Landsat and AVHRR Data, *Remote Sens. Environ.*, **25**, 107-115.
- Natarajan, K., and Kurar, H., 1994a: A regression model for Ömerli Lake water quality monitoring using Landsat imageries, presented at 2. Sinyal İşleme ve Uygulamaları Kurultayı, Gökova, Muğla during 8-9 April, 1994.
- Natarajan, K. and Kurar, H., 1994b: Satellite analysis of environmental changes in the Golden Horn, presented at II Uzaktan Algılama ve Türkiyedeki Uygulamaları Semineri, DSİ Bursa Eğitim Tesisleri, Bursa, Uludağ, 16-22 May, 1994.
- Natarajan, K., and Kurar, H., 1994c: Monitoring of total suspended sediments in Izmit Bay using Landsat spectral radiance, to be presented at the Second Eurasian Symposium on Space Sciences and Technologies, Crimea, Ukraine, September 20-22, 1994.
- Reddy, M. A., 1993: Remote Sensing for Mapping of Suspended Sediments in Krishna Bay Estuary, Andhra Pradesh, India, *Int. J. Remote Sens.*, **14**, 2215-2221.
- Ritchie, J.C., and Cooper, C.M., and Yongquing, J., 1987: Using Landsat Multispectral Scanner Data to Estimate Suspended Sediments in Moon Lake, Mississippi, *Remote Sens. Environ.*, **23**, 65-81.
- Robinove, C.J., 1982: Computation of Physical Values for Landsat Digital Data, *Photogramm. Eng. Remote Sens.*, **48**, 781-784.
- Shih, S.F., and Gervin, J.C., 1980, Ridge Regression Techniques Applied to Landsat Investigation of Water Quality in Lake Okeechobee, *Water Resources Bull.*, **16**, 790-796.

APPLICATION OF MULTISPECTRAL MM-WAVE TECHNIQUE FOR DIAGNOSTICS OF THE DEEP OCEANIC PROCESSES AND CRITICAL SITUATIONS IN THE ATMOSPHERE

I.V. Cherny and G.M. Chernyavskiy
Center for Program Studies, Russian Academy of Sciences,
Moscow 117810, Russia,

ABSTRACT

Paper describes the significant results of airborne studies of some oceanic processes by means multispectral mm-wave imagine technique. The experimental results have been obtained in North Western Pacific on microwave observing the synoptical eddies and frontal zone of Kuroshio current, and the tropical cyclone anomalous trajectory over the ocean. All these processes are characterized by high-contrast spectral variations of sea surface brightness temperature at mm-wave, that allows to classify them. The remote sensing data and in-situ measurements are analyzed. The qualitative model for possibility of microwave diagnostics of the deep oceanic processes and critical situations in the atmosphere is discussed.

1. INTRODUCTION

The development of the theory and practice of passive microwave remote sensing of the ocean-atmosphere system has shown that it is possible and promising to apply the remote methods for determining important meteorological parameters of atmosphere and ocean surface (Ulaby et al., 1981; 1986). For example, the Special Sensor Microwave/Imager (SSM/I), operating at frequencies of 19.35, 22.235, 37.0 and 85.5 GHz, provides the standard meteorological data: total precipitable water in the atmosphere, cloud liquid water content, precipitation, sea surface temperature, wind speed over ocean (Hollinger et al., 1990).

Nevertheless, all the processes taking place on the ocean surface are related in one or another way with the state of deep water layers, even if the surface phenomena occur under direct atmospheric influence. It is valid mostly for anomalous state of the surface.

Presently, a most important problem is to develop aerospace observing technique which could "look into" the ocean depths through the surface. This statement of the problem is quite correct. Indeed, ocean is a thermodynamically nonequilibrium medium due to the presence of temperature and salinity gradients, which form the ocean thermohaline structure. Therefore, the conditions could arise for amplification the influence of depth processes onto the surface at the expense of accumulated oceanic energy (Gus'kov et al., 1991).

It has been experimentally found (Cherny, 1987; 1992; 1993), that the signal which is registered by the remote means at mm-wave is being formed under direct influence of both the process under investigation, taking place at the depth, and another process, certainly connected to the first one and directly characterizing the state of nonequilibrium oceanic medium. The block-diagram, demonstrating the way for diagnostics of the deep oceanic processes and critical situations in the atmosphere with the sea surface microwave emission is shown in Fig.1. The diagnostics of this secondary process, being the result of instability of the ocean thermohaline structure, may bring more information in some cases that of the first one.

Below it is illustrated by the concrete examples. The deep synoptical eddies and mesoscale thermohaline lens structures are manifested in spectral microwave emission of the sea surface. The same microwave effect is appeared in the front of moving tropical cyclone, where some hours later it changes its trajectory.

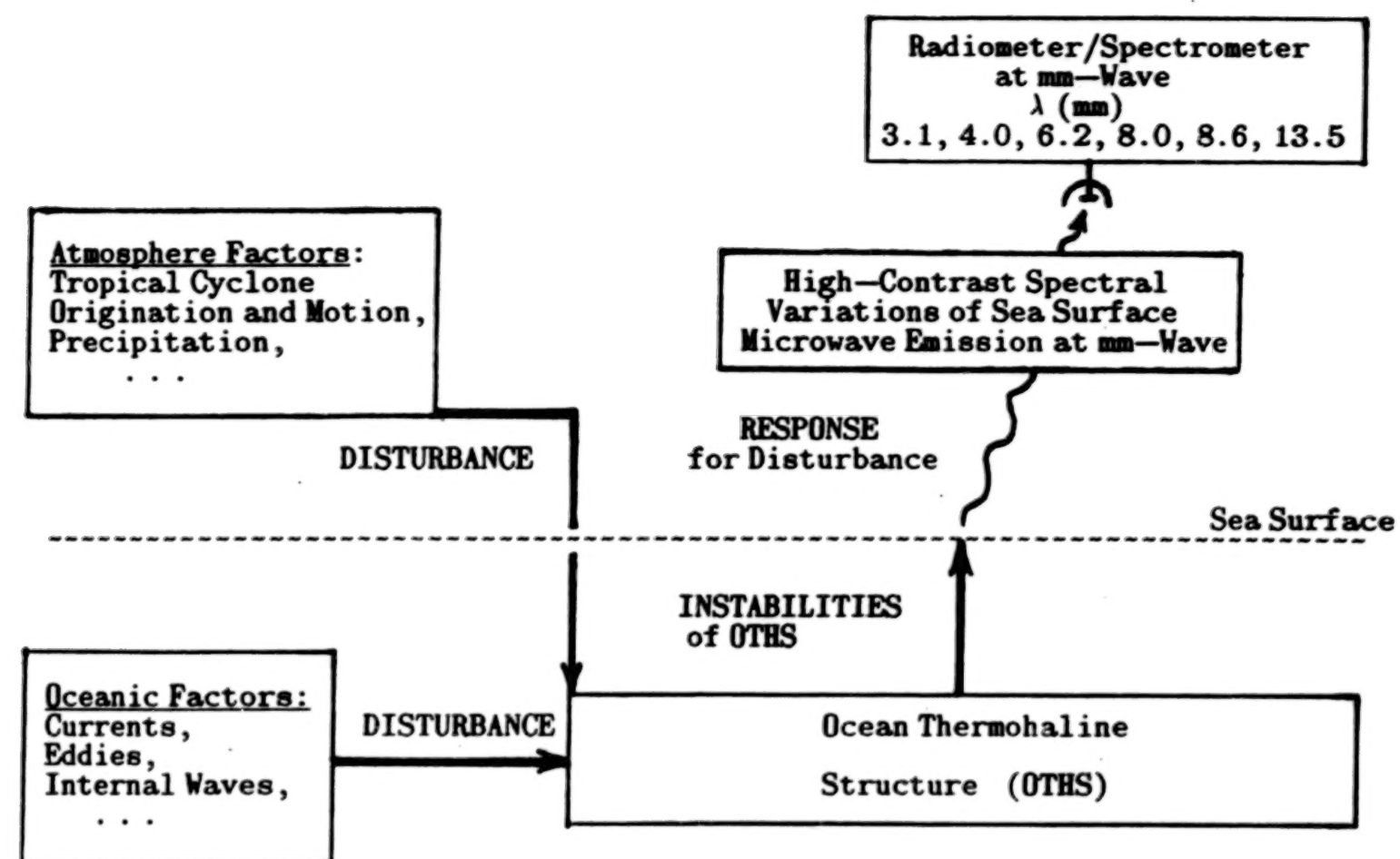


Figure 1. Qualitative model for diagnostics of the deep oceanic processes and critical situations in the atmosphere with the sea surface microwave emission at mm-wave according to (Gus'kov et al., 1991).

000508

BLANK PAGE

2. INSTRUMENTS AND METHODS

The remote sensing of the ocean surface was carried out by means multi-channel radiometer/spectrometer at mm-wave (Cherny et al., 1993). The instrument provides a collection of data over a wide spectrum of mm-wave frequencies available from no other means. The operating wavelengths are the following: 13.5, 8.6, 8.0, 6.2, 4.0 and 3.1 mm. It became possible to conduct concurrently in space and time spectral and polarization measurements by using a multifrequency feedhorn antenna. The fluctuation sensitivities of radiometer channels are 0.03–0.05K at the integration time constant 1s.

Parameters of the multispectral mm-wave imaging technique deployed on research aircraft TU-134 are:

- angle of the antenna beam incidence.....	75° off nadir
- scanning sector (conical scanning in the back hemisphere).....	120°
- scanning period.....	20s
- half-power beamwidth ($\lambda=4.0$ mm).....	2°
- antenna footprint on the surface ($\lambda=4.0$ mm).....	0.12H x 0.45H
	H – flight height
- swath width.....	6H
- surface mapping rate (H=10 km, V=800km/h).....	48000 km ² /h

The data processing system built around IBM PC AT computer performs the complex functioning control, acquisition, storing, preliminary processing, and displaying of data in real-time mode.

3. MICROWAVE OBSERVATIONS OF KUROSHIO RING

On october 1990, jointly the r/v "Academician Lavrentev" and research aircraft TU-134 by means multispectral mm-wave imaging technique studied the Pacific subarctic frontal zone along the 149°E meridian from 34 to 45°N. During this expedition the Kuroshio ring has been detected. The anticyclonic rings with the warm core of 150–300 km are regularly formatted north of the Kuroshio stream and their life time are about 1.5–2 years (Lobanov et al., 1991).

The pattern of experiment is shown in Fig.2. Microwave mapping of the sea surface was carried out on October 18, 20 and 21. The flight height of aircraft was equal to 10 km and swath width was – 60 km. The general length of sectional view reaches 1000 km. Multispectral microwave images of this region obtained on October 20 are shown in Fig.3 at wavelengths 4.0 mm (horizontal polarization) and 6.2, 8.0 and 13.5 mm (vertical polarization).

The hydrological measurements were made by research vessel on October 16–18 between points A–B (see Fig.2). The water temperature distribution of the upper ocean layer (0–300 m) along the 149°E meridian is shown in Fig.4. According to the sounding data the ring has a complicated hydrological structure in the region of the main thermocline. There is a tunnel of the isotherms south of 43°N directly under the sea surface warm core, characterizing the anticyclonic circulation of water masses. At the same time there is a dome of the isotherms north of 43°N at the depth 150–300 m with the horizontal size about 100km. This area is characterized the cyclonic circulation of water masses. This points to the Kuroshio ring consisted of two eddies. The possibility of generation of two coupled oceanic eddies of the opposite sign (cyclone, anticyclone) called as Rossby Soliton was discussed in monograph (Kamenkovich et al., 1987).

We consider mm-wave images at some wavelengths to demonstrate the spectral peculiarities of sea surface brightness temperature due to Kuroshio ring (Fig. 3). The area of the positive brightness temperature contract of 4–5 K and size about 150km is clearly seen on

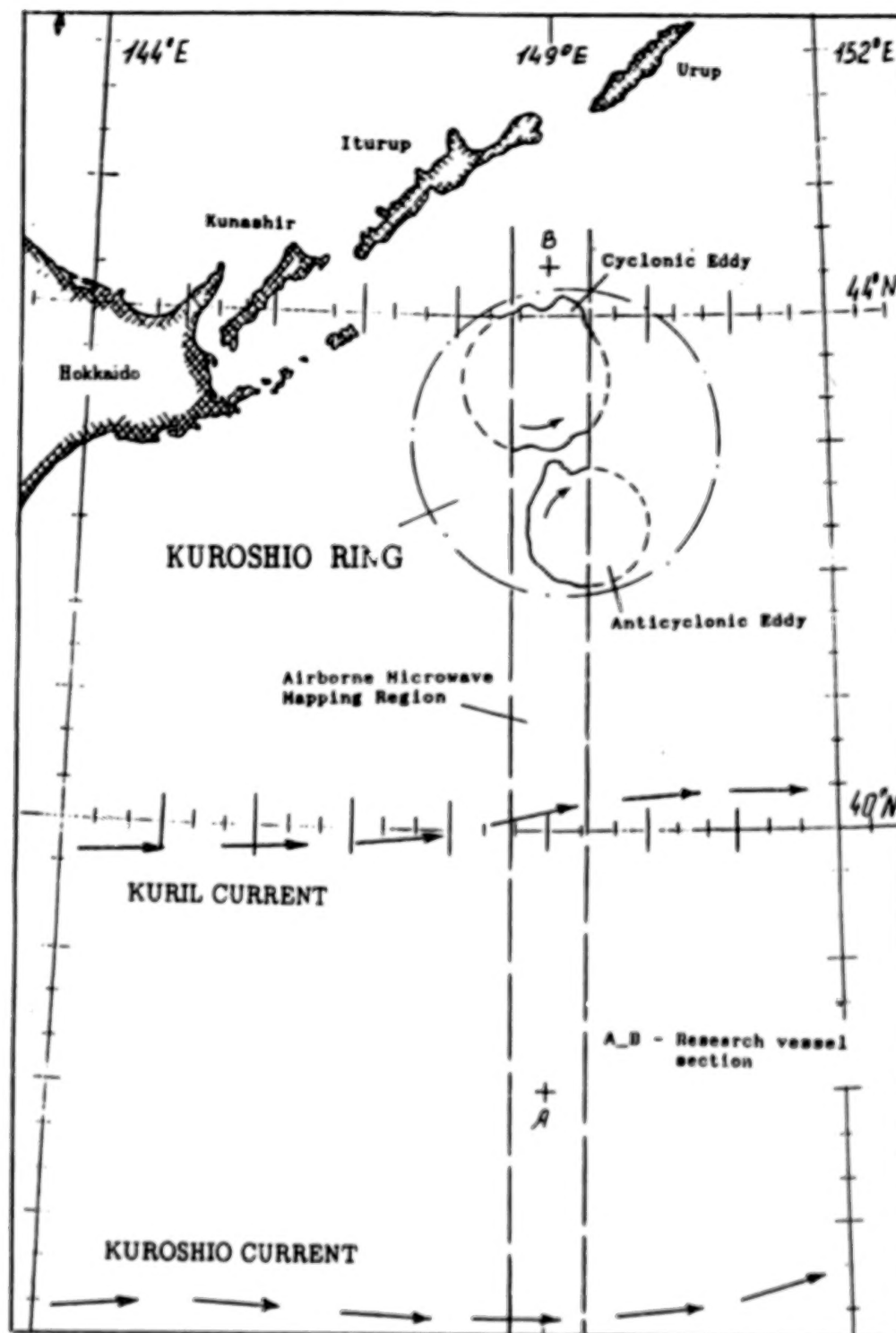


Figure 2. Pattern of experiment on joint studying of Kuroshio ring by aircraft and research vessel. The size and position of anticyclonic and cyclonic eddies are shown according to microwave data.

BLANK PAGE

Figure 3

A-93

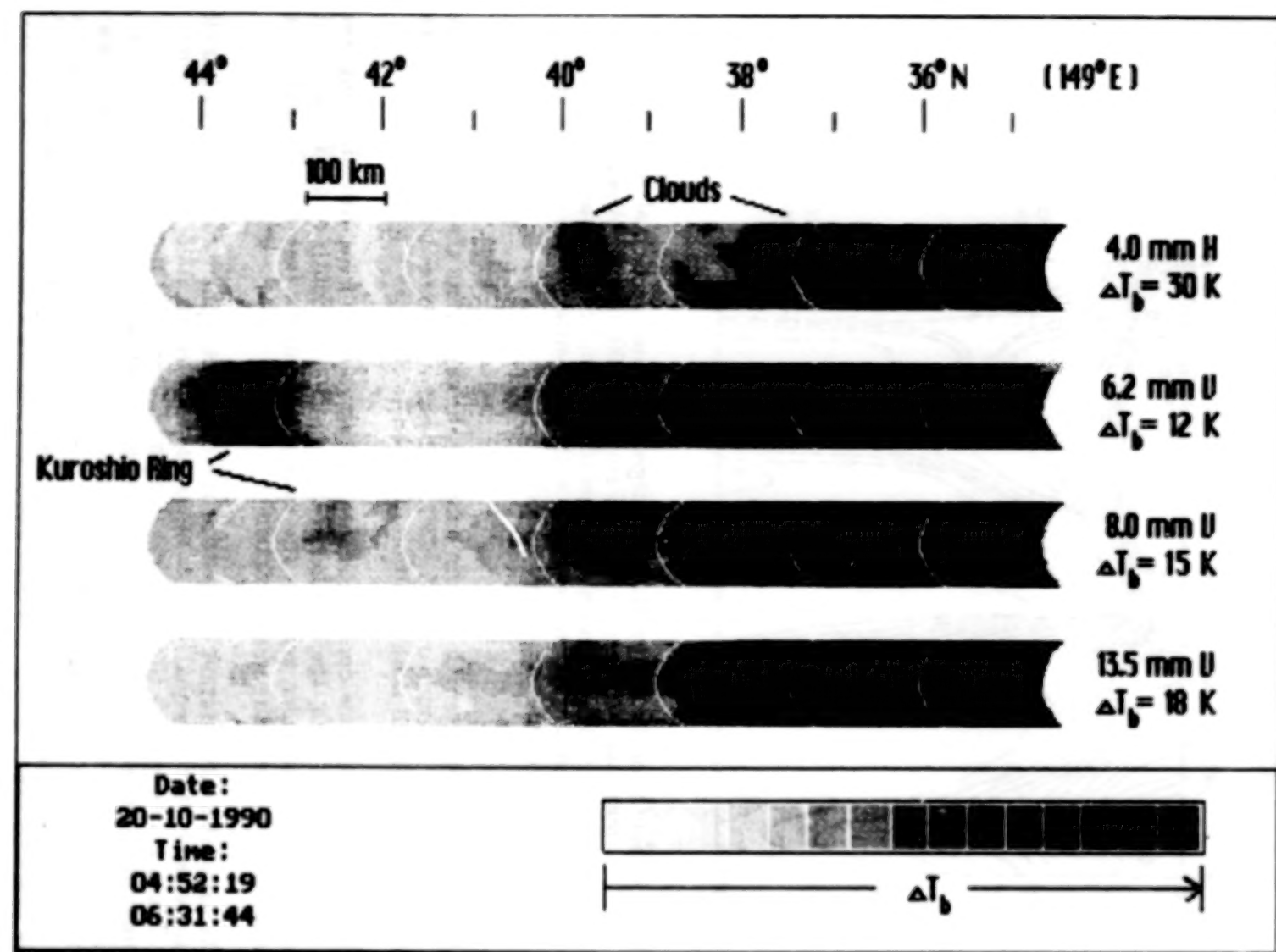


Figure 3. Multispectral microwave images along 149°E meridian on October 20, 1990, by research aircraft TU-134. Kuroshio ring is seen at wavelengths 6.2 mm and 8.0 mm only.

000511

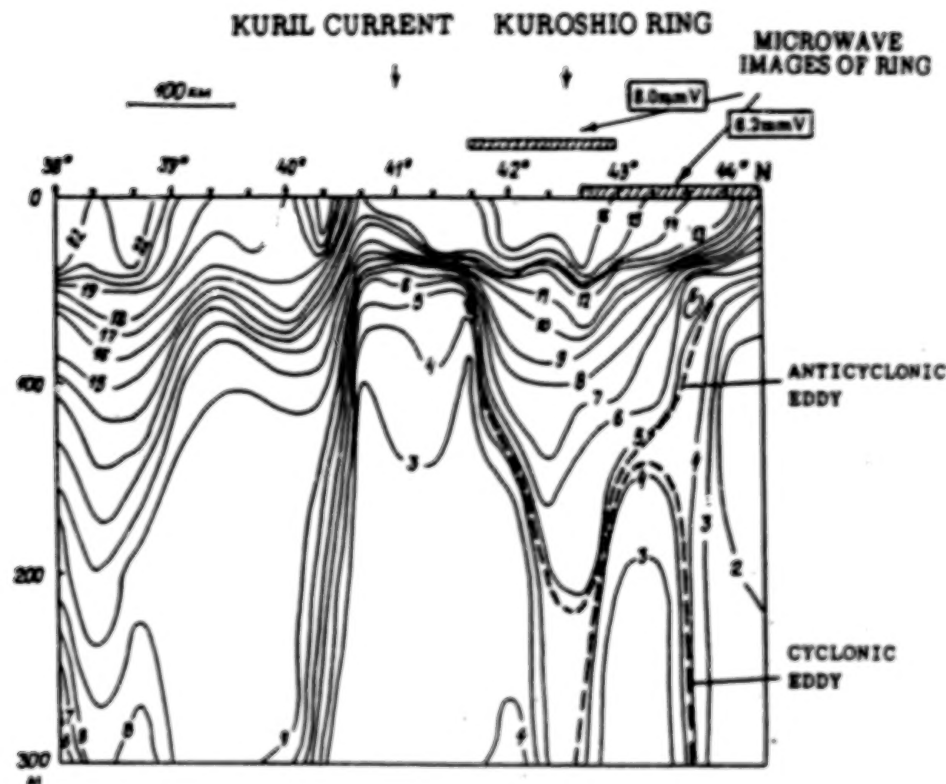


Figure 4. South-north temperature (in degrees Celsius) section along 149°E meridian between October 16 and 18, 1990, by r/v "Academician Lavrentev". Microwave images of Kuroshio ring at wavelengths 6.2 mm and 8.0 mm coincide with the position of the cyclonic and anticyclonic eddies respectively.

the image near 43–44°N at wavelength 6.2 mm only. At the same time the area of similar size is seen only at wavelength 8.0 mm near 42–43°N and has brightness temperature contrast about 2 K. Both areas are located at the position of Kuroshio ring (see Fig. 4).

The weather conditions during microwave observations of the Kuroshio ring were: near surface wind speed – 7 m/s, the weather state – uncloudy. South of 41°N was cloudy. The cumulonimbus clouds are also seen on the microwave images (see Fig. 3), but clouds increase the brightness temperature in all channels.

The calculated attenuation constant of the clear atmosphere for height 10 km (the observation angle was 75°) is equal to 2.4 times at wavelength 13.5 mm, 1.7 times at wavelength 8.0 mm and about 10 times at wavelengths 6.2 and 4.0 mm. Consequently, the brightness temperature contrast of the microwave anomaly at wavelength 8.0 mm must be equal to 3–4 K at sea level. The anomaly position coincides with the position of surface warm core of the anticyclonic eddy (see Fig. 4). Therefore, it should be assumed that the brightness temperature contrast in this case was due to the sea surface temperature variations. The absence of this effect on other images could be explained the more large attenuation constant of the atmosphere at these wavelengths. Although, the spatial configuration of sea surface brightness structure points that it could be caused by another reason.

The more interesting one is the microwave anomaly at wavelength 6.2 mm, because it's brightness temperature contrast at sea level must be equal to about 40–50 K and

no more than 3-4 K at wavelengths 8.0 and 13.5 mm (it takes into account the discrete of brightness scale). From this it follows that the observed effect can not be related to the sea surface temperature variations, as well as, atmosphere influences. Moreover, the sea surface microwave anomaly coincides with the size and position of cyclonic eddy, which is disposed at the depth more than 150 m and where distinctive thermohaline structure exists (see Fig. 4).

Thus, the multispectral mm-wave imaging technique gives the new results for studying of the oceanic rings. It allows to detect not only the warm core of the eddy on the sea surface, but the spatial characteristics of the inner structure of the deep eddy.

The mesoscale structures with the same sea surface microwave effect had been observed in Kuroshio region some years before. Figure 5 shows the hydrological section in temperature field along 149°E meridian across Kuroshio current made on October 1983 by r/v "Professor Bogorov". The shipboard microwave remote sensing of the ocean surface was carried out during this section. It can be seen that sea surface microwave anomalies, which were characterized by high contrast variations of brightness temperature at mm-wave (Cherny, 1987), are located in frontal zone of Kuroshio current where distinct "lens" structures exist at the depth 100-400 m. The spatial size of ocean surface microwave anomalous areas is comparable to the horizontal one of deep water thermic structures.

Note that in all cases the sea surface anomalous effect in microwave emission is related with the complicated hydrological finestructure of water medium.

4. MICROWAVE OBSERVATIONS OF TROPICAL CYCLONE ANOMALOUS TRAJECTORY OVER THE OCEAN SURFACE

The methods of remote diagnostics and prediction of tropical cyclone trajectories are highly important for predicting and warning of natural calamities, specifically in the cases when typhoons and hurricanes drastically change their direction. The anomalous trajectories of tropical cyclone motion can be associated both with external factors - action of the large-scale (background) flow, influence of thermal properties of the sea surface and upper ocean layer, and with asymmetry of the central zone dynamic structure of the tropical cyclone itself (Hain and Sutirin, 1983). By anomalous trajectories is meant changing the velocity of their transitional motion at 5 m/s and more or changing the direction more than 45° during 6 hours.

The result given below demonstrates the possibility of microwave technique for diagnostics of the ocean influence on cyclone trajectory. The spectral variations of sea surface brightness temperature at mm-wave have been detected on the size of 500 km in the front of moving cyclone, where 7-8 hours later it has changed its trajectory.

The microwave mapping region of the Okhotsk Sea on September 4, 1989 and tropical cyclone trajectory on September 4, 5 are shown in Fig. 6. The cyclone was at a filling up stage with the pressure level at the center 1002-1005 mb according to data of Japanese Meteorological Agency.

On September 4 at about 14.00 to 15.00 (everywhere the Vladivostok time will be mentioned) the tropical cyclone entered the Okhotsk Sea with a velocity higher than 40 km/h and went on to move in the north-east direction to its central part. At about 23.00 (September 4) the trajectory of motion changed in the north-west direction towards Sakhalin. In this area the cyclone moved with a velocity of 30 km/h till 14.00 of the next day when its direction changed to the north-east. Thus, the cyclone trajectory is a zigzag curve which outlines the central part of Okhotsk Sea. The motion direction changes at 50-70°, which makes it possible to characterize the cyclone trajectory as anomalous.

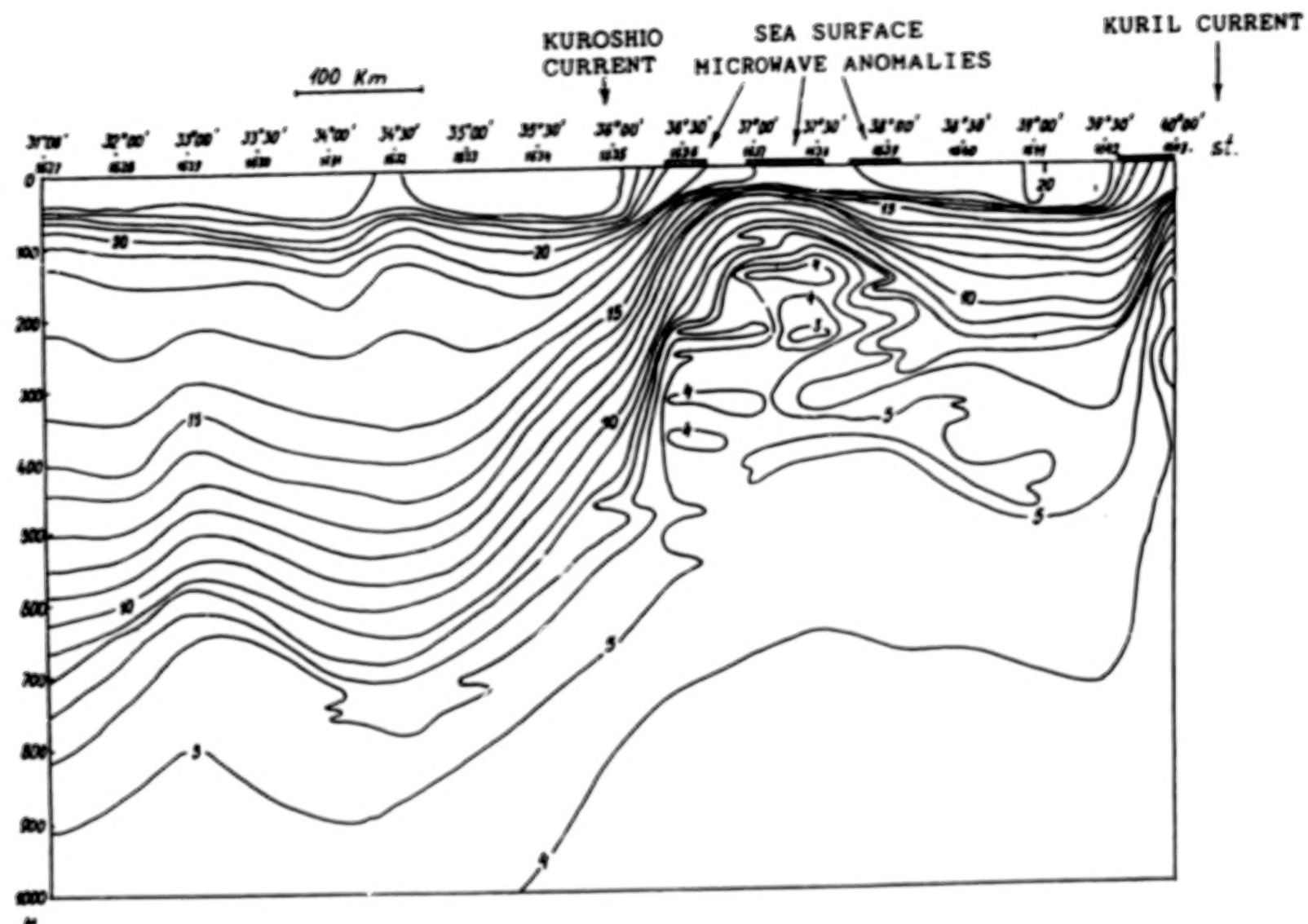


Figure 5. South-north temperature (in degrees Celsius) section along 149°E meridian between October 9 and 12, 1983, by r/v "Professor Bogorov". Sea surface microwave anomalies are located in frontal zone of Kuroshio current.

000514

BLANK PAGE

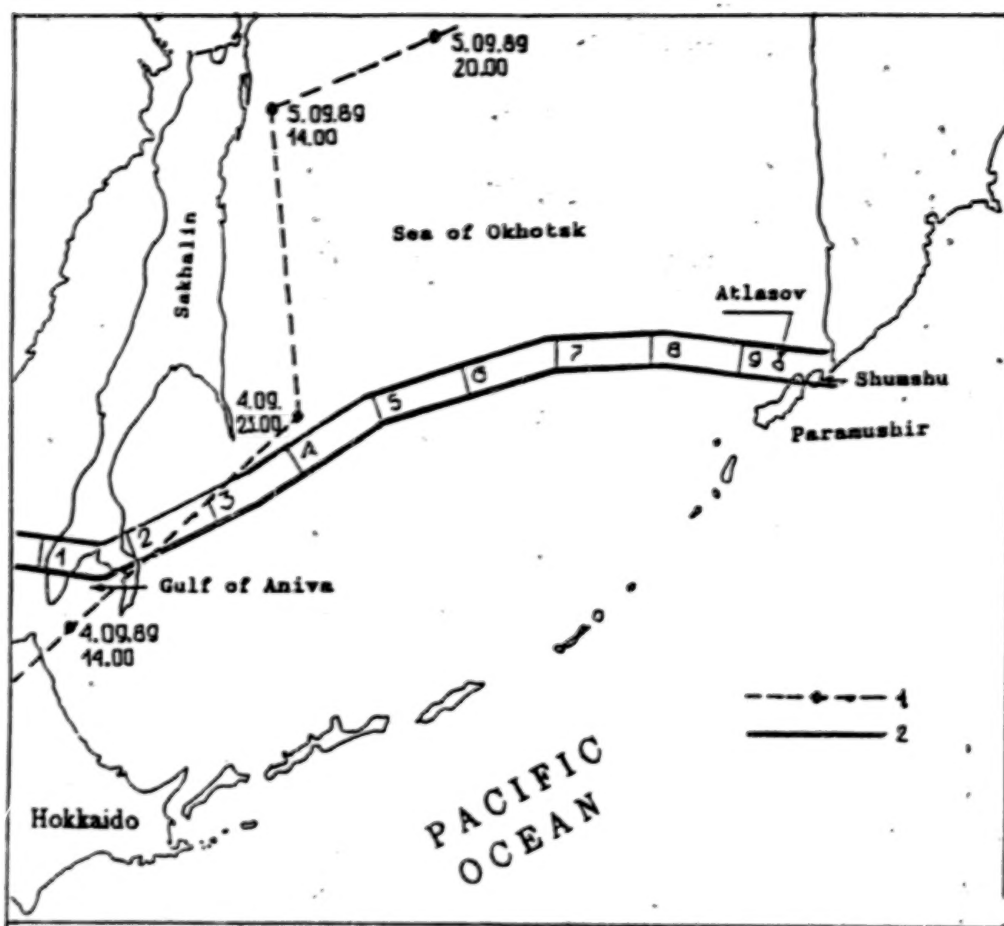


Figure 6. Pattern of the experiment on studying the tropical cyclone anomalous trajectory in Okhotsk Sea on September 4, 1989:
1 - Cyclone trajectory; 2 - Airborne microwave mapping region.

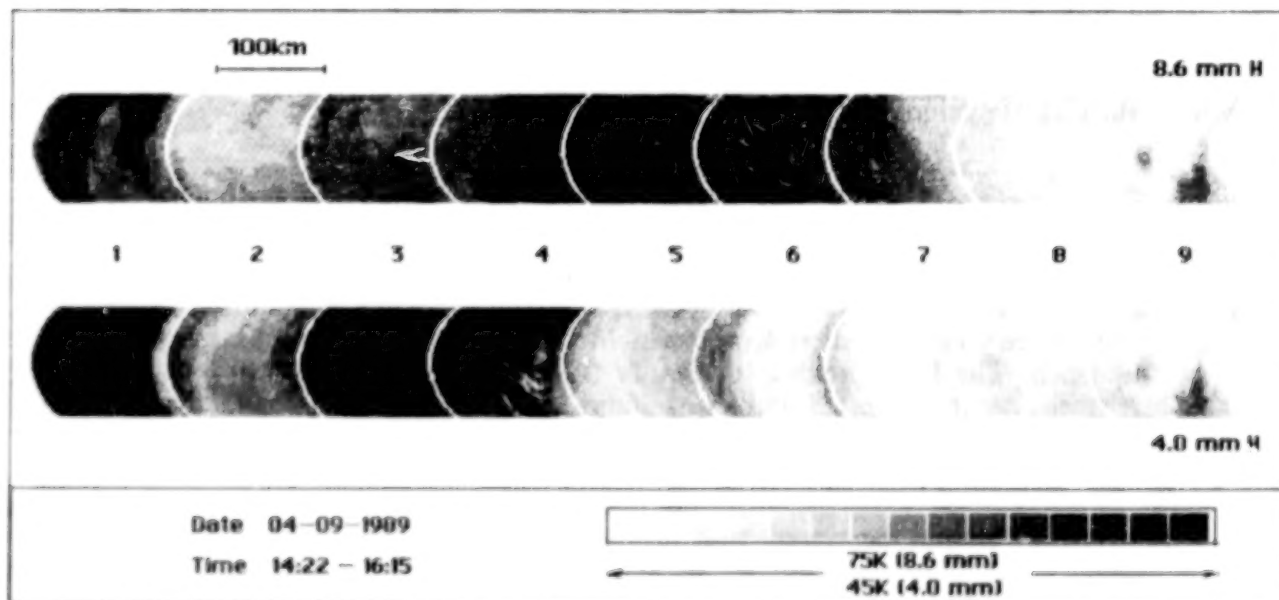


Figure 7. Microwave images of Okhotsk Sea at wavelengths 8.6 mm and 4.0 mm (horizontal polarization). The position of each frame on the flight path is shown in Fig. 6. In the central part a zone of spectral brightness temperature variations is observed (frame 3-7). Area size is about 500 km, where 7-8 hours later the cyclone has changed its trajectory.

Airborne microwave mapping of Okhotsk Sea was conducted on September 4 from 14.22 to 15.15 when the cyclone "eye" was between Hokkaido and Sakhalin and about 7–8 hours before the motion trajectory has been changed. Spectral microwave images at wavelengths 8.6 and 4.0 mm (horizontal polarization) consisted of the subsequent frames are shown on Fig. 7. The flight height of aircraft was equal to 8 km and the swath width was about 50 km. Figure 6 shows the location of each frame along the flight.

The first frame gives Sakhalin covered with cumulonimbus clouds of the cyclone central part at a distance of 100–150 km from its "eye". Spectral images allow for distinguishing the waterland boundary Gulf of Aniva in the channel 8.6 mm only, whereas at wavelength 4.0 mm the upwelling radiation is fully absorbed and cumulonimbus clouds mainly contribute to the antenna temperature.

Of particular interest are the spectral microwave variations of the Okhotsk Sea central part (see frames 3–7 on Fig. 6). For example, at wavelength 8.6 mm the extended region with sharp boundaries about 500 km long (frames 3–7) is observed. This region is characterized by an increase in the brightness temperature on the overage by 30–35 K. At the same time structure fragments ranging from 50 to 150 km are observed at wavelength 4.0mm. Here the given regions are characterized by higher (frames 3 and 4), and lower (frames 5, 6, 7) brightness temperatures relative to the initial level mentioned on frame 2. The brightness temperature variations reach 12–15 K. Note, that during the survey of Okhotsk Sea the homogeneous stratocumulus clouds were observed. Some areas of the land were mapped in given conditions. The Atlasov, Shumshu and Paramushir islands are clearly seen on the images (frame 9).

The analysis suggests that spectral variations of brightness temperature on the microwave images of the Okhotsk Sea central part are obviously caused not by the atmospheric factors. They are in much the same way as phenomena detected in Kuroshio region and in turn could be related to the water thermic inhomogeneities at the depth.

On the other hand, it has been shown (Pudov, 1979), the tropical cyclones reduce speed, make loops or change direction when there are the ocean thermic anomalies on their path, which are comparable-sized to the cyclone active zone. The thermic anomalies include the deep one, because, tropical cyclone interaction with the ocean extends to 1000 m depth (Pudov, 1989). In our case, the detected microwave anomalous region is equal to 500 km and comparable to the size of cyclone active zone.

5. DISCUSSION

Mentioned above experimental data show that some processes in the ocean-atmosphere system cause the high-contrast spectral variations of sea surface brightness temperature at mm-wave. At present time, it is difficult to find a complete physical explanation of this ocean surface microwave phenomenon and it's relation to hydrological processes at the depth. The first attempt to classify the high-contrast spectral variations of sea surface brightness temperature at mm-wave and to show their difference from those caused by the wind stress and direct current influence onto the surface, is discussed in monograph (Raizer and Cherny, 1994).

However, it should be noted that the wide class of processes in the ocean-atmosphere system from mesoscale up to synoptical one are accompanied by spectral peculiarities of sea surface emission at mm-wave frequencies. We discussed the processes such as frontal zone and synoptical eddies of Kuroshio current and tropical cyclone interaction with the ocean. All they disturb in one or another way the ocean thermohaline structure that most likely is responsible for sea surface brightness temperature variations at mm-wave (see Fig. 1).

REFERENCES

- Cherny I.V., 1987: On the Peculiarities of Microwave Emission and Scattering from Sea Surface in the Field of Internal Waves and Frontal Zones, *Preprint IKI AN USSR (Space Research Institute)*, N1285, Moscow, 26 pp.
- Cherny I.V., 1992: The "relic rain" effect on sea surface microwave emission. *Proceedings of IGARSS'92 Symposium*, IEEE 92CH3041-1, Houston, Texas, 254-256.
- Cherny I.V., 1993: Microwave studies of typhoon WARREN generation. *Proceedings of IGARSS'93 Symposium*, IEEE 93CH3294-6, Tokyo, 1913-1915.
- Cherny I.V., A.G. Efimov, G.Ya. Gus'kov, et al., 1993: Airborne multiwavelength microwave imaging sensor. *CO-MEAS'93 Proceedings*, Albuquerque, New Mexico, 170-172.
- Gus'kov G.Ya., S.S. Moiseev and I.V. Cherny, 1991: Secondary Instabilities in the Ocean-Atmosphere System and Microwave Diagnostics of Natural Calamities, *Preprint IKI AN USSR (Space Research Institute)*, N1762, Moscow, 34 pp.
- Hain A.P., and G.G. Sutirin, 1983: *Tropical Cyclones and Their Interaction With the Ocean*, Gidrometeoizdat, Leningrad, 272 pp.
- Hollinger J.P., J.L. Peirce and G.A. Poe, 1990: SSM/I Instrument Evaluation, *IEEE Transactions on Geoscience and Remote Sensing*, vol. 28, N 5, 781-790.
- Kamenkovich V.M., M.N. Koshlyakov, and A.S. Monin, 1987: *Synoptic Eddies in the Ocean*, Gidrometeoizdat, Leningrad, 512 pp.
- Lobanov V.B., et al., 1991: Long-period Evolution of the Warm Kuroshio Eddy", *DAN USSR*, Vol. 317, N4, 984-988.
- Pudov V.D., 1979: On the Influence of Heat Supply of Upper Ocean Layer on Typhoon Trajectories. *Okeanologiya*, v. 19, N 6, 1002-1007.
- Pudov V.D., 1989: Tropical cyclones interaction with the ocean. In *Tropical Cyclones*, V.M. Voloschuk and A.F. Nerushev (Eds.), Gidrometeoizdat, Leningrad, 21-24.
- Raizer V.Yu., and I.V. Cherny, 1994: *Microwave Diagnostics of Subsurface Ocean Layer*, Gidrometeoizdat, Saint-Petersburg.
- Ulaby F.T., R.K. Moore and A.K. Fung, 1981: *Microwave Remote Sensing; Active and Passive*, Vol. 1. Reading, MA: Addison-Wesley.
- , 1986: *Microwave Remote Sensing; Active and Passive*, Vol. 3. Reading, MA: Addison-Wesley.

This paper was not presented at ISSSR '94 and should be recognized as proceedings only status.

**A REVIEW OF PROBLEMS OF LAND USE AND COVER
DELINEATION USING SPOT AND LANDSAT-TM DATA OF
SAO JOSE DOS CAMPOS, BRAZIL**

**Sosthenes Kwadzo Kufogbe
University of Ghana,
Accra, Ghana.**

ABSTRACT

SPOT and Landsat-TM imagery of Sao Jose dos Campos (SJC), Brazil, have been interpreted and integrated in a Geographic Information System (GIS) using the SITIM and SGI softwares of the Instituto Nacional de Pesquisas Espaciais, INPE, Brazil. The higher spatial resolution of SPOT enabled a larger number of land use/cover classes to be identified relative to the Landsat/TM image on the SPOT image. It was difficult to discriminate between transportation network and rivers on the one hand, and the same class of forest or pasture in areas of variable topography on the other. Delineation of spectrally defined classes and recognition of linear features constituted the major problems in the digital classification of the Landsat-TM image. Consequently, the digital classification of the Landsat imagery provided only broad indication of spectrally defined land use/cover classes. The practically oriented procedure involving a combination of manual and photographic techniques which was used in modifying the GIS generated land use/cover map for the final output would be found useful in less developed countries.

1. INTRODUCTION AND BACKGROUND

Data on land use/cover have become prerequisite for optimum development planning requirements of all countries. The data are required not only for existing land use patterns but also their changes through time. The use of remotely sensed imagery is particularly appropriate for the production of such data especially in the form of maps.

While for most developed countries, land use/cover data are available or can be readily made accessible for use in response to planning requirements as expressed above, the need for these data is only now being increasingly recognized or appreciated by government and planning agencies in developing countries.

The use of satellite remote sensing for land use/cover assessment and monitoring is of paramount importance especially in developing countries where regular aerial-photograph coverage is not available. Detailed ground-based surveys of large relatively inaccessible and ecologically complex areas are generally difficult and expensive. Satellite remote sensing and Geographical Information Systems (G.I.S) procedures are therefore considered useful for the mapping and monitoring of changes in such areas, particularly as a means to complement or update conventional data gathering techniques (Nellis, 1986; Weaver, 1984).

The accuracy of image classification is influenced by several factors especially parameters of the remote sensing system, the conditions of data acquisition, the characteristics of the analyzed landscape as well as the type of equipment available (Markham, and Townshend, 1981; Toll, and Kennard, 1984). The difficulties for having spectral characteristics that are constant all over a single image and also for determining "pure pixels" of a landscape unit are particularly limiting factors for automatic classification. The influence of variable topography and small landscape units, for example farm sizes in tropical areas, have also been identified (Gastellu-Etcheberry, and Ducross-Gambart, 1991).

Generally, the finer the spatial resolution of the sensor the larger the number of pure and predominantly pure pixels and the better the accuracy. In this regard the better spatial resolution of SPOT imagery gives considerable advantage over Landsat/TM. The enhanced detail of SPOT therefore allows broader cover types to be mapped more accurately. It is argued, however, that whilst one would intuitively expect an increase in classification accuracy to result from the use of such higher resolution imagery because of the reduced proportion of mixed pixels that may lie across boundaries separating two or more distinct land use/cover types, there is also a corresponding reduction in accuracy as individual components of what a lower resolution sensor would see as being homogeneous are separated by the higher resolution sensor (Mather, 1987). Consequently, other derivatives and combinations of the basic classification procedures are being employed. For example, unsupervised classification may be used generally as a preliminary step in refining knowledge of the spectral classes present in the image so that a subsequent supervised classification can be carried out more effectively. The classes identified then constitute the basis for selecting training samples for use in the supervised procedure such as the Maximum Likelihood Classification (Mather, 1987). The use of textural classification has also been suggested. Textural classification, however, assumes a second stage in the training program with textural characteristics computed for eliminating inter-class confusions that remain after the first stage in the supervised classification. Textural classification is therefore usually applied later in the Maximum Likelihood classification to classes which show confusion identified from the initial classification matrix (Mather, 1987).

Baker et al. (1991) have also discussed two methods for improving mapping classification performance. The first technique involves the use of digital terrain information to reduce the effects of topography on spectral information. The second involves the classification of land use/cover types by using data derived from spectral feature space (Baker, et al., 1991).

The objective of this paper is to present the results of image classification and G.I.S. procedures which address some aspects of the problem using 1988 sub-scenes of Landsat TM and SPOT multispectral images of Sao Jose dos Campos in the Sao Paulo state of Brazil.

2. MATERIALS AND METHODS

Images in both digital and hard copy media were used. The ancilliary material comprised topographical maps and large scale aerial photographs.

2.1 THE STUDY AREA

The location of the study area is approximately south 23:13 and west 45:51 in the state of Sao Paulo (Fig 1). It falls within the broad region known as Vale Paraiba do Sul. Sao Jose dos Campos (SJC), the main municipality in the area, has experienced a very rapid rate of urban growth during the past twenty years due to a very high rate of population increase and industrialization.

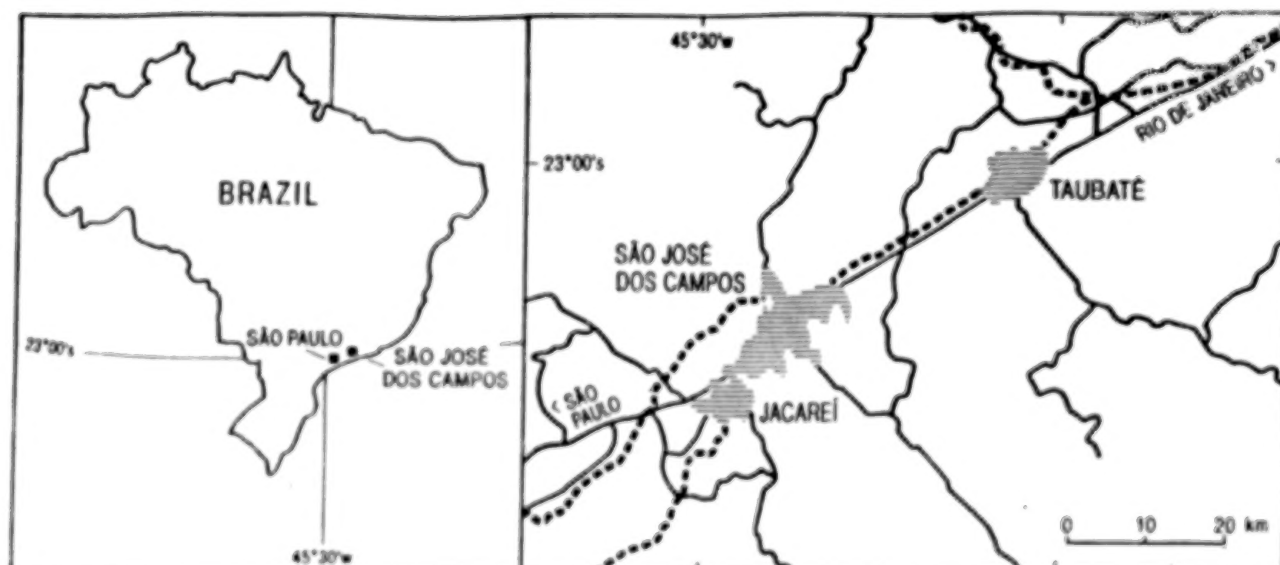


Figure 1. Location of study area.

2.2 IMAGERY

The list of imagery used is provided in Table 1. Aerial photographs, topographical maps and existing land use maps of the study area have also been consulted (Pareira, M.M *et al.*, 1988; INPE, 1991).

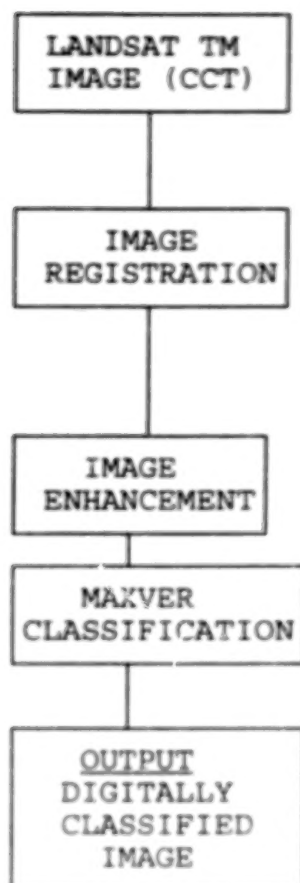
TABLE 1. SETELLITE IMAGERY

Sensor	Orb./pt.	Location	Spatial Resolution	Band	Type	Date
SPOT	718/396c	SJC	20 metres	XS123	Paper	19.7.88
Landsat TM	219/96e	SJC	30 metres	145	CCT	12.9.88

3.0 METHODOLOGICAL PROCEDURES

The methodology developed for this paper emphasizes the integration of both visual and digital techniques for generating land use/cover maps from remotely sensed data (Fig. 2). Due to difficulties encountered in the identification of suitable ground control points (GCPs), the Landsat TM image could not be geometrically registered to any map projection as originally envisaged in the methodological procedures (Fig. 2). Even though the city of SJC has expanded very rapidly during the past twenty years this expansion was not reflected in the only available topographical maps which dated as far back as 1973, and which could have been a most suitable reference for image registration. This shortcoming did not affect the structure of the digital classification procedure. It however did not allow the intergration of the results into the GIS procedure as was the case with the SPOT image.

S I T I M



S G I

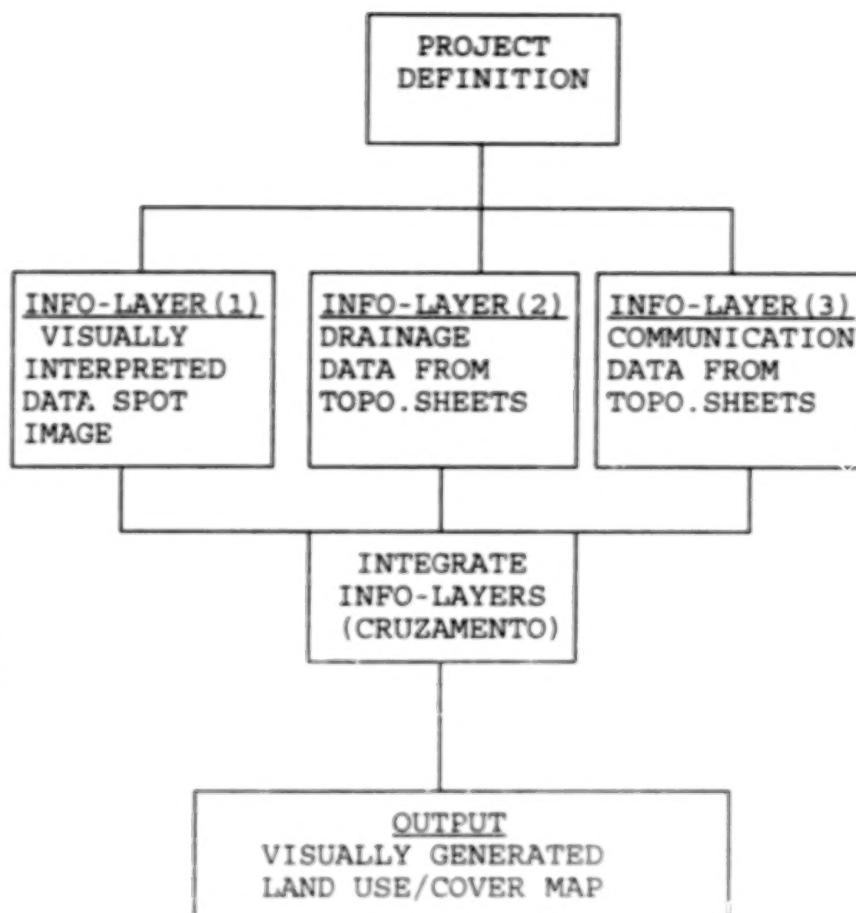


Fig.2 PROCESSING SEQUENCES IN SITIM AND SGI

The geometrically corrected hard copy SPOT image was used in the visual interpretation procedure. Supplementary data were derived on drainage and transportation network from topographical maps. These and the results of the visual classification procedure were digitised as appropriate info-layers in the G.I.S. procedure to generate final land use maps using the SGI¹ software.

¹ Sistema de Informacoes Geograficas (SGI) is the Brasillian equivalent of the GIS software developed by INPE.

4.0 RESULTS AND DISCUSSION

4.1 DIGITAL CLASSIFICATION OF LANDSAT TM IMAGERY

The land use/cover map derived from the Maxver (Maximum Likelihood classification) in SITIM² for the Landsat TM image is shown in Figure 3.



Figure 3. Digital Classification of Landsat TM Image of Sao Jose dos Campos, Brasil. (Original copy in colour)

² Sistema de tratamento de imagens (SITIM) is the image processing system software developed by INPE, Brasil.

The relative distribution of the land use/cover classes identified in the digital classification of the Landsat TM image is shown in Table 2. Two threshold values of the Maxver classification used were 7.80 and 11.30 corresponding to 95% and 99% levels of confidence respectively (Mather, 1988). The result showed that the area of the image left unclassified decreased significantly from 34.2% to 14.7% for the 95% and 99% levels respectively. The improved classification at the 99% threshold level however only resulted in a higher confusion mean value indicating the inability of the algorithm to allocate additional pixels to classes.

TABLE 2. DIGITAL CLASSIFICATION OF LANDSAT TM DATA FOR SJC AT 7.80 AND 11.30 THRESHOLD LEVELS

CLASS	THRESHOLD VALUE			
	(7.80) Area (Km2)	%	(11.30) Area (Km2)	%
Urban mixed	161.3	22.1	189.5	26.0
Planted forest (Eucalyptus)	27.7	3.8	43.9	6.0
Natural forest	39.4	5.4	68.4	9.4
Pasture	126.8	17.4	152.6	20.9
Novo allotamento (peri-urban)	24.6	3.4	39.9	5.5
Water	6.6	0.9	7.3	1.0
Agricultural Land	28.5	3.9	35.5	4.9
Cerrado (Grassland)	23.4	3.2	32.0	4.4
Young Eucalyptus (Euc. 2)	12.7	1.7	15.5	2.1
Burnt area	28.2	4.0	37.2	5.1
Area not classified	249.5	34.2	107.2	14.7
TOTAL	729.0	100.0	729.0	100.0

Source: Maxver classification procedure in SITIM, INPE.

Irrespective of threshold level of classification, urban mixed was the dominant class, accounting for between 22% and 26% of the total image area. Pasture accounted for between 17% to 21% whilst water bodies had the least representation. Quarries were not identified as in the case of the SPOT classification. This was due to the inseparability of this class from the adjacent river banks due to the lower spatial resolution of Landsat/TM. It is important to note that the Landsat TM image was for September, 1988, a period corresponding to the peak of the dry season in the state of Sao Paulo when vegetation cover was almost negligible on the landscape. This made it difficult to distinguish between areas ordinarily classed as agricultural land,

pasture, and the urban periphery, "novo alloteamento", on the image. This anomaly is even more apparent when the results of the digital classification are compared with the more accurate results obtained from the visual interpretation of the SPOT imagery.

The Maxver classification employed in the digital classification relies solely on training data derived from spectral characteristics of classes. An improvement on the result of the classification could, therefore, be the introduction of unsupervised classification procedures in order to determine the quality of the training samples for subsequent re-entry into the basic Maxver classification procedure as discussed earlier. Following the use of a logical combination of both unsupervised and supervised procedures suggested above, the classification could be further improved iteratively through the incorporation of textural analysis as a procedure for resolving only the confused classes observed in the Maxver classification.

The difficulty in eliminating spectral confusion may well be minimised by introducing multi-temporal data since this would eliminate much of the ambiguity between classes due to seasonal changes in spectral characteristics in landscape phenomena particularly in tropical environments. The use of digital terrain information suggested earlier is also another possible solution.

4.2 VISUAL INTERPRETATION OF SPOT IMAGE

The land use/cover classification data produced through the visual interpretation procedure are shown as Table 3 and Figure 4. The dominant land use/cover type identified in the visual interpretation procedure was pasture which accounted for 49.9% of the total image area. Built up areas comprising urban mixed, industrial, peri-urban and chacaras (rural) together accounted for 20%. Natural and planted vegetation were both equally distributed whilst quarry and poultry, both of which may be considered localised phenomena, amounted to only 0.2% (Table 3).

BLANK PAGE

TABLE 3. VISUAL CLASSIFICATION OF SPOT DATA FOR SJC

LAND USE CLASS		CLASSIFIED AREA (Km ²)	(%)
1. SETTLEMENT	1.1 Urban Mixed	58.1	11.4
	1.2 Industrial	8.4	1.7
	1.3 New Allotment	15.7	3.1
	1.4 Chacara (rural)	19.7	3.9
2. AGRICULTURE	2.1 Annual Crops	46.6	9.1
	2.2 Poultry	1.1	0.2
3. NATURAL VEGETATION	3.1 Mata Forest	23.1	4.5
	3.2 Gallery Forest	27.7	5.4
	3.3 Cerrado (Grassland)	7.2	1.4
4. PLANTED VEGETATION	4.1 Planted Forest	42.6	8.4
		254.7	49.9
5. PASTURE		1.1	0.2
6. QUARRY		4.4	0.8
7. WATER	7.1 Rivers		
	7.2 Lakes		
	Reservoirs Dams		
TOTAL		510.4	100.0

Source: GIS (SGI) data; INPE.

A major limitation of the SPOT imagery was the inability to discriminate between communication networks comprising roads, railway and pipeline on the one hand, and rivers on the other. This necessitated the introduction of data from existing topographical maps all of which were however outdated. It was also difficult to associate tonal patterns in areas of varying relief to the same class particularly pasture and forests due to the effects of shadow. Such observations were also made elsewhere (Gastellu-Echegory and Ducross-Gambart, 1991). It was, however, possible to identify localised phenomena particularly quarries due to the relatively high spatial resolution of the SPOT imagery.

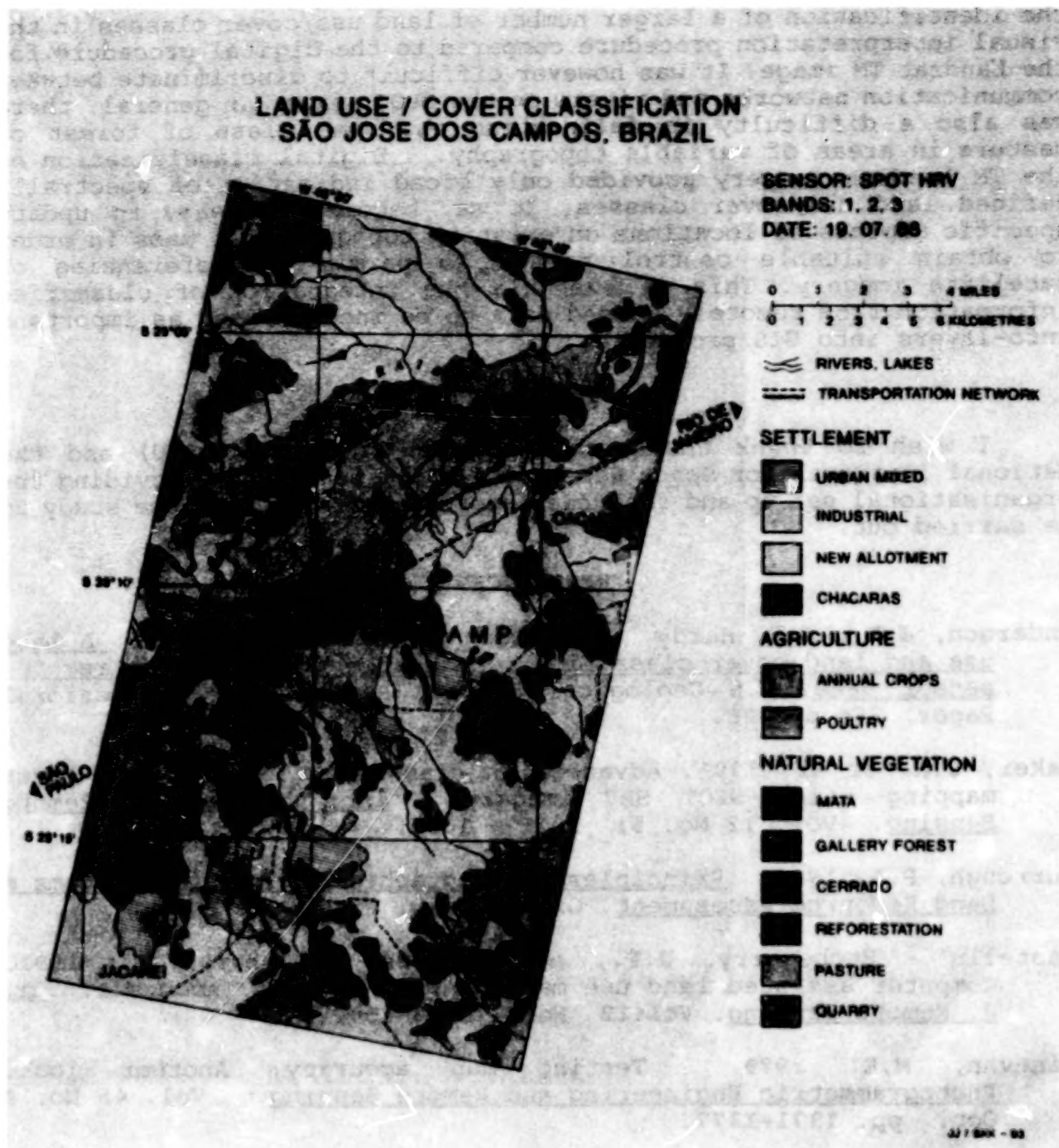


Figure 4. GIS - Generated Land Use map of Sao Jose dos Campos.
(Original copy in colour)

5. SUMMARY AND CONCLUSIONS

The study illustrated practical difficulties that were encountered in digital and visual classification of remotely sensed data of SJC and its integration into G.I.S. for generating a land use map of the municipality. The higher spatial resolution of SPOT enabled the identification of a larger number of land use/cover classes in the visual interpretation procedure compared to the digital procedure for the Landsat TM image. It was however difficult to discriminate between communication networks and rivers on the SPOT image. In general, there was also a difficulty in delineating the same class of forest or pasture in areas of variable topography. Digital classification of the TM Landsat imagery provided only broad indication of spectrally defined land use/cover classes. It may become necessary to update specific aspects of locations on existing topographical maps in order to obtain suitable control points to permit geo-referencing of satellite imagery. This will enable the integration of classified information from remotely sensed data to be incorporated as important info-layers into GIS procedure.

6. ACKNOWLEDGEMENT

I wish to thank the United Nations University (UNU) and the National Institute for Space Research (INPE), Brazil for providing the organisational set up and financial support which enabled the study to be carried out.

REFERENCES

- Anderson, J.R., E.E. Hardy, J.T. Roach and R.E. Witmer. 1976. A Land use and land cover classification system for use with remote-sensor data. U.S Geological Survey, Reston, Va. Professional Paper, 964 pp. 28.
- Baker, J.R. et al. 1991. Advances in classification for land cover mapping using SPOT HRV imagery. Int. Journal of Remote Sensing. Vol. 12 No. 5; 1071 - 1085.
- Burrough, P.A. 1986. Principles of Geographic Information Systems & Land Resource Assessment. Oxford Univ. Press. N.Y.
- Gastellu - Etchegorry, J.P., and Ducross - Gambart, D., 1991. Computer assisted land use mapping with SPOT in Indonesia. Int. J. Remote Sensing. Vol.12 No.7; 1493-1507.
- Ginevan, M.E. 1979. Testing map accuracy: Another look. Photogrammetric Engineering and Remote Sensing. Vol. 45 No. 0 Oct. pp. 1371-1377.
- Governo do Estado de Sao Paulo. 1989. "Recuperacao da qualidade ambiental da Bacia do Rio Paraiba do Sul: subsidios para o disciplinamento do uso e ocupacao do solo na basia hidrografica". Secretaria de Estado do Meio Ambiente.

- Instituto Nacional de Pesquisas Espaciais, INPE, 1991, Cobertura Vegetal e Uso da Terra, CODIVAP, Brasil.
- Markham, B.L. and Townshend, J.R.G. 1981. Land cover classification accuracy as a function of Sensor Spatial resolution. 15th Int. Symp. on Remote Sensing of Environment. Ann Arbor, Michigan: IRM p. 1075-1090.
- Mather, A.S. 1986 Land use. Longman, U.K.
- Mather, P.M. 1987 Computer processing of remotely sensed images: An introduction. John Wiley and Sons., U.K.
- Nellis, M. 1986 Remote Sensing for monitoring rangeland management strategies in the Kansas Flint Hills. Proceedings of the Symposium IV of International Society of Photogrammetry and Remote Sensing, and the Remote Sensing Society: mapping from a modern imagery, held in Ediburgh, Sept. 1986. (Nottingham: Remote Sensing Society) pp. 370-375.
- Pereira, M.N et al. 1988 "Atualizacao do uso da terra do municipio d Sao Jose dos Compos atraves de dados de Sensoriamento Remoto". INPE, 4479 - RPE/562.
- Toll, D.L. and Kennard, R.E 1984 Investigation of SPOT spectral and spatial characteristics for discriminating land use and land cover in Prince George's country, Maryland. Proceedings of SPOT Symposium; Scoltsdale, Arizona, 20-23 May, 1984. (Falls Church, Va: American Society for Photogrammetry). pp. 165-170.
- Van Genderen, J.L. and Lock, B.F. 1977. Testing land use map accuracy. Photogrammetric Engineering and Remote Sensing. 43: 1135-1137.
- Van Wijngaarden, W. and Kooiman, A. 1988. CUMU: Land cover and land use, In: I.T.C. Journal. 1988-1 Enschede, Netherlands. I.T.C. p. 60-66.
- Weaver, R. 1984. Integration of remote sensing data for moorland mapping. Proceedings of 10th Int. Conference of Remote Sensing Soc.: Satellite Remote Sensing: Preview and Review Reading, Sept. 1984 (Reading: Remote Sensing Society) p. 191-211

DETECTION OF RILL EROSION WITH DIGITIZED KFA-1000 SATELLITE PHOTOGRAPHS

Fred Ernst
University of Çukurova
TR-01330 Adana/Turkey

ABSTRACT

The purpose of this paper was to show the usefulness of a texture classification procedure to detect and classify erosion in a direct way. On the base of digitized SOYUZ-KFA-1000 satellite photographs the severity of rill erosion in the northern foothills of the Taurus-Mountains (South Turkey) could be quantified. The image was subdivided into grid cells for each the average density of rill erosion forms was computed. Since very different physical geographic conditions were included in the image, it can be stated that subtle contrast differences do not change the values in the classified image. The proposed method is best suited for detecting rill erosion of marginal lands.

1. INTRODUCTION

Generally, two different approaches for determining soil erosion using remote sensing can be distinguished:

- 1) A direct approach for actual soil erosion detection, where information about erosion is extracted directly from the image, and
- 2) An indirect approach for potential soil erosion assessment, based on the recording of different features of the land (mainly geology, soils, vegetation, land use).

Since the launch of LANDSAT-1 in 1972, many efforts have been made to observe soil degradation with the help of satellite data that has especially been successful in homogeneous landscapes like the Midwestern United States (Weismiller et al., 1983). But, due to the required high spatial resolution, especially if rill erosion is regarded, implementing of the direct approach was usually limited to the use of low-altitude photography (U.S. Department of Agriculture, 1951, Garg and Harrison, 1992). In view of the huge amount of analog data this processing hardly can be automated. This is a reason, research based on the use of low-altitude photography is hindered by the limited area that can be worked on.

Consequently, many investigations covering also greater areas have been carried out by implementing the indirect approach, especially with the help of satellite data. In this technique the purpose of the processing of remote sensing data is usually only to extract information about features like land use or vegetation cover. In a second step, this information serves as an input parameter to complex modelling. A common model represents the Universal Soil Loss Equation (USLE) (Wischmeier and Smith, 1978). The USLE - either in its original form or in some kind of modification - was used in the conjunction with high-altitude color and color infrared (CIR) photography (Morgan et al., 1978), simulated SPOT and LANDSAT-TM satellite data and CIR photography (Cihlar 1987), and LANDSAT-TM data (Traub 1990).

The aim of this research was to detect soil erosion by using the direct approach in conjunction with high-resolution satellite photography (SOYUZ-KFA-1000). A simple method based on a texture enhancement technique is shown that can ease detecting soil erosion in the form of rill erosion and estimate the area effected by.

2. STUDY SITE AND GROUND DATA USED

The geographic area of this research is situated within the rolling foothills of the Middle Taurus Mountains in South Turkey being of about 400 km² in size. Taurus Mountains are parts of the great eurasian alpine mountain chain they are characterized by a complexity of geologic formations, among them young tertiary little stabilized sediments.

Due to cutting and overgrazing since ancient times the vegetation has been degraded heavily. The remaining sparse vegetation of dwarf-shrubs and perennial herbs gives not sufficient resistance to the destroying forces of the water. The extension and severity of erosion in this region have reached a point that required the establishment of one greatest erosion control project of Turkey (Çakıt Çay Erozyon Control Projesi).

During the fieldwork at 97 test sites records concerning vegetation composition and structure, geology, soil, and erosion forms were collected (Ernst, 1993). The test sites were selected in a way that the representation of all landscape ecological units present in the research area were ensured. A careful comparison of the KFA-1000 satellite photograph with the field observation indicated that in some cases rill erosion forms up to about 1 m in width were visible on the photograph.

3. SATELLITE PHOTOGRAPH

Besides on the Salyut and Mir manned space stations, the Russian KFA-1000 camera has flown on certain unmanned Cosmos series low-altitude reconnaissance and Earth resources satellites. The characteristic of the camera is a format of 300 x 300 mm and a principal distance of 1000 mm. By use of the spectrazonal film SN 10 the spectral ranges of 570-670 nm and 670-800 nm are sensed. One photograph covers an area of 81 x 81 km and is delivered at a scale of 1 : 270 000. For this research a special photograph at a scale of 1 : 50 000 acquired on September, 8th 1990 with an excellent quality could be ordered. According to the distributor, SOYUZ KARTA, the photographs have a spatial resolution of about 5 m.

By reasons of the following image processing, the KFA-1000 photograph had to be digitized by scanning. The photograph was scanned using a HEWLETT-PACKARD-IIc scanner with a resolution of 400 dpi, corresponding 3.1 m at ground.

4. IMAGE PROCESSING

All image processing works were done within a PC-based ERDAS™-image processing system, version 7.5 (ERDAS, 1991). First of all, a principal component (PC) transformation (Jensen, 1986) was applied onto the data, for reasons of data reduction and in view of the expected two-dimensionality of the original three band data. The first PC-band accounted for 97,9% of the variance of the data indicating an intrinsic dimensionality of even one. Therefore, it seemed reasonable to use only the first PC-band during all the following image processing steps.

Texture classification can be broadly divided into two major categories. The first is texture segmentation, based on features with a high degree of spatial localization, usually with some form of edge detection. The second category refers to texture classification based on a discrimination function using several texture characteristics. The used classifying techniques lie in the domain of texture segmentation. To enhance line features the spatial frequency characteristics of an image have to be changed. The most common used process is convolution filtering (Jensen, 1986). Within the ERDAS™-image processing system a convolution kernel library is included that was modified for the purposes of this research.

Before any edge detector could be applied, the very high spatial frequency of the data appearing as "salt and pepper" dots had to be reduced. Most of the erroneous pixels could be eliminated by

subsequent applying of an 8 x 8 low-frequency kernel ($f_{ij} = 1$) and a 3 x 3 low-frequency kernel (Fig. 1). The resultant image is now cleaned from "noise" and can be introduced into the real edge detection process. For this purpose a laplacian edge detector (Rosenfeld and Kak, 1982) (Fig. 1) was used which smooths out or zeroes out areas of low spatial frequency, and creates a sharp contrast where spatial frequency is high. The resulting image consisted of edges and zeroes, but at the same time many single pixels that represented obviously "noise" were also generated. The majority of them could be removed with the help of the 5 x 5 low-frequency kernel ($f_{ij} = 1$).

The output of the above described enhancement procedure served as the base file (Fig. 2) for the estimation of erosion severity. To control the success of the applied enhancement techniques the base file was laid over the first PC-band. This way the enhanced line features could be compared visually with

1	1	1
1	2	1
1	1	1

0	1	0
1	-4	1
0	1	0

Figure 1: 3 x 3 low-frequency kernel (left) and Laplacian edge detector (right).



Figure 2: Subset of the enhanced image (1984 rows, 1488 columns) after applying the textural enhancement procedure.

erosion rills detected in the original, little enhanced image. The comparison revealed that nearly all rillerosion forms could be accentuated and that only some very subtle forms were lost. Works on a detailed accuracy assessment are currently under way.

During the last phase an automatic procedure had to be found, enabling the classification of the research area according to erosion severity. To find out the relative location of areas with accelerated erosion a common approach is the overlay of a grid (Garg and Harrison, 1992). In this research a grid with a cell size of 32 x 32 pixels (corresponding approximately 100 x 100 m) was chosen because it provided sufficient accuracy regarding the expanse of the research area. As erosion forms in the base file are represented by values of "one" and the other areas by values of "zero" the degree of erosion severity was computed by averaging the values of each cell separately. The applied algorithm can be written as

$$Mean = \frac{1}{N^2} \cdot \sum_{i=1}^{32} \sum_{j=1}^{32} IM_{(i,j)} \quad (1)$$

whereas "IM" is one cell.

The final processing step was the recoding of the values in each grid cell according to a four-graded erosion severity scheme. Four levels of erosion - nil, little, moderate, severe - were distinguished (Fig. 3). It has to be emphasized that this classification accounts only for the quantity of rill erosion but



Figure 3: Final output of the image subset showing 100 x 100 m cells with their corresponding soil severity classes.

will not give information about the quality of those forms.

5. DISCUSSION AND CONCLUSIONS

The erosion severity classification revealed that the occurrence of severe erosion coincided with areas of highly degraded vegetation, high slope inclination and of young tertiary geological formations.

The present work demonstrates the usefulness of detecting erosion with the help of digitized SOYUZ-KFA-1000 satellite photographs by applying a texture enhancement technique. This work was limited to the detection of rill erosion forms. The outstanding advantage of the KFA-1000 satellite photographs lie in its high spatial resolution. A comparison with the field data revealed, in some cases, indications of detectability of line features even up to 1 m in width. In a research conducted by the Geographic Technology Laboratory at Oregon State University (Rosenfeld et al., 1988) a measurement accuracy of 2 m for medium contrast targets with well-defined edges could be achieved. But these values seem to be somewhat theoretic. Scanning with very high resolutions reduced image quality, by introducing "noise" that hampered further processing. Referring to the used image it seemed more appropriate to set the lower limits by about 3 m. This limit represents not an absolute value. Rather, it should be modified according to the actual image quality.

Besides distortions caused by atmospheric conditions and the sensing system by itself, the detectability of line features will depend on contrast. The contrast can be influenced especially through the brightness of the substrate, cover of vegetation, and the degree of shadowing that will be determined by sun elevation, slope aspect and inclination. As in the used image quite different conditions (except for sun elevation) were included, it can be stated that subtle contrast differences did obviously not change the values in the classified image. Merely, erosion forms occurring in the area where very bright plaster stone cropped out a slight overvaluing were observed. For a more precise detection of rill erosion in areas characterized by a very heterogeneous substrate, a stratification of the image can be recommended. In respect to the coverage of vegetation the used classifier was sensitive to areas by dense vegetation, too. Anyway, severe rill erosion will usually not occur in such areas because a dense vegetation layer impedes erosion best.

An important limitation of the described method has to be cited. Because the classifier is not able to distinguish between different kinds of line features all these features will be regarded as erosion forms although they might represent roads, railways, field boundaries, channels, etc. This means that the application of this method will not give reasonable results in regions intensively cultivated if field sizes are not very big (to many field boundaries) and in suburban areas (too many roads and buildings).

This proposed method is best suited for detecting rill erosion in marginal lands. As in Turkey and many other Mediterranean countries such areas contribute most to the land degradation in this region. By means of the shown simple classifying technique areas of high erosion severity can be identified quickly. The relative low-priced image material (one KFA-1000 photograph covers nearly the same area as a SPOT image by a considerable lower price) allows the handling at a regional scale.

ACKNOWLEDGEMENT

The author would like to thank Mehmet Tankut, ISLEM GEOGRAPHIC INFORMATION SYSTEMS & ENGINEERING LTD., Ankara, for procurement of the KFA-1000 satellite photograph, and Hakan Çağlar, TÜBİTAK Marmara Research Centre, for development of a filtering algorithm.

REFERENCES

- Cihlar, Josef, 1987: A methodology for mapping and monitoring cropland soil erosion, *Can. J. Soil Sci.*, 67, 433-444.

- ERDAS, 1991: *Image processing and multivariate image analysis*, Atlanta.
- Ernst, F., 1993: Erfassung von Pflanzenformationen und Landschaftsschäden in der Südtürkei mit Hilfe von LANDSAT-Bilddaten. Diss. Albert Ludwigs-Universität Freiburg.
- Garg, P.K., and A.R. Harrison, 1992: Land degradation and erosion risk analysis in S.E. Spain: A geographic information system approach, *CATENA*, 19, 411-425.
- Jensen, J. R., 1986: *Introductory digital image processing: A remote sensing perspective*, Englewood Cliffs, New Jersey.
- Morgan, K. M., Lee, G. B., Kiefer, R. W., Daniel, T.C., Bubenzer, G. D., and J. T. Murdock, 1978: Prediction of soil loss on cropland with remote sensing, *J. Soil a. Water Cons.*, 33, 291-293.
- Rosenfeld, A., and A.C. Kak, 1982: *Digital picture processing*, 2. Edition, Vol. I and II, New York.
- Rosenfeld, C.L., Schultz, R.J., and A.J. Kimerling, 1988: Spatial resolution characteristics of Soyuz Karta products from the KFA-1000 camera. Oregon State University, Corvallis.
- Traub, K.-P., 1990: Erfassung der Naturraumgefährdung durch Bodenerosion mit Hilfe digital verarbeiteter Fernerkundungsdaten und Erhebungen im Gelände am Beispiel NW Madagaskar. Diss. Marburg.
- U.S. Department of Agriculture, 1951: *Soil survey manual*, Agr. Handbk. 18, Washington, DC.
- Weismiller, R. A., Van scoyoc, G. E., Pazar, S. E., Latz, K., and M. F. Baumgardner, 1983: Use of soil spectral properties for monitoring soil erosion. In *Soil erosion and conservation*, S.A. El-swaify, and W.C. Moldenhauer, (Eds.), Ankeny, Iowa, 119-127.
- Wischmeier, W.H., and D.D. Smith, 1978: *Predicting rainfall erosion losses. A guide to conservation planning*, Handbook 537, U.S. Dept. Agr., Washington, D.C..

TEMPORAL ENVIRONMENTAL CHANGES IN THE VICINITY OF ATATÜRK DAM USING REMOTE SENSING TECHNIQUES

E. Alparslan, M. T. Aygün and B. Bilge

TÜBİTAK, Marınara Research Centre, Space Technologies Department,
Gebze, 41470 Kocaeli, Turkey

ABSTRACT

Changes in accumulated water capacity in the Atatürk Dam and the water flow pattern around the dam area are studied using LANDSAT TM images acquired in March 1991 and April 1992. This investigation studies the extent of the dam area, water capacity, environmental effects etc. consequent to the construction of the dam using the above LANDSAT imageries.

1. INTRODUCTION

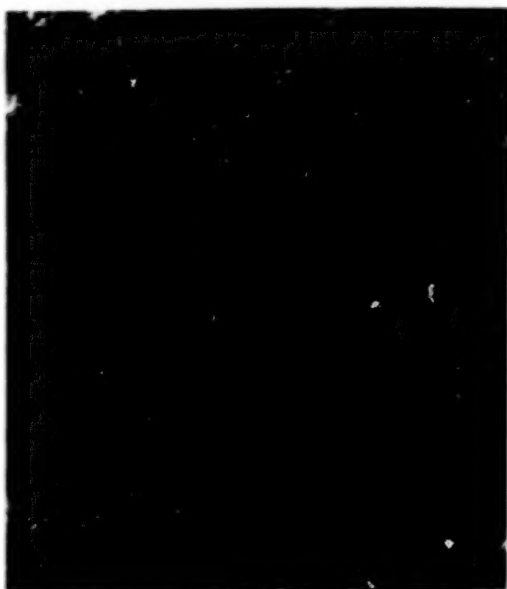
Atatürk Dam is the most significant part of the South Eastern Anatolian Project, and was constructed across Euphrates river in 1990 for irrigation and hydroelectric power, especially for the development of the Eastern region. This dam allows an average annual water flow of $26,654 \text{ km}^3$ and has a total reservoir capacity of 48.7 km^3 and is of considerable socio-economic importance to Turkey in the years to come.

The study area consisting of 2284×2616 pixels covers a geographical area of $5,377.45 \text{ km}^2$ bound between 38 to 39 East longitude and 37 to 38 North latitude. Band 5 image of the study area in years 1991 and 1992 are given in Fig. 1. The histograms of the band 4 images for years 1991 and 1992 are given in Fig. 2.

Classification algorithms applied to the study area are discussed in Sec. 2, while the results obtained are given in Sec. 3.

2. CLASSIFICATION

Of the Landsat TM bands, bands 5, 4 and 3 are used for land use classification purposes because these bands are sufficient for the following reasons: Band 5 in the near-infrared range, namely, 1.55-1.75 microns is preferable from the point of view of plants and soil humidity discrimination; band 4, also in the near-infrared range between 0.76-0.90 microns helps determine the biomass content of vegetation; and band 3 in the visible range between 0.63-0.69 microns helps distinguishing between different plant types because of its sensitivity to chlorophyll in the plants. (NRSC Information Sheet, 1989)

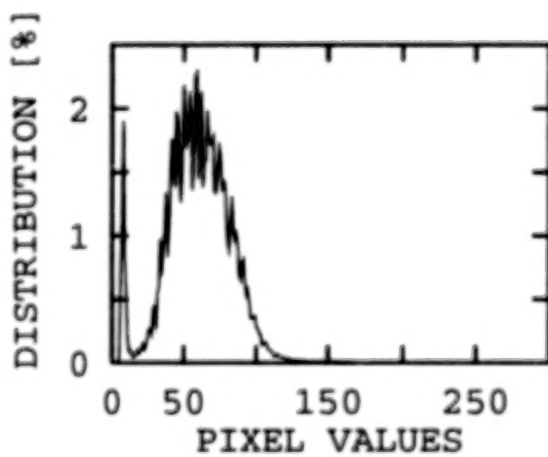


(a)

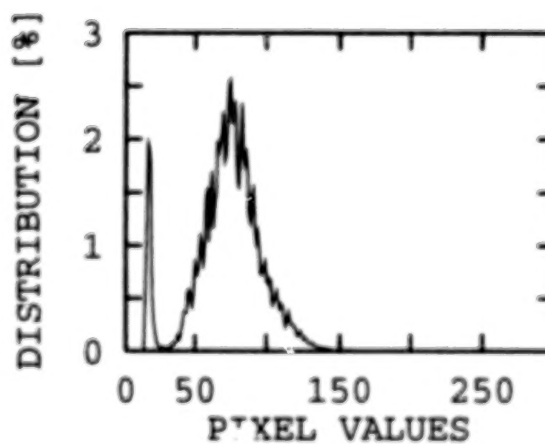


(b)

Figure 1. Landsat TM 5 Image of the Study Area
a) March 1991 b) April 1992



(a)



(b)

Figure 2. Histograms of the Band 4 Images
a) March 1991 b) April 1992

For our case study, twelve classes, which can be visually identified are considered. These classes are namely water, snow, snowy land, two different wheat types, three different rocky land types, two dark soil types and two light colored soil types. Clustering, thresholding and clustering the main principal components are the techniques employed for land use classification and these are elaborated in Sec. 2.1-3.

2.1 CLUSTERING

An unsupervised classification algorithm is applied to the study area to identify twelve classes mentioned above. During the clustering operation, only about ten percent of the whole image has been sampled for preassessment. Then, the full data is used for the final results. In the subsampled image, seeds for twelve classes are generated by picking random pixels. The pixel values for seeds are used as start values for the class means. Each pixel is clustered to the seed yielding the minimum distance. Because of the change in the population of the classes, new means are calculated for each class. Then the pixels are clustered to these new class means. These iterations are continued until the relative change between the new and the previous class means becomes insignificantly small.

2.2 THRESHOLDING

As another approach in discrimination of land use types, visual interpretation has been done on the satellite imagery and different class types are identified by their multispectral signatures. Thresholding method is employed to isolate a class and compare its population with that resulting from unsupervised classification to arrive at a conclusion. Pixels within the multispectral signature are painted black (0), while the rest is kept white (255) to obtain a black and white image to emphasize a class. The results obtained for water surfaces are respectively given in Fig. 4 for years 1991 and 1992.

2.3 CLUSTERING KL-TRANSFORM

Principal components or KL transformation is an orthogonal linear transformation that compresses multidimensional data into fewer dimension without significant loss of information content. This transformation assigns the random variance or noise to eigenvectors with lowest variance (Bartolucci, L. A., et al., 1983)

Clustering algorithm elaborated in Sec. 2.1 is applied to the first three principal components obtained compressing all TM bands excluding the thermal band 6. The results obtained are compared to the techniques in Sec. 2.1-2.

3. RESULTS

The acreage values obtained for water surface and crop in the study area for years 1991 and 1992 are given in Table 1.

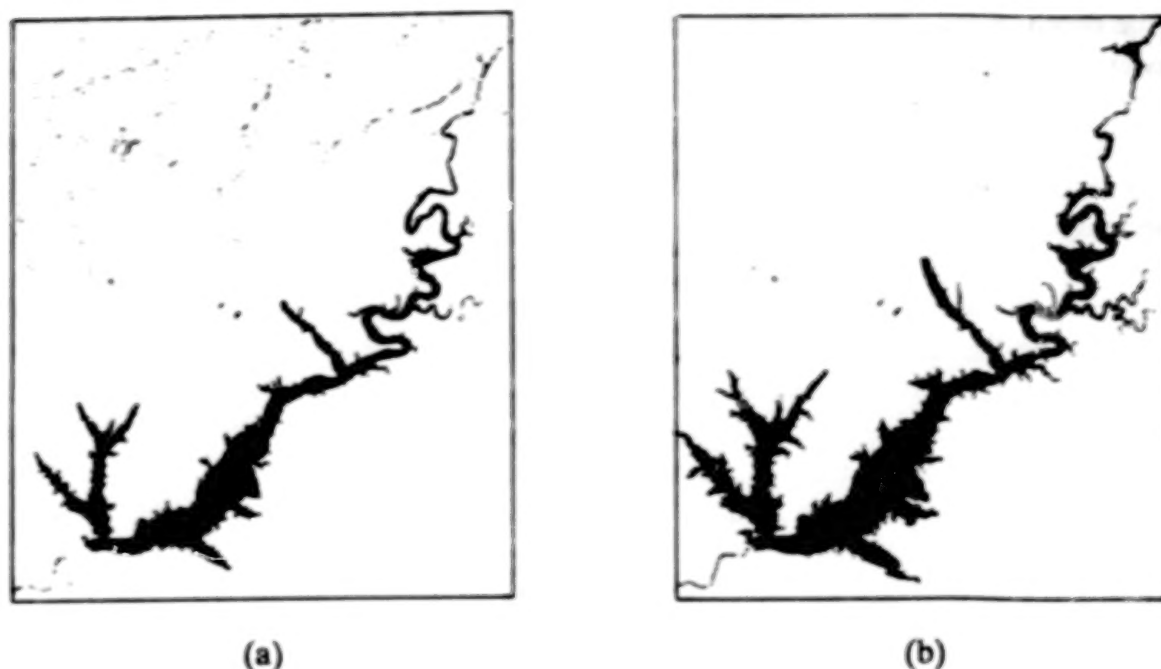


Figure 3. Water Surfaces after Thresholding
a) March 1991 b) April 1992

Table 1. Water Surface and Crop Areas for Different Classification Algorithms

	Clustering (Sampling % 100)		Clustering (Sampling % 10)		Thresholding		KL-Transform	
	Water [ha]	Wheat [ha]	Water [ha]	Wheat [ha]	Water [ha]	Wheat [ha]	Water [ha]	Wheat [ha]
1991	29312	80973	33183	93935	29364	89467	32677	89763
1992	45476	58272	45880	65817	45373	64331	46522	64436
Ratio (92/91)	1.56	0.72	1.38	0.71	1.54	0.72	1.42	0.72

The results obtained through clustering of 10 % subsampled data indicate a 38 % increase in water surface and a 29 % decrease in crop acreage in the year of 1992 compared to the year of 1991.

Thresholding method was applied on TM band 4 for water surfaces and TM band 5 for crop. For the year 1991, the water intensity varies between 5 to 15 while the crop intensity varies between 40 to 58. For the year 1992, the water intensity varies between 13 to 23 while the crop intensity lies between 55 to 75. The LANDSAT TM spectral signatures obtained during 1991-92 in the study area clearly indicate changes in terms

of the depth of the dam. The results obtained through this method are close to that of clustering.

Finally increase in water surface and decrease in crop acreage are found to be 42 % and 28 % respectively when three main principal components of full data is employed during clustering.

The maximum, minimum and average increase and decrease in water surface and crop acreage found by the employed three techniques are given in Table 2. When average values are taken into consideration, increase in water surface is 47 % and decrease in crop acreage is 28 % during the period of investigation. When one considers the fact (Balaban, 1988) that the agricultural land is not planted every year and crop land in 1991 becomes fallow land in 1992 and vice versa, the crop plantation area is approximately 152,000 ha and covers 28% of the study area. For the year 1992, water held in the dam is about 8.5 % of the study area.

Table 2. Max., Min., and Average Changes in Water Surface and Crop Acreage

	Water			Wheat		
	Maximum [ha]	Minimum [ha]	Average [ha]	Maximum [ha]	Minimum [ha]	Average [ha]
1991	33183	29312	31134	93935	80973	88535
1992	45373	46522	45883	66817	58272	63464
Ratio (92/91)			1.47			0.72

This study shows that there has been considerable change in the quantity and extent of the water in the dam during the period of investigation, as well as the environment around the dam site. Consequent to the construction of the dam, the vegetation cover and the surrounding land around the dam site have been considerably affected, creating environmental degradation. Poor vegetation cover, bare soils and dense rocks in the vicinity of the dam area creates a great potential for land erosion. Soil carried by wind and rivers will fill the dam in much shorter time than its expected life time. This event endangers the country's economy and serious protection measures should immediately be taken.

Different techniques employed during this study indicate that clustering KL components yields best results for change detection in water surface and crop acreage. The advantage of KL transform over other methods is because uncorrelated data containing the most information from all six TM bands is employed during clustering.

Using temporal Landsat TM satellite imagery, changes in water surface and vegetation cover in the vicinity of Atatürk dam can be successfully measured. Remote sensing techniques yield more successful results compared to conventional techniques in studying temporal environmental changes as shown in this study.

REFERENCES

- Balaban, A., 1988: South Eastern Anatolian Project Integrated System Planning and Applications Problems, *GAP Agricultural Development Symposium*, Ankara.
- Bartolucci, L. A., et al., 1983: Evaluation of the Radiometric Quality of the TM data Using Clustering, Linear Transformations and Multispectral Distance Measures, *Proc. Landsat 4 Scientific Characterization Early Results Symposium*, NASA Goddard Space Flight Centre, Greenbelt, MD.
- National Remote Sensing Centre(NRSC) Information Sheet, 1989

APPENDIX B
AUTHOR INDEX

000542

APPENDIX B

AUTHOR INDEX

A

Al-Dakan, A., 946
Aldrich, William S., 430
Al-Khodairy, F., 946
Alparslan, Erhan, A-118
Al-Tukhi, Colonel Majdi H., 946
Althouse, Mark L. G., 456
Anderson, Donald E., 562
Anderson, James M., 93
Anderson, John E., 683, 945
Anderson, M., 89
Anderson, Richard, 936
Arnone, R., A-70
Atanassov, Valentin, A-3
Aygün, M. T., A-118

B

Babichenko, Sergei M., 696
Baker, James R., 230
Banninger, C., 878
Barbour, Garth, 880
Barr, Samuel, 477
Basedow, Robert W., 430
Ben-Dor, E., 582
Berger, M., 116
Bilge, B., A-118
Bishop, Kevin D., 133, 775
Blom, Ronald G., 848
Boardman, Joseph W., 302
Boge, Walter G., 59
Bonnet, B., 604, 649
Bostater, Charles, 387, 673
Boycheva, Valentina, A-3
Brockhaus, John A., 805

C

Campbell, James B., 375
Carbary, J. F., 562
Catuogno, Graciela Alicia, 641
Chang, Chein-I, 267, 456
Chang, S.-H., 191
Chedin, A., 604, 649
Chen, Shyh, 635
Chen, Zhikang, 785
Cherny, Igor V., A-89
Chernyavskiy, G. M., A-89
Cheshire, Heather, 805
Choe, Howard C., 246
Chovan, J.D., 246

Chrien, Thomas G., 229
Christensen, Andrew B., 539
Chursin, Alexey A., 604, 649
Conel, James E., 229
Contreras, Amando Leyva, 570
Corl, Phyllis A., 749
Coyle, Chris, 936
Crippen, Robert E., 848
Crowley, G., 562
Curtis, John O., 204
Curtiss, Brian, 195

D

Dalati, Moutaz, 859
Davis, Curtiss O., 661
Day, Richard H., 705
de Jong, Steven M., 842
De Jong, Eric M., 848
Dekker, A. G., 697
Demro, James C., 180
Dilworth, D.S., 612
Dombrowski, Mark, 105
Dudelzak, Alexander E., 696
Duggin, Michael J., 287, 518
Dymond, Kenneth F., 549

E

Eastes, John W., 516
Ediriwickrema, Jayantha, 805
Elderding, George T., 168
Elvidge, Christopher D., 785
Erdman, Carey D., 256, 468
Ernst, Fred, A-112
Estep, Lee, A-70
Estes, John E., 77
Evans, Timothy D., 497

F

Fabi, Ricardo Peralta y, 570
Falcone, Vincent J., 628, 636
Falkov, Edward, 919
Farr, Thomas G., 225, 848
Farrand, William H., 267, 430, 908
Farrington, G.A., 697
Fené, Michael, 149
Fischer, J., 89
Formanjuk, I.M., 919
Forsythe, Jennifer L., 312

G

Gastil, Mary, 691
 Gillespie, Alan R., 312
 Goetz, Alexander F. H., 195, 582
 Gogohia, V. V., A-31
 Golovko, V. F., 604, 649
 Gonzalez, Elisa C., 333
 Granger, J. A., 133, 775
 Granville, V., 310, 311
 Green, Robert O., 229
 Griffin, Michael K., 628, 636
 Gulyaeva, Tamara L., A-38

H

Hall, Carlton, 387
 Hannan, M.A., 946
 Harding, David J., 225
 Harsanyi, Joseph C., 267, 456, 908
 Hatzopoulos, John N., 870
 Hejl, Joseph M., 267
 Henley, Ponder, 497
 Hinnrichs, Michele, 893
 Hinrichs, John, 160
 Hoffmeyer, Paul D., 204
 Holloway, John H., 216
 Holt, Jerald R., 168
 Hoogenboom, H. J., 697
 Horton, Keith A., 160
 Hoskins, G., 813
 Hothem, D., 468
 Husson, Nicole, 604, 649

I

Iliescu, Maria Colette, A-50
 Irvine, John M., 468, 880
 Isaacs, Ronald G., 628, 636

J

Jansen, Wally T., 491, 785
 Jewett, E. L., 133, 775
 Johnson, James R., 594
 Johnson, L., 878

K

Kaufmann, Hermann, 116
 Kelley, Owen, 549
 Kennedy, B.C., 612
 Keramidus, G., 706
 Khorram, Siamak, 805
 Klingelé, E. E., 123

Kosinov, V.A., 919
 Kovalyov, Alexander, 869
 Krumov, Alexandar, A-3
 Kruse, Fred A., 44
 Kufogbe, Sosthenes Kwadzo, A-100
 Kurar, Hikmet, A-79
 Kuzma, Thomas J., 246

L

Lamb, Andrew, 673
 Lamicela, J., 287
 LaPotin, Perry J., 416
 Lazofson, Laurence E., 246
 Leachtenauer, Jon, 468
 Leighty, Brian D., 749
 Leighty, Robert D., 749
 Lillycrop, J., A-70
 Liu, Xiangdong, 375
 Lo, Juliana T., 496
 Lucey, Paul G., 160
 Lukes, George E., 749
 Lynch, David K., 539

M

Ma, Wei-Ming, 673
 Massie, Mark, 893
 Maver, Lawrence A., 468
 Maxwell, J.R., 230
 McCord, Thomas B., 149, 312, 496
 McCoy, Robert P., 549
 McKim, Harlan L., 55, 416
 McRae, Kevin, 705
 Meißner, M., 116
 Meier, Robert R., 549
 Melack, John M., 691
 Melhuish, T. E., 191
 Meng, C.-I., 562
 Mertz, Frederick C., 595
 Metzler, Michael D., 230
 Mohr, Ellen, 468
 Molinelli, Eugene, 707
 Mooradian, Gregory C., 149
 More, Keith A., 216, 612
 Morrison, D., 562
 Muncill, G., 707
 Muramoto, Jo Ann, 936

N

Narayanan, Ram M., 204
 Natarajan, Krishnaier, A-79
 Nikolov, H., A-10, A-11
 Norris, Charles, 635

O

Odenweller, Julic, 468
Orban-Ferauge, F., 310, 311

P

Parson, L., A-70
Pascucci, Richard F., 761
Paxton, L. J., 562
Peterson, D., 878
Petkov, Doyno, A-10, A-16
Philpot, W. N., 287
Pickle, John D., 628, 636
Picone, J. Michael, 549
Podgorny, Igor A., A-59
Poryvkina, Larisa V., 696
Preston, E.B., 246
Provancha, Mark, 387

R

Ramsey III, Elijah W., 705
Rasson, J. P., 310, 311
Ray, Terrill W., 848
Rebbman, Jan, 387
Resmini, Ronald G., 149, 312
Rhoades, Danny W., 204
Rhoads, Donald C., 936
Richards, John A., 62
Richter, R., 287
Rickard, Lee J., 89, 706, 813
Riehl Jr., Ken, 256, 468
Rinker, Jack N., 5, 749
Roads, John, 635
Rock, Barrett N., 737
Rodekoeh, Donn, 954
Romick, G. J., 562
Russell, Edgar E., 168
Rybach, L., 123

S

Sansal, B., A-20
Satterwhite, M.B., 945
Schaum, Alan, 278, 312
Schwarz, G. F., 123
Scott, N. A., 604, 649
Serir, A., A-20
Shapiro, A. T., 582
Sheikho, Kamel M., 929
Shettigara, Vittala K., 403
Sjaved, Gustav M., A-59
Silleos, N., 821
Simental, Edmundo, 333
Simmons, Rulon, 468

Skroch, A., 813
Sorensen, B. M., 191
Spencer, J., 706
Staenz, Karl, 365
Stocker, Alan, 278
Stoner, William W., 430
Sumerling, Gordon M., 403
Sun, X., 93
Sunshine, Jessica M., 312
Susner, Nicholas J., 496
Syrén, Per, 836

T

Teillet, P. M., 365
Theisen, Arnold F., 737
Thomas, Ronald J., 549
Toulios, Leonidas G., 821
Tyuterev, Vl. G., 604, 649

V

van den Bosch, Jeannette, 229
Vasilyev, Oleg B., 570
Velasco, Inés, 641
Velazquez, Agustin Muhlia, 570
Vieglais, D., 387

W

Walter, Fred, 658
Wang, James, 628, 636
Ward, Roger H., 936
Weber, E.J., 612
Weber, Paul, 635
Welch, Ronald M., 570
Westmoreland, Sally, 595
Williams, D. J., 365
Williams, Tim, 160
Witherspoon, Ned H., 216
Wolf, Emil, 71
Woody, Loren M., 180

Y

Yee, J.-H., 562

Z

Zdravev, T., A-10, A-11
Zebker, Howard A., 225
Zywicki, Randall W., 216, 612

APPENDIX C
LIST OF ATTENDEES

000546

APPENDIX C

LIST OF ATTENDEES

A

Al-Shehri, Mohammed Abdullah
Civil Defense Saudi Arabia
P.O. Box 88629
Riyadh 11672, Saudi Arabia
Tel: 966 1 476 0647
Fax: 966 1 477 6579

Al-Tukhi, Majdi H.
Centre for Studies and Research
Directorate of Civil Defence
P.O. Box 88629
Riyadh, Saudi Arabia
Tel: 966-1-232-4776
Fax: 966-1-232-4776

Alessandro, Lawrence P.
ORD/ISRG/ETD
Mail Stop 4132
Washington, DC 20505
Tel: 703/351-2708
Fax: 703/527-8557

Alexander, Robert J.
ORD
6 N. Light Street
Lovettsville, VA 22080
Tel: 703/351-2743

Althouse, Mark L.C.
US Army Edgewood Research,
Development and Engineering Center
SCBRD-RTE
Bldg E5554
APG, MD 21010-5423
Tel: 410/671-3021
Fax: 410/671-4925

Alvarez, Roman
Instituto de Geografia, UNAM
Ciudad Universitaria
Circuito Exterior
AP. 20-850, CP. 01000, Mexico
Tel: 011 525 6224340
Fax: 011 525 6162145

Amlin, Douglas
ASC/REQR
WP AFB, OH 45433
Tel: 513/255-8533
Fax: 513/255-7971

Anderson, Donald E.
The Johns Hopkins University
Applied Physics Laboratory
Johns Hopkins Road
Laurel, MD 20723-6099
Tel: 301/953-6174
Fax: 301/953-6670

Anderson, James M.
University of Dundee
Department of Applied Physics and
Electronic and Manufacturing Engineering
Dundee, DD1 4HN, Scotland
Tel: 0382 344546
Fax: 0382 202830

Anderson, John E.
Corps of Engineers
US Army Topographic Engineering Center
7701 Telegraph Road
Alexandria, VA 22315-3864
Tel: 703/355-3203
Fax: 703/355-3176

B

Baker, James R.
ORD/ETD/627 Ames
M.S. 4132
Washington, DC 20505
Tel: 703/231-4421
Fax: 703/231-7532

Balick, Lee K.
EG&G Energy Measurements, Inc.
MS RSL-19
P.O. Box 1912
Las Vegas, NV 89125
Tel: 702/295-8603
Fax: 702/295-8627

Banninger, C.
Institute for Image Processing and
Computer Graphics Joanneum Research
Wastiangasse 6
A-8010 Graz, Austria
Tel: 1143 3168020735
Fax: 1143 3168020720

242000

Barr, Samuel
US Army Topographic Engineering Center
CETEC-TD-RS
7701 Telegraph Road
Alexandria, VA 22315-3864
Tel: 703/355-3811
Fax: 703/355-3176

Beauregard, John G.
Rockwell International Corporation
2800 Westminster Boulevard
Mail Code SY05, Bldg 90
Seal Beach, CA 90740
Tel: 310/797-4810
Fax: 310/797-1469

Belisle, James
Office of Research and Development
Washington, DC 20505
Tel: 703/351-2540
Fax: 703/527-8357

Bell, Wilbur R.
Office of Research and Development
1000 Independence Avenue, SW
Washington, DC 20585
Tel: 202/586-8859
Fax: 202/586-0485

Birk, Ronald J.
Sverdrup Technology, Inc.
Bldg 1210, South Lobby
Stennis Space Center, MS 39529
Tel: 601/688-2988
Fax: 601/688-3838

Bishop, Kevin D.
Lockheed Palo Alto Research Lab
Bldg 201, Dept 92-80
3251 Hanover Street
Palo Alto, CA 94304
Tel: 415/424-2985
Fax: 415/354-5820

Blackmer, Tracy
University of Nebraska
East Campus
120 Keim Hall
Lincoln, NE 68583
Tel: 402/472-1594

Boardman, Joseph W.
University of Colorado
Center for the Study of Earth from Space
Campus Box 216
Boulder, CO 80309
Tel: 303/492-0594
Fax: 303/492-5070

Boge, Walter E.
Director
US Army Topographic Engineering Center
CETEC-ZA
Cude Building
7701 Telegraph Road
Alexandria, VA 22315-3864
Tel: 703/355-2600
Fax: 703/355-3154

Borstad, Gary
Borstad Associates Ltd
114-9865 West Sanich Road
Sidney, BC Canada V8L 3S1

Bostater, Charles R.
Florida Institute of Technology
Department of Oceanography and
Environmental Science and Ocean Engineering
150 West University Boulevard
Melbourne, FL 32901
Tel: 407/779-1708
Fax: 407/984-8461

Bowler, Dennis
TRW, Inc.
One Space Park, R1/2054
Redondo Beach, CA 90278
Tel: 310/812-9788
Fax: 310/812-0109

Bowman, Anu
Space Application Corporation
4001 North Fairfax Drive, Suite 250
Arlington, VA 22203
Tel: 703/524-0701
Fax: 703/524-2853

Brockhaus, John
North Carolina State University
Computer Graphics Center
Box 7106
Raleigh, NC 27695-7106
Tel: 919/515-3433
Fax: 919/515-3439

Brown, Christopher A.
University of Oklahoma
Health Sciences Center
Department of Occupational
and Environmental Health
801 NE 13th Street, Room 413
Oklahoma City, OK 73190
Tel: 405/271-2070
Fax: 405/271-1971

000548

Bruzewicz, Andrew J.
US Army Corps of Engineers
Remote Sensing/GIS Center
72 Lyme Road
Hanover, NH 03755-1290
Tel: 603/646-4372
Fax: 603/646-4750

Bryski, Daniel D.
Night Vision & Electronic Sensors Directorate
AMSEL-RD-NV-T
Fort Belvoir, VA 22060-5677
Tel: 708/704-3285

Burman, Jerry A.
GTE Government Systems
31717 La Tienda Drive
Box 5027/MS 140
Westlake Village, CA 91359-5027
Tel: 818/706-5636
Fax: 818/706-5050

C

Campbell, James B.
Virginia Tech
Department of Geography
Blacksburg, VA 24061-0115
Tel: 703/231-5841
Fax: 703/231-6367

Catuogno, Graciela Alici
Universidad de Buenos Aires
Departamento de Ciencias de la Atmosfera
Pabellon 2, Ciudad Universitaria
1428 Numez
Buenos Aires, Argentina
Tel: 54-1-750-0051
Fax: 54-1-759-0833

Chrien, Thomas G.
Jet Propulsion Laboratory
Mail Stop 306-336
4800 Oak Grove Drive
Pasadena, CA 91109
Tel: 818/354-2870
Fax: 818/393-4406

Coleman, Gary D.
Hughes Aircraft Company
1100 Wilson Boulevard
Arlington, VA 22209
Tel: 703/284-4330

Colwell, John E.
Naval Research Laboratory
Code 9120
4555 Overlook Avenue, SE
Washington, DC 20375-5320
Tel: 202/279-2422
Fax: 202/404-8240

Comati, Jerry C.
USARDSG-UK
PSC 802, Box 15
FPO AE 09499-1500,
Tel: 44 071 514 4908
Fax: 44 071 724 1433

Connolly, Jr., John I.
OptiMetrics
9906 Manet Road
Burke, VA 22015
Tel: 703/503-3019
Fax: 703/503-3023

Cook, Mark K.
Texas Instruments, Inc.
P.O. Box 405
M/S 3473
Lewisville, TX 75063
Tel: 214/462-4844
Fax: 214/462-5919

Corl, Phyllis A.
US Army Topographic Engineering Center
CETEC-SS
Cude Building (#2592)
7701 Telegraph Road
Alexandria, VA 22315-3864
Tel: 703/355-3313
Fax: 703/355-3176

Coyle, Chris
Science Applications International Corporation
11803 Sorrento Valley Road
San Diego, CA 92121-1006
Tel: 619/792-2123
Fax: 619/792-2635

Croft, Frank
ERDAS, Inc.
2801 Buford Highway, Suite 300
Atlanta, GA 30329
Tel: 404/248-9000
Fax: 404/248-9400

000000

Curtiss, Brian
Analytical Spectral Devices, Inc.
4760 Walnut Street, Suite 105
Boulder, CO 80301
Tel: 303/444-6522
Fax: 303/444-6825

D

Dalati, Moutaz
General Organization for Remote Sensing
Director of International and Scientific Affairs
Haldouni-Street #4
Damascus, Syria
Tel: 963 11 2218764
Fax: 963 11 3320255

Davies, Donald
TRW, Inc.
One Space Park
M.S. 01/1220
Redondo Beach, CA 90278
Tel: 310/812-0293
Fax: 310/812-5160

Davies, Mike
Earth Observation Magazine
13741 E. Rice Place #135
Aurora, CO 80015
Tel: 303/690-2242
Fax: 303/690-2522

Davis, Curtiss O.
Naval Research Laboratory
Code 7212
Washington, DC 20375
Tel: 202/767-9296
Fax: 202/404-7453

de Jong, Steven
University of Utrecht
Department of Physical Geography
P.O. Box 80.115
3508 TC Utrecht, The Netherlands
Tel: 31 30 532749
Fax: 31 30 540604

Deepak, Adarsh
Science and Technology Corporation
101 Research Drive
Hampton, VA 23666
Tel: 804/865-1894
Fax: 804/865-1294

Demro, James C.
Santa Barbara Research Center
75 Coromar Drive
Goleta, CA 93117
Tel: 805/562-4016
Fax: 805/562-7149

Dombrowski, Mark
Surface Optics Corporation
9929 Hibert Street, Suite C
San Diego, CA 92131
Tel: 619/578-8910
Fax: 619/578-0484

Dudelzak, Alexander
Canadian Space Agency
Space Technology
6767 Route de l'Aéroport
St. Hubert, Quebec, J3Y 8Y 9 Canada
Tel: 514/926-4619
Fax: 514/926-4613

Duggin, Michael J.
State University of New York
College of Environmental Science and Forestry
308 Dray Hall
Syracuse, NY 13210
Tel: 315/470-6633
Fax: 315/470-6958

Dymond, Kenneth F.
Naval Research Laboratory
E.O. Hulburt Center for Space Research
Code 7623
Washington, DC 20375
Tel: 202/767-2816
Fax: 202/767-9388

E

Eastes, John W.
US Army Topographic Engineering Center
7701 Telegraph Road
Alexandria, VA 22315-3864
Tel: 703/355-2919
Fax: 703/355-3176

Els, Kenneth E.
Colorado State University
CIRA Foothills Campus
Ft. Collins, CO 80523
Tel: 303/491-8448
Fax: 303/491-8241

Elerding, George T.
Santa Barbara Research Center
75 Coromar Drive
Goleta, CA 93117
Tel: 805/562-7136
Fax: 805/562-7149

Elvidge, Christopher D.
Desert Research Institute
Biological Sciences Center
7010 Dandini Boulevard
Reno, NV 89506-0220
Tel: 702/673-7324
Fax: 702/673-7397

Embutsu, Ichiro
University of California at Santa Barbara
Geography-NCGIA
5704 Ellison Hall
Santa Barbara, CA 93106
Tel: 805/893-7234
Fax: 805/953-7234

Erdman, Carey D.
ITEK Optical Systems
10 Maguire Road
Lexington, MA 02173
Tel: 617/276-2462
Fax: 617/276-3306

Estes, John E.
US Geological Survey
516 National Center
Reston, VA 22092
Tel: 703/648-5752
Fax: 703/648-5792

Evans, Timothy D.
US Army Topographic Engineering Center
CETEC-TD-RS
7701 Telegraph Road
Alexandria, VA 22315-3864
Tel: 703/355-3183
Fax: 703/355-3176

Everding, Charles
Ball Aerospace Systems Division
2875 Presidential Drive, Suite 180
Fairborn, OH 45324-6269
Tel: 513/429-5005
Fax: 513/429-1687

F

Falkov, Edward
State Research Institute
of Aviation Systems (GosNIAS)
7 Vikorenko Str.
Moscow 125319, Russia
Tel: 7 095 157 9295
Fax: 7 095 157 3127

Fischer, Erich M.
Brown University
Department of Geological Sciences
Box 1846
Providence, RI 02912
Tel: 401/863-3485
Fax: 401/863-3978

Fithian, Robert
UTD, Inc.
8560 Cinderbed Road, Suite 1300
Newington, VA 22122
Tel: 703/321-0008
Fax: 703/321-7521

G

Gallo, Laurene
Booz, Allen and Hamilton, Inc.
1953 Gallows Road
Vienna, VA 22180
Tel: 703/902-7000

Gardner, Paul
Excalibur Technologies
2233 Faraday, Suite K
Carlsbad, CA 92008
Tel: 619/438-6604
Fax: 619/438-5418

Gastil, Mary
University of California
Marine Science Institute
Santa Barbara, CA 93106
Tel: 805/893-3879
Fax: 805/893-4724

Gini, Chris
Hughes
1451 23rd Street
Manhattan Beach, CA 90266
Tel: 310/616-8663
Fax: 310/545-4449

Ginsberg, Irving W.
ERIM
P.O. Box 134001
Ann Arbor, MI 48113-4001
Tel: 313/994-1200
Fax: 313/994-4630

Goetz, Alexander
University of Colorado
CSES/CIRES
Boulder, CO 80309-0216
Tel: 303/492-5086
Fax: 303/492-5070

Gomez, Richard
Associate Director of Technology
US Army Topographic Engineering Center
CETEC-TD
Cude Building
7701 Telegraph Road
Alexandria, VA 22315-3864
Tel: 703/355-2600
Fax: 703/355-3154

Gonzalez, Elisa C.
US Army Topographic Engineering Center
7701 Telegraph Road
Alexandria, VA 22315-3864
Tel: 703/355-2538
Fax: 703/355-3176

Graham, Edward Christopher
CSIRO Office of Space Science and Application
(COSSA)
ANU Campus, Acton
Canberra, Australia, 2601
Tel: 61 6 279 0806
Fax: 61 6 279 0812

Granger, Jay
Lockheed Missiles and Space Co., Inc.
3251 Hanover Street
Dept 9280, Bldg 201
Palo Alto, CA 94304
Tel: 415/424-2088
Fax: 415/354-5820

Green, Robert O.
Jet Propulsion Laboratory
California Institute of Technology
Mailstop 306-438
4800 Oak Grove Drive
Pasadena, CA 91109
Tel: 818/354-9136
Fax: 818/393-4406

Grim, Larry
Mesh, Inc.
802 Bethel Road
Oxford, PA 19363
Tel: 610/932-3709
Fax: 610/932-3413

Gursky, Herbert
Naval Research Laboratory
Code 7600
4555 Overlook Avenue, SW
Washington, DC 20375-5352
Tel: 202/767-6343
Fax: 202/404-7296

H

Hack, Thomas
San Diego State University
San Diego, CA 92182-0381
Tel: 619/594-5437
Fax: 619/594-4938

Hall, Carlton R.
The Bionetics Corporation
Mail Code BIO-2
JFK Space Center, FL 32899
Tel: 407/853-3281
Fax: 407/853-2939

Hansen, John V.E.
US Army Topographic Engineering Center
Remote Sensing Lab
7701 Telegraph Road
Alexandria, VA 22315-3864
Tel: 703/355-2663
Fax: 703/355-3176

Harsanyi, Joseph C.
Applied Signal and Image Technology Company
9193 Rolling Meadow Run
Pasadena, MD 21122
Tel: 410/360-2546

Hattendorf, Donald W.
Geodynamics
21171 Western Avenue, #200
Torrance, CA 90501
Tel: 310/781-9535

Hatzopoulos, John N.
University of the Aegean
Department of Environmental Studies
17 Karadoni Street
Mytilene T.K. 81100, Greece
Tel: 30 251 21-286
Fax: 30 251 23-783

Hawkins, S. Roland
Lockheed Palo Alto Research Lab
3251 Hanover Street
Bldg 202, Org 97-80
Palo Alto, CA 94304
Tel: 415/424-2230
Fax: 415/354-5400

Hawtin, Jeanne
Science and Technology Corporation
101 Research Drive
Hampton, VA 23666
Tel: 804/865-7604
Fax: 804/865-8721

Henley, J. Ponder
US Army Topographic Engineering Center
RSL-SRD
7701 Telegraph Road
Alexandria, VA 22315-3864
Tel: 703/355-2643
Fax: 703/355-3176

Herrick, Robert Bruce
TRW, Inc.
One Space Park
M.S. 01/1220
Redondo Beach, CA 90278
Tel: 310/812-4851
Fax: 310/812-5160

Herring, Mark
Jet Propulsion Laboratory
4800 Oak Grove Drive
Mailstop 306-438
Pasadena, CA 91109
Tel: 818/354-6817
Fax: 818/393-4773

Holt, Donn
Center Imagery Office
8401 Old Courthouse Road, Suite 300
Vienna, VA 22182-3820
Tel: 703/285-5833
Fax: 703/285-5245

Honey, Frank R.
SpecTerra Systems Pty Ltd.
2 Leura Street
Nedlands 6009, Western Australia
Tel: 61 9 3862992
Fax: 61 9 3862635

Hoogenboom, Erin
Institute for Environmental Studies
Vrije Universiteit
De Boeleaan 1115
1081 HV Amsterdam, The Netherlands
Tel: 31 20-548 3827
Fax: 31 20-644 5056

Horton, Keith
University of Hawaii
Hawaii Institute of Geophysics and Planetology
2525 Correa Road
Honolulu, HI 96822
Tel: 808/956-3154
Fax: 808/956-6322

Huntington, Jonathan F.
C.S.I.R.O.
Division of Exploration and Mining
51 Defti Road
North Ryde, NSW, 2113, Australia
Tel: 61 2 887 8839
Fax: 61 2 887 8921

Husson, Nicole
Laboratoire de Meteorologie
Dynamique du CNRS
Ecole Polytechnique
91128 Palaiseau Cedex, France
Tel: 33-1 69 33 4802
Fax: 33-1 69 33 3005

I

Irvine, John M.
ERIM
1101 Wilson Boulevard, Suite 1100
Arlington, VA 22209-2248
Tel: 703/528-5250
Fax: 703/524-3527

J

Jansen, Wally T.
WTJ Software Services
809 Lawrence Road
San Mateo, CA 94401
Tel: 415/344-6771
Fax: 415/344-2491

Jenkins, Taunya B.
Praxis, Inc.
6080 Franconia Road
Alexandria, VA 22310
Tel: 202/767-6615
Fax: 202/767-1952

Jewett, Eric L.
Lockheed Palo Alto Research Lab
3251 Hanover Street
Palo Alto, CA 94304
Tel: 415/424-2084
Fax: 415/354-5820

Johnson, James R.
E-Systems Garland Division
P.O. Box 660023
Dallas, TX 75266-0023
Tel: 214/205-7613
Fax: 214/272-8144

Justen, James M.
ORD/CIA
Washington, DC 20505
Tel: 703/351-2540
Fax: 703/527-8357

K

Kanwar, Rameshwar S.
Iowa State University
Department of Agricultural
and Biosystems Engineering
219 Davidson Hall
Ames, IA 50011
Tel: 515/294-4913
Fax: 515/294-2552

Karch, Barry
WL/AARI-4
Bldg 22
2690 C. Street, Suite 1
WP AFB, OH 45433-7408
Tel: 513/255-5922
Fax: 513/255-6144

Kaufmann, Hermann
GeoForschungsCentrum
Telegraphenberg A 17
14473 Potsdam, Germany
Tel: 49-331 288-1150
Fax: 49-331 288-1111

Kelch, David J.
MTL Systems, Inc.
3481 Dayton-Xenia Road
Dayton, OH 45432-2796
Tel: 513/426-3111
Fax: 513/426-8301

Kershenstein, John C.
Naval Research Laboratory
Code 5620
Washington, DC 20375-5338
Tel: 202/767-9313
Fax: 202/404-7493

Kim, Eui-Hong
Systems Engineering Research Institute
Div. of Geo-Environmental Information System
1, Eoeun-dong
Yoosung-koo
TaeJun City 305-333, Korea
Tel: 82 042 869 1551
Fax: 82 042 869 1599

Kroll, James
AFOSR/NL
110 Duncan Avenue, Suite B 115
Bolling AFB, DC 20332-0001
Tel: 202/767-5021
Fax: 202/404-7475

Kruse, Fred A.
University of Colorado at Boulder
Center for the Study of Earth from Space
Campus Box 216
Boulder, CO 80309-0449
Tel: 303/492-6880
Fax: 303/492-5070

Krusinger, Alan E.
US Army Topographic Engineering Center
CETEC-TD-RS
7701 Telegraph Road
Alexandria, VA 22310-3864
Tel: 703/355-3138
Fax: 703/355-7566

L

LaBaw, Clayton
Jet Propulsion Laboratory
California Institute of Technology
MS 11 - 116
4800 Oak Grove Drive
Pasadena, CA 91109
Tel: 818/354-6248

LaPotin, Perry J.
US Army Corps of Engineers
Remote Sensing/GIS Center
72 Lyme Road
Hanover, NH 03755
Tel: 603/646-4408
Fax: 603/646-4750

Lange, James L.
ERIM
2900 Presidential Drive
Fairborn, OH 45324
Tel: 513/426-8299
Fax: 513/426-8989

Lapp, Henry S.
WL/AARI-4
Bldg 22
2690 C Street, Suite 1
WP AFB, OH 45433-7408
Tel: 513/255-5922
Fax: 513/255-6144

Lazofson, Laurence E.
Battelle
505 King Avenue
Columbus, OH 43201-2693
Tel: 614/424-7977
Fax: 614/424-3776

Leighty, Brian D.
Knowledge Sciences, Inc.
8995 Roswell Road, Suite 240
Atlanta, GA 30350
Tel: 404/587-3066
Fax: 404/587-3066

Leighty, Robert D.
Leighty and Associates, Inc.
604 Manor Drive
Vienna, VA 22180
Tel: 703/938-3476
Fax: 703/281-5264

Lemen, Charlotte M.
US Army Topographic Engineering Center
CETEC-ZA
Cude Building
7701 Telegraph Road
Alexandria, VA 22315-3864
Tel: 703/355-2600
Fax: 703/355-3154

Lepley, Larry
G.E.R., Inc.
7925-A N. Oracle Road, #389
Tucson, AZ 85704
Tel: 602/575-8082

Leslie, Daniel H.
W.J. Schafer Associates, Inc.
1901 N. Fort Myer Drive
Arlington, VA 22209
Tel: 703/588-7900
Fax: 703/525-2691

Light, Donald L.
US Geological Survey
MS 511 National Center
Reston, VA 22092
Tel: 703/648-5106
Fax: 703/648-4722

Lucas, James R.
National Geodetic Survey, NOAA
1315 East West Highway
Silver Spring, MD 20910
Tel: 301/713-2650
Fax: 301/713-4581

Lucey, Paul G.
University of Hawaii
Hawaii Institute of Geophysics and Planetology
2525 Correa Road
Honolulu, HI 96822
Tel: 808/956-3137
Fax: 808/956-6322

Lunetta, Ross
Environmental Protection Agency
Environmental Monitoring Systems Lab
Advanced Monitoring Systems Division
P.O. Box 93478
Las Vegas, NV 89193-3478
Tel: 702/798-2175
Fax: 702/798-2692

Lynch, David
The Aerospace Corp
P.O. Box 92957
Los Angeles, CA 90009
Tel: 310/336-6686
Fax: 310/336-1636

Lyon, Ronald J.P.
Stanford University
Applied Earth Sciences Department
Stanford, CA 94305-2115
Tel: 415/725-8077
Fax: 415/725-0979

M

Mah, Grant R.
Hughes STX Corp
EROS Data Center
Mundt Federal Bldg
Sioux Falls, SD 57198
Tel: 605/594-6165
Fax: 605/594-6589

Mandel, Betty
US Army Topographic Engineering Center
CETEC-ZC-A
7701 Telegraph Road
Alexandria, VA 22315-3864
Tel: 703/355-2789
Fax: 703/355-3176

Mason, Jr., Ralph A.
Director of Federal Programs
Earth Satellite Corporation
6011 Executive Boulevard, Suite 400
Rockville, MD 20852
Tel: 301/231-0660
Fax: 301/231-0520

Massie, Mark
Pacific Advanced Technology
1623 Mission Drive, Suite 3
Solvang, CA 93463
Tel: 805/688-2088
Fax: 805/686-2723

McClatchey, Robert A.
Phillips Laboratory/GPA
29 Randolph Road
Hanscom AFB, MA 01731-3010
Tel: 617/377-2975
Fax: 617/377-8892

McCoy, Robert P.
Naval Research Laboratory
Space Science Division
Code 7623
4555 Overlook Avenue, SW
Washington, DC 20375-5320
Tel: 202/767-6109
Fax: 202/404-8090

McDermott, Matthew H.
US Geological Survey
526 National Center
Reston, VA 22092
Tel: 703/648-4654
Fax: 703/648-4270

McKinn, Harlan L.
US Army Corps of Engineers
Remote Sensing/GIS Center
72 Lyme Road
Hanover, NH 03755-1290
Tel: 603/646-4479
Fax: 603/646-4750

McNeilly, John H.
SAIC/CVR
8500 Cinderbed Road
Newington, VA 22122
Tel: 703/550-3736
Fax: 703/550-1986

Mendenhall, Lawrence
Geodynamics Corp
21171 Western Avenue, Suite 100
Torrance, CA 90501
Tel: 310/781-9530
Fax: 310/781-9595

Meredith, Robert E.
OptiMetrics, Inc.
3115 Professional Drive
Ann Arbor, MI 48104-5131
Tel: 313/973-1177
Fax: 313/973-1199

Mertz, Frederick C.
Photon Research Associates, Inc.
10350 North Torrey Pines, Rd., Suite 300
La Jolla, CA 92037
Tel: 619/455-9741
Fax: 619/455-0658

Metzler, Michael D.
ERIM
P.O. Box 134001
Ann Arbor, MI 48113-4001
Tel: 313/994-1200
Fax: 313/994-0944

Molinelli, Eugene
Planning Systems Inc.
7923 Jones Branch Drive
McLean, VA 22102
Tel: 703/734-3400
Fax: 703/734-3456

Mooneyhan, Darden Wayne
Universities Space Research Association
300 D Street SW, Suite 801
Washington, DC 20024
Tel: 202/488-5137
Fax: 202/479-2613

Mooradian, Gregory
SETS Technology
300 Kaheiu Avenue, #10
Mililani, HI 96789
Tel: 808/625-5262
Fax: 808/625-2474

More, Keith A.
Daedalus Enterprises, Inc.
P.O. Box 1869
Ann Arbor, MI 48106
Tel: 313/769-5649
Fax: 313/769-0429

Mulawa, David
TRIFID
680 Craig Road, Suite 308
St. Louis, MO 63141
Tel: 314/991-3095
Fax: 314/991-4059

N

Narayanan, Ram M.
University of Nebraska
Department of Electrical Engineering
209 N Walter Scott Engineering Center
P.O. Box 880511
Lincoln, NE 68588-0511
Tel: 402/472-5141
Fax: 402/472-4732

Nelson, Dianne
US Army Corps of Engineers
Remote Sensing/GIS Center
72 Lyme Road
Hanover, NH 03755-1290
Tel: 603/646-4560
Fax: 603/646-4750

Nguyen, Duong
Geodynamics Corp
304 Inverness Way South, Suite 300
Englewood, CO 80112
Tel: 303/790-0101
Fax: 303/790-7816

Norris, Charles L.
Scripps Institution of Oceanography
Climate Research Division
9500 Gilman Drive, Dept 0224
La Jolla, CA 92093-0224
Tel: 619/534-7557
Fax: 619/534-8561

O

O'Sullivan, Kerry N.
CRA Exploration Pty Ltd.
P.O. Box 3709
Manuka, A.C.T. 2603, Australia
Tel: 61 6 239 6080
Fax: 61 6 295 2655

Ott, Henry H.
TRW, Inc.
One Federal Systems Park Drive
Fairfax, VA 22033
Tel: 703/803-4993
Fax: 703/803-498

P

Pascucci, Richard F.
Autometric, Inc.
5301 Shawnee Road
Alexandria, VA 22312-2333
Tel: 703/658-4115
Fax: 703/658-4021

Peltzer, Gerard
The Aerospace Corp
2350 E. El Segundo Boulevard
El Segundo, CA 90245
Tel: 310/336-1432
Fax: 310/336-1474

Pertica, Alexander J.
Lawrence Livermore National Laboratory
P.O. Box 808, L-407
Livermore, CA 94550
Tel: 510/423-3354
Fax: 510-422-2499

Phelps, Kirkman
CBDCOM
SCBRD-RTE
APG, MD 21010
Tel: 410/671-2675
Fax: 410/671-2649

Phillipson, Warren R.
DOD
6709 Woodstream Drive
Lanham, MD 20706
Tel: 703/351-2136
Fax: 703/527-6139

Porter, Joel
Martin Marietta Astronautics
M/S DC4001
P.O. Box 171
Denver, CO 80201
Tel: 303/977-3233
Fax: 303/971-9827

R

Ramsey III, Elijah W.
National Wetlands Research Center
National Biological Survey
700 Cajundome Boulevard
Lafayette, LA 70506
Tel: 318/266-8575
Fax: 318/266-8513

Rasson, Jean Paul
F.U.N.D.P. University
Laboratory GEOSATEL
Faculte des Sciences
61, rue de Bruxelles
B5000 Namur, Belgium
Tel: 33.81.72.4928
Fax: 33.81.72.4914

Ray, Terrill W.
California Institute of Technology
Division of Geological and Planetary Science
1201 E. California
Mail Code 170-25
Pasadena, CA 91125
Tel: 818/395-3801
Fax: 818/585-1912

Resmini, Ronald G.
SETS Technology, Inc.
300 Kahelu Avenue, #10
Mililani, HI 96789-3911
Tel: 808/625-5262
Fax: 808/625-2474

Richard, Stephen P.
Lockheed Palo Alto Research Lab
3251 Hanover Street
Palo Alto, CA 94304
Tel: 415/424-3189
Fax: 415/354-5820

Richards, John
University College
Department of Electrical Engineering
The University of New South Wales
Australian Defence Force Academy
Campbell ACT 2600, Australia
Tel: 06 268 8592
Fax: 06 268 8443

Rickard, Lee J.
Naval Research Laboratory
Code 7210
4555 Overlook Avenue, SW
Washington, DC 20375-5351
Tel: 202/404-7877
Fax: 202/404-8894

Riehl, Jr., Ken
ITEK Optical Systems
10 Maguire Road
Lexington, MA 02173-3199
Tel: 617/276-2221
Fax: 617/276-3306

Rinker, Betty L.
6911 Andover Drive
Alexandria, VA 22307

Rinker, Jack N.
US Army Topographic Engineering Center
CETEC-SS
Cude Building (#2592)
7701 Telegraph Road
Alexandria, VA 22315-3864
Tel: 703/355-2867
Fax: 703/355-3176

Rubin, Tod D.
Geophysical and Environmental
Research Corporation
One Bennett Common
Millbrook, NY 12545
Tel: 914/677-6100
Fax: 914/677-6106

S

Salazar, Ronald
Jet Propulsion Laboratory
M/S 300-331
4800 Oak Grove Drive
Pasadena, CA 91109
Tel: 818/354-6173
Fax: 818/393-0046

Savage, Wayne
The Scientex Corporation
1655 N. Ft. Myer Drive, Suite 400
Arlington, VA 22209
Tel: 703/276-3377
Fax: 703/276-0996

Scantland, Sylvie
Radarsat International
275 rue Slater, Suite 1203
Ottawa, Ontario, Canada K1P 5H9

Schaum, Alan P.
Naval Research Laboratory
Code 5620
4555 Overlook Avenue
Washington, DC 20375-5320
Tel: 202/767-9366
Fax: 202/404-7493

Schwarz, Georg F.
Institut fur Geophysik
ETH-Honggerberg
CH 8093 Zurich, Switzerland
Tel: 41 1 633 3398
Fax: 41 1 371 2556

Scroggin, James
Science Applications International Corporation
1820 N. Ft Myer
Rosslyn, VA 22209
Tel: 703/351-2708
Fax: 703/527-8357

Sheikho, Kamel M.
Saudi Center for Remote Sensing
P.O. Box 6086
Riyadh 11442, Saudi Arabia
Tel: 966 1 48143544
Fax: 966 1 47842379

Shettigara, Vittala K.
Defense Science and Technical Organization
Electronics Research Laboratory
P.O. Box 1500
Building 79 Labs
Salisbury, SA 5082, Australia
Tel: 61 8 259 7176
Fax: 61 8 259 5619

Silvergate, Peter
Hughes Danbury Optical Systems
100 Wooster Heights Road
Danbury, CT 06810-7589
Tel: 203/797-5566
Fax: 203/797-6259

Simental, Edmundo
US Army Topographic Engineering Center
7701 Telegraph Road
Alexandria, VA 22315-3864
Tel: 703/355-3311
Fax: 703/355-3176

Simmonds, J. Jeff
Jet Propulsion Laboratory
California Institute of Technology
Mail Stop 306-438
4800 Oak Grove Drive
Pasadena, CA 91109
Tel: 818/354-4187
Fax: 818/393-4773

Smart, Robert V.,
US Department of Commerce
NOAA - R/AA
1315 East-West Highway
Rm 11508
Silver Spring, MD 20910-3282
Tel: 301/713-2458
Fax: 301/713-0666

Smiley, Vern N.
NCCOSC RDTE Div 804
53570 Silvergate Avenue, Rm 2070
San Diego, CA 92152-5070
Tel: 619/553-6128
Fax: 619/553-6121

Snapp, Michael
The Aerospace Corporation
13873 Park Center Road, Suite 187
Herndon, VA 22071
Tel: 703/318-5441
Fax: 703/318-5446

Spyak, Paul R.
University of Arizona
Optical Sciences Center
Tucson, AZ 85721
Tel: 602/621-5042
Fax: 602/621-8292

Staenz, Karl
Canada Centre for Remote Sensing
Scene Physics and Analysis Section
Major Projects Office
588 Booth Street, 4th Floor
Ottawa, Ontario, Canada K1A 0Y7
Tel: 613/947-1250
Fax: 613/947-1383

Stoner, William W.
Science Applications International Corporation
6 Fortune Drive
Billerica, MA 01821
Tel: 508/667-6365
Fax: 508/667-8042

Sunshine, Jessica M.
SETS Technology, Inc.
4 Park Street
Brookline, MA 02146
Tel: 617/739-2037
Fax: 617/739-1153

Syrén, Per
Stockholm University
Laboratory of Remote Sensing
Department of Physical Geography
Sandasgatan 2, 10691 Stockholm, Sweden
Tel: 46 8 164799
Fax: 46 8 164810

T

Theisen, Arnold
University of New Hampshire
Complex Systems Research Center
Institute for the Study of Earth, Oceans, and Space
Morse Hall
Durham, NH 03824
Tel: 603/862-1813
Fax: 603/862-0188

Thunen, John G.
Santa Barbara Research Center
75 Coromar Drive
Goleta, CA 93117
Tel: 805/562-7108
Fax: 805/562-7149

Toborg, Scott
Microelectronics and Computer
Technology Corporation
3500 West Dalcones Center
Austin, TX 78759
Tel: 512/338-3208
Fax: 512/338-3838

Tolar, Billy
US Geological Survey
526 National Center
Reston, VA 22092
Tel: 703/648-5660
Fax: 703/648-5660

Toles, Marvin
Hughes Danbury
P.O. Box 2471
El Segundo, CA 90245
Tel: 310/616-4200
Fax: 310/616-4206

Toulios, Leonidas G.
National Agricultural Research Foundation
(N.A.G.R.E.F.)
Institute of Soil Classification and Mapping
1, Theofrastou Str.
41335 Larissa, Greece
Tel: 30 41 660590
Fax: 30 41 232827

Try, Paul D.
Science and Technology Corporation/GEWEX
409 Third Street, SW, Suite 203
Washington, DC 20024
Tel: 202/863-0012

V

Vassiliev, Oleg B.
South Dakota School of Mines and Technology
Institute of Atmospheric Sciences
501 E. St. Joseph Street
Rapid City, SD 57701-3995
Tel: 605/394-2291
Fax: 605/394-6061

W

Walter, Fred
SCIENTIFICO
Scientific Components Company
35985 Row River Road
Cottage Grove, OR 97424
Tel: 503/942-3611
Fax: 503/942-0110

Westmoreland, Sally
San Diego State University
Photon Research Associates, Inc.
10350 North Torrey Pines Road, Suite 300
La Jolla, CA 92037
Tel: 619/455-9741
Fax: 619/455-0658

Weston, Neil D.
NOAA
1315 East-West Highway
SSMC3, N/CG1, 9535
Silver Spring, MD 20910
Tel: 301/713-3235
Fax: 301/713-4175

Wever, G. Pete
Earth Search Sciences
502 N. 3rd Street, #8
McCall, ID 83638
Tel: 208/634-7080
Fax: 208/634-2978

Williams, Timothy J.
University of Hawaii
Hawaii Institute of Geophysics and Planetology
2525 Correa Road
Honolulu, HI 96822
Tel: 808/956-3144
Fax: 808/956-6322

Winterberger, Walter J.
Sverdrup Technology, Inc.
Bldg 260
P.O. Box 1935
Eglin AFB, FL 32542
Tel: 904/729-6359
Fax: 904/729-6377

Zywicki, Randall W.
Daedalus Enterprises, Inc.
Environmental Remote Sensing Technology
P.O. Box 1869
Ann Arbor, MI 48106
Tel: 313/769-5649
Fax: 313/769-0429

Wolf, Emil
University of Rochester
Department of Physics and Astronomy
River Campus Station
Rochester, NY 14627
Tel: 716/275-4397
Fax: 716/473-0687

Woody, Loren M.
Santa Barbara Research Center
75 Coromar Drive
Goleta, CA 93117
Tel: 805/562-7299
Fax: 805/562-7149

Wu, Risa
Sverdrup Technology, Inc.
Bldg 1210
Stennis Space Center, MS 39529
Tel: 601/688-2018
Fax: 601/688-3838

Y

Yingst, Harvey A.
Department of the Army, CECOM
Night Vision and Electronic Sensor Directorate
AMSEL-RD-NV-VISPD-CR
10220 Burbeck Road, Suite 430
Fort Belvoir, VA 22060-5606
Tel: 703/704-2595
Fax: 703/704-2586

Z

Zamudio, Joe
EG&G Energy Measurements
P.O. Box 1912, RSL-19
Las Vegas, NV 89125
Tel: 702/295-8811
Fax: 702/295-8628

Zedar, Nancy
DIA/CEM
3100 Clarendon Boulevard
Arlington, VA 22201-5300
Tel: 703/284-0130
Fax: 703/284-1157

END

DATE FILMED

07 / 15 / 95